International Journal of
Molecular Sciences

Special Issue Reprint

Neurodegenerative Disease

From Molecular Basis to Therapy

Edited by
Claudia Ricci

mdpi.com/journal/ijms

MDPI

Neurodegenerative Disease: From Molecular Basis to Therapy

Neurodegenerative Disease: From Molecular Basis to Therapy

Editor

Claudia Ricci

MDPI

Basel • Beijing • Wuhan • Barcelona • Belgrade • Novi Sad • Cluj • Manchester

Editor
Claudia Ricci
Medical, Surgical and Neurological Sciences
University of Siena
Siena
Italy

Editorial Office
MDPI
St. Alban-Anlage 66
4052 Basel, Switzerland

This is a reprint of articles from the Special Issue published online in the open access journal *International Journal of Molecular Sciences* (ISSN 1422-0067) (available at: www.mdpi.com/journal/ijms/special_issues/9595J0151X).

For citation purposes, cite each article independently as indicated on the article page online and as indicated below:

Lastname, A.A.; Lastname, B.B. Article Title. *Journal Name* **Year**, *Volume Number*, Page Range.

ISBN 978-3-7258-0188-6 (Hbk)
ISBN 978-3-7258-0187-9 (PDF)
doi.org/10.3390/books978-3-7258-0187-9

Contents

About the Editor

Claudia Ricci

Claudia Ricci is Research Scientist at the Neurogenetics Laboratory of the Department of Medical, Surgical and Neurological Sciences of the University of Siena. After a PhD in Biotechnology, she extended her interest to the genetics of cerebral vascular malformations and motor neuron diseases, particularly amyotrophic lateral sclerosis, and increased her expertise in the up-to-date techniques of genetic screening and biomarker research. She also deepened her skills in statistical analysis and bioinformatics tools. She collaborates with the Italian Consortium for the study of genetics in ALS (ITALSGEN) and the Italy-Usa Network and participates in wide studies on the genetic basis of ALS, leading to the identification of several genes related to this disease, including C9orf72, TARDBP, and FUS. Her publication list includes approximately 60 papers in peer-review journals (ORCID 0000-0002-2431-0308). Since 2021, she has been member of the Scientific Committee of the Master's degree programmes "Regulatory Medical Writer" and "Science popularization" of the University of Siena.

Preface

Neurodegenerative diseases are a heterogeneous, largely age-related group of disorders, characterised by the progressive degeneration or death of neurons in the central or peripheral nervous system. The prevalence of these diseases is increasing, in part due to the ageing of the population, with a consequent growing economic burden on healthcare systems. Although, in some cases, these diseases can be managed with treatments, current therapies are mostly symptomatic, do not address the underlying cause of the disease and have little or no effect on disease progression.

Recent advances in neurobiology and neurogenetics provide valuable insights into the pathogenesis of neurodegenerative diseases. This paved the way for the development of molecularly targeted therapies capable of halting or slowing the fundamental pathological processes that cause neuronal damage and consequent cognitive and motor dysfunction. In some cases, neurodegenerative diseases are caused by genetic variants and/or the dysregulation of cellular pathways. Some mechanisms common to several neurodegenerative diseases were identified, such as the presence of misfolded protein aggregates and abnormal protein accumulation, but the molecular mechanisms of neurodegenerative diseases are complex and diverse and may differ between diseases. As progress is made in understanding critical aspects of the underlying molecular pathophysiology, therapeutic strategies continue to evolve.

This Special Issue aims to provide an up-to-date overview of the progress made in research into neurodegenerative diseases, from understanding the molecular basis, to establishing more effective diagnostic tools, to developing new therapies. Some papers focus on Alzheimer's disease, Parkinson's disease, motor neuron disease and Huntington's disease. Others address more general aspects of neurodegeneration, ranging from the common mechanisms of cellular damage to the role of dietary effects on the nervous system.

Overall, this Special Issue highlights the continuing efforts of the scientific community to unravel the pathophysiological mechanisms responsible for neurodegeneration and to identify potential treatments for neurodegenerative diseases. The aim of this research is to understand the molecular bases of disease onset and progression, to achieve earlier diagnosis, to identify novel therapeutic targets and ultimately to develop more effective therapies to counteract the progression of these still fatal diseases.

Claudia Ricci
Editor

International Journal of
Molecular Sciences

MDPI

Editorial

Neurodegenerative Disease: From Molecular Basis to Therapy

Claudia Ricci

Department of Medical, Surgical and Neurological Sciences, University of Siena, 53100 Siena, Italy; claudia.ricci@unisi.it

Neurodegenerative diseases are a heterogeneous group of age-related disorders characterised by the progressive degeneration or death of neurons in the central or peripheral nervous system. The prevalence of these diseases is increasing—in part due to the ageing population—and the economic burden on healthcare systems is growing as a result. Although in some cases these diseases can be managed with treatments, current therapies are mostly symptomatic, do not address the underlying cause of the disease and have very little effect on disease progression. Recent advances in neurobiology and neurogenetics have provided valuable insights into the pathogenesis of neurodegenerative diseases. Genetic, environmental and lifestyle factors contribute to neurodegenerative diseases. Common underlying processes contribute to the degeneration of neurons, but the molecular mechanisms of neurodegenerative diseases are complex and diverse and may differ between conditions. As progress is made in understanding critical aspects of the underlying molecular pathophysiology, therapeutic strategies are evolving and new treatments are being evaluated.

Several papers in this Special Issue focus on Alzheimer's disease (AD), the most common cause of dementia, characterised by memory loss, behavioural disturbances and impaired judgment [1]. The presence of senile plaques, characterised by the aggregation of amyloid beta (Aβ), and the formation of neuronal neurofibrillary tangles (NFTs) are well-known neuropathological hallmarks of AD [2]. Symptoms of AD generally begin with mild memory impairment and progress to various degrees of severe cognitive impairment, including memory loss and difficulty with complex activities of daily living [3,4]. These pre-dementia stages could play a key role in preventive interventions: the development of early and accessible diagnostic methods could help to prevent or delay the progression of cognitive deficits and the onset of AD dementia [5,6].

In this respect, Hunjong Na and colleagues [7] developed the QPLEX™ kit for the early clinical diagnosis of Alzheimer's disease. This kit simultaneously detects amyloid-β1-40, galectin-3 binding protein, angiotensin-converting enzyme and periostin in a few microlitres of peripheral blood and uses an optimised algorithm to screen for AD by correlating with cerebral amyloid deposition. The authors evaluated cognitively normal subjects and patients with subjective cognitive decline, mild cognitive impairment and AD, and showed that the QPLEX™ algorithm values could be used to distinguish the clinical continuum of AD or cognitive function. The QPLEX™ kit could be a valuable tool for health screening and early clinical diagnosis of Alzheimer's disease, as blood-based diagnosis is more accessible, convenient and cost- and time-effective than diagnosis based on cerebral spinal fluid or positron emission tomography.

Another important aspect of dementia research is the development of new therapeutic approaches aimed at curing the disease or alleviating its symptoms. In their research, Nicole E. Eassa and colleagues [8] focused on one of the most common comorbidities associated with Alzheimer's disease, comorbid psychosis, which affects half of all AD patients [9]. Since it is not possible to treat elderly patients with antipsychotics due to an increased risk of premature death, there is a clear need for novel therapeutic options for AD patients with comorbid psychosis. The authors used a viral-mediated approach to express mutated human genes known to contribute to Alzheimer's pathology in a rat

Citation: Ricci, C. Neurodegenerative Disease: From Molecular Basis to Therapy. *Int. J. Mol. Sci.* **2024**, *25*, 967. https://doi.org/10.3390/ijms25020967

Received: 8 January 2024
Accepted: 10 January 2024
Published: 12 January 2024

model. The authors observed a significant increase in dopamine neuron population activity and behavioural deficits in rodent models of psychosis-like symptomatology. Furthermore, systemic administration of an α5-GABAA receptor-selective positive allosteric modulator was able to reverse the aberrant function of the dopaminergic system in AD-AAV rats. This study provides interesting insights for the development of drugs targeting α5-GABAA receptors for patients with Alzheimer's disease and comorbid psychosis.

Hoau-Yan Wang and colleagues [10] investigated the molecular mechanisms of simufilam, a novel oral drug candidate in phase 3 clinical trials for Alzheimer's dementia. Simufilam is a small molecule that binds an altered form of filamin A (FLNA) found in AD. This binding disrupts FLNA's aberrant binding to the α7 nicotinic acetylcholine receptor (α7nAChR), thereby blocking soluble amyloid beta1-42 (Aβ42) signalling via α7nAChR, which hyperphosphorylates tau. The authors showed that simufilam reduces Aβ42 binding to α7nAChR. They also showed that FLNA binds to several inflammatory receptors in addition to Toll-like receptor 4 (TLR4) in postmortem human AD brains and in AD transgenic mice. These aberrant FLNA connections were disrupted by simufilam. Simufilam also reduced inflammatory cytokine release from Aβ42-stimulated human astrocytes. Taken together, these data suggest that simufilam may promote brain health by disrupting abnormal FLNA receptor interactions that are critical for AD pathogenic pathways.

Two reviews summarise the state of the art in understanding the molecular mechanisms responsible for the development of AD and consequently identifying novel drug targets. In their manuscript, Botond Penke and colleagues [11] accurately describe the pathogenesis of AD, its genetic background and the physiological and pathophysiological roles of the Aβ and Tau proteins. They also discuss the various hypotheses that have been proposed to explain AD neurodegeneration. In the second part of the paper, they summarise conventional and novel targets for preventing and/or slowing the progression of AD. The authors conclude that it is not possible to treat all stages of AD with a single drug. A drug combination strategy with multiple molecular targets (amyloid aggregation, clearance, heat shock proteins, autophagy induction, inflammasomes, etc.) should be considered.

The paper by Kseniia Orobets and Andrey Karamyshev [12] reviews the current knowledge on amyloid precursors and Alzheimer's disease. Amyloid precursor protein (APP) is a membrane protein that is thought to play a major role in the pathology of AD. APP is known to follow a non-amyloidogenic pathway under physiological conditions; however, it can progress to an amyloidogenic scenario, leading to the formation of extracellular deleterious Aβ plaques. The authors summarise the biogenesis, processing and mechanisms of action of APP. They conclude that despite decades of research on Alzheimer's disease and APP, not all steps of APP biogenesis have been elucidated and that many questions about APP biogenesis, especially the early steps, interacting partners, the role of APP in microtubules and the potential therapeutic targets, need to be addressed in future studies.

Finally, in their Perspectives paper, Vladimir Volloch and Sophia Rits-Volloch [13] have comprehensively reviewed the molecular basis and potential effective therapies of the Amyloid Cascade Hypothesis 2.0 (ACH2.0) for Alzheimer's disease and age-related cognitive decline (AACD). ACH2.0 is a recently proposed theory of Alzheimer's disease. Its name refers to its predecessor, ACH, although the similarity between the two theories is limited to the recognition of the centrality of amyloid-beta (Aβ) in the disease. In ACH, the disease is caused by secreted extracellular Aβ, while in ACH2.0, it is triggered by Aβ protein precursor (AβPP)-derived intraneuronal Aβ (iAβ) and driven by iAβ generated independently of AβPP. ACH2.0 considers AD as a two-stage disease. In the first, asymptomatic stage, there is a decades-long accumulation of AβPP-derived iAβ via internalisation of secreted Aβ and intracellular retention of a fraction of Aβ produced by AβPP proteolysis. When AβPP-derived iAβ reaches critical levels, it activates a self-sustaining AβPP-independent production of iAβ that drives the second, devastating stage of AD, involving tau pathology and culminating in neuronal loss. The authors analyse the dynamics of iAβ accumulation in health and disease and identify it as a major driver of both

AD and age-related cognitive decline. They discuss the mechanisms potentially involved in the AβPP-independent generation of iAβ and provide mechanistic interpretations for all major aspects of AD and AACD. They conclude that drugs that affect the accumulation of AβPP-derived iAβ may only have a protective effect on AD, whereas targeted degradation of iAβ is the best therapeutic strategy for both prevention and effective treatment of AD and AACD.

Another substantial part of this Special Issue is dedicated to Parkinson's disease (PD). PD is the second most fatal neurodegenerative disorder, identified by neuronal degeneration in the substantia nigra pars and intracellular deposition of Lewy bodies [14]. There is still no clear understanding of the aetiology of Parkinson's disease, and existing treatments only provide effective control of symptoms, without stopping the disease from progressing. Therefore, there is a great need for therapeutic strategies to reduce neuronal death.

One of the possible strategies is to reduce the level of accumulated alpha-synuclein (SNCA) in neurons. Autophagy is the main cellular process for removing toxic protein aggregates responsible for neurodegenerative diseases. It is a complex process involving dozens of proteins [15]. Ibrar Siddique and colleagues [16] have identified a novel regulator (ARL6IP5) of neuronal autophagy whose levels decrease in the brain with age and in Parkinson's disease. Overexpression of ARL6IP5 reduces α-synuclein aggregation and improves cell survival in a mouse model of PD. Interestingly, they showed that ARL6IP5 is an autophagy inducer that enhances autophagosome initiation and elongation. In addition, they showed for the first time that α-synuclein downregulates ARL6IP5, thereby inhibiting autophagy-dependent clearance of toxic aggregates and exacerbating neurodegeneration. Taken together, these results suggest the potential of ARL6IP5 as a target for diseases in which autophagy is deregulated.

In their study, Prachayaporn Prasertsuksri and colleagues [17] have shown that andrographolide (andro) has significant neuroprotective effects against 1-methyl-4-phenylpyridinium (MPP+), a neurotoxin that can cause loss of dopaminergic neurons, in SH-SY5Y cells. Andro reduces cell death by increasing mitophagy and autophagic clearance of alpha-synuclein and by increasing the antioxidant capacity. These results provide evidence that andro could be considered as a potential supplement for the prevention of Parkinson's disease.

SH-SY5Y cells were also used as a model of dopaminergic neurons in the study by Wei Zheng and colleagues [18]. U251 cells were used as a model for astrocytes. The study was designed to investigate the role of leukocyte common antigen-related protein tyrosine phosphatase (LAR) in Parkinson's disease. LAR knockout showed a protective effect in astrocytic cells, reducing cell death and restoring an appropriate cell morphology. The basis of this effect was an enhanced neuroprotective capacity due to the activation of IGF-1R and Akt and the consequent reduction in the Bax/Bcl-2 ratio and suppression of apoptosis. Akt also drove the upregulation of NRF2 and HO-1, resulting in the suppression of ROS production, the preservation of mitochondrial function and increased GDNF production. Higher levels of astrocytic viability and GDNF production also contributed to the increased viability of co-cultured SH-SY5Y neuronal cells in a PD model system. Taken together, these findings suggest that inhibition of LAR may modulate astrocyte viability and function and may provide a novel therapeutic strategy for PD.

Finally, Thomas Stojsavljevic and colleagues [19] focused on another type of therapeutic approach to PD, deep brain stimulation (DBS), which consists of surgically implanting an electrode in the subthalamic nucleus (STN) to send electrical impulses to the targeted regions of the brain. Since the conventional high-frequency (HF) stimulation currently used as standard has several drawbacks, the authors carried out a computational study to overcome the limitations of HF stimulation. The authors stimulated the STN in an adaptive manner, using the interspike time of the neurons to control the stimulation. This protocol eliminated bursts in the synchronised bursting neuronal activity of the STN, which can cause thalamocortical (TC) neurons to fail to respond properly to excitatory cortical

inputs. It also significantly reduced TC relay errors, showing promise for future Parkinson's disease therapeutics.

Among neurodegenerative diseases, amyotrophic lateral sclerosis (ALS) is a rapidly progressive and fatal disorder characterised by progressive degeneration of upper and lower motor neurons in the cerebral cortex, brainstem and spinal cord. The pathophysiological process underlying ALS neurodegeneration is multifactorial and still not fully understood, although dysfunctions in several cellular and molecular processes have been reported, including impaired protein homeostasis, mitochondrial alterations, aberrant RNA metabolism, neuroinflammation, excitotoxicity and oxidative stress [20]. Several studies have implicated aberrant regulation of PKC-mediated signalling pathways in ALS through alterations in either the expression or activity state of several members of the PKC superfamily [21,22]. Valentina La Cognata and colleagues [23] analysed the distribution and cellular localisation of the ε-isozyme of protein kinase C (PKCε), a novel isoform of PKC that represents an attractive target for the treatment of several conditions, including neurodegenerative diseases. In human postmortem motor cortex samples, they found a significant decrease in both PKCε mRNA and protein immunoreactivity in a subset of sporadic ALS patients (ALS-GLIA, defined by an increased expression of genes that mark astrocytes and oligodendrocytes [24]). In addition, NSC-34 cells carrying the human G93A SOD1 mutant exhibited a significant reduction in the phosphoPKCε/panPKCε ratio compared to WT cells. Furthermore, a short pulse activation of PKCε by its agonist Bry-ostatin-1 produced a long-term neuroprotective effect in degenerating G93A SOD1 cells. Taken together, these data support the involvement of PKCε in the ALS pathophysiology and suggest its pharmacological modulation as a potential neuroprotective strategy, at least in a subset of sporadic ALS patients.

Cássia Arruda de Souza Pereira and colleagues [25] focused on Huntington's disease (HD), a progressive neurodegenerative disorder characterised by motor changes, progressive cognitive loss and psychiatric disorders. HD is caused by a mutation in the gene encoding huntingtin (Htt), which results in an expansion of the CAG trinucleotide, leading to abnormal long repeats of polyglutamine (poly-Q) in the N-terminal region of huntingtin which form abnormal conformations and aggregates. HD is also associated with deregulation of calcium (Ca2+) signalling and homeostasis [26,27]. Intracellular Ca2+ is stored in lysosomes, organelles involved in endo-cytic and lysosomal degradation processes, including autophagy [28]. Nicotinic acid adenine dinucleotide phosphate (NAADP) is an intracellular second messenger that promotes Ca2+ release from the endo-lysosomal system via activation of two-pore channels (TPCs) [29]. The authors have shown that in murine astrocytes overexpressing mHtt-Q74, mHtt-Q74 colocalises with the TPC2 receptor in lysosomes, thereby interfering with the physiological function of this channel and inducing Ca2+ re-release from these organelles. Increased Ca2+ levels from the lysosome in turn promote mHtt-Q74 aggregation. Furthermore, autophagy is inhibited in astrocytes overexpressing mHtt-Q74. These results support the hypothesis that lysosomal homeostasis is important in inhibiting mHtt aggregation and highlight the role of autophagy in neuroprotection.

In their concept paper, Dieu Thao Nguyen and colleagues [30] address the issue of obstetric neuropathy in diabetic patients. They propose a "two-hit" model to explain the effects of diabetes on mothers who are already in a putative subclinical state of damage and then experience neuronal damage during childbirth. Pregnant women with diabetes have a damaged nervous system, although the condition may be subclinical: this is the "first hit". The process of childbirth can cause damage to the mother's nervous system during delivery, which is the "second hit". The authors describe the different pathological processes responsible for worsening neuropathy in diabetes mellitus and highlight the risk of obstetric neuropathy.

Two reviews examine the role of appropriate micronutrient supplementation on the nervous system. Zhengyang Quan and colleagues [31] describe the effect of a balanced intake of macro-, micro- and trace elements to improve and/or reduce the risk of depression.

They discuss the effects of glucose, fatty acids, amino acids and mineral elements such as lithium, zinc, magnesium, copper, iron and selenium. These elements exacerbate or alleviate depression by regulating a range of physiological processes, including neural signal transmission, inflammation, oxidative stress, neurogenesis and synaptic plasticity. The paper also looks at the balance of these nutrients in the body, describing the effects of both nutritional deficiencies and episodes of depression.

In their review, Bianca Caroline da Cunha Germano and colleagues [32] summarise the scientific evidence on the effects of vitamin E supplementation on neuroprotection and neurodegeneration in experimental models. Vitamin E supplementation significantly improves memory, cognition, learning, motor function and brain markers associated with neuroregeneration and neuroprotection. It also reduces beta-amyloid (Aβ) deposition and toxicity in experimental models of Alzheimer's disease. Furthermore, it reduces tau protein hyperphosphorylation and increases the levels of superoxide dismutase and brain-derived neurotrophic factor (BDNF) in rodents. For these reasons, the use of vitamin E could prevent and/or delay the progression of degenerative lesions in the central nervous system.

Finally, three papers address the general mechanisms involved in neurodegeneration. In their original article, Paul A. Hyslop and colleagues [33] discussed the origin of elevated S-glutathionylated GAPDH in chronic neurodegenerative diseases. Using biochemical and in silico molecular dynamics simulations, their study elucidates which factors may contribute to the persistence of S-glutathionylated GAPDH in different pathophysiological conditions. The results of the research provide a molecular rationale for how oxidative stress elevates S-glutathionylated GAPDH in neurodegenerative diseases and suggest novel targets for therapeutic intervention.

Alexander Pilski and Steven M. Graves [34] focused on the effects of repeated methamphetamine (meth) administration on substantia nigra pars compacta (SN) and locus coeruleus (LC) neurons in a mouse model. They observed that repeated meth exposure produced SN and LC axonal deficits prior to somatic loss in males, consistent with a dying-back pattern of degeneration, whereas female mice were resistant to chronic meth-induced degeneration. Interestingly, the pattern of degeneration observed in male mice and the sex difference paralleled in Parkinson's disease [35] and patients with a history of meth abuse have been reported to lead to an increased risk of developing Parkinson's disease [36]. In addition, exposure to meth also increases the risk of Alzheimer's disease, as LC degeneration has been linked to pathogeneses associated with this disease [37]. Taken together, these findings suggest that the adverse effects of meth abuse may extend beyond neurotoxicity and represent a potential risk for the development of neurodegenerative diseases. This risk may be restricted to males, as female mice were resistant to meth-induced neurodegeneration.

Finally, the review by Jun-Hao Wen and colleagues [38] recapitulates the main aspects of a topic strictly related to neurodegeneration: cellular protein aggregation. They reviewed the composition and causes of protein aggregation in mammalian cells and summarised the damage caused by protein aggregates, describing how these aggregates affect various cellular functions. They have also highlighted some of the clearance mechanisms involved in removing the aggregates and discussed potential therapeutic strategies targeting protein aggregates in the treatment of ageing and age-related neurodegenerative diseases. Considering that the achievement of this goal requires a more comprehensive understanding of the organisation and relationship between protein homeostasis and protein aggregation, the authors conclude that further studies will be fundamental to follow this path.

In conclusion, this Special Issue highlights the continuing efforts of the scientific community to unravel the pathophysiological mechanisms responsible for neurodegeneration and to identify potential treatments for neurodegenerative diseases. The aim of this research is to understand the molecular basis of disease onset and progression, to obtain an earlier diagnosis, to identify novel therapeutic targets and ultimately to develop more effective therapies to counteract the progression of these still fatal diseases.

Conflicts of Interest: The author declares no conflicts of interest.

References

1. Knopman, D.S.; Amieva, H.; Petersen, R.C.; Chételat, G.; Holtzman, D.M.; Hyman, B.T.; Nixon, R.A.; Jones, D.T. Alzheimer Disease. *Nat. Rev. Dis. Primers* **2021**, *7*, 33. [CrossRef] [PubMed]
2. Zhang, L.; Xia, Y.; Gui, Y. Neuronal ApoE4 in Alzheimer's disease and potential therapeutic targets. *Front. Aging Neurosci.* **2023**, *15*, 1199434. [CrossRef]
3. Kukull, W.A.; Bowen, J.D. Dementia Epidemiology. *Med. Clin. N. Am.* **2002**, *86*, 573–590. [CrossRef]
4. Mantzavinos, V.; Alexiou, A. Biomarkers for Alzheimer's Disease Diagnosis. *Curr. Alzheimer Res.* **2017**, *14*, 1149–1154. [CrossRef] [PubMed]
5. Uzuegbunam, B.C.; Librizzi, D.; Hooshyar Yousefi, B. PET Radiopharmaceuticals for Alzheimer's Disease and Parkinson's Disease Diagnosis, the Current and Future Landscape. *Molecules* **2020**, *25*, 977. [CrossRef] [PubMed]
6. Park, J.-C.; Jung, K.S.; Kim, J.; Jang, J.S.; Kwon, S.; Byun, M.S.; Yi, D.; Byeon, G.; Jung, G.; Kim, Y.K.; et al. Performance of the QPLEX^{TM} Alz plus Assay, a Novel Multiplex Kit for Screening Cerebral Amyloid Deposition. *Alzheimer's Res. Ther.* **2021**, *13*, 12. [CrossRef]
7. Na, H.; Shin, K.Y.; Lee, D.; Yoon, C.; Han, S.-H.; Park, J.-C.; Mook-Jung, I.; Jang, J.; Kwon, S. The QPLEX^{TM} Plus Assay Kit for the Early Clinical Diagnosis of Alzheimer's Disease. *Int. J. Mol. Sci.* **2023**, *24*, 11119. [CrossRef]
8. Eassa, N.E.; Perez, S.M.; Boley, A.M.; Elam, H.B.; Sharmin, D.; Cook, J.M.; Lodge, D.J. A5-GABAA Receptor Modulation Reverses Behavioral and Neurophysiological Correlates of Psychosis in Rats with Ventral Hippocampal Alzheimer's Disease-like Pathology. *Int. J. Mol. Sci.* **2023**, *24*, 11788. [CrossRef]
9. Drevets, W.C.; Rubin, E.H. Psychotic Symptoms and the Longitudinal Course of Senile Dementia of the Alzheimer Type. *Biol. Psychiatry* **1989**, *25*, 39–48. [CrossRef]
10. Wang, H.-Y.; Cecon, E.; Dam, J.; Pei, Z.; Jockers, R.; Burns, L.H. Simufilam Reverses Aberrant Receptor Interactions of Filamin A in Alzheimer's Disease. *Int. J. Mol. Sci.* **2023**, *24*, 13927. [CrossRef]
11. Penke, B.; Szűcs, M.; Bogár, F. New Pathways Identify Novel Drug Targets for the Prevention and Treatment of Alzheimer's Disease. *Int. J. Mol. Sci.* **2023**, *24*, 5383. [CrossRef] [PubMed]
12. Orobets, K.S.; Karamyshev, A.L. Amyloid Precursor Protein and Alzheimer's Disease. *Int. J. Mol. Sci.* **2023**, *24*, 14794. [CrossRef] [PubMed]
13. Volloch, V.; Rits-Volloch, S. The Amyloid Cascade Hypothesis 2.0 for Alzheimer's Disease and Aging-Associated Cognitive Decline: From Molecular Basis to Effective Therapy. *Int. J. Mol. Sci.* **2023**, *24*, 12246. [CrossRef]
14. Kalia, L.V.; Lang, A.E. Parkinson's Disease. *Lancet* **2015**, *386*, 896–912. [CrossRef]
15. He, C.; Klionsky, D.J. Regulation Mechanisms and Signaling Pathways of Autophagy. *Annu. Rev. Genet.* **2009**, *43*, 67–93. [CrossRef]
16. Siddique, I.; Kamble, K.; Gupta, S.; Solanki, K.; Bhola, S.; Ahsan, N.; Gupta, S. ARL6IP5 Ameliorates α-Synuclein Burden by Inducing Autophagy via Preventing Ubiquitination and Degradation of ATG12. *Int. J. Mol. Sci.* **2023**, *24*, 10499. [CrossRef]
17. Prasertsuksri, P.; Kraokaew, P.; Pranweerapaiboon, K.; Sobhon, P.; Chaithirayanon, K. Neuroprotection of Andrographolide against Neurotoxin MPP+-Induced Apoptosis in SH-SY5Y Cells via Activating Mitophagy, Autophagy, and Antioxidant Activities. *Int. J. Mol. Sci.* **2023**, *24*, 8528. [CrossRef]
18. Zheng, W.; Han, X.; Han, B.; Li, G.; Gan, J.; Wang, T.; Xu, B.; He, J.; Du, W.; Cao, X.; et al. LAR Downregulation Protects the Astrocytic U251 and Cocultured SH-SY5Y Cells in a Rotenone-Induced Parkinson's Disease Cell Model. *Int. J. Mol. Sci.* **2023**, *24*, 11111. [CrossRef]
19. Stojsavljevic, T.; Guo, Y.; Macaluso, D. Adaptive Stimulations in a Biophysical Network Model of Parkinson's Disease. *Int. J. Mol. Sci.* **2023**, *24*, 5555. [CrossRef]
20. Mitchell, J.; Borasio, G. Amyotrophic Lateral Sclerosis. *Lancet* **2007**, *369*, 2031–2041. [CrossRef]
21. Tury, A.; Tolentino, K.; Zou, Y. Altered Expression of Atypical PKC and Ryk in the Spinal Cord of a Mouse Model of Amyotrophic Lateral Sclerosis. *Dev. Neurobiol.* **2014**, *74*, 839–850. [CrossRef] [PubMed]
22. Guo, W.; Vandoorne, T.; Steyaert, J.; Staats, K.A.; Van Den Bosch, L. The Multifaceted Role of Kinases in Amyotrophic Lateral Sclerosis: Genetic, Pathological and Therapeutic Implications. *Brain* **2020**, *143*, 1651–1673. [CrossRef] [PubMed]
23. La Cognata, V.; D'Amico, A.G.; Maugeri, G.; Morello, G.; Guarnaccia, M.; Magrì, B.; Aronica, E.; Alkon, D.L.; D'Agata, V.; Cavallaro, S. The ε-Isozyme of Protein Kinase C (PKCε) Is Impaired in ALS Motor Cortex and Its Pulse Activation by Bryostatin-1 Produces Long Term Survival in Degenerating SOD1-G93A Motor Neuron-like Cells. *Int. J. Mol. Sci.* **2023**, *24*, 12825. [CrossRef] [PubMed]
24. Chiu, I.M.; Morimoto, E.T.A.; Goodarzi, H.; Liao, J.T.; O'Keeffe, S.; Phatnani, H.P.; Muratet, M.; Carroll, M.C.; Levy, S.; Tavazoie, S.; et al. A Neurodegeneration-Specific Gene-Expression Signature of Acutely Isolated Microglia from an Amyotrophic Lateral Sclerosis Mouse Model. *Cell Rep.* **2013**, *4*, 385–401. [CrossRef] [PubMed]
25. Pereira, C.A.D.S.; Medaglia, N.D.C.; Ureshino, R.P.; Bincoletto, C.; Antonioli, M.; Fimia, G.M.; Piacentini, M.; Pereira, G.J.D.S.; Erustes, A.G.; Smaili, S.S. NAADP-Evoked Ca^{2+} Signaling Leads to Mutant Huntingtin Aggregation and Autophagy Impairment in Murine Astrocytes. *Int. J. Mol. Sci.* **2023**, *24*, 5593. [CrossRef] [PubMed]

26. Suzuki, M.; Nagai, Y.; Wada, K.; Koike, T. Calcium leak through ryanodine receptor is involved in neuronal death induced by mutant huntingtin. *Biochem. Biophys. Res. Commun.* **2012**, *429*, 18–23. [CrossRef]
27. Jiang, R.; Diaz-Castro, B.; Looger, L.L.; Khakh, B.S. Dysfunctional Calcium and Glutamate Signaling in Striatal Astrocytes from Huntington's Disease Model Mice. *J. Neurosci.* **2016**, *36*, 3453–3470. [CrossRef] [PubMed]
28. Medina, D.L. Lysosomal calcium and autophagy. *Int. Rev. Cell Mol. Biol.* **2021**, *362*, 141–170. [CrossRef]
29. Calcraft, P.J.; Ruas, M.; Pan, Z.; Cheng, X.; Arredouani, A.; Hao, X.; Tang, J.; Rietdorf, K.; Teboul, L.; Chuang, K.-T.; et al. NAADP Mobilizes Calcium from Acidic Organelles through Two-Pore Channels. *Nature* **2009**, *459*, 596–600. [CrossRef]
30. Nguyen, D.T.; Zaferanieh, M.H.; Black, A.C.; Hamedi, K.R.; Goodwin, R.L.; Nathaniel, T.I. Obstetric Neuropathy in Diabetic Patients: The "Double Hit Hypothesis". *Int. J. Mol. Sci.* **2023**, *24*, 6812. [CrossRef]
31. Quan, Z.; Li, H.; Quan, Z.; Qing, H. Appropriate Macronutrients or Mineral Elements Are Beneficial to Improve Depression and Reduce the Risk of Depression. *Int. J. Mol. Sci.* **2023**, *24*, 7098. [CrossRef] [PubMed]
32. Da Cunha Germano, B.C.; De Morais, L.C.C.; Idalina Neta, F.; Fernandes, A.C.L.; Pinheiro, F.I.; Do Rego, A.C.M.; Araújo Filho, I.; De Azevedo, E.P.; De Paiva Cavalcanti, J.R.L.; Guzen, F.P.; et al. Vitamin E and Its Molecular Effects in Experimental Models of Neurodegenerative Diseases. *Int. J. Mol. Sci.* **2023**, *24*, 11191. [CrossRef]
33. Hyslop, P.A.; Boggs, L.N.; Chaney, M.O. Origin of Elevated S-Glutathionylated GAPDH in Chronic Neurodegenerative Diseases. *Int. J. Mol. Sci.* **2023**, *24*, 5529. [CrossRef] [PubMed]
34. Pilski, A.; Graves, S.M. Repeated Methamphetamine Administration Results in Axon Loss Prior to Somatic Loss of Substantia Nigra Pars Compacta and Locus Coeruleus Neurons in Male but Not Female Mice. *Int. J. Mol. Sci.* **2023**, *24*, 13039. [CrossRef] [PubMed]
35. Klein, C.; König, I.R. Exploring Uncharted Territory: Genetically Determined Sex Differences in Parkinson's Disease. *Ann. Neurol.* **2021**, *90*, 15–18. [CrossRef] [PubMed]
36. Granado, N.; Ares-Santos, S.; Moratalla, R. Methamphetamine and Parkinson's Disease. *Park. Dis.* **2013**, *2013*, 308052. [CrossRef]
37. Mercan, D.; Heneka, M.T. The Contribution of the Locus Coeruleus–Noradrenaline System Degeneration during the Progression of Alzheimer's Disease. *Biology* **2022**, *11*, 1822. [CrossRef]
38. Wen, J.-H.; He, X.-H.; Feng, Z.-S.; Li, D.-Y.; Tang, J.-X.; Liu, H.-F. Cellular Protein Aggregates: Formation, Biological Effects, and Ways of Elimination. *Int. J. Mol. Sci.* **2023**, *24*, 8593. [CrossRef]

International Journal of
Molecular Sciences

MDPI

Review

Amyloid Precursor Protein and Alzheimer's Disease

Kseniia S. Orobets and Andrey L. Karamyshev *

Department of Cell Biology and Biochemistry, Texas Tech University Health Sciences Center, Lubbock, TX 79430, USA; korobets@ttuhsc.edu
* Correspondence: andrey.karamyshev@ttuhsc.edu; Tel.: +1-806-743-4102

Abstract: Alzheimer's disease (AD) is one of the most common neurodegenerative disorders associated with age or inherited mutations. It is characterized by severe dementia in the late stages that affect memory, cognitive functions, and daily life overall. AD progression is linked to the accumulation of cytotoxic amyloid beta (Aβ) and hyperphosphorylated tau protein combined with other pathological features such as synaptic loss, defective energy metabolism, imbalances in protein, and metal homeostasis. Several treatment options for AD are under investigation, including antibody-based therapy and stem cell transplantation. Amyloid precursor protein (APP) is a membrane protein considered to play a main role in AD pathology. It is known that APP in physiological conditions follows a non-amyloidogenic pathway; however, it can proceed to an amyloidogenic scenario, which leads to the generation of extracellular deleterious Aβ plaques. Not all steps of APP biogenesis are clear so far, and these questions should be addressed in future studies. AD is a complex chronic disease with many factors that contribute to disease progression.

Keywords: neurodegenerative disease; Alzheimer's disease; amyloid precursor protein (APP); amyloid beta; protein biogenesis; protein transport; membrane proteins; SRP-dependent targeting

Citation: Orobets, K.S.; Karamyshev, A.L. Amyloid Precursor Protein and Alzheimer's Disease. *Int. J. Mol. Sci.* **2023**, *24*, 14794. https://doi.org/10.3390/ijms241914794

Academic Editors: Hari Shanker Sharma and Claudia Ricci

Received: 30 July 2023
Revised: 20 September 2023
Accepted: 26 September 2023
Published: 30 September 2023

1. Introduction

Alzheimer's disease (AD) is a severe neurological disorder and the most common type of dementia across the world. According to Alzheimer's Association, AD contributes to 60–80% of all dementia cases worldwide. As estimated, in 2023, there will be 6.7 million people who are 65 years old or older living in the United States with Alzheimer's disease [1]. It is predicted that a dramatic elevation of AD pathology will occur in the future, with 13.85 million Americans affected by Alzheimer's dementia and 152 million affected around the world by the year 2050 [2,3]. In 2019, the World Health Organization (WHO) reported USD 1.3 trillion as the dementia cost around the world, including care expenses from family members and friends who do not fall into the category of professional caregivers and medical personnel. A huge number of current AD patients, their dramatic increase with an aging population in the near future, and the devastating economic costs put pressure on governments to address these issues through new policies for medical care providers to find efficient ways to treat patients and for the scientific community and pharmacologists to discover the mechanism of this disorder, developing markers for its early detection and finding new potential effective treatment and the disease cure. However, despite the fact that intensive studies and significant funding for Alzheimer's disease research have been undertaken, no breakthrough discovery has been made regarding the mechanism, and many promising therapies have failed; currently, only a few pharmacological treatments have received approval or are under consideration by the FDA, providing only mild improvement in patients [4]. Thus, the significance of the study related to AD is obvious.

Alzheimer's disease is represented in two forms—familial (inherited) and sporadic. Familial AD is the autosomal-dominant form of the disease and is characterized by relatively early onset under the age of 65, contributing to around 1% of all cases [1]. The sporadic form usually develops after 65 years and, therefore, is referred to as late-onset

Alzheimer's disease (LOAD). It is the most common form of AD. Familial and sporadic cases are triggered by mutations in different genes (discussed in detail below) or by alternative mRNA splicing [5]. There are several studied cases with a very early onset of AD reported, suggesting the increasing number of affected people, even in the younger generation [6–9]. With the age of disease decreasing and the general population getting older, the development of functional treatment, preventive medicine, and effective diagnostics stay in the focus of attention and is the most wanted.

The clinical picture of Alzheimer's disease is identical for inherited and familial cases. It comprises memory loss, decreasing thinking skills and solving problems, and the inability to cope with daily tasks. This functional decline is accompanied by changes in personality and behavior and withdrawal from social life and work. Finally, in the late stages, patients are fully dependent on caregivers or special facilities. Alzheimer's disease affects not only patients diagnosed with this disorder but also their families, with the patients being a large burden in many ways. The progression of this disease usually takes years and starts much earlier than the first symptoms can be detected. Biological changes, such as the presence of specific biomarkers in patient samples or the accumulation of pathological hallmarks, can help to diagnose the disease at the so-called preclinical or pre-symptomatic stage [1,10]. Mild cognitive impairment represents the next stage of the disease progression, characterized by mild symptoms without much interference with daily tasks. The final stage is Alzheimer's dementia, which can also be in mild, moderate, or severe, causing minor to drastic interference with everyday life.

Alzheimer's disease has a strong association with genetics and cellular mechanisms, yet it is a chronic and complex disorder where additional risk factors contribute to disease onset and progression. Genetics and age are the strongest and nonmodifiable risk factors. Health factors (heart and blood vessel conditions, hypertension, and diabetes) and behavior factors (diet, physical activity, level of education, and cognitive engagement) are mixed together in an intricate interplay where the variables depend on each other.

2. The Genetics of Alzheimer's Disease

The molecular basis of Alzheimer's disease has been studied for decades. Among the hallmarks of neurodegenerative disorders, the most recent data define not only the aberrant aggregation of proteins but also the dysfunction of neuronal networks, defective energy metabolism, abnormalities in the cytoskeleton, and alterations to protein and metal homeostasis, as well as declining memory, language, and thinking abilities [11].

The most known and studied molecular marker of AD is the accumulation of extracellular plaques built up by amyloid β protein (Aβ) and intracellular neurofibrillary tangles (NFTs) formed by hyperphosphorylated tau-protein in brain neurons. To date, several hypotheses of Alzheimer's disease onset are being discussed in the field. The major hypothesis implicates the defective cleavage of amyloid precursor protein (APP) and the consequent amyloid beta plaque formation as a predominant basis for Alzheimer's disease, giving rise to a downstream cascade that leads to tau-pathology [12]. However, nowadays, there is a tendency to show the interplay between these two factors [13,14].

Although aggregated Aβ and tau are the major characteristics of AD on the microscopic level, the molecular pathology of the disease is not limited to only these two proteins. There is a plethora of genes associated with a higher risk for Alzheimer's disease. Genome-wide association studies (GWASs) help to identify novel mutations in those genes related to the sporadic form of the disease. This topic has been in the research field for years, widening the list of potentially pathogenic mutations and confirming the genetic complexity of Alzheimer's disease [15–17]. There has been progress in genetic screens that are linked to other genes, including *APOE*, *TREM2*, *SORL1*, and *ABCA7*, with the disease [18,19]. Recent studies identified 75 loci for AD (42 of them were new, and 33 were previously found) [20]. Some of these newly identified genes may regulate APP recycling in the endosomal system and modulate APP metabolism by influencing lipid metabolism and inflammation [21–23].

APOE4, a variant of the *APOE* gene, is associated with a high risk of the development of the sporadic form of AD, but the reason for such effect is still not clear. Apolipoprotein E, which is encoded by this gene, regulates lipoprotein uptake and interferes with lipid transport and lipid metabolism in the brain. Defects in *APOE4* lead to the common pathological characteristics of AD, such as mitochondrial dysfunction, changes in synaptic plasticity, and neuroinflammation [24]. Transcriptomic analyses of APOE4 neurons, astrocytes, and microglia-like cells (derived from induced pluripotent stem cells—iPSC) revealed many differentially expressed genes. Notably, in APOE4 neurons, the production of Aβ is increased, as well as the number of endosomes, where major Aβ generation takes place [25]. With elevated neuronal Aβ production, Aβ uptake by astrocytes is compromised, leading to an increase in extracellular amyloid deposition. These events are accompanied by the activation of an inflammatory response in microglia-like cells and the upregulation of proinflammatory genes [26,27]. The removal of the APOE4 allele in a mouse model leads to a decrease in another AD hallmark, hyperphosphorylated tau and tau-associated neurodegeneration in microglia. It indicates that APOE4 affects tau pathology [26,28,29]. Changes in cholesterol metabolism were also observed. Another study using transcriptomic analysis demonstrated alterations in lipid metabolism in APOE4 astrocytes and microglia, resulting in increased cholesterol synthesis in combination with high cholesterol accumulation in lysosomes, suggesting defects in cholesterol turnover in these cell types; however, this was only in humans [30]. Eventually, an oversupply of cholesterol by astrocytes promotes amyloidogenic APP processing in neurons due to the increased formation of lipid rafts, which APP is associated with [31].

Familial forms of AD are connected to the defective proteins involved in the generation of Aβ and are caused by mutations in *PSEN1*, *PSEN2*, or *APP* genes. For the *APP* gene, 25 mutations were described as pathogenic [32]. For *PSEN1* and *PSEN2*, there are around 200 different pathogenic mutations that have been identified as contributing to disease development [33,34]. The *PSEN1* and *PSEN2* genes encode the proteins presenilin 1 and presenilin 2, respectively. Both these proteins modulate the activity of γ-secretase, a membrane-associated complex responsible for the cleavage of different proteins, including APP. It was established that mutations in *PSENs* affect γ-secretase activity through the destabilization of the enzyme-substrate complex. In APP processing, the production of longer Aβ peptides is what stimulates amyloid generation and shifts the balance towards Aβ accumulation [35]. Additionally, it was suggested that *PSENs* mutations trigger pathological alterations in mitochondrial metabolism, which is one of the cellular hallmarks of AD [36]. Mutations in *APP* contribute to AD by increasing the production of the most toxic Aβ42 peptides or through stimulating Aβ aggregation but not through the alterations of APP function [34].

3. Early Biogenesis of Amyloid Precursor Protein

Despite extensive research into APP biology, especially its processing, the early steps of APP biogenesis are still unknown. Generally, newly synthesized proteins are marked with specific targeting signals for the final protein destination. Depending on these signals, the proteins are transported to different organelles such as the endoplasmic reticulum (ER), Golgi apparatus, plasma membrane, nucleus, mitochondrion, endosomes, lysosomes, or peroxisomes. APP is located in the plasma membrane and other membrane organelles. Thus, it must undergo certain trafficking to reach these subcellular locations. Here, we discuss the general protein trafficking pathway in eukaryotic organisms and analyze its relevance to APP biogenesis.

In general, secretory and membrane proteins follow a specific path during their biogenesis. For proper folding and transport, they are targeted to the endoplasmic reticulum with the assistance of the signal recognition particle (SRP), which is a major route of protein transport in eukaryotes [37,38]. SRP is a ribonucleoprotein complex that is able to bind signal peptides and ribosomes, and is able to transport its cargo to the SRP receptor (SR) in the ER membrane. Mutations in the SRP subunits are associated with multiple human

diseases [39]. SRP recognizes a specific part of a polypeptide emerging from the ribosome exit tunnel during translation. This cleavable N-terminal region of secretory proteins is known as a signal peptide; its properties and features were originally described in Dr. G von Heijne's works [40–42]. It was shown that signal peptides do not have amino acid sequence homology; instead, they have common physico-chemical properties, including a stretch of hydrophobic amino acids in the central part. The importance of this signal peptide's parameters was highlighted in several studies [43–46]. The defective signal peptide of preprolactin (PPL) does not allow for normal interaction between SRP and the nascent chain of PPL, triggering a specific mechanism of mRNA degradation, named regulation of aberrant protein production (RAPP) [44]. RAPP is one of the protein quality control mechanisms in eukaryotes, and it is activated when SRP cannot bind the nascent chain and the targeting of secretory and membrane proteins is compromised [47,48]. So far, RAPP has been associated with the degradation of the mRNAs of several different secretory proteins in addition to preprolactin. Thus, it was shown that disease-associated mutations in multiple secretory proteins, including granulin (the protein associated with neurodegenerative disease frontotemporal lobar degeneration or FTLD), activate the RAPP pathway [49,50]. It was also suggested that SRP is involved in alpha-synuclein biogenesis, and RAPP may play a role in Parkinson's disease [51]. Finally, a deep RNA-seq analysis revealed the connection between the loss of SRP interaction with a signal peptide and various metabolic, immune, and age-related disorders, as well as cancer [52]. It was established that RAPP is a general pathway that controls the quality of SRP-dependent secretory and membrane proteins in the ribosome [52]. However, despite the in-depth studies on the interaction between SRP and ribosome-associated polypeptides and the control of their quality during translation, the fundamental questions of which proteins are SRP-dependent and which proteins are SRP-independent have not been answered yet.

Similar to many secretory and membrane proteins, APP has an N-terminal signal peptide, which is remarkably hydrophobic. The APP signal peptide consists of 17 amino acid residues, and five of them are leucines, which makes it a potential candidate for being an SRP substrate. The APP signal sequence marks this protein for ER targeting, but it was linked to SRP only indirectly [53] and was briefly discussed as a client for cotranslational targeting [54]. There are few studies in which the early stages of APP biogenesis are the focus of the interest. APP was identified as a client of the SEC61 translocon, one of the main entry gates to the ER [55]. The SEC61 translocon is a protein complex in the ER membrane, to which SRP cotranslationally brings its cargo [56,57]. SEC61 is one of the major entry points to the ER, and it can be engaged with other trafficking partners [58,59]. Thus, it is still to be determined how APP is targeted to the ER and what partners are involved in its transport; this can shed light on early APP biogenesis and its possible effect on Alzheimer's disease onset.

4. Amyloid Precursor Protein Processing

Amyloid precursor protein is a type I membrane protein. It is encoded by the *APP* gene located on chromosome 21 in humans [60–62]. APP is widely expressed in the body, with higher expression in the neuronal tissues in the brain. Differential processing and alternative splicing generate different isoforms of APP in a tissue-dependent manner [63]. The three major variants are APP695, APP751, and APP770, and all of them are capable of producing amyloid beta [64]. Isoforms APP751 and APP770 are mostly present in non-neuronal tissues, while APP695 is predominantly found in neurons and is considered the most toxic. APP functions are diverse and are associated with the neurogenesis and differentiation of neuronal cells, synaptic mechanisms, cell cycle and adhesion, and calcium metabolism [65–67]. APP-deficient mice exhibit a shortened lifespan, cognitive and learning impairment, and altered metal homeostasis in the brain regions typically affected by the disease [68–70].

APP processing is a multistep mechanism that involves several cleavage events to release different products. APP biogenesis can be divided into distinct general steps, as shown in Figure 1.

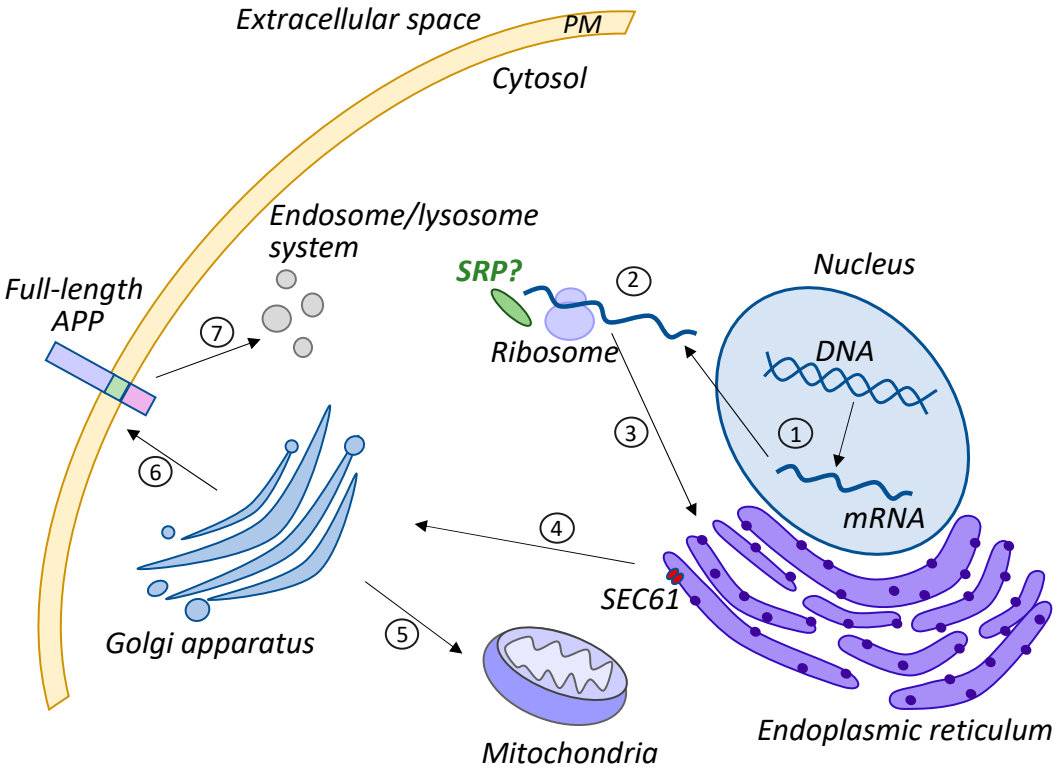

Figure 1. Intracellular APP trafficking. (1) *APP* transcription in the nucleus and mRNA export to the cytoplasm. (2) APP mRNA translation on a ribosome with the assistance of SRP or unestablished targeting factors (no experimental evidence of SRP involvement yet, thus, it is indicated by a question mark). (3) The transport of nascent APP to ER for further biogenesis. (4) The transition to Golgi for post-translational modifications. (5) The transport of full-length APP to mitochondria and the insertion into the mitochondria membrane. (6) The transport of full-length APP to the plasma membrane (PM). (7) The internalization of full-length APP into the endosomal system for further cleavage.

The vast majority of the studies focus on the late stages of APP processing when the full-length APP is inserted into the plasma membrane or other intracellular membrane organelles and undergoes cleavage events. The cleavage of membrane-inserted APP can follow two pathways—amyloidogenic or non-amyloidogenic (the most common one) (Figure 2). Three secretases play a central role in the late processing of APP: α-, β-, and γ-secretase. The non-amyloidogenic pathway starts with α-secretase releasing the N-terminal extracellular soluble APP domain (sAPPα) and the membrane-attached C83 fragment. α-secretase cuts the middle of the Aβ region; thus, this cleavage prevents the further formation of Aβ. Extracellular sAPPα can mitigate amyloid beta production via the inhibition of β-secretase (BACE1), which is the enzyme responsible for one of the steps in the amyloidogenic pathway of APP processing. Thus, sAPPα stimulates the non-amyloidogenic pathway [71,72]. The reintroduction of sAPPα into APP-depleted mouse models leads to the restoration of a normal phenotype, indicating the pivotal role of the sAPPα fragment in development [73].

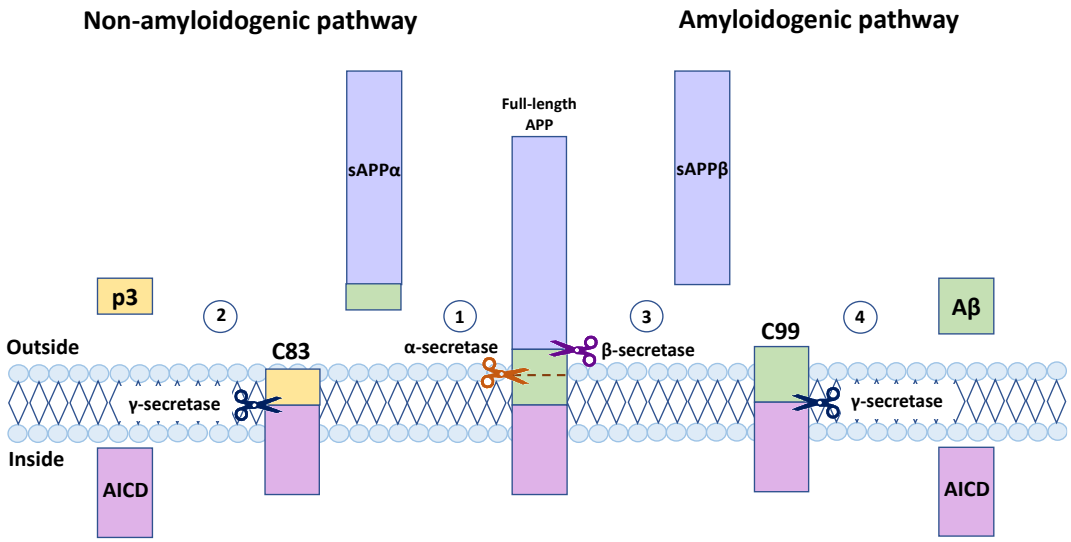

Figure 2. Amyloid precursor protein processing pathways. Full-length APP is inserted into the plasma membrane or intracellular membrane organelles, where it can proceed to the non-amyloidogenic or amyloidogenic pathway. (1) The non-amyloidogenic pathway starts with cleavage by α-secretase, which cuts full-length APP at the Aβ mid-region. This cleavage produces sAPPα and the membrane-bound C83 fragment. (2) The C83 fragment is cleaved further by γ-secretase to release the p3 molecule extracellularly and AICD (amyloid precursor protein intracellular domain) intracellularly. (3) The amyloidogenic pathway starts with β-secretase cleavage, which occurs on the membrane. It produces extracellular sAPPβ and the C99 fragment associated with the membrane. (4) γ-secretase cuts the C99 fragment, and Aβ is released outside of the cell, whereas AICD stays inside.

The first cleavage in the amyloidogenic pathway is performed by β-secretase, also known as β-site APP-cleaving enzyme-1 (BACE1). This cleavage produces the extracellular soluble APP β (sAPPβ) fragment and membrane-bound C99 domain. The importance of BACE1 for the production of aberrant amyloid beta was demonstrated in several studies. Remarkably, the experiments with mouse models for Alzheimer's disease revealed the complete absence of amyloid beta when BACE1 was silenced [74–77]. β-secretase is a membrane-associated enzyme with complex trafficking and diverse cellular routs. It is synthesized in the ER in a proenzyme form, which acquires its full activity after several post-translational modifications in the Golgi, including palmitoylation, glycosylation, acetylation, and phosphorylation, which have been shown to be essential for this enzyme to trigger amyloidogenic events [78,79]. After β-secretase insertion into the plasma membrane lipid rafts, it can be extracellularly released; therefore, APP processing by this enzyme rarely occurs on the plasma membrane. Then, this extracellular BACE1 is endocytosed to appear in the endosomes for functioning or to proceed to the lysosomes for degradation. Inside of the cell, BACE1 is mostly located on the membrane of the trans-Golgi network (TGN) and endosomes, where APP processing takes place [80]. Interestingly, initially, the APP from the plasma membrane is internalized through a clathrin-mediated mechanism, whereas BACE1 uses another clathrin-independent mechanism [81]. The optimal pH for this enzyme is 5.5; therefore, the predominant location of the possible APP processing and generation of Aβ is endosomes and lysosomes. Eventually, APP and β-secretase colocalize in Rab5-positive endosomes, where APP is cleaved by a fully active enzyme [82,83].

The first cleavage in both pathways results in the formation of the C83 and C99 membrane-bound domains in non-amyloidogenic and amyloidogenic scenarios, respectively. The physiological role of the C83 and C99 fragments is still uncharacterized. Both fragments are substrates for the γ-secretase enzyme complex. The cleavage of C83 or C99 by γ-secretase results in the production of amyloid precursor protein intracellular domain

(AICD) in both scenarios, amyloidogenic and non-amyloidogenic. AICD is known as a transcription factor containing the motif YENPTY, facilitating binding to other proteins [84–87]. AICD has been shown to be one of the regulators of APP processing, promoting intracellular APP trafficking. The APP intracellular domain can be phosphorylated at S655, stimulating the non-amyloidogenic pathway due to directing APP from endosomes with active BACE1 to TGN [88–90]. Phosphorylation at the position T668 may promote the amyloidogenic pathway [91], and likely, it interferes with APP intracellular processing [90,92]. Membrane-associated γ-secretase is a complex consisting of at least four transmembrane enzymes—presenilin (PS1 or PS2), presenilin-enhancer 2 (PEN-2), nicastrin (NCT), and anteriorpharynx-defective-1 (APH-1) [93,94]. As mentioned earlier, mutations in *PSEN1* or *PSEN2* genes contribute to the development of familial AD. γ-secretase is not exclusively associated with APP processing. It is implicated in the Notch-pathway and tumorigenesis. There are more than 50 proteins, including E-Cadherin, CD44, and IGF1R (insulin-like growth factor receptor) among γ-secretase's substrates [95,96]. The location of γ-secretase is not limited to the plasma membrane; it is also located in mitochondria and lysosome membranes, as well as in early and late endosomes [97,98]. The ubiquitous localization of this enzyme complex supports the idea of the highly intricate processing of APP with many subcellular loci available for the potential generation of Aβ. Noticeably, the non-amyloidogenic pathway is predominantly associated with the plasma membrane [99,100], whereas amyloidogenic is connected to the endosomal system [82,83,101]. When C83 is cleaved by γ-secretase, another product, p3, is released into extracellular space in the non-amyloidogenic pathway. To date, the biological role of this molecule has not been established.

Amyloid beta is one of the final products in the amyloidogenic pathway of APP processing. It is a small peptide consisting of 37–43 amino acids, where the Aβ42 isoform is known to be the most deleterious. Aβ peptides can form extracellular soluble oligomers and plaques and insoluble fibrils, which are the main hallmark of Alzheimer's disease. This accumulation gives rise to pathological events, such as neuroinflammation, cytotoxic effects, and neuronal death. The aggregation of Aβ and its dynamics in laboratory conditions in vitro has been carefully investigated through various methods, including cryo-electron microscopy, atomic force microscopy, nuclear magnetic resonance, electron paramagnetic resonance, and X-ray [102–106]. Aβ peptides can build up in a different fashion to form diverse structures of β-sheets, depending on the arrangement of monomers and the orientation of β-strands and β-sheets [107]. An intriguing phenomenon of aggregated Aβ peptides was observed in several studies. Amyloids consisting of 2–12 monomers are considered to possess the highest level of toxicity, whereas longer forms can interact with their shorter counterparts to "isolate" them, reducing the harmful effects. Therefore, the aggregation of Aβ, despite being a main pathological signature of the disease, can actually help cells to survive via the mitigation of cytotoxic effects [108,109]. Another deleterious effect of Aβ accumulation is the disruption of the plasma membrane followed by changes in calcium (Ca^{2+}) flux. The pore-forming hypothesis is still controversial; however, growing evidence indicates that, indeed, Aβ oligomers are inserted into the plasma membrane where they form Ca^{2+}-permeable pores and disrupt calcium homeostasis, which also leads to neuronal damage and cell death [110,111].

5. Amyloid Precursor Protein and Mitochondria

It has been known and investigated for years that mitochondria are connected to amyloid precursor protein and Alzheimer's disease. This field can be divided into three major research questions: (1) how is APP transported to mitochondria, and where is it localized? (2) What is the role of APP in mitochondria, and how is mitochondrial metabolism affected during the disease? (3) Can mitochondria be a therapeutic target for AD treatment?

As of today, mitochondrial dysfunction is one of the pathological hallmarks of Alzheimer's disease; nevertheless, this condition is present in the majority of neurodegenerative disorders [112,113]. In addition to the plasma membrane, APP is transported to mitochondria due

to a signal sequence resembling a mitochondrial-targeted signal [114,115]. Initially, although APP was found in the mitochondria of AD patient brain samples, a recent study showed APP presence in both healthy and pathological brains [116,117]. Mitochondrial dysfunction was attributed to Alzheimer's disease, causing defects in metabolism, protein maturation in mitochondria, energy production, oxygen consumption, and mitochondrial calcium homeostasis [118–120]. Multiple attempts were made to assess the changes in mitochondrial metabolism with the overexpression of wild-type APP or its mutated forms. The results vary from one cell line to another as well as between study groups; therefore, there is no consensus about APP effects in mitochondria. A comprehensive review describes, in detail, the results of recent studies on how APP effects mitochondria in in vitro and in vivo models [121]. Mitochondria metabolism seems an appealing target for potential AD therapy. Cell replacement therapy with MSCs or MSC-conditioned media has the potential for a reduction in oxidative stress and the restoration of normal mitochondrial function in a mouse model [122]. Exploiting nanoparticles for targeting mitochondria was also investigated. MSCs-derived extracellular vesicles (EVs) with tyrosine phosphatase-2 (SHP2) deliver SHP2 to the brain, where it induces mitophagy and helps with the clearance of aberrant proteins [123,124].

6. Alzheimer's Disease Is a Complex Disorder

Alzheimer's disease pathology is triggered by genetic factors, such as inherited mutations in familial cases or sporadic mutations with a connection to age. However, there are other factors affecting the disease progression and severity of the symptoms. AD contributing factors are spread over all parts of APP biogenesis (Figure 3).

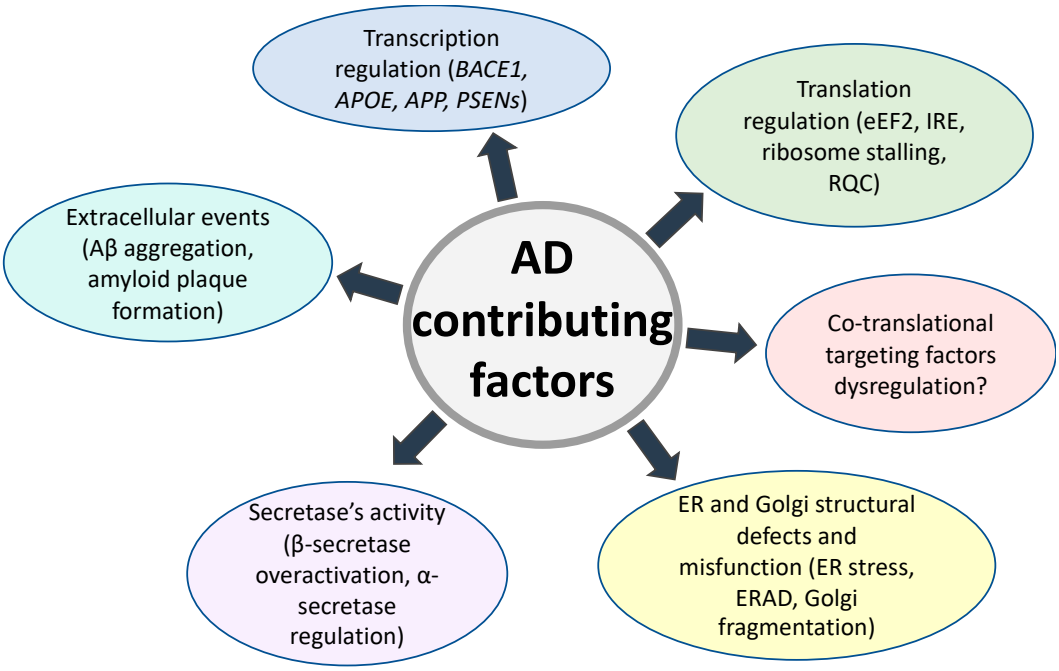

Figure 3. Alzheimer's disease contributing factors.

Versatile evidence indicates that Alzheimer's disease emerges from an imbalance between amyloid plaque accumulation and its degradation. The regulation of amyloid β production starts on the level of transcription. Autophagy is the main cellular mechanism for the clearance of aggregates and aberrant proteins. PPARA/PPARα (peroxisome proliferator-activated receptor alpha) regulates the gene expression of autophagy, with lipid and glucose metabolism genes serving as some of the central regulators for mitochondrial function [125]. The pharmacological targeting of transcription factor PPARA activates autophagy in human microglial and glioma cells expressing APP, which leads to the partial removal of amyloid plaques and causes a shift towards Aβ clearance through

transcriptional regulation [126]. A shift towards amyloid β production can be triggered by the regulation of genes directly involved in APP processing. For instance, *BACE1*, the gene that encodes β-secretase, has several transcription factor-binding sites that allow for the regulation of this gene by multiple transcription factors, for example, peroxisome proliferator-activated receptor gamma (PPARγ), NF-κB, specificity protein 1 (SP1). PPARγ is a nuclear transcription factor that reduces the activity of the *BACE1* promotor when overexpressed. In AD patient, samples of a lower level of PPARγ was detected, suggesting the overactivation of *BACE1* [127]. NF-κB regulates *BACE1* expression differently under different conditions, such as lowering BACE1 expression in physiological conditions but promoting Aβ generation in pathology [128]. SP1 is one of the first identified regulators for *BACE1*, working as an activator for β-secretase expression and also interacting with NF-κB [129,130]. The transcription of *APOE* can be upregulated by cyclic AMP (cAMP), retinoic acid (RA), PPARγ, and Aβ itself. In the case of *APOE* transcriptional regulation via Aβ, it can be considered as a neuroprotective mechanism since ApoE helps prevent against cytotoxicity [131].

APP transcription can be activated in different cell types by heat-shock factor 1 (HSF-1), NF-κB, and Rac1 [128]. *PSEN1* transcriptional regulation has been studied more than *PSEN2* and can be controlled by diverse transcription elements (Ets, ZNF237, cAMP-responsive element-binding protein, and p300) and chromatin modifications [132–134].

The activity of α-secretase is also subject to regulation, leading to changes in the balance of amyloid production. The protease furin effectively promotes the non-amyloidogenic pathway and the production of sAPPα, which, in turn, further stimulates this pathway. When furin is inhibited, the level of sAPPα is decreased (when the APP level is not changed), suggesting amyloidogenic pathway activation [135]. Remarkably, a recent study revealed an interplay between iron overload in neurodegeneration and the downregulation of furin, leading to elevated production of amyloids [136].

Defects in other stages of APP processing may also play a significant role in Aβ accumulation and aggregation. It was shown that alterations to APP mRNA translation can happen in the initiation and elongation steps. Elongation factor eEF2, when phosphorylated, slows down protein synthesis and leads to ribosome stalling. In AD mouse models, the phosphorylation of eEF2 is enhanced, suggesting the involvement of this elongation factor in AD pathology development [137]. Another mechanism that was shown to alter APP mRNA translation is iron-dependent. It was demonstrated that patients with neurodegenerative disorders, such as Alzheimer's or Parkinson's disease, have an elevated level of iron in the brain [138]. Iron toxicity is connected to the generation of reactive oxygen species in the brain following oxidative stress and neuronal death [139]. The iron-responsive element (IRE) of APP mRNA was identified and shown to regulate APP protein expression. When iron is chelated in a neuroblastoma cell line, APP protein synthesis is drastically decreased, demonstrating the involvement of iron in the regulation of APP translation [140]. If ribosomes with an APP nascent chain are stuck in the ER during translation, this activates ribosome-associated quality control (RQC), triggering a down-stream cascade of reactions. Abnormal RQC causes endolysosomal misfunction, which leads to the formation of an amyloid plaque core intracellularly [55]. Yet, as mentioned before, the APP targeting factors are still unestablished, and this can be another aspect of APP processing that might contribute to AD development.

The prevalent part of APP maturation takes place in the ER and Golgi, where post-translational modifications occur; therefore, these subcellular locations are important for physiologically normal APP biogenesis. A plethora of studies have focused on ER stress and its connection to Alzheimer's disease. The unfolded protein response (UPR) is a protein quality control mechanism associated with ER. During mild ER stress, this mechanism is highly functional and beneficial for cells since it works for balancing ER and protein homeostasis [141]. But under severe stress conditions in AD, the UPR turns maladaptive and stimulates apoptosis, increasing neuronal death [142]. Another connection between APP biogenesis and ER was made through ER degradation-enhancing α-mannosidase-like

protein 1 (EDEM1), a targeting factor for misfolded ER proteins. It targets aberrant proteins for degradation in the ER-associated protein degradation (ERAD) pathway [143]. In cell cultures expressing APP, EDEM1 promotes APP targeting from the ER to the cytoplasm, where ERAD takes place. It stimulates the proteosome degradation of APP inside the cell and leads to a consequent decrease in Aβ40-42 production [144]. Golgi fragmentation was reported in AD pathology cases; however, the primary reason and consequence in the APP-Golgi relationship is still poorly understood. It was suggested that despite this, Golgi defects appear as a consequences of AD pathology in the early stages, and these defects also enhance amyloid formation and stimulate the amyloidogenic pathway [145]. The fragmentation of the Golgi apparatus is due to the phosphorylation of Golgi structural proteins (GRASP65), which happens through the Aβ-associated activation of cyclin-dependent kinase-5 (cdk5) [146].

7. Alzheimer's Disease Diagnostic and Treatment

Nowadays, technical progress has allowed for the diagnosis of Alzheimer's disease, even in the preclinical stage. An inadequate level of Aβ and hyperphosphorylated tau protein can be detected in cerebrospinal fluid (CSF). Positron emission tomography (PET) allows for the detection of accumulated amyloids and tau tangles in the brain. Recently, a new diagnostic technique was introduced. Blood-based biomarkers (BBMs) for Alzheimer's disease screening have several advantages, such as the simplicity of the test and its performance (blood tests can be carried out in any medical facility, whereas CSF analysis or PET can only be conducted in specialized clinics), lower cost, and additional biomarkers for neurodegeneration (neurofilament light chain (NfL) and glial fibrillary acidic protein (GFAP)) can be detected [147–149]. Several other methods, such as computed tomography (CT) or magnetic resonance imaging (MRI), may be used to refute Alzheimer's disease pathology or to support other possible diagnoses.

There are many potential options for the treatment of Alzheimer's disease, which are broadly being explored to this day. One of the most promising fields is antibody-based therapy to target Aβ. Several developed immunotherapy compounds have already entered clinical trials; however, many of them failed. By the end of 2022, there were four antibody-based therapeutic agents undergoing the final clinical phase: aducanumab, lecanemab, gantenerumab, and donanemab. These are monoclonal IgG1 antibodies with an affinity to aggregate amyloid beta forms [150]. In spite of high hopes for finding a curative medicine, it is too early to say if some of the suggested options may revolutionize Alzheimer's disease treatment.

Another treatment option that has become widely explored is stem cell therapy. Mesenchymal stem cells (MSCs), neural stem cells (NSCs), and embryonic stem cells (ESCs) are used for transplantation into AD mouse models to evaluate their potential curative effect on neurodegenerative pathology. Among the common effects between these different MSC lines, there has been an increase in synaptic plasticity, mitigation of inflammatory response, improved short-term memory and learning abilities, and cognitive improvement [151–156].

Since the sporadic form of Alzheimer's disease has a strong association with aging, anti-aging therapy is considered another approach for AD treatment, which has been actively investigated. Several existing anti-aging drugs are under investigation with nanoparticle-based delivery agents in animal models [157,158]. Nanoparticle-based treatment delivery is believed to be effective because nanoparticles can penetrate the blood–brain barrier (BBB) efficiently and perform targeted delivery with a lower chance of crossing peripheral circulation.

8. Conclusions

Alzheimer's disease is a complex chronic disorder where genetic defects are enhanced by age, other health conditions, and environmental factors. The investigation of the genetic features of AD using modern technological approaches has allowed for a broader picture of the diagnostics of the disease. Detailed studies on the molecular biology of APP and all

the related products, including secretases, have helped determine the relationship between them and how they affect the amyloidogenic process. Despite decades of research on Alzheimer's disease and APP, we are still far from a complete understanding of its biological basis. Many questions about APP biogenesis, especially the early steps, interacting partners, APP's role in mitochondria, and the potential therapeutic targets, must be addressed in future studies.

Author Contributions: A.L.K. contributed to the conceptualization; K.S.O. wrote the manuscript, designed and prepared figures; and all authors discussed and edited the manuscript. All authors have read and agreed to the published version of the manuscript.

Funding: This work was supported by the Center of Excellence for Translational Neuroscience and Therapeutics (CTNT) and the TTUHSC Office of Research (award number CTNT-OR 2022-04 AKMM).

Institutional Review Board Statement: Not applicable.

Informed Consent Statement: Not applicable.

Data Availability Statement: Not applicable.

Conflicts of Interest: The authors declare no conflict of interest.

References

1. Alzheimer's Association Report. 2023 Alzheimer's disease facts and figures. *Alzheimers Dement.* **2023**, *19*, 1598–1695. [CrossRef] [PubMed]
2. Rajan, K.B.; Weuve, J.; Barnes, L.L.; McAninch, E.A.; Wilson, R.S.; Evans, D.A. Population estimate of people with clinical Alzheimer's disease and mild cognitive impairment in the United States (2020–2060). *Alzheimers Dement.* **2021**, *17*, 1966–1975. [CrossRef]
3. Passeri, E.; Elkhoury, K.; Morsink, M.; Broersen, K.; Linder, M.; Tamayol, A.; Malaplate, C.; Yen, F.T.; Arab-Tehrany, E. Alzheimer's Disease: Treatment Strategies and Their Limitations. *Int. J. Mol. Sci.* **2022**, *23*, 13954. [CrossRef] [PubMed]
4. US Food and Drug Administration. *FDA Grants Accelerated Approval for Alzheimer's Disease Treatment*; US Food and Drug Administration: Rockville, MD, USA, 2023.
5. Course, M.M.; Gudsnuk, K.; Keene, C.D.; Bird, T.D.; Jayadev, S.; Valdmanis, P.N. Aberrant splicing of PSEN2, but not PSEN1, in individuals with sporadic Alzheimer's disease. *Brain* **2023**, *146*, 507–518. [CrossRef]
6. Jia, J.; Zhang, Y.; Shi, Y.; Yin, X.; Wang, S.; Li, Y.; Zhao, T.; Liu, W.; Zhou, A.; Jia, L. A 19-Year-Old Adolescent with Probable Alzheimer's Disease. *J. Alzheimers Dis.* **2023**, *91*, 915–922. [CrossRef] [PubMed]
7. Csaban, D.; Illes, A.; Renata, T.B.; Balicza, P.; Pentelenyi, K.; Molnar, V.; Gezsi, A.; Grosz, Z.; Gal, A.; Kovacs, T.; et al. Genetic landscape of early-onset dementia in Hungary. *Neurol. Sci.* **2022**, *43*, 5289–5300. [CrossRef] [PubMed]
8. Barthélemy, N.R.; Li, Y.; Joseph-Mathurin, N.; Gordon, B.A.; Hassenstab, J.; Benzinger, T.L.S.; Buckles, V.; Fagan, A.M.; Perrin, R.J.; Goate, A.M.; et al. A soluble phosphorylated tau signature links tau, amyloid and the evolution of stages of dominantly inherited Alzheimer's disease. *Nat. Med.* **2020**, *26*, 398–407. [CrossRef]
9. Gordon, B.A.; Blazey, T.M.; Su, Y.; Hari-Raj, A.; Dincer, A.; Flores, S.; Christensen, J.; McDade, E.; Wang, G.; Xiong, C.; et al. Spatial patterns of neuroimaging biomarker change in individuals from families with autosomal dominant Alzheimer's disease: A longitudinal study. *Lancet Neurol.* **2018**, *17*, 241–250. [CrossRef]
10. Porsteinsson, A.P.; Isaacson, R.S.; Knox, S.; Sabbagh, M.N.; Rubino, I. Diagnosis of Early Alzheimer's Disease: Clinical Practice in 2021. *J. Prev. Alzheimers Dis.* **2021**, *8*, 371–386. [CrossRef]
11. Wilson, D.M.; Cookson, M.R.; Van Den Bosch, L.; Zetterberg, H.; Holtzman, D.M.; Dewachter, I. Hallmarks of neurodegenerative diseases. *Cell* **2023**, *186*, 693–714. [CrossRef]
12. Hardy, J.A.; Higgins, G.A. Alzheimer's disease: The amyloid cascade hypothesis. *Science* **1992**, *256*, 184–185. [CrossRef]
13. Edwards, F.A. A Unifying Hypothesis for Alzheimer's Disease: From Plaques to Neurodegeneration. *Trends Neurosci.* **2019**, *42*, 310–322. [CrossRef]
14. Busche, M.A.; Hyman, B.T. Synergy between amyloid-β and tau in Alzheimer's disease. *Nat. Neurosci.* **2020**, *23*, 1183–1193. [CrossRef]
15. Bertram, L.; McQueen, M.B.; Mullin, K.; Blacker, D.; Tanzi, R.E. Systematic meta-analyses of Alzheimer disease genetic association studies: The AlzGene database. *Nat. Genet.* **2007**, *39*, 17–23. [CrossRef]
16. Hollingworth, P.; Harold, D.; Sims, R.; Gerrish, A.; Lambert, J.C.; Carrasquillo, M.M.; Abraham, R.; Hamshere, M.L.; Pahwa, J.S.; Moskvina, V.; et al. Common variants at ABCA7, MS4A6A/MS4A4E, EPHA1, CD33 and CD2AP are associated with Alzheimer's disease. *Nat. Genet.* **2011**, *43*, 429–435. [CrossRef] [PubMed]

17. Lambert, J.C.; Ibrahim-Verbaas, C.A.; Harold, D.; Naj, A.C.; Sims, R.; Bellenguez, C.; DeStafano, A.L.; Bis, J.C.; Beecham, G.W.; Grenier-Boley, B.; et al. Meta-analysis of 74,046 individuals identifies 11 new susceptibility loci for Alzheimer's disease. *Nat. Genet.* **2013**, *45*, 1452–1458. [CrossRef] [PubMed]
18. Selkoe, D.J. SnapShot: Pathobiology of Alzheimer's disease. *Cell* **2013**, *154*, 468–468.e1. [CrossRef] [PubMed]
19. Waring, S.C.; Rosenberg, R.N. Genome-wide association studies in Alzheimer disease. *Arch. Neurol.* **2008**, *65*, 329–334. [CrossRef]
20. Bellenguez, C.; Küçükali, F.; Jansen, I.E.; Kleineidam, L.; Moreno-Grau, S.; Amin, N.; Naj, A.C.; Campos-Martin, R.; Grenier-Boley, B.; Andrade, V.; et al. New insights into the genetic etiology of Alzheimer's disease and related dementias. *Nat. Genet.* **2022**, *54*, 412–436. [CrossRef]
21. Li, R.Y.; Qin, Q.; Yang, H.C.; Wang, Y.Y.; Mi, Y.X.; Yin, Y.S.; Wang, M.; Yu, C.J.; Tang, Y. TREM2 in the pathogenesis of AD: A lipid metabolism regulator and potential metabolic therapeutic target. *Mol. Neurodegener.* **2022**, *17*, 40. [CrossRef] [PubMed]
22. Mishra, S.; Knupp, A.; Szabo, M.P.; Williams, C.A.; Kinoshita, C.; Hailey, D.W.; Wang, Y.; Andersen, O.M.; Young, J.E. The Alzheimer's gene SORL1 is a regulator of endosomal traffic and recycling in human neurons. *Cell. Mol. Life Sci.* **2022**, *79*, 162. [CrossRef] [PubMed]
23. Dib, S.; Pahnke, J.; Gosselet, F. Role of ABCA7 in Human Health and in Alzheimer's Disease. *Int. J. Mol. Sci.* **2021**, *22*, 4603. [CrossRef]
24. Zhao, N.; Liu, C.C.; Qiao, W.; Bu, G. Apolipoprotein E, Receptors, and Modulation of Alzheimer's Disease. *Biol. Psychiatry* **2018**, *83*, 347–357. [CrossRef] [PubMed]
25. Cataldo, A.M.; Peterhoff, C.M.; Troncoso, J.C.; Gomez-Isla, T.; Hyman, B.T.; Nixon, R.A. Endocytic pathway abnormalities precede amyloid beta deposition in sporadic Alzheimer's disease and Down syndrome: Differential effects of APOE genotype and presenilin mutations. *Am. J. Pathol.* **2000**, *157*, 277–286. [CrossRef] [PubMed]
26. Lin, Y.T.; Seo, J.; Gao, F.; Feldman, H.M.; Wen, H.L.; Penney, J.; Cam, H.P.; Gjoneska, E.; Raja, W.K.; Cheng, J.; et al. APOE4 Causes Widespread Molecular and Cellular Alterations Associated with Alzheimer's Disease Phenotypes in Human iPSC-Derived Brain Cell Types. *Neuron* **2018**, *98*, 1141–1154.e7. [CrossRef]
27. de Leeuw, S.M.; Kirschner, A.W.T.; Lindner, K.; Rust, R.; Budny, V.; Wolski, W.E.; Gavin, A.C.; Nitsch, R.M.; Tackenberg, C. APOE2, E3, and E4 differentially modulate cellular homeostasis, cholesterol metabolism, and inflammatory response in isogenic iPSC-derived astrocytes. *Stem Cell Rep.* **2022**, *17*, 110–126. [CrossRef] [PubMed]
28. Wang, C.; Xiong, M.; Gratuze, M.; Bao, X.; Shi, Y.; Andhey, P.S.; Manis, M.; Schroeder, C.; Yin, Z.; Madore, C.; et al. Selective removal of astrocytic APOE4 strongly protects against tau-mediated neurodegeneration and decreases synaptic phagocytosis by microglia. *Neuron* **2021**, *109*, 1657–1674.e7. [CrossRef]
29. Zhao, J.; Fu, Y.; Yamazaki, Y.; Ren, Y.; Davis, M.D.; Liu, C.C.; Lu, W.; Wang, X.; Chen, K.; Cherukuri, Y.; et al. APOE4 exacerbates synapse loss and neurodegeneration in Alzheimer's disease patient iPSC-derived cerebral organoids. *Nat. Commun.* **2020**, *11*, 5540. [CrossRef]
30. Tcw, J.; Qian, L.; Pipalia, N.H.; Chao, M.J.; Liang, S.A.; Shi, Y.; Jain, B.R.; Bertelsen, S.E.; Kapoor, M.; Marcora, E.; et al. Cholesterol and matrisome pathways dysregulated in astrocytes and microglia. *Cell* **2022**, *185*, 2213–2233.e25. [CrossRef]
31. Lee, S.I.; Jeong, W.; Lim, H.; Cho, S.; Lee, H.; Jang, Y.; Cho, J.; Bae, S.; Lin, Y.T.; Tsai, L.H.; et al. APOE4-carrying human astrocytes oversupply cholesterol to promote neuronal lipid raft expansion and Aβ generation. *Stem Cell Rep.* **2021**, *16*, 2128–2137. [CrossRef]
32. Li, N.M.; Liu, K.F.; Qiu, Y.J.; Zhang, H.H.; Nakanishi, H.; Qing, H. Mutations of beta-amyloid precursor protein alter the consequence of Alzheimer's disease pathogenesis. *Neural Regen. Res.* **2019**, *14*, 658–665. [PubMed]
33. Selkoe, D.J. Presenilin, Notch, and the genesis and treatment of Alzheimer's disease. *Proc. Natl. Acad. Sci. USA* **2001**, *98*, 11039–11041. [CrossRef]
34. Weggen, S.; Beher, D. Molecular consequences of amyloid precursor protein and presenilin mutations causing autosomal-dominant Alzheimer's disease. *Alzheimers Res. Ther.* **2012**, *4*, 9. [CrossRef]
35. Szaruga, M.; Munteanu, B.; Lismont, S.; Veugelen, S.; Horré, K.; Mercken, M.; Saido, T.C.; Ryan, N.S.; De Vos, T.; Savvides, S.N.; et al. Alzheimer's-Causing Mutations Shift Aβ Length by Destabilizing γ-Secretase-Aβn Interactions. *Cell* **2017**, *170*, 443–456.e14. [CrossRef]
36. Sarasija, S.; Laboy, J.T.; Ashkavand, Z.; Bonner, J.; Tang, Y.; Norman, K.R. Presenilin mutations deregulate mitochondrial Ca. *Elife* **2018**, *7*, e33052. [CrossRef]
37. Walter, P.; Blobel, G. Translocation of proteins across the endoplasmic reticulum III. Signal recognition protein (SRP) causes signal sequence-dependent and site-specific arrest of chain elongation that is released by microsomal membranes. *J. Cell Biol.* **1981**, *91 Pt 1*, 557–561. [CrossRef] [PubMed]
38. Kellogg, M.K.; Miller, S.C.; Tikhonova, E.B.; Karamyshev, A.L. SRPassing Co-translational Targeting: The Role of the Signal Recognition Particle in Protein Targeting and mRNA Protection. *Int. J. Mol. Sci.* **2021**, *22*, 6284. [CrossRef]
39. Kellogg, M.K.; Tikhonova, E.B.; Karamyshev, A.L. Signal Recognition Particle in Human Diseases. *Front. Genet.* **2022**, *13*, 898083. [CrossRef]
40. von Heijne, G. Signal sequences. The limits of variation. *J. Mol. Biol.* **1985**, *184*, 99–105. [CrossRef]
41. von Heijne, G. Analysis of the distribution of charged residues in the N-terminal region of signal sequences: Implications for protein export in prokaryotic and eukaryotic cells. *EMBO J.* **1984**, *3*, 2315–2318. [CrossRef] [PubMed]
42. von Heijne, G. Protein targeting signals. *Curr. Opin. Cell Biol.* **1990**, *2*, 604–608. [CrossRef] [PubMed]

43. Nilsson, I.; Lara, P.; Hessa, T.; Johnson, A.E.; von Heijne, G.; Karamyshev, A.L. The code for directing proteins for translocation across ER membrane: SRP cotranslationally recognizes specific features of a signal sequence. *J. Mol. Biol.* **2015**, *427 Pt A*, 1191–1201. [CrossRef]
44. Karamyshev, A.L.; Patrick, A.E.; Karamysheva, Z.N.; Griesemer, D.S.; Hudson, H.; Tjon-Kon-Sang, S.; Nilsson, I.; Otto, H.; Liu, Q.; Rospert, S.; et al. Inefficient SRP interaction with a nascent chain triggers a mRNA quality control pathway. *Cell* **2014**, *156*, 146–157. [CrossRef] [PubMed]
45. Karamyshev, A.L.; Tikhonova, E.B.; Karamysheva, Z.N. Translational Control of Secretory Proteins in Health and Disease. *Int. J. Mol. Sci.* **2020**, *21*, 2538. [CrossRef] [PubMed]
46. Tikhonova, E.B.; Karamysheva, Z.N.; von Heijne, G.; Karamyshev, A.L. Silencing of Aberrant Secretory Protein Expression by Disease-Associated Mutations. *J. Mol. Biol.* **2019**, *431*, 2567–2580. [CrossRef]
47. Karamyshev, A.L.; Karamysheva, Z.N. Lost in Translation: Ribosome-Associated mRNA and Protein Quality Controls. *Front. Genet.* **2018**, *9*, 431. [CrossRef] [PubMed]
48. Karamysheva, Z.N.; Karamyshev, A.L. Aberrant protein targeting activates quality control on the ribosome. *Front. Cell Dev. Biol.* **2023**, *11*, 1198184. [CrossRef]
49. Pinarbasi, E.S.; Karamyshev, A.L.; Tikhonova, E.B.; Wu, I.H.; Hudson, H.; Thomas, P.J. Pathogenic Signal Sequence Mutations in Progranulin Disrupt SRP Interactions Required for mRNA Stability. *Cell Rep.* **2018**, *23*, 2844–2851. [CrossRef]
50. Karamysheva, Z.N.; Tikhonova, E.B.; Karamyshev, A.L. Granulin in Frontotemporal Lobar Degeneration: Molecular Mechanisms of the Disease. *Front. Neurosci.* **2019**, *13*, 395. [CrossRef]
51. Hernandez, S.M.; Tikhonova, E.B.; Baca, K.R.; Zhao, F.; Zhu, X.; Karamyshev, A.L. Unexpected Implication of SRP and AGO2 in Parkinson's Disease: Involvement in Alpha-Synuclein Biogenesis. *Cells* **2021**, *10*, 2792. [CrossRef]
52. Tikhonova, E.B.; Gutierrez Guarnizo, S.A.; Kellogg, M.K.; Karamyshev, A.; Dozmorov, I.M.; Karamysheva, Z.N.; Karamyshev, A.L. Defective Human SRP Induces Protein Quality Control and Triggers Stress Response. *J. Mol. Biol.* **2022**, *434*, 167832. [CrossRef] [PubMed]
53. Gadhave, K. The signal peptide of the amyloid precursor protein forms amyloid-like aggregates and enhances Ab42 aggregation. *Cell Rep. Phys. Sci.* **2021**, *2*, 100599. [CrossRef]
54. Selkoe, D.J. Alzheimer's disease: Genes, proteins, and therapy. *Physiol. Rev.* **2001**, *81*, 741–766. [CrossRef]
55. Rimal, S.; Li, Y.; Vartak, R.; Geng, J.; Tantray, I.; Li, S.; Huh, S.; Vogel, H.; Glabe, C.; Grinberg, L.T.; et al. Inefficient quality control of ribosome stalling during APP synthesis generates CAT-tailed species that precipitate hallmarks of Alzheimer's disease. *Acta Neuropathol. Commun.* **2021**, *9*, 169. [CrossRef] [PubMed]
56. Simon, S.M.; Blobel, G. A protein-conducting channel in the endoplasmic reticulum. *Cell* **1991**, *65*, 371–380. [CrossRef]
57. Rapoport, T.A. Protein transport across the endoplasmic reticulum membrane. *FEBS J.* **2008**, *275*, 4471–4478. [CrossRef]
58. Ast, T.; Cohen, G.; Schuldiner, M. A network of cytosolic factors targets SRP-independent proteins to the endoplasmic reticulum. *Cell* **2013**, *152*, 1134–1145. [CrossRef]
59. Liaci, A.M.; Förster, F. Take Me Home, Protein Roads: Structural Insights into Signal Peptide Interactions during ER Translocation. *Int. J. Mol. Sci.* **2021**, *22*, 11871. [CrossRef]
60. Goldgaber, D.; Lerman, M.I.; McBride, O.W.; Saffiotti, U.; Gajdusek, D.C. Characterization and chromosomal localization of a cDNA encoding brain amyloid of Alzheimer's disease. *Science* **1987**, *235*, 877–880. [CrossRef]
61. Yoshikai, S.; Sasaki, H.; Doh-ura, K.; Furuya, H.; Sakaki, Y. Genomic organization of the human amyloid beta-protein precursor gene. *Gene* **1990**, *87*, 257–263. [CrossRef]
62. Lamb, B.T.; Sisodia, S.S.; Lawler, A.M.; Slunt, H.H.; Kitt, C.A.; Kearns, W.G.; Pearson, P.L.; Price, D.L.; Gearhart, J.D. Introduction and expression of the 400 kilobase amyloid precursor protein gene in transgenic mice [corrected]. *Nat. Genet.* **1993**, *5*, 22–30. [CrossRef]
63. Delvaux, E.; Bentley, K.; Stubbs, V.; Sabbagh, M.; Coleman, P.D. Differential processing of amyloid precursor protein in brain and in peripheral blood leukocytes. *Neurobiol. Aging* **2013**, *34*, 1680–1686. [CrossRef]
64. Kang, J.; Müller-Hill, B. Differential splicing of Alzheimer's disease amyloid A4 precursor RNA in rat tissues: PreA4(695) mRNA is predominantly produced in rat and human brain. *Biochem. Biophys. Res. Commun.* **1990**, *166*, 1192–1200. [CrossRef]
65. Korte, M.; Herrmann, U.; Zhang, X.; Draguhn, A. The role of APP and APLP for synaptic transmission, plasticity, and network function: Lessons from genetic mouse models. *Exp. Brain Res.* **2012**, *217*, 435–440. [CrossRef] [PubMed]
66. Soba, P.; Eggert, S.; Wagner, K.; Zentgraf, H.; Siehl, K.; Kreger, S.; Löwer, A.; Langer, A.; Merdes, G.; Paro, R.; et al. Homo- and heterodimerization of APP family members promotes intercellular adhesion. *EMBO J.* **2005**, *24*, 3624–3634. [CrossRef] [PubMed]
67. Yamazaki, T.; Koo, E.H.; Selkoe, D.J. Cell surface amyloid beta-protein precursor colocalizes with beta 1 integrins at substrate contact sites in neural cells. *J. Neurosci.* **1997**, *17*, 1004–1010. [CrossRef] [PubMed]
68. Senechal, Y.; Kelly, P.H.; Dev, K.K. Amyloid precursor protein knockout mice show age-dependent deficits in passive avoidance learning. *Behav. Brain Res.* **2008**, *186*, 126–132. [CrossRef]
69. White, A.R.; Reyes, R.; Mercer, J.F.; Camakaris, J.; Zheng, H.; Bush, A.I.; Multhaup, G.; Beyreuther, K.; Masters, C.L.; Cappai, R. Copper levels are increased in the cerebral cortex and liver of APP and APLP2 knockout mice. *Brain Res.* **1999**, *842*, 439–444. [CrossRef]
70. Zhang, X.; Zhong, W.; Brankačk, J.; Weyer, S.W.; Müller, U.C.; Tort, A.B.; Draguhn, A. Impaired theta-gamma coupling in APP-deficient mice. *Sci. Rep.* **2016**, *6*, 21948. [CrossRef]

71. Young-Pearse, T.L.; Chen, A.C.; Chang, R.; Marquez, C.; Selkoe, D.J. Secreted APP regulates the function of full-length APP in neurite outgrowth through interaction with integrin beta1. *Neural Dev.* **2008**, *3*, 15. [CrossRef]
72. Obregon, D.; Hou, H.; Deng, J.; Giunta, B.; Tian, J.; Darlington, D.; Shahaduzzaman, M.; Zhu, Y.; Mori, T.; Mattson, M.P.; et al. Soluble amyloid precursor protein-α modulates β-secretase activity and amyloid-β generation. *Nat. Commun.* **2012**, *3*, 777. [CrossRef]
73. Ring, S.; Weyer, S.W.; Kilian, S.B.; Waldron, E.; Pietrzik, C.U.; Filippov, M.A.; Herms, J.; Buchholz, C.; Eckman, C.B.; Korte, M.; et al. The secreted beta-amyloid precursor protein ectodomain APPs alpha is sufficient to rescue the anatomical, behavioral, and electrophysiological abnormalities of APP-deficient mice. *J. Neurosci.* **2007**, *27*, 7817–7826. [CrossRef]
74. Farzan, M.; Schnitzler, C.E.; Vasilieva, N.; Leung, D.; Choe, H. BACE2, a beta -secretase homolog, cleaves at the beta site and within the amyloid-beta region of the amyloid-beta precursor protein. *Proc. Natl. Acad. Sci. USA* **2000**, *97*, 9712–9717. [CrossRef] [PubMed]
75. Laird, F.M.; Cai, H.; Savonenko, A.V.; Farah, M.H.; He, K.; Melnikova, T.; Wen, H.; Chiang, H.C.; Xu, G.; Koliatsos, V.E.; et al. BACE1, a major determinant of selective vulnerability of the brain to amyloid-beta amyloidogenesis, is essential for cognitive, emotional, and synaptic functions. *J. Neurosci.* **2005**, *25*, 11693–11709. [CrossRef] [PubMed]
76. Ohno, M.; Chang, L.; Tseng, W.; Oakley, H.; Citron, M.; Klein, W.L.; Vassar, R.; Disterhoft, J.F. Temporal memory deficits in Alzheimer's mouse models: Rescue by genetic deletion of BACE1. *Eur. J. Neurosci.* **2006**, *23*, 251–260. [CrossRef] [PubMed]
77. Ohno, M.; Sametsky, E.A.; Younkin, L.H.; Oakley, H.; Younkin, S.G.; Citron, M.; Vassar, R.; Disterhoft, J.F. BACE1 deficiency rescues memory deficits and cholinergic dysfunction in a mouse model of Alzheimer's disease. *Neuron* **2004**, *41*, 27–33. [CrossRef] [PubMed]
78. Araki, W. Post-translational regulation of the β-secretase BACE1. *Brain Res. Bull.* **2016**, *126 Pt 2*, 170–177. [CrossRef] [PubMed]
79. Andrew, R.J.; Fernandez, C.G.; Stanley, M.; Jiang, H.; Nguyen, P.; Rice, R.C.; Buggia-Prévot, V.; De Rossi, P.; Vetrivel, K.S.; Lamb, R.; et al. Lack of BACE1 S-palmitoylation reduces amyloid burden and mitigates memory deficits in transgenic mouse models of Alzheimer's disease. *Proc. Natl. Acad. Sci. USA* **2017**, *114*, E9665–E9674. [CrossRef] [PubMed]
80. Huse, J.T.; Liu, K.; Pijak, D.S.; Carlin, D.; Lee, V.M.; Doms, R.W. Beta-secretase processing in the trans-Golgi network preferentially generates truncated amyloid species that accumulate in Alzheimer's disease brain. *J. Biol. Chem.* **2002**, *277*, 16278–16284. [CrossRef]
81. Schneider, A.; Rajendran, L.; Honsho, M.; Gralle, M.; Donnert, G.; Wouters, F.; Hell, S.W.; Simons, M. Flotillin-dependent clustering of the amyloid precursor protein regulates its endocytosis and amyloidogenic processing in neurons. *J. Neurosci.* **2008**, *28*, 2874–2882. [CrossRef]
82. Sannerud, R.; Declerck, I.; Peric, A.; Raemaekers, T.; Menendez, G.; Zhou, L.; Veerle, B.; Coen, K.; Munck, S.; De Strooper, B.; et al. ADP ribosylation factor 6 (ARF6) controls amyloid precursor protein (APP) processing by mediating the endosomal sorting of BACE1. *Proc. Natl. Acad. Sci. USA* **2011**, *108*, E559–E568. [CrossRef] [PubMed]
83. Sakurai, T.; Kaneko, K.; Okuno, M.; Wada, K.; Kashiyama, T.; Shimizu, H.; Akagi, T.; Hashikawa, T.; Nukina, N. Membrane microdomain switching: A regulatory mechanism of amyloid precursor protein processing. *J. Cell Biol.* **2008**, *183*, 339–352. [CrossRef]
84. Bukhari, H.; Glotzbach, A.; Kolbe, K.; Leonhardt, G.; Loosse, C.; Müller, T. Small things matter: Implications of APP intracellular domain AICD nuclear signaling in the progression and pathogenesis of Alzheimer's disease. *Prog. Neurobiol.* **2017**, *156*, 189–213. [CrossRef] [PubMed]
85. Greenwood, E.K.; Angelova, D.M.; Büchner, H.M.I.; Brown, D.R. The AICD fragment of APP initiates a FoxO3a mediated response via FANCD2. *Mol. Cell. Neurosci.* **2022**, *122*, 103760. [CrossRef] [PubMed]
86. Zhou, D.; Noviello, C.; D'Ambrosio, C.; Scaloni, A.; D'Adamio, L. Growth factor receptor-bound protein 2 interaction with the tyrosine-phosphorylated tail of amyloid beta precursor protein is mediated by its Src homology 2 domain. *J. Biol. Chem.* **2004**, *279*, 25374–25380. [CrossRef]
87. Chen, W.J.; Goldstein, J.L.; Brown, M.S. NPXY, a sequence often found in cytoplasmic tails, is required for coated pit-mediated internalization of the low density lipoprotein receptor. *J. Biol. Chem.* **1990**, *265*, 3116–3123. [CrossRef]
88. Vieira, S.I.; Rebelo, S.; Domingues, S.C.; da Cruz e Silva, E.F.; da Cruz e Silva, O.A. S655 phosphorylation enhances APP secretory traffic. *Mol. Cell. Biochem.* **2009**, *328*, 145–154. [CrossRef]
89. Vieira, S.I.; Rebelo, S.; Esselmann, H.; Wiltfang, J.; Lah, J.; Lane, R.; Small, S.A.; Gandy, S.; da Cruz e Silva, E.F.; da Cruz e Silva, O.A. Retrieval of the Alzheimer's amyloid precursor protein from the endosome to the TGN is S655 phosphorylation state-dependent and retromer-mediated. *Mol. Neurodegener.* **2010**, *5*, 40. [CrossRef]
90. Jiang, S.; Li, Y.; Zhang, X.; Bu, G.; Xu, H.; Zhang, Y.W. Trafficking regulation of proteins in Alzheimer's disease. *Mol. Neurodegener.* **2014**, *9*, 6. [CrossRef]
91. Lee, M.S.; Kao, S.C.; Lemere, C.A.; Xia, W.; Tseng, H.C.; Zhou, Y.; Neve, R.; Ahlijanian, M.K.; Tsai, L.H. APP processing is regulated by cytoplasmic phosphorylation. *J. Cell Biol.* **2003**, *163*, 83–95. [CrossRef]
92. Suzuki, T.; Nakaya, T. Regulation of amyloid beta-protein precursor by phosphorylation and protein interactions. *J. Biol. Chem.* **2008**, *283*, 29633–29637. [CrossRef]
93. De Strooper, B. Aph-1, Pen-2, and Nicastrin with Presenilin generate an active gamma-Secretase complex. *Neuron* **2003**, *38*, 9–12. [CrossRef]

94. Krishnaswamy, S.; Verdile, G.; Groth, D.; Kanyenda, L.; Martins, R.N. The structure and function of Alzheimer's gamma secretase enzyme complex. *Crit. Rev. Clin. Lab. Sci.* **2009**, *46*, 282–301. [CrossRef]
95. Haapasalo, A.; Kovacs, D.M. The many substrates of presenilin/γ-secretase. *J. Alzheimers Dis.* **2011**, *25*, 3–28. [CrossRef] [PubMed]
96. Beel, A.J.; Sanders, C.R. Substrate specificity of gamma-secretase and other intramembrane proteases. *Cell. Mol. Life Sci.* **2008**, *65*, 1311–1334. [CrossRef] [PubMed]
97. Kanatsu, K.; Tomita, T. Membrane trafficking and proteolytic activity of γ-secretase in Alzheimer's disease. *Biol. Chem.* **2016**, *397*, 827–835. [CrossRef]
98. Hansson, C.A.; Frykman, S.; Farmery, M.R.; Tjernberg, L.O.; Nilsberth, C.; Pursglove, S.E.; Ito, A.; Winblad, B.; Cowburn, R.F.; Thyberg, J.; et al. Nicastrin, presenilin, APH-1, and PEN-2 form active gamma-secretase complexes in mitochondria. *J. Biol. Chem.* **2004**, *279*, 51654–51660. [CrossRef] [PubMed]
99. Sisodia, S.S. Beta-amyloid precursor protein cleavage by a membrane-bound protease. *Proc. Natl. Acad. Sci. USA* **1992**, *89*, 6075–6079. [CrossRef]
100. Carey, R.M.; Balcz, B.A.; Lopez-Coviella, I.; Slack, B.E. Inhibition of dynamin-dependent endocytosis increases shedding of the amyloid precursor protein ectodomain and reduces generation of amyloid beta protein. *BMC Cell Biol.* **2005**, *6*, 30. [CrossRef]
101. Goodger, Z.V.; Rajendran, L.; Trutzel, A.; Kohli, B.M.; Nitsch, R.M.; Konietzko, U. Nuclear signaling by the APP intracellular domain occurs predominantly through the amyloidogenic processing pathway. *J. Cell Sci.* **2009**, *122 Pt 20*, 3703–3714. [CrossRef]
102. Campioni, S.; Mannini, B.; Zampagni, M.; Pensalfini, A.; Parrini, C.; Evangelisti, E.; Relini, A.; Stefani, M.; Dobson, C.M.; Cecchi, C.; et al. A causative link between the structure of aberrant protein oligomers and their toxicity. *Nat. Chem. Biol.* **2010**, *6*, 140–147. [CrossRef]
103. Fitzpatrick, A.W.; Debelouchina, G.T.; Bayro, M.J.; Clare, D.K.; Caporini, M.A.; Bajaj, V.S.; Jaroniec, C.P.; Wang, L.; Ladizhansky, V.; Müller, S.A.; et al. Atomic structure and hierarchical assembly of a cross-β amyloid fibril. *Proc. Natl. Acad. Sci. USA* **2013**, *110*, 5468–5473. [CrossRef]
104. Gu, L.; Liu, C.; Guo, Z. Structural insights into Aβ42 oligomers using site-directed spin labeling. *J. Biol. Chem.* **2013**, *288*, 18673–18683. [CrossRef]
105. Sawaya, M.R.; Sambashivan, S.; Nelson, R.; Ivanova, M.I.; Sievers, S.A.; Apostol, M.I.; Thompson, M.J.; Balbirnie, M.; Wiltzius, J.J.; McFarlane, H.T.; et al. Atomic structures of amyloid cross-beta spines reveal varied steric zippers. *Nature* **2007**, *447*, 453–457. [CrossRef] [PubMed]
106. Scheidt, H.A.; Morgado, I.; Rothemund, S.; Huster, D. Dynamics of amyloid β fibrils revealed by solid-state NMR. *J. Biol. Chem.* **2012**, *287*, 2017–2021. [CrossRef] [PubMed]
107. Eisenberg, D.; Jucker, M. The amyloid state of proteins in human diseases. *Cell* **2012**, *148*, 1188–1203. [CrossRef]
108. Chen, J.; Armstrong, A.H.; Koehler, A.N.; Hecht, M.H. Small molecule microarrays enable the discovery of compounds that bind the Alzheimer's Aβ peptide and reduce its cytotoxicity. *J. Am. Chem. Soc.* **2010**, *132*, 17015–17022. [CrossRef]
109. Zhang, C.; Liu, Y.; Gilthorpe, J.; van der Maarel, J.R. MRP14 (S100A9) protein interacts with Alzheimer beta-amyloid peptide and induces its fibrillization. *PLoS ONE* **2012**, *7*, e32953. [CrossRef]
110. Camandola, S.; Mattson, M.P. Aberrant subcellular neuronal calcium regulation in aging and Alzheimer's disease. *Biochim. Biophys. Acta* **2011**, *1813*, 965–973. [CrossRef]
111. Demuro, A.; Smith, M.; Parker, I. Single-channel Ca(2+) imaging implicates Aβ1-42 amyloid pores in Alzheimer's disease pathology. *J. Cell Biol.* **2011**, *195*, 515–524. [CrossRef] [PubMed]
112. Johri, A.; Beal, M.F. Mitochondrial dysfunction in neurodegenerative diseases. *J. Pharmacol. Exp. Ther.* **2012**, *342*, 619–630. [CrossRef] [PubMed]
113. Moon, H.E.; Paek, S.H. Mitochondrial Dysfunction in Parkinson's Disease. *Exp. Neurobiol.* **2015**, *24*, 103–116. [CrossRef] [PubMed]
114. Anandatheerthavarada, H.K.; Biswas, G.; Mullick, J.; Sepuri, N.B.; Otvos, L.; Pain, D.; Avadhani, N.G. Dual targeting of cytochrome P4502B1 to endoplasmic reticulum and mitochondria involves a novel signal activation by cyclic AMP-dependent phosphorylation at ser128. *EMBO J.* **1999**, *18*, 5494–5504. [CrossRef] [PubMed]
115. Robin, M.A.; Anandatheerthavarada, H.K.; Biswas, G.; Sepuri, N.B.; Gordon, D.M.; Pain, D.; Avadhani, N.G. Bimodal targeting of microsomal CYP2E1 to mitochondria through activation of an N-terminal chimeric signal by cAMP-mediated phosphorylation. *J. Biol. Chem.* **2002**, *277*, 40583–40593. [CrossRef]
116. Devi, L.; Prabhu, B.M.; Galati, D.F.; Avadhani, N.G.; Anandatheerthavarada, H.K. Accumulation of amyloid precursor protein in the mitochondrial import channels of human Alzheimer's disease brain is associated with mitochondrial dysfunction. *J. Neurosci.* **2006**, *26*, 9057–9068. [CrossRef]
117. Vaillant-Beuchot, L.; Mary, A.; Pardossi-Piquard, R.; Bourgeois, A.; Lauritzen, I.; Eysert, F.; Kinoshita, P.F.; Cazareth, J.; Badot, C.; Fragaki, K.; et al. Accumulation of amyloid precursor protein C-terminal fragments triggers mitochondrial structure, function, and mitophagy defects in Alzheimer's disease models and human brains. *Acta Neuropathol.* **2021**, *141*, 39–65. [CrossRef]
118. Mossmann, D.; Vögtle, F.N.; Taskin, A.A.; Teixeira, P.F.; Ring, J.; Burkhart, J.M.; Burger, N.; Pinho, C.M.; Tadic, J.; Loreth, D.; et al. Amyloid-β peptide induces mitochondrial dysfunction by inhibition of preprotein maturation. *Cell Metab.* **2014**, *20*, 662–669. [CrossRef]
119. Sorrentino, V.; Romani, M.; Mouchiroud, L.; Beck, J.S.; Zhang, H.; D'Amico, D.; Moullan, N.; Potenza, F.; Schmid, A.W.; Rietsch, S.; et al. Enhancing mitochondrial proteostasis reduces amyloid-β proteotoxicity. *Nature* **2017**, *552*, 187–193. [CrossRef]

120. Calvo-Rodriguez, M.; Bacskai, B.J. Mitochondria and Calcium in Alzheimer's Disease: From Cell Signaling to Neuronal Cell Death. *Trends Neurosci.* **2021**, *44*, 136–151. [CrossRef]
121. Strope, T.A.; Wilkins, H.M. Amyloid precursor protein and mitochondria. *Curr. Opin. Neurobiol.* **2023**, *78*, 102651. [CrossRef]
122. Lykhmus, O.; Koval, L.; Voytenko, L.; Uspenska, K.; Komisarenko, S.; Deryabina, O.; Shuvalova, N.; Kordium, V.; Ustymenko, A.; Kyryk, V.; et al. Intravenously Injected Mesenchymal Stem Cells Penetrate the Brain and Treat Inflammation-Induced Brain Damage and Memory Impairment in Mice. *Front. Pharmacol.* **2019**, *10*, 355. [CrossRef]
123. Xu, F.; Wu, Y.; Yang, Q.; Cheng, Y.; Xu, J.; Zhang, Y.; Dai, H.; Wang, B.; Ma, Q.; Chen, Y.; et al. Engineered Extracellular Vesicles with SHP2 High Expression Promote Mitophagy for Alzheimer's Disease Treatment. *Adv. Mater.* **2022**, *34*, e2207107. [CrossRef] [PubMed]
124. Yin, T.; Liu, Y.; Ji, W.; Zhuang, J.; Chen, X.; Gong, B.; Chu, J.; Liang, W.; Gao, J.; Yin, Y. Engineered mesenchymal stem cell-derived extracellular vesicles: A state-of-the-art multifunctional weapon against Alzheimer's disease. *Theranostics* **2023**, *13*, 1264–1285. [CrossRef]
125. Vamecq, J.; Latruffe, N. Medical significance of peroxisome proliferator-activated receptors. *Lancet* **1999**, *354*, 141–148. [CrossRef] [PubMed]
126. Luo, R.; Su, L.Y.; Li, G.; Yang, J.; Liu, Q.; Yang, L.X.; Zhang, D.F.; Zhou, H.; Xu, M.; Fan, Y.; et al. Activation of PPARA-mediated autophagy reduces Alzheimer disease-like pathology and cognitive decline in a murine model. *Autophagy* **2020**, *16*, 52–69. [CrossRef] [PubMed]
127. Sastre, M.; Dewachter, I.; Rossner, S.; Bogdanovic, N.; Rosen, E.; Borghgraef, P.; Evert, B.O.; Dumitrescu-Ozimek, L.; Thal, D.R.; Landreth, G.; et al. Nonsteroidal anti-inflammatory drugs repress beta-secretase gene promoter activity by the activation of PPARgamma. *Proc. Natl. Acad. Sci. USA* **2006**, *103*, 443–448. [CrossRef] [PubMed]
128. Chen, X.F.; Zhang, Y.W.; Xu, H.; Bu, G. Transcriptional regulation and its misregulation in Alzheimer's disease. *Mol. Brain* **2013**, *6*, 44. [CrossRef] [PubMed]
129. Christensen, M.A.; Zhou, W.; Qing, H.; Lehman, A.; Philipsen, S.; Song, W. Transcriptional regulation of BACE1, the beta-amyloid precursor protein beta-secretase, by Sp1. *Mol. Cell. Biol.* **2004**, *24*, 865–874. [CrossRef]
130. Hirano, F.; Tanaka, H.; Hirano, Y.; Hiramoto, M.; Handa, H.; Makino, I.; Scheidereit, C. Functional interference of Sp1 and NF-kappaB through the same DNA binding site. *Mol. Cell. Biol.* **1998**, *18*, 1266–1274. [CrossRef] [PubMed]
131. Rossello, X.S.; Igbavboa, U.; Weisman, G.A.; Sun, G.Y.; Wood, W.G. AP-2β regulates amyloid beta-protein stimulation of apolipoprotein E transcription in astrocytes. *Brain Res.* **2012**, *1444*, 87–95. [CrossRef]
132. Das, H.K. Transcriptional regulation of the presenilin-1 gene: Implication in Alzheimer's disease. *Front. Biosci.* **2008**, *13*, 822–832. [CrossRef]
133. Pastorcic, M.; Das, H.K. Regulation of transcription of the human presenilin-1 gene by ets transcription factors and the p53 protooncogene. *J. Biol. Chem.* **2000**, *275*, 34938–34945. [CrossRef]
134. Pastorcic, M.; Das, H.K. Analysis of transcriptional modulation of the presenilin 1 gene promoter by ZNF237, a candidate binding partner of the Ets transcription factor ERM. *Brain Res.* **2007**, *1128*, 21–32. [CrossRef]
135. Hwang, E.M.; Kim, S.K.; Sohn, J.H.; Lee, J.Y.; Kim, Y.; Kim, Y.S.; Mook-Jung, I. Furin is an endogenous regulator of alpha-secretase associated APP processing. *Biochem. Biophys. Res. Commun.* **2006**, *349*, 654–659. [CrossRef]
136. Zhang, Y.; Bai, X.; Yao, S.; Cui, Y.; You, L.H.; Yu, P.; Chang, Y.Z.; Gao, G. Hippocampal Iron Accumulation Impairs Synapses and Memory via Suppressing Furin Expression and Downregulating BDNF Maturation. *Mol. Neurobiol.* **2022**, *59*, 5574–5590. [CrossRef]
137. Beckelman, B.C.; Yang, W.; Kasica, N.P.; Zimmermann, H.R.; Zhou, X.; Keene, C.D.; Ryazanov, A.G.; Ma, T. Genetic reduction of eEF2 kinase alleviates pathophysiology in Alzheimer's disease model mice. *J. Clin. Investig.* **2019**, *129*, 820–833. [CrossRef]
138. Zhang, N.; Yu, X.; Xie, J.; Xu, H. New Insights into the Role of Ferritin in Iron Homeostasis and Neurodegenerative Diseases. *Mol. Neurobiol.* **2021**, *58*, 2812–2823. [CrossRef]
139. Altamura, S.; Muckenthaler, M.U. Iron toxicity in diseases of aging: Alzheimer's disease, Parkinson's disease and atherosclerosis. *J. Alzheimers Dis.* **2009**, *16*, 879–895. [CrossRef]
140. Rogers, J.T.; Randall, J.D.; Cahill, C.M.; Eder, P.S.; Huang, X.; Gunshin, H.; Leiter, L.; McPhee, J.; Sarang, S.S.; Utsuki, T.; et al. An iron-responsive element type II in the 5′-untranslated region of the Alzheimer's amyloid precursor protein transcript. *J. Biol. Chem.* **2002**, *277*, 45518–45528. [CrossRef]
141. Hetz, C. The unfolded protein response: Controlling cell fate decisions under ER stress and beyond. *Nat. Rev. Mol. Cell Biol.* **2012**, *13*, 89–102. [CrossRef]
142. Cozachenco, D.; Ribeiro, F.C.; Ferreira, S.T. Defective proteostasis in Alzheimer's disease. *Ageing Res. Rev.* **2023**, *85*, 101862. [CrossRef]
143. Hosokawa, N.; Wada, I.; Hasegawa, K.; Yorihuzi, T.; Tremblay, L.O.; Herscovics, A.; Nagata, K. A novel ER alpha-mannosidase-like protein accelerates ER-associated degradation. *EMBO Rep.* **2001**, *2*, 415–422. [CrossRef]
144. Nowakowska-Gołacka, J.; Czapiewska, J.; Sominka, H.; Sowa-Rogozińska, N.; Słomińska-Wojewódzka, M. EDEM1 Regulates Amyloid Precursor Protein (APP) Metabolism and Amyloid-β Production. *Int. J. Mol. Sci.* **2021**, *23*, 117. [CrossRef]
145. Joshi, G.; Wang, Y. Golgi defects enhance APP amyloidogenic processing in Alzheimer's disease. *Bioessays* **2015**, *37*, 240–247. [CrossRef]

146. Joshi, G.; Chi, Y.; Huang, Z.; Wang, Y. Aβ-induced Golgi fragmentation in Alzheimer's disease enhances Aβ production. *Proc. Natl. Acad. Sci. USA* **2014**, *111*, E1230–E1239. [CrossRef]
147. Teunissen, C.E.; Verberk, I.M.W.; Thijssen, E.H.; Vermunt, L.; Hansson, O.; Zetterberg, H.; van der Flier, W.M.; Mielke, M.M.; Del Campo, M. Blood-based biomarkers for Alzheimer's disease: Towards clinical implementation. *Lancet Neurol.* **2022**, *21*, 66–77. [CrossRef]
148. Hansson, O. Biomarkers for neurodegenerative diseases. *Nat. Med.* **2021**, *27*, 954–963. [CrossRef]
149. Hansson, O.; Edelmayer, R.M.; Boxer, A.L.; Carrillo, M.C.; Mielke, M.M.; Rabinovici, G.D.; Salloway, S.; Sperling, R.; Zetterberg, H.; Teunissen, C.E. The Alzheimer's Association appropriate use recommendations for blood biomarkers in Alzheimer's disease. *Alzheimers Dement.* **2022**, *18*, 2669–2686. [CrossRef] [PubMed]
150. Söderberg, L.; Johannesson, M.; Nygren, P.; Laudon, H.; Eriksson, F.; Osswald, G.; Möller, C.; Lannfelt, L. Lecanemab, Aducanumab, and Gantenerumab—Binding Profiles to Different Forms of Amyloid-Beta Might Explain Efficacy and Side Effects in Clinical Trials for Alzheimer's Disease. *Neurotherapeutics* **2023**, *20*, 195–206. [CrossRef] [PubMed]
151. Jia, Y.; Cao, N.; Zhai, J.; Zeng, Q.; Zheng, P.; Su, R.; Liao, T.; Liu, J.; Pei, H.; Fan, Z.; et al. HGF Mediates Clinical-Grade Human Umbilical Cord-Derived Mesenchymal Stem Cells Improved Functional Recovery in a Senescence-Accelerated Mouse Model of Alzheimer's Disease. *Adv. Sci.* **2020**, *7*, 1903809. [CrossRef] [PubMed]
152. Neves, A.F.; Camargo, C.; Premer, C.; Hare, J.M.; Baumel, B.S.; Pinto, M. Intravenous administration of mesenchymal stem cells reduces Tau phosphorylation and inflammation in the 3xTg-AD mouse model of Alzheimer's disease. *Exp. Neurol.* **2021**, *341*, 113706. [CrossRef]
153. Yang, H.; Yue, C.; Xie, Z.; Hu, H.; Wei, L.; Wang, P.; Zhao, C.; Bi, J. Intravenous Administration of Human Umbilical Cord Mesenchymal Stem Cells Improves Cognitive Impairments and Reduces Amyloid-Beta Deposition in an AβPP/PS1 Transgenic Mouse Model. *Neurochem. Res.* **2013**, *38*, 2474–2482. [CrossRef] [PubMed]
154. Lim, J.Y.; In Park, S.; Park, S.A.; Jeon, J.H.; Jung, H.Y.; Yon, J.M.; Jeun, S.S.; Lim, H.K.; Kim, S.W. Potential application of human neural crest-derived nasal turbinate stem cells for the treatment of neuropathology and impaired cognition in models of Alzheimer's disease. *Stem Cell Res. Ther.* **2021**, *12*, 402. [CrossRef] [PubMed]
155. Lim, J.Y.; Lee, J.E.; Park, S.A.; Park, S.I.; Yon, J.M.; Park, J.A.; Jeun, S.S.; Kim, S.J.; Lee, H.J.; Kim, S.W.; et al. Protective Effect of Human-Neural-Crest-Derived Nasal Turbinate Stem Cells against Amyloid-β Neurotoxicity through Inhibition of Osteopontin in a Human Cerebral Organoid Model of Alzheimer's Disease. *Cells* **2022**, *11*, 1029. [CrossRef]
156. Zhang, H.A.; Yuan, C.X.; Liu, K.F.; Yang, Q.F.; Zhao, J.; Li, H.; Yang, Q.H.; Song, D.; Quan, Z.Z.; Qing, H. Neural stem cell transplantation alleviates functional cognitive deficits in a mouse model of tauopathy. *Neural Regen. Res.* **2022**, *17*, 152–162. [PubMed]
157. Chu, J.J.; Ji, W.B.; Zhuang, J.H.; Gong, B.F.; Chen, X.H.; Cheng, W.B.; Liang, W.D.; Li, G.R.; Gao, J.; Yin, Y. Nanoparticles-based anti-aging treatment of Alzheimer's disease. *Drug Deliv.* **2022**, *29*, 2100–2116. [CrossRef]
158. Zhong, G.; Long, H.; Zhou, T.; Liu, Y.; Zhao, J.; Han, J.; Yang, X.; Yu, Y.; Chen, F.; Shi, S. Blood-brain barrier Permeable nanoparticles for Alzheimer's disease treatment by selective mitophagy of microglia. *Biomaterials* **2022**, *288*, 121690. [CrossRef]

International Journal of
Molecular Sciences

MDPI

Article

Simufilam Reverses Aberrant Receptor Interactions of Filamin A in Alzheimer's Disease

Hoau-Yan Wang [1,2], Erika Cecon [3], Julie Dam [3], Zhe Pei [1], Ralf Jockers [3] and Lindsay H. Burns [4,*]

[1] Department of Molecular, Cellular and Biomedical Sciences, City University of New York School of Medicine, New York, NY 10031, USA; hwang@med.cuny.edu (H.-Y.W.); zpei@ccny.cuny.edu (Z.P.)
[2] Department of Biology and Neuroscience, Graduate School, City University of New York, New York, NY 10016, USA
[3] Institut Cochin, INSERM, CNRS, Université Paris Cité, 75014 Paris, France; erika.cecon@inserm.fr (E.C.); julie.dam@inserm.fr (J.D.); ralf.jockers@inserm.fr (R.J.)
[4] Cassava Sciences, Inc., Austin, TX 78731, USA
* Correspondence: lburns@cassavascienaces.com

Abstract: Simufilam is a novel oral drug candidate in Phase 3 clinical trials for Alzheimer's disease (AD) dementia. This small molecule binds an altered form of filamin A (FLNA) that occurs in AD. This drug action disrupts FLNA's aberrant linkage to the α7 nicotinic acetylcholine receptor (α7nAChR), thereby blocking soluble amyloid beta$_{1–42}$ (Aβ_{42})'s signaling via α7nAChR that hyperphosphorylates tau. Here, we aimed to clarify simufilam's mechanism. We now show that simufilam reduced Aβ_{42} binding to α7nAChR with a 10-picomolar IC_{50} using time-resolved fluorescence resonance energy transfer (TR-FRET), a robust technology to detect highly sensitive molecular interactions. We also show that FLNA links to multiple inflammatory receptors in addition to Toll-like receptor 4 (TLR4) in postmortem human AD brains and in AD transgenic mice: TLR2, C-X-C chemokine receptor type 4 (CXCR4), C-C chemokine receptor type 5 (CCR5), and T-cell co-receptor cluster of differentiation 4 (CD4). These aberrant FLNA linkages, which can be induced in a healthy control brain by Aβ_{42} incubation, were disrupted by simufilam. Simufilam reduced inflammatory cytokine release from Aβ_{42}-stimulated human astrocytes. In the AD transgenic mice, CCR5–G protein coupling was elevated, indicating persistent activation. Oral simufilam reduced both the FLNA–CCR5 linkage and the CCR5–G protein coupling in these mice, while restoring CCR5's responsivity to C-C chemokine ligand 3 (CCL3). By disrupting aberrant FLNA–receptor interactions critical to AD pathogenic pathways, simufilam may promote brain health.

Keywords: α7 nicotinic acetylcholine receptor; TLR4; TLR2; CXCR4; CD4; CCR5; TR-FRET

Citation: Wang, H.-Y.; Cecon, E.; Dam, J.; Pei, Z.; Jockers, R.; Burns, L.H. Simufilam Reverses Aberrant Receptor Interactions of Filamin A in Alzheimer's Disease. *Int. J. Mol. Sci.* **2023**, *24*, 13927. https://doi.org/10.3390/ijms241813927

Academic Editor: Claudia Ricci

Received: 7 August 2023
Revised: 29 August 2023
Accepted: 4 September 2023
Published: 11 September 2023

1. Introduction

Alzheimer's disease (AD) is the most common neurodegenerative disease and the most common form of dementia, with over 55 million cases worldwide and expected to double every 20 years, underscoring the need for effective disease-modifying treatments [1]. In the U.S., there are 6.7 million people living with AD with an additional 11 million family and friends caring for them [2], totaling 5.3% of the U.S. population.

The FDA has recently approved two anti-amyloid antibody therapies for patients with early AD. These infusion drugs are celebrated as nominal successes, tempered by their modest impact on disease progression, a black box cautionary warning regarding cerebral hemorrhages, the possible need for APOE genotyping and PET scans, the requirement for frequent MRIs to monitor drug-induced brain swelling and brain bleeding, and the inconveniences and exceptional expense of drug infusion therapy, which also limit access to rural or underserved populations [3]. More recently noted is the possible shrinkage of brain volume over time, which is not fully understood [4]. Adding complexity, drug effectiveness may vary by gender and APOE genotype [5] and degree of tau deposition [6].

Finally, the regulatory use of these infusion drugs is restricted to patients with early AD, i.e., mild cognitive impairment and mild AD.

Alternatives to anti-amyloid therapies are sorely needed. Those being investigated clinically include agents targeting tau, neuroinflammation, synaptic plasticity, metabolism or proteostasis [7]. Simufilam is a novel oral drug candidate with preclinical data showing reduced tau hyperphosphorylation and neurofibrillary tangles, reduced neuroinflammation, improved synaptic plasticity and improved insulin receptor signaling. We posit that all these beneficial effects are downstream to restoring the normal conformation of simufilam's target protein, altered FLNA [8–10].

FLNA is a large intracellular scaffolding protein known to interact with over 90 different proteins [11]. It contains 24 immunoglobulin-like repeats, two hinge regions and two rod domains [12,13]. The 24th repeat dimerizes in the membrane to form a V shape inside the cell. Best known for cross-linking actin via the N-terminal domain to provide structure and motility, FLNA also serves as a scaffold for channels, receptors, signaling molecules and even transcription factors, illustrating a role beyond structure [11,14,15]. FLNA is highly expressed in the brain, and its protein interactions are regulated by mechanical forces, phosphorylation, cleavage and other factors [11,13,16,17].

An altered conformation of FLNA would likely alter certain protein interactions or induce aberrant ones. A region of FLNA unfolds under forces as low as 10 pN [17], and stress-induced conformational changes have been hypothesized to play a direct role in signaling, either by disrupting existing interactions or inducing new ones [18]. In an altered conformation implied by a shift in isoelectric focusing point [8,10,19] and a change in solubility [16], FLNA appears to be a critical and deviant receptor-associated protein underlying multiple facets of AD pathology [9,10]. Specifically, deviant FLNA linkages are critical to $A\beta_{42}$-induced tau hyperphosphorylation, leading to neurodegeneration, and to $A\beta_{42}$-induced activation of TLR4, leading to neuroinflammation [9,10]. The disruption of these aberrant receptor interactions by simufilam is coincident with a reversal of the shift in isoelectric focusing, implying a reversion to FLNA's native shape [8,10].

Simufilam's primary mechanism is to disrupt the toxic signaling of soluble $A\beta_{42}$ via the α7nAChR that hyperphosphorylates tau [9,10,20]. The ultra-high-affinity binding of $A\beta_{42}$ for α7nAChR was first published in 2000 [21,22], and this $A\beta_{42}$–α7nAChR interaction was later shown by Wang and other researchers to activate kinases that hyperphosphorylate tau [23–26].

Hyperphosphorylated tau can no longer stabilize microtubules, impairing intraneuronal transport of proteins, which causes the accumulation of hyperphosphorylated tau aggregates, eventual neurodegeneration and tau-containing tangles [27–29]. As increasing soluble $A\beta_{42}$ piles onto this receptor, the $A\beta_{42}$–α7nAChR complex is internalized into the cell by endocytosis, leading to intraneuronal amyloid aggregates and eventual amyloid deposits or dense-core plaques after cell death [30,31]. Hence, this pathogenic signaling pathway of soluble $A\beta_{42}$ mechanistically links the hallmark plaques and tangles [30,32,33].

Simufilam dismantles this prominent AD pathogenic pathway by disrupting the linkage of FLNA with α7nAChR, an interaction critical both to the toxic signaling and to the ultra-high-affinity binding of $A\beta_{42}$ [9]. By disrupting this pathway in the AD brain, simufilam slows or reduces neurodegeneration.

This aberrant FLNA–α7nAChR linkage can be induced in normal tissue by incubation with $A\beta_{42}$, along with the shift in isoelectric focusing point that implies an altered conformation of FLNA [10], and both are reversible by simufilam [8,10]. By disrupting the FLNA–α7nAChR linkage and restoring the native FLNA conformation, simufilam reduced the femtomolar binding affinity of $A\beta_{42}$ for α7nAChR 1000-fold in postmortem brain synaptic membranes and 10,000-fold in SK-N-MC cells [9]. In the current work, we used a cell-based TR-FRET assay [34] to confirm that simufilam reduces $A\beta_{42}$ binding to α7nAChR.

The second pathogenic signaling pathway of soluble amyloid that is disrupted by simufilam is $A\beta_{42}$'s persistent activation of TLR4 by $A\beta_{42}$ binding to the TLR4 co-receptor CD14 [35]. TLR4's activation by $A\beta_{42}$ requires the aberrant linkage of FLNA with TLR4 [8–10]. In a similar mechanism, simufilam disrupts the FLNA–TLR4 linkage to suppress the persistent activation of this receptor and resulting inflammatory cytokine release to suppress neuroinflammation [8–10].

Because neuroinflammation is a prominent AD pathology [36], we explored whether $A\beta_{42}$ may induce FLNA linkages with other inflammatory receptors found on microglia that are involved in a persistent inflammatory response. TLR2 was selected as it is also activated by $A\beta_{42}$ [37], but, unlike TLR4, does not use the CD14 co-receptor for activation and produces different cytokines and chemokines [38]. The chemokine receptors CXCR4 and CCR5 and T-cell receptor CD4 were selected because they act synergistically or stepwise in inflammation. CCR5 is a prominent chemokine receptor upregulated on microglia in AD [39]. CXCR4 and CD4 are also expressed on microglia and often cluster with CCR5 [40].

We assessed whether ex vivo simufilam incubation of postmortem human AD brains or oral administration of simufilam to triple transgenic AD mice could disrupt these additional aberrant FLNA–receptor linkages. Next, to determine whether the FLNA linkages with these receptors may indicate receptor activation and whether simufilam could suppress their activation by disrupting the FLNA–receptor linkages, we tested simufilam's effects on inflammatory cytokine release in human astrocytes stimulated in vitro with $A\beta_{42}$, lipopolysaccharide (LPS; an activator of TLR4), or TLR2 ligands: lipoteichoic acid from Staphylococcus aureus (LTA-SA) and peptidoglycan from Staphylococcus aureus (PGN-SA). Finally, in the brains of the AD transgenic mice, we examined whether the FLNA linkage with CCR5, a G-protein-coupled receptor, was coincident with elevated G protein coupling by CCR5, which would indicate persistent CCR5 activation and potentially an insensitivity to CCR5's natural ligand CCL3. The AD transgenic mice administered oral simufilam in drinking water allowed for the assessment of simufilam's effects on persistent CCR5 activation and dysfunction.

2. Results

2.1. Simufilam Reduced $A\beta_{42}$ Binding to α7nAChR

The effect of simufilam on $A\beta_{42}$ binding to α7nAChR was determined by a TR-FRET assay, which relies on the excitation of $A\beta_{42}$-FAM (donor fluorophore) to produce an energy transfer to SNAP-α7nAChR (acceptor fluorophore) if they are in close proximity (<10 nm; Förster radius). Simufilam reduced $A\beta_{42}$ binding to α7nAChR in a concentration-dependent manner, with a mean IC_{50} of four separate experiments in the pM range (pIC_{50} = 10.9 ± 0.5 or 12.6 pM when converted to molarity) (Figure 1). By comparison, the mean IC_{50} for unlabeled $A\beta_{42}$ was also in the low pM range (pIC_{50} = 11.9 ± 0.5 or 1.3 pM). Because simufilam does not directly interact with either $A\beta_{42}$ or α7nAChR, its reduction in $A\beta_{42}$ binding to α7nAChR in this assay is hypothesized to occur by dissociating FLNA from the $A\beta_{42}$–α7nAChR complex, thereby releasing $A\beta_{42}$ in a concentration-dependent manner. This result corroborates our earlier demonstration that simufilam reduces $A\beta_{42}$ affinity (increasing off rate) for α7nAChRs in SK-N-MC cells and postmortem human brains [9].

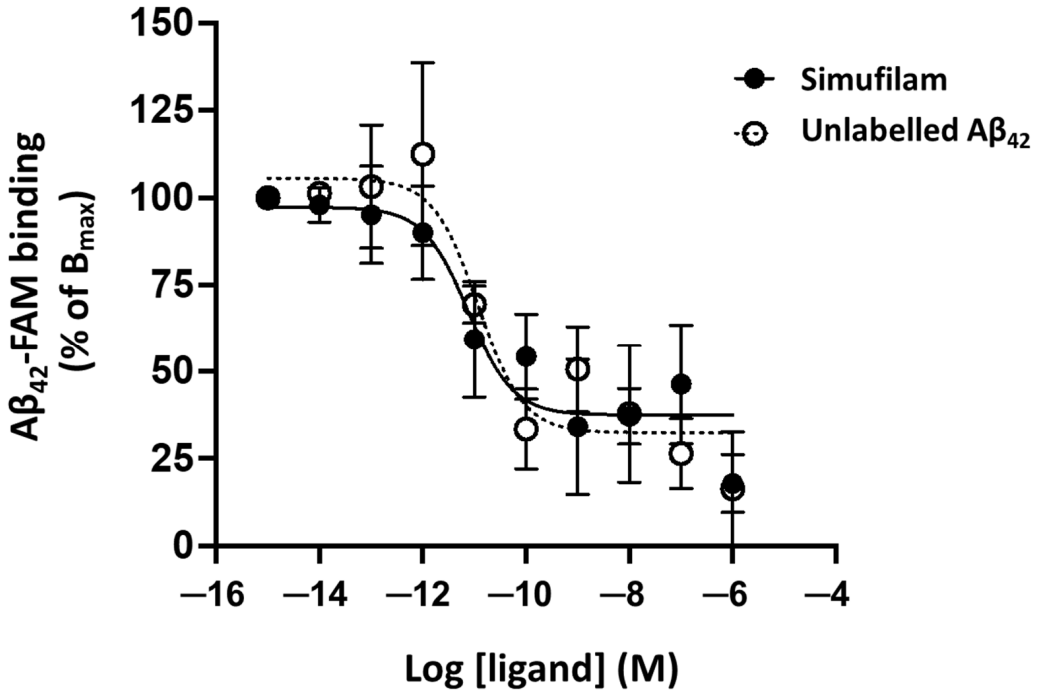

Figure 1. Simufilam reduced $A\beta_{42}$ binding to α7nAChR in a TR-FRET assay. $A\beta_{42}$-FAM binding to SNAP-α7nAChR in HEK293T cells was measured in the presence of increasing concentrations of simufilam or unlabeled $A\beta_{42}$. Data are means of pooled data from 4 separate experiments ± SEM.

2.2. Simufilam Reduced FLNA–TLR2 Linkage and Cytokine Release Stimulated by $A\beta_{42}$ and TLR2 Agonists

Because FLNA also links to TLR4, allowing $A\beta_{42}$'s chronic activation of this receptor via its co-receptor CD14, we next examined whether FLNA might also interact with TLR2, which is stimulated by $A\beta_{42}$ directly [37]. Incubation of a control postmortem human frontal cortex with $A\beta_{42}$ or the TLR2 ligands (LTA-SA or PGN-SA) dramatically elevated the levels of FLNA linkage to TLR2 ($p < 0.001$; Figure 2). Simufilam incubation at 1 or 10 nM reduced these FLNA–TLR2 linkages induced by $A\beta_{42}$ or the TLR2 agonists ($p < 0.01$). The similar effects of 1 and 10 nM simufilam suggest that 1 nM is a saturating concentration and is in accordance with the picomolar IC_{50} demonstrated for reducing $A\beta_{42}$ binding to α7nAChR.

The co-immunoprecipitation experiments to determine protein–protein interactions were conducted with synaptosomes, i.e., sealed presynaptic terminals that can be prepared in high yield (~80%) from brain tissue, which have been used since the 1960s [41–44] and specifically to examine synaptic terminals in AD brain tissue [45].

To assess whether the FLNA linkage represents activation of TLR2 by these ligands and whether its disruption might reduce such activation, we measured cytokine release from human astrocytes stimulated for 24 h with $A\beta_{42}$, the TLR2 agonists or LPS (a TLR4 activator) and measured the effect of simufilam, added 2 h prior to the stimulants, on the cytokine release. Simufilam at 100 fM, 10 pM or 1 nM reduced the release of inflammatory cytokines tumor necrosis factor α (TNFα), interleukin (IL)-6 and IL-1β by approximately 75% or more ($p < 0.001$; Figure 3). It is possible that the lack of concentration response in this experiment is related to the 2 h pre-treatment with simufilam prior to the 16 h incubation with the stimulants, favoring simufilam's prevention of cytokine release.

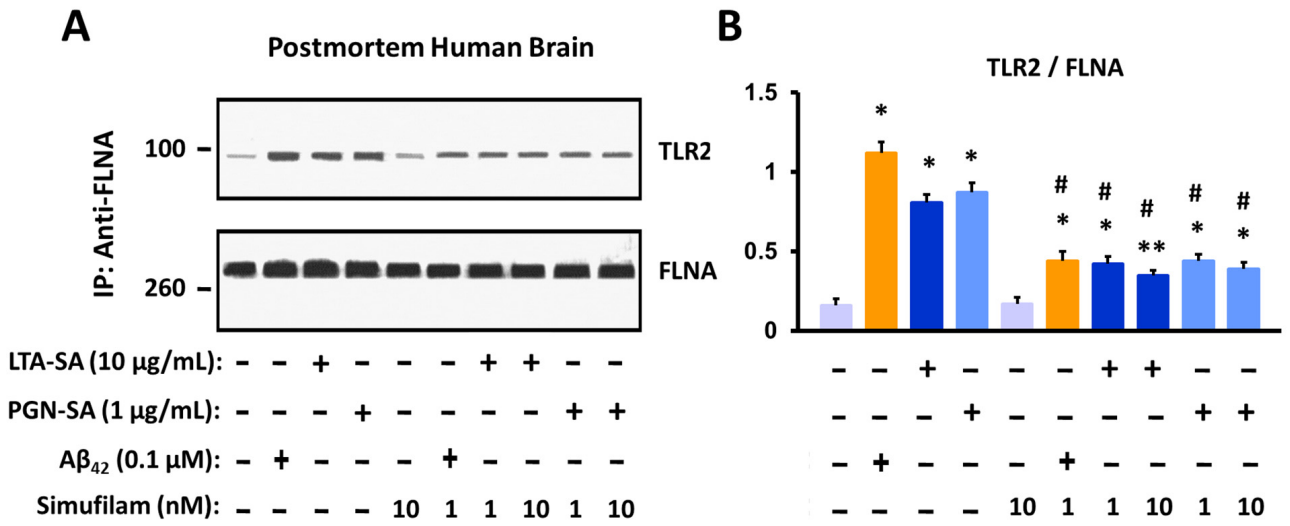

Figure 2. Incubation of postmortem human frontal cortex with TLR2 ligands or Aβ_{42} increases FLNA linkage with TLR2. This FLNA—TLR2 linkage is inhibited by simufilam at 1 or 10 nM. Representative blots (**A**) and densitometric quantitation of blots (**B**). Data are means ± SEM. N = 3. * $p < 0.001$, ** $p < 0.01$ vs. medium alone; # $p < 0.01$ vs. respective stimulant without simufilam.

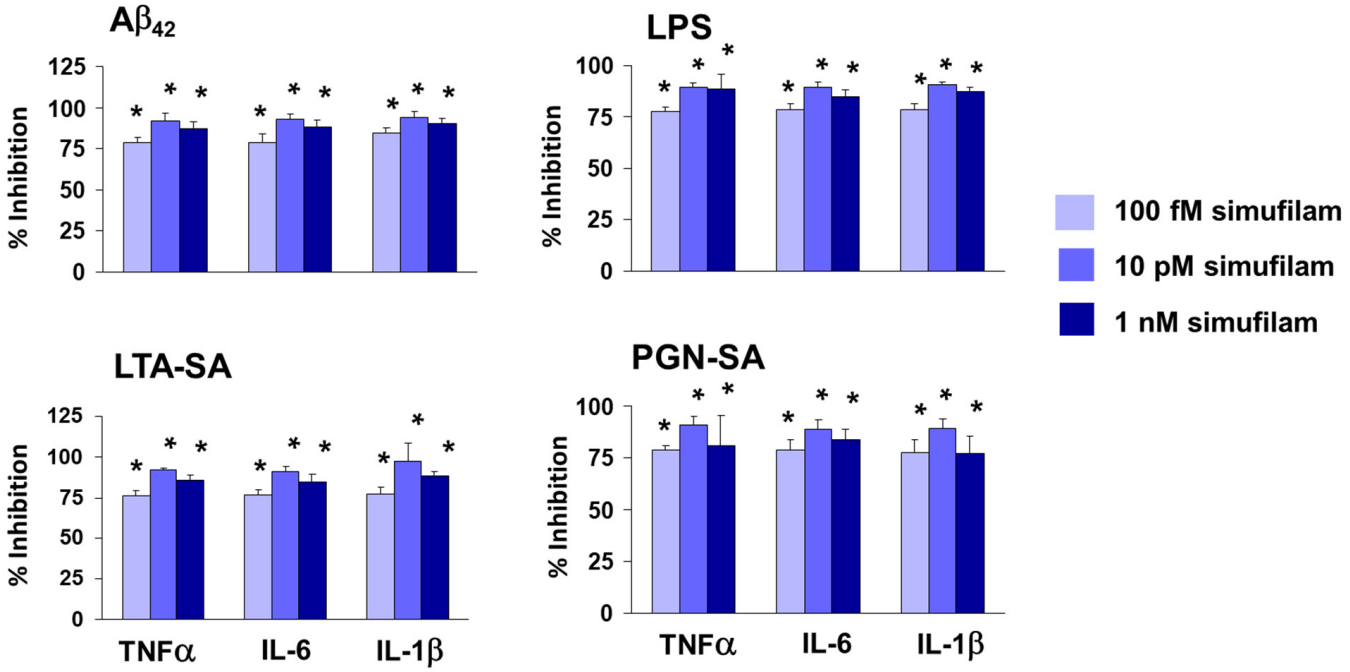

Figure 3. Simufilam inhibits release of inflammatory cytokines by human astrocytes stimulated with Aβ_{42}, LPS or TLR2 ligands LTA-SA and PGN-SA. Data are means ± SEM. N = 3. * $p < 0.001$ simufilam vs. respective stimulant alone.

2.3. Simufilam Reduced FLNA–CXCR4/CD4/CCR5 Linkages

We next broadened our investigation to additional inflammatory receptors: the chemokine receptors CXCR4 and CCR5 and the T cell co-receptor CD4. For FLNA linkages to all three receptors in synaptosomes from AD versus age-, gender- and postmortem-interval-matched healthy control brain tissue, two-way ANOVAs showed highly significant main effects of diagnosis (CXCR4: $F = 22.30$, $p < 0.0001$; CD4: $F = 188.52$, $p < 0.0001$; CCR5: $F = 179.43$, $p < 0.0001$) and treatment (CXCR4: $F = 44.39$, $p < 0.0001$; CD4: $F = 140.48$, $p < 0.0001$; CCR5: $F = 35.78$, $p < 0.0001$) and a diagnosis–treatment interaction (CXCR4:

F = 22.29, $p < 0.0001$; CD4: F = 109.68, $p < 0.0001$; CCR5: F = 79.78, $p < 0.0001$). In postmortem AD brain tissue, FLNA linkages to these three receptors were elevated compared to levels in non-demented control brain tissue ($p < 0.001$; Figure 4). Simufilam incubation of brain tissue (1 nM for 1 h) significantly reduced these elevated linkages in AD brain synaptosomes ($p < 0.01$), while having no effect on the lower levels in control brain synaptosomes.

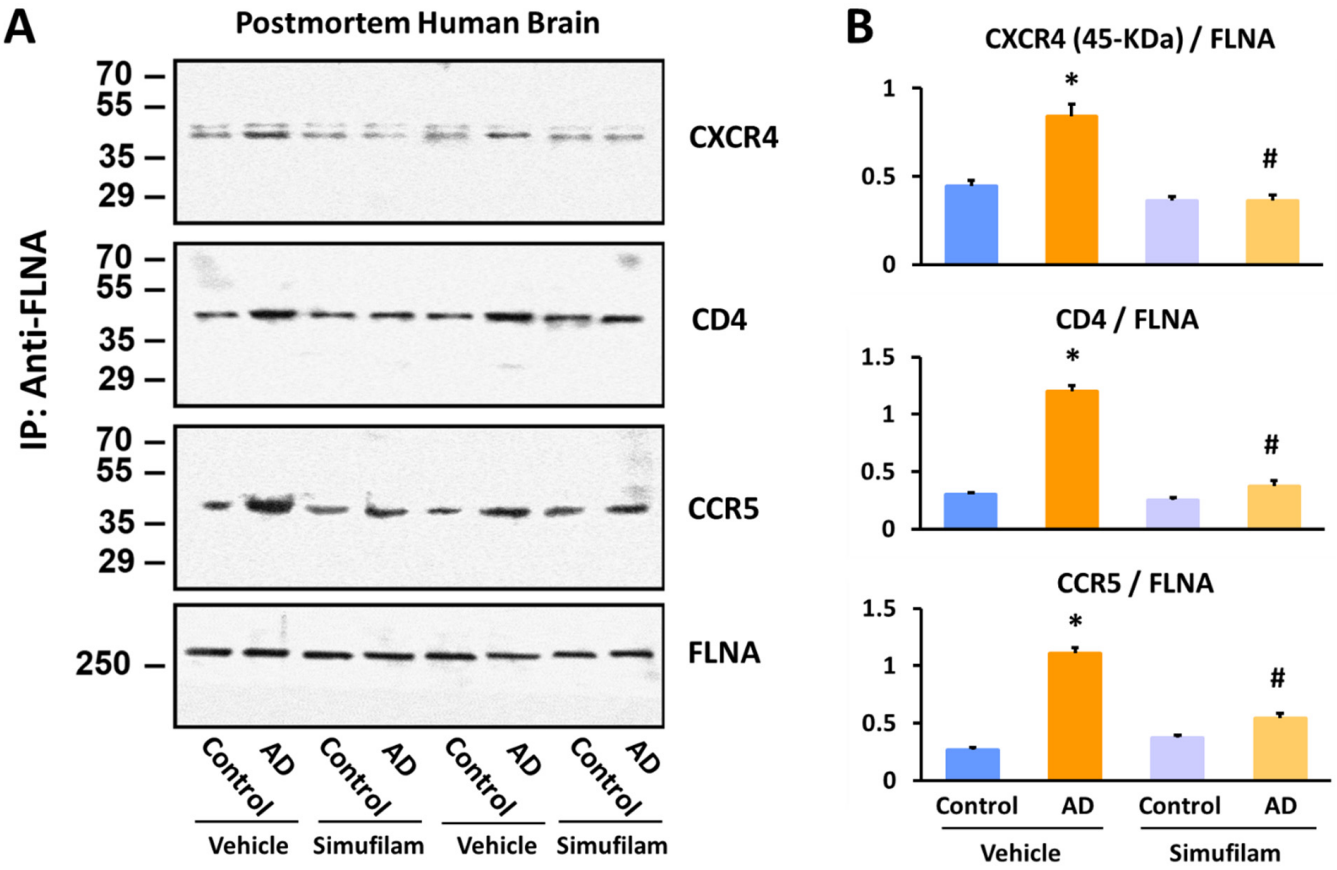

Figure 4. Simufilam incubation (1 nM for 1 h) reduced FLNA linkages with CXCR4, CD4 and CCR5 in AD postmortem brain to levels not different from healthy control brain. Representative blots (**A**) and densitometric quantitation of blots (**B**). Data are means ± SEM. N = 11. * $p < 0.001$ AD vs. control brain tissue incubated with vehicle; # $p < 0.01$ simufilam vs. vehicle incubation of AD brain tissue.

We also examined FLNA linkages with CXCR4, CD4 and CCR5 in synaptosomes from AD triple transgenic mice versus wildtype mice at 6 or 10 months of age after 2 months of oral simufilam via drinking water (Figure 5). We selected 4 months and 8 months to initiate treatment, as these ages correspond to pre-plaque and post-plaque pathology in this transgenic line. The dose of 22 mg/kg/d was based on a prior experiment using 10 mg/kg b.i.d. by i.p. infusion in an acute AD mouse model [9] and the drug's high oral bioavailability.

FLNA–CXCR4 was significantly elevated in 10-month (but not 6-month) transgenic mice vs. wildtypes ($p < 0.001$). FLNA–CD4 was significantly elevated in 6-month transgenics versus wildtypes ($p < 0.001$) but was not significantly different in 10-month transgenic vs. the 10-month wildtypes due to the higher levels of this linkage in the older versus younger wildtypes. FLNA–CCR5 was elevated in transgenics of both ages relative to respective aged wildtypes ($p < 0.001$). All three FLNA linkages were also significantly elevated in the 10-month versus 6-month wildtype mice ($p < 0.001$). Importantly, 2-month oral simufilam treatment significantly reduced FLNA linkages with all three receptors in the transgenics of both ages as well as the FLNA–CCR5 linkage in the 10-month wildtypes ($p < 0.001$).

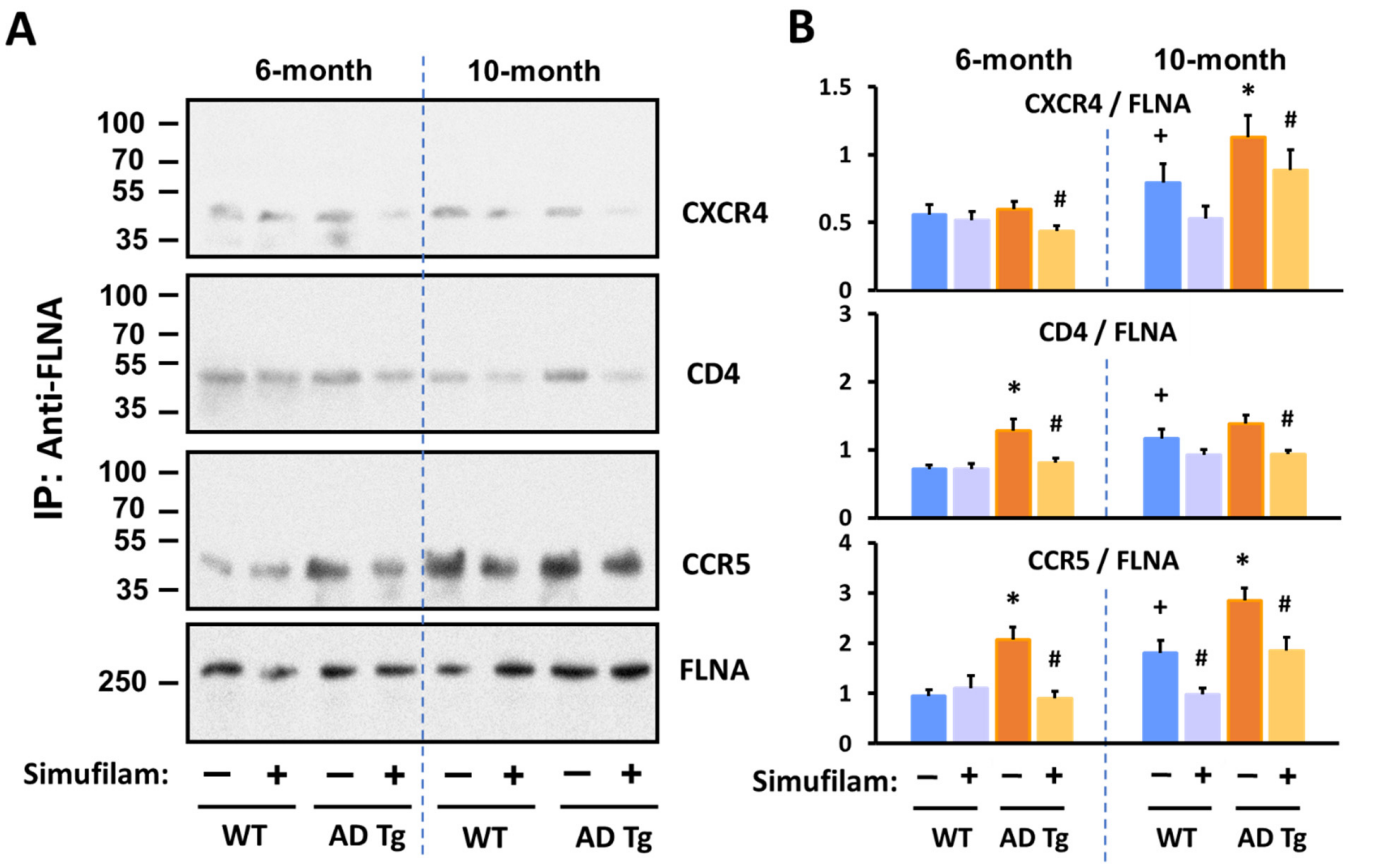

Figure 5. Simufilam reduced FLNA linkages with CXCR4, CD4 and CCR5 in AD triple transgenic mouse brains. Simufilam (22 mg/kg/d) was administered via drinking water for 2 months, starting at 4 months or at 8 months. Simufilam also reduced the slightly lower levels of these FLNA linkages found in 10-month wildtype mice. Representative blots (**A**) and densitometric quantitation of blots (**B**). Data are means ± SEM. N = 5. * $p < 0.001$ AD Tg vs. wildtype; # $p < 0.001$ simufilam vs. water alone in respective age transgenic mice; + $p < 0.001$ vs. 6-month wildtypes.

2.4. Simufilam Reduced Chronic CCR5 Activation in AD Transgenic Mice

To confirm that the FLNA linkage with CCR5 results in CCR5 activation, we measured the level of CCR5–G protein coupling in the transgenic mice given drinking water with or without simufilam for 2 months. Basal (unstimulated) G protein coupling by CCR5 was assessed in synaptic membranes of these mice, and this CCR5–G protein coupling was also measured following stimulation of synaptic membranes with the CCR5 ligand CCL3.

Levels of unstimulated CCR5-coupled Gq/11 protein were elevated in 6-month transgenics compared to wildtypes (Figure 6B; $p < 0.05$), suggesting chronic activation. However, the basal coupling in 10-month transgenics was not significantly higher than basal CCR–G protein coupling in the older wildtypes. Stimulation with CCL3 did not further increase G protein coupling in transgenics of either age. In contrast, the wildtype mice of both ages showed a significant increase in CCR5–G protein coupling after stimulation by CCL3 ($p < 0.01$). Percent stimulation by CCL3 in transgenics was significantly lower than in wildtypes (Figure 6C; $p < 0.01$ for both ages).

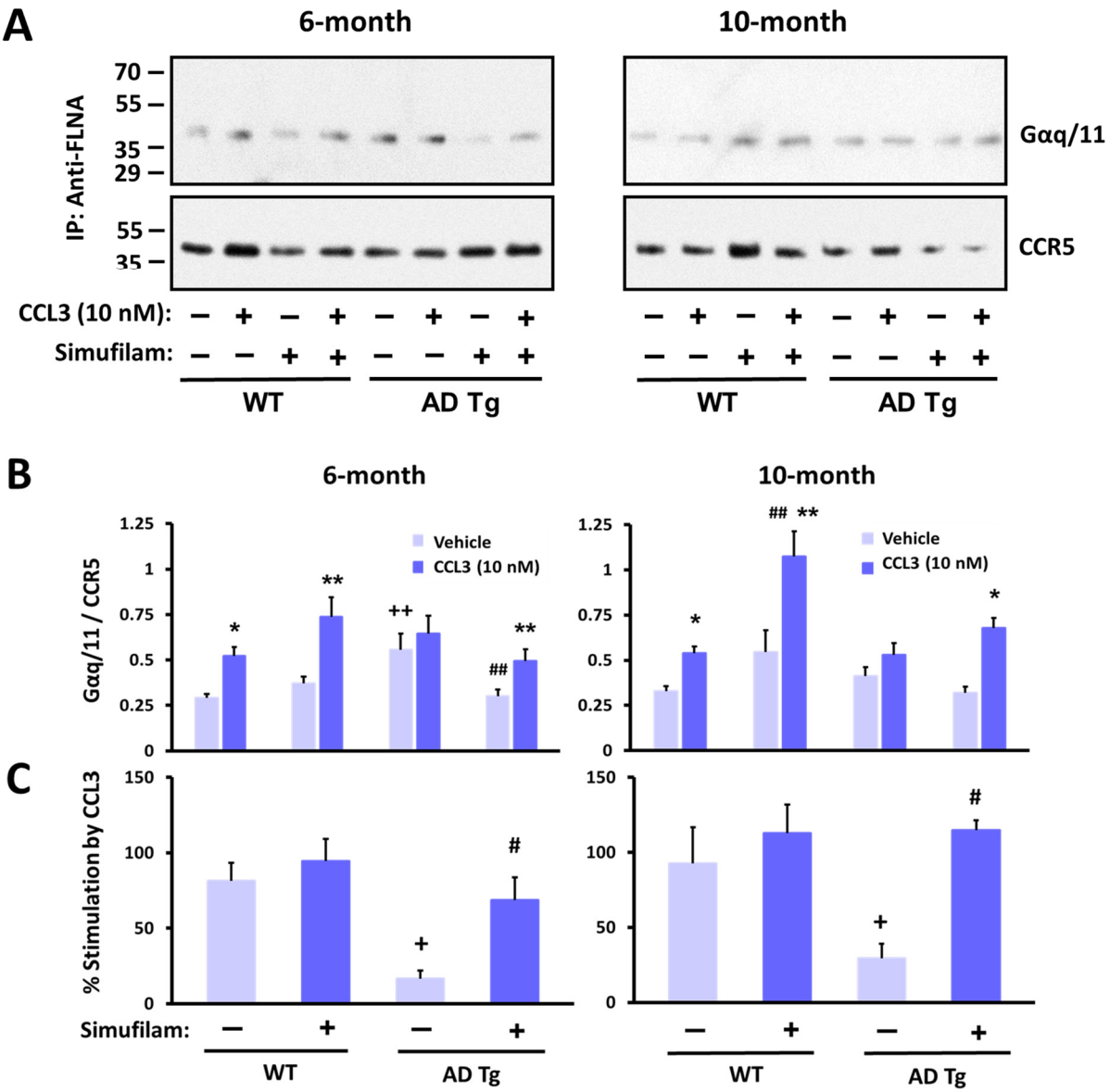

Figure 6. CCR5 coupling to G protein Gaq/11 was elevated in AD transgenic mice versus wildtypes, with little stimulation by the CCR5 ligand CCL3. Oral simufilam (22 mg/kg/d) for 2 months, starting at 4 months or at 8 months, reduced the elevated CCR5–G protein coupling and improved CCL3-induced G protein coupling of CCR5. Representative blots (**A**) densitometric quantitation (**B**) and percent stimulation by CCL3 (**C**). Data are means ± SEM. N = 5 (except N = 4 for 10-month-old wildtypes administered vehicle). * $p < 0.01$, ** $p < 0.05$ CCL3 vs. vehicle in the same group; # $p < 0.01$, ## $p < 0.05$ simufilam vs. vehicle in respective age transgenic/wildtype; + $p < 0.01$, ++ $p < 0.05$ transgenic vs. respective age wildtype.

Simufilam oral treatment for 2 months restored the response to CCL3 in transgenics, primarily by reducing basal levels to that of wildtype controls (Figure 6B; $p < 0.05$ in 6-month transgenics). Although simufilam did not significantly reduce basal CCR5–G protein coupling in 10-month transgenics or significantly enhance the response to CCL3 in these older transgenics, the CCL3 response was significant in simufilam-treated but not vehicle-treated transgenics of both ages (CCL3 vs. vehicle for 6-month transgenics treated with simufilam: $p < 0.05$; CCL3 vs. vehicle for 10-month transgenics treated with simufilam: $p < 0.01$). Interestingly, the absolute CCL3-induced Gq/11 coupling to CCR5 was higher in 10-month simufilam- vs. vehicle-treated wildtypes ($p < 0.05$). Simufilam also improved the percent stimulation by CCL3 in transgenics of both ages (Figure 6C; $p < 0.01$).

3. Discussion

This work further elucidates the mechanism of action of oral AD drug candidate simufilam, i.e., reducing both neurodegeneration and neuroinflammation [8–10,20]. We previously showed that simufilam oral treatment or ex vivo incubation of brain tissue reduced levels of $A\beta_{42}$–α7nAChR and FLNA–α7nAChR complexes [8–10]. We now show that simufilam reduced the binding of $A\beta_{42}$ to α7nAChR in a concentration-dependent manner using TR-FRET, a robust technology for the detection of molecular interactions that are highly sensitive to conformational modifications [46].

The 10 pM IC_{50} of simufilam in inhibiting the binding of $A\beta_{42}$ to α7nAChR in this assay was only 10-fold lower than the 1 pM IC_{50} of unlabeled $A\beta_{42}$ (direct competition) and similar to the pIC_{50}s of several agonists, partial agonists or competitive antagonists of α7nAChR (range: 8.4 to 12.7 pIC_{50}) [34]. Notably, full and partial agonists of α7nAChR were only able to reduce $A\beta_{42}$ binding by 66–83% of the full inhibition by unlabeled $A\beta_{42}$, and only methylylcaconitine, a competitive antagonist, was able to inhibit the $A\beta_{42}$–α7nAChR interaction to the full extent of unlabeled $A\beta_{42}$. Inhibition in this TR-FRET assay was not seen with a non-competitive antagonist or a type 1 positive allosteric modulator of α7nAChR [34]. Simufilam's low picomolar IC_{50} and magnitude of inhibition very close to that of unlabeled $A\beta_{42}$ are unprecedented for its mechanism of binding a receptor-associated protein.

These TR-FRET data corroborate simufilam's reduction in $A\beta_{42}$'s binding affinity of $A\beta_{42}$ for α7nAChR shown by FITC-labeled $A\beta_{42}$ in postmortem human brain and in fresh SK-N-MC cells [9]. The picomolar IC_{50} also agrees with picomolar IC_{50}s for simufilam's inhibition of the $A\beta_{42}$–α7nAChR interaction, tau hyperphosphorylation, and FLNA–α7nAChR/TLR4 interactions calculated for a range of concentrations in postmortem brain [10] and also shown in AD mouse models or AD patient lymphocytes [8–10]. Further support is that two other independent laboratories showed biological activity of simufilam in FLNA-related disorders [47,48]. Together, all these data support simufilam's primary mechanism of reducing soluble $A\beta_{42}$'s signaling that hyperphosphorylates tau. Disrupting $A\beta_{42}$'s pathogenic signaling through α7nAChR would also promote healthy α7nAChR neurotransmission.

Illustrating an additional AD-relevant mechanism of action, simufilam also disrupts an aberrant linkage of FLNA with TLR4, which again is induced by soluble $A\beta_{42}$ binding, in this case to TLR4's co-receptor CD14 [8–10]. Extending the anti-neuroinflammatory mechanism of action of simufilam, we now show that simufilam reduced the $A\beta_{42}$-induced FLNA interactions with additional inflammatory receptors: TLR2, the chemokine receptors CXCR4 and CCR5, and T-cell co-receptor CD4. Postmortem human frontal cortexes from non-demented controls showed FLNA interactions with TLR2 induced by $A\beta_{42}$ or TLR2 agonists; simufilam reduced these linkages. Simufilam's 75% or greater reductions in inflammatory cytokine release from primary human astrocytes stimulated with $A\beta_{42}$ or TLR2/TLR4 agonists suggest that the FLNA–receptor linkages, which are reduced by simufilam, are critical to agonist activation of these receptors.

Both postmortem human AD brain tissue and triple transgenic AD mouse brains showed elevated interactions of FLNA with CXCR4, CCR5 and CD4. Ex vivo simufilam incubation of the postmortem tissue or 2-month oral administration to the mice significantly reduced these linkages, suggesting that simufilam reduced inflammatory signaling. We previously showed that the brains of these same AD transgenic mice treated with 2-month oral simufilam showed reduced FLNA linkages with α7nAChR and TLR4, reduced tau hyperphosphorylation, reduced inflammatory cytokine levels, reduced amyloid deposits and neurofibrillary lesions, improved function of NMDA and insulin receptors, and improved activity-dependent Arc expression (an indicator of synaptic plasticity) [10]. All these drug effects were coincident with the isoelectric focusing point of FLNA shifting back to that of FLNA in wildtype control brains [10].

Finally, the elevated G protein coupling of CCR5 in the triple transgenic AD mice, along with CCR5's insensitivity to further activation by its ligand CCL3 in these transgenics,

provides additional evidence that elevated FLNA linkages to inflammatory receptors in AD imply their chronic activation and resulting neuroinflammation. Simufilam's suppression of the elevated basal CCR5–G protein coupling and improvement to CCR5's responsivity to its ligand CCL3 again support the hypothesis that simufilam reduces chronic activation of multiple inflammatory receptors in AD. Of note, $A\beta_{42}$ also interacts with the A2A adrenergic receptor [49] and the leptin receptor [50] to modify basal or ligand-induced signaling pathways.

Reducing activation of multiple inflammatory receptors would benefit AD. Indeed, 17% of AD therapeutic candidates currently in clinical trials target neuroinflammation [7]. Neuroinflammation in AD is not merely a reaction to plaques and tangles but contributes to disease progression and severity [51]. Although early microglial recruitment promotes clearance of soluble Aβ, as the disease progresses, elevated inflammatory cytokines can lead to insufficient phagocytic clearance of soluble Aβ, resulting in greater toxic signaling via α7nAChR and TLR4/2, intraneuronal Aβ accumulation, tau hyperphosphorylation and further inflammation, leading to extensive neurodegeneration [52,53].

The inflammatory cytokines TNFα, IL-1β and IL-17 can loosen tight junctions and compromise the blood–brain barrier [54], another pathological feature of AD, which enables an influx of immune cells to exacerbate neuroinflammation [55,56]. Because healthy microglia regulate synaptic pruning, synaptic plasticity and learning and memory, abnormal microglial activation and the resulting neuroinflammation have been causally implicated in the cognitive deficits of normal aging, AD and other diseases [57].

By suppressing neuroinflammation, simufilam may also reduce insulin resistance associated with AD: neuroinflammation in both AD and obesity or type 2 diabetes induces insulin resistance and insulin receptor dysfunction [58,59]. TNFα has been shown to induce insulin resistance [60,61]. Neuroinflammation is a critical link between AD, depression, and obesity, with each increasing risk of the others [62]. Indeed, simufilam has been shown to improve brain insulin receptor signaling [9,10]. Illustrating reduced insulin resistance, oral simufilam improved the response to insulin of mammalian target of rapamycin (mTOR) and suppressed mTOR's basal overactivation in lymphocytes of AD subjects [63]. With insulin receptors critical for cell survival and cell health, reduced brain insulin resistance, if translating from the lymphocytes, would lessen this contribution to neurodegeneration.

In addition to the induced aberrant receptor interactions with α7nAChR and multiple inflammatory receptors, the altered conformation of FLNA in AD may impact FLNA's normal protein interactions. We previously showed that FLNA normally interacts with the intracellular phosphatase PTEN and that this healthy FLNA interaction is reduced in AD [63]. There may be other aberrant protein interactions that are reduced and other normal protein interactions that are preserved by restoring FLNA's native shape in AD brains.

4. Materials and Methods

4.1. Materials and Chemicals

$A\beta_{1–42}$ human, LTA-SA and PGN-SA were obtained from Invitrogen. For TR-FRET assays, $A\beta_{1–42}$ human and $A\beta_{42}$-FAM were purchased from Anaspec (Fremont, CA, USA). Recombinant human CCL3/MIP-1 alpha protein was purchased from R&D Systems (Minneapolis, MN, USA). Anti-TLR2 (SC-166900), -CCR5 (SC-17833), -CD4 (SC-19641), and -CXCR4 (SC-53534), -FLNA (SC-7565 [IP], SC-17749 [IP], SC-271440), Gαq/11 (SC-515689), anti-tumor necrosis factor α (TNFα) (SC-8301), anti-Interleukin-6 (IL-6) (SC-7920), anti-Interleukin-1β (IL-1β) (SC-7884) were purchased from Santa Cruz Biotechnology (Santa Cruz, CA, USA). Reacti-Bind NeutrAvidin high-binding capacity coated 96-well plates, covalently conjugated protein A/G-agarose beads, antigen elution buffer and Chemiluminescent reagents were purchased from Pierce-Thermo Scientific (Rockford, IL, USA). Biotinylated anti-IL1β (13-7016-85), anti-TNFα (13-7349-85) and anti-IL-6 (13-7068-85) were purchased from eBioscience (San Diego, CA, USA). LPS, phosphatase inhibitors (Roche), complete mini ethylenediaminetetraacetic acid (EDTA)-free protease inhibitor tablet (Roche), and alkaline phosphatase were purchased from Sigma (St. Louis, MO,

USA). Aβ-derived peptides were dissolved in 50 mM Tris, pH 9.0 containing 10% dimethyl sulfoxide (DMSO) and stored at −80 °C. All test agents were freshly made according to manufacturers' recommendations. If DMSO was used as the solvent, the highest DMSO concentration in the incubation was 1%.

4.2. TR-FRET Binding Assay

$A\beta_{42}$ binding to α7nAChR was monitored by a TR-FRET assay, as previously described [34]. Briefly, HEK293T cells were transfected to express SNAP-α7nAChR and the chaperone protein NACHO [64]. Forty-eight hours post-transfection, surface SNAP-α7nAChR was labeled with the long-lived fluorophore Terbium cryptate (Tb; Lumi4-Tb, Cisbio Bioassays, Codolet, France) by incubating cells with the Tb-conjugated SNAP substrate in Tag-lite labeling medium (100 nM, 1 h, 4 °C). After 3 washes in PBS, cells were distributed into a 384-well plate with assay buffer (Tag-lite medium). To construct the inhibition dose–response curves for simufilam and $A\beta_{42}$, varying concentrations of simufilam or unlabeled $A\beta_{42}$ were added to corresponding wells, followed by 10 nM $A\beta_{42}$-FAM (5-carboxyfluorescein-labeled $A\beta_{42}$) in a final reaction volume of 14 μL. Plates were incubated 2–4 h at room temperature and read in a Tecan F500 plate reader (Tecan; Männedorf, Switzerland) with the following settings: donor excitation at 340 nm; 1st emission detection at 520 nm (acceptor) and 2nd emission at 620 nm (donor); delay: 150 μs; integration time: 500 μs. Data are expressed as the acceptor/donor ratio normalized as % of maximal $A\beta_{42}$-FAM binding (maximal TR-FRET ratio = 100%). Specific binding is defined as the difference between total binding and non-specific binding in the presence of an excess of unlabeled $A\beta_{42}$ (1 μM).

4.3. Postmortem Human Brain Tissue

The postmortem brain study protocol conformed to the tenets of the Declaration of Helsinki as reflected in a previous approval by the City College of New York and the City University of New York Medical School's human research committee. Each participant underwent a uniform clinical evaluation that included a medical history, complete neurological examination, cognitive testing including a mini mental state examination and other cognitive tests on episodic memory, semantic memory and language, working memory, perceptual speed, and visuospatial ability, as well as a psychiatric rating. AD subjects were diagnosed based on NINCDS-ADRDA criteria [65]. Frontal cortices from patients with clinically diagnosed sporadic AD and age-matched, neurotypical persons were obtained from the Harvard Brain Tissue Resource Center (HBTRC, Belmont, MA, USA) and the UCLA Brain Tissue Resource Center (UBTRC, Los Angeles, CA, USA). Both HBTRC and UBTRC are supported in part by the National Institutes of Health. The postmortem time intervals for collecting these brains were under 13 h (mean postmortem intervals for AD and control brain samples were 6.0 ± 0.9 h and 5.8 ± 0.8 h, respectively). Diagnostic neuropathological examination was also conducted on fixed sections stained with hematoxylin and eosin and with modified Bielschowsky silver staining [66] to establish any disease diagnosis according to defined criteria [67]. The presence of both neuritic (amyloid) plaques and neurofibrillary tangles in all AD brains was confirmed by Nissl and Bielschowsky staining and characterized by anti-$A\beta_{42}$ and -neurofibrillary tangle (NFT) immunohistochemistry staining in the frontal and entorhinal cortex, as well as the hippocampus, as described [21]. Control tissues exhibited only minimal, localized microscopic neuropathology of AD (0–3 neuritic plaques/10% field and 0–6 NFTs/10% field in hippocampus). One-gram blocks from Brodmann areas 10 and/or 46 of frontal cortices were dissected from fresh frozen coronal brain sections maintained at −80 °C. Following the removal of white matter, gray matter was divided into ~50 mg blocks on dry ice and returned to −80 °C until use.

4.4. In Vivo Oral Administration of Simufilam

As described [10], 4- and 8-month-old male and female wildtype E129 mice (30–35 g) from Taconic and 3xTg AD mice (containing 3 mutations: APP Swedish, MAPT P301L,

and PSEN1 M146V) of stock supplied by Dr. Frank LaFerla [68] were maintained on a 12 h light/dark cycle with free access to food and water. We first determined the average daily intake of water sweetened with 0.25 g sucralose/100 mL to be ~5 mL. Mice then received either sweetened water alone or with simufilam at 22 mg/kg/d for 2 months. After decapitation, brain regions from one half of the brain were immediately frozen in liquid nitrogen and stored at −80 °C until use. Two equal samples (~5 mg) were separately processed to obtain synaptosomes (P2 fraction) as described [24] for assessments of FLNA linkage to CCR5/CD4/CXCR4 and CCL3-induced Gq/11 recruitment to CCR5. Synaptosomes were washed twice and suspended in 2 mL ice-cold oxygenated Krebs–Ringer solution (K-R: 25 mM HEPES, pH 7.4; 118 mM NaCl, 4.8 mM KCl, 25 mM $NaHCO_3$, 1.3 mM $CaCl_2$, 1.2 mM $MgSO_4$, 1.2 mM KH_2PO_4, 10 mM glucose, 100 mM ascorbic acid) with protease and protein phosphatase inhibitors (Roche Diagnostics, Mannheim, Germany) and aerated for 10 min with 95% O_2/5% CO_2. Protein concentration was determined by the Bradford method (Bio-Rad, Hercules, CA, USA).

4.5. Assessment of Cytokine Levels in Primary Human Astrocytes

Primary astrocyte cultures were prepared according to the provider (Lonza Biosciences, Basel, Switzerland). Adherent astrocytes were trypsinized by 0.25% trypsin-EDTA, collected and sub-cultured in 12-well plates (1.2 mL/well). When 80–85% confluent, cells were incubated with 100 fM, 10 pM or 1 nM simufilam or culture medium only under 5% CO_2 for 2 h, prior to adding 1 μg/mL LPS, 10 μg/mL LTA-SA or 1 μg/mL PGN-SA for an additional 24 h. Levels of TNF-α, IL-6 and IL-1β in 200 μL culture medium were determined, with the medium as the blank. Each well was sampled twice. Biotinylated mouse monoclonal anti-TNFα, -IL-6, and -IL-1β (0.5 mg/well) were coated onto streptavidin-coated plates (Reacti-Bind NeutrAvidin high-binding capacity coated 96-well plate). Plates were washed 3 times with 200 μL ice-cold 50 mM Tris HCl (pH 7.4) and incubated at 30 °C with 100 μL culture medium for 1 h. Plates were washed 3 more times with ice-cold Tris HCl and incubated at 30 °C with 0.5 mg/well unconjugated rabbit anti-TNFα, -IL-6, and -IL-1β for 1 h. After 2 washes with ice-cold Tris HCl, each well was incubated in 0.5 mg/well fluorescein isothiocyanate (FITC)-conjugated anti-rabbit immunoglobulin G (human and mouse absorbed) for 1 h at 30 °C. Plates were again washed 3 times with ice-cold Tris HCl, and residual FITC signals were determined by a multimode plate reader (DTX880, Beckman Coulter, Irving, TX, USA).

4.6. Assessment of FLNA–TLR2 Interaction in Postmortem Human Brain Tissue

Using an established method [9], levels of FLNA linkage to TLR2 were determined by co-immunoprecipitation of synaptosomes prepared from frontal cortical slices from 3 non-demented control subjects [41]. Frontal cortical slices were incubated with K-R, 100 nM $A\beta_{42}$, 10 μg/mL LTA-SA or 1 μg/mL PGN-SA with or without 1 or 10 nM simufilam at 37 °C for 30 min. The incubation mixture (volume 0.5 mL) was aerated for 1 min every 15 min with 95% O_2/5% CO_2. Reactions were terminated by adding 1.5 mL ice-cold Ca^{2+}-free K-R containing protease and protein phosphatase inhibitors, and slices were collected by brief centrifugation and processed to obtain synaptosomes (P2 fraction) as described previously [24].

Synaptosomes (200 μg) were pelleted by centrifugation, solubilized by brief sonication in 250 μL immunoprecipitation buffer (25 mM HEPES, pH 7.5; 200 mM NaCl, 1 mM EDTA, with protease and protein phosphatase inhibitors) and incubated at 4 °C with end-to-end shaking for 1 h. Following dilution with 750 μL ice-cold immunoprecipitation buffer and centrifugation (4 °C) to remove insoluble debris, the FLNA–TLR2 complexes in the lysate were isolated by immunoprecipitation with 16 h incubation at 4 °C with anti-FLNA (SC-7565; 1 μg) immobilized on protein A/G-conjugated agarose beads. Resultant immunocomplexes were pelleted by centrifugation at 4 °C. After 3 washes with 1 mL ice-cold PBS (pH 7.2) and centrifugation, the isolated FLNA–TLR2 complexes were solubilized by boiling for 5 min in 100 μL SDS-polyacrylamide gel electrophoresis (PAGE) sample

preparation buffer (62.5 mM Tris-HCl, pH 6.8; 10% glycerol, 2% SDS; 5% 2-mercaptoethanol, 0.1% bromophenol blue). The TLR2 contents in 50% of the anti-FLNA immunoprecipitates were determined by immunoblotting with mouse monoclonal anti-TLR2 (SC-166900). Blots were then stripped and re-probed with monoclonal anti-FLNA (SC-271440) to ascertain equal immunoprecipitation and loading.

4.7. Assessment of FLNA–CCR5/CD4/CXCR4 Interaction in Postmortem Human Brain and Transgenic AD Mouse Brain

Using the same method [9], the linkage of FLNA with CCR5, CXCR4 and CD4 in synaptosomes from $A\beta_{42}$-incubated frontal slices from 11 sets of age- (66–92 years) and postmortem interval (2–13 h)-matched control and AD subjects (4 females/7 males) with and without 1 nM simufilam were immunoprecipitated with immobilized anti-FLNA (SC-7565). In the experiments using postmortem human brains, frontal cortical slices were incubated with K-R or 1 nM simufilam at 37 °C for 30 min. The incubation mixture (volume 0.5 mL) was aerated for 1 min every 15 min with 95% O_2/5% CO_2. Reactions were terminated by adding 1.5 mL ice-cold Ca^{2+}-free K-R containing protease and protein phosphatase inhibitors, and slices were collected by brief centrifugation and processed to obtain synaptosomes (P2 fraction) as described [24].

Synaptosomes (200 μg) prepared from K-R- or simufilam-incubated postmortem cortical slices or from wildtype or transgenic mice were pelleted by centrifugation, solubilized by brief sonication in 250 μL immunoprecipitation buffer (described above) and incubated at 4 °C with end-to-end shaking for 1 h. Following dilution with 750 μL ice-cold immunoprecipitation buffer and centrifugation (4 °C) to remove insoluble debris, the FLNA–CCR5/CD4/CXCR4 complexes in the lysate were isolated by immunoprecipitation with 16 h incubation at 4 °C with anti-FLNA (1 μg) immobilized on protein A/G-conjugated agarose beads (anti-FLNA for postmortem human brain: SC-7565; for mice: SC-17749). The immunocomplexes were pelleted by centrifugation at 4 °C. After 3 washes with 1 mL ice-cold PBS (pH 7.2) and centrifugation, the isolated FLNA–CCR5/CD4/CXCR4 complexes were solubilized by boiling for 5 min in 100 mL SDS-PAGE sample preparation buffer. Levels of CCR5, CD4, and CXCR4 IRβ in 50% of the anti-FLNA immunoprecipitates were determined by immunoblotting with mouse monoclonal CCR5 (SC-17833), CD4 (SC-19641), and CXCR4 (SC-53534) antibodies, sequentially. A separate set of blots was probed with monoclonal anti-FLNA (SC-271440) to validate equal immunoprecipitation efficiency and loading.

4.8. CCL3-Stimulated Gq/11 Recruitment to CCR5 in Synaptic Membranes

Synaptosomes (P2 fraction) were prepared from snap-frozen parietal cortices of vehicle- and simufilam-treated wildtype and transgenic mice as previously described [69,70]. To further purify synaptosomal factions, the synaptosome-rich P2 fraction was washed twice in 1 mL oxygenated ice-cold K-R with protease and protein phosphatase inhibitors. To obtain membranous fractions of the synaptosomes, washed synaptosomes were sonicated for 10 sec on ice in 0.5 mL hypotonic homogenization solution (25 mM HEPES, pH 7.4; 12 mM NaCl, 0.5 mM KCl, 2.5 mM $NaHCO_3$, 0.1 mM $CaCl_2$, 0.1 mM $MgSO_4$, 0.1 mM KH_2PO_4, 1 mM glucose, 10 mM ascorbic acid, protease and protein phosphatase inhibitors). Samples were then centrifuged at 50,000× *g* for 30 min. The resultant synaptic membrane pellet was resuspended in 0.5 mL K-R, and protein concentrations were determined by the Bradford method. These synaptic membranes were stimulated with the CCR5 ligand CCL3, and levels of CCR5-coupled Gq/11 were determined using an established method [71].

Synaptic membranes (100 μg) were incubated in 200 μL K-R or in 10 nM CCL3 at 37 °C for 10 min. The reaction was stopped by adding 20 mM $MgCl_2$ and centrifuging. The pelleted synaptic membranes were solubilized by brief sonication (10 sec, 50% output, Fisher Scientific, Waltham, MA, USA) on ice in 250 μL immunoprecipitation buffer and solubilized by adding 0.5% digitonin, 0.2% sodium cholate and 0.5% NP-40 and incubated at 4 °C with end-to-end shaking for 1 h. Following dilution with 750 μL ice-cold immuno-

precipitation buffer and centrifugation at 4 °C to remove insoluble debris, the resultant lysate was used to measure levels of CCR5-associated Gq/11 by the quantities of Gαq/11 in the anti-CCR5 immunoprecipitates. Briefly, the CCR5-Gq/11 complexes in the lysate were isolated by immunoprecipitation with 16 h incubation at 4 °C with 1 μg anti-CCR5 (SC-17833) immobilized on protein A/G-conjugated agarose beads. The immunocomplexes were pelleted by centrifugation at 4 °C. After 3 washes with 1 mL ice-cold PBS (pH 7.2) and centrifugation, the isolated CCR5-Gq/11 complexes were solubilized by boiling for 5 min in 100 μL SDS-PAGE sample preparation buffer. Levels of Gαq/11 in 50% of the anti-CCR5 immunoprecipitates were determined by immunoblotting with mouse anti-Gαq/11 (SC-515689). The other 50% of the anti-CCR5 immunoprecipitates were run on separate blots probed with monoclonal anti-CCR5 (SC-17833) to validate equal immunoprecipitation efficiency and loading.

4.9. Statistics

For the TR-FRET assay, nonlinear fitting of the concentration curve and calculation of pIC_{50} was performed using GraphPad Prism software version 9. FLNA–receptor linkages in postmortem brain tissue were analyzed by two-way ANOVA with diagnosis (AD/control) and treatment (simufilam/vehicle) as factors with post hoc *t*-tests for pair-wise comparisons. Student's *t*-test was used for all other statistical analyses.

5. Conclusions

FLNA, in an altered conformation, is a deviant receptor-associated protein critical to AD pathology. Simufilam's disruption of the aberrant FLNA linkage to α7nAChR reduces $A\beta_{42}$'s binding to and pathogenic signaling via this receptor, thereby restoring healthy α7nAChR neurotransmission. Simufilam's disruption of deviant FLNA linkages to multiple inflammatory receptors suppresses neuroinflammation induced by these receptors. The dissociation of FLNA from all these receptors is coincident with simufilam's reversal of an altered conformation of FLNA, as indicated by isoelectric focusing points. It is not surprising that an altered conformation, inducible by soluble $A\beta_{42}$, would lead to aberrant protein interactions. Alternatively, $A\beta_{42}$-induced aberrant protein interactions could induce the altered conformation.

By binding a single protein target, simufilam reduces a predominant neurodegeneration pathway and multiple neuroinflammatory signaling pathways of soluble amyloid and potentially other inflammatory ligands in AD. A multi-pronged therapeutic approach, whether by agents with multiple mechanisms or by drug combinations, may be necessary to treat this devastating disease.

Author Contributions: L.H.B. and H.-Y.W. were involved in study design, interpretation of data, the writing of this article and the decision to submit it for publication. H.-Y.W. and Z.P. conducted and analyzed the co-immunoprecipitation experiments to determine FLNA—receptor interactions. E.C., J.D. and R.J. planned, conducted, analyzed and interpreted the TR-FRET assay work and contributed to writing the article. All authors have read and agreed to the published version of the manuscript.

Funding: This study was funded by Cassava Sciences.

Institutional Review Board Statement: All postmortem tissues were identified by an anonymous identification number, and experiments were performed as a best-matched pair without knowledge of clinical information, therefore receiving IRB exemption. All animal procedures complied with the National Institutes of Health Guide for Care Use of Laboratory Animals and were approved by the City College of New York Animal Care and Use Committee.

Informed Consent Statement: For human postmortem studies, informed consent was obtained for collection and use of clinical, pathological and postmortem data from all subjects or their next of kin in accordance with the Institutional Review Boards at UCLA and Harvard.

Data Availability Statement: The data presented in this work are presented in the article.

Conflicts of Interest: Simufilam is a proprietary drug candidate of Cassava Sciences, Inc. (Austin, TX, USA). L.B. is an employee and shareholder of Cassava Sciences. H.-Y.W. is an employee of City University of New York School of Medicine, is a long-time consultant and scientific advisor to Cassava Sciences, owns an insignificant financial interest (less than $\frac{1}{2}$ of 1%) in the equity of Cassava Sciences, and has consulted to various pharmaceutical companies over the past twenty years. L.H.B and H.-Y.W. are inventors on simufilam patents. None of the authors are due patent royalties. This basic research was conducted in non-GLP compliant facilities. Z.P. is an employee of City University of New York School of Medicine and reports no conflicts of interest. E.C. is an employee of the CNRS and J.D. and R.J. are employees of Inserm; they report no conflict of interest.

References

1. World Health Organization. *Global Status Report on the Public Health Response to Dementia*; World Health Organization: Geneva, Switzerland, 2021; p. 137.
2. 2023 Alzheimer's disease facts and figures. *Alzheimers Dement.* **2023**, *19*, 1598–1695. [CrossRef] [PubMed]
3. Brockmann, R.; Nixon, J.; Love, B.L.; Yunusa, I. Impacts of FDA approval and Medicare restriction on antiamyloid therapies for Alzheimer's disease: Patient outcomes, healthcare costs, and drug development. *Lancet Reg. Health Am.* **2023**, *20*, 100467. [CrossRef]
4. Barkhof, F.; Knopman, D.S. Brain shrinkage in anti-β-amyloid Alzheimer trials: Neurodegeneration or pseudoatrophy? *Neurology* **2023**, *100*, 941–942. [CrossRef]
5. van Dyck, C.H.; Swanson, C.J.; Aisen, P.; Bateman, R.J.; Chen, C.; Gee, M.; Kanekiyo, M.; Li, D.; Reyderman, L.; Cohen, S.; et al. Lecanemab in Early Alzheimer's Disease. *N. Engl. J. Med.* **2023**, *388*, 9–21. [CrossRef] [PubMed]
6. Sims, J.R.; Zimmer, J.A.; Evans, C.D.; Lu, M.; Ardayfio, P.; Sparks, J.; Wessels, A.M.; Shcherbinin, S.; Wang, H.; Monkul Nery, E.S.; et al. Donanemab in early symptomatic Alzheimer disease: The TRAILBLAZER-ALZ 2 randomized clinical trial. *JAMA* **2023**, *330*, 512–527. [CrossRef]
7. Cummings, J.; Zhou, Y.; Lee, G.; Zhong, K.; Fonseca, J.; Cheng, F. Alzheimer's disease drug development pipeline: 2023. *Alzheimers Dement.* **2023**, *9*, e12385. [CrossRef]
8. Wang, H.-Y.; Pei, Z.; Lee, K.-C.; Lopez-Brignoni, E.; Nikolov, B.; Crowley, C.; Marsman, M.; Barbier, R.; Friedmann, N.; Burns, L. PTI-125 reduces biomarkers of Alzheimer's disease in patients. *J. Prev. Alzheimer's Dis.* **2020**, *7*, 256–264. [CrossRef]
9. Wang, H.-Y.; Bakshi, K.; Frankfurt, M.; Stucky, A.; Goberdhan, M.; Shah, S.; Burns, L. Reducing amyloid-related Alzheimer's disease pathogenesis by a small molecule targeting filamin A. *J. Neurosci.* **2012**, *32*, 9773–9784. [CrossRef] [PubMed]
10. Wang, H.-Y.; Lee, K.-C.; Pei, Z.; Khan, A.; Bakshi, K.; Burns, L. PTI-125 binds and reverses an altered conformation of filamin A to reduce Alzheimer's disease pathogenesis. *Neurobiol. Aging* **2017**, *55*, 99–114. [CrossRef]
11. Nakamura, F.; Stossel, T.; Hartwig, J. The filamins: Organizers of cell structure and function. *Cell Adh. Migr.* **2011**, *5*, 160–169. [CrossRef]
12. Nakamura, F.; Osborn, T.; Hartemink, C.; Hartwig, J.; Stossel, T. Structural basis of filamin A functions. *J. Cell Biol.* **2007**, *179*, 1011–1025. [CrossRef] [PubMed]
13. Ruskamo, S.; Gilbert, R.; Hofmann, G.; Jiang, P.; Campbell, I.D.; Ylänne, J.; Pentikäinen, U. The C-terminal rod 2 fragment of filamin A forms a compact structure that can be extended. *Biochem. J.* **2012**, *446*, 261–269. [CrossRef] [PubMed]
14. Zhou, J.; Kang, X.; An, H.; Lv, Y.; Liu, X. The function and pathogenic mechanism of filamin A. *Gene* **2021**, *784*, 145575. [CrossRef]
15. Stossel, T.; Condeelis, J.; Cooley, L.; Hartwig, J.; Noegel, A.; Schleicher, M.; Shapiro, S. Filamins as integrators of cell mechanics and signalling. *Nature* **2001**, *2*, 138–145. [CrossRef]
16. Aumont, E.; Tremblay, C.; Levert, S.; Bennett, D.A.; Calon, F.; Leclerc, N. Evidence of Filamin A loss of solubility at the prodromal stage of neuropathologically-defined Alzheimer's disease. *Front. Aging Neurosci.* **2022**, *14*, 1038343. [CrossRef]
17. Chen, H.; Zhu, X.; Cong, P.; Sheetz, M.P.; Nakamura, F.; Yan, J. Differential mechanical stability of filamin A rod segments. *Biophys. J.* **2011**, *101*, 1231–1237. [CrossRef]
18. Kesner, B.A.; Ding, F.; Temple, B.R.; Dokholyan, N.V. N-terminal strands of filamin Ig domains act as a conformational switch under biological forces. *Proteins* **2010**, *78*, 12–24. [CrossRef]
19. Strang, C.J.; Wales, M.E.; Brown, D.M.; Wild, J.R. Site-directed alterations to the geometry of the aspartate transcarbamoylase zinc domain: Selective alteration to regulation by heterotropic ligands, isoelectric point, and stability in urea. *Biochemistry* **1993**, *32*, 4156–4167. [CrossRef]
20. Burns, L.H.; Pei, Z.; Wang, H.Y. Targeting α7 nicotinic acetylcholine receptors and their protein interactions in Alzheimer's disease drug development. *Drug Dev. Res.* 2023; *online ahead of print*.
21. Wang, H.-Y.; Lee, D.; D'Andrea, M.; Peterson, P.; Shank, R.; Reitz, A. b-Amyloid1-42 binds to a7 nicotinic acetylcholine receptor with high affinity: Implication for Alzheimer's disease pathology. *J. Biol. Chem.* **2000**, *275*, 5626–5632. [CrossRef]
22. Wang, H.-Y.; Lee, D.; Davie, C.; Shank, R. Amyloid peptide Aβ1-42 binds selectively and with picomolar affinity to α7 nicotinic acetylcholine receptors. *J. Neurochem.* **2000**, *75*, 1155–1161. [CrossRef]
23. Dineley, K.; Bell, K.; Bui, D.; Sweatt, J. b-Amyloid peptide activates a7 nicotinic acetylcholine receptors expressed in xenopus oocytes. *J. Biol. Chem.* **2002**, *227*, 25056–25061. [CrossRef] [PubMed]

24. Wang, H.-Y.; Li, W.; Benedetti, N.; Lee, D. α7 nicotinic acetylcholine receptors mediate β-amyloid peptide-induced tau protein phosphorylation. *J. Biol. Chem.* **2003**, *278*, 31547–31553. [CrossRef] [PubMed]
25. El Kouhen, R.; Hu, M.; Anderson, D.J.; Li, J.; Gopalakrishnan, M. Pharmacology of alpha7 nicotinic acetylcholine receptor mediated extracellular signal-regulated kinase signalling in PC12 cells. *Br. J. Pharmacol.* **2009**, *156*, 638–648. [CrossRef] [PubMed]
26. Hu, M.; Waring, J.; Gopalakrishnan, M.; Li, J. Role of GSK-3beta activation and alpha7 nAChRs in Abeta(1-42)-induced tau phosphorylation in PC12 cells. *J. Neurochem.* **2008**, *106*, 1371–1377. [CrossRef]
27. Alonso, A.; Grundke-Iqbal, I.; Barra, H.; Iqbal, K. Abnormal phosphorylation of tau and the mechanism of Alzheimer neurofibrillary degeneration: Sequestration of microtubule-associated proteins 1 and 2 and the disassembly of microtubules by the abnormal tau. *PNAS* **1997**, *94*, 298–303. [CrossRef]
28. Alonso, A.; Zaidi, T.; Grundke-Iqbal, I.; Iqbal, K. Role of abnormally phosphorylated tau in the breakdown of microtubules in Alzheimer disease. *PNAS* **1994**, *91*, 5562–5566. [CrossRef]
29. Pîrşcoveanu, D.F.V.; Pirici, I.; Tudorică, V.; Bălşeanu, T.A.; Albu, V.C.; Bondari, S.; Bumbea, A.M.; Pîrşcoveanu, M. Tau protein in neurodegenerative diseases—A review. *Rom. J. Morphol. Embryol.* **2017**, *58*, 1141–1150.
30. D'Andrea, M.; Nagele, R.; Wang, H.-Y.; Peterson, P.; Lee, D. Evidence that neurones accumulating amyloid can undergo lysis to form amyloid plaques in Alzheimer's disease. *Histopathology* **2001**, *38*, 120–134. [CrossRef]
31. Nagele, R.; D'Andrea, M.; Anderson, W.; Wang, H.-Y. Accumulation of beta-amyloid1-42 in neurons is facilitated by the alpha7 nicotinic acetylcholine receptor in Alzheimer's disease. *Neuroscience* **2002**, *110*, 199–211. [CrossRef]
32. Povala, G.; Bellaver, B.; De Bastiani, M.A.; Brum, W.S.; Ferreira, P.C.L.; Bieger, A.; Pascoal, T.A.; Benedet, A.L.; Souza, D.O.; Araujo, R.M.; et al. Soluble amyloid-beta isoforms predict downstream Alzheimer's disease pathology. *Cell Biosci.* **2021**, *11*, 204. [CrossRef]
33. Dziewczapolski, G.; Glogowski, C.; Masliah, E.; Heinemann, S. Deletion of the α7 Nicotinic Acetylcholine Receptor Gene Improves Cognitive Deficits and Synaptic Pathology in a Mouse Model of Alzheimer's Disease. *J. Neurosci.* **2009**, *29*, 8805–8815. [CrossRef]
34. Cecon, E.; Dam, J.; Luka, M.; Gautier, C.; Chollet, A.M.; Delagrange, P.; Danober, L.; Jockers, R. Quantitative assessment of oligomeric amyloid β peptide binding to α7 nicotinic receptor. *Br. J. Pharmacol.* **2019**, *176*, 3475–3488. [CrossRef]
35. Gambuzza, M.; Sofo, V.; Salmeri, F.; Soraci, L.; Marino, S.; Bramanti, P. Toll-like receptors in Alzheimer's disease: A therapeutic perspective. *CNS Neurol. Disord. Drug Targets* **2014**, *13*, 1542–1558. [CrossRef]
36. Calsolaro, V.; Edison, P. Neuroinflammation in Alzheimer's disease: Current evidence and future directions. *Alzheimers Dement.* **2016**, *12*, 719–732. [CrossRef]
37. Liu, S.; Liu, Y.; Hao, W.; Wolf, L.; Kiliaan, A.J.; Penke, B.; Rübe, C.E.; Walter, J.; Heneka, M.T.; Hartmann, T.; et al. TLR2 is a primary receptor for Alzheimer's amyloid β peptide to trigger neuroinflammatory activation. *J. Immunol.* **2012**, *188*, 1098–1107. [CrossRef]
38. Re, F.; Strominger, J.L. Toll-like receptor 2 (TLR2) and TLR4 differentially activate human dendritic cells. *J. Biol. Chem.* **2001**, *276*, 37692–37699. [CrossRef]
39. Xia, M.Q.; Qin, S.X.; Wu, L.J.; Mackay, C.R.; Hyman, B.T. Immunohistochemical study of the beta-chemokine receptors CCR3 and CCR5 and their ligands in normal and Alzheimer's disease brains. *Am. J. Pathol.* **1998**, *153*, 31–37. [CrossRef]
40. Singer, I.I.; Scott, S.; Kawka, D.W.; Chin, J.; Daugherty, B.L.; DeMartino, J.A.; DiSalvo, J.; Gould, S.L.; Lineberger, J.E.; Malkowitz, L.; et al. CCR5, CXCR4, and CD4 are clustered and closely apposed on microvilli of human macrophages and T cells. *J. Virol.* **2001**, *75*, 3779–3790. [CrossRef]
41. Whittaker, V.P. Thirty years of synaptosome research. *J. Neurocytol.* **1993**, *22*, 735–742. [CrossRef]
42. Fein, J.A.; Sokolow, S.; Miller, C.A.; Vinters, H.V.; Yang, F.; Cole, G.M.; Gylys, K.H. Co-localization of amyloid beta and tau pathology in Alzheimer's disease synaptosomes. *Am. J. Pathol.* **2008**, *172*, 1683–1692. [CrossRef]
43. Gylys, K.H.; Fein, J.A.; Wiley, D.J.; Cole, G.M. Rapid annexin-V labeling in synaptosomes. *Neurochem. Int.* **2004**, *44*, 125–131. [CrossRef] [PubMed]
44. Kamat, P.K.; Kalani, A.; Tyagi, N. Method and validation of synaptosomal preparation for isolation of synaptic membrane proteins from rat brain. *MethodsX* **2014**, *1*, 102–107. [CrossRef] [PubMed]
45. Sokolow, S.; Henkins, K.M.; Williams, I.A.; Vinters, H.V.; Schmid, I.; Cole, G.M.; Gylys, K.H. Isolation of synaptic terminals from Alzheimer's disease cortex. *Cytom. A* **2012**, *81*, 248–254. [CrossRef] [PubMed]
46. Ergin, E.; Dogan, A.; Parmaksiz, M.; Elçin, A.E.; Elçin, Y.M. Time-resolved fluorescence resonance energy transfer [TR-FRET] assays for biochemical processes. *Curr. Pharm. Biotechnol.* **2016**, *17*, 1222–1230. [CrossRef] [PubMed]
47. Marra, G.; Treppiedi, D.; Di Muro, G.; Mangili, F.; Catalano, R.; Esposito, E.; Nozza, E.; Locatelli, M.; Lania, A.; Sala, E.; et al. *A Novel Filamin A-Binding Molecule May Significantly Enhance Somatostatin Receptor Type 2 Antitumoral Actions in Growth Hormone-Secreting PitNET Cells*; European Congress of Endocrinology: Istanbul, Turkey, 2023.
48. Zhang, L.; Huang, T.; Teaw, S.; Nguyen, L.H.; Hsieh, L.S.; Gong, X.; Burns, L.H.; Bordey, A. Filamin A inhibition reduces seizure activity in a mouse model of focal cortical malformations. *Sci. Transl. Med.* **2020**, *12*, eaay0289. [CrossRef] [PubMed]
49. Zhang, F.; Gannon, M.; Chen, Y.; Yan, S.; Zhang, S.; Feng, W.; Tao, J.; Sha, B.; Liu, Z.; Saito, T.; et al. β-amyloid redirects norepinephrine signaling to activate the pathogenic GSK3β/tau cascade. *Sci. Transl. Med.* **2020**, *12*, eaay6931. [CrossRef]
50. Cecon, E.; Lhomme, T.; Maurice, T.; Luka, M.; Chen, M.; Silva, A.; Wauman, J.; Zabeau, L.; Tavernier, J.; Prévot, V.; et al. Amyloid beta peptide is an endogenous negative allosteric modulator of leptin receptor. *Neuroendocrinology* **2021**, *111*, 370–387. [CrossRef]

51. Heneka, M.T.; Carson, M.J.; El Khoury, J.; Landreth, G.E.; Brosseron, F.; Feinstein, D.L.; Jacobs, A.H.; Wyss-Coray, T.; Vitorica, J.; Ransohoff, R.M.; et al. Neuroinflammation in Alzheimer's disease. *Lancet Neurol.* **2015**, *14*, 388–405.
52. Hickman, S.E.; Allison, E.K.; El Khoury, J. Microglial dysfunction and defective beta-amyloid clearance pathways in aging Alzheimer's disease mice. *J. Neurosci.* **2008**, *28*, 8354–8360. [CrossRef]
53. Zhang, F.; Jiang, L. Neuroinflammation in Alzheimer's disease. *Neuropsychiatr. Dis. Treat.* **2015**, *11*, 243–256. [CrossRef]
54. Steinman, L. Inflammatory cytokines at the summits of pathological signal cascades in brain diseases. *Sci. Signal.* **2013**, *6*, pe3. [CrossRef]
55. Zlokovic, B.V. Neurovascular pathways to neurodegeneration in Alzheimer's disease and other disorders. *Nat. Rev. Neurosci.* **2011**, *12*, 723–738. [CrossRef]
56. Zipser, B.D.; Johanson, C.E.; Gonzalez, L.; Berzin, T.M.; Tavares, R.; Hulette, C.M.; Vitek, M.P.; Hovanesian, V.; Stopa, E.G. Microvascular injury and blood-brain barrier leakage in Alzheimer's disease. *Neurobiol. Aging* **2007**, *28*, 977–986. [CrossRef]
57. Cornell, J.; Salinas, S.; Huang, H.Y.; Zhou, M. Microglia regulation of synaptic plasticity and learning and memory. *Neural. Regen. Res.* **2022**, *17*, 705–716. [PubMed]
58. Shoelson, S.E.; Lee, J.; Goldfine, A.B. Inflammation and insulin resistance. *J. Clin. Investig.* **2006**, *116*, 1793–1801. [CrossRef]
59. Ferreira, S.T.; Clarke, J.R.; Bomfim, T.R.; De Felice, F.G. Inflammation, defective insulin signaling, and neuronal dysfunction in Alzheimer's disease. *Alzheimers Dement.* **2014**, *10* (Suppl. 1), S76–S83. [CrossRef]
60. Hotamisligil, G.S.; Shargill, N.S.; Spiegelman, B.M. Adipose expression of tumor necrosis factor-alpha: Direct role in obesity-linked insulin resistance. *Science* **1993**, *259*, 87–91. [CrossRef]
61. Feinstein, R.; Kanety, H.; Papa, M.Z.; Lunenfeld, B.; Karasik, A. Tumor necrosis factor-alpha suppresses insulin-induced tyrosine phosphorylation of insulin receptor and its substrates. *J. Biol. Chem.* **1993**, *268*, 26055–26058. [CrossRef]
62. Ly, M.; Yu, G.Z.; Mian, A.; Cramer, A.; Meysami, S.; Merrill, D.A.; Samara, A.; Eisenstein, S.A.; Hershey, T.; Babulal, G.M.; et al. Neuroinflammation: A modifiable pathway linking obesity, Alzheimer's disease, and depression. *Am. J. Geriatr. Psychiatry* **2023**, *31*, 853–866. [CrossRef]
63. Wang, H.-Y.; Pei, Z.; Lee, K.-C.; Nikolov, B.; Doehner, T.; Puente, J.; Friedmann, N.; Burns, L. Simufilam suppresses overactive mTOR and restores its sensitivity to insulin in Alzheimer's disease patient lymphocytes. *Front. Aging* **2023**, *4*, 1175601. [CrossRef]
64. Gu, S.; Matta, J.A.; Lord, B.; Harrington, A.W.; Sutton, S.W.; Davini, W.B.; Bredt, D.S. Brain α7 Nicotinic Acetylcholine Receptor Assembly Requires NACHO. *Neuron* **2016**, *89*, 948–955. [CrossRef]
65. McKhann, G.; Drachman, D.; Folstein, M.; Katzman, R.; Price, D.; Stadlan, E. Clinical diagnosis of Alzheimer's disease: Report of the NINCDS-ADRDA Work Group under the auspices of Department of Health and Human Services Task Force on Alzheimer's disease. *Neurology* **1984**, *34*, 939–944. [CrossRef] [PubMed]
66. Yamamoto, T.; Hirano, A. A comparative study of modified Bielschowsky, Bodian and thioflavin S stains on Alzheimer's neurofibrillary tangles. *Neuropathol. Appl. Neurobiol.* **1986**, *12*, 3–9. [CrossRef] [PubMed]
67. Hyman, B.; Trojanowski, J. Consensus recommendations for the postmortem diagnosis of Alzheimer disease from the National Institute on Aging and the Reagan Institute Working Group on diagnostic criteria for the neuropathological assessment of Alzheimer disease. *J. Neuropathol. Exp. Neurol.* **1997**, *56*, 1095–1097. [CrossRef]
68. Oddo, S.; Caccamo, A.; Shepherd, J.D.; Murphy, M.P.; Golde, T.E.; Kayed, R.; Metherate, R.; Mattson, M.P.; Akbari, Y.; LaFerla, F.M. Triple-transgenic model of Alzheimer's disease with plaques and tangles: Intracellular Abeta and synaptic dysfunction. *Neuron* **2003**, *39*, 409–421. [CrossRef]
69. Wang, H.-Y.; Friedman, E. Effects of lithium on receptor-mediated activation of G proteins in rat brain cortical membranes. *Neuropharmacology* **1999**, *38*, 403–414. [CrossRef]
70. Wang, L.; Gintzler, A. Bimodal opioid regulation of cyclic AMP formation: Implications for positive and negative coupling of opiate receptors to adenylyl cyclase. *J. Neurochem.* **1994**, *63*, 1726–1730. [CrossRef]
71. Weis, W.I.; Kobilka, B.K. The Molecular Basis of G Protein-Coupled Receptor Activation. *Annu. Rev. Biochem.* **2018**, *87*, 897–919. [CrossRef]

International Journal of
Molecular Sciences

MDPI

Article

Repeated Methamphetamine Administration Results in Axon Loss Prior to Somatic Loss of Substantia Nigra Pars Compacta and Locus Coeruleus Neurons in Male but Not Female Mice

Alexander Pilski and Steven M. Graves *

Department of Pharmacology, University of Minnesota, Minneapolis, MN 55455, USA; pilsk001@umn.edu
* Correspondence: gravess@umn.edu

Abstract: Methamphetamine (meth) is a neurotoxic psychostimulant that increases monoamine oxidase (MAO)-dependent mitochondrial oxidant stress in axonal but not somatic compartments of substantia nigra pars compacta (SNc) and locus coeruleus (LC) neurons. Chronic meth administration results in the degeneration of SNc and LC neurons in male mice, and MAO inhibition is neuroprotective, suggesting that the deleterious effects of chronic meth begin in axons before advancing to the soma of SNc and LC neurons. To test this hypothesis, mice were administered meth (5 mg/kg) for 14, 21, or 28 days, and SNc and LC axonal lengths and numbers of neurons were quantified. In male mice, the SNc and LC axon lengths decreased with 14, 21, and 28 days of meth, whereas somatic loss was only observed after 28 days of meth; MAO inhibition (phenelzine; 20 mg/kg) prevented axonal and somatic loss of SNc and LC neurons. In contrast, chronic (28-day) meth had no effect on the axon length or numbers of SNc or LC neurons in female mice. The results demonstrate that repeated exposure to meth produces SNc and LC axonal deficits prior to somatic loss in male subjects, consistent with a dying-back pattern of degeneration, whereas female mice are resistant to chronic meth-induced degeneration.

Keywords: methamphetamine; neurodegeneration; substantia nigra pars compacta; locus coeruleus; monoamine oxidase; sex difference

Citation: Pilski, A.; Graves, S.M. Repeated Methamphetamine Administration Results in Axon Loss Prior to Somatic Loss of Substantia Nigra Pars Compacta and Locus Coeruleus Neurons in Male but Not Female Mice. *Int. J. Mol. Sci.* **2023**, *24*, 13039. https://doi.org/10.3390/ijms241713039

Academic Editor: Claudia Ricci

Received: 29 July 2023
Revised: 17 August 2023
Accepted: 19 August 2023
Published: 22 August 2023

1. Introduction

Methamphetamine (meth) is an addictive psychostimulant with escalating rates of abuse in the United States [1–3]. In addition to being highly addictive, meth is also neurotoxic [4,5]. Clinical evidence from human meth users shows decreased dopamine content, tyrosine hydroxylase (TH) and dopamine transporter (DAT) expressions, and vesicular monoamine transporter 2 (VMAT2) and DAT binding in the striatum, suggesting nigrostriatal axon loss [6–13]. Similar outcomes are reported in rodents using acute binge paradigms wherein subjects are administered a single high-dose bolus or multiple injections in a single day, which result in decreased dopamine tissue content; DAT, VMAT2, and TH immunoreactivity; DAT and VMAT2 binding; DAT protein expression; and TH and VMAT2 activity [14–35]. We have recently reported that the deleterious effects of meth extend beyond nigrostriatal axons. More specifically, chronic (28-day) meth (5 mg/kg; i.p.) administration to male mice results in overt SNc degeneration that is linked to meth-induced axonal mitochondrial oxidant stress [36–38].

Meth binds to and induces dysfunction of monoamine reuptake proteins as well as VMAT2. In dopaminergic neurons, the consequence of binding to and inducing dysfunction of VMAT2 is increased cytosolic dopamine concentrations [39,40], which increases mitochondrial oxidant stress in axonal but not somatic subcellular compartments [36,38]. This meth-induced axonal mitochondrial oxidant stress results from MAO metabolism of dopamine, which generates free electrons that are transferred to the mitochondrial intermembrane space [38]. The in vivo administration of meth (5 mg/kg) for 28 consecutive

days to male mice results in SNc degeneration (both axonal and somatic), which is prevented by a mitochondrial antioxidant (mitoTEMPO) or a MAO inhibitor [36]. Together, these data suggest that meth-induced MAO-dependent axonal mitochondrial oxidant stress is necessary for degeneration.

In addition to SNc dopamine neurons, meth similarly impacts locus coeruleus (LC) norepinephrine neurons [41]. Like in SNc neurons, meth increases MAO-dependent axonal but not somatic mitochondrial oxidant stress in LC neurons [42]. Furthermore, chronic in vivo administration of meth results in a loss of LC axon length and the number of norepinephrine neurons in the LC of male mice, both of which are prevented by MAO inhibition [42]. Therefore, meth-induced MAO-dependent axonal mitochondrial oxidant stress appears to be necessary for chronic meth-induced LC degeneration, just as in SNc neurons [36,37,42]. However, the manner in which SNc and LC degeneration progresses during chronic meth administration is unclear.

Given that meth increases axonal but not somatic mitochondrial oxidant stress in SNc and LC neurons, and that MAO inhibition is neuroprotective [36,37,42], we hypothesized that chronic meth administration would result in axon loss first, followed by somatic loss, consistent with a dying-back pattern of neurodegeneration. To test this hypothesis, male mice were administered meth (5 mg/kg; i.p.) or saline for 14, 21, or 28 consecutive days, after which the axon lengths and numbers of SNc and LC neurons were stereologically quantified. To confirm MAO-dependence of degeneration, a separate group of mice were treated with the MAO inhibitor phenelzine (20 mg/kg; i.p.) as a 30-min pretreatment prior to each meth injection. To determine whether SNc and LC neurons in female subjects are similarly vulnerable to chronic meth-induced degeneration, female subjects were administered saline or meth (5 mg/kg; i.p.) for 28 consecutive days, and axon lengths and numbers of neurons in the SNc and LC were stereologically quantified.

2. Results

2.1. Chronic Methamphetamine Administration Resulted in Axonal Loss Prior to Somatic Loss of Substantia Nigra Pars Compacta Dopamine Neurons in Male Mice

In ex vivo brain slices, the bath perfusion of meth (10 μM) increased MAO-dependent axonal but not somatic mitochondrial oxidant stress in SNc neurons [38]; in vivo, the chronic administration of meth (5 mg/kg; i.p.) for 28 consecutive days resulted in degeneration of SNc dopamine neurons, which is prevented by pretreating subjects with a mitochondrial antioxidant or a MAO inhibitor [36,37]; this suggests that meth-induced MAO-dependent axonal mitochondrial oxidant stress is a driver of degeneration, and that the deleterious effects of repeated meth exposure impact the axons first. To test whether axonal loss precedes somatic loss, male mice were administered saline or meth (5 mg/kg) for 14, 21, or 28 consecutive days, after which brains were collected and SNc axon lengths in the dorsolateral striatum (DLS) and numbers of dopamine neurons in the SNc were stained for TH (TH^+). The lengths of TH^+ axons in the DLS and numbers of TH^+ neurons in the SNc were stereologically quantified by an experimenter blinded to the treatment histories. Fourteen days of meth administration decreased SNc axonal lengths in the DLS (Figure 1A,B), but had no effect on the numbers of TH^+ neurons in the SNc (Figure 1F,G). Similarly, 21 days of meth (5 mg/kg) decreased SNc axonal lengths in the DLS (Figure 1C), but still had no effect on the numbers of TH^+ SNc neurons (Figure 1H). However, consistent with prior studies [36,37], a chronic 28-day treatment of meth resulted in a decrease in both SNc axonal length (Figure 1D,E) and numbers of TH^+ neurons in the SNc (Figure 1I,J). We have previously shown that rasagiline, a MAO-B inhibitor with FDA approval for the treatment of Parkinson's disease, prevents chronic meth-induced SNc degeneration [36,37]. In the current study, we tested a second clinically available MAO inhibitor, phenelzine, which inhibits both MAO-A and MAO-B isoforms, and is FDA-approved for the treatment of panic disorder, social anxiety disorder, and treatment-resistant depression. Pre-treating mice with phenelzine (20 mg/kg) 30 min prior to each meth administration prevented both axonal (Figure 1D) and somatic loss of SNc dopamine neurons (Figure 1I).

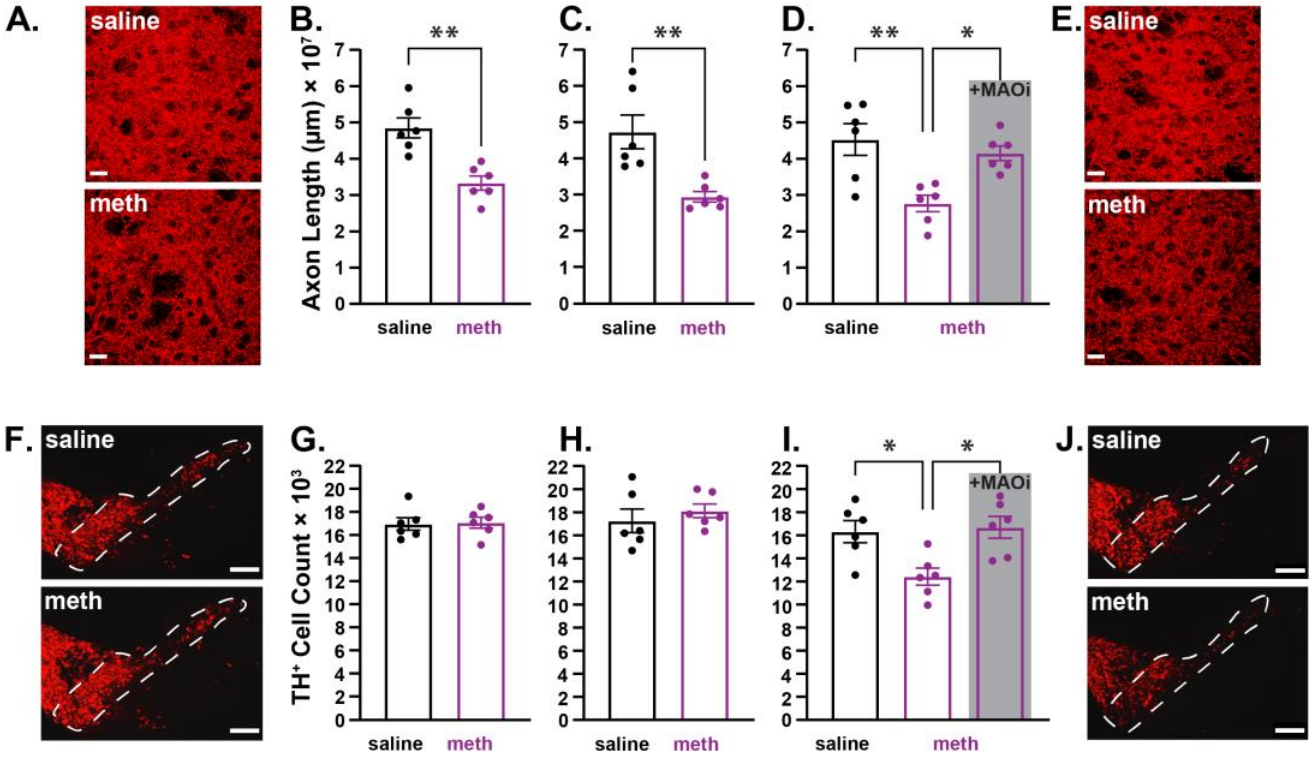

Figure 1. Repeated methamphetamine administration in male mice resulted in axon loss prior to somatic loss in substantia nigra pars compacta dopamine neurons. Male mice were treated with saline or methamphetamine (meth; 5 mg/kg) for 14, 21, or 28 consecutive days, after which substantia nigra pars compacta (SNc) axonal lengths in the dorsolateral striatum (DLS) and numbers of dopamine neurons in the SNc were stereologically quantified. (**A**) Representative images of SNc axons stained for tyrosine hydroxylase (TH^+; red) in the DLS from a male mouse treated with saline (**top**) and meth (**bottom**) for 14 consecutive days; scale bars denote 20 µm. (**B**) SNc axon length decreased in mice treated with meth for 14 days ($n = 6$) compared to saline-treated control mice ($n = 6$). Data analyzed using unpaired *t*-test ($t(10) = 4.483$, $p = 0.0012$, two-tailed). (**C**) Administration of meth (5 mg/kg) for 21 days also decreased SNc axonal length (saline: $n = 6$; meth: $n = 6$; $t(10) = 3.669$, $p = 0.0043$, two-tailed). (**D**) Male mice were administered saline ($n = 6$), meth ($n = 6$) or meth with a 30-min phenelzine (20 mg/kg; +MAOi; $n = 6$) pretreatment for 28 days; 28-day meth treatment decreased SNc axonal length, and this decrease was prevented by pretreatment with phenelzine. Data analyzed using one-way ANOVA ($F_{(2,15)} = 9.108$, $p = 0.0026$) with Tukey's post hoc analysis (saline vs. meth, $p = 0.0028$; saline vs. +MAOi, $p = 0.6713$; meth vs. +MAOi, $p = 0.0158$). (**E**) Representative images of SNc axons stained for tyrosine hydroxylase (TH^+) in the DLS from a male mouse treated with saline (**top**) and meth (5 mg/kg; **bottom**) for 28 consecutive days; scale bars denote 20 µm. (**F**) Representative images of TH^+ SNc neurons from a male mouse treated with saline (**top**) and meth (**bottom**) for 14 consecutive days; scale bars denote 200 µm. (**G**) The numbers of TH^+ neurons in the SNc did not decrease in mice treated with meth ($n = 6$) for 14 days compared to saline-treated mice ($n = 6$). Data analyzed using unpaired *t*-test ($t(10) = 0.1675$, $p = 0.8703$, two-tailed). (**H**) Administration of meth (5 mg/kg) for 21 days also did not alter the number of TH^+ neurons in the SNc (saline: $n = 6$; meth: $n = 6$; $t(10) = 0.7319$, $p = 0.4810$, two-tailed). (**I**) Male mice were administered saline ($n = 6$), meth ($n = 6$), or meth with a 30-min phenelzine (20 mg/kg; +MAOi; $n = 6$) pretreatment for 28 consecutive days; 28-day meth treatment decreased the number of TH^+ SNc neurons, and this decrease was prevented by pretreatment with phenelzine. Data analyzed using one-way ANOVA ($F_{(2,15)} = 7.095$, $p = 0.0068$) with Tukey's post hoc analysis (saline vs. meth, $p = 0.0188$; saline vs. +MAOi, $p = 0.9515$; meth vs. +MAOi, $p = 0.0103$). (**J**) Representative images of TH^+ SNc neurons from a male mouse treated with saline (**top**) and meth (**bottom**) for 28 consecutive days; scale bars denote 200 µm; * $p \leq 0.05$, ** $p \leq 0.01$.

2.2. Chronic Administration of Methamphetamine Resulted in Axonal Loss Prior to Somatic Loss of Locus Coeruleus Norepinephrine Neurons in Male Mice

In addition to targeting dopaminergic neurons, meth also binds to and induces dysfunction of VMAT2 in LC norepinephrine neurons [41]. Consistent with meth effects in SNc dopamine neurons [36,37], meth increases MAO-dependent mitochondrial oxidant stress in LC axons but not in the soma, and chronic in vivo meth administration to male mice results in LC degeneration that is prevented by MAO inhibition [42]. To test whether meth-induced LC degeneration follows the same pattern as that observed in SNc neurons (i.e., axonal loss prior to somatic loss; Figure 1), LC axons in the M1 motor cortex were stained for the norepinephrine transporter (NET^+), and norepinephrine neurons in the LC were stained for TH from male mice treated with saline or meth (5 mg/kg; i.p.) for 14, 21, or 28 days. Consistent with the results in SNc neurons from male mice (Figure 1), chronic meth administration resulted in LC axon loss in the M1 motor cortex prior to somatic loss (Figure 2). Repeated meth administration for 14 (Figure 2A,B) and 21 (Figure 2C) days decreased LC axonal length, but had no effect on the number of TH^+ neurons in the LC (Figure 2F–H), whereas 28 days of administration significantly decreased both axonal length (Figure 2D,E) and the number of TH^+ LC neurons (Figure 2I,J); 28-day meth-induced deficits in LC axon lengths and numbers of TH^+ LC neurons were prevented by pre-treating with the MAO inhibitor phenelzine (20 mg/kg; Figure 2D,I).

2.3. Female Mice were Resistant to Chronic Methamphetamine-Induced Degeneration of Substantia Nigra Pars Compacta Dopamine Neurons

Acute binge models wherein subjects are repeatedly administered meth over the course of one day or given a single high dose consistently show deleterious effects on SNc axons in male subjects [14,17,21,22,25,27], whereas female subjects are resistant to the deleterious effects of an acute meth binge [43–50]. To determine whether SNc neurons in female subjects are similarly resistant to the effects of chronic meth, female mice were administered saline or meth (5 mg/kg) for 28 consecutive days followed by stereological analysis of SNc axonal lengths in the DLS and numbers of TH^+ neurons in the SNc. Congruent with results from studies using acute binge models [43–50], female mice were resistant to chronic meth-induced degeneration of SNc neurons. There was no difference in the length of SNc axons in the DLS (Figure 3A,B) or the number of TH^+ neurons in the SNc (Figure 3C,D) between mice administered saline or meth for 28 consecutive days.

2.4. Female Mice were Resistant to Chronic Methamphetamine-Induced Degeneration of Locus Coeruleus Norepinephrine Neurons

To determine whether LC neurons were resistant to chronic meth-induced degeneration in female mice, the lengths of NET^+ LC axons in the M1 motor cortex and numbers of TH^+ cells in the LC were quantified after chronic 28-day administration of saline or meth (5 mg/kg). Consistent with results in SNc dopamine neurons (Figure 3), LC norepinephrine neurons in female mice were resistant to chronic meth-induced degeneration. There were no differences in the lengths of NET^+ axons in the M1 motor cortex (Figure 4A,B) or numbers of TH^+ neurons in the LC between female subjects treated with saline or meth (Figure 4C,D).

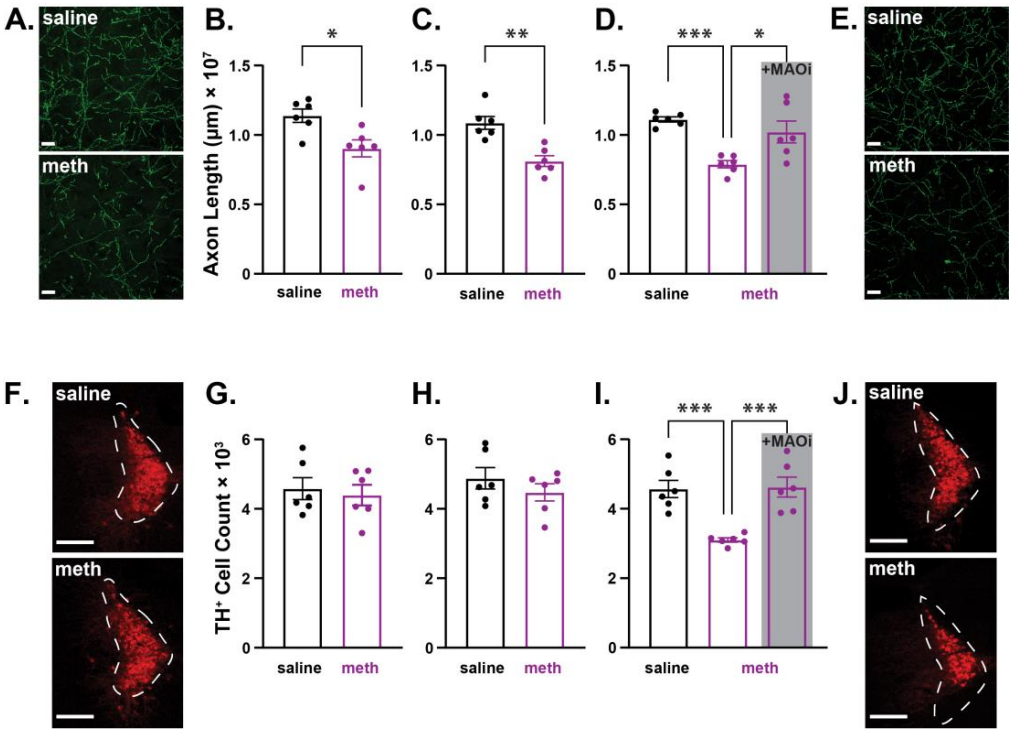

Figure 2. Repeated methamphetamine administration in male mice resulted in axonal loss prior to somatic loss in locus coeruleus norepinephrine neurons. Male mice were treated with saline or methamphetamine (meth; 5 mg/kg) for 14, 21, or 28 consecutive days, after which locus coeruleus (LC) axonal lengths in the M1 motor cortex and numbers of norepinephrine neurons in the LC were stereologically quantified. (**A**) Representative images of LC axons stained for the norepinephrine transporter (NET^+; green) in the M1 motor cortex from a male mouse treated with saline (**top**) and meth (**bottom**) for 14 consecutive days; scale bars denote 20 μm. (**B**) LC axonal length decreased in mice treated with meth for 14 days ($n = 6$) compared to saline-treated control mice ($n = 6$). Data analyzed using unpaired *t*-test ($t(10) = 3.102$, $p = 0.0131$, two-tailed). (**C**) Administration of meth for 21 consecutive days also decreased LC axonal length (saline: $n = 6$; meth: $n = 6$; $t(10) = 4.562$, $p = 0.0010$, two-tailed). (**D**) Male mice were administered saline ($n = 6$), meth ($n = 6$) or meth with a 30-min phenelzine (20 mg/kg; +MAOi; $n = 6$) pretreatment for 28 consecutive days, and LC axonal lengths in the M1 motor cortex were stereologically quantified. Chronic 28-day meth treatment decreased LC axonal length compared to saline-treated controls, and this decrease was prevented by pretreatment with phenelzine. Data analyzed using one-way ANOVA ($F_{(2,15)} = 11.41$, $p = 0.0010$) with Tukey's post hoc analysis (saline vs. meth, $p = 0.0009$; saline vs. +MAOi, $p = 0.4192$; meth vs. +MAOi, $p = 0.0119$). (**E**) Representative images of NET^+ LC axons in the M1 motor cortex from a male mouse treated with saline (**top**) and meth (**bottom**) for 28 consecutive days; scale bars denote 20 μm. (**F**) Representative images of LC neurons stained for tyrosine hydroxylase (TH^+; red) from a male mouse treated with saline (**top**) and meth (**bottom**) for 14 consecutive days; scale bars denote 200 μm. (**G**) The numbers of TH^+ LC neurons did not decrease in mice treated with meth for 14 days ($n = 6$) compared to saline-treated control mice ($n = 6$). Data analyzed using unpaired *t*-test ($t(10) = 0.4326$, $p = 0.6745$, two-tailed). (**H**) Administration of meth for 21 consecutive days also did not decrease the number of TH^+ LC neurons (saline: $n = 6$; meth: $n = 6$; $t(10) = 1.026$, $p = 0.3293$, two-tailed). (**I**) Repeated 28-day meth treatment decreased the number of TH^+ LC neurons compared to saline-treated controls, and this decrease was prevented by pretreatment with phenelzine (saline: $n = 6$, meth: $n = 6$, and +MAOi $n = 6$ mice). Data analyzed using one-way ANOVA ($F_{(2,15)} = 15.08$, $p = 0.0003$) with Tukey's post hoc analysis (saline vs. meth, $p = 0.0008$; saline vs. +MAOi, $p = 0.9837$; meth vs. +MAOi, $p = 0.0006$). (**J**) Representative images of TH^+ LC neurons from a male mouse treated with saline (**top**) and meth (**bottom**) for 28 consecutive days; scale bars denote 200 μm; * $p \leq 0.05$, ** $p \leq 0.01$ *** $p \leq 0.001$.

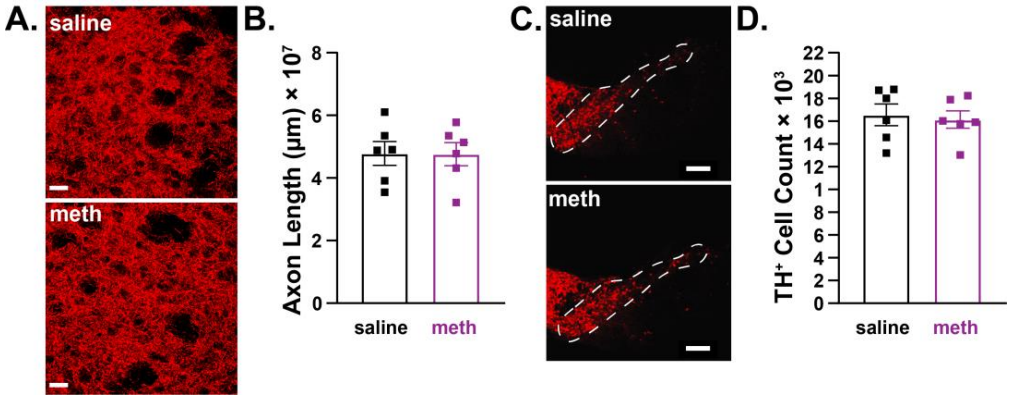

Figure 3. Chronic methamphetamine administration had no effect on axon length or numbers of tyrosine hydroxylase-stained substantia nigra pars compacta dopamine neurons in female mice. Female mice were treated with saline or methamphetamine (meth; 5 mg/kg) for 28 consecutive days, after which substantia nigra pars compacta (SNc) axonal length in the dorsolateral striatum (DLS) and numbers of dopamine neurons in the SNc were stereologically quantified. (**A**) Representative images of SNc axons stained for tyrosine hydroxylase (TH^+; red) in the DLS from a female mouse treated with saline (**top**) and meth (**bottom**) for 28 consecutive days; scale bars denote 20 μm. (**B**) SNc axonal length was unchanged by 14 days of meth (n = 6) compared to saline-treated mice (n = 6). Data analyzed using unpaired t-test ($t(10)$ = 0.03984, p = 0.9690, two-tailed). (**C**) Representative images of SNc neurons stained for tyrosine hydroxylase (TH^+) from a female mouse treated with saline (**top**) and meth (**bottom**) for 28 consecutive days; scale bars denote 200 μm. (**D**) The numbers of TH^+ SNc dopamine neurons in female mice were unchanged by chronic meth administration (saline: n = 6 mice; meth: n = 6 mice). Data analyzed using unpaired t-test ($t(10)$ = 0.3416, p = 0.7397, two-tailed).

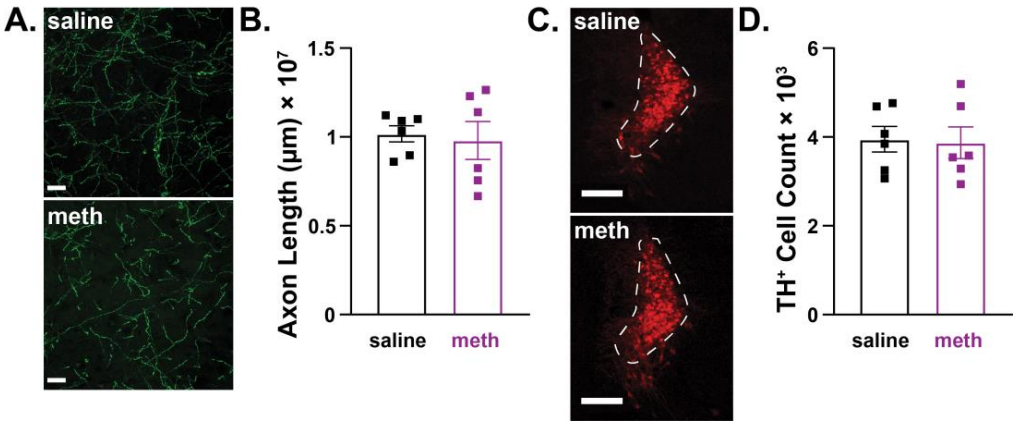

Figure 4. Chronic methamphetamine administration had no effect on axon lengths or numbers of locus coeruleus norepinephrine neurons in female mice. Female mice were treated with saline or methamphetamine (meth; 5 mg/kg) for 28 consecutive days, after which locus coeruleus (LC) axonal lengths in the M1 motor cortex and numbers of norepinephrine neurons in the LC were stereologically quantified. (**A**) Representative images of LC axons stained for the norepinephrine transporter (NET^+; green) in the M1 motor cortex from a female mouse treated with saline (**top**) and meth (**bottom**) for 28 days; scale bars denote 20 μm. (**B**) NET^+ LC axonal length was unchanged by 28-day meth (n = 6) compared to saline-treated control mice (n = 6). Data analyzed using unpaired t-test ($t(10)$ = 0.3210, p = 0.7548, two-tailed). (**C**) Representative images of LC neurons stained for tyrosine hydroxylase (TH^+; red) from a female mouse treated with saline (**top**) and meth (**bottom**) for 28 consecutive days; scale bars denote 200 μm. (**D**) The numbers of TH^+ LC neurons were unchanged by chronic 28-day treatment of meth (n = 6) compared to saline-treated control mice (n = 6). Data analyzed using unpaired t-test ($t(10)$ = 0.1698, p = 0.8692, two-tailed).

3. Discussion

We recently reported that chronic 28-day in vivo administration of meth (5 mg/kg) results in a loss of SNc dopamine and LC norepinephrine neurons in male mice [36,37,42]. Results from the current study extend these findings to show that in both SNc dopamine and LC norepinephrine neurons, meth administration produces axonal deficits prior to somatic loss, suggesting that chronic meth administration produces a dying-back pattern of degeneration in both SNc and LC neurons. The observed losses of TH^+ neurons in the SNc and LC are unlikely to be the result of phenotypic suppression, as our prior studies have shown decreased numbers of NeuN-, the neuronal-specific nuclear splicing regulator Fox 3 [51] stained cells in the SNc and LC [36,42], supporting the interpretation of overt cell loss. Furthermore, the number of SNc neurons and optical density of nigrostriatal axons fluorescently labelled by genetically encoded TdTomato were also decreased by chronic 28-day meth [37]. However, it is possible that phenotypic suppression occurs prior to cell loss, as recently reported in a mouse model of Parkinson's disease [52]. Our prior studies also demonstrated the neuroprotective efficacy of rasagiline and isradipine [36,37,42]. Rasagiline is an irreversible MAO-B inhibitor that is FDA-approved for treatment of Parkinson's disease, and isradipine is an L-type calcium channel inhibitor that is an FDA-approved dihydropyridine antihypertensive medication. Current results expand the list of clinically available medications that attenuate meth-induced degeneration to include phenelzine, an irreversible MAO-A/B inhibitor FDA-approved for treatment-resistant depression, panic disorder, and social anxiety disorder. MAO inhibition using the MAO-A selective inhibitor clorgyline also attenuates meth-induced mitochondrial oxidant stress in SNc axons [38]; future studies will be necessary to determine whether MAO-A inhibition is similarly effective at preventing meth-induced SNc and/or LC degeneration. A third key outcome from our investigation is a robust sex difference wherein female subjects were resistant to chronic meth-induced degeneration.

Chronic 28-day meth administration to male mice resulted in a ~30% decrease in the numbers of TH^+ neurons in the SNc and LC as well as in corresponding axon lengths in the DLS and M1 motor cortex, a magnitude of effect that is consistent with our prior studies [36,42]. However, the same treatment paradigm had no effect on the axon length or number of SNc or LC neurons in female mice. Female subjects have similarly been shown to be resistant to the neurotoxicity that results from an acute meth binge [43–50]. The mechanism underlying these observed sex differences regarding meth neurotoxicity is unclear. One potential mechanism may be linked to L-type calcium channels. $Cav_{1.3}$ L-type calcium channel activity contributes to mitochondrial oxidant stress in SNc and LC neurons [53–57]; inhibition of L-type calcium channels with isradipine attenuates mitochondrial oxidant stress in SNc and LC neurons, is neuroprotective in mouse models of Parkinson's disease, and prevents chronic meth-induced degeneration of SNc and LC neurons in male mice [36,42,54,56,58,59]. In cultured striatal neurons, 17β-estradiol inhibits L-type calcium channel-mediated currents, and the magnitude of this effect is larger in neurons from female subjects [60]. Therefore, we would predict that mitochondrial oxidant stress in SNc and LC neurons from female subjects would be less than that in males due to inhibition of L-type calcium channels by endogenous 17β-estradiol, and that this endogenous mechanism of L-type calcium channel inhibition could potentially account for the observed sex difference. Future studies are needed to test this hypothesis and determine the impact of sex hormones on mitochondrial oxidant stress and its implications for neurodegeneration. Whether the observed resistance to meth-induced degeneration in females is long-lasting is also in need of further study. In male rats trained to self-administer meth for 14 days, evidence of nigrostriatal axon loss did not become apparent until 14 days of abstinence, with evidence of SNc degeneration appearing at 28 days of abstinence [61]. This suggests that degenerative processes may continue to evolve throughout periods of abstinence. Further investigation is needed to fully examine and explore mechanisms of potential degeneration during abstinence, and whether resistance to degeneration in female subjects persists. Overall, the neurotoxic effects of meth on catecholaminergic systems

and the possibility of continued degeneration during abstinence raise significant concerns regarding the potential impact of meth abuse on neurodegenerative diseases.

Parkinson's disease (PD) is the most common neurodegenerative movement disorder, and the second-most common neurodegenerative disease overall. The deleterious effects of meth are strikingly similar to the neurodegeneration seen in PD. In PD, both SNc and LC neurons are particularly vulnerable to degeneration [62,63], a feature recapitulated by chronic meth administration [36,42]. Neurodegeneration in PD has been hypothesized to advance in a dying-back pattern wherein nigrostriatal axons are lost, followed by overt SNc degeneration [64–66] in a manner that is analogous to the observed effects of chronic meth on both SNc and LC neurons in male mice. Indeed, clinical research has demonstrated that at PD onset, patients display more severe markers of striatal axon loss than SNc cell loss, with axonal loss progressing faster than cell loss in the following 10 years [67]. Like in SNc neurons, LC axon loss also appears to occur prior to somatic loss of LC norepinephrine neurons in PD [68,69]. Meth treatment in rodents has also been shown to increase the expression of α-synuclein, a hallmark of PD, in the nigrostriatal system and gut [70–72]. Another parallel between meth-induced neurotoxicity and PD is the presence of a sex difference, with female subjects displaying relative resistance in both cases. In humans, the incidence of idiopathic PD is approximately 1.5x more common in men than women, and has an earlier onset [73]. Given the similarities between meth neurotoxicity and PD, it is perhaps not surprising that meth abuse is associated with an increased the risk for developing PD [74–79], although see [80,81]. Whether disease trajectory and severity are altered in PD patients with a history of meth abuse is unclear; further research is required to determine longitudinal effects, and to explore potential converging or overlapping mechanisms driving this degeneration. In addition to PD, our findings, past and present, on meth-induced neurodegeneration share connections with another neurodegenerative disorder: Alzheimer's disease (AD).

AD is the most common neurodegenerative disease and most common form of dementia, accounting for between 50–75% of dementia cases worldwide [82,83]. In AD, hippocampal and cortical degeneration is quite prominent; however, monoaminergic neurons, including LC neurons, are also vulnerable to degeneration. Clinical studies report an approximate 38–88% loss of TH^+, neuromelanin-, and dopamine β-hydroxylase-labeled LC neurons in post-mortem tissue [84–86]. Clinical studies also report that AD patients have decreased LC volume [87] and decreased LC signal intensity in neuromelanin-sensitive MRI scans [88,89]. Importantly, decreases in TH^+ LC neurons are associated with worsened cognitive function and increased AD neuropathology in human subjects [84]. Preclinical AD rodent models also show LC degeneration. Aged APP/PS1 mice have fewer TH^+ and NET^+ LC neurons than age-matched controls [90–93]. This loss of TH^+ LC neurons is also observed in the Tau P301S/DBH mouse model [94]. The presence of AD-related pathology in the LC and LC neuron loss may even occur during pre-symptomatic and mild cognitive impairment stages of AD prior to glutamatergic degeneration [95,96]. LC degeneration and loss of noradrenergic signaling is particularly concerning in AD, as it may contribute to disease progression and pathogenesis; pre-clinical studies show that noradrenergic signaling attenuates amyloid-β deposition, and lesioning the LC increases amyloid-β pathology and neuroinflammation [97–101]. Additionally, LC lesions in a mouse tauopathy model of AD increases hippocampal degeneration, inflammation, and mortality [97]. Therefore, the LC appears to play a protective role in AD. Although there is a paucity of studies examining the relationship between meth and AD in vivo, 15 mg/kg (i.p.) of meth injected every 12 h for 8 weeks increases amyloid-β protein and amyloid precursor protein levels in the hippocampus of non-transgenic C57Bl/6J mice [102]. Additionally, meth exposure in vitro has also shown increased amyloid-β and hyperphosphorylated tau pathology [102–104]. While epidemiological evidence linking meth and AD is lacking, the neurotoxic effect of chronic meth on LC neurons shown in the current report and prior study [42] suggest that a history of meth abuse could be a potential risk factor for AD, and is in need of further investigation.

4. Conclusions

We recently reported that chronic 28-day administration of meth results in axonal and somatic degeneration of SNc dopamine and LC norepinephrine neurons in male mice [36,37,42]. These deleterious effects of meth were further shown to be prevented by administration of the clinically available MAO-B inhibitor rasagiline and L-type calcium channel inhibitor isradipine. Results from the current report expand upon our prior studies to show that in male mice, axon loss precedes somatic loss in both SNc and LC neurons with 14- and 21-day administration of meth, decreasing axonal length without altering the number of SNc or LC neurons; meanwhile, consistent with our prior investigations [36,37,42], 28 days of meth resulted in both axonal and somatic loss. Similar to the neuroprotective effect of the MAO-B inhibitor rasagiline [36,37,42], phenelzine, a non-specific MAO-A/B inhibitor that is also clinically available, prevented meth-induced neurodegeneration. In stark contrast to results in male mice, we found that female mice were resistant to meth-induced SNc and LC degeneration. The pattern of degeneration observed in male mice and the sex difference parallels that seen in Parkinson's disease, the most common neurodegenerative movement disorder, and patients with a history of meth abuse are reported to have an increased risk for developing Parkinson's disease [74,75,79]. Whether the mechanisms underlying degeneration are shared between meth and Parkinson's disease requires further investigation. In addition to concerns for Parkinson's disease, we believe there may also be increased risk for Alzheimer's disease, the most common neurodegenerative disease. LC neurons degenerate in Alzheimer's disease, and LC degeneration has been linked to pathogeneses related to Alzheimer's [105]. Taken together, the deleterious effects of meth abuse may extend beyond neurotoxicity, and perhaps set the stage for the development of Parkinson's and/or Alzheimer's disease. Based on the current report, it would seem that this potential risk is relegated to male subjects, given that female mice were resistant to meth induced neurodegeneration; however, further study is needed to determine whether the observed resistance in females persists, or if perhaps the deleterious effects of meth simply take longer to manifest.

5. Materials and Methods

5.1. Experimental Subjects

Male and female C57Bl/6J mice were bred in-house. All subjects were group housed, maintained on a 12-h light/dark cycle, and provided free access to food and water in the home cage throughout the study. The procedures were reviewed and approved by the University of Minnesota Animal Care and use Committee, and conform to the National Institutes of Health Guide for the Care and Use of Laboratory Animals.

5.2. In Vivo Drug Administration

The male and female mice began in vivo treatments at approximately 8 weeks of age. The subjects were administered saline (10 mL/kg; General Laboratory Products) or (+)-methamphetamine hydrochloride (meth, 5 mg/kg; Sigma-Aldrich, St. Louis, MO, USA) for 14, 21, or 28 consecutive days in the home cage. To test whether monoamine oxidase (MAO) inhibition prevents degeneration, the irreversible MAO-A/B inhibitor phenelzine (20 mg/kg; Sigma-Aldrich) was administered as a 30-min pretreatment prior to each meth injection. Meth and phenelzine were dissolved in sterile saline, and all of the injections were intraperitoneal. The dose of meth and 28-day duration were based on our prior studies demonstrating meth-induced degeneration of SNc and LC neurons in male mice [36,37,42]. The dose of phenelzine (20 mg/kg) was chosen based on it being a behaviorally relevant dose in mice [106].

5.3. Immunohistochemistry

The tissue collection, sectioning, processing, and staining procedures were consistent with our prior studies [36,42]. The mice were euthanized within 12 h of the last treatment via terminal anesthesia using ketamine (50 mg/kg)/xylazine (4.5 mg/kg) followed by

transcardial perfusion with 4% paraformaldehyde in phosphate-buffered saline (PBS). The brains were extracted, post-fixed overnight in 4% paraformaldehyde in PBS, and cryoprotected in 30% sucrose in PBS. The fixed brains were sectioned (40 μm) using a microtome (Leica SM2010R, Deerfield, IL, USA), and sections spanning the dorsolateral striatum (DLS), anterior portion of the primary motor cortex (M1), substantia nigra pars compacta (SNc), and locus coeruleus (LC) were collected. Every third brain section spanning the SNc and LC was stained for tyrosine hydroxylase (TH^+), resulting in 11–13 SNc and 7–8 LC sections. Antibodies were tested for non-specific staining in-house by incubating the tissue with either primary or secondary antibody omission; fluorescent staining was not observed after primary or secondary antibody omission. Additionally, as per manufacturer websites, rabbit anti-TH polyclonal primary antibody (AB152, Millipore, Burlington, MA, USA) was tested in the corpus striatum, sympathetic nerve terminal, and adrenal gland tissue as positive controls, with liver tissue as a negative control, and Western blot analysis; mouse IgG1 anti-NET primary antibody (MA5-24647, ThermoFisher, Waltham, MA, USA) was tested in rat locus coeruleus, mouse cortex and hippocampus, and human prostate, placenta, and locus coeruleus tissue as positive controls. Secondary antibodies (Alexa 555 donkey anti-rabbit (A-31572, Invitrogen, Waltham, MA, USA) and Alexa 488 donkey anti-mouse (A-21202, Invitrogen)) have been evaluated by the manufacturer for non-specific staining in cell cultures using primary antibody exclusion and isotype controls. For the striatum and primary motor cortex, every sixth section was stained for TH^+ and the norepinephrine transporter (NET^+), respectively, resulting in 4 sections for each region. Prior to immunostaining, the sections were first treated with 20% formic acid for antigen retrieval, followed by blocking with 5% normal donkey serum. TH^+ staining of the SNc, LC, and DLS sections consisted of incubation with the primary antibody (rabbit anti-TH polyclonal AB152, Millipore 1:2000), followed by washing and incubation with Alexa 555 donkey anti-rabbit secondary antibody (A-31572, Invitrogen, 1:200). NET^+ staining of LC axons in the primary motor cortex were carried out using mouse IgG1 anti-NET primary antibody (MA5-24647, ThermoFisher; 1:1000) and Alexa 488 donkey anti-mouse (A-21202, Invitrogen) secondary antibody (1:200). The stained sections were mounted on glass slides (Electron Microscopy Sciences, Hatfield, PA, USA) with ProLong Diamond Antifade Mountant (Invitrogen), then coverslipped and stored at −20 °C.

5.4. Stereological Quantification

The stained sections were analyzed using a Zeiss microscope with a motorized stage and digital camera controlled by StereoInvestigator software version 2020 (MBF Bioscience, Williston, VT, USA). Anatomical boundaries were delineated using a 2.5X/0.085NA objective lens and stereological counting using the optical fractionator and Spaceballs probes performed using a 63×/1.4NA lens. Using the optical fractionator probe, cells were individually marked within counting frames, and total numbers of cells were calculated with StereoInvestigator software. The Spaceballs probe uses a virtual hemisphere superimposed over tissue through the *z*-plane; the axons were marked where they crossed the hemispheres at counting sites, and total axon lengths were calculated using StereoInvestigator software. For further reading on the optical fractionator and Spaceballs probes, see [107,108]. The TH^+ cells were counted throughout the SNc with a 150 μm × 150 μm counting frame and grid size of 250 μm × 275 μm [36]. A 150 μm × 150 μm counting frame and 275 μm × 175 μm grid size was used to count the LC neurons [42]. Somatic counting in the SNc and LC was performed using the optical fractionator probe with 3 μm guard zones; the stereological parameters used resulted in a Gunderson coefficient of error (m = 1) of 0.03 (SNc TH^+ neurons) and 0.05 (LC TH^+ neurons) or less. The SNc axons in the dorsolateral striatum (DLS) and LC axons in the primary motor cortex were quantified using the Spaceballs probe with a hemisphere of 7 μm and 20 μm radius, respectively. For SNc axons in the DLS a grid size of 275 μm × 275 μm, was used [36], and for LC axons in the primary motor cortex a grid size of 250 μm × 250 μm was used [42]. Quantification of SNc axons in the DLS and LC axons in the primary motor cortex was carried out using a guard zone of 3 μm;

the described parameters resulted in a Gundersen coefficient of error (m = 1) of 0.08 (DLS TH^+ axons) and 0.06 (motor cortex NET^+ axons) or less. All stereological counting was performed by an experimenter blinded to the treatment conditions.

5.5. Statistical Analysis

All datasets passed Shapiro–Wilk normality testing, and were analyzed using unpaired Student *t*-tests or one-way ANOVAs with Tukey's post hoc analysis; $\alpha = 0.05$. The statistical analyses were performed using GraphPad Prism Software, and data are presented as histograms depicting mean and standard error of the mean overlayed with individual dot plots. Detailed statistical reporting for all of the experiments is provided in the figure legends.

Author Contributions: S.M.G. and A.P. designed the experiments, and drafted and reviewed the manuscript. A.P. conducted the experiments and analyzed the data. All authors have read and agreed to the published version of the manuscript.

Funding: This research was funded by National Institutes of Health grants DA051450 and AG070962 (to S.M.G.) and DA054779 (to A.P.).

Institutional Review Board Statement: Experimental protocols and procedures were reviewed and approved by the University of Minnesota Institutional Animal Care and Use Committee (protocol code 2208-40331A; date of approval 17 March 2023).

Informed Consent Statement: Not applicable.

Data Availability Statement: Data will be made available upon reasonable request.

Conflicts of Interest: The authors declare no conflict of interest.

References

1. Substance Abuse and Mental Health Services Administration. *Key Substance Use and Mental Health Indicators in the United States: Results from the 2016 National Survey on Drug Use and Health*; Substance Abuse and Mental Health Services Administration: Rockville, MD, USA, 2017.
2. Substance Abuse and Mental Health Services Administration. *Key Substance Use and Mental Health Indicators in the United States: Results from the 2021 National Survey on Drug Use and Health*; Substance Abuse and Mental Health Services Administration: Rockville, MD, USA, 2022.
3. Jones, C.M.; Houry, D.; Han, B.; Baldwin, G.; Vivolo-Kantor, A.; Compton, W.M. Methamphetamine use in the United States: Epidemiological update and implications for prevention, treatment, and harm reduction. *Ann. N. Y. Acad. Sci.* **2022**, *1508*, 3–22. [CrossRef] [PubMed]
4. Jayanthi, S.; Daiwile, A.P.; Cadet, J.L. Neurotoxicity of methamphetamine: Main effects and mechanisms. *Exp. Neurol.* **2021**, *344*, 113795. [CrossRef] [PubMed]
5. Shaerzadeh, F.; Streit, W.J.; Heysieattalab, S.; Khoshbouei, H. Methamphetamine neurotoxicity, microglia, and neuroinflammation. *J. Neuroinflam.* **2018**, *15*, 341. [CrossRef] [PubMed]
6. McCann, U.D.; Wong, D.F.; Yokoi, F.; Villemagne, V.; Dannals, R.F.; Ricaurte, G.A. Reduced striatal dopamine transporter density in abstinent methamphetamine and methcathinone users: Evidence from positron emission tomography studies with [^{11}C]WIN-35,428. *J. Neurosci.* **1998**, *18*, 8417–8422. [CrossRef]
7. Volkow, N.D.; Chang, L.; Wang, G.J.; Fowler, J.S.; Leonido-Yee, M.; Franceschi, D.; Sedler, M.J.; Gatley, S.J.; Hitzemann, R.; Ding, Y.S.; et al. Association of dopamine transporter reduction with psychomotor impairment in methamphetamine abusers. *Am. J. Psychiatry* **2001**, *158*, 377–382. [CrossRef]
8. McCann, U.D.; Kuwabara, H.; Kumar, A.; Palermo, M.; Abbey, R.; Brasic, J.; Ye, W.; Alexander, M.; Dannals, R.F.; Wong, D.F.; et al. Persistent cognitive and dopamine transporter deficits in abstinent methamphetamine users. *Synapse* **2008**, *62*, 91–100. [CrossRef]
9. Johanson, C.E.; Frey, K.A.; Lundahl, L.H.; Keenan, P.; Lockhart, N.; Roll, J.; Galloway, G.P.; Koeppe, R.A.; Kilbourn, M.R.; Robbins, T.; et al. Cognitive function and nigrostriatal markers in abstinent methamphetamine abusers. *Psychopharmacology* **2006**, *185*, 327–338. [CrossRef]
10. Sekine, Y.; Iyo, M.; Ouchi, Y.; Matsunaga, T.; Tsukada, H.; Okada, H.; Yoshikawa, E.; Futatsubashi, M.; Takei, N.; Mori, N. Methamphetamine-related psychiatric symptoms and reduced brain dopamine transporters studied with PET. *Am. J. Psychiatry* **2001**, *158*, 1206–1214. [CrossRef]
11. Moszczynska, A.; Callan, S.P. Molecular, Behavioral, and Physiological Consequences of Methamphetamine Neurotoxicity: Implications for Treatment. *J. Pharmacol. Exp. Ther.* **2017**, *362*, 474. [CrossRef]

12. Wilson, J.M.; Kalasinsky, K.S.; Levey, A.I.; Bergeron, C.; Reiber, G.; Anthony, R.M.; Schmunk, G.A.; Shannak, K.; Haycock, J.W.; Kish, S.J. Striatal dopamine nerve terminal markers in human, chronic methamphetamine users. *Nat. Med.* **1996**, *2*, 699–703. [CrossRef]
13. Kitamura, O.; Tokunaga, I.; Gotohda, T.; Kubo, S. Immunohistochemical investigation of dopaminergic terminal markers and caspase-3 activation in the striatum of human methamphetamine users. *Int. J. Leg. Med.* **2007**, *121*, 163–168. [CrossRef]
14. Ares-Santos, S.; Granado, N.; Espadas, I.; Martinez-Murillo, R.; Moratalla, R. Methamphetamine causes degeneration of dopamine cell bodies and terminals of the nigrostriatal pathway evidenced by silver staining. *Neuropsychopharmacology* **2014**, *39*, 1066–1080. [CrossRef] [PubMed]
15. Blaker, A.L.; Rodriguez, E.A.; Yamamoto, B.K. Neurotoxicity to dopamine neurons after the serial exposure to alcohol and methamphetamine: Protection by COX-2 antagonism. *Brain Behav. Immun.* **2019**, *81*, 317–328. [CrossRef]
16. Dang, D.K.; Shin, E.J.; Nam, Y.; Ryoo, S.; Jeong, J.H.; Jang, C.G.; Nabeshima, T.; Hong, J.S.; Kim, H.C. Apocynin prevents mitochondrial burdens, microglial activation, and pro-apoptosis induced by a toxic dose of methamphetamine in the striatum of mice via inhibition of p47phox activation by ERK. *J. Neuroinflam.* **2016**, *13*, 12. [CrossRef] [PubMed]
17. Eyerman, D.J.; Yamamoto, B.K. Lobeline attenuates methamphetamine-induced changes in vesicular monoamine transporter 2 immunoreactivity and monoamine depletions in the striatum. *J. Pharmacol. Exp. Ther.* **2005**, *312*, 160–169. [CrossRef] [PubMed]
18. Eyerman, D.J.; Yamamoto, B.K. A rapid oxidation and persistent decrease in the vesicular monoamine transporter 2 after methamphetamine. *J. Neurochem.* **2007**, *103*, 1219–1227. [CrossRef] [PubMed]
19. Frey, K.; Kilbourn, M.; Robinson, T. Reduced striatal vesicular monoamine transporters after neurotoxic but not after behaviorally-sensitizing doses of methamphetamine. *Eur. J. Pharmacol.* **1997**, *334*, 273–279. [CrossRef]
20. Fumagalli, F.; Gainetdinov, R.R.; Valenzano, K.J.; Caron, M.G. Role of dopamine transporter in methamphetamine-induced neurotoxicity: Evidence from mice lacking the transporter. *J. Neurosci.* **1998**, *18*, 4861–4869. [CrossRef]
21. Granado, N.; Ares-Santos, S.; O'Shea, E.; Vicario-Abejón, C.; Colado, M.I.; Moratalla, R. Selective vulnerability in striosomes and in the nigrostriatal dopaminergic pathway after methamphetamine administration: Early loss of TH in striosomes after methamphetamine. *Neurotox. Res.* **2010**, *18*, 48–58. [CrossRef]
22. Granado, N.; Ares-Santos, S.; Tizabi, Y.; Moratalla, R. Striatal Reinnervation Process after Acute Methamphetamine-Induced Dopaminergic Degeneration in Mice. *Neurotox. Res.* **2018**, *34*, 627–639. [CrossRef]
23. Guillot, T.S.; Shepherd, K.R.; Richardson, J.R.; Wang, M.Z.; Li, Y.; Emson, P.C.; Miller, G.W. Reduced vesicular storage of dopamine exacerbates methamphetamine-induced neurodegeneration and astrogliosis. *J. Neurochem.* **2008**, *106*, 2205–2217. [CrossRef] [PubMed]
24. Hogan, K.A.; Staal, R.G.; Sonsalla, P.K. Analysis of VMAT2 binding after methamphetamine or MPTP treatment: Disparity between homogenates and vesicle preparations. *J. Neurochem.* **2000**, *74*, 2217–2220. [CrossRef] [PubMed]
25. Lohr, K.M.; Stout, K.A.; Dunn, A.R.; Wang, M.; Salahpour, A.; Guillot, T.S.; Miller, G.W. Increased Vesicular Monoamine Transporter 2 (VMAT2; Slc18a2) Protects against Methamphetamine Toxicity. *ACS Chem. Neurosci.* **2015**, *6*, 790–799. [CrossRef]
26. Mark, K.A.; Soghomonian, J.J.; Yamamoto, B.K. High-dose methamphetamine acutely activates the striatonigral pathway to increase striatal glutamate and mediate long-term dopamine toxicity. *J. Neurosci.* **2004**, *24*, 11449–11456. [CrossRef] [PubMed]
27. McConnell, S.E.; O'Banion, M.K.; Cory-Slechta, D.A.; Olschowka, J.A.; Opanashuk, L.A. Characterization of binge-dosed methamphetamine-induced neurotoxicity and neuroinflammation. *Neurotoxicology* **2015**, *50*, 131–141. [CrossRef] [PubMed]
28. Moszczynska, A.; Yamamoto, B.K. Methamphetamine oxidatively damages parkin and decreases the activity of 26S proteasome in vivo. *J. Neurochem.* **2011**, *116*, 1005–1017. [CrossRef] [PubMed]
29. Northrop, N.A.; Yamamoto, B.K. Cyclooxygenase activity contributes to the monoaminergic damage caused by serial exposure to stress and methamphetamine. *Neuropharmacology* **2013**, *72*, 96–105. [CrossRef]
30. O'Callaghan, J.P.; Miller, D.B. Neurotoxicity profiles of substituted amphetamines in the C57BL/6J mouse. *J. Pharmacol. Exp. Ther.* **1994**, *270*, 741–751.
31. Reichel, C.M.; Ramsey, L.A.; Schwendt, M.; McGinty, J.F.; See, R.E. Methamphetamine-induced changes in the object recognition memory circuit. *Neuropharmacology* **2012**, *62*, 1119–1126. [CrossRef]
32. Salvatore, M.F.; Nejtek, V.A.; Khoshbouei, H. Prolonged increase in ser31 tyrosine hydroxylase phosphorylation in substantia nigra following cessation of chronic methamphetamine. *Neurotoxicology* **2018**, *67*, 121–128. [CrossRef]
33. Seiden, L.S.; Commins, D.L.; Vosmer, G.; Axt, K.; Marek, G. Neurotoxicity in dopamine and 5-hydroxytryptamine terminal fields: A regional analysis in nigrostriatal and mesolimbic projections. *Ann. N. Y. Acad. Sci.* **1988**, *537*, 161–172. [CrossRef] [PubMed]
34. Sonsalla, P.K.; Jochnowitz, N.D.; Zeevalk, G.D.; Oostveen, J.A.; Hall, E.D. Treatment of mice with methamphetamine produces cell loss in the substantia nigra. *Brain Res.* **1996**, *738*, 172–175. [CrossRef] [PubMed]
35. Truong, J.G.; Wilkins, D.G.; Baudys, J.; Crouch, D.J.; Johnson-Davis, K.L.; Gibb, J.W.; Hanson, G.R.; Fleckenstein, A.E. Age-dependent methamphetamine-induced alterations in vesicular monoamine transporter-2 function: Implications for neurotoxicity. *J. Pharmacol. Exp. Ther.* **2005**, *314*, 1087–1092. [CrossRef] [PubMed]
36. Du, Y.; Lee, Y.B.; Graves, S.M. Chronic methamphetamine-induced neurodegeneration: Differential vulnerability of ventral tegmental area and substantia nigra pars compacta dopamine neurons. *Neuropharmacology* **2021**, *200*, 108817. [CrossRef]
37. Graves, S.M.; Schwarzschild, S.E.; Tai, R.A.; Chen, Y.; Surmeier, D.J. Mitochondrial oxidant stress mediates methamphetamine neurotoxicity in substantia nigra dopaminergic neurons. *Neurobiol. Dis.* **2021**, *156*, 105409. [CrossRef]

38. Graves, S.M.; Xie, Z.; Stout, K.A.; Zampese, E.; Burbulla, L.F.; Shih, J.C.; Kondapalli, J.; Patriarchi, T.; Tian, L.; Brichta, L.; et al. Dopamine metabolism by a monoamine oxidase mitochondrial shuttle activates the electron transport chain. *Nat. Neurosci.* **2020**, *23*, 15–20. [CrossRef]
39. Sulzer, D.; Sonders, M.S.; Poulsen, N.W.; Galli, A. Mechanisms of neurotransmitter release by amphetamines: A review. *Prog. Neurobiol.* **2005**, *75*, 406–433. [CrossRef]
40. Freyberg, Z.; Sonders, M.S.; Aguilar, J.I.; Hiranita, T.; Karam, C.S.; Flores, J.; Pizzo, A.B.; Zhang, Y.; Farino, Z.J.; Chen, A.; et al. Mechanisms of amphetamine action illuminated through optical monitoring of dopamine synaptic vesicles in Drosophila brain. *Nat. Commun.* **2016**, *7*, 10652. [CrossRef]
41. Rothman, R.B.; Baumann, M.H.; Dersch, C.M.; Romero, D.V.; Rice, K.C.; Carroll, F.I.; Partilla, J.S. Amphetamine-type central nervous system stimulants release norepinephrine more potently than they release dopamine and serotonin. *Synapse* **2001**, *39*, 32–41. [CrossRef]
42. Du, Y.; Choi, S.; Pilski, A.; Graves, S.M. Differential vulnerability of locus coeruleus and dorsal raphe neurons to chronic methamphetamine-induced degeneration. *Front. Cell Neurosci.* **2022**, *16*, 949923. [CrossRef]
43. Bourque, M.; Dluzen, D.E.; Di Paolo, T. Male/Female differences in neuroprotection and neuromodulation of brain dopamine. *Front. Endocrinol.* **2011**, *2*, 35. [CrossRef] [PubMed]
44. Bourque, M.; Liu, B.; Dluzen, D.E.; Di Paolo, T. Sex differences in methamphetamine toxicity in mice: Effect on brain dopamine signaling pathways. *Psychoneuroendocrinology* **2011**, *36*, 955–969. [CrossRef] [PubMed]
45. Liu, B.; Dluzen, D.E. Effect of estrogen upon methamphetamine-induced neurotoxicity within the impaired nigrostriatal dopaminergic system. *Synapse* **2006**, *60*, 354–361. [CrossRef] [PubMed]
46. Dluzen, D.E.; Mcdermott, J.L. Estrogen, Testosterone, and Methamphetamine Toxicity. *Ann. N. Y. Acad. Sci.* **2006**, *1074*, 282–294. [CrossRef]
47. Dluzen, D.E.; McDermott, J.L. Neuroprotective role of estrogen upon methamphetamine and related neurotoxins within the nigrostriatal dopaminergic system. *Ann. N. Y. Acad. Sci.* **2000**, *914*, 112–126. [CrossRef]
48. Gajjar, T.M.; Anderson, L.I.; Dluzen, D.E. Acute effects of estrogen upon methamphetamine induced neurotoxicity of the nigrostriatal dopaminergic system. *J. Neural Transm.* **2003**, *110*, 1215–1224. [CrossRef]
49. Dluzen, D.E.; Anderson, L.I.; Pilati, C.F. Methamphetamine–gonadal steroid hormonal interactions:: Effects upon acute toxicity and striatal dopamine concentrations. *Neurotoxicol. Teratol.* **2002**, *24*, 267–273. [CrossRef]
50. Liu, B.; Dluzen, D.E. Effects of Estrogen and Related Agents upon Methamphetamine-Induced Neurotoxicity within an Impaired Nigrostriatal Dopaminergic System of Ovariectomized Mice. *Neuroendocrinology* **2006**, *83*, 295–302. [CrossRef]
51. Kim, K.K.; Adelstein, R.S.; Kawamoto, S. Identification of neuronal nuclei (NeuN) as Fox-3, a new member of the Fox-1 gene family of splicing factors. *J. Biol. Chem.* **2009**, *284*, 31052–31061. [CrossRef]
52. González-Rodríguez, P.; Zampese, E.; Stout, K.A.; Guzman, J.N.; Ilijic, E.; Yang, B.; Tkatch, T.; Stavarache, M.A.; Wokosin, D.L.; Gao, L.; et al. Disruption of mitochondrial complex I induces progressive parkinsonism. *Nature* **2021**, *599*, 650–656. [CrossRef]
53. Guzman, J.N.; Sánchez-Padilla, J.; Chan, C.S.; Surmeier, D.J. Robust pacemaking in substantia nigra dopaminergic neurons. *J. Neurosci.* **2009**, *29*, 11011–11019. [CrossRef] [PubMed]
54. Guzman, J.N.; Sanchez-Padilla, J.; Wokosin, D.; Kondapalli, J.; Ilijic, E.; Schumacker, P.T.; Surmeier, D.J. Oxidant stress evoked by pacemaking in dopaminergic neurons is attenuated by DJ-1. *Nature* **2010**, *468*, 696–700. [CrossRef]
55. Matschke, L.A.; Bertoune, M.; Roeper, J.; Snutch, T.P.; Oertel, W.H.; Rinné, S.; Decher, N. A concerted action of L- and T-type Ca^{2+} channels regulates locus coeruleus pacemaking. *Mol. Cell Neurosci.* **2015**, *68*, 293–302. [CrossRef] [PubMed]
56. Sanchez-Padilla, J.; Guzman, J.N.; Ilijic, E.; Kondapalli, J.; Galtieri, D.J.; Yang, B.; Schieber, S.; Oertel, W.; Wokosin, D.; Schumacker, P.T.; et al. Mitochondrial oxidant stress in locus coeruleus is regulated by activity and nitric oxide synthase. *Nat. Neurosci.* **2014**, *17*, 832–840. [CrossRef] [PubMed]
57. Zampese, E.; Surmeier, D.J. Calcium, Bioenergetics, and Parkinson's Disease. *Cells* **2020**, *9*, 2045. [CrossRef]
58. Chan, C.S.; Guzman, J.N.; Ilijic, E.; Mercer, J.N.; Rick, C.; Tkatch, T.; Meredith, G.E.; Surmeier, D.J. 'Rejuvenation' protects neurons in mouse models of Parkinson's disease. *Nature* **2007**, *447*, 1081–1086. [CrossRef]
59. Ilijic, E.; Guzman, J.N.; Surmeier, D.J. The L-type channel antagonist isradipine is neuroprotective in a mouse model of Parkinson's disease. *Neurobiol. Dis.* **2011**, *43*, 364–371. [CrossRef]
60. Mermelstein, P.; Becker, J.; Surmeier, D. Estradiol reduces calcium currents in rat neostriatal neurons via a membrane receptor. *J. Neurosci.* **1996**, *16*, 595–604. [CrossRef]
61. Kousik, S.M.; Carvey, P.M.; Napier, T.C. Methamphetamine self-administration results in persistent dopaminergic pathology: Implications for Parkinson's disease risk and reward-seeking. *Eur. J. Neurosci.* **2014**, *40*, 2707–2714. [CrossRef]
62. Sulzer, D.; Surmeier, D.J. Neuronal vulnerability, pathogenesis, and Parkinson's disease. *Mov. Disord.* **2013**, *28*, 41–50. [CrossRef]
63. Surmeier, D.J.; Obeso, J.A.; Halliday, G.M. Selective neuronal vulnerability in Parkinson disease. *Nat. Rev. Neurosci.* **2017**, *18*, 101–113. [CrossRef] [PubMed]
64. O'Keeffe, G.W.; Sullivan, A.M. Evidence for dopaminergic axonal degeneration as an early pathological process in Parkinson's disease. *Park. Relat. Disord.* **2018**, *56*, 9–15. [CrossRef] [PubMed]
65. Tagliaferro, P.; Burke, R.E. Retrograde Axonal Degeneration in Parkinson Disease. *J. Park. Dis.* **2016**, *6*, 1–15. [CrossRef] [PubMed]
66. Kurowska, Z.; Kordower, J.H.; Stoessl, A.J.; Burke, R.E.; Brundin, P.; Yue, Z.; Brady, S.T.; Milbrandt, J.; Trapp, B.D.; Sherer, T.B.; et al. Is Axonal Degeneration a Key Early Event in Parkinson's Disease? *J. Park. Dis.* **2016**, *6*, 703–707. [CrossRef]

67. Cheng, H.C.; Ulane, C.M.; Burke, R.E. Clinical progression in Parkinson disease and the neurobiology of axons. *Ann. Neurol.* **2010**, *67*, 715–725. [CrossRef]
68. Baloyannis, S.J.; Costa, V.; Baloyannis, I.S. Morphological alterations of the synapses in the locus coeruleus in Parkinson's disease. *J. Neurol. Sci.* **2006**, *248*, 35–41. [CrossRef]
69. Doppler, C.E.J.; Kinnerup, M.B.; Brune, C.; Farrher, E.; Betts, M.; Fedorova, T.D.; Schaldemose, J.L.; Knudsen, K.; Ismail, R.; Seger, A.D.; et al. Regional locus coeruleus degeneration is uncoupled from noradrenergic terminal loss in Parkinson's disease. *Brain* **2021**, *144*, 2732–2744. [CrossRef]
70. Persons, A.L.; Desai Bradaric, B.; Kelly, L.P.; Kousik, S.M.; Graves, S.M.; Yamamoto, B.K.; Napier, T.C. Gut and brain profiles that resemble pre-motor and early-stage Parkinson's disease in methamphetamine self-administering rats. *Drug Alcohol. Depend.* **2021**, *225*, 108746. [CrossRef]
71. Fornai, F.; Lenzi, P.; Ferrucci, M.; Lazzeri, G.; di Poggio, A.B.; Natale, G.; Busceti, C.L.; Biagioni, F.; Giusiani, M.; Ruggieri, S.; et al. Occurrence of neuronal inclusions combined with increased nigral expression of alpha-synuclein within dopaminergic neurons following treatment with amphetamine derivatives in mice. *Brain Res. Bull.* **2005**, *65*, 405–413. [CrossRef]
72. Butler, B.; Gamble-George, J.; Prins, P.; North, A.; Clarke, J.T.; Khoshbouei, H. Chronic Methamphetamine Increases Alpha-Synuclein Protein Levels in the Striatum and Hippocampus but not in the Cortex of Juvenile Mice. *J. Addict. Prev.* **2014**, *2*, 6.
73. Klein, C.; König, I.R. Exploring Uncharted Territory: Genetically Determined Sex Differences in Parkinson's Disease. *Ann. Neurol.* **2021**, *90*, 15–18. [CrossRef] [PubMed]
74. Callaghan, R.C.; Cunningham, J.K.; Sajeev, G.; Kish, S.J. Incidence of Parkinson's disease among hospital patients with methamphetamine-use disorders. *Mov. Disord.* **2010**, *25*, 2333–2339. [CrossRef] [PubMed]
75. Callaghan, R.C.; Cunningham, J.K.; Sykes, J.; Kish, S.J. Increased risk of Parkinson's disease in individuals hospitalized with conditions related to the use of methamphetamine or other amphetamine-type drugs. *Drug Alcohol. Depend.* **2012**, *120*, 35–40. [CrossRef] [PubMed]
76. Granado, N.; Ares-Santos, S.; Moratalla, R. Methamphetamine and Parkinson's disease. *Park. Dis.* **2013**, *2013*, 308052. [CrossRef]
77. Moratalla, R.; Khairnar, A.; Simola, N.; Granado, N.; García-Montes, J.R.; Porceddu, P.F.; Tizabi, Y.; Costa, G.; Morelli, M. Amphetamine-related drugs neurotoxicity in humans and in experimental animals: Main mechanisms. *Prog. Neurobiol.* **2017**, *155*, 149–170. [CrossRef]
78. Lappin, J.M.; Darke, S. Methamphetamine and heightened risk for early-onset stroke and Parkinson's disease: A review. *Exp. Neurol.* **2021**, *343*, 113793. [CrossRef]
79. Curtin, K.; Fleckenstein, A.E.; Robison, R.J.; Crookston, M.J.; Smith, K.R.; Hanson, G.R. Methamphetamine/amphetamine abuse and risk of Parkinson's disease in Utah: A population-based assessment. *Drug Alcohol. Depend.* **2015**, *146*, 30–38. [CrossRef]
80. Moszczynska, A.; Fitzmaurice, P.; Ang, L.; Kalasinsky, K.S.; Schmunk, G.A.; Peretti, F.J.; Aiken, S.S.; Wickham, D.J.; Kish, S.J. Why is parkinsonism not a feature of human methamphetamine users? *Brain* **2004**, *127*, 363–370. [CrossRef]
81. Kish, S.J.; Boileau, I.; Callaghan, R.C.; Tong, J. Brain dopamine neurone 'damage': Methamphetamine users vs. Parkinson's disease—A critical assessment of the evidence. *Eur. J. Neurosci.* **2017**, *45*, 58–66. [CrossRef]
82. Prince, M.; Albanese, E.; Guerchet, M.; Prina, M. *World Alzheimer Report 2014. Dementia and Risk Reduction: An Analysis of Protective and Modifiable Risk Factors*; Alzheimer's Disease International: London, UK, 2014.
83. Lane, C.A.; Hardy, J.; Schott, J.M. Alzheimer's disease. *Eur. J. Neurol.* **2018**, *25*, 59–70. [CrossRef]
84. Kelly, S.C.; He, B.; Perez, S.E.; Ginsberg, S.D.; Mufson, E.J.; Counts, S.E. Locus coeruleus cellular and molecular pathology during the progression of Alzheimer's disease. *Acta Neuropathol. Commun.* **2017**, *5*, 8. [CrossRef]
85. Iversen, L.L.; Rossor, M.N.; Reynolds, G.P.; Hills, R.; Roth, M.; Mountjoy, C.Q.; Foote, S.L.; Morrison, J.H.; Bloom, F.E. Loss of pigmented dopamine-beta-hydroxylase positive cells from locus coeruleus in senile dementia of Alzheimer's type. *Neurosci. Lett.* **1983**, *39*, 95–100. [CrossRef]
86. German, D.C.; Manaye, K.F.; White, C.L., III; Woodward, D.J.; McIntire, D.D.; Smith, W.K.; Kalaria, R.N.; Mann, D.M.A. Disease-specific patterns of locus coeruleus cell loss. *Ann. Neurol.* **1992**, *32*, 667–676. [CrossRef]
87. Dutt, S.; Li, Y.; Mather, M.; Nation, D.A. Brainstem Volumetric Integrity in Preclinical and Prodromal Alzheimer's Disease. *J. Alzheimer's Dis.* **2020**, *77*, 1579–1594. [CrossRef] [PubMed]
88. Hou, R.; Beardmore, R.; Holmes, C.; Osmond, C.; Darekar, A. A case-control study of the locus coeruleus degeneration in Alzheimer's disease. *Eur. Neuropsychopharmacol.* **2021**, *43*, 153–159. [CrossRef] [PubMed]
89. Betts, M.J.; Cardenas-Blanco, A.; Kanowski, M.; Spottke, A.; Teipel, S.J.; Kilimann, I.; Jessen, F.; Düzel, E. Locus coeruleus MRI contrast is reduced in Alzheimer's disease dementia and correlates with CSF Aβ levels. *Alzheimer's Dement* **2019**, *11*, 281–285. [CrossRef]
90. Liu, L.; Luo, S.; Zeng, L.; Wang, W.; Yuan, L.; Jian, X. Degenerative alterations in noradrenergic neurons of the locus coeruleus in Alzheimer's disease. *Neural Regen. Res.* **2013**, *8*, 2249–2255. [CrossRef]
91. O'Neil, J.N.; Mouton, P.R.; Tizabi, Y.; Ottinger, M.A.; Lei, D.L.; Ingram, D.K.; Manaye, K.F. Catecholaminergic neuronal loss in locus coeruleus of aged female dtg APP/PS1 mice. *J. Chem. Neuroanat.* **2007**, *34*, 102–107. [CrossRef]
92. Jardanhazi-Kurutz, D.; Kummer, M.P.; Terwel, D.; Vogel, K.; Dyrks, T.; Thiele, A.; Heneka, M.T. Induced LC degeneration in APP/PS1 transgenic mice accelerates early cerebral amyloidosis and cognitive deficits. *Neurochem. Int.* **2010**, *57*, 375–382. [CrossRef]

93. Liu, Y.; Yoo, M.J.; Savonenko, A.; Stirling, W.; Price, D.L.; Borchelt, D.R.; Mamounas, L.; Lyons, W.E.; Blue, M.E.; Lee, M.K. Amyloid pathology is associated with progressive monoaminergic neurodegeneration in a transgenic mouse model of Alzheimer's disease. *J. Neurosci.* **2008**, *28*, 13805–13814. [CrossRef]
94. Kang, S.S.; Liu, X.; Ahn, E.H.; Xiang, J.; Manfredsson, F.P.; Yang, X.; Luo, H.R.; Liles, L.C.; Weinshenker, D.; Ye, K. Norepinephrine metabolite DOPEGAL activates AEP and pathological Tau aggregation in locus coeruleus. *J. Clin. Investig.* **2020**, *130*, 422–437. [CrossRef] [PubMed]
95. Ehrenberg, A.J.; Nguy, A.K.; Theofilas, P.; Dunlop, S.; Suemoto, C.K.; Di Lorenzo Alho, A.T.; Leite, R.P.; Diehl Rodriguez, R.; Mejia, M.B.; Rüb, U.; et al. Quantifying the accretion of hyperphosphorylated tau in the locus coeruleus and dorsal raphe nucleus: The pathological building blocks of early Alzheimer's disease. *Neuropathol. Appl. Neurobiol.* **2017**, *43*, 393–408. [CrossRef]
96. Braun, D.J.; Van Eldik, L.J. In vivo Brainstem Imaging in Alzheimer's Disease: Potential for Biomarker Development. *Front. Aging Neurosci.* **2018**, *10*, 266. [CrossRef] [PubMed]
97. Chalermpalanupap, T.; Schroeder, J.P.; Rorabaugh, J.M.; Liles, L.C.; Lah, J.J.; Levey, A.I.; Weinshenker, D. Locus Coeruleus Ablation Exacerbates Cognitive Deficits, Neuropathology, and Lethality in P301S Tau Transgenic Mice. *J. Neurosci.* **2018**, *38*, 74–92. [CrossRef] [PubMed]
98. Heneka, M.T.; Ramanathan, M.; Jacobs, A.H.; Dumitrescu-Ozimek, L.; Bilkei-Gorzo, A.; Debeir, T.; Sastre, M.; Galldiks, N.; Zimmer, A.; Hoehn, M.; et al. Locus ceruleus degeneration promotes Alzheimer pathogenesis in amyloid precursor protein 23 transgenic mice. *J. Neurosci.* **2006**, *26*, 1343–1354. [CrossRef]
99. Kalinin, S.; Gavrilyuk, V.; Polak, P.E.; Vasser, R.; Zhao, J.; Heneka, M.T.; Feinstein, D.L. Noradrenaline deficiency in brain increases beta-amyloid plaque burden in an animal model of Alzheimer's disease. *Neurobiol. Aging* **2007**, *28*, 1206–1214. [CrossRef]
100. Kelly, S.C.; McKay, E.C.; Beck, J.S.; Collier, T.J.; Dorrance, A.M.; Counts, S.E. Locus Coeruleus Degeneration Induces Forebrain Vascular Pathology in a Transgenic Rat Model of Alzheimer's Disease. *J. Alzheimer's Dis.* **2019**, *70*, 371–388. [CrossRef]
101. Heneka, M.T.; Galea, E.; Gavriluyk, V.; Dumitrescu-Ozimek, L.; Daeschner, J.; O'Banion, M.K.; Weinberg, G.; Klockgether, T.; Feinstein, D.L. Noradrenergic depletion potentiates beta -amyloid-induced cortical inflammation: Implications for Alzheimer's disease. *J. Neurosci.* **2002**, *22*, 2434–2442. [CrossRef]
102. Gao, Z.-x.; Zhang, C.; Lu, J.-c.; Zhao, X.; Qiu, H.; Wang, H.-j. Pathological methamphetamine exposure triggers the accumulation of neuropathic protein amyloid-β by inhibiting UCHL1. *NeuroToxicology* **2021**, *86*, 19–25. [CrossRef]
103. Zhu, Y.; Wang, X.; Hu, M.; Yang, T.; Xu, H.; Kang, X.; Chen, X.; Jiang, L.; Gao, R.; Wang, J. Targeting Aβ and p-Tau Clearance in Methamphetamine-Induced Alzheimer's Disease-Like Pathology: Roles of Syntaxin 17 in Autophagic Degradation in Primary Hippocampal Neurons. *Oxid. Med. Cell Longev.* **2022**, *2022*, 3344569. [CrossRef]
104. Nopparat, C.; Boontor, A.; Panmanee, J.; Govitrapong, P. Melatonin Attenuates Methamphetamine-Induced Alteration of Amyloid β Precursor Protein Cleaving Enzyme Expressions via Melatonin Receptor in Human Neuroblastoma Cells. *Neurotox. Res.* **2022**, *40*, 1086–1095. [CrossRef]
105. Mercan, D.; Heneka, M.T. The Contribution of the Locus Coeruleus-Noradrenaline System Degeneration during the Progression of Alzheimer's Disease. *Biology* **2022**, *11*, 1822. [CrossRef] [PubMed]
106. Kleinridders, A.; Cai, W.; Cappellucci, L.; Ghazarian, A.; Collins, W.R.; Vienberg, S.G.; Pothos, E.N.; Kahn, C.R. Insulin resistance in brain alters dopamine turnover and causes behavioral disorders. *Proc. Natl. Acad. Sci. USA* **2015**, *112*, 3463–3468. [CrossRef] [PubMed]
107. West, M.J. Space Balls Revisited: Stereological Estimates of Length With Virtual Isotropic Surface Probes. *Front. Neuroanat.* **2018**, *12*, 49. [CrossRef] [PubMed]
108. Deniz, Ö.G.; Altun, G.; Kaplan, A.A.; Yurt, K.K.; von Bartheld, C.S.; Kaplan, S. A concise review of optical, physical and isotropic fractionator techniques in neuroscience studies, including recent developments. *J. Neurosci. Methods* **2018**, *310*, 45–53. [CrossRef]

International Journal of
Molecular Sciences

MDPI

Article

The ε-Isozyme of Protein Kinase C (PKCε) Is Impaired in ALS Motor Cortex and Its Pulse Activation by Bryostatin-1 Produces Long Term Survival in Degenerating SOD1-G93A Motor Neuron-like Cells

Valentina La Cognata [1,†], Agata Grazia D'Amico [2,†], Grazia Maugeri [2], Giovanna Morello [1], Maria Guarnaccia [1], Benedetta Magrì [2], Eleonora Aronica [3], Daniel L. Alkon [4], Velia D'Agata [2] and Sebastiano Cavallaro [1,*]

[1] Institute for Biomedical Research and Innovation, National Research Council, 95126 Catania, Italy
[2] Section of Human Anatomy and Histology, Department of Biomedical and Biotechnological Sciences, University of Catania, 95123 Catania, Italy
[3] Department of (Neuro) Pathology, Amsterdam UMC, University of Amsterdam, Amsterdam Neuroscience, Meibergdreef 9, 1105 Amsterdam, The Netherlands
[4] Synaptogenix, Inc., New York, NY 10036, USA
* Correspondence: sebastiano.cavallaro@cnr.it
† These authors contributed equally to this work.

Abstract: Amyotrophic lateral sclerosis (ALS) is a rapidly progressive and ultimately fatal neurodegenerative disease, characterized by a progressive depletion of upper and lower motor neurons (MNs) in the brain and spinal cord. The aberrant regulation of several PKC-mediated signal transduction pathways in ALS has been characterized so far, describing either impaired expression or altered activity of single PKC isozymes (α, β, ζ and δ). Here, we detailed the distribution and cellular localization of the ε-isozyme of protein kinase C (PKCε) in human postmortem motor cortex specimens and reported a significant decrease in both PKCε mRNA (*PRKCE*) and protein immunoreactivity in a subset of sporadic ALS patients. We furthermore investigated the steady-state levels of both pan and phosphorylated PKCε in doxycycline-activated NSC-34 cell lines carrying the human wild-type (WT) or mutant G93A SOD1 and the biological long-term effect of its transient agonism by Bryostatin-1. The G93A-SOD1 cells showed a significant reduction of the phosphoPKCε/panPKCε ratio compared to the WT. Moreover, a brief pulse activation of PKCε by Bryostatin-1 produced long-term survival in activated G93A-SOD1 degenerating cells in two different cell death paradigms (serum starvation and chemokines-induced toxicity). Altogether, the data support the implication of PKCε in ALS pathophysiology and suggests its pharmacological modulation as a potential neuroprotective strategy, at least in a subgroup of sporadic ALS patients.

Keywords: PKCε; *PRKCE*; amyotrophic lateral sclerosis; neurodegeneration; Bryostatin-1

Citation: La Cognata, V.; D'Amico, A.G.; Maugeri, G.; Morello, G.; Guarnaccia, M.; Magrì, B.; Aronica, E.; Alkon, D.L.; D'Agata, V.; Cavallaro, S. The ε-Isozyme of Protein Kinase C (PKCε) Is Impaired in ALS Motor Cortex and Its Pulse Activation by Bryostatin-1 Produces Long Term Survival in Degenerating SOD1-G93A Motor Neuron-like Cells. *Int. J. Mol. Sci.* **2023**, *24*, 12825. https://doi.org/10.3390/ijms241612825

Academic Editor: Claudia Ricci

Received: 11 July 2023
Revised: 12 August 2023
Accepted: 14 August 2023
Published: 15 August 2023

1. Introduction

Amyotrophic lateral sclerosis (ALS) is a fatal adult-onset neurodegenerative disorder characterized by the progressive degeneration of upper and lower motor neurons (MNs) in the cortex, brainstem and spinal cord. Motor neuron deterioration results in muscle weakness and, ultimately, in death due to respiratory failure, typically within 3–5 years after diagnosis [1,2].

The majority of cases (90%) are sporadic (SALS) without a family history, while the remaining 10% of ALS patients are inherited (familial ALS or FALS) [1,3,4]. Approximately 12% of familial cases and 2% of sporadic ALS cases are caused by mutations in the Cu/Zn superoxide dismutase 1 (*SOD1*) gene, one of the first discovered ALS genes [5–8]. The clinical presentation of SALS and FALS are similar, and treatment options remain

primarily supportive so far. Indeed, the two current FDA-approved drugs, i.e., the anti-excitotoxic Riluzole (Rilutek) and the antioxidant Edaravone, are able to extend the lifespan of patients by a few months and counteract disease progression without a real resolutive outcome [9,10].

The pathogenic process underlying ALS neurodegeneration is multifactorial and still not fully determined, although dysfunctions in several cellular and molecular processes have been reported so far, including impaired protein homeostasis, mitochondrial alterations, aberrant RNA metabolism, neuroinflammation, excitotoxicity and oxidative stress [11]. In the last few years, our research group and others have demonstrated that sporadic ALS is a phenotypically and genetically heterogenous disease, and SALS patients may be taxonomized into distinct molecular subtypes based on postmortem motor cortex transcriptomic signatures [11–16]. This evidence emphasized the idea that molecular-based studies aimed at uncovering the disease etiopathogenesis, as well as at characterizing biomarkers or effective treatments, require updating and necessitate accurate stratified case monitoring [11].

Multiple studies have implicated deregulation in ALS of the protein kinase C (PKC)-mediated signal transduction mechanisms, through changes in either the expression or activity state of several members of the PKC superfamily [17–22]. This latter consists of 10 related serine/threonine protein kinases (isozymes) that can be grouped into three subclasses, according to structural motifs and activation requirements: (i) classical (also termed conventional) cPKCs (α, β and γ) require both diacyl glycerol (DAG) and a calcium ion for activation, (ii) novel nPKCs (δ, ε, η and θ) require DAG but not by calcium [23], and (iii) atypical aPKCs (ζ and τ/γ) are insensitive to calcium and DAG but are activated by other lipids or by phosphorylation [23,24].

The novel ε isoform (PKCε) is a finely regulated enzyme known for its important roles in the nervous [25,26], cardiac [27] and immune systems [28]. Currently, it represents an attractive target for the treatment of several conditions, such as inflammation, ischemia, addiction, pain, anxiety and cancer [24], and has recently gained attention in Alzheimer's disease (AD) for its role in both memory formation and regulation of β-amyloid misfolded proteins [29,30]. The PKCε enzyme shares many structural features with the other members of the PKC family, including the DAG (C1) and the C2-like phospholipid-binding domains, the pseudo-substrate (PS) site, the catalytic terminal C3 and C4 domains containing the ATP binding site, the substrate recognition site and the kinase domain [24]. Like the other PKC isozymes, PKCε must be primed through phosphorylation to display full enzymatic activity and respond to allosteric regulators. Phosphorylation can occur at three conserved sites in the catalytic domain: the activation loop (Thr-566), the Thr-Pro turn motif (Thr-710) and the hydrophobic Phe-Ser-Tyr motif (Ser-729) [24]. Following activation, PKCε translocases into specific subcellular compartments (e.g., perinuclear/Golgi site) and changes the substrate kinetics [31].

One of the most potent PKCε activators is the marine natural product Bryostatin-1, a macrocyclic lactone originally isolated from *Bugula neritina*. This molecule has long been investigated in neuroscience for its interesting ameliorative effects on neuronal structure and function in in vitro studies, as well as for the pro-cognitive and antidepressant outcomes in vivo in animal models, thus entering into human clinical trials for treating AD [32,33]. Bryostatin-1 produces a time-dependent biphasic effect on PKCε levels: firstly, it binds and activates PKCε, promoting its translocation from cytosol to membrane fractions [34]; then, PKCε is proteolytically degraded during the so-called downregulation step and, lastly, undergoes a phase of de novo protein synthesis which restores PKCε normal levels and induces the production of additional trophic factors (e.g., BDNF) [32,34].

The aberrant regulation of α, β, ζ and δ PKC isozymes in ALS has been previously described [17–22,35,36], but nothing is known about the contribution of the ε isoform in the ALS pathophysiology. In the present work, we investigated the PKCε mRNA (*PRKCE*) expression level and the PKCε protein cellular expression and localization in human postmortem motor cortex specimens from control and ALS patients' subtypes.

Furthermore, we evaluated the steady-state levels of pan and phosphorylated PKCε in murine NSC-34 motor neuron-like cells expressing human wild-type (WT) or mutant G93A-SOD1 [37] and inspected the biological long-term effect of PKCε activation by Bryostatin-1.

2. Results

2.1. PKCε Is Expressed by Different Cell Types in Human Primary Motor Cortex

In order to understand the biological role of PKCε in the pathophysiology of the human motor cortex, we first investigated its cellular distribution in postmortem cortical specimens from control patients by fluorescence immunohistochemistry. Double labeling with fluorescent antibodies revealed a widely panPKCε immunoreactivity in the cortical neurons (MAP2$^+$ or NF-H$^{+)}$, microglial cells (CD11b$^+$) and oligodendrocytes (OLIG2$^+$), but barely in the astrocytes (GFAP$^+$) (Figures 1 and 2).

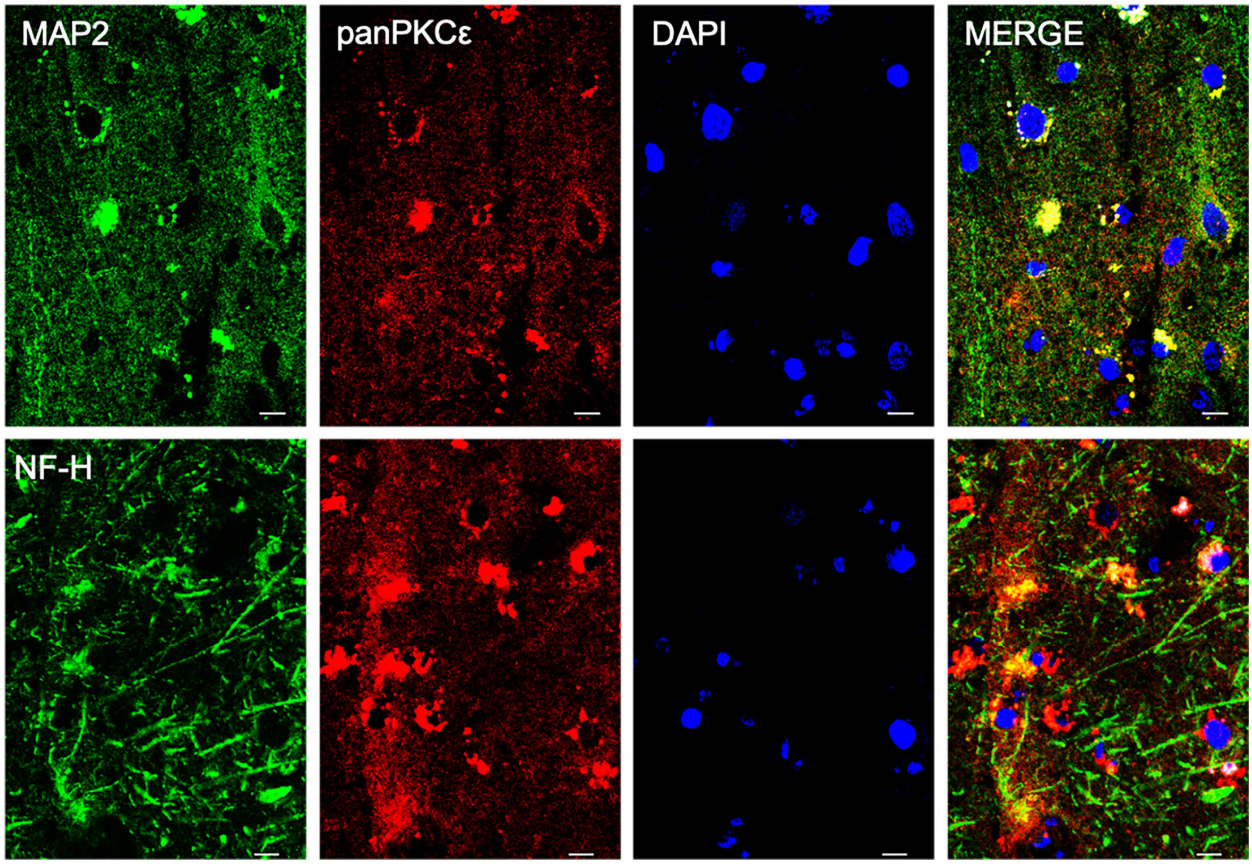

Figure 1. PKCε is expressed by cortical neurons in human primary motor cortex. Representative photomicrographs show panPKCε expressed in cortical neuronal cells (MAP2$^+$ or NF-H$^+$) examined under a Nikon A1 confocal inverted microscope equipped with a Plan Apochromat lambda 60×/1.4 oil immersion lens (Nikon, Tokyo, Japan). Scale bar 10 μm.

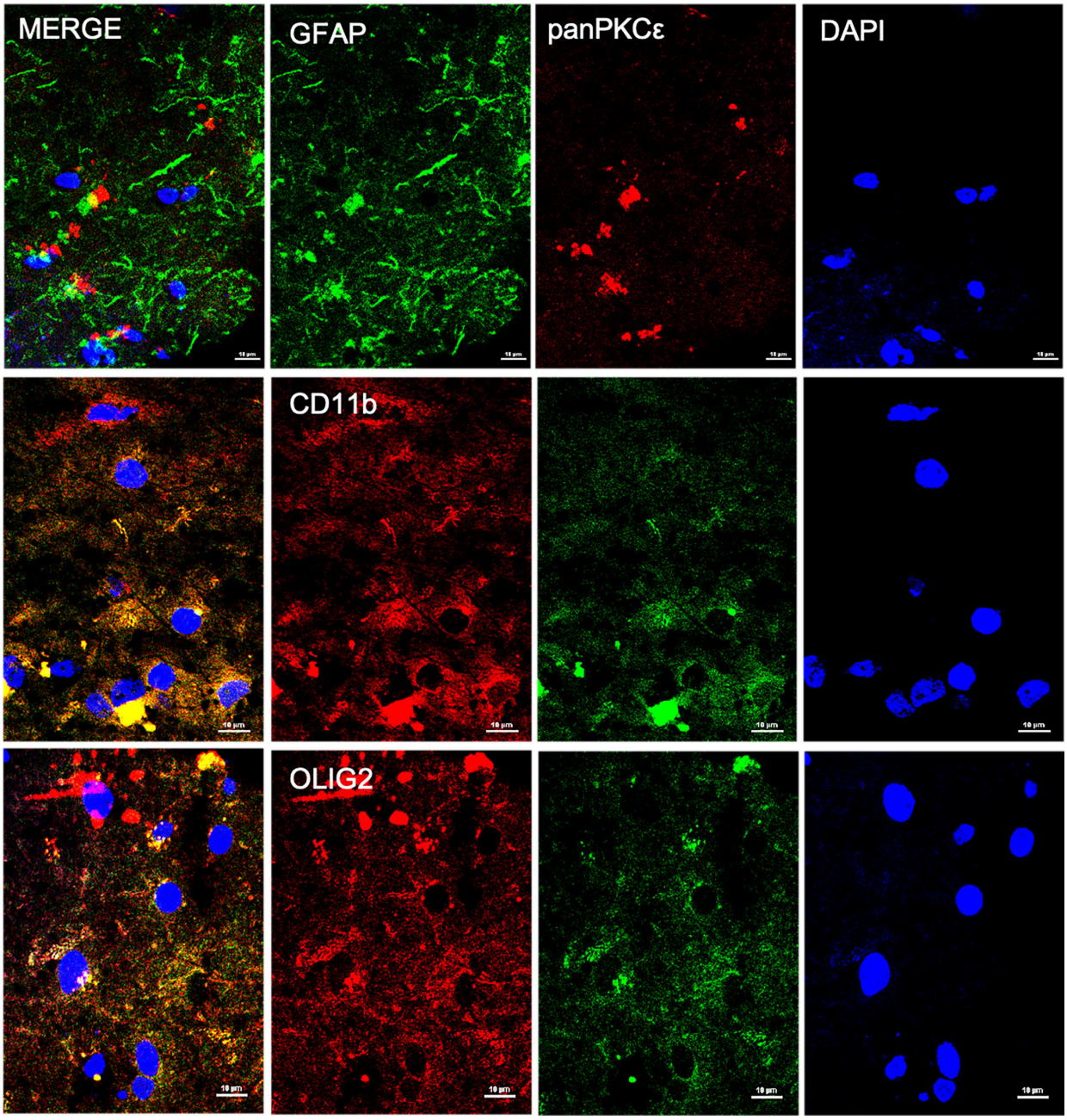

Figure 2. PKCε is expressed by non-neuronal cells in human primary motor cortex. Representative photomicrographs show panPKCε expressed in microglial cells ($CD11b^+$) and oligodendrocytes ($OLIG2^+$) but barely in astrocytes ($GFAP^+$). Slides were examined under a Nikon A1 confocal inverted microscope equipped with a Plan Apochromat lambda 60×/1.4 oil immersion lens (Nikon, Tokyo, Japan). Scale bar 10 μm.

2.2. PRKCE mRNA Expression Level Is Reduced in Motor Cortex in a Subset of ALS Patients

To characterize the biological significance of PKCε in ALS, we first compared the expression level of PKCε encoding-gene (*PRKCE*) in control and ALS motor cortex subgroups from two independent RNA gene-expression studies.

The first analysis relied on the E-MTAB-2325 transcriptomic dataset, which collected the whole-genome microarray RNA profiles of the motor cortex from 31 sporadic ALS samples and 10 controls. The previous examination of these RNA profiles had revealed a clear transcriptional-based clustering of subjects into three distinct groups: control (n = 10), SALS1 (n = 18) and SALS2 (n = 13) subtypes, each associated with different molecular

features and potential drug targets [14,16,38]. Among the multiple differentially expressed genes, *PRKCE* emerged as significantly decreased in SALS2 (not in SALS1) patients compared to the controls (Figure 3a).

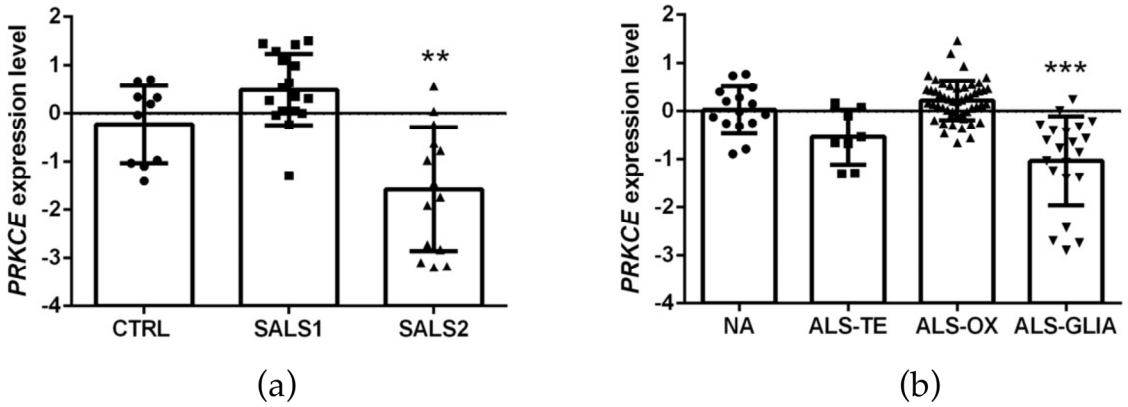

Figure 3. PKCε mRNA (*PRKCE*) is downregulated in motor cortex in a subset of sporadic ALS patients. (**a**). Transcriptomic data extrapolated from E-MTAB-2325 dataset showing a statistically significant downregulation of *PRKCE* mRNA expression level in motor cortex in a subset of sporadic ALS patients (SALS2) compared to CTRL (control = 10, SALS1 = 18, SALS2 = 13 patients, respectively). (**b**). Transcriptomic data derived from GSE124439 dataset showing a statistically significant downregulation of *PRKCE* mRNA expression level in motor cortex in a subset of ALS patients (ALS-Glia) compared to non-neurological controls (NA) (NA = 15, ALS-TE = 8, ALS-OX = 51, ALS-Glia = 21 patients, respectively). Data were extrapolated from ArrayExpress (http://www.ebi.ac.uk/arrayexpress/ accessed on 1 June 2021) and Gene Expression Omnibus (https://www.ncbi.nlm.nih.gov/geo/ accessed on 1 January 2023), respectively, and analyzed as described in the Materials and Methods section. Tukey–Kramer post hoc test: ** $p < 0.01$ vs. CTRL, *** $p < 0.001$ vs. NA. Circles, squares or triangles indicate the *PRKCE* expression level of single patients for each experimental group from the two datasets.

To corroborate this observation, we further explored the cortical *PRKCE* mRNA level in a second bulk transcriptome study (i.e., the GSE124439 dataset), which profiled by RNA-sequencing 80 ALS and 15 non-neurological control (NA) motor cortex areas (both medial and lateral) [15], and stratified the ALS patients into three distinct molecular subtypes: (i) ALS-TE, marked by retrotransposon re-activation as a dominant feature ($n = 8$); (ii) ALS-OX, showing evidence of oxidative and proteotoxic stress ($n = 51$); (iii) ALS-Glia, with strong signatures of glial activation and inflammation ($n = 21$) [15]. Interestingly, a significant downregulation of *PRKCE* mRNA was observed only in the ALS-Glia patients (Figure 3b).

2.3. PKCε Immunoreactivity Is Decreased in Both ALS Postmortem Primary Motor Cortex and SOD1-G93A NSC-34 Cells

To characterize the global protein expression and phosphorylation state of PKCε in the human control and SALS2 motor cortex samples, we performed fluorescent immunohistochemistry studies. Staining with both anti-panPKCε and anti-phosho-S729-PKCε antibodies revealed an overall decreased immunoreactivity for both antibodies in the motor cortex (NF-H$^+$ area) of SALS2 patients compared to controls (Figure 4).

Considering that the SALS2 subcluster was the only one showing significant deregulation in SOD1 expression level [16,38], we decided to inspect PKCε expression in vitro in the widely used murine cellular humanized ALS model, i.e., NSC-34 over-expressing WT or mutated human SOD1-G93A under doxycycline activation, as previously reported [39]. Consistent with the human-derived motor cortex data, we detected a downregulation of the panPKCε and phosphoPKCε immunoreactivity in G93A NSC-34 cells compared to WT (Figure 5) and used this model for the following studies.

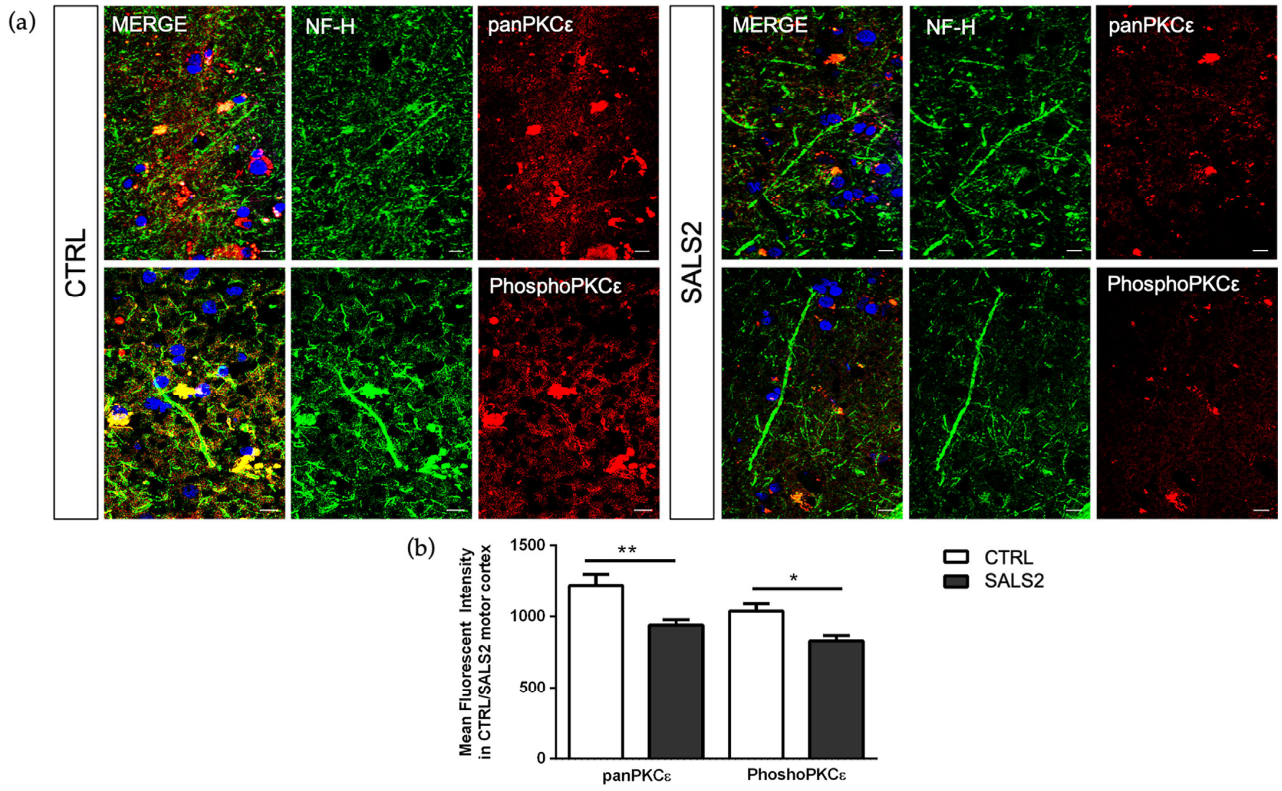

Figure 4. The panPKCε and phosphoPKCε levels are reduced in motor cortex area of SALS2 patients. (**a**). Representative images showing panPKCε and phosphoPKCε immunoreactivity in motor cortex area (characterized by NF-H positive staining) of control and SALS2 patients. (**b**). Fluorescence mean intensity, quantified by examining samples under a Nikon A1 confocal inverted microscope equipped with a Plan Apochromat lambda 60×/1.4 oil immersion lens (Nikon, Tokyo, Japan). The mean intensity of TRITC channel was extrapolated from multiple regions of interest (ROI) and normalized to the background by using the NIS-Elements AR (Advanced Research) software (version 4.60). Scale bar 10 µm. Tukey–Kramer post hoc test: ** $p < 0.01$ SALS2 vs CTRL for panPKCε, * $p < 0.05$ SALS2 vs. CTRL for phosphoPKCε.

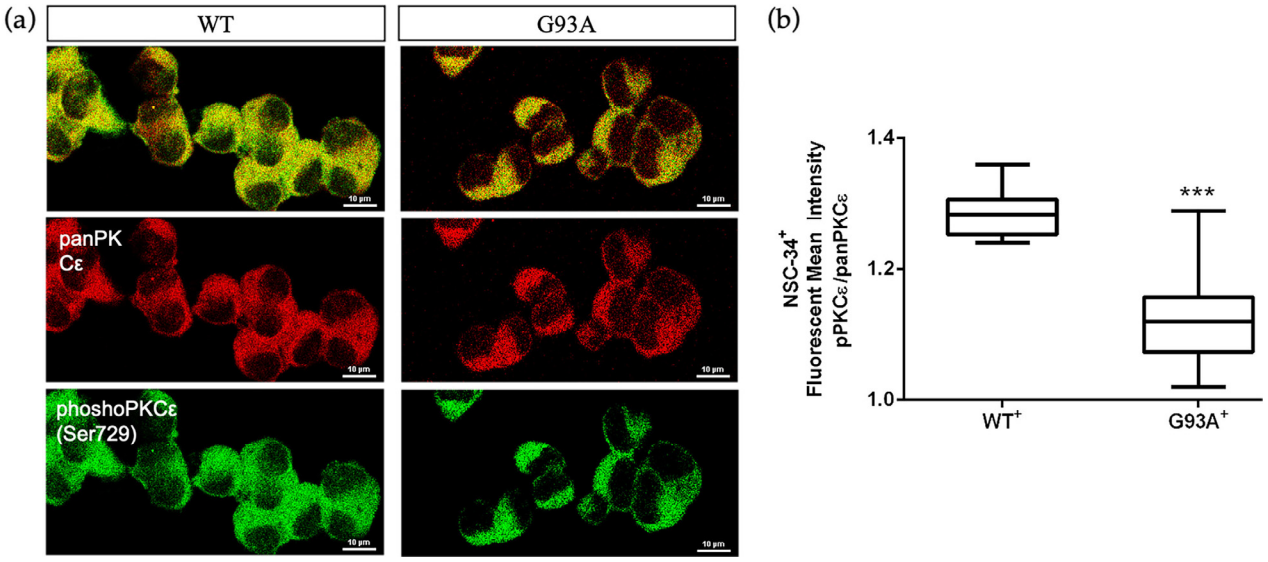

Figure 5. Immunoreactivity ratio of phosphoPKCε/panPKCε is reduced in SOD1-G93A NSC-34 cells. (**a**). Representative images showing panPKCε and phosphoPKCε immunoreactivity in WT and

SOD1-G93A NSC-34 cells. (**b**). Fluorescence mean intensity, quantified by examining samples under a Nikon A1 confocal inverted microscope equipped with a Plan Apochromat lambda 60×/1.4 oil immersion lens (Nikon, Tokyo, Japan). The mean intensity of each channel was extrapolated from multiple regions of interest (ROI) and normalized to the background by using the NIS-Elements AR (Advanced Research) software (version 4.60). Scale bar 10 µm. Tukey–Kramer post hoc test: *** $p < 0.001$ vs. WT.

2.4. A Pulse Activation by Bryostatin-1 Promotes Long-Term Cell Survival in Degenerating SOD1-G93A NSC-34 Cells and Changes the phosphoPKCε/panPKCε Ratio

Based on the observed PKCε downregulation in the ALS condition, we wondered about the downstream pharmacological effects of PKCε agonism in vitro and examined the biological outcomes of PKCε pulse activation by Bryostatin-1 in WT and G93A NSC-34 cells in two different paradigms of cell death models. Induction to apoptosis in both WT and G93A doxy-activated cells was prompted by: (i) serum starvation at either 24 or 48 h, or (ii) co-incubation with toxic chemokines (i.e., MIP2α and GROα) for 48 h. This second apoptosis model derives from previous observations conducted in our laboratories [40], which highlighted the vulnerability of G93A cells to MIP2α and GROα ligand treatment. Indeed, in the chemokines-induced cell death paradigm, the G93A NSC-34 cells displayed more sensitivity to apoptosis compared to the WT NSC-34, showing a peculiar significant reduction of cell viability in the presence of GROα and MIP2α (Figure 6b).

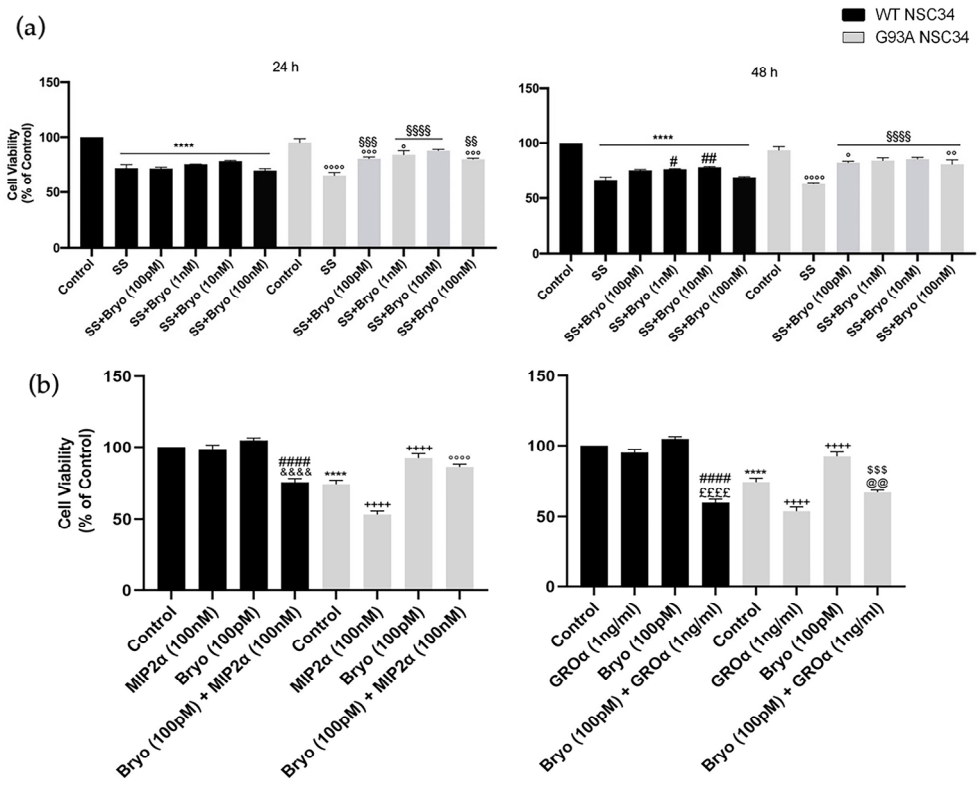

Figure 6. A pulse activation of PKCε by Bryostatin-1 produces long-term survival in degenerating mutant SOD1-G93A cells. (**a**). Cell viability of WT and SOD1-G93A NSC-34 cultured in normal growth medium (Control), serum starvation (ss) and exposed at different concentrations of Bryostatin-1 for 10 min after 24 and 48 h. Normal growth medium-cultured cells were used as controls. Results are representative of at least three independent experiments and values are expressed as a percentage of control (**** vs. Control WT, $^{\circ}$ or $^{\circ\circ}$ or $^{\circ\circ\circ}$ or $^{\circ\circ\circ\circ}$ vs. Control G93A, $^{\#}$ or $^{\#\#}$ vs. SS WT, §§ or §§§ or §§§§ vs. SS G93A as determined by one-way ANOVA followed by Tukey–Kramer post hoc test). (**b**). Cell viability of WT and SOD1-G93A NSC-34 cultured for 48 h in normal growth medium (Control), in combination with toxic chemokines (GROα and MIP2α) and exposed to Bryostatin-1 (100 pMol) for

10 min. Normal growth medium-cultured cells were used as controls. Results are representative of at least three independent experiments and values are expressed as a percentage of control (**** $p < 0.0001$ vs. control WT, $^{++++}$ $p < 0.0001$ vs. control G93A, $^{\#\#\#\#}$ $p < 0.0001$ vs. Bryo WT, $^{\$\$\$}$ $p < 0.001$ vs. Bryo G93A, $^{\circ\circ\circ\circ}$ $p < 0.0001$ vs. MIP2α G93A, $^{\&\&\&\&}$ $p < 0.0001$ vs. MIP2α WT, $^{££££}$ $p < 0.0001$ vs. GROα WT, $^{@@}$ $p < 0.0001$ vs. GROα G93A as determined by one-way ANOVA followed by Tukey–Kramer post hoc test).

The cells were then exposed to a pulse treatment (10 min) with Bryostatin-1. We used increasing concentrations of Bryostatin-1 (100 pM, 1 nM, 10 nM and 100 nM) in the serum deprivation condition (Figure 6a) and a single dose (100 pM) in the chemokines-induced toxicity paradigm (Figure 6b). In both apoptotic paradigms, the PKCε pulse activation by Bryostatin-1 determined a significant increase in cellular viability in degenerating G93A NSC-34 cells compared to the untreated controls (Figure 6a).

Previous data on Bryostatin-1 showed it produces a time-dependent biphasic effect on PKCε levels since it immediately binds PKCε promoting its self-phosphorylation and translocation from cytosol to membrane fractions [34,41], and then the enzyme undergoes a downregulation phase for several hours, followed by de novo synthesis. We therefore measured PKCε immunoreactivity after 48 h from Bryostatin-1 pulse activation and, concordantly with previous observations, detected late decreased levels of the phosphoPKCε/panPKCε ratio in both the WT and G93A NSC-34 cells (Figure 7).

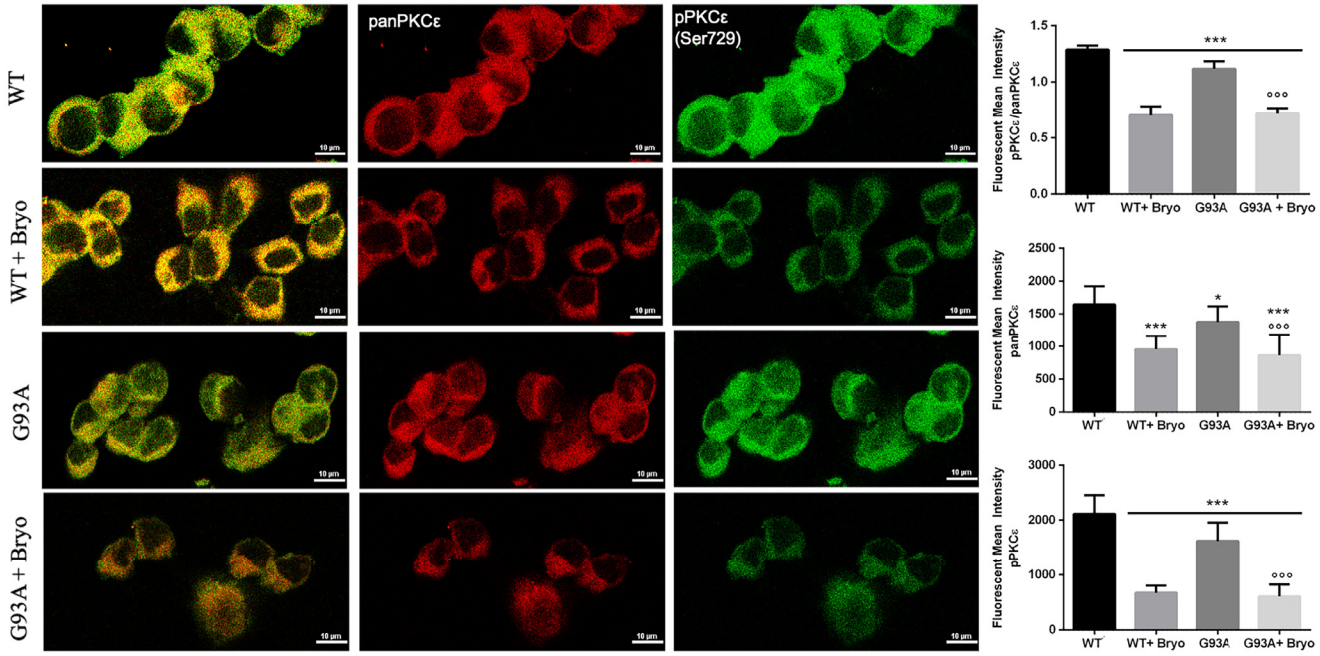

Figure 7. A transient treatment with Bryostatin-1 induces reduction of PKCε expression level in both WT and SOD1-G93A cells. Representative images showing panPKCε and phosphoPKCε immunoreactivity in WT and SOD1-G93A NSC-34 cells after 48 h from the 10 min pulse activation by Bryostatin-1. Fluorescence was quantified by examining samples under a Nikon A1 confocal inverted microscope equipped with a Plan Apochromat lambda 60×/1.4 oil immersion lens (Nikon, Tokyo, Japan). The mean intensity of each channel was extrapolated from multiple regions of interest (ROI) and normalized to the background by using the NIS-Elements AR (Advanced Research) software (version 4.60). Scale bar 10 μm. Tukey–Kramer post hoc test: *** $p < 0.001$ or * $p < 0.05$ vs. WT, $^{\circ\circ\circ}$ $p < 0.001$ vs. G93A.

3. Discussion

The mechanisms underlying motor neuron cell death and axonal degeneration in ALS still remain elusive, partly due to our incomplete knowledge of the biological mechanisms

controlling neuronal degeneration. In this study, we focused our attention on the ε-isozyme of PKC (PKCε), a versatile enzyme regulating a number of cellular processes including proliferation, differentiation, chemotaxis, neurogenesis of cortical area, outgrowth of neurites, memory, synaptic growth and synaptogenesis, and mitochondria-mediated regulation of free radical production and apoptosis [17,42–46].

PKCε is widely expressed throughout the body, predominantly in brain regions [25,36,47] such as the hippocampus, Calleja's islands, olfactory tubercle, cerebral cortex, septal nuclei, nucleus accumbens, frontal cortex, striatum and caudate putamen [45]. In the present study, we detailed PKCε distribution in the postmortem human primary motor cortex, describing its expression in cortical neurons ($MAP2^+$ or $NF\text{-}H^+$), microglial cells ($CD11b^+$) and oligodendrocytes ($OLIG2^+$), but barely in astrocytes ($GFAP^+$).

Despite a number of former studies highlighted a significant deregulation of other PKC-isozymes (α, β, ζ and δ) in the motor neurons of ALS patients and in SOD1-G93A murine models [17–19,35,36], no previous studies have investigated the role of the ε-isozyme in ALS pathophysiology. Here, we observed that PKCε mRNA expression level does not show differences when ALS is considered as a single entity, while it displays a significant downregulation in particular molecular subtypes of sporadic ALS patients obtained by bulk transcriptomic-based profiling (SALS2 from Aronica et al. [16] and ALS-Glia subset from Tam et al. [15]). Then, focusing the immunofluorescence analysis on postmortem SALS2 primary motor cortex areas, we disclosed a concordant significant downregulation of both panPKCε and phospho-Ser729-PKCε expression compared to the controls. Such PKCε downregulation may be the result of the selective motor neuronal depletion in terminal ALS patients, which are usually characterized by extensive astrocytosis.

As previously described, the SALS2 subcluster was the only one showing significant deregulation of the *SOD1* expression level [16,38]. Therefore, we decided to inspect PKCε-mediated biological effects in an ALS in vitro model characterized by overexpression of WT and mutant SOD1, i.e., NSC-34 carrying WT or mutated human SOD1 (G93A). Consistent with the human-derived motor cortex data, we detected a downregulation of phosphoPKCε/panPKCε ratio immunoreactivity in G93A NSC-34 cells compared to WT.

Given the decreased PKCε expression and its impaired phosphorylation state in ALS, we investigated the long-term biological effect of Bryostatin-1, a macrolide lactone and potent agonist of PKCε [32] in both WT and G93A NSC-34 motor neuron-like cells [37], triggered to death by two different apoptotic ways (growth factor starvation and chemokines-induced toxicity). The in vitro assays revealed that a PKCε pulse activation treatment (10 min) by Bryostatin-1 plays a long-term neuroprotective action in degenerating cells, especially in the G93A background. This finding is in agreement with previous studies showing that Bryostatin-1 increases cortical synaptogenesis and is useful in enhancing learning and memory in preclinical models of AD [32,33,48]. Moreover, the transient brief activation was sufficient to prompt a shift down of the phosphoPKCε/panPKCε ratio level in both WT and mutant G93A NSC-34 cells, a finding that could represent the well-documented downregulation phenomenon resulting from PKCε C1 domain activation in neurons [32,49–51].

Of course, the study has several limitations, such as the unknown precise time course of PKCε turnover, and the used murine cell-based model, which does not exhaustively recapitulate the complex ALS portrait. Nonetheless, these findings, along with the well-characterized multiplicity of PKCε functions and variation in cellular and tissue distribution, could raise some interesting considerations about the contribution of the ε isozyme kinase in the pathogenesis of ALS [21]. Indeed, a kinase alteration could impact the production of trophic factors (e.g., BDNF) for neuronal survival, cell cycle checkpoints regulating neuronal death and survival, axonal transport and the stimulation of excitatory amino acid receptors and Ca^{2+} channels [22]. Moreover, in other neurodegenerative diseases, Bryostatin-1 proved to revert synaptic loss and restore cognitive functions [41,52]. In Alzheimer's models and patients, for example, it is able to increase synaptogenesis

through the increase in BDNF, and, therefore, it is emerging as a potential neuroprotective treatment [41,52].

Although the mechanisms described in this work are still preliminary, and the number of analyzed patients is few, the results encourage additional preclinical and clinical investigations to guide new directions in the knowledge of ALS pathophysiology. Moreover, since deregulated expression of *SOD1* was exclusively found in SALS2 but not in SALS1 patients [16,38], and the sporadic ALS-Glia human subset shares some transcriptional signatures with murine SOD1-G93A spinal microglia [15,53], SOD1-G93A NSC-34 may represent a suitable preclinical model to investigate a distinct subset of ALS human pathology.

4. Materials and Methods

4.1. Transcriptomic Profiling

For this study, we referred to a previously described bulk transcriptome dataset [16,54] available at ArrayExpress (http://www.ebi.ac.uk/arrayexpress/ accessed on 1 June 2021) with the accession number E-MTAB-2325 (https://www.ebi.ac.uk/biostudies/arrayexpress/studies/E-MTAB-2325/ accessed on 1 June 2021) The dataset consists of the expression profiles of motor cortexes from SALS (n = 31) and control (n = 10) subjects produced with 4 × 44 K Whole Human Genome Oligo expression microarrays (Agilent Technologies, Santa Clara, CA, USA). A detailed description of the subject characteristics (origin, source code, age, gender, race, disease state, survival time from diagnosis date and postmortem interval) and experimental procedures have been previously reported [16,54,55]. Raw intensity signals from motor cortex sample hybridization were thresholded to 1, log2-transformed, normalized and baselined to the median of all the samples by using GeneSpring GX (Agilent Technologies, Santa Clara, CA, USA). Values from probes targeting *PRKCE* were extrapolated for the following analysis.

To further investigate the *PRKCE* mRNA levels in the ALS motor cortex, we used a second independent transcriptome study (GSE124439 dataset), which profiled, by RNA sequencing, a number of frontal and motor cortex specimens from a large cohort of ALS (n = 148) and non-neurological (NA) subjects (n = 28) [15]. The data from this dataset were downloaded from the Gene Expression Omnibus (https://www.ncbi.nlm.nih.gov/geo/ accessed on 1 January 2023), imported on GeneSpring GX (Agilent Technologies), thresholded to 1 and baselined to the median of all the samples. Signals from ALS (n = 80) and control (n = 15) primary motor cortex (both medial and lateral) samples were used for further analysis.

4.2. Fluorescent Immunohistochemistry

Postmortem frozen sections (10 μm) of motor cortex samples from control and ALS patients were collected and processed in order to perform immunofluorescence analyses, as described elsewhere [12,16,56]. We used the following primary antibodies: anti-PKCε (PA5-102580, Thermo Fisher Scientific, Waltham, MA, USA, 1:200 and sc-1681, Santa Cruz Biotechnology, Inc. Dallas, TX, USA, 1:250), anti-phosho-S729-PKCε (#44-977G, Thermo Fisher Scientific, Waltham, MA, USA, 1:250), anti-MAP2 (M13-13-1500, Thermo Fisher Scientific, Waltham, MA, USA, 1:300), anti-NF-H (ab187374, Abcam, Cambridge, UK, 1:200), anti-CD11b (ab133357, Abcam, Cambridge, UK, 1:500) and anti-GFAP (MAB360, Merck Millipore, Burlington, MA, USA, 1:500). TRITC- and FITC-conjugated secondary antibodies (Goat anti-rabbit 111-025-003 and Goat anti-mouse 115-095-003, Jackson Laboratories Inc., Baltimore, PA, USA) were used for 1 h at room temperature in the dark. The slides were washed 3 times in PBS after every step, mounted with glycerol mounting medium containing DAPI and analyzed with a Nikon A1 confocal inverted microscope equipped with a Plan Apochromat lambda 60×/1.4 oil immersion lens (Nikon, Tokyo, Japan). Fluorescence was quantified by analyzing the mean intensity of each channel from multiple regions of interest (ROI), normalized to the background by using the NIS-Elements AR (Advanced Research, Nikon, Tokyo, Japan) software (version 4.60).

4.3. Cell Culture

A mouse motor neuron-like hybrid NSC-34 cell line (kindly provided by Dr. Cinzia Volontè from the National Research Council, Institute for Systems Analysis and Computer Science "Antonio Ruberti") [57] was stably transfected with the pTet-ON plasmid (Clontech, Palo Alto, CA, USA) coding for the reverse tetracycline-controlled transactivator, used to construct inducible cell lines expressing the cDNAs encoding human wild-type-SOD1 (WT) or human SOD1 mutant G93A (SOD1-G93A), as previously described [39,58], and listed hereafter as WT and G93A NSC-34 cells. The treatment with doxycycline (2 μg/mL) for 24 h was used to induce WT and mutant G93A SOD1 expression.

4.4. Immuno-Cytofluorescence

NSC-34 cells expressing human WT or SOD1-G93A were cultured on glass cover slips, fixed in 4% paraformaldehyde and processed in order to perform an immunofluorescence assay [12,59]. The samples were probed with specific primary antibodies: anti-PKCε (sc-1681, Santa Cruz Biotechnology, Inc. Dallas, TX, USA, 1:200), anti-phosho-S729-PKCε (#44-977G, Thermo Fisher Scientific, Waltham, MA, USA, 1:200); Alexa Fluor 488 Goat anti-rabbit and Alexa Fluor 594 Goat anti-mouse were used as secondary antibodies (Jackson Immuno-research). The analyses were performed by using confocal microscopy, as reported elsewhere [60]. The fluorescence was quantified by extrapolating the mean intensity of each channel from multiple regions of interest (ROI) and normalized to the background [12] by using the NIS-Elements AR (Advanced Research) software.

4.5. Cellular Viability Assay

Cell viability was assessed using the colorimetric reagent-based MTT cell proliferation kit I, based on the 3-[4,5-dimethylthiazol-2-yl]-2,5-diphenyltetrazolium bromide (Roche Diagnostics, Germany) salt, as previously described [58,61]. Briefly, after 24 hours from the doxycycline (2 μg/mL) induction, the cells were prompted to apoptosis by serum starvation or chemokines-induced toxicity (GROα, 1 ng/mL and MIP2α, 100 nM) (SRP4210 and SRP4251, Sigma-Aldrich, Munich, Germany). The cells were incubated for 10 min (pulse treatment) with Bryostatin-1 at different concentrations (100 pM, 1 nM, 10 nM and 100 nM, Calbiochem, Merck Millipore, Burlington, Massachusetts) and allowed to grow for 24 or 48 h. Subsequently, 0.5 mg/mL of MTT was added to each well and incubated for 4 h at 37 °C. The reaction was stopped by adding 100 μL of solubilization solution, then, formazan, formed by the cleavage of the yellow tetrazolium salt MTT, was measured spectrophotometrically by absorbance change at 550–600 nm using a microplate reader (BioRad (Hercules, CA, USA)). Six replicate wells were used for each group. The controls included untreated cells, whereas the medium alone was used as a blank.

4.6. Statistical Analysis

The data are represented as the mean ± standard error of the mean. *t*-tests and one-way analysis of variance were used to compare differences among groups, and statistical significance was assessed by the Tukey–Kramer post hoc test. The level of significance for all the statistical tests was set at $p \leq 0.05$. All the statistics were run using the Prism 5.0a (GraphPad Software Inc., La Jolla, CA, USA) software package.

5. Conclusions

Taken together, our findings suggest that PKCε alteration could play a role in ALS pathophysiology, and PKCε agonism by Bryostatin-1 may represent a potential neuroprotective strategy against motor neuronal degeneration in a specific subgroup of sporadic ALS patients. The evidence reported here suggests that cellular-based in vitro models may be suitable to investigate specific molecular subgroups, thus representing an interesting starting point for future preclinical and clinical studies aimed at developing patient-tailored pharmacological treatments.

Author Contributions: Conceptualization, D.L.A. and S.C.; data curation, V.L.C., A.G.D. and G.M. (Grazia Maugeri); formal analysis, V.L.C., A.G.D., G.M. (Grazia Maugeri) and V.D.; funding acquisition, S.C.; investigation, V.L.C., A.G.D., G.M. (Grazia Maugeri), G.M. (Giovanna Morello), M.G., B.M. and V.D.; methodology, V.L.C., A.G.D. and G.M. (Grazia Maugeri); resources, E.A.; supervision, V.D. and S.C.; writing—original draft, V.L.C.; writing—review and editing, V.L.C. and S.C. All authors have read and agreed to the published version of the manuscript.

Funding: This research was funded by the IRIB-CNR project "A multi-omics approach for the study of neurodegeneration" (grant number: DSB.AD007.304 to S.C). EA was supported by ALS Stichting (grant "ALS Tissue Bank–NL").

Institutional Review Board Statement: The study was conducted in accordance with the Declaration of Helsinki, approved by an ethical committee (Ethics Committee of the Amsterdam Academic Medical Center, approved protocol: W11_073) for medical research and has been performed in accordance with ethical standards, as previously reported [16,62].

Informed Consent Statement: Informed consent was obtained from all individual participants included in the study for the use of tissue and for access to medical records for research purposes.

Data Availability Statement: Transcriptional data are available at EBI ArrayExpress database with the accession number E-MTAB-8635 (https://www.ebi.ac.uk/arrayexpress/experiments/E-MTAB-8635/ accessed on 1 June 2021) and at the Gene Expression Omnibus with the accession number GSE124439 (https://www.ncbi.nlm.nih.gov/geo/query/acc.cgi?acc=GSE124439 accessed on 1 January 2023).

Acknowledgments: The authors gratefully acknowledge Cristina Calì, Alfia Corsino, Maria Patrizia D'Angelo and Francesco Marino for their administrative and technical support.

Conflicts of Interest: The authors declare no conflict of interest.

References

1. Mathis, S.; Goizet, C.; Soulages, A.; Vallat, J.M.; Masson, G.L. Genetics of amyotrophic lateral sclerosis: A review. *J. Neurol. Sci.* **2019**, *399*, 217–226. [CrossRef] [PubMed]
2. Mitchell, J.D.; Borasio, G.D. Amyotrophic lateral sclerosis. *Lancet* **2007**, *369*, 2031–2041. [CrossRef] [PubMed]
3. Gentile, G.; Morello, G.; La Cognata, V.; Guarnaccia, M.; Conforti, F.L.; Cavallaro, S. Dysregulated miRNAs as Biomarkers and Therapeutical Targets in Neurodegenerative Diseases. *J. Pers. Med.* **2022**, *12*, 770. [CrossRef] [PubMed]
4. Gentile, G.; La Cognata, V.; Cavallaro, S. The contribution of CNVs to the most common aging-related neurodegenerative diseases. *Aging Clin. Exp. Res.* **2021**, *33*, 1187–1195. [CrossRef] [PubMed]
5. Rosen, D.R.; Siddique, T.; Patterson, D.; Figlewicz, D.A.; Sapp, P.; Hentati, A.; Donaldson, D.; Goto, J.; O'Regan, J.P.; Deng, H.X.; et al. Mutations in Cu/Zn superoxide dismutase gene are associated with familial amyotrophic lateral sclerosis. *Nature* **1993**, *362*, 59–62. [CrossRef] [PubMed]
6. Valentine, J.S.; Doucette, P.A.; Zittin Potter, S. Copper-zinc superoxide dismutase and amyotrophic lateral sclerosis. *Annu. Rev. Biochem.* **2005**, *74*, 563–593. [CrossRef]
7. Mulligan, V.K.; Chakrabartty, A. Protein misfolding in the late-onset neurodegenerative diseases: Common themes and the unique case of amyotrophic lateral sclerosis. *Proteins* **2013**, *81*, 1285–1303. [CrossRef]
8. Akçimen, F.; Lopez, E.R.; Landers, J.E.; Nath, A.; Chiò, A.; Chia, R.; Traynor, B.J. Amyotrophic lateral sclerosis: Translating genetic discoveries into therapies. *Nat. Rev. Genet.* **2023**, *24*, 642–658. [CrossRef]
9. Johnson, S.A.; Fang, T.; De Marchi, F.; Neel, D.; Van Weehaeghe, D.; Berry, J.D.; Paganoni, S. Pharmacotherapy for Amyotrophic Lateral Sclerosis: A Review of Approved and Upcoming Agents. *Drugs* **2022**, *82*, 1367–1388. [CrossRef]
10. Turner, M.R.; Parton, M.J.; Leigh, P.N. Clinical trials in ALS: An overview. *Semin. Neurol.* **2001**, *21*, 167–175. [CrossRef]
11. La Cognata, V.; Morello, G.; Cavallaro, S. Omics Data and Their Integrative Analysis to Support Stratified Medicine in Neurodegenerative Diseases. *Int. J. Mol. Sci.* **2021**, *22*, 4820. [CrossRef]
12. La Cognata, V.; Golini, E.; Iemmolo, R.; Balletta, S.; Morello, G.; De Rosa, C.; Villari, A.; Marinelli, S.; Vacca, V.; Bonaventura, G.; et al. CXCR2 increases in ALS cortical neurons and its inhibition prevents motor neuron degeneration in vitro and improves neuromuscular function in SOD1G93A mice. *Neurobiol. Dis.* **2021**, *160*, 105538. [CrossRef] [PubMed]
13. Morello, G.; Spampinato, A.G.; Cavallaro, S. Molecular Taxonomy of Sporadic Amyotrophic Lateral Sclerosis Using Disease-Associated Genes. *Front. Neurol.* **2017**, *8*, 152. [CrossRef] [PubMed]
14. Morello, G.; Spampinato, A.G.; Conforti, F.L.; D'Agata, V.; Cavallaro, S. Selection and Prioritization of Candidate Drug Targets for Amyotrophic Lateral Sclerosis Through a Meta-Analysis Approach. *J. Mol. Neurosci.* **2017**, *61*, 563–580. [CrossRef] [PubMed]
15. Tam, O.H.; Rozhkov, N.V.; Shaw, R.; Kim, D.; Hubbard, I.; Fennessey, S.; Propp, N.; Consortium, N.A.; Fagegaltier, D.; Harris, B.T.; et al. Postmortem Cortex Samples Identify Distinct Molecular Subtypes of ALS: Retrotransposon Activation, Oxidative Stress, and Activated Glia. *Cell Rep.* **2019**, *29*, 1164–1177 e1165. [CrossRef] [PubMed]

16. Aronica, E.; Baas, F.; Iyer, A.; ten Asbroek, A.L.; Morello, G.; Cavallaro, S. Molecular classification of amyotrophic lateral sclerosis by unsupervised clustering of gene expression in motor cortex. *Neurobiol. Dis.* **2015**, *74*, 359–376. [CrossRef] [PubMed]
17. Dave, K.R.; Raval, A.P.; Purroy, J.; Kirkinezos, I.G.; Moraes, C.T.; Bradley, W.G.; Perez-Pinzon, M.A. Aberrant deltaPKC activation in the spinal cord of Wobbler mouse: A model of motor neuron disease. *Neurobiol. Dis.* **2005**, *18*, 126–133. [CrossRef]
18. Tury, A.; Tolentino, K.; Zou, Y. Altered expression of atypical PKC and Ryk in the spinal cord of a mouse model of amyotrophic lateral sclerosis. *Dev. Neurobiol.* **2014**, *74*, 839–850. [CrossRef]
19. Lanius, R.A.; Paddon, H.B.; Mezei, M.; Wagey, R.; Krieger, C.; Pelech, S.L.; Shaw, C.A. A role for amplified protein kinase C activity in the pathogenesis of amyotrophic lateral sclerosis. *J. Neurochem.* **1995**, *65*, 927–930. [CrossRef]
20. Guo, W.; Vandoorne, T.; Steyaert, J.; Staats, K.A.; Van Den Bosch, L. The multifaceted role of kinases in amyotrophic lateral sclerosis: Genetic, pathological and therapeutic implications. *Brain* **2020**, *143*, 1651–1673. [CrossRef]
21. Lanuza, M.A.; Just-Borras, L.; Hurtado, E.; Cilleros-Mane, V.; Tomas, M.; Garcia, N.; Tomas, J. The Impact of Kinases in Amyotrophic Lateral Sclerosis at the Neuromuscular Synapse: Insights into BDNF/TrkB and PKC Signaling. *Cells* **2019**, *8*, 1578. [CrossRef] [PubMed]
22. Krieger, C.; Hu, J.H.; Pelech, S. Aberrant protein kinases and phosphoproteins in amyotrophic lateral sclerosis. *Trends Pharmacol. Sci.* **2003**, *24*, 535–541. [CrossRef] [PubMed]
23. Sipka, S.; Biro, T.; Czifra, G.; Griger, Z.; Gergely, P.; Brugos, B.; Tarr, T. The role of protein kinase C isoenzymes in the pathogenesis of human autoimmune diseases. *Clin. Immunol.* **2022**, *241*, 109071. [CrossRef] [PubMed]
24. Newton, P.M.; Messing, R.O. The substrates and binding partners of protein kinase Cepsilon. *Biochem. J.* **2010**, *427*, 189–196. [CrossRef]
25. Shirai, Y.; Adachi, N.; Saito, N. Protein kinase Cepsilon: Function in neurons. *FEBS J.* **2008**, *275*, 3988–3994. [CrossRef]
26. Van Kolen, K.; Pullan, S.; Neefs, J.M.; Dautzenberg, F.M. Nociceptive and behavioural sensitisation by protein kinase Cepsilon signalling in the CNS. *J. Neurochem.* **2008**, *104*, 1–13. [CrossRef]
27. Churchill, E.N.; Mochly-Rosen, D. The roles of PKCdelta and epsilon isoenzymes in the regulation of myocardial ischaemia/reperfusion injury. *Biochem. Soc. Trans.* **2007**, *35*, 1040–1042. [CrossRef]
28. Aksoy, E.; Goldman, M.; Willems, F. Protein kinase C epsilon: A new target to control inflammation and immune-mediated disorders. *Int. J. Biochem. Cell Biol.* **2004**, *36*, 183–188. [CrossRef]
29. Alkon, D.; Sun, M.K.; Thompson, R. Evidence of significant cognitive improvement over baseline in advanced Alzheimer's disease (AD) patients: A regenerative therapeutic strategy. *Alzheimers Dement.* **2021**, *17*, e050013. [CrossRef]
30. Etcheberrigaray, R.; Tan, M.; Dewachter, I.; Kuiperi, C.; Van der Auwera, I.; Wera, S.; Qiao, L.; Bank, B.; Nelson, T.J.; Kozikowski, A.P.; et al. Therapeutic effects of PKC activators in Alzheimer's disease transgenic mice. *Proc. Natl. Acad. Sci. USA* **2004**, *101*, 11141–11146. [CrossRef]
31. Xu, T.R.; He, G.; Dobson, K.; England, K.; Rumsby, M. Phosphorylation at Ser729 specifies a Golgi localisation for protein kinase C epsilon (PKCepsilon) in 3T3 fibroblasts. *Cell. Signal.* **2007**, *19*, 1986–1995. [CrossRef]
32. Nelson, T.J.; Sun, M.K.; Lim, C.; Sen, A.; Khan, T.; Chirila, F.V.; Alkon, D.L. Bryostatin Effects on Cognitive Function and PKCvarepsilon in Alzheimer's Disease Phase IIa and Expanded Access Trials. *J. Alzheimers Dis.* **2017**, *58*, 521–535. [CrossRef] [PubMed]
33. Ly, C.; Shimizu, A.J.; Vargas, M.V.; Duim, W.C.; Wender, P.A.; Olson, D.E. Bryostatin 1 Promotes Synaptogenesis and Reduces Dendritic Spine Density in Cortical Cultures through a PKC-Dependent Mechanism. *ACS Chem. Neurosci.* **2020**, *11*, 1545–1554. [CrossRef] [PubMed]
34. Reynolds, N.J.; Baldassare, J.J.; Henderson, P.A.; Shuler, J.L.; Ballas, L.M.; Burns, D.J.; Moomaw, C.R.; Fisher, G.J. Translocation and Downregulation of Protein Kinase C Isoenzymes-α and -ε by Phorbol Ester and Bryostatin-1 in Human Keratinocytes and Fibroblasts. *J. Investig. Dermatol.* **1994**, *103*, 364–369. [CrossRef]
35. Nagao, M.; Kato, S.; Oda, M.; Hirai, S. Decrease of protein kinase C in the spinal motor neurons of amyotrophic lateral sclerosis. *Acta Neuropathol.* **1998**, *96*, 52–56. [CrossRef] [PubMed]
36. Hu, J.H.; Chernoff, K.; Pelech, S.; Krieger, C. Protein kinase and protein phosphatase expression in the central nervous system of G93A mSOD over-expressing mice. *J. Neurochem.* **2003**, *85*, 422–431. [CrossRef] [PubMed]
37. Ferri, A.; Cozzolino, M.; Crosio, C.; Nencini, M.; Casciati, A.; Gralla, E.B.; Rotilio, G.; Valentine, J.S.; Carri, M.T. Familial ALS-superoxide dismutases associate with mitochondria and shift their redox potentials. *Proc. Natl. Acad. Sci. USA* **2006**, *103*, 13860–13865. [CrossRef]
38. Morello, G.; Spampinato, A.G.; Cavallaro, S. Neuroinflammation and ALS: Transcriptomic Insights into Molecular Disease Mechanisms and Therapeutic Targets. *Mediat. Inflamm.* **2017**, *2017*, 7070469. [CrossRef]
39. D'Amico, A.G.; Maugeri, G.; Saccone, S.; Federico, C.; Cavallaro, S.; Reglodi, D.; D'Agata, V. PACAP Modulates the Autophagy Process in an In Vitro Model of Amyotrophic Lateral Sclerosis. *Int. J. Mol. Sci.* **2020**, *21*, 2943. [CrossRef]
40. La Cognata, V.; D'Amico, A.G.; Maugeri, G.; Morello, G.; Guarnaccia, M.; Magrì, B.; Aronica, E.; D'Agata, V.; Cavallaro, S. CXCR2 Is Deregulated in ALS Spinal Cord and Its Activation Triggers Apoptosis in Motor Neuron-Like Cells Overexpressing hSOD1-G93A. *Cells* **2023**, *12*, 1813. [CrossRef]
41. Tian, Z.; Lu, X.-T.; Jiang, X.; Tian, J. Bryostatin-1: A promising compound for neurological disorders. *Front. Pharmacol.* **2023**, *14*, 7411. [CrossRef]

42. Sunesson, L.; Hellman, U.; Larsson, C. Protein kinase Cepsilon binds peripherin and induces its aggregation, which is accompanied by apoptosis of neuroblastoma cells. *J. Biol. Chem.* **2008**, *283*, 16653–16664. [CrossRef] [PubMed]
43. Zeidman, R.; Pettersson, L.; Sailaja, P.R.; Truedsson, E.; Fagerstrom, S.; Pahlman, S.; Larsson, C. Novel and classical protein kinase C isoforms have different functions in proliferation, survival and differentiation of neuroblastoma cells. *Int. J. Cancer* **1999**, *81*, 494–501. [CrossRef]
44. Zeidman, R.; Lofgren, B.; Pahlman, S.; Larsson, C. PKCepsilon, via its regulatory domain and independently of its catalytic domain, induces neurite-like processes in neuroblastoma cells. *J. Cell. Biol.* **1999**, *145*, 713–726. [CrossRef]
45. Chen, Y.; Tian, Q. The role of protein kinase C epsilon in neural signal transduction and neurogenic diseases. *Front. Med.* **2011**, *5*, 70–76. [CrossRef]
46. Matsuzaki, S.; Szweda, P.A.; Szweda, L.I.; Humphries, K.M. Regulated production of free radicals by the mitochondrial electron transport chain: Cardiac ischemic preconditioning. *Adv. Drug Deliv. Rev.* **2009**, *61*, 1324–1331. [CrossRef]
47. Patten, S.A.; Sihra, R.K.; Dhami, K.S.; Coutts, C.A.; Ali, D.W. Differential expression of PKC isoforms in developing zebrafish. *Int. J. Dev. Neurosci.* **2007**, *25*, 155–164. [CrossRef]
48. Sen, A.; Nelson, T.J.; Alkon, D.L.; Hongpaisan, J. Loss in PKC Epsilon Causes Downregulation of MnSOD and BDNF Expression in Neurons of Alzheimer's Disease Hippocampus. *J. Alzheimers Dis.* **2018**, *63*, 1173–1189. [CrossRef] [PubMed]
49. Wender, P.A.; Lippa, B.; Park, C.-M.; Irie, K.; Nakahara, A.; Ohigashi, H. Selective binding of bryostatin analogues to the cysteine rich domains of protein kinase C isozymes. *Bioorg. Med. Chem. Lett.* **1999**, *9*, 1687–1690. [CrossRef]
50. Lorenzo, P.S.; Bogi, K.; Hughes, K.M.; Beheshti, M.; Bhattacharyya, D.; Garfield, S.H.; Pettit, G.R.; Blumberg, P.M. Differential roles of the tandem C1 domains of protein kinase C delta in the biphasic down-regulation induced by bryostatin 1. *Cancer Res.* **1999**, *59*, 6137–6144. [PubMed]
51. Alkon, D.L.; Epstein, H.; Kuzirian, A.; Bennett, M.C.; Nelson, T.J. Protein synthesis required for long-term memory is induced by PKC activation on days before associative learning. *Proc. Natl. Acad. Sci. USA* **2005**, *102*, 16432–16437. [CrossRef] [PubMed]
52. Mizutani, K.; Sonoda, S.; Wakita, H.; Takahashi, Y. Effects of exercise and bryostatin-1 on functional recovery and posttranslational modification in the perilesional cortex after cerebral infarction. *NeuroReport* **2023**, *34*, 267–272. [CrossRef] [PubMed]
53. Chiu, I.M.; Morimoto, E.T.; Goodarzi, H.; Liao, J.T.; O'Keeffe, S.; Phatnani, H.P.; Muratet, M.; Carroll, M.C.; Levy, S.; Tavazoie, S.; et al. A neurodegeneration-specific gene-expression signature of acutely isolated microglia from an amyotrophic lateral sclerosis mouse model. *Cell Rep.* **2013**, *4*, 385–401. [CrossRef]
54. La Cognata, V.; Gentile, G.; Aronica, E.; Cavallaro, S. Splicing Players Are Differently Expressed in Sporadic Amyotrophic Lateral Sclerosis Molecular Clusters and Brain Regions. *Cells* **2020**, *9*, 159. [CrossRef] [PubMed]
55. Fetoni, A.R.; Zorzi, V.; Paciello, F.; Ziraldo, G.; Peres, C.; Raspa, M.; Scavizzi, F.; Salvatore, A.M.; Crispino, G.; Tognola, G.; et al. Cx26 partial loss causes accelerated presbycusis by redox imbalance and dysregulation of Nfr2 pathway. *Redox Biol.* **2018**, *19*, 301–317. [CrossRef]
56. Bonaventura, G.; Iemmolo, R.; D'Amico, A.G.; La Cognata, V.; Costanzo, E.; Zappia, M.; D'Agata, V.; Conforti, F.L.; Aronica, E.; Cavallaro, S. PACAP and PAC1R are differentially expressed in motor cortex of amyotrophic lateral sclerosis patients and support survival of iPSC-derived motor neurons. *J. Cell. Physiol.* **2018**, *233*, 3343–3351. [CrossRef]
57. Cashman, N.R.; Durham, H.D.; Blusztajn, J.K.; Oda, K.; Tabira, T.; Shaw, I.T.; Dahrouge, S.; Antel, J.P. Neuroblastoma x spinal cord (NSC) hybrid cell lines resemble developing motor neurons. *Dev. Dyn.* **1992**, *194*, 209–221. [CrossRef]
58. Maugeri, G.; D'Amico, A.G.; Rasa, D.M.; Federico, C.; Saccone, S.; Morello, G.; La Cognata, V.; Cavallaro, S.; D'Agata, V. Molecular mechanisms involved in the protective effect of pituitary adenylate cyclase-activating polypeptide in an in vitro model of amyotrophic lateral sclerosis. *J. Cell. Physiol.* **2019**, *234*, 5203–5214. [CrossRef]
59. Bonaventura, G.; Iemmolo, R.; Attaguile, G.A.; La Cognata, V.; Pistone, B.S.; Raudino, G.; D'Agata, V.; Cantarella, G.; Barcellona, M.L.; Cavallaro, S. iPSCs: A Preclinical Drug Research Tool for Neurological Disorders. *Int. J. Mol. Sci.* **2021**, *22*, 4596. [CrossRef]
60. Zohar, O.; Reiter, Y.; Bennink, J.R.; Lev, A.; Cavallaro, S.; Paratore, S.; Pick, C.G.; Brooker, G.; Yewdell, J.W. Cutting edge: MHC class I-Ly49 interaction regulates neuronal function. *J. Immunol.* **2008**, *180*, 6447–6451. [CrossRef]
61. D'Amico, A.G.; Scuderi, S.; Maugeri, G.; Cavallaro, S.; Drago, F.; D'Agata, V. NAP reduces murine microvascular endothelial cells proliferation induced by hyperglycemia. *J. Mol. Neurosci.* **2014**, *54*, 405–413. [CrossRef] [PubMed]
62. Morello, G.; Guarnaccia, M.; Spampinato, A.G.; Salomone, S.; D'Agata, V.; Conforti, F.L.; Aronica, E.; Cavallaro, S. Integrative multi-omic analysis identifies new drivers and pathways in molecularly distinct subtypes of ALS. *Sci. Rep.* **2019**, *9*, 9968. [CrossRef] [PubMed]

International Journal of
Molecular Sciences

MDPI

Article

Molecular Changes in the Brain of the Wintering *Calidris pusilla* in the Mangroves of the Amazon River Estuary

Patrick Douglas Corrêa Pereira [1], Ediely Pereira Henrique [1,†], Emanuel Ramos da Costa [1], Anderson de Jesus Falcão [1], Mauro André Damasceno de Melo [1], Maria Paula Cruz Schneider [2], Rommel Mario Rodriguez Burbano [2], Daniel Guerreiro Diniz [3,4], Nara Gyzely de Morais Magalhães [1], David Francis Sherry [5], Cristovam Wanderley Picanço Diniz [3,*] and Cristovam Guerreiro-Diniz [1]

[1] Laboratório de Biologia Molecular e Neuroecologia, Campus Bragança, Instituto Federal de Educação, Ciência e Tecnologia do Pará, Bragança 68600-000, PA, Brazil; pereira.d.c.patrick@gmail.com (P.D.C.P.)
[2] Laboratório de Citogenética Humana, Universidade Federal do Pará, Belém 66075-110, PA, Brazil
[3] Laboratório de Investigações em Neurodegeneração e Infecção, Hospital Universitário João de Barros Barreto, Instituto de Ciências Biológicas, Universidade Federal do Pará, Belém 66075-110, PA, Brazil
[4] Laboratório de Microscopia Eletrônica, Seção de Hepatologia, Instituto Evandro Chagas, Belém 66093-020, PA, Brazil
[5] Department of Psychology, Advanced Facility for Avian Research, University of Western Ontario, London, ON N6G 1G9, Canada
* Correspondence: cwpdiniz@ufpa.br
† Deceased.

Abstract: Migrant birds prepare differently to fly north for breeding in the spring and for the flight to lower latitudes during autumn, avoiding the cold and food shortages of the Northern Hemisphere's harsh winter. The molecular events associated with these fundamental stages in the life history of migrants include the differential gene expression in different tissues. Semipalmated sandpipers (*Calidris pusilla*) are Arctic-breeding shorebirds that migrate to the coast of South America during the non-breeding season. In a previous study, we demonstrated that between the beginning and the end of the wintering period, substantial glial changes and neurogenesis occur in the brain of *C. pusilla*. These changes follow the epic journey of the autumn migration when a 5-day non-stop transatlantic flight towards the coast of South America and the subsequent preparation for the long-distance flight of the spring migration takes place. Here, we tested the hypothesis that the differential gene expressions observed in the brains of individuals captured in the autumn and spring windows are consistent with the previously described cellular changes. We searched for differential gene expressions in the brain of the semipalmated sandpiper, of recently arrived birds (RA) from the autumnal migration, and that of individuals in the premigratory period (PM) in the spring. All individuals were collected in the tropical coastal of northern Brazil in the mangrove region of the Amazon River estuary. We generated a de novo neurotranscriptome for *C. pusilla* individuals and compared the gene expressions across libraries. To that end, we mapped an RNA-Seq that reads to the *C. pusilla* neurotranscriptome in four brain samples of each group and found that the differential gene expressions in newly arrived and premigratory birds were related with neurogenesis, metabolic pathways (ketone body biosynthetic and the catabolic and lipid biosynthetic processes), and glial changes (astrocyte-dopaminergic neuron signaling, astrocyte differentiation, astrocyte cell migration, and astrocyte activation involved in immune response), as well as genes related to the immune response to virus infections (Type I Interferons), inflammatory cytokines (IL-6, IL-1β, TNF, and NF-κB), NLRP3 inflammasome, anti-inflammatory cytokines (IL-10), and cell death pathways (pyroptosis- and caspase-related changes).

Keywords: brain transcriptome; migratory birds; spring migration; wintering; *Calidris pusilla*

Citation: Pereira, P.D.C.; Henrique, E.P.; da Costa, E.R.; Falcão, A.d.J.; de Melo, M.A.D.; Schneider, M.P.C.; Burbano, R.M.R.; Diniz, D.G.; Magalhães, N.G.d.M.; Sherry, D.F.; et al. Molecular Changes in the Brain of the Wintering *Calidris pusilla* in the Mangroves of the Amazon River Estuary. *Int. J. Mol. Sci.* **2023**, *24*, 12712. https://doi.org/10.3390/ijms241612712

Academic Editor: Claudia Ricci

Received: 30 June 2023
Revised: 30 July 2023
Accepted: 1 August 2023
Published: 12 August 2023

1. Introduction

Each year, migratory birds undergo behavioral, cellular, and molecular changes associated with migration and reproduction [1–5]. During autumn, they fly towards lower latitudes for the wintering period, where they find milder temperatures and food, and experience progressive functional changes at all levels in preparation for the spring migration, when they fly north for reproduction [6–8]. The spring migration requires a preparation for the long-distance migratory flights by fueling at the wintering sites, when fat accumulation, metabolic enzymatic changes, and lipogenesis in the liver with subsequent transport to the skeletal muscle indicates a readiness for departure [9].

Previous reports in different species investigated migratory changes at the molecular [10,11], cellular [12–15], and systemic changes [16–19]. These adaptive responses take hold during spring and autumn migrations, when migratory birds shift between two life history states (LHS) [20], with contrasting seasonal phenotypic profiles that emerge before and after reproduction, respectively [6]. These states occur in association with distinct regulatory strategies at the transcriptional level in autumn and spring based on the differential expressions of hypothalamic genes. [4,21]. For example, after seasonal LHS photoperiod induction, the Black-headed Bunting songbird, *Emberiza melanocephala*, showed significant differences between the spring premigratory and postmigratory phenotypes in the activity-rest pattern, body fattening, weight gain, testis size, heart and intestine weights, blood glucose, and triglyceride levels [6].

Many species of shorebirds migrate to low-latitude climate zones around the equator to escape the harsh northern winter climate and lack of food. This tropical region around the equator, which remains stable from year to year, is an area rich in food resources and has warmer temperatures with little annual variation, allowing migratory birds to recover from the autumnal long journey and prepare for the long migratory flights in spring and [22–25].

Due to the stability of the environment at lower latitudes, the endogenous rhythms imposed by the internal clocks in combination with the wintering and stopover locations weather, wind favorable conditions and temperature raise may determine the timing of the vernal migration [26–31].

The semipalmated sandpiper *C. pusilla* performs a remarkable five to six days nonstop flight across the Atlantic Ocean from James Bay (Ontario, Canada) or from the Bay of Fundy (between New Brunswick and Nova Scotia, Canada) to coastal South America, Caribbean, and Central America, before moving on to their wintering area in Brazil [25,32]. This species arrives on the coast of Venezuela [33] and in the Brazilian Coast [34] between the middle of August and early September and stays at resource-rich locations until April/May, when birds start the vernal migration [33]. In these areas, these migratory shorebirds spend a large portion of the non-breeding season [35], where they exchange feathers, increase body mass [36], and decrease corticosterone levels [33], maximizing their fitness in preparation for the next long flight of spring migration.

There is not a single report related to brain molecular changes associated with the wintering period following the long, uninterrupted migratory flight across the Atlantic Ocean (in fall), or the preparation for the multiple stopover migratory flight for breeding (in spring) in this species. Similarly, the brain transcriptome before and after reproduction remains to be investigated. Since the ribonucleic acids represent the genomic expressions by linking the genotype to the phenotype [37], we compared two snapshots of transcripts in the brains of recently arrived and pre-migratory semipalmated sandpiper (*Calidris pusilla*), captured respectively at two time windows of the wintering period: August/September (fall) and April/May (spring).

We have previously demonstrated that the autumn migration and subsequent recovery to the spring migration promotes substantial glial changes and neurogenesis in the brain of *C. pusilla* [12,14,38]. Here, we tested the hypothesis that the differential gene expressions observed in the brains of individuals captured in the autumn and spring windows during the wintering period at the mangrove region of the estuary of the Amazon River are in line with those changes.

In the absence of a sequenced genome to guide the reconstruction process, the transcriptome was assembled de novo based on RNA-sequencing reads (RNA-Seq) and annotation [39]. We searched for differential gene expressions in the brain of this latitudinal migrant species, and the results were used to interpret the functional implications of the genomic expressions [40].

2. Results

2.1. Sequencing Assembly of Semipalmated Sandpiper Transcriptome

The RNA telencephalon tissues of *C. pusilla* were sequenced in an Ion Proton Sequencer. Eight samples generated a total of 130,275,514 single-end raw reads, of these, 66.1% survived the trimming/short-reads removal phase and were used for transcriptome assembly, producing a total of 266,414 transcripts.

2.2. Gene Expression between Experimental Groups

The transcript expression data were obtained via mapping back the reads to the assembled transcripts. The volcano plot in Figure 1 exhibits the statistical significance of the difference relative to the amplitude of difference for every single gene in the comparison between recently arrived and premigratory birds' brains, through the negative base-10 log and base-2 log fold-change, respectively. See [41] for a detailed explanation of the volcano plot representation. The present report revealed 615 differentially expressed genes (DEGs) in the brains of recently arrived and premigratory groups: 356 upregulated and 259 downregulated genes (Figure 1 and Supplementary File S1).

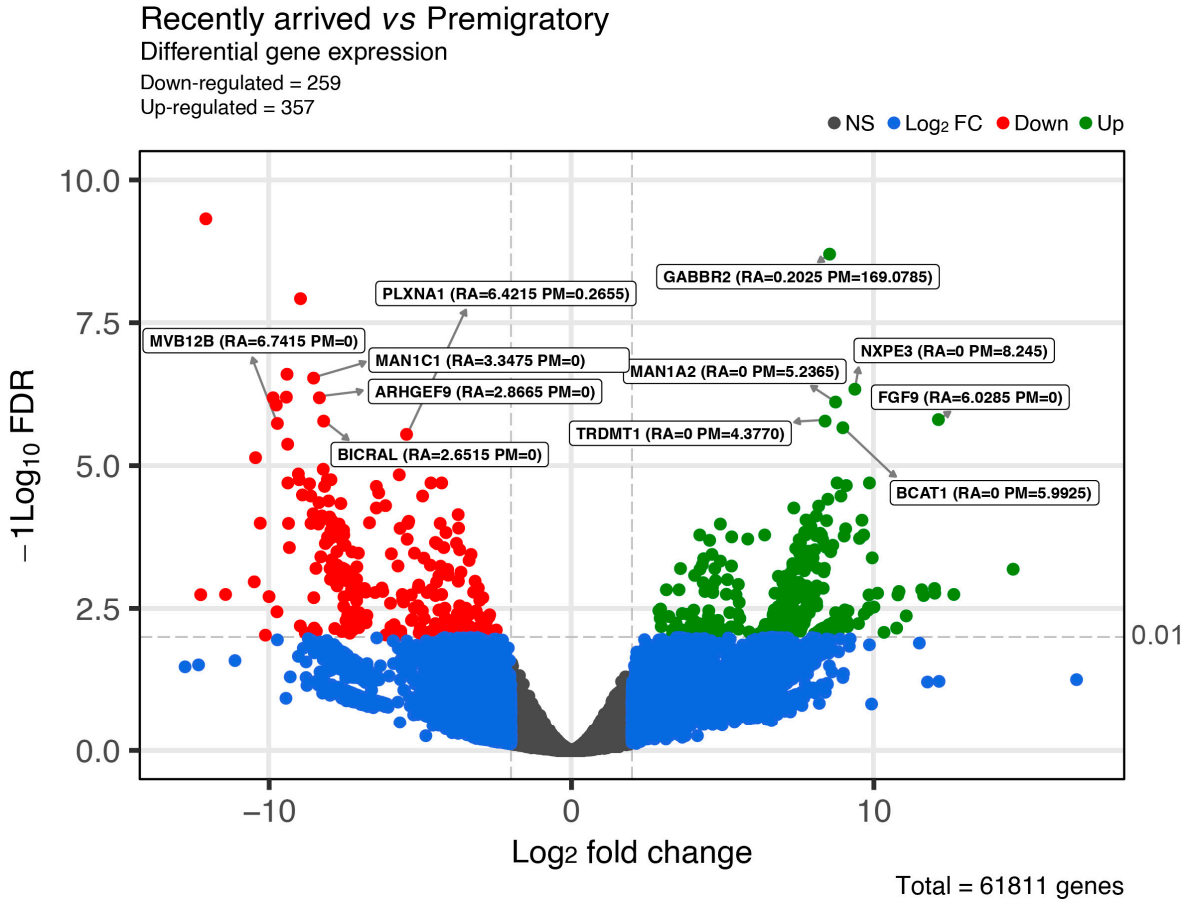

Figure 1. Volcano plot of differentially expressed genes between the pairwise comparison of premigratory and recently arrived groups. The vertical axis shows −log10 adjusted *p*-value (FDR logarithmized significant *p*-values) and the horizontal axis shows the Log_2Fold Change (change in the

gene expression level). Eleven of the greater top 20 differentially expressed genes are identified by indicating between brackets, normalized correspondent values between samples comparisons for recently arrived (RA) and premigratory (PM) groups. Abbreviations: *GABBR2* = Gamma-Aminobutyric Acid Type B Receptor Subunit 2; *NXPE3* = Neuroexophilin and PC-Esterase domain family member 3; *FGF9* = Fibroblast Growth Factor 9; *TRDMT1* = TRNA Aspartic Acid Methyltransferase 1; *BCAT1* = Branched Chain Amino Acid Transaminase 1; *ARHGEF9* = Cdc42 Guanine Nucleotide Exchange Factor 9; *MVB12B* = Multivesicular Body Subunit 12B; *BICRAL* = BICRA like Chromatin Remodeling Complex Associated Protein; *PLXNA1* = Plexin A1, *MAN1C1* = Mannosidase Alpha Class 1C Member 1; *MAN1A2* = Mannosidase Alpha Class 1A Member 2.

Figure 2 is a large-scale snapshot of the genomic differential expressions in the brains of RA and PM *C. pusilla* datasets. The heat map of the expression shows two clusters of genes with opposed patterns, showing a unique profile for each cluster among the experimental groups (Figure 2 and Supplementary File S1 shows an expanded version of the heatmap, as presented in Figure 2).

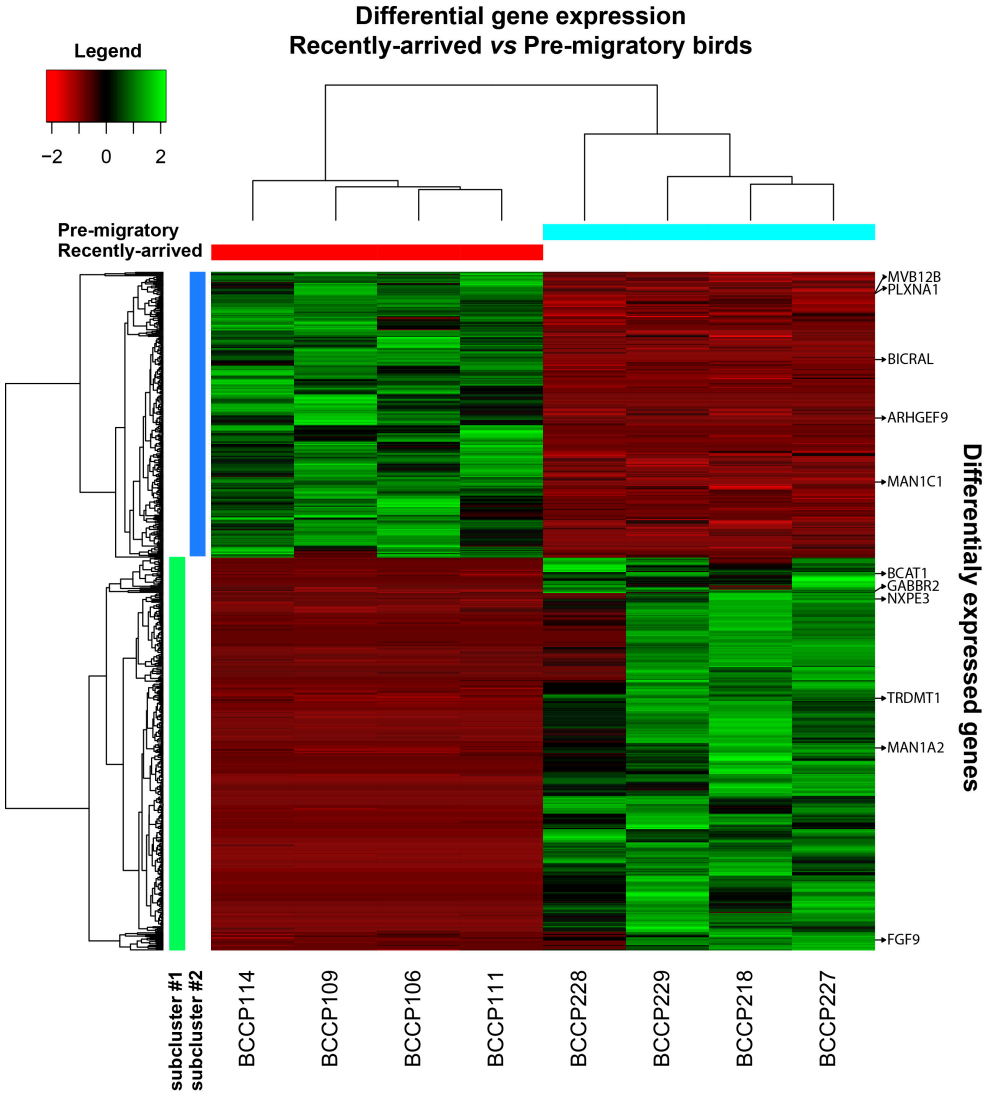

Figure 2. Hierarchical cluster analysis of the differential gene expressions (DEGs) and transcriptome RNA-sequencing heat maps of these genes in the brains of recently arrived (RC) and pre-migratory (PM) *Calidris pusilla* (adjusted p-cutoff of 0.01 for classification as differentially expressed). Top: Dendrogram

of the distribution of individuals according to differentially expressed genes in the brains of RC (red bar) and PM (blue bar) (same dataset in Figure 1). The detailed dendrogram on the left identifies upregulated (green) and downregulated (red) genes in each biological replicate of distinct RC and PM individuals. The brighter the color, the more differentially expressed a gene is. Colored bars under the left dendrogram (light green and blue) indicate the two groups of genes with contrasting expression patterns (see Figure 3). Bottom: Individual identifications on subclusters 1 and 2. Abbreviations: *GABBR2* = Gamma-Aminobutyric Acid Type B Receptor Subunit 2; *NXPE3* = Neuroexophilin and PC-Esterase domain family member 3; *FGF9* = Fibroblast Growth Factor 9; *TRDMT1* = TRNA Aspartic Acid Methyltransferase 1; *BCAT1* = Branched Chain Amino Acid Transaminase 1; *ARHGEF9* = Cdc42 Guanine Nucleotide Exchange Factor 9; *MVB12B* = Multivesicular Body Subunit 12B; *BICRAL* = BICRA like Chromatin Remodeling Complex Associated Protein; *PLXNA1* = Plexin A1; *MAN1C1* = Mannosidase Alpha Class 1C Member 1; *MAN1A2* = Mannosidase Alpha Class 1A Member 2.

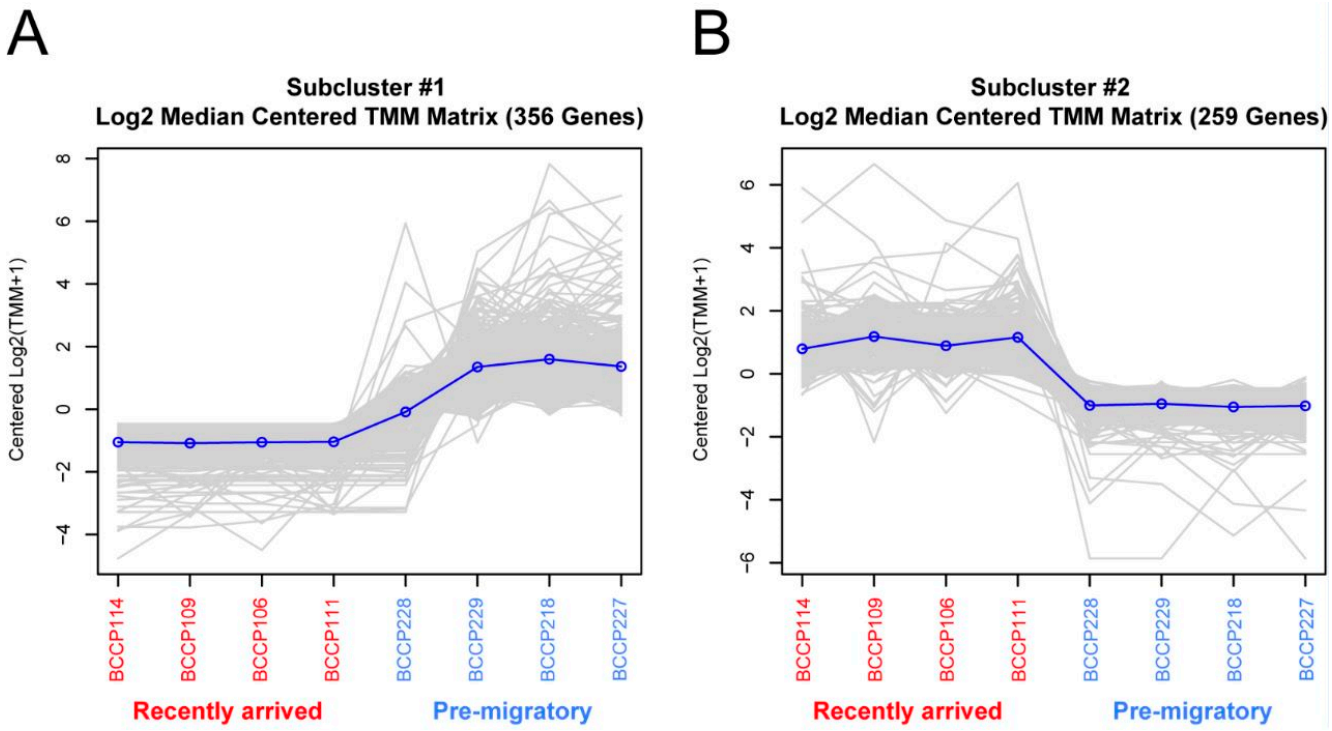

Figure 3. Differential gene expressions on subclusters 1 (**A**) and 2 (**B**) indicated in Figure 2. The expression in recently arrived (red) and pre-migratory (blue) individuals is expressed in *y* axis as TMM (Trimmed Mean of M-values; M = $\log_2$RA/PM); for detailed explanation, see [42].

2.3. Gene Ontology and Functional Analysis

A gene ontology (GO) annotation analysis was performed for the brain transcriptome of the RA and PM *C. pusilla* (the full annotation report is in Supplementary File S1). We found a total of 4656 enriched terms for the RA birds and 1859 terms for the PM birds. From these numbers, 923 belongs to Cellular Component (CC); 1730 to Molecular Function (MF); and 3862 to Biological Process (BP). The terms annotated in the gene ontology (GO) for the transcriptome showed different functional roles that may reflect pre- and post-breeding fundamental stages in the life history of this long-distance migrant species. Table 1 lists the top 11 differentially expressed genes with their respective enriched GO terms related to the biological process exhibiting significant differential expressions.

Table 1. *Calidris pusilla* top 11 differentially expressed genes and their respective enriched Biological Process GO terms showing significant differential expressions in the brains of autumn recently arrived and spring pre-migratory semipalmated sandpipers.

Sequence ID	Gene Symbol	GO IDs	GO Names
		Up-Regulated Genes	
TRINITY_DN40544_c0_g1	*GABBR2*	GO:0007186; GO:0007214;	G protein-coupled receptor signaling pathway; Gamma-aminobutyric acid signaling pathway;
TRINITY_DN3467_c1_g1	*MAN1A2*	GO:0005975; GO:0006491;	Carbohydrate metabolic process; N-glycan processing;
TRINITY_DN41739_c0_g1	*BCAT1*	GO:0009082; GO:0009098; GO:0009099;	Branched-chain amino acid biosynthetic process; Leucine biosynthetic process; Valine biosynthetic process;
TRINITY_DN56325_c0_g1	*NXPE3*	GO:0008150;	Encode a member of neurexophilin family of neuropeptide-like glycoproteins
TRINITY_DN62709_c0_g1	*FGF9*	GO:0000122; GO:0001525; GO:0001649; GO:0001654; GO:0001934; GO:0002053; GO:0002062; GO:0006606; GO:0008543; GO:0008584; GO:0010628; GO:0030178; GO:0030238; GO:0030326; GO:0030334; GO:0030949; GO:0032927; GO:0042472; GO:0045880; GO:0048505; GO:0048566; GO:0048706; GO:0050679; GO:0051781; GO:0060045; GO:0060484; GO:0090263; GO:1904707;	Negative regulation of transcription by RNA polymerase II; Angiogenesis; Osteoblast differentiation; Eye development; Positive regulation of protein phosphorylation; Positive regulation of mesenchymal cell proliferation; Chondrocyte differentiation; Protein import into nucleus; Fibroblast growth factor receptor signaling pathway; Male gonad development; Positive regulation of gene expression; Negative regulation of Wnt signaling pathway; Male sex determination; Embryonic limb morphogenesis; Regulation of cell migration; Positive regulation of vascular endothelial growth factor receptor signaling pathway; Positive regulation of activin receptor signaling pathway; Inner ear morphogenesis; positive regulation of smoothened signaling pathway; Regulation of timing of cell differentiation; Embryonic digestive tract development; Embryonic skeletal system development; Positive regulation of epithelial cell proliferation; Positive regulation of cell division; Positive regulation of cardiac muscle cell proliferation; Lung-associated mesenchyme development; Positive regulation of canonical Wnt signaling pathway; Positive regulation of vascular associated smooth muscle cell proliferation;
TRINITY_DN147173_c0_g1	*TRDMT1*	GO:0030488; GO:0036416;	tRNA methylation; A stabilization;
		Downregulated Genes	
TRINITY_DN1477_c0_g1	*PLXNA1*	GO:0007162; GO:0008360; GO:0030334; GO:0043087; GO:0050772; GO:1902287	Negative regulation of cell adhesion; Regulation of cell shape; Regulation of cell migration; Regulation of GTPase activity; Positive regulation of axonogenesis; Semaphorin-plexin signaling pathway involved in axon guidance;
TRINITY_DN161848_c0_g1	*BICRAL*	GO:0045893;	Positive regulation of DNA-templated transcription;
TRINITY_DN51404_c0_g1	*ARHGEF9*	GO:0050790;	Regulation of catalytic activity;
TRINITY_DN123969_c0_g1	*MVB12B*	GO:0015031; GO:0019075; GO:0042058; GO:0046755;	Protein transport; Virus maturation; Regulation of epidermal growth factor receptor signaling pathway; Viral budding;
TRINITY_DN13053_c4_g1	*MAN1C1*	GO:0005975; GO:0006491; GO:0004571; GO:0005509; GO:0000139; GO:0005783; GO:0016020	Carbohydrate metabolic process; *N*-glycan processing; Mannosyl-oligosaccharide 1,2-α-mannosidase activity; Calcium ion binding; Golgi membrane; Endoplasmic reticulum; membrane

Previous analysis of the genes illustrated in Table 1 in other species revealed their involvement in a variety of biological processes that, when examined from the perspective of differential gene expressions in the brain of *C. pusilla*, raises relevant questions about the contribution of the wintering period for the spring migration. Indeed, the top six upregulated (*GABBR2*, *MAN1A2*, *BCAT1*, *NXPE3*, *FGF9*, and *TRDMT1*) and the top four downregulated (*PLXNA1*, *BICRAL*, *ARHGEF9*, and *MVB12B*) differentially expressed

genes in the brains of RA and PM individuals are involved in distinct biological processes, as indicated by GO names in Table 1.

In addition, another group of genes (not included in Table 1) related to the phenotypic metabolic changes of migrant birds were also found as differentially expressed: the ZNF703 gene, associated with ketone body biosynthetic and catabolic processes upregulated in RA individuals; AGMO, associated with the lipid biosynthetic process upregulated in PM birds. Upregulated genes in RA birds were also related with astrocyte-dopaminergic neuron signaling (ATXN1), astrocyte cell migration (SCRIB), and astrocyte activation and differentiation (ZNF703). In contrast, in PM birds, upregulated genes related to astrocytes functions were limited to the gene associated with the activation for immune response (APP) and the gene CTNNB1 associated with astrocyte-dopaminergic neuron signaling.

Finally, we found a positive regulation of genes related to immune response to virus infections (Type I Interferons, inflammatory cytokines (IL-6, TNF and NF-κB), NLRP3 inflammasome, anti-inflammatory cytokines (IL-10), and cell death pathways (pyroptosis and apoptosis)) in RA individuals.

3. Discussion

In this study, we performed de novo assembly of RNA extracted from the brains of *C. pusilla* that were collected before and after breeding, seven months apart, during the wintering period, and we compared the transcriptomic changes. Samples were collected in September/October, when the birds had just completed their autumnal migration, and in April/May, when the birds became ready for the spring migration. We found 259 upregulated and 357 downregulated genes differentially expressed in the brains of recently arrived and pre-migratory birds. We confirmed the hypothesis that the brain molecular changes observed in recently arrived and premigratory birds during the wintering period were coherent with previously described cellular changes in the same species and time windows [12,14,38]. In addition, significant changes were found in the differential expressions of genes related to the inflammatory and anti-inflammatory response to virus infections, and this included Type I Interferons, IL-6, IL-1β, TNF, and NF-κB, NLRP3 inflammasome, anti-inflammatory cytokines (IL-10) and cell death pathways (pyroptosis- and caspase-related apoptosis).

3.1. GABBR2 and ARHGEF9 Differential Expressed Genes in Wintering C. pusilla

Notably, *GABBR2* and *ARHGEF9* exhibit contrasting differential gene expressions related to the inhibitory activity in the brain of *C. pusilla* (Figure 1). The upregulation of the synthesis of Subunit 2 of the Gamma-Aminobutyric Acid Receptor Type B may provide an increase in the GABAergic transmission in the brain as the spring migration approaches. It is important to highlight that the hippocampal circuits involved in the learning and memory [43] and social interaction [44] seem to be important for the long flights of migrations. Social interaction between birds of the same group may facilitate collective behavior to form flocks and organize flights during the migration for energy savings [45]. Of note, in a previous study, we found in a shorebird of the same family (Scolopacidae) a significant increase in parvalbuminergic neurons in the hippocampal formation of this species, in the premigratory groups captured in the wintering period, at the same time point and place [46]. If this observation about the PV neurons of the hippocampal formation extends to *C. pusilla*, it is reasonable to raise the hypothesis that GABAergic adaptive changes may be required for the spring migratory flight. In contrast, since autumn migration has been left behind, and long-distance flights will not be required during the wintering period, GABAB expressions may not be required to the same extent. In addition, parvalbumin-expressing basket-cell network plasticity induced by experience regulates adult learning [47], and hippocampal early-born and late-born PV neurons are recruited in rule consolidation and new information acquisition through the excitation and inhibition, respectively [48,49]. Learning and memory is modulated via hippocampal GABAergic activity through the GABB receptor and metabotropic glutamate receptor-

dependent cooperative long-term potentiation, suggesting that GABAergic synapses may contribute to functional synaptic plasticity in the adult hippocampus [50,51]. Indeed, the synaptic plasticity of inhibitory neurons provides long-lasting changes in the hippocampal network, and this is a key component of memory formation [52,53]. Distinct interneuron types contribute to the temporal binding of hippocampal ensembles, synaptic plasticity, and the acquisition of spatial and contextual information [53,54]. This hippocampal activity is part of the neuronal network used to integrate the multisensory navigational information (magnetic field, celestial cues, and geographical cues) in the hippocampal formation, and this is important to define flight direction and stopover recognition during the spring long-distance migration, back to the breeding niches [55–57].

In line with these findings is the differential downregulation of the Guanine Nucleotide Exchange Factor *ARHGEF9* that is essential for the synaptic localization and maintenance of GABAA receptors in the postsynaptic neuronal membrane in the hippocampus [58–60]. This gene synthesizes collybistin, a guanine nucleotide exchange factor that seems essential to materialize this operation [58]. Important to remember is that GABA type A receptor is a ionotropic ligand-gated chloride channel which mediates fast inhibitory signals through rapid postsynaptic hyperpolarization, whereas GABA type B is a metabotropic receptor producing slow and prolonged inhibitory signals via G proteins and second messengers involved in pre- and postsynaptic inhibition, the regulation of Ca^{2+}, and K channels [61].

Thus, related to brain inhibition in this species, many questions emerge to be explored in future studies. For example: what is the functional role of such contrasting differential gene expressions for the GABAA and GABAB receptors found in the brains of newly arrived and pre-migratory individuals? It is important to highlight that although our samples were separated by 7 to 8 months (wintering period), the time windows studied were close to the reproductive period. In fact, the autumn migration takes place two months after breeding (August and September), and the spring migration back to the breeding site takes place two months before breeding (April and May). Due to this proximity to the reproduction period, we can ask whether the physiological changes induced before and after reproduction would differentially modulate these receptors in the brain. As the expression of the $GABA_A$ receptor subunit transcriptional regulation is affected by sexual hormones [62], and as hormone levels may be not by the same before and after reproduction [63], the differential expressions of the GABAA receptors may change. It remains, however, to be investigated in detail, the physiological implications of these differential gene expressions regulating the GABAergic receptors in the wintering *C. pusilla* at lower latitudes.

Since our sample did not distinguish the different areas of the nervous system, nor did it examine the expression in different neuronal types, it is worth asking whether these receptors are differentially expressed in different brain areas and in different neuronal types in further investigations.

3.2. Gene Differential Expressions Related with Metabolic Pathways, Glial Changes, Neurogenesis, and Anti-Virus Response in Recently Arrived and Premigratory C. pusilla

Migratory birds have no access to supplementary water or nutrition during non-stop multi-day flight, and body fat and protein stores provide both fuel and life support. Long-distance migratory flights require lipid reserves [64], and they must have everything on board before departure [65]. Indeed, it has been demonstrated that higher levels βOHB in the blood, as is expected during the fasting period, is associated with the transatlantic flight, can meet all basal requirements, and only around half of the energy is necessary for neuronal activity [66]. *Calidris pusilla* must fast for 5–6 days during the long flight [32], and when glucose is in short supply, the brain increases ketone body metabolism [66]. The brains of migratory birds can adapt to the utilization of ketone bodies for its energy requirements during the fasting state, and this may lead to a high demand for astrocytes to take up, synthesize, and release fatty acids, which are alternative sources of energy that can be released as β-hydroxybutyrate, a ketone body that can fuel brain cells, including

astrocytes, neurons, and oligodendrocytes [67]. Coherently, we found in the present report differential gene expressions related to ketone body biosynthetic and catabolic processes (ZNF703) in recently arrived individuals, whereas differential expressions of the lipid biosynthetic process (AGMO) were found in premigratory birds.

Accordingly, in previous reports, we hypothesized that long flights may affect astrocytes, and we previously demonstrated the contrasting astrocyte changes in recently arrived and premigratory *C. pusilla* [14]. In the present report, we found that astrocyte-related genes were differentially expressed, indicating the upregulation of astrocyte-dopaminergic neuron signaling (ATXN1), astrocyte cell migration (SCRIB), and astrocyte activation and differentiation (ZNF703) in recently arrived individuals, whereas differential gene expressions in premigratory birds related to astrocytes were limited to astrocyte activation involved in immune response (APP) and astrocyte-dopaminergic neuron signaling (CTNNB1). We have no explanation for the contrasting expressions of CTNNB1 and ATXN1.

We have recently searched for virus transcripts in the brain of *C. pusilla* using the pipeline VIRTUS (v.1.2.1) and VIRTUS2 (v.2.0), using as reference the genome and transcriptome of *Calidris pugnax* (Accession code ASM143184v1), followed by NCBI Ref-Seq Viral Genomes [68]. We found 370 virus species in the brain of *C. pusilla*, three of which (Simbu orthobunyavirus—NC_018477, *Choristoneura fumiferana* granulovirus—NC_008165, and Shamonda orthobunyavirus—NC_018464) were differentially expressed [69]. The stopovers in bird migration may contribute to the recovery of the constitutive immune function, which is compromised during migration [70], whereas a non-stop transatlantic flight may not allow the innate immune system to recover before the arrival at the final destination and may affect the ability of the bird, in this instance, to clear a virus [17].

As the primary function of the immune system is, however, the recognition and elimination of the invading pathogens (resistance) [71,72], or alternatively, the control of the damage induced by a given burden (tolerance) [73], we suggest that *C. pusilla* may have developed these immunological mechanisms and may function as a virus reservoir.

The interferon system provides the first line of defense against viral infection in vertebrates with type I IFN, promoting humoral immunity [74], and both type I and III IFNs, associated with the adoption of an anti-viral state in infected and neighboring cells [75,76]. Inflammatory cytokine production follows the signaling pathways activated by viral (mainly DNA and RNA virus) pathogen-associated molecular patterns [77].

In the present report, we found the positive regulation of NLRP3 inflammasome complex assembling in recently arrived *C. pusilla*, suggesting an ongoing inflammation. NLR family pyrin domain containing 3 (NRLP3) has been linked to viral-induced inflammation [78]. Inflammasomes activate inflammatory caspases promoting the maturation of IL-1β and IL-18, while inducing cell death by pyroptosis [79]. Though some inflammasome genes were also expressed in birds, little is known about the role of inflammasomes in avian responses [80].

Coherently, with differential virus transcripts in the brain of *C. pusilla*, we found significant differential expressions of genes related to the inflammatory and anti-inflammatory response to virus infections, and this included Type I Interferons, IL-6, IL-1β, TNF, and NF-κB, anti-inflammatory cytokines (IL-10), and cell death pathways (pyroptosis- and caspase-binding).

Concluding Remarks

In the present work, we used information from the genomic studies of other species to speculate about the functional significance of the genes of *C. pusilla* that are being differentially expressed through wintering in recently arrived (in the fall) and premigratory (spring) individuals. To our knowledge, this is the first study demonstrating differential gene expression patterns in the brain tissue of migratory birds in natural environments throughout two different time windows of the wintering period, leading to phenotypic changes.

Gene expressions and phenotypes seem to reflect the bird physiology in these two time points of the wintering period. Indeed, we found contrasting differential expressions of

genes that regulate the inhibitory neuronal activity in the brain, phenotypic expressions of astrocytes, metabolic pathways, and innate immune response.

Further studies dedicated to brain-specific gene expression signatures and environment-mediated changes, in correlation with recently arrived and premigratory bird's gene expression patterns, may elucidate the complex network of modifications to the brain transcriptome.

4. Materials and Methods

4.1. Bird Sampling and Ethics Recommendations for the Use of Animals in Research

We used a total of eight *C. pusilla* individuals, all collected in Otelina Island (0°45′42.57″ S and 46°55′51.86″ W), four of which were collected during the period between September and October (Recently arrived birds), and the other four between April and May (Premigratory birds). Birds were captured under license N° 44551-2 from the Chico Mendes Institute for the conservation of Biodiversity (ICMBio). All procedures were carried out in accordance with the Association for the Study of Animal Behavior/Animal Behavior Society Guidelines for the Use of Animals in Research. All efforts were made to minimize the number of animals used, stress, and discomfort.

4.2. Transcardiac Perfusion with RNA Later and RNA-Sequencing

The birds were transcardially perfused with a saline solution, followed by RNA Later® Solution. The brains were removed from the skull and stored at −20 °C prior to sequencing. Telencephalic tissues were homogenized for extraction and sequencing. The total RNA was extracted according to the manufacturer's suggested protocol for isolating the RNA from the tissues, and the mRNA was isolated and purified using the Dynabeads™ mRNA DIRECT™ Micro Purification kit (Thermo Fisher Scientific, São Paulo, SP, Brazil). For the conversion of RNA into cDNA, we used the Ion Total RNA-Seq Kit v2 (Thermo Fisher Scientific, São Paulo, SP, Brazil). The template preparation was performed in the Ion One Touch 2 Instrument with the OT2 200 kit (Life Technologies, São Paulo, SP, Brazil). The fragment sequencing was performed in the Ion PI chip v2 via the Ion Proton System Instrument. Eight single-ends read FASTQ files were generated that referenced the eight biological replicates (four individuals from the RA group and four from the PM group).

4.3. Filtering, Trimming, and Transcriptome Assembly

To verify the quality of the sequenced transcriptome, we used the software FastQC 0.18 [81], and for cleaning up the low-quality reads, we used the Trimmomatic 0.36 [82]. To perform the de novo assembly, we used the Trinity 2.11 [83] according to the default parameters and the Salmon v1.0 software to quantify the transcript expressions [84].

4.4. Differential Expression Discovery and Functional Annotation

We used the EdgeR v3.38.4 package to run the differential expression analysis [85] and Blast2GO [86] to identify the differentially expressed transcripts via several Blast+ v2.14.0 [87] searches. In an attempt to identify the maximum number of valid hits, we blasted our differentially expressed transcripts using Uniprot SwissProt and TrEMBL [88], NCBI non-redundant proteins and nucleotides (nr and nt) [89], RefSeq Protein and RNA [89], Uniref [90], and GenPept [91]. After the Blast+ phase, we ran the Blast2GO v6.0 functional annotation protocol according to the user manual and default parameters [86,92].

The volcano plot exhibits a false discovery rate (FDR) as their significance values (y-axis) [93], which were transformed to their $-\log 10$. The higher the position of a point, the more significant its value. The positive fold change values (to the right) correspond to the upregulated and negative fold change values (to the left), which represents the downregulated genes. The vertical line at log 2 ratio = zero indicates fold change = one. Thresholds were based on the following cutoffs: FDR-values below 0.01 and log fold-changes above 4. In this plot, each dot (regardless of color) represents a gene, and the color of each dot defines its significance in relation to the levels set in the graph. Gray dots represent genes that did not show a differential expression (not significant), and blue

dots are significant only for Log2FC > 4. Red and green dots above the horizontal dashed line are significant for both Log2FC and FDR and highlights genes with FDR < 0.01 and fold changes above 4. The top 11 differentially expressed genes are indicated with their labels and their expression values are indicated as TMM (Trimmed Mean of M-values; M = log2RA/PM).

5. Conclusions

In the present work, we compared the brain transcriptomes of *C. pusilla* at two time points of the winter period: after breeding and a long-distance uninterrupted autumnal flight across the Atlantic Ocean, and before breeding, at the end of the winter period and before the spring migratory flight back to the reproductive site [11,94]. We quantified differentially expressed genes of recently arrived and premigratory individuals and used information from the genomic studies of other species to speculate about the functional significance of this differential expression. The underlying assumption was that genomic functional regions are conserved in birds and mammals through evolution [95,96]. Although this is a limited way to interpret the results [96,97], it is reasonable to use this approach as a first step towards a detailed molecular-based guide for formulating and testing new hypotheses. We have previously demonstrated that the autumn migration and subsequent recovery to the spring migration promotes substantial glial changes and neurogenesis in the brain of *C. pusilla* [14,38]. Here, we confirmed the hypothesis that the differential gene expressions observed in the brains of individuals captured in the autumn and spring windows accompany phenotypic changes previously described for this species in the same wintering periods.

Since the functional genomic analysis referred to in the present report is based on different species, and the whole genome of *C. pusilla* is not available, a deeper understanding of the biology of its transcriptome and functional implications are necessary.

Supplementary Materials: The supporting information can be downloaded at: https://www.mdpi.com/article/10.3390/ijms241612712/s1.

Author Contributions: Conceptualization, P.D.C.P., E.R.d.C., M.P.C.S., R.M.R.B., D.G.D., N.G.d.M.M., D.F.S., C.W.P.D. and C.G.-D.; Methodology, P.D.C.P., E.P.H., E.R.d.C., A.d.J.F., M.A.D.d.M., N.G.d.M.M., C.W.P.D. and C.G.-D.; Software, P.D.C.P. and D.G.D.; Validation, M.A.D.d.M., R.M.R.B., D.G.D. and C.W.P.D.; Formal analysis, P.D.C.P., E.R.d.C., A.d.J.F., M.A.D.d.M., M.P.C.S., R.M.R.B., D.G.D., N.G.d.M.M., C.W.P.D. and C.G.-D.; Investigation, P.D.C.P., E.P.H., A.d.J.F., M.A.D.d.M., R.M.R.B., D.G.D., N.G.d.M.M., D.F.S., C.W.P.D. and C.G.-D.; Resources, M.P.C.S., R.M.R.B., C.W.P.D. and C.G.-D.; Data curation, P.D.C.P., M.A.D.d.M., M.P.C.S., D.G.D., N.G.d.M.M., D.F.S. and C.W.P.D.; Writing—original draft, P.D.C.P., E.P.H., D.G.D., N.G.d.M.M., C.W.P.D. and C.G.-D.; Writing—review & editing, P.D.C.P., D.G.D., N.G.d.M.M., C.W.P.D. and C.G.-D.; Visualization, E.P.H., A.d.J.F., M.A.D.d.M., M.P.C.S., D.F.S., C.W.P.D. and C.G.-D.; Supervision, M.A.D.d.M., N.G.d.M.M., D.F.S., C.W.P.D. and C.G.-D.; Project administration, C.W.P.D. and C.G.-D.; Funding acquisition, P.D.C.P., E.P.H., E.R.d.C., A.d.J.F., M.A.D.d.M., R.M.R.B., D.G.D., N.G.d.M.M., D.F.S., C.W.P.D. and C.G.-D. All authors have read and agreed to the published version of the manuscript.

Funding: This research was supported by: Coordenação de Aperfeiçoamento de Pessoal de Nível Superior (CAPES) Programa Ciências do Mar II; the Brazilian Research Council (CNPq) Edital Universal Grant number 440722/2014-4; Fundação Amazônia Paraense de Amparo à Pesquisa (FAPESPA) Programa de Apoio a Núcleos Emergentes Convenio 03/2017; and Financiadora de Estudos e Projetos (FINEP) MCTI/FINEP/CT-INFRA—PROINFRA—02/2014/27; PAPQ-Propesp/Federal University of Pará (UFPA); Federal Institute of Education; Science and Technology of Pará (IFPA)—Campus Bragança; Natural Sciences and Engineering Research Council of Canada (NSERC); and the Canadian Bureau for International Education (CBIE).

Institutional Review Board Statement: The birds were captured under license N° 44551-2 from the Chico Mendes Institute for the conservation of Biodiversity (ICMBio). All procedures were carried out in accordance with the Association for the Study of Animal Behavior/Animal Behavior Society Guidelines for the Use of Animals in Research. All efforts were made to minimize the number of animals used, stress, and discomfort. The use of animals in this work was approved by Prof.

Barbarella de Matos Macchi, the Coordinator of the Ethics Committee on the Use of Animals at the Federal University of Pará, Brazil.

Informed Consent Statement: Not applicable.

Data Availability Statement: The authors declare that, under request, all qualitative and quantitative data will be shared and genetic information, such as raw RNA-Seq data, has be deposited in the NCBI SRA at the following link https://www.ncbi.nlm.nih.gov/bioproject/PRJNA898584 (accessed on 30 June 2023).

Conflicts of Interest: The authors declare no conflict of interest.

Abbreviations

RA	Recent Arrived Birds
PM	Premigratory
DEGs	Differentially Expressed Genes
FDR	False Discovery Rate
Log2FC	Log2 Fold Change
GO	Gene Ontology
CC	Cellular Component
MF	Molecular Function
BP	Biological Process
IDs	Identifications
TPM	Transcript Per Million
TMM	Trimmed Mean of M values

References

1. Kimmitt, A.A. Females as the Gatekeepers to Seasonal Breeding: What We Can Learn by Studying Reproductive Mechanisms in Both Sexes. *Integr. Comp. Biol.* **2020**, *60*, 703–711. [CrossRef] [PubMed]
2. Lifjeld, J.T.; Kleven, O.; Fossoy, F.; Jacobsen, F.; Laskemoen, T.; Rudolfsen, G.; Robertson, R.J. When Older Males Sire More Offspring-Increased Attractiveness or Higher Fertility? *Behav. Ecol. Sociobiol.* **2022**, *76*, 61. [CrossRef]
3. Yoshimura, T. Thyroid hormone and seasonal regulation of reproduction. *Front. Neuroendocrinol.* **2013**, *34*, 157–166. [CrossRef]
4. Sharma, A.; Das, S.; Komal, R.; Malik, S.; Rani, S.; Kumar, V. Seasonal reproductive state determines gene expression in the hypothalamus of a latitudinal migratory songbird during the spring and autumn migration. *Mol. Cell Endocrinol.* **2020**, *508*, 110794. [CrossRef]
5. Costa, J.S.; Hahn, S.; Araujo, P.M.; Dhanjal-Adams, K.L.; Rocha, A.D.; Alves, J.A. Linking migratory performance to breeding phenology and productivity in an Afro-Palearctic long-distance migrant. *Sci. Rep.* **2021**, *11*, 23258. [CrossRef] [PubMed]
6. Trivedi, A.K.; Kumar, J.; Rani, S.; Kumar, V. Annual life history-dependent gene expression in the hypothalamus and liver of a migratory songbird: Insights into the molecular regulation of seasonal metabolism. *J. Biol. Rhythms* **2014**, *29*, 332–345. [CrossRef] [PubMed]
7. Sharma, A.; Singh, D.; Malik, S.; Gupta, N.J.; Rani, S.; Kumar, V. Difference in control between spring and autumn migration in birds: Insight from seasonal changes in hypothalamic gene expression in captive buntings. *Proc. Biol. Sci.* **2018**, *285*, 20181531. [CrossRef] [PubMed]
8. Sharma, A.; Kumar, V. Metabolic plasticity mediates differential responses to spring and autumn migrations: Evidence from gene expression patterns in migratory buntings. *Exp. Physiol.* **2019**, *104*, 1841–1857. [CrossRef]
9. Sharma, A.; Singh, D.; Gupta, P.; Bhardwaj, S.K.; Kaur, I.; Kumar, V. Molecular changes associated with migratory departure from wintering areas in obligate songbird migrants. *J. Exp. Biol.* **2021**, *224*, jeb242153. [CrossRef]
10. Frias-Soler, R.C.; Kelsey, N.A.; Villarin Pildain, L.; Wink, M.; Bairlein, F. Transcriptome signature changes in the liver of a migratory passerine. *Genomics* **2022**, *114*, 110283. [CrossRef]
11. Frias-Soler, R.C.; Pildain, L.V.; Parau, L.G.; Wink, M.; Bairlein, F. Transcriptome signatures in the brain of a migratory songbird. *Comp. Biochem. Physiol. Part D Genom. Proteom.* **2020**, *34*, 100681. [CrossRef] [PubMed]
12. Henrique, E.P.; de Oliveira, M.A.; Paulo, D.C.; Pereira, P.D.C.; Dias, C.; de Siqueira, L.S.; de Lima, C.M.; Miranda, D.A.; do Rego, P.S.; Araripe, J.; et al. Contrasting migratory journeys and changes in hippocampal astrocyte morphology in shorebirds. *Eur. J. Neurosci.* **2021**, *54*, 5687–5704. [CrossRef]
13. de Almeida Miranda, D.; Araripe, J.; de Morais Magalhaes, N.G.; de Siqueira, L.S.; de Abreu, C.C.; Pereira, P.D.C.; Henrique, E.P.; da Silva Chira, P.A.C.; de Melo, M.A.D.; do Rego, P.S.; et al. Shorebirds' Longer Migratory Distances Are Associated With Larger ADCYAP1 Microsatellites and Greater Morphological Complexity of Hippocampal Astrocytes. *Front. Psychol.* **2021**, *12*, 784372. [CrossRef] [PubMed]

14. Carvalho-Paulo, D.; de Morais Magalhaes, N.G.; de Almeida Miranda, D.; Diniz, D.G.; Henrique, E.P.; Moraes, I.A.M.; Pereira, P.D.C.; de Melo, M.A.D.; de Lima, C.M.; de Oliveira, M.A.; et al. Hippocampal Astrocytes in Migrating and Wintering Semipalmated Sandpiper *Calidris pusilla*. *Front. Neuroanat.* **2017**, *11*, 126. [CrossRef]
15. DeMoranville, K.J.; Corder, K.R.; Hamilton, A.; Russell, D.E.; Huss, J.M.; Schaeffer, P.J. PPAR expression, muscle size and metabolic rates across the gray catbird's annual cycle are greatest in preparation for fall migration. *J. Exp. Biol.* **2019**, *222 Pt 14*, jeb198028. [CrossRef] [PubMed]
16. Guglielmo, C.G. Obese super athletes: Fat-fueled migration in birds and bats. *J. Exp. Biol.* **2018**, *221* (Suppl. S1), jeb165753. [CrossRef] [PubMed]
17. Schmaljohann, H.; Eikenaar, C.; Sapir, N. Understanding the ecological and evolutionary function of stopover in migrating birds. *Biol. Rev. Camb. Philos. Soc.* **2022**, *97*, 1231–1252. [CrossRef]
18. Catry, T.; Granadeiro, J.P.; Gutierrez, J.S.; Correia, E. Stopover use of a large estuarine wetland by dunlins during spring and autumn migrations: Linking local refuelling conditions to migratory strategies. *PLoS ONE* **2022**, *17*, e0263031. [CrossRef]
19. Elowe, C.R.; Gerson, A.R. Migratory disposition alters lean mass dynamics and protein metabolism in migratory white-throated sparrows (*Zonotrichia albicollis*). *Am. J. Physiol. Regul. Integr. Comp. Physiol.* **2022**, *323*, R98–R109. [CrossRef]
20. Malik, S.; Singh, S.; Rani, S.; Kumar, V. Life at a different pace: Annual itineraries are conserved in seasonal songbirds. *J. Biosci.* **2014**, *39*, 485–491. [CrossRef] [PubMed]
21. Sharma, A.; Singh, D.; Das, S.; Kumar, V. Hypothalamic and liver transcriptome from two crucial life-history stages in a migratory songbird. *Exp. Physiol.* **2018**, *103*, 559–569. [CrossRef]
22. Albert, S.; Wolfe, J.D.; Kellerman, J.; Sherry, T.; Stutchbury, B.J.M.; Bayly, N.J.; Ruiz-Sánchez, A. Habitat ecology of Nearctic–Neotropical migratory landbirds on the nonbreeding grounds. *Condor* **2020**, *122*, duaa055. [CrossRef]
23. Gratto-Trevor, C.; Morrison, R.; Mizrahi, D.; Lank, D.; Hicklin, P.; Spaans, A. Migratory connectivity of Semipalmated Sandpipers: Winter distribution and migration routes of breeding populations. *Waterbirds* **2012**, *35*, 83–95. [CrossRef]
24. Hicklin, P.; Gratto-Trevor, C.L.; Poole, A.F. Semipalmated Sandpiper (*Calidris pusilla*). The Birds of North. America Online. 2010. Available online: https://www.birds-of-north-america.net/Semipalmated_Sandpiper.html (accessed on 20 January 2023).
25. Hicklin, P. The migration of shorebirds in the Bay of Fundy. *Wilson Bull.* **1987**, *99*, 540–570.
26. Gwinner, E. Circadian and circannual programmes in avian migration. *J. Exp. Biol.* **1996**, *199 Pt 1*, 39–48. [CrossRef] [PubMed]
27. Haest, B.; Huppop, O.; Bairlein, F. The influence of weather on avian spring migration phenology: What, where and when? *Glob. Chang. Biol.* **2018**, *24*, 5769–5788. [CrossRef]
28. Marra, P.P.; Francis, C.M.; Mulvihill, R.S.; Moore, F.R. The influence of climate on the timing and rate of spring bird migration. *Oecologia* **2005**, *142*, 307–315. [CrossRef]
29. Horton, K.G.; Van Doren, B.M.; La Sorte, F.A.; Cohen, E.B.; Clipp, H.L.; Buler, J.J.; Fink, D.; Kelly, J.F.; Farnsworth, A. Holding steady: Little change in intensity or timing of bird migration over the Gulf of Mexico. *Glob. Chang. Biol.* **2019**, *25*, 1106–1118. [CrossRef]
30. Huppop, O.; Huppop, K. North Atlantic Oscillation and timing of spring migration in birds. *Proc. Biol. Sci.* **2003**, *270*, 233–240. [CrossRef]
31. Haest, B.; Huppop, O.; Bairlein, F. Weather at the winter and stopover areas determines spring migration onset, progress, and advancements in Afro-Palearctic migrant birds. *Proc. Natl. Acad. Sci. USA* **2020**, *117*, 17056–17062. [CrossRef]
32. Brown, S. The Remarkable Odyssey of a Semipalmated Sandpiper. In *Shorebird Science*; Manomet Soaring Solutions Grounded Science: Coats Island, NU, Canada, 2014.
33. Mata, A.; Marin, G.; Rodriguez, J.P.; Yurai Guerrero, H.; Cardillo, E. Plasma corticosterone levels of semipalmated sandpiper *Calidris pusilla* overwintering in a tropical coastal lagoon of northeastern Venezuela: Effect of capture and handling. *Ann. N. Y. Acad. Sci.* **2009**, *1163*, 460–463. [CrossRef]
34. Larrazábal, M.; Azevedo-Júnior, S.d.; Pena, O. Monitoramento de aves limícolas na Salina diamante Branco, galinhos, Rio grande do Norte, Brasil. *Rev. Bras. Zool.* **2002**, *19*, 1081–1089. [CrossRef]
35. Linhart, R.; Hamilton, D.; Paquet, J.; Monteiro, J.; Ramires, G.; Mobley, J. Movement and habitat use of non-breeding Semipalmated Sandpiper (*Calidris pusilla*) at the Banco dos Cajuais in Northeast Brazil. In *Conservation Science and Practice*; Wiley: Hoboken, NJ, USA, 2022; p. e12683. Available online: wileyonlinelibrary.com/journal/csp2 (accessed on 3 February 2022).
36. Fedrizzi, C.E.; Azevedo Júnior, S.M.d.; Larrazábal, M.E.L.d. Body mass and acquisition of breeding plumage of wintering *Calidris pusilla* (Linnaeus) (Aves, Scolopacidae) in the coast of Pernambuco, north-eastern Brazil. *Rev. Bras. Zool.* **2004**, *21*, 249–252. [CrossRef]
37. Buccitelli, C.; Selbach, M. mRNAs, proteins and the emerging principles of gene expression control. *Nat. Rev. Genet.* **2020**, *21*, 630–644. [CrossRef]
38. de Morais Magalhaes, N.G.; Guerreiro Diniz, C.; Guerreiro Diniz, D.; Pereira Henrique, E.; Correa Pereira, P.D.; Matos Moraes, I.A.; Damasceno de Melo, M.A.; Sherry, D.F.; Wanderley Picanco Diniz, C. Hippocampal neurogenesis and volume in migrating and wintering semipalmated sandpipers (*Calidris pusilla*). *PLoS ONE* **2017**, *12*, e0179134. [CrossRef] [PubMed]
39. Raghavan, V.; Kraft, L.; Mesny, F.; Rigerte, L. A simple guide to de novo transcriptome assembly and annotation. *Brief. Bioinform.* **2022**, *23*, bbab563. [CrossRef] [PubMed]
40. Wang, Z.; Gerstein, M.; Snyder, M. RNA-Seq: A revolutionary tool for transcriptomics. *Nat. Rev. Genet.* **2009**, *10*, 57–63. [CrossRef] [PubMed]

41. McDermaid, A.; Monier, B.; Zhao, J.; Liu, B.; Ma, Q. Interpretation of differential gene expression results of RNA-seq data: Review and integration. *Brief. Bioinform.* **2019**, *20*, 2044–2054. [CrossRef]
42. Zhao, Y.; Li, M.C.; Konate, M.M.; Chen, L.; Das, B.; Karlovich, C.; Williams, P.M.; Evrard, Y.A.; Doroshow, J.H.; McShane, L.M. TPM, FPKM, or Normalized Counts? A Comparative Study of Quantification Measures for the Analysis of RNA-seq Data from the NCI Patient-Derived Models Repository. *J. Transl. Med.* **2021**, *19*, 269. [CrossRef]
43. Barkan, S.; Yom-Tov, Y.; Barnea, A. Exploring the Relationship between Brain Plasticity, Migratory Lifestyle, and Social Structure in Birds. *Front. Neurosci.* **2017**, *11*, 139. [CrossRef]
44. Rytova, V.; Ganella, D.E.; Hawkes, D.; Bathgate, R.A.D.; Ma, S.; Gundlach, A.L. Chronic activation of the relaxin-3 receptor on GABA neurons in rat ventral hippocampus promotes anxiety and social avoidance. *Hippocampus* **2019**, *29*, 905–920. [CrossRef] [PubMed]
45. Ling, H.; McLvor, G.E.; van der Vaart, K.; Vaughan, R.T.; Thornton, A.; Ouellette, N.T. Costs and benefits of social relationships in the collective motion of bird flocks. *Nat. Ecol. Evol.* **2019**, *3*, 943–948. [CrossRef] [PubMed]
46. Guerreiro, L.C.F.; Henrique, E.P.; da Silva Rosa, J.B.; Pereira, P.D.C.; de Abreu, C.C.; Fernandes, T.N.; de Morais Magalhaes, N.G.; de Jesus Falcao da Silva, A.; da Costa, E.R.; Guerreiro-Diniz, C.; et al. Plasticity in the hippocampal formation of shorebirds during the wintering period: Stereological analysis of parvalbumin neurons in Actitis macularius. *Learn. Behav.* **2022**, *50*, 45–54. [CrossRef]
47. Donato, F.; Rompani, S.B.; Caroni, P. Parvalbumin-expressing basket-cell network plasticity induced by experience regulates adult learning. *Nature* **2013**, *504*, 272–276. [CrossRef]
48. Caroni, P. Regulation of Parvalbumin Basket cell plasticity in rule learning. *Biochem. Biophys. Res. Commun.* **2015**, *460*, 100–103. [CrossRef] [PubMed]
49. Caroni, P. Inhibitory microcircuit modules in hippocampal learning. *Curr. Opin. Neurobiol.* **2015**, *35*, 66–73. [CrossRef]
50. Patenaude, C.; Chapman, C.A.; Bertrand, S.; Congar, P.; Lacaille, J.C. GABAB receptor- and metabotropic glutamate receptor-dependent cooperative long-term potentiation of rat hippocampal GABAA synaptic transmission. *J. Physiol.* **2003**, *553 Pt 1*, 155–167. [CrossRef]
51. Patenaude, C.; Massicotte, G.; Lacaille, J.C. Cell-type specific GABA synaptic transmission and activity-dependent plasticity in rat hippocampal stratum radiatum interneurons. *Eur. J. Neurosci.* **2005**, *22*, 179–188. [CrossRef]
52. Honore, E.; Khlaifia, A.; Bosson, A.; Lacaille, J.C. Hippocampal Somatostatin Interneurons, Long-Term Synaptic Plasticity and Memory. *Front. Neural Circuits* **2021**, *15*, 687558. [CrossRef]
53. Topolnik, L.; Tamboli, S. The role of inhibitory circuits in hippocampal memory processing. *Nat. Rev. Neurosci.* **2022**, *23*, 476–492. [CrossRef]
54. Chamberland, S.; Topolnik, L. Inhibitory control of hippocampal inhibitory neurons. *Front. Neurosci.* **2012**, *6*, 165. [CrossRef]
55. Mouritsen, H.; Heyers, D.; Gunturkun, O. The Neural Basis of Long-Distance Navigation in Birds. *Annu. Rev. Physiol.* **2016**, *78*, 133–154. [CrossRef]
56. Tyagi, T.; Bhardwaj, S.K. Magnetic Compass Orientation in a Palaearctic-Indian Night Migrant, the Red-Headed Bunting. *Animals* **2021**, *11*, 1541. [CrossRef] [PubMed]
57. Gronroos, J.; Muheim, R.; Akesson, S. Orientation and autumn migration routes of juvenile sharp-tailed sandpipers at a staging site in Alaska. *J. Exp. Biol.* **2010**, *213*, 1829–1835. [CrossRef] [PubMed]
58. Papadopoulos, T.; Eulenburg, V.; Reddy-Alla, S.; Mansuy, I.M.; Li, Y.; Betz, H. Collybistin is required for both the formation and maintenance of GABAergic postsynapses in the hippocampus. *Mol. Cell Neurosci.* **2008**, *39*, 161–169. [CrossRef] [PubMed]
59. Ibaraki, K.; Mizuno, M.; Aoki, H.; Niwa, A.; Iwamoto, I.; Hara, A.; Tabata, H.; Ito, H.; Nagata, K.I. Biochemical and Morphological Characterization of a Guanine Nucleotide Exchange Factor ARHGEF9 in Mouse Tissues. *Acta Histochem. Cytochem.* **2018**, *51*, 119–128. [CrossRef] [PubMed]
60. Chiou, T.T.; Bonhomme, B.; Jin, H.; Miralles, C.P.; Xiao, H.; Fu, Z.; Harvey, R.J.; Harvey, K.; Vicini, S.; De Blas, A.L. Differential regulation of the postsynaptic clustering of gamma-aminobutyric acid type A (GABAA) receptors by collybistin isoforms. *J. Biol. Chem.* **2011**, *286*, 22456–22468. [CrossRef] [PubMed]
61. Smart, T.G.; Stephenson, F.A. A half century of gamma-aminobutyric acid. *Brain Neurosci. Adv.* **2019**, *3*, 2398212819858249. [CrossRef]
62. Agrawal, J.; Dwivedi, Y. GABA(A) Receptor Subunit Transcriptional Regulation, Expression Organization, and Mediated Calmodulin Signaling in Prefrontal Cortex of Rats Showing Testosterone-Mediated Impulsive Behavior. *Front. Neurosci.* **2020**, *14*, 600099. [CrossRef]
63. Blank, M.H.; de Oliveira, M.J.; Cubas, Z.S.; de Morae, W.; Moreira, N.; Pereira, R.J.G. Fecal sex steroids and reproductive behaviors in harpy eagles (*Harpia harpyja*). *Zoo Biol.* **2020**, *39*, 315–324. [CrossRef]
64. Landys, M.M.; Piersma, T.; Guglielmo, C.G.; Jukema, J.; Ramenofsky, M.; Wingfield, J.C. Metabolic profile of long–distance migratory flight and stopover in a shorebird. *Proc. R. Soc. B Biol. Sci.* **2005**, *272*, 295–302. [CrossRef] [PubMed]
65. Guglielmo, C.G. Move that fatty acid: Fuel selection and transport in migratory birds and bats. *Integr. Comp. Biol.* **2010**, *50*, 336–345. [CrossRef] [PubMed]
66. Chowdhury, G.M.; Jiang, L.; Rothman, D.L.; Behar, K.L. The contribution of ketone bodies to basal and activity-dependent neuronal oxidation in vivo. *J. Cereb. Blood Flow. Metab.* **2014**, *34*, 1233–1242. [CrossRef] [PubMed]

67. Achanta, L.B.; Rae, C.D. β-Hydroxybutyrate in the Brain: One Molecule, Multiple Mechanisms. *Neurochem. Res.* **2017**, *42*, 35–49. [CrossRef]
68. Brister, J.R.; Ako-adjei, D.; Bao, Y.; Blinkova, O. NCBI Viral Genomes Resource. *Nucleic Acids Res.* **2015**, *43*, D571–D577. [CrossRef]
69. Pereira, P.D.C. Genes inflammatory response, tolerance, and resistance to virus infections in migratory birds, bats, and rodents. *Front. Immunol.* 2023; *under review*.
70. Eikenaar, C.; Hegemann, A.; Packmor, F.; Kleudgen, I.; Isaksson, C. Not just fuel: Energy stores are correlated with immune function and oxidative damage in a long-distance migrant. *Curr. Zool.* **2020**, *66*, 21–28. [CrossRef] [PubMed]
71. Medzhitov, R.; Schneider, D.S.; Soares, M.P. Disease tolerance as a defense strategy. *Science* **2012**, *335*, 936–941. [CrossRef]
72. Rivas, F.V.; Chervonsky, A.V.; Medzhitov, R. ART and immunology. *Trends Immunol.* **2014**, *35*, 451. [CrossRef]
73. Raberg, L.; Graham, A.L.; Read, A.F. Decomposing health: Tolerance and resistance to parasites in animals. *Philos. Trans. R. Soc. Lond. B Biol. Sci.* **2009**, *364*, 37–49. [CrossRef]
74. Zhong, C.; Liu, F.; Hajnik, R.J.; Yao, L.; Chen, K.; Wang, M.; Liang, Y.; Sun, J.; Soong, L.; Hou, W.; et al. Type I Interferon Promotes Humoral Immunity in Viral Vector Vaccination. *J. Virol.* **2021**, *95*, e0092521. [CrossRef] [PubMed]
75. de Weerd, N.A.; Nguyen, T. The interferons and their receptors--distribution and regulation. *Immunol. Cell Biol.* **2012**, *90*, 483–491. [CrossRef] [PubMed]
76. Zhou, P.; Tachedjian, M.; Wynne, J.W.; Boyd, V.; Cui, J.; Smith, I.; Cowled, C.; Ng, J.H.; Mok, L.; Michalski, W.P.; et al. Contraction of the type I IFN locus and unusual constitutive expression of IFN-α in bats. *Proc. Natl. Acad. Sci. USA* **2016**, *113*, 2696–2701. [CrossRef]
77. Carty, M.; Guy, C.; Bowie, A.G. Detection of Viral Infections by Innate Immunity. *Biochem. Pharmacol.* **2021**, *183*, 114316. [CrossRef] [PubMed]
78. Ahn, M.; Anderson, D.E.; Zhang, Q.; Tan, C.W.; Lim, B.L.; Luko, K.; Wen, M.; Chia, W.N.; Mani, S.; Wang, L.C.; et al. Dampened NLRP3-mediated inflammation in bats and implications for a special viral reservoir host. *Nat. Microbiol.* **2019**, *4*, 789–799. [CrossRef]
79. Broz, P.; Dixit, V.M. Inflammasomes: Mechanism of assembly, regulation and signalling. *Nat. Rev. Immunol.* **2016**, *16*, 407–420. [CrossRef]
80. Vrentas, C.E.; Schaut, R.G.; Boggiatto, P.M.; Olsen, S.C.; Sutterwala, F.S.; Moayeri, M. Inflammasomes in livestock and wildlife: Insights into the intersection of pathogens and natural host species. *Vet. Immunol. Immunopathol.* **2018**, *201*, 49–56. [CrossRef] [PubMed]
81. FastQC: A Quality Control Tool for High Throughput Sequence Data. 2016. Available online: https://www.bioinformatics.babraham.ac.uk/projects/fastqc/ (accessed on 30 June 2023).
82. Bolger, A.M.; Lohse, M.; Usadel, B. Trimmomatic: A flexible trimmer for Illumina sequence data. *Bioinformatics* **2014**, *30*, 2114–2120. [CrossRef]
83. Grabherr, M.G.; Haas, B.J.; Yassour, M.; Levin, J.Z.; Thompson, D.A.; Amit, I.; Adiconis, X.; Fan, L.; Raychowdhury, R.; Zeng, Q. Full-length transcriptome assembly from RNA-Seq data without a reference genome. *Nat. Biotechnol.* **2011**, *29*, 644–652. [CrossRef]
84. Patro, R.; Duggal, G.; Love, M.I.; Irizarry, R.A.; Kingsford, C. Salmon provides fast and bias-aware quantification of transcript expression. *Nat. Methods* **2017**, *14*, 417–419. [CrossRef]
85. Robinson, M.D.; McCarthy, D.J.; Smyth, G.K. edgeR: A Bioconductor package for differential expression analysis of digital gene expression data. *Bioinformatics* **2010**, *26*, 139–140. [CrossRef] [PubMed]
86. Conesa, A.; Gotz, S.; Garcia-Gomez, J.M.; Terol, J.; Talon, M.; Robles, M. Blast2GO: A universal tool for annotation, visualization and analysis in functional genomics research. *Bioinformatics* **2005**, *21*, 3674–3676. [CrossRef]
87. Altschul, S.F.; Gish, W.; Miller, W.; Myers, E.W.; Lipman, D.J. Basic local alignment search tool. *J. Mol. Biol.* **1990**, *215*, 403–410. [CrossRef] [PubMed]
88. UniProt Consortium, T. UniProt: The universal protein knowledgebase. *Nucleic Acids Res.* **2018**, *46*, 2699. [CrossRef] [PubMed]
89. Pruitt, K.D.; Tatusova, T.; Maglott, D.R. NCBI reference sequences (RefSeq): A curated non-redundant sequence database of genomes, transcripts and proteins. *Nucleic Acids Res.* **2007**, *35*, D61–D65. [CrossRef]
90. Suzek, B.E.; Huang, H.; McGarvey, P.; Mazumder, R.; Wu, C.H. UniRef: Comprehensive and non-redundant UniProt reference clusters. *Bioinformatics* **2007**, *23*, 1282–1288. [CrossRef] [PubMed]
91. Sayers, E.W.; Cavanaugh, M.; Clark, K.; Ostell, J.; Pruitt, K.D.; Karsch-Mizrachi, I. GenBank. *Nucleic Acids Res.* **2019**, *47*, D94–D99. [CrossRef] [PubMed]
92. Gotz, S.; Garcia-Gomez, J.M.; Terol, J.; Williams, T.D.; Nagaraj, S.H.; Nueda, M.J.; Robles, M.; Talon, M.; Dopazo, J.; Conesa, A. High-throughput functional annotation and data mining with the Blast2GO suite. *Nucleic Acids Res.* **2008**, *36*, 3420–3435. [CrossRef]
93. Benjamini, Y.; Hochberg, Y. Controlling the false discovery rate: A practical and powerful approach to multiple testing. *J. R. Stat. Soc. Ser. B Methodol.* **1995**, *57*, 289–300. [CrossRef]
94. Frias-Soler, R.C.; Villarin Pildain, L.; Hotz-Wagenblatt, A.; Kolibius, J.; Bairlein, F.; Wink, M. De novo annotation of the transcriptome of the Northern Wheatear (*Oenanthe oenanthe*). *PeerJ* **2018**, *6*, e5860. [CrossRef]
95. Guigo, R.; de Hoon, M. Recent advances in functional genome analysis. *F1000Research* **2018**, *7*, 1968. [CrossRef] [PubMed]

96. Colquitt, B.M. Organizational Conservation and Flexibility in the Evolution of Birdsong and Avian Motor Control. *Brain Behav. Evol.* **2022**, *97*, 255–264. [CrossRef] [PubMed]
97. Prather, J.F.; Okanoya, K.; Bolhuis, J.J. Brains for birds and babies: Neural parallels between birdsong and speech acquisition. *Neurosci. Biobehav. Rev.* **2017**, *81 Pt B*, 225–237. [CrossRef]

International Journal of
Molecular Sciences

MDPI

Perspective

The Amyloid Cascade Hypothesis 2.0 for Alzheimer's Disease and Aging-Associated Cognitive Decline: From Molecular Basis to Effective Therapy

Vladimir Volloch [1,*] and Sophia Rits-Volloch [2,3,*]

[1] Department of Developmental Biology, Harvard School of Dental Medicine, Boston, MA 02115, USA
[2] Division of Molecular Medicine, Children's Hospital, Boston, MA 02115, USA
[3] Department of Biological Chemistry and Molecular Pharmacology, Harvard Medical School, Boston, MA 02115, USA
* Correspondence: vladimir.volloch@gmail.com (V.V.); rits@crystal.harvard.edu (S.R.-V.)

Abstract: With the long-standing amyloid cascade hypothesis (ACH) largely discredited, there is an acute need for a new all-encompassing interpretation of Alzheimer's disease (AD). Whereas such a recently proposed theory of AD is designated ACH2.0, its commonality with the ACH is limited to the recognition of the centrality of amyloid-β (Aβ) in the disease, necessitated by the observation that *all* AD-causing mutations affect, in one way or another, Aβ. Yet, even this narrow commonality is superficial since AD-causing Aβ of the ACH differs distinctly from that specified in the ACH2.0: Whereas in the former, the disease is caused by secreted extracellular Aβ, in the latter, it is triggered by Aβ-protein-precursor (AβPP)-derived *intraneuronal* Aβ (*i*Aβ) and driven by *i*Aβ generated *independently* of AβPP. The ACH2.0 envisions AD as a two-stage disorder. The first, asymptomatic stage is a decades-long accumulation of AβPP-derived *i*Aβ, which occurs via internalization of secreted Aβ and through intracellular retention of a fraction of Aβ produced by AβPP proteolysis. When AβPP-derived *i*Aβ reaches critical levels, it activates a self-perpetuating AβPP-independent production of *i*Aβ that drives the second, devastating AD stage, a cascade that includes tau pathology and culminates in neuronal loss. The present study analyzes the dynamics of *i*Aβ accumulation in health and disease and concludes that it is the prime factor driving both AD and aging-associated cognitive decline (AACD). It discusses mechanisms potentially involved in AβPP-independent generation of *i*Aβ, provides mechanistic interpretations for all principal aspects of AD and AACD including the protective effect of the Icelandic AβPP mutation, the early onset of FAD and the sequential manifestation of AD pathology in defined regions of the affected brain, and explains why current mouse AD models are neither adequate nor suitable. It posits that while drugs affecting the accumulation of AβPP-derived *i*Aβ can be effective only protectively for AD, the targeted degradation of *i*Aβ is the best therapeutic strategy for both prevention and effective treatment of AD and AACD. It also proposes potential *i*Aβ-degrading drugs.

Keywords: the amyloid cascade hypothesis 2.0 (ACH2.0); intraneuronal Aβ (*i*Aβ); Aβ protein precursor (AβPP)-independent generation of *i*Aβ; aging-related cognitive dysfunction (AACD); *i*Aβ depletion therapy for AD and AACD; BACE1 and BACE2 activators as AD and AACD drugs

Citation: Volloch, V.; Rits-Volloch, S. The Amyloid Cascade Hypothesis 2.0 for Alzheimer's Disease and Aging-Associated Cognitive Decline: From Molecular Basis to Effective Therapy. *Int. J. Mol. Sci.* **2023**, *24*, 12246. https://doi.org/10.3390/ijms241512246

Academic Editor: Claudia Ricci

Received: 19 July 2023
Revised: 26 July 2023
Accepted: 27 July 2023
Published: 31 July 2023

1. Introduction

The designation of the recently proposed interpretation of Alzheimer's disease (AD) and aging-associated cognitive decline (AACD), amyloid cascade hypothesis 2.0 (ACH2.0), refers to its predecessor, the ACH. However, despite the similarity of names, the commonality between these two theories of AD is restricted to the recognition of the centrality of amyloid-beta (Aβ) in the disease. But even this narrow commonality is rather superficial: whereas in the ACH, AD is caused by extracellular Aβ produced and secreted in the Aβ protein precursor (AβPP)-proteolytic pathway, in the ACH2.0, the disease is triggered by

AβPP-derived intraneuronal Aβ (*i*Aβ) accumulated to sufficient levels and is driven by *i*Aβ generated independently of AβPP. The rationale for the

ACH2.0, as well as its various aspects, has been discussed in detail elsewhere [1–3]. The present discourse takes the preceding studies as the established point of departure. One of its main objectives is to analyze the kinetic parameters of the ACH.2.0. As detailed below, this analysis concludes that the dynamics of *i*Aβ accumulation plays the key role in the commencement and progression of both AD and AACD. This notion is best illustrated by the observations that *all* known AD-causing mutations elevate the rate of *i*Aβ accumulation, whereas the mutation that protects from both AD and AACD suppresses it [4,5]. The dynamics of *i*Aβ accumulation points to feasible options of interference with AD and AACD and its understanding is essential for the development of the efficient therapeutic strategies, which are discussed in detail below.

To better orient the reader, the following few sections (Sections 2–6), preceding the analysis of the dynamics of *i*Aβ accumulation, briefly summarize four main principles of the ACH 2.0 (for detailed description and analysis see [1,2]). They are: (1)—AD and AACD are caused and driven by intra- rather than extracellular Aβ; (2)—AD (but not AACD) is a two-stage disease; (3)—the symptomatic second stage of AD is driven by *i*Aβ produced in the AβPP-independent pathway; (4)—*i*Aβ generated independently of AβPP is retained intraneuronally, perpetuates its own production and renders AβPP-derived *i*Aβ irrelevant for the progression of AD due to its marginal (in comparison with *i*Aβ produced independently of AβPP) contribution into the cellular *i*Aβ pool.

2. Amyloid Cascade Hypothesis: A Proposition in Distress

In 1992, Hardy and Higgins proposed the long-standing amyloid cascade hypothesis, ACH, for AD [6]. They formulated it as follows: "Our hypothesis is that deposition of amyloid β protein, the main component of the plaques, is the causative agent of Alzheimer's pathology and that the neurofibrillary tangles, cell loss, vascular damage, and dementia follow as the direct result of this deposition" [6]. The principal basis for this assertion was, in addition to the prominent occurrence of Aβ plaques, the then recent discovery of a mutation within AβPP [7] that affected the generation of Aβ in the AβPP proteolytic pathway and segregated with, and apparently caused, familial AD (FAD). At the time, the ACH appeared to be consistent with all preceding observations; it was widely accepted and formed the long-lasting foundation for basic and clinical research. Consequently, extracellular Aβ and its production in the AβPP proteolytic/secretory pathway became the major therapeutic targets of the disease. The research and development efforts resulted in numerous candidate AD drugs. Many of those drugs exhibited dramatic successes in preclinical studies and animal trials. As an example, suppression of BACE1 activity, and thus of Aβ production, by different means resulted in a significant improvement of neurophysiological functions and, moreover, in the dramatic reversal of AD symptoms in animal models where Aβ was overproduced exogenously [8–10].

However, with few exceptions (lecanemab and donanemab, which are marginally effective in very early symptomatic AD but apparently act preventively rather than curatively [3]), all AD candidate drugs showed no efficacy whatsoever in symptomatic AD clinical trials, which were consequently declared failures. On the other hand, the close analysis of the results of "failed" clinical trials indicates that many candidate AD drugs succeeded remarkably in their mechanistic mission. For example, verubecestat, a BACE1 inhibitor, effectively suppressed production of Aβ in the AβPP proteolytic pathway and substantially cleared extracellular Aβ in AD patients, as reflected in the up to 80% reduction, in a dose-dependent manner, of the levels of Aβ in CSF [11,12]. The observations that the drug effectively accomplished exactly what it was designed for without eliciting any clinical improvements in patients implied that the underlying theory of AD, the ACH, is incorrect and mandated different interpretation of the disease. Failures of clinical trials of ACH-based AD drugs were exacerbated by observations showing that there is no good correlation between extracellular Aβ deposit levels and the occurrence of the disease. Indeed,

a significant subset of the general human population develops, with aging, excessive levels of extracellular Aβ, comparable with or greater than those typically seen in AD, yet shows no cognitive dysfunction or AD pathology [13–19]. In a diametrically opposite example, some individuals with cognitive AD symptoms and the occurrence of AD pathology show no excessive levels of extracellular Aβ [20]. Taken cumulatively, the above considerations apparently rule out the causative role of extracellular Aβ in AD.

3. The Centrality of Amyloid-β Is Requisite for Any Theory of AD: ACH2.0

Yet another set of observations powerfully attests to the centrality and the causative role of Aβ in AD. In the over three decades since the discovery of the first Aβ-affecting, AD-causing mutation [7], many more mutations that cause AD have been detected and characterized. *All* of them, with no exception, affect either the structure of Aβ or various aspects of its production in the AβPP proteolytic pathway. Moreover, the mutation known to confer on its carriers the protection from both AD and AACD replaces a single amino acid within Aβ [4,5]. In other words, introduce a single Aβ modification and cause AD; substitute a single Aβ residue and protect from both AD and AACD. It is hardly conceivable to make a more persuasive case for the centrality and causative role of Aβ in AD. It follows that these two attributes, i.e., the centrality and the causative role of Aβ are requisite for *any* theory of AD. At first glance, this statement seems to contradict the concluding remark of the preceding section. The two notions, however, are not mutually exclusive. Considerations of the preceding section indeed rule out the causative role of extracellular Aβ but not that of the another pool of amyloid-beta: *intraneuronal* Aβ, *i*Aβ.

The causative role of *i*Aβ is the central tenet of the ACH2.0, which envisions AD as a two-stage disease. In the first, asymptomatic stage, AβPP-derived Aβ accumulates, in a decades-long process, to critical levels that cause the activation of the second, devastating AD stage that is anchored and driven by an agent which is independent of AβPP and which sustains and perpetuates its own production [1,2]. In terms of the ACH2.0, this agent is *i*Aβ generated in the AβPP-independent pathway [1]. Potentially, as discussed in [2], the agent driving the stage two of AD can be other than *i*Aβ. However, because all known AD-associated mutations affect Aβ, it is highly plausible that this agent is, in fact, *i*Aβ. It appears, therefore, that *i*Aβ, differentially produced in two distinct, albeit related, pathways, runs the entire course of the disease. Two key features of the *i*Aβ driving the second, symptomatic, AD stage are suggested by the following empirical data. (a) Since suppression of the production of AβPP-derived Aβ during the symptomatic stage of AD has no effect whatsoever on the progression of AD [11,12], this *i*Aβ pool must be produced in the AβPP-independent pathway. (b) Since the depletion of extracellular Aβ in human clinical trials showed no efficacy whatsoever [11,12], the bulk of Aβ produced in the AβPP-independent pathway must be retained intraneuronally. The physiological occurrence of cellular mechanisms capable of generating Aβ independently of AβPP (summarized in Sections 22–24 of the present study) provides additional support to the above notions.

The crucial role of the AβPP proteolytic/secretory pathway in only the first, pre-symptomatic stage of AD explains why drugs targeting extracellular AβPP-derived Aβ or its production by the AβPP proteolysis did not and indeed *could not* have any effect on the progression of the disease (driven at this stage by *i*Aβ produced independently of AβPP) in symptomatic AD patients despite effectively fulfilling their mechanistic purpose. By the same logic, the overall success of the same drugs in animal models suggests that no second AD stage occurs there, consistent with the inability to obtain full spectrum of AD pathology in those experimental systems (reviewed in [1] and further discussed below). On the other hand, the ACH2.0 predicts that, if administered pre-symptomatically, prior to the activation of the AβPP-independent *i*Aβ production pathway, these drugs could be effective preventively by precluding AβPP-derived Aβ from reaching the levels triggering the second AD stage [1,2]. The results obtained in clinical trials of lecanemab and donanemab substantiate this notion [3].

4. Two Sources of AβPP-Derived Intraneuronal Aβ

As discussed above, in the framework of the ACH2.0, it is assumed that in the second, symptomatic AD stage, the bulk, or the entire output, of the AβPP-independent *i*Aβ production pathway is not secreted but retained within the cell [1,2]; this stimulates and perpetuates its own production and thus drives the disease [1]. As for the sources of AβPP-derived *i*Aβ, crucial in the first, asymptomatic AD stage, those are well understood and are briefly summarized as follows.

4.1. Influx of iAβ via the Uptake of Extracellular Amyloid-β

Multiple studies of the role of *i*Aβ in AD indicated that it is the major trigger of AD pathology [21–32]. They also showed that the levels of *i*Aβ, rather than those of Aβ plaques, correlate with the loss of neurons in studied systems [33]. As for how AβPP-derived Aβ accumulates intraneuronally, there are two recognized venues. The first venue is the well-documented importation of extracellular Aβ by the cell. Soluble Aβ was shown to be taken up inside the cell by endocytosis [34]. Importantly, extracellular $A\beta_{42}$ is imported twice as efficiently as the other species of extracellular soluble Aβ [35]. The more efficient uptake of $A\beta_{42}$ leads to higher rates of its accumulation as *i*Aβ and, in combination with its augmented cytotoxicity (apparently due to its increase propensity to aggregate), appears to play a decisive role in the occurrence of FAD in carriers of mutations, both in AβPP and in presenilins (PSEN), resulting in the elevated production of $A\beta_{42}$ versus other Aβ species [36]. Multiple studies suggested that oligomerization of extracellular Aβ is a precondition for its importation inside the cell [37–39], a notion consistent with the increased cytotoxicity of extracellular Aβ in oligomeric conformation [34]. $A\beta_{42}$ was shown to form oligomeric structures and thus to enter the cell significantly more efficiently than other Aβ species [37,38]. The importation of extracellular Aβ is mediated by and was demonstrated to be dependent on the isoform of ApoE expressed by the cell [38]. Interestingly, ApoE4 appears to be significantly more effective in facilitating the importation of extracellular Aβ than other ApoE isoforms [26,38]. Importantly, this particular ApoE isoform is also the major risk factor for the occurrence of AD, consistent with the proposed role of *i*Aβ in the disease. Cellular uptake of extracellular Aβ was also shown to be facilitated by LRP [40], by the *α7* nicotinic acetylcholine receptor [41–43], by the RAGE (receptor for advanced glycation) [44–46], by the FPRL1 (formyl peptide receptor-like1) [47], and by NMDA (N-methyl-d-aspartate) receptors [48]. While its importation occurs also in normal individuals [49], the relative efficiency of its cellular uptake appears, as discussed below, to play a significant role in the occurrence of AD.

4.2. A Fraction of the C99 Fragment of AβPP Undergoes the Gamma-Cleavage on Intracellular Membranes; the Resulting Aβ Is Retained Intraneuronally

The second venue for the occurrence of *i*Aβ is the intracellular retention of a fraction of Aβ generated by AβPP proteolysis. The occurrence of this phenomenon is dependent on the site where the gamma-cleavage of the C99 fragment of AβPP takes place. The bulk of these cleavages occur on the plasma membrane, with the resulting Aβ being exported into the extracellular space. On the other hand, gamma-secretase cleavages have been also documented on intracellular membranes [50–52], with the resulting Aβ being retained intraneuronally. The locations of such cleavages include the lysosomes, mitochondria, endosomes, Golgi apparatus as well as the TGN (trans-Golgi network), and the ER (endoplasmic reticulum). Cleavages on the ER and TGN membranes appear to be specific to neuronal cells [53,54]. Gamma-cleavages at these locations produce, apparently, different species of iAβ. Those occurring on the ER membranes generate mostly *i*$A\beta_{42}$ while those taking place on the TGN membranes produce iAβ enriched in $A\beta_{40}$ species [53–58].

Given that AD is caused by *i*Aβ, it could be predicted that the increase in the proportion of Aβ produced on intracellular membranes and thus retained as *i*Aβ would facilitate the occurrence of AD. This is exactly what occurs in carriers of the Swedish FAD mutation. This mutation significantly increases a fraction of AβPP/C99 processed at the intracellular

membrane locations [59]. This results in the elevated levels of *i*Aβ and, consequently triggers FAD [59]. In another example where the above prediction is borne out, certain PSEN mutations facilitate gamma-cleavage on intracellular membranes and thus cause the elevation in *i*Aβ levels and the occurrence of FAD [60].

To summarize, a compendium of empirical data referenced above is presented below. It is either consistent with or is strongly indicative of the notion that AβPP-derived *i*Aβ causes AD and drives its first stage:

1. AD is caused by Aβ and not by tau protein. The mutations of the former lead to the pathological formation of tau tangles and the disease; the reverse does not occur [20,61].
2. The correlation between levels of extracellular Aβ and AD is poor:
   (a) The excessive deposition of extracellular Aβ is often not accompanied by AD [13–19].
   (b) The occurrence of AD (as judged by cognitive symptoms as well as by PET scan and postmortem analysis) is not always accompanied by excessive deposition of extracellular Aβ [20].
3. A fraction of Aβ produced in the AβPP proteolytic pathway was shown to physiologically accumulate within neurons via two defined mechanisms [21–60]; discussed above.
4. AD is associated with multiple factors that enable and promote the intraneuronal accumulation of *i*Aβ produced in the AβPP proteolytic pathway:
   (a) Cytotoxic $A\beta_{42}$ is taken up by the cell twice as efficiently as other isoforms of Aβ [35];
   (b) ApoE4, a major AD risk factor, is significantly more efficient in the internalization of extracellular Aβ than other species of ApoE [26,38];
   (c) The "toxicity" of extracellular Aβ in oligomeric form is due to its efficient cellular uptake [34,37–39].
5. Mutations that either cause AD or that protect from AD were shown to interfere with accumulation of *i*Aβ:
   (a) The Swedish AβPP mutation that causes familial AD was shown to expedite AβPP processing on internal membranes and thus to increase the retention of AβPP-derived Aβ within neurons [59];
   (b) The Flemish AβPP, FAD-causing, mutation elevates levels of *i*Aβ by suppressing physiologically occurring BACE2-mediated *i*Aβ cleavage [62];
   (c) The Icelandic AβPP mutation that protects from both AD and AACD decreases levels of *i*Aβ by significantly increasing the efficiency of BACE1-mediated *i*Aβ cleavage [4,5];
   (d) Certain PSEN FAD-causing mutations enhance the cellular uptake of extracellular Aβ by shifting the gamma-cleavage to position 42 of Aβ, thus elevating the proportion of $A\beta_{42}$ produced in the AβPP proteolytic/secretory pathway [36];
   (e) Some PSEN FAD-causing mutations increase the retention of Aβ produced in the AβPP proteolytic pathway within neuronal cells by facilitating the gamma-cleavage of C99 on internal (rather than on plasma) membranes [60].
6. The correlation between levels of *i*Aβ in AD-affected neurons and the incidence of AD biomarkers was shown to be good [33,49].
7. The results of preclinical and human clinical trials indicate that AβPP-derived *i*Aβ drives the first stage of AD but plays no significant role in the second stage of the disease [8–12].

5. Mechanistic Aspects of the ACH2.0

As was mentioned above, the Amyloid Cascade Hypothesis 2.0 posits that AD is a two-stage disease [1,2]. The first stage is a slow, decades-long accumulation of AβPP-derived *i*Aβ. Upon reaching a critical threshold, it mediates the activation of the second AD stage, which is relatively (to the first stage) fast. More precisely, it triggers the initiation

of the pathway that generates an agent, which drives the second AD stage. This agent is presumed to be capable of (a) anchoring a cascade that includes tau pathology and leads to neuronal death and (b) sustaining its own production [2]. It could be argued that the second requirement is redundant in view of the continuous influx of AβPP-derived *i*Aβ. However, this is not the case, because suppression of the AβPP proteolytic pathway at symptomatic phase of the disease (i.e., at the stage two of AD) in human clinical trials had no effect whatsoever on the progression of AD [11,12], consistent with the autonomous operation of the pathway that produces an agent which drives the second AD stage. As argued above, it is highly plausible that the second AD stage-driving agent is *i*Aβ generated in the AβPP-independent pathway; it is at the heart of Alzheimer's pathology, and it is of great interest how AβPP-derived *i*Aβ triggers its production. Plausibly, this occurs via the elicitation of the integrated stress response, ISR (although additional or alternative pathways cannot be excluded) [1,2].

5.1. Plausible Involvement of the Integrated Stress Response in Generation of an Agent Driving the Second Stage of AD

The integrated stress response, ISR, is a signaling cascade that takes place in eukaryotic cells and is triggered by a large variety of cellular stresses [63–72]. It is termed "integrated" because all events that initiate it lead to a common and central occurrence: the activation of eIF2α (a subunit of eukaryotic translation initiation factor 2) by its phosphorylation at a specific site (serine 51). Four kinases (comprising the family of eIF2α kinases) are capable of enacting this phosphorylation/activation event. They are PKR, PERK, GCN2, and HRI. Phosphorylation of eIF2α elicits the ISR. This manifests itself as an acute decline in the protein synthesis output. The reduction in the global cellular protein synthesis occurs via the suppression of the cap-dependent initiation of translation. Concurrently, the ISR promotes cap-independent translation of selected mRNA species; among those are mRNAs encoding specific transcription factors. The ISR-induced transcription factors, or translation products of the genes activated by these factors, may include components critical for the activation of the AβPP-independent *i*Aβ production or, alternatively, of the pathway generating the agent (if other than *i*Aβ) which drives the second stage of AD [1,2].

5.2. PKR Kinase Is Activated by iAβ and, in Turn, Elicits the ISR and Triggers the Second Stage of AD

In the majority of human population, AβPP-derived *i*Aβ does not reach the ISR-eliciting levels within the human lifespan and no AD occurs. On the other hand, when it does reach the ISR-eliciting levels, it mediates the elicitation of the integrated stress response. Elicitation of the ISR in AD can occur via two distinct pathways. In the first pathway, the ISR is triggered by the *i*Aβ-mediated activation of the PKR kinase. Indeed, experimental data obtained with both, established human cell lines and with human primary neuronal cells demonstrated the activation of PKR by Aβ cytotoxicity [73]. These results were corroborated in experiments with animal models exogenously overexpressing Aβ [74,75]. A linkage between PKR and AD in human patients was established by showing that degenerating neuronal cells are positive for both activated PKR and eIF2α (indicating that phosphorylated PKR has elicited the ISR in these cells and plausibly contributed to their degeneration via the ISR-triggered apoptotic pathway) [76,77]. As to how *i*Aβ triggers the phosphorylation and activation of PKR, experiments with animal models indicated that this might occur through TNFα [78]. Alternatively, PACT (PKR activator) could mediate the interaction between *i*Aβ and the kinase; this possibility was suggested by the observation of the co-localization of PACT and activated PKR in degenerating human neurons [79]. *i*Aβ-mediated activation of PKR through the elevation of PACT levels was also indicated by its observed suppression in human neuroblastoma cells following the cells' exposure to PACT shRNA [79].

5.3. HRI Kinase Activation Is Triggered by iAβ-Mediated Mitochondrial Dysfunction; Elicitation of the ISR Follows

The association of AD with mitochondrial distress is well established [80–96]. It is, in fact, one of the earliest observed events in the progression of the disease. Experimentally, the exogenous overexpression of Aβ in cell-based studies and in animal models was demonstrated to be sufficient to initiate mitochondrial distress and trigger cellular stress response. In this respect, a recent work by Brewer et al. [97] described a phenomenon whereby "long" Aβ species $A\beta_{45}$ and $A\beta_{49}$, generated due to incomplete activity of gamma-secretases, accumulate intraneuronally (rather than being exported). The levels of $i A\beta_{45}$ in mitochondria, endosomes, and autophagosomes are significantly elevated with aging; this results in mitochondrial dysfunction [97]. For mitochondrial dysfunction to translate into the cellular stress response, the stress signal has to be transmitted from the organelle to the cytosol. Until recently, it was not entirely clear how it occurs. Studies by Guo et al. [98] and by Fessler et al. [99] provided the answer. They demonstrated that mitochondrial distress activates the mitochondrial protease OMA1. In turn, the activated OMA1 cleaves another mitochondrial protein, DELE1. One of the resulting fragments of DELE1 is exported into the cytosol. There, it binds to the HRI kinase; this results in the phosphorylation and activation of HRI, thus continuing the cascade and leading, through the phosphorylation eIF2α, to the elicitation of the ISR. Data indicate that this signaling pathway is operative in neuronal cells [99].

6. Self-Perpetuating, AβPP-Independent Generation of *i*Aβ: The Engine That Drives the Second Stage of AD

In light of the above considerations and to simplify further discussion, the present study provisionally assumes that the agent driving the second AD stage is *i*Aβ produced in the AβPP-independent manner. This is a "safe" assumption because (a) it is highly plausible that this is the case and (b) if the agent in question is not *i*Aβ, neither the logic of the thesis nor the underlying concepts would be affected [2]; in essence, any potential agent would have to be able to drive the AD pathology and to sustain and perpetuate its own production pathway.

To summarize the preceding sections, it has been proposed that in the first AD stage, AβPP-derived *i*Aβ accumulates, in a decades-long process, to the critical over-the threshold levels. This leads to the activation of the PKR kinase and, through mitochondrial distress, of the OMA1-DELE1-HRI signaling pathway. Consequently, eIF2α is phosphorylated and the integrated stress response elicited. The induction of certain genes' expression within the framework of the ISR provides crucial component(s) required for the operation of the AβPP-independent Aβ generation pathway and causes its activation. The product of this pathway is, in fact, *i*Aβ (i.e., intraneuronal rather than extracellular Aβ) because the majority of it, if not the complete output of the pathway, is not secreted but, instead, is retained within the neurons. The substantially increased influx of *i*Aβ rapidly elevates its steady-state levels; pathways leading to the elicitation of the integrated stress response are sustained, and the activity of the AβPP-independent *i*Aβ generation pathway, and, consequently, uninterrupted influx of *i*Aβ, are perpetuated. These continuous cycles of the *i*Aβ-stimulated propagation of its own production constitute an engine that drives the disease, the AD Engine. Its operation is illustrated in Figure 1.

The decades-long accumulation of AβPP-derived *i*Aβ (left box in Figure 1) leading to the activation of the AβPP-independent *i*Aβ production and, consequently, of the AD Engine is referred hereafter as "the first stage of AD". It should be emphasized, however, that it becomes such only post-factum, provided the disease actually occurs. Otherwise this is a normal physiological process common to healthy individuals and future AD patients. Only if and when AβPP-derived iAβ reaches the critical threshold and the AβPP-independent Aβ generation pathway and, consequently, the self-sustaining AD Engine (arched arrows-connected boxes in Figure 1) is activated (referred to henceforth as the symptomatic "second stage of AD") does the disease commence, and "the first stage of AD"

earns its name. In this terminology, therefore, "the second stage of AD" is synonymous with "AD"; both terms are used interchangeably below.

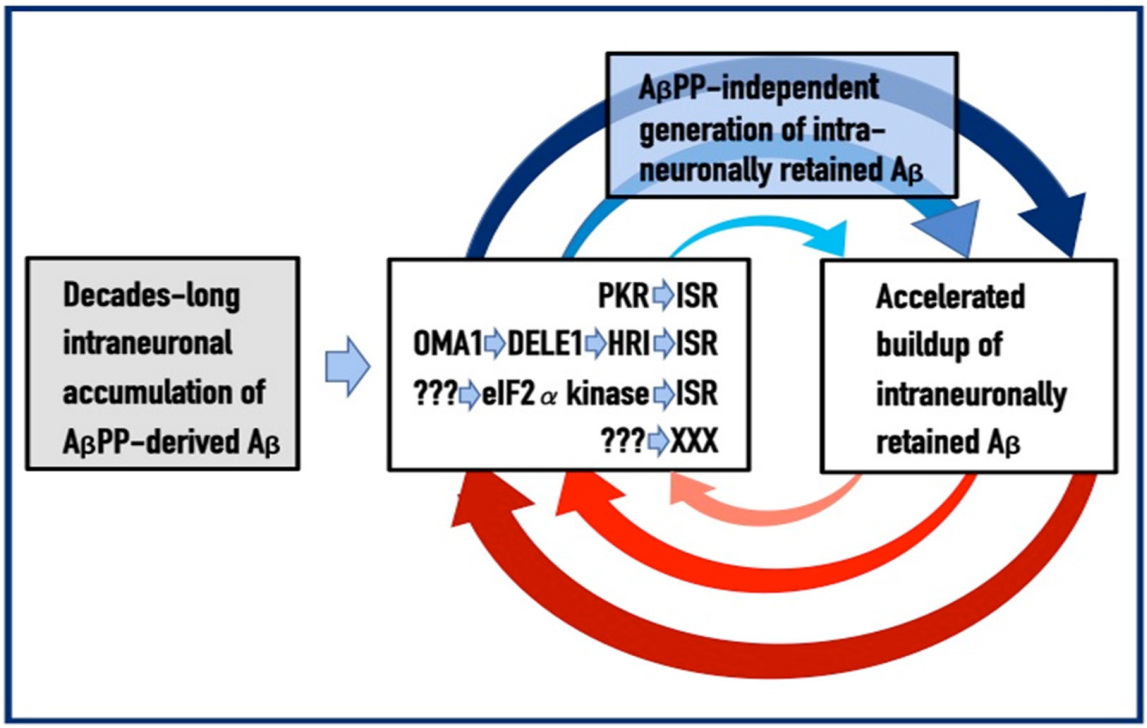

Figure 1. Mechanistic aspects of *i*Aβ dynamics in the ACH2.0 perspective: The AD Engine. *Left box*: The life-long accumulation of intraneuronal Aβ (*i*Aβ) produced in the AβPP proteolytic pathway. Two distinct processes contribute to this accumulation: importation of secreted extracellular Aβ inside the cell and retention within the neuron of a fraction of Aβ generated by gamma-cleavage of the C99 fragment of AβPP on intracellular rather than on plasma membranes. Such accumulation of *i*Aβ is a normal physiological process common to healthy individuals and future AD patients. It becomes detrimental if and when it reaches the critical threshold and activates the second, symptomatic stage of AD. In the majority of population this threshold is not reached within the lifespan of an individual and no AD occurs. *Middle box*: When *i*Aβ, accumulated in a life-long process, reaches the critical threshold invoked above, it mediates the elicitation of the integrated stress response, ISR (or of a yet undefined pathway marked XXX). This occurs via the documented activation of two eIF2α kinases, PKR and HRI (other eIF2α kinases, or yet unidentified mediators denoted "???" could be also involved). Activated PKR and/or HRI phosphorylate eIF2α and thus trigger the ISR. *Top box*: The ISR manifests itself as an acute decline in the protein synthesis output. The reduction in the global cellular protein synthesis occurs via the suppression of the cap-dependent initiation of translation. Concurrently, the ISR promotes cap-independent translation of selected mRNA species; among those are mRNAs encoding specific transcription factors. The ISR-induced transcriptions factors, or translation products of the genes activated by these factors, plausibly include components critical for the activation of the AβPP-independent *i*Aβ generation pathway. The bulk, if not the whole *i*Aβ output is retained within affected neurons. *Right box*: The increased influx of *i*Aβ generated in the AβPP-independent manner substantially elevates its steady-state levels. *Arched arrows*: As the result of a drastic augmentation of *i*Aβ levels, pathways leading to the elicitation of the integrated stress response are sustained, and the activity of the AβPP-independent *i*Aβ generation pathway and uninterrupted influx of *i*Aβ are perpetuated. These continuous cycles of *i*Aβ-stimulated propagation of its own production constitute an engine that drives AD, the AD Engine. Only when the AD Engine is activated does the disease commence. A possibility that the agent driving the second AD stage is not *i*Aβ cannot be excluded; this would not, however, change the logic of the thesis and is discussed in detail in [2].

Since the symptomatic stage, i.e., stage two of AD, requires the activation of the AβPP-independent *i*Aβ production pathway and, consequently, of the AD Engine, factors determining the attainment of the critical AD Engine-activating threshold by AβPP-derived *i*Aβ play the key role in defining the susceptibility to AD. These factors and the dynamics of AβPP-derived iAβ accumulation are discussed in detail in the following sections below.

7. The Dynamics of Aβ Accumulation and of the Disease in AD-Affected Human Population: Comparison of the ACH and ACH2.0 Perspectives

As described in the preceding sections, in the framework of the ACH2.0 the kinetics and even the occurrence of AD depend on the accumulation of *i*Aβ. Only when it reaches the critical threshold and triggers the activation of its own production in the AβPP-independent mode does the symptomatic stage of the disease commence. If this threshold is not reached within the lifetime of an individual, no AD occurs; in fact, this is what happens in the majority of the human population. The following sections below are concerned with the dynamics of *i*Aβ accumulation and, consequently, of the disease. In this respect, it is instructive to compare these dynamics in two paradigms: the ACH and the ACH2.0. Both presume that the agent that drives AD is Aβ. The similarity, however, ends here. Whereas the ACH is centered on extracellular Aβ produced and secreted in the AβPP proteolytic pathway, in the ACH2.0, the disease is caused by *i*Aβ. No less importantly, the dynamics of *i*Aβ, or of extracellular Aβ in the case of the ACH, accumulation in the two paradigms are radically distinct. These dynamics are diagrammatically depicted in Figure 2 (each continuous line denotes an individual AD patient).

Panel **A** (sporadic AD) and panel **B** (FAD) illustrate the ACH-based interpretation of AD. Blue lines represent the kinetics of accumulation of secreted extracellular Aβ, whereas red lines represent the kinetics of neurodegeneration; both are single-phased. The kinetics of the neuronal damage can be further separated into two stages, asymptomatic (red lines) and symptomatic (red blocks). The latter commences when the levels of secreted Aβ and the corresponding extent of neurodegeneration reach and cross the threshold **T**. In this paradigm, Aβ is generated exclusively by AβPP proteolysis and is secreted outside the cell. As it accumulates, it causes neuronal damage commencing early in life; the extent of this damage is proportional to the extent of extracellular Aβ accumulation. Neuronal damages accrue with time and manifest as AD symptoms late in life in cases of SAD, starting at the mid-sixties, or much earlier in cases of FAD, where levels of extracellular Aβ reach the **T** threshold sooner. In its symptomatic stage, the disease is deemed untreatable. There are presently no preventive treatments for AD. In the ACH paradigm, were such treatments to exist, they would be fruitless late in life: even if the AD symptoms did not yet manifest, the irreversible neurodegeneration already occurred.

In the ACH2.0 paradigm, the principal feature of the dynamics of *i*Aβ accumulation and of the disease (SAD: panel **C**; FAD: panel **D**) is that both are biphasic. In the first stage, Aβ is produced exclusively by AβPP proteolysis. *i*Aβ is derived only from AβPP and accrues very slowly, over the bulk of individual's lifespan. Its accumulation occurs through the importation of extracellular Aβ inside the cell and via the intraneuronal retention of Aβ generated by gamma-cleavage of C99 on intracellular membranes. Both processes, and the resulting accumulation of *i*Aβ, are normal physiological occurrences and take place not only in future AD patients but also in healthy individuals, as well as in non-human mammals. Until and unless the **T1** threshold is crossed, there is no significant neurodegeneration and no disease at this stage (black indicator lines). The second stage commences when levels of *i*Aβ produced in the AβPP proteolytic pathway reach and cross the **T1** threshold. This triggers cellular processes culminating in the initiation of AβPP-independent production of *i*Aβ, consequent activation of the AD Engine, commencement of the second AD stage, and symptomatic manifestation of AD. This stage appears to be exclusive to humans or at least species-specific, probably because the AβPP-independent *i*Aβ production pathway is (see below).

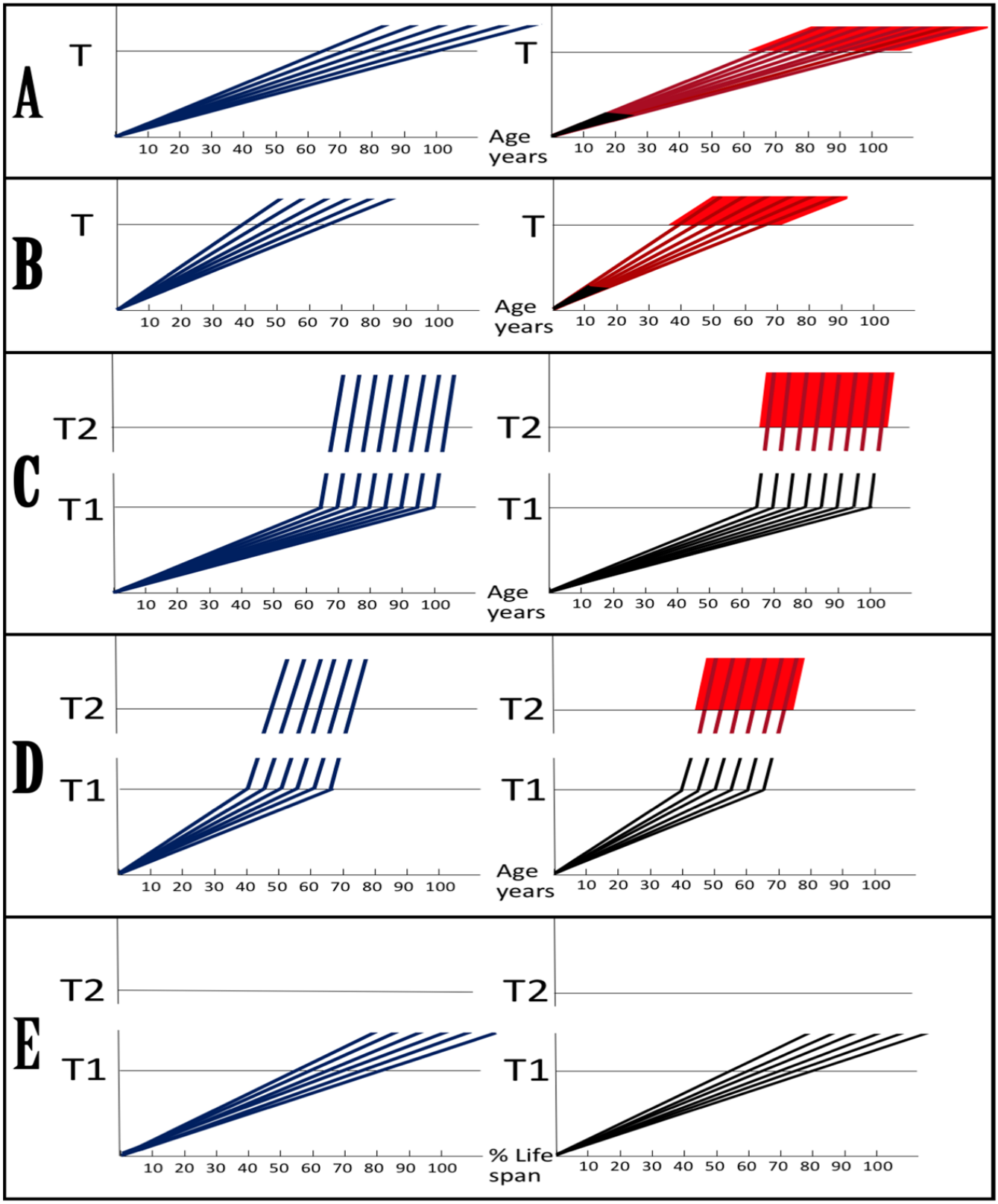

Figure 2. Dynamics of Aβ accumulation and the disease in AD-affected population: ACH and ACH2.0 perspectives. *Blue lines*: Levels of Aβ (panels **A**,**B**) or *i*Aβ (panels **C**–**E**). *Red lines*: Degree of

neuronal damage. *Black lines*: Indicator lines; no noticeable neuronal damage. *Red blocks*: Apoptotic zone. Threshold **T**: The level of Aβ and the consequent level of neurodegeneration causing symptomatic manifestation of AD. Threshold **T1**: The level of AβPP-derived *i*Aβ triggering cellular processes leading to the activation of the AβPP-independent generation of *i*Aβ. Threshold **T2**: The level of *i*Aβ and the consequent degree of neurodegeneration causing cellular commitment to apoptosis and acute AD symptoms. Panels **A**,**B** (SAD, FAD respectively): Dynamics of AD in the ACH perspective. Extracellular Aβ accumulates and the degree of neuronal damage increases proportionally. When the **T** threshold is crossed, the symptomatic AD stage commences. Panels **C**,**D** (SAD, FAD respectively): Dynamics of AD in the ACH2.0 perspective. Following crossing of the **T1** threshold by *i*Aβ produced in the AβPP proteolytic pathway, its generation in the AβPP-independent pathway commences. Since the entire Aβ output of the AβPP-independent pathway is retained intraneuronally, the rate of *i*Aβ accumulation greatly accelerates and its levels substantially and rapidly increase, which causes, via the cascade involving tau pathology, significant neuronal damage and triggers initial AD symptoms. When *i*Aβ, and the consequent degree of neuronal damage reach and cross the **T2** threshold, the cell apoptotic pathway is triggered and acute AD symptoms manifest. (Panel **E**)*: iAβ dynamics in subjects (including non-human mammals) with an inoperative second stage.* AβPP-derived *i*Aβ reaches and crosses the **T1** threshold but the AβPP-independent *i*Aβ generation pathway remains inoperative. Neither levels of *i*Aβ causing AD-related damage nor the **T2** threshold are reached, no AD occurs.

Since the entire Aβ output of the AβPP-independent pathway is retained intraneuronally, in the second AD stage the rate of *i*Aβ accumulation greatly accelerates and its levels substantially and rapidly increase, which causes, via the cascade involving tau pathology, significant neuronal damage and triggers the initial AD symptoms (red lines). When *i*Aβ, and the consequent degree of neuronal damage reach and cross the **T2** threshold, the irreversible apoptotic pathway is triggered (red blocks), and acute AD symptoms manifest. In contrast to the ACH-based interpretation of the disease, in the ACH2.0 paradigm preventive treatment, if and when available, would be successful at any time before the second phase is initiated. If the latter were precluded, e.g., via suppression of the AβPP-independent *i*Aβ generation pathway (panel E), no AD would occur; this is the scenario that plays out in some, or possibly in all, non-human mammals.

8. The *i*Aβ Dynamics in the Affected Neuronal Population of an Individual Patient in the ACH2.0 Perspective

The dynamics of *i*Aβ accumulation and of the disease in AD-affected human population, discussed in the preceding section, presents a "coarse-grained" picture of the evolution of AD. To gain a better understanding, one should consider the *i*Aβ dynamics in the affected neuronal population of an individual AD patient; it's understanding could be instrumental in defining therapeutic strategies applicable in the ACH2.0 framework. Two principal, conceptually distinct, versions of such dynamics could be envisaged in the ACH2.0 perspective. In one version, illustrated in Figure 3, panels **A** and **B** (every continuous blue line represents a single affected neuron), individual neurons reach and cross the **T1** threshold with a stochastic distribution within a broad time interval, which primarily determines the duration of the disease. Subsequent to the **T1** threshold crossing by AβPP-derived *i*Aβ, the AβPP-independent *i*Aβ generation pathway and, consequently, the AD Engine are activated, the rate of *i*Aβ accumulation and its cellular levels are sharply elevated, and neuronal damage rapidly increases. Following crossing of the **T2** threshold, neurons enter the apoptotic pathway and are ultimately lost. When a sufficient fraction of neurons lose their functionality or die, acute AD symptoms manifest, as shown in panel **A** of Figure 3. With the progression of the disease, additional neurons cross first the **T1** and then the **T2** thresholds, and the disease reaches its end stage, as shown in panel **B** of Figure 3.

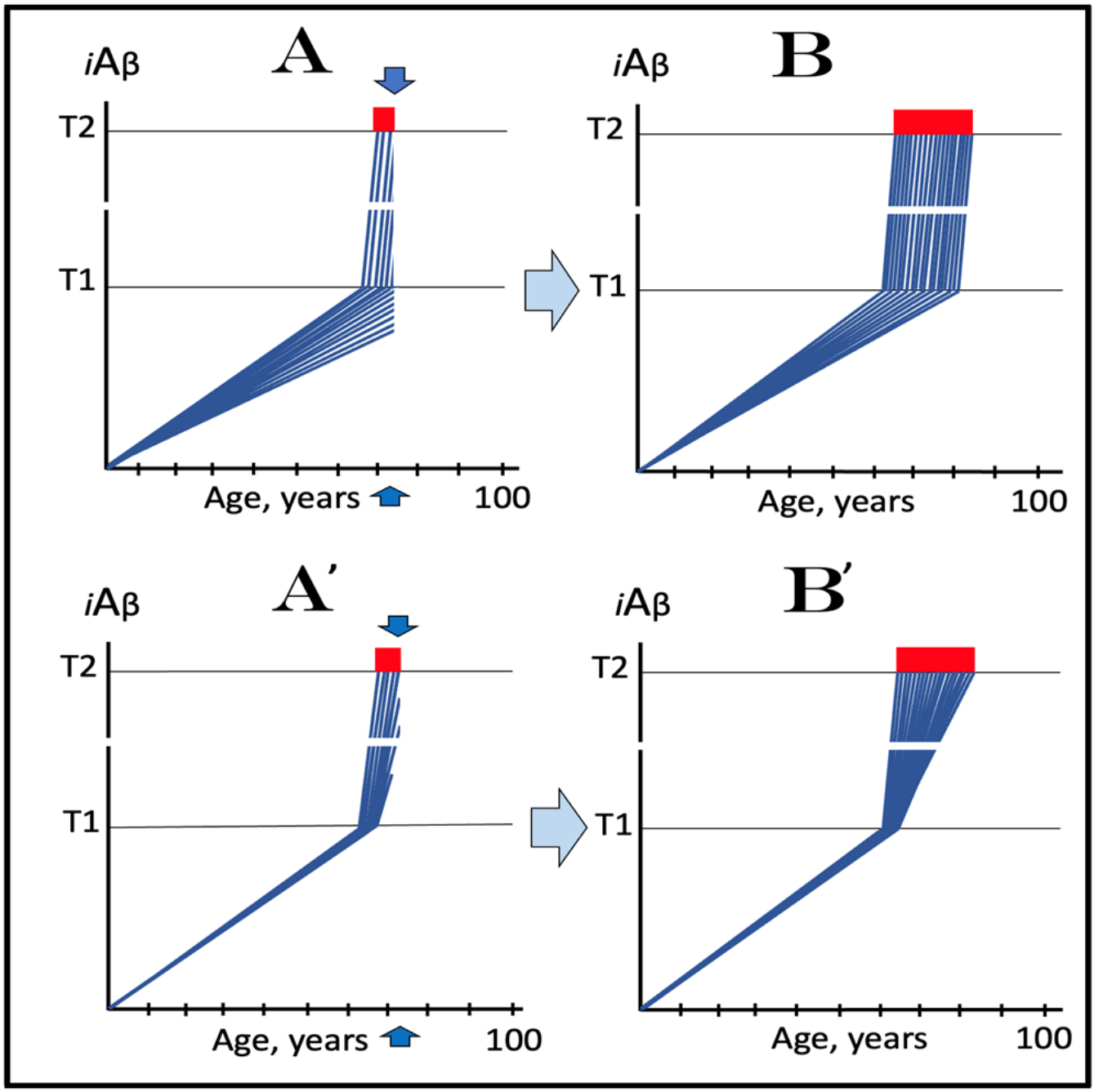

Figure 3. *i*Aβ dynamics in the affected neuronal population of an individual patient in the ACH2.0 perspective. *Blue lines*: Levels of *i*Aβ in individual AD-affected neurons. Threshold **T1**: The level of AβPP-derived *i*Aβ triggering cellular processes leading to the activation of the AβPP-independent generation of *i*Aβ. Threshold **T2**: The level of *i*Aβ and the consequent degree of neurodegeneration causing cellular commitment to apoptosis and acute AD symptoms. *Red blocks*: Apoptotic zone. *Vertical blue arrows*: Commencement of the occurrence of AD symptoms. *Panel **A***: Individual neurons reach and cross the **T1** threshold with a stochastic distribution within a broad time interval, which primarily determines the duration of the disease. Subsequent to the **T1** threshold crossing by AβPP-derived *i*Aβ, the AβPP-independent *i*Aβ generation pathway is activated, the rate of *i*Aβ accumulation and its cellular levels are sharply elevated, and neuronal damage rapidly increases.

Following crossing of the **T2** threshold, neurons enter the apoptotic pathway and are ultimately lost. When sufficient fraction of neurons lose their functionality or die, AD symptoms manifest while a substantial proportion of affected neurons have not yet crossed the **T1** threshold. *Panel **B***: With the progression of the disease, additional neurons cross first the **T1** and then the **T2** thresholds and the disease reaches its end stage. *Panel **A**'*: The neuronal crossing of the **T1** threshold occurs within relatively short time interval. Subsequent to the crossing of the **T1** threshold, the affected neurons advance toward and cross the **T2** threshold in a broad stochastic distribution; the temporal duration of this distribution determines the duration of the disease. When the neuronal damage or loss occurred to a degree sufficient for symptomatic manifestation of the disease, the majority, if not the entire population, of the affected neurons already crossed the **T1** threshold. *Panel **B**'*: As the disease progresses, more neurons reach the **T2** threshold and enter the apoptotic pathway; eventually, the end stage is reached.

However, in the face of the empirical data, this scenario is, apparently, unviable. Indeed, as shown in panel **A** of Figure 3, when a fraction of affected neurons reaches the **T2** threshold and AD symptoms manifest, a large proportion of affected neurons have not yet crossed the **T1** threshold. If, at this time, the generation of Aβ in the AβPP proteolytic pathway were repressed, for example, by BACE1 inhibitors shown capable of effectively achieving this [11,12], the accumulation AβPP-derived *i*Aβ should be slowed. Consequently, crossing of the **T1** threshold by the affected neurons should also be slowed or precluded, and the progression of AD should be, likewise, slowed or arrested. However, in human clinical trials of verubecestat, these effects were seen neither with mild to moderate [11] nor with prodromal patients [12] despite the observed strong inhibition of Aβ production in the AβPP proteolytic pathway.

Another version of *i*Aβ dynamics in the affected neuronal population of individual AD patient is illustrated in Figure 3, panels **A**′ and **B**′. The main feature, suggested by experimental data [11,12] and distinguishing this version from the above described version, is the duration of the neuronal crossing of the **T1** threshold: here, it occurs within relatively short time interval. Subsequent to the crossing of the **T1** threshold, the affected neurons advance toward and cross the **T2** threshold in a broad stochastic distribution; the temporal duration of this distribution determines the duration of the disease in this version. Importantly, when the neuronal damage and/or loss occurred to a degree sufficient for symptomatic manifestation of the disease, the majority, if not the entire population, of the affected neurons, have already crossed the **T1** threshold, as shown in Figure 3, panel **A**′. Since, subsequent to the **T1** threshold crossing, the AβPP-independent *i*Aβ generation pathway is activated in all or nearly all affected neurons, BACE1 inhibitors (or drugs targeting the accumulation of AβPP-derived *i*Aβ) would be rendered therapeutically ineffective, a notion that was indeed corroborated by the empirical data [11,12].

As the disease progresses, more neurons reach the **T2** threshold and enter the apoptotic pathway; eventually, the end stage is reached, as shown in panel **B**′ of Figure 3. The above two versions of *i*Aβ dynamics in the affected neuronal population are just basic outlines of the process. Intermediary versions that combine features of the two basic scenarios can also be envisioned. However, the essential requirement of any version is that by the time AD symptoms manifest, the levels of *i*Aβ produced in the AβPP proteolytic pathway have already crossed the **T1** threshold, and the second AD stage has commenced in the majority of affected neurons.

9. The Dynamics of AD in the ACH2.0 Perspective: Effect of the Rate of Accumulation of AβPP-Derived *i*Aβ in the Affected Neuronal Population of an AD Patient

As discussed above, in the framework of the ACH2.0, the "second stage of AD" is, de facto, symptomatic AD, i.e., the stage where AD-causing, *i*Aβ-mediated neurodegeneration actually takes place. Moreover, as argued in the preceding sections, the "first AD stage" becomes such only post-factum, if and when AβPP-derived *i*Aβ levels cross the **T1** threshold and the disease actually occurs. Otherwise, it is a normal physiological process

shared by healthy individuals and (future) AD patients; if the stage two of AD, i.e., the self-perpetuating AβPP-independent *i*Aβ generation pathway, is "cancelled", as depicted in the panel **E** of Figure 2 above, and only the AβPP proteolytic pathway remains operational, there could be no AD because AβPP-derived *i*Aβ would not reach AD neurodegeneration-causing levels within the lifespan of an individual. The second AD stage (synonymous with AD, as defined above) commences when the levels of AβPP-derived *i*Aβ reach and cross the **T1** threshold and trigger the activation of the AβPP-independent *i*Aβ production pathway and the consequent operation of the self-sustaining AD Engine. Accordingly, in the ACH2.0 perspective the susceptibility to AD is defined by two factors, which determine the timing of the **T1** crossing by AβPP-derived *i*Aβ: the rate of accumulation of AβPP-derived *i*Aβ and the extent of the **T1** threshold. In the present section, we consider the effect of the former in SAD (or prospective SAD) with a given, relatively low, extent of the **T1** threshold (and, consequently, insignificant extent of AβPP-derived *i*Aβ accumulation-related cell damage prior to the **T1** threshold's crossing), within temporal boundaries of the symptomatic stage between 65 and 100 years of age (the former reflects a statistical age of the onset of SAD and the latter is a reasonable cut-off, i.e., the assumed lifespan; increasing this number would not change the logic but would make the figure more cumbersome). The present section analyzes only the effect of the rate of accumulation of AβPP-derived *i*Aβ on its crossing (or not crossing) the **T1** threshold and the consequent occurrence of AD. This analysis is not concerned with the rate of accumulation of *i*Aβ (mostly *i*Aβ generated independently of AβPP) in the second AD stage. The latter does not impact the former in any way, and its effect on the progression of the second AD stage is discussed below (Section 20).

Figure 4 illustrates the effect of the rate of AβPP-derived *i*Aβ accumulation on the timing of the commencement of the second AD stage. In panel **A**, the rate is such that AD symptoms manifest at about 65 years of age. As the rate decreases, the timing of AβPP-derived *i*Aβ crossing of the **T1** threshold, and, consequently, of the commencement of stage two of AD, increases. In panel **B**, this timing is such that AD symptoms manifest at about 85 years of age. In panel **C**, AβPP-derived *i*Aβ crosses the **T1** threshold and initiates the AβPP-independent *i*Aβ production pathway so late that, while the manifestation of AD symptoms commences, the disease does not run its complete course within the lifespan of an individual. In panel **D**, the rate of AβPP-derived *i*Aβ accumulation is sufficiently low for it not to reach the **T1** threshold within the lifespan of an individual. Importantly, in contrast to the analogous process in panels **A** through **C**, the process depicted in panel **D** is *not* "the first AD stage" because the **T1** threshold is not crossed and the disease does not occur. This scenario (panel **D**) describes, in fact, individuals that do not develop AD in their lifetime, the current majority of the general population. These individuals do not develop the disease not because they are "resistant" to it but because they simply run out of time, that is, the *lifetime*, to do so. The "resistance to AD" is conferred by the low rate of AβPP-derived *i*Aβ accumulation, as shown in Figure 4, or by the high extent of the **T1** threshold, as discussed in the following section, or by the combination of both; in all cases, the **T1** threshold is not reached and the second AD stage is not triggered within the lifespan of an individual.

It is of a substantial interest that *all* known mutation(s) or factors that protect from AD have the same underlying mode of operation: they all reduce the rate of AβPP-derived *i*Aβ accumulation and prevent (or delay) the crossing of the **T1** threshold by AβPP-derived *i*Aβ within individual's lifespan, whereas, as described below, *all* known FAD-causing mutations increase the rate of AβPP-derived *i*Aβ accumulation and accelerate the crossing of the **T1** threshold. It follows, from the above considerations, that given a sufficiently long lifespan, AD is an inevitable disorder. As a case in point, if one extrapolates the kinetics of AβPP-derived *i*Aβ accumulation in panel **D** of Figure 4, the crossing of the **T1** threshold and the commencement of the stage two of AD would occur at about 120 years of age, provided an individual in question is still alive. Such longevity is, apparently, a currently improbable and/or infrequent occurrence, but it is, possibly, attainable in the not-

so-distant future. The anticipated increase in longevity would inevitably be accompanied by a corresponding increase in the incidence of AD if the population were not treated preventively.

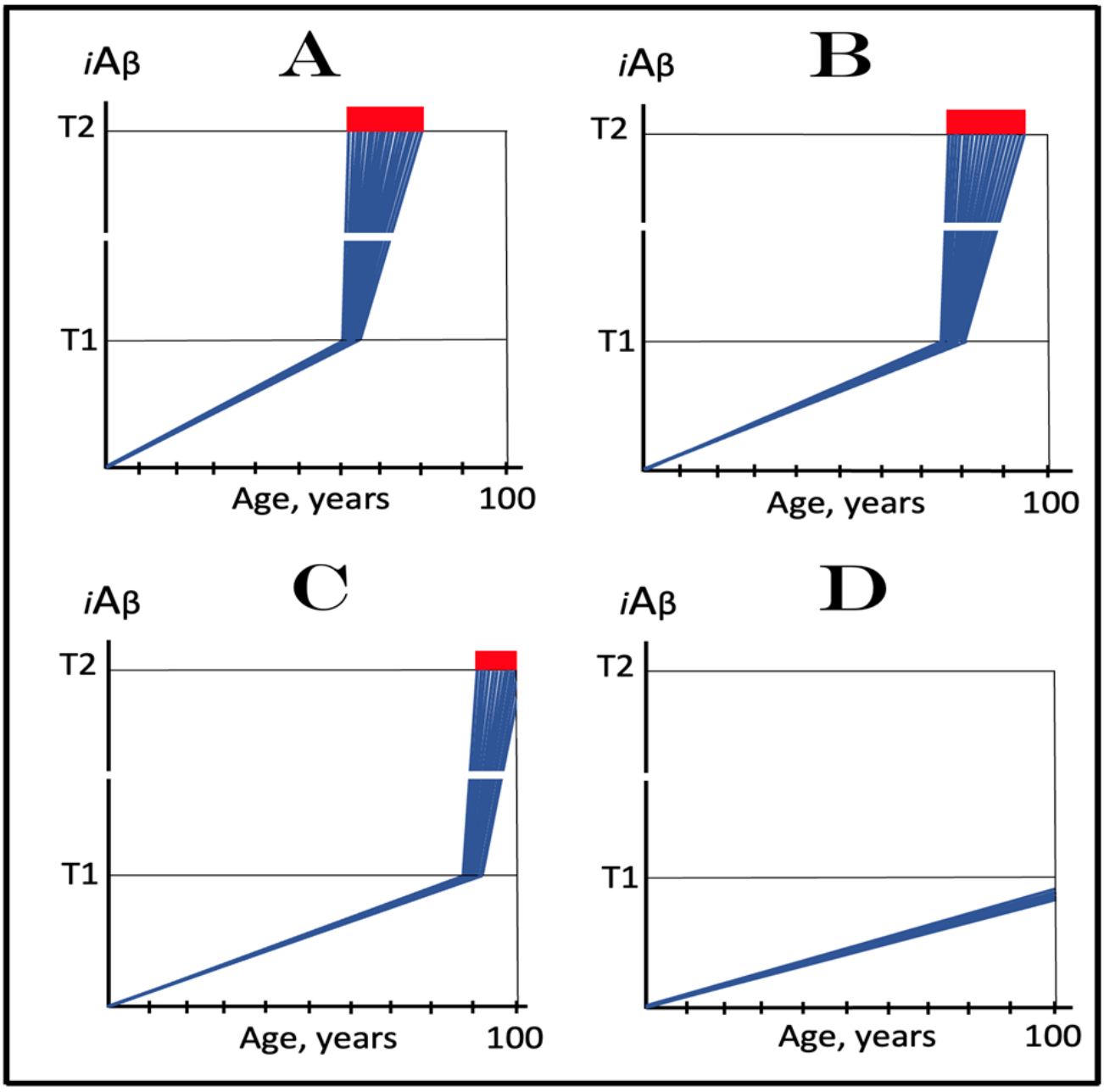

Figure 4. Dynamics of AD: Effect of the rate of accumulation of AβPP-derived *i*Aβ. *iAβ*: Intraneuronal Aβ levels; ***T1***: The level of *i*Aβ that triggers elicitation of the integrated stress response, initiation of AβPP-independent generation of *i*Aβ, and activation of the AD Engine. ***T2***: The level of *i*Aβ that triggers cell's commitment to the apoptotic pathway. *Red blocks*: Fraction of affected neurons either committed to apoptosis or dead. The **T1** threshold is constant and is chosen deliberately low, so that the extent of AβPP-derived *i*Aβ-accumulation-related neuronal damage prior to the **T1** threshold's crossing is insignificant and inconsequential. The Figure does not consider the effect of the rate of *i*Aβ (mostly *i*Aβ generated independently of AβPP) accumulation in the second AD stage, which is assumed constant for purposes of this analysis. The lifespan is assumed to end at 100 years of age. In *panel **A***, the rate of AβPP-derived *i*Aβ accumulation is such that AD symptoms manifest

at about 65 years of age (statistical age of the commencement of AD). As the rate of AβPP-derived *i*Aβ accumulation decreases, the timing of its reaching and crossing the **T1** threshold, and consequently of the commencement of stage two of AD, increases. In *panel **B***, this timing is such that AD symptoms manifest at about 85 years of age. In *panel **C***, AβPP-derived *i*Aβ crosses the **T1** threshold and initiates the AβPP-independent *i*Aβ production pathway so late that, while the manifestation of AD symptoms commences, the disease does not run its complete course within the lifespan of an individual. In *panel* **D**, the rate of AβPP-derived *i*Aβ accumulation is sufficiently low for it not to reach the **T1** threshold within the lifespan of an individual. Therefore, the depicted process is, in contrast to the analogous process in panels **A** through **C**, *not* "the first stage of AD". Note that given a sufficient lifespan, AβPP-derived *i*Aβ would eventually cross the **T1** threshold and AD would inevitably occur.

10. The Dynamics of AD and AACD in the ACH2.0 Perspective: Effect of the Extent of the T1 Threshold in the Affected Neuronal Population of an AD Patient—AACD as an Extended Segment of the Stage One of AD

The present section analyzes effects of the extent of the **T1** threshold and considers the nature of AACD. The mechanistic definition of AACD has been provided previously in [2]. It is based on the understanding of the nature of an AACD-causing agent. What is the cause of AACD? To answer this question, we would like to invoke again the principal basis for the formulation of the ACH. It was the discovery of a single mutation affecting Aβ and segregating with FAD [7]. This observation was deemed sufficient to deduce, by extrapolation, that Aβ causes FAD. In case of AACD, we have an observation of a similar nature and comparable caliber: a mutation affecting Aβ, in fact a mutation of Aβ, the Icelandic mutation [4,5], protects from AACD as well as from AD. Applying the same logic, one can, by inversion, infer that Aβ causes AACD. The nature of AACD, i.e., in what manner Aβ executes its causative action in AACD, is indicated by the analysis of the effect of the extent of the **T1** threshold on the dynamics of AD (and apparently of AACD) within the same temporal boundaries as those utilized in the preceding section. In this analysis, the rate of accumulation of AβPP-derived Aβ is presumed to be constant, a given. The extent of the **T1** threshold, however, is increasing in succeeding panels of Figure 5. As in the preceding section, this analysis is not concerned with the effects of changes in the rate of *i*Aβ accumulation above the **T1** threshold or in the extent of the **T2** threshold, the parameters discussed in Section 20 below.

In panel **A** of Figure 5, the **T1** threshold is chosen deliberately low, low enough that the accumulation of AβPP-derived *i*Aβ results in no significant cellular damage. It is logically reasonable, however, to assume that with the **T1** threshold of variable extent, this is not always the case. As the extent of **T1** increases, AβPP-derived *i*Aβ is bound to reach the sub-**T1** level, inadequate to trigger the second AD stage but sufficient to cause the consequential neuronal damage. To indicate the extent of *i*Aβ accumulation where such damage commences, another threshold, the $\mathbf{T^0}$, is introduced in panel **B** of Figure 5. We posit that it is this AβPP-derived *i*Aβ-inflicted neuronal damage, occurring between the thresholds $\mathbf{T^0}$ and **T1** which causes AACD (when in such cases the **T1** threshold is crossed, AACD morphs, by definition, into AD; see the following section on the subject), that the differential in *i*Aβ levels between the extents of the $\mathbf{T^0}$ and **T1** thresholds constitutes the "AACD Zone" (gradient-pink boxes in Figure 5), and that the duration (time period between the $\mathbf{T^0}$ and **T1** threshold crossings by AβPP-derived *i*Aβ) and the consequent severity of AACD depend on the size of the AACD Zone, i.e., the $\mathbf{T1/T^0}$ differential, and the rate of AβPP-derived *i*Aβ accumulation (the lower the rate, the longer it takes to traverse the differential and the longer the duration).

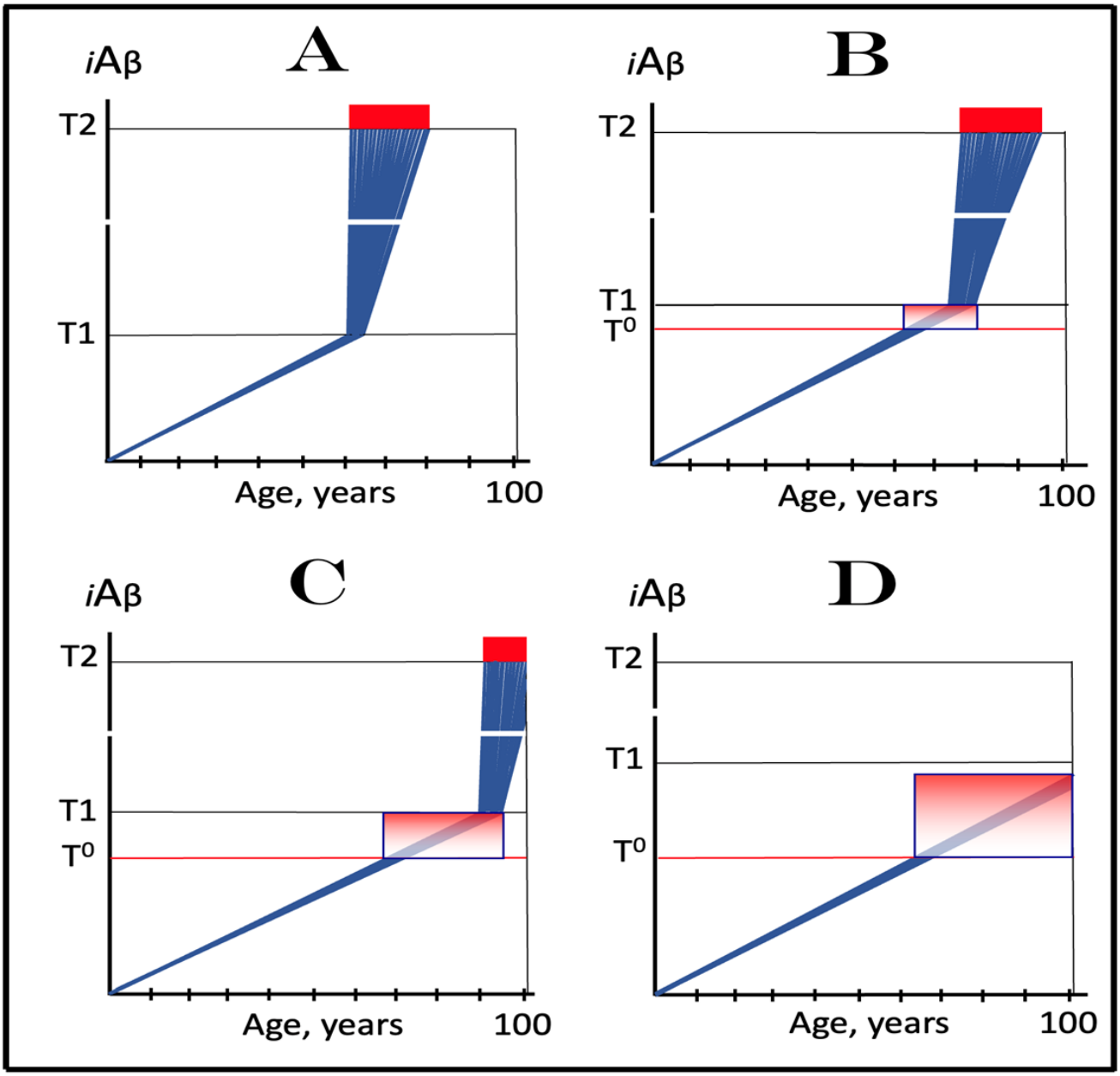

Figure 5. Dynamics of AD and AACD: Effect of the extent of the T1 threshold. *iA*β: Intraneuronal Aβ levels. ***T*^{0}**: *i*Aβ levels that trigger neuronal damage manifesting as AACD. ***T1***: *i*Aβ level that triggers elicitation of the integrated stress response, initiation of AβPP-independent generation of *i*Aβ and the activation of the AD Engine. ***T2***: *i*Aβ level that triggers cell's commitment to the apoptotic pathway. *Red blocks*: Fraction of affected neurons either committed to apoptosis or dead. *Gradient-pink boxes*: "AACD Zone", the differential between the **T^{0}** and **T1** threshold levels of AβPP-derived *i*Aβ (more precisely, between the **T^{0}** and the maximum level reached by AβPP-derived *i*Aβ short of the **T1** threshold). The rate of accumulation of AβPP-derived *i*Aβ and the extent of the **T^{0}** threshold are constant, and the lifespan is assumed to terminate at 100 years of age; the only variable is the extent of the **T1** threshold. In *panel **A***, the **T1** threshold is chosen deliberately low, so that the accumulation of AβPP-derived *i*Aβ results in no significant neuronal damage. With the increase of the extent of the **T1** threshold, such damage would inevitably occur at the sub-**T1** levels of AβPP-derived *i*Aβ; to indicate the extent of *i*Aβ accumulation where such damage commences, another threshold, the **T^{0}** is introduced in *panel **B*** and it is posited that it is this AβPP-derived *i*Aβ-inflicted neuronal damage,

occurring between the thresholds $\mathbf{T^0}$ and **T1** which causes AACD (on the more precise definition of the upper AACD boundary, see text). In *panel **C***, the extent of the **T1** threshold increases. With the rate of AβPP-derived *i*Aβ accumulation and the extent of the $\mathbf{T^0}$ threshold remaining constant, the AACD Zone increases accordingly, as does the duration and the severity of the dysfunction. While the timing of the commencement of AACD does not change with the increasing extent of the **T1** threshold, the timing of the commencement of the second AD stage increases in a direct proportion, and the probability of developing AD within the remaining lifespan decreases in an inverse proportion to the increase in the extent of the **T1** threshold. In *panel **D***, the extent of the **T1** threshold is such that the level of AβPP-derived *i*Aβ does not reach the **T1** threshold within the lifespan of an individual. With the extent of the $\mathbf{T^0}$ threshold and the rate of AβPP-derived *i*Aβ accumulation fixed, the timing of the commencement of AACD remains constant, but the AACD Zone further increases. On the other hand, since the **T1** threshold is not crossed, there is no activation of the AβPP-independent *i*Aβ production pathway, no stage two of AD ensues, no AD occurs. Note, however, that the **T1** threshold would be crossed and AD would certainly occur provided the lifespan is long enough.

In panel **C** of Figure 5, the extent of the **T1** threshold increases. With the rate of AβPP-derived *i*Aβ accumulation and the extent of the $\mathbf{T^0}$ threshold remaining constant, the AACD Zone increases accordingly, as does the duration and the severity of the dysfunction (it is assumed that higher levels of AβPP-derived *i*Aβ over the $\mathbf{T^0}$ threshold equals greater neuronal cells damage). Importantly, while the timing of the commencement of AACD does not change with the increasing extent of the **T1** threshold (it depends solely on the extent of the $\mathbf{T^0}$ threshold and the rate of accumulation of AβPP-derived *i*Aβ, both parameters constant in the present narrative), the timing of the commencement of the second AD stage increases in a direct proportion, and the probability of developing AD within the remaining lifespan decreases in an inverse proportion of the increase in the extent of the **T1** threshold. Finally, in panel **D** of Figure 5, the extent of the **T1** threshold is such that the level of AβPP-derived *i*Aβ does not reach it within the lifespan of an individual. With the extent of the $\mathbf{T^0}$ threshold and the rate of AβPP-derived *i*Aβ accumulation fixed, the timing of the commencement of AACD remains constant, but the AACD Zone, as well as the duration and the severity of the dysfunction further increase. On the other hand, since the **T1** threshold is not crossed, there is no activation of the AβPP-independent *i*Aβ production pathway, no stage two of AD ensues, no AD occurs (note, however, that the **T1** threshold would be crossed and AD would occur provided the lifespan is long enough). It appears, therefore, that a kind of a trade-off is in play: A decrease in the probability of AD (or its delay and, possibly, avoidance) due to the elevated **T1** threshold is paid for by the increased probability of the occurrence of AACD. Any cognitively functional individual would probably embrace such trade-off. But, potentially, there is no need to choose a lesser of two evils; as described elsewhere [1,2] and discussed below, *a single, once-in-a-lifetime-only administration of a preventive or curative treatment is apparently capable of protecting from both AD and AACD for the remaining lifespan of an individual regardless of the extent of the **T1** threshold.*

To summarize, in light of the above, in the ACH2.0 framework, AACD is defined as the symptomatic manifestation of the neuronal cell damage caused by AβPP-derived *i*Aβ accumulated to the concentration range between the $\mathbf{T^0}$ and **T1** thresholds [2], a process that evolves into AD if and when *i*Aβ levels reach and cross the **T1** threshold and activate the AβPP-independent *i*Aβ generation pathway. Its occurrence requires a relatively high extent of the **T1** threshold, certainly in excess of that of the $\mathbf{T^0}$ threshold. In this context, AACD can be considered an extended stage One of AD, or, more precisely, an extended segment of the first AD stage; "extended" in terms of the augmented (in comparison with AD that is not preceded by AACD) capacity to accumulate AβPP-derived *i*Aβ prior to the **T1** threshold crossing [2]. Importantly, statistical age of the onset of AACD is greater than that of the onset of SAD [100,101]. This observation is consistent with the notion that in the population that eventually develops AACD, *the $\boldsymbol{T^0}$ threshold is higher than the **T1** threshold in the SAD-predisposed population*, i.e., that *the low extents of the **T1** threshold appear*

to be a predisposition contributing to the occurrence of SAD. This notion is of a considerable importance for two reasons. First, drugs targeting the accumulation of AβPP-derived *i*Aβ, which are inapplicable at the second AD stage (symptomatic AD), could be nevertheless effective in the treatment of symptomatic AACD (see below). Second, any preventive treatment effective for AD would be equally effective in prevention of AACD.

11. Symptoms of AACD-Associated Cognitive Impairment May Overlap with and Could Be Indistinguishable from Those of AD-Associated Mild Cognitive Impairment

From the definition of AACD as the symptomatic manifestation of the neuronal cell damage caused by *i*Aβ accumulated within a certain concentration range [2], it follows that symptoms of AACD may overlap with and could be indistinguishable from those of AD-associated mild cognitive impairment. Indeed, consider the situation depicted in Figure 6. In panels **A** through **C** of Figure 6, all kinetic parameters are, with one exception, constant. These parameters include the extents of the $\mathbf{T^0}$ and **T2** thresholds as well as the rate of *i*Aβ accumulation. The only exception is the extent of the **T1** threshold. In panel **A** of Figure 6 it is high and is not reached within the lifespan of an individual. AACD commences with the crossing of the $\mathbf{T^0}$ threshold and continues for the remaining portion of the lifespan (gradient-pink box). In this case, *i*Aβ-caused cognitive impairment is clearly attributable solely to AACD. In panel **B** of Figure 6, the **T1** threshold is lowered. The same range of *i*Aβ within the gradient-pink box as shown in panel **A** is divided in panel **B** into two portions: pre-**T1** crossing and post-**T1** crossing. Because the range of *i*Aβ within gradient-pink boxes is the same in panels **A** and **B**, symptoms are also the same. But pre-**T1** crossing they are AACD-associated cognitive impairment (AACD-CI), whereas post-**T1** crossing they constitute AD-associated mild cognitive impairment (AD-MCI). In panel **C** of Figure 6, the same *i*Aβ range within the gradient-pink box as in panels **A** and **B** occurs entirely post-**T1** crossing. Since the *i*Aβ range within the box is the same as in panels **A** and **B**, the symptoms also are, but now they constitute, in their entirety, AD-associated mild cognitive impairment. Note that, since the rate of *i*Aβ accumulation is greater post-**T1** than pre-**T1** crossing, the duration of symptoms decreases in successive panels of Figure 6.

Conceivably, it could be argued that the above terminological distinctions are purely semantic; after all, the same symptoms are caused by *i*Aβ of any origin within a certain range of concentration, and the symptoms are the symptoms, regardless of what name you attach to them. This, however, is certainly not the case in the situation under discussion: here, the distinction is not semantic but functional because mechanisms underpinning the two conditions (AACD-CI and AD-MCI) are distinctly different. Indeed, due to its underlying mechanism (i.e., the accumulation of AβPP-derived *i*Aβ to a certain range), AACD-CI can be treated by drugs reducing the influx of AβPP-derived *i*Aβ and thus suppressing its rate of accumulation [1–3], whereas the same drugs would be completely ineffective in the treatment of AD-MCI, which is driven by *i*Aβ produced independently from AβPP [1–3]. On the other hand, drugs reducing *i*Aβ levels via its targeted degradation regardless of its origin (i.e., both AβPP-derived and produced independently of AβPP), such as the enhancers of *i*Aβ-cleaving activities of BACE1 and BACE2, would be equally effective in treatment of both AACD-CI and AD-MCI [1–3] (further discussed below). In light of the above, since the symptoms of AACD-CI and AD-MCI could be overlapping, the determination of their origin could be of substantial importance. To determine whether AβPP-derived *i*Aβ levels have crossed the **T1** threshold is, however, challenging. Since the **T1** threshold differs individually, the objective operational criterion to determine it's crossing by AβPP-derived *i*Aβ is the detection of the activity of AβPP-independent *i*Aβ production pathway. The feasible means to assess the activity of this pathway are addressed below (Sections 22 and 26).

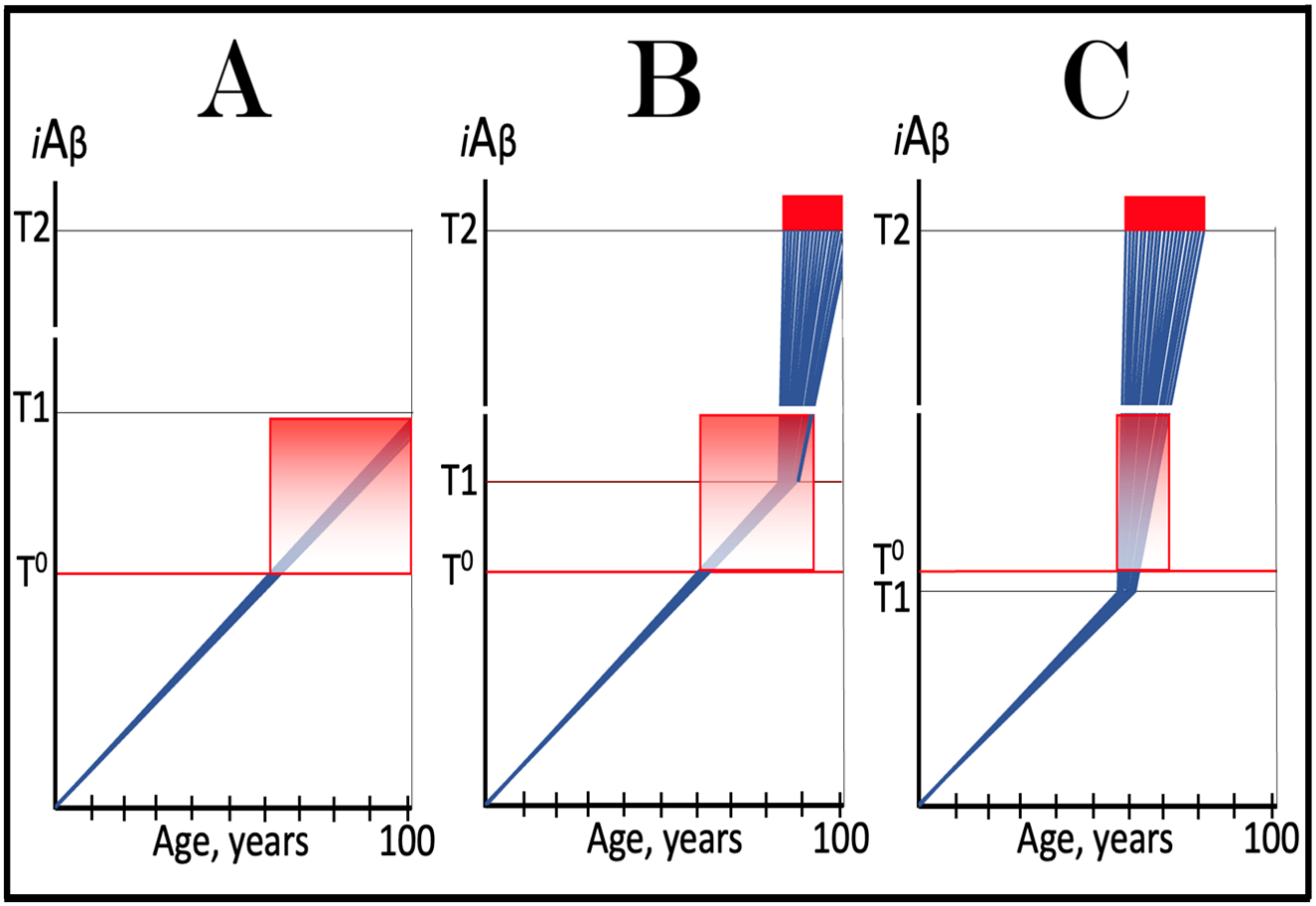

Figure 6. Symptoms of AACD-associated cognitive impairment may overlap with and could be indistinguishable from those of AD-associated mild cognitive impairment. *iA*β: Intraneuronal Aβ levels. ***T*^{0}**: *i*Aβ levels that trigger neuronal damage manifesting as AACD. ***T1***: *i*Aβ level that triggers elicitation of the integrated stress response, initiation of AβPP-independent generation of *i*Aβ, and the activation of the AD Engine. ***T2***: *i*Aβ level that triggers cell's commitment to apoptosis. *Red blocks*: Fraction of affected neurons either committed to apoptosis or dead. *Gradient-pink boxes*: "AACD Zone", the differential between the **T^{0}** and **T1** threshold levels of AβPP-derived *i*Aβ. The rate of accumulation of AβPP-derived *i*Aβ and the extent of the **T^{0}** threshold are constant, and the lifespan is assumed to terminate at 100 years of age; the only variable is the extent of the **T1** threshold. In panel **A** the **T1** is high and is not reached within the lifespan of an individual. AACD commences with the crossing of the **T^{0}** threshold and continues for the remaining portion of the lifespan (gradient-pink box). In this case, *i*Aβ-caused cognitive impairment is clearly attributable to AACD. In panel **B,** the T1 threshold is lowered. The same range of *i*Aβ within the gradient-pink box as shown in panel **A** is divided in panel **B** into two portions: pre-**T1** crossing and post-**T1** crossing. Because the range of *i*Aβ within the gradient-pink boxes in panels **A** and **B** is the same, the symptoms are also the same. But pre-**T1** crossing, they comprise AACD-associated cognitive impairment, whereas post-**T1** crossing, they constitute AD-associated mild cognitive impairment. In panel **C**, the same *i*Aβ range within the gradient-pink box as in panels **A** and **B** occurs entirely post-**T1** crossing. Since the *i*Aβ range within the box is the same as in other panels, the symptoms also are, but now they constitute, in their entirety, AD-associated mild cognitive impairment. Note that since the rate of *i*Aβ accumulation is greater post-**T1** than pre-**T1** crossing, the duration of symptoms decreases in successive panels.

12. Putative Principles of the AD and AACD Dynamics

The line of reasoning pursued in the preceding sections suggests the following putative principles of the AD and AACD dynamics. These principles are concerned with events occurring within the first stage of AD and do not address the processes taking place at the

second AD stage, which are discussed in detail below. Moreover, the kinetics of stage Two of AD influences neither that of its stage One nor any of the principles formulated below.

1. At a given extent of the **T1** threshold, the timing of the commencement of the second AD stage (effectively the timing of AD, referred to below as such) is inversely proportional to the rate of accumulation of AβPP-derived *i*Aβ.
2. At a given rate of accumulation of AβPP-derived *i*Aβ, the timing of the commencement of AD is directly proportional to the extent of the **T1** threshold.
3. In the both cases mentioned above, either the rate of AβPP-derived *i*Aβ accumulation or the extent of the **T1** threshold or the combination of both could be such that the timing of the commencement of AD would exceed the lifespan of an individual.
4. Combination of the rate of accumulation of AβPP-derived *i*Aβ and the extent of the **T1** threshold determine the susceptibility of an individual to AD within a typical lifespan.
5. Regardless of the rate of AβPP-derived *i*Aβ accumulation and of the extent of the **T1** threshold, the occurrence of AD is inevitable given sufficient duration of the lifespan.
6. At a given extent of the **T1** threshold and regardless of the rate of AβPP-derived *i*Aβ accumulation, AACD would not occur if the **T1** threshold is sufficiently low (not exceeding the $\mathbf{T^0}$ threshold), but AD may occur, subject to the rate of *i*Aβ accumulation.
7. When the extent of the **T1** threshold is sufficiently high, i.e., exceeds that of the $\mathbf{T^0}$ threshold, and the extent of the $\mathbf{T^0}$ threshold is constant, the timing of the commencement of AACD is inversely proportional to the rate of accumulation of AβPP-derived *i*Aβ.
8. With the extent of the $\mathbf{T^0}$ threshold and the rate of AβPP-derived *i*Aβ accumulation fixed, the timing of the commencement of AACD remains constant, but the AACD Zone increases in direct proportion to the increasing extent of the **T1** threshold.
9. At a given rate of accumulation of AβPP-derived *i*Aβ, the duration and severity of AACD are directly proportional to the differential between the extents of the $\mathbf{T^0}$ and **T1** thresholds (the "AACD Zone").
10. Given the extent of the $\mathbf{T^0}$ threshold is always lower than that of the **T1** threshold and regardless of the rate of AβPP-derived *i*Aβ accumulation and of the extent of the **T1** threshold, AACD would inevitably occur given sufficient duration of the lifespan.
11. The **T1** threshold is a demarcation line between AD and AACD; when it is crossed by the bulk (or sufficient fraction) of affected neurons, AACD evolves into AD.
12. Given a limited lifespan and sufficient AACD Zone, AACD may develop without AβPP-derived *i*Aβ reaching the **T1** threshold.
13. Given a limited lifespan, AACD is not always followed by AD (but AD will always follow if the lifespan is long enough).
14. Given the sufficiently high **T1** threshold, if AD occurs, it is always preceded by AACD.

13. Potential Fluidity of Kinetic Parameters Defining the Dynamics and Occurrence of AD and AACD

The preceding sections depicted the kinetic parameters that define the occurrence of AD and AACD as constant throughout the lifetime. This, however, is not necessarily the case. In principle, the incidence of both conditions, AD and AACD, is determined primarily by the following three parameters: the extents of the $\mathbf{T^0}$ and **T1** thresholds and the rate of accumulation of AβPP-derived *i*Aβ. The crossing of the $\mathbf{T^0}$ threshold by AβPP-derived *i*Aβ activates AACD; that of the **T1** threshold triggers AD. Each of these parameters is potentially variable and can modulate with age in both linear and non-linear manner. Since the crossing of the $\mathbf{T^0}$ and **T1** thresholds triggers the commencement of AACD and of AD respectively, it can be assumed that increases in the extents of the $\mathbf{T^0}$ and **T1** thresholds in a time-dependent manner during the lifetime would delay or prevent the occurrence of AACD and AD and the lowering of these thresholds would accelerate the commencement of both conditions. Similarly, the time-dependent reduction in the rate of accumulation of AβPP-derived *i*Aβ would delay or prevent the incidence of both conditions, whereas

its increase as a function of time would accelerate the commencement of both AACD and AD. In any case it should be emphasized that, importantly, even with the time-dependent modulation of the extents of the relevant thresholds or the potential aging-related variability of the rate of accumulation of AβPP-derived *i*Aβ, the dynamic aspects of the **T^0** and **T1** crossings would remain subjects to the same logic as applied above and would be fully consistent with the proposed therapeutic strategies for AD and AACD discussed below.

14. Protection from AD and AACD Conferred by the Icelandic AβPP Mutation Is Due to Dynamic Changes in *i*Aβ Accumulation: Mechanistic Interpretation in the ACH2.0 Perspective

The validity of any novel concept demands that it is consistent with all prior observations and is capable of explaining all outstanding unexplained phenomena and making meaningful predictions. The ACH2.0 does all of this. It explains, as discussed above, why numerous candidate AD drugs showed no efficacy in human clinical trials (due to the occurrence of AβPP-independent production of *i*Aβ) yet were very effective in animal studies (due to the lack of the second AD stage, i.e., the absence of the generation of *i*Aβ independently of AβPP in animal models). It predicts that at least some of those drugs could be effective in prevention of AD and in the treatment of AACD but that conceptually different types of drugs are required for the treatment of symptomatic AD [1–3]. It also predicts the occurrence in human AD-affected neurons of C99 and Ab species that contain additional methionine residue at their N-terminus (discussed below). The present and several following sections consider the phenomena of protection from AD and AACD and of causation of the early onset of AD (FAD) and provide the mechanistic interpretation of both occurrences in terms of the ACH2.0 and, more specifically, in terms of the dynamics of accumulation of AβPP-derived *i*Aβ.

The Icelandic AβPP mutation A673T, also known as Aβ mutation A3T since it occurs *within* Aβ, was shown to protect its carriers from AD by augmenting the efficiency of BACE1-mediated cleavage at the β′ site within Aβ [1,2]. Remarkably, it also protects from the pervasive aging-associated cognitive decline, AACD [1,2]. This is a striking observation. It implies that Aβ is involved in AACD, and that its role in this dysfunction is apparently similar, i.e., causative, to the role it performs in AD. Considering the dynamics of *i*Aβ accumulation within the ACH2.0 framework, described above, it is clear how the Icelandic mutation protects from AD. It does so by increasing the rate of BACE1 cleavage at the β′ site within Aβ segment of the precursor molecule as well as within already formed *i*Aβ, thus lowering the rate of accumulation of AβPP-derived *i*Aβ. Indeed, in the mutation carriers less Aβ is produced in the AβPP proteolytic pathway and more *i*Aβ is cleaved at the β′ site, therefore the steady state influx of *i*Aβ is lowered and the rate of its accumulation is reduced. Consequently, AβPP-derived *i*Aβ levels do not reach the **T1** threshold within the lifespan of a mutation carrier (or reach it much later than in wild-type AβPP carriers), and the disease either does not occur or is delayed. As for AACD, its definition as the extended segment of the first AD stage, commencing with the crossing of the **T^0** threshold by AβPP-derived *i*Aβ, provides the explanation for how the Icelandic mutation protects from aging-associated cognitive decline: in exactly the same manner that it renders protection from AD, namely by lowering the rate of AβPP-derived *i*Aβ accumulation with the result that *i*Aβ levels do not reach the **T^0** threshold within the lifetime of a mutation carrier (or reach it at a substantially later age than in wild-type AβPP carriers).

The above mechanistic interpretation of the protective effect of the Icelandic mutation in AD and AACD is illustrated in Figure 7. Panels **A**, **B**, and **C** of Figure 7 depict diagrammatically three principal variants of the *i*Aβ-caused diseases, i.e., AD and AACD, occurring in wild-type AβPP carriers. In these panels, the rate of AβPP-derived *i*Aβ accumulation is constant, a given, and so is the extent of the **T^0** threshold; the lifespan in each case is assumed to end at 100 years of age. On the other hand, the extent of the **T1** threshold is variable and dictates whether AACD and AD do or do not occur. In panel **A** of Figure 7, the **T1** threshold is below the AβPP-derived *i*Aβ level required for the initiation of AACD (**T^0** threshold). When the **T1** threshold is reached, the AβPP-independent *i*Aβ generation

pathway is activated and AD commences. When *i*Aβ (mostly produced at this point independently of AβPP) levels reach the $\mathbf{T^0}$ threshold, AD-MCI symptoms would occur, as discussed above, and morph rapidly into AD.

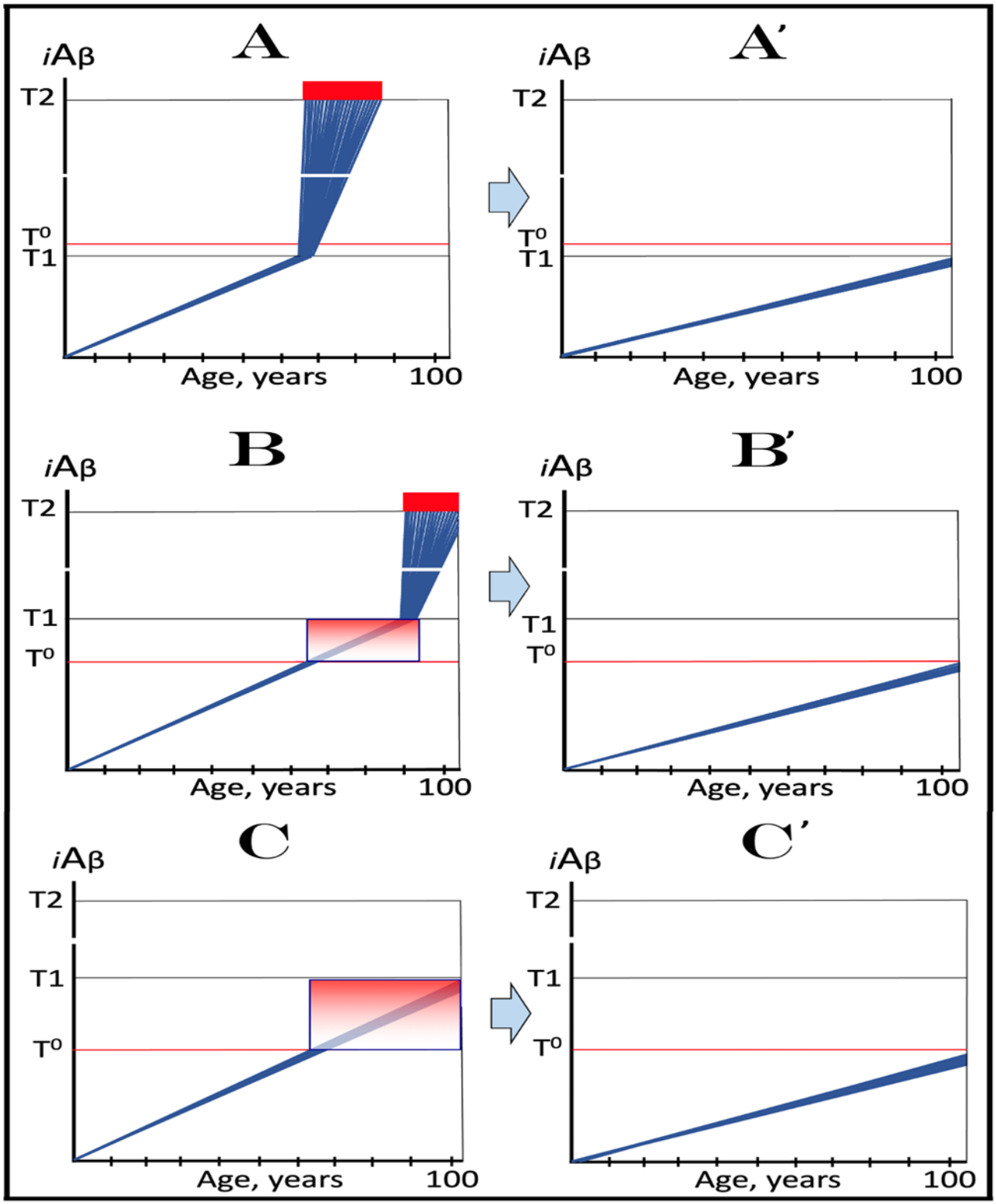

Figure 7. Protective effect of the Icelandic mutation for AD and AACD: Mechanistic interpretation in the ACH2.0 perspective. *iA*β: Intraneuronal Aβ levels. $\boldsymbol{T^0}$: *i*Aβ levels that trigger neuronal damage

manifesting as AACD. ***T1***: *i*Aβ level that triggers elicitation of the integrated stress response, initiation of AβPP-independent generation of *i*Aβ, and the activation of the AD Engine. ***T2***: *i*Aβ level that triggers cell's commitment to the apoptotic pathway. *Red blocks*: Fraction of affected neurons either committed to apoptosis or dead. *Gradient-pink boxes*: "AACD Zone", the differential between the $\mathbf{T^0}$ and **T1** threshold levels of AβPP-derived *i*Aβ (more precisely, between the $\mathbf{T^0}$ and the maximum level reached by AβPP-derived *i*Aβ short of the T1 threshold). *Panels **A**, **B**, and **C*** depict three principal variants of the *i*Aβ-caused disease occurring in wild-type AβPP carriers. The rate of AβPP-derived *i*Aβ accumulation is assumed constant and so is the extent of the $\mathbf{T^0}$ threshold; the lifespan in each case is limited to 100 years of age. On the other hand, the extent of the **T1** threshold is variable and dictates whether AACD and AD do or do not occur. In *panel **A***, the **T1** threshold is below the AβPP-derived *i*Aβ level ($\mathbf{T^0}$ threshold) required for the initiation of AACD. When the **T1** threshold is reached, the AβPP-independent *i*Aβ generation pathway is activated and AD commences. In *panel **B***, the $\mathbf{T^0}$ threshold level is below that of the T1 threshold. When the levels of AβPP-derived *i*Aβ reach the former, AACD commences and persists until AβPP-derived *i*Aβ crosses the latter, i.e., for the duration of the AACD Zone (gradient-pink box), whereupon it evolves into AD. In *panel **C***, the extent of the **T1** threshold is such that at a given rate of accumulation of AβPP-derived *i*Aβ, the **T1** threshold cannot be reached, the AβPP-independent *i*Aβ generation pathway cannot be activated, and AD cannot occur within the lifetime of an individual. When AβPP-derived *i*Aβ levels cross the $\mathbf{T^0}$ threshold, AACD commences and continues for the remaining part of the lifespan. *Panels **A**′, **B**′, and **C**′* depict mechanistic interpretation of the protective effect of the Icelandic AβPP mutation within the framework of the ACH2.0. In all three variants of potential AD/AACD, the rate of accumulation of AβPP-derived *i*Aβ is lowered. In *panel **A**′*, it is such that levels of AβPP-derived *i*Aβ do not reach the T1 threshold within the lifespan of an individual. In *panels **B**′ and **C**′*, the rate of accumulation of AβPP-derived iAβ is rendered such that its levels do not reach the $\mathbf{T^0}$ (and **T1**) threshold within the individual's lifetime. Accordingly, in all three variants, neither AACD nor AD occurs within the lifespan of the Icelandic mutation carriers (or occurs substantially later than in wild-type AβPP carriers).

Panel **B** of Figure 7 depicts a scenario where the $\mathbf{T^0}$ threshold level is below that of the **T1** threshold. When the levels of AβPP-derived *i*Aβ reach the former, AACD commences and persists until AβPP-derived *i*Aβ crosses the latter, i.e., for the duration of the AACD Zone (shown as gradient-pink boxes in Figure 7), whereupon it evolves into AD. In panel **C** of Figure 7, the extent of the **T1** threshold is such that at a given rate of accumulation of AβPP-derived *i*Aβ, the **T1** threshold cannot be reached, the AβPP-independent *i*Aβ generation pathway cannot be activated and AD cannot occur within the lifetime of an individual. When AβPP-derived *i*Aβ levels cross the $\mathbf{T^0}$ threshold, AACD commences and continues (increasing in severity with elevating levels of *i*Aβ) for the remaining part of the lifespan.

Panels **A**′, **B**′, and **C**′ of Figure 7 depict mechanistic interpretation of the protective effect of the Icelandic mutation within the framework of the ACH2.0. In all three variants of potential AD/AACD, the rate of accumulation of AβPP-derived *i*Aβ is lowered. In panel **A**′ of Figure 7, it is such that neither the levels of AβPP-derived *i*Aβ do reach the **T1** threshold within the lifespan of an individual nor AD occurs. In panels **B**′ and **C**′ of Figure 7, the rate of accumulation of AβPP-derived iAβ is rendered such that neither levels of AβPP-derived *i*Aβ reach the $\mathbf{T^0}$ (and, of course, **T1**) threshold within the individual's lifetime, nor AACD (and, of course, AD) ensues. Thus, in all three variants discussed above, neither AACD nor AD occur within the lifespan of the Icelandic mutation carriers (or occur substantially later than in wild type AβPP carriers).

15. Confirmation of the Concept: Effect of the Flemish Aβ Mutation as the Ultimate Empirical Test in Nature-Conducted Experiment

Conceptually, the notion that the persistent suppression of the rate of *i*Aβ accumulation protects from AD could be assessed empirically. An experiment can be envisioned where a physiologically occurring cleavage within Aβ (which indeed takes place as discussed below) is suppressed, a scenario which is diametrically opposite to that happening in Icelandic mutation carriers. The suppression of Aβ cleavage would result in its increased production, in the elevated steady-state influx of *i*Aβ, and, consequently, in the augmented rate of *i*Aβ accumulation, the accelerated crossing of the **T1** threshold, and the early activation of the AβPP-independent *i*Aβ production and of the second AD stage. Thus, if the concept, linking the rate of *i*Aβ accumulation to the occurrence of AD, were correct, early-onset AD should result. *Just this experiment was, in fact, carried out by nature in the form of the Flemish A692G AβPP mutation*. It is also known as the A21G Aβ Aβ mutation because it affects the residue 21 of Aβ, which contiguously follows cleaving sites of BACE2 at residues 19 and 20 within Aβ. A21G substitution suppresses the physiologically operating cleaving activity of BACE2 within Aβ segment of the precursor molecule as well as within already formed *i*Aβ. This increases the production of Aβ in the AβPP proteolytic pathway and decreases cleavages of already formed *i*Aβ, thus elevating the steady-state influx of *i*Aβ and augmenting the rate of *i*Aβ accumulation (further discussed in the following section). The result is the early-onset FAD that manifests symptomatically at the mid-forties [62,102,103]. *The outcome of this "natural" experiment, therefore, constitutes a confirmation of the concept connecting the rate of iAβ accumulation and the occurrence of AD.*

16. Dynamics of the Early Onset of FAD: Mechanistic Interpretation in the ACH2.0 Perspective

16.1. Category One of FAD: Mutations Causing the Elevation in the Rate of Accumulation of AβPP-Derived iAβ

The Flemish FAD mutation is one of many causing the early onset of the disease. In the ACH2.0 perspective, the modus operandi of every such mutation is essentially the same: Acceleration of the crossing of the **T1** threshold by AβPP-derived *i*Aβ. As for how this is achieved, FAD mutations can be separated into two categories. One category is exemplified by Flemish [62] and Swedish [59] AβPP mutations, as well as by presenilins mutations that facilitate gamma-cleavage of C99 on the internal membranes, thus increasing the intraneuronal retention of AβPP-derived Aβ [60]. In these cases, the core causative event is the increase in the steady-state influx of AβPP-derived *i*Aβ and consequent elevation of the rate of its accumulation. In Flemish FAD mutation case, this is due to suppression of physiologically operating activity of BACE2 that cleaves Aβ segment within AβPP and the C99 fragment as well as within *i*Aβ. In case of the Swedish FAD [59] and certain PSEN [60] mutants, the increase in the steady-state influx of *i*Aβ is due to the augmented gamma-cleavage of the C99 fragment on the intracellular membranes rather than on the plasma membrane, which results in the increased intraneuronal retention of AβPP-derived *i*Aβ. Consequently, in either case, the rate of AβPP-derived *i*Aβ accumulation increases in comparison with wild-type AβPP carriers.

In wild-type AβPP carriers, two possible scenarios can play out. In the first scenario, which occurs in the majority of the population, the **T1** threshold is not crossed within the lifespan of an individual, and no AD occurs (Figure 8, panel **A**). In the other scenario (in both scenarios the extent of the **T1** is assumed to be lower than that of $\mathbf{T^0}$ threshold), *i*Aβ levels reach and cross the **T1** threshold and late-onset AD ensues (Figure 8, panel **B**). In carriers of the first category of FAD mutations with the extent of the **T1** lower than that of $\mathbf{T^0}$ threshold, AβPP-derived *i*Aβ accumulates faster, the **T1** threshold is reached sooner, and the early onset of AD results (Figure 8, panels **A′** and **B′**).

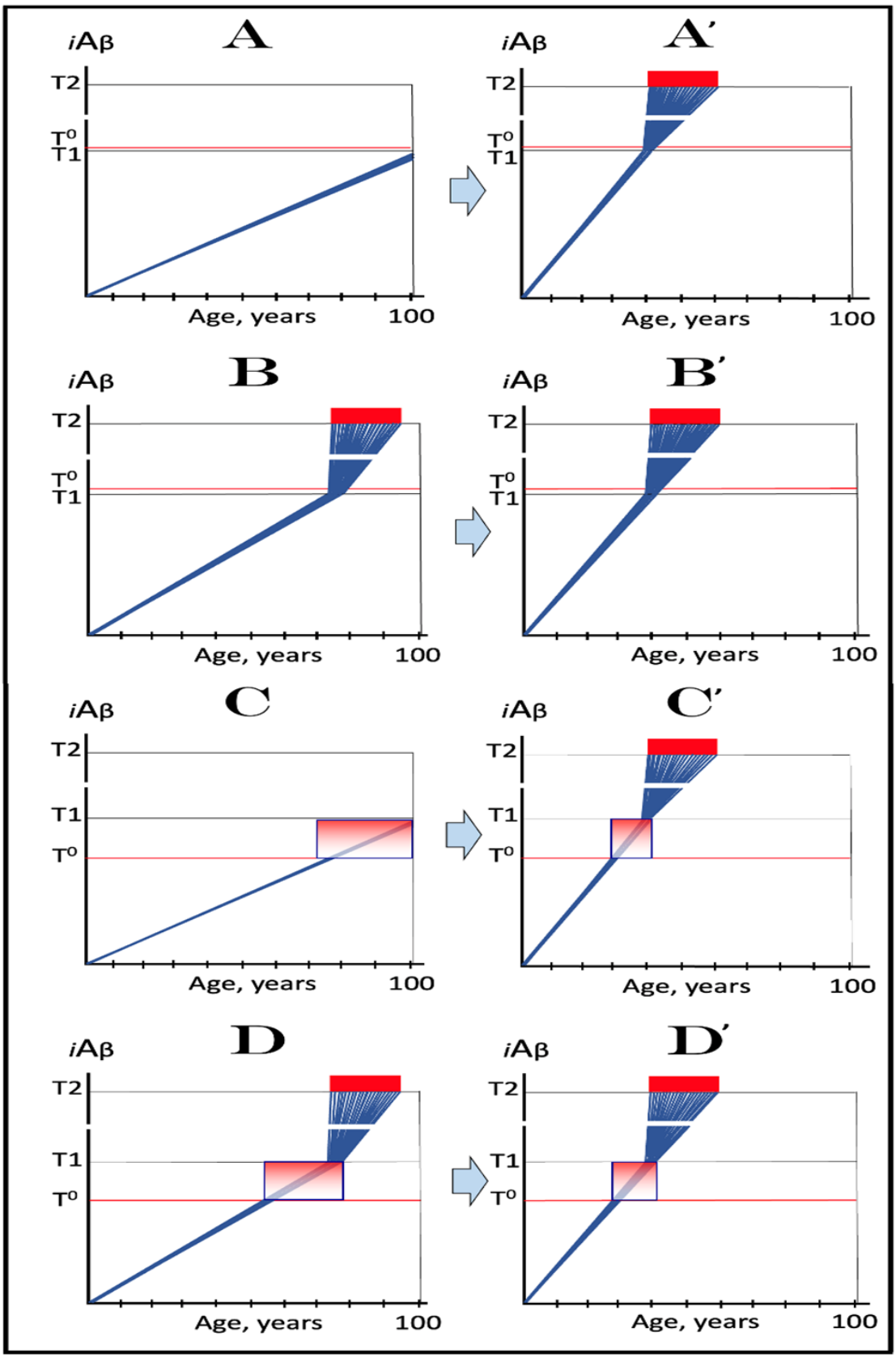

Figure 8. Early onset of AD in carriers of category One FAD mutations: Mechanistic interpretation in the ACH2.0 perspective. *iA*β: Intraneuronal Aβ levels. T^0: *i*Aβ levels that trigger neuronal damage

manifesting as AACD. ***T1***: *i*Aβ level that triggers elicitation of the integrated stress response, initiation of AβPP-independent generation of *i*Aβ, and the activation of the AD Engine. ***T2***: *i*Aβ level that triggers cell's commitment to the apoptotic pathway. *Red blocks*: Fraction of affected neurons either committed to apoptosis or dead. *Gradient-pink boxes*: "AACD Zone", the differential between the $\mathbf{T^0}$ and **T1** threshold levels of AβPP-derived *i*Aβ (more precisely, between the $\mathbf{T^0}$ and the maximum level reached by AβPP-derived *i*Aβ short of the **T1** threshold). Assumed lifespan: 100 years. *Panels **A**, **B**, **C**, **D***: Kinetics of *i*Aβ accumulation and progression of disease in wild-type AβPP carriers. Panels **A** and **B**: The extent of the $\mathbf{T^0}$ threshold exceed that of the **T1**; no AACD occurs. Panel **A**: The **T1** threshold is not crossed; no AD occurs. Panel **B**: The **T1** threshold is reached and crossed; the late onset AD ensues. Panels **C** and **D**: The $\mathbf{T^0}$ threshold is lower than the **T1**. Panel **C**: The **T1** threshold is not crossed; AACD commences upon crossing of the $\mathbf{T^0}$ threshold and continues for the remaining lifespan. Panel **D**: Both the $\mathbf{T^0}$ and **T1** thresholds are crossed; AACD commences upon the crossing of the former and evolves into late onset AD when the latter is reached. *Panels **A′**, **B′**, **C′**, **D′***: Dynamics of *i*Aβ accumulation and progression of disease in carriers of category One FAD mutations. The steady-state influx of AβPP-derived *i*Aβ is increased and its rate of accumulation augmented. Consequently, the **T1** threshold is reached earlier, AβPP-independent production of *i*Aβ is activated sooner, and the early-onset AD ensues. Panels **A′** and **B′**: The $\mathbf{T^0}$ levels exceed those of **T1**; no AACD occurs. Panels **C′** and **D′**: The extent of the $\mathbf{T^0}$ threshold is lower than that of the **T1** threshold, and the early-onset AD is preceded by the AACD phase. Due to the steepness of AβPP-derived *i*Aβ accumulation, the duration of the AACD phase is much shorter in mutants than in wild-type AβPP carriers; it rapidly evolves (upon crossing of the **T1** threshold by AβPP-derived *i*Aβ) into early onset AD and therefore could be hard to diagnose as a separate condition. Note that the only dynamic alteration caused by category One FAD mutations is the augmentation of the rate of accumulation of AβPP-derived *i*Aβ.

In wild-type AβPP cases where the extent of the $\mathbf{T^0}$ threshold is lower than that of the **T1**, there are also several possibilities. If the $\mathbf{T^0}$ and **T1** thresholds are not crossed, neither AACD nor AD occurs (not shown). If the $\mathbf{T^0}$ threshold is crossed but the **T1** is not, AACD would commence and continue for the remaining part of the lifespan (Figure 8, panel **C**). If both, the $\mathbf{T^0}$ and **T1** thresholds were crossed, AACD would be followed by the late onset AD (Figure 8, panel **D**). In carriers of the first category of FAD mutations with the $\mathbf{T^0}$ threshold is lower than the **T1**, due to the augmented accumulation of AβPP-derived *i*Aβ the early onset AD would occur and would be preceded by the AACD stage (Figure 8, panels **C′** and **D′**). However, due to the steep rate of *i*Aβ accumulation in FAD cases, the AACD stage would be of substantially shorter duration in FAD mutation carriers (Figure 8, panels **C′** and **D′**) than in their wild-type AβPP counterparts (Figure 8, panels **C** and **D**). In the former, unlike in the latter, AACD would rapidly evolve into AD upon crossing of the **T1** threshold, and could be hard to diagnose as a separate condition.

*16.2. Category Two of FAD: Mutations That Both Accelerate the Rate of AβPP-Derived iAβ Accumulation and Lower the **T1** Threshold*

Another category of FAD mutations includes those, both in AβPP and in presenilins, which cause the increased production of $A\beta_{42}$ [36]. Two factors are at play in the attainment of the **T1** threshold by AβPP-derived *i*Aβ in this category. (a) The first factor is the accelerated cellular uptake of secreted soluble $A\beta_{42}$, which was shown to oligomerize and be taken up by cells twice more efficiently than $A\beta_{40}$ [35]. This results in the accelerated (in comparison with the wild-type) steady-state influx of *i*Aβ, which, in turn, leads to the augmented rate of *i*Aβ accumulation. (b) The second factor is the reduction of the extent of the **T1** threshold due to the documented increased (in comparison with other Aβ species) toxicity of intracellular $A\beta_{42}$. The increased toxicity translates into increased cellular stress and in the reduction in the levels of $i\mathrm{A}\beta_{42}$ required for elicitation of the ISR, i.e., in the lowering of the **T1** threshold (the $\mathbf{T^0}$ threshold is, probably, also lowered). Cumulatively, these two factors substantially accelerate, in comparison with wild-type AβPP carriers, the

crossing of the **T1** threshold by AβPP-derived *i*Aβ and the consequent commencement of the second AD stage in carriers of the second category of FAD mutations.

This brings about the early onset of AD as shown in Figure 9. The scenarios playing out in wild-type AβPP carriers are similar to those described in the preceding section: In cases where the $\mathbf{T^0}$ exceeds the **T1** threshold, no crossing of the **T1** threshold within an individual's lifetime and no AD (Figure 9, panel **A**) or the crossing of the **T1** threshold, followed by the late onset AD (Figure 9, panel **B**). In carriers of the second category of FAD mutations, both the rate of accumulation of AβPP-derived *i*Aβ is augmented and the T1 threshold is lowered. Consequently in cases with the extent of **T1** lower than that of $\mathbf{T^0}$, the **T1** threshold is reached and crossed substantially sooner and the early onset of AD ensues (Figure 9, panels **A**′ and **B**′).

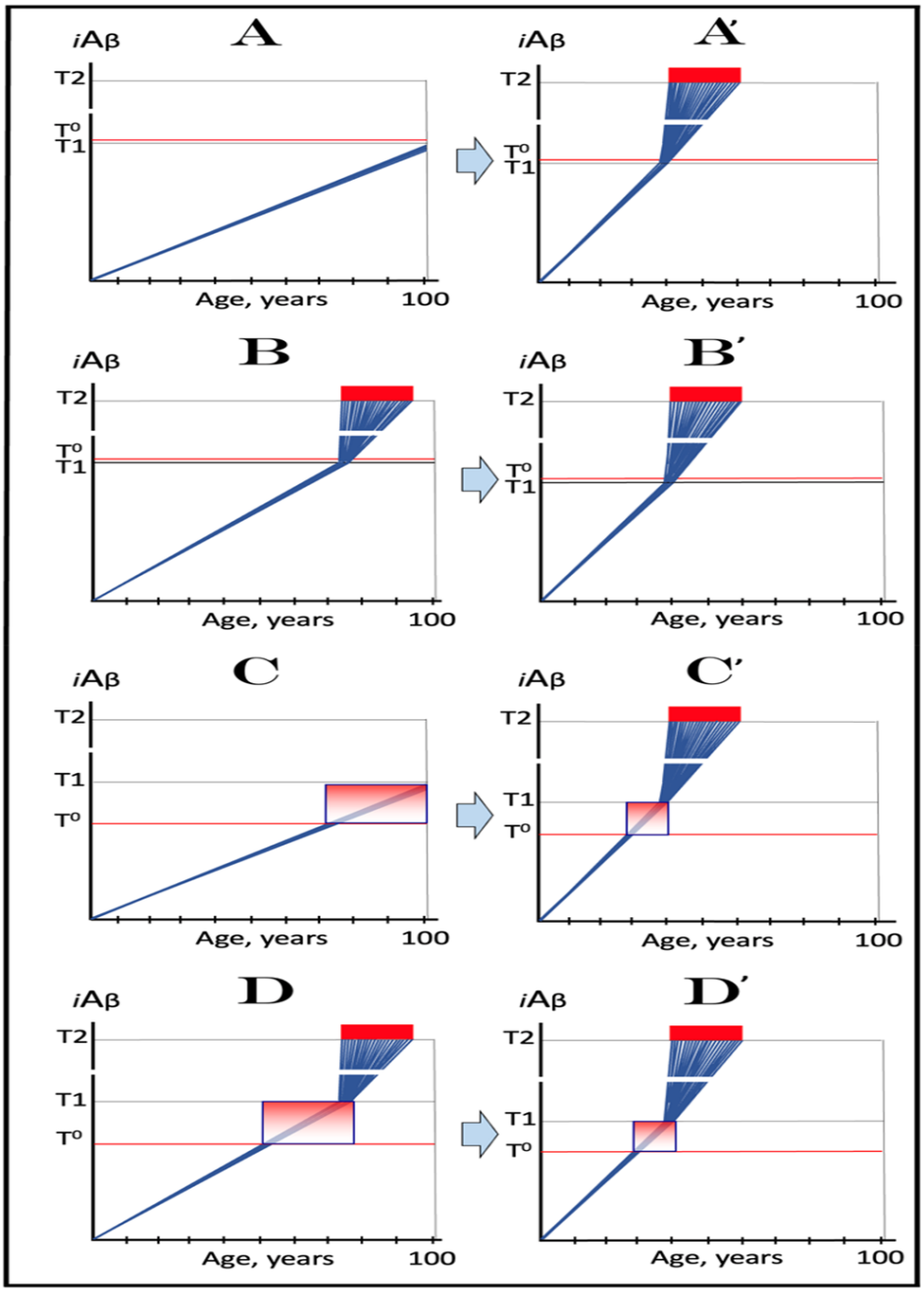

Figure 9. Early onset of AD in carriers of category Two FAD mutations: Mechanistic interpretation in the ACH2.0 perspective. *iA*β: Intraneuronal Aβ levels. $\boldsymbol{T^0}$: *i*Aβ levels that trigger neuronal damage

manifesting as AACD. *T1*: *i*Aβ level that triggers elicitation of the integrated stress response, initiation of AβPP-independent generation of *i*Aβ and the activation of the AD Engine. ***T2***: *i*Aβ level that triggers cell's commitment to the apoptotic pathway. *Red blocks*: Fraction of affected neurons either committed to apoptosis or dead. *Gradient-pink boxes*: "AACD Zone", the differential between the $\mathbf{T^0}$ and **T1** threshold levels of AβPP-derived *i*Aβ (more precisely, between the $\mathbf{T^0}$ and the maximum level reached by AβPP-derived *i*Aβ short of the **T1** threshold). Assumed lifespan: 100 years. *Panels **A**, **B**, **C**, **D***: Kinetics of *i*Aβ accumulation and progression of disease in wild-type AβPP carriers. Panels **A** and **B**: The $\mathbf{T^0}$ levels exceed those of T1; no AACD occurs. Panel **A**: The **T1** threshold is not crossed; no AD occurs. Panel **B**: The **T1** threshold is reached and crossed; the late onset AD ensues. Panels **C** and **D**: The $\mathbf{T^0}$ threshold is lower than **T1**. Panel **C**: The **T1** threshold is not crossed; AACD commences upon crossing of the $\mathbf{T^0}$ threshold and continues for the remaining lifespan. Panel **D**: Both the $\mathbf{T^0}$ and **T1** thresholds are crossed; AACD commences upon crossing of the former and evolves into late onset AD when the latter is reached. *Panels **A′**, **B′**, **C′**, **D′***: Dynamics of *i*Aβ accumulation and progression of disease in carriers of category two FAD mutations, which cause not only the augmentation of steady-state influx of AβPP-derived *i*Aβ and the increase in its rate of accumulation but also the reduction in the extent of the **T1** threshold. The **T1** threshold is reached earlier, AβPP-independent production of *i*Aβ is activated sooner, and the early-onset AD ensues. Panels **A′** and **B′**: The $\mathbf{T^0}$ levels exceed those of T1; no AACD occurs. Panels **C′** and **D′**: The extent of the $\mathbf{T^0}$ threshold is lower than that of the **T1** threshold, and the early-onset AD is preceded by the AACD phase. Due to the steepness of AβPP-derived *i*Aβ accumulation, the duration of the AACD phase is much shorter than in wild-type AβPP carriers; it rapidly evolves (upon crossing of the **T1** threshold by AβPP-derived *i*Aβ) into early onset AD and therefore could be hard to diagnose as a separate condition. Note that dynamic changes caused by category two FAD mutations are not only the increase in the rate of accumulation of AβPP-derived *i*Aβ but also the reduction in the extent of the **T1** and, probably, $\mathbf{T^0}$ thresholds.

In wild-type AβPP cases where the extent of the $\mathbf{T^0}$ threshold is lower than that of the **T1**, the possible scenarios are also similar to those discussed in the preceding section, namely (a) no $\mathbf{T^0}$ and **T1** threshold crossing and, consequently, no AD and AACD (not shown); (b) crossing of the $\mathbf{T^0}$ but not of the **T1** threshold, resulting in in AACD continuing for the remaining lifespan and no AD (Figure 9, panel **C**); and (c) crossing of both the $\mathbf{T^0}$ and **T1** thresholds leading to AACD that would be followed by the late onset AD (Figure 9, panel **D**).

In carriers of the second category of FAD mutations, in cases where the $\mathbf{T^0}$ threshold is lower than the **T1**, both the $\mathbf{T^0}$ and **T1** thresholds are crossed, and the early onset AD is preceded by the AACD stage (Figure 9, panels **C′** and **D′**). Due to the steep rate of *i*Aβ accumulation, however, the AACD phase in mutation carriers would be of substantially shorter duration than in wild-type counterparts; would relatively rapidly morph, upon crossing of the **T1** threshold by AβPP-derived *i*Aβ, into AD; and would, possibly, be unnoticeable or hard to diagnose as a separate condition (Figure 9, panels **D/D′**). Note that in panels **A′**, **B′**, **C′** and **D′**, not only is the rate of *i*Aβ accumulation augmented, but the extent of the **T1** threshold is also lowered.

17. Protective Icelandic AβPP Mutation as the Ultimate Guide for AD and AACD Therapy

Consider the following: Not only do multiple mutations affecting, apparently solely, Aβ cause AD, but also the Icelandic mutation *within* Aβ protects from both AD and AACD. This is the ultimate argument for the causative role of Aβ in AD and AACD, and a persuasive and defining guide for therapeutic strategies for both conditions. How to prevent and treat AD and AACD according to this guide? The answer is straightforward: Emulate what the Icelandic mutation does. Then, what exactly does the Icelandic mutation do? It simply augments the efficiency of BACE1 cleavage at the β′ site within *i*Aβ and thus reduces the steady-state influx of AβPP-derived *i*Aβ and lowers the rate of its accumulation; ultimately, it delays or prevents (within limits of the lifespan) the crossing of the **T^0** and/or **T1** thresholds and, consequently, the occurrence of AD and AACD. How to imitate this? This can be accomplished in two ways.

17.1. Prevention of AD and AACD by Simulation of the Mode of Operation of the Icelandic AβPP Mutation

One way is literally. The Icelandic mutation persistently, from birth, reduces the steady-state influx of AβPP-derived *i*Aβ. To imitate this literally, drugs, possibly the existing ones, can be used to accomplish the same. BACE1 inhibitors appear capable of accomplishing this by suppressing the overall AβPP-based production of Aβ; so do, albeit to a lesser extent, antibodies targeting extracellular Aβ (e.g., lecanemab and donanemab [3]) by suppressing its cellular uptake, i.e., its conversion to *i*Aβ. This would reduce the steady-state influx of AβPP-derived *i*Aβ, lower the rate of its accumulation, and delay or prevent the crossing of the **T1** and **T^0** thresholds and the occurrence of AD and AACD. To literally imitate the effect of the Icelandic mutation, such drugs would have to be administered unremittingly for the entire life, starting early. On the other hand, the outcomes of clinical trials of lecanemab and donanemab (analyzed in [3]) indicate that the type of drug, which targets the influx of AβPP-derived *i*Aβ, can be employed preventively relatively late in life, provided that their administration commences prior to the **T^0** and **T1** crossings and that their effect is sufficiently potent to preclude further accumulation of AβPP-derived *i*Aβ for the duration of the treatment [3].

The potential outcomes of treatment with such drugs, initiated late in life, are illustrated in Figure 10. *Panels* **A, B**, and **C** depict the accumulation of *i*Aβ and progression of disease in untreated patients with different relative extents of the **T^0** and **T1** thresholds in three principal variants of AD/AACD discussed above (see for comparison Figure 7 above). In panel **A** of Figure 10, the **T1** threshold is lower than **T^0** and its crossing triggers AD. In panel A′, a drug is administered, prior to the **T1** crossing, that precludes further accumulation of AβPP-derived *i*Aβ and prevents AD for the duration of the treatment (orange box). In panel **B**, the **T^0** is lower than **T1** and AD is preceded by AACD. In panel **B′**, a drug is administered prior to the **T^0** crossing. It stops further accumulation of AβPP-derived *i*Aβ and prevents both AACD and AD for the duration of the treatment. In panel **C,** the **T1** threshold is not crossed and the **T^0** crossing triggers AACD that continues for the remaining lifespan of an individual. In panel **C′**, a drug is administered *after* the **T^0** crossing. It precludes further accumulation of AβPP-derived *i*Aβ and stops or slows the progression of AACD for the duration of the treatment. *Thus a drug, which suppresses the accumulation of AβPP-derived iAβ, can be only preventive for AD but may constitute a valid treatment for AACD*. This is because, whereas AACD is caused by AβPP-derived *i*Aβ, AD is driven by *i*Aβ produced independently of AβPP and is, therefore, insensitive to drugs targeting AβPP-derived *i*Aβ [1,2].

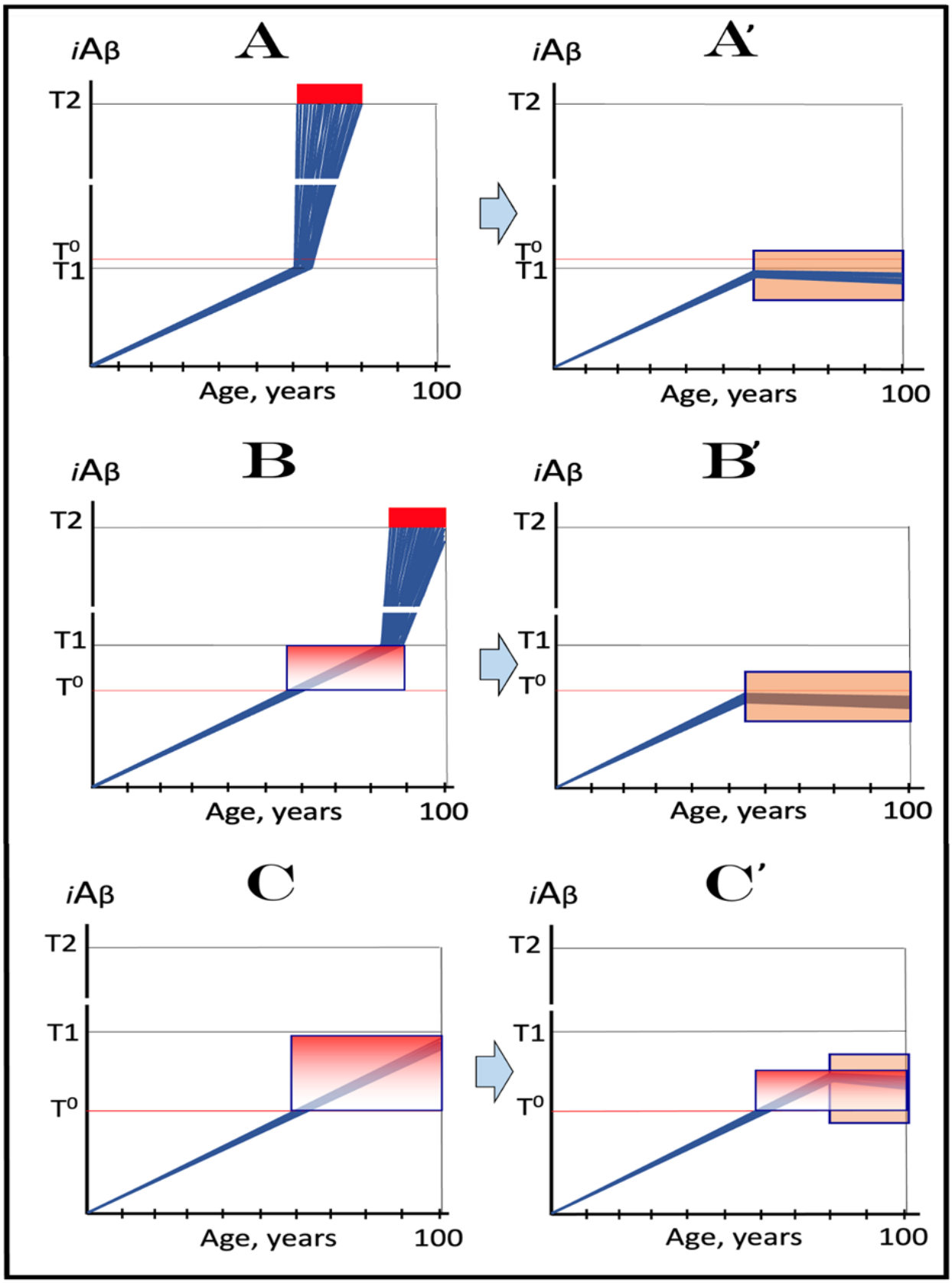

Figure 10. The Icelandic AβPP mutation as the ultimate guide for AD and AACD therapy: Effect of the imitation of the mode of mutation's operation. *iA*β: Intraneuronal Aβ levels. T^0: *i*Aβ levels that

trigger neuronal damage manifesting as AACD. ***T1***: *i*Aβ level that triggers elicitation of the integrated stress response, initiation of AβPP-independent generation of *i*Aβ and the activation of the AD Engine. ***T2***: *i*Aβ level that triggers cell's commitment to the apoptotic pathway. *Red blocks*: Fraction of affected neurons either committed to apoptosis or dead. *Gradient-pink Boxes*: "AACD Zone", the differential between the $\mathbf{T^0}$ and **T1** threshold levels of AβPP-derived *i*Aβ (more precisely, between the $\mathbf{T^0}$ and the maximum level reached by AβPP-derived *i*Aβ short of the **T1** threshold). *Orange boxes:* Duration of treatment's administration. The lifespan is assumed to terminate at 100 years of age. *Panels **A**, **B**, **C**:* Dynamics of *i*Aβ accumulation in AD-affected neurons and the progression of the disease in the wild-type AβPP carriers in the absence of treatment. In panel ***A***, the $\mathbf{T^0}$ levels exceed those of **T1** and no AACD occurs. In panels ***B*** and ***C***, the $\mathbf{T^0}$ threshold is lower than **T1**. AACD commences upon crossing of the $\mathbf{T^0}$ threshold and evolves into AD when the **T1** threshold is crossed (panel **B**) or continues for the remaining lifespan if the **T1** threshold is not crossed (panel **C**). *Panels **A'**, **B'***: Dynamics of AβPP-derived *i*Aβ accumulation under a drug that suppresses its steady-state influx and precludes its further accumulation. The crossing of the **T1** and $\mathbf{T^0}$ thresholds is prevented and no disease ensues for the duration of the treatment. *Panel **C'***: The same drug is administered *after* the $\mathbf{T^0}$ crossing. It precludes further accumulation of AβPP-derived *i*Aβ and stops or slows the progression of AACD for the duration of the treatment. *Thus, a drug, which suppresses the accumulation of AβPP-derived iAβ, can be only preventive for AD but may constitute a valid treatment for AACD*.

17.2. The Mode of Operation of the Protective Icelandic AβPP Mutation Is Physiologically Constrained and Can Be Substantially Improved Upon: Transient, Short-Duration iAβ Depletion Therapy for AD and AACD

Another way to emulate the Icelandic mutation is to follow the essential logic (i.e., the spirit rather than the letter) of its operation but do one better. We can achieve the same outcome, namely the extension of the duration of time required for AβPP-derived *i*Aβ to reach the **T1** and/or $\mathbf{T^0}$ thresholds, in a stepwise manner by transiently depleting the levels of *i*Aβ before they cross the $\mathbf{T^0}$ and **T1** thresholds, thus collapsing its population and forcing the resumption of its accumulation from a lower baseline, an objective that can be accomplished by just a few, possibly a single, strategically timed transient *i*Aβ depletion treatments.

This strategy is illustrated in panels **A/A', B/B'** and **C/C'** of Figure 11. Panels **A, B** and **C** show the dynamics of accumulation of *i*Aβ and progression of disease in untreated patients with different relative extents of the $\mathbf{T^0}$ and **T1** thresholds in three principal variants of AD/AACD discussed above. In panel **A** of Figure 11, the crossing of the **T1** threshold triggers the commencement of AD. In panel **A**′ a transient treatment is administered prior to the **T1** crossing, which depletes *i*Aβ. Following the depletion, AβPP-derived *i*Aβ accumulation resumes from a low baseline and its levels, as shown, would not reach the **T1** threshold within the lifetime of the treated individual. No **T1** crossing would take place, no AβPP-independent *i*Aβ production would be activated, no AD would occur.

In panel **B** of Figure 11, AD is preceded by AACD. In panel **B**′, a transient *i*Aβ depletion treatment is implemented before the $\mathbf{T^0}$ threshold crossing. The de novo accumulation of AβPP-derived *i*Aβ resumes from a low baseline. The $\mathbf{T^0}$ (and **T1**) threshold is not crossed within the remaining lifetime of the treated individual, nor does AACD (and AD) occur.

In panel **C** of Figure 11, the $\mathbf{T^0}$ threshold is crossed and AACD is triggered but the **T1** threshold is not reached within an individual's lifespan. In panel **C**′, a transient *i*Aβ depletion treatment is applied to AACD patient *after* the $\mathbf{T^0}$ but prior to the **T1** threshold crossing. *Following the depletion, iAβ levels are well below the $\mathbf{T^0}$ threshold and the patient is technically cured of AACD* (subject to complete recovery of the affected neurons following the *i*Aβ depletion treatment). As shown, de novo accumulating AβPP-derived *i*Aβ does not reach the $\mathbf{T^0}$ threshold, and AACD does not recur within the remaining lifetime of the treated patient.

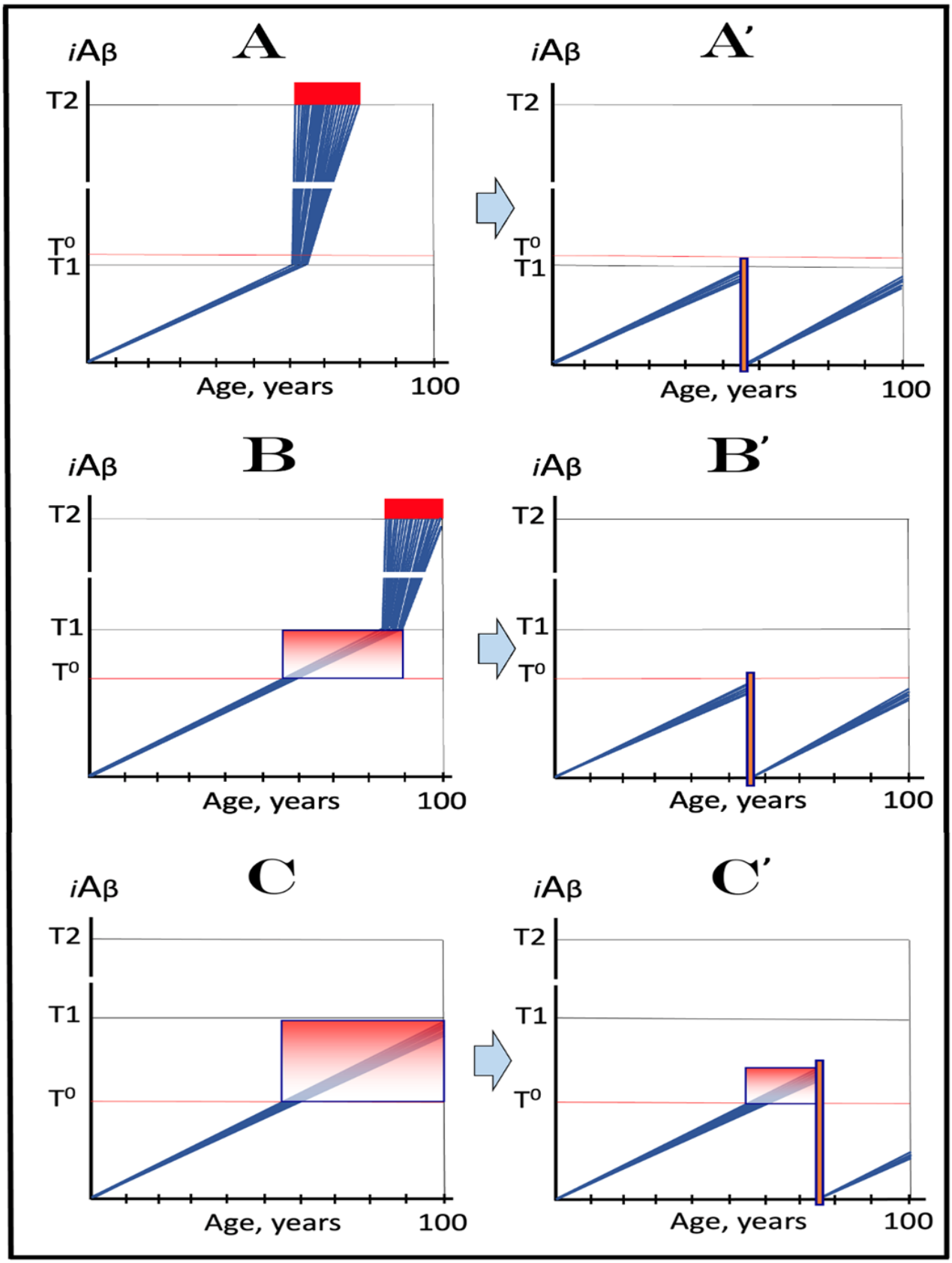

Figure 11. Protective action of the Icelandic AβPP mutation can be improved upon: effect of the transient depletion of *i*Aβ. *iA*β: Intraneuronal Aβ levels. T^0: *i*Aβ levels that trigger neuronal damage

manifesting as AACD. ***T1***: *i*Aβ level that triggers elicitation of the integrated stress response, initiation of AβPP-independent generation of *i*Aβ and the activation of the AD Engine. ***T2***: *i*Aβ level that triggers cell's commitment to the apoptotic pathway. *Red blocks*: Fraction of affected neurons either committed to apoptosis or dead. *Gradient-pink boxes*: "AACD Zone", the differential between the $\mathbf{T^0}$ and **T1** threshold levels of AβPP-derived *i*Aβ (more precisely, between the $\mathbf{T^0}$ and the maximum level reached by AβPP-derived *i*Aβ short of the **T1** threshold). *Orange boxes:* Duration of treatment's administration. The lifespan is assumed to terminate at 100 years of age. *Panels **A**, **B**, **C**:* Dynamics of *i*Aβ accumulation in AD-affected neurons and the progression of the disease in the wild-type AβPP carriers in the absence of treatment. In panel ***A***, the $\mathbf{T^0}$ levels exceed those of **T1** and no AACD occurs. In panels ***B*** and ***C***, the $\mathbf{T^0}$ threshold is lower than **T1**. AACD commences upon crossing of the $\mathbf{T^0}$ threshold and evolves into AD when the **T1** threshold is crossed (panel **B**) or continues for the remaining lifespan if the **T1** threshold is not crossed (panel **C**). *Panels **A′**, **B′***: Dynamics of AβPP-derived *i*Aβ accumulation following a transient *i*Aβ depletion treatment administered prior to the crossing of the T1 and T^0 thresholds. The *i*Aβ population is collapsed and its accumulation is resumed from a low baseline. The duration of the treatment is defined by the desired extent of *i*Aβ depletion and could be as short as few days, akin to an antibiotic treatment's regimen. As shown, *i*Aβ is completely (or nearly completely) depleted and its build-up to the **T1** and $\mathbf{T^0}$ levels would exceed an individual's lifespan; no disease would occur. *Panel **C′***: A transient *i*Aβ depletion treatment is applied to AACD patient after the $\mathbf{T^0}$ crossing. *Following the depletion, iAβ levels are well below the $\mathbf{T^0}$ threshold and the patient is technically cured of AACD* (subject to complete recovery of the affected neurons following the *i*Aβ depletion treatment). As shown, de novo accumulating AβPP-derived *i*Aβ does not reach the $\mathbf{T^0}$ threshold and AACD does not recur within the remaining lifetime of the treated patient. Note that whereas complete or nearly complete *i*Aβ depletion is shown in panels **A′**–**C′**, any reduction in its baseline would be therapeutically beneficial in proportion to the extent of the depletion.

The transient *i*Aβ depletion treatment option is clearly the preferable as well as the enactable one: Just find a way, any way, to transiently deplete *i*Aβ. It is a "one better" scenario versus the mode of operation of the Icelandic AβPP mutation. Indeed, the latter is physiologically constrained because the physiology, being inertial and limited to "continuous" processes, is incapable of sharply discontinuous transient actions available to us as illustrated in panels **A′, B′** and **C**′ of Figure 11. The identical end-results, in terms of the prevention of the **T1** and $\mathbf{T^0}$ thresholds crossing and, consequently, of the occurrence of AD and AACD, are reached in panels **A′** and **B**′ of Figure 11 versus panels **A′** and **B′** of Figure 10, but these results are achieved with the drastic disparity in the duration of the treatment.

The duration of the *i*Aβ depletion treatment is defined by the desired extent of depletion and potentially could be as short as few days, a regimen possibly akin to that of an antibiotic treatment. Importantly, the *i*Aβ depletion does not need to be complete to be effective; any reduction in its baseline would be therapeutically meaningful and beneficial (in proportion to the extent of the depletion) because it would increase the duration of time required for the crossing of the $\mathbf{T^0}$ and **T1** thresholds and for the occurrence of AACD and AD, thus causing, if not the prevention, then at least a delay in the commencement of a disease. Moreover, the same therapeutic strategy, i.e., transient *i*Aβ depletion treatment, is also applicable to symptomatic stages of both AD and is discussed and illustrated in following sections below.

As for the treatment of AACD patients (panels **C**′ of Figures 10 and 11), whereas the suppression of the rate of accumulation of AβPP-derived *i*Aβ (Figure 10) can at best stop the progression of the disease, sufficient *i*Aβ depletion (Figure 11) is potentially capable of curing the condition. Drugs suppressing AβPP-derived *i*Aβ accumulation are likely incapable of its sufficiently deep depletion [3] and a principally different type of drugs could be necessitated. Such type of AD/AACD drugs, capable of targeted degradation of *i*Aβ, as well as potential outcomes of its implementation, is discussed in the following sections below.

18. ACH2.0-Based Therapeutic Strategy for Treatment of AD at Its Symptomatic Stages

The preceding section described therapeutic strategies for the prevention of AD and AACD and for the treatment of AACD in symptomatic patients. These strategies are based on the ACH2.0 interpretation of both conditions and guided by our understanding of the mechanism of action of the protective Icelandic Aβ mutation. As discussed in the present section, the same guiding principles can be also applied for achieving the, arguably, ultimate goal: Effective treatment of AD at its symptomatic stages. To better orient the reader, a compendium of potential therapeutic options for symptomatic AD is briefly analyzed as follows.

18.1. Therapeutic Options for the Symptomatic Stages of AD

18.1.1. Approaches That Failed or Are Impractical

As was mentioned above, a number of ACH-based candidate AD drugs were developed and performed spectacularly in preclinical studies. They all failed as spectacularly in human clinical trials when administered at various symptomatic stages of AD. In the framework of the ACH2.0, this failure was inevitable because, in this paradigm, the occurrence of AD symptoms signifies that the AβPP-independent, self-sustaining *i*Aβ generation pathway had been activated in most or in all affected neurons (the recently observed effect of lecanemab and donanemag in symptomatic AD appears to be due to the early timing of its administration; the drugs target preventively a marginal subset of affected neurons that did not yet reach and cross the **T1** threshold, hence their marginal effect [3]). At this point the contribution of the AβPP proteolytic pathway into neuronal *i*Aβ pool is rendered negligible and insignificant (in comparison with the contribution of the AβPP-independent *i*Aβ generation pathway) and any attempted interference with this pathway or with secreted Aβ produced in this pathway would be futile [1–3].

The consequence of the above considerations is that the only potentially successful therapeutic strategy subsequent to symptomatic manifestation of AD is targeting the AD Engine or the components thereof. The components of the AD Engine are lucidly depicted in Figure 1 above. They include *i*Aβ, a mediator in the self-perpetuating cycle that constitutes the AD Engine; the compounds and processes necessary for the initiation of the AβPP-independent *i*Aβ production, such as the *i*Aβ-mediated activation of eIF2α kinases; the integrated stress response; and, finally, the AβPP-independent pathway of *i*Aβ generation. The rationale for the AD-Engine-targeting strategy is obvious. The principal product of the AD Engine is *i*Aβ. It not only propagates the activity of the Engine but also drives the AD pathology. A successful interference with the operation of the AD Engine would, therefore, not only cease the *i*Aβ production in the AβPP-independent pathway but would also interrupt the progression of the disease.

Implementing this strategy, however, is not simple. Inhibiting cellular pathways that are required for and result in the initiation of the AβPP-independent production of *i*Aβ would be quite demanding either because of the built-in redundancies or due to the principal function of a putative target in normal cellular physiology. For example, the ISR was shown to be elicited in neuronal cells by the activated PKR and HRI kinases via the phosphorylation of eIF2α. To suppress the latter, both PKR and HRI need to be inhibited. However, even if the concurrent inhibition of both kinases were feasible, it would be unproductive in preventing phosphorylation of eIF2α because such inhibition would result in a compensatory activation of alternative eIF2α kinases [63]. Interfering with the eIF2α to P-eIF2α conversion upstream of the ISR via the manipulation of PP1 phosphatase, CReP, or GADD34 [63] is not feasible because of the principal role of eIF2α in cellular functioning. Likewise, and for the same reason not feasible is the interference with the downstream ISR targets such as ATF4, ATF5 and CHOP transcription factors [63].

Targeting the AβPP-independent *i*Aβ generation pathway is also problematic for more than one reason. First, the nature of the mechanism enabling this pathway is not understood with sufficient certainty; whereas the asymmetric amplification of AβPP mRNA is the most likely possibility (see below), the three other mechanisms described below are

also optionally valid [1]. The second reason is that the underlying mechanism could be physiologically vital and cannot be interfered with by a broad approach. Thus, for example, mRNA amplification in mammalian cells was shown to be crucial for multiple fundamental cellular functions [104–107] and, as such, cannot be manipulated without a probable detrimental effect. One plausible way to interfere narrowly and *specifically* with the AβPP-independent *i*Aβ production (regardless of the nature of the underlying mechanism) is via site-specific intervention at the ATG encoding Met671 of AβPP and/or surrounding nucleotides [1]. If the initiation of translation from this position were disabled, no AβPP-independent *i*Aβ production would occur (see details below). This approach, presumably through genome editing, is, however, currently unfeasible in humans (but can be used in experimental models). It should be also noted that even if the disabling of the AβPP-independent *i*Aβ production pathway were feasible, it would not interfere in any way with the occurrence of AACD, which is driven solely by AβPP-derived *i*Aβ because in such a case, as described above, AACD would commence when AβPP-derived *i*Aβ levels reach the $\mathbf{T^0}$ threshold and would continue for the remaining lifespan of an individual.

Therefore, the sole remaining therapeutic option for symptomatic stages of AD is lowering the levels of *i*Aβ below those needed for the activation of the AβPP-independent *i*Aβ production pathway and, consequently, for the operation of the AD Engine. An apparent logical approach toward this goal is the suppression of the activity of gamma-secretase. This would alter the generation of *i*Aβ not only by AβPP proteolysis but also in the AβPP-independent pathway (see details below) and would eventually lower its levels. This strategy was tried, with detrimental results, in multiple studies, including clinical trials [108–111], and was eventually forsaken. The reasons for this failure eventually become clear: gamma secretase is an important member of the Notch pathway with many C99-unrelated substrates and, therefore, cannot be interfered with without deleterious consequences. Modulating gamma-secretase activity with the goal of producing shorter, more benign isoforms of Aβ has also proven so far less than satisfactory [110–113].

18.1.2. Potentially Feasible Therapeutic Strategy: Activation of Alpha-Secretase

Another strategy to lower levels of *i*Aβ is the activation of alpha-secretase. This would increase the cleavage within Aβ, at its lysine 16, and, consequently, would both reduce the rate of *i*Aβ production and deplete its preexisting pool. This possibility was addressed [114–119] and the evidence of therapeutic benefits of such an approach has been obtained in multiple studies [119–122]. This strategy, however, is burdened with potential complications of the same type that invalidated therapeutic application of gamma-secretase inhibitors. This is because alpha-secretase belongs to the ADAM family of proteases. Its exogenous overexpression in cellular models (i.e., the increase in its activity) affected more than three hundred genes [123]. Moreover, it appears that alpha-secretase is involved in certain Notch-controlled pathways [124]. These considerations explain the well-justified prudence with advancing the utilization of alpha-secretase-activating agents as potential AD therapy.

18.2. Activation of Aβ-Cleaving Activities of BACE1 and/or BACE2: A Rational, Intuitive and Feasible Therapeutic Option in the ACH2.0 Perspective

There is, however, one potential therapeutic option that offers all benefits described above but without associated disadvantages. In this approach, the stated goal of lowering *i*Aβ level, and potentially substantially depleting it, is achieved by its targeted degradation via the activation of Aβ-cleaving capabilities of one or both variants of beta-secretase, BACE1 and BACE2. In view of the previously attempted extensive utilization of BACE1 inhibitors as potential AD drugs, a project that required tremendous investment of funds, research, and development efforts, the proposed use of the diametrically opposite strategy, namely the employment of BACE1 and BACE2 activators, may appear radical and counter-intuitive. It is, however, neither. *The proposed utilization of BACE1/BACE2 activators (or, in fact, of any other suitable iAβ-depleting agent) is a no less justifiable, rational, logical, intuitive and*

feasible AD therapy in the ACH2.0 paradigm than the attempted employment of BACE inhibitors was (when it was proposed and implemented) in the ACH perspective.

To appreciate the above assertion, consider the following brief summary of the relevant empirical data [4,5,125–128]:

(**a**) It was demonstrated that BACE1 cleaves not only at the β site, thus generating the N-terminus of C99 and of Aβ, but also at the β′ site ten residues downstream. (**b**) BACE1 cleavage at the β′ site occurs equally efficiently within AβPP, C99 and Aβ. (**c**) Exogenous overexpression of BACE1 in mouse models increased the rate of cleavage at the β′ site as well as the ratio of the N-truncated versus full-size Aβ. (**d**) Exogenous overexpression of human BACE1 substantially decreased Aβ deposition in mouse brain. (**e**) As described above, the protection conferred by the Icelandic AβPP mutation upon its carriers is apparently due to the elevated rate of BACE1 cleavage at the β′ site.

In addition to the β′ site cleavage, multiple studies [129–132] demonstrated that BACE1 cleaves also at residues 34/35 of human Aβ; the rate of this cleavage increased significantly when BACE1 was overproduced exogenously. The BACE1 cleavage at residues 34/35 of Aβ produces $Aβ_{34}$, an intermediate in Aβ clearing. It appears, therefore, that a sufficient elevation of Aβ-cleaving activities of BACE1 is capable of depleting neurons of iAβ, thus ceasing the progression of AD if implemented at symptomatic stages or preventing its occurrence if employed prior to manifestation of AD symptoms.

BACE2 activation could be equally, if not more effective in depleting *i*Aβ in affected neurons. Whereas it is capable of cleavage at the β site of AβPP, its *main* activity is to cleave *within* Aβ in two positions, at residues 19 and 20 (both phenylalanines) [102]. It appears that the physiological role of BACE2 is to limit the generation of Aβ. When BACE2 is inhibited in model systems, the production of Aβ substantially increases [103]. This BACE2 function appears to be a naturally occurring protective mechanism, a notion that is strongly supported by the effect of the Flemish FAD mutation at the residue 21 of Aβ. The Flemish FAD mutation suppresses the capacity of BACE2 to cleave within Aβ. This results in the elevation of *i*Aβ levels in mutation carriers and, consequently in the early onset of AD [62].

Therapeutically, the activation of BACE2 at the symptomatic stages of AD would deplete *i*Aβ and stop the progression of the disease. When implemented prior to manifestation of the symptoms, it would prevent the disease. This strategy constitutes, in fact, the augmentation of the physiological protective function of BACE2. Since the cleavage within Aβ (rather than at the β site) is the predominant activity of BACE2 and because it appears to be employed physiologically in the protective role, the employment of BACE2 activators is, apparently, physiologically more suitable than that of BACE1 enhancers. If only one, BACE1 or BACE2, protease can be manipulated in the therapeutic application, the utilization of BACE2 activation seems more advantageous. On the other hand, it would be most efficient in concert with the activation of BACE1. This is because the two not only target discrete Aβ sites but are also situated in distinct subcellular locations [133].

Potentially, a treatment, which activates Aβ-cleaving capabilities of BACE1- and/or BACE2 and is administered for only limited duration, could accomplish a sufficient depletion of *i*Aβ and thus open the possibility of once-in-a-lifetime-only curative or preventive therapy for AD (as described in Section 17.2 above, it would be no less efficient in the prevention and treatment of AACD). This possibility is further discussed and illustrated in the following section below.

19. AD Therapy at Symptomatic Stages: Once-in-a Lifetime Transient *i*Aβ Depletion Therapy via Its Targeted Degradation Would Potentially Stop the Progression of the Disease

As described above, the AD Engine, i.e., the AβPP-independent *i*Aβ production pathway, which drives the disease, requires certain levels of *i*Aβ for its activation and operation. These levels are maintained by the continuous influx of *i*Aβ generated in the AβPP-independent pathway and, in turn, sustain and perpetuate the operation of the pathway and of the Engine. The goal of the proposed *i*Aβ depletion therapy at the symptomatic

stages of AD is to bring *i*Aβ levels below the **T1** threshold, the *i*Aβ level required for the activation of the AβPP-independent *i*Aβ production pathway. When this happens, the AβPP-independent *i*Aβ production would be switched off, the influx of *i*Aβ generated in this pathway would cease, the AD Engine would be rendered inoperative, the progression of the disease would stop and AD-affected neurons that remained viable would be allowed to recover and reconnect. The depletion of *i*Aβ would not affect, however, the AβPP proteolytic pathway; it would remain operational regardless of the *i*Aβ levels. If the *i*Aβ depletion treatment were transient, the duration of its effect would be identical to the time interval required for the restoration of *i*Aβ (produced at this point solely in the AβPP proteolytic pathway) to the **T1** threshold levels, for the consequent re-activation of the AβPP-independent *i*Aβ production pathway and the AD Engine, and for the recurrence of the disease. The therapeutic efficiency of the transient *i*Aβ depletion treatment would, therefore, directly depend on the degree of depletion: the "deeper" it is, the more time is required for the restoration of the levels of AβPP-derived Aβ to the **T1** threshold and consequent activation of the AβPP-independent *i*Aβ production pathway and the recurrence of the disease. Ultimately, with the *i*Aβ depletion sufficiently "deep", the duration required for the de novo accumulation of AβPP-derived *i*Aβ to the **T1** threshold would exceed the remaining lifespan of a patient and the disease would not recur.

Figure 12 illustrates the effects of *i*Aβ depletion therapy administered at various symptomatic stages of AD. In this Figure, it is presumed that the transient elevation of Aβ-cleaving activities of BACE1 and/or BACE2, or the limited-duration employment of any other appropriate *i*Aβ depletion agent, results in complete or nearly complete (sufficiently "deep", as discussed above) depletion of *i*Aβ. It is also envisioned that the rate of accumulation of *i*Aβ produced in the AβPP proteolytic pathway and the extent of the **T1** threshold following *i*Aβ depletion therapy are similar to the same values prior to the depletion treatment. As depicted in Figure 12, the *i*Aβ depletion treatment is implemented either when symptomatic manifestation of the disease has just commenced (panel **A**) or at more and more advanced stages of AD (panels **B** through **D**). At each stage depicted in the figure, the transient administration of the *i*Aβ depletion therapy results in a "deep" reset of the level of *i*Aβ in neurons that survived and remained viable.

At the early symptomatic stage of AD (panel **A** of Figure 12), this category includes the majority of the affected neurons. Following the reset of the *i*Aβ levels, the activity of the AβPP-independent *i*Aβ production pathway ceases, operation of the AD Engine stops, and viable affected neurons are allowed to recover and reconnect. The production of *i*Aβ at this stage occurs only in the AβPP proteolytic pathway. The accumulation of newly produced *i*Aβ commences from a low baseline, and its build-up to the **T1** threshold would be of a long duration, exceeding that of the remaining lifespan of a patient. Consequently, the AβPP-independent *i*Aβ generation pathway would not be activated, the AD Engine would remain inoperative and the AD would not recur within patient's lifetime. Since the majority of AD-affected neurons would be redeemed, the prognosis for patient stabilization and, possibly, a significant cognitive recovery would be good.

With the progression of AD, at its more advanced stages, increasing number of the affected neurons cross the **T2** threshold and commit apoptosis. This leaves progressively smaller number of the affected neurons that retained their viability and can be redeemed. This progression is depicted in panels **B, C**, and **D**. The administration of transient *i*Aβ depletion therapy and the following reset of the *i*Aβ baseline would result in inactivation of the AβPP-independent *i*Aβ production pathway, and would allow the ever decreasing number of viable AD-affected neurons to recover and restore their functionality. At this point, the prospect of stopping the progression of the disease is, apparently, as good as at the early stages of the disease, but cognitive functions would be increasingly unlikely to be significantly restored; the probability of such an occurrence would be proportional to the fraction of the affected neurons that were redeemed by *i*Aβ depletion via its targeted degradation by the Aβ-cleaving activities of BACE1 and/or BACE2 or by any other suitable

agent. As reasoned above, following the *i*Aβ depletion, the disease would not recur within the remaining patient's lifespan.

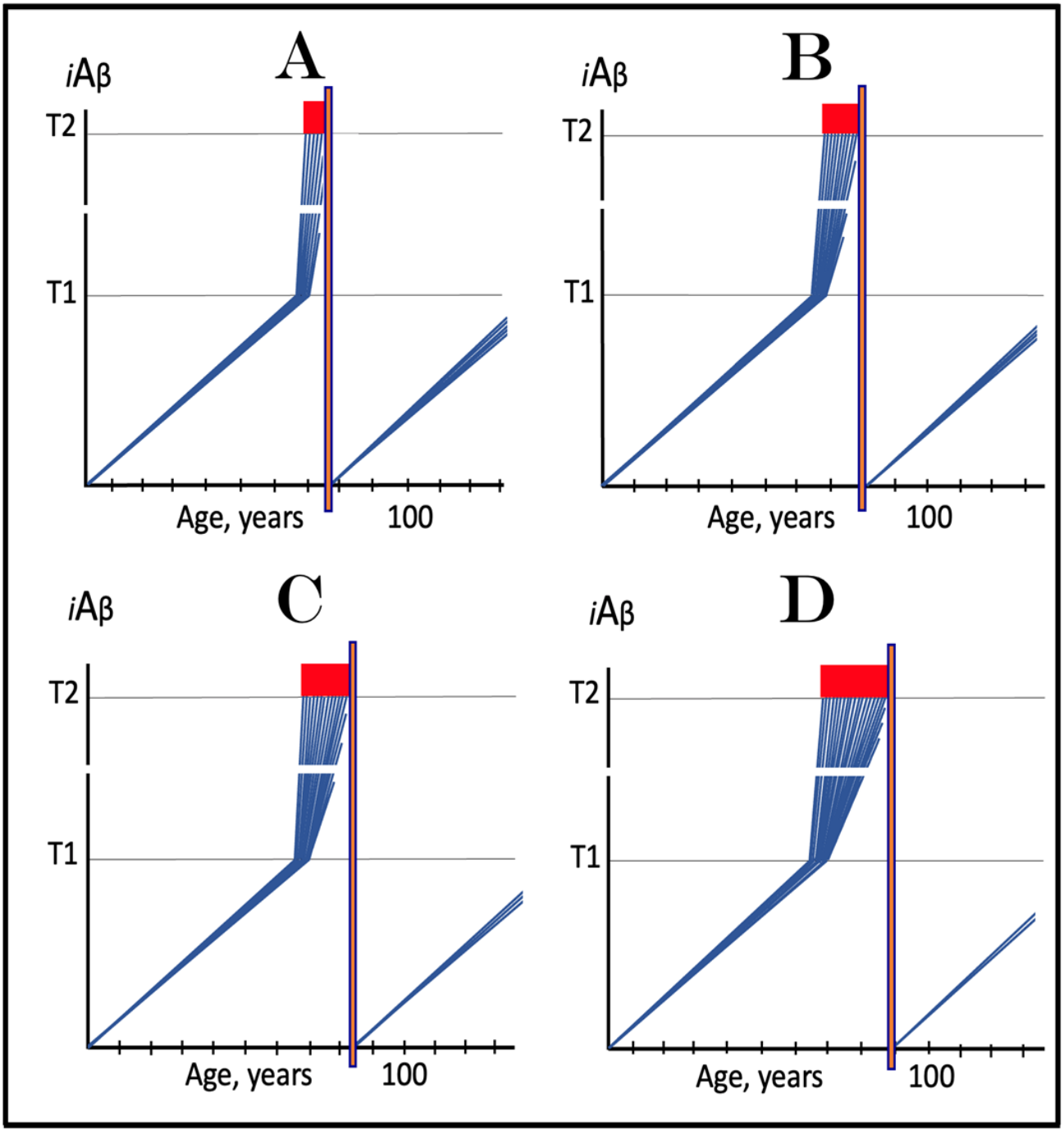

Figure 12. Effect of transient *i*Aβ depletion therapy via its targeted degradation at various symptomatic stages of AD. Blue lines: affected neurons. *iA*β: Level of intraneuronal Aβ. ***T1*** *threshold*: Levels of *i*Aβ triggering elicitation of the ISR, initiation of AβPP-independent production of *i*Aβ, activation of the AD Engine, and the commencement of the second stage of AD. ***T2*** *threshold*: Levels of *i*Aβ triggering neurons' entrance into the apoptotic pathway. *Red blocks*: Apoptotic zone. *Orange boxes:* Active transient *i*Aβ depletion via its targeted degradation by Aβ-cleaving activities of BACE1 and/or BACE2 or by any other suitable agent; levels of *i*Aβ are reset and the accumulation

of AβPP-derived *i*Aβ resumes from a low baseline. *Panel **A***: The transient *i*Aβ depletion therapy is implemented at the early symptomatic stage of AD, when the bulk of the affected neurons are still viable. Following the reset of *i*Aβ levels, its build-up starts de novo, supported only by the AβPP proteolytic pathway. It is anticipated that *i*Aβ levels will not reach the **T1** threshold and AD will not recur within the remaining lifetime of an SAD patient. *Panels **B**, **C**, and **D***: The transient *i*Aβ depletion treatment is implemented at progressively advanced stages of AD. The results are analogous to those depicted in panel **A**. However, at this AD stages increasing number of affected neurons cross the **T2** threshold and commit apoptosis. This leaves a progressively smaller number of affected neurons that retained their viability and can be redeemed.

20. Dynamics of *i*Aβ Accumulation and of the Disease at Symptomatic AD Stage

Above, we analyzed the dynamics of accumulation of AβPP-derived *i*Aβ and the role of the extents of the $\mathbf{T^0}$ and **T1** thresholds in the commencement of AACD and of the second, symptomatic, stage of AD. The event that signifies and defines the second AD stage is the activation of the self-perpetuating AβPP-independent *i*Aβ production pathway, which drives the disease [1–3]. At this stage, the accumulation of *i*Aβ produced by AβPP proteolysis continues, presumably at the same rate as prior to the crossing of the **T1** threshold, but now it is rendered marginal and inconsequential (due to its now marginal contribution into the *i*Aβ pool) because the entire output of Aβ produced independently of AβPP is retained intraneuronally and perpetuates the operation of AβPP-independent *i*Aβ generation pathway, i.e., its own production [1–3]. Whereas at the first, asymptomatic, AD stage, the AβPP-derived *i*Aβ-initiated cascade is relatively benign and involves the activation of eIF2α kinases and elicitation of the ISR, at the second AD stage *i*Aβ produced independently of AβPP drives a much more perilous cascade that involves the formation, presumably through a chain of events, including the *i*Aβ-mediated inhibition of the ubiquitin–proteasome system [134–137], of tau tangles, and ultimately results in neuronal loss.

The factors determining the dynamics of *i*Aβ accumulation and of the disease at the second AD stage are superficially similar to those operating at the first stage of AD: a rate of accumulation and the extent of a threshold. But at the second AD stage, these parameters are the rate of accumulation of *i*Aβ produced independently of AβPP (rather than of AβPP-derived *i*Aβ) and the extent of the **T2** (rather than of **T1**) threshold, which is a "point of no return" since its crossing triggers the apoptotic pathway. Accordingly, the timing of the end stage of the disease is inversely proportional to the rate of *i*Aβ accumulation and directly proportional to the extent of the **T2** threshold. Indeed, the higher the rate of *i*Aβ accumulation, the faster the progression of AD and the sooner would the end stage be reached; the higher the extent of the **T2** threshold, the greater the timing of the occurrence of the end stage of the disease.

These relationships are presented diagrammatically in Figure 13. In this Figure, the kinetic parameters of AβPP-derived *i*Aβ accumulation up to and including the crossing of the **T1** threshold are identical in all panels whereas the kinetic parameters following the **T1** crossing and the commencement of the second AD stage are different. In panels **A** and **A′**, the extent of the **T2** threshold is the same, but the rates of accumulation of *i*Aβ produced in the AβPP-independent *i*Aβ production pathway are different. It is much greater in panel **A** than in panel **A′**. Accordingly, as discussed above, the rate of progression of the disease is much slower, the timing of its symptomatic manifestation is significantly greater, and its duration is substantially longer in panel **A′** than in panel **A**.

In panels **B** and **B′**, both the extent of the **T2** threshold and the initial (fastest) rate of accumulation of *i*Aβ produced independently of AβPP are identical but the stochastic distribution of the latter in the affected neurons is much wider in panel **B′** than in panel **B**. Accordingly, the duration of the disease is significantly longer in panel **B′** than in panel **B**. In panels **C** and **C′**, the rate of accumulation of *i*Aβ produced in the AβPP-independent *i*Aβ production pathway and it stochastic distribution in the affected neurons are the same, but the extents of the **T2** threshold differ. In panel **C′**, it is substantially higher than in panel

C. Consequently, the timing of the symptomatic manifestation of the disease is greater and the duration of the disease is significantly longer in panel **C′** than in panel **C**.

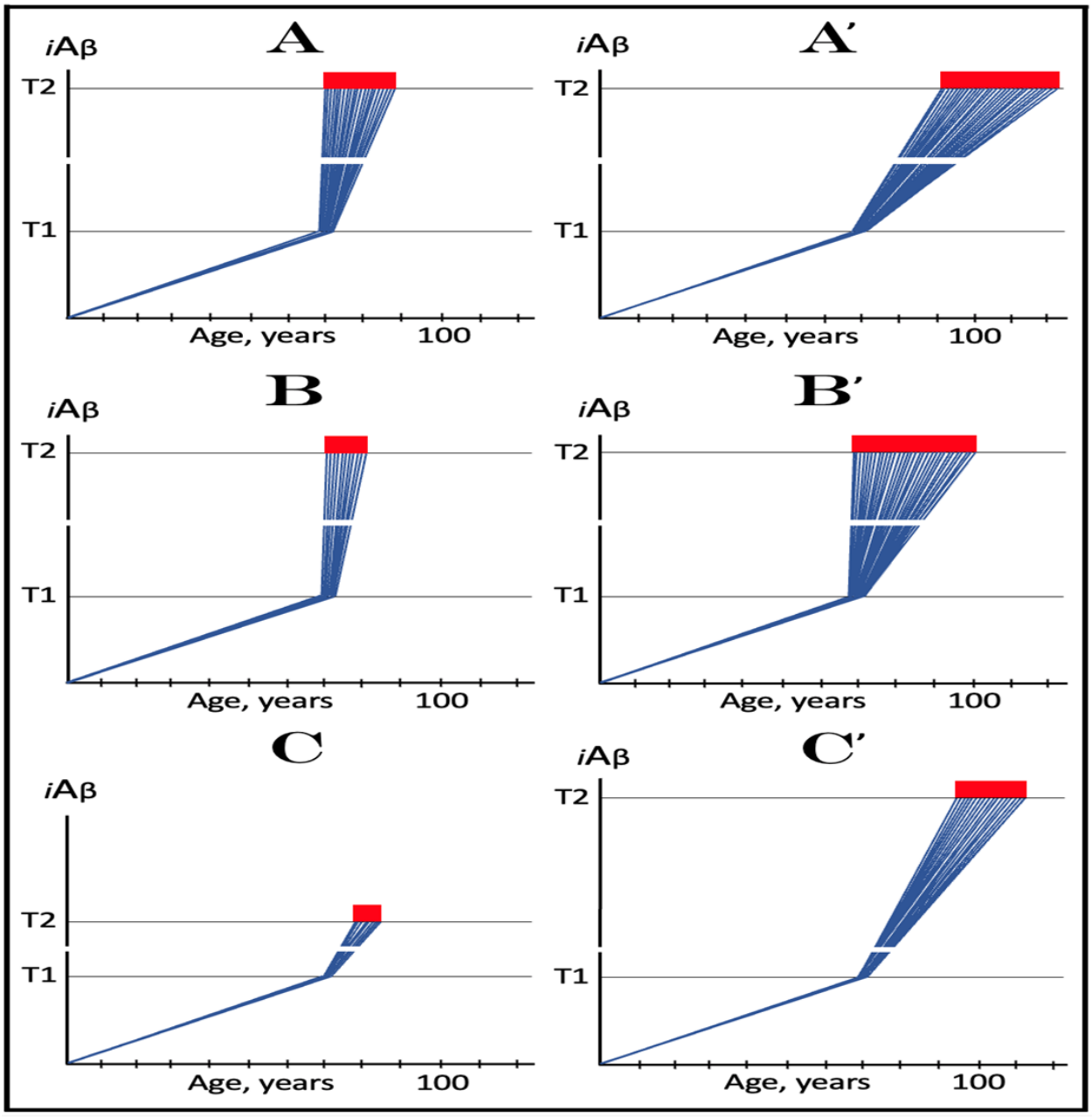

Figure 13. Dynamics of *i*Aβ accumulation and of the disease at the second, symptomatic stage of AD. *Blue lines*: Affected neurons. *iA*β: Levels of intraneuronal Aβ. ***T1*** *threshold*: Levels of *i*Aβ triggering elicitation of the ISR, initiation of AβPP-independent production of *i*Aβ, activation of the AD Engine and the commencement of the second stage of AD. ***T2*** *threshold*: Levels of *i*Aβ triggering neurons' entrance into the apoptotic pathway. *Red blocks*: Apoptotic zone. All kinetic parameters up to and including the crossing of the **T1** threshold are identical in all panels whereas the kinetic parameters following the **T1** crossing and the commencement of the second AD stage are different. In panels **A** and **A′,** the extent of the **T2** threshold is the same but the rates of accumulation of *i*Aβ produced in the AβPP-independent *i*Aβ production pathway are different. It is much greater in panel **A** than in panel **A′**. Accordingly, the rate of progression of the disease is much slower, the timing of its symptomatic manifestation is significantly greater, and its duration is substantially longer in panel **A′** than in panel **A.** In panels **B** and **B′,** both the extent of the **T2** threshold and the initial (fastest) rate of accumulation

of *i*Aβ produced independently of AβPP are identical but the stochastic distribution of the latter in the affected neurons is much wider in panel **B′** than in panel **B**. Accordingly, the duration of the disease is significantly longer in panel **B′** than in panel **B**. In panels **C** and **C′,** the rate of accumulation of *i*Aβ produced in the AβPP-independent *i*Aβ production pathway and it's stochastic distribution in the affected neurons are the same but the extents of the **T2** threshold differ. In panel **C′,** it is substantially higher than in panel **C**. Consequently, the timing of the symptomatic manifestation of the disease is greater and the duration of the disease is significantly longer in panel **C′** than in panel **C**.

None of the kinetic parameters discussed in the present section and illustrated in Figure 13 have a conceptual impact on the proposed therapeutic strategy at symptomatic stages of AD, namely the *i*Aβ depletion via its targeted degradation by the Aβ-cleaving activities of BACE1 and/or BACE2 or by any other suitable agent. On the other hand, their combined variability offers a plausible explanation for a well-documented phenomenon: a sequential manifestation of AD pathology in the defined rejoins of the affected brain. This aspect of the disease is discussed in the following section below.

21. Sequential Manifestation of the AD Pathology in Defined Brain Compartments. Implications for the *i*Aβ Depletion Therapy at the Early Symptomatic Stages of AD

21.1. Rate of Accumulation of iAβ Produced Independently of AβPP May Differ in Diverse Regions of the Affected Brain

It could be presumed that the stochastically distributed (in individual AD-affected neurons) rate of accumulation of *i*Aβ produced in the AβPP-independent *i*Aβ generation pathway in the second, symptomatic stage of AD and the extent of the **T2** threshold are patient-specific and identical throughout the affected brain. This assumption would imply that the rate of temporal progression of the AD pathology is also the same throughout the AD-affected brain. This implication, however, is patently invalid because one of the principal documented features of AD is the temporally sequential nature of the occurrence of the AD pathology in the various defined regions of the affected brain.

Above, we concluded, on the basis of the available empirical data, that in the majority of, if not in all, AD-affected neurons, *i*Aβ levels reach and cross the **T1** threshold within a narrow time window. This means that the second stage of AD commences within close temporal proximity in all neurons affected by the disease. Yet, it is the basic knowledge that the AD pathology occurs in different defined parts of the brain as a widely distributed temporal function. Indeed, anatomical and histological studies of AD-affected brains concluded that the neurodegeneration begins within the second layer of the entorhinal cortex followed by its occurrence in the hippocampus, temporal cortex, frontoparietal cortex, and subcortical nuclei [138]. Moreover, each compartment of the brain exhibits the neuropathology in the gradual and defined manner. For example, in the hippocampus, the CA1 area is affected first, followed sequentially by the areas CA2, CA3 and DG [139].

The question is then, how to reconcile the relatively concurrent **T1** crossings and the commencement of the second AD stage in all affected neurons, throughout the entire brain, with the widely spread, over many years, effects of the disease in various compartments of the brain? One plausible answer lies in the variably wide stochastic distribution of the rate of accumulation of *i*Aβ produced independently of AβPP in and, consequently, of the distribution of the **T2** threshold (assumed in this interpretation to be the same throughout the affected brain) crossings by the affected neurons, postulated in the preceding section. It necessitates that different (yet overlapping) segments of the overall stochastic distribution spectrum represent affected neurons from different, distinctly defined parts of the brain; i.e., *i*Aβ crosses the **T2** threshold sequentially in diverse regions of the AD-affected brain. For this to occur, the average rate of *i*Aβ accumulation should differ in different parts of the brain due to either diverse, brain compartment-specific efficiencies of the AβPP-independent *i*Aβ generation pathway or varied rates of *i*Aβ clearing. In each defined brain compartment, the stochastic nature of the **T2** threshold crossings would be local yet overlapping to form the overall spectrum that defines the duration of AD.

This notion is illustrated in Figure 14. In this Figure, the lines of different colors above the **T1** threshold represent *i*Aβ levels in the affected neurons in defined regions of the afflicted brain whereas panels **A** through **D** of Figure 14 provide diagrammatic snapshots of progressive stages of AD. Panel **A** of Figure 14 illustrates an early AD stage. Only a fraction of the affected neurons in only a single defined brain compartment reached and crossed the **T2** threshold and committed apoptosis. In panels **B** and **C**, as the disease progresses, all affected neurons in the first (red) compartment cross the **T2** threshold and commit apoptosis, and similar accession toward and crossing of the **T2** threshold occurs sequentially in the defined compartments of the affected brain. In panel **D**, all affected neurons reached and crossed the **T2** threshold in all defined compartments of the afflicted brain; this is the end stage of the disease.

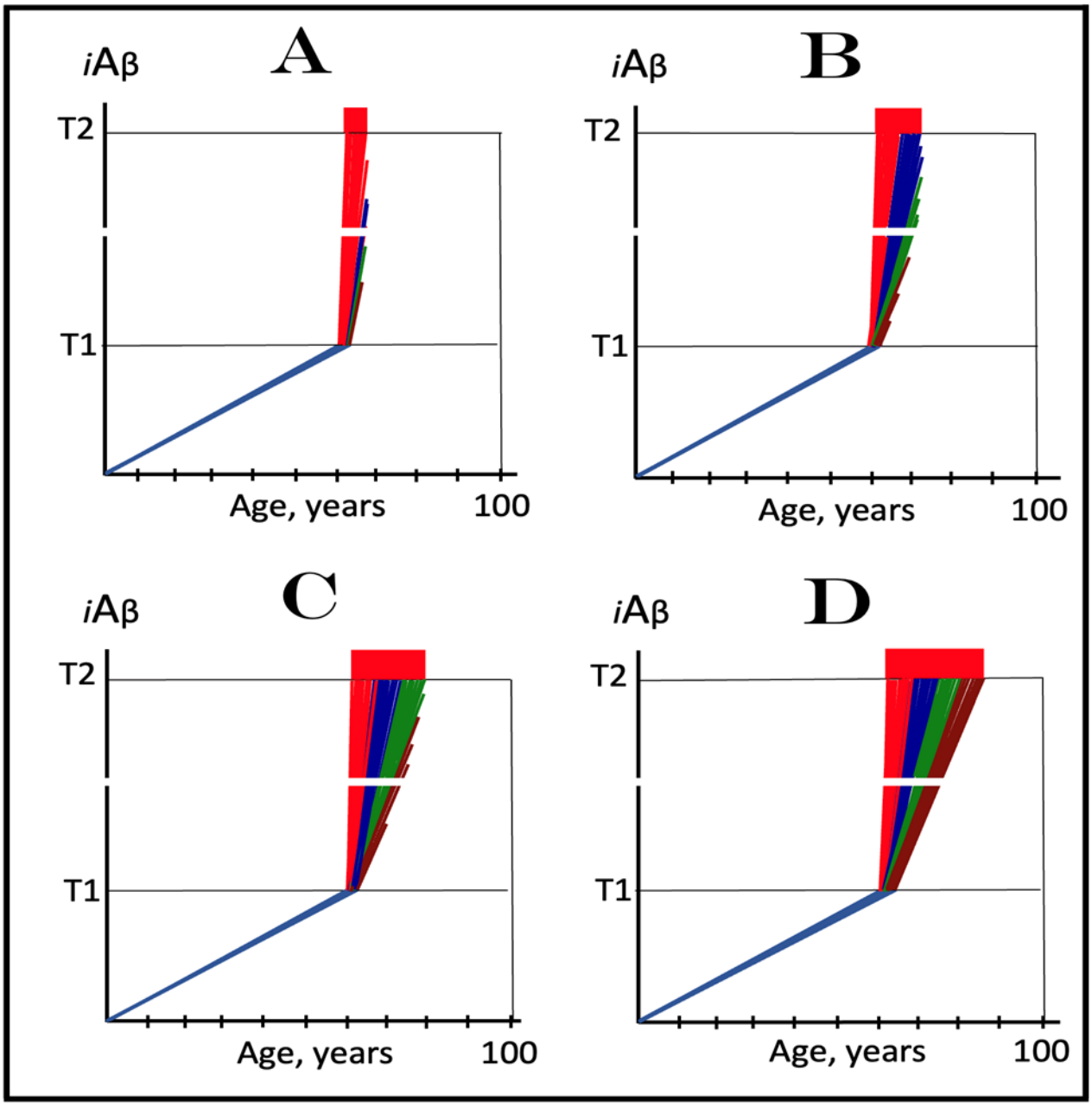

Figure 14. Sequential manifestation of the AD pathology in defined brain compartments: The rate of accumulation of *i*Aβ produced independently of AβPP differs in diverse regions of the affected brain.

*i*Aβ: Level of intraneuronal Aβ. ***T1*** *threshold*: Level of *i*Aβ level triggering elicitation of the ISR, initiation of AβPP-independent production of *i*Aβ, activation of the AD Engine and the commencement of the second stage of AD. ***T2*** *threshold*: Levels of *i*Aβ triggering neurons' entrance into the apoptotic pathway. *Red blocks*: Apoptotic zone. Each line represents individual affected neurons. *Lines of different colors above the* ***T1*** *threshold*: The affected neurons in various defined parts of the AD-afflicted brain. The rate of *i*Aβ accumulation differs in different parts of the brain, due to either diverse, brain compartment-specific, efficiencies of the AβPP-independent *i*Aβ generation pathway or varied rates of *i*Aβ clearing. *Panel* ***A***: The early symptomatic stage of AD. Only the entorhinal cortex and possibly the hippocampus are affected; neither significant accumulation of *i*Aβ produced in the AβPP-independent pathway, nor AD neuropathology yet occurred in other brain compartments. *Panels* ***B***, ***C***, ***D***: With the progression of AD toward the end stage (panel **D**), *i*Aβ produced in the AβPP-independent pathway accumulates and the AD pathology commences and expends in temporally sequential manner in other defined compartments of the affected brain. Note that if the therapeutic intervention, via transient administration of BACE1 and/or BACE2 activators or of other *i*Aβ-depleting agents, were implemented at an early symptomatic stage of AD (panel **A**), the progression of the disease in the brain compartment already affected at this stage would cease, and the AD pathology would not commence, due to *i*Aβ depletion, in other brain compartments, which would remain largely intact. The progression of AD in the affected brain compartment would not resume and other brain compartments would stay pathology-free for the remaining lifespan of a patient.

The above interpretation of the sequential manifestation of AD pathology in the defined regions of the affected brain has an important implication for treatment of the disease. If the transient *i*Aβ depletion therapy via its targeted degradation by Aβ-cleaving activities of BACE1 and/or BACE2 or by any other suitable *i*Aβ-depleting agent were implemented at an early symptomatic stage of AD, the progression of the disease in the early-affected brain compartment (e.g., panel **A** of Figure 14) would cease, and the AD pathology *would not* occur, due to *i*Aβ depletion, in other brain compartments where it did not yet commence or progressed only insignificantly. *In the early-affected brain region, the disease would not recur (for the reasons discussed in* Section 19*), and other brain compartments would stay pathology-free for the remaining lifespan of a patient.*

21.2. An Alternative Interpretation of Sequential Manifestation of AD Pathology: The Extent of the ***T2*** *Threshold May Differ in Diverse Defined Regions of the Affected Brain*

Assigning different segments of the overall stochastic distribution of the rate of *i*Aβ accumulation in individual affected neurons at the second AD stage to different defined compartments of the brain is not the only scenario capable of explaining temporally sequential occurrence of the AD pathology in the affected brain. Another potential scenario is that in symptomatic AD *i*Aβ levels in affected neurons increase toward the **T2** threshold with the same rate and same stochastic distribution in all brain regions, but the extent of the **T2** threshold differs in different brain compartments. This scenario is illustrated in panel **A** of Figure 15, which shows the dynamics of *i*Aβ accumulation toward the **T2** threshold in different regions in the AD-affected brain (different brain compartments are signified by different colors). The rate of AβPP-independent *i*Aβ accumulation and its stochastic distribution are identical throughout the entire AD-affected brain, but the extents of the **T2** threshold are different in diverse defined brain compartments. Consequently, the **T2** threshold is reached and the affected neurons commit to apoptosis and die at different times in different brain regions. With the variable extents of the **T2** threshold, the affected neurons commit to the apoptotic pathway in a defined brain region-specific mode, and the AD pathology manifests in a sequential temporal order in defined brain compartments. This scenario explains the sequential appearance of lesions associated with the neuronal death and is consistent with the observed sequential appearance of tau tangles (formed in live cells presumably prior to the **T2** threshold crossing) in various defined regions of the AD-affected brain [138].

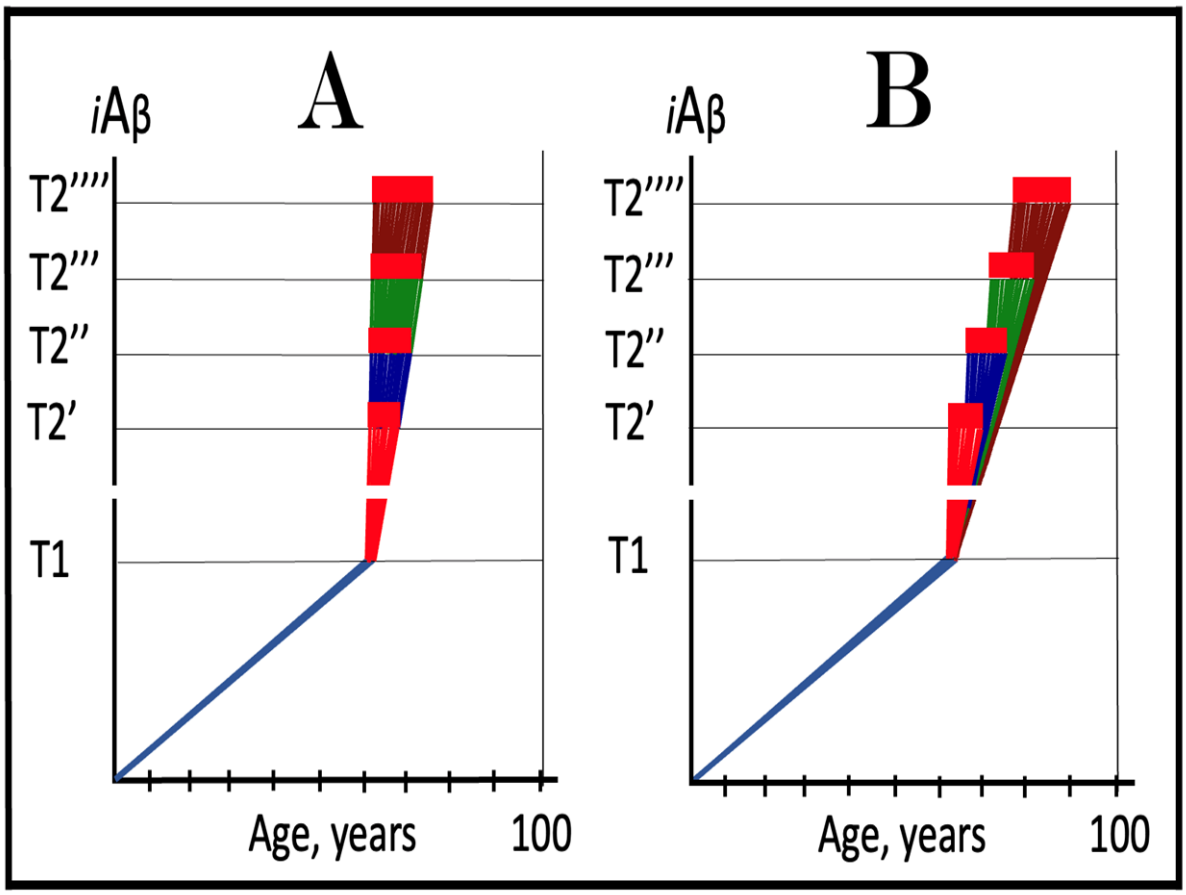

Figure 15. Sequential manifestation of the AD pathology in defined brain compartments: The extent of the **T2** threshold is variable, either separately or simultaneously with the rate of AβPP-independent *i*Aβ accumulation, in distinct defined regions of the affected brain. *iA*β: Level of intraneuronal Aβ. ***T1*** *threshold*: Level of *i*Aβ level triggering elicitation of the ISR, initiation of AβPP-independent production of *i*Aβ, activation of the AD Engine, and the commencement of the second stage of AD. ***T2*** *threshold*: Levels of *i*Aβ triggering neurons' entrance into the apoptotic pathway. *Red blocks*: Apoptotic zone. Each line represents individual affected neurons. ***T2'*** *through* ***T2''''***: Extents of the **T2** threshold in separate define brain compartments. *Lines of different colors above the* ***T1*** *threshold*: The affected neurons in various defined parts (signified by different colors) of the AD-afflicted brain. Dynamics of *i*Aβ accumulation and the disease in separate defined brain regions are superimposed. Levels of AβPP-derived *i*Aβ reach and cross the T1 threshold in a narrow temporal window in all affected neurons throughout the entire brain. Following the T1 crossing, the bulk of *i*Aβ is produced in the AβPP-independent pathway. *Panel* ***A***: The rate of AβPP-independent *i*Aβ accumulation and its stochastic distribution are identical throughout the entire AD-affected brain, but extents of the **T2** threshold are different in diverse defined brain compartments. The **T2** threshold is reached and the affected neurons commit to apoptosis and die at different times in different brain regions; consequently, the AD pathology manifests in a sequential temporal order. *Panel* ***B***: Both the rate of AβPP-independent *i*Aβ accumulation and the extent of the **T2** threshold are variable in separate defined regions of the affected brain and both contribute to sequential temporal manifestation of the AD pathology by determining the timing of its occurrence. Note that the extents of temporal shifts (e.g., in the **T2** threshold crossings) could be significantly greater when both parameters are variable in defined regions of the brain. The depicted inverse proportionality between rates of AβPP-independent *i*Aβ accumulation and extents of the **T2** threshold (panel **B**) is shown for purposes of comparison and graphic convenience only; it is just one of multiple possible combinations of these two parameters in various defined regions of the AD-affected brain.

21.3. A Combination of Two Variable Kinetic Parameters Could Be Responsible for Sequential Manifestation of AD Pathology in Defined Brain Regions

On the other hand, it is distinctly possible that the observed sequential temporal occurrence of the AD pathology in defined brain regions involves a combination of variable kinetic parameters, for example, differential rates of AβPP-independent accumulation of *i*Aβ and differential extents of the **T2** threshold in various defined compartments of the AD-affected brain. This combined scenario is shown in panel **B** of Figure 15. In this scenario, both the rate of AβPP-independent *i*Aβ accumulation and the extent of the **T2** threshold are variable in separate defined regions (signified by different colors) of the affected brain, and both contribute to sequential temporal manifestation of the AD pathology by determining the timing of its occurrence. Note that the extents of temporal shifts (e.g., in the **T2** threshold crossings) could be significantly greater when both parameters (rather than only one as shown in panel **A** of Figure 15) are variable in defined regions of the brain. The depicted inverse proportionality between rates of AβPP-independent *i*Aβ accumulation and extents of the **T2** threshold in panel **B** is shown for purposes of comparison and graphic convenience only; it is just one of multiple possible combinations of these two parameters in various defined regions of the AD-affected brain. Importantly, the proposed transient *i*Aβ depletion therapy via its targeted degradation by Aβ-cleaving activities of BACE1 and/or BACE2 activators or by any other suitable *i*Aβ-depleting agent is equally applicable in all scenarios discussed above.

22. Cellular Mechanisms Capable of the iAβ Generation Independently of AβPP

Generation of *i*Aβ in the AβPP-independent manner is one of the central tenets of the ACH2.0. Indeed, in this theory of AD, the activation of the self-perpetuating AβPP-independent *i*Aβ production pathway is the pivotal event in the etiology of AD, which marks the commencement of the disease. Because of its presumably vast output, this is the process that, when active, renders the contribution of the AβPP proteolytic pathway to the cellular *i*Aβ pool insignificant for progression of the disease and its targeting for therapeutic purposes futile. This is why the understanding of the mechanism that generates *i*Aβ independently from AβPP is of crucial importance for elucidating the disease. Moreover, as discussed above, because of its presumed role, this mechanism and its components constitute the prime therapeutic targets in AD.

22.1. The Centrality of the AUG Codon for Met671 of AβPP in the Presumed AβPP-Independent Production of iAβ

At least four known cellular mechanisms (see below) are capable of producing Aβ independently of AβPP. As elaborated below, they all share the key common feature: In every conceivable mechanism of AβPP-independent generation of Aβ, translation initiates at the AUG encoding methionine 671 of AβPP. The possibility that, in AD, Aβ is produced independently from AβPP by translation initiating at this AUG codon was first posited by Breimer and Danny in 1987 [140], the year when human AβPP cDNA was synthesized, cloned and sequenced simultaneously by several groups [141–143]. In their study [140], Breimer and Danny noted that C99 and Aβ-encoding portion of human AβPP DNA is preceded immediately, contiguously and in-frame by the ATG which encodes methionine 671 of AβPP. Importantly, this ATG is embedded in the optimal translation initiation nucleotide context (Kozak motif), the arrangement exceptional in the human AβPP gene, where of 20 in-frame Met-encoding ATG codons (including the ATG encoding the translation-initiating Met), only the ATG encoding Met671 is found in the nucleotide context optimal for the initiation of translation [140].

Breimer and Denny argued [140] that such a favorable and unique positioning of the ATG encoding Met671 of the AβPP may be not random but rather reveals the underlying physiological function. They proposed that this function could be the initiation of translation of AβPP mRNA within its coding region, a mechanism that could be *inducible and operative in AD* (discussed in more detail below). They also argued that translation initiated

at the AUG encoding Met671 of AβPP would result in C99 because the initiating Met would be removed co-translationally by N-terminal methionine aminopeptidases 1 and 2 (MAP1 and MAP2); the gamma-cleavage of C99 would, in turn, generate Aβ. Thus, in the Breimer and Danny's version of events, C99 and Aβ could be produced independently of AβPP but would be identical in all respects to and indistinguishable from their counterparts produced by the AβPP proteolysis [140].

22.2. C100 (Met-C99) and Met-iAβ Produced Independently of AβPP Can Be Distinguished from Their Counterparts Resulting from the AβPP Proteolysis: The Key to Evaluating the Validity of the ACH2.0

Breimer and Danny's presumption that C99 and Aβ generated independently of AβPP via the initiation of translation from the AUG encoding Met671 would be indistinguishable from their counterparts produced in the AβPP proteolytic pathway [140] was, however, subsequently proven to be incorrect. Indeed, as detailed below, the ensuing studies of the processing of the N-terminal translation-initiating methionine in eukaryotic cells have shown that MAP1 and MAP2 would be incapable of removing (co-translationally) the translation-initiating methionine preceding C99 and Aβ and that, in this case, the primary translation product would be C100 (i.e., N-terminal Met-C99), which can be processed by gamma-cleavage into Met-Aβ, both readily distinguishable from C99 and Aβ produced in the AβPP proteolytic pathway; eventually, the N-terminal methionine would be removed, but, importantly, *post-* rather than co-translationally and by aminopeptidases other than MAP1/MAP2.

Translation of the bulk of cellular proteins is initiated from N-terminal methionine. This methionine, however, is not always cleaved-off co-translationally by MAP1 and/or MAP2. For this to occur, both N-terminal Met and the residue that follows it should be accommodated within the active site of the enzyme. This is, therefore, a geometric problem and, with the invariable N-terminal Met, the feasibility of cleavage is strictly a function of the size of a residue that follows it [144–146]. The size of a residue is directly defined by the radius of gyration (RG) of its side chain. The smallest RG, zero, is in glycine, which does not have a side chain. The RG is 0.77 Angstroms in alanine, 1.08 Angstroms in serine, 1.22 Angstroms in cysteine, 1.24 Angstroms in threonine, 1.25 Angstroms in proline and 1.29 Angstroms in valine. It steadily increases and reaches its highest value (2.38 Angstroms) in arginine.

The N-terminal Met can be cleaved-off co-translationally by MAP1 and/or MAP2 *only* if it is followed by one of the seven smallest residues listed above [147]. The position following methionine 671 of AβPP is occupied by aspartate (RG 1.43 Angstroms). Consequently, if translation initiates from the AUG codon for methionine 671 of AβPP, this methionine would not be removed co-translationally and the resulting primary product would be not C99 but C100, i.e., Met-C99. In cases such as this, where the translation-initiating methionine is not removed by MAP1/MAP2, it is ultimately cleaved-off by one of numerous aminopeptidases with a broad specificity [148], as happens, for example, with γ-actin where the penultimate residue is glutamate, with RG of 1.77 Angstroms, and where the N-terminal methionine is cleaved–off by an aminopeptidase distinct from MAP1/MAP2 [149]. It should be emphasized that the cleavage of translation-initiating methionine by an aminopeptidase that is not MAP1/MAP2 does invariably occur post-translationally.

It follows, in light of the above considerations, that if *i*Aβ is generated in AD independently of AβPP by initiation of translation from the AUG encoding methionine 671 of AβPP, pools of Met-C99 (i.e., C100) and, potentially, of Met-Aβ would occur in the affected human neurons. These pools would represent the equilibrium of several dynamic processes, namely gamma-cleavage of C100 yielding Met-Aβ, conversion of C100 into C99 via the removal on the N-terminal methionine by aminopeptidases other than MAP1/MAP2, and conversion of Met-Aβ into Aβ trough the same mechanism. Relative rates of these dynamic processes would define sizes of the Met-C99 and Met-Aβ pools, but their steady-state populations would certainly occur and could be detected in live neuronal cells (see below

on human neuronal cells-based AD model, Section 26). These populations, however, would not occur in post-mortem samples since in dying cells, the production of C100 would stop long before the operation of aminopeptidases terminates; consequently, with the influx of C100 and Met-Aβ ceased and aminopeptidases active, the N-terminal Met in question would be removed in its entirety. The presumed ability to distinguish between C100 and *i*Aβ generated independently of AβPP and their counterparts produced by AβPP proteolysis is the key to assaying the validity of the ACH2.0 (see Section 26 below).

22.3. Potential Mechanisms of AβPP-Independent Generation of iAβ: Internal Initiation of Translation within the Intact Human AβPP mRNA from the AUG Encoding Met671

Potentially, there are two categories of the mechanisms of AβPP-independent generation of iAβ. One consists of the proposal of Breimer and Danny [140] that in AD, C99 and Aβ could be produced independently of AβPP by translation of the intact human AβPP mRNA initiating within its coding region with Met671. Two research groups attempted to test this proposal. The rationale in both studies was that a manipulation of AβPP DNA (and, consequently, AβPP mRNA) upstream from the ATG encoding Met671 should be inconsequential for translation initiating at this site, and would not interfere with it. In one study, various frame-shift mutations, introduced at the upstream positions, were utilized [150]. Another group inserted a translational stop codon upstream of the ATG in question [151]. In both cases the reasoning was simple: if the internal initiation of translation from the AUG encoding Met671 of AβPP does occur, C99 (and Aβ) would be produced from mutation-carrying AβPP mRNAs; if it does not, neither C99 nor Aβ would be generated. In both cases, C99 and Aβ were not detected, and the postulated phenomenon was declared as "ruled out" [150,151].

But did the above referenced studies really rule out this possibility? The answer is a resolute "NO". The experimental approaches that both studies have employed to assess the validity of the proposed mechanism resulted in apparently typical cases of comparing the proverbial apples and oranges. The proposal by Breimer and Danny [140] postulated the AβPP-independent production of C99 and Aβ via internal initiation of translation in AD-affected neurons in a *disease-inducible* manner. However, in both studies [150,151] referred to above, the determination ruling out this phenomenon was made in non-neuronal cells and certainly not under the AD conditions. It is, therefore, patently inapplicable to the processes taking place in AD. Consequently, the proposal by Breimer and Danny [140] remains potentially valid and should be re-assessed, along with other possible mechanisms discussed below in the present and following sections, in the suitable AD model (see Section 26 on this subject).

22.4. Potential Mechanisms of AβPP-Independent Production of iAβ: Utilization of 5′-Truncated AβPP mRNA Where the AUG Encoding Met671 Is the First Translation Initiation Codon

22.4.1. Internal Initiation of Transcription Upstream from the ATG Encoding Met671 of AβPP

The other category of potential mechanisms of AβPP-independent *i*Aβ generation includes the processes utilizing 5′-truncated AβPP mRNA. It is not difficult to envision that if AβPP mRNA were 5′-truncated in such a way that the first functional in-frame translation initiation codon would be the AUG encoding Met671, a conventional (rather than internally initiated) translation would result in the C100 fragment of AβPP as its primary product. One mechanism capable of generating such truncated mRNA is the internal initiation of transcription. This should take place well within the AβPP coding region but upstream of the AβPP gene segment encoding C99, in such a position that in the resulting mRNA the AUG encoding Met671 of AβPP would be the first functional translation initiation codon. The occurrence of such process would necessitate expression of a suitable transcription factor, or a cofactor, and could be induced upon the elicitation of the integrated stress response.

22.4.2. Targeted Site-Specific Cleavage of AβPP mRNA Upstream from Its C99-Encoding Segment

Another mechanism possibly responsible for the production of suitably 5′-truncated AβPP mRNA is the targeted site-specific cleavage of the intact AβPP mRNA at an appropriate position within its coding region, i.e., upstream from the C99-encoding segment of mRNA. The activation of such a mechanism would require the ISR-enabled expression of a suitable nuclease activity. mRNA produced by the above mentioned two mechanisms would be similar in that they would be encoding the same primary product, namely the C100 fragment of AβPP. On the other hand, they would be distinguishably different: whereas the mRNA product of the internal initiation of transcription would terminate with the cap structure at its 5′ end, the cleavage-resulting mRNA would be cap-less.

22.4.3. Potential Generation of C100-Encoding mRNA by the Asymmetric Amplification of Human AβPP mRNA

The third and, arguably, most plausible potential mechanism underlying AβPP-independent generation of *i*Aβ in AD is asymmetric RNA-dependent AβPP mRNA amplification. This mechanism is of significant interest because it also offers mechanistic explanation as to why AD is species-specific and possibly human-specific and why it certainly cannot occur in mice and mouse models, even upon an acute exogenous overexpression of human Aβ. Importantly, human AβPP mRNA appears to be its eligible template. If indeed operational in AD, this mechanism would, as detailed below, produce mRNA where the AUG encoding Met671 of AβPP is the first translation initiation codon; it is briefly discussed in the following section.

23. RNA-Dependent Amplification of Mammalian mRNA: Human AβPP mRNA Is Uniquely Eligible for the Process That Would Generate mRNA Encoding the C100 Fragment of AβPP

23.1. The Chimeric Pathway of Mammalian RNA-Dependent mRNA Amplification

RNA-dependent amplification of mammalian mRNA can occur in two consecutive stages, a "chimeric" pathway that potentially could be followed by a PCR-like mRNA amplification (for detailed discussion see [104–107,152–157]). Only the former is relevant to the subject of the present study. The mRNA amplification pathway of interest is "chimeric" because the resulting product of amplification contains covalently attached sense and antisense RNA segments. The amplified mRNA may be identical to its gene-transcribed progenitor in that it retains the intact protein coding capacity. On the other hand, it is of great potential relevance for AD because the amplification process can also produce mRNA molecules with 5′-truncated coding regions. In fact, the amplification of human AβPP mRNA resulting in 5′-truncated mRNA encoding the C100 fragment of AβPP is indeed plausible and is discussed below.

The chimeric pathway of mammalian mRNA amplification is illustrated diagrammatically in Figure 16 and can be briefly summarized as follows. The process is initiated by synthesis of the antisense complement of gene-transcribed mRNA progenitor by the RNA-dependent RNA polymerase (RdRp). It results in a double-stranded structure containing both sense and antisense RNA strands. Strands are then separated by a helicase complex that starts at the poly(A) segment of the 3′-terminal poly(A)-containing strand and moves along it. When separated, sense RNA can be reused as amplification template. Antisense RNA, on the other hand, folds into a self-priming configuration and is extended into the sense RNA. Such folding requires the occurrence of two complementary and topologically compatible elements (nucleotide sequences) within the antisense RNA [158]. One element must be 3′-terminal (the terminal complementary element, TCE), the other (the internal complementary element, ICE) can be located potentially anywhere within antisense RNA.

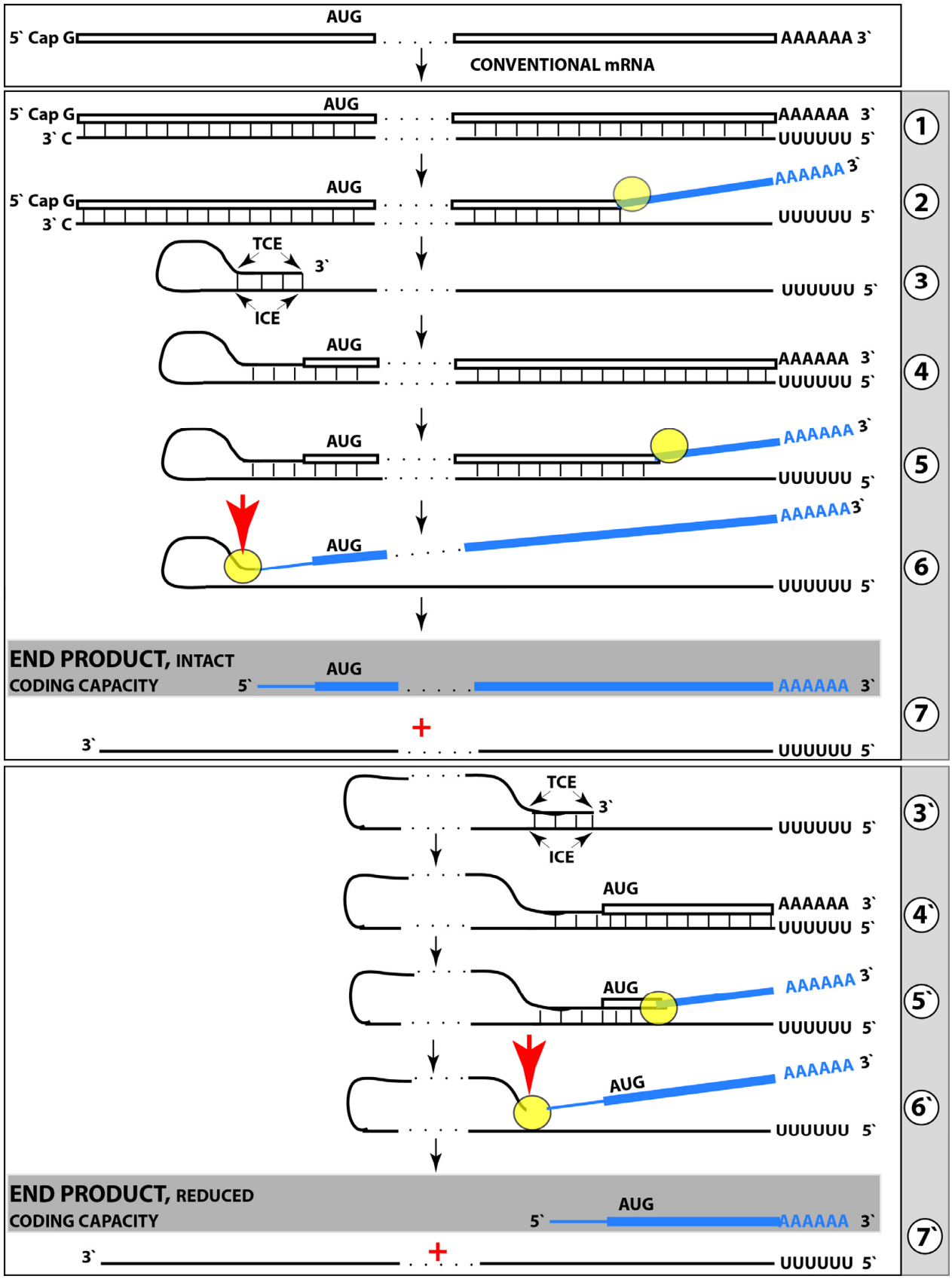

Figure 16. Principal stages of mammalian RNA-dependent mRNA amplification. *Boxed line*: Sense RNA. *Single line*: Antisense RNA. "*AUG*": Codon for translation-initiating methionine."*TCE*": 3′-terminal complementary element of the antisense RNA; "*ICE*": Internal complementary element of the antisense

RNA. *Filled yellow circle*: Helicase/nucleotide-modifying activity complex. *Blue lines* (single and boxed): RNA strands following their separation by a helicase/modifying activity. *Red arrows*: Site of cleavage of the chimeric intermediate. ***Top*** *panel*: The progenitor of the mRNA amplification pathway: conventional, genome-transcribed mRNA. ***Middle*** *panel*: Projected stages of the chimeric pathway of mammalian mRNA amplification. The internal complementary element (ICE) is situated within a portion of antisense RNA corresponding to the 5′UTR of conventional mRNA progenitor; consequently, the chimeric RNA end product contains the entire coding region of conventional mRNA. Stage **1**: RdRp-mediated transcription of the antisense RNA from the gene-transcribed sense RNA progenitor. Stage **2**: Strand separation; helicase activity mounts 3′ poly(A) of the sense RNA and moves along it. Stage **3**: TCE/ICE-facilitated folding of antisense RNA into self-priming conformation. Stage **4**: 3′ terminus of the antisense RNA is extended into the sense RNA. Stage **5**: Double-stranded portion of the hairpin structure is separated into sense and antisense RNA by helicase activity. Stage **6**: When helicase reaches single-stranded portion of hairpin structure, it (or associated activity) cleaves the chimeric intermediate. Stage **7**: 3′-trucated antisense RNA and chimeric RNA end products of the chimeric mRNA amplification pathway. ***Bottom*** *panel*: The ICE element is situated within a segment of antisense RNA corresponding to the coding region of conventional mRNA. Consequently, the amplified chimeric RNA end-product contains a 5′-truncated coding region of conventional mRNA. The translational outcome is decided by the location of the 5′-most translation initiation codon; if it is in-frame, translation would yield the C-terminal fragment of conventionally encoded polypeptide. Stages **3**′ through **7**′ correspond to stages **3** through **7**.

When the extension of self-primed antisense into sense RNA strand is completed, it results in a hairpin structure. Complementary strands in this structure are separated by a helicase activity invoked above. When helicase complex reaches the single-stranded portion (loop) of the hairpin structure, it cleaves the RNA molecule at the 3′ end of the loop or at a TCE/ISE mismatch. The cleavage produces two end products of the chimeric amplification pathway. One product is 3′-truncated antisense RNA missing either a part of or the entire TCE element. Another product is the chimeric mRNA. It contains 5′-truncated sense RNA and a covalently bound portion of the antisense RNA (in fact, its cleaved-off 3′-terminal segment). Whereas the antisense end product of the chimeric pathway can be utilized as initial template (progenitor) in the PCR-like mRNA amplification pathway (outside the scope of the present discussion; described in detail in [105,106,156]), the chimeric RNA end product of amplification is a functional mRNA and can be translated into a protein [105,106]. The potential protein product of the chimeric mRNA translation are not necessarily identical to that translated from gene-transcribed mRNA progenitor of amplification; two potential typical outcomes are discussed below.

23.2. Chimeric RNA End Products May Retain the Intact Protein Coding Content of the Conventional mRNA Progenitor

Translational outcomes of the chimeric pathway of RNA-dependent mRNA amplification include but are not limited to a protein encoded by the gene-transcribed mRNA progenitor. Chimeric RNA end product of amplification may encode only the C-terminal portion of the corresponding conventionally produced protein. It may join the C-terminal portion of conventionally produced protein with a polypeptide encoded elsewhere in the genome, i.e., the amplification process is able to produce a polypeptide encoded non-contiguously in the genome. Alternatively, the chimeric RNA end product of amplification may encode a polypeptide entirely unrelated to that translated from the conventional mRNA progenitor (for detailed discussion of the above possibilities see [156]). Which translational scenario plays out with a given mRNA species depends principally on the position of the ICE element within the antisense RNA, which, in turn, determines the site of initiation of the extension of the antisense into the sense RNA. The middle panel of Figure 16 illustrates the simplest scenario where the internal complementary element is situated within antisense RNA segment corresponding to the 5′ untranslated region of the gene-transcribed progenitor mRNA. In this scenario, the extension of self-primed anti-

sense RNA would produce a portion of the 5′UTR and the entire coding region of mRNA progenitor. Consequently, the chimeric RNA end product of amplification would differ from corresponding conventionally produced mRNA only in its 5′UTR region and, upon translation, would produce protein identical to the conventionally generated polypeptide.

23.3. Chimeric RNA End Products May Encode the C-Terminal Fragment of Conventionally Generated Polypeptide

The 3′ terminal complementary element of the antisense RNA is, by definition, invariably 3′-terminal. On the other hand, the internal complementary element can be literally anywhere within the antisense RNA. A possibility, which is of great interest because it is relevant to the subject of AβPP-independent generation of Aβ, is one whereby the ICE element is located in a portion of the antisense RNA corresponding to the coding region of conventional gene-transcribed mRNA progenitor. This particular scenario is illustrated in the bottom panel of Figure 16. In this case, the extension of self-primed antisense RNA would produce only the 3′ portion of conventional mRNA containing only the 3′ portion of its coding region. Accordingly, the chimeric RNA end product of amplification would contain 5′ truncated coding region of conventional mRNA. The translational product generated from such RNA would be defined by the location of the first, 5′-most AUG or another translation initiation-competent codon. If this codon were in-frame, translation of the chimeric RNA product of mRNA amplification would produce the C-terminal fragment of conventional mRNA progenitor-encoded protein. This type of the chimeric mRNA amplification pathway would be asymmetric: Indeed, only the 3′-terminal segment of the coding region would be amplified, and its translation would generate only the C-terminal segment of conventionally produced protein. Asymmetric chimeric mRNA amplification pathway can also result in several additional interesting translational outcomes, which are outside of the scope of the present discussion and are described elsewhere [156].

24. Human AβPP mRNA Is an Eligible RdRp Template: Projected Pathway of Asymmetric Amplification Resulting in Chimeric mRNA Encoding the C100 Fragment of AβPP

The asymmetric chimeric pathway of RNA-dependent mRNA amplification described above is potentially capable, if applicable to AβPP mRNA, of generating mRNA encoding C100 fragment independently of AβPP. The asymmetry involved in producing 5′-truncated AβPP mRNA where the AUG codon for methionine 671 is the 5′-most translation initiation codon is, however, extensive. The AUG encoding methionine 671 of AβPP is located more than two thousand nucleotides downstream from the 5′ end of AβPP mRNA. Consequently, the TCE and ICE complementary elements within the antisense RNA (if they occur in the first place) would be as distant from each other. Provided that the TCE and ICE do occur in suitable positions, the question is: would the required antisense RNA folding be feasible, i.e., would the complementary elements be topologically compatible in folded antisense AβPP conformation? The general approach (i.e., not only for AβPP mRNA but for any mRNA species) to assess this is as follows.

24.1. Assessment of the Eligibility of an mRNA for RNA-Dependent Amplification: General Approach

In this general approach, the mRNA of interest is reverse transcribed into an antisense cDNA. The mRNA template is removed by RNase H activity (which cleaves RNA in double-stranded RNA/DNA substrate and usually occurs in preparations of reverse transcriptase, RTase, unless removed genetically) concurrently with the reverse transcription progression and mRNA template's engagement in a double-stranded structure with newly synthesized cDNA (thus forming RNase H substrate). Provided the mRNA of interest is fully transcribed, provided the TCE and ICE elements occur within the antisense strand, and provided they are topologically compatible, the antisense strand would fold into self-priming conformation and would be extended (by RTase, which is capable of utilizing both RNA and DNA templates) into the sense strand. Such extension could be easily detected by

nucleotide sequencing, and the junction between the sense and antisense segments would indicate the position of the ICE element and enable the identification of both TCE and ICE.

24.2. Human AβPP mRNA Is Eligible for RNA-Dependent Amplification

Just such an assessment was actually inadvertently performed for human AβPP mRNA. Soon after human AβPP cDNA was sequenced [141–143], but before the genomic sequence upstream of the human AβPP gene was defined, one research group reported the detection and sequencing of much longer human AβPP cDNA, which was significantly extended at its 3′ end [159]. The authors hypothesized that it originated from 5′-extended AβPP mRNA whose transcription was initiated at the alternative transcription initiation site upstream from originally reported 5′ end of the human AβPP gene (based on the AβPP cDNA sequencing, [141–143]). Soon after [159] was published, however, the genomic region upstream of human AβPP was sequenced [160], and it became apparent that the observed human AβPP cDNA extension seen in [159] could not have originated by alternative initiation of transcription upstream from AβPP gene. Consequently, following the publication of genomic nucleotide sequence upstream from the human AβPP gene [160], the authors of [159] declared their result an artifact and published a correction to this effect [159]. However, a close analysis of human AβPP cDNA extension obtained in [159] showed that the extended portion is, in fact, a perfect segment of human AβPP sense strand, and that it was derived by the extension of folded and self-primed AβPP cDNA (antisense strand) that occurred about 2000 nucleotides from the 3′ terminus of the AβPP cDNA. The sense/antisense junction within extended AβPP cDNA defined the site of the initiation of extension and enabled the determination of sequences of the TCE and ICE elements [161–163]. Moreover, this analysis showed that the first, 5′-most translation initiation codon within the sense segment of the extended AβPP cDNA is, in fact, the ATG encoding Met671 of AβPP [161–163]. The projected folding, self-priming and the extension of human antisense RNA AβPP strand, as well as the cleavage generating the mRNA encoding the C100 fragment of human AβPP, are illustrated in Figure 17. Note that stages **a**, **b**, and **c** of asymmetric RNA-dependent AβPP mRNA amplification depicted in Figure 17 correspond to stages **3′** through **6′** shown in Figure 16.

As shown in Figure 17, the human antisense AβPP RNA contains the TCE and ICE elements (the TCE becomes such only if it has the complementary and topologically compatible ICE partner; otherwise it is just a 3′ terminal RNA segment). The distance between the TCE and ICE is quite large, about two thousand nucleotides, yet they guide the folding of the antisense RNA into a self-priming conformation. The TCE element acts as a primer and is extended by RdRp into sense RNA strand (transcribing, in fact, a 5′ portion of the antisense RNA template). Sense and antisense RNA strands are then separated by helicase activity (not shown in Figure 2). When helicase reaches the single-stranded portion of the molecule, it, or associated activity, cleaves it. In Figure 2, the cleavage is shown to occur at the 5′ end of the TCE element (i.e., the 3′ end of the single-stranded loop of the hairpin structure), but it could also occur at one of the TCE/ICE mismatches. This cleavage produces the chimeric end product of asymmetric RdRp-mediated, RNA-dependent amplification of human AβPP mRNA. Its sense RNA segment consists of severely 5′ truncated coding region of AβPP mRNA continued into its 3′ untranslated region. In terms of the translational outcome, the most important feature of this amplified RNA is the presence of in-frame translation initiation codon. It occurs 58 nucleotides downstream from the sense/antisense junction, and *it is the AUG codon for methionine 671 of AβPP.* Thus, *the chimeric RNA end product of the asymmetric amplification of human AβPP mRNA would produce, upon its translation, the C100 fragment of AβPP*. Importantly, this mode of production, eventually resulting in Aβ, would be completely independent of AβPP.

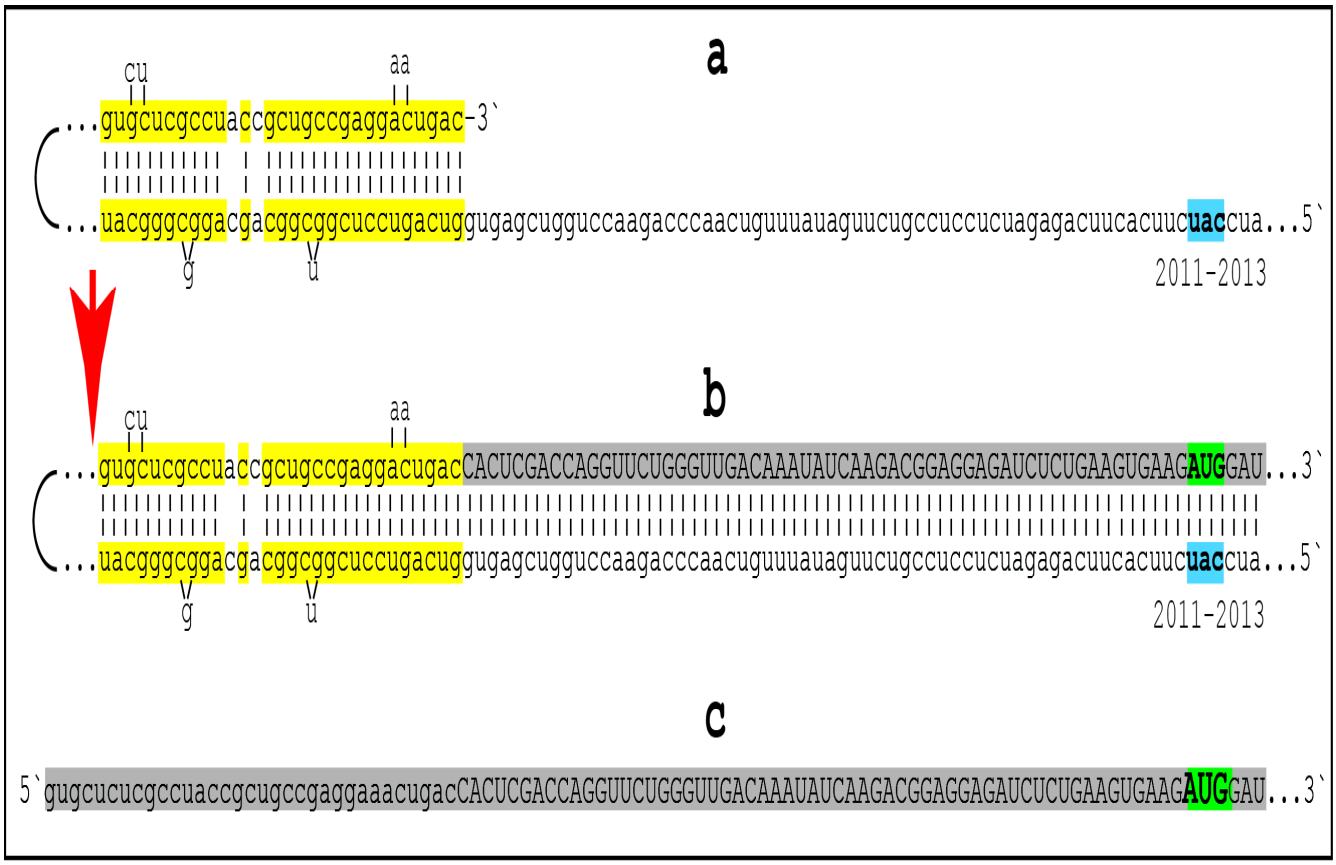

Figure 17. Chimeric pathway of human AβPP mRNA amplification resulting in mRNA encoding the C100 fragment of AβPP: Projected principal stages. *Lowercase letters*: Nucleotide sequence of the antisense RNA. *Uppercase letters*: Nucleotide sequence of the sense RNA. Highlighted *in yellow*: The 3′ terminal (**top**) and the internal (**bottom**) elements of the human antisense AβPP RNA. "*2011–2013*": Nucleotide positions (from the 3′ terminus of the antisense AβPP RNA) of the "uac" (highlighted *in blue*) corresponding to the "AUG" (highlighted *in green*) encoding Met671 in the human AβPP mRNA. *Panel **a***: TCE/ICE-facilitated folding of the human AβPP antisense RNA into self-priming configuration. *Panel **b***: Extension of self-primed AβPP antisense RNA into sense RNA (highlighted *in gray*). *Red arrow*: Cleavage of chimeric RNA intermediate following separation of sense and antisense RNA (not shown). The cleavage is shown at the 5′ end of the TCE element; it may also occur at one of the TCE/ICE mismatches. *Panel* **c**: Chimeric RNA end product of RNA-dependent amplification of human AβPP mRNA (highlighted *in gray*). It consists of antisense portion (the TCE or part thereof) extended into 5′ truncated coding region of human AβPP mRNA. Its first, 5′-most translation initiation codon is the in-frame AUG (highlighted *in green*) that encodes Met671 of human AβPP; when translated, it would produce the C100 fragment of AβPP.

25. The Unique Eligibility of Human AβPP mRNA for Asymmetric RNA-Dependent Amplification Provides Explanation for Species-Specificity, Possibly Human-Specificity, of AD

The potential utilization of the asymmetric AβPP mRNA amplification in the second stage of AD provides an explanation as to why AD appears to be human-specific (or, at least, species-specific; indeed, it does not occur even in long-living mammals, such as elephants). As was mentioned above, at least two requirements have to be met for RNA-dependent mRNA amplification to occur: (a) the occurrence of two complementary elements, TCE and ICE, on the antisense strand and, if this is satisfied, (b) topographical compatibility of the TCE and ICE, i.e., the sufficient spatial proximity in the folded antisense configuration allowing their interaction and formation of a self-priming structure. It appears that in non-human mammals even the first requirement is not met [156]. It certainly

is not met in mice, where AβPP antisense RNA segments corresponding to the TCE and ICE elements of human AβPP antisense RNA show little, if any, complementarity [161–163]. Moreover, this requirement is not met in human AβPP mRNA exogenously overexpressed in mice because its 5′-terminal region is substantially modified during the construction of expression vectors or of transgenes, and therefore it loses its RdRp eligibility. This can be the reason why transgenic AD models do not and apparently cannot exhibit the full spectrum of AD pathology. Importantly, however, as argued above, the absence of the operative AβPP-independent *i*Aβ generation pathway does not preclude in any way the occurrence of AACD.

26. Testing the Validity of the ACH2.0 and the Potential of the BACE1/BACE2 Activation-Mediated *i*Aβ Depletion Therapy

26.1. Human-Neuronal-Cell-Based AD Model

26.1.1. Rationale

For two reasons, the best conceivable AD model is, arguably, that based on human neuronal cells. The first reason is that such model utilizes cells originating from the species known to be affected by AD. The second reason is that, as discussed above, AD appears to be human-specific or, at least, species-specific [152–157], i.e., human cells seem to possess unique feature(s), possibly the ability to produce *i*Aβ in the AβPP-independent mode [156] or enact some other mechanism(s) enabling the second AD stage, that are, because of the structure of their AβPP mRNA or for other reasons, unavailable in non-human mammalian species [161–163]. Since human neurons are intrinsically capable of the molecular processes underlying the disease and, more specifically, are capable of enabling the stage two of AD, the design principles to generate the AD model are relatively straightforward; they aim to trigger the second stage of AD and to activate the AβPP-independent *i*Aβ generation pathway and, consequently, the AD Engine. Once this occurs, the progression of cellular AD pathology, driven by the AβPP-independent *i*Aβ production pathway, would become self-sustaining and irreversible (unless intervened in therapeutically). Moreover, as described below, the ability of a human neuronal cells-based AD model system to support the formation of hyperphosphorylated tau tangles, the major cellular AD hallmark, has been proven experimentally [61].

26.1.2. Cultured Human Neuronal Cells Are Capable of Displaying Full Spectrum of Cellular AD Pathology

Another decisive advantage of a human neuronal cells-based AD model is its apparent capacity to present the complete spectrum of cellular AD pathology, including the formation of neurofibrillary tangles (NFTs). Exogenous overexpression of Aβ in human neuronal cells cultured in matrigel was indeed shown to trigger the formation of this principal AD hallmark [61]. In the study under discussion, the authors adopted the ACH-based interpretation of the observed phenomenon and ascribed it to the effects of overexpressed extracellular Aβ produced in the AβPP proteolytic pathway. The ACH2.0-based interpretation of the same results offers a completely different picture. It suggests that in their experiments authors inadvertently activated the AβPP-independent *i*Aβ generation pathway and, consequently, ignited the AD Engine. In this study [61], investigators utilized polycistronic lentiviral construct to acutely overexpress human AβPP cDNA carrying the London FAD mutation V717I as well as the Swedish FAD mutation K670N/M671L. From the same construct, they also overexpressed PSEN1 carrying the FAD mutation ΔE9. Following the introduction of lentiviral construct, human neural progenitor cells were cultured and differentiated in matrigel [61]. To understand how the mutations employed in this study could facilitate the activation of the AβPP-independent *i*Aβ generation pathway, it is important to review their function. The Swedish FAD mutation furthers, as discussed above, the gamma-cleavage of C99 on intracellular membranes and, consequently, facilitates the retention of *i*Aβ produced by the AβPP proteolysis [59]. The London FAD mutation significantly increases production of $A\beta_{42}$ isoform and so does the PSEN1 mutation utilized in

this study. Both mutations substantially accelerate the accumulation of AβPP-derived *i*Aβ. This occurs for three reasons. First, secreted Aβ does not diffuse in the matrigel. Second, secreted $A\beta_{42}$ is internalized preferentially and with augmented efficiency (versus other Aβ species) [35]. Third, as discussed above, intraneuronal $A\beta_{42}$ lowers (in comparison with other Aβ isoforms) the **T1** threshold and thus facilitates the activation of the AβPP-independent *i*Aβ production pathway. Therefore, $i A\beta_{42}$ rapidly reaches the **T1** threshold and triggers the endogenous AβPP-independent generation of *i*Aβ. The drastically increased levels of *i*Aβ drive cellular AD pathology, apparently including the formation of NFTs. The high *i*Aβ levels indeed were shown to inhibit the ubiquitin–proteasome system, facilitate the accumulation and phosphorylation of tau protein and promote the formation of NFTs [134–137]. Whereas the human-neuronal-cell-based AD model employed in [61] can be utilized for testing (see below) the validity of the ACH2.0 (in fact, it is currently the only existing AD model suitable for this purpose), the following section describes simpler and more streamlined approaches to generate a human-neuronal-cell-based model capable of accomplishing this objective.

26.2. Human-Neuronal-Cell-Based AD Model: Principles of Design

Within the framework of the ACH2.0, the most "physiological" (i.e., imitating the processes that occur in the disease) approach to ignite the AD Engine, i.e., to activate the endogenous AβPP-independent *i*Aβ production and to initiate the second stage of AD, is to rapidly accumulate *i*Aβ to the **T1** threshold. Considering, as described above, that in AD-predisposed individuals, the **T1** threshold could be significantly lower than in general population, it may be useful to utilize neurons differentiated from iPSCs of AD patients who developed AD in their middle to late sixties. Rapid accumulation of *i*Aβ can be accomplished by transiently and exogenously expressing $A\beta_{42}$ (because it further lowers the **T1** threshold) from DNA constructs or from transfected mRNA, or by importing it directly by electroporation or by other suitable technique. The expression constructs should encode $A\beta_{42}$ rather than AβPP or C99; the resulting peptide would be *i*Aβ (i.e., it would not be secreted). If, in an exogenous *i*Aβ expression construct, translation would initiate from the AUG contiguously preceding the Aβ segment of the expression vector, the resulting primary product would be Met-Aβ. However, the principal detection assays in the validation procedure would be for the occurrence of endogenously produced C100 and Met-Aβ, and the presence of exogenously generated Met-Aβ would interfere with the detection of its endogenous counterpart.

A solution to the above problem is to arrange for a co-translational removal of the translation-initiating methionine by MAP1 or MAP2. This can be accomplished by inserting, immediately following the initiating methionine, one of the seven residues (listed above) that are compatible with the operation of MAP1/MAP2 [147]. The best choice appears to be Val because it would confer the longest half-life, according to the N-end rule [146]. However, when the N-terminal methionine is followed by valine, its removal by MAP1/MAP2 depends on the next downstream residue. If it is aspartate, as is the case in Aβ, the initiating methionine cannot be cleaved-off by MAP1/MAP2 [147], and the resulting primary translation product would be Met-Val-Aβ. The next best choice, in accordance with the N-end rule, is Gly. In this case, the translation initiating methionine will be removed co-translationally by MAP1 or MAP2 [147] and the primary translation product would be Gly-Aβ, which can be readily distinguished from the Met-Aβ presumably generated endogenously in the AβPP-independent manner. In a complementary approach, if exogenously expressed *i*Aβ contains one of FAD mutations, say the Swedish mutation, not present in the endogenously produced Aβ, this feature would assist in distinguishing between the two.

On the other hand, however, the identification of the endogenously produced C100 fragment of AβPP would be fully satisfactory, at least initially, for the purpose of the validation of the ACH2.0. If such a procedure is adopted, Met-Aβ can be unreservedly expressed exogenously in human neuronal cells with the aim to activate the endogenous AβPP-

independent C100 and *i*Aβ production. Such an approach would not interfere with the C100-based detection procedure.

Alternative, albeit less "physiological", approaches, which bypass the *i*Aβ accumulation stage, include the induction of mitochondrial dysfunction resulting in the HRI activation or stressor-specific activation of one of the other eIF2α kinases, all leading to the elicitation of the ISR and, provided that the ISR alone is sufficient to activate the AβPP-independent *i*Aβ generation pathway and, consequently, the AD Engine, resulting in the commencement of the second AD stage.

26.3. Testing for the Principal Hallmark of the ACH2.0: AβPP-Independent Generation of iAβ

As was discussed above, the AβPP-independent generation of *i*Aβ may conceivably occur via four distinct mechanisms: (a) internal initiation of transcription of the AβPP gene, (b) site-specific cleavage of AβPP mRNA, (c) asymmetric RNA-dependent amplification of AβPP mRNA, and (d) internal initiation of translation within AβPP mRNA. All these mechanisms have one common principal feature: in each, the AβPP-independent generation of *i*Aβ occurs via translation initiated at the AUG codon encoding Met671 of AβPP. Accordingly, the primary translation product in every mechanism is the C100 fragment of AβPP, i.e., N-terminal methionine-containing C99. This is because, as described above, the N-terminal methionine cannot be removed co-translationally by MAP1 or MAP2, and its removal is effected only post-translationally by an aminopeptidase(s) with broad specificity. Consequently, in neuronal cells with the activated AβPP-independent *i*Aβ production pathways, steady-state pools of N-terminal-Met-containing C99 and Met-Aβ should be present; either of these pools would constitute the unique identifier of the activity of the pathway. Therefore, the detection of either or both would provide an unambiguous proof of the operation of the AβPP-independent *i*Aβ generation pathway.

If such proof were obtained, a question could be addressed which of the four mechanisms described above enables the operation of the AβPP-independent *i*Aβ production pathway. Three of the four could be identified by the analysis of mRNA encoding the C100 fragment (the only requirement for such mRNA is that the first functional translation initiation codon is the AUG encoding Met671 in AβPP mRNA). If the mRNA in question were capped at its 5′ terminus, it would suggest its origin via the internal initiation of transcription within the AβPP gene. If the mRNA in question were an uncapped suitable fragment of AβPP mRNA, its origin is likely a site-specific cleavage of AβPP mRNA. The observation that RNA of interest is chimeric, i.e., contains an antisense segment at its 5′ portion, with the predictable sequence and position of the sense/antisense junction, identical to or resembling that shown in Figure 17 (cleavage of the pinhead chimeric RNA intermediate could occur at TCE/ICE mismatches, and the remaining antisense self-priming structure could be stable enough to initiate a new extension cycle, thus generating slightly different sense/antisense junction sequences, a phenomenon termed the "Chimeric Junction Shift"; see ref. [156]), would indicate the occurrence of the asymmetric RNA-dependent amplification of AβPP mRNA. If none of the above were detected, the internal initiation of translation of AβPP mRNA would be indicated. The occurrence of the latter could be tested in ways conceptually similar to those employed in the original testing of this notion (when it was arbitrarily "ruled out" [150,151]) but in the proper human neuronal cells-based model system. This can be accomplished by editing-in the endogenous AβPP gene either a frame-changing mutation or a stop codon mutation upstream from the AUG encoding Met671 of AβPP. If the internal initiation of AβPP mRNA translation does occur, these mutations should not interfere with it; if it does not, no Aβ would be produced endogenously. The criteria of the endogenous origin could be the presence of N-terminal Met on C99 or *i*Aβ. Alternatively, as described above, an arbitrary FAD mutation could be introduced within the exogenously produced *i*Aβ to distinguish it from its endogenously derived counterparts. A possible involvement of the internal ribosome entry site (IRES) in the internal initiation of translation of AβPP mRNA can be also studied using standard methods of analysis [164–169]. If, on the other hand, no pools of either C100 or Met-Aβ are

detected in the human-neuronal-cell-based AD model despite the occurrence of NFTs, the conclusion, apparently unlikely but nevertheless possible, would be that the agent driving the second AD stage is not *i*Aβ, a scenario considered in detail in [2].

26.4. Testing the Therapeutic Potential of the BACE1/BACE2 Activation-Mediated iAβ Depletion Therapy

To assess the therapeutic potential of *i*Aβ depletion, BACE1 and/or BACE2 can be exogenously overexpressed from either a constitutive or an inducible promoter (the latter to allow evaluation at the different mechanistic stages). Assaying options for the assessment of the effects and consequences of BACE overexpression would depend on the determination of the pathway underlying operation of the AD Engine, as described in the preceding section. If this pathway is the AβPP-independent *i*Aβ production, the assaying could be extensive. It would include monitoring the levels of the intact *i*Aβ (expected to be reduced by Aβ-cleaving activities of BACE1 and BACE2) and testing the activity of the AβPP-independent *i*Aβ production pathway by examining the occurrence of C100 (Met-C99) and of Met-Aβ. If the *i*Aβ depletion were successful, the AD Engine's operation would cease. Consequently, C100 influx would stop and it, as well as Met-Aβ, would dissipate (this is why these species cannot be present in postmortem samples: in dying neurons, the production of Met-C99 and Met-*i*Aβ would cease while aminopeptidases are still operational; consequently no N-terminal methionine would remain); thus, the occurrence of C100 and/or Met-Aβ, or lack thereof, would report on the activity of the AβPP-independent pathway of its production. If, on the other hand, the second AD stage is driven not by *i*Aβ but by another, yet unidentified, agent, assaying options would be limited to determining levels of the intact *i*Aβ and to monitoring hyperphosphorylation of tau protein and the formation of NFTs; in any case, the potential therapeutic effects of the *i*Aβ depletion treatment could be quantified. The ability to regulate the activity of the AβPP-independent *i*Aβ generation pathway and, even more importantly, to control the formation of NFTs via BACE-mediated *i*Aβ depletion would constitute a proof of principle for the utilization of BACE activators (or other *i*Aβ-depleting agents) as potential AD drugs and would justify a major effort to develop such agents.

As for assessing effects of the proposed therapy in AACD, this can be and indeed was performed numerous times with successful outcomes (using drugs suppressing the accumulation of AβPP-derived *i*Aβ) in currently available transgenic mouse models where, as argued above, the second AD stage does not occur. This is because, whereas these models do not develop AD, the neuronal damage and the cognitive dysfunction symptoms that they exhibit are, at least in part and possibly in full, caused by *i*Aβ (produced by AβPP proteolysis and both internalized and retained intraneuronally) and are equivalent to the pathology displayed in AACD. Moreover, whenever the effective BACE1- and/or BACE2-activating (or any suitable *i*Aβ-depleting) candidate drugs are available, their effect on AACD could be tested in mouse models exogenously overexpressing Aβ. Because of the lack of definitive cellular AACD-specific markers, it is currently not feasible to test directly the therapeutic potential of the *i*Aβ depletion in AACD in humans or in the human-neuronal-cell AD model. However, because the age of onset of AACD is apparently greater than that of typical SAD [100,101], any human clinical trials testing the effect of the *i*Aβ depletion in prevention of SAD would, by default, also test the effect of the *i*Aβ depletion therapy in prevention of AACD.

27. Conclusions

The recently posited amyloid cascade hypothesis 2.0 envisions AD as a two-stage disorder. The first stage is a life-long accumulation of intraneuronal AβPP-derived *i*Aβ. This occurs via cellular uptake of secreted Aβ and through retention of a fraction of Aβ produced by AβPP proteolysis. When AβPP-derived *i*Aβ reaches critical **T1** threshold, it activates a self-sustaining production of an agent that drives the second AD stage, i.e., a cascade including tau pathology and culminating in neuronal loss. It is highly probable

that this agent is *i*Aβ generated independently of AβPP. The detection of a single AβPP mutation affecting Aβ and causing familial AD [7] was deemed sufficient to formulate the ACH. In the thirty years that followed, many additional FAD mutations were detected. All of them, without a single exception, affect, in one way or another, Aβ. This is consistent with the notion that *i*Aβ, differentially derived, runs the entire course of AD, a concept supported by the occurrence of several cellular mechanisms capable of producing *i*Aβ independently of AβPP. The rate of accumulation of AβPP-derived *i*Aβ and the extent of the **T1** threshold determine the timing of the commencement of the second AD stage and, given the limited lifespan, define the susceptibility to AD.

The present study analyzes the dynamics of AβPP-derived *i*Aβ and the role of the extent of the **T1** threshold in the disease. It formulates principles of dynamics of AD and of aging-associated cognitive dysfunction and defines AACD as an extended segment of the first AD stage, thus incorporating it into the ACH2.0. It explains why only a fraction of the population develops sporadic AD and AACD and why both pathologies are age-dependent. It provides mechanistic interpretations for all principal aspects of AD and AACD, including the protective effect of Icelandic AβPP mutation, the early onset of FAD and the temporally sequential manifestation of AD in defined regions of the affected brain, and explains mechanisms underlying the observed effect of lecanemab and donanemab at the early symptomatic stage of AD. It offers a therapeutic strategy that emulates and substantially improves upon the mode of operation of the Icelandic AβPP mutation, which confers on its carriers protection from both AD and AACD. It also posits that a single, once-in-a-lifetime-only, administration of *i*Aβ depletion treatment via transient activation of BACE1 and/or BACE2, exploiting their Aβ-cleaving activities, or by any other suitable means, would not only prevent AD and AACD but would also be effective at the symptomatic stages of both disorders. Validation of the ACH2.0 and of the effectiveness of the proposed ACH2.0-based *i*Aβ depletion therapy would justify a major effort to develop operative BACE1 and BACE2 activators, or other suitable *i*Aβ-depleting agents, as potential preventive and curative AD and AACD drugs.

The postulated greatly accelerated production of the C99 fragment in the AβPP-independent pathway in symptomatic AD is not only responsible for the augmented generation of *i*Aβ but is also consistent with a growing body of evidence indicating the deleterious role of AβPP intracellular domain (AICD) in the disease. AICD is generated by the epsilon cleavage of C99 downstream and, apparently, independently from the gamma cleavage [170]. AICD interacts with numerous regulatory proteins and signaling pathways [171–181]. It is involved in transcriptional regulation, apoptosis, and cytoskeletal dynamics [182,183]. It affects expression of neprilysin [184] and contributes to tau phosphorylation [171,182]. It alters neuron firing, modifies hippocampus oscillations, and impairs spatial memory encoding [185]. Within the framework of the ACH2.0, the levels of AICD increase significantly in the second, symptomatic AD stage due to the operation of the AβPP-independent *i*Aβ production pathway. Indeed, the primary translation product of this pathway is C100, which gives rise not only to *i*Aβ but also to AICD. The levels of the latter increase in parallel with those of the former, hence its deleterious effect. In this sense the increase in AICD levels in symptomatic AD is a direct result of the activity of the AβPP-independent *i*Aβ (and AICD) production pathway and thus the integral part of the ACH2.0. Importantly, the therapeutic strategies proposed in the present study apply to AICD as well as to *i*Aβ. When implemented preventively, they would preclude the activation of the AβPP-independent *i*Aβ *and AICD* generation pathway. Consequently, there would be no increase in the levels of either *i*Aβ or AICD. When employed in symptomatic AD, the targeted *i*Aβ degradation and its consequent depletion would stop the operation of the AβPP-independent *i*Aβ generation pathway; the production of AICD in this pathway would also cease.

Whereas AD and AACD are associated with aging, they are not the typical aging-caused diseases. They are linked with aging due to the slow rate of the accumulation of *i*Aβ produced in the AβPP proteolytic pathway, a process which occurs presumably linearly

from the childhood and whereby *i*Aβ levels start reaching the thresholds that trigger sporadic AD or AACD only in the seventh or eighth decade of life. The occurrence of the disease is the function of a sufficient *i*Aβ accumulation, not of the "aging" per se. Indeed, in the past, with shorter average lifespan and the "aging" occurring earlier, a smaller fraction of the population was reaching their sixties and seventies, and, accordingly, the prevalence of AD was lower than currently. Likewise, prolonging the human lifespan would not shift the occurrence of both conditions to the more advanced "new old age"; instead, it would commence at about the same age (sixties and seventies) as now, constituting a "new middle age". At the current average lifespan of nearly eighty years, *i*Aβ levels reach the AD-triggering threshold in the advanced age in only about 10% of the population; this fraction is, however, the proverbial "tip of the iceberg". Given a sufficiently long lifetime, the occurrence of both AD and AACD would *inevitably* become nearly universal since, in the absence of preventive treatment, the disease-triggering *i*Aβ thresholds would be eventually crossed in every (or nearly every) individual, i.e., the entire "iceberg" would be eventually affected. Indeed, with the presumed linear rate of accumulation of AβPP-derived *i*Aβ, the anticipated, potentially highly substantial, increase in longevity in the near future would be accompanied by a corresponding increase in the prevalence, possibly approaching the entirety of the population, of AD and AACD. The proposed once-in-a-lifetime (or twice in a 150-year-long lifetime) preventive *i*Aβ depletion treatment provides an attractive solution.

Author Contributions: Conceptualization and draft preparation, V.V.; conceptualization and review, S.R.-V. All authors have read and agreed to the published version of the manuscript.

Funding: This research is supported by The National Institutes of Health under project number NIH R21 GM056179 and NIH RO1 AR036819.

Institutional Review Board Statement: Not applicable.

Informed Consent Statement: Not applicable.

Data Availability Statement: Not applicable.

Acknowledgments: Authors are grateful to Bjorn R. Olsen (Harvard Medical School) for his support, to Hailong Gao (Children's Hospital, Boston) for the assistance with figures' preparation, and to Michael J. Foley and his associates for logistical support.

Conflicts of Interest: The authors declare no conflict of interest.

References

1. Volloch, V.; Rits-Volloch, S. The Amyloid Cascade Hypothesis 2.0: On the possibility of once-in-a-lifetime-only treatment for prevention of Alzheimer's disease and for Its potential cure at symptomatic stages. *J. Alzheimer's Dis. Rep.* **2022**, *6*, 369–399. [CrossRef] [PubMed]
2. Volloch, V.; Rits-Volloch, S. The Amyloid Cascade Hypothesis 2.0: Generalization of the Concept. *J. Alzheimer's Dis. Rep.* **2023**, *7*, 21–35. [CrossRef] [PubMed]
3. Volloch, V.; Rits-Volloch, S. Effect of Lecanemab and Donanemab in Early Alzheimer's Disease: Mechanistic Interpretation in the Amyloid Cascade Hypothesis 2.0 Perspective. *J. Alzheimer's Dis.* **2023**, *93*, 1277–1284. [CrossRef] [PubMed]
4. Jonsson, T.; Atwal, J.K.; Steinberg, S.; Snaedal, J.; Jonsson, P.V.; Bjornsson, S.; Stefansson, H.; Sulem, P.; Gudbjartsson, D.; Maloney, J.; et al. A mutation in APP protects against Alzheimer's disease and age-related cognitive decline. *Nature* **2012**, *488*, 96–99. [CrossRef] [PubMed]
5. Harper, A.R.; Nayee, S.; Topol, E.J. Protective alleles and modifier variants in human health and disease. *Nat. Rev. Genet.* **2015**, *16*, 689–701. [CrossRef] [PubMed]
6. Hardy, J.A.; Higgins, G.A. Alzheimer's disease: The amyloid cascade hypothesis. *Science* **1992**, *256*, 184–185. [CrossRef]
7. Goate, A.; Chartier-Harlin, M.C.; Mullan, M.; Brown, J.; Crawford, F.; Fidani, L.; Giuffra, L.; Haynes, A.; Irving, N.; James, L.; et al. Segregation of a missense mutation in the amyloid precursor protein gene with familial Alzheimer's disease. *Nature* **1991**, *349*, 704–706. [CrossRef]
8. Keskin, A.D.; Kekuš, M.; Adelsberger, H.; Neumann, U.; Shimshek, D.R.; Song, B.; Zott, B.; Peng, T.; Förstl, H.; Staufenbiel, M.; et al. BACE inhibition-dependent repair of Alzheimer's pathophysiology. *Proc. Natl. Acad. Sci. USA* **2017**, *114*, 8631–8636. [CrossRef]
9. Hu, X.; Das, B.; Hou, H.; He, W.; Yan, R. BACE1 deletion in the adult mouse reverses preformed amyloid deposition and improves cognitive functions. *J. Exp. Med.* **2018**, *10*, 1084. [CrossRef]

10. Kennedy, M.E.; Stamford, A.W.; Chen, X.; Cox, K.; Cumming, J.N.; Dockendorf, M.F.; Egan, M.; Ereshefsky, L.; Hodgson, R.A.; Hyde, L.A.; et al. The BACE1 inhibitor verubecestat (MK-8931) reduces CNS β-amyloid in animal models and in Alzheimer's disease patients. *Sci. Transl. Med.* **2016**, *8*, 363ra150. [CrossRef] [PubMed]
11. Egan, M.F.; Kost, J.; Tariot, P.N.; Aisen, P.S.; Cummings, J.L.; Vellas, B.; Sur, C.; Mukai, Y.; Voss, T.; Furtek, C.; et al. Randomized trials of verubecestat for mild-to-moderate Alzheimer's disease. *N. Engl. J. Med.* **2018**, *378*, 1691–1703. [CrossRef]
12. Egan, M.F.; Kost, J.; Voss, T.; Mukai, Y.; Aisen, P.S.; Cummings, J.L.; Tariot, P.N.; Vellas, B.; van Dyck, C.H.; Boada, M.; et al. Randomized trial of verubecestat for prodromal Alzheimer's disease. *N. Engl. J. Med.* **2019**, *380*, 1408–1420. [CrossRef] [PubMed]
13. Katzman, R.; Terry, R.; DeTeresa, R.; Brown, T.; Davies, P.; Fuld, P.; Rebing, X.; Peck, A. Clinical, pathological, and neurochemical changes in dementia: A subgroup with preserved mental status and numerous neocortical plaques. *Ann. Neurol.* **1988**, *23*, 138–144. [CrossRef] [PubMed]
14. Delaere, P.; Duyckaerts, C.; Masters, C.; Beyreuther, K.; Piette, F.; Hauw, J. Large amounts of neocortical beta A4 deposits without neuritic plaques nor tangles in a psychometrically assessed, non-demented person. *Neurosci. Lett.* **1990**, *116*, 87–93. [CrossRef] [PubMed]
15. Dickson, D.; Crystal, H.; Mattiace, L.; Masur, D.; Blau, A.; Davies, P.; Yen, S.; Aronson, M. Identification of normal and pathological aging in prospectively studied nondemented elderly humans. *Neurobiol. Aging* **1992**, *13*, 178–189. [CrossRef]
16. Aizenstein, H.; Nebes, R.; Saxton, J.; Price, J.; Mathis, C.; Tsopelas, N.; Ziolko, S.; James, J.; Snitz, B.; Houck, P.; et al. Frequent amyloid deposition without significant cognitive impairment among the elderly. *Arch. Neurol.* **2008**, *65*, 1509–1517. [CrossRef]
17. Klunk, W.; Mathis, C.; Price, J.; DeKosky, S.; Lopresti, B.; Tsopelas, N.; Saxton, J.; Nebes, R. Amyloid imaging with PET in Alzheimer's disease, mild cognitive impairment, and clinically unimpaired subjects. In *PET in the Evaluation of Alzheimer's Disease and Related Disorders*; Silverman, D., Ed.; Springer: New York, NY, USA, 2009; pp. 119–147.
18. Villemagne, V.; Pike, K.; Chételat, G.; Ellis, K.; Mulligan, R.; Bourgeat, P.; Ackermann, U.; Jones, G.; Szoeke, C.; Salvado, O.; et al. Longitudinal assessment of Abeta and cognition in aging and Alzheimer disease. *Ann. Neurol.* **2011**, *69*, 181–192. [CrossRef]
19. Seto, M.; Weiner, R.L.; Dumitrescu, L.; Hohman, T.J. Protective genes and pathways in Alzheimer's disease: Moving towards precision interventions. *Mol. Neurodegener.* **2021**, *16*, 29. [CrossRef]
20. Makin, S. The amyloid hypothesis on trial. *Nature* **2018**, *559*, S4–S7. [CrossRef]
21. Casas, C.; Sergeant, N.; Itier, J.M.; Blanchard, V.; Wirths, O.; Van Der Kolk, N.; Vingtdeux, V.; Van De Steeg, E.; Ret, G.; Canton, T.; et al. Massive CA1/2 neuronal loss with intraneuronal and N-terminal truncated Abeta42 accumulation in a novel Alzheimer transgenic model. *Am. J. Pathol.* **2004**, *165*, 1289–1300. [CrossRef]
22. Bayer, T.A.; Wirths, O. Review on the APP/PS1KI mouse model: Intraneuronal Abeta accumulation triggers axonopathy, neuron loss and working memory impairment. *Genes Brain Behav.* **2008**, *7*, 6–11. [CrossRef] [PubMed]
23. Bayer, T.A.; Breyhan, H.; Duan, K.; Rettig, J.; Wirths, O. Intraneuronal beta-amyloid is a major risk factor--novel evidence from the APP/PS1KI mouse model. *Neurodegener. Dis.* **2008**, *5*, 140–142. [CrossRef]
24. Wirths, O.; Breyhan, H.; Cynis, H.; Schilling, S.; Demuth, H.U.; Bayer, T.A. Intraneuronal pyroglutamate-Abeta 3–42 triggers neurodegeneration and lethal neurological deficits in a transgenic mouse model. *Acta Neuropathol.* **2009**, *118*, 487–496. [CrossRef]
25. Christensen, D.Z.; Bayer, T.A.; Wirths, O. Intracellular Aβ triggers neuron loss in the cholinergic system of the APP/PS1KI mouse model of Alzheimer's disease. *Neurobiol. Aging* **2010**, *31*, 1153–1163. [CrossRef]
26. Christensen, D.Z.; Schneider-Axmann, T.; Lucassen, P.J.; Bayer, T.A.; Wirths, O. Accumulation of intraneuronal Abeta correlates with ApoE4 genotype. *Acta Neuropathol.* **2010**, *119*, 555–566. [CrossRef]
27. Bayer, T.A.; Wirths, O. Intracellular accumulation of amyloid-Beta—A predictor for synaptic dysfunction and neuron loss in Alzheimer's disease. *Front. Aging Neurosci.* **2010**, *2*, 8. [CrossRef]
28. Bayer, T.A.; Wirths, O. Intraneuronal Aβ as a trigger for neuron loss: Can this be translated into human pathology? *Biochem. Soc. Trans.* **2011**, *39*, 857–861. [CrossRef]
29. Wirths, O.; Bayer, T.A. Intraneuronal Aβ accumulation and neurodegeneration: Lessons from transgenic models. *Life Sci.* **2012**, *91*, 1148–1152. [CrossRef]
30. Kumar, S.; Wirths, O.; Theil, S.; Gerth, J.; Bayer, T.A.; Walter, J. Early intraneuronal accumulation and increased aggregation of phosphorylated Abeta in a mouse model of Alzheimer's disease. *Acta Neuropathol.* **2013**, *125*, 699–709. [CrossRef] [PubMed]
31. Ripoli, C.; Cocco, S.; Li Puma, D.D.; Piacentini, R.; Mastrodonato, A.; Scala, F.; Puzzo, D.; D'Ascenzo, M.; Grassi, C. Intracellular accumulation of amyloid-β (Aβ) protein plays a major role in Aβ-induced alterations of glutamatergic synaptic transmission and plasticity. *J. Neurosci.* **2014**, *34*, 12893–12903. [CrossRef] [PubMed]
32. Scala, F.; Fusco, S.; Ripoli, C.; Piacentini, R.; Li Puma, D.D.; Spinelli, M.; Laezza, F.; Grassi, C.; D'Ascenzo, M. Intraneuronal Aβ accumulation induces hippocampal neuron hyperexcitability through A-type K(+) current inhibition mediated by activation of caspases and GSK-3. *Neurobiol. Aging* **2015**, *36*, 886–900. [CrossRef] [PubMed]
33. Christensen, D.Z.; Kraus, S.L.; Flohr, A.; Cotel, M.C.; Wirths, O.; Bayer, T.A. Transient intraneuronal Abeta rather than extracellular plaque pathology correlates with neuron loss in the frontal cortex of APP/PS1KI mice. *Acta Neuropathol.* **2008**, *116*, 647–655. [CrossRef] [PubMed]
34. Chafekar, S.; Baas, F.; Scheper, W. Oligomer-specific amyloid-beta toxicity in cell models is mediated by selective uptake. *Biochem. Biophys. Acta* **2008**, *9*, 523–531.

35. Wesen, E.; Jeffries, G.; Dzebo, M.; Esbjorner, M. Endocytic uptake of monomeric amyloid-β peptides is clathrin- and dynamin-independent and results in selective accumulation of Aβ(1–42) compared to Aβ(1–40). *Sci. Rep.* **2017**, *7*, 2021. [CrossRef] [PubMed]
36. Kumar-Singh, S.; Theuns, J.; Van Broeck, B.; Pirici, D.; Vennekens, K.L.; Corsmit, E.; Cruts, M.; Dermaut, B.; Wang, R.; Van Broeckhoven, C. Mean age-of-onset of familial Alzheimer disease caused by presenilin mutations correlates with both increased Abeta42 and decreased Abeta40. *Hum. Mutat.* **2006**, *27*, 686–695. [CrossRef]
37. Hu, X.; Crick, S.L.; Bu, G.; Frieden, C.; Pappu, R.V.; Lee, J.-M. Amyloid seeds formed by cellular uptake, concentration, and aggregation of the amyloid-beta peptide. *Proc. Natl. Acad. Sci. USA* **2009**, *106*, 20324–20329. [CrossRef]
38. Yajima, R.; Tokutake, T.; Koyama, A.; Kasuga, K.; Tezuka, T.; Nishizawa, M.; Ikeuchi, T. ApoE-isoform-dependent cellular uptake of amyloid-β is mediated by lipoprotein receptor LR11/SorLA. *Biochem. Biophys. Res. Comm.* **2015**, *456*, 482–488. [CrossRef]
39. Omtri, R.S.; Davidson, M.W.; Arumugam, B.; Poduslo, J.F.; Kandimalla, K.K. Differences in the cellular uptake and intracellular itineraries of amyloid beta proteins 40 and 42: Ramifications for the Alzheimer's drug discovery. *Mol. Pharm.* **2012**, *9*, 1887. [CrossRef]
40. Bu, G.; Cam, J.; Zerbinatti, C. LRP in amyloid-β production and metabolism. *Ann. N. Y. Acad. Sci.* **2006**, *1086*, 35–53. [CrossRef]
41. Wang, H.Y.; Lee, D.H.; D'Andrea, M.R.; Peterson, P.A.; Shank, R.P.; Reitz, A.B. β-Amyloid1–42 binds to α7 nicotinic acetylcholine receptor with high affinity. Implications for Alzheimer's disease pathology. *J. Biol. Chem.* **2000**, *275*, 5626–5632. [CrossRef]
42. Nagele, R.; D'Andrea, M.; Anderson, W.; Wang, H. Intracellular accumulation of Aβ42 in neurons is facilitated by the α7 nicotinic acetylcholine receptor in Alzheimer's disease. *Neuroscience* **2002**, *110*, 199–211. [CrossRef] [PubMed]
43. Oddo, S.; Caccamo, A.; Green, K.N.; Liang, K.; Tran, L.; Chen, Y.; Leslie, F.M.; LaFerla, F.M. Chronic nicotine administration exacerbates tau pathology in a transgenic model of Alzheimer's disease. *Proc. Natl. Acad. Sci. USA* **2005**, *102*, 3046–3051. [CrossRef] [PubMed]
44. Yan, S.D.; Chen, X.I.; Fu, J.; Chen, M.; Zhu, H.; Roher, A.; Slattery, T.; Zhao, L.; Nagashima, M.; Morser, J.; et al. RAGE and amyloid-β peptide neurotoxicity in Alzheimer's disease. *Nature* **1996**, *382*, 685–691. [CrossRef] [PubMed]
45. Sasaki, N.; Toki, S.; Chowei, H.; Saito, T.; Nakano, N.; Hayashi, Y.; Takeuchi, M.; Makita, Z. Immunohistochemical distribution of the receptor for advanced glycation end products in neurons and astrocytes in Alzheimer's disease. *Brain Res.* **2001**, *888*, 256–262. [CrossRef]
46. Deane, R.; Du Yan, S.; Submamaryan, R.K.; LaRue, B.; Jovanovic, S.; Hogg, E.; Welch, D.; Manness, L.; Lin, C.; Yu, J.; et al. RAGE mediates amyloid-β peptide transport across the blood–brain barrier and accumulation in brain. *Nature Med.* **2003**, *9*, 907–913. [CrossRef]
47. Iribarren, P.; Zhou, Y.; Hu, J.; Le, Y.; Wang, J. Role of formyl peptide receptor-like 1 (FPRL1/FPR2) in mononuclear phagocyte responses in Alzheimer disease. *Immunol. Res.* **2005**, *31*, 165–176. [CrossRef]
48. Snyder, E.M.; Nong, Y.; Almeida, C.G.; Paul, S.; Moran, T.; Choi, E.Y.; Nairn, A.C.; Salter, M.W.; Lombroso, P.J.; Gouras, G.K.; et al. Regulation of NMDA receptor trafficking by amyloid-β. *Nature Neurosci.* **2005**, *8*, 1051–1058. [CrossRef]
49. LaFerla, F.; Green, K.; Oddo, S. Intracellular amyloid-beta in Alzheimer's disease. *Nat. Rev. Neurosci.* **2007**, *8*, 499–509. [CrossRef]
50. Kinoshita, A.; Fukumoto, H.; Shah, T.; Whelan, C.M.; Irizarry, M.C.; Hyman, B.T. Demonstration by FRET of BACE interaction with the amyloid precursor protein at the cell surface and in early endosomes. *J. Cell Sci.* **2003**, *116*, 3339–3346. [CrossRef]
51. Xu, H.; Greengard, P.; Gandy, S. Regulated formation of Golgi secretory vesicles containing Alzheimer β-amyloid precursor protein. *J. Biol. Chem.* **1995**, *270*, 23243–23245. [CrossRef]
52. Mizuguchi, M.; Ikeda, K.; Kim, S. Differential distribution of cellular forms of β-amyloid precursor protein in murine glial cell cultures. *Brain Res.* **1992**, *584*, 219–225. [CrossRef] [PubMed]
53. Cook, D.G.; Forman, M.S.; Sung, J.C.; Leight, S.; Kolson, D.L.; Iwatsubo, T.; Lee, V.M.Y.; Doms, R.W. Alzheimer's A-42 is generated in the endoplasmic reticulum/intermediate compartment of NT2N cells. *Nature Med.* **1997**, *3*, 1021–1023. [CrossRef] [PubMed]
54. Hartmann, T.; Bieger, S.C.; Brühl, B.; Tienari, P.J.; Ida, N.; Allsop, D.; Roberts, G.W.; Masters, C.L.; Dotti, C.G.; Unsicker, K.; et al. Distinct sites of intracellular production for Alzheimer's disease A β40/42 amyloid peptides. *Nature Med.* **1997**, *3*, 1016–1020. [CrossRef] [PubMed]
55. Wild-Bode, C.; Yamazaki, T.; Capell, A.; Leimer, U.; Steiner, H.; Ihara, Y.; Haass, C. Intracellular generation and accumulation of amyloid beta-peptide terminating at amino acid 42. *J. Biol. Chem.* **1997**, *272*, 16085–16088. [CrossRef] [PubMed]
56. Lee, S.J.; Liyanage, U.; Bickel, P.E.; Xia, W.; Lansbury, P.T., Jr.; Kosik, K.S. A detergent-insoluble membrane compartment contains Aβ in vivo. *Nature Med.* **1998**, *4*, 730–734. [CrossRef]
57. Skovronsky, D.; Doms, R.; Lee, V. Detection of a novel intraneuronal pool of insoluble amyloid β protein that accumulates with time in culture. *J. Cell Biol.* **1998**, *141*, 1031–1039. [CrossRef]
58. Manczak, M.; Anekonda, T.S.; Henson, E.; Park, B.S.; Quinn, J.; Reddy, P.H. Mitochondria are a direct site of Aβ accumulation in Alzheimer's disease neurons: Implications for free radical generation and oxidative damage in disease progression. *Hum. Mol. Genet.* **2006**, *15*, 1437–1449. [CrossRef]
59. Martin, B.; Schrader-Fischer, G.; Busciglio, J.; Duke, M.; Paganetti, P.; Yankner, B. Intracellular accumulation of beta-amyloid in cells expressing the Swedish mutant amyloid precursor protein. *J. Biol. Chem.* **1995**, *270*, 26727–26730. [CrossRef]
60. Sannerud, R.; Esselens, C.; Ejsmont, P.; Mattera, R.; Rochin, L.; Tharkeshwar, A.K.; De Baets, G.; De Wever, V.; Habets, R.; Baert, V.; et al. Restricted Location of PSEN2/gamma-secretase determines substrate specificity and generates an intracellular Abeta pool. *Cell* **2016**, *166*, 193–208. [CrossRef]

61. Choi, S.H.; Kim, Y.H.; Hebisch, M.; Sliwinski, C.; Lee, S.; D'Avanzo, C.; Chen, H.; Hooli, B.; Asselin, C.; Muffat, J.; et al. A three-dimensional human neural cell culture model of Alzheimer's disease. *Nature* **2014**, *515*, 274–278. [CrossRef]
62. De Jonghe, C.; Zehr, C.; Yager, D.; Prada, C.M.; Younkin, S.; Hendriks, L.; Van Broeckhoven, C.; Eckman, C.B. Flemish and Dutch mutations in amyloid beta precursor protein have different effects on amyloid beta secretion. *Neurobiol. Dis.* **1998**, *5*, 281–286. [CrossRef] [PubMed]
63. Pakos-Zebrucka, K.; Koryga, I.; Mnich, K.; Ljujic, M.; Samali, A.; Gorman, A.M. The integrated stress response. *EMBO Rep.* **2016**, *17*, 1374–1395. [CrossRef] [PubMed]
64. Ron, D. Translational control in the endoplasmic reticulum stress response. *J. Clin. Investig.* **2002**, *110*, 1383–1388. [CrossRef] [PubMed]
65. Harding, H.P.; Zhang, Y.; Zeng, H.; Novoa, I.; Lu, P.D.; Calfon, M.; Sadri, N.; Yun, C.; Popko, B.; Paules, R.S.; et al. An integrated stress response regulates amino acid metabolism and resistance to oxidative stress. *Mol. Cell* **2003**, *11*, 619–633. [CrossRef]
66. Brostrom, C.O.; Prostko, C.R.; Kaufman, R.J.; Brostrom, M.A. Inhibition of translational initiation by activators of the glucose-regulated stress protein and heat shock protein stress response systems. Role of the interferon-inducible double-stranded RNA-activated eukaryotic initiation factor 2alpha kinase. *J. Biol. Chem.* **1996**, *271*, 24995–25002. [CrossRef]
67. Dever, T.E.; Feng, L.; Wek, R.C.; Hinnebusch, A.G. Phosphorylation of initiation factor 2 alpha by protein kinase GCN2 mediates gene-specific translational control of GCN4 in yeast. *Cell* **1992**, *68*, 585–596. [CrossRef]
68. Wek, R.C.; Jiang, H.Y.; Anthony, T.G. Coping with stress: eIF2 kinases and translational control. *Biochem. Soc. Trans.* **2006**, *34*, 7–11. [CrossRef]
69. Rzymski, T.; Milani, M.; Pike, L.; Buffa, F.; Mellor, H.R.; Winchester, L.; Pires, I.; Hammond, E.; Ragoussis, I.; Harris, A.L. Regulation of autophagy by ATF4 in response to severe hypoxia. *Oncogene* **2010**, *29*, 4424–4435. [CrossRef]
70. Ye, J.; Kumanova, M.; Hart, L.S.; Sloane, K.; Zhang, H.; De Panis, D.N.; Bobrovnikova-Marjon, E.; Diehl, J.A.; Ron, D.; Koumenis, C. The GCN2-ATF4 pathway is critical for tumour cell survival and proliferation in response to nutrient deprivation. *EMBO J.* **2010**, *29*, 2082–2096. [CrossRef]
71. Garcia, M.A.; Meurs, E.F.; Esteban, M. The dsRNA protein kinase PKR: Virus and cell control. *Biochimie* **2007**, *89*, 799–811. [CrossRef]
72. Harding, H.P.; Zhang, Y.; Ron, D. Protein translation and folding are coupled by an endoplasmic-reticulum-resident kinase. *Nature* **1999**, *397*, 271–274. [CrossRef] [PubMed]
73. Chang, R.C.; Suen, K.C.; Ma, C.H.; Elyaman, W.; Ng, H.K.; Hugon, J. Involvement of double-stranded RNA-dependent protein kinase and phosphorylation of eukaryotic initiation factor-2alpha in neuronal degeneration. *J. Neurochem.* **2002**, *83*, 1215–1225. [CrossRef] [PubMed]
74. Peel, A.L. PKR activation in neurodegenerative disease. *J. Neuropathol. Exp. Neurol.* **2004**, *63*, 97–105. [CrossRef] [PubMed]
75. Peel, A.L.; Bredesen, D.E. Activation of the cell stress kinase PKR in Alzheimer's disease and human amyloid precursor protein transgenic mice. *Neurobiol. Dis.* **2003**, *14*, 52–62. [CrossRef] [PubMed]
76. Chang, R.C.; Wong, A.K.; Ng, H.K.; Hugon, J. Phosphorylation of eukaryotic initiation factor-2alpha (eIF2alpha) is associated with neuronal degeneration in Alzheimer's disease. *Neuroreport* **2002**, *13*, 2429–2432. [CrossRef] [PubMed]
77. Onuki, R.; Bando, Y.; Suyama, E.; Katayama, T.; Kawasaki, H.; Baba, T.; Tohyama, M.; Taira, K. An RNA-dependent protein kinase is involved in tunicamycin-induced apoptosis and Alzheimer's disease. *EMBO J.* **2004**, *23*, 959–968. [CrossRef]
78. Lourenco, M.V.; Clarke, J.R.; Frozza, R.L.; Bomfim, T.R.; Forny-Germano, L.; Batista, A.F.; Sathler, L.B.; Brito-Moreira, J.; Amaral, O.B.; Silva, C.A.; et al. TNF-alpha mediates PKR-dependent memory impairment and brain IRS-1 inhibition induced by Alzheimer's beta-amyloid oligomers in mice and monkeys. *Cell Metab.* **2013**, *18*, 831–843. [CrossRef]
79. Paquet, C.; Mouton-Liger, F.; Meurs, E.F.; Mazot, P.; Bouras, C.; Pradier, L.; Gray, F.; Hugon, J. The PKR activator PACT is induced by Abeta: Involvement in Alzheimer's disease. *Brain Pathol.* **2012**, *22*, 219–229. [CrossRef]
80. Zhu, X.; Perry, G.; Moreira, P.I.; Aliev, G.; Cash, A.D.; Hirai, K.; Smith, M.A. Mitochondrial abnormalities and oxidative imbalance in Alzheimer disease. *J. Alzheimer's Dis.* **2006**, *9*, 147–153. [CrossRef]
81. Blass, J.P. The mitochondrial spiral. An adequate cause of dementia in the Alzheimer's syndrome. *Ann. N. Y. Acad. Sci.* **2000**, *924*, 170–183. [CrossRef]
82. Manczak, M.; Park, B.S.; Jung, Y.; Reddy, P.H. Differential expression of oxidative phosphorylation genes in patients with Alzheimer's disease: Implications for early mitochondrial dysfunction and oxidative damage. *Neuromol. Med.* **2004**, *5*, 147–162. [CrossRef] [PubMed]
83. Qin, W.; Haroutunian, V.; Katsel, P.; Cardozo, C.P.; Ho, L.; Buxbaum, J.D.; Pasinetti, G.M. PGC-1alpha expression decreases in the Alzheimer disease brain as a function of dementia. *Arch. Neurol.* **2009**, *66*, 352–361. [CrossRef] [PubMed]
84. Du, H.; Guo, L.; Yan, S.; Sosunov, A.A.; McKhann, G.M.; Yan, S.S. Early deficits in synaptic mitochondria in an Alzheimer's disease mouse model. *Proc. Natl. Acad. Sci. USA* **2010**, *107*, 18670–18675. [CrossRef]
85. Lin, M.T.; Simon, D.K.; Ahn, C.H.; Kim, L.M.; Beal, M.F. High aggregate burden of somatic mtDNA point mutations in aging and Alzheimer's disease brain. *Hum. Mol. Genet.* **2002**, *11*, 133–145. [CrossRef] [PubMed]
86. Calkins, M.; Manczak, M.; Mao, P.; Shirendeb, U.; Reddy, P.H. Impaired mitochondrial biogenesis, defective axonal transport of mitochondria, abnormal mitochondrial dynamics and synaptic degeneration in a mouse model of Alzheimer's disease. *Hum. Mol. Genet.* **2011**, *20*, 4515–4529. [CrossRef] [PubMed]

87. Anandatheerthavarada, H.K.; Biswas, G.; Robin, M.A.; Avadhani, N.G. Mitochondrial targeting and a novel transmembrane arrest of Alzheimer's amyloid precursor protein impairs mitochondrial function in neuronal cells. *J. Cell Biol.* **2003**, *161*, 41–54. [CrossRef]
88. Caspersen, C.; Wang, N.; Yao, J.; Sosunov, A.; Chen, X.; Lustbader, J.W.; Xu, H.W.; Stern, D.; McKhann, G.; Du Yan, S. Mitochondrial Abeta: A potential focal point for neuronal metabolic dysfunction in Alzheimer's disease. *FASEB J.* **2005**, *19*, 2040–2041. [CrossRef] [PubMed]
89. Chen, J.X.; Yan, S.S. Role of mitochondrial amyloid-beta in Alzheimer's disease. *J. Alzheimer's Dis.* **2010**, *20*, S569–S578. [CrossRef]
90. Hansson Petersen, C.A.; Alikhani, N.; Behbahani, H.; Wiehager, B.; Pavlov, P.F.; Alafuzoff, I.; Leinonen, V.; Ito, A.; Winblad, B.; Glaser, E.; et al. The amyloid beta-peptide is imported into mitochondria via the TOM import machinery and localized to mitochondrial cristae. *Proc. Natl. Acad. Sci. USA* **2008**, *105*, 13145–13150. [CrossRef]
91. de la Monte, S.M.; Luong, T.; Neely, T.R.; Robinson, D.; Wands, J.R. Mitochondrial DNA damage as a mechanism of cell loss in Alzheimer's disease. *Lab. Investig.* **2000**, *80*, 1323–1335. [CrossRef]
92. Brooks, W.M.; Lynch, P.J.; Ingle, C.C.; Hatton, A.; Emson, P.C.; Faull, R.L.; Starkey, M.P. Gene expression profiles of metabolic enzyme transcripts in Alzheimer's disease. *Brain Res.* **2007**, *1127*, 127–135. [CrossRef] [PubMed]
93. Wang, X.; Perry, G.; Smith, M.A.; Zhu, X. Amyloid-beta-derived diffusible ligands cause impaired axonal transport of mitochondria in neurons. *Neurodegener. Dis.* **2007**, *7*, 56–59. [CrossRef] [PubMed]
94. Wang, X.; Su, B.; Fujioka, H.; Zhu, X. Dynamin-like protein 1 reduction underlies mitochondrial morphology and distribution abnormalities in fibroblasts from sporadic Alzheimer's disease patients. *Am. J. Pathol.* **2008**, *173*, 470–482. [CrossRef] [PubMed]
95. Wang, X.; Su, B.; Lee, H.G.; Li, X.; Perry, G.; Smith, M.A.; Zhu, X. Impaired balance of mitochondrial fission and fusion in Alzheimer's disease. *J. Neurosci.* **2009**, *29*, 9090–9103. [CrossRef] [PubMed]
96. Wang, X.; Su, B.; Siedlak, S.L.; Moreira, P.I.; Fujioka, H.; Wang, Y.; Casadesus, G.; Zhu, X. Amyloid-beta overproduction causes abnormal mitochondrial dynamics via differential modulation of mitochondrial fission/fusion proteins. *Proc. Natl. Acad. Sci. USA* **2008**, *105*, 19318–19323. [CrossRef]
97. Brewer, G.; Herrera, R.; Philipp, S.; Sosna, J.; Reyes-Ruiz, J.; Glabe, C. Age-Related Intraneuronal Aggregation of Amyloid-β in Endosomes, Mitochondria, Autophagosomes, and Lysosomes. *J. Alzheimer's Dis.* **2020**, *73*, 229–246. [CrossRef]
98. Guo, X.; Aviles, G.; Liu, Y.; Tian, R.; Unger, B.A.; Lin, Y.-H.T.; Wiita, A.P.; Xu, K.; Correia, M.A.; Kampmann, M. Mitochondrial stress is relayed to the cytosol by an OMA1-DELE1-HRI pathway. *Nature* **2020**, *579*, 427–432. [CrossRef]
99. Fessler, E.; Eckl, E.-M.; Schmitt, S.; Mancilla, I.A.; Meyer-Bender, M.F.; Hanf, M.; Philippou-Massier, J.; Krebs, S.; Zischka, H.; Jae, L.T. A pathway coordinated by DELE1 relays mitochondrial stress to the cytosol. *Nature* **2020**, *579*, 433–437. [CrossRef]
100. Tucker-Drob, E.M. Cognitive Aging and Dementia: A Life Span Perspective. *Annu. Rev. Dev. Psychol.* **2019**, *1*, 177–196. [CrossRef]
101. Matthews, F.E.; Arthur, A.; Barnes, L.E.; Bond, J.; Jagger, C.; Robinson, L.; Brayne, C.; Medical Research Council Cognitive Function and Ageing Collaboration. A two-decade comparison of prevalence of dementia in individuals aged 65 years and older from three geographical areas of England: Results of the Cognitive Function and Ageing Study I and II. *Lancet* **2013**, *382*, 1405–1412. [CrossRef]
102. Farzan, M.; Schnitzler, C.E.; Vasilieva, N.; Leung, D.; Choe, H. BACE2, a β-secretase homolog, cleaves at the β site and within the amyloid-β region of the amyloid-β precursor protein. *Proc. Natl. Acad. Sci. USA* **2000**, *97*, 9712–9717. [CrossRef] [PubMed]
103. Yan, R.; Munzner, J.; Shuck, M.; Bienkowski, M. BACE2 functions as an alternative alpha secretase in cells. *J. Biol. Chem.* **2001**, *276*, 34019–34027. [CrossRef] [PubMed]
104. Volloch, V.; Schweitzer, B.; Rits, S. Antisense Globin RNA in Murine Erythroid Tissues: Structure, Origin and Possible Function. *Proc. Natl. Acad. Sci. USA* **1996**, *93*, 2476–2481. [CrossRef] [PubMed]
105. Volloch, V. Protein-encoding RNA-to-RNA information transfer in mammalian cells: Principles of RNA-dependent mRNA amplification. *Ann. Integr. Mol. Med.* **2019**, *1*, 1002. [CrossRef] [PubMed]
106. Rits, S.; Olsen, B.; Volloch, V. Protein-encoding RNA to RNA information transfer in mammalian cells: RNA-dependent mRNA amplification. Identification of chimeric RNA intermediates and putative RNA end products. *Ann. Integr. Mol. Med.* **2019**, *1*, 1003.
107. Volloch, V.; Rits, S.; Olsen, B. RNA-dependent amplification of mammalian mRNA encoding extracellular matrix proteins: Identification of chimeric RNA intermediates for 1alpha, 1beta, and 1gamma chains of laminin. *Ann. Integr. Mol. Med.* **2019**, *1*, 1004.
108. Henley, D.B.; Sundell, K.L.; Sethuraman, G.; Dowsett, S.A.; May, P.C. Safety profile of semagacestat, a gamma-secretase inhibitor: IDENTITY trial findings. *Curr. Med. Res.* **2014**, *30*, 2021–2032. [CrossRef]
109. Tagami, S.; Yanagida, K.; Kodama, T.S.; Takami, M.; Mizuta, N.; Oyama, H.; Nishitomi, K.; Chiu, Y.-W.; Okamoto, T.; Ikeuchi, T.; et al. Semagacestat Is a Pseudo-Inhibitor of γ-Secretase. *Cell Rep.* **2017**, *21*, 259–273. [CrossRef]
110. Imbimbo, B.; Giardina, G. γ-secretase inhibitors and modulators for the treatment of Alzheimer's disease: Disappointments and hopes. *Curr. Top. Med. Chem.* **2011**, *11*, 1555–1570. [CrossRef]
111. Zhao, J.; Liu, X.; Xia, W. Targeting Amyloidogenic Processing of APP in Alzheimer's Disease. *Front. Mol. Neurosci.* **2020**, *13*, 137. [CrossRef]
112. Mekala, S.; Nelson, G.; Li, Y. Recent developments of small molecule γ-secretase modulators for Alzheimer's disease. *RSC Med. Chem.* **2020**, *11*, 1003–1022. [CrossRef]

113. Rynearson, K.D.; Ponnusamy, M.; Prikhodko, O.; Xie, Y.; Zhang, C.; Nguyen, P.; Hug, B.; Sawa, M.; Becker, A.; Spencer, B.; et al. Preclinical validation of a potent γ-secretase modulator for Alzheimer's disease prevention. *J. Exp. Med.* **2021**, *218*, e20202560. [CrossRef] [PubMed]
114. Jäger, S.; Leuchtenberger, S.; Martin, A.; Czirr, E.; Wesselowski, J.; Dieckmann, M.; Waldron, E.; Korth, C.; Koo, E.H.; Heneka, M.; et al. Alpha-secretase mediated conversion of the amyloid precursor protein derived membrane stub C99 to C83 limits Aβ generation. *J. Neurochem.* **2009**, *6*, 1369–1382. [CrossRef]
115. Kuhn, P.H.; Wang, H.; Dislich, B.; Colombo, A.; Zeitschel, U.; Ellwart, J.W.; Kremmer, E.; Roßner, S.; Lichtenthaler, S.F. ADAM10 is the physiologically relevant, constitutive α-secretase of the amyloid precursor protein in primary neurons. *EMBO J.* **2010**, *29*, 3020–3032. [CrossRef]
116. Lichtenthaler, S. Alpha-secretase in Alzheimer's disease. *J. Neurochem.* **2011**, *116*, 10–21. [CrossRef]
117. Postina, R. Activation of alpha secretase cleavage. *J. Neurochem.* **2012**, *120*, 46–54. [CrossRef] [PubMed]
118. Endres, K.; Deller, T. Regulation of Alpha-Secretase ADAM10 In vitro and In vivo: Genetic, Epigenetic, and Protein-Based Mechanisms. *Front. Mol. Neurosci.* **2017**, *10*, 56. [CrossRef] [PubMed]
119. Ray, B.; Maloney, B.; Sambamurti, K.; Karnati, H.K.; Nelson, P.T.; Greig, N.H.; Lahiri, D.K. Rivastigmine modifies the α-secretase pathway and potentially early Alzheimer's disease. *Nat. Transl Psychiatry* **2020**, *10*, 47. [CrossRef]
120. Fahrenholz, F. Alpha-secretase as a therapeutic target. *Curr. Alzheimer Res.* **2007**, *4*, 412–417. [CrossRef]
121. Postina, R.; Schroeder, A.; Dewachter, I.; Bohl, J.; Schmitt, U.; Kojro, E.; Prinzen, C.; Endres, K.; Hiemke, C.; Blessing, M.; et al. A disintegrin- metalloproteinase prevents amyloid plaque formation and hippocampal defects in an Alzheimer disease mouse model. *J. Clin. Investig.* **2004**, *113*, 1456–1464. [CrossRef]
122. MacLeod, R.; Hillert, E.; Cameron, R.; Baillie, G. The role and therapeutic targeting of α-, β- and γ-secretase in Alzheimer's disease. *Future Sci.* **2015**, *1*, FSO11. [CrossRef] [PubMed]
123. Prinzen, C.; Trumbach, D.; Wurst, W.; Endres, K.; Postina, R.; Fahrenholz, F. Differential gene expression in ADAM10 and mutant ADAM10 transgenic mice. *BMC Genom.* **2009**, *10*, 66. [CrossRef] [PubMed]
124. Jorissen, E.; Prox, J.; Bernreuther, C.; Weber, S.; Schwanbeck, R.; Serneels, L.; Snellinx, A.; Craessaerts, K.; Thathiah, A.; Tesseur, I.; et al. The disintegrin/metal-loproteinase ADAM10 is essential for the establishment of the brain cortex. *J. Neurosci.* **2010**, *30*, 4833–4844. [CrossRef] [PubMed]
125. Huse, J.; Liu, K.; Pijak, D.; Carlin, D.; Lee VDoms, R. Beta-secretase processing in the trans-Golgi network preferentially generates truncated amyloid species that accumulate in Alzheimer's disease brain. *J. Biol. Chem.* **2002**, *277*, 16278–16284. [CrossRef] [PubMed]
126. Liu, K.; Doms, R.; Lee, M. Glu11 site cleavage and N-terminally truncated A beta production upon BACE overexpression. *Biochemistry* **2002**, *41*, 3128–3136. [CrossRef]
127. Lee, E.B.; Zhang, B.; Liu, K.; Greenbaum, E.A.; Doms, R.W.; Trojanowski, J.Q.; Lee, V.M.-Y. BACE overexpression alters the subcellular processing of APP and inhibits Aβ deposition in vivo. *J. Cell Biol.* **2005**, *168*, 291–302. [CrossRef]
128. Kimura, A.; Hata, S.; Suzuki, T. Alternative selection of beta-site APP-cleaving enzyme 1 (BACE1) cleavage sites in amyloid beta-protein precursor (APP) harboring protective and pathogenic mutations within the Abeta sequence. *J. Biol. Chem.* **2016**, *291*, 24041–24053. [CrossRef]
129. Fluhrer, R.; Multhaup, G.; Schlicksupp, A.; Okochi, M.; Takeda, M.; Lammich, S.; Willem, M.; Westmeyer, G.; Bode, W.; Walter, J.; et al. Identification of a beta-secretase activity, which truncates amyloid beta-peptide after its presenilin-dependent generation. *J. Biol. Chem.* **2003**, *278*, 5531–5538. [CrossRef]
130. Shi, X.P.; Tugusheva, K.; Bruce, J.E.; Lucka, A.; Wu, G.X.; Chen-Dodson, E.; Price, E.; Li, Y.; Xu, M.; Huang, Q.; et al. Beta-secretase cleavage at amino acid residue 34 in the amyloid beta peptide is dependent upon gamma-secretase activity. *J. Biol. Chem.* **2003**, *278*, 21286–21294. [CrossRef]
131. Liebsch, F.; Kulic, L.; Teunissen, C.; Shobo, A.; Ulku, I.; Engelschalt, V.; Hancock, M.A.; van der Flier, W.M.; Kunach, P.; Rosa-Neto, P.; et al. Abeta34 is a BACE1-derived degradation intermediate associated with amyloid clearance and Alzheimer's disease progression. *Nat. Commun.* **2019**, *10*, 2240. [CrossRef]
132. Garcia-Gonzales, L.; Pilat, D.; Rivera, S. Emerging Alternative Proteinases in APP Metabolism and Alzheimer's Disease Pathogenesis. *Front. Aging Neurosci.* **2019**, *11*, 244. [CrossRef]
133. Basi, G.; Frigon, N.; Barbour, R.; Doan, T.; Gordon, G.; McConlogue, L.; Sinha, S.; Zeller, M. Antagonistic effects of beta-site amyloid precursor protein-cleaving enzymes 1 and 2 on beta-amyloid peptide production in cells. *J. Biol. Chem.* **2003**, *278*, 31512–31520. [CrossRef] [PubMed]
134. Almeida, C.; Takahashi, R.; Gouras, G. β-amyloid accumulation impairs multivesicular body sorting by inhibiting the ubiquitin–proteasome system. *J. Neurosci.* **2006**, *26*, 4277–4288. [CrossRef] [PubMed]
135. Gregori, L.; Fuchs, C.; Figueiredo-Pereira, M.; Van Nostrand, W.; Goldgaber, D. Amyloid β-protein inhibits ubiquitin-dependent protein degradation in vitro. *J. Biol. Chem.* **1995**, *270*, 19702–19708. [CrossRef]
136. Oh, S.; Hong, H.S.; Hwang, E.; Sim, H.J.; Lee, W.; Shin, S.J.; Mook-Jung, I. Amyloid peptide attenuates the proteasome activity in neuronal cells. *Mech. Ageing Dev.* **2005**, *126*, 1292–1299. [CrossRef] [PubMed]
137. Tseng, B.; Green, K.; Chan, J.; Blurton-Jones, M.; LaFerla, F. Aβ inhibits the proteasome and enhances amyloid and tau accumulation. *Neurobiol. Aging* **2008**, *29*, 1607–1618. [CrossRef] [PubMed]

138. Asai, H.; Ohkawa, N.; Saitoh, Y.; Ghandour, K.; Murayama, E.; Nishizono, H.; Matsuo, M.; Hirayama, T.; Kaneko, R.; Muramatsu, S.I.; et al. Pcdhβ deficiency affects hippocampal CA1 ensemble activity and contextual fear discrimination. *Mol. Brain* **2020**, *13*, 7. [CrossRef]
139. Rao, Y.L.; Ganaraja, B.; Murlimanju, B.V.; Joy, T.; Krishnamurthy, A.; Agrawal, A. Hippocampus and its involvement in Alzheimer's disease: A review. *3 Biotech.* **2022**, *12*, 55. [CrossRef]
140. Breimer, L.; Denny, P. Alzheimer amyloid aspects. *Nature* **1987**, *326*, 749–750. [CrossRef]
141. Kang, J.; Lemaire, H.G.; Unterbeck, A.; Salbaum, J.M.; Masters, C.L.; Grzeschik, K.H.; Multhaup, G.; Beyreuther, K.; Müller-Hill, B. The precursor of Alzheimer's disease amyloid A4 protein resembles a cell-surface receptor. *Nature* **1987**, *325*, 733–736. [CrossRef]
142. Robakis, N.K.; Ramakrishna, N.; Wolfe, G.; Wisniewski, H.M. Molecular cloning and characterization of a cDNA encoding the cerebrovascular and the neuritic plaque amyloid peptides. *Proc. Natl. Acad. Sci. USA* **1987**, *84*, 4190–4194. [CrossRef] [PubMed]
143. Tanzi, R.E.; Gusella, J.F.; Watkins, P.C.; Bruns, G.A.; St George-Hyslop, P.; Van Keuren, M.L.; Patterson, D.; Pagan, S.; Kurnit, D.M.; Neve, R.L. Amyloid beta protein gene: cDNA, mRNA distribution, and genetic linkage near the Alzheimer locus. *Science* **1987**, *235*, 880–884. [CrossRef] [PubMed]
144. Frottin, F.; Martinez, A.; Peinot, P.; Mitra, S.; Holz, R.; Giglione, C.; Meinnel, T. The proteomics of N-terminal methionine cleavage. *Mol Cell Proteom.* **2006**, *5*, 2336–2349. [CrossRef]
145. Xiao, Q.; Zhang, F.; Nacev, B.; Liu, J.; Pei, D. Protein N-Terminal Processing: Substrate Specificity of Escherichia coli and Human Methionine Aminopeptidases. *Biochemistry* **2010**, *49*, 5588–5599. [CrossRef] [PubMed]
146. Varshavsky, A. The N-end rule pathway and regulation by proteolysis. *Protein. Sci.* **2011**, *20*, 1298–1345. [CrossRef]
147. Wingfield, P. N-Terminal Methionine Processing. *Curr. Protoc. Protein. Sci.* **2017**, *88*, 6.14.1–6.14.3. [CrossRef] [PubMed]
148. Varland, S.; Osberg, C.; Arnesen, T. N-terminal modifications of cellular proteins: The enzymes involved, their substrate specificities and biological effects. *Proteomics* **2015**, *15*, 2385–2401. [CrossRef]
149. Polevoda, B.; Sherman, F. N-terminal acetyltransferases and sequence requirements for N-terminal acetylation of eukaryotic proteins. *J. Mol. Biol.* **2003**, *325*, 595–622. [CrossRef]
150. Citron, M.; Haass, C.; Selkoe, D. Production of amyloid beta peptide by cultured cells: No evidence for internal initiation of translation at Met596. *Neurobiol. Aging.* **1993**, *14*, 571–573. [CrossRef]
151. Macq, A.; Philippe, B.; Octave, N. The amyloid peptide of Alzheimer's disease is not produced by internal initiation of translation generating C-terminal amyloidogenic fragments of its precursor. *Neurosci. Lett.* **1994**, *182*, 227–230. [CrossRef]
152. Volloch, V.; Olsen, B.; Rits, S. Precursor-independent overproduction of beta-amyloid in AD: Mitochondrial dysfunction as possible initiator of asymmetric RNA-dependent APP mRNA amplification. An engine that drives Alzheimer's disease. *Ann. Integr. Mol. Med.* **2019**, *1*, 1005. [CrossRef]
153. Volloch, V.; Olsen, B.; Rits, S. AD "Statin": Alzheimer's disorder is a "fast" disease preventable by therapeutic intervention initiated even late in life and reversible at the early stages. *Ann. Integr. Mol. Med.* **2020**, *2*, 1006. [CrossRef]
154. Volloch, V.; Olsen, B.; Rits, S. Alzheimer's disease is driven by intraneuronally retained beta-amyloid produced in the AD-specific, APP-independent pathway: Current perspective and experimental models for tomorrow. *Ann. Integr. Mol. Med.* **2020**, *2*, 1007.
155. Volloch, V.; Olsen, B.; Rits, S. Alzheimer's disease prevention and treatment: Case for optimism. *Ann. Integr. Mol. Med.* **2020**, *2*, 1008. [CrossRef] [PubMed]
156. Volloch, V.; Rits-Volloch, S. News from Mars: Two-tier paradox, intracellular PCR, chimeric junction shift, dark matter mRNA and other remarkable features of mammalian RNA-dependent mRNA amplification. Implications for Alzheimer's disease, RNA-based vaccines and mRNA therapeutics. *Ann. Integr. Mol. Med.* **2021**, *2*, 131–173. [CrossRef] [PubMed]
157. Volloch, V.; Rits-Volloch, S. Alzheimer's disease is driven by beta-amyloid generated in the amyloid precursor protein-independent pathway and retained intraneuronally: Research and therapeutic strategies in a new AD paradigm. *Ann. Integr. Mol. Med.* **2021**, *2*, 1010. [CrossRef]
158. Volloch, V.; Schwetizer, B.; Rits, S. Evolutionarily Conserved Elements in the 5′-untranslated Region of β Globin mRNA Mediate Site-specific Priming of a Unique Hairpin Structure during cDNA Synthesis. *Nucl. Acids Res.* **1994**, *22*, 5302–5309. [CrossRef]
159. Mita, S.; Sadlock, J.; Herbert, J.; Schon, E. A cDNA specifying the human amyloid beta precursor protein encodes a 95-kDa polypeptide. *Nucl. Acids Res.* **1988**, *16*, 9351, Correction in *Nucl. Acids Res.* **1988**, *16*, 11402. [CrossRef]
160. Salbaum, J.; Weidemann, A.; Lemaire, H.; Masters, C.; Beyreuther, K. The promoter of Alzheimer's disease amyloid A4 precursor gene. *EMBO J.* **1988**, *7*, 2807–2813. [CrossRef] [PubMed]
161. Volloch, V. A mechanism for β-amyloid overproduction in Alzheimer's disease: Precursor-independent generation of β-amyloid via antisense RNA-primed mRNA synthesis. *FEBS Lett.* **1996**, *390*, 124–128. [CrossRef]
162. Volloch, V. Mechanism for β-amyloid overproduction in sporadic Alzheimer's Disease: Possible antisense RNA-mediated generation of a 5′-truncated ßAPP mRNA encoding 12 kDa C-terminal fragment of βAPP, the immediate precursor of Aβ. In *Molecular Mechanisms of Dementia*; Wasco, W., Tanzi, R., Eds.; Humana Press: New York, NY, USA, 1997.
163. Volloch, V. Possible mechanism for resistance to Alzheimer's disease (AD) in mice suggests new approach to generate a mouse model for sporadic AD and may explain familial resistance to AD in man. *Exp. Neurobiol.* **1997**, *144*, 214–218. [CrossRef] [PubMed]
164. Hellen, C.U.; Sarnow, P. Internal ribosome entry sites in eukaryotic mRNA molecules. *Genes Dev.* **2001**, *15*, 1593–1612. [CrossRef] [PubMed]
165. Yang, T.; Wang, C.; Tsai, H.; Liu, C. Human IRES Atlas: An integrative platform for studying IRES-driven translational regulation in humans. *Database* **2021**, *2021*, baab025. [CrossRef] [PubMed]

166. Kieft, J.S.; Costantino, D.A.; Filbin, M.E.; Hammond, J.; Pfingsten, J.S. Structural methods for studying IRES function. *Methods Enzymol.* **2007**, *430*, 333–371. [PubMed]
167. Wang, Q.S.; Au, H.H.; Jan, E. Methods for studying IRES-mediated translation of positive-strand RNA viruses. *Methods* **2013**, *59*, 167–179. [CrossRef]
168. Thompson, S.R. So you want to know if your message has an IRES? *WIREs RNA* **2012**, *3*, 697–705. [CrossRef]
169. Francisco-Velilla, R.; Fernandez-Chamorro, J.; Lozano, G.; Diaz-Toledano, R.; Martínez-Salas, E. RNA–protein interaction methods to study viral IRES elements. *Methods* **2015**, *91*, 3–12. [CrossRef]
170. Pardossi-Piquard, R.; Checler, F. The physiology of the β-amyloid precursor protein intracellular domain AICD. *J. Neurochem.* **2011**, *120*, 109–124. [CrossRef]
171. Szögi, T.; Schuster, I.; Borbély, E.; Gyebrovszki, A.; Bozsó, Z.; Gera, J.; Rajkó, R.; Sántha, M.; Penke, B.; Fülöp, L. Effects of the Pentapeptide P33 on Memory and Synaptic Plasticity in APP/PS1 Transgenic Mice: A Novel Mechanism Presenting the Protein Fe65 as a Target. *Int. J. Mol. Sci.* **2019**, *20*, 3050. [CrossRef]
172. Borg, J.-P.; Yang, Y.; De Taddeo-Borg, M.; Margolis, B.; Turner, R.S. The X11α protein slows cellular amyloid precursor protein processing and reduces Aβ40 and Aβ42 secretion. *J. Biol. Chem.* **1998**, *273*, 14761–14766. [CrossRef]
173. Dunning, C.J.R.; Black, H.L.; Andrews, K.L.; Davenport, E.C.; Conboy, M.; Chawla, S.; Dowle, A.A.; Ashford, D.; Thomas, J.R.; Evans, G.J.O. Multisite tyrosine phosphorylation of the N-terminus of Mint1/X11α by Src kinase regulates the trafficking of amyloid precursor protein. *J. Neurochem.* **2016**, *137*, 518–527. [CrossRef]
174. Miller, C.C.J.; McLoughlin, D.M.; Lau, K.-F.; Tennant, M.E.; Rogelj, B. The X11 proteins, Aβ production and Alzheimer's disease. *Trends Neurosci.* **2006**, *29*, 280–285. [CrossRef]
175. Tamayev, R.; Zhou, D.; D'Adamio, L. The interactome of the amyloid β precursor protein family members is shaped by phosphorylation of their intracellular domains. *Mol. Neurodegener.* **2009**, *4*, 28. [CrossRef] [PubMed]
176. Hoe, H.-S.; Tran, T.S.; Matsuoka, Y.; Howell, B.W.; Rebeck, G.W. DAB1 and Reelin Effects on Amyloid Precursor Protein and ApoE Receptor 2 Trafficking and Processing. *J. Biol. Chem.* **2006**, *281*, 35176–35185. [CrossRef] [PubMed]
177. Russo, C.; Dolcini, V.; Salis, S.; Venezia, V.; Zambrano, N.; Russo, T.; Schettini, G. Signal Transduction through Tyrosine-phosphorylated C-terminal Fragments of Amyloid Precursor Protein via an Enhanced Interaction with Shc/Grb2 Adaptor Proteins in Reactive Astrocytes of Alzheimer's Disease Brain. *J. Biol. Chem.* **2002**, *277*, 35282–35288. [CrossRef]
178. Tarr, P.E.; Roncarati, R.; Pelicci, G.; Pelicci, P.G.; D'Adamio, L. Tyrosine phosphorylation of the β-amyloid precursor protein cytoplasmic tail promotes interaction with Shc. *J. Biol. Chem.* **2002**, *277*, 16798–16804. [CrossRef]
179. Bukhari, H.; Glotzbach, A.; Kolbe, K.; Leonhardt, G.; Loosse, C.; Mueller, T. Small things matter: Implications of APP intracellular domain AICD nuclear signaling in the progression and pathogenesis of Alzheimer's disease. *Prog. Neurobiol.* **2017**, *156*, 189–213. [CrossRef]
180. Chang, K.-A.; Kim, H.-S.; Ha, T.-Y.; Ha, J.-W.; Shin, K.Y.; Jeong, Y.H.; Lee, J.-P.; Park, C.-H.; Kim, S.; Baik, T.-K.; et al. Phosphorylation of amyloid precursor protein (APP) at Thr668 regulates the nuclear translocation of the APP intracellular domain and induces neurodegeneration. *Mol. Cell. Biol.* **2006**, *26*, 4327–4338. [CrossRef]
181. Ando, K.; Iijima, K.-I.; Elliott, J.I.; Kirino, Y.; Suzuki, T. Phosphorylation-dependent regulation of the interaction of amyloid precursor protein with Fe65 affects the production of β-amyloid. *J. Biol. Chem.* **2001**, *276*, 40353–40361. [CrossRef]
182. Müller, T.; Meyer, H.E.; Egensperger, R.; Marcus, K. The amyloid precursor protein intracellular domain (AICD) as modulator of gene expression, apoptosis, and cytoskeletal dynamics-relevance for Alzheimer's disease. *Prog. Neurobiol.* **2008**, *85*, 393–406. [CrossRef]
183. Shu, R.; Wong, W.; Ma, Q.H.; Yang, Z.Z.; Zhu, H.; Liu, F.J.; Wang, P.; Ma, J.; Yan, S.; Polo, J.M.; et al. APP intracellular domain acts as a transcriptional regulator of miR-663 suppressing neuronal differentiation. *Cell Death Dis.* **2015**, *6*, e1651. [CrossRef] [PubMed]
184. Grimm, M.O.; Mett, J.; Stahlmann, C.P.; Grösgen, S.; Haupenthal, V.J.; Blümel, T.; Hundsdörfer, B.; Zimmer, V.C.; Mylonas, N.T.; Tanila, H.; et al. APP intracellular domain derived from amyloidogenic β- and γ-secretase cleavage regulates neprilysin expression. *Front. Aging. Neurosci.* **2015**, *7*, 77. [CrossRef] [PubMed]
185. Pousinha, P.A.; Mouska, X.; Bianchi, D.; Temido-Ferreira, M.; Rajão-Saraiva, J.; Gomes, R.; Fernandez, S.P.; Salgueiro-Pereira, A.R.; Gandin, C.; Raymond, E.F.; et al. The Amyloid Precursor Protein C-Terminal Domain Alters CA1 Neuron Firing, Modifying Hippocampus Oscillations and Impairing Spatial Memory Encoding. *Cell Rep.* **2019**, *29*, 317–331.e5. [CrossRef] [PubMed]

International Journal of
Molecular Sciences

MDPI

Article

α5-GABAA Receptor Modulation Reverses Behavioral and Neurophysiological Correlates of Psychosis in Rats with Ventral Hippocampal Alzheimer's Disease-like Pathology

Nicole E. Eassa [1,2], Stephanie M. Perez [1,2,*], Angela M. Boley [1,2], Hannah B. Elam [1,2], Dishary Sharmin [3], James M. Cook [3] and Daniel J. Lodge [1,2]

[1] Department of Pharmacology and Center for Biomedical Neuroscience, UT Health San Antonio, San Antonio, TX 78229, USA; eassa@livemail.uthscsa.edu (N.E.E.); boley@uthscsa.edu (A.M.B.); elamh@livemail.uthscsa.edu (H.B.E.); lodged@uthscsa.edu (D.J.L.)
[2] South Texas Veterans Health Care System, Audie L. Murphy Division, San Antonio, TX 78229, USA
[3] Department of Chemistry and Biochemistry, Milwaukee Institute of Drug Discovery, University of Wisconsin-Milwaukee, Milwaukee, WI 53211, USA; dsharmin@uwm.edu (D.S.); capncook@uwm.edu (J.M.C.)
* Correspondence: perezsm@uthscsa.edu

Abstract: Of the 35 million people in the world suffering from Alzheimer's Disease (AD), up to half experience comorbid psychosis. Antipsychotics, used to treat psychosis, are contraindicated in elderly patients because they increase the risk of premature death. Reports indicate that the hippocampus is hyperactive in patients with psychosis and those with AD. Preclinical studies have demonstrated that the ventral hippocampus (vHipp) can regulate dopamine system function, which is thought to underlie symptoms of psychosis. A viral-mediated approach was used to express mutated human genes known to contribute to AD pathology: the Swedish (K670N, M671L), Florida (I716V), and London (V717I) mutations of amyloid precursor protein and two mutations (M146L and L286V) of presenilin 1 specifically in the vHipp, to investigate the selective contribution of AD-like pathology in this region. We observed a significant increase in dopamine neuron population activity and behavioral deficits in this AD-AAV model that mimics observations in rodent models with psychosis-like symptomatologies. Further, systemic administration of MP-III-022 (α5-GABAA receptor selective positive allosteric modulator) was able to reverse aberrant dopamine system function in AD-AAV rats. This study provides evidence for the development of drugs that target α5-GABAA receptors for patients with AD and comorbid psychosis.

Keywords: Alzheimer's disease; psychosis; dopamine; ventral hippocampus; parvalbumin; α5-GABAA

Citation: Eassa, N.E.; Perez, S.M.; Boley, A.M.; Elam, H.B.; Sharmin, D.; Cook, J.M.; Lodge, D.J. α5-GABAA Receptor Modulation Reverses Behavioral and Neurophysiological Correlates of Psychosis in Rats with Ventral Hippocampal Alzheimer's Disease-like Pathology. *Int. J. Mol. Sci.* **2023**, *24*, 11788. https://doi.org/10.3390/ijms241411788

Academic Editor: Alberto Pérez-Mediavilla

Received: 6 July 2023
Revised: 18 July 2023
Accepted: 20 July 2023
Published: 22 July 2023

1. Introduction

Alzheimer's Disease (AD) is the most common neurodegenerative disease, affecting an estimated 6.7 million Americans age 65 and older [1] and is known to cause a progressive cognitive decline, but it is less appreciated that half of these patients also suffer with comorbid psychosis (hallucinations and delusions) [2]. Elderly patients are unable to be treated with antipsychotics (the standard-of-care) given that the Food and Drug Administration issued a black box warning contraindicating their use in the elderly due to an increased risk of premature death. AD patients suffering from comorbid psychosis are clearly in need of novel therapeutic options.

Dopamine system dysfunction has been demonstrated to underlie symptoms of psychosis and is likely attributable to aberrant regulation by afferent brain regions [3,4]. The hippocampus is one such region upstream of the dopamine system that is a key site of pathology in patients with AD [5] and displays aberrant activity in psychosis [6]. In preclinical studies, our laboratory, along with others, has shown that hyperactivity of the ventral hippocampus (vHipp) drives dopamine system dysfunction in the ventral tegmental area

(VTA) via a multi-synaptic circuit in rodent models used to study psychosis [7]. Further, we have shown that increasing expression of the α5 subunit of the GABAA receptor in the vHipp reverses neuronal and behavioral deficits analogous to psychosis [8]. Given that the endogenous expression of α5 is highly specific to the hippocampus [9], systemic administration of positive allosteric modulators of α5 (α5-PAMs), which were developed as nootropic drugs that work by normalizing the excitation/inhibition (E/I) balance, may serve as a novel therapeutic option for patients with comorbid psychosis by reversing aberrant hippocampal drive of the dopamine system.

Previous studies have demonstrated that amyloid beta (Aβ) plaques, which accumulate in the hippocampus and other cortical areas, induce hyperactivity in the vHipp and psychosis-like neuronal and behavioral pathology in a rat model used to study sporadic AD [10]. In order to investigate this pathophysiology in a circuit-specific manner, and determine whether an α 5-PAM, MP-III-022, is able to reverse this, here we virally expressed two mutated human genes known to contribute to AD pathology, the Swedish (K670N, M671L), Florida (I716V), and London (V717I) mutations of human amyloid precursor protein (hAPP) and two mutations (M146L and L286V) of presenilin 1 (hPSEN1), specifically in the vHipp. Once the rats reached adulthood, corresponding to the age of AD pathology in humans, we examined neuronal pathology in the vHipp and VTA and cognitive and behavioral phenotypes consistent with AD and comorbid psychosis. These studies establish a circuit-specific rationale for targeting the hippocampus, using the selective α5-PAM, MP-III-022 [11], to reverse downstream dopamine system dysfunction, which will lay the groundwork for developing therapeutic options for AD patients with comorbid psychosis.

2. Results

2.1. AAV-AD Rats Display Impairments in Hippocampal Activity That Are Reversed by Systemic Administration of the Selective α5-PAM, MP-III-022

Hippocampal hyperactivity has been observed in rodent models that display psychosis-related pathologies [12–14]; however, AAV-AD rats (n = 77 neurons; 0.78 ± 0.07 Hz) did not exhibit a vHipp firing frequency different from control rats (n = 93 neurons; 0.73 ± 0.06 Hz; Figure 1B). Additionally, vHipp firing rates of control (n = 87 neurons; 0.87 ± 0.06 Hz) or AAV-AD rats (n = 78 neurons; 0.70 ± 0.05 Hz) were not affected by the selective α5-PAM, MP-III-022 (Figure 1B). Recordings of spontaneous oscillatory activity in the vHipp (Figure 1C–F) revealed a main effect (n = 4–7 rats per group; three-way ANOVA; $F_{Strain}(1, 119) = 0.32$; $F_{Frequency}(4, 119) = 19.31$; $p < 0.001$; $F_{Treatment}(1, 119) = 2.58$; $F_{Strain \times Treatment}(1, 119) = 6.95$; $p = 0.01$; Holm Sidak; $t = 2.51$; $p = 0.01$), whereby we observed an overall decrease in oscillatory activity in AAV-AD rats when compared to controls. Interestingly, this was reversed by the systemic administration of MP-III-022 ($t = 2.83$; $p = 0.006$; Figure 1C,D).

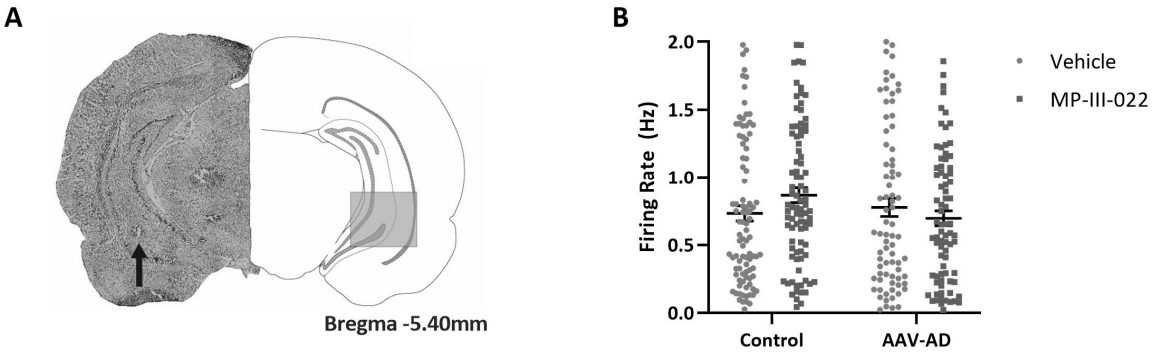

Figure 1. *Cont.*

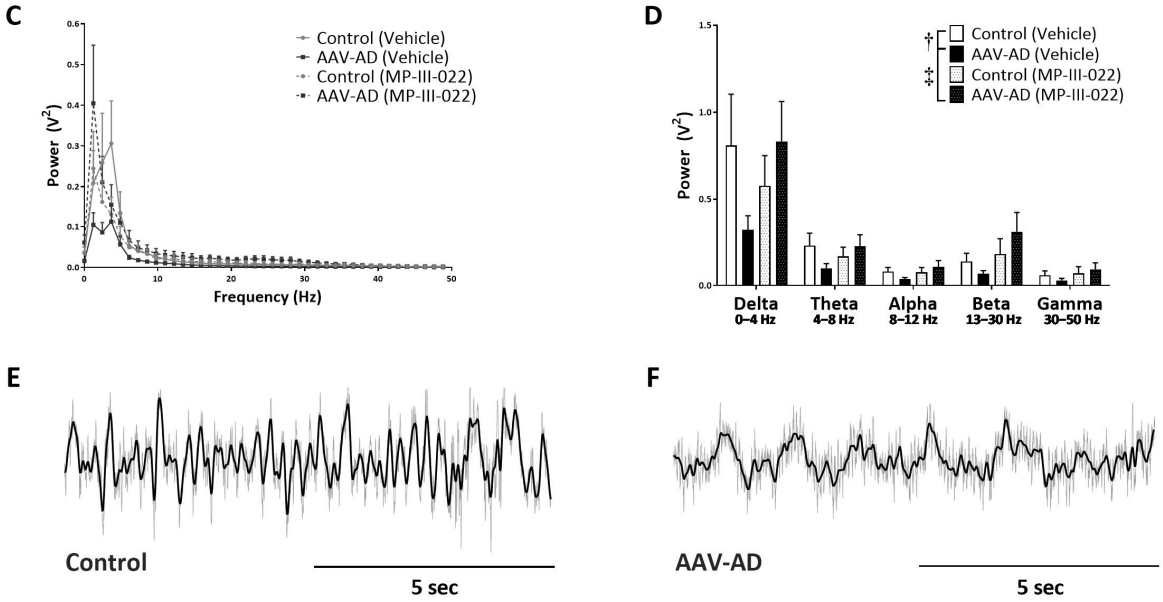

Figure 1. Impaired ventral hippocampal oscillatory activity reversed by MP−III−022 in AAV−AD rats. Representative brain slice with an electrode track (indicated by black arrow) in the ventral hippocampus ((**A**), left) and corresponding schematic of the brain section ((**A**), right). The average firing rate of spontaneously active putative pyramidal neurons in the ventral hippocampus (vHipp) is unchanged between treatment groups and unaffected by treatment with the selective α5−GABAA PAM, MP−III−022 (**B**). AAV−AD rats display a significant decrease in oscillatory power when compared to eGFP controls, which was reversed by the systemic administration of MP−III−022 (**C**,**D**). Representative trace of spontaneous local field potential oscillations filtered for delta (dark line) in the vHipp of a control (**E**) and AAV−AD rat (**F**). † denotes a significant main effect; $p = 0.014$. ‡ denotes a significant main effect; $p = 0.006$.

2.2. AAV-AD Rats Exhibit Aberrant Dopamine System Function That Is Reversed by Systemic Administration of the Selective α5-PAM, MP-III-022

Various models used to study psychosis display a significant increase in VTA dopamine neuron population activity [7,14–17]. Consistent with these data, the population activity of AAV-AD rats (n = 10; 1.60 ± 0.13 cells per track) was significantly higher than controls (n = 10 rats; 1.05 ± 0.08 cells per track; two-way ANOVA; $F_{Strain}(1, 34) = 6.61$; $p = 0.02$; $F_{Treatment}(1, 34) = 9.48$; $p = 0.004$; $F_{Strain \times Treatment}(2, 34) = 8.25$; $p = 0.007$; Holm-Sidak; $t = 4.16$; $p < 0.001$; Figure 2B). Systemic administration of the selective α5-PAM, MP-III-022 reversed increases in population activity in AAV-AD rats (n = 8 rats; 1.00 ± 0.06 cells per track; $t = 4.29$; $p < 0.001$) and did not have an effect in control rats (n = 7 rats; 1.03 ± 0.08 cells per track). No significant differences in average firing rate (n = 44–98 dopamine neurons per group; Figure 2C) or bursting pattern (n = 44–98 dopamine neurons per group; Figure 2D) were observed between any groups.

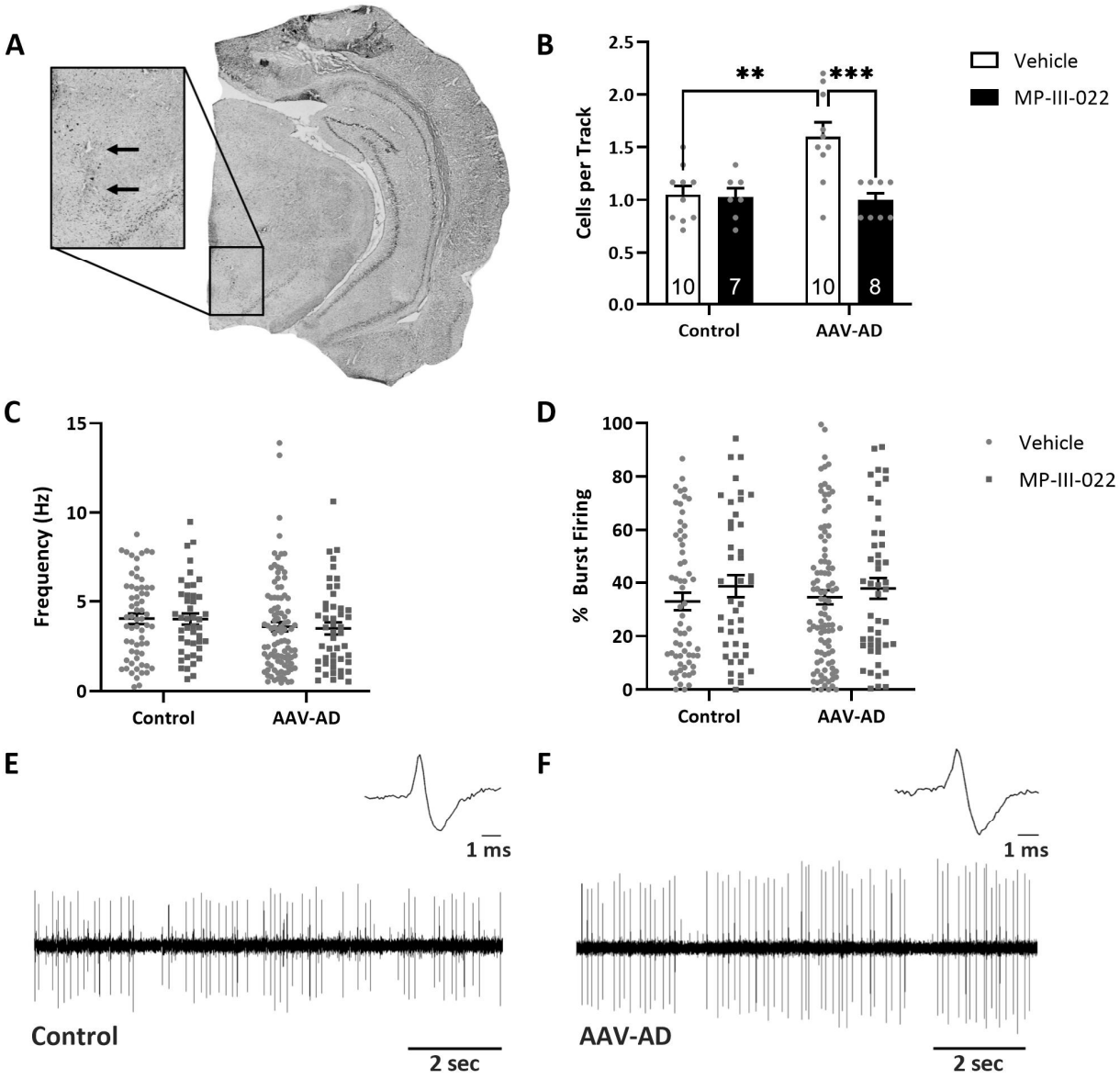

Figure 2. Aberrant ventral tegmental area activity is restored by MP-III-022 in AAV-AD rats. Representative brain slice with an electrode track (indicated by black arrows) in the ventral tegmental area (**A**). Dopamine neuron population activity (average number of spontaneously active dopamine neurons per electrode track) is significantly increased in AAV-AD rats, which is reversed by systemic administration of the selective α5-GABAA PAM, MP-III-022 (**B**). The average firing rate (**C**) or bursting pattern (**D**) was not altered in control or AAV-AD rats or by systemic MP-III-022 administration. Representative dopamine recording and action potential from a control (**E**) and AAV-AD (**F**) rat. ** $p < 0.005$, *** $p < 0.0001$.

2.3. AAV-AD Rats Do Not Display Cognitive Deficits but Exhibit Specific Deficits in a dopamine-Dependent Behavior, Which Was Reversed By Systemic Administration of the Selective α5-PAM, MP-III-022

Deficits in cognitive tasks are a consistent observation in rodent models of AD; however, given that this is a vHipp-specific model, no deficits in spatial learning and memory were observed. Here, we calculated the percent spontaneous alternations in the Y-maze and did not observe any difference between groups (n = 9–11 rats per group; Figure 3A), indicating that this model does not produce working memory deficits. Similarly, sensorimotor gating deficits have been observed in models used to study psychosis, as well as in models of AD; however, we did not observe a PPI deficit between groups (n = 10–11 rats per group;

Figure 3B). Rodent models used to study psychosis commonly display deficits in dopamine-dependent measures, such as exaggerated responses to acute systemic administration of psychotomimetic drugs. Here, we demonstrate that baseline locomotor activity is consistent across all groups (n = 10–11 rats per group), while MK-801-induced locomotor activity was elevated in AAV-AD rats when compared to controls (three-way ANOVA; $F_{Strain}(1, 385) = 0.008$; $F_{Treatment}(1, 385) = 0.67$; $F_{Time}(8, 385) = 3.35$; $p = 0.001$; $F_{Strain \times Treatment}(1, 385) = 10.85$; $p = 0.001$; Holm Sidak; $t = 2.23$; $p = 0.026$; Figure 3C). Further, this increase was reversed following systemic administration of the selective α5-PAM, MP-III-022 (Holm-Sidak; $t = 2.87$; $p = 0.004$).

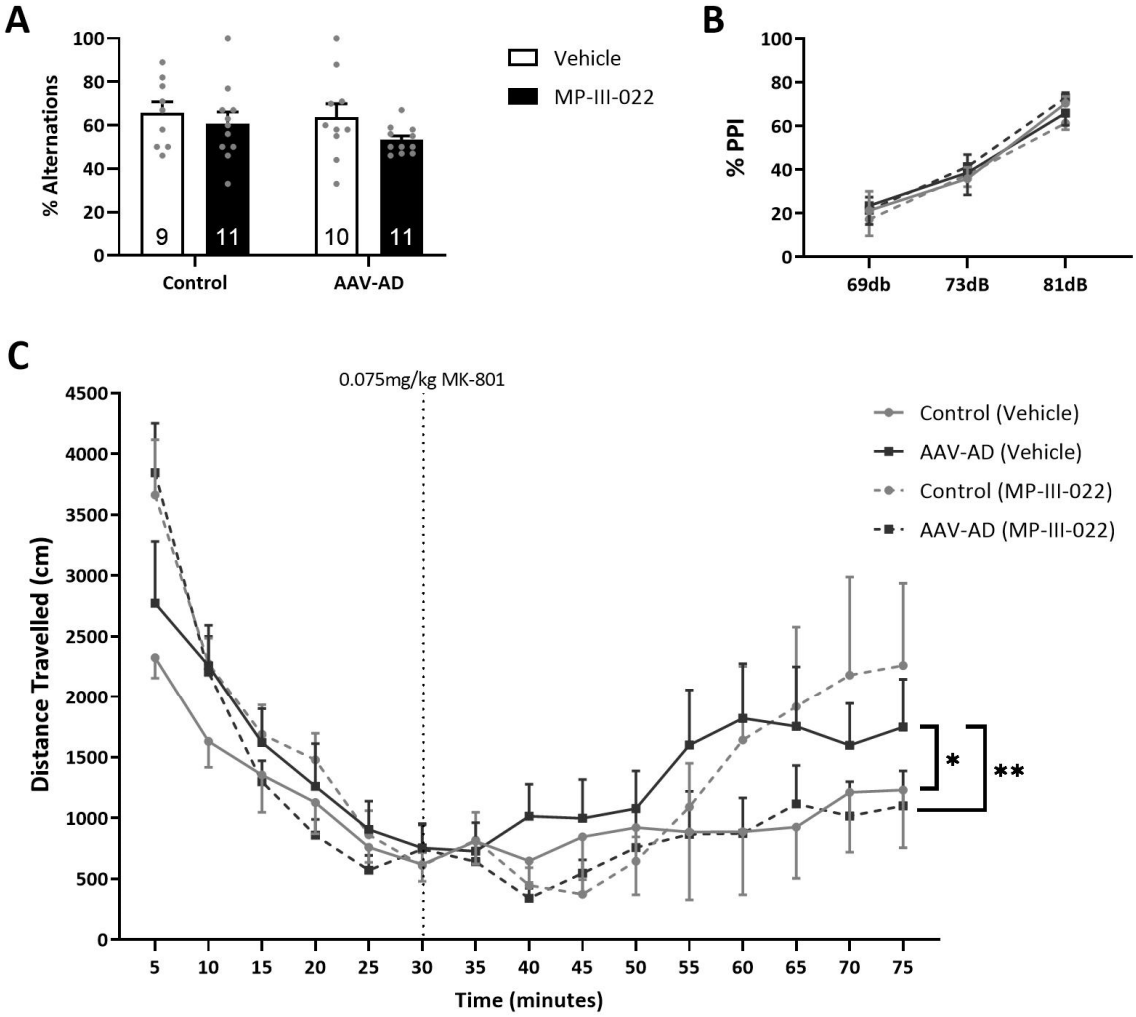

Figure 3. AAV-AD rats exhibit an enhanced sensitivity to the locomotor-inducing effects of MK-801, which are reversed by MP-II-022. No significant working memory deficits were observed between any groups in Y-maze (**A**). Additionally, no significant sensorimotor gating differences were observed, as measured by pre-pulse inhibition of startle (**B**). AAV-AD rats displayed an enhanced locomotor response to MK-801, which was reversed by the systemic administration of the selective α5-GABAA positive allosteric modulator, MP-III-022 (**C**). * $p = 0.026$, ** $p = 0.004$.

2.4. Parvalbumin Positive Interneurons are Decreased in AAV-AD Rats

A decrease in the number of PV interneurons has been previously reported in post-mortem studies from AD patients [18,19] and rodent models used to study psychosis [13,20]. Further, this has been correlated with VTA dopamine neuron population activity [15]. Here, we found a significant decrease in the number of PV neurons in the vHipp of AAV-AD rats (n = 13 rats; 5.79 ± 0.62 PV cells/mm^2) when compared to controls (n = 13 rats; 7.82 ± 0.64 PV cells/mm^2; *t*-test; $t = 2.28$ with 24 degrees of freedom; $p = 0.03$; Figure 4A). In addition, there is a trend whereby a decrease in vHipp PV interneurons corresponds

with an increase in VTA dopamine neuron population activity (n = 13; linear regression; R = 0.40; r^2 = 0.16; analysis of variance; $F_{Regression}(1, 12) = 2.10$; $p = 0.18$; Figure 4C).

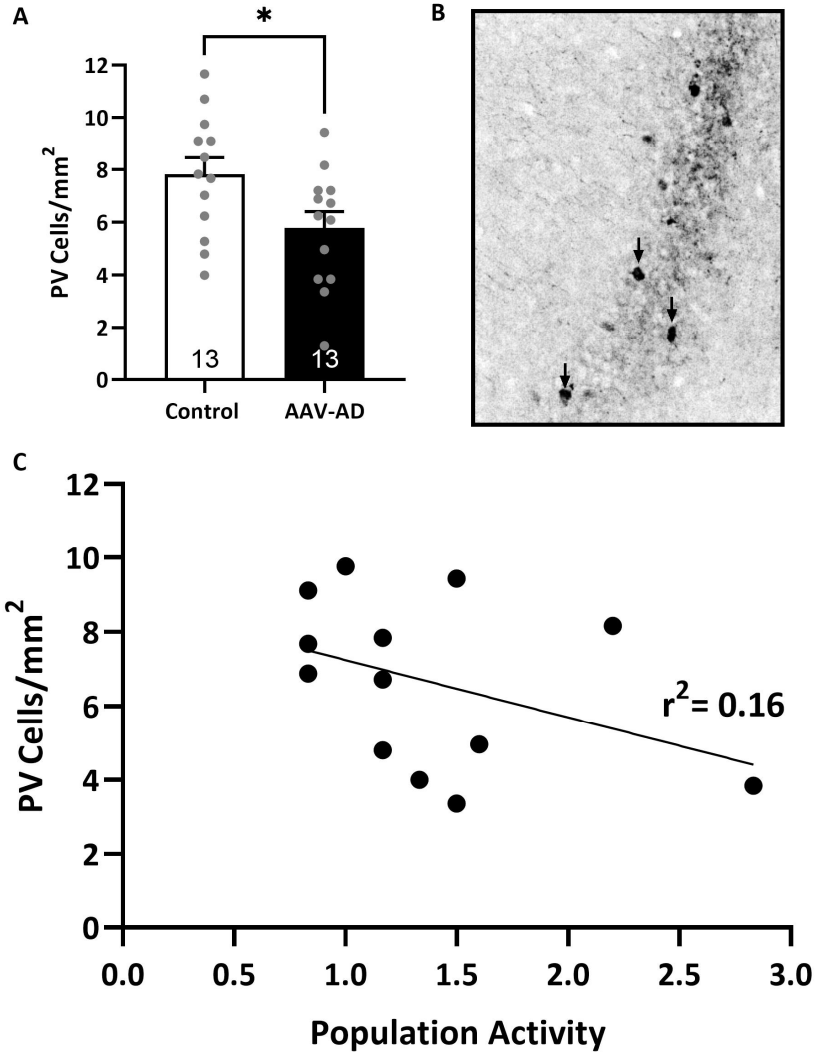

Figure 4. AAV-AD rats exhibit a significant decrease in the number of parvalbumin-positive (PV) interneurons in the vHipp. AAV-AD rats exhibit significantly less parvalbumin-positive inhibitory interneurons in the vHipp (**A**). Representative coronal brain section containing the ventral hippocampus (vHipp) displaying parvalbumin (converted to greyscale and indicated by black arrows; (**B**)). Scatterplot depicting correlation between dopamine neuron population activity and the number of PV interneurons in the vHipp. Black dots represent individual rats. (**C**). * $p = 0.032$.

3. Discussion

Every year, in the United States alone, AD accrues a healthcare system burden of $340 billion [21]. Half of these AD patients also suffer from comorbid psychosis [2], which disproportionately contributes to the burden of the illness on society due to more advanced disease stage and increased adverse health outcomes [22]. Among these is an increased risk for mortality, and drugs that directly target dopamine system dysfunction that underlies symptoms of psychosis further increase the risk of death two-fold in the elderly population [23]. There is clearly a need to develop therapeutics that alleviate symptoms of psychosis in this patient population.

AD comes in two forms: familial early-onset AD, which is over 90% heritable and manifests prior to the age of 65 [24], and sporadic late-onset AD, which is more common, up to 78% heritable, and presents after the age of 65 [25]. The pathophysiology of sporadic AD is not as well understood and is likely due to a combination of genetic and

environmental risk factors, but the pathophysiology of familial AD is more well-defined to specific causative genes and serves as a simpler starting point to exploring circuit-specific mechanisms. Our studies utilized a circuit-specific version of a rat model that recapitulates many of the features of familial AD in a manner that is translatable to relevant disease progression milestones seen in humans. Rats that globally express familial mutations in the hAPP+hPSEN1 genes accumulate Aβ plaques and display cognitive impairments beginning at 6 months of age, which corresponds to middle age in humans, and experience 40% degeneration of hippocampal neurons by 12 months of age, which corresponds to later adulthood [26,27]. This is consistent with humans, in whom Aβ plaques are thought to manifest as soon as 20 years prior to AD diagnosis [28], and the earlier soluble forms are thought to initiate disruptions to E/I ratio and network activity [29] that leads to cognitive dysfunction and comorbid symptoms such as psychosis in AD. Decreases in GABAergic interneurons positive for the calcium-binding protein PV, which synapse onto the cell body and axon hillock of glutamatergic pyramidal cell neurons they regulate, have been heavily implicated in the pathophysiology of both AD and psychosis [19], including ventral hippocampal disruptions to coordinated neuronal firing in a rat model used to study psychosis [20].

Here, in AAV-AD rats, we saw a 26% decrease in PV inhibitory interneurons, consistent with that seen in mice that globally express the same mutations [30] and neuronal and behavioral phenotypes consistent with comorbid psychosis in AD. Although our data do not display hippocampal hyperactivity as measured by firing rates of putative pyramidal cells using in vivo extracellular electrophysiology, this is consistent with the findings of a bigenic rat model used to study familial AD, in which patch clamp electrophysiology was instead able to measure other features consistent with hippocampal hyperactivity, such as increased resting membrane potential and wider action potential length in putative pyramidal cells [31]. Further, our data do demonstrate a decrease in vHipp oscillatory activity, which occurs at the population level in the context of hippocampal hyperactivity, specifically in the lower frequency delta bands (0–4 Hz) of hAPP + hPSEN1 rats compared to eGFP controls, which is restored by MP-III-022 compared to vehicle treatment.

These deficits in PV expression and spontaneous oscillatory activity in the vHipp likely drive downstream effects in the VTA and psychosis-like behaviors. AAV-AD rats displayed a nearly two-fold elevation in population activity and increased sensitivity to psychomotor stimulants in the locomotor activity assay, consistent with rodent models of psychosis [7,14–17] and sporadic AD [10], which were both reversed by administration of MP-III-022 compared to the vehicle. Interestingly, reduced PV neuron expression is likely to disinhibit pyramidal neurons due to reduced perisomatic and axon initial segment inhibition, whereas α5-PAM increases dendritic inhibition on the same neurons. The dendritic inhibition corresponds to SST input rather than PV input, thus representing a novel finding where deficits in PV function can be rescued through an SST-mediated cell mechanism (α5-PAM). Similar to our rodent model used to study sporadic AD [10], there were no significant differences in inhibition of the startle reflex; however, sensorimotor gating deficits can occur in numerous pathologies and thus may not always be as penetrant of a trait as increased sensitivity to psychomotor stimulants that are more specifically characteristic of psychosis in the clinic [32]. Additionally, these results were not surprising given that sensorimotor gating deficits involve brain regions that were not altered by pathology specific to the vHipp [33]. There were no significant differences in the percentage of spontaneous alternations in the Y-maze cognitive assay, which served to confirm the specificity of AD pathology specific to the vHipp in the model we used in this study, given deficits in short-term working memory would be expected with AD pathology in the dorsal hippocampus.

Since the hippocampus is a common site of primary pathology in both AD and psychosis, and previous work from our lab has shown hyperactivity of the hippocampus is both necessary and sufficient to induce neuronal and behavioral deficits analogous to psychosis in rats, these studies set out to establish that AD-like pathology specific to the vHipp is not

only sufficient to model comorbid psychosis, but also necessary, given that drugs specific to the hippocampus may serve as a viable therapeutic strategy to target this pathophysiology in a circuit-specific manner. We found that viral expression of hAPP+hPSEN1 decreases oscillations and PV interneuron number in the vHipp, leading to increases in dopamine neuron population activity in the VTA and increased sensitivity to psychomotor stimulants. Furthermore, these deficits were reversed by the systemic administration of MP-III-022. These data mirror clinical and post-mortem brain studies [19,29], as well as preclinical work in other AD models [34]. Taken together, this work provides a circuit-based rationale for the use of AAV-AD rats as a translatable model that can be used to study drugs that target hippocampus-specific pathophysiology upstream of dopamine dysfunction that affects millions of patients worldwide who have no viable therapeutic options.

4. Materials and Methods

4.1. Animals

To generate a rodent model of AD (AAV-AD model; Figure 5), with pathological alterations restricted to the vHipp, we utilized high-titer adeno-associated viruses (AAV). Survival surgeries were performed in a semi-sterile environment under general anesthesia. Male (~325–350 g) Sprague-Dawley rats (Envigo, Indianapolis, IN, USA) were anesthetized with Fluriso™ (2–5% Isoflurane, USP with oxygen flow at 1 L/min) and placed in a stereotaxic apparatus (Kopf, Tujunga, CA, USA) using blunt atraumatic ear bars. A core body temperature of 37 °C was maintained. A mixture of two AAV9 containing vectors each expressing either the mutated form of hAPP (2.09×10^{13} GC/mL; pAAV[Exp]-CMV>{mutant hAPP}:WPRE) or hPSEN1 (6.28×10^{13} GC/mL; pAAV[Exp]-CMV>{hPSEN1}:T2A:TurboGFP:WPRE) containing a GFP reporter and driven by the CMV promotor were bilaterally injected (0.5 ul) into the vHipp (A/P: −5.3 mm and M/L: ±5.0 mm from Bregma; D/V: −9.0 mm ventral of the brain surface). Control rats were bilaterally injected with an AAV expressing eGFP (2.09 × 1013 GC/mL; pAAV[Exp]-CMV>EGFP:WPRE). Rats received post-operative ketoprofen (5 mg/kg; s.c.) and were housed in groups of 2–3 until ~8 months of age prior to behavioral testing and electrophysiological recordings. An experimental timeline is depicted in Figure 1A. A subset of control and AAV-AD rats were treated systemically with either vehicle (1% Tween 80, 14% propylene glycol, in distilled water) or the selective α5-PAM, MP-III-022 (10 mg/kg; i.p.), 20 min prior to any electrophysiological or behavioral testing. The dose was chosen based on previously published literature using this compound [11,35,36].

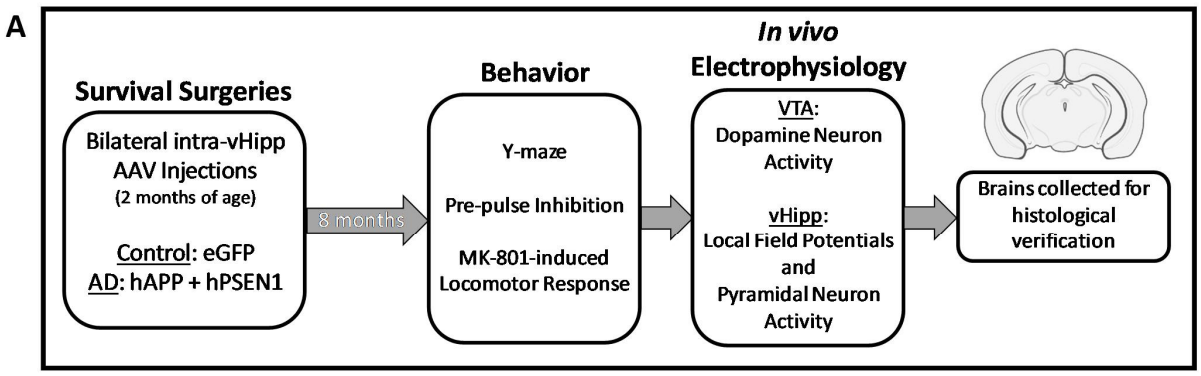

Figure 5. *Cont.*

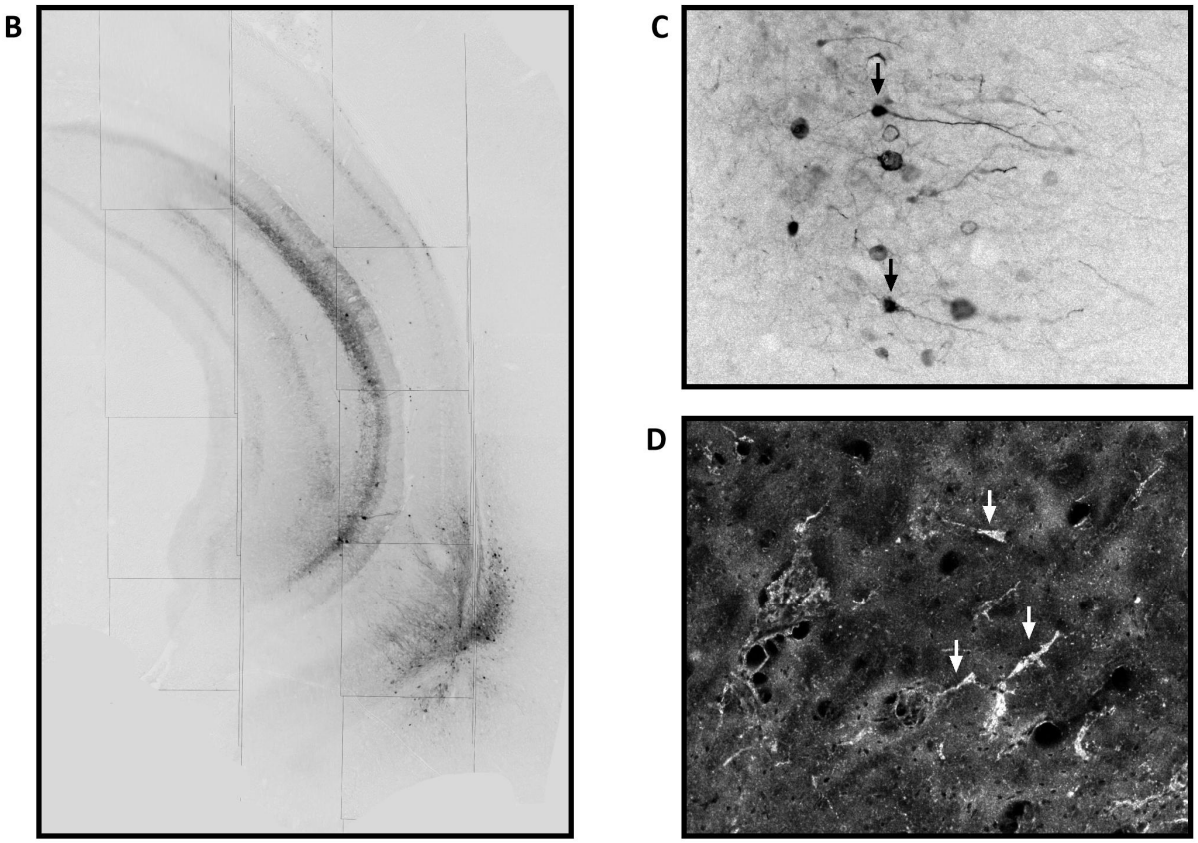

Figure 5. Verification of the AAV-AD model. Schematic representation of the experimental timeline (**A**). Representative coronal brain slice verifying viral reporter expression within the ventral hippocampus. Black arrows indicate representative neurons (converted to greyscale (**B**,**C**)). Representative dark field image of a silver-stained ventral hippocampal coronal brain slice, with pathological deposits in the vHipp of AAV-AD rats, indicated by the white arrows in (**D**). Icons used were adapted from BioRender.com (2022). Retrieved from http://app.biorender.com/illustrations (accessed on 5 May 2022).

4.2. In Vivo Extracellular Electrophysiology Recordings

For non-survival surgery, rats were anesthetized with chloral hydrate (400 mg/kg; i.p.) prior to placement in a stereotaxic apparatus (Kopf; Tujunga, CA, USA). This anesthetic is required for dopamine neuron physiology, as it does not significantly alter dopamine activity when compared to recordings in freely moving animals [37]. A core body temperature of 37 °C was maintained, and supplemental anesthesia was administered as required to maintain suppression of the limb withdrawal reflex. Extracellular glass microelectrodes (impedance 6–10 MΩ) were lowered into the vHipp (A/P: −5.3 and M/L: ±5.0 mm from Bregma; D/V: −4.5 to −9.0 mm ventral of the brain surface) or VTA (A/P: −5.3 mm and M/L: ±0.6 mm from Bregma; D/V: −6.5 to −9.0 mm ventral of the brain surface). The firing frequency of spontaneously active putative pyramidal neurons in the vHipp was measured and identified as previously published (neurons with firing frequencies less than 2 Hz) [12,13,38]. Local field potential (LFP) oscillatory activity was generated from the vHipp using open filter settings (Low Pass Filter: 0.3 Hz; High Pass Filter: 1000 Hz) and recorded for a minimum of ten minutes. Oscillations were quantified with commercially available computer software (LabChart version 8; ADInstruments, Chalgrove, Oxfordshire, UK). Spontaneously active dopamine neurons were identified using previously established criteria [39,40]: (1) action potential duration > 2 ms and (2) frequency between 0.5 and 15 Hz. Three parameters of dopamine activity were measured: (1) population activity (the number of spontaneously active dopamine neurons encountered per track);

(2) basal firing rate; (3) and the proportion of action potentials occurring in bursts (defined as the incidence of spikes with <80 ms between them; termination of the burst is defined by >160 ms between spikes). Recordings typically lasted for ~2–4 h. Electrophysiological recordings were analyzed by two-way ANOVA (strain × frequency) followed by a Holm-Sidak post-hoc test.

4.3. Y-Maze Spontaneous Alternation Assay

The Y-maze consists of three plastic arms (81 cm long × 20.32 cm wide × 20 cm high) separated by 120-degree angles. Rats were placed inside the same arm facing the center of the maze and allowed to move freely for 10 min. During this time, the number and order of arm entries (defined as at least 80% of the front of the rat entering an arm from the center of the maze) were recorded. To calculate percent alternations, the number of alternations (triad containing entry to all three arms) was divided by the total number of entries minus 2 and multiplied by 100. Y-maze data were analyzed by two-way ANOVA followed by a Holm-Sidak post hoc test.

4.4. Pre-Pulse Inhibition of Startle (PPI)

Rats were placed in a sound-attenuated chamber (SD Instruments; San Diego, CA, USA) and allowed to acclimate to 65 dB background noise for 5 min prior to exposure to 10 startle-only trials [40 ms, 120 dB, 15 s average inter-trial intervals (ITIs)], followed by 24 trials where a pre-pulse (20 ms at 69 dB, 73 dB, and 81 dB) was presented 100 ms prior to a startle pulse. Each pre-pulse was presented six times in a pseudo-random order (15 s ITI). Startle responses were measured from 10 to 80 ms after the onset of the startle-only pulse and recorded using SR-Lab Analysis Software (https://sandiegoinstruments.com/product/sr-lab-startle-response/ accessed on 5 May 2022). PPI data were analyzed by three-way ANOVA (strain × treatment × dB) followed by a Holm-Sidak post hoc test.

4.5. Stimulant-Induced Locomotor Activity

Rats were placed in an open field arena (Med Associates, St. Albans, VT, USA) and spontaneous locomotor activity in the x-y plane was determined by beam breaks and recorded with Open Field Activity software (version 5). After 30 min of baseline recording, all rats were injected with the NMDA receptor antagonist, MK-801 (0.075 mg/kg, i.p.), and recorded for an additional 45 min. Locomotor data were analyzed by two separate (baseline and following MK-801) three-way ANOVAs (strain × treatment × time) followed by a Holm-Sidak post hoc test.

4.6. Immunohistochemistry

At the cessation of all experiments, rats were transcardially perfused with saline (150 mL), and brains were extracted and post-fixed for at least 24 h (4% formaldehyde in 0.1 M phosphate buffered saline (PBS) prior to cryoprotecting in 10% sucrose (dissolved in PBS), and coronally sectioned (50 µm) using a cryostat (Leica, Buffalo Grove, IL, USA). A subset of vHipp slices was mounted and cover slipped with Prolong™ Gold anti-fade mountant to verify viral expression (by GFP fluorescent reporter; Figure 2B,C). To verify the presence of amyloid plaques in the vHipp, a subset of slices containing the vHipp were silver stained using the FD NeuroSilver Kit II according to the manufacturer's directions, and cover slipped with Permount® (Figure 1C). A separate subset of slices containing the vHipp was used to detect the expression of PV (Figure 5B). In short, slices were washed three times (10 min each) in PBS, blocked (2% normal goat serum and 0.3% Triton™ X 100 in PBS) for 30 min at room temperature, and incubated with rabbit anti-parvalbumin primary antibody (1:1000) overnight at 4 °C. After washing (three times in PBS for 10 min each), slices were incubated with AlexaFluor® 594 goat anti-rabbit immunoglobin G (H + L) (1:1000) for 1 h at room temperature. Slices were wet mounted, and cover slipped with ProLong™ Gold anti-fade mountant. Sections were imaged using an AxioCam ICc 1 (Zeiss, Jena, Germany) camera attached to an Axio Lab.A1 (Zeiss, Jena, Germany) microscope.

The number of PV-positive cells within the vHipp was counted on six sections per animal, in an area approximately −6.0 to −8.5 mm ventral of the skull surface and ±4.0 to 6.0 mm lateral of the midline.

4.7. Histology

A subset of brains was post-fixed (4% formaldehyde in PBS), cryoprotected (10% *w*/*v* sucrose in PBS) until saturated, and coronally sectioned (25 µm) on a cryostat (Leica, Buffalo Grove, IL, USA). Sections were mounted onto gelatin-chrome-coated slides, stained with neutral red (0.1%) and thionin acetate (0.01%), and cover slipped with DPX mountant for histological verification of electrode tracks within the vHipp (Figure 2A) or VTA (Figure 3A) [41].

4.8. Analysis

Electrophysiological analysis of vHipp and dopamine neuron activity was performed with commercially available computer software (LabChart version 8; ADInstruments, Dunedin, New Zealand; Chalgrove, Oxfordshire, UK). Locomotor activity was collected with Activity Monitor software (version 5; MED Associates; St. Albans, VT, USA). PPI data were collected using SR-Lab™ Analysis Software (https://sandiegoinstruments.com/product/sr-lab-startle-response/ accessed on 5 May 2022) (SD Instruments; San Diego, CA, USA). All data were analyzed using Prism software (version 10; GraphPad Software Inc.; San Diego, CA, USA). Data are represented as mean ± SEM with n values representing the number of animals per experimental group unless otherwise stated. Data were analyzed using a *t*-test, linear regression, or two- or three-way analysis of variance (ANOVA), and the Holm-Sidak post hoc test was used when significant interactions were determined. Statistics were calculated using SigmaPlot (version 12; Systat Software Inc.; Chicago, IL, USA) and significance was determined at $p < 0.05$.

4.9. Materials

Proprietary compound, MP-III-022, was generated by the University of Wisconsin in Milwaukee. Plasmids were generated and packaged into AAV by VectorBuilder (Chicago, IL, USA). FlurisoTM was purchased from MWI Animal Health (Boise, ID, USA). Chloral hydrate (C8383), Ketoprofen (K2012), MK-801 (M107), Propylene Glycol (P4347), Tween® 80 (P1754), and DPX mountant (06522) were sourced from Sigma-Aldrich (St. Louis, MO, USA). Anti-parvalbumin antibody (ab11427) was purchased from Abcam (Boston, MA, USA). AlexaFluor® 594 goat anti-rabbit immunoglobin G (H + L) (A-11012) was purchased from Invitrogen (Waltham, MA, USA). Invitrogen™ ProLong™ Gold antifade mountant (P36930) and Permount™ mounting medium (SP15) were purchased from Thermo Fisher Scientific (Waltham, MA, USA). FD NeuroSilver Kit II (PK301) was sourced from FD NeuroTechnologies, Inc. (Columbia, MD, USA). All other chemicals and reagents were either analytical or laboratory-grade and purchased from standard suppliers. Interventional studies involving animals or humans and other studies that require ethical approval must list the authority that provided approval and the corresponding ethical approval code.

Author Contributions: Conceptualization, D.J.L. and S.M.P.; formal analysis, S.M.P. and N.E.E.; resources, J.M.C. and D.S.; data curation, S.M.P., N.E.E., A.M.B. and H.B.E.; writing—original draft preparation, S.M.P. and N.E.E.; writing—review and editing, D.J.L., S.M.P. and N.E.E.; supervision, D.J.L. and S.M.P.; project administration, S.M.P.; funding acquisition, D.J.L. and J.M.C. All authors have read and agreed to the published version of the manuscript.

Funding: This work was supported by Merit Awards #BX004693 (D.J.L.) and #BX004646 (D.J.L.) from the United States Department of Veterans Affairs, Biomedical Laboratory Research and Development Service, the San Antonio Nathan Shock Center of Excellence Pilot Grant (S.M.P.), NIH Jointly Sponsored Predoctoral Training Program in the Neurosciences training grant T32 NS082145 (N.E.E.), and South Texas Medical Scientist Training Program (STX-MSTP) NIH T32GM113896 (N.E.E.). Funding for chemistry and HR spectroscopy was provided by the National Science Foundation CHE-1625735

(J.M.C.), the National Institute on Drug Abuse DA054177 and DA043204 (J.M.C.), and the National Institute on Alcohol Abuse and Alcoholism AA029023 (J.M.C.).

Institutional Review Board Statement: All experiments were performed in accordance with the guidelines outlined in the USPH Guide for the Care and Use of Laboratory Animals and were approved by the Institutional Animal Care and Use Committees of UT Health San Antonio and the U.S. Department of Veterans Affairs.

Informed Consent Statement: Not applicable.

Data Availability Statement: Data available on request.

Conflicts of Interest: J.M.C. is a coinventor or listed on U.S. patent applications that cover GABAergic ligands and their use in brain disorders. D.J.L. has an active collaboration with Sosei-Heptares; these are both unrelated to the work described in the current article. All other authors report no biomedical financial interests or potential conflicts of interest.

References

1. Rajan, K.B.; Weuve, J.; Barnes, L.L.; McAninch, E.A.; Wilson, R.S.; Evans, D.A. Population estimate of people with clinical Alzheimer's disease and mild cognitive impairment in the United States (2020–2060). *Alzheimer's Dement.* **2021**, *17*, 1966–1975. [CrossRef]
2. Drevets, W.C.; Rubin, E.H. Psychotic symptoms and the longitudinal course of senile dementia of the Alzheimer type. *Biol. Psychiatry* **1989**, *25*, 39–48. [CrossRef] [PubMed]
3. Abi-Dargham, A. Do we still believe in the dopamine hypothesis? New data bring new evidence. *Int. J. Neuropsychopharmacol.* **2004**, *7* (Suppl. S1), S1–S5. [CrossRef]
4. Laruelle, M.; Abi-Dargham, A. Dopamine as the wind of the psychotic fire: New evidence from brain imaging studies. *J. Psychopharmacol.* **1999**, *13*, 358–371. [CrossRef]
5. Palop, J.J.; Chin, J.; Roberson, E.D.; Wang, J.; Thwin, M.T.; Bien-Ly, N.; Yoo, J.; Ho, K.O.; Yu, G.Q.; Kreitzer, A.; et al. Aberrant excitatory neuronal activity and compensatory remodeling of inhibitory hippocampal circuits in mouse models of Alzheimer's disease. *Neuron* **2007**, *55*, 697–711. [CrossRef]
6. Schobel, S.A.; Kelly, M.A.; Corcoran, C.M.; Van Heertum, K.; Seckinger, R.; Goetz, R.; Harkavy-Friedman, J.; Malaspina, D. Anterior hippocampal and orbitofrontal cortical structural brain abnormalities in association with cognitive deficits in schizophrenia. *Schizophr. Res.* **2009**, *114*, 110–118. [CrossRef] [PubMed]
7. Lodge, D.J.; Grace, A.A. Aberrant hippocampal activity underlies the dopamine dysregulation in an animal model of schizophrenia. *J. Neurosci.* **2007**, *27*, 11424–11430. [CrossRef] [PubMed]
8. Donegan, J.J.; Boley, A.M.; Yamaguchi, J.; Toney, G.M.; Lodge, D.J. Modulation of extrasynaptic GABAA alpha 5 receptors in the ventral hippocampus normalizes physiological and behavioral deficits in a circuit specific manner. *Nat. Commun.* **2019**, *10*, 2819. [CrossRef]
9. Fritschy, J.M.; Mohler, H. GABAA-receptor heterogeneity in the adult rat brain: Differential regional and cellular distribution of seven major subunits. *J. Comp. Neurol.* **1995**, *359*, 154–194. [CrossRef]
10. Perez, S.M.; Boley, A.M.; McCoy, A.M.; Lodge, D.J. Aberrant dopamine system function in the ferrous amyloid buthionine (FAB) rat model for Alzheimer's disease. *Int. J. Mol. Sci.* **2023**, *24*, 7196. [CrossRef]
11. Stamenic, T.T.; Poe, M.M.; Rehman, S.; Santrac, A.; Divovic, B.; Scholze, P.; Ernst, M.; Cook, J.M.; Savic, M.M. Ester to amide substitution improves selectivity, efficacy and kinetic behavior of a benzodiazepine positive modulator of GABA(A) receptors containing the alpha5 subunit. *Eur. J. Pharmacol.* **2016**, *791*, 433–443. [CrossRef] [PubMed]
12. Perez, S.M.; Lodge, D.J. Hippocampal interneuron transplants reverse aberrant dopamine system function and behavior in a rodent model of schizophrenia. *Mol. Psychiatry* **2013**, *18*, 1193–1198. [CrossRef] [PubMed]
13. Boley, A.M.; Perez, S.M.; Lodge, D.J. A fundamental role for hippocampal parvalbumin in the dopamine hyperfunction associated with schizophrenia. *Schizophr. Res.* **2014**, *157*, 238–243. [CrossRef]
14. Perez, S.M.; Boley, A.; Lodge, D.J. Region specific knockdown of Parvalbumin or Somatostatin produces neuronal and behavioral deficits consistent with those observed in schizophrenia. *Transl. Psychiatry* **2019**, *9*, 264. [CrossRef]
15. Perez, S.M.; Aguilar, D.D.; Neary, J.L.; Carless, M.A.; Giuffrida, A.; Lodge, D.J. Schizophrenia-Like Phenotype Inherited by the F2 Generation of a Gestational Disruption Model of Schizophrenia. *Neuropsychopharmacology* **2016**, *41*, 477–486. [CrossRef]
16. Perez, S.M.; Chen, L.; Lodge, D.J. Alterations in dopamine system function across the estrous cycle of the MAM rodent model of schizophrenia. *Psychoneuroendocrinology* **2014**, *47*, 88–97. [CrossRef]
17. Aguilar, D.D.; Chen, L.; Lodge, D.J. Increasing Endocannabinoid Levels in the Ventral Pallidum Restores Aberrant Dopamine Neuron Activity in the Subchronic PCP Rodent Model of Schizophrenia. *Int. J. Neuropsychopharmacol.* **2015**, *18*, pyu035. [CrossRef] [PubMed]
18. Satoh, J.; Tabira, T.; Sano, M.; Nakayama, H.; Tateishi, J. Parvalbumin-immunoreactive neurons in the human central nervous system are decreased in Alzheimer's disease. *Acta Neuropathol.* **1991**, *81*, 388–395. [CrossRef]

19. Brady, D.R.; Mufson, E.J. Parvalbumin-immunoreactive neurons in the hippocampal formation of Alzheimer's diseased brain. *Neuroscience* **1997**, *80*, 1113–1125. [CrossRef]
20. Lodge, D.J.; Behrens, M.M.; Grace, A.A. A loss of parvalbumin-containing interneurons is associated with diminished oscillatory activity in an animal model of schizophrenia. *J. Neurosci.* **2009**, *29*, 2344–2354. [CrossRef]
21. 2023 Alzheimer's disease facts and figures. *Alzheimer's Dement.* **2023**, *19*, 1598–1695. [CrossRef]
22. Murray, P.S.; Kumar, S.; Demichele-Sweet, M.A.; Sweet, R.A. Psychosis in Alzheimer's disease. *Biol. Psychiatry* **2014**, *75*, 542–552. [CrossRef]
23. Kales, H.C.; Kim, H.M.; Zivin, K.; Valenstein, M.; Seyfried, L.S.; Chiang, C.; Cunningham, F.; Schneider, L.S.; Blow, F.C. Risk of mortality among individual antipsychotics in patients with dementia. *Am. J. Psychiatry* **2012**, *169*, 71–79. [CrossRef]
24. Marchani, E.E.; Bird, T.D.; Steinbart, E.J.; Rosenthal, E.; Yu, C.E.; Schellenberg, G.D.; Wijsman, E.M. Evidence for three loci modifying age-at-onset of Alzheimer's disease in early-onset PSEN2 families. *Am. J. Med. Genet. Part B Neuropsychiatr. Genet.* **2010**, *153B*, 1031–1041.
25. Pedersen, W.A.; McCullers, D.; Culmsee, C.; Haughey, N.J.; Herman, J.P.; Mattson, M.P. Corticotropin-releasing hormone protects neurons against insults relevant to the pathogenesis of Alzheimer's disease. *Neurobiol. Dis.* **2001**, *8*, 492–503. [CrossRef]
26. Cohen, R.M.; Rezai-Zadeh, K.; Weitz, T.M.; Rentsendorj, A.; Gate, D.; Spivak, I.; Bholat, Y.; Vasilevko, V.; Glabe, C.G.; Breunig, J.J.; et al. A transgenic Alzheimer rat with plaques, tau pathology, behavioral impairment, oligomeric abeta, and frank neuronal loss. *J. Neurosci.* **2013**, *33*, 6245–6256. [CrossRef] [PubMed]
27. Jawhar, S.; Trawicka, A.; Jenneckens, C.; Bayer, T.A.; Wirths, O. Motor deficits, neuron loss, and reduced anxiety coinciding with axonal degeneration and intraneuronal Abeta aggregation in the 5XFAD mouse model of Alzheimer's disease. *Neurobiol. Aging* **2012**, *33*, 196.e29–196.e40. [CrossRef] [PubMed]
28. Gordon, B.A.; Blazey, T.M.; Su, Y.; Hari-Raj, A.; Dincer, A.; Flores, S.; Christensen, J.; McDade, E.; Wang, G.; Xiong, C.; et al. Spatial patterns of neuroimaging biomarker change in individuals from families with autosomal dominant Alzheimer's disease: A longitudinal study. *Lancet Neurol.* **2018**, *17*, 241–250. [CrossRef] [PubMed]
29. Palop, J.J.; Mucke, L. Network abnormalities and interneuron dysfunction in Alzheimer disease. *Nat. Rev. Neurosci.* **2016**, *17*, 777–792. [CrossRef] [PubMed]
30. Giesers, N.K.; Wirths, O. Loss of Hippocampal Calretinin and Parvalbumin Interneurons in the 5XFAD Mouse Model of Alzheimer's Disease. *ASN Neuro* **2020**, *12*, 1759091420925356. [CrossRef]
31. Sosulina, L.; Mittag, M.; Geis, H.R.; Hoffmann, K.; Klyubin, I.; Qi, Y.; Steffen, J.; Friedrichs, D.; Henneberg, N.; Fuhrmann, F.; et al. Hippocampal hyperactivity in a rat model of Alzheimer's disease. *J. Neurochem.* **2021**, *157*, 2128–2144. [CrossRef]
32. Janowsky, D.S.; el-Yousel, M.K.; Davis, J.M.; Sekerke, H.J. Provocation of schizophrenic symptoms by intravenous administration of methylphenidate. *Arch. Gen. Psychiatry* **1973**, *28*, 185–191. [CrossRef] [PubMed]
33. Davis, M.; Gendelman, D.S.; Tischler, M.D.; Gendelman, P.M. A primary acoustic startle circuit: Lesion and stimulation studies. *J. Neurosci.* **1982**, *2*, 791–805. [CrossRef] [PubMed]
34. Krivinko, J.M.; Koppel, J.; Savonenko, A.; Sweet, R.A. Animal Models of Psychosis in Alzheimer Disease. *Am. J. Geriatr. Psychiatry* **2020**, *28*, 1–19. [CrossRef] [PubMed]
35. Perez, S.M.; McCoy, A.M.; Prevot, T.D.; Mian, M.Y.; Carreno, F.R.; Frazer, A.; Cook, J.M.; Sibille, E.; Lodge, D.J. Hippocampal alpha5-GABA(A) Receptors Modulate Dopamine Neuron Activity in the Rat Ventral Tegmental Area. *Biol. Psychiatry Glob. Open Sci.* **2023**, *3*, 78–86. [CrossRef]
36. Santrac, A.; Batinic, B.; Stamenic, T.T.; Arandelovic, J.; Sharmin, D.; Knutson, D.E.; Cook, J.M.; Savic, M.M. Positive modulation of alpha5GABAA receptors leads to dichotomous effects in rats on memory pattern and GABRA5 expression in prefrontal cortex and hippocampus. *Behav. Brain Res.* **2022**, *416*, 113578. [CrossRef]
37. Hyland, B.I.; Reynolds, J.N.; Hay, J.; Perk, C.G.; Miller, R. Firing modes of midbrain dopamine cells in the freely moving rat. *Neuroscience* **2002**, *114*, 475–492. [CrossRef]
38. Shah, A.; Lodge, D.J. A loss of hippocampal perineuronal nets produces deficits in dopamine system function: Relevance to the positive symptoms of schizophrenia. *Transl. Psychiatry* **2013**, *3*, e215. [CrossRef]
39. Grace, A.A.; Bunney, B.S. Intracellular and extracellular electrophysiology of nigral dopaminergic neurons--1. Identification and characterization. *Neuroscience* **1983**, *10*, 301–315. [CrossRef]
40. Ungless, M.A.; Grace, A.A. Are you or aren't you? Challenges associated with physiologically identifying dopamine neurons. *Trends Neurosci.* **2012**, *35*, 422–430. [CrossRef]
41. Paxinos, G.; Watson, C. *The Rat Brain in Stereotaxic Coordinates*, 2nd ed.; Academic Press: Sydney, Australia, 1986.

International Journal of
Molecular Sciences

MDPI

Review

Vitamin E and Its Molecular Effects in Experimental Models of Neurodegenerative Diseases

Bianca Caroline da Cunha Germano [1], Lara Cristina Carlos de Morais [2,3], Francisca Idalina Neta [3,4], Amélia Carolina Lopes Fernandes [3,4], Francisco Irochima Pinheiro [5,6], Amália Cinthia Meneses do Rego [5], Irami Araújo Filho [5,6], Eduardo Pereira de Azevedo [5], José Rodolfo Lopes de Paiva Cavalcanti [2,3,4], Fausto Pierdona Guzen [2,3,4,5,*] and Ricardo Ney Cobucci [1,5,6,7]

1 Postgraduate Program in Science Applied to Women's Health, Federal University of Rio Grande do Norte (UFRN), Natal 59072-970, Brazil; bianca@ufrn.br (B.C.d.C.G.); ricardo.cobucci.737@ufrn.edu.br (R.N.C.)
2 Postgratuate Program in Health and Society, Department of Biomedical Sciences, Faculty of Health Sciences, State University of Rio Grande do Norte (UERN), Mossoró 59607-360, Brazil; laracarlos@alu.uern.com.br (L.C.C.d.M.); rodolfolopes@uern.br (J.R.L.d.P.C.)
3 Laboratory of Experimental Neurology, Department of Biomedical Sciences, Faculty of Health Sciences, State University of Rio Grande do Norte (UERN), Mossoró 59607-360, Brazil; franciscaidalina@alu.uern.br (F.I.N.); ameliacarolina@alu.uern.br (A.C.L.F.)
4 Postgraduate Program in Physiological Sciences, Department of Biomedical Sciences, Faculty of Health Sciences, State University of Rio Grande do Norte (UERN), Mossoró 59607-360, Brazil
5 Postgraduate Program in Biotechnology, Health School, Potiguar University (UnP), Natal 59056-000, Brazil; irochima@gmail.com (F.I.P.); irami.filho@gmail.com (I.A.F.); azevedoep@hotmail.com (E.P.d.A.)
6 Medical School, Health School, Potiguar University (UnP), Natal 59056-000, Brazil
7 Postgraduate Program in Health Sciences, Federal University of Rio Grande do Norte (UFRN), Natal 59078-900, Brazil
* Correspondence: faustoguzen@uern.br; Tel.: +55-84-33152248

Abstract: With the advancement of in vivo studies and clinical trials, the pathogenesis of neurodegenerative diseases has been better understood. However, gaps still need to be better elucidated, which justifies the publication of reviews that explore the mechanisms related to the development of these diseases. Studies show that vitamin E supplementation can protect neurons from the damage caused by oxidative stress, with a positive impact on the prevention and progression of neurodegenerative diseases. Thus, this review aims to summarize the scientific evidence of the effects of vitamin E supplementation on neuroprotection and on neurodegeneration markers in experimental models. A search for studies published between 2000 and 2023 was carried out in the PubMed, Web of Science, Virtual Health Library (BVS), and Embase databases, in which the effects of vitamin E in experimental models of neurodegeneration were investigated. A total of 5669 potentially eligible studies were identified. After excluding the duplicates, 5373 remained, of which 5253 were excluded after checking the titles, 90 articles after reading the abstracts, and 11 after fully reviewing the manuscripts, leaving 19 publications to be included in this review. Experiments with in vivo models of neurodegenerative diseases demonstrated that vitamin E supplementation significantly improved memory, cognition, learning, motor function, and brain markers associated with neuroregeneration and neuroprotection. Vitamin E supplementation reduced beta-amyloid (Aβ) deposition and toxicity in experimental models of Alzheimer's disease. In addition, it decreased tau-protein hyperphosphorylation and increased superoxide dismutase and brain-derived neurotrophic factor (BDNF) levels in rodents, which seems to indicate the potential use of vitamin E in preventing and delaying the progress of degenerative lesions in the central nervous system.

Keywords: experimental models of neurological diseases; vitamin E; alpha tocopherol; experimental models

Citation: da Cunha Germano, B.C.; de Morais, L.C.C.; Idalina Neta, F.; Fernandes, A.C.L.; Pinheiro, F.I.; do Rego, A.C.M.; Araújo Filho, I.; de Azevedo, E.P.; de Paiva Cavalcanti, J.R.L.; Guzen, F.P.; et al. Vitamin E and Its Molecular Effects in Experimental Models of Neurodegenerative Diseases. *Int. J. Mol. Sci.* **2023**, *24*, 11191. https://doi.org/10.3390/ijms241311191

Academic Editor: Claudia Ricci

Received: 16 May 2023
Revised: 26 June 2023
Accepted: 27 June 2023
Published: 7 July 2023

1. Introduction

Over the past few years, as a result of the steady rise in life expectancy, a significant increase in the prevalence of neurodegenerative diseases (NDD) has been evident, which has resulted in increased health risks and more demanding research into new and more efficient therapies [1]. In addition, the great majority of NDD are debilitating and untreatable, resulting in suffering for the affected patients and their families [2–4].

The disorders start by affecting neurons in a gradual process, resulting in degeneration and/or death of some neurons, which might lead to impaired physical movements and cognitive function [5]. In fact, some neurodegenerative diseases, such as Alzheimer's disease (AD), Parkinson's disease (PD), and dementia with Lewy bodies, have some common clinical manifestations such as abnormal protein deposition, inflammation, mitochondrial deficits, intracellular Ca^{2+} overload, abnormal cellular transport, uncontrolled generation of reactive oxygen species (ROS), and excitotoxicity. Thus, the existence of convergent neurodegeneration pathways in such diseases becomes clear [6]. However, there are still no therapeutic strategies that can prevent, reduce, or stop the progression of these diseases, even though some drugs are able to treat only the symptoms [7].

Some natural products exhibit a variety of neuroprotective activities, which include targeting mitochondrial dysfunction, excitotoxicity, inflammation, apoptosis, oxidative stress, and protein folding [8–12]. One of these products from natural sources with reported neuroprotective activity is vitamin E (VE), which is formed by different fat-soluble compounds found in plants and is divided into tocopherols and tocotrienols. Each type is formed by four homologs according to the number and location of the methyl groups, being classified as α-, β-, γ-, and δ-tocopherol and as α-, β-, γ-, and δ-tocotrienol [13].

The effects of α-tocopherol (α-Toc) on the central nervous system (CNS) have been reported for over 50 years [14]. A relationship between brain health and α-tocopherol levels has been hypothesized, especially in diseases associated with oxidative stress such as ataxias, AD, and PD [15]. Therefore, VE deficiency might lead to progressive neurological disorders such as spinocerebellar ataxia as a result of the death of peripheral nerves. Thus, long-term α-Toc supplementation may prevent the progression of nervous system degeneration caused by VE deficiency [16,17].

In this perspective, both tocopherol transfer protein (TTP) and vitamin E have important functions in the CNS, as they are necessary for embryonic development, neurogenesis, neuroprotection, and cognition [18]. Furthermore, it acts as a peroxyl-radical-scavenging antioxidant that inhibits free radical-mediated lipid peroxidation [19]. Moreover, studies indicate that α-Toc reduces lipid peroxidation caused by lipopolysaccharide (LPS), microglia, and interleukin-6 (IL-6) [20,21], in addition to having a positive effect on neuroplasticity [22]. In fact, αToc is able to break the oxidant chain found in lipoproteins and cellular compartments such as cell membranes, preventing lipid peroxidation and thus preserving membrane integrity [23,24].

Ambrogini et al. reported that α-tocopherol can protect against kainate-induced cell death in the hippocampus, thereby preserving its synaptic plasticity and function [25]. Moreover, other studies have evidenced the antioxidant activity of VE and αToc in the CNS with significant improvements in memory and motor function, as well as a marked increase in the levels of neuroprotective, neuroregenerative, and anti-inflammatory components [26,27]. However, there are a very limited number of reviews about the effects of VE supplementation on animal models of neurodegenerative diseases.

Considering that the studies published so far show positive effects of VE and αToc on the CNS, this narrative review aims to analyze the scientific evidence of the effects of VE and αToc supplementation in animal models of neurodegenerative diseases.

2. Methodology

A search for studies published between January 2000 and April 2023 was carried out in Medline databases through PubMed, Web of Science, Virtual Health Library (BVS), and Embase, in which the effects of vitamin E in experimental models of neurodegeneration

were investigated. The search strategy consisted of a combination of Medical Subject Headings (MeSH) terms "neurodegenerative diseases" and "alpha-tocopherol" (Medline and Web of Science); "degenerative disease" and "alpha-tocopherol" (Embase); and "chronic disease" and "alpha-tocopherol" (BVS). The search strategy performed in PubMed can be verified in the Supplementary Material Table S1.

Studies involving the effects of VE on memory, cognition, learning, motor coordination, neuroprotection, neuroregeneration, inflammatory markers, and biomarkers of oxidative stress in experimental models of neurodegeneration were included in this review. Studies that met one of the following criteria were excluded: (1) Review studies; (2) Non-peer-reviewed studies (such as guidelines and preprints); (3) studies performed with vitamin E associated with other herbal supplements, drugs, or therapies; (4) double publication: if the article appeared more than once in one of the databases, only the original manuscript was included; (5) experimental models other than small rodents (rats and mice) or cell culture; (6) studies carried out with extracts of more than one oil or with the use of parts of the plant that are not the seed, such as the stem, leaf, fruit, root, and flower.

The results of the eligible studies are described herein as a narrative synthesis that summarizes the characteristics of the study, the studied population (animals), as well as the type of VE and αToc supplementation used.

3. Results

The search strategy used in this study resulted in 5669 potentially eligible articles. After excluding the duplicates, 5373 articles remained, of which 5253 were excluded after checking the titles, 90 after reading the abstracts, and 11 after the complete review of the manuscripts, leaving a total of 19 publications to be included in this review.

The included studies are presented in Table 1 with the following information: author, year of publication, species, control group, induction method, experimental model of neurodegeneration, type of VE supplementation and administration method, supplementation time and data collection, the dose used, and the main results.

Table 1. Characteristics and main findings of the studies included in this review.

Reference	Species/Strain	Gender	Control Group	Induction Method	Experimental Model	Type of Subst.	Duration	Dose	Admin. Route	Data Collection Time	Outcome Measure-ment	Main Findings
Sung 2003 [28]	Tg 2576 mice	M/F	Placebo	Transgenic rats	AD [a]	Vitamin E	6 to 8 months	2 mg/g	Oral	8 months	Neuroprotection	Reduced lipid peroxidation, soluble Aβ [b] and amyloid plaque deposition
Conte et al., 2004 [29]	Tg 2576 mice	F	Normal chow	RCBI [c]	AD [a]	Vitamin E	4 weeks before lesion and 8 weeks after	2 mg/g	Injection into the left parieto-temporal region.	8 weeks	Neuroprotection	Reduced BLP (Brain Lipid Peroxidation) Alleviated the learning deficit Improved behavioral commitment
Garcia-Alloza 2006 [30]	APPswe/PS1d9 mice	*	2 received distilled water 2 received cremophor 25% in distilled water	Transgenic rats	AD [a]	Trolox (Vitamin E)	15 days	1 day before sugery 210 mg/kg, and after for 15 days	Gavage	15 days	Neuroregeneration	Slowed the progress of AD [a] Significantly reduced oxidative stress Changed the structures of the neurites
Annaházi, 2007 [31]	Wistar rats	M	Operated group Nothing applied	Chronic brain hypop-erfusion	Brain injury in bilateral common carotid arteries	α-tocopherol	5 days before surgery and 5 days after	100 mg/kg	Intraperitoneal	17 days	Neuroprotection	Improved the learning process Prevented loss of stained pyramidal cells in the CA1 hippocampus Preserved dendritic arborizations Attenuated microglial activation
Pasbakhsh, 2009 [32]	Sprague-Dawley rats	M	Sham group operated + Sham group treated with vehicle + sham group treated with vitamin E	6-OHDA [d]	PD [e] initial model	Vitamin E	8 weeks	D-a-tocopheryl succinate (16 mg/kg, i.m, Bioglan, UK) and 0.8 mL/kg of propylene glycol	Intramuscular	2 weeks after surgery	Neuroprotection	Delayed functional decline
Tiwari et al., 2009 [33]	Wistar rats	M	Injected citrate buffer	ST′Z [f]	AD [a] Cognitive deficit	α-tocopherol	21 days after lesion	100 mg/kg	Oral	21 days	Neuroprotection	Prevention of cognitive impairment Prevented a reduction in the levels of GSH [g] and catalase Reduced MDA [h], nitrite and cholinesterase activity

Table 1. *Cont.*

Reference	Species/Strain	Gender	Control Group	Induction Method	Experimental Model	Type of Subst.	Duration	Dose	Admin. Route	Data Collection Time	Outcome Measurement	Main Findings
Bostanci, 2010 [34]	Wistar rats	M	Saline solution	Iron	Neurotoxicity Oxidative stress	α-tocopherol	10 days	100 mg/kg/day	Intraperitoneal	10 days	Neuroprotection	Attenuated the loss of neurons Decreased cell loss in the hippocampus and substantia nigra Protective effect on pyramidal cells of the hippocampus
Alzoubi, 2012 [35]	Wistar rats	M	Vehicle	Sleep deprivation	Memory deficit Learning impairment	Vitamin E	6 weeks	100 mg/kg	Oral by gavage	6 weeks	Neuroprotection	Prevented memory impairment It normalized the reduction in oxidative stress markers (GSH [g]/GSSG [i]), SOD [j] and GPx [k] catalase activity
Desrumaux, 2013 [36]	PLTO-KO mice	M	3 µL of vehicle	Aβ [b] 25–35	AD [a] Memory impairment	Vitamin E	10 days	800 mg/kg	Oral	10 days	Neuroprotection	Reduced short-term memory impairment Prevented PLTP-KO [l] compromise
Ishihara, 2013 [37]	3 Tg—AD [a] mice	*	Normal diet	Transgenic rats	AD [a] pathogenesis Cognitive deficit	α-tocopherol	4 months	1.342 mg/g and normal diet 0.076 mg/g	Oral	4 months and 4 days	Neuroprotection	Prevented cognitive impairment Attenuated the reduction in GSH [g] levels and the increase in GSSG [i] and TBARS [m] Decreased the levels of reactive radicals in the brain
An, 2016 [38]	Sprague Dawley rats	M	Saline solution	HAL [n]	Orofacial dyskinesia VCM [o]	α-tocopherol	5 weeks	20 mg/kg/day	Oral	5 weeks from the last administration	Neuroprotection	Reduced stereotypical behavior Decreased the expression of anti-apoptotic protein Bcl-2 [p] Increased the expression of pro-apoptotic Bax [q] protein Decreased Bax [q]/Bcl-2 [p] ratio in prefrontal cortex, striatum, substantia nigra, and globus pallidus

Table 1. *Cont.*

Reference	Species/Strain	Gender	Control Group	Induction Method	Experimental Model	Type of Subst.	Duration	Dose	Admin. Route	Data Collection Time	Outcome Measurement	Main Findings
Wang, 2016 [39]	APPswe/PS1dE9 mice	M	Saline solution	Transgenic rats	AD [a]	α-tocopherol	4 weeks	100 mg/kg	Oral gavage	4 weeks	Neuroprotection Neuroregeneration	Improved memory impairment Improved cognitive dysfunction Counteracted oxidative stress Decreased the levels of Aβ [b] oligomer
Liu, 2019 [40]	C57BL/6J mice	M	0 mg kg –1 day –1 of PM 2.5 [r]	PM 2.5 [r]	Cognitive deficit Oxidative stress	Vitamin E	7 days	50 mg/kg^{-1} day^{-1}	Intragastric	7 days	Neuroprotection Neuroregeneration	Improved cognitive function Reduced cellular damage Increased the number of cells Decreased the expression of Aβ [b] 1–42 Reduced oxidative stress
Jahanshahi, 2020 [41]	Wistar rats	M	No medication	Scopolamin	AD [a]	Vitamin E	14 days after induction	25, 50, and 100 mg/kg/day	Intraperitoneal	16 days	Neuroprotection	Amyloid plaque reduction Prevented an increase in neurofibrillary tangles in hippocampal subregions
Rana et al., 2020 [42]	Wistar rats	M	Vehicle	TBI [s]	Cognitive impairment Motor damage	α-tocopherol	28 days after induction	5 mg/kg, po. 10 mg/kg, po.	Weight drop model	28 days	Neuroprotection Neuromodulation	Attenuated locomotor performance Reduced cognitive impairment Reduced neuroinflammatory markers Restored neurotransmitter levels Balanced oxidative stress
Nesari, 2021 [43]	Wistar rats	M	DMSO [t] + Saline solution	Lactacystin	Proteasome inhibition Oxidative stress Memory impairment	α-tocopherol	5 days before induction	60 and 200 mg/kg, i.p.	Bilateral hippocampal injection	7 days	Neuroprotection	High doses of α-tocopherol exhibited remarkable mitochondrial protection Improved memory impairment Increased the levels of glutathione

Table 1. *Cont.*

Reference	Species/Strain	Gender	Control Group	Induction Method	Experimental Model	Type of Subst.	Duration	Dose	Admin. Route	Data Collection Time	Outcome Measure-ment	Main Findings
Shahidi, 2021 [44]	Wistar rats	M	Saline solution + Non operated	Aβ [b] 25–35	AD [a]	Vitamin E	10 days	200 mg/kg	Oral by gavage	2 weeks 10 days	Neuroprotection	Improved passive avoidance of memory impairment The amplitude of the PS [u] was increased Alleviated LTP [v] deficiency Reverted the increase in Bcl-2 [p] and Bax [q] ratio in the hippocampus
Singh, 2022 [45]	Wistar rats	M	Ropinirol	Rotenona	Sintomas semelhantes a PD [e]	Tocopherol	40 days	5 and 10 mg/kg	Intraperitoneal	41 days	Neuroprotection and neuroin-flammation	Attenuated behavioral changes Enhanced the expression of neurotransmitters Reduced the levels of inflammatory markers
Iqbal, 2022 [46]	Albino swiss mice	M	CMC [w]	HAL [n]	PD [e]	Tocopherol	23 days	5, 10, 20 and 40 mg/kg	Oral route	23 days	Neuroprotection	Increased the levels of antioxidant enzymes and neurotransmitters Decreased the levels of inflammatory cytokines and the expression of α-synuclein mRNA

* = not mentioned; [a] AD = Alzheimer's disease; [b] Aβ = β-amyloid; [c] RCBI = repetitive concussive brain injury; [d] 6-OHDA = 6-hydroxydopamin; [e] PD = Parkinson's disease; [f] STZ = streptozotocin; [g] GSH = glutathione; [h] MDA = malondialdehyde; [i] GSSG = oxidized glutathione; [j] SOD = superoxide dismutase; [k] GPx = glutathione peroxidase; [l] PLTP-KO = plasma phospholipid transfer protein-deficient; [m] TBARS = thiobarbituric acid-reactive substance; [n] HAL = haloperidol; [o] VCM = vacuum chewing movements; [p] BCL-2 = B-cell lymphoma 2; [q] BAX= B-cell lymphoma 2 associated protein X; [r] PM 2.5 = ambient fine particulate matter (aerodynamic diameter < 2.5 um, PM 2.5); [s] TBI = traumatic brain injury; [t] DMSO = dimethylsulfoxide; [u] PS = population increase; [v] LTP = long-term potentiation; [w] CMC = carboxymethylcellulose.

3.1. Neuroprotective Mechanisms of Vitamin E in Neurodegenerative Diseases

3.1.1. Memory and Learning

The study by Alzoubi [35] was carried out using Wistar rats as the animal model, in which they were deprived of sleep followed by oral administration of VE (100 mg/kg) for six weeks. Such a procedure was able to prevent memory impairment (Figure 1).

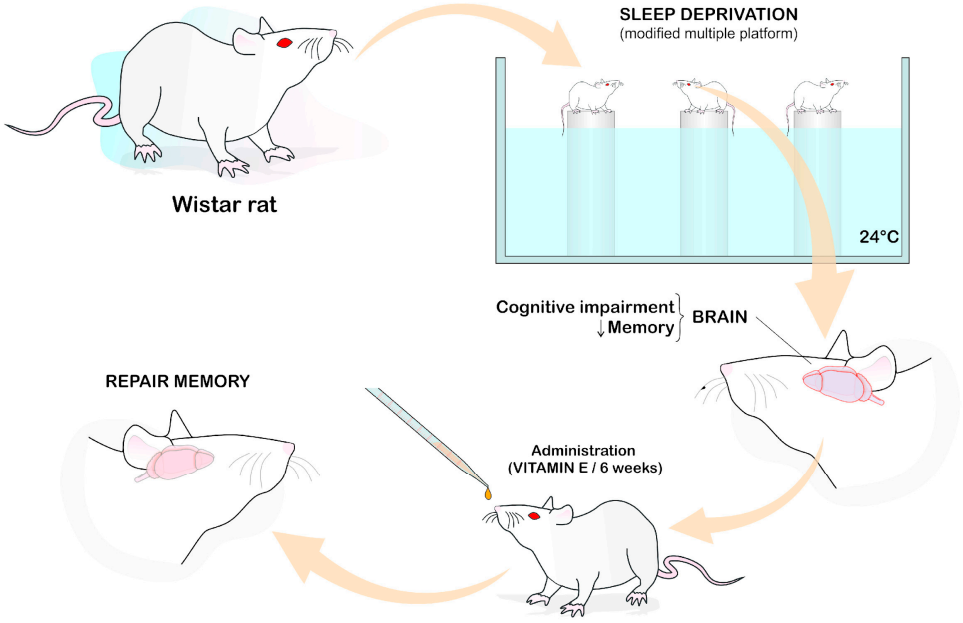

Figure 1. Vitamin E and memory. Illustration demonstrates that sleep deprivation impairs cognition/memory. The role of vitamin E in memory repair after its administration for 6 weeks in Wistar rats with sleep deprivation-induced memory impairment using the modified multiple platform method. (Illustration performed by Dr. Francisco Irochima).

Desrumaux et al. used PLTO-KO mice that were deficient in plasma phospholipid transfer and were induced to develop memory deficit and Alzheimer's disease (AD) through β 25–35 administration. The animals were supplemented with vitamin E (800 mg/kg orally) for 10 days, whose effect on short-term memory impairment was considered satisfactory [36].

Wang et al. conducted their studies using APPswe/PS1dE9 transgenic mice. After developing AD-triggering Aβ deposits, the animals received αToc, 100 mg/kg, orally for four weeks. The authors concluded that supplementation with αToc had positive effects on memory preservation [39].

Nesari et al. supplemented αToc (60 and 200 mg/kg) for five days after causing proteasome inhibition and memory deficit in Wister rats through lactacystin induction. The authors reported benefits only in those rats that received the highest doses of αToc [43].

Finally, Shadini et al. induced AD in Wistar rats through β 25–35 administration. VE supplementation (200 mg/kg orally) for 10 days resulted in the passive avoidance of memory impairment [44].

In addition, other studies investigated the effectiveness of VE and αToc on learning. The experiment conducted by Conte et al. with AD-induced Tg 2576 mice investigated the administration of 2 IU/g of VE for four weeks before repetitive concussive brain injury (RCBI), followed by another eight weeks of vitamin supplementation after the onset of AD. The authors reported a potential effect of VE supplementation on alleviating the learning deficit [29].

Likewise, Annaházi et al. studied the effect of α-Toc administration in Wistar rats with chronic cerebral hypoperfusion generated by brain injury in the bilateral common carotid

arteries. The α-Toc administration (100 mg/kg) for five days before the injury and the same dose for another five days after the injury was able to improve the learning process [31].

3.1.2. Cognitive

Concerning the effects of VE on cognitive functions, a study investigated the administration of α-Toc (100 mg/kg) for 21 days to Wistar rats subjected to streptozotocin (ST'Z) injury for AD and cognitive deficit induction. Such a protocol was able to successfully prevent cognitive impairment by protecting the animals' brains against oxidative stress and eliminating nitrosative stress and acetylcholinesterase activity [33].

Ishihara et al. obtained similar results, but with a dose of α-TOH of 1.342 mg/kg for six months in 3 tg-AD mice with AD and cognition impairment triggered by Aβ accumulation in the brain. This dose of α-TOH was able to reduce oxidative stress by attenuating the expression of the brain-derived neurotrophic factor [37].

Wang et al. reported improvement in cognitive dysfunction related to spatial memory due to a protective effect that resulted in a reduction in lipid peroxidation and a decrease in the release of inflammatory mediators (IL-1 and IL-6) through the oral administration of α-Toc (100 mg/kg for four weeks) in transgenic APPswe/PS1dE9 mice previously induced to develop AD [39].

Liu et al. used C57BL/6J transgenic mice in which PM 2.5 was administered to induce cognitive deficit. The administration of VE (60 mg/kg/day for seven days) resulted in improved cognitive function, which was correlated with the ability to memorize and learn on the Morris water maze test (MWM), suggesting that it was associated with reduced oxidative stress [40].

Finally, Rana et al. used α-Toc, 5–10 mg/kg over 28 days after induction of traumatic brain injury (TBI) in Wistar rats, resulting in reduced cognitive impairment. The use of such a protocol of α-Toc supplementation reduced neuroinflammatory markers, restored neurotransmitter levels, and restored oxidative stress balance [42].

3.1.3. Motor Coordination

The studies included in this section investigated whether VE and α-Toc supplementation generated a positive impact in animal models with motor and behavioral impairments, even though they used different experimental models.

In one study, Tg 2576 mice were induced to develop AD through repetitive concussive brain injury (RCBI) in the left parietal-temporal region. Briefly, 2 IU/g of VE was administered for four weeks before and eight weeks after the lesion, and an improvement in behavior caused by RCBI was observed with cerebral lipid peroxidation secondary to brain trauma [29].

In another study, Sprague-Dawley rats were used, and they were fed for five weeks with α-Toc (20 mg/kg/day, orally) after being induced to develop orofacial dyskinesia and vacuum chewing movements (MVC) by haloperidol (HAL). It was observed a reduction in the stereotyped behavior of chewing movements after α-Toc administration [38].

Finally, Wistar rats were induced to exhibit motor impairment by a TBI lesion, whose locomotor deficit was attenuated when supplemented with 5–10 mg/kg of α-Toc for 28 days [42].

3.1.4. Oxidative Stress and Neurodegenerative Diseases

VE supplementation can cause changes in the CNS and positively impact oxidative stress. In the study conducted by Sung et al., AD-induced Tg 2576 mice were supplemented with vitamin E (2 IU/g) for 8 months. The authors found a reduction in lipid peroxidation as well as a decrease in the levels of soluble Aβ and in amyloid plaque deposition [28].

Garcia-Alloza et al. carried out a study with AD-induced APPswe/PS1d9 mice. The oral administration of VE (210 mg/kg) 1 day before and 15 days after surgery was able to reduce AD progress, decrease oxidative stress, and reduce damage to the neurite structures [30].

In addition, Bostanci et al. administered α-Toc (100 mg/kg/day) for 10 days to Wistar rats previously induced to neurotoxicity and oxidative stress, after which they found that the loss of neurons was attenuated and a neuroprotective effect was observed [34].

Singh and Chauhan induced Parkinson's-like symptoms in Wistar rats, followed by the administration of tocopherol (5 and 10 mg/kg) intraperitoneally for 40 days. Such a procedure attenuated behavioral changes, in addition to improving the expression of neurotransmitters and reducing the levels of inflammatory markers [45].

Iqbal et al. carried out a study with Swiss albino mice with PD induced by haloperidol. Oral administration of tocopherol (5, 10, 20, and 40 mg/kg) for 23 days was able to increase the levels of antioxidant enzymes and neurotransmitters and decrease the levels of inflammatory cytokines and α-synuclein mRNA expression [46].

3.1.5. Neuroprotection and Neuroregeneration

VE and α-Toc have shown a neuroprotective effect in several neurodegenerative models. Supplementation with vitamin E and α-Toc has been able to reach the entire CNS, hippocampus, neurons, memory functions, behavior, learning, and cognition, thus protecting from oxidative stress, which is the main cause of neurodegenerative disorders [28–32,34–38,41,43,44].

When VE was administered to transgenic mice APPswe/PS1d9 with induced AD, a regenerative effect was observed, thereby slowing the progress of AD, reducing oxidative stress, and altering structures in neurons that resulted in neuroprotection [30].

In another study, Wang et al. [39] used APPswe/Ps1dE9 mice with AD and supplemented them with 100 mg/kg of α-Toc for four weeks, while Liu et al. [40] used C57Bl/6J mice with induced cognitive deficit and oxidative stress and supplemented them with VE for seven days at 50 mg/kg/day. On the other hand, Rana et al. [42] induced cognitive deficit and motor impairment in Wistar rats by means of TBI, followed by supplementation with α-Toc for 28 days at 5–10 mg/kg. These authors reported that vitamin E and α-Toc supplementation was able to protect and regenerate the CNS of the animals, despite the diversity of induced neurodegenerative diseases, the doses of VE and α-Toc, and the heterogeneity in the duration of the experiments (Figure 2).

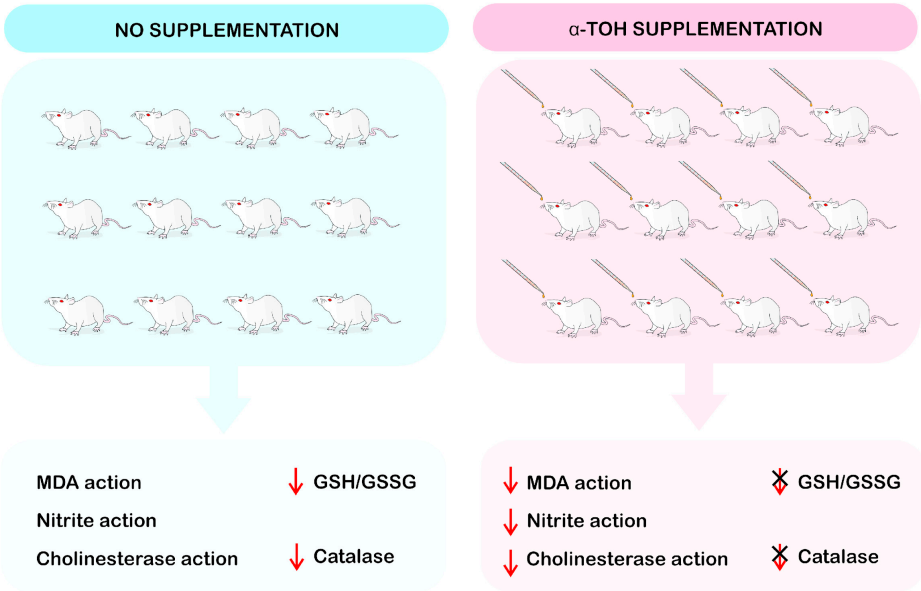

Figure 2. Biochemical effects of vitamin E supplementation in rats. The groups treated with α-TOH (α-tocopherol) supplementation resulted in reduced levels of malondialdehyde (MDA), nitrites, and cholinesterase, in addition to preventing the loss of glutathione (GSH) and oxidized glutathione (GSSG) when compared to non-supplemented animals, which had a decrease in GSH/GSSG and Catalase (Illustration performed by Dr. Francisco Irochima).

4. Discussion

The studies analyzed in this review evidenced that VE supplementation is able to reduce oxidative stress and lipid peroxidation as well as inhibit the brain inflammatory process in animal models of neurodegenerative diseases. Considering that there is scientific evidence that links oxidative stress to CNS inflammation with the onset and progression of neurodegenerative diseases, the results of this review point to a beneficial effect of supplementation with foods rich in α-tocopherol.

The studies included in this review showed that VE supplementation had a positive effect on oxidative stress through a reduction in lipid peroxidation and senile plaques as a result of its anti-inflammatory effect on the CNS. VE has the ability to regulate the gene expression of proteins involved in the cellular redox state and, consequently, oxidative stress. In fact, the studies demonstrate that α-Toc supplementation acts on lipid peroxidation [47]. Similarly, a previous study reported that vitamin E has fat-soluble antioxidant capacity, efficiently eliminating membrane lipid peroxidation and protecting against free radical damage while maintaining membrane integrity [18]. In this perspective, a study conducted by Takatsu and colleagues demonstrated that vitamin E improves the cognitive deficit caused by aging, not only through its neuroprotective activity but also through its antioxidant effect [48].

Another study demonstrated the potential ability of VE to counteract the effects of traumatic brain injury (TBI) on the molecular substrates underlying synaptic plasticity and cognitive function in the hippocampus in rat models. The results suggested that dietary VE supplementation may protect the brain against the effects of mild TBI on synaptic plasticity and cognition by using molecular systems associated with long-term maintenance of synaptic plasticity, such as BDNF and its downstream effectors in preserving activity, synaptic, synapsin I, CREB, and CaMKII [49]. Other studies in this review corroborate this neuroregenerative effect, which has resulted in delaying the progression of AD, increasing cell number, reducing cell damage, changing neurite structure, reducing oxidative stress, and significantly improving cognitive functions [30,39,40].

Mangialasche and colleagues reported in their study that low levels of vitamin E are found in older adults with AD and mild cognitive impairment [50]. From this perspective, the relationship between increased levels of VE and a reduction in the incidence of cognitive impairment cannot be ruled out. Based on these results, it is understood that high levels of VE (α-Toc and γ-tocopherol) might play a preventive role in reducing the risk of cognitive impairment [51]. Therefore, it is possible to infer that the elevation of plasma α-Toc may result in better global cognition and a reduction in total brain atrophy [52]. In fact, different authors found similar results, showing that VE supplementation is a potential alternative to improve the cognitive function of animals [29,31,33,35–37,39,42–44].

Furthermore, this review analyzed studies in which VE and α-Toc were able to cause a significant improvement in motor activity by reducing the Bax/Bcl-2 ratio in the prefrontal cortex, striatum, substantia nigra, and globus pallidus, in addition to restoring neurotransmitter levels. Therefore, VE and α-Toc supplementation have demonstrated a potential effect on motor changes caused by neurodegenerative diseases through a reduction in stereotyped behaviors and functional decline [29,38,42,52]. In fact, previous studies have reported that the substantia nigra is an area of the midbrain responsible for controlling motor activity, which indicates that neurodegeneration of dopaminergic neurons in this region can result in the genesis of Parkinson's disease (PD) and other motor dysfunctions [53].

Ulatowski et al. reported that VE deficiency causes dysfunction in the cerebellum, degeneration of its neurons, premature death, and ataxia [54]. Purkinje cerebellar cells also undergo deterioration, being the main integrators of neural circuits in this region. VE-deficient TTP null mice show a high degree of atrophy of Purkinje neurons and reduced neuronal connectivity, highlighted by reduced neuronal arborization. In this perspective, Yokota et al. demonstrated that α-Toc supplementation almost completely corrected the abnormalities in a mouse model with α-TTP gene mutations that are linked to isolated LV ataxia deficiency (AVED). These authors concluded that α-tocopherol supplementa-

tion suppressed lipid peroxidation and almost completely prevented the development of neurological symptoms [55].

El-Shaer et al., using an experimental model of exposure to an electromagnetic field, evaluated the effects on the structural properties of the cerebellum and the possible neuroprotective effects of VE. The submission to magnetism caused demyelination and degeneration of axons in the molecular and granular layers, as well as a reduction in Purkinje cells and pyknotic nuclei. However, supplementation with VE enabled a reduction in neuropathological changes in all the aforementioned cerebellar areas [56].

In addition, some studies have reported that VE supplementation is able to reduce the neurodegenerative process involved in PD. This disease is characterized by the degeneration of dopaminergic neurons in the substantia pars compacta in the substantia nigra. In addition, it is associated with reduced levels of dopamine in the nigrostriatal pathway in the brain [57,58]. Although the genesis of PD is uncertain, oxidative stress is one of the main mechanisms involved in its underlying pathophysiology [57,59]. This review demonstrated that VE was able to reduce the progression of the degenerative process associated with PD through a reduction in oxidative stress. Therefore, it is believed that vitamin E causes neuronal resistance and recovery of the atrophied neurons, thus delaying their functional decline [32,45,46].

VE administration (α-Toc and Trolox) has the ability to reverse synaptic plasticity abnormalities in PINK1 -/- mice. The PINK1 haploinsufficiency precipitates mitochondrial functioning, impairing mitophagy and energy production on demand, therefore being responsible for the reduced release of synaptic vesicles at dopaminergic terminals and the subsequent breakdown of corticostriatal synaptic plasticity [60–63]. In this review, Rana and colleagues found similar results in which αToc restored altered neurotransmitter levels after TBI induction [42]. In this study, VE and α-Toc positively interfered in inhibiting or inactivating neuroinflammatory and neuroprotective substances, as well as markers of oxidative stress in the CNS, through a reduction in GSH/GSSG, catalase, and superoxide dismutase (SOD) activity, in addition to the mediators interleukin-1 beta (IL-1β), IL-6, and tumor necrosis factor-alpha (TNF-α).

The antioxidant system has other important components, such as SOD, which plays a fundamental role in protecting cells against the deteriorating and ROS scavenging effects [64,65], portraying the function of SOD as having the ability to catalyze the conversion of superoxide radicals to hydrogen peroxide and molecular oxygen, whereas CAT catalyzes the breakdown of toxic H_2O_2 into water and oxygen. In addition, there are other enzymes that inactivate hydrogen peroxide, a potent ROS that has the ability to convert into a stable product, such as glutathione peroxidase (GPx) [66]. Ward and colleagues [67] stated that the aging process causes different cellular changes, such as increased intracellular Ca^{2+} levels, which cause low-grade inflammation in the CNS and peripheral systems. Furthermore, they reported that low-grade inflammation causes the release of IL-1β, IL-6, and TNF-α. However, it has been reported that VE and/or LTB supplementation decreases TNF-α and IL-6 levels, reducing DNA fragmentation and MAPK signaling pathways. Thus, VE supplementation was able to inhibit oxidative damage in vivo in systemic vasculitides [68,69].

In addition, Celikoglu et al. [70] demonstrated that VE alleviated the oxidative stress induced by mercury, causing increased activities of SOD, catalase, and glutathione peroxidase. Furthermore, α-Toc supplementation resulted in a protective effect against oxidative brain damage through a reduction in lipid peroxidation and improved brain antioxidant capacity by increasing GSH levels [71,72].

Studies carried out using elderly rodents have shown that the BDNF system is affected at several levels with aging, which includes reduced transcription, synthesis, and protein processing [73]. These reductions are related to hippocampal shrinkage [74], spatial memory decline [75], and neuronal atrophy [76]. However, VE was able to promote an enhancement in cognition mediated by BDNF through its ability to regulate the production of CaMK in the hippocampus, whereas α-Toc was able to increase the molecular factors associated with

memory consolidation such as BDNF, CREB, and synapsin I, all of which can be affected by oxidative stress [49,77,78].

Although the studies with animal models of neurodegenerative diseases that underwent supplementation with VE or α-Toc have shown potential in preventing and controlling the progression of these diseases, there are limitations in this review that may compromise the extrapolation of results. The diversity found in the amount of supplementation used, as well as in the administration route and in the heterogeneity of the evaluation of the effects on the CNS, are limitations that need to be pointed out. In addition, it is important to emphasize that only in vivo studies were included in this review, and even with scientifically validated evidence, there is a conviction that the results cannot yet be fully extrapolated to humans.

5. Conclusions

VE and α-Toc have the potential to significantly improve cognition, memory, learning, motor function, and disease progression in animal models of neurodegenerative diseases, playing a preventive role.

Therefore, the promising results shown in the in vivo studies indicate that vitamin E can reduce oxidative stress and lipid peroxidation and inhibit the brain inflammatory process, whose mechanisms are present in different neurodegenerative diseases. However, there is a need to confirm these findings in controlled clinical trials that assess the efficacy of vitamin E supplementation in humans with such CNS pathologies.

Supplementary Materials: The following supporting information can be downloaded at: https://www.mdpi.com/article/10.3390/ijms241311191/s1.

Funding: CAPES code 001.

Acknowledgments: The authors thank the Brazilian agencies the National Council for Scientific and Technological Development (CNPq) and the Coordination for the Improvement of Higher Education Personnel (CAPES) for fellowships and financial support.

Conflicts of Interest: The authors declare no conflict of interest.

References

1. Heemels, M.T. Neurodegenerative diseases. *Nature* **2016**, *539*, 179. [CrossRef]
2. Guo, L.; Lee, V.M.Y. Cell-to-cell transmission of pathogenic proteins in neurodegenerative diseases. *Nat. Med.* **2014**, *20*, 130–138. [CrossRef] [PubMed]
3. Jucker, M.; Walker, L.C. Self-propagation of pathogenic protein aggregates in neurodegenerative diseases. *Nature* **2013**, *501*, 45–51. [CrossRef] [PubMed]
4. Prusiner, S.B. A Unifying Role for Prions in Neurodegenerative Diseases. *Science* **2012**, *336*, 1511–1513. [CrossRef] [PubMed]
5. Chekani, F.; Bali, V.; Aparasu, R.R. Quality of life of patients with Parkinson's disease and neurodegenerative dementia: A nationally representative study. *Res. Soc. Adm. Pharm.* **2016**, *12*, 604–613. [CrossRef]
6. Dadhania, V.P.; Trivedi, P.P.; Vikram, A.; Tripathi, D.N. Nutraceuticals against Neurodegeneration: A Mechanistic Insight. *Curr. Neuropharmacol.* **2016**, *14*, 627–640. [CrossRef]
7. Rasool, M.; Malik, A.; Qureshi, M.S.; Manan, A.; Pushparaj, P.N.; Asif, M.; Qazi, M.H.; Qazi, A.M.; Kamal, M.A.; Gan, S.H.; et al. Recent Updates in the Treatment of Neurodegenerative Disorders Using Natural Compounds. *Evid. Based Complement. Alternat. Med.* **2014**, *2014*, 979730. [CrossRef]
8. Leonoudakis, D.; Rane, A.; Angeli, S.; Lithgow, G.J.; Andersen, J.K.; Chinta, S.J. Anti-Inflammatory and Neuroprotective Role of Natural Product Securinine in Activated Glial Cells: Implications for Parkinson's Disease. *Mediat. Inflamm.* **2017**, *2017*, 8302636. [CrossRef]
9. Bagli, E.; Goussia, A.; Moschos, M.M.; Agnantis, N.; Kitsos, G. Natural Compounds and Neuroprotection: Mechanisms of Action and Novel Delivery Systems. *In Vivo* **2016**, *30*, 535–547.
10. Starkov, A.A.; Beal, F.M. Portal to Alzheimer's disease. *Nat. Med.* **2008**, *14*, 1020–1021. [CrossRef]
11. Venkatesan, R.; Ji, E.; Kim, S.Y. Phytochemicals That Regulate Neurodegenerative Disease by Targeting Neurotrophins: A Comprehensive Review. *BioMed Res. Int.* **2015**, *2015*, 814068. [CrossRef]
12. Deshpande, P.; Gogia, N.; Singh, A. Exploring the efficacy of natural products in alleviating Alzheimer's disease. *Neural Regen. Res.* **2019**, *14*, 1321. [CrossRef]

13. Jiang, Q. Natural forms of vitamin E: Metabolism, antioxidant, and anti-inflammatory activities and their role in disease prevention and therapy. *Free Radic. Biol. Med.* **2014**, *72*, 76–90. [CrossRef] [PubMed]
14. Ulatowski, L.; Ghelfi, M.; West, R.; Atkinson, J.; Finno, C.J.; Manor, D. The tocopherol transfer protein mediates vitamin E trafficking between cerebellar astrocytes and neurons. *J. Biol. Chem.* **2022**, *298*, 101–712. [CrossRef]
15. Lee, P.; Ulatowski, L.M. Vitamin E: Mechanism of transport and regulation in the CNS. *IUBMB Life* **2019**, *71*, 424–429. [CrossRef]
16. Kohlschütter, A.; Finckh, B.; Nickel, M.; Bley, A.; Hübner, C. First Recognized Patient with Genetic Vitamin E Deficiency Stable after 36 Years of Controlled Supplement Therapy. *Neurodegener. Dis.* **2020**, *20*, 35–38. [CrossRef] [PubMed]
17. Head, B.; Traber, M.G. Expanding role of vitamin E in protection against metabolic dysregulation: Insights gained from model systems, especially the developing nervous system of zebrafish embryos. *Free Radic. Biol. Med.* **2021**, *176*, 80–91. [CrossRef] [PubMed]
18. Traber, M. Vitamin E: Necessary nutrient for neural development and cognitive function. *Proc. Nutr. Soc.* **2021**, *80*, 319–326. [CrossRef]
19. Jiang, Q.; Im, S.; Wagner, J.G.; Hernandez, M.L.; Peden, D.B. Gamma-tocopherol, a major form of vitamin E in diets: Insights into antioxidant and anti-inflammatory effects, mechanisms, and roles in disease management. *Free Radic. Biol. Med.* **2022**, *178*, 347–359. [CrossRef]
20. Shibata, H.; Katsuki, H.; Okawara, M.; Kume, T.; Akaike, A. C-Jun N-terminal kinase inhibition and α-tocopherol protect midbrain dopaminergic neurons from interferon-γ/lipopolysaccharide-induced injury without affecting nitric oxide production. *J. Neurosci. Res.* **2006**, *83*, 102–109. [CrossRef]
21. Godbout, J. α-Tocopherol reduces lipopolysaccharide-induced peroxide radical formation and interleukin-6 secretion in primary murine microglia and in brain. *J. Neuroimmunol.* **2004**, *149*, 101–109. [CrossRef] [PubMed]
22. Hernangomez, M.; Carrillo-Salinas, F.; Mecha, M.; Correa, F.; Mestre, L.; Loria, F.; Feliu, A.; Docagne, F.; Guaza, C. Brain Innate Immunity in the Regulation of Neuroinflammation: Therapeutic Strategies by Modulating CD200-CD200R Interaction Involve the Cannabinoid System. *Curr. Pharm. Des.* **2014**, *20*, 4707–4722. [CrossRef] [PubMed]
23. Brigelius-Flohé, R.; Davies, K.J.A. Is vitamin E an antioxidant, a regulator of signal transduction and gene expression, or a 'junk' food? Comments on the two accompanying papers: "Molecular mechanism of α-tocopherol action" by A. Azzi and "Vitamin E, antioxidant and nothing more" by M. Traber and J. Atkinson. *Free Rad. Biol. Med.* **2007**, *43*, 2–3. [CrossRef] [PubMed]
24. Traber, M.G.; Atkinson, J. Vitamin E, antioxidant and nothing more. *Free Rad. Biol. Med.* **2007**, *43*, 4–15. [CrossRef]
25. Ambrogini, P.; Minelli, A.; Galati, C.; Betti, M.; Lattanzi, D.; Ciffolilli, S.; Piroddi, M.; Galli, F.; Cuppini, R. Post-Seizure α-Tocopherol Treatment Decreases Neuroinflammation and Neuronal Degeneration Induced by Status Epilepticus in Rat Hippocampus. *Mol. Neurobiol.* **2014**, *50*, 246–256. [CrossRef]
26. Icer, M.A.; Arslan, N.; Gezmen-Karadag, M. Effects of vitamin E on neurodegenerative diseases: An update. *Acta Neurobiol. Exp.* **2021**, *81*, 21–33. [CrossRef]
27. Regner-Nelke, L.; Nelke, C.; Schroeter, C.B.; Dziewas, R.; Warnecke, T.; Ruck, T.; Meuth, S.G. Enjoy Carefully: The Multifaceted Role of Vitamin E in Neuro-Nutrition. *Int. J. Mol. Sci.* **2021**, *22*, 10087. [CrossRef]
28. Sung, S.; Yao, Y.; Uryu, K.; Yang, H.; Lee, V.M.Y.; Trojanowski, J.Q.; Praticò, D. Early Vitamin E supplementation in young but not aged mice reduces Aβ levels and amyloid deposition in a transgenic model of Alzheimer's disease. *FASEB J.* **2004**, *18*, 323–325. [CrossRef]
29. Conte, V.; Uryu, K.; Fujimoto, S.; Yao, Y.; Rokach, J.; Longhi, L.; Trojanowski, J.Q.; Lee, V.M.Y.; McIntosh, T.K.; Pratico, D. Vitamin E reduces amyloidosis and improves cognitive function in Tg2576 mice following repetitive concussive brain injury. *J. Neurochem.* **2004**, *90*, 758–764. [CrossRef]
30. Garcia-Alloza, M.; Dodwell, S.A.; Meyer-Luehmann, M.; Hyman, B.T.; Bacskai, B.J. Plaque-Derived Oxidative Stress Mediates Distorted Neurite Trajectories in the Alzheimer Mouse Model. *J. Neuropathol. Exp. Neurol.* **2006**, *65*, 1082–1089. [CrossRef]
31. Annaházi, A.; Mracskó, É.; Süle, Z.; Karg, E.; Penke, B.; Bari, F.; Farkas, E. Pre-treatment and post-treatment with α-tocopherol attenuates hippocampal neuronal damage in experimental cerebral hypoperfusion. *Eur. J. Pharmacol.* **2007**, *571*, 120–128. [CrossRef] [PubMed]
32. Pasbakhsh, P.; Omidi, N.; Mehrannia, K.; Sobhani, A.G.; Kashani, I.R.; Abbasi, M.; Valeshabad, A.K. The protective effect of vitamin E on locus coeruleus in early model of Parkinson's disease in rat: Immunoreactivity evidence. *Iran. Biomed. J.* **2008**, *12*, 217–222. [CrossRef] [PubMed]
33. Tiwari, V.; Kuhad, A.; Bishnoi, M.; Chopra, K. Chronic treatment with tocotrienol, an isoform of vitamin E, prevents intracerebroventricular streptozotocin-induced cognitive impairment and oxidative–nitrosative stress in rats. *Pharmacol. Biochem. Behav.* **2009**, *93*, 183–189. [CrossRef] [PubMed]
34. Bostanci, M.Ö.; Bas, O.; Bagirici, F. Alpha-Tocopherol Decreases Iron-Induced Hippocampal and Nigral Neuron Loss. *Cell. Mol. Neurobiol.* **2010**, *30*, 389–394. [CrossRef]
35. Alzoubi, K.H.; Khabour, O.F.; Rashid, B.A.; Damaj, I.M.; Salah, H.A. The neuroprotective effect of vitamin E on chronic sleep deprivation-induced memory impairment: The role of oxidative stress. *Behav. Brain Res.* **2012**, *226*, 205–210. [CrossRef]
36. Desrumaux, C.; Pisoni, A.; Meunier, J.; Deckert, V.; Athias, A.; Perrier, V.; Villard, V.; Lagrost, L.; Verdier, J.M.; Maurice, T. Increased Amyloid-β Peptide-Induced Memory Deficits in Phospholipid Transfer Protein (PLTP) Gene Knockout Mice. *Neuropsychopharmacology* **2013**, *38*, 817–825. [CrossRef]

37. Ishihara, Y.; Itoh, K.; Mitsuda, Y.; Shimada, T.; Kubota, T.; Kato, C.; Song, S.Y.; Kobayashi, Y.; Yasumoto, S.M.; Sekita, S.; et al. Involvement of brain oxidation in the cognitive impairment in a triple transgenic mouse model of Alzheimer's disease: Noninvasive measurement of the brain redox state by magnetic resonance imaging. *Free Radic. Res.* **2013**, *47*, 731–739. [CrossRef]
38. An, H.M.; Tan, Y.L.; Shi, J.; Wang, Z.; Lv, M.H.; Soares, J.C.; Zhou, D.; Yang, F.; Zhang, X.Y. Ginkgo biloba leaf extract and alpha-tocopherol attenuate haloperidol-induced orofacial dyskinesia in rats: Possible implication of antiapoptotic mechanisms by preventing Bcl-2 decrease and Bax elevation. *Phytomedicine* **2016**, *23*, 1653–1660. [CrossRef]
39. Wang, S.; Yang, S.; Liu, W.; Zhang, Y.; Xu, P.; Wang, T.; Ling, T.; Liu, R. Alpha-tocopherol quinine ameliorates spatial memory deficits by reducing beta-amyloid oligomers, neuroinflammation and oxidative stress in transgenic mice with Alzheimer's disease. *Behav. Brain Res.* **2016**, *296*, 109–117. [CrossRef]
40. Liu, X.; Zhang, Y.; Yang, X. PM $_{2.5}$ induced neurodegenerative-like changes in mice and the antagonistic effects of vitamin E. *Toxicol. Res.* **2019**, *8*, 172–179. [CrossRef]
41. Jahanshahi, M.; Nikmahzar, E.; Sayyahi, A. Vitamin E therapy prevents the accumulation of congophilic amyloid plaques and neurofibrillary tangles in the hippocampus in a rat model of Alzheimer's disease. *Iran. J. Basic Med. Sci.* **2020**, *23*, 86–92. [CrossRef]
42. Rana, A.; Singh, S.; Deshmukh, R.; Kumar, A. Pharmacological potential of tocopherol and doxycycline against traumatic brain injury-induced cognitive/motor impairment in rats. *Brain Inj.* **2020**, *34*, 1039–1050. [CrossRef]
43. Nesari, A.; Mansouri, M.T.; Khodayar, M.J.; Rezaei, M. Preadministration of high-dose alpha-tocopherol improved memory impairment and mitochondrial dysfunction induced by proteasome inhibition in rat hippocampus. *Nutr. Neurosci.* **2021**, *24*, 119–129. [CrossRef]
44. Shahidi, S.; Ghahremanitamadon, F.; Asl, S.S.; Komaki, A.; Afshar, S.; Hashemi-Firouzi, N. Electrophysiological, Behavioral and Molecular Study of Vitamin E and Ginkgo biloba in a Rat Model of Alzheimer's Disease. *Res. J. Pharmacogn. (RJP)* **2021**, *8*, 39–51.
45. Singh, S.; Chauhan, K. Pharmacological Approach using Doxycycline and Tocopherol in Rotenone induced Oxidative Stress, Neuroinflammation and Parkinson's like symptoms. *Int. J. Neurosci.* **2022**, *28*, 192–205. [CrossRef]
46. Iqbal, A.; Anwar, F.; Saleem, U.; Khan, S.S.; Karim, A.; Ahmad, B.; Gul, M.; Iqbal, Z.; Ismall, T. Inhibition of Oxidative Stress and the NF-κB Pathway by a Vitamin E Derivative: Pharmacological Approach against Parkinson's Disease. *OCS Omega* **2022**, *7*, 45088–45095. [CrossRef] [PubMed]
47. Zappe, K.; Pointner, A.; Switzeny, O.J.; Magnet, U.; Tomeva, E.; Heller, J.; Mare, G.; Wagner, K.-H.; Knasmueller, S.; Haslberger, A.G. Counteraction of Oxidative Stress by Vitamin E Affects Epigenetic Regulation by Increasing Global Methylation and Gene Expression of *MLH1* and *DNMT1* Dose Dependently in Caco-2 Cells. *Oxid. Med. Cell. Longev.* **2018**, *2018*, 3734250. [CrossRef] [PubMed]
48. Takatsu, H.; Owada, K.; Abe, K.; Nakano, M.; Urano, S. Effect of Vitamin E on Learning and Memory Deficit in Aged Rats. *J. Nutr. Sci. Vitaminol.* **2009**, *55*, 389–393. [CrossRef]
49. Wu, A.; Ying, Z.; Gomez-Pinilla, F. Vitamin E Protects Against Oxidative Damage and Learning Disability After Mild Traumatic Brain Injury in Rats. *Neurorehabil. Neural Repair.* **2010**, *24*, 290–298. [CrossRef]
50. Mangialasche, F.; Xu, W.; Kivipelto, M.; Costanzi, E.; Ercolani, S.; Pigliautile, M.; Cecchetti, R.; Baglioni, M.; Simmons, A.; Soininen, H.; et al. Tocopherols and tocotrienols plasma levels are associated with cognitive impairment. *Neurobiol. Aging* **2012**, *33*, 2282–2290. [CrossRef]
51. Mangialasche, F.; Solomon, A.; Kåreholt, I.; Hooshmand, B.; Cecchetti, R.; Fratiglioni, L.; Soininen, H.; Laatikainen, T.; Mecocci, P.; Kivipelto, M. Serum levels of vitamin E forms and risk of cognitive impairment in a Finnish cohort of older adults. *Exp. Gerontol.* **2013**, *48*, 1428–1435. [CrossRef]
52. Bowman, G.L.; Silbert, L.C.; Howieson, D.; Dodge, H.H.; Traber, M.G.; Frei, B.; Kaye, J.A.; Shannon, J.; Quinn, J.F. Nutrient biomarker patterns, cognitive function, and MRI measures of brain aging. *Neurology* **2012**, *78*, 241–249. [CrossRef] [PubMed]
53. Liu, X.; Deng, F.; Chen, L. Parkinsonism Caused by Viral Encephalitis Affecting the Bilateral Substantia Nigra. *Clin. Neuroradiol.* **2019**, *29*, 571–573. [CrossRef] [PubMed]
54. Ulatowski, L.; Parker, R.; Warrier, G.; Sultana, R.; Butterfield, D.A.; Manor, D. Vitamin E is essential for Purkinje neuron integrity. *Neuroscience* **2014**, *260*, 120–129. [CrossRef] [PubMed]
55. Yokota, T.; Igarashi, K.; Uchihara, T.; Jishage, K.; Tomita, H.; Inaba, A.; Li, Y.; Arita, M.; Suzuki, H.; Mizusawa, H.; et al. Delayed-onset ataxia in mice lacking α-tocopherol transfer protein: Model for neuronal degeneration caused by chronic oxidative stress. *Proc. Natl. Acad. Sci. USA* **2001**, *98*, 15185–15190. [CrossRef]
56. El-shaer, N.; El Attar, A. A Study on the Effect of Vitamin E on Histomorphological and Immunohistochemical Changes Induced By Electromagnetic Field. *Egypt Acad. J. Biol. Sci. B Zool.* **2019**, *11*, 85–99. [CrossRef]
57. Blesa, J.; Trigo-Damas, I.; Quiroga-Varela, A.; Jackson-Lewis, V.R. Oxidative stress and Parkinson's disease. *Front. Neuroanat.* **2015**, *9*, 91. [CrossRef]
58. Moon, H.E.; Paek, S.H. Mitochondrial Dysfunction in Parkinson's Disease. *Exp. Neurobiol.* **2015**, *24*, 103–116. [CrossRef]
59. Schapira, A.H. Mitochondria in the aetiology and pathogenesis of Parkinson's disease. *Lancet Neurol.* **2008**, *7*, 97–109. [CrossRef]
60. Pickrell, A.M.; Youle, R.J. The Roles of PINK1, Parkin, and Mitochondrial Fidelity in Parkinson's Disease. *Neuron* **2015**, *85*, 257–273. [CrossRef]
61. Kitada, T.; Pisani, A.; Porter, D.R.; Yamaguchi, H.; Tscherter, A.; Martella, G.; Bonsi, P.; Zhang, C.; Pothos, E.N.; Shen, J. Impaired dopamine release and synaptic plasticity in the striatum of *PINK1* -deficient mice. *Proc. Natl. Acad. Sci. USA* **2007**, *104*, 11441–11446. [CrossRef]

62. Madeo, G.; Schirinzi, T.; Martella, G.; Latagliata, E.C.; Puglisi, F.; Shen, J.; Valente, E.M.; Federici, M.; Mercuri, N.B.; Puglisi-Allegra, S.; et al. *PINK1* heterozygous mutations induce subtle alterations in dopamine-dependent synaptic plasticity. *Mov. Disordem.* **2014**, *29*, 41–53. [CrossRef]
63. Martella, G.; Madeo, G.; Maltese, M.; Vanni, V.; Puglisi, F.; Ferraro, E.; Schirinzi, T.; Valente, E.M.; Bonanni, L.; Shen, J.; et al. Exposure to low-dose rotenone precipitates synaptic plasticity alterations in PINK1 heterozygous knockout mice. *Neurobiol. Dis.* **2016**, *91*, 21–36. [CrossRef]
64. Rahman, H.; Qureshi, M.; Khan, R. Influence of Dietary Zinc on Semen Traits and Seminal Plasma Antioxidant Enzymes and Trace Minerals of Beetal Bucks. *Reprod. Dom. Anim.* **2014**, *49*, 1004–1007. [CrossRef]
65. Boujbiha, M.A.M.; Hamden, K.; Guermazi, F.; Bouslama, A.; Omezzine, A.; El Feki, A. Impairment of Spermatogenesis in Rats by Mercuric Chloride: Involvement of Low 17β-Estradiol Level in Induction of Acute Oxidative Stress. *Biol. Trace Elem. Res.* **2011**, *142*, 598–610. [CrossRef] [PubMed]
66. Naz, S.; Idris, M.; Khalique, M.A.; Zia-Ur-Rahman; Alhidary, I.A.; Abdelrahman, M.M.; Khan, R.U.; Chand, N.; Farooq, U.; Ahmad, S. The activity and use of zinc in poultry diets. *World's Poult. Sci. Journal.* **2016**, *72*, 159–167. [CrossRef]
67. Ward, R.J. Ageing neuroinflammation and neurodegeneration. *Front./Biosci.* **2015**, *7*, 433. [CrossRef] [PubMed]
68. Chon, H.; Choi, B.; Jeong, G.; Lee, E.; Lee, S. Suppression of proinflammatory cytokine production by specific metabolites of Lactobacillus plantarum 10hk2 via inhibiting NF-κB and p38 MAPK expressions. *Comp. Immunol. Microbiol. Infect. Dis.* **2010**, *33*, e41–e49. [CrossRef] [PubMed]
69. Saito, T.; Sugimoto, N.; Ohta, K.; Shimizu, T.; Ohtani, K.; Nakayama, Y.; Nakamura, T.; Hitomi, Y.; Nakamura, H.; Koizumi, S.; et al. Phosphodiesterase Inhibitors Suppress *Lactobacillus casei* Cell-Wall-Induced NF-κ B and MAPK Activations and Cell Proliferation through Protein Kinase A—Or Exchange Protein Activated by cAMP-Dependent Signal Pathway. *Sci. World J.* **2012**, *2012*, 748572. [CrossRef]
70. Celikoglu, E.; Aslanturk, A.; Kalender, Y. Vitamin E and Sodium Selenite Against Mercuric Chloride-Induced Lung Toxicity in the Rats. *Braz. Arch. Biol. Technol.* **2015**, *58*, 587–594. [CrossRef]
71. Chaudhary, G.; Sinha, K.; Gupta, Y.K. Protective effect of exogenous administration of α -tocopherol in middle cerebral artery occlusion model of cerebral ischemia in rats. *Fundam Clin. Pharmacol.* **2003**, *17*, 703–707. [CrossRef] [PubMed]
72. Tovmasyan, A.; Sheng, H.; Weitner, T.; Arulpragasam, A.; Lu, M.; Warner, D.S.; Vujaskovic, Z.; Spasojevic, I.; Batinic-Haberle, I. Design, Mechanism of Action, Bioavailability and Therapeutic Effects of Mn Porphyrin-Based Redox Modulators. *Med. Princ. Pract.* **2013**, *22*, 103–130. [CrossRef] [PubMed]
73. Calabrese, F.; Guidotti, G.; Racagni, G.; Riva, M.A. Reduced neuroplasticity in aged rats: A role for the neurotrophin brain-derived neurotrophic factor. *Neurobiol. Aging* **2013**, *34*, 2768–2776. [CrossRef] [PubMed]
74. Erickson, K.I.; Prakash, R.S.; Voss, M.W.; Chaddock, L.; Heo, S.; McLaren, M.; Pence, B.D.; Martin, S.A.; Vieira, V.J.; Woods, A.; et al. Brain-Derived Neurotrophic Factor Is Associated with Age-Related Decline in Hippocampal Volume. *J. Neurosci.* **2010**, *30*, 5368–5375. [CrossRef]
75. von Bohlen und Halbach, O. Involvement of BDNF in age-dependent alterations in the hippocampus. *Front. Aging Neurosci.* **2010**, *2*, 36. [CrossRef]
76. Murer, M.G.; Yan, Q.; Raisman-Vozari, R. Brain-derived neurotrophic factor in the control human brain, and in Alzheimer's disease and Parkinson's disease. *Prog. Neurobiol.* **2001**, *63*, 71–124. [CrossRef]
77. Guimarães, M.R.M.; Murad, L.B.; Paganelli, A.; de Oliveira, C.A.B.; Vianna, L.M.A. Effects of alpha-tocopherol associated with lovastatin on brain tissue and memory function in SHRSPs. *Physiol. Behav.* **2015**, *149*, 303–309. [CrossRef]
78. Murad, L.B.; Guimarães, M.R.M.; Paganelli, A.; de Oliveira, C.A.B.; Vianna, L.M. Alpha-tocopherol in the brain tissue preservation of stroke-prone spontaneously hypertensive rats. *J. Physiol. Biochem.* **2014**, *70*, 49–60. [CrossRef]

International Journal of
Molecular Sciences

MDPI

Article

LAR Downregulation Protects the Astrocytic U251 and Cocultured SH-SY5Y Cells in a Rotenone-Induced Parkinson's Disease Cell Model

Wei Zheng [1,†], Xiao Han [1,†], Bing Han [1], Gang Li [1], Jing Gan [1], Tian Wang [2], Bo Xu [1], Jie He [1], Wenxiao Du [3], Xiaolin Cao [3] and Zhenhua Wang [1,*]

[1] Center for Mitochondria and Healthy Aging, College of Life Sciences, Yantai University, Yantai 264005, China; weizheng@ytu.edu.cn (W.Z.)
[2] School of Pharmacy, Yantai University, Yantai 264005, China
[3] College of Life Sciences, Yantai University, Yantai 264005, China
* Correspondence: skywzh@ytu.edu.cn
† These authors contributed equally to this work.

Abstract: Leukocyte common antigen-related protein tyrosine phosphatase (LAR) is a member of the protein tyrosine phosphatase family that serves as a key regulator of cellular survival. It is also involved in neurodevelopment and brain disorders. This study was designed to investigate the role of LAR in a cell-based model of Parkinson's disease (PD) in which U251 and SH-SY5Y cells were used as models of astrocytes and dopaminergic neurons, respectively. Cell viability, cell death, cell morphology, protein phosphorylation and expression, ATP levels, reactive oxygen species (ROS) generation, and mitochondrial membrane potential were analyzed in the wild-type (WT) and heterozygous LAR-knockout astrocytoma U251 cells to assess the cell state, signal transduction, and mitochondrial function. LAR downregulation showed a protective effect in rotenone-exposed U251 cells by increasing cell viability, reducing cell mortality, and restoring appropriate cellular morphology. LAR downregulation enhanced IGF-1R phosphorylation and downstream signal transduction as evidenced by increases in the Akt and GSK-3β phosphorylation, as well as the upregulation of NRF2 and HO-1. The downregulation of LAR also augmented DJ-1 levels in these cells. The enhanced Akt and GSK-3β phosphorylation contributed to a reduced Bax/Bcl2 ratio and suppressed apoptosis after rotenone exposure. Heterozygous LAR-knockout U251 cells exhibited higher mitochondrial function evidenced by increased mitochondrial membrane potential, ATP contents, and reduced ROS production compared to the WT cells following rotenone exposure. Further studies showed that the astrocytic protection mediated by the heterozygous knockout of LAR was associated with the activation of Akt. A specific Akt inhibitor, MK2206, reduced the cell viability, Akt and GSK3β phosphorylation, and HO-1 and NRF2 expression in U251 cells exposed to rotenone. Astrocytes provide structural and metabolic support to maintain neuronal health. Astrocytic glial cell-derived neurotrophic factor (GDNF) production is vital for dopaminergic neuron survival. Heterozygous LAR-knockout U251 cells produced higher amounts of GDNF than the WT cells. The SH-SY5Y cells cocultured with heterozygous LAR-knockout U251 cells exhibited greater viability than that of cells cocultured with WT U251 cells in response to rotenone. Together, these findings demonstrate that the heterozygous knockout of LAR in astrocytes can play a key role in protecting both astrocytic cells and cocultured neurons in a rotenone-induced cell-based model of PD. This neuroprotective effect is attributable to the augmentation of IGF1R-Akt-GDNF signaling and the maintenance of astrocytic mitochondrial function.

Keywords: LAR; Parkinson's disease; astrocyte; mitochondrial function; neuron; rotenone

Citation: Zheng, W.; Han, X.; Han, B.; Li, G.; Gan, J.; Wang, T.; Xu, B.; He, J.; Du, W.; Cao, X.; et al. LAR Downregulation Protects the Astrocytic U251 and Cocultured SH-SY5Y Cells in a Rotenone-Induced Parkinson's Disease Cell Model. *Int. J. Mol. Sci.* **2023**, *24*, 11111. https://doi.org/10.3390/ijms241311111

Academic Editors: Claudia Ricci and Patrizia Hrelia

Received: 8 May 2023
Revised: 23 June 2023
Accepted: 30 June 2023
Published: 5 July 2023

1. Introduction

Parkinson's disease (PD) is a common neurodegenerative disease that causes severe movement disorders [1], with over 8.5 million PD patients throughout the world as of 2019 [2]. To date, no curative treatments for PD have been developed [2]. Degeneration of dopaminergic neurons in the substantia nigra pars compacta and dopamine loss in the striatum are the most prominent features of PD [3]. These impairments lead to tremors, postural instability, and bradykinesia [3]. Current evidence suggests that PD is caused by a combination of several factors, including environmental toxins, genetic mutations, and aging [4]. The main pathological mechanisms underlying PD include α-synuclein accumulation, mitochondrial dysfunction, and oxidative stress in neuronal cells [5]. In addition, non-neuronal cells including astrocytes also play important roles in the progression of PD [5–7].

Astrocytes, the most abundant glial cell type in the central nervous system (CNS), play a crucial role in sustaining neuron health [5]. Increasing evidence suggests that astrocyte dysfunction and death also lead to dopaminergic neuron degeneration in PD [8–10]. Astrocytes not only provide structural support to neurons but also regulate extracellular ion balance in the central nervous system [8] and transport glutamine to neurons [11]. They are important components for the maintenance of the blood–brain barrier, which is disrupted in PD patients [11]. During neuroinflammation, astrocytes surround the inflammatory location and create a barrier between the inflammatory tissue and healthy cells, thus playing a neuroprotective role [11]. Antioxidants and neurotrophic factors produced by astrocytes are essential for dopaminergic neuron development and survival [12,13]. α-Synuclein aggregation within dopaminergic neurons is a hallmark of PD that leads to Lewy body formation in neurons, disrupts normal cellular function, and results in neuron cell death [5]. α-Synuclein aggregates can be released by neurons into the extracellular space via exocytosis, whereupon they can be engulfed and degraded by the astrocytes [14–16]. As such, astrocytes protect dopaminergic neurons by clearing the excess harmful α-synuclein [5]. Mitochondrial dysfunction is another major mediator of PD development and progression [17]. Worn-out mitochondria are usually removed through mitophagy to maintain neuronal health [18,19]. Astrocytes are also responsible for the clearance of these damaged mitochondria from neurons [20]. Recent work has shown that induced pluripotent stem cell-derived astrocytes from humans can also donate healthy mitochondria to dopaminergic neurons and rescue them from neurotoxicity [21].

Rotenone is a natural compound that can be extracted from the seeds and roots of several leguminous and liana plants and is used as a broad-spectrum insecticide [22]. As rotenone can induce typical PD characteristics, including Lewy body formation in neurons of the substantia nigra and neurodegeneration, rotenone-exposed animal and cell models are frequently used as experimental tools for studies of PD [23]. Rotenone causes mitochondrial malfunction, excessive production of reactive oxygen species (ROS), and neuronal death by inhibiting mitochondrial complex I and inducing α-synuclein aggregation [24–26]. Mitochondria also regulate astrocyte functions, mitochondrial dysfunction in astrocytes causes imbalanced glutamate metabolism, neuronal excitotoxicity, and ROS overproduction [7,27,28]. These factors are contributors to the pathogenesis of PD [7].

Leukocyte common antigen-related protein tyrosine phosphatase (LAR) is a member of the protein tyrosine phosphatase (PTP) family and serves as a key regulator of phosphorylation signal transduction and downstream physiological effects including cell survival, proliferation, and differentiation [29]. Prior work has shown that LAR plays a role in neurodevelopment and brain disorders [29]. LAR suppresses the phosphorylation of receptor tyrosine kinases including ephrin type-A receptor 2 (EphA2), epidermal growth factor receptor (EGFR), and insulin-like growth factor-1 receptor (IGF-1R) and, therefore, reduces downstream signaling activity mediated through pathways including the PI3K-Akt pathway [30–32]. PI3K-Akt signaling promotes cell survival and reduces apoptosis in the CNS [33]. Akt is also among the most important apoptosis-inhibiting proteins [33]. A member of the PTP family, PTP1B, was recently shown to play an important role in PD [34].The

aim of this study was to explore the role of LAR in PD using a rotenone-induced cell model. U251 and SH-SY5Y cells were employed as models for astrocytes and dopaminergic neurons, respectively.

2. Results

2.1. LAR Expression Is Reduced in D1 and D2 Cells Compared with WT U251 Cells

Western blot experiments were used to confirm LAR levels in the U251 cell lines. As expected, the LAR levels in the heterozygous LAR-knockout D1 and D2 cells were markedly reduced and were at approximately 20% of the levels observed in WT cells (Figure 1A).

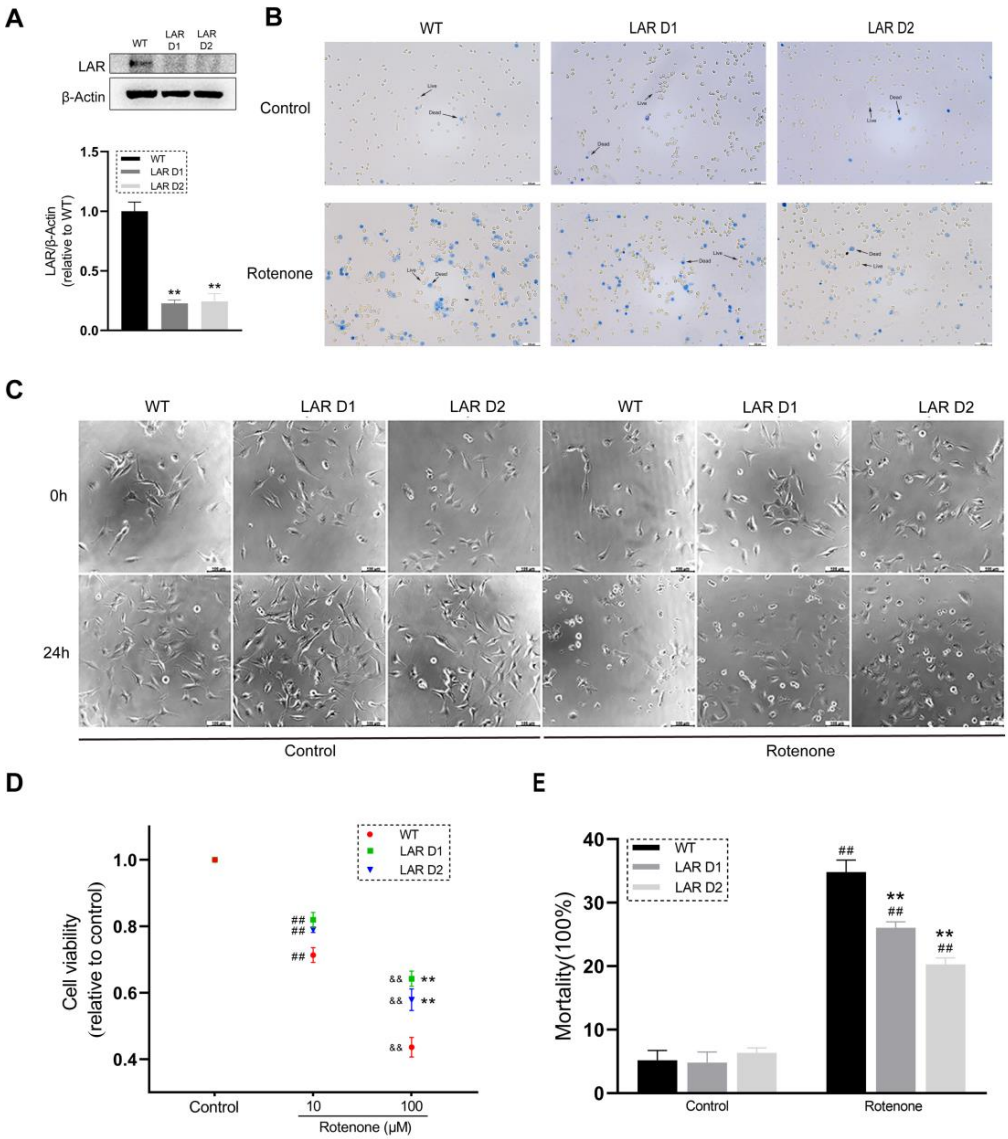

Figure 1. Heterozygous LAR knockout protects astrocytic U251 cells from rotenone toxicity. (**A**) Representative Western blotting results for LAR in WT and heterozygous LAR knockout D1 and D2 U251 cells with corresponding quantification normalized to β-actin. (**B**) Images of trypan blue stained WT, D1, and D2 U251 cells treated with or without rotenone. Scale bar = 100 μm. (**C**) Cell morphology images of WT, D1, and D2 U251 cells treated with or without 100 μM rotenone. Scale bar = 100 μm. (**D**) Scatter plot quantification analysis of the viability of the U251 cell lines after being exposed to rotenone. (**E**) Quantification of U251 cell mortality after being exposed to rotenone. Data are the means ± SEM from triplicate experiments. ## $p < 0.01$ vs. control, ** $p < 0.01$ vs. WT cells, && $p < 0.01$ vs. 10 μM rotenone group.

2.2. Heterozygous LAR Knockout Increases U251 Cell Viability and Maintains Normal Cell Morphology in the Presence of Rotenone

The cell viability and morphology in cells treated with or without rotenone were examined to study the impact of LAR on astrocyte survival in conditions of rotenone toxicity. Rotenone significantly reduced the viability of the U251 cell lines. The D1 and D2 cells exhibited relatively higher viability than WT cells following exposure to a 100 μM rotenone concentration (Figure 1D), which also altered the morphology of these cell lines. The D1 and D2 cells exhibited more normal morphological characteristics compared with WT cells following rotenone treatment (Figure 1C).

2.3. Reductions in LAR Expression Reduce Cell Mortality following Rotenone Exposure

Exposure to a 100 μM rotenone dose led to higher mortality in U251 cells, whereas a significantly reduced mortality was evident for the D1 and D2 cells (Figure 1B,E). As a result, a 100 μM rotenone dose was used for the following experiments.

2.4. Rotenone Induces Greater Increases in DJ-1 Expression and Akt Phosphorylation in D1 and D2 Cells

To explore the mechanistic basis of the higher cell viability and lower cell mortality observed for the heterozygous LAR-knockout cells after rotenone exposure, Akt phosphorylation and protein deglycase-1 (DJ-1) protein levels were measured. The DJ-1 levels in the U251 cell lines increased upon rotenone exposure, and D1 and D2 cells expressed significantly higher level of DJ-1 relative to WT cells (Figure 2A). Akt phosphorylation was also enhanced in these U251 cell lines after rotenone challenge, with these increases being markedly higher in the D1 and D2 cells relative to WT cells in the presence of rotenone (Figure 2B). The DJ-1 and P-Akt levels of D1 and D2 seemed to be slightly higher than those of the WT in the absence of rotenone, but these differences were not statistically significant (Figure 2A,B).

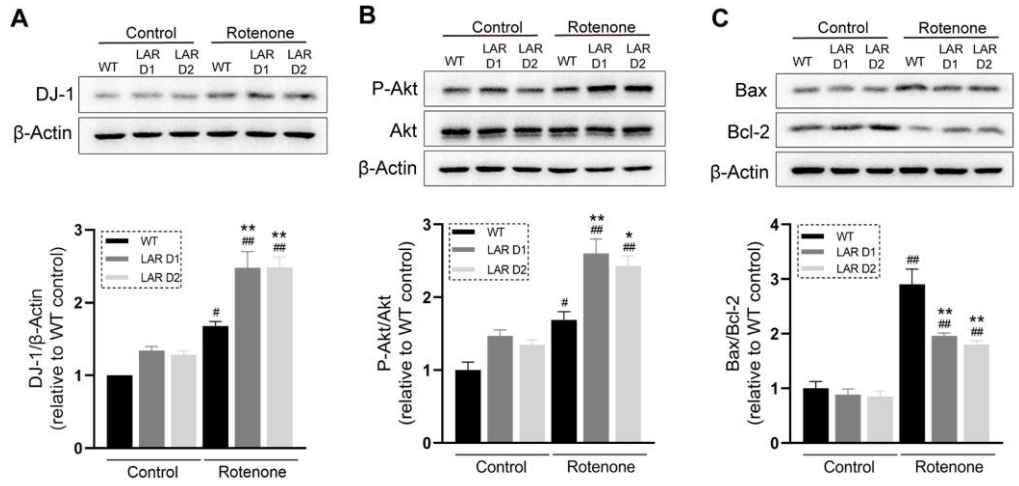

Figure 2. Heterozygous LAR knockout modulates Akt phosphorylation and DJ-1, Bax, and Bcl-2 protein levels in U251 cells. (**A**) Representative Western blotting results for DJ-1 and β-actin and corresponding quantification, with β-actin used for normalization. (**B**) Representative Western blotting results for P-Akt, Akt, and β-actin and corresponding quantification, with Akt used to normalize P-Akt levels. (**C**) Representative Western blotting results for Bax, Bcl-2, and β-actin and corresponding quantification, with data indicating the Bax levels relative to Bcl-2 levels in these samples. Data are the means ± SEM from triplicate experiments. # $p < 0.05$, ## $p < 0.01$ vs. control, * $p < 0.05$, ** $p < 0.01$ vs. WT.

2.5. Rotenone Induces Greater Increases in the Bax/Bcl-2 Ratio in WT U251 Cells

The Bax/Bcl-2 ratio increased in these U251 cell lines after rotenone exposure, with WT cells manifesting a higher Bax/Bcl-2 ratio than the LAR heterozygous knockout cell lines (Figure 2C).

2.6. Akt Inhibition Reduces the Viability of Rotenone-Treated U251 Cell Lines

The Akt-specific inhibitor MK2206 was used to test whether Akt signaling is involved in the observed differences in viability between WT and D1 or D2 cells. MK2206 reduced Akt phosphorylation by ~50% in these U251 cell lines (Figure 3A). Cotreatment with MK2206 and rotenone additionally suppressed the viability of all cell lines when compared with rotenone exposure alone (Figure 3B).

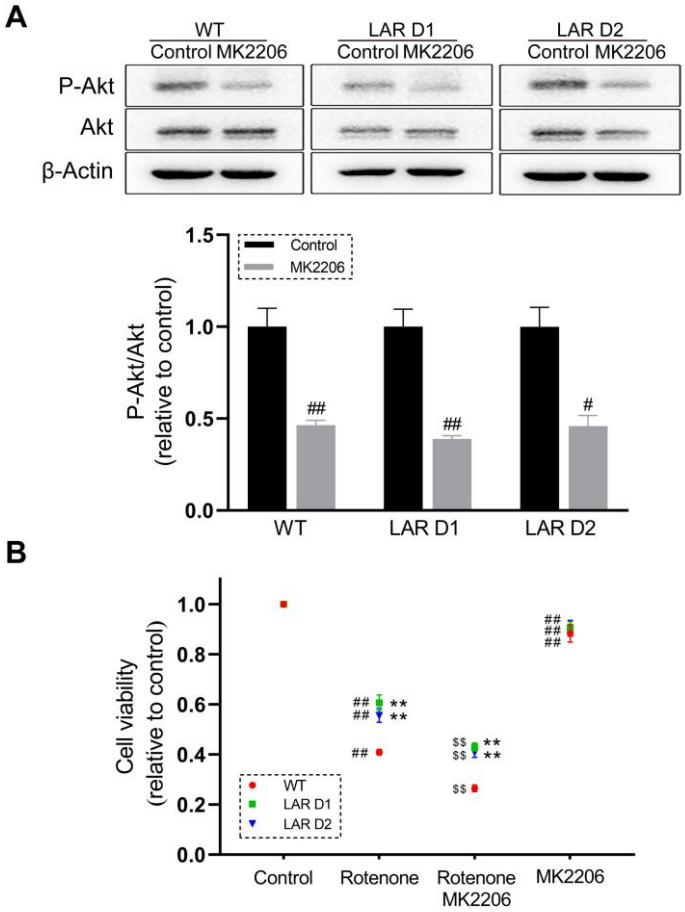

Figure 3. Akt inhibition further suppresses the viability of the U251 cell lines in the presence of rotenone. (**A**) Representative Western blotting results for Akt, P-Akt, and β-actin levels, with corresponding quantification in which P-Akt levels were normalized to total Akt levels. (**B**) Scatter plot quantification of the viability of U251 cell lines after being exposed to rotenone and MK2206. Data are the means ± SEM from triplicate experiments. # $p < 0.05$, ## $p < 0.01$ vs. control, ** $p < 0.01$ vs. WT, $$ $p < 0.01$ vs. rotenone group.

2.7. Rotenone Induces Greater Increases in GSK-3β and Akt Phosphorylation Levels in D1 and D2 Cells That Are Reversed by MK2206 Treatment

The phosphorylation of Akt and the downstream signaling protein glycogen synthase kinase 3β (GSK-3β) were next analyzed in the absence or presence of rotenone and MK2206. Rotenone increased GSK-3β and Akt phosphorylation in the U251 cell lines. These phosphorylation increases were significantly greater in the D1 and D2 cells compared with the WT cells. Cotreatment with rotenone and MK2206 reduced the observed GSK-3β and Akt phosphorylation levels compared with rotenone treatment alone (Figure 4A–C).

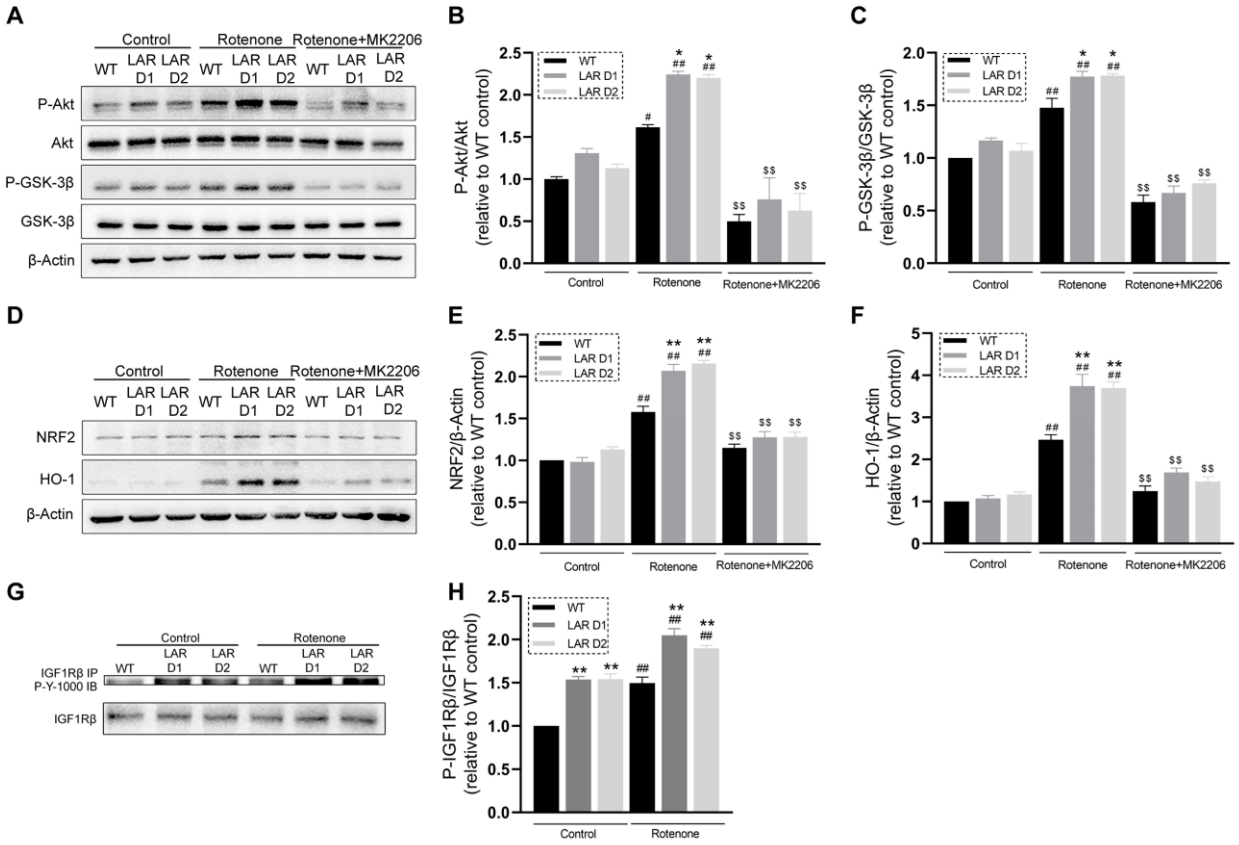

Figure 4. Heterozygous LAR knockout potentiates IGF-1R-Akt signaling, increased GSK-3β phosphorylation and promoted NRF2 and HO-1 expression in the presence of rotenone, while Akt inhibition suppressed these changes. (**A**) Representative Western blotting results for P-Akt, Akt, P-GSK-3β, GSK-3β, and β-actin. (**B**) The quantification of P-Akt levels which were normalized to total Akt. (**C**) The quantification of P-GSK-3β levels were normalized to total GSK-3β. (**D**) Representative Western blotting results for NRF2, HO-1, and β-actin. (**E**) The quantification of NRF2 levels were normalized to β-actin. (**F**) The quantification of HO-1 levels were normalized to β-actin. (**G**) Representative Western blotting results for P-IGF-1R and IGF-1R. (**H**) The quantification of P-IGF-1R levels were normalized to IGF-1R. Data are the means ± SEM from triplicate experiments. # $p < 0.05$, ## $p < 0.01$ vs. control, * $p < 0.05$, ** $p < 0.01$ vs. WT, \$\$ $p < 0.01$ vs. rotenone group.

2.8. Rotenone Induces Greater Increases in HO-1 and NRF2 Protein Levels in D1 and D2 Cells That Are Reversed by MK2206 Treatment

In response to rotenone exposure, these U251 cell lines showed elevated levels of nuclear factor erythroid 2-related factor 2 (NRF2) and heme oxygenase-1 (HO-1). In D1 and D2 cells, these increases were significantly greater than in the WT cells. Cotreatment with rotenone and MK2206 significantly reduced the NRF2 and HO-1 levels compared with rotenone exposure alone (Figure 4D–F).

2.9. Heterozygous LAR Knockout Enhances Rotenone-Induced IGF-1Rβ Phosphorylation

An immunoprecipitation approach was used to assess IGF-1R phosphorylation, revealing that rotenone exposure promoted IGF-1R phosphorylation in the U251 cells. The IGF-1R phosphorylation in D1 and D2 cells was significantly enhanced relative to the WT cells (Figure 4G,H).

2.10. Heterozygous LAR Knockout Suppresses Rotenone-Induced ROS Production, While Cotreatment with Rotenone and MK2206 Induces More ROS Production than Rotenone Alone

Next, ROS production was measured, revealing that rotenone exposure led to ROS overproduction in these U251 cell lines. In comparison to the D1 and D2 cells, ROS levels

were noticeably higher in WT cells (Figure 5A). Cotreatment with both rotenone and MK2206 led to further increases in ROS production compared with rotenone exposure alone (Figure 5A). WT cells also had considerably greater ROS levels compared to D1 and D2 cells cotreated with rotenone and MK2206 (Figure 5A).

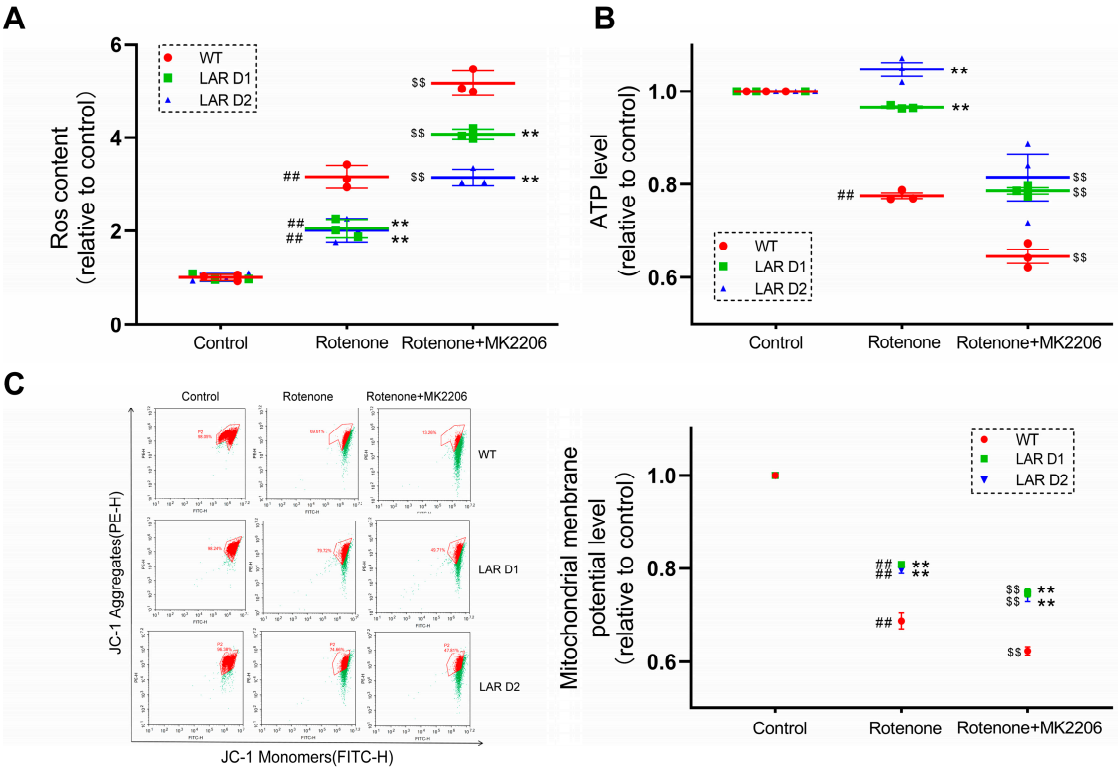

Figure 5. Heterozygous LAR knockout reduces ROS production and promotes mitochondrial function under conditions of rotenone exposure, while Akt inhibition further increases ROS production and suppresses mitochondrial function under conditions of rotenone treatment. (**A**) Quantitative analysis of the ROS production by U251 cell lines treated with or without rotenone and MK2206. (**B**) Quantitative analysis of ATP levels in U251 cells treated with or without rotenone and MK2206. (**C**) JC-1 fluorescent signal as measured via flow cytometry with corresponding quantification of the mitochondrial membrane potential levels in U251 cell lines treated with or without rotenone and MK2206. Red dots represent the JC-1 fluorescent signal in the untreated cells, green dots represent the JC-1 signal change after rotenone and MK2206 exposure. Data are the means ± SEM from triplicate experiments. ## $p < 0.01$ vs. control, ** $p < 0.01$ vs. WT, $$ $p < 0.01$ vs. rotenone alone.

2.11. Heterozygous LAR Knockout Enhances Mitochondrial Membrane Potential (ΔΨm) under Rotenone Exposure and Cotreatment with Rotenone and MK2206

Next, mitochondrial membrane potential was measured in these cells, revealing that rotenone exposure led to a reduction in ΔΨm in the U251 cell lines. Notably, ΔΨm was substantially lower in the WT cells than in the D1 and D2 cells. Cotreatment with rotenone and MK2206 further reduced ΔΨm values in these U251 cells, and the ΔΨm values in the WT cells remained significantly lower than those in the D1 and D2 cells (Figure 5C).

2.12. Heterozygous LAR Knockout Cells Exhibit Higher ATP Levels than WT Cells after Rotenone Exposure and Cotreatment with Rotenone and MK2206

An analysis of the ATP levels showed that rotenone treatment decreased ATP levels in the WT cells, with the ATP levels in these WT cells being considerably lower compared to the ATP levels in the D1 and D2 cells after rotenone exposure. Cotreatment with rotenone and MK2206 additionally decreased ATP levels in these U251 cell lines (Figure 5B).

2.13. Astrocytic Heterozygous LAR Knockout Contributes to Enhanced GDNF Production and Exerts Stronger Neuroprotective Effects on SH-SY5Y Cells

The GDNF levels were measured, and they were shown to be considerably elevated in D1 and D2 cells compared to WT cells in both the presence and absence of rotenone (Figure 6A). The SH-SY5Y cells were cocultured with the U251 cell lines either with or without rotenone to assess how LAR affects the neuroprotective properties of these astrocytes (Figure 6B). In comparison to SH-SY5Y cells cocultured with WT U251 cells, the viability of SH-SY5Y cells cocultured with D1 or D2 U251 cells after rotenone exposure was significantly improved (Figure 6C).

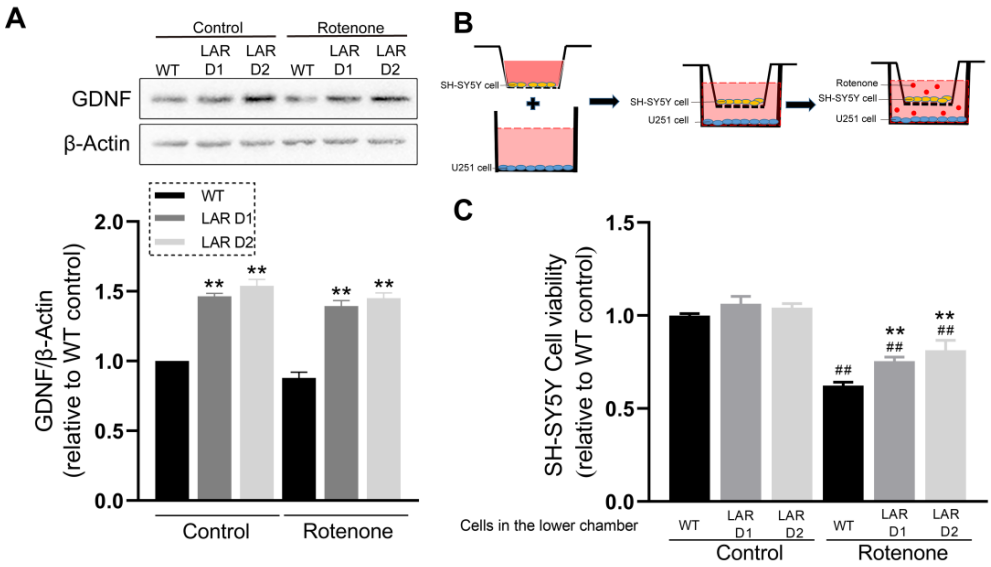

Figure 6. Heterozygous LAR knockout potentiates astrocytic GDNF production and neuroprotective activity. (**A**) Representative Western blotting results for GDNF and β-actin with corresponding quantification in which β-actin was used for normalization. (**B**) Schematic diagram showing the set-up used for the cell coculture assay. (**C**) Quantitative analysis of SH-SY5Y cell viability following coculture with the indicated U251 lines treated with or without rotenone. Data are the means ± SEM from triplicate experiments. ## $p < 0.01$ vs. control, ** $p < 0.01$ vs. WT.

3. Discussion

The CNS consumes high amounts of glucose and oxygen and engages in continuous metabolic activity to satisfy its own energy demands [35]. This characteristic leads to the production of a large volume of ROS [35]. In the neurons of the substantia nigra, the metabolism of cytosolic free dopamine causes additional ROS generation, which makes this area of the brain especially vulnerable to oxidative stress [36]. This is a major contributor to neurodegeneration in PD [37]. Astrocytes surrounding the neurons play key roles in antioxidant production, ROS detoxification, and neuroprotection [38]. However, when the amount of ROS exceeds the detoxifying capacity of these astrocytes, ROS can cause mitochondrial dysregulation, additional ROS production, $\Delta\Psi m$ reduction, and cytochrome c release into the cytoplasm [39,40]. These processes, consequently, cause the activation of caspases, astrocyte apoptosis, and the loss of their neuroprotective function [39,40].

Previous studies have shown that the rotenone treatment of rat C6 astrocytoma cells reduces mitochondrial activity, increases ROS production, and decreases the viability of these cells [41]. Here, rotenone exposure markedly reduced the viability and increased the mortality of the astrocytic U251 cells. Heterozygous LAR knockout rescued these cells from rotenone toxicity. Morphological analyses revealed that rotenone altered cell morphology, while decreased LAR expression partially restored the normal morphology of these cells. Rotenone exposure also induced the overproduction of ROS and $\Delta\Psi m$ decreases in these astrocytic cells, while the heterozygous knockout of LAR reversed these effects.

Rotenone additionally lowered the levels of ATP in WT cells without any comparable effect in LAR heterozygous knockout cells. These findings suggest that heterozygous LAR knockout protects astrocytic mitochondrial function and thus shields these cells from mitochondria-mediated cell death.

In order to explore the molecular mechanisms underlying the astrocytic-protective function of heterozygous LAR knockout, the phosphorylation of Akt and the DJ-1, Bcl-2, and Bax protein levels in these cells were measured. DJ-1 is primarily expressed in astrocytes and is upregulated under conditions of oxidative stress, playing important roles in neuroprotection, antioxidant activity, and mitochondrial function [5]. It activates Akt by suppressing PTEN [42–44]. Akt is crucial for cell survival, and its disruption is common in PD [45,46]. Selective loss of dopaminergic neurons frequently coincides with decreased Ser473 Akt phosphorylation within the brain in the context of PD [47]. The activation of Akt contributes to the upregulation of Bcl-2 and inhibition of Bax [48,49]. Oligomers formed by translocated Bax on the mitochondrial outer membrane cause pores in the membrane that allows for the release of cytochrome c and subsequent cell death [39]. Bcl-2 binds to Bax and prevents this Bax oligomerization, thereby inhibiting consequent pore formation [50]. The ratio between Bax and Bcl-2 is usually used as an indicator of apoptosis [50]. In the present study, rotenone exposure increased DJ-1 expression in U251 cells, which may be due to oxidative stress. DJ-1 levels in the LAR-downregulated cells were significantly higher than that of WT after rotenone exposure. Akt, being downstream of DJ-1, displayed a similar phosphorylation pattern. Rotenone enhanced Akt phosphorylation, while heterozygous LAR knockout further increased Akt phosphorylation in the presence of rotenone. The Bax/Bcl-2 ratio was increased in rotenone-exposed cells, while LAR-downregulated D1 and D2 cells exhibited a lower Bax/Bcl-2 ratio compared with the WT after rotenone exposure. These results suggest that rotenone exposure increases DJ-1 protein expression in turn enhancing Akt phosphorylation. These increases were further promoted by the heterozygous knockout of LAR. The increased levels of Akt phosphorylation observed in the LAR-downregulated cells contributed to a reduction in the Bax/Bcl-2 ratio, thereby protecting against rotenone-induced apoptosis (Figure 7). However, the mechanistic cause for the increase in the DJ-1 levels in the heterozygous LAR knockout cells under rotenone treatment still needs to be further studied.

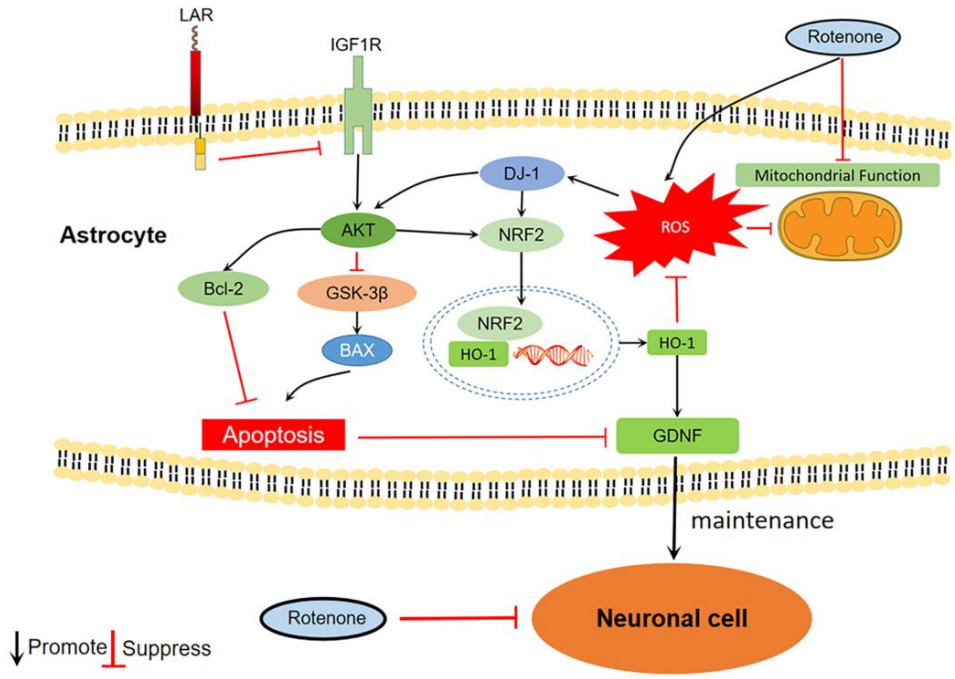

Figure 7. A schematic overview of the molecular mechanisms underlying LAR-mediated activity.

As Akt phosphorylation was prominently enhanced in the LAR-downregulated cells, the Akt-specific inhibitor MK2206 was used to test whether this activation of Akt signaling pathway was responsible for the higher viability of the heterozygous LAR knockout cells. MK2206 inhibited Akt in these U251 cell lines as expected. The U251 cell lines viability was significantly decreased when cotreated with rotenone and MK2206. This shows that increased Akt phosphorylation is a significant factor in the increased cell viability reported in LAR-downregulated cell lines.

Glycogen synthase kinase 3β (GSK-3β) is an activator of neuronal apoptosis [51]. It phosphorylates Bax and promotes its translocation to the mitochondria and consequent cell death [51]. As a direct substrate, GSK-3β is inhibited by Akt through phosphorylation at Ser9 [52]. NRF2 is a master transcriptional regulator of cellular anti-oxidative response. It is constantly degraded by the proteasome because it interacts with the Kelch-like ECH-associated protein 1 (KEAP1) under normal circumstances [53]. Oxidative stress changes the structure of KEAP1 and prevents NRF2 degradation. NRF2 can then be translocated to the nucleus and binds to antioxidant-response element (ARE) sequences in the chromosomal DNA [53]. Many antioxidant proteins, such as HO-1, are expressed as a result of this process [53]. NRF2 also upregulates key antioxidant mediators including superoxide dismutase (SOD) and glutathione (GSH) [54]. Astrocytic NRF2 activation plays a major role in neuroprotection [55]. Importantly, Akt assists NRF2 activation by inhibiting its interaction with KEAP1, and DJ-1 upregulates NRF2 expression [56]. The GSK-3β and Akt phosphorylation, along with the protein HO-1 and NRF2 levels, were determined in untreated cells, rotenone-exposed cells, and cells cotreated with rotenone and MK2206 to gain insight into the molecular mechanism involved in the LAR-related astrocytic protection against rotenone toxicity. The HO-1 and NRF2 protein levels were increased in response to rotenone, along with GSK-3β and Akt phosphorylation. Cotreatment of cells with rotenone and MK2206 inhibited GSK-3β and Akt phosphorylation and expression of HO-1 and NRF2 compared to only rotenone treatment. Cotreatment with MK2206 and rotenone also additionally increased ROS production and reduced $\Delta\Psi m$ and ATP levels compared with rotenone alone. This indicates that higher levels of Akt phosphorylation in the heterozygous LAR-knockout cells contribute to the enhanced phosphorylation and inactivation of GSK-3β, thus suppressing the Bax/Bcl-2 ratio and apoptotic cell death. In heterozygous LAR-knockout cells, hyper-phosphorylated Akt together with upregulated DJ-1 promote the expression of NRF2 which triggers the production of a range of intracellular antioxidants. This action significantly reduces the ROS levels in these cells, preserves normal mitochondrial function, and suppresses cell death (Figure 7). Akt thus plays a central role in these signaling pathways.

To determine why Akt signaling is markedly stronger in the heterozygous LAR-knockout cells, a search for upstream proteins was conducted, revealing that IGF-1R phosphorylation was significantly upregulated in the heterozygous LAR-knockout cells. IGF-1 and its corresponding cell surface transmembrane receptor IGF-1R are essential regulators of multiple cell functions including survival, proliferation, antioxidant activity, and neuroprotection [57,58]. Ligand binding to the IGF-1R extracellular α-subunit induces a conformational change for this receptor, which then leads to the autophosphorylation of the tyrosine residues of the IGF1R transmembrane β-subunit [59]. As a result, the PI3K-Akt pathway and various subsequent signaling cascades are activated [57,58]. LAR directly dephosphorylates IGF-1R and thus abrogates downstream cell proliferation and migration [30]. In the present study, rotenone exposure increased IGF-1R phosphorylation in the U251 cells, while the reduction of LAR expression promoted IGF-1R phosphorylation. This indicates that LAR suppresses Akt signaling by dephosphorylating and suppressing IGF-1R in astrocytes. When LAR protein levels are reduced, IGF-1R is hyper-phosphorylated, contributing to the hyper-activation of Akt and its downstream signaling pathway (Figure 7). Intracellular ROS can cause the oxidation of active-site cysteines present in protein tyrosine phosphatases (PTPs), thereby reducing their activity [60]. Since some other PTPs also dephosphorylate IGF-1R [61], the elevated levels of IGF-1R phosphorylation observed

under conditions of rotenone exposure may be due to the partial inhibition of these PTPs by ROS overproduction.

Astrocytes are essential mediators of neuroprotection that function by producing GDNF, which is important for dopaminergic neuron survival [8]. To investigate the effect of LAR heterozygous knockout on astrocytic GDNF production and its neuroprotective capability in this rotenone-induced PD model system, the cocultures of wild-type (WT) U251 or LAR heterozygous knockout U251 cells with SH-SY5Y cells were treated with or without rotenone. Astrocytic GDNF production was found to be significantly higher when LAR was heterozygously knocked out. Since HO-1 overexpression in substantia nigra upregulates GDNF production in glial cells [62], the higher GDNF level in LAR heterozygous knockout cells may be induced by the higher HO-1 and NRF2 levels. Moreover, the SH-SY5Y cells cocultured with U251 cells were less likely to survive after being exposed to rotenone. Under rotenone-inducing conditions, the SH-SY5Y cells cocultured with the LAR heterozygous knockout U251 cells showed markedly increased vitality compared to SH-SY5Y cells cocultured with WT U251 cells. This suggests that LAR heterozygous knockout astrocytic cells possess stronger neuroprotective capabilities in the context of PD due to their greater viability and more robust GDNF production (Figure 7).

4. Materials and Methods

4.1. Cell Culture

Human U251 glioblastoma cells were purchased from the Cell Bank of the Chinese Academy of Sciences (Shanghai, China). The heterozygous LAR-knockout cell lines LAR D1 and LAR D2 are two different cell monoclones generated by UBIGENE, Guangzhou, China with the wild-type U251 cells (WT) using a CRISPR/cas9 technique. These cells were cultured using DMEM (Gibco, Waltham, MA, USA), supplemented with 10% fetal bovine serum (FBS, TIANHANG, Huzhou, Zhejiang, China) and penicillin/streptomycin (Gibco, Waltham, MA, USA) in a 37 °C 5% CO_2 incubator.

4.2. Cell Viability and Morphology Analyses

An MTT assay was used to measure cell viability. Briefly, the U251 WT, LAR D1, and LAR D2 cell lines were exposed to 10 or 100 μM rotenone (Sigma-Aldrich, St. Louis, MO, USA) for 24 or 72 h with or without 100 nM MK2206 (Absin, Shanghai, China) at 37 °C. The cells on a 96-well plate were then treated with 0.5 mg/mL MTT. After 3 h, the growth media was discarded, and 150 μL of DMSO was added to each well before the plates were oscillated for 15 min to distribute the solution. SpectraMax Paradigm Multi-Mode Microplate Reader (Molecular Devices, San Jose, CA, USA) absorbance values at 595 nm were determined for each well. After 24 h of treatment with 100 μM rotenone, the cell morphology was analyzed by taking images of the WT, LAR D1, and LAR D2 cells under a microscope (Leica Microsystems CMS GmbH, Wetzlar, Germany).

4.3. Cell Mortality Assay

The cell mortality was assessed via trypan blue staining. The U251 WT, LAR D1, and LAR D2 cell lines cultured in 6-well plates were treated with 100 μM rotenone for 24 h. The cells were then removed from each well using PBS, centrifuged at 1500× *g* for 1 min, and resuspended in 1 mL of PBS. Next, 100 μL of 0.08% Trypan Blue was added to each 100 μL of cell suspension, and the resulting mixtures were incubated for 3 min at room temperature. The cells were subsequently counted using a cell counter (Denovix, Wilmington, DE, USA). Approximately 3 × 500 cells were assessed for Trypan Blue staining for each sample. Cell mortality was calculated as 100% × number of Trypan Blue stained cells/total cell number. In addition, the stained cell suspension was mixed evenly before depositing a droplet onto a microscope slide for imaging with a microscope (Leica Microsystems CMS GmbH, Wetzlar, Germany).

4.4. Western Blotting and Protein Immunoprecipitation

U251 cell lines were exposed to 100 μM rotenone and 100 nM MK2206 for 90 min or 24 h for analyses of phosphorylation and protein levels, respectively. After treatment, cells were placed on ice and rinsed with pre-cooled PBS twice. Lysis buffer (150 mmol/L NaCl, 100 mg/mL PMSF, 1% NP-40, 50 mmol/L Tris–HCl (pH 7.4), 0.1% SDS) was then added to these cells prior to incubation on ice for 15 min. Collected cells were centrifuged (15 min, 13,000× *g*, 4 °C), after which supernatants were collected. Protein levels therein were detected with an enhanced BCA protein detection kit (Beyotime Biotechnology, Shanghai, China). For immunoprecipitation experiments, IGF-1R was precipitated from cell lysate samples containing an equal amount of protein using anti-IGF-1Rβ (Cell Signaling Technology, Danvers, MA, USA) followed by incubation with protein A agarose beads (Absin, Shanghai, China). Samples were separated via 5%, 6%, 10%, 12%, or 15% gels SDS-PAGE (Mini-PROTEAN, Bio-Rad, Hercules, CA, USA) based on protein size. Separated proteins were transferred onto Immunobilon-P PVDF membranes (Millipore, Burlington, MA, USA), which were subsequently blocked using 5% BSA (Sigma-Aldrich, St. Louis, MO, USA) in TBS-T solution (10 mmol/L Tris-base, 68 mmol/L NaCl, pH 7.5, 0.1% Tween 20) for 1 h at room temperature. After incubating in the suggested concentration of primary antibody overnight at 4 °C, membranes were washed thoroughly with TBS-T, and incubated in the corresponding peroxidase-conjugated secondary antibody for 1 h followed by an additional round of washing. Proteins were visualized with a 5200 Multi Luminescent image analyzer (Tanon Science and Technology, Shanghai, China), and Image Proplus 6.0 was used for quantification. The following antibodies were used in this study (all from Cell Signaling Technology unless otherwise indicated): LAR, IGF-1Rβ, Akt, Phospho-Akt Ser473, GSK-3β, Phospho-GSK-3β Ser9, Bax, Bcl-2, DJ-1, NRF2, HO-1, Phospho-Tyrosine PY1000, and GDNF (Abcam, Cambridge, UK) (Table 1). Horseradish peroxidase (HRP) Goat anti-Rabbit immunoglobulin G (IgG) was used as the secondary antibody.

Table 1. The primary antibodies used.

Antibody	Catalogue Number	Animal	Dilution
Akt	4060	Rabbit	1:2000
Bax	41162	Rabbit	1:1000
Bcl-2	15071	Mouse	1:1000
DJ-1	5933	Rabbit	1:1000
GDNF	Ab176564	Rabbit	1:2000
GSK-3β	12456	Rabbit	1:1000
HO-1	26416	Rabbit	1:1000
IGF-1Rβ	9750	Rabbit	1:1000
LAR	61611	Rabbit	1:1000
NRF2	12721	Rabbit	1:1000
Phospho-Akt Ser473	4060	Rabbit	1:2000
Phospho-GSK-3β Ser9	9323	Rabbit	1:1000
PY1000	8954	Rabbit	1:2000

4.5. ROS Analyses

Cells were incubated with rotenone and MK2206 for 6 h before they were washed three times with pre-warmed DMEM. Then, 10 μM of DCFH-DA fluorescent probe was added to the cells. The probe was removed after 30 min incubation at 37 °C. The cells were then collected and centrifuged at 900× *g* for 5 min. The cell pellet was resuspended with PBS, the fluorescent signal from DCFH-DA bound to the cell was analyzed us-

ing an ACEA Novocyte flow cytometer (ACEA Biosciences, San Diego, CA, USA) and Novo Express software (version 1.6.1).

4.6. Measurement of Mitochondrial Membrane Potential ($\Delta\Psi m$)

Following incubation with rotenone and MK2206 for 24 h, cells were washed three times using pre-warmed DMEM followed by incubation with 5 μg/mL of the fluorescent probe JC-1 (Thermo Fisher Scientific, Waltham, MA, USA) for 30 min at 37 °C. The cells were washed again with pre-warmed PBS and digested with trypsin. The collected cells were centrifuged (5 min, 900× *g*) and resuspended using PBS, after which the fluorescent JC-1 signal was detected with an ACEA Novocyte flow cytometer (ACEA Biosciences, San Diego, CA, USA) and the Novo Express software (version 1.6.1). The ratio of red to green fluorescence was analyzed to calculate the mitochondrial membrane potential (ΔΨm).

4.7. ATP Assay

Cellular ATP content was analyzed with a luciferase-based luminescence-enhanced ATP assay kit (Beyotime, Shanghai, China). Following rotenone treatment for 24 h, cells were rinsed using chilled PBS and lysed with chilled ATP-releasing buffer. Following lysate centrifugation (5 min, 12,000× *g*, 4 °C), supernatants were collected and combined with an ATP testing working solution. ATP levels in these samples were then measured with a plate reader as above (Molecular Devices, Sacramento, CA, USA).

4.8. Cell Coculture

Transwell Polyester membrane chambers (Corning, New York, NY, USA) were used for U251-SH-SY5Y cell coculture. Cell culture medium was added to the upper and lower chambers and incubated overnight at 37 °C. SH-SY5Y cells were seeded in the upper chambers, while the U251 WT, LAR D1, or LAR D2 cell lines were seeded in the lower chambers. After 24 h, a normal culture medium or medium containing rotenone was added to the upper and lower chambers (Figure 6B). After 72 h, 0.5 mg/mL MTT was added to each upper chamber and incubated for 3 h, after which this medium was replaced with 200 μL of DMSO. This solution was then transferred into a 96-well plate, and the absorbance at 595 nm was analyzed using a plate reader as above (Molecular Devices, San Jose, CA, USA).

4.9. Statistical Analyses

Data are the means ± SEM. The analyses were carried out with GraphPad Prism 8.0. All data were analyzed via one-way ANOVAs with Tukey's post hoc test. $p < 0.05$ was the cut-off for statistical significance.

5. Conclusions

In conclusion, this study found that heterozygous LAR-knockout grants astrocytic cells a higher degree of viability, enhanced GDNF production, and stronger neuroprotective capacity in a cell-based model of PD. The mechanistic basis for these effects is associated with the activation of IGF-1R and Akt. Akt activation leads to the Bax/Bcl-2 ratio reduction and cell apoptosis suppression. Akt and DJ-1 further drives the upregulation of NRF2 and HO-1, consequently suppressing ROS production, preserving mitochondrial function, and increasing GDNF production. These higher levels of astrocytic viability and GDNF production also contributed to the augmented viability of cocultured neuronal SH-SY5Y cells in a rotenone-induced PD model system. Thus, inhibiting LAR to modulate the viability and function of astrocytes offers a novel therapeutic strategy for PD as LAR performs a vital role in the neuroprotective function of astrocytes.

Author Contributions: Conceptualization, W.Z.; Data curation, X.H.; Formal analysis, W.Z. and X.H.; Funding acquisition, G.L.; Investigation, W.Z. and X.H.; Methodology, W.Z. and Z.W.; Project administration, W.Z. and Z.W.; Resources, W.Z., B.H., G.L., J.G., T.W. and Z.W.; Software, Z.W.; Supervision, Z.W.; Validation, W.Z., X.H. and W.D.; Writing—original draft, W.Z. and X.H.; Writing—

review and editing, G.L., J.G., T.W., B.X., J.H., W.D., X.C. and Z.W. All authors have read and agreed to the published version of the manuscript.

Funding: This work was supported by the Qinghai Province Applied Basic Research Project (2020-ZJ-905).

Institutional Review Board Statement: Not applicable.

Informed Consent Statement: Not applicable.

Data Availability Statement: Not applicable.

Conflicts of Interest: The authors declare no conflict of interest.

References

1. Dorsey, E.; Sherer, T.; Okun, M.S.; Bloem, B.R. The Emerging Evidence of the Parkinson Pandemic. *J. Park. Dis.* **2018**, *8*, S3–S8. [CrossRef] [PubMed]
2. World Health Organization (WHO). Parkinson Disease. 2022. Available online: https://www.who.int/news-room/fact-sheets/detail/parkinson-disease (accessed on 25 April 2023).
3. Thomas, B.; Beal, M.F. Parkinson's disease. *Hum. Mol. Genet.* **2007**, *16*, R183–R194. [CrossRef] [PubMed]
4. Johnson, M.E.; Stecher, B.; Labrie, V.; Brundin, L.; Brundin, P. Triggers, Facilitators, and Aggravators: Redefining Parkinson's Disease Pathogenesis. *Trends Neurosci.* **2019**, *42*, 4–13. [CrossRef] [PubMed]
5. Miyazaki, I.; Asanuma, M. Neuron-Astrocyte Interactions in Parkinson's Disease. *Cells* **2020**, *9*, 2623. [CrossRef]
6. Maragakis, N.J.; Rothstein, J.D. Mechanisms of Disease: Astrocytes in neurodegenerative disease. *Nat. Clin. Pract. Neurol.* **2006**, *2*, 679–689. [CrossRef]
7. Bantle, C.M.; Hirst, W.D.; Weihofen, A.; Shlevkov, E. Mitochondrial Dysfunction in Astrocytes: A: A Role in Parkinson's Disease? *Front. Cell Dev. Biol.* **2020**, *8*, 608026. [CrossRef]
8. Booth, H.D.E.; Hirst, W.D.; Wade-Martins, R. The Role of Astrocyte Dysfunction in Parkinson's Disease Pathogenesis. *Trends Neurosci.* **2017**, *40*, 358–370. [CrossRef]
9. Kuter, K.; Olech, L.; Glowacka, U. Prolonged Dysfunction of Astrocytes and Activation of Microglia Accelerate Degeneration of Dopaminergic Neurons in the Rat Substantia Nigra and Block Compensation of Early Motor Dysfunction Induced by 6-OHDA. *Mol. Neurobiol.* **2018**, *55*, 3049–3066. [CrossRef]
10. Min, K.J.; Jeong, H.K.; Kim, B.; Hwang, D.H.; Shin, H.Y.; Nguyen, A.T.; Kim, J.H.; Jou, I.; Kim, B.G.; Joe, E.H. Spatial and temporal correlation in progressive degeneration of neurons and astrocytes in contusion-induced spinal cord injury. *J. Neuroinflamm.* **2012**, *9*, 100. [CrossRef]
11. Sofroniew, M.V.; Vinters, H.V. Astrocytes: Biology and pathology. *Acta Neuropathol.* **2010**, *119*, 7–35. [CrossRef]
12. Lin, L.F.; Doherty, D.H.; Lile, J.D.; Bektesh, S.; Collins, F. GDNF: A glial cell line-derived neurotrophic factor for midbrain dopaminergic neurons. *Science* **1993**, *260*, 1130–1132. [CrossRef]
13. Scharr, D.G.; Sieber, B.A.; Dreyfus, C.F.; Black, I.B. Regional and cell-specific expression of GDNF in rat brain. *Exp. Neurol.* **1993**, *124*, 368–371. [CrossRef]
14. Stefanis, L.; Emmanouilidou, E.; Pantazopoulou, M.; Kirik, D.; Vekrellis, K.; Tofaris, G.K. How is alpha-synuclein cleared from the cell? *J. Neurochem.* **2019**, *150*, 577–590. [CrossRef]
15. Choi, I.; Zhang, Y.; Seegobin, S.P.; Pruvost, M.; Wang, Q.; Purtell, K.; Zhang, B.; Yue, Z. Microglia clear neuron-released alpha-synuclein via selective autophagy and prevent neurodegeneration. *Nat. Commun.* **2020**, *11*, 1386. [CrossRef]
16. Morales, I.; Sanchez, A.; Puertas-Avendaño, R.; Rodriguez-Sabate, C.; Perez-Barreto, A.; Rodriguez, M. Neuroglial transmitophagy and Parkinson's disease. *Glia* **2020**, *68*, 2277–2299. [CrossRef]
17. Borsche, M.; Pereira, S.L.; Klein, C.; Grünewald, A. Mitochondria and Parkinson's Disease: Clinical, Molecular, and Translational Aspects. *J. Park. Dis.* **2021**, *11*, 45–60. [CrossRef]
18. Lazarou, M.; Sliter, D.A.; Kane, L.A.; Sarraf, S.A.; Wang, C.; Burman, J.L.; Sideris, D.P.; Fogel, A.I.; Youle, R.J. The ubiquitin kinase PINK1 recruits autophagy receptors to induce mitophagy. *Nature* **2015**, *524*, 309–314. [CrossRef]
19. Springer, W.; Kahle, P.J. Regulation of PINK1-Parkin-mediated mitophagy. *Autophagy* **2011**, *7*, 266–278. [CrossRef]
20. Davis, C.H.O.; Kim, K.Y.; Bushong, E.A.; Mills, E.A.; Boassa, D.; Shih, T.; Kinebuchi, M.; Phan, S.; Zhou, Y.; Bihlmeyer, N.A.; et al. Transcellular degradation of axonal mitochondria. *Proc. Natl. Acad. Sci. USA* **2014**, *111*, 9633–9638. [CrossRef]
21. Cheng, X.-Y.; Biswas, S.; Li, J.; Mao, C.-J.; Chechneva, O.; Chen, J.; Li, K.; Li, J.; Zhang, J.-R.; Liu, C.-F.; et al. Human iPSCs derived astrocytes rescue rotenone-induced mitochondrial dysfunction and dopaminergic neurodegeneration in vitro by donating functional mitochondria. *Transl. Neurodegener.* **2020**, *9*, 13. [CrossRef]
22. Wikipedia. Rotenone. 2022. Available online: https://xgoogle.xyz/extdomains/zh.wikipedia.org/zh-cn/%E9%AD%9A%E8%97%A4%E9%85%AE (accessed on 26 April 2023).
23. Ibarra-Gutierrez, M.T.; Serrano-Garcia, N.; Orozco-Ibarra, M. Rotenone-Induced Model of Parkinson's Disease: Beyond Mitochondrial Complex I Inhibition. *Mol. Neurobiol.* **2023**, *60*, 1929–1948. [CrossRef] [PubMed]

24. Betarbet, R.; Canet-Aviles, R.M.; Sherer, T.B.; Mastroberardino, P.G.; McLendon, C.; Kim, J.H.; Lund, S.; Na, H.M.; Taylor, G.; Bence, N.F.; et al. Intersecting pathways to neurodegeneration in Parkinson's disease: Effects of the pesticide rotenone on DJ-1, alpha-synuclein, and the ubiquitin-proteasome system. *Neurobiol. Dis.* **2006**, *22*, 404–420. [CrossRef] [PubMed]
25. Li, N.; Ragheb, K.; Lawler, G.; Sturgis, J.; Rajwa, B.; Melendez, J.A.; Robinson, J.P. Mitochondrial complex I inhibitor rotenone induces apoptosis through enhancing mitochondrial reactive oxygen species production. *J. Biol. Chem.* **2003**, *278*, 8516–8525. [CrossRef] [PubMed]
26. Watabe, M.; Nakaki, T. Rotenone induces apoptosis via activation of bad in human dopaminergic SH-SY5Y cells. *J. Pharmacol. Exp. Ther.* **2004**, *311*, 948–953. [CrossRef]
27. Armada-Moreira, A.; Gomes, J.I.; Pina, C.C.; Savchak, O.K.; Gonçalves-Ribeiro, J.; Rei, N.; Pinto, S.; Morais, T.P.; Martins, R.S.; Ribeiro, F.F.; et al. Going the Extra (Synaptic) Mile: Excitotoxicity as the Road Toward Neurodegenerative Diseases. *Front. Cell. Neurosci.* **2020**, *14*, 90. [CrossRef]
28. Kirkley, K.S.; Popichak, K.A.; Hammond, S.L.; Davies, C.; Hunt, L.; Tjalkens, R.B. Genetic suppression of IKK2/NF-kappaB in astrocytes inhibits neuroinflammation and reduces neuronal loss in the MPTP-Probenecid model of Parkinson's disease. *Neurobiol. Dis.* **2019**, *127*, 193–209. [CrossRef]
29. Cornejo, F.; Cortés, B.I.; Findlay, G.M.; Cancino, G.I. LAR Receptor Tyrosine Phosphatase Family in Healthy and Diseased Brain. *Front. Cell Dev. Biol.* **2021**, *9*, 659951. [CrossRef]
30. Niu, X.L.; Li, J.; Hakim, Z.S.; Rojas, M.; Runge, M.S.; Madamanchi, N.R. Leukocyte antigen-related deficiency enhances insulin-like growth factor-1 signaling in vascular smooth muscle cells and promotes neointima formation in response to vascular injury. *J. Biol. Chem.* **2007**, *282*, 19808–19819. [CrossRef]
31. Hashimoto, N.; Zhang, W.R.; Goldstein, B.J. Insulin receptor and epidermal growth factor receptor dephosphorylation by three major rat liver protein-tyrosine phosphatases expressed in a recombinant bacterial system. *Biochem. J.* **1992**, *284 Pt 2*, 569–576. [CrossRef]
32. Lee, H.; Bennett, A.M. Receptor protein tyrosine phosphatase-receptor tyrosine kinase substrate screen identifies EphA2 as a target for LAR in cell migration. *Mol. Cell Biol.* **2013**, *33*, 1430–1441. [CrossRef]
33. Meng, Y.; Wang, W.; Kang, J.; Wang, X.; Sun, L. Role of the PI3K/AKT signalling pathway in apoptotic cell death in the cerebral cortex of streptozotocin-induced diabetic rats. *Exp. Ther. Med.* **2017**, *13*, 2417–2422. [CrossRef]
34. Feng, C.-W.; Chen, N.-F.; Chan, T.-F.; Chen, W.-F. Therapeutic Role of Protein Tyrosine Phosphatase 1B in Parkinson's Disease via Antineuroinflammation and Neuroprotection In Vitro and In Vivo. *Park. Dis.* **2020**, *2020*, 8814236. [CrossRef]
35. Fraunberger, E.A.; Scola, G.; Laliberté, V.L.; Duong, A.; Andreazza, A.C. Redox Modulations, Antioxidants, and Neuropsychiatric Disorders. *Oxidative Med. Cell. Longev.* **2016**, *2016*, 4729192. [CrossRef]
36. Miyazaki, I.; Asanuma, M. Dopaminergic neuron-specific oxidative stress caused by dopamine itself. *Acta Med. Okayama* **2008**, *62*, 141–150.
37. Rizor, A.; Pajarillo, E.; Johnson, J.; Aschner, M.; Lee, E. Astrocytic Oxidative/Nitrosative Stress Contributes to Parkinson's Disease Pathogenesis: The Dual Role of Reactive Astrocytes. *Antioxidants* **2019**, *8*, 265. [CrossRef]
38. McBean, G.J. Cysteine, Glutathione, and Thiol Redox Balance in Astrocytes. *Antioxidants* **2017**, *6*, 62. [CrossRef]
39. Ryter, S.W.; Kim, H.P.; Hoetzel, A.; Park, J.W.; Nakahira, K.; Wang, X.; Choi, A.M. Mechanisms of cell death in oxidative stress. *Antioxid. Redox Signal.* **2007**, *9*, 49–89. [CrossRef]
40. Gollihue, J.L.; Norris, C.M. Astrocyte mitochondria: Central players and potential therapeutic targets for neurodegenerative diseases and injury. *Ageing Res. Rev.* **2020**, *59*, 101039. [CrossRef]
41. Swarnkar, S.; Singh, S.; Goswami, P.; Mathur, R.; Patro, I.K.; Nath, C. Astrocyte activation: A key step in rotenone induced cytotoxicity and DNA damage. *Neurochem. Res.* **2012**, *37*, 2178–2189. [CrossRef]
42. Baulac, S.; Lu, H.; Strahle, J.; Yang, T.; Goldberg, M.S.; Shen, J.; Schlossmacher, M.G.; Lemere, C.A.; Lu, Q.; Xia, W. Increased DJ-1 expression under oxidative stress and in Alzheimer's disease brains. *Mol. Neurodegener.* **2009**, *4*, 12. [CrossRef]
43. Aleyasin, H.; Rousseaux, M.W.; Marcogliese, P.C.; Hewitt, S.J.; Irrcher, I.; Joselin, A.P.; Parsanejad, M.; Kim, R.H.; Rizzu, P.; Callaghan, S.M.; et al. DJ-1 protects the nigrostriatal axis from the neurotoxin MPTP by modulation of the AKT pathway. *Proc. Natl. Acad. Sci. USA* **2010**, *107*, 3186–3191.
44. Zhao, Y.; Han, Y.; Wang, Z.; Chen, T.; Qian, H.; He, J.; Li, J.; Han, B.; Wang, T. Rosmarinic acid protects against 1-methyl-4-phenyl-1,2,3,6-tetrahydropyridine-induced dopaminergic neurotoxicity in zebrafish embryos. *Toxicol. In Vitro* **2020**, *65*, 104823. [CrossRef] [PubMed]
45. Brunet, A.; Bonni, A.; Zigmond, M.J.; Lin, M.Z.; Juo, P.; Hu, L.S.; Anderson, M.J.; Arden, K.C.; Blenis, J.; Greenberg, M.E. Greenberg, Akt promotes cell survival by phosphorylating and inhibiting a Forkhead transcription factor. *Cell* **1999**, *96*, 857–868. [CrossRef] [PubMed]
46. Furlong, R.M.; Lindsay, A.; Anderson, K.E.; Hawkins, P.T.; Sullivan, A.M.; O'Neill, C. The Parkinson's disease gene PINK1 activates Akt via PINK1 kinase-dependent regulation of the phospholipid PI(3,4,5)P(3). *J. Cell Sci.* **2019**, *132*, jcs233221. [CrossRef]
47. Greene, L.A.; Levy, O.; Malagelada, C. Akt as a victim, villain and potential hero in Parkinson's disease pathophysiology and treatment. *Cell Mol. Neurobiol.* **2011**, *31*, 969–978. [CrossRef]
48. Yamaguchi, H.; Wang, H.G. The protein kinase PKB/Akt regulates cell survival and apoptosis by inhibiting Bax conformational change. *Oncogene* **2001**, *20*, 7779–7786. [CrossRef]

49. Pugazhenthi, S.; Nesterova, A.; Sable, C.; Heidenreich, K.A.; Boxer, L.M.; Heasley, L.E.; Reusch, J.E.B. Akt/protein kinase B up-regulates Bcl-2 expression through cAMP-response element-binding protein. *J. Biol. Chem.* **2000**, *275*, 10761–10766. [CrossRef]
50. Naseri, M.H.; Mahdavi, M.; Davoodi, J.; Tackallou, S.H.; Goudarzvand, M.; Neishabouri, S.H. Up regulation of Bax and down regulation of Bcl2 during 3-NC mediated apoptosis in human cancer cells. *Cancer Cell Int.* **2015**, *15*, 55. [CrossRef]
51. Linseman, D.A.; Butts, B.D.; Precht, T.A.; Phelps, R.A.; Le, S.S.; Laessig, T.A.; Bouchard, R.J.; Florez-McClure, M.L.; Heidenreich, K.A. Glycogen synthase kinase-3beta phosphorylates Bax and promotes its mitochondrial localization during neuronal apoptosis. *J. Neurosci.* **2004**, *24*, 9993–10002. [CrossRef]
52. Hermida, M.A.; Kumar, J.D.; Leslie, N.R. GSK3 and its interactions with the PI3K/AKT/mTOR signalling network. *Adv. Biol. Regul* **2017**, *65*, 5–15. [CrossRef]
53. Li, H.X.; Wang, T.H.; Wu, L.X.; Xue, F.S.; Zhang, G.H.; Yan, T. Role of Keap1-Nrf2/ARE signal transduction pathway in protection of dexmedetomidine preconditioning against myocardial ischemia/reperfusion injury. *Biosci. Rep.* **2022**, *42*, BSR20221306. [CrossRef]
54. Ma, Q. Role of nrf2 in oxidative stress and toxicity. *Annu. Rev. Pharmacol. Toxicol.* **2013**, *53*, 401–426. [CrossRef]
55. Vargas, M.R.; Johnson, J.A. The Nrf2-ARE cytoprotective pathway in astrocytes. *Expert Rev. Mol. Med.* **2009**, *11*, e17. [CrossRef]
56. Im, J.-Y.; Lee, K.-W.; Woo, J.-M.; Junn, E.; Mouradian, M.M. DJ-1 induces thioredoxin 1 expression through the Nrf2 pathway. *Hum. Mol. Genet.* **2012**, *21*, 3013–3024. [CrossRef]
57. Castilla-Cortázar, I.; Aguirre, G.A.; Femat-Roldán, G.; Martin-Estal, I.; Espinosa, L. Is insulin-like growth factor-1 involved in Parkinson's disease development? *J. Transl. Med.* **2020**, *18*, 70. [CrossRef]
58. Hua, H.; Kong, Q.; Yin, J.; Zhang, J.; Jiang, Y. Insulin-like growth factor receptor signaling in tumorigenesis and drug resistance: A challenge for cancer therapy. *J. Hematol. Oncol.* **2020**, *13*, 64. [CrossRef]
59. Leroith, D.; Werner, H.; Beitner-Johnson, D.; Roberts, C.T., Jr. Molecular and cellular aspects of the insulin-like growth factor I receptor. *Endocr. Rev.* **1995**, *16*, 143–163. [CrossRef]
60. Chiarugi, P. Reactive oxygen species as mediators of cell adhesion. *Ital. J. Biochem.* **2003**, *52*, 28–32. [CrossRef]
61. Fan, G.; Lin, G.; Lucito, R.; Tonks, N.K. Protein-tyrosine phosphatase 1B antagonized signaling by insulin-like growth factor-1 receptor and kinase BRK/PTK6 in ovarian cancer cells. *J. Biol. Chem.* **2013**, *288*, 24923–24934. [CrossRef]
62. Hung, S.Y.; Liou, H.C.; Fu, W.M. The mechanism of heme oxygenase-1 action involved in the enhancement of neurotrophic factor expression. *Neuropharmacology* **2010**, *58*, 321–329. [CrossRef]

International Journal of
Molecular Sciences

MDPI

Article

The QPLEX™ Plus Assay Kit for the Early Clinical Diagnosis of Alzheimer's Disease

Hunjong Na [1,2,†], Ki Young Shin [3,†], Dokyung Lee [2], Changsik Yoon [2], Sun-Ho Han [4,5,6], Jong-Chan Park [4,5,6], Inhee Mook-Jung [4,5,6], Jisung Jang [2,*] and Sunghoon Kwon [1,2,3,*]

1 Department of Electrical and Computer Engineering, Seoul National University, Seoul 08826, Republic of Korea
2 QuantaMatrix Inc., Seoul 08506, Republic of Korea
3 Bio-MAX Institute, Seoul National University, Seoul 08826, Republic of Korea
4 Department of Biochemistry and Biomedical Sciences, College of Medicine, Seoul National University, Seoul 03080, Republic of Korea
5 Neuroscience Research Institute, Medical Research Center, College of Medicine, Seoul National University, Seoul 03080, Republic of Korea
6 SNU Dementia Research Center, College of Medicine, Seoul National University, Seoul 03080, Republic of Korea
* Correspondence: jjang@quantamatrix.com (J.J.); skwon@snu.ac.kr (S.K.)
† These authors contributed equally to this work.

Abstract: We recently developed a multiplex diagnostic kit, QPLEX™ Alz plus assay kit, which captures amyloid-β1-40, galectin-3 binding protein, angiotensin-converting enzyme, and periostin simultaneously using microliters of peripheral blood and utilizes an optimized algorithm for screening Alzheimer's disease (AD) by correlating with cerebral amyloid deposition. Owing to the demand for early AD detection, we investigate the potential of our kit for the early clinical diagnosis of AD. A total of 1395 participants were recruited, and their blood samples were analyzed with the QPLEX™ kit. The average of QPLEX™ algorithm values in each group increased gradually in the order of the clinical progression continuum of AD: cognitively normal (0.382 ± 0.150), subjective cognitive decline (0.452 ± 0.130), mild cognitive impairment (0.484 ± 0.129), and AD (0.513 ± 0.136). The algorithm values between each group showed statistically significant differences among groups divided by Mini-Mental State Examination and Clinical Dementia Rating. The QPLEX™ algorithm values could be used to distinguish the clinical continuum of AD or cognitive function. Because blood-based diagnosis is more accessible, convenient, and cost- and time-effective than cerebral spinal fluid or positron emission tomography imaging-based diagnosis, the QPLEX™ kit can potentially be used for health checkups and the early clinical diagnosis of AD.

Keywords: Alzheimer's disease; dementia; cognition; peripheral blood; algorithm; early diagnosis

Citation: Na, H.; Shin, K.Y.; Lee, D.; Yoon, C.; Han, S.-H.; Park, J.-C.; Mook-Jung, I.; Jang, J.; Kwon, S. The QPLEX™ Plus Assay Kit for the Early Clinical Diagnosis of Alzheimer's Disease. *Int. J. Mol. Sci.* **2023**, *24*, 11119. https://doi.org/10.3390/ijms241311119

Academic Editor: Claudia Ricci

Received: 1 June 2023
Revised: 2 July 2023
Accepted: 3 July 2023
Published: 5 July 2023

1. Introduction

The development of Alzheimer's disease (AD), the most common form of dementia, is slow and persistent, with a pre-symptom stage lasting over several years to decades [1–4]. As of 2023, the prevalence of Alzheimer's dementia among the older population (aged 65 years and older) in the United States is estimated to be approximately 6.7 million individuals [5]. The prominent neuropathological features of AD primarily involve the presence of senile plaques, characterized by the aggregation of amyloid-β (Aβ), and the formation of neuronal neurofibrillary tangles (NFTs) [6]. Generally, AD symptoms begin with mild memory impairment and progress to diverse cognitive impairments, including memory disorder and dysfunctions in complex daily activities [7,8]. The early clinical diagnosis of AD can be defined by means of criteria such as neuropsychological tests [9–11]: (a) subjective cognitive decline (SCD) is a continued decline in the self-reported experience in cognitive performance compared to the subject's previously normal state [12]; and

(b) mild cognitive impairment (MCI) is characterized by objective cognitive impairment, including impairment of memory (amnestic) or judgment (non-amnestic) [13]. Both groups are in transitional stages between normal cognition and dementia [14]. The symptoms of SCD are among the early signs of pathological brain aging [15]. Individuals with SCD behavior are associated with Aβ deposition [16]. MCI is also a precursor to AD characterized by neurocognitive dysfunction [17]. Based on estimates for the year 2023, it is projected that approximately 8–11% of the American population aged 65 years and older, corresponding to approximately 5–7 million older individuals, may exhibit MCI [5] and approximately 10–15% of individuals with MCI develop dementia yearly, while 1–2% of unaffected individuals develop dementia [18,19]. These pre-dementia stages could serve as populations for dementia prevention clinical trials [12]. The development of early and accessible diagnostic methods can help to prevent or delay the progression of cognitive deficits and the onset of full-blown AD dementia [20,21]; therefore, targeting the critical precursor steps of SCD or MCI may have a strong potential for the early clinical diagnosis of AD [22].

Increasing efforts to discover biomarkers for AD in the cerebral spinal fluid (CSF) or blood have been ongoing for decades and have led to the discovery of potential biomarkers. CSF analysis revealed amyloid-β1-42 (Aβ42) proteins, Aβ42/Aβ40 ratio, total tau proteins, phosphorylated tau proteins, and neurogranin can be used as a biomarker for AD. In the blood, Aβ42/Aβ40 ratio, amyloid precursor protein (APP)669-711/Aβ42 ratio, tau proteins, and neurofilament light were suggested as biomarkers for AD [23]. Some candidates are related directly to the core pathological features of AD, while others are linked closely to the neurodegeneration of the brain. Compared to CSF-based diagnosis, peripheral blood-based diagnosis has the advantages of reducing the patient's burden, shortening the inspection time, and lowering the cost of sample collection and examination as a non-invasive method. With these advantages, blood-based diagnosis can be included in health checkups and used for early diagnosis. Although many peripheral biomarkers for AD diagnosis have been reported in recent decades [24–26], few have proven to be useful in commercially developed diagnostic kits. Screening peripheral biomarkers for brain diseases has many challenges, such as problems with the sensitivity and specificity of the assay and careful validation work. Such biomarkers can be detectable at relatively low concentrations in the blood because the blood–brain barrier limits the movement of molecules between the central nervous system and the blood vessel system [27]. It is also technically difficult to detect various biomarkers simultaneously within a single assay system [21]. Therefore, it was suggested that multiple combinations of effective peripheral biomarkers with highly sensitive assays might increase diagnostic success for AD [28].

In previous studies, we revealed a novel blood-based biomarker panel consisting of galectin-3 binding protein (LGALS3BP), amyloid-β1-40 (Aβ40), angiotensin-converting enzyme (ACE), and periostin (POSTN) [28,29]. It was demonstrated that LGALS3BP exerts a regulatory role in Aβ production by directly interacting with amyloid precursor protein (APP), consequently impeding APP processing by β-secretase [30]. ACE has been implicated in the processing and metabolism of amyloid β (Aβ) [31]. Therefore, the administration of ACE inhibitors in hypertensive patients diagnosed with AD has been correlated with increased handgrip strength (HGS), preservation of physical capacity, and the prevention of neuromuscular junction (NMJ) degradation [32]. In a recent study, researchers observed a noteworthy relationship between elevated plasma POSTN levels and the progressive decline in physical and cognitive capacities among older adults [33]. We have already produced a bioanalytical platform that can measure four biomarkers with tens of microliters of peripheral blood, the so-called Quantamatrix's multiplexed diagnostics platform (QPLEX™; Quantamatrix Inc., Seoul, Republic of Korea) Alz plus assay kit. Subsequently, we designed an optimal algorithm, the QPLEX™ algorithm, using the results of the QPLEX™ Alz plus assay kit to predict cerebral amyloid deposition. When the algorithm value exceeds the cutoff value, we assume that the participants may be at risk for AD. The current study shows that a QPLEX™ Alz plus assay kit could be used

for cerebral amyloid deposition diagnosis [21,34,35]. However, all studies were developed and applied with the Korean Brain Aging Study for the Early diagnosis and prediction of Alzheimer's disease (KBASE) cohort. Therefore, applying the kit and the algorithm to other independent cohorts is necessary to verify the performance and bias.

In this paper, our goal is to investigate the potential of the QPLEX™ Alz plus assay kit for the early clinical diagnosis of AD in another independent cohort in South Korea. First, we checked the relationship between the QPLEX™ algorithm values and the four clinically separated groups: cognitively normal individuals (CN), SCD, MCI, and AD. Second, we explored the relationship between our algorithm values and groups divided by the scores of the Mini-Mental State Examination (MMSE) and Clinical Dementia Rating (CDR). The MMSE is a screening tool that provides information about global cognition, and the CDR is a composite evaluation used mainly to determine the presence/absence of functional impairment. Finally, we analyzed the relationship between our algorithm values and the subgroups fractionalized by some factors known to influence the onset of AD, such as sex, age, depression, or apolipoprotein E (ApoE) genotype. The comorbidity of depression is frequently observed in individuals with dementia [36]. As in the case of those three factors, ApoE has been implicated in the pathological changes in AD, including the accumulation of Aβ and tau proteins, which subsequently contribute to neuroinflammation and neuronal injury, ultimately leading to impaired cognitive functions associated with learning and memory [6]. Moreover, we checked the influence of other factors, such as education years, hypertension, diabetes, hyperlipidemia, stroke, angina, thyroid, surgical history, cancer, family history, drinking, smoking, body mass index (BMI), and anxiety. However, at least in our data, there were no significant differences between clinically separated groups (Supplementary Table S1), so we did not include them in the in-depth analysis.

2. Results

2.1. Characteristics of the Participants

This study included 1395 participants (aged 41–92 years) classified into four groups divided by the clinical continuum of AD: 71 CN, 275 SCD, 857 MCI, and 192 AD. The demographic details are shown in Table 1. There were significant differences among the clinically separated groups in terms of age, MMSE score, and CDR score. Moreover, there were significant differences between groups in all the MMSE and CDR test sub-categories.

Table 1. Demographic data of the participants (N = 1395).

	CN	SCD	MCI	AD
Number	71 (5%)	275 (20%)	857 (61%)	192 (14%)
Age	61.49 ± 9.44	69.79 ± 7.80 [a]	72.86 ± 8.15 [a]	70.26 ± 9.44 [a]
Sex (M/F)	24/47	81/194	297/560	78/114
ApoE genotype (ε4 +/−)	8/63	71/204	314/543	92/100
MMSE total	27.93 ± 2.24	27.92 ± 1.91	24.31 ± 4.06 [a]	19.33 ± 4.73 [a]
Orientation	9.85 ± 0.36	9.84 ± 0.43	8.59 ± 1.69 [a]	5.94 ± 2.07 [a]
Immediate recall	2.96 ± 0.20	2.96 ± 0.22	2.90 ± 0.37	2.81 ± 0.49 [a]
Attention and Calculation	4.21 ± 1.12	4.17 ± 1.03	3.32 ± 1.51 [a]	2.36 ± 1.75 [a]
Memory recall	2.37 ± 0.76	2.27 ± 0.96	1.35 ± 1.11 [a]	0.66 ± 0.99 [a]
Language	7.59 ± 0.77	7.74 ± 0.56	7.32 ± 1.01 [a]	6.92 ± 1.34 [a]
Copying	0.94 ± 0.23	0.94 ± 0.24	0.81 ± 0.39 [a]	0.65 ± 0.48 [a]
CDR score	0.18 ± 0.24	0.46 ± 0.14 [a]	0.50 ± 0.16 [a]	0.94 ± 0.49 [a]
CDR SB	0.21 ± 0.30	0.67 ± 0.48 [a]	1.63 ± 1.35 [a]	5.65 ± 2.87 [a]
Memory	0.18 ± 0.24	0.46 ± 0.15 [a]	0.60 ± 0.28 [a]	1.24 ± 0.57 [a]
Orientation	0.00 ± 0.00	0.05 ± 0.18	0.32 ± 0.36 [a]	1.07 ± 0.55 [a]
Judgment and Problem-solving	0.01 ± 0.06	0.07 ± 0.18	0.28 ± 0.33 [a]	0.95 ± 0.53 [a]

Table 1. *Cont.*

	CN	SCD	MCI	AD
Community Affairs	0.00 ± 0.00	0.03 ± 0.12	0.19 ± 0.32 [a]	0.97 ± 0.61 [a]
Home and Hobbies	0.02 ± 0.10	0.06 ± 0.17	0.20 ± 0.32 [a]	0.95 ± 0.61 [a]
Personal care	0.00 ± 0.00	0.01 ± 0.05	0.04 ± 0.23	0.47 ± 0.68 [a]

Data represent mean ± standard deviation; [a], $p < 0.05$ compared with the CN group, one-way *ANOVA* with Student–Newman–Keuls *post hoc* comparison; CN, cognitively normal; SCD, subjective cognitive decline; MCI, mild cognitive impairment; AD, Alzheimer's disease; ApoE, Apolipoprotein E; MMSE, Mini-Mental State Examination; CDR, Clinical Dementia Rating; CDR SB, Clinical Dementia Rating Sum of Boxes.

2.2. Demographic Characteristics of the Two Groups Divided by the QPLEX™ Algorithm

In Table 2, QM Alz-N indicates the negative group below the cutoff value and QM Alz-P indicates the positive group equal to or higher than the cutoff value, as classified by the QPLEX™ algorithm. Previous results have shown that a score equal to or higher than the cutoff value indicates a high possibility of cerebral amyloid deposition. Significant differences were demonstrated between QM Alz-N and QM Alz-P in age and CDR (CDR SB, memory, orientation, judgment and problem-solving, community affairs, home and hobbies, and personal care). Except for immediate recall and copying, the scores of other MMSE items (orientation, attention and calculation, memory recall, and language) in QM Alz-N were significantly higher than those in QM Alz-P.

Table 2. Demographic characteristics of the two groups divided by the QPLEX™ algorithm.

	QM Alz-N	QM Alz-P	*p*-Value
Number	595	800	
Age	70.71 ± 9.04	71.76 ± 8.49	$p = 0.0283$
Sex (M/F)	212/383	268/532	
ApoE genotype (ε4 +/−)	184/411	301/499	
MMSE total	25.15 ± 4.28	24.05 ± 4.70	$p < 0.0001$
Orientation	8.80 ± 1.75	8.34 ± 2.03	$p < 0.0001$
Immediate recall	2.92 ± 0.34	2.90 ± 0.38	*N.S.*
Attention and Calculation	3.53 ± 1.50	3.31 ± 1.58	$p = 0.0068$
Memory recall	1.62 ± 1.13	1.39 ± 1.18	$p = 0.0002$
Language	7.43 ± 0.94	7.31 ± 1.07	$p = 0.0289$
Copying	0.84 ± 0.36	0.81 ± 0.40	*N.S.*
CDR score	0.50 ± 0.24	0.57 ± 0.32	$p < 0.0001$
CDR SB	1.60 ± 1.82	2.16 ± 2.38	$p < 0.0001$
Memory	0.58 ± 0.37	0.68 ± 0.43	$p < 0.0001$
Orientation	0.29 ± 0.43	0.40 ± 0.49	$p < 0.0001$
Judgment and Problem-solving	0.25 ± 0.38	0.36 ± 0.46	$p < 0.0001$
Community Affairs	0.20 ± 0.38	0.30 ± 0.49	$p < 0.0001$
Home and Hobbies	0.21 ± 0.37	0.31 ± 0.49	$p < 0.0001$
Personal care	0.06 ± 0.27	0.11 ± 0.39	$p = 0.0059$

Data represent mean ± standard deviation; QM Alz-N, the negative group that has below-cutoff values in the QPLEX™ algorithm, resulting from the QPLEX™ kit; QM Alz-P, the positive group that has values equal to or over the cutoff values in the QPLEX™ algorithm, resulting from the QPLEX™ kit; *N.S.*, not significant; ApoE, Apolipoprotein E; MMSE, Mini-Mental State Examination; CDR, Clinical Dementia Rating; CDR SB, Clinical Dementia Rating Sum of Boxes.

2.3. Difference in the QPLEX™ Algorithm Values among Clinically Separated, MMSE-Separated, or CDR-Separated Groups

The average of QPLEX™ algorithm values in each group increased in the order of the clinical progression continuum of AD: CN (0.382 ± 0.150), SCD (0.452 ± 0.130), MCI (0.484 ± 0.129), and AD (0.513 ± 0.136) (Figure 1A). Moreover, the algorithm values between each group showed statistically significant differences ($p < 0.01$). Further, we compared the values of the QPLEX™ algorithm to cognitive evaluation scores of MMSE

or CDR (Figure 1B,C). When the groups were divided according to the clinical criteria of each cognitive evaluation, the values of the QPLEX™ algorithm were significantly different among groups in both MMSE and CDR. The MMSE score and algorithm values were analyzed by defining 24 to 30 as normal, 20 to 23 as mild AD dementia, and less than 20 as AD dementia [37]. The algorithm values showed significant differences among the MMSE-separated groups. Furthermore, the CDR score was analyzed by defining 0 as normal, 0.5 as questionable, 1 as mild dementia, and 2 or more as dementia [38]. Similarly, the QPLEX™ algorithm value showed a statistically significant difference among the CDR-separated groups.

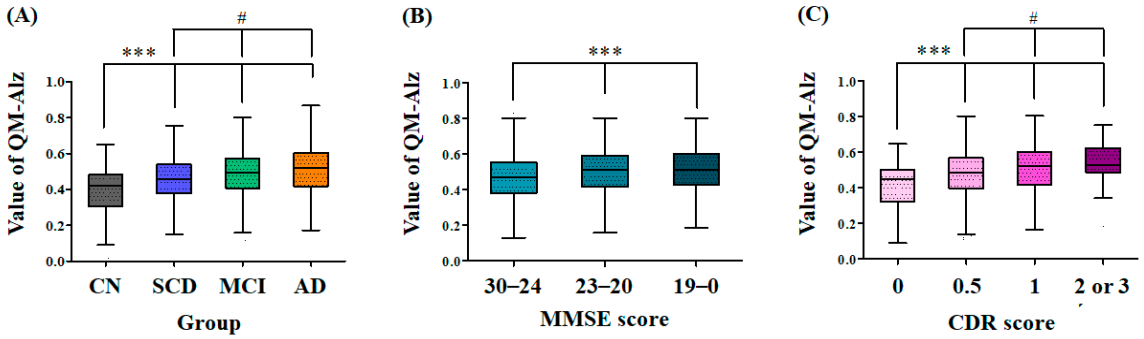

Figure 1. Difference of the QPLEX™ algorithm values among the clinically separated groups, MMSE-separated, or CDR-separated groups. The values of the QPLEX™ algorithm showed statistically significant differences among the (**A**) four clinically separated groups (CN (n = 71), SCD (n = 275), MCI (n = 857), and AD (n = 192)), (**B**) MMSE-separated groups (30–24 (n = 923), 23–20 (n = 265), and 19–0 (n = 207)), and (**C**) CDR-separated groups (CDR 0 (n = 98), CDR 0.5 (n = 1153), CDR 1 (n = 117), and CDR 2 (n = 27)). Data represent mean ± standard deviation. *** $p < 0.01$ compared with the (**A**) CN group, (**B**) the group ranging from 24 to 30 in MMSE scores, and (**C**) the group scoring 0 in CDR, one-way *ANOVA* with Student–Newman–Keuls *post hoc* comparison, respectively; $^{\#}$ $p < 0.05$ compared with the (**A**) SCD group, and (**C**) the group scoring 0.5 in CDR, one-way *ANOVA* with Student–Newman–Keuls *post hoc* comparison, respectively; CN, cognitively normal; SCD, subjective cognitive decline; MCI, mild cognitive impairment; AD, Alzheimer's disease; MMSE, Mini-Mental State Examination; CDR, Clinical Dementia Rating.

2.4. Comparison of the QPLEX™ Algorithm Values among the Individual Subgroups Fractionized by Sex, Age, Depression, or ApoE Genotype

We further analyzed whether the clinically separated groups had a significant difference in the QPLEX™ algorithm values even when the participant groups were fractionized by various factors (Figure 2). When the groups were fractionized according to age, sex, or depression, the difference in the algorithm values between the two groups was not significant (Figure 2A,D,G). However, the QPLEX™ algorithm values showed significant differences among the clinically separated subgroups fractionized by age or sex (Figure 2B,C,E,F). In participants without depression, significant differences between subgroups were maintained (Figure 2H). Conversely, in participants with depression, only CN and AD were significantly distinguished, while SCD and MCI were not distinguished (Figure 2I). When the participant groups were fractionated according to ApoE genotyping, the algorithm values of the ApoE ε4-negative group were significantly lower than those of the ApoE ε4-positive group (Figure 2J). In the ApoE ε4-negative group, there was a significant difference in algorithm values among the four subgroups (Figure 2K). However, in the ApoE ε4-positive group, there was no significant difference between the CN subgroup and the other subgroups (Figure 2L). There were only eight CN participants in the ApoE ε4-positive group, which was not a large enough sample size to analyze the statistical significance. However, the algorithm values of the AD subgroup were significantly higher than those of the SCD subgroup in the ApoE ε4-positive group.

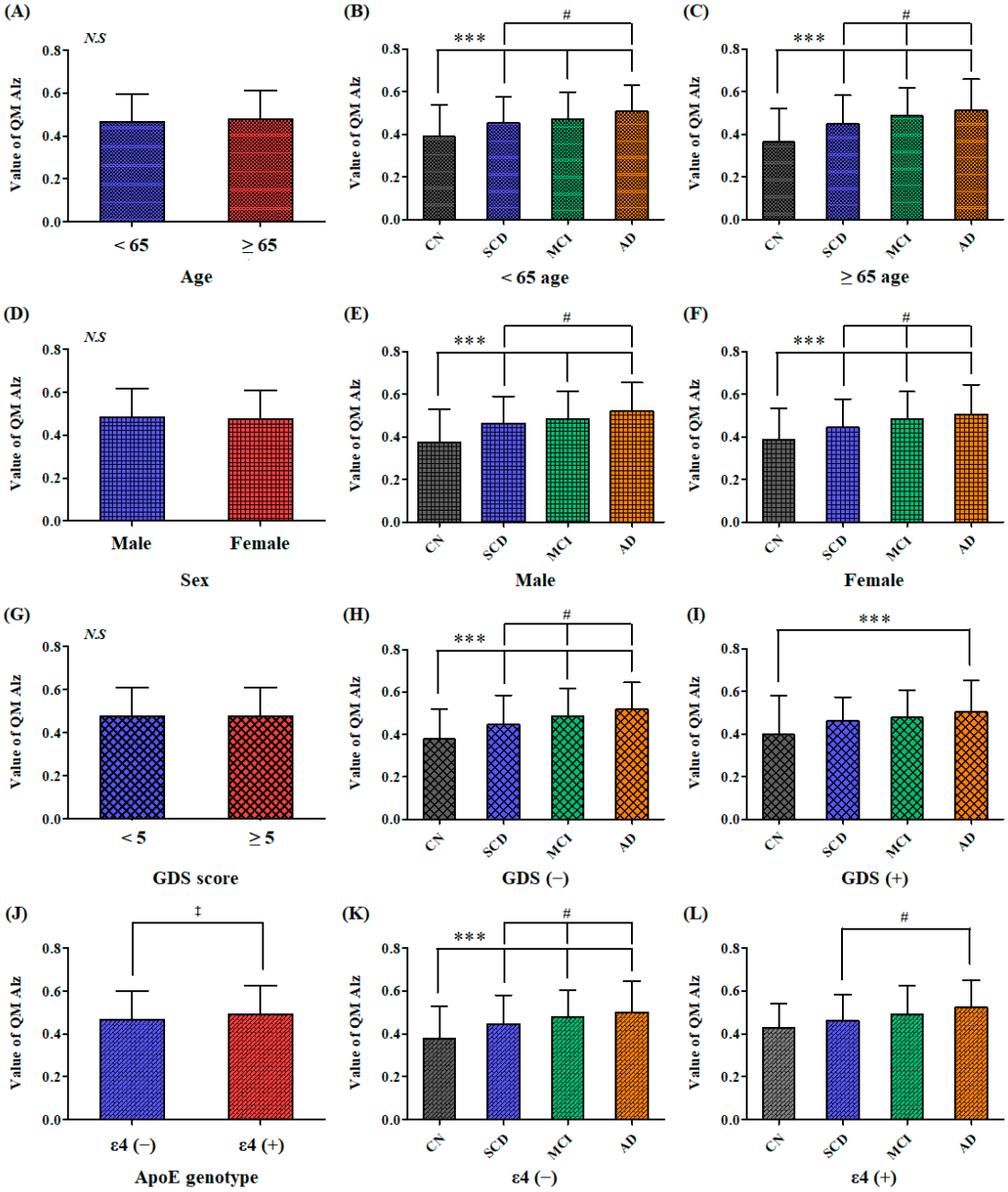

Figure 2. Difference of the QPLEX™ algorithm values within the subdivided groups by various factors. (**A**) Comparison between the groups under 65 and over 65. (**B**,**C**) Comparison among the clinically separated subgroups by age. (**D**) Comparison between the male and female groups. (**E**,**F**) Comparison among the clinically separated subgroups by sex. (**G**) Comparison between the group without depression and the group with depression. (**H**,**I**) Comparison among the clinically separated subgroups by depression. (**J**) Comparison between ApoE ε4-negative (ε4 (−)) and ApoE ε4-positive (ε4 (+)) group. (**K**,**L**) Comparison among the clinically separated subgroups by ApoE genotype. Data represent mean ± standard deviation; *N.S.*, no significance; ‡ $p < 0.01$ compared with the ε4 (−) group, an independent t-test; *** $p < 0.05$ compared with the CN group, one-way *ANOVA* with Student–Newman–Keuls *post hoc* comparison; # $p < 0.05$ compared with the SCD group, one-way *ANOVA* with Student–Newman–Keuls *post hoc* comparison; CN, cognitively normal; SCD, subjective cognitive decline; MCI, mild cognitive impairment; AD, Alzheimer's disease; GDS, Geriatric Depression Scale; ApoE, Apolipoprotein E.

2.5. ANCOVA Results to Adjust for Covariates, such as Age, Sex, Depression, and ApoE Genotype

The distribution of age, sex, depression, and ApoE genotype differed for each clinical group. When the analysis of covariance (*ANCOVA*) was performed to exclude the effects of these covariates, significant differences were shown between clinical groups regardless of age, sex, or geriatric depression scale (GDS) score (Figure 3A–C). In contrast, when the ApoE genotype was set as a covariate, there was no statistical significance between MCI and AD (Figure 3D). When age, sex, depression, and ApoE genotype were set as covariates simultaneously, there were significant differences between all clinical groups (Figure 3E).

(A)

	CN	SCD	MCI	AD
CN	-	0.0015	<0.0001	<0.0001
SCD	0.0015	-	0.0066	<0.0001
MCI	<0.0001	0.0066	-	0.0212
AD	<0.0001	<0.0001	0.0212	-

(B)

	CN	SCD	MCI	AD
CN	-	0.0004	<0.0001	<0.0001
SCD	0.0004	-	0.0035	<0.0001
MCI	<0.0001	0.0035	-	0.0361
AD	<0.0001	<0.0001	0.0361	-

(C)

	CN	SCD	MCI	AD
CN	-	0.0004	<0.0001	<0.0001
SCD	0.0004	-	0.0034	<0.0001
MCI	<0.0001	0.0034	-	0.0319
AD	<0.0001	<0.0001	0.0319	-

(D)

	CN	SCD	MCI	AD
CN	-	0.0007	<0.0001	<0.0001
SCD	0.0007	-	0.0060	<0.0001
MCI	<0.0001	0.0060	-	*N.S.*
AD	<0.0001	<0.0001	*N.S.*	-

(E)

	CN	SCD	MCI	AD
CN	-	0.0024	<0.0001	<0.0001
SCD	0.0024	-	0.0180	0.0001
MCI	<0.0001	0.0180	-	0.0454
AD	<0.0001	0.0001	0.0454	-

Figure 3. Bonferroni-corrected *p*-values of *ANCOVA*. *p*-values of *ANCOVA* when covariates were set as (**A**) age, (**B**) sex, (**C**) GDS score, (**D**) ApoE genotype, and (**E**) all four factors combined. *ANCOVA*, analysis of covariance; *N.S.*, not significant; GDS, Geriatric Depression Scale; ApoE, Apolipoprotein E.

3. Discussion

The QPLEX™ Alz plus assay kit adopts a bead-based 3D suspension array system to enhance reactivity and improve sensitivity. As a result, the kit can analyze rare or volume-limited samples, and only 20 μL undiluted human plasma was used per assay in this study. Moreover, the kit is a well-implemented multi-platform capable of measuring four peripheral biomarkers at once using a limited sample and combining them into an algorithm. In previous studies, we identified that these four biomarkers are related to AD [28,29]. Aβ40 is the most representative biomarker of AD. ACE is known as an endopeptidase related to blood pressure control [39,40], but it also acts as an inhibitor of Aβ aggregation [41–43]. ACE level and activity were lower in AD patients than in CN individuals [44]. POSTN is related to inflammatory diseases [45,46], and can be found in the cerebral cortex of AD patients [47]. It may be that inflammation is activated and POSTN levels are elevated during AD pathogenesis. LGALS3BP is a receptor for galectin-3, and the binding of LGALS3BP to its ligand inhibits neutrophil activation [48,49].

This study was performed on another independent cohort, including many more participants (n = 1395) compared with the previous studies (n = 300) [21,34]. The target for health checkups are individuals with CN, SCD, or MCI who may potentially develop AD dementia. We included more subjects (n = 1103) with CN, SCD, or MCI than those (n = 236) in the previous studies.

In this paper, we demonstrated that the QPLEX™ Alz plus assay kit could be a useful tool for the early clinical diagnosis of AD. The QPLEX™ algorithm was developed to determine the presence of cerebral amyloid deposition; however, we hypothesized that it could also be used to differentiate between CN and AD based on the fact that, statistically,

CN has less amyloid deposition compared to AD. The results suggest that the kit can indeed distinguish the groups according to the clinical progression continuum of AD: CN, SCD, MCI, and AD (Figure 1A). AD neuropathological changes initially target specific brain regions associated with memory, language, and cognitive functions. Consequently, the prodromal symptoms primarily present as impairments in memory, language, and cognitive abilities [5]. Further, there was a significant difference in algorithm values between groups correlating with the score ranges of the MMSE or CDR test (Figure 1B,C) related to memory, language, and cognitive abilities. This implies that the kit can differentiate among groups based on the severity of dementia.

For early diagnosis to be meaningful, it must also be valid for people under the age of 65 years. The correlation between algorithm values and clinical progress was present in patients above 65 years and below 65 years (Figure 2B,C). There were also significant algorithmic value differences among clinical progression in both males and females without bias (Figure 2E,F). This means that the kit can be used regardless of the age and sex of the patient. Notably, a correlation between algorithm values and clinical progression was observed in the absence of depression, but the presence of depression appears to impact the diagnostic accuracy of the QPLEX™ kit. With depression, only CN showed a significant difference with AD (Figure 2I). Although the specific subgroup differences may vary depending on the presence of depression, the QPLEX™ algorithm value proves to be highly valuable in differentiating between CN and AD, regardless of the presence or absence of depression. Further research on our kit is necessary to incorporate depression and effectively distinguish various clinical symptoms. Conversely, the presence or absence of the ApoE gene shows a significant difference in the QPLEX™ algorithm value (Figure 2J), because people with the ApoE gene are more likely to develop MCI or AD [50,51]. Additional research on the QPLEX™ kit will be necessary to differentiate various clinical symptoms while incorporating ApoE results in the future.

We also performed *ANCOVA* to adjust for covariates, such as age, sex, depression, and ApoE genotype (Figure 3). Although the distribution of age, sex, and depression differed between cognitive states, the *ANCOVA* results adjusted for these covariates showed statistically significant differences among all clinical groups (Figure 3A–C). These also indicate that the QPLEX™ kit can distinguish the cognitive states regardless of age, sex, and depression. In *ANCOVA* with ApoE genotype set as a covariate, significant differences were present among all groups except between the MCI and AD groups (Figure 3D). This lack of significance between MCI and AD can be attributed to the fact that high ApoE positivity was considered, but differences in the other factors were not adjusted for. When age, sex, depression, and ApoE genotype were all set as covariates, the QPLEX™ algorithm values showed significant differences among all groups (Figure 3E). The *ANCOVA* results confirm that the QPLEX™ algorithm values are related to cognitive states.

One intended application of the kit is for use in routine screening for AD among the general population. Our kit has four main advantages that make it highly suitable for this purpose: Firstly, it detects multiple biomarkers, which has been shown to increase the accuracy of diagnosing AD [28], predicting the conversion from MCI to AD [52,53], identifying MCI patients susceptible to AD [54], and predicting cerebral Aβ deposition [24,26,28]. Secondly, it detects these biomarkers in blood samples, which are easier to acquire and more cost- and time-effective than detecting biomarkers in CSF [25,55–59]. Thirdly, it requires only a small sample volume of 20 μL undiluted plasma per analysis. Fourthly, the kit utilizes highly stable magnetic beads that are amenable to automation [21].

Additionally, as in previous studies, participants were analyzed by dividing them into negative and positive, based on the algorithm cutoff value (Table 2). The *t*-test results show a statistically significant difference between QM Alz-N and QM Alz-P in all items of MMSE and CDR except for immediate recall and copying of MMSE. However, the magnitude of the difference seems small. This can be explained by the characteristics of the PREMIER cohort, and we used the CDR score as an example. The purpose of the consortium is early diagnosis, especially focusing on changes in blood biomarkers, genetic data, and

pathological data during the progression from MCI to AD with a longitudinal study; hence, more than half of the recruited participants had MCI (Table 1). The proportion of SCD and MCI participants exceeded 80% of the total cohort, with 93% of participants in these categories having a CDR score of 0.5. As a result, the CDR scores converged to 0.5 for both QM Alz-N and QM Alz-P. In the KBASE cohort, CDR scores differed according to the clinical state, but there was no difference according to amyloid deposition [21]. When the KBASE cohort was classified by PET results, there seemed to be a difference in CDR scores between the two groups, but this is a result of the difference in the CN/MCI/dementia ratio [34].

The study also had some limitations. First, proteomics screening and statistical analysis show that blood biomarkers LGALS3BP, ACE, and POSTN effectively screen for cerebral amyloid depositions and clinically diagnose Alzheimer's disease, but the theoretical basis is still lacking. Additional research will be needed to supplement these theoretical grounds. Second, a longitudinal study will be needed to observe the change in our assay depending on the disease progression. Third, owing to limitations in accessibility, the study was conducted only for the Korean cohort. Analysis of cohorts of different regions and races is needed to confirm the possibility of universal applicability. Fourth, various types of dementia or MCI need to be compared using our assay to investigate the possibility of distinguishing these from one another. Fifth, there were only eight participants in the ApoE ε4-positive CN group, which was an insufficient sample size for statistical significance analysis. ApoE positivity is distributed with a lower probability in the CN group, and the recruitment rate for the CN group was low due to the characteristics of the cohort, resulting in a shortage of participants in the ApoE ε4-positive CN group. Sixth, only cognition tests, such as MMSE and CDR, were utilized in this study. However, there is a need for additional validation of the relationship between the QPLEX™ algorithm and other more sensitive and specific tests, such as the Montreal Cognitive Assessment (MoCA). Seventh, we only conducted the prediction of cerebral amyloid deposition using the QPLEX™ algorithm. However, since tauopathy is highly relevant in the pathophysiology and progression of AD, future research and validation will also be necessary using tau PET.

In conclusion, the QPLEX™ Alz plus assay kit, a multiplex system to analyze four blood biomarkers consisting of LGALS3BP, Aβ40, ACE, and POSTN simultaneously, showed potential as a screening tool for AD. In particular, our kit could be a useful detection tool for the early clinical diagnosis of AD, i.e., for SCD or MCI. Our kit could be a helpful diagnostic tool for cognitive impairments at health checkups because the kit can measure multiple blood biomarkers using only tens of microliters of blood.

4. Materials and Methods

4.1. Participants

In total, 1633 participants were included from 14 referral hospitals in the Republic of Korea. Most of the participants were recruited from the Samsung Medical Center (n = 579), the Soonchunhyang University Bucheon Hospital (n = 313), and the Kangwon National University Hospital (n = 265). The rest (n = 476) were from 11 hospitals across Korea, including the Korea University Guro Hospital (n = 56). These participants were recruited from a nationally funded, nationwide multicenter study named Precision medicine platform for mild cognitive impairment, based on Multi-omics, Imaging, Evidence-based R&BD (PREMIER) consortium (conducted between May 2019 and December 2022) in South Korea [60]. The aim of this consortium is to establish a platform for the development of the early diagnosis and precision medicine-based treatment of dementia by enrolling participants with various cognitive states, developing blood-based biomarkers, generating genetic data, and developing imaging-data- and clinical-data-based algorithms as a diagnostic or predictive tool. According to the purpose of the consortium, the cohort recruited mainly MCI participants at the pre-stage of dementia.

4.2. Clinical Diagnosis

An experienced neurologist diagnosed participants with SCD, MCI, or AD dementia according to relevant diagnostic criteria [61]. Based on the recommendation of Molinuevo et al. [62], the criteria for SCD are as follows: (1) self-experienced persistent decline in cognitive performance compared to previously normal state, (2) normal performance on all neuropsychological tests, and (3) cannot be explained by other psychiatric or neurologic diseases. Based on Petersen's criteria [63], the criteria for MCI are as follows: (1) cognitive complaint, preferably corroborated by an informant; (2) objective cognitive impairment for age and educational level; (3) relatively preserved general cognition; (4) intact activities of daily living; and (5) not demented. The criteria for AD dementia are based on the proposal by the National Institute on Aging—Alzheimer's Association (NIA–AA) Research Framework [64]. AD patients exhibited CDR scores ranging from 0.5 to 3, and their MMSE scores were 10 or higher, indicating their suitability for Seoul neuropsychological screening battery-dementia version (SNSB-D) testing [65].

4.3. Cognition Tests

All participants underwent MMSE and CDR (Table 1). The MMSE consists of tests for orientation, immediate recall, attention and calculation, memory recall, language, and copying. The CDR consists of tests for memory, orientation, judgment and problem-solving, community affairs, home and hobbies, and personal care. The details and protocols of neuropsychological assessment are described in a previous report [66]. The diverse interpretation of the MMSE scores and their relationship with the severity of dementia were depicted as several steps [3,67–69]. Using one of the ranging methods of MMSE, we split the participants into three groups: normal, with a score range from 24 to 30; mild dementia, with a score range from 20 to 23; and moderate to severe dementia, with a score range below 19 [37]. The CDR scale is a global clinical staging method for AD [70]. Using a simplified description of the AD stages according to the CDR score, we also split CDR groups as follows: 0 = no dementia or normal; 0.5 = questionable; 1 = mild; and 2 to 3 = moderate to severe [38].

4.4. Short Geriatric Depression Scale—Korean Version (SGDS-K)

The SGDS-K, which stands for the Korean version of the Elderly Depression Scale [71], was derived from the Geriatric Depression Scale (GDS) [72]. It comprises 15 yes/no questions, resulting in a total score of 15 points. The SGDS-K evaluates symptoms of depression experienced during the previous week [73,74]. Using one of the ranging methods of GDS, we split the participants into two groups: normal, with a score range from 0 to 4, and depression, with a score range of 5 or higher [75,76].

4.5. Blood Sampling and Storage

Whole-blood samples were collected in K2 EDTA tubes (BD Vacutainer Systems, Plymouth, UK). The blood sample tubes were centrifuged at 700× g for 5 min at room temperature, and plasma supernatants were stored at −80 °C [21,34].

4.6. Exclusion Criteria of the Participants

Figure 4 shows the criteria and number for the inclusion and exclusion of participants. A total of 1633 participants were recruited. Among them, those without blood samples (n = 10), ApoE genotype (n = 19), MMSE (n = 57), CDR (n = 70) tests missing, or with other forms of disease (N = 82) were excluded from the analysis. Finally, QPLEX™ assay and data analysis were performed on 1395 participants.

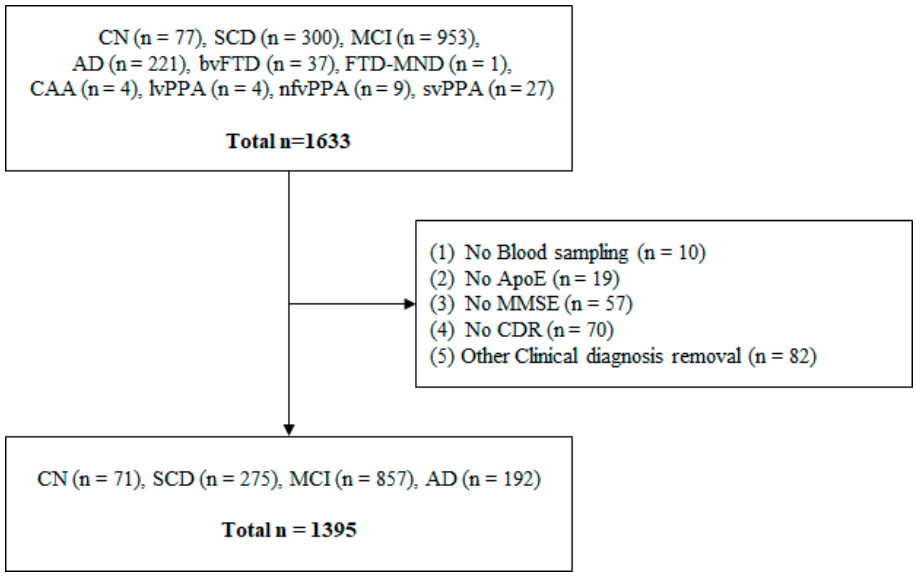

Figure 4. Flowchart for participant selection. CN, cognitively normal; SCD, subjective cognitive decline; MCI, mild cognitive impairment; AD, Alzheimer's disease; bvFTD, behavioral variant frontotemporal dementia; FTD-MND, frontotemporal dementia with motor neuron disease; CAA, cerebral amyloid angiopathy; lvPPA, logopenic variant primary progressive aphasia; nfvPPA, nonfluent/agrammatic variant primary progressive aphasia; svPPA, semantic variant primary progressive aphasia; ApoE, apolipoprotein E; MMSE, Mini-Mental State Examination; CDR, clinical dementing rating.

4.7. QPLEX™ Alz Plus Assay

QPLEX™ kit is a bead-based 3D suspension array system for multiplex analysis in a single well [77,78]. The micro-sized beads, referred to as microdisks, are graphically encoded using photolithography. By reacting multiple microdisks pre-coupled with specific markers according to their specific codes, and analyzing the fluorescence signal for each code, multiple markers can be analyzed simultaneously in one well. Briefly, 35 µL diluted human plasma samples and 35 µL biotin-conjugated detection antibodies were incubated with microdisks in a 96-well plate for 90 min at room temperature with shaking at 1000 rpm. The reacted microdisks were washed with 0.1% BSA buffer and incubated with 50 µL of 2 µL/mL R-phycoerythrin-conjugated streptavidin for 15 min at room temperature with shaking at 1000 rpm. After three washes, the microdisks were re-suspended in 100 µL of 0.1% BSA buffer and analyzed with Quantamatrix's multiplex assay platform (QMAP™).

The QPLEX™ algorithm was developed to diagnose cerebral amyloid deposition. This algorithm was developed through logistic regression with the quantitative values of LGALS3BP, Aβ40, ACE, and POSTN obtained from the QPLEX™ Alz plus assay kit as the independent variables and the results of PET imaging performed at the Seoul National University Hospital as the dependent variables [21,34]. Subsequently, the cutoff value, sensitivity, and specificity were obtained through receiver operating characteristic (ROC) curve analysis. The equation of the QPLEX™ algorithm was as follows:

$$P_i = \frac{E}{1+E}$$

$$E = \exp(a_1 \times LGALS3BP + a_2 \times A\beta40 + a_3 \times ACE + a_4 \times POSTN + C)$$

(P_i, predicted probabilities; a_n, coefficient values for each biomarker, with $a_1 = -0.00066$, $a_2 = 0.008$, $a_3 = -0.00662$, and $a_4 = 0.13224$; and $C = 1.24777$, which is a constant. The quantitative values of each biomarker obtained with the QPLEX™ Alz plus kit were multiplied by the coefficient values, and P_i was calculated).

The cutoff value to maximize sensitivity and specificity for screening cerebral amyloid deposition determined by ROC curve analysis was 0.461.

4.8. Data Analysis

All statistical analyses were performed using Medcalc 20.115 (Ostend, Belgium), and the figures were generated using GraphPad Prism 5 (San Diego, CA, USA). The comparison between groups was performed with an independent t-test, analysis of variance (*ANOVA*) with a Student–Newman–Keuls *post hoc* test, or *ANCOVA*. $p < 0.05$ was considered statistically significant. In *ANCOVA*, the *p*-value was Bonferroni-corrected. Figure 5 illustrates the overall data analysis process, showing the criteria used to create subgroups and the number of participants in each subgroup.

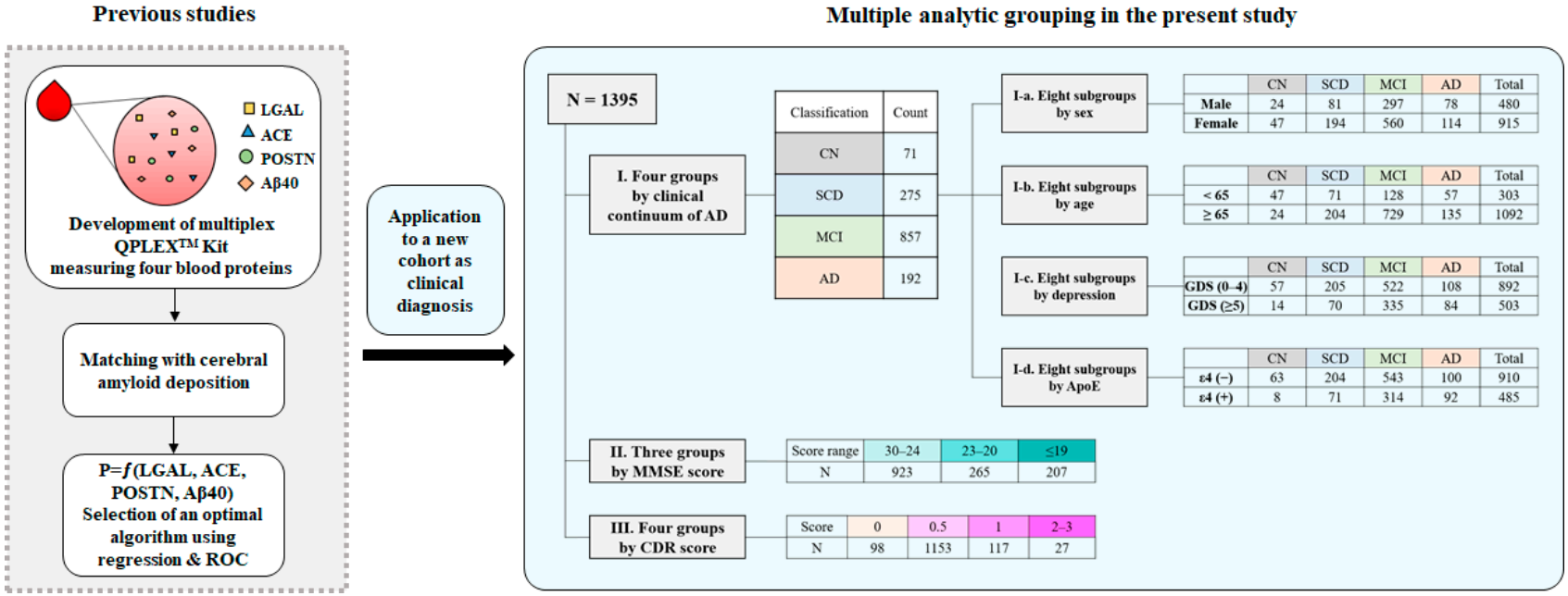

Figure 5. Overall data analysis process flow. In previous studies, we developed the QPLEX™ kit to quantify four blood biomarkers (LGAL, ACE, POSTN, and Aβ40) and indicated its optimal algorithm to screen cerebral amyloid deposition. In this study, we applied the kit and algorithm to a new additional cohort for the clinical diagnosis of AD. A total of 1395 participants were divided according to the clinical continuum of AD, MMSE score, and CDR score, and the differences in algorithm values among groups were compared. The clinical continuum of AD was further analyzed by subdividing according to sex, age, and ApoE genotype. According to the clinical criteria, the MMSE scores were grouped into normal from 24 to 30, mild AD dementia from 20 to 23, and AD dementia for scores lower than 20. Similarly, the CDR scores were grouped into normal for 0, questionable for 0.5, mild dementia for 1, and dementia for two or more. LGAL, galectin-3 binding protein; ACE, angiotensin-converting enzyme; POSTN, periostin; Aβ40, amyloid-β1-40; ROC, receiver operating characteristic; CN, cognitively normal; SCD, subjective cognitive decline; MCI, mild cognitive impairment; AD, Alzheimer's disease; ApoE, Apolipoprotein E; MMSE, Mini-Mental State Examination; CDR, Clinical Dementia Rating.

I-a. Eight subgroups by sex	CN	SCD	MCI	AD	Total
Male	24	81	297	78	480
Female	47	194	560	114	915

I-b. Eight subgroups by age	CN	SCD	MCI	AD	Total
< 65	47	71	128	57	303
≥ 65	24	204	729	135	1092

I-c. Eight subgroups by depression	CN	SCD	MCI	AD	Total
GDS (0–4)	57	205	522	108	892
GDS (≥5)	14	70	335	84	503

I-d. Eight subgroups by ApoE	CN	SCD	MCI	AD	Total
ε4 (−)	63	204	543	100	910
ε4 (+)	8	71	314	92	485

Supplementary Materials: The following supporting information can be downloaded at: https://www.mdpi.com/article/10.3390/ijms241311119/s1.

Author Contributions: Conceptualization, H.N., K.Y.S. and J.J.; methodology, D.L. and C.Y.; software, H.N.; validation, H.N., K.Y.S. and J.J.; formal analysis, H.N., K.Y.S. and J.J.; investigation, H.N., K.Y.S. and J.J.; resources, S.K.; data curation, H.N.; writing, H.N. and K.Y.S.; visualization, H.N., D.L. and C.Y.; supervision, S.-H.H., J.-C.P., I.M.-J. and S.K.; project administration, S.K.; funding acquisition, S.K. All authors have read and agreed to the published version of the manuscript.

Funding: This research was funded by a grant of the Korea Health Technology R&D Project through the Korea Health Industry Development Institute (KHIDI), funded by the Ministry of Health & Welfare, Republic of Korea, grant number HI19C1132.

Institutional Review Board Statement: The study was conducted in accordance with the Declaration of Helsinki, and approved by the Institutional Review Board of the Samsung Medical Center (IRB No. 2020-01-024[M1]) and each center.

Informed Consent Statement: Informed consent was obtained from all subjects involved in the study. Written informed consent was obtained from the patients to publish this paper.

Data Availability Statement: The data presented in this study are available in the insert article.

Conflicts of Interest: Hunjong Na, Dokyung Lee, Changsik Yoon, and Jisung Jang are employees of QuantaMatrix Inc. Sunghoon Kwon is the CEO of QuantaMatrix Inc. The remaining authors have no conflict of interest to declare.

References

1. Jack, C.R., Jr.; Knopman, D.S.; Jagust, W.J.; Petersen, R.C.; Weiner, M.W.; Aisen, P.S.; Shaw, L.M.; Vemuri, P.; Wiste, H.J.; Weigand, S.D.; et al. Tracking pathophysiological processes in Alzheimer's disease: An updated hypothetical model of dynamic biomarkers. *Lancet Neurol.* **2013**, *12*, 207–216. [CrossRef]
2. Villemagne, V.L.; Burnham, S.; Bourgeat, P.; Brown, B.; Ellis, K.A.; Salvado, O.; Szoeke, C.; Macaulay, S.L.; Martins, R.; Maruff, P.; et al. Amyloid beta deposition, neurodegeneration, and cognitive decline in sporadic Alzheimer's disease: A prospective cohort study. *Lancet Neurol.* **2013**, *12*, 357–367. [CrossRef]
3. Joshi, A.S. Drug prescription patterns in patients with Alzheimer's disease in an urban Neuro-speciality clinic in Western India. *Natl. J. Physiol. Pharm. Pharmacol.* **2019**, *9*, 1073–1080. [CrossRef]
4. World-Health-Organization. Dementia. 2023. Available online: https://www.who.int/news-room/fact-sheets/detail/dementia (accessed on 1 June 2023).
5. Alzheimer's Association. 2023 Alzheimer's disease facts and figures. *Alzheimers Dement.* **2023**, *19*, 1598–1695. [CrossRef]
6. Zhang, L.; Xia, Y.; Gui, Y. Neuronal ApoE4 in Alzheimer's disease and potential therapeutic targets. *Front. Aging Neurosci.* **2023**, *15*, 1199434. [CrossRef]
7. Kukull, W.A.; Bowen, J.D. Dementia epidemiology. *Med. Clin. N. Am.* **2002**, *86*, 573–590. [CrossRef]
8. Mantzavinos, V.; Alexiou, A. Biomarkers for Alzheimer's Disease Diagnosis. *Curr. Alzheimer Res.* **2017**, *14*, 1149–1154. [CrossRef]
9. Albert, M.S.; DeKosky, S.T.; Dickson, D.; Dubois, B.; Feldman, H.H.; Fox, N.C.; Gamst, A.; Holtzman, D.M.; Jagust, W.J.; Petersen, R.C.; et al. The diagnosis of mild cognitive impairment due to Alzheimer's disease: Recommendations from the National Institute on Aging-Alzheimer's Association workgroups on diagnostic guidelines for Alzheimer's disease. *Alzheimers Dement.* **2011**, *7*, 270–279. [CrossRef]
10. Sperling, R.A.; Aisen, P.S.; Beckett, L.A.; Bennett, D.A.; Craft, S.; Fagan, A.M.; Iwatsubo, T.; Jack, C.R., Jr.; Kaye, J.; Montine, T.J.; et al. Toward defining the preclinical stages of Alzheimer's disease: Recommendations from the National Institute on Aging-Alzheimer's Association workgroups on diagnostic guidelines for Alzheimer's disease. *Alzheimers Dement.* **2011**, *7*, 280–292. [CrossRef]
11. Giacomucci, G.; Mazzeo, S.; Bagnoli, S.; Ingannato, A.; Leccese, D.; Berti, V.; Padiglioni, S.; Galdo, G.; Ferrari, C.; Sorbi, S.; et al. Plasma neurofilament light chain as a biomarker of Alzheimer's disease in Subjective Cognitive Decline and Mild Cognitive Impairment. *J. Neurol.* **2022**, *269*, 4270–4280. [CrossRef]
12. Jessen, F.; Amariglio, R.E.; van Boxtel, M.; Breteler, M.; Ceccaldi, M.; Chetelat, G.; Dubois, B.; Dufouil, C.; Ellis, K.A.; van der Flier, W.M.; et al. A conceptual framework for research on subjective cognitive decline in preclinical Alzheimer's disease. *Alzheimers Dement.* **2014**, *10*, 844–852. [CrossRef] [PubMed]
13. Davis, M.; O'Connell, T.; Johnson, S.; Cline, S.; Merikle, E.; Martenyi, F.; Simpson, K. Estimating Alzheimer's Disease Progression Rates from Normal Cognition Through Mild Cognitive Impairment and Stages of Dementia. *Curr. Alzheimer Res.* **2018**, *15*, 777–788. [CrossRef]
14. Brodaty, H.; Heffernan, M.; Kochan, N.A.; Draper, B.; Trollor, J.N.; Reppermund, S.; Slavin, M.J.; Sachdev, P.S. Mild cognitive impairment in a community sample: The Sydney Memory and Ageing Study. *Alzheimers Dement.* **2013**, *9*, 310–317.e311. [CrossRef]

15. Wirth, M.; Schwarz, C.; Benson, G.; Horn, N.; Buchert, R.; Lange, C.; Kobe, T.; Hetzer, S.; Maglione, M.; Michael, E.; et al. Effects of spermidine supplementation on cognition and biomarkers in older adults with subjective cognitive decline (SmartAge)-study protocol for a randomized controlled trial. *Alzheimers Res. Ther.* **2019**, *11*, 36. [CrossRef]
16. Amariglio, R.E.; Becker, J.A.; Carmasin, J.; Wadsworth, L.P.; Lorius, N.; Sullivan, C.; Maye, J.E.; Gidicsin, C.; Pepin, L.C.; Sperling, R.A.; et al. Subjective cognitive complaints and amyloid burden in cognitively normal older individuals. *Neuropsychologia* **2012**, *50*, 2880–2886. [CrossRef] [PubMed]
17. Chandra, A.; Dervenoulas, G.; Politis, M. Alzheimer's Disease Neuroimaging, I. Magnetic resonance imaging in Alzheimer's disease and mild cognitive impairment. *J. Neurol.* **2019**, *266*, 1293–1302. [CrossRef] [PubMed]
18. Shah, Y.; Tangalos, E.G.; Petersen, R.C. Mild cognitive impairment. When is it a precursor to Alzheimer's disease? *Geriatrics* **2000**, *55*, 62, 65–68. [PubMed]
19. Busse, A.; Bischkopf, J.; Riedel-Heller, S.G.; Angermeyer, M.C. Mild cognitive impairment: Prevalence and predictive validity according to current approaches. *Acta Neurol. Scand.* **2003**, *108*, 71–81. [CrossRef] [PubMed]
20. Uzuegbunam, B.C.; Librizzi, D.; Hooshyar Yousefi, B. PET Radiopharmaceuticals for Alzheimer's Disease and Parkinson's Disease Diagnosis, the Current and Future Landscape. *Molecules* **2020**, *25*, 977. [CrossRef]
21. Park, J.C.; Jung, K.S.; Kim, J.; Jang, J.S.; Kwon, S.; Byun, M.S.; Yi, D.; Byeon, G.; Jung, G.; Kim, Y.K.; et al. Performance of the QPLEX Alz plus assay, a novel multiplex kit for screening cerebral amyloid deposition. *Alzheimers Res. Ther.* **2021**, *13*, 12. [CrossRef]
22. Petersen, R.C. Early diagnosis of Alzheimer's disease: Is MCI too late? *Curr. Alzheimer Res.* **2009**, *6*, 324–330. [CrossRef]
23. Blennow, K.; Zetterberg, H. Biomarkers for Alzheimer's disease: Current status and prospects for the future. *J. Intern. Med.* **2018**, *284*, 643–663. [CrossRef] [PubMed]
24. Han, S.H.; Park, J.C.; Mook-Jung, I. Amyloid beta-interacting partners in Alzheimer's disease: From accomplices to possible therapeutic targets. *Prog. Neurobiol.* **2016**, *137*, 17–38. [CrossRef] [PubMed]
25. Hampel, H.; O'Bryant, S.E.; Molinuevo, J.L.; Zetterberg, H.; Masters, C.L.; Lista, S.; Kiddle, S.J.; Batrla, R.; Blennow, K. Blood-based biomarkers for Alzheimer disease: Mapping the road to the clinic. *Nat. Rev. Neurol.* **2018**, *14*, 639–652. [CrossRef]
26. Park, J.C.; Han, S.H.; Mook-Jung, I. Peripheral inflammatory biomarkers in Alzheimer's disease: A brief review. *BMB Rep.* **2020**, *53*, 10–19. [CrossRef] [PubMed]
27. Zetterberg, H.; Burnham, S.C. Blood-based molecular biomarkers for Alzheimer's disease. *Mol. Brain* **2019**, *12*, 26. [CrossRef]
28. Park, J.C.; Han, S.H.; Lee, H.; Jeong, H.; Byun, M.S.; Bae, J.; Kim, H.; Lee, D.Y.; Yi, D.; Shin, S.A.; et al. Prognostic plasma protein panel for Abeta deposition in the brain in Alzheimer's disease. *Prog. Neurobiol.* **2019**, *183*, 101690. [CrossRef]
29. Park, J.C.; Han, S.H.; Cho, H.J.; Byun, M.S.; Yi, D.; Choe, Y.M.; Kang, S.; Jung, E.S.; Won, S.J.; Kim, E.H.; et al. Chemically treated plasma Abeta is a potential blood-based biomarker for screening cerebral amyloid deposition. *Alzheimers Res. Ther.* **2017**, *9*, 20. [CrossRef]
30. Seki, T.; Kanagawa, M.; Kobayashi, K.; Kowa, H.; Yahata, N.; Maruyama, K.; Iwata, N.; Inoue, H.; Toda, T. Galectin 3-binding protein suppresses amyloid-beta production by modulating beta-cleavage of amyloid precursor protein. *J. Biol. Chem.* **2020**, *295*, 3678–3691. [CrossRef]
31. Nassan, M.; Daghlas, I.; Piras, I.S.; Rogalski, E.; Reus, L.M.; Pijnenburg, Y.; Cuddy, L.K.; Saxena, R.; Mesulam, M.M.; Huentelman, M. Evaluating the association between genetically proxied ACE inhibition and dementias. *Alzheimers Dement.* **2023**. [CrossRef]
32. Qaisar, R.; Karim, A.; Iqbal, M.S.; Alkahtani, S.A.; Ahmad, F.; Kamli, H. ACE Inhibitors Improve Skeletal Muscle by Preserving Neuromuscular Junctions in Patients with Alzheimer's Disease. *J. Alzheimers Dis.* **2023**, 1–10. [CrossRef]
33. Sanchez-Sanchez, J.L.; Ader, I.; Jeanson, Y.; Planat-Benard, V.; Vellas, B.; Casteilla, L.; de Souto-Barreto, P. Periostin Plasma Levels and Changes on Physical and Cognitive Capacities in Community-Dwelling Older Adults. *J. Gerontol. A Biol. Sci. Med. Sci.* **2023**, *78*, 424–432. [CrossRef]
34. Kim, H.J.; Park, J.C.; Jung, K.S.; Kim, J.; Jang, J.S.; Kwon, S.; Byun, M.S.; Yi, D.; Byeon, G.; Jung, G.; et al. The clinical use of blood-test factors for Alzheimer's disease: Improving the prediction of cerebral amyloid deposition by the QPLEX(TM) Alz plus assay kit. *Exp. Mol. Med.* **2021**, *53*, 1046–1054. [CrossRef]
35. Lee, D.; Park, J.C.; Jung, K.S.; Kim, J.; Jang, J.S.; Kwon, S.; Byun, M.S.; Yi, D.; Byeon, G.; Jung, G.; et al. Application of QPLEX(TM) biomarkers in cognitively normal individuals across a broad age range and diverse regions with cerebral amyloid deposition. *Exp. Mol. Med.* **2022**, *54*, 61–71. [CrossRef]
36. Carey, M.; Mansfield, E.; Cameron, E.; Boyes, A.; Browne, W.; Dizon, J.; Sanson-Fisher, R. Depression and thoughts of self-harm and suicide among people living with dementia: Results of a cross-sectional survey. *Psychogeriatrics* **2023**. [CrossRef]
37. Psych-Congress-Network. Mini-Mental State Examination (MMSE). 2016. Available online: https://www.hmpgloballearningnetwork.com/site/pcn/mini-mental-state-examination-mmse (accessed on 1 June 2023).
38. Arrighi, H.M.; Neumann, P.J.; Lieberburg, I.M.; Townsend, R.J. Lethality of Alzheimer disease and its impact on nursing home placement. *Alzheimer Dis. Assoc. Disord.* **2010**, *24*, 90–95. [CrossRef]
39. Reid, I.A. Interactions between ANG II, sympathetic nervous system, and baroreceptor reflexes in regulation of blood pressure. *Am. J. Physiol.* **1992**, *262*, E763–E778. [CrossRef]
40. Inagami, T. The renin-angiotensin system. *Essays Biochem.* **1994**, *28*, 147–164.
41. Oba, R.; Igarashi, A.; Kamata, M.; Nagata, K.; Takano, S.; Nakagawa, H. The N-terminal active centre of human angiotensin-converting enzyme degrades Alzheimer amyloid beta-peptide. *Eur. J. Neurosci.* **2005**, *21*, 733–740. [CrossRef]

42. Hemming, M.L.; Selkoe, D.J. Amyloid beta-protein is degraded by cellular angiotensin-converting enzyme (ACE) and elevated by an ACE inhibitor. *J. Biol. Chem.* **2005**, *280*, 37644–37650. [CrossRef]
43. Hu, J.; Igarashi, A.; Kamata, M.; Nakagawa, H. Angiotensin-converting enzyme degrades Alzheimer amyloid beta-peptide (A beta); retards A beta aggregation, deposition, fibril formation; and inhibits cytotoxicity. *J. Biol. Chem.* **2001**, *276*, 47863–47868. [CrossRef]
44. Jochemsen, H.M.; Teunissen, C.E.; Ashby, E.L.; van der Flier, W.M.; Jones, R.E.; Geerlings, M.I.; Scheltens, P.; Kehoe, P.G.; Muller, M. The association of angiotensin-converting enzyme with biomarkers for Alzheimer's disease. *Alzheimers Res. Ther.* **2014**, *6*, 27. [CrossRef]
45. Johansson, M.W.; Annis, D.S.; Mosher, D.F. alpha(M)beta(2) integrin-mediated adhesion and motility of IL-5-stimulated eosinophils on periostin. *Am. J. Respir. Cell Mol. Biol.* **2013**, *48*, 503–510. [CrossRef]
46. Liu, A.Y.; Zheng, H.; Ouyang, G. Periostin, a multifunctional matricellular protein in inflammatory and tumor microenvironments. *Matrix Biol.* **2014**, *37*, 150–156. [CrossRef]
47. Inoue, M.; Yagishita, S.; Itoh, Y.; Koyano, S.; Amano, N.; Matsushita, M. Eosinophilic bodies in the cerebral cortex of Alzheimer's disease cases. *Acta Neuropathol.* **1996**, *92*, 555–561. [CrossRef]
48. Laubli, H.; Alisson-Silva, F.; Stanczak, M.A.; Siddiqui, S.S.; Deng, L.; Verhagen, A.; Varki, N.; Varki, A. Lectin galactoside-binding soluble 3 binding protein (LGALS3BP) is a tumor-associated immunomodulatory ligand for CD33-related Siglecs. *J. Biol. Chem.* **2014**, *289*, 33481–33491. [CrossRef]
49. Inohara, H.; Raz, A. Identification of human melanoma cellular and secreted ligands for galectin-3. *Biochem. Biophys. Res. Commun.* **1994**, *201*, 1366–1375. [CrossRef]
50. Patel, S.; Wei, J.; Shi, Z.; Rifkin, A.S.; Zheng, S.L.; Gelfman, E.; Duggan, D.; Helfand, B.T.; Hulick, P.J.; Xu, J. Refining Risk for Alzheimer's Disease Among Heterozygous APOEvarepsilon4 Carriers. *J. Alzheimers Dis.* **2023**, 1–7. [CrossRef]
51. Wang, J.; Wang, M.; Ren, S.; Huang, L.; He, K.; Li, J.; Hua, F.; Guan, Y.; Guo, Q.; Huang, Q.; et al. The Effect of Gender and APOE varepsilon4 Status on Brain Amyloid-beta Deposition in Different Age Groups of Mild Cognitively Impaired Individuals: A PET-CT Study. *J. Alzheimers Dis.* **2023**, 1–13. [CrossRef]
52. Gomar, J.J.; Bobes-Bascaran, M.T.; Conejero-Goldberg, C.; Davies, P.; Goldberg, T.E. Alzheimer's Disease Neuroimaging, I. Utility of combinations of biomarkers, cognitive markers, and risk factors to predict conversion from mild cognitive impairment to Alzheimer disease in patients in the Alzheimer's disease neuroimaging initiative. *Arch. Gen. Psychiatry* **2011**, *68*, 961–969. [CrossRef]
53. Shaffer, J.L.; Petrella, J.R.; Sheldon, F.C.; Choudhury, K.R.; Calhoun, V.D.; Coleman, R.E.; Doraiswamy, P.M. Alzheimer's Disease Neuroimaging, I. Predicting cognitive decline in subjects at risk for Alzheimer disease by using combined cerebrospinal fluid, MR imaging, and PET biomarkers. *Radiology* **2013**, *266*, 583–591. [CrossRef]
54. Frolich, L.; Peters, O.; Lewczuk, P.; Gruber, O.; Teipel, S.J.; Gertz, H.J.; Jahn, H.; Jessen, F.; Kurz, A.; Luckhaus, C.; et al. Incremental value of biomarker combinations to predict progression of mild cognitive impairment to Alzheimer's dementia. *Alzheimers Res. Ther.* **2017**, *9*, 84. [CrossRef]
55. Jammeh, E.; Zhao, P.; Carroll, C.; Pearson, S.; Ifeachor, E. Identification of blood biomarkers for use in point of care diagnosis tool for Alzheimer's disease. In Proceedings of the 38th Annual International Conference of the IEEE Engineering in Medicine and Biology Society (EMBC), Orlando, FL, USA, 16–20 August 2016; pp. 2415–2418. [CrossRef]
56. Kitamura, Y.; Usami, R.; Ichihara, S.; Kida, H.; Satoh, M.; Tomimoto, H.; Murata, M.; Oikawa, S. Plasma protein profiling for potential biomarkers in the early diagnosis of Alzheimer's disease. *Neurol. Res.* **2017**, *39*, 231–238. [CrossRef]
57. Mattsson, N.; Andreasson, U.; Zetterberg, H.; Blennow, K. Alzheimer's Disease Neuroimaging, I. Association of Plasma Neurofilament Light with Neurodegeneration in Patients with Alzheimer Disease. *JAMA Neurol.* **2017**, *74*, 557–566. [CrossRef]
58. O'Bryant, S.E.; Mielke, M.M.; Rissman, R.A.; Lista, S.; Vanderstichele, H.; Zetterberg, H.; Lewczuk, P.; Posner, H.; Hall, J.; Johnson, L.; et al. Blood-based biomarkers in Alzheimer disease: Current state of the science and a novel collaborative paradigm for advancing from discovery to clinic. *Alzheimers Dement.* **2017**, *13*, 45–58. [CrossRef]
59. Altuna-Azkargorta, M.; Mendioroz-Iriarte, M. Blood biomarkers in Alzheimer's disease. *Neurologia* **2021**, *36*, 704–710. [CrossRef]
60. Jung, S.H.; Kim, H.R.; Chun, M.Y.; Jang, H.; Cho, M.; Kim, B.; Kim, S.; Jeong, J.H.; Yoon, S.J.; Park, K.W.; et al. Transferability of Alzheimer Disease Polygenic Risk Score Across Populations and Its Association with Alzheimer Disease-Related Phenotypes. *JAMA Netw. Open* **2022**, *5*, e2247162. [CrossRef]
61. Chin, J.; Kim, D.E.; Lee, H.; Yun, J.; Lee, B.H.; Park, J.; Yeom, J.; Shin, D.S.; Na, D.L. A Validation Study of the Inbrain CST: A Tablet Computer-based Cognitive Screening Test for Elderly People with Cognitive Impairment. *J. Korean Med. Sci.* **2020**, *35*, e292. [CrossRef]
62. Molinuevo, J.L.; Rabin, L.A.; Amariglio, R.; Buckley, R.; Dubois, B.; Ellis, K.A.; Ewers, M.; Hampel, H.; Kloppel, S.; Rami, L.; et al. Implementation of subjective cognitive decline criteria in research studies. *Alzheimers Dement.* **2017**, *13*, 296–311. [CrossRef]
63. Petersen, R.C.; Smith, G.E.; Waring, S.C.; Ivnik, R.J.; Tangalos, E.G.; Kokmen, E. Mild cognitive impairment: Clinical characterization and outcome. *Arch. Neurol.* **1999**, *56*, 303–308. [CrossRef]
64. Jack, C.R., Jr.; Bennett, D.A.; Blennow, K.; Carrillo, M.C.; Dunn, B.; Haeberlein, S.B.; Holtzman, D.M.; Jagust, W.; Jessen, F.; Karlawish, J.; et al. Contributors. NIA-AA Research Framework: Toward a biological definition of Alzheimer's disease. *Alzheimers Dement.* **2018**, *14*, 535–562. [CrossRef]

65. Kang, S.H.; Lee, K.H.; Chang, Y.; Choe, Y.S.; Kim, J.P.; Jang, H.; Shin, H.Y.; Kim, H.J.; Koh, S.B.; Na, D.L.; et al. Gender-specific relationship between thigh muscle and fat mass and brain amyloid-beta positivity. *Alzheimers Res. Ther.* **2022**, *14*, 145. [CrossRef]
66. Kim, K.W.; Woo, S.Y.; Kim, S.; Jang, H.; Kim, Y.; Cho, S.H.; Kim, S.E.; Kim, S.J.; Shin, B.S.; Kim, H.J.; et al. Disease progression modeling of Alzheimer's disease according to education level. *Sci. Rep.* **2020**, *10*, 16808. [CrossRef]
67. Ong, H.L.; Subramaniam, M.; Abdin, E.; Wang, P.; Vaingankar, J.A.; Lee, S.P.; Shafie, S.; Seow, E.; Chong, S.A. Performance of Mini-Mental State Examination (MMSE) in long-stay patients with schizophrenia or schizoaffective disorders in a psychiatric institute. *Psychiatry Res.* **2016**, *241*, 256–262. [CrossRef]
68. Iqbal, G.; Braidy, N.; Ahmed, T. Blood-Based Biomarkers for Predictive Diagnosis of Cognitive Impairment in a Pakistani Population. *Front. Aging Neurosci.* **2020**, *12*, 223. [CrossRef]
69. Eftychios, A. Alzheimer Disease and Music-Therapy: An Interesting Therapeutic Challenge and Proposal. *Advances in Alzheimer's Disease* **2021**, *10*, 1–18. [CrossRef]
70. Morris, J.C. Clinical dementia rating: A reliable and valid diagnostic and staging measure for dementia of the Alzheimer type. *Int. Psychogeriatr.* **1997**, *9* (Suppl. 1), 173–176, discussion 177–178. [CrossRef]
71. Bae, J.N.; Cho, M.J. Development of the Korean version of the Geriatric Depression Scale and its short form among elderly psychiatric patients. *J. Psychosom. Res.* **2004**, *57*, 297–305. [CrossRef]
72. Sheikh, J.I.; Yesavage, J.A. Geriatric Depression Scale (GDS): Recent evidence and development of a shorter version. *Clin. Gerontol. J. Aging Ment. Health* **1986**, *5*, 165–173. [CrossRef]
73. Kim, Y.; Jang, H.; Kim, S.J.; Cho, S.H.; Kim, S.E.; Kim, S.T.; Kim, H.J.; Moon, S.H.; Ewers, M.; Im, K.; et al. Vascular Effects on Depressive Symptoms in Cognitive Impairment. *J. Alzheimers Dis.* **2018**, *65*, 597–605. [CrossRef]
74. Min, K.C.; Kim, E.H.; Woo, H.S.; Song, C.S. Effectiveness of an Online Dementia Prevention Program on Cognitive Function and Depression in Community-Dwelling Older Adults during the COVID-19 Pandemic in Korea. *Healthcare* **2023**, *11*, 1376. [CrossRef]
75. Sinha, S.P.; Shrivastava, S.R.; Ramasamy, J. Depression in an older adult rural population in India. *MEDICC Rev.* **2013**, *15*, 41–44. [CrossRef]
76. Nikmat, A.W.; Azhar, Z.I.; Shuib, N.; Hashim, N.A. Psychometric Properties of Geriatric Depression Scale (Malay Version) in Elderly with Cognitive Impairment. *Malays. J. Med. Sci.* **2021**, *28*, 97–104. [CrossRef] [PubMed]
77. Kim, H.; Kim, J.; Kim, E.G.; Heinz, A.J.; Kwon, S.; Chun, H. Optofluidic in situ maskless lithography of charge selective nanoporous hydrogel for DNA preconcentration. *Biomicrofluidics* **2010**, *4*, 43014. [CrossRef]
78. Kim, L.N.; Kim, M.; Jung, K.; Bae, H.J.; Jang, J.; Jung, Y.; Kim, J.; Kwon, S. Shape-encoded silica microparticles for multiplexed bioassays. *Chem. Commun.* **2015**, *51*, 12130–12133. [CrossRef]

International Journal of
Molecular Sciences

MDPI

Article

ARL6IP5 Ameliorates α-Synuclein Burden by Inducing Autophagy via Preventing Ubiquitination and Degradation of ATG12

Ibrar Siddique †, Kajal Kamble ‡, Sakshi Gupta ‡, Kavita Solanki, Sumnil Bhola, Nuzhat Ahsan and Sarika Gupta *

Molecular Science Laboratory, National Institute of Immunology, New Delhi 110067, India
* Correspondence: sarika@nii.ac.in; Tel.: +91-11-2670-3666
† Current address: Department of Neurology, David Geffen School of Medicine, University of California, Los Angeles, CA 90095, USA.
‡ These authors contributed equally to this work.

Abstract: Recent advanced studies in neurodegenerative diseases have revealed several links connecting autophagy and neurodegeneration. Autophagy is the major cellular degradation process for the removal of toxic protein aggregates responsible for neurodegenerative diseases. More than 30 autophagy-related proteins have been identified as directly participating in the autophagy process. Proteins regulating the process of autophagy are much more numerous and unknown. To address this, in our present study, we identified a novel regulator (ARL6IP5) of neuronal autophagy and showed that the level of ARL6IP5 decreases in the brain with age and in Parkinson's disease in mice and humans. Moreover, a cellular model of PD (Wild type and A53T mutant α-synuclein overexpression) has also shown decreased levels of ARL6IP5. ARL6IP5 overexpression reduces α-synuclein aggregate burden and improves cell survival in an A53T model of Parkinson's disease. Interestingly, detailed mechanistic studies revealed that ARL6IP5 is an autophagy inducer. ARL6IP5 enhances Rab1-dependent autophagosome initiation and elongation by stabilizing free ATG12. We report for the first time that α-synuclein downregulates ARL6IP5 to inhibit autophagy-dependent clearance of toxic aggregates that exacerbate neurodegeneration.

Keywords: ARL6IP5 (ADP-ribosylation-like factor 6 interacting protein 5); Parkinson's disease (PD); autophagy; neurodegeneration; α-synuclein; SH-SY5Y cells

Citation: Siddique, I.; Kamble, K.; Gupta, S.; Solanki, K.; Bhola, S.; Ahsan, N.; Gupta, S. ARL6IP5 Ameliorates α-Synuclein Burden by Inducing Autophagy via Preventing Ubiquitination and Degradation of ATG12. *Int. J. Mol. Sci.* **2023**, *24*, 10499. https://doi.org/10.3390/ijms241310499

Academic Editor: Claudia Ricci

Received: 14 May 2023
Revised: 1 June 2023
Accepted: 1 June 2023
Published: 22 June 2023

1. Introduction

Parkinson's disease (PD) is the second most fatal neurodegenerative disorder, identified by neuronal degeneration in the substantia nigra pars compacta (SNpc) and intracellular deposition of Lewy bodies [1]. The most common symptoms of PD are divided into motor and non-motor symptoms. Motor symptoms include mainly tremor, bradykinesia, and rigidity, while non-motor symptoms consist of rapid eye movement, sleeping disorder, olfactory dysfunction, anosmia, constipation, urinary dysfunction, cognitive impairment, and depression [2]. There is still no clear understanding of the etiology of Parkinson's disease, despite decades of vigorous research. As existing treatments provide only symptomatic relief, there is a high need for therapeutic strategies to reduce the accumulated α-synuclein (SNCA) level in neurons. Neurons are post-mitotic cells that highly depend on the basal autophagy to maintain their proteostasis.

The ubiquitin proteasomal system (UPS) and autophagy are the two main protein degradation pathways of eukaryotes. UPS degrades short-lived soluble proteins, while autophagy degrades long-lived insoluble aggregates [3]. As a result of autophagy, cells survive adverse conditions, such as nutrient deprivation, the accumulation of aggregated proteins, the emergence of damaged organelles, and the recycling of receptors. Autophagy

plays a pivotal role in maintaining protein homeostasis. Dysfunctional autophagy was identified as the main cause of many neurodegenerative disorders [4]. The process of autophagy can be divided into mechanistically distinct steps, which include induction, cargo recognition and selection, autophagosome formation, autophagosome-lysosome fusion, and breakdown of the cargo followed by release of the degradation products in the form of small peptides back into the cytoplasm [5]. The 1990s saw an era of autophagy research, leading to the characterization of this phenomenon at the molecular level [6]. In 1993, Tsukada and Ohsumi performed the isolation and characterization of 15 *S. cerevisiae* mutants that displayed defective autophagy and named them *apg1-15* (autophagy) [7]. Further research was done to find the more defective mutants by other researchers. In 2003, a unified nomenclature for the so-called autophagy-related genes/proteins, ATGs, was proposed [8]. Recently, yeast ATG39 and ATG40 have been identified as receptors that are apparently involved in the selective removal of the cytoplasmic and perinuclear ER and the nucleus [9]. Most of the yeast ATG proteins have mammalian homologs [10]. Different sets of ATG proteins are involved in these steps and comprise the core autophagic machinery. Besides the ATG proteins, certain non-ATG proteins are required for autophagy, such as certain specific Sec-proteins that are important for autophagosome formation [11]. Moreover, Trs85 is another protein that is a component in the TRAPP (transport protein particle) complexes, which mediate ER-to-Golgi and intra-Golgi trafficking and are found in both nonselective autophagy and selective autophagy [12]. The number of such autophagy-regulating proteins is increasing with research.

ADP-ribosylation-like factor 6 interacting protein 5 (ARL6IP5) is also known as JWA in humans, Addicsin in mice, and GTRAP 3-18 or JM4 in rats [13]. This protein belongs to the PRAF3 family as it has a functionally large prenylated acceptor domain 1, mainly involved in intracellular protein trafficking [14]. ARL6IP5 is an established negative regulator of the EAAC1 transporter [15]. This protein has been extensively studied in the field of cancer metastasis, yet the functions of ARL6IP5 are less well characterized [16–18]. In a small study, siRNA ARL6IP5 expression reduced autophagy in cancer cells [19]. In the present study, we identified ARL6IP5 as an ATG12 interacting protein and a novel regulator/inducer of autophagy that could reduce α-synuclein aggregates in situ. Our detailed findings thereby establish the critical role of the ARL6IP5/Rab1/ATG12 axis for neuroprotection in PD.

2. Results

2.1. The Level of ARL6IP5 Decreases with Age and Parkinson's Disease

To study the role of ARL6IP5 in aging and neurodegenerative diseases, we checked the age-dependent (4, 8, and 12 months) change in the level of ARL6IP5 in the wild-type C57BL6 mouse brain (WT) and PD transgenic mouse model (A53T mutant) (Tg) (Figure 1A,B). We observed a decrease in ARL6IP5 level with aging in both WT and Tg mice. For WT mice, there was a decrease 25 $\pm$ 7%, p = 0.12, n = 3 and 44 $\pm$ 17%, p = 0.0015, n = 3 at the age of 8 months and 12 months, respectively, in the ARL6IP5 level as compared to 4 months. Tg mice had a trend showing lower levels of ARL6IP5 as compared to wild-type controls for all time points but with high p-value (Figure 1A,B). Data clearly suggest that ARL6IP5 levels decline with aging, which shows a synergic effect with α-synuclein overexpression.

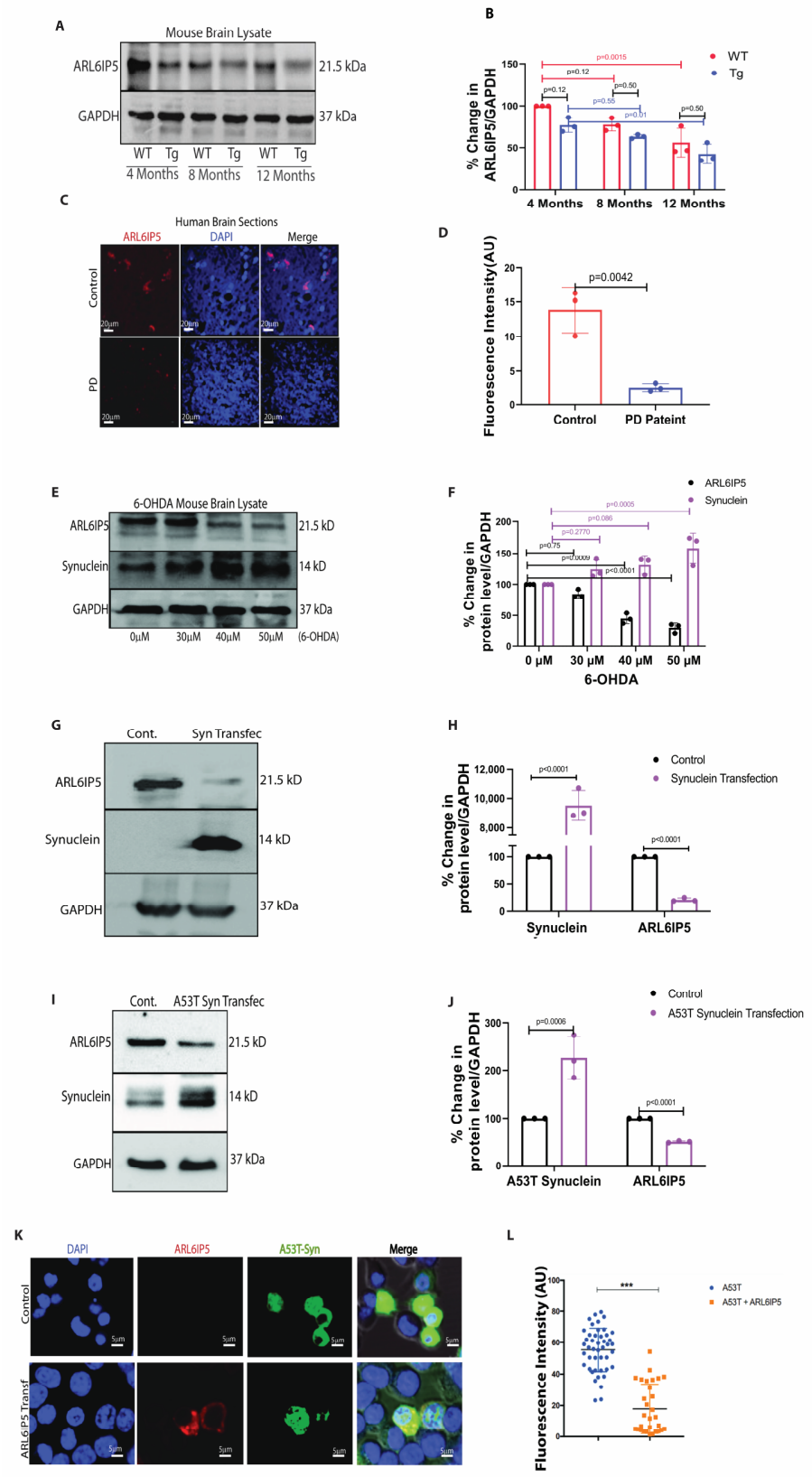

Figure 1. ARL6IP5 level decreases with age and PD. (**A**) Immunoblot showing age-dependent protein level of ARL6IP5 in WT and Tg mice brains. (**B**) Densitometric analysis of ARL6IP5 in the WT and Tg brains with respect to loading control GAPDH. *p*-value was calculated using two-way ANOVA with post hoc Tukey test. (**C**) ARL6IP5 (red) signals were detected in Parkinson's patients and control sample's mid-brain sections, as shown in representative IHC images. Scale bars, 20 µm.

(**D**) Graph showing fluorescence intensity quantification. *p*-value was calculated using unpaired two-tailed Student *t*-test. (**E**) Immunoblots showing protein level of ARL6IP5 and α-synuclein upon treatment of 30, 40, 50 μM 6-OHDA for 30 days (**F**) Graph showing the densitometric analysis of ARL6IP5 level in 6-OHDA treated mice brains using GAPDH as a loading control. *p*-value was calculated using two-way ANOVA with Tukey post hoc method. (**G**) Immunoblots showing protein level of ARL6IP5 in α-synuclein overexpressed stable SH-SY5Y cells. (**H**) Densitometric analysis of ARL6IP5 in SH-SY5Y cells stably expressing α-synuclein as shown in graph with GAPDH as a loading control. *p*-value was calculated using one-way ANOVA with post hoc Tukey test. (**I**) Decreased ARL6IP5 protein level in A53T over expressed stable SH-SY5Y cells. (**J**) Graph showing densitometric analysis of ARL6IP5 in A53T overexpressed stable SHSY-5Y cells. *p*-value was calculated using one-way ANOVA with post hoc Tukey test. (**K**) Immunofluorescence representative image of SH-SY5Y cells expressing GFP-α-synuclein (green), stained for ARL6IP5 (red) in normal and ARL6IP5 overexpressing condition and nucleus (blue). Scale bars, 5 μm. (**L**) Graph showing the fluorescence intensity of A53T-α-synuclein in control and ARL6IP5 overexpressing condition, $n = 40$ cells were analyzed randomly. *p*-value was calculated using unpaired two-tailed Student *t*-test. *** $p < 0.001$. Results from three independent experiments are presented.

To revalidate our immunoblot data, we performed immunofluorescence in the brain sections of the WT and Tg mice models of PD at 12 months of age. As shown in Supplementary Figure S1A,B, the α-synuclein aggregate burden was higher (56 ± 19%, $p = 0.0039$, $n = 3$) in the Tg mouse model of PD compared to WT and agrees with the disease burden, and ARL6IP5 was decreased (71 ± 14%, $p = 0.0002$, $n = 3$) as compared to WT. After confirming the disease burden histologically in mice, we detected the level of ARL6IP5 in the human brain sections and were excited to see the decrease (85 ± 28%, $p = 0.0042$, $n = 3$) in its level in the PD patients' brain samples as compared to healthy controls (Figure 1C,D). Additionally, we assessed the level of ARL6IP5 in the brain lysates of 6-OHDA-induced Parkinson's disease in mice. 6-hydroxydopamine (6-OHDA) is a synthetic organic neurotoxin. Injection of the neurotoxin, 6-OHDA in substantia niagra of brain reproduces several non-motor comorbidities commonly associated with PD, including cognitive deficits, depression, anxiety and deposition of α-synuclein in the brain [20,21]. C57BL6 mice were intracranially injected with various doses of 6-OHDA stereotaxically or injected with vehicle to further validate our findings. Interestingly, the level of ARL6IP5 significantly decreases (20 ± 11% $p = 0.75$, $n = 3$, 60 ± 23%, $p = 0.0009$, $n = 3$, and 75 ± 15% $p < 0.0001$, $n = 3$ at the doses of 30 μM, 40 μM, and 50 μM, respectively) in the 6-OHDA-induced mouse model of PD as compared to the sham control (Figure 1E,F).

To further understand the role of ARL6IP5 in neurodegeneration, we developed a cellular model of PD by stably expressing wild-type and A53T mutant α-synuclein in the SHSY5Y neuronal cell line. In accordance with animal data, there was a significant reduction (80 ± 24%, $p < 0.0001$, $n = 3$) in ARL6IP5 levels in cells overexpressing α-synuclein and reduction (60 ± 25%, $p < 0.0001$, $n = 3$) in A53T mutant α-synuclein overexpression compared to control cells (Figure 1I,J). SH-SY5Y cells stably expressing mutant GFP-A53T α-synuclein were transfected with ARL6IP5, and the level of green fluorescence (as a measure of expression of A53T α-synuclein) was measured. We found a decrease (28 ± 33 in ARL6IP5 transfected cells from 58 ± 24 in control cells, $p < 0.0001$) in the level of A53T-α-synuclein fluorescence with ARL6IP5 expression (Figure 1K,L). This indicates a direct role of ARL6IP5 in aging and PD-like neurodegenerative diseases.

2.2. Beneficial Role of ARL6IP5 Overexpression in PD

Having learned that α-synuclein (WT/A53T) overexpression reduces ARL6IP5 levels, we wanted to check the change in toxicity and aggregate of α-synuclein (WT/A53T) when the level of ARL6IP5 is overexpressed. The toxicity of cellular aggregate was checked using the A11 antibody as previously described [22]. We were delighted to detect a significant reduction in A11 reactivity (31 ± 15%, $p = 0.49$, $n = 3$ in α-synuclein, and 20 ± 16%, $p = 0.47$, $n = 3$ in A53T) with ARL6IP5 overexpression as compared to the basal ARL6IP5 condition

(Figure 2A,B). To further confirm the beneficial role of ARL6IP5, we carried out siRNA-mediated knockdown of ARL6IP5 in a cellular model of PD. The toxicity was confirmed with the LDH assay, α-synuclein overexpression in the knockdown condition of ARL6IP5 shows more (15 ± 7%, $p = 0.018$, $n = 6$) toxicity than α-synuclein overexpression alone (Figure 2C).

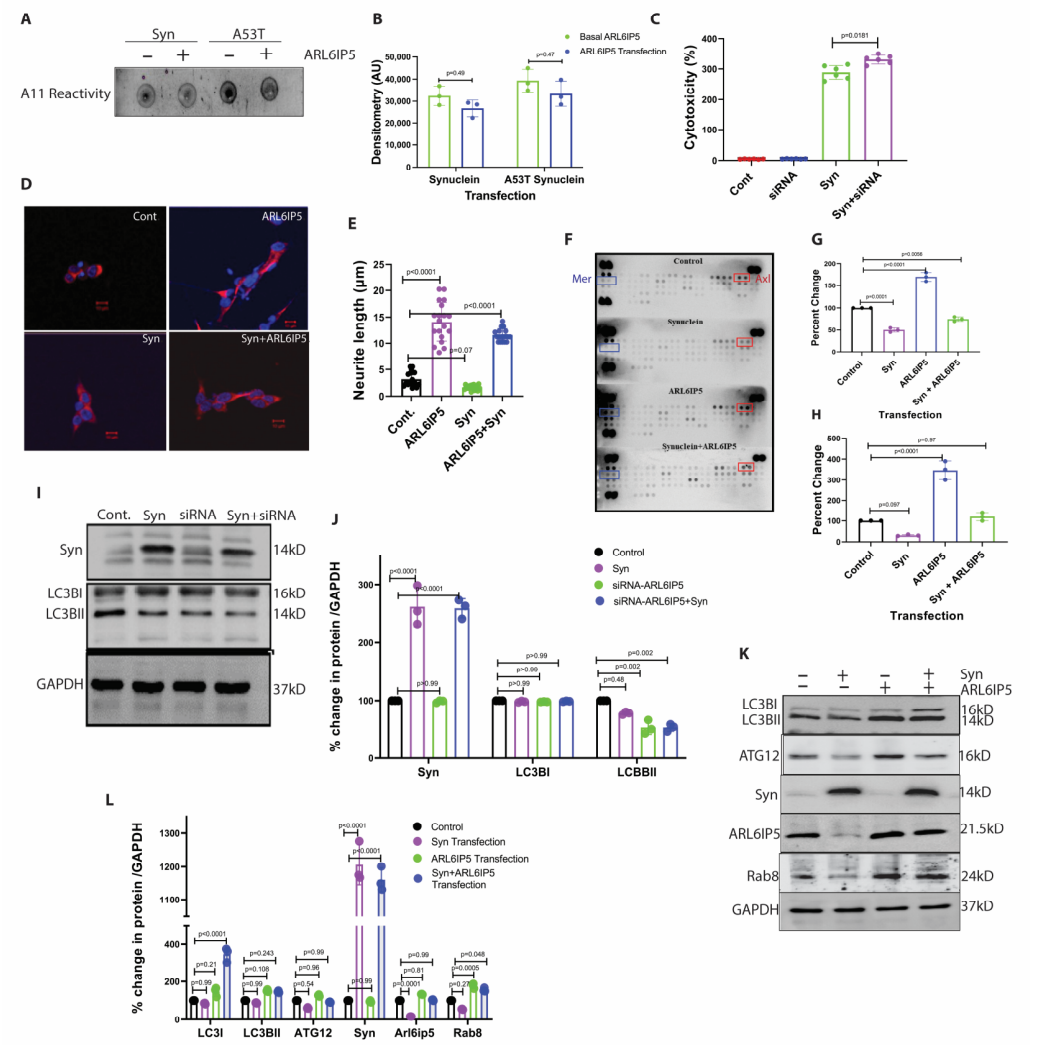

Figure 2. ARL6IP5 overexpression reduces α-synuclein aggregates burden and induces differentiation. (**A**) Representative dot-blot showing A11 reactivity for α-synuclein aggregates in the basal and overexpressed ARL6IP5 condition. (**B**) Densitometric analysis of A11 reactivity. *p*-value was calculated using one-way ANOVA with post hoc Tukey test. (**C**) Graph showing LDH activity in the supernatant samples from control, ARL6IP5 knockdown condition, in α-synuclein overexpressed stable cell line, and in knockdown ARL6IP5 and α-synuclein overexpressed condition. *p*-value was calculated using one-way ANOVA with Tukey test. (**D**) Representative confocal images of SH-SY5Y cells stained for MAP-2 (red). The nuclei are stained with DAPI (blue) for reference. n = 25. Scale bars, 10 µm. Neurite length was measured using the Image-J software version 1.53t. (**E**) Graph showing neurite lengths of SH-SY5Y cells in control, ARL6IP5 overexpressing, α-synuclein overexpressing, and ARL6IP5 and α-synuclein co-expressing conditions. *p*-value was calculated using one-way ANOVA with Tukey test. (**F**) Phospho-kinase array showing the Mer and Axl kinase levels in control, α-synuclein overexpressing, ARL6IP5 overexpressing, and α-synuclein and ARL6IP5 co-expressing conditions. (**G**,**H**) Graph showing the densitometric analysis of Mer and Axl levels, respectively. *p*-value was calculated using one-way ANOVA with post hoc Tukey test. (**I**) Representative blot showing the levels of autophagy proteins LC3BI, and LC3BII in control, α-synuclein overexpressing, ARL6IP5 knockdown, and ARL6IP5 knockdown condition with overexpressing α-synuclein, while

GAPDH was used as the loading control. (**J**) Densitometric analysis graph of α-synuclein, LC3B1 and LC3BII. *p*-value was calculated using two-way ANOVA with post hoc Tukey test. (**K**) Representative blot showing the levels of LC3BI, LC3BII, ATG12, α-synuclein ARL6IP5, and Rab8 in control, α-synuclein overexpressing, ARL6IP5 overexpressing, and α-synuclein and ARL6IP5 co-expressing conditions. (**L**) Densitometric analysis of LC3BI, LC3BII, ATG12, α-synuclein, ARL6IP5, and Rab8. *p*-value was calculated using two-way ANOVA with post hoc Tukey test. Results from three independent experiments are presented.

Till now, our study has confirmed the beneficial role of ARL6IP5 in preventing disease pathogenesis by reducing the burden and toxicity of α-synuclein aggregates. Thus, we proceeded to investigate the molecular mechanisms that ensure cell viability. Subsequently, we planned to investigate the underlying pathways. We studied the effect of ARL6IP5 on cell differentiation and surface receptor tyrosine kinase. The microscopic studies have shown that overexpression of ARL6IP5 induces neuronal differentiation, which was further confirmed by neurite length, which was found to increase (3 ± 2 μm in normal condition to 13 ± 5 μm in ARL6IP5 overexpression condition, $p < 0.0001$, $n = 20$), while α-synuclein overexpression reduced neurite length, which was again restored after co-expression of ARL6IP5 (2 ± 1 μm in α-synuclein overexpression and 11 ± 4 μm in overexpression condition, $p < 0.0001$, $n = 20$) (Figure 2D,E). The role of TAM receptors in neuronal survival and pathological protein aggregate clearance has been suggested [23]. We decided to check using Receptor tyrosine kinase (RTK) array analysis, which revealed a significant increase in the phosphorylation of the TAM receptor family kinases Axl and Mer (Figure 2F–H) in ARL6IP5 overexpression. For Axl, α-synuclein overexpression reduced ($54 \pm 11\%$, $p < 0.0001$, $n = 3$ as compared to control) its phosphorylation, which was increased ($171 \pm 32\%$, $p < 0.0001$, $n = 3$ as compared to control) in the ARL6IP5 overexpressing condition, and phosphorylation was restored ($72 \pm 35\%$, $p = 0.056$, $n = 3$ as compared to control) in co-expression. For Mer, α-synuclein overexpression reduced ($74 \pm 15\%$, $p = 0.097$, $n = 3$ as compared to control) its phosphorylation, which was increased ($321 \pm 24\%$, $p < 0.0001$, $n = 3$ as compared to control) in ARL6IP5 overexpressing condition, and phosphorylation was restored ($110 \pm 34\%$, $p = 0.97$, $n = 3$ as compared to control) in co-expression. Together, all these results suggest that ARL6IP5 restores the cellular conditions that were altered by the overexpression of α-synuclein.

Next, we investigated the plausible cellular degradation pathways involved in the removal of α-synuclein cytosolic aggregates. We observed that overexpression of ARL6IP5 does not significantly affect the proteasomal degradation pathway (Supplementary Figure S2A–C). In the case of α-synuclein, chaperon-mediated degradation plays a pivotal role in reducing neurotoxicity [24], hence, we studied the levels of p62 and HSC-70 (Supplementary Figure S2D–I). However, no significant change in the levels of these chaperones was observed upon ARL6IP5 overexpression. Therefore, we ventured into studying the effect of ARL6IP5 overexpression on the cellular bulk degradation process, autophagy. LC3BI is a soluble protein and remains in the cytoplasm. During the formation of autophagosome, LC3BI converts into LC3BII and is incorporated into the membrane of the autophagosome. We measured autophagy by analyzing the level of LCBII, which is a standard marker of autophagy [25]. As shown in Figure 2I,J, the overexpression of α-synuclein disrupted/inhibited ($20 \pm 8\%$, $p = 0.48$, $n = 3$, as compared to control) the process of autophagy significantly, which was also inhibited ($45 \pm 13\%$, $p = 0.002$, $n = 3$ as compared to control) by the knockdown of ARL6IP5, and shows a synergic effect in inhibition of autophagy ($51 \pm 23\%$, $p = 0.002$, $n = 3$), when α-synuclein is overexpressed, and ARL6IP5 is knockdown. Results strongly suggest that ARL6IP5 increases autophagy, so we decided to overexpress ARL6IP5 in α-synuclein overexpression condition and see if it ameliorates the α-synuclein pathology condition via autophagy. Overexpression of ARL6IP5 increased ($150 \pm 54\%$, $p = 0.108$, $n = 3$ as compared to control) autophagy. Autophagy was also increased ($135 \pm 23\%$, $p = 0.243$, $n = 3$ as compared to control) by ARL6IP5 in α-synuclein overexpressing condition, which was decreased ($80 \pm 23\%$, $p = 0.99$, $n = 3$ as compared to control) in α-synuclein overexpressing

condition only. We also checked for the autophagy-related protein ATG12, which was decreased (60 ± 24%, $p = 0.54$, $n = 3$) in α-synuclein overexpressing condition and elevated (126 ± 30%, $p = 0.96$, $n = 3$ as compared to control) in ARL6IP5 overexpressing condition, which was normalized (92 ± 34%, $p = 0.99$, $n = 3$ as compared to control) when α-synuclein was co-expressed with ARL6IP5. Rab8 also has a role in autophagosome membrane maturation [26], so we also checked the level of Rab8. Rab8 followed the same pattern as ATG12 and was reduced (55 ± 25%, $p = 0.27$, $n = 3$) in α-synuclein overexpressing condition, upregulated (177 ± 45%, $p= 0.0005$, $n = 3$ as compared to control) in the ARL6IP5 overexpressing condition and remained upregulated (155 ± 46%, $p = 0.048$, $n = 3$ as compared to control) when ARL6IP5 and α-synuclein co-expressed together (Figure 2K,L). These data strongly support that ARL6IP5 upregulates autophagy, which needs to be investigated further.

2.3. ARL6IP5 Induces Autophagy Comparable to Other Standard Chemical Inducers in SH-SY5Y Cells

We performed a detailed study to understand the mechanism of ARL6IP5-induced autophagy in the neuron. Firstly, we compared the ARL6IP5-induced autophagy with other autophagy inducers. SH-SY5Y cells were grown to 60% confluency and transfected with 5 μg of the flag-ARL6IP5 construct for 36 h. For another method of autophagy induction, we used serum starvation for 2 h [27], rapamycin (1 μM) for 2 h [28], and MeβCD (100 μm) for 24 h [29,30]. ARL6IP5 overexpression increased 261 ± 11%, $p < 0.0001$ the level of LC3BII by, while serum starvation induced 162 ± 62%, $p = 0.107$, Rapamycin induced 254 ± 45%, $p = 0.74$ and MeβCD induced 167 ± 7%, $p = 0.365$ as compared to control. (Figure 3A,B). We also confirmed autophagy induction by ARL6IP5 using GFP-LC3BI [31], which is a soluble cytoplasmic protein. When autophagy is induced, GFP-LC3BI converts into GFP-LC3BII and becomes part of the autophagosome membrane, resulting in the formation of a fluorescence puncta [32]. We counted the number of autophagic puncta in randomly selected ~25 cells from each group. ARL6IP5 overexpressing cells found to have 32 ± 6, $p < 0.0001$ puncta, serum starvation has an average of 30 ± 5, $p < 0.0001$ puncta, rapamycin produced the 30 ± 6, $p < 0.0001$ puncta, MeβCD induced the number of puncta to 29 ± 5, $p < 0.0001$ as compared to control cells, showed an average of 8 ± 2.2 (Figure 3C,D). These findings suggest that ARL6IP5 overexpression induces autophagy, which is comparable in level to the autophagy induced with other standard methods. This suggests that ARL6IP5 may have a role in autophagy regulation, prompting us to investigate further detailed mechanisms.

For our next experiment, we used an empty vector as the transfection control to rule out the possibility of autophagy induction by the transfection reagent. We found a 195 ± 25%, $p = 0.0001$ increase in autophagy measured by the level of LC3BII after ARL6IP5 transfection. Only a marginal induction of 111 ± 10%, $p = 0.46$ percent, was observed after the transfection of empty vector as compared to control (Figure 3E,F). We further wanted to confirm the role of ARL6IP5 in autophagy by downregulating its expression. We transfected cells with siRNA of ARL6IP5 and confirmed the downregulation of protein to 16 ± 3 %, $p < 0.0001$ after 48 h using Western blot technique. When we re-probed the blot to see the level of autophagy using LC3BII, it was reduced to 58 ± 5%, $p < 0.0001$, as compared to control. (Figure 3G,H). We confirmed the phenomenon using GFP-LC3BI and found that the number of autophagy puncta was 8 ± 2 per cell in normal condition. The number of puncta per cell was increased to 32 ± 6, $p < 0.0001$ after ARL6IP5 transfection and reduced less than normal to 3 ± 1, $p = 0.47$ puncta per cell under ARL6IP5 knockdown condition as compared to control (Figure 3I,J).

Another critical question here is whether the autophagy induced by ARL6IP5 overexpression is typical and whether it causes bulk autophagic flux. To address this question, we used the mCherry-GFP-LC3BI vector, which allows us to track the different stages of autophagy [33]. In the absence of autophagy, RFP-GFP fluorescence in the cytoplasm results in combined yellow fluorescence. When autophagy is induced, this protein is incorporated into the autophagosome membrane, forming a yellow punctum. When the autophagosome

fuses with the lysosome, which has a low pH, the GFP protein is denaturized, and the green fluorescence is lost. The formation of red puncta indicates the fusion of the autophagosome with the lysosome, and the loss of fluorescence indicates the degradation of autophagosome cargo by autophagy (Figure 3K).

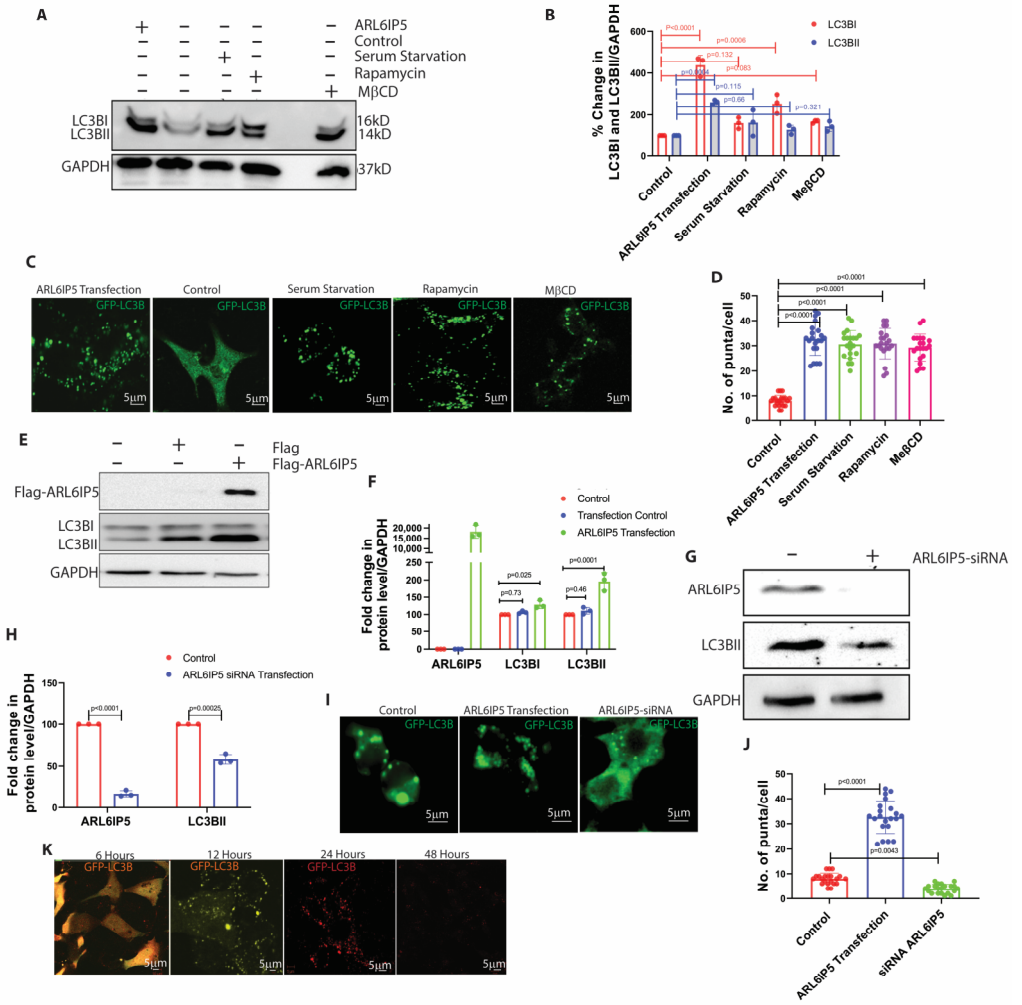

Figure 3. ARL6IP5 regulates autophagy. (**A**) Representative blot showing the levels of LC3BI, and LC3BII, in ARL6IP5 overexpressing, control, serum-starved, rapamycin-treated, and MβCD treated SH-SY5Y cells. GAPDH was used as the loading control. (**B**) Densitometric analysis of LC3BI and LC3BII is shown in image 3A. *p*-value was calculated using two-way ANOVA with post hoc Tukey test. (**C**) Representative confocal images showing the autophagy induction in the form of puncta formation in ARL6IP5 overexpressing, control, serum starved, rapamycin treated, and MβCD treated conditions. Scale bars, 5 μm. (**D**) Graph showing the number of puncta counted in ARL6IP5 overexpressing, control, serum-starved, rapamycin-treated, and MβCD treated conditions. $n = 25$ cells. *p*-value was calculated using one-way ANOVA with post hoc Tukey test. (**E**) Representative blot showing the levels of LC3BI and LC3BII in control and after Flag transfection, Flag-ARL6IP5 transfection conditions. (**F**) Densitometric analysis of the levels of LC3BI, and LC3BII in control, transfection control, and ARL6IP5 transfection conditions. *p*-value was calculated using one-way ANOVA with post hoc Tukey test. (**G**) Representative blot showing the level of LC3BII, in control and ARL6IP5 knockdown condition. (**H**) Densitometric analysis showing the level of ARL6IP5 and LC3BII in control and siRNA-ARL6IP5 knockdown condition. *p*-value was calculated using one-way ANOVA with post hoc Tukey test. (**I**) Representative confocal images showing the puncta formation levels in control, ARL6IP5 overexpressing, and ARL6IP5 knockdown conditions. $n = 25$. Scale bars, 5 μm. (**J**) Graph showing the number of puncta in individual cell in control, ARL6IP5 overexpressing, and knockdown conditions. *p*-value was calculated using one-way ANOVA with post hoc Tukey

test. (**K**) Representative confocal images showing the various stages of the autophagy process using GFP-RFP-LC3B. First panel shows the protein in the cytoplasm giving yellow fluorescence (scale bar, 5 μm), second panel shows the formation of autophagosome (scale bar, 5 μm), third panel shows the fusion of autophagosome with lysosome (scale bar, 5 μm), and fourth panel shows the degradation of autophagosomes (scale bar, 5 μm). Results from three independent experiments are presented.

2.4. ARL6IP5 Is a Downstream Autophagy Regulator

Next, we wanted to know whether ARL6IP5 overexpression induces autophagy to get rid of the toxic aggregates formed in the cell or if it is part of the typical autophagy induction process. We used standard chemical inducers to induce autophagy and measured the level of ARL6IP5 as autophagy increased. After treatment with rapamycin, serum starvation, MβCD and trehalose, the levels of LC3BII increased by 212 ±7, $p < 0.0001$, 265 ± 10, $p < 0.0001$, 169 ± 14, $p < 0.0001$ and 165 ± 12, $p < 0.0001$ percent, respectively, as compared to control. While the level of ARL6IP5 was also increased to 159 ± 8, $p < 0.0001$, 138 ± 6, $p < 0.0001$, 164 ± 2, $p < 0.0001$ and 133 ± 6, $p < 0.0001$ percent as compared to control, respectively (Figure 4A,B). We further wanted to check the level of autophagy induction using a chemical inducer in the ARL6IP5 knockdown condition. After ARL6IP5 suppression using siRNA, we induced autophagy with serum starvation, rapamycin, MeβCD, and trehalose and found 50 ± 3%, $p < 0.0001$, 76 ± 2%, $p < 0.0001$, 63 ± 0.2%, $p < 0.0001$ and 68 ± 3%, $p < 0.0001$ percent reductions in LC3BII levels as compared to control autophagy induction (Figure 4C,D). A significant decrease in autophagy level with autophagy inducer in ARL6IP5 knockdown conditions strongly suggests that ARL6IP5 is involved in the regulation of the process of autophagy.

2.5. ARL6IP5 Overexpression Increase ATG12 by Preventing Its Ubiquitination

The results strongly suggest that ARL6IP5 plays a role in the regulation of autophagy, making it worthwhile to investigate the mechanism by which ARL6IP5 induces autophagy. The first step was to check for the levels of other autophagy-related proteins in the ARL6IP5 overexpressed and downregulated conditions. Surprisingly, the only autophagy-related protein upregulated by ARL6IP5 overexpression was ATG12, which increased by 227 ± 57%, $p < 0.0001$ as compared to control (Figure 4E,F), while ATG5, which works with ATG12 in autophagic membrane propagation [34], remained unchanged (Figure 4E,F). The combined ATG5-ATG12 band was also increased by 308 ± 14%, $p < 0.0001$ with ARL6IP5 overexpression as compared to control, which was contributed solely by ATG12 (Figure 4E,F). ARL6IP5 and ATG12 expression were also checked by knocking down ARL6IP5, and as anticipated, the level of free ATG12 was drastically reduced to 15 ± 3%, $p < 0.0001$ (Figure 4G,H). There was no significant difference observed in the ATG5 and ATG5 + ATG12 levels.

To further understand the relationship between ARL6IP5 and ATG12, we decided to co-immunoprecipitate ARL6IP5 after overexpressing it for 24 h. We found that ATG5 and ATG12 co-immunoprecipitated with the ARL6IP5, suggesting their interactions (Figure 5A). We also confirmed this interaction by detecting flag-ARL6IP5 after immunoprecipitating ATG12 (Figure 5B). All co-immunoprecipitation experiments were conducted in the ARL6IP5 overexpression condition, and hence we decided to conduct further study in the presence of basal ARL6IP5 expression level. We found that ATG12 co-immunoprecipitated with basal ARL6IP5 (Figure 5C), indicating that these two proteins interact under normal cellular physiological conditions. We also checked the interaction of Rab1 and ARL6IP5, as previously reported [35], using co-immunoprecipitation (Figure 5D). Interaction was also confirmed by the co-immunofluorescence (Figure 5E). We found co-localization of the red (ARL6IP5) and green (ATG5/ATG12 (80 ± 23%, $n = 12$, and 86 ± 18%, $n = 12$, respectively) in the cells (Figure 5F). It was previously reported that ATG12 is a highly unstable protein when it is not combined with ATG5 and is susceptible to ubiquitination and proteasomal degradation [36]. ATG12 is a limiting factor in the process of autophagy, stabilization of ATG12 may lead to increased autophagy. Since we know that elevating cellular levels of

ATG12 through ARL6IP5 overexpression leads to increased autophagy, it is interesting to compare the levels of ATG12 ubiquitination under the overexpressing and downregulating conditions. We immunoprecipitated the ATG12 in the ARL6IP5 overexpressing condition and found a 56 ± 4%, $p = 0.0032$ reduction in ubiquitination and a 169 ± 19%, $p = 0.0001$ increase in ubiquitination after siRNA knockdown of ARL6IP5 as compared to control (Figure 5G–I). Taken together, these data suggest that ARL6IP5 interacts with ATG12 and prevents its ubiquitination, resulting in the upregulation of autophagy.

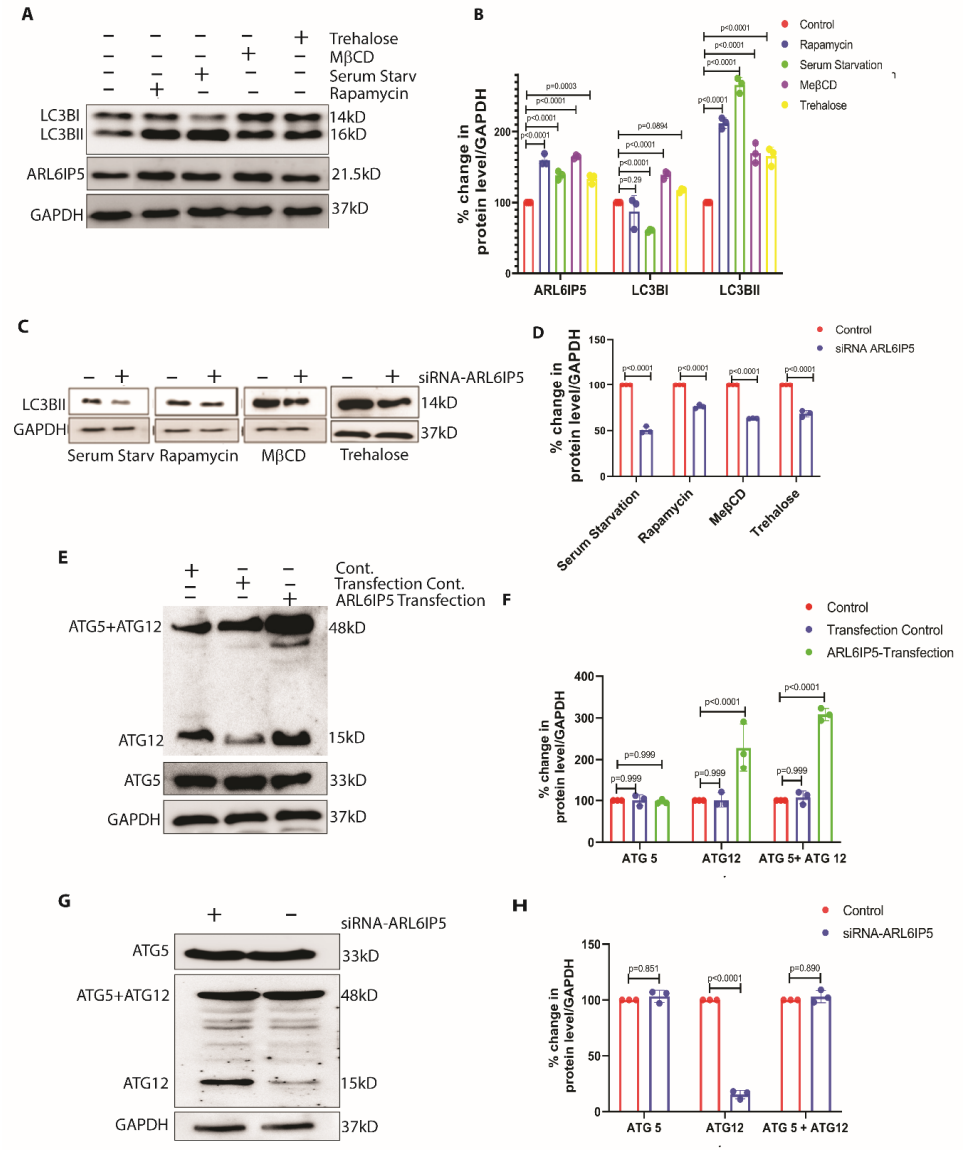

Figure 4. ARL6IP5 regulates autophagy via ATG12. (**A**) Representative blot showing the levels of LC3BI, LC3BII, and ARL6IP5 in control and after the induction of autophagy with Trehalose, MβCD, serum starvation, and rapamycin, respectively. (**B**) Graph showing the densitometric analysis of ARL6IP5, LC3B1 and LC3BII in control and with treatment with autophagy inducers shown in (**A**). *p*-value was calculated using two-way ANOVA with post hoc Tukey test. (**C**) Representative blot showing the levels of LC3BII, in control and ARL6IP5 knockdown conditions treated with autophagy inducers serum starvation, rapamycin, MβCD, and trehalose, respectively. (**D**) Densitometric analysis showing the levels of LC3BII, in control and ARL6IP5 knockdown conditions with autophagy inducers, as shown in (**C**). *p*-value was calculated using multiple *t*-test with two-stage linear step-up procedure. (**E**) Representative immunoblot showing the levels of ATG5 + ATG12, ATG12, and ATG5 in control, transfection control, and ARL6IP5 transfection conditions. (**F**) Densitometric analysis of the levels of ATG12, ATG5, and ATG12 + ATG5 from the blot (**F**). *p*-value was calculated using

two-way ANOVA with post hoc Tukey test. (**G**) Representative blot showing the levels of ATG5 + ATG12, ATG5, and ATG12 in control and ARL6IP5 knockdown condition. (**H**) Densitometric analysis of the levels of ATG12, ATG5, and ATG5 + ATG12 in control and ARL6IP5 knockdown condition. Results from three independent experiments are presented. *p*-value was calculated using multiple *t*-test with two-stage linear step-up procedure.

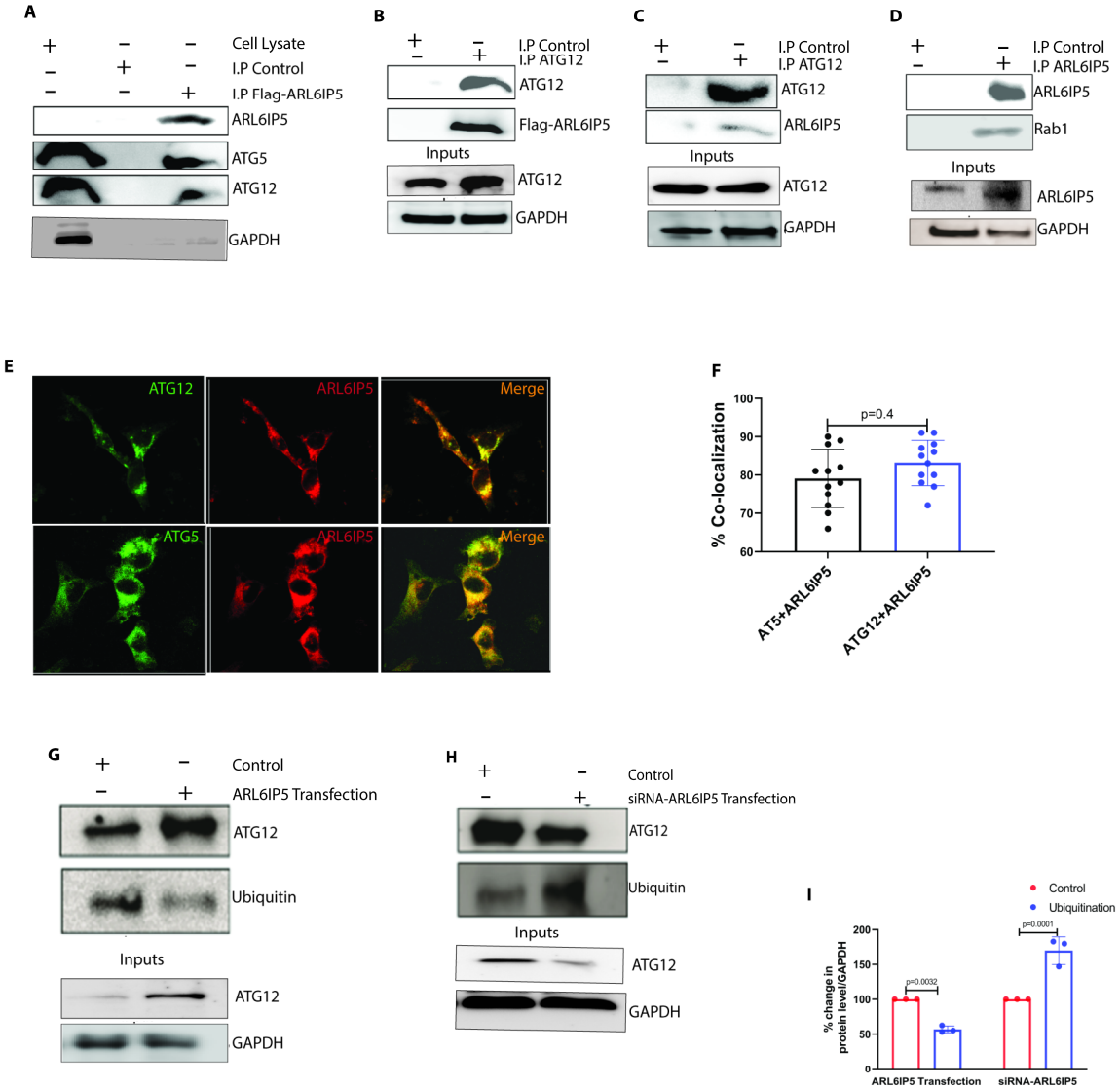

Figure 5. ARL6IP5 interacts with ATG12 and prevents its ubiquitination. (**A**) Representative blot showing the immunoprecipitation of ATG5, and ATG12 with ARL6IP5. (**B**) Representative blot showing the immunoprecipitation of overexpressed Flag-ARL6IP5 with ATG12 and GAPDH in the lysate. (**C**) Representative blot showing the immunoprecipitation of basal ARL6IP5 with ATG12 and GAPDH in the lysate. (**D**) Representative blot showing the immunoprecipitation of Rab1 with ARL6IP5 and GAPDH in the lysate. (**E**) Representative confocal images showing the co-localization (yellow) of ATG12 (green) and ARL6IP5 (red) (upper panel) and co-localization of ATG5 (green) and ARL6IP5 (red) (lower panel). Scale bars, 5 µm (**F**) Graph showing the percent of localization calculated by measuring the yellow area in the cell. *p*-value was calculated using unpaired two-tailed Student *t*-test. (**G**) Representative blot showing the levels of ATG12 ubiquitination in control and ARL6IP5 overexpressing condition. GAPDH was measured in the lysate. (**H**) Representative blot showing the levels of ATG12 ubiquitination in control and ARL6IP5 knockdown condition. GAPDH was measured in the lysate. (**I**) Densitometry analysis of the levels of ubiquitination in control and

ARL6IP5 overexpressing and ARL6IP5 knockdown conditions. *p*-value was calculated using multiple *t*-test with two-stage linear step-up procedure. Results from three independent experiments are presented.

3. Discussion

The extended studies we conducted on understanding the role of ARL6IP5 in Parkinson's disease and aging revealed it was downregulated in the brain as it aged, and this downregulation was even more pronounced in PD animal, human, and cellular models. These findings were sufficient to hypothesize the pivotal role of ARL6IP5 in PD. ARL6IP5 is a membrane resident protein of ER, mainly studied in the field of cancer [16–18]. No literature is available to predict its role in synucleopathy and neuronal autophagy. To decipher the role of ARL6IP5 in PD, we first studied the effect of overexpression and knockdown of ARL6IP5 in PD cellular model. The beneficial and pro-survival effects of ARL6IP5 overexpression in the cellular model of PD confirmed its pivotal role in neuronal physiology. This suggests that α-synuclein-mediated downregulation of ARL6IP5 might be an initial step involved in disease pathogenesis. The detailed mechanistic studies to understand its beneficial effect revealed that overexpression of ARL6IP5 significantly reduced toxic aggregates, reduced toxicity in LDH assay, and induced differentiation in the cellular model of PD (Figure 2A–D). The RTKs array was performed to understand their involvement in ARL6IP5-mediated neuronal survival. The analysis indicated activation of TAM pathway specifically upon ARL6IP5 overexpression (Figure 2F–H). TAM pathways play a key role in neuron survival and homeostasis [37], and its induction in ARL6IP5-mediated neuronal survival indicates its regulation by ARL6IP5. We further ventured to find out the intracellular pathway involved in removing toxic α-synuclein aggregates. The α-synuclein aggregates, being cytosolic, are removed by all cellular degradation pathways viz proteasomal, chaperon-mediated, and autophagy, depending on the size of the aggregates. We did not find significant changes in proteasomal- and chaperon-mediated degradation pathways (Supplementary Figure S2). Interestingly, the process of autophagy, which was significantly reduced in A53T cellular model of PD, was augmented significantly upon ARL6IP5 overexpression, indicating its role in autophagy regulation. As we mentioned above, disruption/deregulation of the process of autophagy in neurons is linked to degeneration of dopaminergic neurons, leading to PD. Thus, ARL6IP5-mediated induction of autophagy and α-synuclein mediated downregulation of ARL6IP5 in PD constitute key findings of our study.

We extended our study to understand the ARL6IP5 mediated regulation of macroautophagy. We were stunned to find that overexpressing ARL6IP5 in the SH-SY5Y cells induces autophagy, which is comparable to the autophagy induced by the standard chemical inducers of autophagy (Figure 3A–D). To confirm the phenomenon, we knockdown the ARL6IP5 and found a significant reduction in the basal level and chemically induced autophagy (Figure 3G–J). In ARL6IP5 overexpressing condition, we found that the level of free ATG12 is increased, which is highly susceptible to degradation [36]. ATG12 interacts with ATG5 and ATG16L and contributes to the elongation of autophagosome membrane [38]. In overexpressing and downregulating conditions of ARL6IP5, we found that free ATG12 increased (Figure 4E,F) and decreases (Figure 4G,H), respectively, and significantly, suggesting that ARL6IP5 stabilized ATG12. Post-translational modifications like ubiquitination plays an important role in the regulation of ATG12 cellular degradation. In the next experiment, we confirmed that ARL6IP5 inhibits the ubiquitination of ATG12 and hence its degradation (Figure 5G–I), which is the cause of elevated autophagy.

ARL6IP5 negatively regulates the Rab1 [35], function of transporting proteins from ER to Golgi. Rab1 plays an important role in the formation of the phagophore assembly site (PAS) [39], where the formation of autophagic membrane start. We have shown that overexpression of ARL6IP5 induces autophagy, suggesting that ARL6IP5 changes role of Rab1 from protein transportation to autophagy induction. Thus, ARL6IP5 is a downstream regulator of autophagy and might play a pivotal role in autophagosome

membrane formation. This hypothesis also suggests that ARL6IP5 can induce autophagy in more than one way, which warrants independent investigation.

4. Material and Methods

4.1. Plasmids

Flag-ARL6IP5 plasmid was a kind gift from professor Jianwei Zhou, Department of Molecular Cell Biology and Toxicology, School of Public Health, Nanjing Medical University, 101 Lonamian Avenue, Jiangning District, Nanjing, 211166, China, EGFP-LC3BII plasmid was a kind gift from Dr. Dhiraj Kumar from ICGEB, New Delhi India and GFP-RFP-LC3BII (Addgene, Watertown, MA, USA # 84573), α-synuclein (Addgene #51437), GFP-A53T (Addgene #40823), pcDNA 3.1 vector (Invitrogen, Waltham, MA, USA V79020), siRNA targeting ARL6IP5(human) (Sigma, St. Louis, MO, USA #EHU041951)

4.2. Protein Extraction and Estimation

After the completion of the experiment, cells were lysed using 70 µL of lysis buffer (Promega, Madison, WI, USA, A1731) in each well. Protein concentration was measured after adding Bradford reagent (Thermo-Fisher Scientific, Waltham, MA, USA, 23236) and reading absorbance at 595 nm on a microplate reader (Infinite M200 ProMicroplate Reader TECAN, Seestrasse, Mannidorf, Switzerland).

4.3. Microscopy

Cells were fixed after the completion of the experiment using 4% PFA, after a wash, cells were covered by mounting media containing DAPI (Thermo-Fisher, P36961) and coverslip. Images were taken using a confocal microscope (ZEISS LSM 500, Oberkochen, Baden-Württemberg, Germany) at 63× magnification.

4.4. Reagents

Sodium bicarbonate (Sigma #S6014), L-glutamine (100× (Gibco #25030081), Trypsin EDTA (0.25%) (Gibco, Waltham, MA, USA #25200056), Opti-MEM (Gibco #31985062), 6-Hydroxydopamine hydrobromide (Sigma-Aldrich #H116), MG132 (Calbiochem, Burlington, MA, USA, #474790), Baf A1 (CST, Danver, MA, USA #54645), Chloroquine diphosphate salt (Sigma #C6628), Rapamycin (Calbiochem #553210), Methyl β-cyclodextrin (Sigma #C4555), Bovine Serum Albumin (HiMedia, Thane, Maharashtra, India #MB083), Lactate dehydrogenase activity assay kit (Sigma-Aldrich #MAK066), RTK kit (R&D Systems, Minneapolis, Min, USA, ARY001B), poly L-lysine (Sigma #P3513), paraformaldehyde (Sigma # 158127).

4.5. Antibodies

Antibodies against ARL6IP5 (Sigma#HPA015540, 1:1000 dilution), α-synuclein (CST #2628), GAPDH (sc-47724), Ubiquitin (CST #3933), HSC 70 (CST #8444), Beta-actin (Sigma #A5441), LC3A/B (MBL #M186-3, 1:1000 dilution), p62 (CST #8025), LC3IIB (CST #2775), Flag (Sigma #F7425), ATG 3(CST #3415), Rab1 (CST #12375), ATG5 (CST #8540), ATG12 (CST #2010), Rab8 (CST #6975)

4.6. In-Vivo Mouse Model Study

A53T α-synuclein transgenic line (Strain #: **004479**) and wild-type C57BL/6J (Strain #:**000664**) mice were procured from Jackson Laboratories and bred and maintained by the National Institute of Immunology small animal facility. Homozygous SNCA and wild-type littermates were used in this study. Animal handling and treatment strategies, including experiments, were carried out according to the standard guidelines of the Institutional Animal Ethics Committee (IAEC). Animal usage protocols were approved by the IAEC (Project # 345/14). Mice were anesthetized using xylazine (10mg/kg) plus ketamine(100mg/kg) and perfused transcardially using 0.1 M PBS, pH 7.4, containing 1% protease and phosphatase inhibitors (Sigma-Aldrich), following 4% (w/v) paraformaldehyde in 0.1 M PBS for fixation.

4.7. Cell Culture

Undifferentiated human neuroblastoma SH-SY5Y cells were maintained in high glucose DMEM medium supplemented with 10% fetal bovine serum (FBS) and 1% and 2% glutamine. Cells were grown at 37 °C in a humidified CO_2 incubator with 5% CO_2. Cells were tested for mycoplasma contamination using EZ-PCR Mycoplasma test kit (Biological Industries, Beit-Haemek, Israel). Cells were found to be negative for mycoplasma contamination.

4.8. Transfection

SH-SY5Y cells were seeded in 6-well plate and proceeded further for transfection and knockdown experiments after attending the desired confluency. Transient transfection was carried out with 2 μg of plasmid DNA using Lipofectamine with LTX plus (Thermo-Fisher Scientific, A12621) reagent by the manufacture's protocol. The knockdown experiments were carried out with ARL6IP5 siRNA using Lipofectamine RNAi-MAX (Thermo-Fisher, 13778100) transfection reagent by the manufacture's protocol.

For generation of stable cell lines, SH-SY5Y cells were transiently transfected, and single cells were selected for protein expression by drug-resistance (neomycin) or fluorescence-activated cell sorting. Stable cell lines generated were characterized by immunoblotting.

4.9. Protein Extraction and Estimation

Cells were lysed with cold RIPA lysis buffer (Sigma- Aldrich #R0278) supplemented with 1X protease inhibitor cocktail (Sigma, P8340) and phosphatase inhibitor cocktail (Sigma, P0044). Post-nuclear lysates were subjected to protein estimation via the Pierce™ BCA protein assay kit (ThermoScientific #23225) using a TECAN Infinite M–200plate reader (Tecan Group Ltd., Männedorf, Switzerland) containing MagellanTM data analysis software version 6.6.0.1; Tecan.

4.10. Immunoblotting

In Laemmli loading buffer [5% -mercaptoethanol, 0.05% bromophenol blue, 75 mM Tris HCl (pH 6.8), 2% SDS, and 10% glycerol], an equal amount of protein sample (50 g) was heat denatured at 37 °C for 30 min or 95 °C for 10 min. Protein samples were separated using 10%, 12%, and 14% SDS-PAGE (BioRad, Hercules, CA, USA). Resolved proteins were electroblotted on a 0.45 μm nitrocellulose membrane (MDI Membrane Technology, Ambala, India) in a glycine/methanol transfer buffer (20 mM Tris-base, 150 mM glycine, and 20% methanol) using the PROTEAN Mini Cell system (BioRad). The protein blots were blocked for 60 min and cut into 2–3 stripes (according to the molecular weight of the protein that needs to be probed) and again blocked for 30 min at room temperature with 5% BSA in 1× TBST. Blots were probed overnight at 4 °C with respective primary antibodies, followed by three 10-min washes with 1× TBST. Secondary antibody incubation was carried out with HRP-conjugated IgG goat anti-rabbit IgG and IgG goat anti-mouse for 90 min at room temperature. The membrane was washed three times with an interval of 10 min each, and then bands were detected with Clarity Western ECL substrate (Bio-Rad) in the LAS-4000 Fujifilm chemiluminescent gel documentation unit (GE Healthcare Life Sciences, Piscataway, NJ, USA). To normalize protein loading control, mouse anti-actin, and anti-GAPDH antibodies were used. Protein bands were analyzed by Multi Gauge Image Reader software version 2.0 (Fujifilm, Tokyo, Japan).

4.11. Immunohistochemistry

The paraffinized human midbrain sections of Parkinson's disease and a control sample were obtained from the Brain bank of NIMHANS, Bangalore, India, with human ethics committee approval. The sections were deparaffinized, and optimized antigen retrieval (AR) was carried out with heat-mediated AR in citrate buffer (pH 6.0), followed by permeabilization with 0.2% triton X-100 in 1× PBS. The sections were washed three times with 1× PBS at 5-min intervals. Blocking was carried out with 10% goat serum for 90 min followed by primary antibody incubation at 4 °C in a humid chamber. Sections were

again washed and incubated with Alexa fluor tagged secondary antibody for 90 min at room temperature. After three consecutive washes with 1× PBS, cells were treated with mounting media containing DAPI (ThermoFisher, P36961). Images were scanned using a confocal microscope (Zeiss LSM 980) at 63× magnification.

For mouse samples, SNCA transgenic and wild-type mice PFA fixed brains were cut into 10 µm thick sections using cryotome. Sections were heated in citrate buffer (pH = 6) for 15 min for antigen retrieval. Sections were blocked in 5% BSA at room temperature for 1 h. Sections were then washed thrice with PBS-T and incubated overnight in primary antibody (1:100) at 4 °C. Sections were again washed thrice with PBS-T and incubated in secondary antibody (1:100) for 1 h at room temperature. Sections were then washed thrice with PBS-T and covered with mounting media with DAPI (Thermo-Fisher, P36961) and coverslip. Slides were stored at 4 °C until microscopic analysis.

4.12. Immunofluorescence

Cells were seeded on poly L-lysine-coated coverslips. After reaching the required confluency, cells were transfected and fixed after the completion of the experiment using 4% (wt/vol) PFA for 15 min at room temperature, followed by three washes of 1× PBS for each of the next 5 min. Then, cells were covered by mounting media containing DAPI (ThermoFisher, P36961). Images were taken using a confocal microscope (ZEISS LSM 510) at 63× magnification.

4.13. Immunoprecipitation

After completion of the experiment, 200 µg of total protein from the cell lysate was incubated overnight on a slow rotation with 2 µg of primary antibody at 4 °C. Then, 40 µL of protein-A agarose beads were added to the lysate and incubated for another 2 h on slow rotation at room temperature. Lysate was centrifuged for 1 min at 1000 rpm to settle beads, and pelleted beads were washed three times using 1× PBS. Finally, SDS buffer was added to the pellet and heated at 95 °C for 10 min to remove all the protein attached to the antibody and further proceed for the immunoblotting. Total lysate was also utilized to run the western blot for checking the expression of the housekeeping gene GAPDH as a means of verifying equal protein loading.

4.14. Lactate Dehydrogenase Activity Assay

Cells were seeded in a 6-well plate, and co-transfection was carried out for 36 h. The supernatant fractions were collected and subjected to an assay for lactase dehydrogenase activity using the manufacturer's protocol.

4.15. RTK Assay

The RTK assay was carried out using a human phospho-RTK array kit (Catalog no.# ARY001B). The assay was carried out according to manufacturer's protocol.

4.16. Statistical Analysis

The data represented here are the means of three independent experiments, and the error bars represent the standard deviation (SD) between the experiments. Statistical analysis was performed using GraphPad Prism 8 (San Diego, CA, USA). Two tailed student *t*-tests and a one-way ANOVA using the Bonferroni post hoc method were applied to determine the significance among groups as indicated in the figures or figure legends. Statistical significances were represented by mentioning the *p*-values.

5. Conclusions

The significant decrease in the ARL6IP5 in PD and aging brain suggest its role in neurodegeneration, including PD pathogenesis. We have clearly shown that overexpression of ARL6IP5 ameliorates disease burden and improves neuronal survival. Our detailed analysis showed that ARL6IP5 is an ER resident protein playing a key role in autophagophore

formation. Upregulation of ARL6IP5 can induce autophagy independently of the upstream initiation signal. Autophagy induction with standard methods also increased the ARL6IP5 level. Interestingly, the downregulation of ARL6IP5 downregulated autophagy even in the presence of autophagy inducers, establishing ARL6IP5 as a key protein involved in the process of pre-autophagophore formation. This is a key finding as the process of pre-autophagophore formation is not well defined. This shows the potential of ARL6IP5 as a target for diseases where autophagy is deregulated.

Supplementary Materials: The following supporting information can be downloaded at: https://www.mdpi.com/article/10.3390/ijms241310499/s1.

Author Contributions: S.G. (Sarika Gupta).: conceived the idea and designed the study. I.S., S.G. (Sakshi Gupta), K.K., K.S., S.B. and N.A. performed the experiments. I.S., K.K. and S.G. (Sakshi Gupta) analyzed the data. I.S., K.K., and S.G. (Sarika Gupta) wrote the manuscript. The authors read and approved the final manuscript. All authors have read and agreed to the published version of the manuscript.

Funding: Authors wants to acknowledge Science and Engineering Research Board, Department of Science and technology, Gov. of India (SERB) Grant (File Number: EMR/2016/006368) and National Institute of Immunology (core grant to Sarika Gupta). ICMR-RA fellowship to Sakshi Gupta, Department of Biotechnology JRF and SRF fellowship to K.K., S.B. and N.A., Govt. of India for the support of this work.

Institutional Review Board Statement: Animal handling and treatment strategies including experiments were carried out according to the standard guidelines of Institutional Animal Ethics Committee (IAEC). Animal usage protocols were approved by the IAEC (Project # 345/14).

Informed Consent Statement: Not applicable.

Conflicts of Interest: The authors declare that they have no known competing interests that could have appeared to influence the work reported in this paper.

References

1. Kalia, L.V.; Lang, A.E. Parkinson's disease. *Lancet* **2015**, *386*, 896–912. [CrossRef]
2. Armstrong, M.J.; Okun, M.S. Diagnosis and Treatment of Parkinson Disease: A Review. *JAMA* **2020**, *323*, 548–560. [CrossRef] [PubMed]
3. Kocaturk, N.M.; Gozuacik, D. Crosstalk between Mammalian Autophagy and the Ubiquitin-Proteasome System. *Front. Cell Dev. Biol.* **2018**, *6*, 128. [CrossRef]
4. Menzies, F.M.; Fleming, A.; Caricasole, A.; Bento, C.F.; Andrews, S.P.; Ashkenazi, A.; Fullgrabe, J.; Jackson, A.; Jimenez Sanchez, M.; Karabiyik, C.; et al. Autophagy and Neurodegeneration: Pathogenic Mechanisms and Therapeutic Opportunities. *Neuron* **2017**, *93*, 1015–1034. [CrossRef] [PubMed]
5. He, C.; Klionsky, D.J. Regulation mechanisms and signaling pathways of autophagy. *Annu. Rev. Genet.* **2009**, *43*, 67–93. [CrossRef] [PubMed]
6. Yang, Z.; Klionsky, D.J. Eaten alive: A history of macroautophagy. *Nat. Cell Biol.* **2010**, *12*, 814–822. [CrossRef]
7. Tsukada, M.; Ohsumi, Y. Isolation and characterization of autophagy-defective mutants of Saccharomyces cerevisiae. *FEBS Lett.* **1993**, *333*, 169–174. [CrossRef]
8. Klionsky, D.J.; Cregg, J.M.; Dunn, W.A., Jr.; Emr, S.D.; Sakai, Y.; Sandoval, I.V.; Sibirny, A.; Subramani, S.; Thumm, M.; Veenhuis, M.; et al. A unified nomenclature for yeast autophagy-related genes. *Dev. Cell* **2003**, *5*, 539–545. [CrossRef]
9. Mochida, K.; Oikawa, Y.; Kimura, Y.; Kirisako, H.; Hirano, H.; Ohsumi, Y.; Nakatogawa, H. Receptor-mediated selective autophagy degrades the endoplasmic reticulum and the nucleus. *Nature* **2015**, *522*, 359–362. [CrossRef]
10. Zhang, S.; Hama, Y.; Mizushima, N. The evolution of autophagy proteins-diversification in eukaryotes and potential ancestors in prokaryotes. *J. Cell Sci.* **2021**, *134*, jcs233742. [CrossRef]
11. Ishihara, N.; Hamasaki, M.; Yokota, S.; Suzuki, K.; Kamada, Y.; Kihara, A.; Yoshimori, T.; Noda, T.; Ohsumi, Y. Autophagosome requires specific early Sec proteins for its formation and NSF/SNARE for vacuolar fusion. *Mol. Biol. Cell* **2001**, *12*, 3690–3702. [CrossRef] [PubMed]
12. Meiling-Wesse, K.; Epple, U.D.; Krick, R.; Barth, H.; Appelles, A.; Voss, C.; Eskelinen, E.L.; Thumm, M. Trs85 (Gsg1), a component of the TRAPP complexes, is required for the organization of the preautophagosomal structure during selective autophagy via the Cvt pathway. *J. Biol. Chem.* **2005**, *280*, 33669–33678. [CrossRef] [PubMed]
13. Butchbach, M.E.; Lai, L.; Lin, C.L. Molecular cloning, gene structure, expression profile and functional characterization of the mouse glutamate transporter (EAAT3) interacting protein GTRAP3-18. *Gene* **2002**, *292*, 81–90. [CrossRef]

14. Ingley, E.; Williams, J.H.; Walker, C.E.; Tsai, S.; Colley, S.; Sayer, M.S.; Tilbrook, P.A.; Sarna, M.; Beaumont, J.G.; Klinken, S.P. A novel ADP-ribosylation like factor (ARL-6), interacts with the protein-conducting channel SEC61beta subunit. *FEBS Lett.* **1999**, *459*, 69–74. [CrossRef] [PubMed]
15. Lin, C.I.; Orlov, I.; Ruggiero, A.M.; Dykes-Hoberg, M.; Lee, A.; Jackson, M.; Rothstein, J.D. Modulation of the neuronal glutamate transporter EAAC1 by the interacting protein GTRAP3-18. *Nature* **2001**, *410*, 84–88. [CrossRef]
16. Liang, Y.; Qian, C.; Xie, Y.; Huang, X.; Chen, J.; Ren, Y.; Fu, Z.; Li, Y.; Zeng, T.; Yang, F.; et al. JWA suppresses proliferation in trastuzumab-resistant breast cancer by downregulating CDK12. *Cell Death Discov.* **2021**, *7*, 306. [CrossRef]
17. Wang, W.; Yang, J.; Yu, Y.; Deng, J.; Zhang, H.; Yao, Q.; Fan, Y.; Zhou, Y. Expression of JWA and XRCC1 as prognostic markers for gastric cancer recurrence. *Int. J. Clin. Exp. Pathol.* **2020**, *13*, 3120–3127.
18. Ren, Y.; Chen, D.; Zhai, Z.; Chen, J.; Li, A.; Liang, Y.; Zhou, J. JAC1 suppresses proliferation of breast cancer through the JWA/p38/SMURF1/HER2 signaling. *Cell Death Discov.* **2021**, *7*, 85. [CrossRef]
19. Qian, Z.Y.; Wei, B.; Wang, J.R.; Wang, Q.L.; Gao, Y.; Chen, X.F. [Autophagy regulated by JWA influenced sensitivity of esophageal cancer to cisplatin]. *Zhonghua Yi Xue Za Zhi* **2017**, *97*, 2141–2144. [CrossRef]
20. Masini, D.; Plewnia, C.; Bertho, M.; Scalbert, N.; Caggiano, V.; Fisone, G. A Guide to the Generation of a 6-Hydroxydopamine Mouse Model of Parkinson's Disease for the Study of Non-Motor Symptoms. *Biomedicines* **2021**, *9*, 598. [CrossRef]
21. Choi, D.H.; Choi, I.A.; Lee, C.S.; Yun, J.H.; Lee, J. The Role of NOX4 in Parkinson's Disease with Dementia. *Int. J. Mol. Sci.* **2019**, *20*, 696. [CrossRef] [PubMed]
22. Bigi, A.; Ermini, E.; Chen, S.W.; Cascella, R.; Cecchi, C. Exploring the Release of Toxic Oligomers from α-Synuclein Fibrils with Antibodies and STED Microscopy. *Life* **2021**, *11*, 431. [CrossRef] [PubMed]
23. Tondo, G.; Perani, D.; Comi, C. TAM Receptor Pathways at the Crossroads of Neuroinflammation and Neurodegeneration. *Dis. Markers* **2019**, *2019*, 2387614. [CrossRef] [PubMed]
24. Vogiatzi, T.; Xilouri, M.; Vekrellis, K.; Stefanis, L. Wild type alpha-synuclein is degraded by chaperone-mediated autophagy and macroautophagy in neuronal cells. *J. Biol. Chem.* **2008**, *283*, 23542–23556. [CrossRef]
25. Mizushima, N.; Yoshimori, T. How to interpret LC3 immunoblotting. *Autophagy* **2007**, *3*, 542–545. [CrossRef]
26. Corbier, C.; Sellier, C. C9ORF72 is a GDP/GTP exchange factor for Rab8 and Rab39 and regulates autophagy. *Small GTPases* **2017**, *8*, 181–186. [CrossRef]
27. Xu, H.D.; Wu, D.; Gu, J.H.; Ge, J.B.; Wu, J.C.; Han, R.; Liang, Z.Q.; Qin, Z.H. The pro-survival role of autophagy depends on Bcl-2 under nutrition stress conditions. *PLoS ONE* **2013**, *8*, e63232. [CrossRef]
28. Lin, X.; Han, L.; Weng, J.; Wang, K.; Chen, T. Rapamycin inhibits proliferation and induces autophagy in human neuroblastoma cells. *Biosci. Rep.* **2018**, *38*, BSR20181822. [CrossRef]
29. Dai, S.; Dulcey, A.E.; Hu, X.; Wassif, C.A.; Porter, F.D.; Austin, C.P.; Ory, D.S.; Marugan, J.; Zheng, W. Methyl-beta-cyclodextrin restores impaired autophagy flux in Niemann-Pick C1-deficient cells through activation of AMPK. *Autophagy* **2017**, *13*, 1435–1451. [CrossRef]
30. Tanida, I.; Ueno, T.; Kominami, E. LC3 and Autophagy. *Methods Mol. Biol.* **2008**, *445*, 77–88. [CrossRef]
31. Hansen, T.E.; Johansen, T. Following autophagy step by step. *BMC Biol.* **2011**, *9*, 39. [CrossRef] [PubMed]
32. Yoshii, S.R.; Mizushima, N. Monitoring and Measuring Autophagy. *Int. J. Mol. Sci.* **2017**, *18*, 1865. [CrossRef] [PubMed]
33. Kaizuka, T.; Morishita, H.; Hama, Y.; Tsukamoto, S.; Matsui, T.; Toyota, Y.; Kodama, A.; Ishihara, T.; Mizushima, T.; Mizushima, N. An Autophagic Flux Probe that Releases an Internal Control. *Mol. Cell* **2016**, *64*, 835–849. [CrossRef] [PubMed]
34. Romanov, J.; Walczak, M.; Ibiricu, I.; Schuchner, S.; Ogris, E.; Kraft, C.; Martens, S. Mechanism and functions of membrane binding by the Atg5-Atg12/Atg16 complex during autophagosome formation. *EMBO J.* **2012**, *31*, 4304–4317. [CrossRef]
35. Maier, S.; Reiterer, V.; Ruggiero, A.M.; Rothstein, J.D.; Thomas, S.; Dahm, R.; Sitte, H.H.; Farhan, H. GTRAP3-18 serves as a negative regulator of Rab1 in protein transport and neuronal differentiation. *J. Cell Mol. Med.* **2009**, *13*, 114–124. [CrossRef]
36. Haller, M.; Hock, A.K.; Giampazolias, E.; Oberst, A.; Green, D.R.; Debnath, J.; Ryan, K.M.; Vousden, K.H.; Tait, S.W. Ubiquitination and proteasomal degradation of ATG12 regulates its proapoptotic activity. *Autophagy* **2014**, *10*, 2269–2278. [CrossRef]
37. Burstyn-Cohen, T.; Hochberg, A. TAM Signaling in the Nervous System. *Brain Plast.* **2021**, *7*, 33–46. [CrossRef]
38. Mizushima, N.; Ohsumi, Y.; Yoshimori, T. Autophagosome formation in mammalian cells. *Cell Struct. Funct.* **2002**, *27*, 421–429. [CrossRef]
39. Lipatova, Z.; Segev, N. A Ypt/Rab GTPase module makes a PAS. *Autophagy* **2012**, *8*, 1271–1272. [CrossRef]

International Journal of
Molecular Sciences

MDPI

Review

Cellular Protein Aggregates: Formation, Biological Effects, and Ways of Elimination

Jun-Hao Wen, Xiang-Hong He, Ze-Sen Feng, Dong-Yi Li, Ji-Xin Tang * and Hua-Feng Liu *

Guangdong Provincial Key Laboratory of Autophagy and Major Chronic Non-Communicable Diseases, Institute of Nephrology, Affiliated Hospital of Guangdong Medical University, Zhanjiang 524001, China
* Correspondence: tangjixin@gdmu.edu.cn (J.-X.T.); liuhf@gdmu.edu.cn (H.-F.L.)

Abstract: The accumulation of protein aggregates is the hallmark of many neurodegenerative diseases. The dysregulation of protein homeostasis (or proteostasis) caused by acute proteotoxic stresses or chronic expression of mutant proteins can lead to protein aggregation. Protein aggregates can interfere with a variety of cellular biological processes and consume factors essential for maintaining proteostasis, leading to a further imbalance of proteostasis and further accumulation of protein aggregates, creating a vicious cycle that ultimately leads to aging and the progression of age-related neurodegenerative diseases. Over the long course of evolution, eukaryotic cells have evolved a variety of mechanisms to rescue or eliminate aggregated proteins. Here, we will briefly review the composition and causes of protein aggregation in mammalian cells, systematically summarize the role of protein aggregates in the organisms, and further highlight some of the clearance mechanisms of protein aggregates. Finally, we will discuss potential therapeutic strategies that target protein aggregates in the treatment of aging and age-related neurodegenerative diseases.

Keywords: protein aggregates; proteostasis; aging; age-related neurodegenerative diseases; autophagy; ubiquitin-proteasome system

Citation: Wen, J.-H.; He, X.-H.; Feng, Z.-S.; Li, D.-Y.; Tang, J.-X.; Liu, H.-F. Cellular Protein Aggregates: Formation, Biological Effects, and Ways of Elimination. *Int. J. Mol. Sci.* **2023**, *24*, 8593. https://doi.org/10.3390/ijms24108593

Academic Editor: Claudia Ricci

Received: 22 April 2023
Revised: 6 May 2023
Accepted: 8 May 2023
Published: 11 May 2023

1. Introduction

As the material basis of vita, proteins play essential roles in various forms of life activities in organisms. Therefore, it is important to maintain the correct conformation of protein in mammalian cells. Mammalian cells have developed a system called proteostasis network to maintain more than 10,000 different proteins' correct conformation [1]. In healthy mammalian cells, a proteostasis network contains molecular chaperones and proteolytic machinery and their regulators, which coordinate with each other to ensure the maintenance of proteostasis [1]. However, it is a challenging task to maintain proteostasis, especially in the face of various external and endogenous stresses that accumulated in aging. These stresses can result in a decrease in proteostasis network capacity and proteome integrity, causing the accumulation of misfolded and aggregated proteins, which will specifically affect the postmitotic cell types such as neurons [2,3]. As the symbol of proteostasis imbalance, protein aggregation can be found in aging cells and tissues and damaged organs [4,5]. Moreover, recent findings establish a central role of enhanced proteostasis to prevent the aging of somatic stem cells in adult organisms. Notably, proteostasis is also required for the biological purpose of adult germline stem cells, which are to be passed from one generation to the next. Beyond these links between proteostasis and stem cell function, these insights demonstrate that embryonic stem cells and induced pluripotent stem cells exhibit an endogenous proteostasis network that not only delays senescence but also maintains the ability to reproduce. Besides the essential roles of the proteostasis network in postmitotic neurons, it also play important roles in maintaining stem cell function [6], such as modulating stem cells pluripotency and differentiation as well as suppressing aggregation of disease-related proteins [7].

As the hallmark of aging, loss of proteostasis can be found in many age-related diseases and degenerative diseases, such as Alzheimer's disease (AD), Parkinson's disease (PD), Huntington's disease (HD), and idiopathic cardiomyopathy [8–13]. Protein aggregates caused by loss of proteostasis can lead to cell dysfunction via damaging the lysosomes, inducing endoplasmic reticulum stress (ER-stress), causing DNA damage, and perturbating Ca^{2+}, all of which can promote the progression of age-related diseases [14].

In this review, we will briefly summarize the composition and causes of protein aggregates in mammalian cells, and then we will systematically introduce the function of protein aggregates in mammalian cells, and further highlight some of ways to the clear the protein aggregates. Finally, we will discuss potential therapeutic strategies that target protein aggregates for the treatment of aging and age-related neurodegenerative diseases.

2. The Components of Protein Aggregates

Protein aggregates can be formed from almost all kinds of proteins in cells. The state of protein aggregates covers liquid (monomer), liquid-like or solid-like (oligomers), and solid (insoluble aggregation) [15]. In aging *C. elegans*, though the most abundant proteins were 10 times more soluble than the least abundant proteins, the most abundant proteins contribute most to the total aggregate load [16]. Apparently, the high solubility of abundant proteins is insufficient to protect them from age-dependent aggregation. Interestingly, in long-lived daf-16 mutant *C. elegans*, protein aggregates were accumulated significantly more than that of age-matched WT animals [16]. This phenomenon suggests that long-lived daf-16 mutant worms can handle protein aggregates well, driving aberrant, potentially toxic proteins into aggregates. Packing up damaged abundant proteins and separating them in order to prevent proteostasis imbalance can help daf-16 mutant worms live longer.

In the organism proteome, most proteins have special segments that are not likely to form a defined 3D structure which is characterized by their biased amino acid composition and low sequence complexity. These structures are known as intrinsically disordered proteins (IDPs) and intrinsically disordered protein regions (IDPRs) [17,18]. It may explain why protein aggregates are mainly formed by the most abundant proteins. Because the most abundant proteins contain IDPRs, when facing stress environments, they tend to perform liquid-liquid phase separation (LLPS) and turn into protein aggregates if stress factors persist [19]. In most cases, protein phase separation is closely linked with the presence of IDRs and IDPRs in the phase-separated proteins [20]. However, IDPs and IDPRs do play a key role in life activities such as protein modification and cellular signaling and regulation [21]. IDPs and IDPRs are the key structures to regulate cellular signals, as these motifs combine varieties of molecules to cascade or terminate signals, and they also promote flexible sites for post-translational modification to assist the activity of the kinase. Also, IDPs and IDPRs can regulate the amount of kinase by forming LLPS in order to trap some kinases and restrict those activities [18].

Besides the most abundant proteins, protein aggregates also contain other matter. Nucleic acids, such as RNA, can intertwine proteins, aggravating protein aggregate accumulation [22,23]. Eukaryotic cells have numerous dynamic membrane-less organelles, called RNP granules, such as nucleolus, Cajal bodies, stress granules, and P-bodies. These organelles can bind with RNA to perform physiological functions. In addition, aberrant regulation of RNA-RNP combination could explain the reason for the pathological stress granules formation in certain diseases [24,25]. In protein aggregates, RNAs are likely to act as 'scaffolds', which string misfolded proteins together [25–27]. RNA-dependent protein aggregates were widely found in degenerative diseases. In amyotrophic lateral sclerosis (ALS) and frontotemporal dementia (FTD), misfolded TDP-43 protein did not perform the function of protecting mRNA, rather than wrap around with mRNA and other proteins [28]. This process accelerates the formation of protein aggregates and makes removal more difficult. Once proteostasis is damaged, proteins and RNA can wrap together and change the stability of LLPS, promoting solid-like aggregates accumulation [25]. However, as the longest cells in the body with the most longevity, neurons use LLPS to create separate

compartments for RNA and protein in order to transport matter and keep biochemical reaction accurately conducted [27]. This phenomenon could explain why neurons tend to form protein aggregates which cause cell dysfunction.

A relatively simple composition of protein aggregates also causes diseases. In AD patients' neurons, β-amyloid 1–42 (Aβ 1–42) and tau protein aggregates are the most significant factors causing neurodegeneration [29–31]. Lewy bodies, which are accumulated by misfolded α-synuclein (α-syn), can be found in PD patients' substantia nigra. They disrupt normal cellular architecture so that cell function is damaged, eventually leading to cell death [9,32,33]. Abnormal accumulation of Huntingtin (Htt) protein in the corpus striatum causes disordered motor movements, personality changes, and premature death in patients [10]. In cardiovascular diseases, protein aggregates also play a key role in the initiation process of diseases. In mouse models, αB-crystallin (CryAB) aggregates in cardiomyocytes can cause cardiac failure when the mouse is still at a young age [34]. High-temperature requirement protein A1 (HTRA1) aggregations and HTRA1 substrates accumulation are the key links for cerebral autosomal dominant arteriopathy with subcortical infarcts and leukoencephalopathy (CADASIL) [35]. How to clear protein aggregates is the key strategy to resist some hereditary cardiomyopathies. Not only do permanent cells such as neurons and myocardial cells face protein aggregation challenges, but highly active transporting epithelia such as renal tubules are also at risk of protein aggregates due to high protein turnover and/or oxidative stress. When stress load increases, such as aldosterone stimulation, renal tubule cells keratin 5, the ribosomal protein RPL27, ataxin-3, and even HSPs would be abnormally found accumulating in protein aggregates [36]. The influence of protein aggregates in renal tubule cells on renal function has still not been understood so far.

3. Protein Aggregation Caused by Losing of Proteostasis

A proteostasis network is required for mammalian cells to keep protein quality control, reduce misfolded protein, and maintain proteostasis [37], but as time went by, the ability of mammalian cells to keep proteostasis declined with aging. There are many reasons for organism proteostasis imbalance, which can be attributed to four points: first, there are not enough molecular chaperones in the cytoplasm to help proteins correctly fold; second, cells cannot appropriately react to endoplasmic reticulum stress (ER stress); third, digestion of damaged proteins is blocked for lysosomes degradation; fourth, protein aggregates accumulate due to above reasons [37]. Therefore, protein aggregate is the outcome event of proteostasis imbalance in the proteome, and it is the connector that leads to cell structure and function damage, aggravating organ failure.

The proteostasis network can maintain protein quality by correctly guiding polypeptide chain folding, maintaining the structure of proteins, and digesting damaged proteins [2]. However, in normal cells, some common proteins are close to their solubility limits [38,39] or are indeed supersaturated [16,40], which makes them stay in metastable 'subproteome'. When the intracellular environment is perturbated, the metastable 'subproteome' aggregates into insoluble proteins, interfering with vital movement. In order to handle these insoluble proteins, more molecular chaperones could combine with them, this process aggravating polypeptide chain misfolding for lack of available molecular chaperones. If unfold protein response (UPR) was not activated in a timely manner, the cells would be caught in a vicious circle of proteostasis imbalance. However, protein aggregating also interacts with proteostasis, playing a special role in maintaining proteostasis. Intracellular environment perturbating can cause LLPS and even accumulation of protein aggregates. The intermediates process, LLPS, can also maintain proteostasis in some special ways. When misfolded proteins are in LLPS state, this special state equally limits them to a designated space in the cell. Moreover, proteasomes and related marker proteins such as p62/SQSTM1 also recruit into LLPS. This process improves the efficiency of proteasomes and autolysosomes to clear misfolded proteins [41,42].

Protein aggregates, such as amyloid deposition, can be found from Alzheimer's disease to type II diabetes, most of which are typical age-related diseases [5]. Protein aggregates are particularly prominent in the pathogenesis of neurological diseases [30], such as Aβ 1–42 for Alzheimer's disease [29], tau aggregation for Alzheimer's disease [31],α-syn for Parkinson's disease [9], and Rosenthal fibers for Alexander disease [43]. In molecular structure, amyloid deposition and many protein aggregates were characterized by β-sheet, and hydrogen bonding is the key structure to maintaining β-sheet [5]. Due to hydrogen bonding and β-sheet, the amyloid state has a lower free energy (G) than the native state ($\Delta G < 0$), which means that the protein native state is kinetically metastable [38,44]. Once the intracellular environment fluctuates, such as heat stress and oxidative stress [45], the protein's native state would spontaneously transform into an amyloid state from receiving enough activation energy to get over the energy barrier. As a molecular structural property of proteins, too many free radicals in the cytoplasm may accelerate the native protein's transformation into the amyloid state in aging cells.

Staying in metastable 'subproteome', many proteins would trend to LLPS and even aggregation. However, this process is reversible in most situations when stress disappeared. However, some mutations in RNA-binding proteins (RBPs) can accelerate the process of LLPS and turn RBPs from reversible fibrils to irreversible fibrils [46,47]. In many neurodegenerative diseases, LLPS is the primary process of forming amyloid proteins such as α-syn, FUS, tau, and TDP-43, all of which can aggregate and form into amyloid proteins through irreversible LLPS and damage to neurons [48,49].

4. The Harm of Protein Aggregates

Protein aggregates are the normal matter of cellular metabolism, all cells must handle protein aggregates, however, if the cells could not eliminate protein aggregates below the threshold, they would damage cells in many ways and accelerate cell aging [14] (Figure 1). The ways that protein aggregates damage cells are multitudinous, weaving together with mutual promotion, becoming a complex network. For example, protein aggregates disrupt the membrane system, causing an imbalance of calcium homeostasis and lysosomal function incompetence. ROS, a by-product of protein aggregates, not only destroys DNA, but also disrupts the protein synthesis environment, which causes more serious consequences such as protein synthesis error and aggregates accumulation, creating a vicious circle. Therefore, stopping the interference of protein aggregates and breaking the chain of destructive effects is the key target of treatment for protein aggregate accumulation.

4.1. Interference with Lysosomal Function

Protein aggregate accumulations can be partially attributed to lysosome dysfunction. Correspondingly, lysosome dysfunction is also the phenotypic of protein aggregates accumulation [50,51]. The current study shows that protein aggregates interfere with lysosome via directly damaging lysosome structure and function, or disturbing lysosomal-associated genes expression and fusion to indirectly reduce degradation capacity. In Alzheimer's disease models, though Aβ 1–42 aggregations were wrapped by autolysosomes, they still stayed in autolysosomes and even destroyed the integrity of autolysosomes, which caused leakage of hydrolase and broader cellular dysfunction [50]. However, improving the activity of autophagy could delay the onset of neurodegenerative disorders because it would reduce protein aggregate accumulation [52]. In addition, we should pay attention to another phenomenon: protein aggregates interfere with lysosomal gene expression. Also in Alzheimer's disease, tau proteins accumulate into aggregates, which is another hallmark pathology. Abnormal tau accumulation could inhibit the transcription of IST1 expression, the key factor of autophagosome formation, via activating the CEBPB-ANP32A-INHAT pathway [51]. Upregulating IST1 or downregulating ANP32A can break the vicious cycle and reduce protein aggregates. Besides inhibiting gene expression, tau aggregations could also accelerate microtubule disassembly, inducing a massive buildup of autophagosomes in neuronal processes [53,54]. Therefore, tau aggregations accumulation can also impair

autolysosome formation by disrupting microtubule dynamics and axonal transport. Analogously, in Parkinson's Disease, α-syn protein aggregating also harms the degradations of autolysosomes [55]. The α-syn protein not only disrupts microglial autophagy initiation via Tlr4-dependent p38 and Akt-mTOR signaling in substantia nigra, but also piles up in autolysosomes to hamper them, degrading metabolic wastes [55]. This adverse outcome accelerates the apoptosis of microglia cells and inflammatory infiltration of the substantia nigra and drives the progression of Parkinson's disease. We summarize that protein aggregates interfere with lysosome function via two pathways: first, directly damaging the lysosome structure and function which cause metabolic waste accumulating in cytoplasmic and leakage of hydrolases; and second, disturbing lysosomal associated genes expression or fusion of lysosomes to indirectly reduce degradation capacity. Both of these pathways break the intracellular environment, interweaving with each other and causing a more complex mechanism of injury.

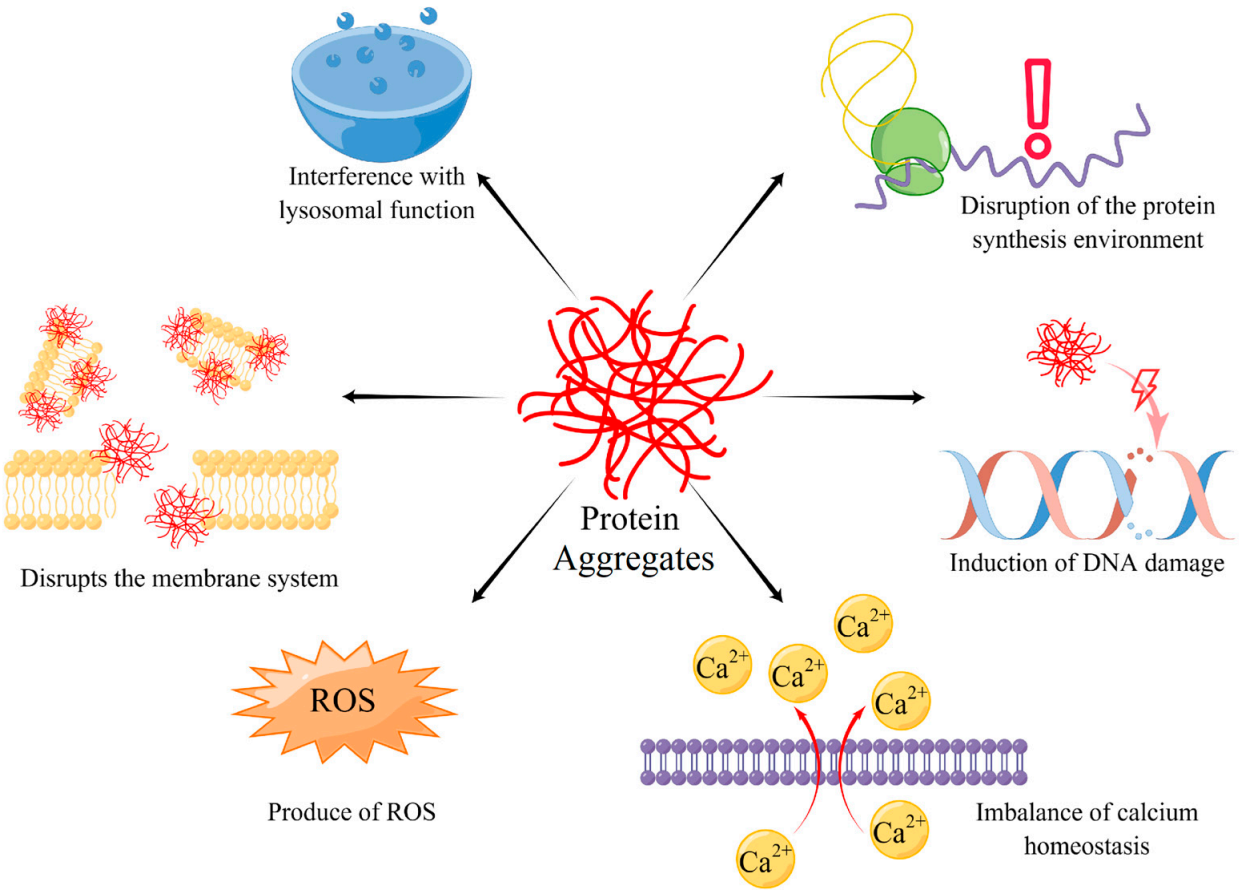

Figure 1. Six main ways of protein aggregates damage the metabolism of cells. They contain interference with lysosomal function, disruption of protein synthesis environment, damage DNA, disturb calcium homeostasis, produce ROS, and injure the membrane system.

4.2. Disruption of the Protein Synthesis Environment

Misfolded proteins are the key elements of protein aggregates, which means that any reason for protein synthesis interference could exacerbate protein aggregate accumulation [56]. Similarly, protein aggregates can disrupt the protein synthesis environment via induction of ER stress. In PD patient midbrain cultures, α-synuclein was aggregated, the aggregates induce ER fragmentation and compromise ER protein folding capacity, leading to protein misfolding and aggregation [57]. In the amyotrophic lateral sclerosis (ALS) mouse model, the aggregates-related protein C9orf72 can cause ER stress response [58]. Therefore, reducing ER stress is also a potential target for weakening protein aggregates' influence. Many studies prove that limiting ER stress and activating UPS can relieve the negative impact of

protein aggregates [56,59]. Some researchers suggest that ROS may be the key mediator between protein aggregates and ER stress [60,61]. However, we still do not comprehensively know how protein aggregates destroy the protein synthesis environment.

4.3. Induction of DNA Damage

DNA damage is a key symbol of cell aging and also a typical outcome of protein aggregate accumulation [62]. We notice that in many neurodegenerative diseases characterized by protein aggregates, neurons are observed DNA damage [29,63–65]. Focusing on DNA injury mechanism, protein aggregates damage DNA via three main modes: (1) Touching DNA and directly destroying its structure. (2) Injuring DNA indirectly through mediums such as ROS. (3) Interfering with the DNA repair system, causing an accumulation of damages [62]. These modes are not separately fought; they intertwine with each other and mutually reinforce. A. Suram et al. research showed that Aβ 1–42 has DNA-nicking activity similar to nuclease [21]. Further studies revealed that Aβ 1–42 causes open circular and linear forms in supercoiled DNA and also clearly evidenced the physical association of protein-DNA complex via transmission electron microscopy (TEM). The broken DNA was repaired via homology recombination which may generate frameshift mutation. Meanwhile, in the α-syn aggregation cell model, ROS accumulation was observed because of α-syn aggregation induction. ROS is the key poison that can damage DNA structure. V. Vasquez et al. observed that α-syn overexpression and oxidative stress significantly enhanced DNA damage in the neuronal genome [64]. While protein aggregates can injure DNA, the DNA damage repair system executes the task of protecting and repairing fragile genetic material. However, protein aggregates also interfere with this life-saving straw. Lior Weissman et al. found that AD patients' brain has base excision repair (BER) deficiencies, suggesting a decreased capacity to repair oxidative DNA damage [65]. Tyler Fortuna et al. attempted to relieve the symptom of protein aggregates accumulation in neurons by improving DNA damage repair ability. And the result shows that superior DNA repair abilities suppress protein aggregates-mediated neuropathogenesis and toxicity in vivo [63].

4.4. Imbalance of Calcium Homeostasis

Calcium is the key ion of life activities, performing as an electrical signal carrier, a messenger, and the catalytically active center of many enzymes. Cells have an ingenious mechanism to maintain calcium concentration. However, protein aggregates can destroy the balance of calcium exchange, causing more disorder in biochemical metabolism [12,61,66]. Some researchers have discovered that certain types of protein aggregates could insert into membrane structures and play the role of a non-selective ion channel [66–69]. For example, Aβ 1–42, a typical protein aggregation, can form a pore transmembrane structure with an 8–25 nm outer diameter and 2–6 nm inner diameter [68,69]. Those aggregates channels can appear in the cytomembrane, changing the resting potential, but can also appear in the smooth endoplasmic reticulum, the largest calcium store in cells. When a pore transmembrane structure is formed in smooth endoplasmic reticulum, it means that lots of calcium ions have been lost to the cytoplasm, causing a disorder in metabolism. Furthermore, protein aggregates can increase membrane conductance and permeability to charged species by spreading the lipid head groups apart, consequently thinning the bilayer and lowering the permeability barrier, causing calcium ions to transmembrane flow [70–72]. To maintain calcium homeostasis, the calcium pump must keep working, which wastes precious energy in the neuron. On the other hand, calcium homeostasis is more similar to a result of the contents disclosure of membrane system disruption. Interestingly, protein aggregates are seen not to change calcium homeostasis via activating calcium channel protein. This is because even when calcium channels are blocked, the effect of calcium imbalance still existed [67]. Limiting the disruption of calcium homeostasis by protein aggregates is the key tool to preventing cellular senescence and degeneration.

4.5. Disrupts the Membrane System and Production of ROS

The membrane system separates different cell biochemical reactions and provides a smooth environment for metabolic processes. The interaction of protein aggregates with lipid membranes has been widely reported [73–76]. This primarily occurs through a physical mode of punching holes in the membrane and even emulsifying lipid bilayers. Entering into the membrane and creating transmembrane pores is one mode that not only causes membrane disruption, but also calcium imbalance [67,68]. Alternatively, a carpeting effect of Aβ 1–42 has been proposed, which is thought to result in a general increase in membrane conductance either by membrane thinning or a lateral spreading of lipid headgroups [70–72]. Even protein aggregates such as surfactants can disrupt the integrity of the membrane via emulsifying lipid bilayers [69,77]. Terminating the impact of protein aggregates on cellular membranes is the target of potential treatment.

ROS is the by-product of protein aggregates, which can attack any substance in the cell due to its strong oxidation [60,61,66,78]. In general, it is not clear why protein aggregates or their precursors trigger ROS production. Various hypotheses have been put forward, including an increase in oxidative metabolism to clear the excess of free Ca^{2+}, the impairment of the functionality of the ER, and mitochondria ROS production [79]. Reacting with transition element ions, such as Fe^{2+} and Cu^{2+}, protein aggregates subsequently converted to hydroxyl radicals. However, hydroxyl radical formation was inhibited by the inclusion of catalase or metal chelators [79].

5. The Way to Eliminate Protein Aggregates

Because protein aggregates are vital in influencing proteostasis imbalance, organisms developed many ways to protect themselves from protein aggregates. The methods of resisting protein aggregates can be summarized as following points: (1) Refolding misfolded proteins and depolymerizing aggregates. (2) Degrading protein aggregates via ubiquitin-proteasome pathway (UPP) or autophagy-lysosome pathway (ALP). (3) Alleviate protein aggregates load via asymmetric cell division (ACD) or exocytosis [80,81]. All of these are protecting proteostasis balance.

Refolding and depolymerizing protein aggregates are the first choice of cells to maintain proteostasis balance in a normal state for saving precious resources [23]. Though cells are still healthy, protein aggregates can be produced for intracellular environment fluctuations. Recycling or rescuing misfolded proteins in an efficient and economical way is of particular importance. Molecular chaperones can perform this task well [2,23]. The heat shock protein family (HSPs) is the most typical molecular chaperone protecting proteostasis. ATP-dependent HSP70 is the most important protein that can depolymerize misfolded proteins with the assistance of HSP110 (Figure 2A). In addition to HSP70, small heat shock proteins (sHSP) also play a role in repairing misfolded proteins by actively gathering them, separating damaged proteins into small protein aggregates, and preventing further misfolding. Interestingly, besides HPS, ubiquitin, the tag protein of protein aggregates, can also execute the mission of depolymerizing protein aggregates [22]. Ubiquitin can break the structure of the C-terminal ubiquitin-associating domain (UAB), a key construction of protein oligomerization and LLPS. Via combining polyubiquitylation in UAB, protein aggregates in LLPS can depolymerize again and return to the soluble state. This is precisely because refolding and depolymerizing protein aggregates requires many molecular chaperones. When facing stress, cells could be confronted with a dilemma, which is the lack of available molecular chaperones if ER-stress response cannot activate and produce enough molecular chaperones [82]. ER-stress response deficiency causes insufficient synthesis of molecular chaperones. Therefore, there is a complex interaction network between protein aggregating and proteostasis.

The ubiquitin-proteasome pathway (UPP) or autophagy-lysosome pathway (ALP) are the key systems of protein quality control in cells [83] (Figure 2B). Both of them are degraded misfolded proteins, but they handle different types of misfolded proteins. Because of the limitation of the narrow channel of the proteasome, UPS primarily deals with soluble

misfolded proteins and unfolded polypeptides. When facing the gathering of misfolded proteins and even protein aggregates, UPP is helpless. To eliminate these damaged proteins, ALP was applied to wrap up protein aggregates and combine with the lysosome for enzymolysis [84,85]. To label the protein aggregates and target them to UPP and ALP, ubiquitin (Ub) is necessary for marking protein aggregates. Protein aggregates can be identified and conjugated ubiquitin by a hierarchically acting enzymatic cascade. Via Ub-conjugating enzyme linking Ub thioester, activated Ub, to substrate specificity [84,86]. When substrates are progressively modified with Ub, either at the N terminus (Met1) or at a lysine side chain of Ub, various linear or branched Ub chains are built. Poly-Ub link as a potent signal, recruiting intrinsic Ub receptors of the proteasome (Rpn10 or Rpn13) or shuttle factors that are equipped with both a Ub-binding domain and a domain that binds to the proteasome and guides ubiquitinated protein to the proteasome. When aggregates surpass the processing limitation of the proteasome, Ub chains can combine with autophagy receptors such as P62, NBR1, and TAX1BP1 [87]. After that, those receptors induce autophagosome, enveloping the protein aggregates and fusing with the lysosome to digest them.

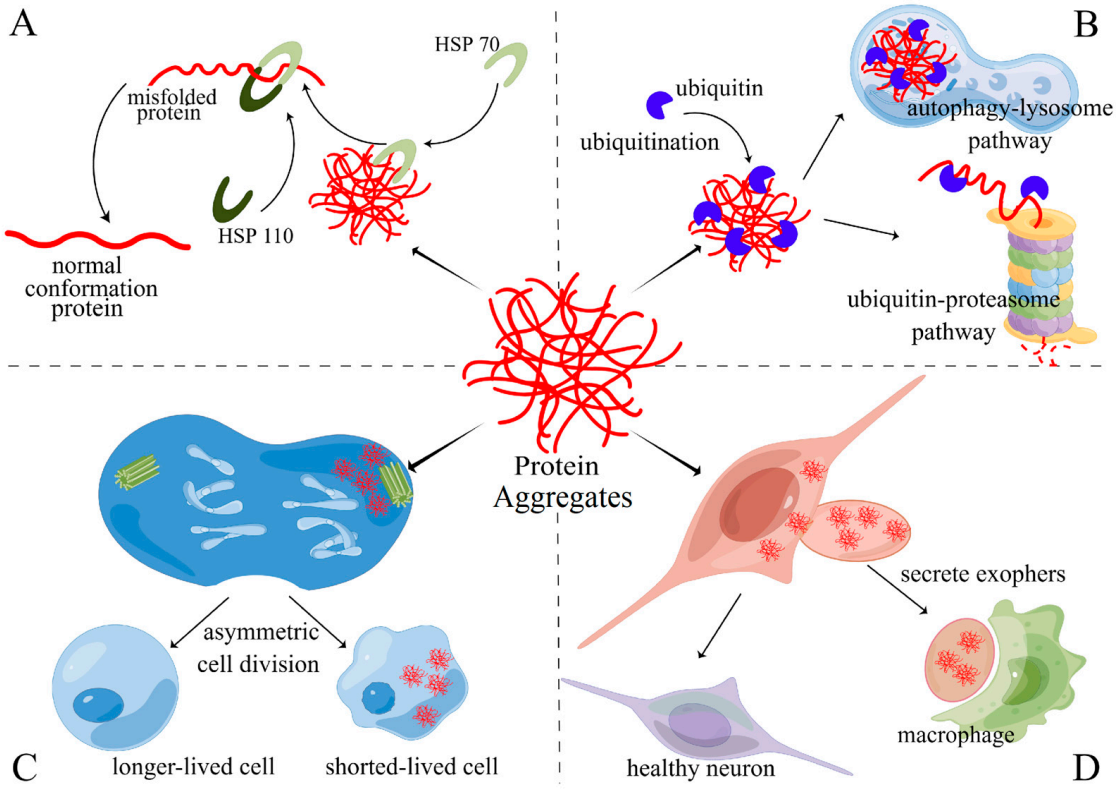

Figure 2. An organism can clear protein aggregates through four pathways: (**A**) HSPs family associate refolding and depolymerizing. In metazoa, HSP70 locate in protein aggregates, and with the help of HSP110, it applies pulling forces to aggregates that disentangle trapped polypeptides; (**B**) ubiquitin-proteasome pathway (UPP) and autophagy-lysosome pathway (ALP) can deal with protein aggregates when their scale exceeds the ability of HSPs family, UUP often degrades soluble misfolded proteins and aggregates, while insoluble proteins or aggregates were disposed of by ALP; (**C**) asymmetric cell division (ACD) can birth a healthier cell with fewer protein aggregates at the cost of another daughter cell with more protein aggregates and shorter life; (**D**) secrete exophers which contain protein aggregates are a useful way for G0 cells such as neurons, exophers would be cleared by macrophages.

For resting cells or dividing cells, asymmetric cell division (ACD) is also a good way to reduce protein aggregates in daughter cells [80,81,88] (Figure 2C). G0 cells such as mature neurons or myocardial cells cannot reduce protein aggregates via ACD, which

may explain why the nervous system and cardiovascular system are sensitive to protein aggregates. However, they can secrete aggregates via exocytosis as well. Interestingly, in neuron development, ACD is the main way to protect daughter cells from protein aggregates [88]. In embryonic *Drosophila* neuroblast, protein aggregates were transported to the microtubule organizing center (MTOC) and interacted with the peri-centriolar material (PCM) by dynein [89]. When centrosomes separated from each other during mitosis, the mother centrosome (older centrosome) would drag the PCM to one side of the cell. In this process, protein aggregates can also be enriched to one side of the spindle body. The daughter centrosome would form the new PCM with fewer protein aggregates [90–92]. Finally, the daughter cell, which inherits the protein aggregates, could undergo apoptosis, while the other cell would survive for obtaining better resources [93,94]. A mature cell that has lost the ability to divide can also discard protein aggregates through extruded membrane-surrounded vesicles called "exophers" that can harbor protein aggregates and organelles [95,96] (Figure 2D). Similar to ACD, the thin thread-like tube can induce protein aggregates accumulating on one side of the neuron, and then form a compartment, which is an average of 3.8 μm large, the same as a neuron. Exophers ultimately disconnect from the originating neuron [95]. This process is similar to mitosis, other than the nucleus, mother cells are completely retained. This pattern to remove protein aggregates may be the supplement measure for permanent cells for losing the ability of mitosis [96].

Though there are no pieces of evidence revealing that cells can dismantle mature protein aggregates and amyloid fibrils into soluble proteins through the molecular chaperone pathway, some chemical chaperones were found to destabilize or disaggregate misfolded or aggregated states of polypeptide chains by regulating the viscosity, melting point, and ionic strength of biological fluids. For example, tauroursodeoxycholic acid (TUDCA) supplementation can prevent cognitive impairment and amyloid deposition in APP/PS1 mice [97]. Besides bile acids, trehalose and betaine can also disrupt protein aggregate into protein soluble assemblies by changing ionic strength and stabilizing hydrophobic amino acids from hydrophobic protein–protein interactions [98,99]. Catechin derivatives, non-steroidal anti-inflammatory drugs (NSAIDs), anthracycline, and tetracycline derivatives also show the ability to disassemble protein aggregate. However, they still need more research to clarify the mechanism and reveal potential risks before use in clinical treatment [100–103].

6. The Function of Protein Aggregates in Development of Aging-Related Diseases

Much evidence discovered that protein aggregates have a close relationship with aging-related diseases. Limiting protein aggregates can be a useful method to change the development of diseases. From neurodegenerative diseases to diabetes and idiopathic cardiomyopathy, protein aggregation is the key factor that promotes disease development. Inhibiting the formation of protein aggregation or promoting the elimination of protein aggregation also show a good effect on aging related diseases.

Neurodegenerative diseases are the best-known diseases caused by protein aggregates, so they have been intensively studied. People proposed many hypotheses to explain the reason protein aggregates cause neurodegenerative diseases. Alzheimer's disease, Parkinson's disease, Huntington's disease, and Alexander's disease are all found to be linked to protein aggregates [9,29,31,43]. Though they accumulated different kinds of protein aggregates in different locations of the brain, they do lead to dysfunction, atrophy even, and apoptosis in the corresponding parts [9,32,33]. These abnormalities of cells and tissues present with all the familiar neural symptoms we know. Current studies have suggested that clearing protein aggregates or delaying protein aggregates accumulation can effectively slow down the progression of symptoms. Therefore, clearing protein aggregates is expected to become a treatment for neurodegenerative diseases.

Diabetes and idiopathic cardiomyopathy have the same pathological processes as neurodegenerative diseases. Many pieces of research prove that protein aggregates can accumulate in corresponding organs, causing symptoms such as inadequate insulin secretion or cardiac failure [5,34]. In the kidney, some evidence also remind us that protein aggregates

can accumulate in renal tubular epithelial cells in a high load and high-pressure state [36]. Also, in chronic kidney disease (CKD) disease models, protein aggregates were significantly increased [104]. Clearing protein aggregates in renal tubular epithelial cells may be an effective way to delay the process of CKD. However, the status of protein aggregates in CKD still needs more research to clarify which role protein aggregates play in CKD.

Interestingly, protein aggregation accumulation also has a good result in a special aging related disease, which is cancer. Some researchers discovered that promoting protein aggregation accumulation can accelerate oncocytes apoptosis and immunogenic cell death [105,106]. Oncocytes were in a hypersynthetic and hypermetabolic state, which cause more sensitivity to protein aggregation. Metabolic processes and the membrane system of oncocytes are disrupted by increasing the load of protein aggregation, So as to achieve the purpose of inhibiting the growth of cancer tissue.

7. Conclusions

Protein aggregation is a basic component of cells, the balance of protein aggregation is the key process for cells to keep protein homeostasis. In aging cells, this balance can be broken for lysosome degradation, ER stress, UPS, and so on. Also, protein aggregation accumulation could promote cell aging through breaking protein homeostasis. This sets in motion a self-propagating cycle that exacerbates proteome imbalance and eventually leads to protein homeostasis collapse and disease occurrence. Metabolism of protein aggregation depends on UPP, ALP, ACD, and exophers. Most of them are age-dependent decline, so it can explain why age is the major risk factor for aggregate-deposition diseases, and the nervous and cardiovascular are the generally damaged target systems of protein aggregation. Damage to the protein homeostasis network also injures the cells through a series of interactions. In these interactions, membrane system disruption, DNA damage, protein synthesis environment confusion, and lysosomal function disability are the key links, and they can mutually reinforce. Therefore, regulating protein aggregation is a useful pathway for therapeutic intervention of aging-related diseases and degenerative diseases, even cancer. However, achieving this goal requires a comprehensive understanding of the organization and relationship between protein homeostasis and protein aggregation.

Author Contributions: Conceptualization, J.-X.T. and H.-F.L.; methodology, J.-H.W.; investigation, J.-H.W.; resources, X.-H.H.; writing—original draft preparation, J.-H.W. and Z.-S.F.; writing—review and editing, J.-H.W., X.-H.H., J.-X.T. and H.-F.L.; visualization, D.-Y.L.; supervision, J.-X.T., H.-F.L.; project administration, J.-X.T. and H.-F.L.; funding acquisition, J.-X.T. and H.-F.L. All authors have read and agreed to the published version of the manuscript.

Funding: This work was supported by grants from the National Natural Science Foundation of China (81974095) and the Natural Science Foundation of Guangdong Province (2019A1515110152, 2023A1515012187), Guangdong Provincial Key Laboratory of Autophagy and Major Chronic Non-Communicable Diseases (2022B1212030003), Discipline Construction Project of Guangdong Medical University (4SG21229G).

Institutional Review Board Statement: This study does not involve humans or animals.

Data Availability Statement: Not applicable.

Acknowledgments: The authors acknowledge Xiaojun Guo for administrative assistance. Pictures were drawn by Figdraw.

Conflicts of Interest: The authors declare no conflict of interest.

References

1. Balch, W.E.; Morimoto, R.I.; Dillin, A.; Kelly, J.W. Adapting Proteostasis for Disease Intervention. *Science* **2008**, *319*, 916–919. [CrossRef] [PubMed]
2. Hipp, M.S.; Kasturi, P.; Hartl, F.U. The proteostasis network and its decline in ageing. *Nat. Rev. Mol. Cell Biol.* **2019**, *20*, 421–435. [CrossRef] [PubMed]

3. López-Otín, C.; Blasco, M.A.; Partridge, L.; Serrano, M.; Kroemer, G. The Hallmarks of Aging. *Cell* **2013**, *153*, 1194–1217. [CrossRef] [PubMed]
4. Ross, C.A.; Poirier, M.A. Protein aggregation and neurodegenerative disease. *Nat. Med.* **2004**, *10*, S10–S17. [CrossRef]
5. Knowles, T.; Vendruscolo, M.; Dobson, C.M. The amyloid state and its association with protein misfolding diseases. *Nat. Rev. Mol. Cell Biol.* **2014**, *15*, 384–396. [CrossRef]
6. Llamas, E.; Alirzayeva, H.; Loureiro, R.; Vilchez, D. The intrinsic proteostasis network of stem cells. *Curr. Opin. Cell Biol.* **2020**, *67*, 46–55. [CrossRef]
7. Bohnert, K.A.; Kenyon, C. A lysosomal switch triggers proteostasis renewal in the immortal *C. elegans* germ lineage. *Nature* **2017**, *551*, 629–633. [CrossRef]
8. Cheng, J.; North, B.J.; Zhang, T.; Dai, X.; Tao, K.; Guo, J.; Wei, W. The emerging roles of protein homeostasis-governing pathways in Alzheimer's disease. *Aging Cell* **2018**, *17*, e12801. [CrossRef]
9. Shults, C.W. Lewy bodies. *Proc. Natl. Acad. Sci. USA* **2006**, *103*, 1661–1668. [CrossRef]
10. Arrasate, M.; Finkbeiner, S. Protein aggregates in Huntington's disease. *Exp. Neurol.* **2012**, *238*, 1–11. [CrossRef]
11. Sanbe, A.; Osinska, H.; Saffitz, J.E.; Glabe, C.G.; Kayed, R.; Maloyan, A.; Robbins, J. Desmin-related cardiomyopathy in transgenic mice: A cardiac amyloidosis. *Proc. Natl. Acad. Sci. USA* **2004**, *101*, 10132–10136. [CrossRef]
12. Gianni, D.; Li, A.; Tesco, G.; McKay, K.; Moore, J.; Raygor, K.; Rota, M.; Gwathmey, J.K.; Dec, G.W.; Aretz, T.; et al. Protein Aggregates and Novel Presenilin Gene Variants in Idiopathic Dilated Cardiomyopathy. *Circulation* **2010**, *121*, 1216–1226. [CrossRef]
13. Hofmann, C.; Katus, H.A.; Doroudgar, S. Protein Misfolding in Cardiac Disease. *Circulation* **2019**, *139*, 2085–2088. [CrossRef]
14. Zaman, M.; Khan, A.N.; Zakariya, S.M.; Khan, R.H. Protein misfolding, aggregation and mechanism of amyloid cytotoxicity: An overview and therapeutic strategies to inhibit aggregation. *Int. J. Biol. Macromol.* **2019**, *134*, 1022–1037. [CrossRef]
15. Alberti, S.; Hyman, A.A. Biomolecular condensates at the nexus of cellular stress, protein aggregation disease and ageing. *Nat. Rev. Mol. Cell Biol.* **2021**, *22*, 196–213. [CrossRef]
16. Walther, D.M.; Kasturi, P.; Zheng, M.; Pinkert, S.; Vecchi, G.; Ciryam, P.; Morimoto, R.I.; Dobson, C.M.; Vendruscolo, M.; Mann, M.; et al. Widespread Proteome Remodeling and Aggregation in Aging *C. elegans*. *Cell* **2015**, *161*, 919–932. [CrossRef]
17. Kulkarni, P.; Uversky, V.N. Intrinsically Disordered Proteins in Chronic Diseases. *Biomolecules* **2019**, *9*, 147. [CrossRef]
18. Wright, P.E.; Dyson, H.J. Intrinsically disordered proteins in cellular signalling and regulation. *Nat. Rev. Mol. Cell Biol.* **2014**, *16*, 18–29. [CrossRef]
19. Abyzov, A.; Blackledge, M.; Zweckstetter, M. Conformational Dynamics of Intrinsically Disordered Proteins Regulate Biomolecular Condensate Chemistry. *Chem. Rev.* **2022**, *122*, 6719–6748. [CrossRef]
20. Banani, S.F.; Lee, H.O.; Hyman, A.A.; Rosen, M.K. Biomolecular condensates: Organizers of cellular biochemistry. *Nat. Rev. Mol. Cell Biol.* **2017**, *18*, 285–298. [CrossRef]
21. Uversky, V.N. The Mysterious Unfoldome: Structureless, Underappreciated, Yet Vital Part of Any Given Proteome. *J. Biomed. Biotechnol.* **2009**, *2010*, 568068. [CrossRef] [PubMed]
22. Dao, T.P.; Kolaitis, R.-M.; Kim, H.J.; O'donovan, K.; Martyniak, B.; Colicino, E.; Hehnly, H.; Taylor, J.P.; Castañeda, C.A. Ubiquitin Modulates Liquid-Liquid Phase Separation of UBQLN2 via Disruption of Multivalent Interactions. *Mol. Cell* **2018**, *69*, 965–978.e6. [CrossRef] [PubMed]
23. Wallace, E.W.; Kear-Scott, J.L.; Pilipenko, E.V.; Schwartz, M.H.; Laskowski, P.R.; Rojek, A.E.; Katanski, C.D.; Riback, J.A.; Dion, M.F.; Franks, A.M.; et al. Reversible, Specific, Active Aggregates of Endogenous Proteins Assemble upon Heat Stress. *Cell* **2015**, *162*, 1286–1298. [CrossRef] [PubMed]
24. Lin, Y.; Protter, D.S.W.; Rosen, M.K.; Parker, R. Formation and Maturation of Phase-Separated Liquid Droplets by RNA-Binding Proteins. *Mol. Cell* **2015**, *60*, 208–219. [CrossRef] [PubMed]
25. Tauber, D.; Tauber, G.; Khong, A.; Van Treeck, B.; Pelletier, J.; Parker, R. Modulation of RNA Condensation by the DEAD-Box Protein eIF4A. *Cell* **2020**, *180*, 411–426.e16. [CrossRef]
26. Louka, A.; Zacco, E.; Temussi, P.A.; Tartaglia, G.G.; Pastore, A. RNA as the stone guest of protein aggregation. *Nucleic Acids Res.* **2020**, *48*, 11880–11889. [CrossRef]
27. Roden, C.; Gladfelter, A.S. RNA contributions to the form and function of biomolecular condensates. *Nat. Rev. Mol. Cell Biol.* **2020**, *22*, 183–195. [CrossRef]
28. Johnson, B.; Snead, D.; Lee, J.J.; McCaffery, J.M.; Shorter, J.; Gitler, A.D. TDP-43 is Intrinsically Aggregation-prone, and Amyotrophic Lateral Sclerosis-linked Mutations Accelerate Aggregation and Increase Toxicity. *J. Biol. Chem.* **2009**, *284*, 20329–20339. [CrossRef]
29. Suram, A.; Hegde, M.; Rao, K. A new evidence for DNA nicking property of amyloid β-peptide (1–42): Relevance to Alzheimer's disease. *Arch. Biochem. Biophys.* **2007**, *463*, 245–252. [CrossRef]
30. Armstrong, R.A.; Lantos, P.L.; Cairns, N.J. What determines the molecular composition of abnormal protein aggregates in neurodegenerative disease? *Neuropathology* **2008**, *28*, 351–365. [CrossRef]
31. Yin, Y.; Gao, D.; Wang, Y.; Wang, Z.-H.; Wang, X.; Ye, J.; Wu, D.; Fang, L.; Pi, G.; Yang, Y.; et al. Tau accumulation induces synaptic impairment and memory deficit by calcineurin-mediated inactivation of nuclear CaMKIV/CREB signaling. *Proc. Natl. Acad. Sci. USA* **2016**, *113*, E3773–E3781. [CrossRef]
32. Polymeropoulos, M.H.; Lavedan, C.; Leroy, E.; Ide, S.E.; Dehejia, A.; Dutra, A.; Dutra, A.; Pike, B.; Root, H.; Rubenstein, J.; et al. Mutation in the α-Synuclein Gene Identified in Families with Parkinson's Disease. *Science* **1997**, *276*, 2045–2047. [CrossRef]

33. Singleton, A.B.; Farrer, M.; Johnson, J.; Singleton, A.; Hague, S.; Kachergus, J.; Hulihan, M.; Peuralinna, T.; Dutra, A.; Nussbaum, R.; et al. alpha-Synuclein Locus Triplication Causes Parkinson's Disease. *Science* **2003**, *302*, 841. [CrossRef]
34. Xu, N.; Gulick, J.; Osinska, H.; Yu, Y.; McLendon, P.M.; Shay-Winkler, K.; Robbins, J.; Yutzey, K.E. Ube2v1 Positively Regulates Protein Aggregation by Modulating Ubiquitin Proteasome System Performance Partially Through K63 Ubiquitination. *Circ. Res.* **2020**, *126*, 907–922. [CrossRef]
35. Zellner, A.; Scharrer, E.; Arzberger, T.; Oka, C.; Domenga-Denier, V.; Joutel, A.; Lichtenthaler, S.F.; Müller, S.A.; Dichgans, M.; Haffner, C. CADASIL brain vessels show a HTRA1 loss-of-function profile. *Acta Neuropathol.* **2018**, *136*, 111–125. [CrossRef]
36. Cheema, M.U.; Poulsen, E.T.; Enghild, J.J.; Hoorn, E.; Fenton, R.A.; Praetorius, J. Aldosterone and angiotensin II induce protein aggregation in renal proximal tubules. *Physiol. Rep.* **2013**, *1*, e00064. [CrossRef]
37. Koga, H.; Kaushik, S.; Cuervo, A.M. Protein homeostasis and aging: The importance of exquisite quality control. *Ageing Res. Rev.* **2011**, *10*, 205–215. [CrossRef]
38. Baldwin, A.J.; Knowles, T.P.J.; Tartaglia, G.G.; Fitzpatrick, A.W.; Devlin, G.L.; Shammas, S.L.; Waudby, C.A.; Mossuto, M.F.; Meehan, S.; Gras, S.L.; et al. Metastability of Native Proteins and the Phenomenon of Amyloid Formation. *J. Am. Chem. Soc.* **2011**, *133*, 14160–14163. [CrossRef]
39. Tartaglia, G.G.; Pechmann, S.; Dobson, C.M.; Vendruscolo, M. Life on the edge: A link between gene expression levels and aggregation rates of human proteins. *Trends Biochem. Sci.* **2007**, *32*, 204–206. [CrossRef]
40. Ciryam, P.; Tartaglia, G.G.; Morimoto, R.I.; Dobson, C.M.; Vendruscolo, M. Widespread Aggregation and Neurodegenerative Diseases Are Associated with Supersaturated Proteins. *Cell Rep.* **2013**, *5*, 781–790. [CrossRef]
41. Amzallag, E.; Hornstein, E. Crosstalk between Biomolecular Condensates and Proteostasis. *Cells* **2022**, *11*, 2415. [CrossRef]
42. Yasuda, S.; Tsuchiya, H.; Kaiho, A.; Guo, Q.; Ikeuchi, K.; Endo, A.; Arai, N.; Ohtake, F.; Murata, S.; Inada, T.; et al. Stress- and ubiquitylation-dependent phase separation of the proteasome. *Nature* **2020**, *578*, 296–300. [CrossRef] [PubMed]
43. Heaven, M.R.; Flint, D.; Randall, S.M.; Sosunov, A.A.; Wilson, L.; Barnes, S.; Goldman, J.E.; Muddiman, D.C.; Brenner, M. Composition of Rosenthal Fibers, the Protein Aggregate Hallmark of Alexander Disease. *J. Proteome Res.* **2016**, *15*, 2265–2282. [CrossRef] [PubMed]
44. Gazit, E. The "Correctly Folded" state of proteins: Is it a metastable state? *Angew. Chem. Int. Ed.* **2002**, *41*, 257–259. [CrossRef]
45. Sies, H.; Berndt, C.; Jones, D.P. Oxidative Stress. *Annu. Rev. Biochem.* **2017**, *86*, 715–748. [CrossRef]
46. Zhang, H.; Ji, X.; Li, P.; Liu, C.; Lou, J.; Wang, Z.; Wen, W.; Xiao, Y.; Zhang, M.; Zhu, X. Liquid-liquid phase separation in biology: Mechanisms, physiological functions and human diseases. *Sci. China Life Sci.* **2020**, *63*, 953–985. [CrossRef]
47. Gui, X.; Luo, F.; Li, Y.; Zhou, H.; Qin, Z.; Liu, Z.; Gu, J.; Xie, M.; Zhao, K.; Dai, B.; et al. Structural basis for reversible amyloids of hnRNPA1 elucidates their role in stress granule assembly. *Nat. Commun.* **2019**, *10*, 2006. [CrossRef]
48. Zbinden, A.; Pérez-Berlanga, M.; De Rossi, P.; Polymenidou, M. Phase Separation and Neurodegenerative Diseases: A Disturbance in the Force. *Dev. Cell* **2020**, *55*, 45–68. [CrossRef]
49. Ray, S.; Singh, N.; Kumar, R.; Patel, K.; Pandey, S.; Datta, D.; Mahato, J.; Panigrahi, R.; Navalkar, A.; Mehra, S.; et al. α-Synuclein aggregation nucleates through liquid–liquid phase separation. *Nat. Chem.* **2020**, *12*, 705–716. [CrossRef]
50. Ling, D.; Song, H.-J.; Garza, D.; Neufeld, T.P.; Salvaterra, P.M. Abeta42-Induced Neurodegeneration via an Age-Dependent Autophagic-Lysosomal Injury in Drosophila. *PLoS ONE* **2009**, *4*, e4201. [CrossRef]
51. Feng, Q.; Luo, Y.; Zhang, X.-N.; Yang, X.-F.; Hong, X.-Y.; Sun, D.-S.; Li, X.-C.; Hu, Y.; Li, X.-G.; Zhang, J.-F.; et al. MAPT/Tau accumulation represses autophagy flux by disrupting IST1-regulated ESCRT-III complex formation: A vicious cycle in Alzheimer neurodegeneration. *Autophagy* **2019**, *16*, 641–658. [CrossRef]
52. Ravikumar, B.; Vacher, C.; Berger, Z.; Davies, J.E.; Luo, S.; Oroz, L.G.; Scaravilli, F.; Easton, D.F.; Duden, R.; O'Kane, C.J.; et al. Inhibition of mTOR induces autophagy and reduces toxicity of polyglutamine expansions in fly and mouse models of Huntington disease. *Nat. Genet.* **2004**, *36*, 585–595. [CrossRef]
53. Nixon, R.A. The role of autophagy in neurodegenerative disease. *Nat. Med.* **2013**, *19*, 983–997. [CrossRef]
54. Ambegaokar, S.S.; Jackson, G.R. The downward spiral of tau and autolysosomes: A new hypothesis in neurodegeneration. *Autophagy* **2012**, *8*, 1144–1145. [CrossRef]
55. Tu, H.; Yuan, B.; Hou, X.; Zhang, X.; Pei, C.; Ma, Y.; Yang, Y.; Fan, Y.; Qin, Z.; Liu, C.; et al. α-synuclein suppresses microglial autophagy and promotes neurodegeneration in a mouse model of Parkinson's disease. *Aging Cell* **2021**, *20*, e13522. [CrossRef]
56. Hamdan, N.; Kritsiligkou, P.; Grant, C.M. ER stress causes widespread protein aggregation and prion formation. *J. Cell Biol.* **2017**, *216*, 2295–2304. [CrossRef]
57. Stojkovska, I.; Wani, W.Y.; Zunke, F.; Belur, N.R.; Pavlenko, E.A.; Mwenda, N.; Sharma, K.; Francelle, L.; Mazzulli, J.R. Rescue of α-synuclein aggregation in Parkinson's patient neurons by synergistic enhancement of ER proteostasis and protein trafficking. *Neuron* **2021**, *110*, 436–451.e11. [CrossRef]
58. Kramer, N.J.; Haney, M.S.; Morgens, D.W.; Jovičić, A.; Couthouis, J.; Li, A.; Ousey, J.; Ma, R.; Bieri, G.; Tsui, C.K.; et al. CRISPR–Cas9 screens in human cells and primary neurons identify modifiers of C9ORF72 dipeptide-repeat-protein toxicity. *Nat. Genet.* **2018**, *50*, 603–612. [CrossRef]
59. Frakes, A.E.; Metcalf, M.G.; Tronnes, S.U.; Bar-Ziv, R.; Durieux, J.; Gildea, H.K.; Kandahari, N.; Monshietehadi, S.; Dillin, A. Four glial cells regulate ER stress resistance and longevity via neuropeptide signaling in *C. elegans*. *Science* **2020**, *367*, 436–440. [CrossRef]

60. Schubert, D.; Behl, C.; Lesley, R.; Brack, A.; Dargusch, R.; Sagara, Y.; Kimura, H. Amyloid peptides are toxic via a common oxidative mechanism. *Proc. Natl. Acad. Sci. USA* **1995**, *92*, 1989–1993. [CrossRef]
61. Mattson, M.P. Pathways towards and away from Alzheimer's disease. *Nature* **2004**, *430*, 631–639. [CrossRef] [PubMed]
62. Ainslie, A.; Huiting, W.; Barazzuol, L.; Bergink, S. Genome instability and loss of protein homeostasis: Converging paths to neurodegeneration? *Open Biol.* **2021**, *11*, 200296. [CrossRef] [PubMed]
63. Fortuna, T.R.; Kour, S.; Anderson, E.N.; Ward, C.; Rajasundaram, D.; Donnelly, C.J.; Hermann, A.; Wyne, H.; Shewmaker, F.; Pandey, U.B. DDX17 is involved in DNA damage repair and modifies FUS toxicity in an RGG-domain dependent manner. *Acta Neuropathol.* **2021**, *142*, 515–536. [CrossRef] [PubMed]
64. Vasquez, V.; Mitra, J.; Hegde, P.M.; Pandey, A.; Sengupta, S.; Mitra, S.; Rao, K.; Hegde, M.L. Chromatin-Bound Oxidized α-Synuclein Causes Strand Breaks in Neuronal Genomes in in vitro Models of Parkinson's Disease. *J. Alzheimer's Dis.* **2017**, *60*, S133–S150. [CrossRef] [PubMed]
65. Weissman, L.; Jo, D.-G.; Sørensen, M.M.; de Souza-Pinto, N.C.; Markesbery, W.R.; Mattson, M.P.; Bohr, V.A. Defective DNA base excision repair in brain from individuals with Alzheimer's disease and amnestic mild cognitive impairment. *Nucleic Acids Res.* **2007**, *35*, 5545–5555. [CrossRef]
66. Bucciantini, M.; Calloni, G.; Chiti, F.; Formigli, L.; Nosi, D.; Dobson, C.M.; Stefani, M. Prefibrillar Amyloid Protein Aggregates Share Common Features of Cytotoxicity. *J. Biol. Chem.* **2004**, *279*, 31374–31382. [CrossRef]
67. Demuro, A.; Mina, E.; Kayed, R.; Milton, S.C.; Parker, I.; Glabe, C.G. Calcium Dysregulation and Membrane Disruption as a Ubiquitous Neurotoxic Mechanism of Soluble Amyloid Oligomers. *J. Biol. Chem.* **2005**, *280*, 17294–17300. [CrossRef]
68. Bode, D.C.; Baker, M.D.; Viles, J.H. Ion Channel Formation by Amyloid-β42 Oligomers but Not Amyloid-β40 in Cellular Membranes. *J. Biol. Chem.* **2017**, *292*, 1404–1413. [CrossRef]
69. Bode, D.C.; Freeley, M.; Nield, J.; Palma, M.; Viles, J.H. Amyloid-β oligomers have a profound detergent-like effect on lipid membrane bilayers, imaged by atomic force and electron microscopy. *J. Biol. Chem.* **2019**, *294*, 7566–7572. [CrossRef]
70. Valincius, G.; Heinrich, F.; Budvytyte, R.; Vanderah, D.J.; McGillivray, D.; Sokolov, Y.; Hall, J.E.; Lösche, M. Soluble Amyloid β-Oligomers Affect Dielectric Membrane Properties by Bilayer Insertion and Domain Formation: Implications for Cell Toxicity. *Biophys. J.* **2008**, *95*, 4845–4861. [CrossRef]
71. Sokolov, Y.; Kozak, J.A.; Kayed, R.; Chanturiya, A.; Glabe, C.; Hall, J.E. Soluble Amyloid Oligomers Increase Bilayer Conductance by Altering Dielectric Structure. *J. Gen. Physiol.* **2006**, *128*, 637–647. [CrossRef]
72. Kayed, R.; Sokolov, Y.; Edmonds, B.; McIntire, T.M.; Milton, S.C.; Hall, J.E.; Glabe, C.G. Permeabilization of Lipid Bilayers Is a Common Conformation-dependent Activity of Soluble Amyloid Oligomers in Protein Misfolding Diseases. *J. Biol. Chem.* **2004**, *279*, 46363–46366. [CrossRef]
73. Williams, T.L.; Serpell, L.C. Membrane and surface interactions of Alzheimer's Aβ peptide—Insights into the mechanism of cytotoxicity. *FEBS J.* **2011**, *278*, 3905–3917. [CrossRef]
74. Canale, C.; Oropesa-Nuñez, R.; Diaspro, A.; Dante, S. Amyloid and membrane complexity: The toxic interplay revealed by AFM. *Semin. Cell Dev. Biol.* **2017**, *73*, 82–94. [CrossRef]
75. Butterfield, S.M.; Lashuel, H.A. Amyloidogenic Protein-Membrane Interactions: Mechanistic Insight from Model Systems. *Angew. Chem. Int. Ed.* **2010**, *49*, 5628–5654. [CrossRef]
76. Green, J.; Kreplak, L.; Goldsbury, C.; Blatter, X.L.; Stolz, M.; Cooper, G.; Seelig, A.; Kistler, J.; Aebi, U. Atomic Force Microscopy Reveals Defects Within Mica Supported Lipid Bilayers Induced by the Amyloidogenic Human Amylin Peptide. *J. Mol. Biol.* **2004**, *342*, 877–887. [CrossRef]
77. Sasahara, K.; Morigaki, K.; Shinya, K. Effects of membrane interaction and aggregation of amyloid β-peptide on lipid mobility and membrane domain structure. *Phys. Chem. Chem. Phys.* **2013**, *15*, 8929–8939. [CrossRef]
78. Butterfield, D.; Drake, J.; Pocernich, C.; Castegna, A. Evidence of oxidative damage in Alzheimer's disease brain: Central role for amyloid β-peptide. *Trends Mol. Med.* **2001**, *7*, 548–554. [CrossRef]
79. Tabner, B.J.; Turnbull, S.; El-Agnaf, O.M.; Allsop, D. Formation of hydrogen peroxide and hydroxyl radicals from Aβ and α-synuclein as a possible mechanism of cell death in Alzheimer's disease and Parkinson's disease. *Free. Radic. Biol. Med.* **2002**, *32*, 1076–1083. [CrossRef]
80. Mogk, A.; Bukau, B.; Kampinga, H.H. Cellular Handling of Protein Aggregates by Disaggregation Machines. *Mol. Cell* **2018**, *69*, 214–226. [CrossRef]
81. Singhvi, A.; Garriga, G. Asymmetric divisions, aggresomes and apoptosis. *Trends Cell Biol.* **2009**, *19*, 1–7. [CrossRef] [PubMed]
82. Kropski, J.A.; Blackwell, T.S. Endoplasmic reticulum stress in the pathogenesis of fibrotic disease. *J. Clin. Investig.* **2018**, *128*, 64–73. [CrossRef] [PubMed]
83. Pohl, C.; Dikic, I. Cellular quality control by the ubiquitin-proteasome system and autophagy. *Science* **2019**, *366*, 818–822. [CrossRef]
84. Dikic, I. Proteasomal and Autophagic Degradation Systems. *Annu. Rev. Biochem.* **2017**, *86*, 193–224. [CrossRef] [PubMed]
85. Wurzer, B.; Zaffagnini, G.; Fracchiolla, D.; Turco, E.; Abert, C.; Romanov, J.; Martens, S. Oligomerization of p62 allows for selection of ubiquitinated cargo and isolation membrane during selective autophagy. *eLife* **2015**, *4*, e08941. [CrossRef]
86. Akopian, D.; Rape, M. Principles of Ubiquitin-Dependent Signaling. *Annu. Rev. Cell Dev. Biol.* **2018**, *34*, 137–162. [CrossRef]
87. Sarraf, S.A.; Shah, H.V.; Kanfer, G.; Pickrell, A.M.; Holtzclaw, L.A.; Ward, M.E.; Youle, R.J. Loss of TAX1BP1-Directed Autophagy Results in Protein Aggregate Accumulation in the Brain. *Mol. Cell* **2020**, *80*, 779–795.e10. [CrossRef]

88. Rujano, M.A.; Bosveld, F.; Salomons, F.A.; Dijk, F.; Van Waarde, M.A.W.H.; van der Want, J.; De Vos, R.A.I.; Brunt, E.R.; Sibon, O.C.M.; Kampinga, H.H. Polarised Asymmetric Inheritance of Accumulated Protein Damage in Higher Eukaryotes. *PLoS Biol.* **2006**, *4*, e417. [CrossRef]
89. Garcia-Mata, R.; Gao, Y.-S.; Sztul, E. Hassles with Taking Out the Garbage: Aggravating Aggresomes. *Traffic* **2002**, *3*, 388–396. [CrossRef]
90. Rebollo, E.; Sampaio, P.; Januschke, J.; Llamazares, S.; Varmark, H.; González, C. Functionally Unequal Centrosomes Drive Spindle Orientation in Asymmetrically Dividing Drosophila Neural Stem Cells. *Dev. Cell* **2007**, *12*, 467–474. [CrossRef]
91. Rusan, N.M.; Peifer, M. A role for a novel centrosome cycle in asymmetric cell division. *J. Cell Biol.* **2007**, *177*, 13–20. [CrossRef]
92. Yamashita, Y.M.; Mahowald, A.P.; Perlin, J.R.; Fuller, M.T. Asymmetric Inheritance of Mother Versus Daughter Centrosome in Stem Cell Division. *Science* **2007**, *315*, 518–521. [CrossRef]
93. Cordes, S.; Frank, C.A.; Garriga, G. The *C. elegans* MELK ortholog PIG-1 regulates cell size asymmetry and daughter cell fate in asymmetric neuroblast divisions. *Development* **2006**, *133*, 2747–2756. [CrossRef]
94. Frank, C.A.; Hawkins, N.C.; Guenther, C.; Horvitz, H.R.; Garriga, G.C. *elegans* HAM-1 positions the cleavage plane and regulates apoptosis in asymmetric neuroblast divisions. *Dev. Biol.* **2005**, *284*, 301–310. [CrossRef]
95. Melentijevic, I.; Toth, M.L.; Arnold, M.L.; Guasp, R.J.; Harinath, G.; Nguyen, K.C.; Taub, D.; Parker, J.A.; Neri, C.; Gabel, C.V.; et al. *C. elegans* neurons jettison protein aggregates and mitochondria under neurotoxic stress. *Nature* **2017**, *542*, 367–371. [CrossRef]
96. Nicolás-Ávila, J.A.; Lechuga-Vieco, A.V.; Esteban-Martínez, L.; Sánchez-Díaz, M.; Díaz-García, E.; Santiago, D.J.; Rubio-Ponce, A.; Li, J.L.; Balachander, A.; Quintana, J.A.; et al. A Network of Macrophages Supports Mitochondrial Homeostasis in the Heart. *Cell* **2020**, *183*, 94–109.e23. [CrossRef]
97. Lo, A.C.; Callaerts-Vegh, Z.; Nunes, A.F.; Rodrigues, C.M.; D'Hooge, R. Tauroursodeoxycholic acid (TUDCA) supplementation prevents cognitive impairment and amyloid deposition in APP/PS1 mice. *Neurobiol. Dis.* **2013**, *50*, 21–29. [CrossRef]
98. Natalello, A.; Liu, J.; Ami, D.; Doglia, S.M.; de Marco, A. The osmolyte betaine promotes protein misfolding and disruption of protein aggregates. *Proteins Struct. Funct. Bioinform.* **2008**, *75*, 509–517. [CrossRef]
99. Liu, R.; Barkhordarian, H.; Emadi, S.; Park, C.B.; Sierks, M.R. Trehalose differentially inhibits aggregation and neurotoxicity of beta-amyloid 40 and 42. *Neurobiol. Dis.* **2005**, *20*, 74–81. [CrossRef]
100. Almeida, Z.L.; Brito, R.M.M. Amyloid Disassembly: What Can We Learn from Chaperones? *Biomedicines* **2022**, *10*, 3276. [CrossRef]
101. Hirohata, M.; Ono, K.; Naiki, H.; Yamada, M. Non-steroidal anti-inflammatory drugs have anti-amyloidogenic effects for Alzheimer's β-amyloid fibrils in vitro. *Neuropharmacology* **2005**, *49*, 1088–1099. [CrossRef] [PubMed]
102. Forloni, G.; Colombo, L.; Girola, L.; Tagliavini, F.; Salmona, M. Anti-amyloidogenic activity of tetracyclines: Studies in vitro. *FEBS Lett.* **2001**, *487*, 404–407. [CrossRef] [PubMed]
103. Andrich, K.; Bieschke, J. The Effect of (−)-Epigallo-catechin-(3)-gallate on Amyloidogenic Proteins Suggests a Common Mechanism. *Nat. Compd. Ther. Agents Amyloidogenic Dis.* **2015**, *863*, 139–161. [CrossRef]
104. Brijmohan, A.S.; Batchu, S.N.; Majumder, S.; Alghamdi, T.A.; Thieme, K.; McGaugh, S.; Liu, Y.; Advani, S.L.; Bowskill, B.B.; Kabir, M.G.; et al. HDAC6 Inhibition Promotes Transcription Factor EB Activation and Is Protective in Experimental Kidney Disease. *Front. Pharmacol.* **2018**, *9*, 34. [CrossRef]
105. McGrail, D.J.; Garnett, J.; Yin, J.; Dai, H.; Shih, D.J.; Lam, T.N.A.; Li, Y.; Sun, C.; Li, Y.; Schmandt, R.; et al. Proteome Instability Is a Therapeutic Vulnerability in Mismatch Repair-Deficient Cancer. *Cancer Cell* **2020**, *37*, 371–386.e12. [CrossRef]
106. Kumar, S.; Stokes, J.; Singh, U.P.; Gunn, K.S.; Acharya, A.; Manne, U.; Mishra, M. Targeting Hsp70: A possible therapy for cancer. *Cancer Lett.* **2016**, *374*, 156–166. [CrossRef]

International Journal of
Molecular Sciences

MDPI

Article

Neuroprotection of Andrographolide against Neurotoxin MPP$^+$-Induced Apoptosis in SH-SY5Y Cells via Activating Mitophagy, Autophagy, and Antioxidant Activities

Prachayaporn Prasertsuksri [1], Pichnaree Kraokaew [1], Kanta Pranweerapaiboon [1,2], Prasert Sobhon [1] and Kulathida Chaithirayanon [1,*]

[1] Department of Anatomy, Faculty of Science, Mahidol University, Bangkok 10400, Thailand; prachayaporn.prs@student.mahidol.ac.th (P.P.)
[2] Chulabhorn International College of Medicine, Thammasat University, Pathumthani 12120, Thailand
* Correspondence: kulathida.cha@mahidol.edu

Abstract: Parkinson's disease (PD) is associated with dopaminergic neuron loss and alpha-synuclein aggregation caused by ROS overproduction, leading to mitochondrial dysfunction and autophagy impairment. Recently, andrographolide (Andro) has been extensively studied for various pharmacological properties, such as anti-diabetic, anti-cancer, anti-inflammatory, and anti-atherosclerosis. However, its potential neuroprotective effects on neurotoxin MPP$^+$-induced SH-SY5Y cells, a cellular PD model, remain uninvestigated. In this study, we hypothesized that Andro has neuroprotective effects against MPP$^+$-induced apoptosis, which may be mediated through the clearance of dysfunctional mitochondria by mitophagy and ROS by antioxidant activities. Herein, Andro pretreatment could attenuate MPP$^+$-induced neuronal cell death that was reflected by reducing mitochondrial membrane potential (MMP) depolarization, alpha-synuclein, and pro-apoptotic proteins expressions. Concomitantly, Andro attenuated MPP$^+$-induced oxidative stress through mitophagy, as indicated by increasing colocalization of MitoTracker Red with LC3, upregulations of the PINK1–Parkin pathway, and autophagy-related proteins. On the contrary, Andro-activated autophagy was compromised when pretreated with 3-MA. Furthermore, Andro activated the Nrf2/KEAP1 pathway, leading to increasing genes encoding antioxidant enzymes and activities. This study elucidated that Andro exhibited significant neuroprotective effects against MPP$^+$-induced SH-SY5Y cell death in vitro by enhancing mitophagy and clearance of alpha-synuclein through autophagy, as well as increasing antioxidant capacity. Our results provide evidence that Andro could be considered a potential supplement for PD prevention.

Keywords: Parkinson's disease; andrographolide; MPP$^+$; SH-SY5Y cells; ROS; Nrf2; mitophagy

Citation: Prasertsuksri, P.; Kraokaew, P.; Pranweerapaiboon, K.; Sobhon, P.; Chaithirayanon, K. Neuroprotection of Andrographolide against Neurotoxin MPP$^+$-Induced Apoptosis in SH-SY5Y Cells via Activating Mitophagy, Autophagy, and Antioxidant Activities. *Int. J. Mol. Sci.* **2023**, *24*, 8528. https://doi.org/10.3390/ijms24108528

Academic Editor: Claudia Ricci

Received: 12 April 2023
Revised: 6 May 2023
Accepted: 8 May 2023
Published: 10 May 2023

1. Introduction

Parkinson's disease (PD) is a progressive neurological disorder frequently found in elderlies. Globally, the number of individuals with PD has more than doubled to over 6 million. This disease mainly affects motor and non-motor systems due to the loss of dopaminergic neurons (DA) in the substantia nigra pars compacta and striatal terminal, respectively [1]. The loss of DA is caused by aging, gene mutations, and neurotoxin exposures such as 1-methyl-4-phenylpyridinium (MPP$^+$), 6-hydroxydopamine (6-OHDA), and agricultural toxins. In particular, neurotoxin MPP$^+$ has been widely applied in the in vitro cellular models of PD owing to its ability to generate excessive reactive oxygen species (ROS) [2]. The ensuing oxidative stress causes depolarization of mitochondrial membrane potential ($\Delta\psi M$), which leads to the impairment of mitochondria through the inhibition of the electron transport chain (ETC) at the complex I, resulting in ATP depletion and thus initiating the death of DA neurons [3–6]. In addition, a recent study has shown

that MPP^+ increases the accumulation of misfolded alpha-synuclein, which contributes further to PD progression [7].

Normally, mitophagy helps regulate mitochondrial number and quality by eliminating damaged or dysfunctional mitochondria by using common mediators with the autophagic process [8]. In addition, PTEN-induced kinase 1 (PINK1) and Parkin RBR E3 ubiquitin-protein ligase (Parkin) are markers of dysfunctional mitochondria destined for mitophagy in neurodegenerative diseases such as PD [9–11]. In this regard, the dimerization of PINK1 at the outer mitochondrial membrane (OMM) recruits and phosphorylates Parkin, followed by ubiquitination (Ub) of damaged mitochondria. Poly-Ub chains are subsequently phosphorylated by PINK1 and serve as an 'eat me' signal for the autophagic machinery. Adaptor proteins (p62, OPTN (optineurin), NDP52 (nuclear dot protein 52 kDa) recognize phosphorylated poly-Ub chains, resulting in the initiation of autophagosome around dysfunctional mitochondria and binding with LC3, which leads to fusion with lysosome and degradation. Thus, autophagy is an important mechanism that plays a major role in removing damaged organelles (such as mitochondria) and proteins (such as misfolded alpha-synuclein) via autophagosome–lysosome fusion and degradation. Impaired autophagy leads to accumulations of dysfunctional mitochondria and alpha-synuclein, which subsequently leads to neuron death.

Various medications such as levodopa, carbidopa, bromocriptine, entacapone, and deep brain stimulation have been applied to cure PD. However, these pharmacologic agents provide only symptomatic relief of PD, but not cure [12,13]. Hence, discoveries of natural products may prevent or decelerate the progression of PD. The potential anti-PD action of natural products could be conveniently screened by determining their ability to attenuate damage in a cellular model of PD, such as MPP^+-induced SH-SY5Y cells. Interestingly, andrographolide (Andro), a natural product isolated from *Andrographis paniculata*, was found to exhibit many pharmacological activities, especially antioxidant and anti-inflammatory properties [14]. For instance, Andro could increase the expression of nuclear factor erythroid 2-related factor 2 (Nrf2)/heme oxygenase 1 (HO-1) in rats with middle cerebral artery occlusion (MCAO)-induced ischemic stroke, which upregulated p38 MAPK signaling [15]. Mechanistically, dissociation of the KEAP1/Nrf2 complex induces Nrf2 nuclear translocation, which triggers the transcription of antioxidant enzymes such as heme oxygenase-1 (HO-1), superoxide dismutase (SOD), catalase (CAT), and glutathione peroxidase (GPx) [16]. Moreover, Andro ameliorated the inflammatory response in microglia by activating the Nrf2/HO-1 pathway and inhibiting NF-κB expression [17]. More importantly, a recent study demonstrated that Andro suppresses NLRP3 inflammasome activation in MPP^+ and LPS-induced microglia through the induction of Parkin-mediated mitophagy in in vitro and in vivo models of Parkinson's disease [18]. Nevertheless, whether Andro could provide neuroprotection against MPP^+ insult in human neuroblastoma SH-SY5Y cell line remains uninvestigated. Therefore, in the present study, we investigated whether Andro could prevent MPP^+-induced death of SH-SY5Y cells, serving as an in vitro model of PD, via inductions of mitophagy–autophagy and antioxidant mechanisms.

2. Results

2.1. Andrographolide Mitigates Death of Human Neuroblastoma SH-SY5Y Cells Induced by MPP^+

To study the neuroprotection of Andro, we first evaluated the cytotoxicity effect of 0.02% of DMSO, a solvent of Andro. There was no cytotoxic effect in that group in comparison with the control (Supplementary Figure S1). Thus, DMSO at 0.02% was used as a control in these experimental studies. Various concentrations (0.1, 0.25, 0.5, 0.75, 1, 1.25, 1.5, 2, 2.5, and 3 μM) of Andro did not show any cytotoxicity towards the neuroblastoma cell line SH-SY5Y after 24 h when compared to the control group. Interestingly, a drastic increase in cell viability was observed at the concentration of 1.5 μM of Andro (Figure 1A). Conversely, Andro at 6 μM could contribute to cytotoxicity in these cells.

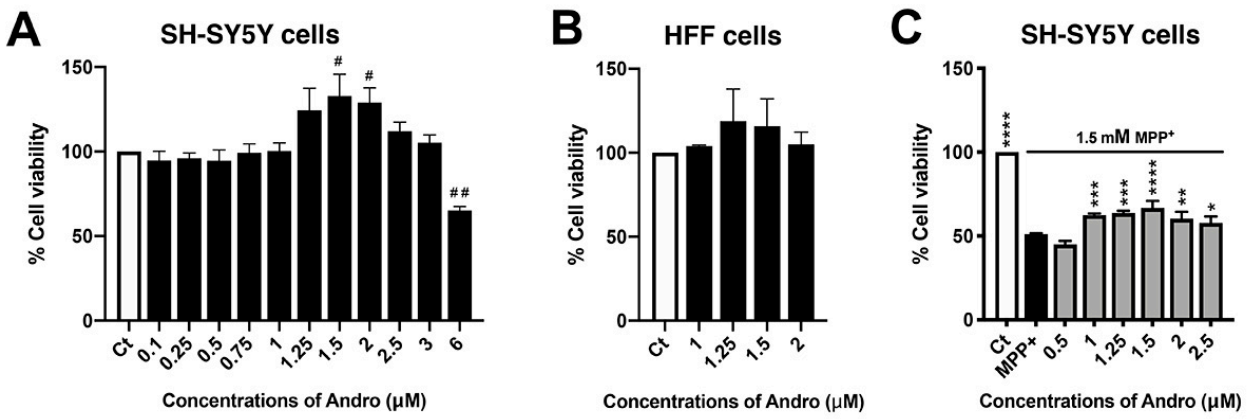

Figure 1. Cytotoxicity and protective effect of andrographolide (Andro) on SH-SY5Y and HFF cells. Cell viability was evaluated by MTT assay. (**A**) SH-SY5Y cells were treated with 0.1, 0.25, 0.5, 0.75, 1, 1.25, 1.5, 2, 2.5, 3, and 6 μM of Andro for 24 h. (**B**) HFF cells were treated with 1, 1.25, 1.5, and 2 μM of Andro for 24 h. (**C**) Neuroprotective effect of Andro on MPP^+-induced SH-SY5Y cells toxicity. SH-SY5Y cells were treated with or without 0.5, 1, 1.25, 1.5, 2, 2.5 μM of Andro for 24 h, followed by treatment with MPP^+ 1.5 mM for 24 h. * $p < 0.05$, ** $p < 0.01$, *** $p < 0.001$, **** $p < 0.0001$—statistical significance versus MPP^+-treated group. # $p < 0.05$, ## $p < 0.01$—statistical significance versus control group (data are mean ± SD, $n = 3$).

Moreover, Andro has no cytotoxic activity on normal cell line, such as human foreskin fibroblast (HFF) cells (Figure 1B). To determine the effective concentration of Andro for neuroprotection, SH-SY5Y cells were pretreated with Andro at 0.5, 1, 1.25, 1.5, 2, and 2.5 μM for 24 h and then exposed to 1.5 mM MPP^+ for 24 h. We found that 1.5 μM of Andro pretreatment significantly ameliorated MPP^+-induced neuronal cell death as compared with the MPP^+ exposure group (Figure 1C). Therefore, 1.5 μM of Andro was selected to investigate the neuroprotective effects of Andro in further studies.

2.2. Andrographolide Ameliorates MPP^+-Induced SH-SY5Y Cells Apoptosis through Protecting Mitochondrial Dysfunction

To examine the protective effect of Andro on MPP^+-induced SH-SY5Y cells, the mitochondrial membrane potential (MMP) depolarization was detected by JC-1 staining as an indicator of cell apoptosis. JC-1 forms aggregates in energized mitochondria, which exhibits red fluorescence (dimer) in healthy cells. In contrast, the apoptotic or unhealthy cells with low MMP retain the original green fluorescence (monomer) [19]. MPP^+ is one of the neurotoxins that cause MMP depolarization, as detected in Parkinson's disease [5,20–23]. Remarkably, the cells pretreated with Andro at 1.5 μM showed significantly increased red fluorescence intensity which indicates healthy mitochondria, while the cells treated with MPP^+ at 1.5 mM alone showed a significantly reduced intensity of red fluorescence while increasing that of green fluorescence, indicating the occurrence of MMP depolarization (Figure 2A,B). To further explore the impact of Andro on the apoptosis pathway during the course of MPP^+ induction, we observed the expressions of proteins in MPP^+-induced SH-SY5Y cells. MPP^+ exposure significantly increases not only the levels of pro-apoptotic proteins, including cleaved-caspase-3, cytochrome c, and Bax, but also a pathogenic hallmark of PD, alpha-synuclein. Notably, pretreatment with Andro significantly downregulated these proteins as reflected by the decreases in protein expression in cleaved-caspase-3, Bax, and alpha-synuclein in comparison to the MPP^+-treated group. Moreover, pretreatment with Andro tended to decrease cytochrome c when compared with MPP^+ at 1.5 mM alone. Additionally, pretreatment with Andro significantly increased Bcl2 expression compared with the untreated control and MPP^+-treated groups (Figure 2C,D). In order to investigate the neuroprotective effect of Andro on MPP^+-induced SH-SY5Y cells, the expression of tyrosine hydroxylase (TH), which is an enzyme that catalyzes dopamine synthesis, was

also observed. We found that pretreatment with Andro significantly increased TH compared with the control and MPP^+-treated groups (Figure 2C,D). Accordingly, these findings suggest that Andro ameliorated MPP^+-induced apoptosis in SH-SY5Y cells by preventing mitochondrial dysfunction.

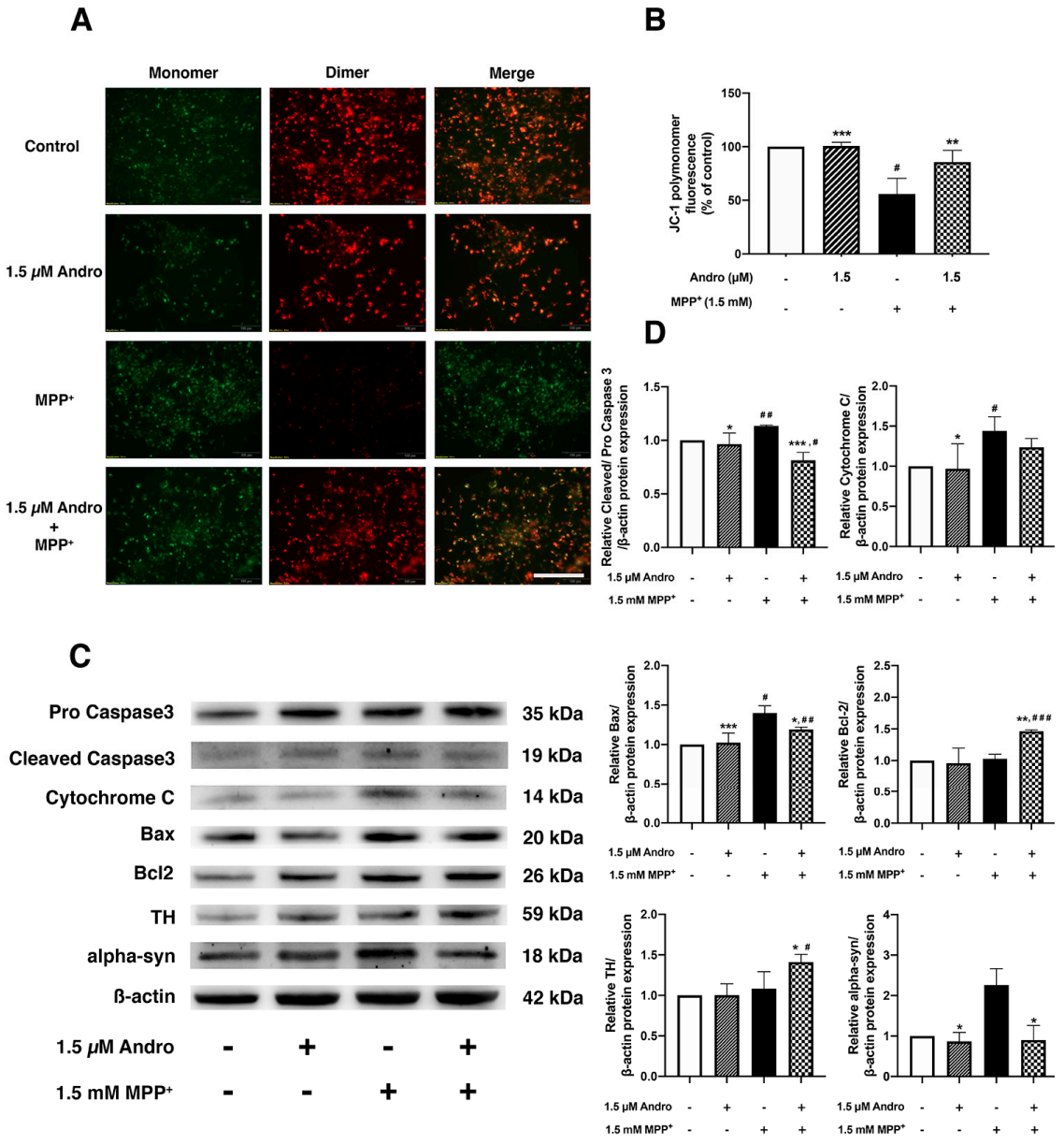

Figure 2. Protective effect of andrographolide on MPP^+-induced neuronal death through inhibition of apoptotic pathway. SH-SY5Y cells were treated with or without 1.5 μM of Andro for 24 h, followed by exposure with MPP^+ 1.5 mM for 16 h. (**A**) MMP was assessed by JC-1 staining. Green JC-1 monomers indicate depolarized MMP and red JC-1 dimers indicate normal MMP. Merged panel represents colocalization of green monomer and red dimer fluorescences. Scale bar: 50 μm. (**B**) Quantification of relative fluorescence between red and green in each group was measured by a microplate reader ($n = 3$). (**C**) Representative immunoblots of pro-caspase-3, cleaved-caspase-3, cytochrome c, Bax, Bcl2, TH, and alpha-synuclein. (**D**) Quantification of relative protein bands density normalized by β-actin in SH-SY5Y cells treated with or without 1.5 μM of Andro for 24 h, then treated with 1.5 mM of MPP^+ for 16 h. * $p < 0.05$, ** $p < 0.01$, *** $p < 0.001$-statistical significance versus MPP^+-treated group. # $p < 0.05$, ## $p < 0.01$, ### $p < 0.001$-statistical significance versus control group (data are mean ± SD, $n = 3$).

2.3. Andrographolide Enhanced Mitophagy and Autophagy Induction to Eliminate Damaged Mitochondrial and Accumulation of Alpha-Synuclein

Autophagy impairment leads to accumulations of damaged mitochondria and toxic alpha-synuclein [24–26]. After treatment with MPP^+, the morphology of mitochondria was observed by staining with MitoTracker Red. We found that after treatment with 1.5 μM of Andro, mitochondria appeared as interconnected red filamentous structures similar to those of the control group. In contrast, cells treated with MPP^+ exhibited abnormal mitochondria that appeared and fragmented condensed red dots (Supplementary Figure S2). Therefore, we studied the mitophagic effect, a clearance of defective mitochondria, under MPP^+-induced toxicity, including pretreatment with Andro. To demonstrate whether pretreatment with Andro stimulated mitophagy, the colocalization of mitochondria and autophagosomes in SH-SY5Y cells was performed by staining with MitoTracker Red (a marker for mitochondria) and LC3 (a marker for autophagosome). In order to analyze the colocalization of mitochondria and autophagosomes, Manders' coefficient (MCC) was used to quantify the degree of colocalization between the two markers. This MCC is calculated by dividing the number of pixels in which the two structures colocalized, resulting in a value ranging from 0 to 1 that reflects the degree of colocalization [27]. It was found that pretreatment with Andro at 1.5 μM significantly increased the intensity of MCC compared with the MPP^+-treated group (Figure 3A,B). Moreover, there was an increased LC3 puncta in the pretreatment with Andro as compared with the MPP^+-treated group. In a previous report [18], Andro inhibited inflammation in microglia by promoting mitophagy via the activation of Parkin. To further assess how Andro triggers mitochondrial autophagy, 3-methyladenine (3-MA), an autophagy inhibitor, was used to block the initiation of autophagy [28,29]. The results revealed that the ratio of p-mTOR/mTOR protein expression, which is a negative indicator of autophagy, was decreased in pretreatment with Andro compared with the MPP^+-treated group, whereas SH-SY5Y cells exposed to 3-MA followed by pretreatment with Andro showed a slightly increased p-mTOR/mTOR ratio when compared with Andro pretreatment. In autophagy, LC3-phosphatidylethanolamine conjugate (LC3), the mammalian ortholog of the yeast autophagy-related gene 6 (Beclin1), and lysosomal-associated membrane protein 1 (LAMP1) are involved in the autophagosome formation. We found that pretreatment with Andro tended to increase LC3B/A and LAMP1 and significantly increased Beclin1 in comparison with MPP^+ exposure. Correspondingly, 3-MA significantly decreased the expression of LC3B/A compared to pretreatment with Andro. As reported previously [30], Andro could attenuate chronic unpredictable mild stress-induced depressive-like behavior in mice through upregulation of autophagy. To corroborate this finding, p62/SQSTM1, an autophagosome-linked cargo protein that signifies the fusion of autophagosomes with lysosomes, was measured by Western blot, which showed a significant increase in p62 in the MPP^+-treated group compared with the control group. This increase in p62 indicates the impairment of autophagosome degradation by the accumulation of p62, whereas pretreatment with Andro decreased p62 expression, as compared with the MPP^+-treated group.

We next investigated the protective effect of Andro on mitophagy induction during MPP^+ treatment of SH-SY5Y cells. PINK1 and Parkin are important factors that regulate mitophagy [31]. Pretreatment with Andro significantly increased PINK1 expression and tended to increase the expression of Parkin when compared with the MPP^+-treated group. In contrast, exposure with 3-MA followed by pretreatment with Andro compromised the effect of Andro in facilitating mitophagy induction by significantly decreasing expression of PINK1 and Parkin when compared with pretreatment with Andro without prior 3-MA treatment (Figure 3C,D). Thus, these results suggested that Andro has a neuroprotective effect by enhancing autophagy and mitophagy, which facilitates clearances of alpha-synuclein and damaged mitochondria.

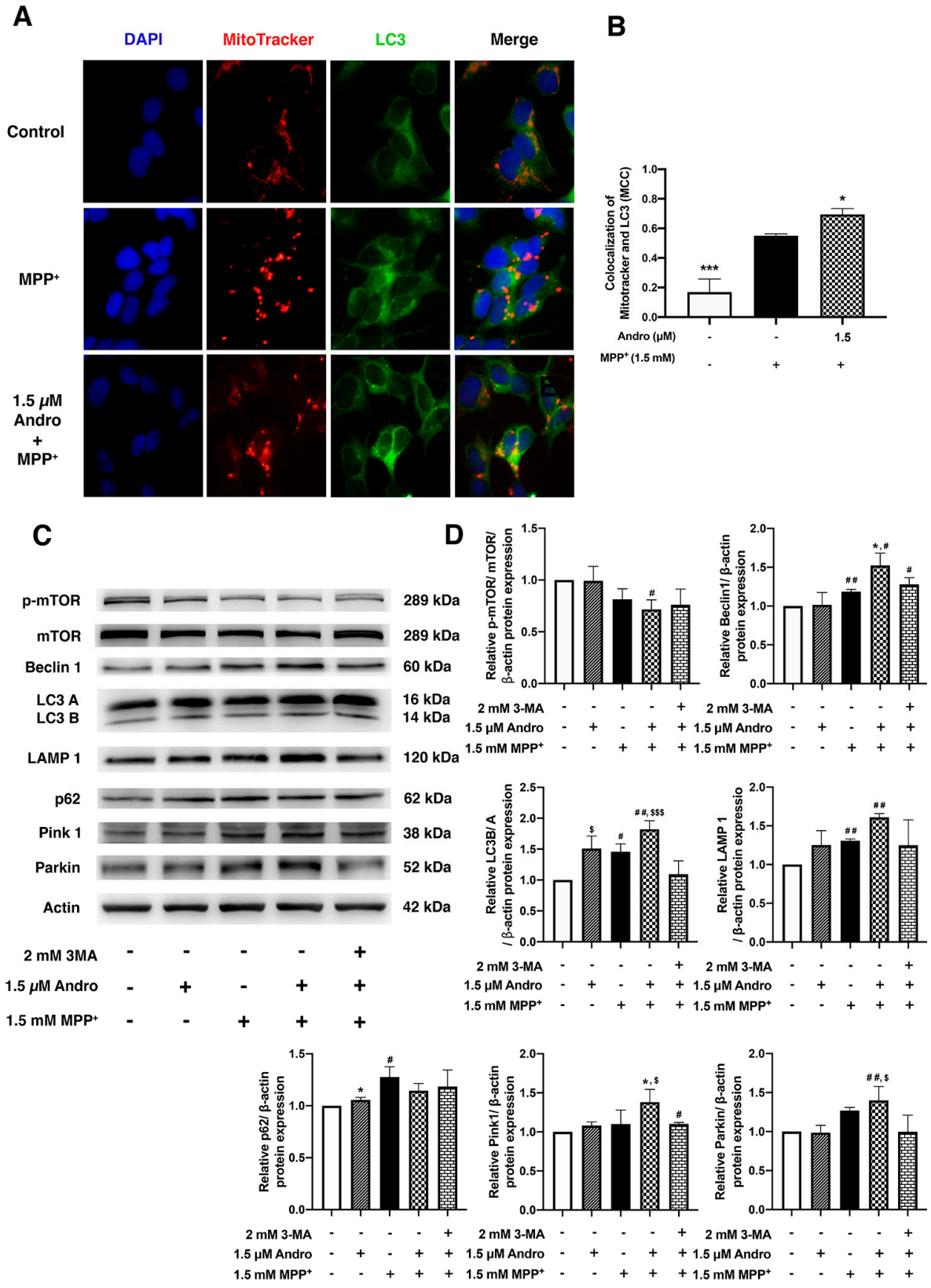

Figure 3. Protective effect of andrographolide against MPP$^+$-induced SH-SY5Y cell death by enhancing autophagy and mitophagy induction. SH-SY5Y cells were incubated with or without 1.5 μM of Andro

for 24 h, followed by incubation of MPP^+ 1.5 mM for 16 h. (**A**) Representative immunofluorescence images of MitoTracker Red and LC3 (green) and nuclei were counterstained with DAPI (blue). Merged panel represents colocalization of mitophagy induction. Scale bar: 50 μm. (**B**) The Manders' coefficient (MCC) was calculated from 3 independent experiments (at least 6 random fields were analyzed per condition) and quantified by using ImageJ. (**C**) Immunoblot of mTOR, p-mTOR, Beclin1, LC3B/A, LAMP1, p62, PINK1, Parkin. (**D**) Quantification of bands intensity normalized by β-actin in SH-SY5Y cells treated with or without 2 mM of 3-MA prior to incubation with or without 1.5 μM of Andro for 24 h, then treated with 1.5 mM of MPP^+ for 16 h. * $p < 0.05$, *** $p < 0.001$-statistical significance versus MPP^+-treated group. # $p < 0.05$, ## $p < 0.01$-statistical significance versus control group. $ $p < 0.05$, $$$ $p < 0.001$-statistical significance versus 3-MA group (data are mean ± SD, $n = 3$).

2.4. Andrographolide Exerted Antioxidant Effect against ROS Generated in MPP^+-Treated SH-SY5Y Cells via Nrf2 Activation

The amount of intracellular ROS generated as the result of MPP^+ treatment was measured by live-cell imaging and a microplate reader. We found that intracellular ROS accumulation was visibly increased in the MPP^+ exposure group compared with the control. In contrast, Andro pretreatment reduced the intensity of intracellular ROS as compared with the MPP^+-treated group (Figure 4A). Correspondingly, the quantification of ROS measured by microplate reader was significantly reduced in Andro pretreated samples compared to the MPP^+-treated group (Figure 4C). We next demonstrated the activation of transcription factor Nrf2, which plays a key role in the antioxidant pathway, through its nuclear translocation by examining the colocalization of Nrf2 and DAPI in the nuclei of SH-SY5Y cells. We found that MPP^+ treatment significantly diminished the Nrf2 nuclear translocation as compared with the control group, whereas Andro pretreatment at 1.5 μM significantly increased Nrf2 nuclear translocation compared with the MPP^+-treated group (Figure 4B,D). These findings implied that Andro reduced ROS generation by promoting nuclear translocation, leading to the activation of Nrf2.

2.5. Andrographolide Activated Nrf2, Which Leads to the Upregulations of Antioxidant Enzymes to Counteract Oxidative Stress in MPP^+-Treated SH-SY5Y Cells

In order to investigate the effect of Andro on Nrf2 activation, antioxidant protein and gene expressions, including antioxidant activities, were determined. NAC is commonly used as an antioxidant inducer [32]; thus, NAC was used as a positive control in the experiments. When analyzed by Western blot, the expression of KEAP1 levels was significantly decreased in the cells pretreated with Andro compared with the control and MPP^+-treated groups, while the Nrf2 nuclear translocation was increased in the Andro pretreatment group as compared with the MPP^+-treated group. Accordingly, the expression of HO-1 levels was significantly increased in the cells pretreated with Andro compared with the control and MPP^+-treated groups (Figure 5A,B), while treatment with NAC tended to increase Nrf2 nuclear translocation and HO-1 compared with the control group. Next, to verify whether Andro is able to activate the expression of genes encoding antioxidant enzymes activity during the course of MPP^+ treatment, RT-qPCR was performed. We found that the MPP^+-treated group downregulated mRNA expressions of SOD1 and GSTP1 compared with the control group. In contrast, pretreatment with Andro drastically upregulated SOD1, CAT, GSTP1, and HO-1 gene expression compared with the MPP^+-treated group (Figure 5C), while treatment with NAC did not exhibit a significant difference compared with the control group. Thus, these results indicated that Andro induced antioxidant activity by upregulating antioxidant genes against ROS generated in MPP^+-treated SH-SY5Y cells. Furthermore, the activities of SOD and GPx antioxidant enzymes were evaluated, as shown in Figure 5D, where the activities of SOD and GPx enzymes in Andro pretreatment were significantly upregulated in comparison with the MPP^+-treated group. Thus, these data confirmed that in addition to activations of autophagy and mitophagy, Andro could

also activate antioxidant activities via Nrf2/HO-1 signaling pathway to attenuate oxidative stress in MPP^+-treated SH-SY5Y cells.

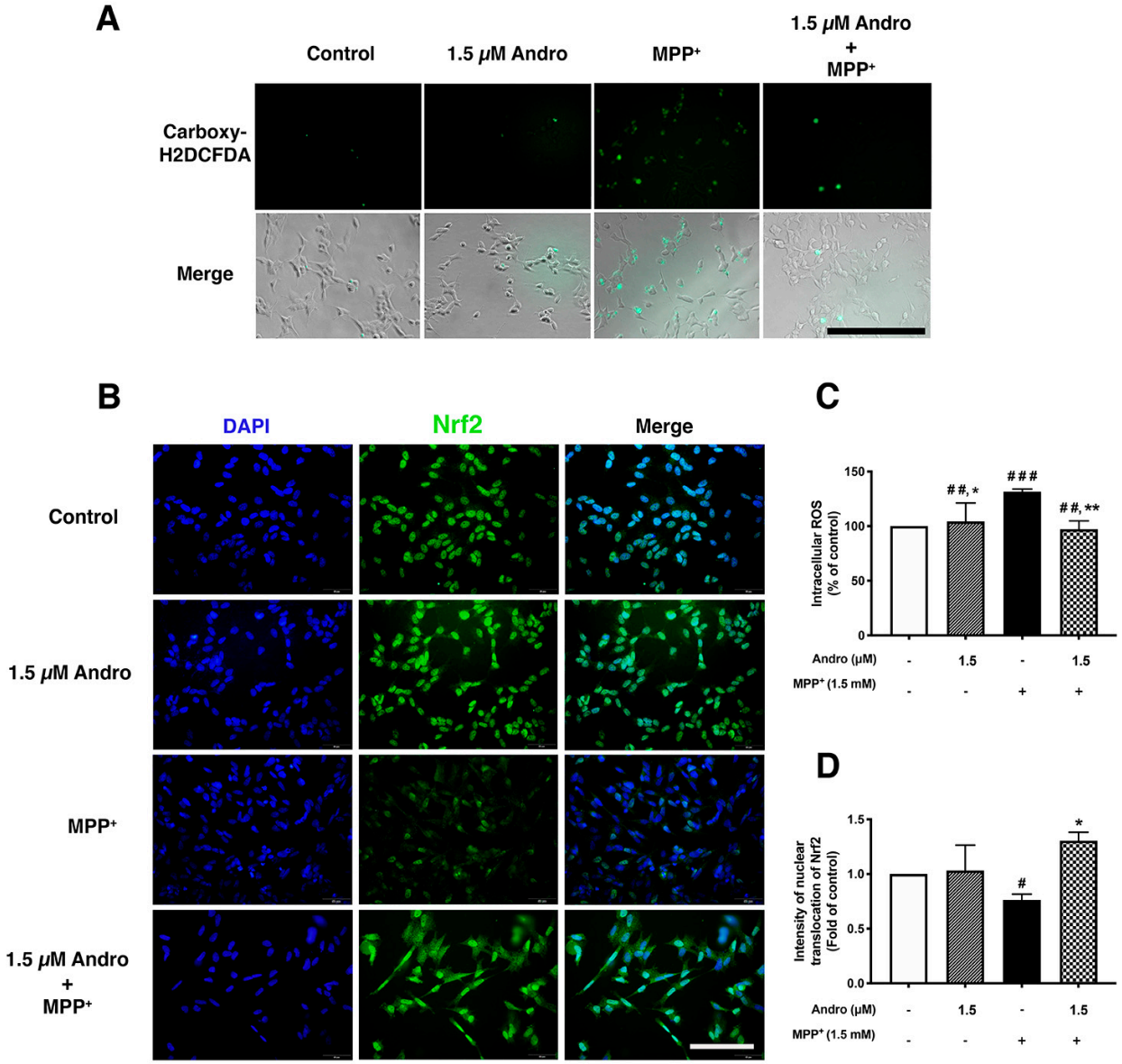

Figure 4. Antioxidant effect of andrographolide via Nrf2 activation in MPP^+-induced toxicity in SH-SY5Y cells. The ROS generation was induced by incubation of SH-SY5Y cells with MPP^+ 1.5 mM for 2 h after incubation with or without 1.5 μM of Andro for 24 h. (**A**) Intracellular ROS was measured by carboxy-DH2DCFDA staining, and green fluorescence was observed under IX83 Inverted microscope. Scale bar: 100 μm. (**B**) Representative images of Nrf2 staining (green) and DAPI (blue) which indicated nuclear translocation by observing the colocalization of Nrf2 and DAPI in SH-SY5Y cells treated with 1.5 μM of Andro for 24 h prior to being treated with 1.5 mM of MPP^+ for 16 h. Scale bar: 50 μm. (**C**) Quantification of intracellular ROS fluorescence intensity in each group was measured by microplate reader. (n = 3). (**D**) Quantification of Nrf2 nuclear translocation intensity was calculated from 3 independent experiments (at least 6 random fields were analyzed per condition) and quantified by using ImageJ. * $p < 0.05$, ** $p < 0.01$-statistical significance versus MPP^+-treated group. # $p < 0.05$, ## $p < 0.01$, ### $p < 0.001$-statistical significance versus control group (data are mean ± SD, n = 3).

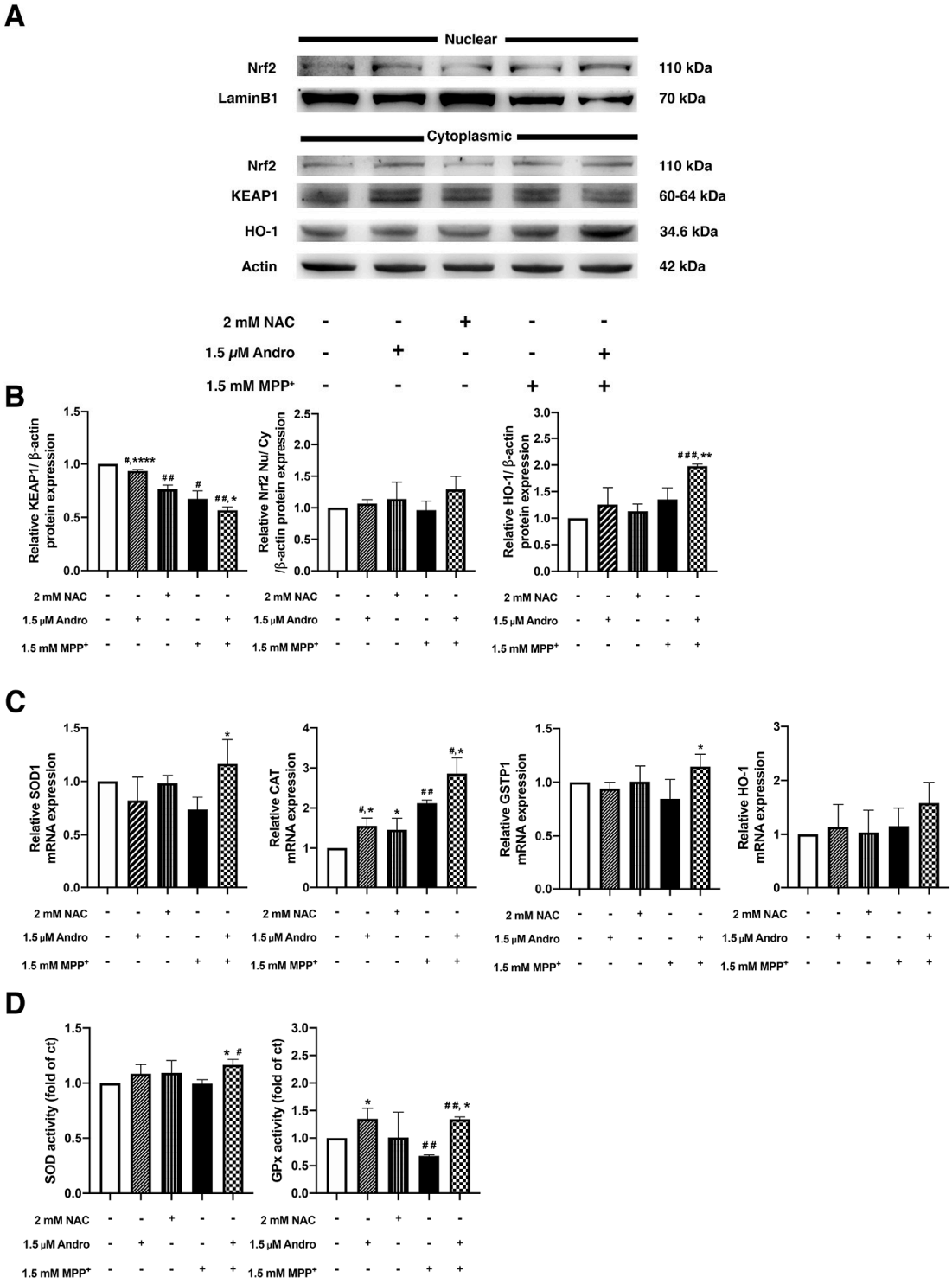

Figure 5. Antioxidant effect of andrographolide via Nrf2 activation in MPP^+-induced SH-SY5Y cells. (**A**) The immunoblots of Nrf2 in nuclear and cytoplasmic fractions, KEAP1 and HO-1. (**B**) Quantification of band intensity normalized by β-actin. (**C**) The antioxidant mRNA levels of SOD1, CAT, GSTP1, and HO-1 were evaluated by RT-qPCR assay. SH-SY5Y cells were incubated with or without 1.5 μM of Andro or 2 mM NAC for 12 h, followed by incubation of MPP^+ 1.5 mM for 8 h. (**D**) The antioxidant activities of SOD and GPx enzymes in SH-SY5Y cells treated with or without 1.5 μM of Andro or 2 mM of NAC for 24 h prior to incubated with 1.5 mM of MPP^+ for 16 h. * $p < 0.05$, ** $p < 0.01$, **** $p < 0.0001$-statistical significance versus MPP^+-treated group. # $p < 0.05$, ## $p < 0.01$, ### $p < 0.001$-statistical significance versus control group (data are mean ± SD, $n = 3$).

3. Discussion

Despite many studies reporting on various pharmacological activities of andrographolide, we are the first to report that Andro pretreatment could prevent MPP^+-induced SH-SY5Y cell death by promoting mitophagy along with autophagy through its ability to activate PINK-Parkin and LC3 B/A, respectively. Moreover, Andro could decrease intracellular oxidative stress by activating Nrf2, which upregulated the expression of genes encoding antioxidant enzymes, thereby alleviating cell damage and death.

We have shown that MPP^+ at 1.5 mM triggered mitochondrial damage in SH-SY5Y cells that led to increased ROS production, resulting in increased mitochondrial membrane depolarization, which caused cell apoptosis. These defective mitochondria were removed by the Andro-initiated mitophagy and autophagy as demonstrated by colocalization of MitoTracker red and LC3, as well as the upregulations of PINK1 and Parkin proteins in MPP^+-treated SH-SY5Y cells that were pretreated with Andro. These results were similar to those reported previously by Ahmed et al. [18], where Andro prevented the loss of dopaminergic neurons in NLRP inflammasome-induced microglial-mediated neuroinflammation in PD by promoting mitophagy of defective mitochondria. Moreover, it has been reported that Andro protects neurons by inhibiting excessive dynamin-related protein 1 (DRP1)-mediated mitochondrial fission, which is responsible for maintaining the function of mitochondria against rotenone- or MPTP-induced damage in in vitro and in vivo models, respectively [33]. Furthermore, we also demonstrated that Andro decreased the expression of p-mTOR, which is a negative regulator of autophagy. Then, the autophagy-related proteins that are involved in autophagosome–lysosome formation were increased, including Beclin1, LC3 B/A, and LAMP1. Defective mitochondria expressed PINK1 on the outer membrane, followed by Parkin, which was subsequently ubiquitinylated and recruited autophagy-forming molecules such as p62 and LC3 B/A to initiate mitophagy. Meanwhile, our study revealed that MPP^+ exposure slightly upregulated autophagy-related proteins but impaired autophagosome degradation, as shown by the accumulation of p62 in cells exposed to only MPP^+. This accumulation of p62 leads to autophagy impairment which leads to the accumulation of mitochondria and protein dysfunction. In consonance with Sakamoto and Rokad [28,34], human neuroblastoma SH-SY5Y cells were exposed to low concentrations of MPP^+ at 10 and 200 μM can enhance autophagosome in an earlier stage of autophagy but impair autophagosome degradation, leading to cell death. Due to the assembly of MPP^+ exposure, alpha-synuclein is then upregulated in SH-SY5Y cells [35,36]. Interestingly, Andro pretreatment resulted in decreased p62 expression, leading to decreasing alpha-synuclein accumulation in the cell, as shown in Figure 2C. On the contrary, treatment with 3-MA showed a decline in autophagy induction. Therefore, Andro provides neuroprotection by enhancing mitophagy and autophagy, which eliminates damaged mitochondria and alpha-synuclein accumulations.

As a consequence of defective mitochondria accumulation, ROS generation is increased, which impairs energy production. In addition, the overproduction of ROS-mediated oxidative stress can promote the release of cytochrome c, which subsequently triggers apoptosis of dopaminergic neurons [37]. Recently, it was reported that MPP^+ induced intracellular ROS generation in cerebellar granule neurons, neuroblastoma, and N27 dopaminergic cells from damaged mitochondria, which caused apoptotic cell death [38,39]. We also found that Andro reduced ROS generation produced by MPP^+ in SH-SY5Y cells by inducing Nrf2 antioxidant activation. Likewise, Andro exhibited an antioxidant effect against oxidative stress in the AD model based on the activation of the Nrf2 pathway [40]. Several studies reported that Nrf2 is a crucial defensive mechanism against oxidative stress through its ability to upregulate antioxidant and detoxifying genes in age-related diseases, including AD and PD [16,41]. Normally, Nrf2 is localized in the cytosol and interacts with KEAP1 under a basal condition. This interaction between KEAP1 and Nrf2 promotes Nrf2 ubiquitination that subsequently leads to proteasomal degradation [42,43]. Oxidative stress and Nrf2 activators can trigger Nrf2 activation by releasing Nrf2 from KEAP1 and allowing Nrf2 to translocate into the nucleus, where it activates the expres-

sions of antioxidant enzymes to eliminate ROS and facilitate neuronal survival in many neurological diseases [44–47]. In our present study, we found that MPP^+ decreased Nrf2 nuclear translocation while pretreatment with Andro facilitated Nrf2 nuclear translocation and increased expressions of SOD1, CAT, HO-1, and GSTP1 genes expressions, as well as SOD1 and GPx enzyme activities. These findings indicated that Andro decreased oxidative stress and protected cells from apoptosis by promoting antioxidant activities through the activation of the Nrf2 pathway. Andro might also directly promote cell survival as it was found that pretreatment with Andro diminished pro-apoptotic proteins, including caspase-3, BAX, and cytochrome c, while increased Bcl2, an anti-apoptotic protein. Accordingly, Andro directly promoted the expression of TH, which was responsible for DA synthesis in SH-SY5Y cells.

Taken together, our study demonstrated that Andro showed a neuroprotective effect against MPP^+-induced neurotoxicity by mediating mitophagy and autophagy, which facilitated the elimination of defective mitochondria and alpha-synuclein degradation. Concomitantly, Andro activated the antioxidant Nrf2 pathway to counteract ROS build-up from defective mitochondria, which directly attenuated cell apoptosis. Thus, it is to be hoped that this study provides evidence to support the neuroprotective ability of Andro that may be considered as a potential therapeutic or supplement in the prevention of PD. However, further studies are needed to determine the proposed properties in in vivo mouse models, as well as stringent clinical trials in humans.

4. Materials and Methods

4.1. Cell Culture

Neuroblastoma SH-SY5Y cell line (ATCC# CRL-2266) and HFF cell line (ATCC# SCRC-1041) were purchased from American Type Culture Collections (ATCC, Manassas, VA, USA). SH-SY5Y and HFF cell lines were cultured in Dulbecco's Modified Eagle's Medium/Nutrient Mixture F-12 (DMEM/F-12) and DMEM high glucose (4.5 g/L), respectively, and supplemented with 10% fetal bovine serum (FBS) and 1% penicillin/streptomycin at 37 °C in a relatively humidified atmosphere with 5% CO_2. The cultured cells were maintained at 37 °C in 5% CO_2. The media were changed 2–3 times per week. SH-SY5Y and HFF cells have been used between passage numbers 31–34 and 17–20, respectively.

4.2. Cell Viability Assay

Andrographolide was purchased from Sigma-Aldrich (St. Louis, MO, USA, 365645). The purity (TLC) of this compound is $\geq$ 98%, with a formula weight of 350.45 g/mol. To examine the ability of andrographolide to prevent SH-SY5Y cell death from MPP^+ exposure, SH-SY5Y cells (8000 cells/well) were cultured in 96-well plates for 24 h in a humidified 5% CO_2 atmosphere at 37 °C. Cells were incubated with Andro that was dissolved in dimethyl sulfoxide (DMSO for cell culture; Sigma-Aldrich, USA) at designated concentrations for 24 h. After that, the solution was removed and treated with 1.5 mM of MPP^+ for 24 h. Ultimately, cell viability was determined by adding 5 mg/mL MTT (3-(4,5-dimethylthiazol-2-yl)-2,5-diphenyltetrazolium bromide; Sigma-Aldrich, USA) for 2 h. At the indicated time, the supernatant was discarded, and formazan crystals were dissolved by adding 100 µL of dimethyl sulfoxide (DMSO; Sigma-Aldrich, USA). The absorbance was read by a microplate reader (Versamax Spectrophotometer, MA, USA) at 570 nm and 690 nm as modified from [48]. The percentage of cell viability was calculated in comparison with the untreated group.

4.3. Mitochondrial Membrane Potential Analysis

Mitochondrial membrane potential (MMP) is an important indicator of mitochondrial function. JC-1 Mitochondrial membrane potential assay kit (Abcam, ab113850, Cambridge, UK) was used to determine MMP. JC-1 staining indicates the healthy mitochondria by emitting red fluorescence, whereas unhealthy cells showed a decrease in red fluorescence and an increase in green fluorescence, which represent the remaining monomers in the cyto-

plasm. Hence, the ratio of red/green serves as an indicator of loss of MMP. The experiment was conducted as previously reported [49]. Cells were seeded at 15,000 cells/well in a black and flat bottom 96-well microplate and incubated with Andro at designated concentrations for 24 h, followed by treatment with MPP^+ at 1.5 mM for 16 h. Then, the cells were washed with PBS and incubated with 10 µM of JC-1 dye in a dark room at 37 °C and 5% CO_2 for 10 min. After washing with PBS, the quantification of relative fluorescence between red and green intensity was measured by a fluorescence microplate reader (TECAN Spark 10M, Bioexpress, Männedorf, CH, USA). The red fluorescence intensity (polymerized form of JC-1) was measured at an Ex/Em of 535/590 nm, and the green fluorescence intensity (monomerized form of JC-1) was measured at an Ex/Em of 490/530 nm. Furthermore, JC-1-stained cells were observed under a fluorescence microscope (Olympus BX53, Tokyo, Japan).

4.4. Immunofluorescence Staining

SH-SY5Y cells were grown on poly-l-lysine coated coverslips to improve cell attachment in 6-well culture plates at a density of 1.5×10^5 cells per well. Then, cells were pretreated with Andro at designated concentrations for 24 h, followed by exposure to 1.5 mM MPP^+ for 16 h. After that, treated cells were incubated with MitoTracker Red (Cell Signaling) for 30 min at 37 °C, then fixed with cold methanol for 15 min at −20 °C and washed three times with PBS for 5 min. Treated cells were permeabilized with 0.25% Triton-X-100 in PBS and blocked with 1% bovine serum albumin, 10% normal goat serum, and 0.3% glycine in PBST for 2 h. Subsequently, cells were incubated with anti-LC3 primary antibody (Cell Signaling Technology, Danvers, MA, USA) at 1:200 in a dark humidity box at 4 °C overnight, then incubated with a secondary antibody (Invitrogen, Alexa Fluor 488) goat anti-rabbit IgG (H+L) at 1:500 dilution for 2 h. Finally, the images were taken with a fluorescence microscope (Olympus BX53, Tokyo, Japan).

4.5. Intracellular ROS Measurement

To determine the ROS generation induced by MPP^+ in SH-SY5Y cells, the ROS level was examined by staining with Dichloro-dihydro-fluorescein diacetate (DCFH-DA), a fluorescence probe used for detecting the level of ROS. Intracellular ROS was measured by a protocol modified from a previous report [50]. SH-SY5Y cells were cultured in a black and flat bottom 96-well microplate and exposed to designated concentrations of Andro for 24 h, followed by treatment with 1.5 mM MPP^+ for 2 h. After washing with cold PBS, cells were incubated with 5 µM DCFH-DA (ThermoFisher Scientific, Waltham, MA, USA) in phenol red-free culture medium for 45 min at 37 °C in a dark room. Finally, the fluorescence intensity was detected at excitation and emission wavelengths of 488 nm and 525 nm by TECAN Spark 10M (Bioexpress, Männedorf, CH). Alternatively, SH-SY5Y cells were cultured in a 12-well microplate and exposed to designated concentrations as mentioned above, then observed under a fluorescence microscope (live-cell fluorescence imaging system, IX-83ZDC).

4.6. Nrf2 Nuclear Translocation

Nuclear translocation of Nrf2 was evaluated by immunofluorescence staining following a protocol previously reported [15]. SH-SY5Y cells were plated on the coverslips. After being treated with designated concentrations of Andro for 24 h and MPP^+ for another 16 h, cells were washed three times with PBS and fixed with 4% paraformaldehyde for 15 min at room temperature. Treated cells were then washed three times with PBS and blocked with a blocking buffer (containing 0.3% Triton X-100 and 1% BSA in PBS) for 1 h. Afterward, cells were incubated with anti-Nrf2 antibody (Abcam, ab137550) at 1:200 dilution overnight at 4 °C, followed by a secondary antibody goat anti-rabbit IgG (H+L) (Invitrogen, Alexa Fluor 488) at 1:500 dilution for 1 h at 37 °C. The nuclei were counterstained with DAPI. The fluorescence images were taken by fluorescence microscope (Olympus BX53, Tokyo, Japan), and the intensity of Nrf2 expression was quantified by Image J software version 1.52k.

4.7. Real-Time Quantitative Reverse Transcription Polymerase Chain Reaction (RT-qPCR) for Determinations of Nrf2-Dependent Antioxidant Genes

SH-SY5Y cells were treated with or without 2 mM of NAC or pretreated with 1.5 μM of Andro for 12 h, followed by incubation with or without 1.5 mM of MPP^+ for 8 h. After treatment, RNA was extracted by Total RNA Mini Kit (Blood/Culture cell) (Geneaid, RB300, New Taipei, Taiwan). Then, iScript Reverse Transcription Supermix (Bio-Rad, 170-8841, Heracles, CA, USA) was used for reverse RNA to cDNA. Real-time qPCR was performed by using 10 μL iTaq Universal SYBR Green Supermix (Bio-Rad, 172-5121), and PCR conditions were optimized by using a real-time thermocycler (Bio-rad/CFX96 touch). Nrf2-dependent antioxidant genes were amplified by using the following primers: GAPDH (forward: 5′-GACAGTCAGCCGCATCTTCT-3′, reverse: 5′-GCGCCCAATACGACCAAATC-3′); SOD1 (forward: 5′-GATGACTTGGGCAAAGGTGG-3′, reverse: 5′-TACACCACAAGCCAAACG ACT-3′); CAT (forward: 5′-CTTCGACCCAAGCAACATGC-3′, reverse: 5′-GCGGTGAGTGT CAGGATAGG-3′); HO-1 (forward: 5′-AGGGAATTCTCTTGGCTGGC-3′, reverse: 5′-GACAGCTGCCACATTAGGGT-3′); and GSTP1 (forward: 5′-AAGTTCCAGGACGGAGA CCT-3′, reverse: 5′-AAGTTCCAGGACGGAGACCT-3′). Fold change in gene expression was calculated by using $2^{-\Delta\Delta Ct}$ method.

4.8. Western Blot Analysis

SH-SY5Y cells were cultured on a 6-well plate in culture medium for 24 h. Cells were treated with or without an autophagy inhibitor, 3-MA at 2 mM (Sigma-Aldrich, 5142-23-4) for 2 h, or treated with NAC at 2 mM, or incubated with designated concentrations of Andro for 24 h followed by exposure with MPP^+ for 16 h. Western blot was performed as previously described [18,19]. Treated cells were lysed with 1xRIPA buffer (25 mM Tris HCl pH 7.6, 150 mM NaCl, 1% NP-40, 1% sodium deoxycholate, 0.1% SDS) and PMSF as a non-specific protein inhibitor on ice for 10 min. To investigate the nuclear translocation of Nrf2, nuclear protein extraction was performed by using Nuclear Extraction Kit (Abcam, ab113474). These lysates were centrifugated at 12,000 RPM for 15 min at 4 °C. The supernatants were collected, and protein concentrations were estimated by BCA protein assay kit (ThermoFisher Scientific, 23225). Twenty micrograms of protein were electrophoresed and transferred to nitrocellulose membranes. These nitrocellulose membranes were blocked with TBST containing 5% BSA for 2 h and then incubated overnight at 4 °C with primary antibodies directed against caspase-3 (Cell Signaling Technology, #9662) at 1:1000, cytochrome c (Abcam, ab110325) at 1:1000, Bax (Cell Signaling Technology, #2774) at 1:700, Bcl-2 (Cell Signaling Technology, #4223) at 1:700, TH (Abcam, ab112) at 1:500, alpha-syn (Cell Signaling Technology, #2647) at 1:700, β-actin (Abcam, ab8227) at 1:1000, mTOR (Cell Signaling Technology, #2972) at 1:1000, p- mTOR (Cell Signaling Technology, #2971) at 1:1000, Beclin1 (Cell Signaling Technology, #3738) at 1:1000, LC3A/B (Cell Signaling Technology, #4108) at 1:700, LAMP1 (Cell Signaling Technology, #9091) at 1:1000, SQSTM1/p62 (Cell Signaling Technology, #5114) at 1:1000, PINK 1 (Abcam, ab216144) at 1:1000, Parkin (Abcam, ab77924) at 1:700, Nrf2 (Abcam, ab137550) at 1:700, Lamin B1 (Abcam, ab65986) at 1:700, KEAP1 (Cell Signaling Technology, #4678) at 1:700, and HO-1 (Abcam, ab13243) at 1:1000 followed by HRP-conjugated anti-rabbit or anti-mouse IgG (Abcam, ab6721 and ab mouse ab6789) at 1:700 at 1:5000 dilution with TBST at room temperature for 2 h. Chemiluminescent signal was observed by NovexTM ECL chemiluminescent substrate reagent kit (ThermoFisher Scientific, MA, USA) on chemiluminescent gel document (Alliance Q9 mini, VT, USA) and was analyzed by Image J software.

4.9. Antioxidant Enzymes Detection Assay

To measure the activities of antioxidant enzymes (SOD and GPx), the cells were treated with designated concentrations of Andro for 24 h, followed by MPP^+ for 16 h, then lysed, and the supernatants were collected. Then, the enzyme activities were determined by using SOD and GPx Activity Assay Kit (Abcam, ab65354, and ab102530). The absorbance

was evaluated by a microplate reader (Versamax Spectrophotometer, USA) at 450 nm and 340 nm for SOD and GPx activities, respectively.

4.10. Statistical Analysis

All values are presented as the mean ± standard deviation (SD). Data were collected from at least three independent experiments and analyzed using GraphPad Prism software version 8.2.1 (GraphPad Software, San Diego, CA, USA). Comparisons among multiple groups were performed using one-way ANOVA with Dunnett's multiple comparisons test. One sample t-test was used to compare with the control group without SD. A p-value < 0.05 was considered statistically significant.

5. Conclusions

The neuroprotective effect of andrographolide on a PD cellular model was demonstrated by using MPP^+-induced neuronal toxicity in SH-SY5Y cells, in which andrographolide promoted mitophagy mediated by PINK/Parkin signaling pathway and autophagy as indicated by the upregulations of Beclin1, LC3, and LAMP1. These actions help to eliminate defective mitochondria and alpha-synuclein. Simultaneously, Andro promoted Nrf2 activation, which induced expressions of genes encoding antioxidant enzymes and enzyme activities to counteract oxidative stress. Andrographolide might also directly prevent cell apoptosis by upregulation of mitochondrial membrane potential and Bcl2 and downregulations of cytochrome c, BAX, and cleaved-caspase-3.

Supplementary Materials: The following supporting information can be downloaded at: https://www.mdpi.com/article/10.3390/ijms24108528/s1.

Author Contributions: Conceptualization, P.P. and K.C.; methodology, P.P., P.K. and K.P.; validation, K.C. and P.S.; formal analysis, P.P.; investigation, P.P.; resources, K.C.; writing—original draft preparation, P.P.; writing—review and editing, K.C. and P.S.; visualization, P.P.; supervision, K.C.; project administration, K.C.; funding acquisition, K.C. All authors have read and agreed to the published version of the manuscript.

Funding: This research was funded by the Development and Promotion of Science and Technology Talents Project, DPST, to P.P., and CIF grant, Faculty of Science, Mahidol University to K.C.

Institutional Review Board Statement: Not applicable.

Data Availability Statement: The data supporting the conclusion in this study are available on request from the corresponding author.

Conflicts of Interest: The authors declare no conflict of interest.

References

1. Cacabelos, R. Parkinson's disease: From pathogenesis to pharmacogenomics. *Int. J. Mol. Sci.* **2017**, *18*, 551. [CrossRef] [PubMed]
2. Xicoy, H.; Wieringa, B.; Martens, G.J. The SH-SY5Y cell line in Parkinson's disease research: A systematic review. *Mol. Neurodegener.* **2017**, *12*, 1–11. [CrossRef] [PubMed]
3. Blum, D.; Torch, S.; Lambeng, N.; Nissou, M.-F.; Benabid, A.-L.; Sadoul, R.; Verna, J.-M. Molecular pathways involved in the neurotoxicity of 6-OHDA, dopamine and MPTP: Contribution to the apoptotic theory in Parkinson's disease. *Prog. Neurobiol.* **2001**, *65*, 135–172. [CrossRef] [PubMed]
4. Di Monte, D.A.; Lavasani, M.; Manning-Bog, A.B. Environmental factors in Parkinson's disease. *Neurotoxicology* **2002**, *23*, 487–502. [CrossRef]
5. Richardson, J.R.; Fitsanakis, V.; Westerink, R.H.; Kanthasamy, A.G. Neurotoxicity of pesticides. *Acta Neuropathol.* **2019**, *138*, 343–362. [CrossRef]
6. Schober, A. Classic toxin-induced animal models of Parkinson's disease: 6-OHDA and MPTP. *Cell Tissue Res.* **2004**, *318*, 215–224. [CrossRef]
7. Jethva, P.N.; Kardani, J.R.; Roy, I. Modulation of α-synuclein aggregation by dopamine in the presence of MPTP and its metabolite. *FEBS J.* **2011**, *278*, 1688–1698. [CrossRef]
8. Palikaras, K.; Lionaki, E.; Tavernarakis, N. Mechanisms of mitophagy in cellular homeostasis, physiology and pathology. *Nat. Cell Biol.* **2018**, *20*, 1013–1022. [CrossRef]
9. Dernie, F. Mitophagy in Parkinson's disease: From pathogenesis to treatment target. *Neurochem. Int.* **2020**, *138*, 104756. [CrossRef]

10. Liu, J.; Liu, W.; Li, R.; Yang, H. Mitophagy in Parkinson's disease: From pathogenesis to treatment. *Cells* **2019**, *8*, 712. [CrossRef]
11. Quinn, P.M.; Moreira, P.I.; Ambrósio, A.F.; Alves, C.H. PINK1/PARKIN signalling in neurodegeneration and neuroinflammation. *Acta Neuropathol. Commun.* **2020**, *8*, 1–20. [CrossRef] [PubMed]
12. Armstrong, M.J.; Okun, M.S. Diagnosis and treatment of Parkinson disease: A review. *JAMA* **2020**, *323*, 548–560. [CrossRef]
13. Connolly, B.S.; Lang, A.E. Pharmacological treatment of Parkinson disease: A review. *JAMA* **2014**, *311*, 1670–1683. [CrossRef]
14. Wang, T.; Liu, B.; Zhang, W.; Wilson, B.; Hong, J.-S. Andrographolide reduces inflammation-mediated dopaminergic neurodegeneration in mesencephalic neuron-glia cultures by inhibiting microglial activation. *J. Pharmacol. Exp. Ther.* **2004**, *308*, 975–983. [CrossRef] [PubMed]
15. Yen, T.-L.; Chen, R.-J.; Jayakumar, T.; Lu, W.-J.; Hsieh, C.-Y.; Hsu, M.-J.; Yang, C.-H.; Chang, C.-C.; Lin, Y.-K.; Lin, K.-H. Andrographolide stimulates p38 mitogen-activated protein kinase–nuclear factor erythroid-2-related factor 2–heme oxygenase 1 signaling in primary cerebral endothelial cells for definite protection against ischemic stroke in rats. *Transl. Res.* **2016**, *170*, 57–72. [CrossRef] [PubMed]
16. Vasconcelos, A.R.; Dos Santos, N.B.; Scavone, C.; Munhoz, C.D. Nrf2/ARE pathway modulation by dietary energy regulation in neurological disorders. *Front. Pharmacol.* **2019**, *10*, 33. [CrossRef]
17. Xu, Y.; Tang, D.; Wang, J.; Wei, H.; Gao, J. Neuroprotection of Andrographolide Against Microglia-Mediated Inflammatory Injury and Oxidative Damage in PC12 Neurons. *Neurochem. Res.* **2019**, *44*, 2619–2630. [CrossRef] [PubMed]
18. Ahmed, S.; Kwatra, M.; Panda, S.R.; Murty, U.; Naidu, V. Andrographolide suppresses NLRP3 inflammasome activation in microglia through induction of parkin-mediated mitophagy in in-vitro and in-vivo models of Parkinson disease. *Brain Behav. Immun.* **2021**, *91*, 142–158. [CrossRef]
19. Sivandzade, F.; Bhalerao, A.; Cucullo, L. Analysis of the mitochondrial membrane potential using the cationic JC-1 dye as a sensitive fluorescent probe. *Bio-Protocol* **2019**, *9*, e3128. [CrossRef] [PubMed]
20. Liao, Z.; Gong, Z.; Wang, Z.; Yang, W.; Liu, W.; Hou, L.; Liu, X.; Hua, J.; Wang, B.; Li, N. The Degradation of TMEM166 by Autophagy Promotes AMPK Activation to Protect SH-SY5Y Cells Exposed to MPP^+. *Cells* **2022**, *11*, 2706. [CrossRef]
21. Rani, L.; Ghosh, B.; Ahmad, M.H.; Mondal, A.C. Evaluation of Potential Neuroprotective Effects of Vanillin Against MPP^+/MPTP-Induced Dysregulation of Dopaminergic Regulatory Mechanisms in SH-SY5Y Cells and a Mouse Model of Parkinson's Disease. *Mol. Neurobiol.* **2023**, 1–23. [CrossRef]
22. Rausch, W.-D.; Wang, F.; Radad, K. From the tyrosine hydroxylase hypothesis of Parkinson's disease to modern strategies: A short historical overview. *J. Neural Transm.* **2022**, *129*, 487–495. [CrossRef]
23. Wu, X.; Ren, Y.; Wen, Y.; Lu, S.; Li, H.; Yu, H.; Li, W.; Zou, F. Deacetylation of ZKSCAN3 by SIRT1 induces autophagy and protects SN4741 cells against MPP^+-induced oxidative stress. *Free Radic. Biol. Med.* **2022**, *181*, 82–97. [CrossRef] [PubMed]
24. Albanese, F.; Novello, S.; Morari, M. Autophagy and LRRK2 in the aging brain. *Front. Neurosci.* **2019**, *13*, 1352. [CrossRef]
25. Karabiyik, C.; Lee, M.J.; Rubinsztein, D.C. Autophagy impairment in Parkinson's disease. *Essays Biochem.* **2017**, *61*, 711–720. [PubMed]
26. Reeve, A.; Simcox, E.; Turnbull, D. Ageing and Parkinson's disease: Why is advancing age the biggest risk factor? *Ageing Res. Rev.* **2014**, *14*, 19–30. [CrossRef] [PubMed]
27. Dunn, K.W.; Kamocka, M.M.; McDonald, J.H. A practical guide to evaluating colocalization in biological microscopy. *Am. J. Physiol. Cell Physiol.* **2011**, *300*, C723–C742. [CrossRef]
28. Sakamoto, S.; Miyara, M.; Sanoh, S.; Ohta, S.; Kotake, Y. Mild MPP^+ exposure-induced glucose starvation enhances autophagosome synthesis and impairs its degradation. *Sci. Rep.* **2017**, *7*, 46668. [CrossRef]
29. Zhong, J.; Xie, J.; Xiao, J.; Li, D.; Xu, B.; Wang, X.; Wen, H.; Zhou, Z.; Cheng, Y.; Xu, J. Inhibition of PDE4 by FCPR16 induces AMPK-dependent autophagy and confers neuroprotection in SH-SY5Y cells and neurons exposed to MPP^+-induced oxidative insult. *Free Radic. Biol. Med.* **2019**, *135*, 87–101. [CrossRef] [PubMed]
30. Geng, J.; Liu, J.; Yuan, X.; Liu, W.; Guo, W. Andrographolide triggers autophagy-mediated inflammation inhibition and attenuates chronic unpredictable mild stress (CUMS)-induced depressive-like behavior in mice. *Toxicol. Appl. Pharmacol.* **2019**, *379*, 114688. [CrossRef]
31. Yang, X.; Pan, W.; Xu, G.; Chen, L. Mitophagy: A crucial modulator in the pathogenesis of chronic diseases. *Clin. Chim. Acta* **2020**, *502*, 245–254. [CrossRef] [PubMed]
32. Tenório, M.C.d.S.; Graciliano, N.G.; Moura, F.A.; Oliveira, A.C.M.d.; Goulart, M.O.F. *N*-acetylcysteine (NAC): Impacts on human health. *Antioxidants* **2021**, *10*, 967. [CrossRef] [PubMed]
33. Geng, J.; Liu, W.; Gao, J.; Jiang, C.; Fan, T.; Sun, Y.; Qin, Z.H.; Xu, Q.; Guo, W.; Gao, J. Andrographolide alleviates Parkinsonism in MPTP-PD mice via targeting mitochondrial fission mediated by dynamin-related protein 1. *Br. J. Pharmacol.* **2019**, *176*, 4574–4591. [CrossRef] [PubMed]
34. Rokad, D.; Ghaisas, S.; Harischandra, D.S.; Jin, H.; Anantharam, V.; Kanthasamy, A.; Kanthasamy, A.G. Role of neurotoxicants and traumatic brain injury in α-synuclein protein misfolding and aggregation. *Brain Res. Bull.* **2017**, *133*, 60–70. [CrossRef]
35. Duka, T.; Sidhu, A. The neurotoxin, MPP^+, induces hyperphosphorylation ofTau, in the presence of α-Synuclein, in SH-SY5Y neuroblastoma cells. *Neurotox. Res.* **2006**, *10*, 1–10. [CrossRef]
36. Shasi, V.; Sonya, C.; Srigiridhar, K.; Joy, J.; Cecilia, J.; Kalyanaman, B. α-Synuclein up-regulation and aggregation during MPP-induced apoptosis in neuroblastoma cells. *J. Biol. Chem.* **2004**, *279*, 15+204–225+247.

37. Chen, C.; Turnbull, D.M.; Reeve, A.K. Mitochondrial dysfunction in Parkinson's disease—Cause or consequence? *Biology* **2019**, *8*, 38. [CrossRef]
38. Kalivendi, S.V.; Kotamraju, S.; Cunningham, S.; Shang, T.; Hillard, C.J.; Kalyanaraman, B. 1-Methyl-4-phenylpyridinium (MPP^+)-induced apoptosis and mitochondrial oxidant generation: Role of transferrin-receptor-dependent iron and hydrogen peroxide. *Biochem. J.* **2003**, *371*, 151–164. [CrossRef]
39. Zawada, W.M.; Banninger, G.P.; Thornton, J.; Marriott, B.; Cantu, D.; Rachubinski, A.L.; Das, M.; Griffin, W.S.T.; Jones, S.M. Generation of reactive oxygen species in 1-methyl-4-phenylpyridinium (MPP^+) treated dopaminergic neurons occurs as an NADPH oxidase-dependent two-wave cascade. *J. Neuroinflamm.* **2011**, *8*, 129. [CrossRef]
40. Lindsay, C.B.; Zolezzi, J.M.; Rivera, D.S.; Cisternas, P.; Bozinovic, F.; Inestrosa, N.C. Andrographolide reduces neuroinflammation and oxidative stress in aged Octodon degus. *Mol. Neurobiol.* **2020**, *57*, 1131–1145. [CrossRef]
41. Francisqueti-Ferron, F.V.; Ferron, A.J.T.; Garcia, J.L.; Silva, C.C.V.d.A.; Costa, M.R.; Gregolin, C.S.; Moreto, F.; Ferreira, A.L.A.; Minatel, I.O.; Correa, C.R. Basic concepts on the role of nuclear factor erythroid-derived 2-like 2 (Nrf2) in age-related diseases. *Int. J. Mol. Sci.* **2019**, *20*, 3208. [CrossRef] [PubMed]
42. Jaramillo, M.C.; Zhang, D.D. The emerging role of the Nrf2–Keap1 signaling pathway in cancer. *Genes Dev.* **2013**, *27*, 2179–2191. [CrossRef] [PubMed]
43. Ma, Q. Role of nrf2 in oxidative stress and toxicity. *Annu. Rev. Pharmacol. Toxicol.* **2013**, *53*, 401. [CrossRef] [PubMed]
44. Zhang, M.; An, C.; Gao, Y.; Leak, R.K.; Chen, J.; Zhang, F. Emerging roles of Nrf2 and phase II antioxidant enzymes in neuroprotection. *Prog. Neurobiol.* **2013**, *100*, 30–47. [CrossRef]
45. Hannan, M.A.; Dash, R.; Sohag, A.A.M.; Haque, M.N.; Moon, I.S. Neuroprotection against oxidative stress: Phytochemicals targeting TrkB signaling and the Nrf2-ARE antioxidant system. *Front. Mol. Neurosci.* **2020**, *13*, 116. [CrossRef]
46. Sivandzade, F.; Prasad, S.; Bhalerao, A.; Cucullo, L. NRF2 and NF-$_k$B interplay in cerebrovascular and neurodegenerative disorders: Molecular mechanisms and possible therapeutic approaches. *Redox Biol.* **2019**, *21*, 101059. [CrossRef]
47. Vomhof-DeKrey, E.E.; Picklo Sr, M.J. The Nrf2-antioxidant response element pathway: A target for regulating energy metabolism. *J. Nutr. Biochem.* **2012**, *23*, 1201–1206. [CrossRef]
48. Pranweerapaiboon, K.; Garon, A.; Seidel, T.; Janta, S.; Plubrukarn, A.; Chaithirayanon, K.; Langer, T. In vitro and in silico studies of holothurin A on androgen receptor in prostate cancer. *J. Biomol. Struct. Dyn.* **2021**, *40*, 12674–12682. [CrossRef]
49. Noonong, K.; Sobhon, P.; Sroyraya, M.; Chaithirayanon, K. Neuroprotective and Neurorestorative Effects of Holothuria scabra Extract in the MPTP/MPP+-Induced Mouse and Cellular Models of Parkinson's Disease. *Front. Neurosci.* **2020**, *14*, 575459. [CrossRef]
50. Lee, D.-H.; Kim, C.-S.; Lee, Y.J. Astaxanthin protects against MPTP/MPP^+-induced mitochondrial dysfunction and ROS production in vivo and in vitro. *Food Chem. Toxicol.* **2011**, *49*, 271–280. [CrossRef]

International Journal of
Molecular Sciences

MDPI

Review

Appropriate Macronutrients or Mineral Elements Are Beneficial to Improve Depression and Reduce the Risk of Depression

Zhengyang Quan, Hui Li, Zhenzhen Quan * and Hong Qing *

Key Laboratory of Molecular Medicine and Biotherapy, School of Life Science, Beijing Institute of Technology, Beijing 100081, China
* Correspondence: qzzbit2015@bit.edu.cn (Z.Q.); hqing@bit.edu.cn (H.Q.)

Abstract: Depression is a common mental disorder that seriously affects the quality of life and leads to an increasing global suicide rate. Macro, micro, and trace elements are the main components that maintain normal physiological functions of the brain. Depression is manifested in abnormal brain functions, which are considered to be tightly related to the imbalance of elements. Elements associated with depression include glucose, fatty acids, amino acids, and mineral elements such as lithium, zinc, magnesium, copper, iron, and selenium. To explore the relationship between these elements and depression, the main literature in the last decade was mainly searched and summarized on PubMed, Google Scholar, Scopus, Web of Science, and other electronic databases with the keywords "depression, sugar, fat, protein, lithium, zinc, magnesium, copper, iron, and selenium". These elements aggravate or alleviate depression by regulating a series of physiological processes, including the transmission of neural signals, inflammation, oxidative stress, neurogenesis, and synaptic plasticity, which thus affect the expression or activity of physiological components such as neurotransmitters, neurotrophic factors, receptors, cytokines, and ion-binding proteins in the body. For example, excessive fat intake can lead to depression, with possible mechanisms including inflammation, increased oxidative stress, reduced synaptic plasticity, and decreased expression of 5-Hydroxytryptamine (5-HT), Brain Derived Neurotrophic Factor (BDNF), Postsynaptic density protein 95(PSD-95), etc. Supplementing mineral elements, such as selenium, zinc, magnesium, or lithium as a psychotropic medication is mostly used as an auxiliary method to improve depression with other antidepressants. In general, appropriate nutritional elements are essential to treat depression and prevent the risk of depression.

Keywords: depression; macronutrients; mineral elements; appropriate supplementation; overdose or deficiency

Citation: Quan, Z.; Li, H.; Quan, Z.; Qing, H. Appropriate Macronutrients or Mineral Elements Are Beneficial to Improve Depression and Reduce the Risk of Depression. *Int. J. Mol. Sci.* **2023**, *24*, 7098. https://doi.org/10.3390/ijms24087098

Academic Editor: Claudia Ricci

Received: 6 March 2023
Revised: 6 April 2023
Accepted: 9 April 2023
Published: 12 April 2023

1. Introduction

Depression is one of the most common mental disorders globally, with an estimated 280 million people in the world suffering from it [1]. At worst, severe depression can lead to suicide. Not only does depression bring mental problems to the patients themselves, but it also causes financial and social burdens to their families and society [2].

The monoamine theory has influenced the development of major antidepressant treatments, including monoamine oxidase inhibitors (MAOIs), selective serotonin reuptake inhibitors (SSRIs), and serotonin-norepinephrine reuptake inhibitors (SNRIs). These inhibitors are functional by increasing monoamine levels (5-hydroxytryptamine, norepinephrine) to treat depression [3]. With accumulated studies on depression, other biochemical and physiological factors have also been implicated in the pathogenesis of depression, including brain-derived neurotrophic factor (BDNF)-related neurotrophic atrophy [4], inflammation [5], hypothalamic–pituitary–adrenal (HPA) axis dysfunction [6], etc. Among them, the role of nutrients in depression has attracted more and more attention [7].

The nutritional elements have been reported to help maintain a stable mental state, and an imbalance of them is closely related to depression [8]. As shown in Figure 1, this review

will explore the relationship between the imbalance of some nutrients and depression and summarize that the excess or deficiency of nutrients can increase the incidence of depression, thus maintaining the balance of corresponding nutrients can help reduce the incidence of depression. Moreover, appropriate supplementation of some mineral elements is considered to help treat depressed patients. The possible physiological processes and molecular mechanisms involved are discussed based on experiments.

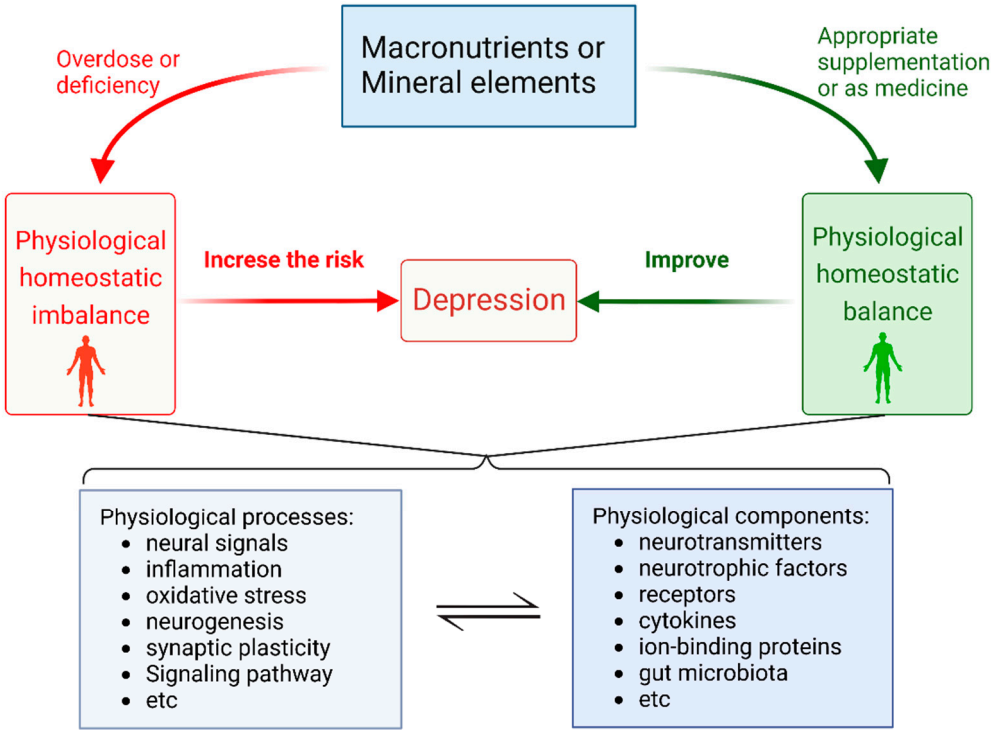

Figure 1. Illustrating the relationship between depression and macronutrients or mineral elements and possible mechanisms including physiological processes and components.

2. Overdose or Deficiency of Macronutrients Elements Increase the Risk of Depression

2.1. Dietary Sugars

Glucose is the primary source of energy for the human brain. ATP produced by glucose metabolism is the basis for maintaining neuronal and non-neuronal cell functions in the brain, such as producing neurotransmitters and nerve impulses [9]. Most sugars are metabolized in the body to produce glucose. There are many sugars in sweets, beverages, and candies. Many studies have shown that the excessive intake of sweets, sugar-sweetened beverages, and candy increases the risk of depression. Guo et al. have shown that regular consumption of sugar-sweetened beverages might increase the risk of depression in older Americans [10]. A study by Vermeulen et al. in a Dutch population also showed that a dietary pattern high in sugar (HS) increases the risk of depression [11]. The result of a 3-year follow-up survey by Shimmura et al. showed that high candy consumption significantly increases the risk of depression among Japanese workers, with 16.8% of high candy eaters experiencing depressive symptoms [12]. A study by Kashino et al. also showed that Japanese people who drink ≥4 cups of sugar-sweetened beverages per week have a 91% higher risk of depression than those who drink <1 cup/week [13]. A meta-analysis study indicated that people who consume 2 cups of cola per day have a 5% increased risk of depression, while those who consume the equivalent of 3 cans of cola per day have an approximately 25% increased risk of depression [14]. The research among Chinese people has also demonstrated that a high-sugar diet increases the odds of depression [15,16]. A study in the Spanish population found that consumption of added sugars was associated with a significantly increased risk of depression but no significant association between the

consumption of sugar-sweetened beverages and the risk of depression [17]. A study on the Korean population suggested that beverage intake increases the risk of depression in women but decreases the risk in men. The differences may be due to different statistical methods for sugar intake and evaluation criteria for depression [18]. Moreover, a high-sugar diet is prone to diabetes and obesity, which are also risk factors for depression [19,20]. In addition to sugar, sugary drinks and desserts may add sweeteners and other ingredients, the excessive intake of which may also be associated with the occurrence of depression, but there is currently a lack of relevant research with follow-up studies. A study has shown that fasting blood glucose concentrations (FBG) were significantly elevated in major depressed patients compared to healthy subjects (4.73 ± 0.45 vs. 4.52 ± 0.43 mmol/L, $p < 0.01$) [21].

The possible physiological processes and physiological components of a high-sugar diet affecting depression might be considered in the following pathways: 1. Neural signals: it affects the content of 5-Hydroxytryptamine (5-HT) in the brain. Animal experiments showed that a high-sugar diet reduces the activity of dendritic 5-HT-1A receptors, which may impede the feedback control of serotonin synthesis and release in the hypothalamus leading to a decrease in 5-HT [22]. 5-HT is a crucial monoamine neurotransmitter, and its decreased content in the brain is one of the critical factors leading to depression [23]. 2. Inflammation and pro-inflammatory factors. A meta-analysis study by Köhler et al. indicated that pro-inflammatory factors such as interleukin-6(IL-6), tumor necrosis factor-α(TNF-α), interleukin-13(IL-13), interleukin-12(IL-12), etc., are significantly elevated in major depressive disorder (MDD) patients, which associates inflammation with depression [24]. Lipopolysaccharide (LPS) is a commonly used inflammatory inducer. Experimental studies have shown that LPS induces inflammation in rodents at the same time as depression-like symptoms [25,26], indicating there might be a correlation between inflammation and depression. Do et al. showed that a high-sugar diet could induce inflammation and depression-like behavior in mice. Moreover, they found that a high-sugar diet may induce inflammation by altering the gut microbiota and intestinal permeability [27]. 3. Synaptic plasticity and the expression of brain-derived neurotrophic factor (BDNF). The level of BDNF in the serum of patients with MDD is significantly lower than that of healthy patients, and after receiving antidepressant treatment, the level of BDNF in the patient's body is significantly increased. BDNF can be used as a biomarker of depression or as a measure of antidepressant efficacy predictors [28]. Another study showed that low plasma BDNF is associated with suicidal behavior in major depression [29]. BDNF is widely expressed in the developing and adult mammalian brain and has been implicated in development, neural regeneration, synaptic transmission, synaptic plasticity, and neurogenesis [30]. A deficiency of BDNF or Trk receptors does not induce depression, but antidepressants are required to increase BDNF activity and restore neuronal networks [31]. In rodent models, a high-glucose diet can reduce the expression of BDNF, synapsin I, cyclic AMP-responsive element-binding protein (CREB), and growth-associated protein 43, which affect synaptic plasticity [32]. Another study showed that after one week of feeding rats with high sugar and fat, dendritic spines and dendritic branches in the CA1 region of the rat brain were significantly reduced [33].

2.2. Dietary Fat

A study showed that fat content is a risk factor for depression [34]. Fat accumulation in the body leads to obesity, which is also a risk factor for depression. A meta-analysis displayed that obese individuals have an 18% increased risk of depression [35]. An intracerebral study showed a 40% increased risk of depression in obese adolescents [36]. After dietary fat is metabolized and absorbed by the human body, it will be mainly converted into triglycerides (TG), total cholesterol (TC), etc. High-density lipoprotein cholesterol (HDL-C) and low-density lipoprotein cholesterol (LDL-C) are the main components of total cholesterol. TG, TC, HDL-C, and LDL-C are four items of blood lipid tests [37]. Peng et al. showed that HDL-C in the blood is significantly higher in major depressed patients compared to healthy subjects (1.31 ± 0.32 vs. 1.24 ± 0.300 mmol/L, $p < 0.01$); however, there

are no significant changes in LDL-C, TC, and TG [21]. Another study showed a significant association between high levels of HDL-C (≥1.04 mmol/L) and depression in adult men and between high levels of TG (≥1.7 mmol/L) and depression in adult women [38]. However, Enko et al. observed that HDL-C is significantly lower in major depressed patients compared to healthy subjects (1.43 [1.97–4.01] vs. 1.60 [1.23–1.89] mmol/L, $p = 0.049$), and TG is significantly higher (1.08 [0.76–1.54] vs. 0.84 [0.63–1.32] g/L, $p = 0.014$) [39]. A recent Mendelian randomization analysis by So et al. reported a positive association of HDL-C with major depressed patients, but increased HDL-C is causally associated with fewer depressive symptoms. The reasons for the discrepancy may involve the different evaluation criteria for depression and the heterogeneity of samples [40]. It suggests that abnormal HDL-C and TG may be risk factors for depression, which need further research. In addition to research in humans, there is a similar phenomenon in rodents. Mice given a high-fat diet (HFD) for 12 weeks developed depressive-like behaviors, and then switching the high-fat diet to a standard diet for 4 weeks eliminated the depressive-like behaviors in mice [41]. After administration of an HFD in BALB/c mice, high-density lipoprotein cholesterol and low-density lipoprotein cholesterol are strongly associated with depressive-like behavior [42]. The study by Anders et al. showed HFD could exacerbate depressive-like behaviors in the Flinders Sensitive Line (FSL) rat [43]. Another study also suggested that olive leaf extract may prevent depression by inhibiting fat mass and weight gain in mice fed with a high-fat diet [44].

The possible physiological processes and mechanisms of a high-fat diet affecting depression are summarized as follows: 1. Neural signals: 5-HT, glutamatergic receptor, $GABA_A$ receptor, glutamate, and aspartate transporter. After feeding with HFD for 14 weeks, Wu et al. found a significant decrease in the 5-HT system expression in the hippocampus of C57BL/6 mice [45]. A study also showed that HFD attenuated the inhibitory effect of escitalopram, a selective serotonin reuptake inhibitor (SSRI), on 5-HT reabsorption in the brain, reducing the concentration of 5-HT in synapses [46]. A high-fat diet administration of intestinal 5-HT synthesis inhibitors can attenuate depression-like behaviors in mice with high-fat diet-induced depression [47]. Long-term use of HFD can induce depressive-like behavior in rats and lead to decreased expression levels of the AMPA receptor (GlutA2) and GABA receptor (GAD65) [48]. HFD-induced depression correlates with the desensitization of GABAergic AgRP (agouti-related peptide) neurons in the hypothalamus, which plays a fundamental role in the control of appetite and body weight [49]. A recent study suggested that feeding mice an HFD causes the downregulation of glutamate transporter 1 (GLT-1), leading to glutamate overactivation, which in turn leads to depression [50]. 2. Inflammation and oxidative stress. A high-fat diet can induce an increase in proinflammatory cytokines in the rat hippocampus and depression-like behaviors [46]. In HFD-fed rats, depressive-like behaviors develop due to the overproduction of proinflammatory cytokines TNF-tumor necrosis factor alpha (TNF-α), interleukin-6 (IL-6), and interleukin-1 beta (IL-1β), the oxidative stress-related elevation of thiobarbituric acid-responsive substances (TABRS), and the down-regulation of antioxidant enzymes catalase (CAT) and glutathione peroxidase (GPX). Antidepressant agomelatine (AGO) eliminated depression in HFD rats, reduced the activity of inflammatory cytokines (TNF-α, IL-6, and IL-1β), TABRS, and restored the activity of CAT and GPX [51]. The antidepressant simvastatin (SMV) might also ameliorate depression by reducing inflammation in the brains of HFD-fed mice [45,52]. 3. Synaptic plasticity. Studies have shown that HFD also affects synaptic plasticity by reducing the expression of βIII-tubulin, postsynaptic density protein 95(PSD-95), synaptosomal-associated Protein, 25 kDa (SNAP-25), and neurotrophic factor-3 when it causes depression-like behavior in rats [48]. 4. The involvement of signaling pathways. HFD may induce depression in rats by desensitizing the Akt/GSK3β signaling pathway to 5-HT in the DG subgranular region of the hippocampal dentate gyrus, and returning to a normal diet can rescue the Akt/GSK3β response to 5-HT and alleviate depression-like behaviors [53]. Mice exposed to an HFD show accumulated fatty acids in the hypothalamus, leading to depression by inhibiting the cAMP/PKA signaling cascade [54]. HFD might also

inhibit AMPK phosphorylation and induce mTOR phosphorylation to suppress autophagy, thus leading to depression-like behavior in mice [55]. 5. Other related receptor proteins: leptin receptor long isoform (LepRb), cannabinoid receptor type 1 (CNR1). LepRb plays an important role in regulating depression and anxiety-related behaviors, and selective deletion induces depression-related behaviors [56,57]. Yang et al. showed that high fat can cause depressive-like behaviors in rats and result in reduced levels of LepRb protein and mRNA in the hippocampus and hypothalamus [58]. CNR1, an important component of the endocannabinoid system, plays an important role in depression [59]. CNR1-deficient mice can also be used to model depression in mice [60]. A study showed that pregnant rats fed an HFD led to depressive-like behaviors in their offspring, with a decrease in the *Cnr1* mRNA levels in the prefrontal cortex in the male offspring [61].

2.3. Dietary Protein

There are fewer studies on the relationship between dietary protein and depression. Low-protein diets are associated with an increased risk of depression in the U.S. and Korean populations. Among macronutrients carbohydrates, protein, and fat, the prevalence of depression decreases significantly in both the United States and South Korea when the proportion of calories consumed from protein increases by 10% [62]. Another study in the United States showed that an increase in protein intake reduces the risk of depression in men but increases the risk of depression in women [63]. A cross-sectional study suggested that total protein intake from milk and dairy products may reduce the risk of depressive symptoms in U.S. adults [64]. In a population of Japanese male workers, a study suggested that low protein intake may be associated with a higher prevalence of depressive symptoms [65]. Peng et al. showed that total protein (TP) is significantly decreased in major depressed patients compared to healthy subjects (4.73 ± 0.45 vs. 4.52 ± 0.43 mmol/L, $p < 0.01$) [21]. Red and processed meats contain protein and saturated fat, and excessive consumption of either could slightly increase the risk of depression [66]. Low protein intake reduces depressive symptoms in diabetic patients [67]. Milk is also rich in protein and fat, and intake of skim milk is inversely associated with depression, while whole milk is positively associated with depression [68].

Dietary protein is rich in amino acids, which can supplement the amino acids required by the human body to maintain normal physiological functions. Tryptophan in dietary protein is a precursor for the synthesis of serotonin, and an increase in serotonin in the brain is the key to treating depression [69]. A survey by Euter et al. found that a diet low in tryptophan is associated with a higher risk of depression [70]. Subchronic tryptophan depletion is also used as an animal model of depression [71]. Tryptophan in dietary protein is also a precursor compound for synthesizing dopamine, which has also been implicated in antidepressant therapy [72]. In milk proteins, alpha-lactalbumin [73] and lactoferrin [74] also help improve depression-like symptoms in mice.

3. Overdose or Deficiency of Mineral Element Increase the Risk in Depression

3.1. Zinc(Zn)

Zinc is an essential trace element that plays an important role in many biochemical and physiological processes in relation to brain growth and function [75]. Studies in many national populations, such as the United States [76], Australia [77], and Japan [78–80], found that a lack of dietary zinc intake increases the risk of depression. Two other studies have shown that insufficient dietary zinc intake leads to depressive symptoms in women but not in men [81,82]. Al-Fartusie et al. showed that zinc in serum is significantly lower in major depressed patients compared to healthy subjects (0.72 ± 0.08 vs. 0.96 ± 0.11 mg/L, $p < 0.01$) [83]. Islam et al. found the same experimental results [84]. In rodents, a zinc-deficient diet also induced depressive-like behavior [85–87].

We also summarized the possible physiological processes and mechanisms of zinc in depression. 1. It is related to zinc transporters (ZnTs). In mammals, zinc homeostasis is primarily regulated by ZnTs [88]. A study showed that there are significant increases in

protein levels of ZnT1, ZnT4, and ZnT5 in the prefrontal cortex in MDD but a reduced protein level of ZnT3 [89]. Zinc transporter 3 (ZnT3) plays an important role in concentrating zinc ions within synaptic vesicles in a subset of the brain's glutamatergic neurons [90]. In the stress-induced rat depression model, total zinc levels were reduced, and the mRNA expression of *ZnT1* and *ZnT3* was significantly reduced in the hippocampus [91]. Neurogenesis in the hippocampus was reduced in both rats fed with a zinc-deficient diet and *ZnT3* knockout mice, but it was resumed after a normal zinc diet treatment [92]. 2. It is related to Zn^{2+}-activated G protein-coupled receptor 39 (GPR39). GPR39 senses changes in extracellular zinc concentrations, which results in the activation of an intracellular signaling pathway to regulate the expression of genes associated with depression, such as BNDF and 5-HT [93,94]. GPR39 knockout causes depressive-like behavior in mice [95]. Depressive-like symptoms were observed in *GPR39* knockout mice, accompanied by decreased *CREB* and *BDNF* expression [96]. The GPR39 protein can bind to 5-HT1A and form a 5-HT1A-GPR39 complex that is regulated by zinc concentration [97]. 3. Inflammation and oxidative stress. After giving rats a zinc-deficient diet for 6 weeks, Doboszewska et al. found that it causes depressive behavior and increases the oxidation/inflammation parameters IL-1 and TBARS in rats [98]. 4. N-methyl-d-aspartate (NMDA). NMDA has emerged as a therapeutic target for depression therapy in clinical and preclinical studies. Since increasing evidence has supported the disruption of glutamate homeostasis and neurotransmission in depressed subjects [99]. A study has shown that in rats, zinc deficiency-induced depression-like behaviors are associated with increased NMDAR (GluN1, GluN2A, GluN2B), decreased AMPAR(GluA1), p-CREB, and BDNF in the hippocampus to change the NMDAR neuronal signal [100]. Another study also showed that in rats, zinc deficiency-induced depression-like behaviors are associated with increased NMDAR (GluN2A and GluN2B), decreased PSD-95, p-CREB, and BDNF in the hippocampus [101].

3.2. Magnesium (Mg)

Magnesium is one of the most important minerals in the human body and is involved in various biological processes in the brain and the fluidity of neuronal membranes, maintaining the stability of brain function [102]. Multiple studies have shown that dietary magnesium intake is inversely associated with the risk of depression [103–105]. Moreover, magnesium in serum is significantly lower in major depressed patients compared to healthy subjects (1.10 ± 0.11 vs. 1.64 ± 0.15 mg/L, $p < 0.01$) [79]. Like humans, a magnesium-deficient diet induces rodent depression-like behaviors [106,107].

The possible regulatory mechanisms of magnesium in depression could involve gut microbiota, NMDA nerve signaling, and oxidative stress: Magnesium deficiency diet might lead to depression-like behavior possibly by altering intestinal microbiome composition and inducing homeostasis of the microbiome–gut–brain axis in mice [107]. Another study showed that dietary Mg supplementation increases bacteria involved in intestinal health and metabolic homeostasis and reduces bacteria involved in inflammation and human diseases [108]. Ghafari et al. showed that enhancement of depressive-like behaviors induced by dietary magnesium restriction is associated with decreased levels of amygdala-hypothalamic proteins of GluN1-containing NMDA complexes [109]. Whittle et al. showed that mice fed a low Mg-containing diet (10% of the daily requirement) exhibit depression-like behavior and elevated expression of N(G), N(G)-dimethylarginine dimethylaminohydrolase 1 (DDAH1), manganese-superoxide dismutase (MnSOD), and glutamate dehydrogenase 1 (GDH1) related to oxidative stress [110]. Another study also showed that depression is associated with a decrease in magnesium concentrations in the human body, which leads to an increase in GPX associated with oxidative stress [111].

3.3. Copper(Cu)

Copper is an important trace element required by essential enzymes. However, copper also leads to the production of toxic reactive oxygen species due to its redox activity, so copper uptake is strictly controlled [112]. It was reported that the serum of major patients

with depression contains higher levels of copper compared to healthy subjects (1.55 ± 0.12 vs. 1.12 ± 0.13 mg/L, $p < 0.01$) [79]. And the same results were given by the Islam team [84] and the Ni team [113]. A study found that women with lower levels of magnesium and higher levels of Cu are more likely to suffer from depression [114]; while it is contradictory that the correlation between serum copper and the severity of depression was not found in another study [115].

Copper might influence depression via inflammation, oxidative stress, or synaptic plasticity. Copper exposure increases depression-like behavior and activates inflammation-related microglia in *APOE4* transgenic mice [116]. Melatonin (Mel) attenuates CU-induced oxidative stress and depression-like behavior by decreasing lipid peroxidation (LPO) and nitric oxide (NO) levels and enhancing superoxide dismutase (SOD) and catalase (CAT) activities in the rat hippocampus [117]. Liu et al. showed that copper levels are increased in the hippocampus of stressed mice, which can affect synaptic function by inhibiting the expression of GluN2B and PSD95 [118].

3.4. Iron(Fe)

Iron is an essential trace element for human growth and development and plays a key role in ensuring normal brain development and function [119]. Several studies have revealed that dietary iron deficiency increases the risk of depression [76,80,82,120,121]. In a case-control study, mothers with postpartum iron deficiency were shown to be three times more likely to develop postpartum depression [122]. Postpartum iron supplementation helps reduce postpartum depression [123]. Serum iron concentration was significantly decreased in many patients with major depression compared to healthy subjects (1.02 ± 0.02 vs. 1.30 ± 0.03 mg/L, $p < 0.05$ mg/L) [84]. A survey study found that people with a history of iron deficiency anemia have a higher risk of depression [124]. A study of type I diabetes and depression found that patients with iron deficiency have a higher incidence of depression [125]. Not only does iron deficiency increase the incidence of depression, but iron excess is also associated with depression. A study indicated significant iron deposition in the thalamus of patients with depression [126].

The mechanism by which iron induces depression is unclear, although it may be partially related to the level of BDNF and oxidative stress. Brain-derived neurotrophic factor (BDNF) is widely expressed in developing and adult mammalian brains and is associated with development, neural regeneration, synaptic transmission, synaptic plasticity, and neurogenesis [31,127]. Ceruloplasmin is a ferroxidase involved in iron metabolism by converting Fe (2+) to Fe (3+). Texel et al. found that ceruloplasmin knock-out mice produce anxiety-like behaviors with significantly decreased levels of Fe and BDNF in the hippocampus [128]. Other studies have also shown that a low dose of iron is associated with low BDNF expression in the rat hippocampus [129,130]. A high dose of iron, possibly from iron accumulation, induces depressive-like behavior in rats [131]. Iron deposition is closely related to depression, and the possible mechanism is that iron deposition leads to increased production of reactive oxygen species, which in turn causes neuronal damage in the brain [132,133].

As Table 1 showed, we summarize the serum or blood Levels of elements in healthy subjects or major depressed patients and the possible mechanisms.

Table 1. Summarize the possible mechanism for overdose or deficiency of macronutrients and mineral elements to increase the risk of depression.

Category		How to Increase the Risk of Depression	Serum or Blood Levels in Healthy Subjects	Serum or Blood Levels in Major Depressed Patients	Physiological Processes and Physiological Components
Macronutrients	Dietary sugars	Overdose	FBG: 4.52 ± 0.43 mmol/L	FBG:4.73 ± 0.45 mmol/L ** [21]	1. Neural signals: 5-HT↓ [22]
					2. Inflammation: pro-inflammatory factors such as IL-6, TNF-α, etc. ↑ [24]; gut microbiota [27]
					3. Synaptic plasticity: synapsin I and BDNF↓ [32]; Dendrite spines and dendritic branches↓ [33]
	Dietary fat	Overdose	TG: 1.08 [0.76–1.54] g/L	TG: 0.84 [0.63–1.32] g/L * [39]	1. Neural signals: 5-HT↓ [45]; 5-HT reabsorption↓ [46]; Intestinal 5-HT↑ [47]; GlutA2 and GAD65↓ [48]; desensitization of GABAergic AgRP neuron [49]; GLT-1↓ [50]
					2. Inflammation: pro-inflammatory factors such as IL-6, IL-1, TNF-α, etc. ↑ [45,46,51,52]
					3. Oxidative stress: TABRS, CAT, GPX↑ [51]
			HDL-C: 1.24 ± 0.30 mmol/L	HDL-C: 1.31 ± 0.32 mmol/L ** [21]	4. Synaptic plasticity: synapsin I and BDNF↓ [32]; βIII-tubulin, PSD-95, SNAP-25, and Neurotrophin-3↓ [48]
					5. Signaling pathway: Akt/GSK3β↓ [53]; cAMP/PKA↓ [54]; AMPK↓ [55].
					6. Other related receptor proteins: LepRb↓ [58], CNR1↓ [61]
	Dietary protein	Deficiency	TP: 68.72 ± 5.23 g/L	TP: 66.72 ± 5.10 g/L ** [21]	May be related to synthesis of 5-HT and dopamine [71,72]
Mineral elements	Zinc	Deficiency	0.96 ± 0.11 mg/L	0.72 ± 0.08 mg/L ** [83]	1. ZnT3↓ [89,91]; *ZnT3* knockout induced decreased hippocampal neurogenesis [92]
					2. GPR39 knockout [95]; GPR39 knockout induced decreased CREB and BDNF expression [96]
					3. Oxidation/inflammation parameters: IL-1 and TBARS↑ [98]
					4. Neural signals: NMDAR(GluN2A, GluN2B) ↑ [100,111]
	Magnesium	Deficiency	1.64 ± 0. 15 mg/L	1.10 ± 0.11 mg/L ** [83]	1. Gut microbiota [107]
					2. Neural signals: GluN1↓ [109]
					3. Oxidative stress: DDAH1, MnSOD, and GDH1↑ [110]; GPX↑ [111]
	Copper	Overdose	1.12 ± 0.13 mg/L	1.55 ± 0.12 mg/L ** [83]	1. Inflammation↑ [116]
					2. Oxidative stress: SOD and CAT↑ [117]
					3. Synaptic plasticity: GluN2B, PSD95↓ [118]
	Iron	Deficiency/ overdose	1.30 ± 0.03 mg/L	1.02 ± 0.02 mg/L * [84]	May be related to BDNF↓ [129,130] and oxidative stress↑ [133]

Note: ↓: indicates lower or reduced; ↑: indicates increase or promotion. Depressed patients compared to healthy subjects, * $p < 0.05$; ** $p < 0.01$. Full name and abbreviation: fasting blood glucose (FBG), triglycerides (TG), high-density lipoprotein cholesterol (HDL-C), total protein (TP), 5-hydroxytryptamine (5-HT), interleukin-6 (IL-6), tumor necrosis factor-α (TNF-α), brain-derived neurotrophic factor (BDNF), glucose transporter A2 (GlutA2), glutamic acid decarboxylase 65-kilodalton isoform (GAD65), gamma-aminobutyric acid (GABA), agouti-related protein (AgRP), glutamate transporter 1 (GLT-1), interleukin-1 (IL-1), thiobarbituric acid reactive substances (TBARS), catalase (CAT), glutathione peroxidase (GPX), postsynaptic density protein 95 (PSD-95), synaptosomal-associated protein, 25 kDa (SNAP-25), protein kinase B (AKT), glycogen synthase kinase-3 (GSK3β), cyclic adenylic acid (cAMP), protein kinase A(PKA), adenosine 5′-monophosphate (AMP)-activated protein kinase (AMPK), leptin receptor (LepRb), cannabinoid receptor 1 (CNR1), zinc transporter 3 (ZnT3), G-protein coupled receptor 39 (GPR39), cAMP response element-binding protein (CREB), N-methyl-d-aspartate (NMDA) receptor 2A (GluN2A), N-methyl-d-aspartate receptor 2B (GluN2B), N-methyl-d-aspartate receptor 1 (GluN1), N(G), N(G)-dimethylarginine dimethylaminohydrolase 1 (DDAH1), manganese-superoxide dismutase (MnSOD), glutamate dehydrogenase 1 (GDH1), superoxide dismutase (SOD).

4. Appropriate Supplementation of Some Mineral Elements or as Medication Can Help Alleviate Depression

4.1. Selenium(Se) Supplementation

Selenium is an essential trace element required for a variety of physiological functions, including thyroid hormone metabolism, protection against oxidative stress, and immune-related functions [134]. A cross-sectional study on US adults showed an inverse association between dietary selenium intake and depressive symptoms [76,135]. A survey on a Chinese rural elderly population [136] and a cross-sectional study on a Brazilian rural population [137] also indicated that higher selenium levels are associated with a lower prevalence of depression. The optimal doses for serum selenium in young Australians are between ~82 μg/L and 85 μg/L, which results in a reduced risk of depressive symptoms [138]. Studies have shown that selenium supplementation may be an effective way to prevent postpartum depression [139,140]. However, a study on US youth found the opposite: higher selenium exposure levels are associated with increased depressive symptoms [141]. Therefore, selenium supplementation for depression requires the first measurement of selenium levels in depressed people, and further clinical studies are required. Selenium supplementation in rodents is beneficial for treating depression. The salt form of selenium, sodium selenite, had antidepressant effects in rodents [142]. Sodium selenite can increase the antidepressant effect of imipramine, fluoxetine, and tianeptine and reduce immobility time on the forced swim test (FST) after the administration of antidepressants [143].

The regulatory mechanisms of selenium in the treatment of depression are limited due to few experimental studies: 1. Anti-oxidative stress. Selenium can reverse arsenic-induced deterioration, alleviate depressive-like behaviors in the rat hippocampus, and reduce malondialdehyde levels and acetylcholinesterase activity [144]. Another study demonstrated that selenium could inhibit LPS-induced oxidative damage by increasing antioxidants [145]. 2. Anti-inflammatory. Fluoride treatment reduces dopamine and norepinephrine secretion, activates inflammation in microglia, and leads to depression-like behavior. While selenium treatment can activate the JAK2/STAT3 pathway, restore dopamine and norepinephrine secretion, reduce IL-1β secretion, and increase the number of viable cortical neurons, thus alleviating fluoride-induced depressive-like behavior [146].

4.2. Zinc(Zn) Supplementation

Section 2.1 of the article suggests that a zinc-deficient diet increases the risk of depression, and in fact, appropriate zinc supplementation can help treat depression. Clinical studies have shown that zinc supplementation, individually or in combination with antidepressants, may help reduce depressive symptoms, and the dose and treatment course of zinc in clinical trials were 25~220 mg for 6 to 12 weeks [147–149]. In chronic stress-induced rodent models of depression, zinc supplementation can reduce depressive-like behavior [150]. For depressed patients, zinc levels should be first measured. If zinc deficiency occurs, appropriate supplementation should be carried out, and zinc levels should be monitored during treatment.

The mechanisms of zinc treatment for depression are related to the levels of BDNF and anti-inflammation. A study showed that zinc enhances the antidepressant efficacy of imipramine by increasing the concentration of BDNF in the prefrontal cortex [151]. Kirsten et al. reported that zinc can inhibit LPS-induced depression-like behaviors caused by inflammation in rats and reduce the expression of inflammation-related factors IFN-γ [99].

4.3. Magnesium (Mg) Supplementation

Depressed patients with magnesium deficiency take 500 mg of magnesium oxide tablets daily for ≥8 weeks to alleviate depressive symptoms [152]. It is effective that over-the-counter magnesium chloride (248 mg of elemental magnesium per day) is taken by adults with mild to moderate symptoms of depression for 6 weeks [153]. A recent clinical study tracking the electroencephalogram in MDD patients showed that magnesium can enhance fluoxetine treatment in response to depression treatment [154]. As with the other

elements above, an initial measurement of magnesium levels is required in depressed patients, followed by supplementing appropriately and monitoring magnesium levels during treatment.

The following are possible mechanisms of magnesium therapy for depression: 1. 5-HT. Poleszak et al. found that the antidepressant-like effects of magnesium are significantly reduced in mice pretreated with serotonin synthesis inhibitors [155]. 2. Anti-inflammation. Cyclophosphamide (CYP)-induced inflammation causes depression-like behaviors in rats and increases the inflammatory factors TNF-α and IL6, while supplementation with magnesium L-threonate could reduce the inflammatory response and depression-like behaviors [156]. 3. NMDA. Magnesium could treat depression-like behavior induced by chronic mild stress in rats, and concomitantly restore the levels of GluN1 and GluN2A and increase the levels of GluN2B and PSD-95 [157].

4.4. Lithium(Li) as a Psychotropic Medication

Lithium as a psychotropic medication has been used to treat bipolar disorder (BD) and prevent suicidal and depressive/manic episodes [158]. Lithium also plays an important role in the treatment of unipolar depression. Barroilhet et al. showed that a low dose of lithium in the body can help prevent suicide caused by depression, but a higher dose (over 1.0 mmol/L) has specific toxic side effects [159]. Adding trace amounts of lithium to drinking water may reduce suicide risk in the general population [160]. The addition of lithium to both imipramine and fluvoxamine in phase II is more effective for treating depression than the phase I drug alone [161]. Lithium has also been recommended in multiple depression medication guidelines [162]. Lithium is clinically effective as long-term monotherapy and supplemental antidepressant therapy for depression [163]. A cohort study in Finland reported that, compared to lithium combined with antidepressants, lithium alone has a lower risk for patients with significant depression readmitted to the hospital [164]. Other studies have also shown the benefits of lithium in treating depression [165,166]. Vázquez et al. summarized the dose and treatment course of lithium in clinical trials as 600~1200 mg for 1 to 6 weeks [167]. Since a higher dose (over 1.0 mmol/L) has specific toxic side effects, in the clinic, the lithium content should be first detected in depressed patients and then monitored regularly.

The possible physiological processes and mechanisms of lithium treatment for depression are considered as follows: 1. Hippocampal neurogenesis. Hippocampal adult neurogenesis is defined as new neurons generated in the dentate gyrus of the hippocampus and integrated into neural circuits during adulthood, which can repair nerve damage and increase neuroplasticity [168]. Hippocampal volume is reduced in the brains of depressed patients but increases after 3 years of antidepressant treatment, suggesting that antidepressants could induce hippocampal neurogenesis to alleviate depression [169]. In rodents, impaired neurogenesis can induce depression-like behaviors in animals [170]. An experimental study showed that both lithium alone and combined with fluoxetine could increase neurogenesis and eliminate depression-like behavior in resistant depression models. Moreover, lithium combined with fluoxetine has fewer side effects than lithium alone [171]. 2. BDNF. A survey has shown lithium can enhance serum BDNF levels in depressed patients [172]. Another study showed that lithium exerts an antidepressant effect by increasing BDNF and thereby increasing the firing activity of VTA-mPFC DA neurons in depressive-like mice [173]. 3. The blood–brain barrier (BBB). Disruption of the BBB leads to a disturbance of brain homeostasis that may be a key factor in the development of depression [174]. Lithium exerts antidepressant effects by protecting against the destruction of the BBB/neurovascular unit (NVU) in the chronic mild stress (CMS) rat model [175].

In Table 2, we summarize daily dose and course of mineral elements to treat depressed patients in clinical trials and the possible mechanisms.

Table 2. A summary of the benefits of proper supplementation with some mineral elements or as medication that can help improve depression.

Category			Daily Dose and Course of Treatment in Depressed Patients in Clinical Trials	Physiological Processes and Physiological Components
Mineral elements	Proper supplementation	Selenium	—	1. Anti-oxidative stress [144,145]
				2. Anti-inflammatory: pro-inflammatory factors IL-1↓ [146]
		Zinc	25~220 mg for 8 to 12 weeks [147–149]	1. Anti-inflammatory: IFN-γ↓ [99]
				2. BDNF↑ [151]
		Magnesium	248~500 mg for 6 to 8 weeks [152,153]	1. 5-HT↑ [155]
				2. Anti-inflammation: TNF-α and IL6↓ [156]
				3. Glutamate signaling↑ [157]
	Psychotropic medication	Lithium	600~1200 mg for 1 to 6 weeks [167]	1. Hippocampal neurogenesis↑ [171]
				2. BDNF↑ [172,173]
				3. Protects the blood–brain barrier [175]

Note: ↓: indicates lower or reduced; ↑: indicates increase or promotion. —: not applicable. Full name and abbreviation: brain-derived neurotrophic factor (BDNF), interleukin-1 (IL-1), interferon-gamma (IFN-γ), 5-hydroxytryptamine (5-HT), tumor necrosis factor-α (TNF-α), interleukin-6 (IL-6).

5. Conclusions

Nutrients are indispensable to the human body and affect the normal physiological functions of the human body. As shown in Table 1, nutrient imbalances, including macronutrients (dietary sugars, fat, and protein) and mineral elements (zinc, magnesium, copper, and iron), may increase the occurrence of depression. Several clinical and non-clinical studies have shown that nutrients also affect the function of antidepressants. As summarized in Table 2, appropriate doses of selenium, zinc, magnesium, and lithium are beneficial for reducing depression. Magnesium and zinc deficiencies increase the risk of depression, and appropriate magnesium and zinc supplementation can also help improve depression. Therefore, as described in Figure 2, in addition to conventional drug treatment of depression, it also needs to pay attention to the level of the patient's own nutritional elements, the timely supplementation of the lacking nutritional elements, the control of excessive nutritional elements, and the balance of these nutrients in the body. Moreover, nutritional elements such as lithium, selenium, zinc, magnesium, etc., for depression treatment should be based on elemental levels in the body and during treatment. Excessive elemental supplementation may be harmful; therefore, supplementation should be appropriate and follow the doctor's advice and not be haphazard or uncontrolled.

In the serum or blood levels of depressed patients, fasting blood glucose, high-density lipoprotein-cholesterol, and copper are significantly elevated, while total protein, zinc, magnesium, and iron are significantly decreased [21,83,84], so further research should be conducted on whether these elements can be used as indicators for the prevention and treatment of depression.

This review summarizes the functions and mechanisms of some nutrients in depression research. Nevertheless, further studies are still required. For example, the intake of dietary sugar, fat, and protein in life also contains some additives such as sweeteners, preservatives, and other ingredients, and their relationships with depression are not clear, which should be addressed in follow-up studies. Furthermore, the nutritional elements associated with depression not only include those summarized in the article but also involve vitamins [176–178], folic acid [179], N-acetylcysteine [180], S-adenozylmetionine [181], dietary fiber [182], etc., which also need to be considered. This article suggests that to better

prevent and treat depression, people should gradually focus on the role of nutrients in depression and their daily diet, such as low-sugar and low-fat diets.

In general, we summarized the involvement of some nutritional elements in depression and elucidated their related regulatory mechanisms. It may inspire novel preventive and therapeutic strategies for depression.

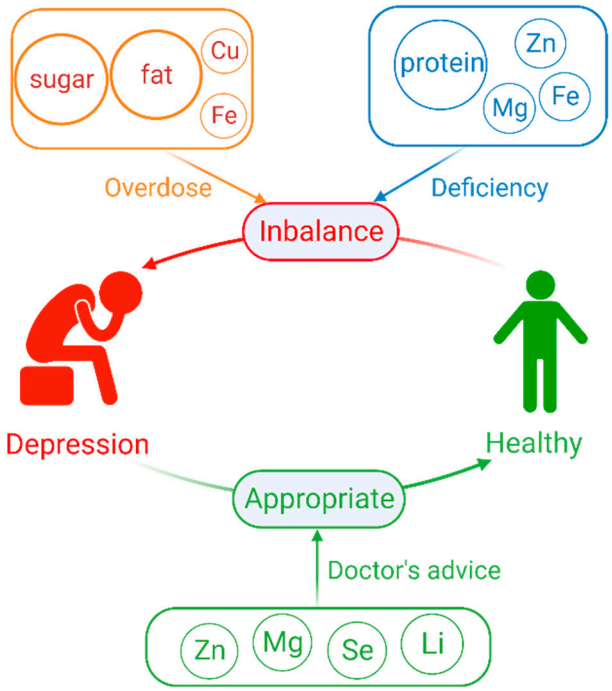

Figure 2. Summarize the relationship between depression and elements. Cu (copper), Fe (iron), Zn (zinc), Mg (magnesium), Se (selenium), Li (lithium).

Author Contributions: H.Q. and Z.Q. (Zhenzhen Quan) contributed to organizing this article and revising its content; Z.Q. (Zhengyang Quan) was responsible for searching literature and writing the manuscript; H.L. provided some valuable advice for this article. All authors have read and agreed to the published version of the manuscript.

Funding: This work was funded by the Ministry of Science and Technology Key project (Grant No. 2022ZD0206800), the National Natural Science Foundation of China under grants No. 92049102 and No. 82001167, Beijing Nova Program (Grant No. 20220484083).

Institutional Review Board Statement: Not applicable.

Informed Consent Statement: Not applicable.

Data Availability Statement: Not applicable.

Conflicts of Interest: The authors declare no conflict of interest.

References

1. World Health Organization. Depression. Available online: http://www.who.int/mediacentre/factsheets/fs369/en/ (accessed on 1 May 2021).
2. Mrazek, D.A.; Hornberger, J.C.; Altar, C.A.; Degtiar, I. A review of the clinical, economic, and societal burden of treatment-resistant depression: 1996–2013. *Psychiatr. Serv.* **2014**, *65*, 977–987. [CrossRef] [PubMed]
3. Hamon, M.; Blier, P. Monoamine neurocircuitry in depression and strategies for new treatments. *Prog. Neuro-Psychopharmacol. Biol. Psychiatry* **2013**, *45*, 54–63. [CrossRef] [PubMed]
4. Yu, H.; Chen, Z.-Y. The role of BDNF in depression on the basis of its location in the neural circuitry. *Acta Pharmacol. Sin.* **2011**, *32*, 3–11. [CrossRef] [PubMed]
5. Beurel, E.; Toups, M.; Nemeroff, C.B. The Bidirectional Relationship of Depression and Inflammation: Double Trouble. *Neuron* **2020**, *107*, 234–256. [CrossRef]

6. Dwyer, J.B.; Aftab, A.; Radhakrishnan, R.; Widge, A.; Rodriguez, C.I.; Carpenter, L.L.; Nemeroff, C.B.; McDonald, W.M.; Kalin, N.H. Hormonal Treatments for Major Depressive Disorder: State of the Art. *Am. J. Psychiatry* **2020**, *177*, 686–705. [CrossRef]
7. Aly, J.; Engmann, O. The Way to a Human's Brain Goes Through Their Stomach: Dietary Factors in Major Depressive Disorder. *Front. Neurosci.* **2020**, *14*, 582853. [CrossRef] [PubMed]
8. Shayganfard, M. Are Essential Trace Elements Effective in Modulation of Mental Disorders? Update and Perspectives. *Biol. Trace Elem. Res.* **2022**, *200*, 1032–1059. [CrossRef]
9. Mergenthaler, P.; Lindauer, U.; Dienel, G.A.; Meisel, A. Sugar for the brain: The role of glucose in physiological and pathological brain function. *Trends Neurosci.* **2013**, *36*, 587–597. [CrossRef]
10. Guo, X.; Park, Y.; Freedman, N.D.; Sinha, R.; Hollenbeck, A.R.; Blair, A.; Chen, H. Sweetened beverages, coffee, and tea and depression risk among older US adults. *PLoS ONE* **2014**, *9*, e94715. [CrossRef]
11. Vermeulen, E.; Stronks, K.; Snijder, M.B.; Schene, A.H.; Lok, A.; de Vries, J.H.; Visser, M.; Brouwer, I.A.; Nicolaou, M. A combined high-sugar and high-saturated-fat dietary pattern is associated with more depressive symptoms in a multi-ethnic population: The HELIUS (Healthy Life in an Urban Setting) study. *Public Health Nutr.* **2017**, *20*, 2374–2382. [CrossRef]
12. Shimmura, N.; Nanri, A.; Kashino, I.; Kochi, T.; Eguchi, M.; Kabe, I.; Mizoue, T. Prospective association of confectionery intake with depressive symptoms among Japanese workers: The Furukawa Nutrition and Health Study. *Br. J. Nutr.* **2022**, *128*, 139–144. [CrossRef] [PubMed]
13. Kashino, I.; Kochi, T.; Imamura, F.; Eguchi, M.; Kuwahara, K.; Nanri, A.; Kurotani, K.; Akter, S.; Hu, H.; Miki, T.; et al. Prospective association of soft drink consumption with depressive symptoms. *Nutrition* **2021**, *81*, 110860. [CrossRef] [PubMed]
14. Hu, D.; Cheng, L.; Jiang, W. Sugar-sweetened beverages consumption and the risk of depression: A meta-analysis of observational studies. *J. Affect. Disord.* **2019**, *245*, 348–355. [CrossRef]
15. Yu, B.; He, H.; Zhang, Q.; Wu, H.; Du, H.; Liu, L.; Wang, C.; Shi, H.; Xia, Y.; Guo, X.; et al. Soft drink consumption is associated with depressive symptoms among adults in China. *J. Affect. Disord.* **2015**, *172*, 422–427. [CrossRef] [PubMed]
16. Zhang, X.; Huang, X.; Xiao, Y.; Jing, D.; Huang, Y.; Chen, L.; Luo, D.; Chen, X.; Shen, M. Daily intake of soft drinks is associated with symptoms of anxiety and depression in Chinese adolescents. *Public Health Nutr.* **2019**, *22*, 2553–2560. [CrossRef] [PubMed]
17. Sanchez-Villegas, A.; Zazpe, I.; Santiago, S.; Perez-Cornago, A.; Martinez-Gonzalez, M.A.; Lahortiga-Ramos, F. Added sugars and sugar-sweetened beverage consumption, dietary carbohydrate index and depression risk in the Seguimiento Universidad de Navarra (SUN) Project. *Br. J. Nutr.* **2018**, *119*, 211–221. [CrossRef]
18. Kim, J.-M.; Lee, E. Association between Soft-Drink Intake and Obesity, Depression, and Subjective Health Status of Male and Female Adults. *Int. J. Environ. Res. Public Health* **2021**, *18*, 10415. [CrossRef]
19. Pinna, F.; Suprani, F.; Deiana, V.; Lai, L.; Manchia, M.; Paribello, P.; Somaini, G.; Diana, E.; Nicotra, E.F.; Farci, F.; et al. Depression in Diabetic Patients: What Is the Link With Eating Disorders? Results of a Study in a Representative Sample of Patients With Type 1 Diabetes. *Front. Psychiatry* **2022**, *13*, 848031. [CrossRef]
20. Borgland, S.L. Can treatment of obesity reduce depression or vice versa? *J. Psychiatry Neurosci.* **2021**, *46*, E313–E318. [CrossRef]
21. Peng, Y.-F.; Xiang, Y.; Wei, Y.-S. The significance of routine biochemical markers in patients with major depressive disorder. *Sci. Rep.* **2016**, *6*, 34402. [CrossRef]
22. Inam, Q.-u.-A.; Jabeen, B.; Haleem, M.A.; Haleem, D.J. Long-term consumption of sugar-rich diet decreases the effectiveness of somatodendritic serotonin-1A receptors. *Nutr. Neurosci.* **2008**, *11*, 277–282. [CrossRef] [PubMed]
23. Haase, J.; Brown, E. Integrating the monoamine, neurotrophin and cytokine hypotheses of depression—A central role for the serotonin transporter? *Pharmacol. Ther.* **2015**, *147*, 1–11. [CrossRef] [PubMed]
24. Köhler, C.A.; Freitas, T.H.; Maes, M.; de Andrade, N.Q.; Liu, C.S.; Fernandes, B.S.; Stubbs, B.; Solmi, M.; Veronese, N.; Herrmann, N.; et al. Peripheral cytokine and chemokine alterations in depression: A meta-analysis of 82 studies. *Acta Psychiatr. Scand.* **2017**, *135*, 373–387. [CrossRef] [PubMed]
25. Sabedra Sousa, F.S.; Birmann, P.T.; Bampi, S.R.; Fronza, M.G.; Balaguez, R.; Alves, D.; Leite, M.R.; Nogueira, C.W.; Brüning, C.A.; Savegnago, L. Lipopolysaccharide-induced depressive-like, anxiogenic-like and hyperalgesic behavior is attenuated by acute administration of α-(phenylselanyl) acetophenone in mice. *Neuropharmacology* **2019**, *146*, 128–137. [CrossRef] [PubMed]
26. Casaril, A.M.; Domingues, M.; de Andrade Lourenço, D.; Birmann, P.T.; Padilha, N.; Vieira, B.; Begnini, K.; Seixas, F.K.; Collares, T.; Lenardão, E.J.; et al. Depression- and anxiogenic-like behaviors induced by lipopolysaccharide in mice are reversed by a selenium-containing indolyl compound: Behavioral, neurochemical and computational insights involving the serotonergic system. *J. Psychiatr. Res.* **2019**, *115*, 1–12. [CrossRef]
27. Do, M.H.; Lee, E.; Oh, M.-J.; Kim, Y.; Park, H.-Y. High-Glucose or -Fructose Diet Cause Changes of the Gut Microbiota and Metabolic Disorders in Mice without Body Weight Change. *Nutrients* **2018**, *10*, 761. [CrossRef]
28. Sen, S.; Duman, R.; Sanacora, G. Serum brain-derived neurotrophic factor, depression, and antidepressant medications: Meta-analyses and implications. *Biol. Psychiatry* **2008**, *64*, 527–532. [CrossRef]
29. Kim, Y.K.; Lee, H.P.; Won, S.D.; Park, E.Y.; Lee, H.Y.; Lee, B.H.; Lee, S.W.; Yoon, D.; Han, C.; Kim, D.J.; et al. Low plasma BDNF is associated with suicidal behavior in major depression. *Prog. Neuropsychopharmacol. Biol. Psychiatry* **2007**, *31*, 78–85. [CrossRef]
30. Colucci-D'Amato, L.; Speranza, L.; Volpicelli, F. Neurotrophic Factor BDNF, Physiological Functions and Therapeutic Potential in Depression, Neurodegeneration and Brain Cancer. *Int. J. Mol. Sci.* **2020**, *21*, 7777. [CrossRef]
31. Björkholm, C.; Monteggia, L.M. BDNF—A key transducer of antidepressant effects. *Neuropharmacology* **2016**, *102*, 72–79. [CrossRef]

32. Molteni, R.; Barnard, R.J.; Ying, Z.; Roberts, C.K.; Gómez-Pinilla, F. A high-fat, refined sugar diet reduces hippocampal brain-derived neurotrophic factor, neuronal plasticity, and learning. *Neuroscience* **2002**, *112*, 803–814. [CrossRef] [PubMed]
33. Calvo-Ochoa, E.; Hernández-Ortega, K.; Ferrera, P.; Morimoto, S.; Arias, C. Short-term high-fat-and-fructose feeding produces insulin signaling alterations accompanied by neurite and synaptic reduction and astroglial activation in the rat hippocampus. *J. Cereb. Blood Flow Metab.* **2014**, *34*, 1001–1008. [CrossRef] [PubMed]
34. Speed, M.S.; Jefsen, O.H.; Børglum, A.D.; Speed, D.; Østergaard, S.D. Investigating the association between body fat and depression via Mendelian randomization. *Transl. Psychiatry* **2019**, *9*, 184. [CrossRef] [PubMed]
35. Mannan, M.; Mamun, A.; Doi, S.; Clavarino, A. Is there a bi-directional relationship between depression and obesity among adult men and women? Systematic review and bias-adjusted meta analysis. *Asian J. Psychiatry* **2016**, *21*, 51–66. [CrossRef] [PubMed]
36. Mannan, M.; Mamun, A.; Doi, S.; Clavarino, A. Prospective Associations between Depression and Obesity for Adolescent Males and Females—A Systematic Review and Meta-Analysis of Longitudinal Studies. *PLoS ONE* **2016**, *11*, e0157240. [CrossRef]
37. Panth, N.; Dias, C.B.; Wynne, K.; Singh, H.; Garg, M.L. Medium-chain fatty acids lower postprandial lipemia: A randomized crossover trial. *Clin. Nutr.* **2020**, *39*, 90–96. [CrossRef]
38. Oh, J.; Kim, T.-S. Serum lipid levels in depression and suicidality: The Korea National Health and Nutrition Examination Survey (KNHANES) 2014. *J. Affect. Disord.* **2017**, *213*, 51–58. [CrossRef]
39. Enko, D.; Brandmayr, W.; Halwachs-Baumann, G.; Schnedl, W.J.; Meinitzer, A.; Kriegshäuser, G. Prospective plasma lipid profiling in individuals with and without depression. *Lipids Health Dis.* **2018**, *17*, 149. [CrossRef]
40. So, H.-C.; Chau, C.K.-L.; Cheng, Y.-Y.; Sham, P.C. Causal relationships between blood lipids and depression phenotypes: A Mendelian randomisation analysis. *Psychol. Med.* **2021**, *51*, 2357–2369. [CrossRef]
41. Braga, S.P.; Delanogare, E.; Machado, A.E.; Prediger, R.D.; Moreira, E.L.G. Switching from high-fat feeding (HFD) to regular diet improves metabolic and behavioral impairments in middle-aged female mice. *Behav. Brain Res.* **2021**, *398*, 112969. [CrossRef]
42. Yu, H.; Qin, X.; Yu, Z.; Chen, Y.; Tang, L.; Shan, W. Effects of high-fat diet on the formation of depressive-like behavior in mice. *Food Funct.* **2021**, *12*, 6416–6431. [CrossRef] [PubMed]
43. Abildgaard, A.; Solskov, L.; Volke, V.; Harvey, B.H.; Lund, S.; Wegener, G. A high-fat diet exacerbates depressive-like behavior in the Flinders Sensitive Line (FSL) rat, a genetic model of depression. *Psychoneuroendocrinology* **2011**, *36*, 623–633. [CrossRef] [PubMed]
44. Mikami, T.; Kim, J.; Park, J.; Lee, H.; Yaicharoen, P.; Suidasari, S.; Yokozawa, M.; Yamauchi, K. Olive leaf extract prevents obesity, cognitive decline, and depression and improves exercise capacity in mice. *Sci. Rep.* **2021**, *11*, 12495. [CrossRef] [PubMed]
45. Wu, H.; Lv, W.; Pan, Q.; Kalavagunta, P.K.; Liu, Q.; Qin, G.; Cai, M.; Zhou, L.; Wang, T.; Xia, Z.; et al. Simvastatin therapy in adolescent mice attenuates HFD-induced depression-like behavior by reducing hippocampal neuroinflammation. *J. Affect. Disord.* **2019**, *243*, 83–95. [CrossRef]
46. Hersey, M.; Woodruff, J.L.; Maxwell, N.; Sadek, A.T.; Bykalo, M.K.; Bain, I.; Grillo, C.A.; Piroli, G.G.; Hashemi, P.; Reagan, L.P. High-fat diet induces neuroinflammation and reduces the serotonergic response to escitalopram in the hippocampus of obese rats. *Brain Behav. Immun.* **2021**, *96*, 63–72. [CrossRef] [PubMed]
47. Pan, Q.; Liu, Q.; Wan, R.; Kalavagunta, P.K.; Liu, L.; Lv, W.; Qiao, T.; Shang, J.; Wu, H. Selective inhibition of intestinal 5-HT improves neurobehavioral abnormalities caused by high-fat diet mice. *Metab. Brain Dis.* **2019**, *34*, 747–761. [CrossRef]
48. Liu, S.; Xiu, J.; Zhu, C.; Meng, K.; Li, C.; Han, R.; Du, T.; Li, L.; Xu, L.; Liu, R.; et al. Fat mass and obesity-associated protein regulates RNA methylation associated with depression-like behavior in mice. *Nat. Commun.* **2021**, *12*, 6937. [CrossRef]
49. Xia, G.; Han, Y.; Meng, F.; He, Y.; Srisai, D.; Farias, M.; Dang, M.; Palmiter, R.D.; Xu, Y.; Wu, Q. Reciprocal control of obesity and anxiety-depressive disorder via a GABA and serotonin neural circuit. *Mol. Psychiatry* **2021**, *26*, 2837–2853. [CrossRef]
50. Tsai, S.-F.; Hsu, P.-L.; Chen, Y.-W.; Hossain, M.S.; Chen, P.-C.; Tzeng, S.-F.; Chen, P.-S.; Kuo, Y.-M. High-fat diet induces depression-like phenotype via astrocyte-mediated hyperactivation of ventral hippocampal glutamatergic afferents to the nucleus accumbens. *Mol. Psychiatry* **2022**, *27*, 4372–4384. [CrossRef]
51. Rebai, R.; Jasmin, L.; Boudah, A. Agomelatine effects on fat-enriched diet induced neuroinflammation and depression-like behavior in rats. *Biomed. Pharmacother. Biomed. Pharmacother.* **2021**, *135*, 111246. [CrossRef] [PubMed]
52. Wang, H.; Zhou, J.; Liu, Q.Z.; Wang, L.L.; Shang, J. Simvastatin and Bezafibrate ameliorate Emotional disorder Induced by High fat diet in C57BL/6 mice. *Sci. Rep.* **2017**, *7*, 2335. [CrossRef] [PubMed]
53. Arcego, D.M.; Toniazzo, A.P.; Krolow, R.; Lampert, C.; Berlitz, C.; Dos Santos Garcia, E.; do Couto Nicola, F.; Hoppe, J.B.; Gaelzer, M.M.; Klein, C.P.; et al. Impact of High-Fat Diet and Early Stress on Depressive-Like Behavior and Hippocampal Plasticity in Adult Male Rats. *Mol. Neurobiol.* **2018**, *55*, 2740–2753. [CrossRef] [PubMed]
54. Vagena, E.; Ryu, J.K.; Baeza-Raja, B.; Walsh, N.M.; Syme, C.; Day, J.P.; Houslay, M.D.; Baillie, G.S. A high-fat diet promotes depression-like behavior in mice by suppressing hypothalamic PKA signaling. *Transl. Psychiatry* **2019**, *9*, 141. [CrossRef] [PubMed]
55. Li, Y.; Cheng, Y.; Zhou, Y.; Du, H.; Zhang, C.; Zhao, Z.; Chen, Y.; Zhou, Z.; Mei, J.; Wu, W.; et al. High fat diet-induced obesity leads to depressive and anxiety-like behaviors in mice via AMPK/mTOR-mediated autophagy. *Exp. Neurol.* **2022**, *348*, 113949. [CrossRef] [PubMed]
56. Liu, W.; Liu, J.; Xia, J.; Xue, X.; Wang, H.; Qi, Z.; Ji, L. Leptin receptor knockout-induced depression-like behaviors and attenuated antidepressant effects of exercise are associated with STAT3/SOCS3 signaling. *Brain Behav. Immun.* **2017**, *61*, 297–305. [CrossRef]

57. Guo, M.; Huang, T.-Y.; Garza, J.C.; Chua, S.C.; Lu, X.-Y. Selective deletion of leptin receptors in adult hippocampus induces depression-related behaviours. *Int. J. Neuropsychopharmacol.* **2013**, *16*, 857–867. [CrossRef]
58. Yang, J.L.; Liu, D.X.; Jiang, H.; Pan, F.; Ho, C.S.; Ho, R.C. The Effects of High-fat-diet Combined with Chronic Unpredictable Mild Stress on Depression-like Behavior and Leptin/LepRb in Male Rats. *Sci. Rep.* **2016**, *6*, 35239. [CrossRef]
59. Gallego-Landin, I.; García-Baos, A.; Castro-Zavala, A.; Valverde, O. Reviewing the Role of the Endocannabinoid System in the Pathophysiology of Depression. *Front. Pharm.* **2021**, *12*, 762738. [CrossRef]
60. Valverde, O.; Torrens, M. CB1 receptor-deficient mice as a model for depression. *Neuroscience* **2012**, *204*, 193–206. [CrossRef]
61. Gawliński, D.; Gawlińska, K.; Smaga, I. Maternal High-Fat Diet Modulates Gene Expression in Male Rat Offspring. *Nutrients* **2021**, *13*, 2885. [CrossRef]
62. Oh, J.; Yun, K.; Chae, J.-H.; Kim, T.-S. Association Between Macronutrients Intake and Depression in the United States and South Korea. *Front. Psychiatry* **2020**, *11*, 207. [CrossRef] [PubMed]
63. Wolfe, A.R.; Arroyo, C.; Tedders, S.H.; Li, Y.; Dai, Q.; Zhang, J. Dietary protein and protein-rich food in relation to severely depressed mood: A 10 year follow-up of a national cohort. *Prog. Neuro-Psychopharmacol. Biol. Psychiatry* **2011**, *35*, 232–238. [CrossRef] [PubMed]
64. Li, Y.; Zhang, C.; Li, S.; Zhang, D. Association between dietary protein intake and the risk of depressive symptoms in adults. *Br. J. Nutr.* **2020**, *123*, 1290–1301. [CrossRef] [PubMed]
65. Nanri, A.; Eguchi, M.; Kuwahara, K.; Kochi, T.; Kurotani, K.; Ito, R.; Pham, N.M.; Tsuruoka, H.; Akter, S.; Jacka, F.; et al. Macronutrient intake and depressive symptoms among Japanese male workers: The Furukawa Nutrition and Health Study. *Psychiatry Res.* **2014**, *220*, 263–268. [CrossRef]
66. Nucci, D.; Fatigoni, C.; Amerio, A.; Odone, A.; Gianfredi, V. Red and Processed Meat Consumption and Risk of Depression: A Systematic Review and Meta-Analysis. *Int. J. Environ. Res. Public Health* **2020**, *17*, 6686. [CrossRef]
67. Ciarambino, T.; Ferrara, N.; Castellino, P.; Paolisso, G.; Coppola, L.; Giordano, M. Effects of a 6-days-a-week low protein diet regimen on depressive symptoms in young-old type 2 diabetic patients. *Nutrition* **2011**, *27*, 46–49. [CrossRef]
68. Sun, J.; Wang, W.; Zhang, D. Associations of different types of dairy intakes with depressive symptoms in adults. *J. Affect. Disord.* **2020**, *274*, 326–333. [CrossRef]
69. Badawy, A.A. B. Tryptophan: The key to boosting brain serotonin synthesis in depressive illness. *J. Psychopharmacol.* **2013**, *27*, 878–893. [CrossRef]
70. Reuter, M.; Zamoscik, V.; Plieger, T.; Bravo, R.; Ugartemendia, L.; Rodriguez, A.B.; Kirsch, P. Tryptophan-rich diet is negatively associated with depression and positively linked to social cognition. *Nutr. Res.* **2021**, *85*, 14–20. [CrossRef]
71. Franklin, M.; Bermudez, I.; Murck, H.; Singewald, N.; Gaburro, S. Sub-chronic dietary tryptophan depletion—An animal model of depression with improved face and good construct validity. *J. Psychiatr. Res.* **2012**, *46*, 239–247. [CrossRef]
72. Papakostas, G.I. Dopaminergic-based pharmacotherapies for depression. *Eur. Neuropsychopharmacol.* **2006**, *16*, 391–402. [CrossRef] [PubMed]
73. Vekovischeva, O.Y.; Peuhkuri, K.; Bäckström, P.; Sihvola, N.; Pilvi, T.; Korpela, R. The effects of native whey and α-lactalbumin on the social and individual behaviour of C57BL/6J mice. *Br. J. Nutr.* **2013**, *110*, 1336–1346. [CrossRef] [PubMed]
74. Takeuchi, T.; Matsunaga, K.; Sugiyama, A. Antidepressant-like effect of milk-derived lactoferrin in the repeated forced-swim stress mouse model. *J. Vet. Med. Sci.* **2017**, *79*, 1803–1806. [CrossRef] [PubMed]
75. Szewczyk, B.; Kubera, M.; Nowak, G. The role of zinc in neurodegenerative inflammatory pathways in depression. *Prog. Neuro-Psychopharmacol. Biol. Psychiatry* **2011**, *35*, 693–701. [CrossRef] [PubMed]
76. Li, Z.; Wang, W.; Xin, X.; Song, X.; Zhang, D. Association of total zinc, iron, copper and selenium intakes with depression in the US adults. *J. Affect. Disord.* **2018**, *228*, 68–74. [CrossRef]
77. Vashum, K.P.; McEvoy, M.; Milton, A.H.; McElduff, P.; Hure, A.; Byles, J.; Attia, J. Dietary zinc is associated with a lower incidence of depression: Findings from two Australian cohorts. *J. Affect. Disord.* **2014**, *166*, 249–257. [CrossRef]
78. Anbari-Nogyni, Z.; Bidaki, R.; Madadizadeh, F.; Sangsefidi, Z.S.; Fallahzadeh, H.; Karimi-Nazari, E.; Nadjarzadeh, A. Relationship of zinc status with depression and anxiety among elderly population. *Clin. Nutr. ESPEN* **2020**, *37*, 233–239. [CrossRef]
79. Nakamura, M.; Miura, A.; Nagahata, T.; Shibata, Y.; Okada, E.; Ojima, T. Low Zinc, Copper, and Manganese Intake is Associated with Depression and Anxiety Symptoms in the Japanese Working Population: Findings from the Eating Habit and Well-Being Study. *Nutrients* **2019**, *11*, 847. [CrossRef]
80. Miki, T.; Kochi, T.; Eguchi, M.; Kuwahara, K.; Tsuruoka, H.; Kurotani, K.; Ito, R.; Akter, S.; Kashino, I.; Pham, N.M.; et al. Dietary intake of minerals in relation to depressive symptoms in Japanese employees: The Furukawa Nutrition and Health Study. *Nutrition* **2015**, *31*, 686–690. [CrossRef]
81. Maserejian, N.N.; Hall, S.A.; McKinlay, J.B. Low dietary or supplemental zinc is associated with depression symptoms among women, but not men, in a population-based epidemiological survey. *J. Affect. Disord.* **2012**, *136*, 781–788. [CrossRef]
82. Thi Thu Nguyen, T.; Miyagi, S.; Tsujiguchi, H.; Kambayashi, Y.; Hara, A.; Nakamura, H.; Suzuki, K.; Yamada, Y.; Shimizu, Y.; Nakamura, H. Association between Lower Intake of Minerals and Depressive Symptoms among Elderly Japanese Women but Not Men: Findings from Shika Study. *Nutrients* **2019**, *11*, 389. [CrossRef] [PubMed]
83. Al-Fartusie, F.S.; Al-Bairmani, H.K.; Al-Garawi, Z.S.; Yousif, A.H. Evaluation of Some Trace Elements and Vitamins in Major Depressive Disorder Patients: A Case-Control Study. *Biol. Trace Elem. Res.* **2019**, *189*, 412–419. [CrossRef] [PubMed]

84. Islam, M.R.; Islam, M.R.; Shalahuddin Qusar, M.M.A.; Islam, M.S.; Kabir, M.H.; Mustafizur Rahman, G.K.M.; Islam, M.S.; Hasnat, A. Alterations of serum macro-minerals and trace elements are associated with major depressive disorder: A case-control study. *BMC Psychiatry* **2018**, *18*, 94. [CrossRef] [PubMed]
85. Whittle, N.; Lubec, G.; Singewald, N. Zinc deficiency induces enhanced depression-like behaviour and altered limbic activation reversed by antidepressant treatment in mice. *Amino Acids* **2009**, *36*, 147–158. [CrossRef]
86. Tassabehji, N.M.; Corniola, R.S.; Alshingiti, A.; Levenson, C.W. Zinc deficiency induces depression-like symptoms in adult rats. *Physiol. Behav.* **2008**, *95*, 365–369. [CrossRef]
87. Młyniec, K.; Nowak, G. Zinc deficiency induces behavioral alterations in the tail suspension test in mice. Effect of antidepressants. *Pharmacol. Rep. PR* **2012**, *64*, 249–255. [CrossRef]
88. Thingholm, T.E.; Rönnstrand, L.; Rosenberg, P.A. Why and how to investigate the role of protein phosphorylation in ZIP and ZnT zinc transporter activity and regulation. *Cell Mol. Life Sci.* **2020**, *77*, 3085–3102. [CrossRef]
89. Rafalo-Ulinska, A.; Piotrowska, J.; Kryczyk, A.; Opoka, W.; Sowa-Kucma, M.; Misztak, P.; Rajkowska, G.; Stockmeier, C.A.; Datka, W.; Nowak, G.; et al. Zinc transporters protein level in postmortem brain of depressed subjects and suicide victims. *J. Psychiatr. Res.* **2016**, *83*, 220–229. [CrossRef]
90. McAllister, B.B.; Dyck, R.H. Zinc transporter 3 (ZnT3) and vesicular zinc in central nervous system function. *Neurosci. Biobehav. Rev.* **2017**, *80*, 329–350. [CrossRef]
91. Dou, X.; Tian, X.; Zheng, Y.; Huang, J.; Shen, Z.; Li, H.; Wang, X.; Mo, F.; Wang, W.; Wang, S.; et al. Psychological stress induced hippocampus zinc dyshomeostasis and depression-like behavior in rats. *Behav. Brain Res.* **2014**, *273*, 133–138. [CrossRef]
92. Suh, S.W.; Won, S.J.; Hamby, A.M.; Yoo, B.H.; Fan, Y.; Sheline, C.T.; Tamano, H.; Takeda, A.; Liu, J. Decreased brain zinc availability reduces hippocampal neurogenesis in mice and rats. *J. Cereb. Blood Flow Metab.* **2009**, *29*, 1579–1588. [CrossRef]
93. Laitakari, A.; Liu, L.; Frimurer, T.M.; Holst, B. The Zinc-Sensing Receptor GPR39 in Physiology and as a Pharmacological Target. *Int. J. Mol. Sci.* **2021**, *22*, 3872. [CrossRef] [PubMed]
94. Siodłak, D.; Nowak, G.; Mlyniec, K. Interaction between zinc, the GPR39 zinc receptor and the serotonergic system in depression. *Brain Res. Bull.* **2021**, *170*, 146–154. [CrossRef]
95. Młyniec, K.; Gaweł, M.; Nowak, G. Study of antidepressant drugs in GPR39 (zinc receptor$^{-/-}$) knockout mice, showing no effect of conventional antidepressants, but effectiveness of NMDA antagonists. *Behav. Brain Res.* **2015**, *287*, 135–138. [CrossRef] [PubMed]
96. Młyniec, K.; Budziszewska, B.; Holst, B.; Ostachowicz, B.; Nowak, G. GPR39 (zinc receptor) knockout mice exhibit depression-like behavior and CREB/BDNF down-regulation in the hippocampus. *Int. J. Neuropsychopharmacol.* **2014**, *18*, pyu002. [CrossRef] [PubMed]
97. Mlyniec, K. Interaction between Zinc, GPR39, BDNF and Neuropeptides in Depression. *Curr. Neuropharmacol.* **2021**, *19*, 2012–2019. [CrossRef] [PubMed]
98. Doboszewska, U.; Szewczyk, B.; Sowa-Kućma, M.; Noworyta-Sokołowska, K.; Misztak, P.; Gołębiowska, J.; Młyniec, K.; Ostachowicz, B.; Krośniak, M.; Wojtanowska-Krośniak, A.; et al. Alterations of Bio-elements, Oxidative, and Inflammatory Status in the Zinc Deficiency Model in Rats. *Neurotox. Res.* **2016**, *29*, 143–154. [CrossRef] [PubMed]
99. Kirsten, T.B.; Cabral, D.; Galvão, M.C.; Monteiro, R.; Bondan, E.F.; Bernardi, M.M. Zinc, but not paracetamol, prevents depressive-like behavior and sickness behavior, and inhibits interferon-gamma and astrogliosis in rats. *Brain Behav. Immun.* **2020**, *87*, 489–497. [CrossRef]
100. Doboszewska, U.; Szewczyk, B.; Sowa-Kućma, M.; Młyniec, K.; Rafało, A.; Ostachowicz, B.; Lankosz, M.; Nowak, G. Antidepressant activity of fluoxetine in the zinc deficiency model in rats involves the NMDA receptor complex. *Behav. Brain Res.* **2015**, *287*, 323–330. [CrossRef]
101. Doboszewska, U.; Sowa-Kućma, M.; Młyniec, K.; Pochwat, B.; Hołuj, M.; Ostachowicz, B.; Pilc, A.; Nowak, G.; Szewczyk, B. Zinc deficiency in rats is associated with up-regulation of hippocampal NMDA receptor. *Prog. Neuro-Psychopharmacol. Biol. Psychiatry* **2015**, *56*, 254–263. [CrossRef]
102. Botturi, A.; Ciappolino, V.; Delvecchio, G.; Boscutti, A.; Viscardi, B.; Brambilla, P. The Role and the Effect of Magnesium in Mental Disorders: A Systematic Review. *Nutrients* **2020**, *12*, 1661. [CrossRef]
103. Tarleton, E.K.; Kennedy, A.G.; Rose, G.L.; Crocker, A.; Littenberg, B. The Association between Serum Magnesium Levels and Depression in an Adult Primary Care Population. *Nutrients* **2019**, *11*, 1475. [CrossRef] [PubMed]
104. Sun, C.; Wang, R.; Li, Z.; Zhang, D. Dietary magnesium intake and risk of depression. *J. Affect. Disord.* **2019**, *246*, 627–632. [CrossRef] [PubMed]
105. Li, B.; Lv, J.; Wang, W.; Zhang, D. Dietary magnesium and calcium intake and risk of depression in the general population: A meta-analysis. *Aust. N. Z. J. Psychiatry* **2017**, *51*, 219–229. [CrossRef] [PubMed]
106. Singewald, N.; Sinner, C.; Hetzenauer, A.; Sartori, S.B.; Murck, H. Magnesium-deficient diet alters depression- and anxiety-related behavior in mice—Influence of desipramine and Hypericum perforatum extract. *Neuropharmacology* **2004**, *47*, 1189–1197. [CrossRef]
107. Winther, G.; Pyndt Jørgensen, B.M.; Elfving, B.; Nielsen, D.S.; Kihl, P.; Lund, S.; Sørensen, D.B.; Wegener, G. Dietary magnesium deficiency alters gut microbiota and leads to depressive-like behaviour. *Acta Neuropsychiatr.* **2015**, *27*, 168–176. [CrossRef]

108. Del Chierico, F.; Trapani, V.; Petito, V.; Reddel, S.; Pietropaolo, G.; Graziani, C.; Masi, L.; Gasbarrini, A.; Putignani, L.; Scaldaferri, F.; et al. Dietary Magnesium Alleviates Experimental Murine Colitis through Modulation of Gut Microbiota. *Nutrients* **2021**, *13*, 4188. [CrossRef]
109. Ghafari, M.; Whittle, N.; Miklósi, A.G.; Kotlowski, C.; Kotlowsky, C.; Schmuckermair, C.; Berger, J.; Bennett, K.L.; Singewald, N.; Lubec, G. Dietary magnesium restriction reduces amygdala-hypothalamic GluN1 receptor complex levels in mice. *Brain Struct. Funct.* **2015**, *220*, 2209–2221. [CrossRef]
110. Whittle, N.; Li, L.; Chen, W.-Q.; Yang, J.-W.; Sartori, S.B.; Lubec, G.; Singewald, N. Changes in brain protein expression are linked to magnesium restriction-induced depression-like behavior. *Amino Acids* **2011**, *40*, 1231–1248. [CrossRef]
111. Opanković, A.; Milovanović, S.; Radosavljević, B.; Čavić, M.; Besu Žižak, I.; Bukumirić, Z.; Latas, M.; Medić, B.; Vučković, S.; Srebro, D.; et al. Correlation of Ionized Magnesium with the Parameters of Oxidative Stress as Potential Biomarkers in Patients with Anxiety and Depression: A Pilot Study. *Dose Response* **2022**, *20*, 15593258221116741. [CrossRef]
112. Scheiber, I.F.; Mercer, J.F.B.; Dringen, R. Metabolism and functions of copper in brain. *Prog. Neurobiol.* **2014**, *116*, 33–57. [CrossRef] [PubMed]
113. Ni, M.; You, Y.; Chen, J.; Zhang, L. Copper in depressive disorder: A systematic review and meta-analysis of observational studies. *Psychiatry Res.* **2018**, *267*, 506–515. [CrossRef] [PubMed]
114. Szkup, M.; Jurczak, A.; Brodowska, A.; Brodowska, A.; Noceń, I.; Chlubek, D.; Laszczyńska, M.; Karakiewicz, B.; Grochans, E. Analysis of Relations Between the Level of Mg, Zn, Ca, Cu, and Fe and Depressiveness in Postmenopausal Women. *Biol. Trace Elem. Res.* **2017**, *176*, 56–63. [CrossRef] [PubMed]
115. Styczeń, K.; Sowa-Kućma, M.; Siwek, M.; Dudek, D.; Reczyński, W.; Misztak, P.; Szewczyk, B.; Topór-Mądry, R.; Opoka, W.; Nowak, G. Study of the Serum Copper Levels in Patients with Major Depressive Disorder. *Biol. Trace Elem. Res.* **2016**, *174*, 287–293. [CrossRef]
116. Xu, J.; He, K.; Zhang, K.; Yang, C.; Nie, L.; Dan, D.; Liu, J.; Zhang, C.-E.; Yang, X. Low-Dose Copper Exposure Exacerbates Depression-Like Behavior in ApoE4 Transgenic Mice. *Oxidative Med. Cell. Longev.* **2021**, *2021*, 6634181. [CrossRef]
117. Lamtai, M.; Zghari, O.; Azirar, S.; Ouakki, S.; Mesfioui, A.; El Hessni, A.; Berkiks, I.; Marmouzi, I.; Ouichou, A. Melatonin modulates copper-induced anxiety-like, depression-like and memory impairments by acting on hippocampal oxidative stress in rat. *Drug Chem. Toxicol.* **2021**, *45*, 1707–1715. [CrossRef]
118. Liu, X.; Lin, C.; Wang, S.; Yu, X.; Jia, Y.; Chen, J. Effects of high levels of copper on the depression-related memory disorders. *J. Gerontol. A Biol. Sci. Med. Sci.* **2022**, *78*, 611–618. [CrossRef]
119. Barks, A.; Hall, A.M.; Tran, P.V.; Georgieff, M.K. Iron as a model nutrient for understanding the nutritional origins of neuropsychiatric disease. *Pediatr. Res.* **2019**, *85*, 176–182. [CrossRef]
120. Li, Z.; Li, B.; Song, X.; Zhang, D. Dietary zinc and iron intake and risk of depression: A meta-analysis. *Psychiatry Res.* **2017**, *251*, 41–47. [CrossRef]
121. Portugal-Nunes, C.; Castanho, T.C.; Amorim, L.; Moreira, P.S.; Mariz, J.; Marques, F.; Sousa, N.; Santos, N.C.; Palha, J.A. Iron Status is Associated with Mood, Cognition, and Functional Ability in Older Adults: A Cross-Sectional Study. *Nutrients* **2020**, *12*, 3594. [CrossRef]
122. Hameed, S.; Naser, I.A.; Al Ghussein, M.A.; Ellulu, M.S. Is iron deficiency a risk factor for postpartum depression? A case-control study in the Gaza Strip, Palestine. *Public Health Nutr.* **2021**, *25*, 1631–1638. [CrossRef] [PubMed]
123. Tian, Y.; Zheng, Z.; Ma, C. The effectiveness of iron supplementation for postpartum depression: A protocol for systematic review and meta-analysis. *Medicine* **2020**, *99*, e23603. [CrossRef] [PubMed]
124. Hidese, S.; Saito, K.; Asano, S.; Kunugi, H. Association between iron-deficiency anemia and depression: A web-based Japanese investigation. *Psychiatry Clin. Neurosci.* **2018**, *72*, 513–521. [CrossRef]
125. Bergis, D.; Tessmer, L.; Badenhoop, K. Iron deficiency in long standing type 1 diabetes mellitus and its association with depression and impaired quality of life. *Diabetes Res. Clin. Pract.* **2019**, *151*, 74–81. [CrossRef] [PubMed]
126. Zhang, W.; Zhou, Y.; Li, Q.; Xu, J.; Yan, S.; Cai, J.; Jiaerken, Y.; Lou, M. Brain Iron Deposits in Thalamus Is an Independent Factor for Depressive Symptoms Based on Quantitative Susceptibility Mapping in an Older Adults Community Population. *Front. Psychiatry* **2019**, *10*, 734. [CrossRef] [PubMed]
127. Autry, A.E.; Monteggia, L.M. Brain-derived neurotrophic factor and neuropsychiatric disorders. *Pharm. Rev.* **2012**, *64*, 238–258. [CrossRef]
128. Texel, S.J.; Camandola, S.; Ladenheim, B.; Rothman, S.M.; Mughal, M.R.; Unger, E.L.; Cadet, J.L.; Mattson, M.P. Ceruloplasmin deficiency results in an anxiety phenotype involving deficits in hippocampal iron, serotonin, and BDNF. *J. Neurochem.* **2012**, *120*, 125–134. [CrossRef]
129. Tran, P.V.; Carlson, E.S.; Fretham, S.J.B.; Georgieff, M.K. Early-life iron deficiency anemia alters neurotrophic factor expression and hippocampal neuron differentiation in male rats. *J. Nutr.* **2008**, *138*, 2495–2501. [CrossRef]
130. Tran, P.V.; Fretham, S.J.B.; Carlson, E.S.; Georgieff, M.K. Long-term reduction of hippocampal brain-derived neurotrophic factor activity after fetal-neonatal iron deficiency in adult rats. *Pediatr. Res.* **2009**, *65*, 493–498. [CrossRef]
131. Mehrpouya, S.; Nahavandi, A.; Khojasteh, F.; Soleimani, M.; Ahmadi, M.; Barati, M. Iron administration prevents BDNF decrease and depressive-like behavior following chronic stress. *Brain Res.* **2015**, *1596*, 79–87. [CrossRef]

132. Wang, F.; Zhang, M.; Li, Y.; Li, Y.; Gong, H.; Li, J.; Zhang, Y.; Zhang, C.; Yan, F.; Sun, B.; et al. Alterations in brain iron deposition with progression of late-life depression measured by magnetic resonance imaging (MRI)-based quantitative susceptibility mapping. *Quant. Imaging Med. Surg.* **2022**, *12*, 3873–3888. [CrossRef] [PubMed]
133. Youdim, M.B. H. Monoamine oxidase inhibitors, and iron chelators in depressive illness and neurodegenerative diseases. *J. Neural Transm.* **2018**, *125*, 1719–1733. [CrossRef]
134. Baldessarini, R.J.; Tondo, L.; Vázquez, G.H. Pharmacological treatment of adult bipolar disorder. *Mol. Psychiatry* **2019**, *24*, 198–217. [CrossRef] [PubMed]
135. Barroilhet, S.A.; Ghaemi, S.N. When and how to use lithium. *Acta Psychiatr. Scand.* **2020**, *142*, 161–172. [CrossRef]
136. Memon, A.; Rogers, I.; Fitzsimmons, S.M.D.D.; Carter, B.; Strawbridge, R.; Hidalgo-Mazzei, D.; Young, A.H. Association between naturally occurring lithium in drinking water and suicide rates: Systematic review and meta-analysis of ecological studies. *Br. J. Psychiatry J. Ment. Sci.* **2020**, *217*, 667–678. [CrossRef] [PubMed]
137. Birkenhäger, T.K.; van den Broek, W.W.; Mulder, P.G.; Bruijn, J.A.; Moleman, P. Comparison of two-phase treatment with imipramine or fluvoxamine, both followed by lithium addition, in inpatients with major depressive disorder. *Am. J. Psychiatry* **2004**, *161*, 2060–2065. [CrossRef]
138. Taylor, R.W.; Marwood, L.; Oprea, E.; DeAngel, V.; Mather, S.; Valentini, B.; Zahn, R.; Young, A.H.; Cleare, A.J. Pharmacological Augmentation in Unipolar Depression: A Guide to the Guidelines. *Int. J. Neuropsychopharmacol.* **2020**, *23*, 587–625. [CrossRef] [PubMed]
139. Undurraga, J.; Sim, K.; Tondo, L.; Gorodischer, A.; Azua, E.; Tay, K.H.; Tan, D.; Baldessarini, R.J. Lithium treatment for unipolar major depressive disorder: Systematic review. *J. Psychopharmacol.* **2019**, *33*, 167–176. [CrossRef]
140. Tiihonen, J.; Tanskanen, A.; Hoti, F.; Vattulainen, P.; Taipale, H.; Mehtälä, J.; Lähteenvuo, M. Pharmacological treatments and risk of readmission to hospital for unipolar depression in Finland: A nationwide cohort study. *Lancet Psychiatry* **2017**, *4*, 547–553. [CrossRef]
141. Maruki, T.; Utsumi, T.; Takeshima, M.; Fujiwara, Y.; Matsui, M.; Aoki, Y.; Toda, H.; Watanabe, N.; Watanabe, K.; Takaesu, Y. Efficacy and safety of adjunctive therapy to lamotrigine, lithium, or valproate monotherapy in bipolar depression: A systematic review and meta-analysis of randomized controlled trials. *Int. J. Bipolar Disord.* **2022**, *10*, 24. [CrossRef]
142. Rakofsky, J.J.; Lucido, M.J.; Dunlop, B.W. Lithium in the treatment of acute bipolar depression: A systematic review and meta-analysis. *J. Affect. Disord.* **2022**, *308*, 268–280. [CrossRef] [PubMed]
143. Vázquez, G.H.; Bahji, A.; Undurraga, J.; Tondo, L.; Baldessarini, R.J. Efficacy and Tolerability of Combination Treatments for Major Depression: Antidepressants plus Second-Generation Antipsychotics vs. Esketamine vs. Lithium. *J. Psychopharmacol.* **2021**, *35*, 890–900. [CrossRef] [PubMed]
144. Denoth-Lippuner, A.; Jessberger, S. Formation and integration of new neurons in the adult hippocampus. *Nat. Rev. Neurosci.* **2021**, *22*, 223–236. [CrossRef] [PubMed]
145. Frodl, T.; Jäger, M.; Smajstrlova, I.; Born, C.; Bottlender, R.; Palladino, T.; Reiser, M.; Möller, H.-J.; Meisenzahl, E.M. Effect of hippocampal and amygdala volumes on clinical outcomes in major depression: A 3-year prospective magnetic resonance imaging study. *J. Psychiatry Neurosci.* **2008**, *33*, 423–430. [PubMed]
146. Egeland, M.; Guinaudie, C.; Du Preez, A.; Musaelyan, K.; Zunszain, P.A.; Fernandes, C.; Pariante, C.M.; Thuret, S. Depletion of adult neurogenesis using the chemotherapy drug temozolomide in mice induces behavioural and biological changes relevant to depression. *Transl. Psychiatry* **2017**, *7*, e1101. [CrossRef]
147. Kin, K.; Yasuhara, T.; Kawauchi, S.; Kameda, M.; Hosomoto, K.; Tomita, Y.; Umakoshi, M.; Kuwahara, K.; Kin, I.; Kidani, N.; et al. Lithium counteracts depressive behavior and augments the treatment effect of selective serotonin reuptake inhibitor in treatment-resistant depressed rats. *Brain Res.* **2019**, *1717*, 52–59. [CrossRef]
148. Ricken, R.; Adli, M.; Lange, C.; Krusche, E.; Stamm, T.J.; Gaus, S.; Koehler, S.; Nase, S.; Bschor, T.; Richter, C.; et al. Brain-derived neurotrophic factor serum concentrations in acute depressive patients increase during lithium augmentation of antidepressants. *J. Clin. Psychopharmacol.* **2013**, *33*, 806–809. [CrossRef]
149. Liu, D.; Tang, Q.-Q.; Wang, D.; Song, S.-P.; Yang, X.-N.; Hu, S.-W.; Wang, Z.-Y.; Xu, Z.; Liu, H.; Yang, J.-X.; et al. Mesocortical BDNF signaling mediates antidepressive-like effects of lithium. *Neuropsychopharmacol. Off. Publ. Am. Coll. Neuropsychopharmacol.* **2020**, *45*, 1557–1566. [CrossRef]
150. Wu, S.; Yin, Y.; Du, L. Blood-Brain Barrier Dysfunction in the Pathogenesis of Major Depressive Disorder. *Cell. Mol. Neurobiol.* **2021**, *42*, 2571–2591. [CrossRef]
151. Taler, M.; Aronovich, R.; Henry Hornfeld, S.; Dar, S.; Sasson, E.; Weizman, A.; Hochman, E. Regulatory effect of lithium on hippocampal blood-brain barrier integrity in a rat model of depressive-like behavior. *Bipolar Disord.* **2021**, *23*, 55–65. [CrossRef]
152. Barchielli, G.; Capperucci, A.; Tanini, D. The Role of Selenium in Pathologies: An Updated Review. *Antioxidants* **2022**, *11*, 251. [CrossRef]
153. Ghimire, S.; Baral, B.K.; Feng, D.; Sy, F.S.; Rodriguez, R. Is selenium intake associated with the presence of depressive symptoms among US adults? Findings from National Health and Nutrition Examination Survey (NHANES) 2011–2014. *Nutrition* **2019**, *62*, 169–176. [CrossRef] [PubMed]
154. Gao, S.; Jin, Y.; Unverzagt, F.W.; Liang, C.; Hall, K.S.; Cao, J.; Ma, F.; Murrell, J.R.; Cheng, Y.; Li, P.; et al. Selenium level and depressive symptoms in a rural elderly Chinese cohort. *BMC Psychiatry* **2012**, *12*, 72. [CrossRef] [PubMed]

155. Ferreira de Almeida, T.L.; Petarli, G.B.; Cattafesta, M.; Zandonade, E.; Bezerra, O.M.d.P.A.; Tristão, K.G.; Salaroli, L.B. Association of Selenium Intake and Development of Depression in Brazilian Farmers. *Front. Nutr.* **2021**, *8*, 671377. [CrossRef]
156. Conner, T.S.; Richardson, A.C.; Miller, J.C. Optimal serum selenium concentrations are associated with lower depressive symptoms and negative mood among young adults. *J. Nutr.* **2015**, *145*, 59–65. [CrossRef]
157. Leung, B.M.Y.; Kaplan, B.J.; Field, C.J.; Tough, S.; Eliasziw, M.; Gomez, M.F.; McCargar, L.J.; Gagnon, L. Prenatal micronutrient supplementation and postpartum depressive symptoms in a pregnancy cohort. *BMC Pregnancy Childbirth* **2013**, *13*, 2. [CrossRef]
158. Mokhber, N.; Namjoo, M.; Tara, F.; Boskabadi, H.; Rayman, M.P.; Ghayour-Mobarhan, M.; Sahebkar, A.; Majdi, M.R.; Tavallaie, S.; Azimi-Nezhad, M.; et al. Effect of supplementation with selenium on postpartum depression: A randomized double-blind placebo-controlled trial. *J. Matern. Fetal Neonatal Med. Off. J. Eur. Assoc. Perinat. Med. Fed. Asia Ocean. Perinat. Soc. Int. Soc. Perinat. Obstet.* **2011**, *24*, 104–108. [CrossRef]
159. Colangelo, L.A.; He, K.; Whooley, M.A.; Daviglus, M.L.; Morris, S.; Liu, K. Selenium exposure and depressive symptoms: The Coronary Artery Risk Development in Young Adults Trace Element Study. *Neurotoxicology* **2014**, *41*, 167–174. [CrossRef]
160. Kędzierska, E.; Dudka, J.; Poleszak, E.; Kotlińska, J.H. Antidepressant and anxiolytic-like activity of sodium selenite after acute treatment in mice. *Pharmacol. Rep. PR* **2017**, *69*, 276–280. [CrossRef] [PubMed]
161. Kędzierska, E.; Dąbkowska, L.; Obierzyński, P.; Polakowska, M.; Poleszak, E.; Wlaź, P.; Szewczyk, K.; Kotlińska, J. Synergistic Action of Sodium Selenite with some Antidepressants and Diazepam in Mice. *Pharmaceutics* **2018**, *10*, 270. [CrossRef]
162. Samad, N.; Rao, T.; Rehman, M.H.U.; Bhatti, S.A.; Imran, I. Inhibitory Effects of Selenium on Arsenic-Induced Anxiety-/Depression-Like Behavior and Memory Impairment. *Biol. Trace Elem. Res.* **2022**, *200*, 689–698. [CrossRef] [PubMed]
163. Zhang, B.; Guo, Y.; Yan, S.; Guo, X.; Zhao, Y.; Shi, B. The protective effect of selenium on the lipopolysaccharide-induced oxidative stress and depressed gene expression related to milk protein synthesis in bovine mammary epithelial cells. *Biol. Trace Elem. Res.* **2020**, *197*, 141–148. [CrossRef]
164. Yang, J.; Li, H.; Hao, Z.; Jing, X.; Zhao, Y.; Cheng, X.; Ma, H.; Wang, J.; Wang, J. Mitigation Effects of Selenium Nanoparticles on Depression-Like Behavior Induced by Fluoride in Mice via the JAK2-STAT3 Pathway. *ACS Appl. Mater. Interfaces* **2022**, *14*, 3685–3700. [CrossRef]
165. Yosaee, S.; Clark, C.C.T.; Keshtkaran, Z.; Ashourpour, M.; Keshani, P.; Soltani, S. Zinc in depression: From development to treatment: A comparative/dose response meta-analysis of observational studies and randomized controlled trials. *Gen. Hosp. Psychiatry* **2022**, *74*, 110–117. [CrossRef] [PubMed]
166. Ranjbar, E.; Shams, J.; Sabetkasaei, M.; M-Shirazi, M.; Rashidkhani, B.; Mostafavi, A.; Bornak, E.; Nasrollahzadeh, J. Effects of zinc supplementation on efficacy of antidepressant therapy, inflammatory cytokines, and brain-derived neurotrophic factor in patients with major depression. *Nutr. Neurosci.* **2014**, *17*, 65–71. [CrossRef]
167. Donig, A.; Hautzinger, M. Zinc as an adjunct to antidepressant medication: A meta-analysis with subgroup analysis for different levels of treatment response to antidepressants. *Nutr. Neurosci.* **2022**, *25*, 1785–1795. [CrossRef]
168. Misztak, P.; Sowa-Kućma, M.; Pańczyszyn-Trzewik, P.; Szewczyk, B.; Nowak, G. Antidepressant-like Effects of Combined Fluoxetine and Zinc Treatment in Mice Exposed to Chronic Restraint Stress Are Related to Modulation of Histone Deacetylase. *Molecules* **2021**, *27*, 22. [CrossRef]
169. Rafało-Ulińska, A.; Poleszak, E.; Szopa, A.; Serefko, A.; Rogowska, M.; Sowa, I.; Wójciak, M.; Muszyńska, B.; Krakowska, A.; Gdula-Argasińska, J.; et al. Imipramine Influences Body Distribution of Supplemental Zinc Which May Enhance Antidepressant Action. *Nutrients* **2020**, *12*, 2529. [CrossRef] [PubMed]
170. Rajizadeh, A.; Mozaffari-Khosravi, H.; Yassini-Ardakani, M.; Dehghani, A. Effect of magnesium supplementation on depression status in depressed patients with magnesium deficiency: A randomized, double-blind, placebo-controlled trial. *Nutrition* **2017**, *35*, 56–60. [CrossRef]
171. Tarleton, E.K.; Littenberg, B.; MacLean, C.D.; Kennedy, A.G.; Daley, C. Role of magnesium supplementation in the treatment of depression: A randomized clinical trial. *PLoS ONE* **2017**, *12*, e0180067. [CrossRef]
172. Skalski, M.; Mach, A.; Januszko, P.; Ryszewska-Pokraśniewicz, B.; Biernacka, A.; Nowak, G.; Pilc, A.; Poleszak, E.; Radziwoń-Zaleska, M. Pharmaco-Electroencephalography-Based Assessment of Antidepressant Drug Efficacy-The Use of Magnesium Ions in the Treatment of Depression. *J. Clin. Med.* **2021**, *10*, 3135. [CrossRef]
173. Poleszak, E. Modulation of antidepressant-like activity of magnesium by serotonergic system. *J. Neural Transm.* **2007**, *114*, 1129–1134. [CrossRef]
174. Chen, J.-L.; Zhou, X.; Liu, B.-L.; Wei, X.-H.; Ding, H.-L.; Lin, Z.-J.; Zhan, H.-L.; Yang, F.; Li, W.-B.; Xie, J.-C.; et al. Normalization of magnesium deficiency attenuated mechanical allodynia, depressive-like behaviors, and memory deficits associated with cyclophosphamide-induced cystitis by inhibiting TNF-α/NF-κB signaling in female rats. *J. Neuroinflamm.* **2020**, *17*, 99. [CrossRef]
175. Pochwat, B.; Szewczyk, B.; Sowa-Kucma, M.; Siwek, A.; Doboszewska, U.; Piekoszewski, W.; Gruca, P.; Papp, M.; Nowak, G. Antidepressant-like activity of magnesium in the chronic mild stress model in rats: Alterations in the NMDA receptor subunits. *Int. J. Neuropsychopharmacol.* **2014**, *17*, 393–405. [CrossRef]
176. Ronaldson, A.; Arias de la Torre, J.; Gaughran, F.; Bakolis, I.; Hatch, S.L.; Hotopf, M.; Dregan, A. Prospective associations between vitamin D and depression in middle-aged adults: Findings from the UK Biobank cohort. *Psychol. Med.* **2022**, *52*, 1866–1874. [CrossRef] [PubMed]
177. Ding, J.; Zhang, Y. Associations of Dietary Vitamin C and E Intake With Depression. A Meta-Analysis of Observational Studies. *Front. Nutr.* **2022**, *9*, 857823. [CrossRef]

178. Wu, Y.; Zhang, L.; Li, S.; Zhang, D. Associations of dietary vitamin B1, vitamin B2, vitamin B6, and vitamin B12 with the risk of depression: A systematic review and meta-analysis. *Nutr. Rev.* **2022**, *80*, 351–366. [CrossRef] [PubMed]
179. Lam, N.S.K.; Long, X.X.; Li, X.; Saad, M.; Lim, F.; Doery, J.C.; Griffin, R.C.; Galletly, C. The potential use of folate and its derivatives in treating psychiatric disorders: A systematic review. *Biomed. Pharmacother.* **2022**, *146*, 112541. [CrossRef]
180. Smaga, I.; Frankowska, M.; Filip, M. N-acetylcysteine as a new prominent approach for treating psychiatric disorders. *Br. J. Pharmacol.* **2021**, *178*, 2569–2594. [CrossRef]
181. Ullah, H.; Di Minno, A.; Esposito, C.; El-Seedi, H.R.; Khalifa, S.A.M.; Baldi, A.; Greco, A.; Santonastaso, S.; Cioffi, V.; Sperandeo, R.; et al. Efficacy of a food supplement based on S-adenosyl methionine and probiotic strains in subjects with subthreshold depression and mild-to-moderate depression: A monocentric, randomized, cross-over, double-blind, placebo-controlled clinical trial. *Biomed. Pharmacother.* **2022**, *156*, 113930. [CrossRef] [PubMed]
182. Xia, Y.; Liu, Y.; Zhang, S.; Zhang, Q.; Liu, L.; Meng, G.; Wu, H.; Sun, S.; Wang, X.; Zhou, M.; et al. Associations between different types and sources of dietary fibre intake and depressive symptoms in a general population of adults: A cross-sectional study. *Br. J. Nutr.* **2021**, *125*, 1281–1290. [CrossRef] [PubMed]

International Journal of
Molecular Sciences

MDPI

Concept Paper

Obstetric Neuropathy in Diabetic Patients: The "Double Hit Hypothesis"

Dieu Thao Nguyen, Mohammad Hooshmand Zaferanieh, Asa C. Black, Jr., Kamron Reza Hamedi, Richard L. Goodwin and Thomas I. Nathaniel *

Greenville School of Medicine, University of South Carolina, 607 Grove Road, Greenville, SC 29605, USA
* Correspondence: nathanit@greenvillemed.sc.edu; Tel.: +1-8644559846; Fax: +1-8644558404

Abstract: The two-hit model has been proposed to explain the effects of diabetes on mothers who are already in a putative subclinical damaged state and then undergo neuronal damage during the delivery process. However, the anatomical and pathophysiological mechanisms are not well understood. Our overarching hypothesis in this review paper is that pregnant women who are diabetic have a damaged peripheral nervous system, constituting the "first hit" hypothesis. The delivery process itself—the "second hit"—can produce neurological damage to the mother. Women with diabetes mellitus (DM) are at risk for neurological damage during both hits, but the cumulative effects of both "hits" pose a greater risk of neurological damage and pathophysiological changes during delivery. In our analysis, we introduce the different steps of our concept paper. Subsequently, we describe each of the topics. First, we outline the mechanisms by which diabetes acts as a detrimental variable in neuropathy by focusing on the most common form of diabetic neuropathy, diabetic distal symmetrical polyneuropathy, also known as distal sensorimotor neuropathy. The possible role of macrosomia in causing diabetic neuropathy and obstetric neurological injury is discussed. Second, we describe how vaginal delivery can cause various obstetrical neurological syndromes and pathophysiological changes. Third, we highlight the risk of obstetric neuropathy and discuss anatomical sites at which lesions may occur, including lesions during delivery. Fourth, we characterize the pathophysiological pathways involved in the causation of diabetic neuropathy. Finally, we highlight diabetic damage to sensory vs. motor nerves, including how hyperglycemia causes different types of damage depending on the location of nerve cell bodies.

Keywords: diabetic neuropathy; neurological damage during delivery

Citation: Nguyen, D.T.; Zaferanieh, M.H.; Black, A.C., Jr.; Hamedi, K.R.; Goodwin, R.L.; Nathaniel, T.I. Obstetric Neuropathy in Diabetic Patients: The "Double Hit Hypothesis". *Int. J. Mol. Sci.* **2023**, *24*, 6812. https://doi.org/10.3390/ijms24076812

Academic Editors: Claudia Ricci and Luisa Agnello

Received: 1 February 2023
Revised: 27 March 2023
Accepted: 30 March 2023
Published: 6 April 2023

1. Introduction

Diabetes mellitus (DM) describes a state of chronic hyperglycemia that affects more than 460 million individuals worldwide [1]. The number of patients with DM has been projected to rise to 700 million worldwide by 2045 [2]. Two types of diabetes mellitus are currently recognized based on their etiologies: Type 1 and Type 2. Type 1 DM describes an autoimmune disease process in which pancreatic beta cells have been targeted for destruction; therefore, there is insufficient insulin production, leading to hyperglycemia. Type 2 DM has been characterized as hyperglycemia due to insulin resistance. Patients with Type 2 DM produce insulin; however, the body does not respond appropriately [1].

Diabetic distal symmetrical polyneuropathy, or distal symmetrical sensorimotor neuropathy (DSSPN), is the most common form of diabetic neuropathy [3,4]. It is responsible for foot lesions, including ulcers and amputations [5]. The lesions manifest in a "stocking and glove" pattern. This form of diabetic neuropathy begins by damaging the sensory axons of the feet first and then the hands. Thus, the symptoms are correlated with the length of the axon. This form disturbs sensory function first and then damages the autonomic nervous system and somatic motor function. Pre-diabetic conditions exhibit a similar pattern [6]. Chronic hyperglycemia damages Schwann cells, which are responsible

for the myelination of axons in the peripheral nervous system. It has been noted that there are features of demyelination in patients with severe cases of hyperglycemia. The current literature has only determined that Wallerian degeneration is involved in signaling pathways that induce axonal degeneration [4].

2. The Mechanisms of Diabetic Neuropathies Are Complex

The pathogenesis of diabetic neuropathy is complex [7]. Diabetic distal symmetrical polyneuropathy (DSP) is a length-dependent polyneuropathy. It is generally considered to be multi-factorial. DSP is considered to involve interactions between glycemic control, the duration of diabetes, and neuronal attrition related to age, hypertension, and body weight. Alterations seen in DSP include segmental demyelination, microangiopathy, and Wallerian degeneration. Apoptosis of dorsal root ganglia is an important mechanistic consideration that causes the loss of unmyelinated and myelinated fibers. Entrapment neuropathies are also common in the diabetic population, affecting one in every three patients [8,9]. Dellon [10] suggested three mechanisms that cause diabetic patients to be more susceptible to peripheral neuropathy. The osmotic hypothesis [11] postulates that there is an increase in the conversion of glucose to sorbitol in the diabetic population. Sorbitol has hydrophilic characteristics, which increase water concentration in the nerves, causing osmotic swelling. It has been shown that the median and tibial nerves in patients with diabetes have significantly larger cross-sectional areas than in a healthy, non-diabetic control group [12]. The swelling in a defined area, such as the carpal or tarsal tunnel, can lead to compressive neuropathy (Figure 1). Second, an abnormal metabolic state and high sorbitol concentration in diabetic patients can impair the nerve regeneration pathway [13] (Figure 1). Lastly, hyperglycemia can produce high amounts of advanced glycation end products (AGE) that can bind to collagen in the peripheral nerve and nearby ligaments, altering the biomechanical AGE properties of both the nerve and ligament. The hyperglycemic state is an additional mechanism that can cause compressive neuropathy when swelling occurs in a restricted space [9,13]. A different concept involves the role of inflammation and vascular complications, especially concerning pain [14]. Vascular injury in diabetes is often mediated by the development of atherosclerosis (Figure 1). Hyperglycemia leads to dyslipidemias, encouraging the formation of foam cells. These cells contribute to the buildup of plaques in the blood vessels. These foam cells also release cytokines that stimulate endothelial cells to produce reactive oxygen species (ROS). ROS use the NF-κB pathways to cause leukocyte recruitment and apoptosis, leading to inflammation, ischemia, and cellular nerve damage [15].

Diabetes mellitus targets the axons of sensory neurons, autonomic nervous system neurons, and motor neurons [4]. Schwann cells are damaged in hyperglycemia, and in more severe cases, demyelination of the axons occurs, which is reflected in the stocking-glove pattern of damage (Figure 1). The axons of the neurons supplying the feet are longer than those supplying the hand, so the most significant damage appears first in the feet (length-dependent demyelination) [4]. Considering the role of Schwann cells in the maintenance and repair of axons, damage to Schwann cells may play a key role in the failure of axons to be maintained or repaired.

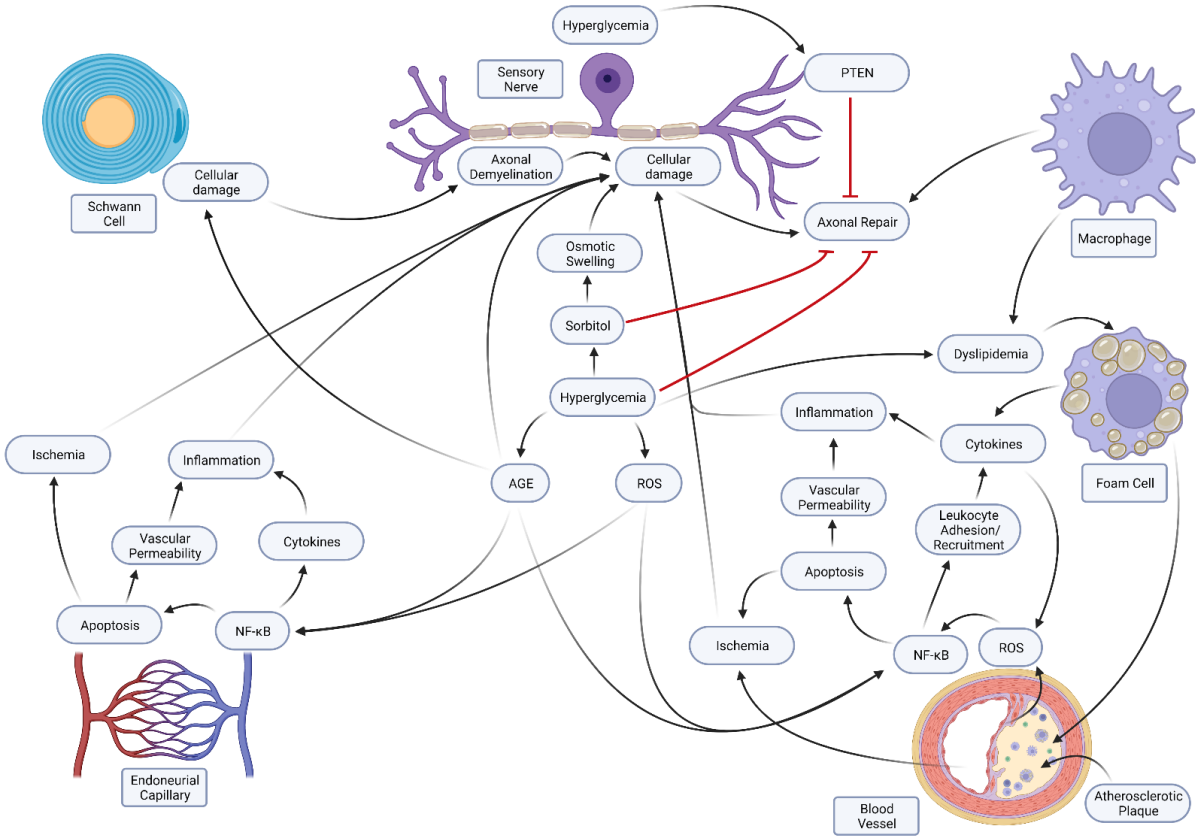

Figure 1. Pathways Involved in diabetic neuropathy: hyperglycemia causes diabetic neuropathy through several pathways. Elevated blood glucose leads to an increased conversion of glucose to sorbitol. Sorbitol can cause osmotic swelling, causing compression neuropathy, and can inhibit axonal repair mechanisms. Hyperglycemia can also cause direct damage to nerve cells through the stimulation of the PTEN (phosphatase and tensin homolog) pathway. Hyperglycemia causes Schwann cell toxicity, thereby producing advanced glycation end products (AGEs) and leading to axonal demyelination. Macrophages are important for nerve repair and regeneration, but can be inhibited by hyperglycemia. Hyperglycemia also leads to dyslipidemia and the formation of foam cells from macrophages. These foam cells contribute to the formation of atherosclerotic plaques, leading to vascular and endoneurial microvascular damage to produce reactive oxygen species (ROS). ROS use the NF-κB pathways to cause leukocyte recruitment and apoptosis, leading to inflammation, ischemia, and cellular nerve damage [16].

Diabetic neurons have an elevated expression of PTEN [17]. PTEN expression inhibits the transduction pathways that are activated by growth factors and required for neuronal regeneration [17,18]. PTEN gene expression persists after injury, thereby interfering with neuronal regeneration. Inhibiting PTEN removes the roadblock to regeneration [18]. The effects on sensory and motor neurons differ somewhat, modeling how general diabetic neuropathy usually affects the functions of sensory neurons. Sensory neuron losses occur first in diabetic mice [19], whose dorsal root ganglia exhibit an increased expression of PTEN compared to littermate controls. This causes neuronal cell death in sensory neurons by disrupting their repair processes. Motor neurons exhibit a distal loss of axon terminals but no perikaryal dropouts (Figure 2). In diabetic mice, the result is the survival of motor neurons but the loss of motor units and neuromuscular junctions, producing a loss of motor function. It has been postulated that the differences between the sensory and motor neurons in terms of the blood–brain barrier can explain the relative vulnerability of sensory neurons compared to motor neurons (Figure 2). The cell bodies of sensory neurons are located in the dorsal root ganglia. In contrast, the cell bodies of motor neurons are located in the anterior horn of the spinal cord. The blood–neuron interface is less well-protected in

the dorsal root ganglion than in the spinal cord [20–22]. It is noteworthy to point out that surgical decompression can be an effective treatment for diabetic neuropathy [23].

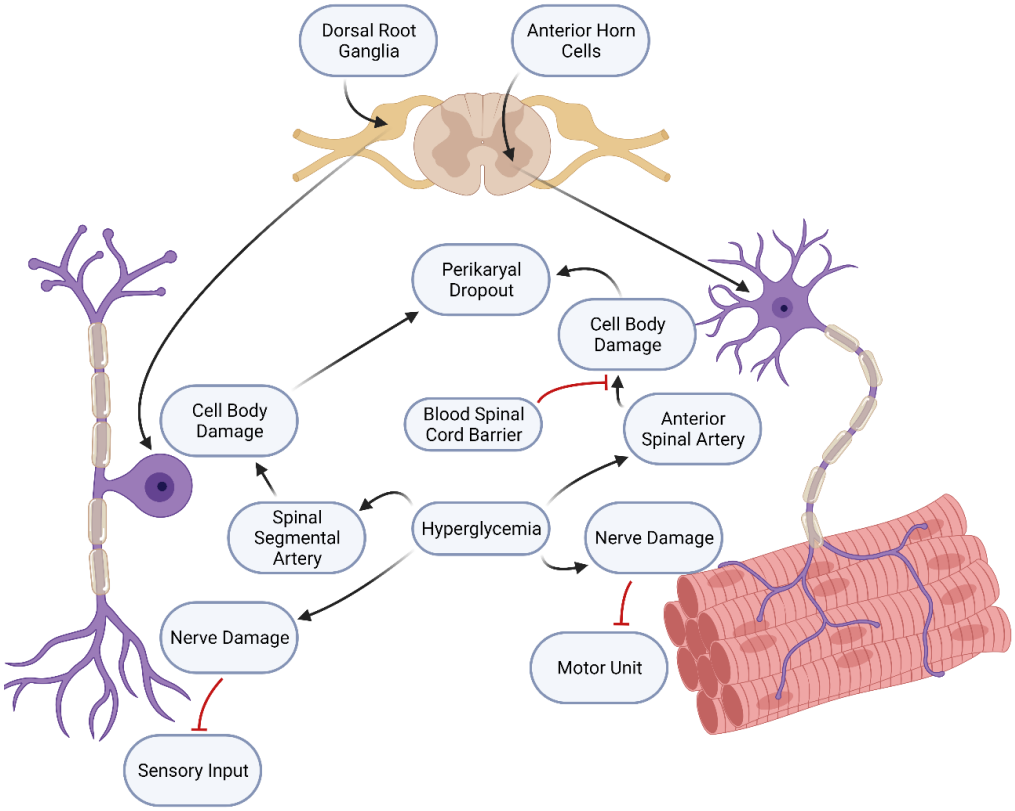

Figure 2. Diabetic damage to sensory vs. motor nerves: hyperglycemia causes different types of damage, depending on the location of nerve cell bodies. Sensory nerve cell bodies are located in the dorsal root ganglia, which are supplied by spinal segmental arteries. Hyperglycemia in this blood supply causes axonal damage and cell body damage, leading to a loss of sensory input and perikaryal dropout. Motor nerve cell bodies are located in the anterior horns of the spinal cord. The blood–spinal cord barrier, similar to the blood–brain barrier, protects these cell bodies from the damaging effects of hyperglycemia. However, the axons of motor nerves and their motor units can still be damaged, leading to the loss of motor function.

Macrophages may play a role in the axonal damage associated with diabetes mellitus. Associated delays in macrophage invasion and the removal of macrophages have been noted in diabetic mice (Figure 1). This raises the possibility that abnormalities in macrophage participation in axonal regeneration following injury may be deficient or defective since macrophage invasion and removal are different in diabetic mice compared to littermate controls [24]. Alterations in energy metabolism caused by diabetes mellitus may play a role in diabetic neuropathy. The substrate overload in diabetes mellitus leads to the formation of acylcarnitines, which are toxic to Schwann cells and dorsal root ganglion cells [5]. Microcirculatory changes may also damage neurons since the dysfunction of the microcirculatory system is strongly associated with diabetic neuropathy [25]. In this concept, damage to the microcirculation leads to neuronal damage. The pathways that damage this microcirculation are similar to those in other diabetes-associated vasculitides [26]. Endoneurial capillary density is increased in diabetic patients, and findings in rats support this concept [4]. Central nervous system (CNS) changes may also occur, increasing sensitivity to pain [27].

2.1. Macrosomic Babies Play a Role in Causing Diabetic Neuropathy and Obstetric Neurological Injury

Gestational diabetes mellitus (GDM) occurs when a previously non-diabetic woman becomes pregnant and develops diabetes mellitus during her pregnancy. Pregnancy places metabolic stress on the mother and can contribute to a state of insulin resistance. As a result, the pancreas will have to produce more insulin to compensate for the resistance of cells to bring in glucose. When the pancreas cannot produce enough insulin, the mother will be hyperglycemic, resembling Type 2 DM [1]. It is noted that approximately 4–14% of pregnancies have complications related to GDM [27].

Diabetes mellitus, coupled with the delivery of a macrosomic baby (>4000 gm) in a short (five feet or less in height) mother, increases the risk of postpartum femoral neuropathy [28]. Diabetes during the gestational period is a known risk factor for causing the development of macrosomic babies, which are risk factors for obstetric radiculopathy, plexopathy, or neuropathy due to cephalopelvic disproportion [29] (Figure 3). The mechanisms that precede fetal macrosomia have been shown to originate from maternal glycemic impairment. High blood glucose levels can travel from the mother's placenta into fetal circulation. Thus, by the second trimester, the fetal pancreas can respond by releasing insulin to combat the hyperglycemic state, leading to hyperinsulinemia in the fetus. The coupling of the effects of hyperinsulinemia and hyperglycemia can lead to increased fat and protein storage in the fetus and ultimately produce a macrosomic fetus [30].

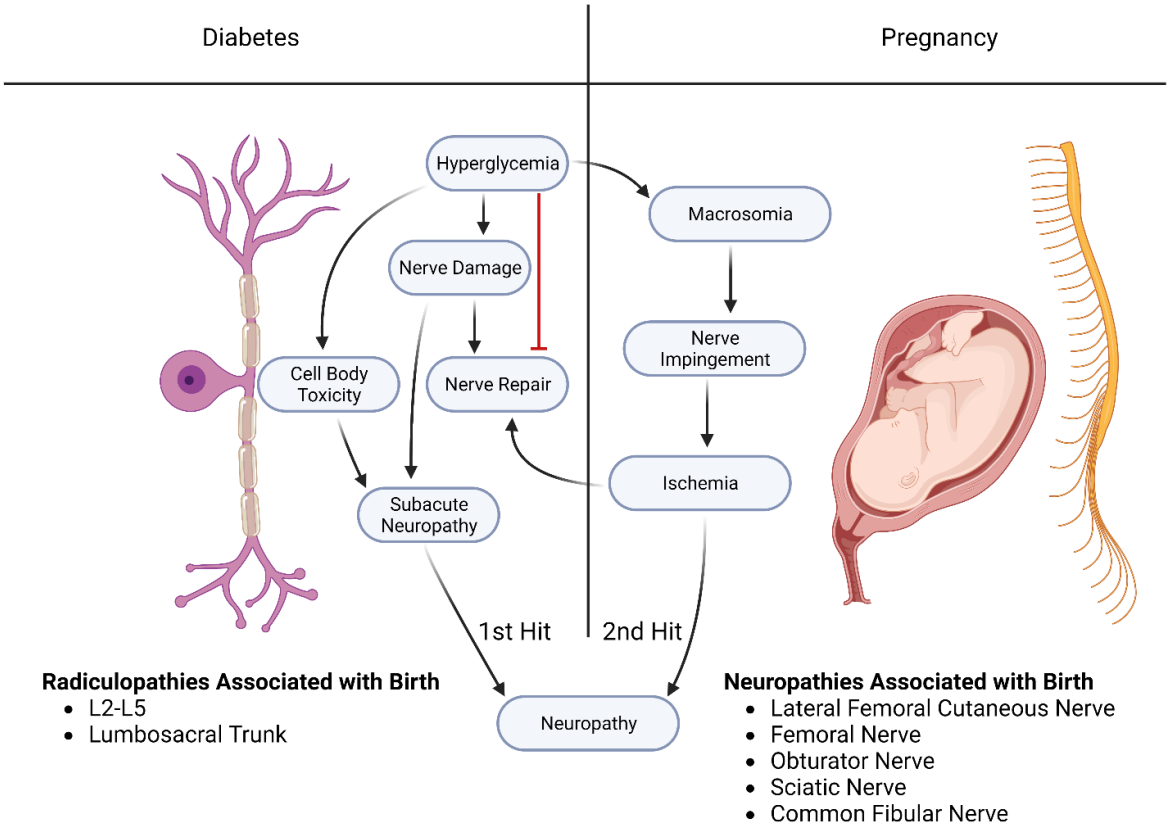

Figure 3. Two-hit hypothesis of diabetic neuropathy in pregnancy: The first hit is believed to be caused by the pathways previously discussed, leading to cell body toxicity and nerve damage. This damage may lead to subacute neuropathy with few symptoms. Diabetes is a common cause of macrosomia, which increases the risk of compression neuropathies during vaginal birth. This compression damage, combined with impaired nerve repair pathways, leads to the second hit, causing the more frequent or severe radiculopathies and neuropathies seen in vaginal births with diabetic mothers.

2.2. Mechanism of Injury for Obstetric Lower Extremity Neuropathies

2.2.1. Vaginal Delivery can Cause Various obstetrical Neurological Syndromes

Several clinical neurological conditions are observed during the delivery process and puerperium. These conditions are sometimes referred to as postpartum or intrapartum obstetric neuropathies (sometimes plexopathies) and involve the pelvis and lower limb of the patient. It is estimated that the incidence of such conditions is around 1% of all births [31–33]. Specific types include femoral neuropathy, lumbosacral plexopathy, lateral femoral cutaneous neuropathy, common fibular neuropathy, deep fibular neuropathy, and radiculopathy. In addition, pregnancy can exacerbate the development of neuropathies in women with insulin-dependent diabetes mellitus [33].

2.2.2. Obstetric Lesions of Direct Branches of the Lumbosacral Plexus

A lesion of the lateral femoral cutaneous nerve beneath the inguinal ligament is integral to obstetric neuropathy at parturition [34]. Furthermore, this is one of the most common lesions in the delivery process (38% of obstetric lesions [32,33]).

The femoral nerve is a major motor and sensory nerve that also passes beneath the inguinal ligament. When the patient is in the dorsal lithotomy position for hours, excessively abducting and flexing the hips, the inguinal ligament compresses the nerve as it does the lateral femoral cutaneous nerve [35]. An obstetric femoral neuropathy causes significant difficulty in trying to walk. Obstetric femoral neuropathy accounts for 35% of obstetric lesions [33,35].

Two other neuropathies may arise, including (1) obturator nerve neuropathy and (2) sciatic nerve neuropathy. A lesion of the obturator nerve in the delivery process accounts for 5% of cases [32,33]. The sciatic nerve is a major posterior nerve of the lumbosacral plexus. It passes out of the pelvis and divides into the common fibular and tibial divisions. These then pass into the popliteal fossa to form the common fibular and tibial nerves. The mechanism of injury of the sciatic nerve in delivery is uncertain. A lesion of the sciatic nerve properly accounts for 3% of obstetric lesions [32,33]. One proposed mechanism leading to the irritation of this nerve may be the prolonged spasming of adjacent musculatures, such as the piriformis muscle [36,37]. Sometimes the common fibular division of the sciatic nerve passes through the piriformis muscle. When the muscle becomes spastic, pain may be felt along the distribution of the common fibular nerve [38].

2.2.3. Obstetric Lesions of Nerves That Supply the Leg and Foot

The sciatic nerve forms the common fibular nerve and the tibial nerve. The common fibular nerve passes around the neck of the fibula, where it is subject to injury compression. The common fibular nerve is at risk in obstetrical deliveries. When a woman lies in the dorsal lithotomy position, she has the thigh bent (flexed) at the hip and the legs bent (flexed) at the knee. This position puts pressure on the common fibular nerve. Sometimes the patient or an attendant tries to hold the lower limbs in this position for hours during delivery. These actions can cause compression of the common fibular nerve and the obstruction of its blood supply [39,40]. Damage to the nerve can cause pain and numbness due to hyperactivity of the small-diameter pain fibers and hypoactivity of the sensory fibers that supply fine touch to the distribution area. The destruction of the large-diameter motor fibers causes a loss of blood supply and death to the axon at the point of compression. The most significant result is the presence of a foot drop. Common fibular nerve lesions account for 5% of obstetric lesions [32,33].

3. Obstetrical Neuropathies

3.1. Compressive Neuropathies

In compression neuropathy, a structure such as the patient's hand or the baby's head compresses the nerve, obstructing its blood supply. The resulting anoxia damages the axons of the nerve. The larger fibers have a higher oxygen demand and die first. These fibers mediate delicate touch. The smaller fibers mediate pain and temperature sensation.

They take longer to die. The pain fibers may become hyperactive and cause pain [41]. The axons die at the point of injury, continuing down the segments distal to the lesion. This is termed Wallerian degeneration [42]. These changes have been studied using magnetic resonance neurography [43]. Because the cell body in the dorsal root ganglion is still viable, the axons will regenerate at a rate of 1–2 mm/day. The peripheral nervous system is noted for its ability to undergo repair. The critical role of Schwann cells in repairing injured axons makes them a prerequisite for nerve repair [19,44,45]. Injury causes Schwann cells to de-differentiate, allowing them to initiate the activity of genes that underlie the repair process. Unfortunately, aging and prolonged injury can limit the ability of Schwann cells to initiate repair [46].

3.2. Diabetes-Potentiated Compression Injuries

The specific mechanism involved in the role of diabetes in postpartum neuropathy is not well understood. Compared to matched controls (4.8%), pregnancies among patients with Type 1 diabetes exhibit a 10-fold increase in the prevalence of postpartum neuropathy [31]. These diabetic individuals may have pre-existing (subacute) nerve damage. The subacute injury has yet to manifest clinically; however, further insult can lead to the overt manifestation of symptoms. This could represent anatomical sites already at high risk of either nerve compression or nerve entrapment [32]. Additionally, diabetes-potentiated compression injuries have previously been documented to occur with an increased incidence involving the lateral femoral cutaneous, peroneal (fibular) nerves, ulnar nerve, and median nerve [10]. It has also been suggested that diabetes may increase the risk of femoral nerve compression [33]. Given this predisposition, the pre-existing damage may become more severe when obstetric nerve damage occurs following the delivery process. Such occurrences highlight the importance of further inquiry into the involvement of diabetes in postpartum neuropathy.

4. How Diabetes Mellitus Produces Nerve Damage That can Be Potentiated by Any Injury Occurring during Delivery

4.1. Hypothesis: Diabetes Mellitus Produces Nerve Damage That can Be Potentiated by Any Injury Occurring during Delivery

One possibility is that parturition can potentiate nerve damage acquired from the diabetic disease process through a double-hit model. The double-hit syndrome can be observed with the first insult coming from the effects of diabetes [10], the mechanisms of which have been outlined above. Subsequently, a second compressive insult may take place as a result of a variety of factors. This could range from the prolonged placement of the patient's legs in the lithotomy position to the positioning of the fetal head and cephalopelvic disproportion [30], as stated above. The additive consequences of the delivery process can further potentiate damage to a nerve that is already impaired by diabetes. This theory can be limiting as it implies compression is the only cause of nerve neuropathy. However, aside from compression alone, different, multifaceted disease processes contribute to a nerve's susceptibility to damage.

4.1.1. Diabetes Mellitus Produces a More Severe Neuropathy through a Two-Fold Pathological Process

First, the neurons of diabetics are injured directly by the disease process. The second hit occurs during the attempt to repair the injured neurons, when the regeneration process is subject to molecular blockade [17]. This process involves the PTEN (phosphatase and tensin homolog) gene. PTEN regulates axonal growth by inhibiting the transduction pathway through the P13K pathway, preventing neuronal regeneration. Following an axonal injury, as in diabetes, PTEN expression continues, causing an ongoing regenerative block (second hit) [17]. The regeneration of peripheral nerves is impaired in diabetic mice in which diabetes was induced by treatment with streptozotocin [47]. Considerable delays of up to 8–10 weeks were observed in the regrowth of myelinated axons in diabetic mice [46,47].

4.1.2. Support for the Two-Hit Hypothesis

The concept that neurological injury can be divided into a two-step ("hit") process has been advanced in different ways. The first example of a two-hit process involves the concept that damage to a neuron by diabetes ("first hit") can then interfere with the repair process in the damaged neuron ("second hit"). The "first hit" in this concept involves the effects of diabetes mellitus in altering the neurons themselves. In this model, the first hit is the diabetic damage to the neuron that causes it to express elevated levels of PTEN (see above). The "second hit" involves the expression of PTEN, which damages the regenerative capacity of sensory neurons first and motor neurons afterward [14]. Mature neurons, such as those exposed to diabetes mellitus, have a diminished capacity for regeneration [17], which may involve the downregulation of receptors for growth factors.

4.1.3. A Second Example of a Two-Hit Process Involves the Neuronal Damage Caused by Diabetes

In this concept, the first hit involves the effects of diabetes on the axons of the median nerve in the carpal tunnel. The carpal tunnel is a "choke point" in which stressors such as diabetes, pregnancy, and overuse syndromes can damage the axons of the median nerve, causing pain in the distal branches of the median nerve. If the effects are severe enough, motor disturbances can cause loss of function and even atrophy of the thenar muscles of the thumb. Carpal tunnel syndrome is a compressive injury that affects the diabetic population three times more often than the normal population. Although up to one-third of the diabetic population may have carpal tunnel syndrome confirmed through electrophysiological studies, only about 5.8% of these patients will present with clinical symptoms [10]. Therefore, it is likely that diabetic patients may experience different neuropathies, much like that of the axons of the median nerve, without observable symptoms. However, these preceding subclinical neurological conditions can exacerbate the injury during delivery. The two-hit model we have proposed can explain the effects of diabetes on mothers who are already in a putative subclinical damaged state [10] and then undergo neuronal damage during the delivery process.

5. Summary and Conclusions

In this review paper, we discussed how the two-hit model can explain the effects of diabetes on mothers who are already in a putative subclinical damaged state and then undergo neuronal damage during the delivery process. In our review, we discussed how pregnant women who are diabetic have a damaged nervous system, although the condition may be subclinical. This constitutes the "first hit". The delivery process may cause damage to the nervous system of the mother during delivery. This constitutes the "second hit". Our hypothesis is that pregnant women who have diabetes mellitus are at risk for neurological damage during both hits, but the cumulative effects of both "hits" poses a greater risk of neurological damage during delivery. To support our hypothesis, we discussed how diabetes mellitus produces a more severe neuropathy through different pathological processes. We conclude that diabetic pregnant patients who may have clinical or subclinical neuropathies can acquire a second insult during the delivery process that can exacerbate the presentation of a previously damaged nerve, resulting in symptoms that could interfere with their ability to carry out daily activities and maintain their quality of life.

Author Contributions: Conceptualization, D.T.N., M.H.Z. and A.C.B.J.; methodology, A.C.B.J.; software, D.T.N., M.H.Z., A.C.B.J. and T.I.N.; validation, D.T.N., M.H.Z., A.C.B.J. and T.I.N.; formal analysis, D.T.N., M.H.Z., A.C.B.J. and T.I.N.; investigation, D.T.N., M.H.Z., A.C.B.J. and T.I.N.; resources, K.R.H. and R.L.G.; data curation, A.C.B.J. and T.I.N..; writing—original draft preparation, D.T.N., M.H.Z. and A.C.B.J.; writing—review and editing, D.T.N., M.H.Z., A.C.B.J., T.I.N. and R.L.G.; visualization, K.R.H.; supervision, A.C.B.J. and T.I.N.; project administration, A.C.B.J. and T.I.N.; funding acquisition, A.C.B.J. and T.I.N. All authors have read and agreed to the published version of the manuscript.

Funding: This research received no external funding.

Institutional Review Board Statement: Not applicable.

Informed Consent Statement: Not applicable.

Data Availability Statement: Not applicable.

Conflicts of Interest: The authors declare no conflict of interest.

References

1. Sempere-Bigorra, M.; Julián-Rochina, I.; Cauli, O. Differences and Similarities in Neuropathy in Type 1 and 2 Diabetes: A Systematic Review. *J. Pers. Med.* **2021**, *11*, 230. [CrossRef]
2. Saeedi, P.; Petersohn, I.; Salpea, P.; Malanda, B.; Karuranga, S.; Unwin, N.; Colagiuri, S.; Guariguata, L.; Motala, A.A.; Ogurtsova, K.; et al. Global and regional diabetes mellitus prevalence estimates for 2019 and projections for 2030 and 2045: Results from the International Diabetes Federation Diabetes Atlas, 9th edition. *Diabetes Res. Clin. Pract.* **2019**, *157*, 107843. [CrossRef]
3. Iqbal, Z.; Azmi, S.; Yadav, R.; Ferdousi, M.; Kumar, M.; Cuthbertson, D.J.; Lim, J.; Malik, R.A.; Alam, U. Diabetic peripheral neuropathy: Epidemiology, Diagnosis, and Pharmacotherapy. *Clin. Ther.* **2018**, *40*, 828–849. [CrossRef] [PubMed]
4. Feldman, E.L.; Callaghan, B.C.; Pop-Bosul, R.P. Diabetic Neuropathy. *Nat. Rev. Dis. Prim.* **2019**, *5*, 41. [CrossRef]
5. Callaghan, B.C.; Price, R.S.; Feldman, E. Diagnostic and therapeutic advances: Distal symmetric polyneuropathy. *JAMA* **2015**, *314*, 2172–2181. [CrossRef] [PubMed]
6. Feldman, E.L.; Nave, K.-A.; Jensen, T.S.; Bennett, D.L.H. New Horizons in Diabetic Neuropathy: Mechanisms, Bioenergetics, and Pain. *Neuron* **2017**, *93*, 1296–1313. [CrossRef] [PubMed]
7. Vinik, A.; Mehrabyan, A.; Colen, L.; Boulton, A. Focal Entrapment Neuropathies in Diabetes. *Diabetes Care* **2004**, *27*, 1783–1788. [CrossRef]
8. Watanabe, T.; Ito, H.; Sekine, A.; Katano, Y.; Nishimura, T.; Kato, Y.; Takeda, J.; Seishima, M.; Matsuoka, T. Sonographic Evaluation of the Peripheral Nerve in Diabetic Patients: The relationship between nerve conduction studies, echo intensity and cross-sectional area. *J. Ultrasound Med.* **2010**, *29*, 697–708. [CrossRef]
9. Dellon, A.L. Susceptibility of nerve in diabetes to compression: Implications for pain treatment. *Plast. Reconstr. Surg.* **2014**, *134*, 142S–150S. [CrossRef] [PubMed]
10. Smith, S.; Normahani, P.; Lane, T.; Hohenschurz-Schmidt, D.; Oliver, N.; Davies, A.H. Pathogenesis of Distal Symmetrical Polyneuropathy in Diabetes. *Life* **2022**, *12*, 1074. [CrossRef]
11. Macaré van Maurik, J.F.; Schouten, M.E.; ten Katen, I.; van Hal, M.; Peters, E.J.; Kon, M. Ultrasound findings after surgical compression of the tarsal tunnel in patients with painful diabetic polyneuropathy: A prospective randomized study. *Diabetes Care* **2014**, *37*, 3762–3772. [CrossRef]
12. Thaisetthawatkul, P.; Dyck, P.J.B. Treatment of Diabetic and Nondiabetic Lumbosacral Radiculoplexus Neuropathy. *Curr. Treat. Options Neurol.* **2010**, *12*, 95–99. [CrossRef]
13. Pop-Busui, R.; Ang, L.; Holmes, C.; Gallagher, K.; Feldman, E.L. Inflammation as a therapeutic target for diabetic neuropathies. *Curr. Diabetes Rep.* **2016**, *16*, 29. [CrossRef]
14. Singh, B.; Singh, V.; Krishnan, A.; Koshy, K.; Martinez, J.A.; Cheng, C.; Almquist, C.; Zochodne, D.W. Regeneration of diabetic axons is enhanced by selective knockdown of the PTEN gene. *Brain* **2014**, *137*, 1051–1067. [CrossRef] [PubMed]
15. Rask-Madsen, C.; King, G.L. Vascular Complications of Diabetes: Mechanisms of Injury and Protective Factors. *Cell Metab.* **2013**, *17*, 20–33. [CrossRef] [PubMed]
16. Christie, K.J.; Webber, C.A.; Martinez, J.A.; Singh, B.; Zochodne, D.W. PTEN Inhibition to Facilitate Intrinsic Regenerative Outgrowth of Adult Peripheral Axons. *J. Neurosci.* **2010**, *30*, 9306–9315. [CrossRef]
17. Ramji, N.; Toth, C.; Kennedy, J.; Zochodne, D.W. Does diabetes mellitus target motor neurons? *Neurobiol. Dis.* **2007**, *26*, 301–311. [CrossRef] [PubMed]
18. Kennedy, J.M.; Zochodne, D.W. Experimental Diabetic Neuropathy With Spontaneous Recovery: Is there irreparable damage? *Diabetes* **2005**, *54*, 830–837. [CrossRef]
19. Kennedy, J.M.; Zochodne, D.W. Impaired peripheral nerve regeneration in diabetes mellitus. *J. Peripher. Nerv. Syst.* **2005**, *10*, 144–157. [CrossRef]
20. Wang, P.H.; Yang, C.-C.; Su, W.-R.; Wu, P.-T.; Cheng, S.-C.; Jou, I.-M. Effects of decompression on behavioral, electrophysiologic, and histomorphologic recovery in a chronic sciatic nerve compression model of streptozotocin-induced diabetic rats. *J. Pain Res.* **2017**, *10*, 643–652. [CrossRef]
21. Kennedy, J.M.; Zochodne, D.W. Influence of Experimental Diabetes on the Microcirculation of Injured Peripheral Nerve. *Diabetes* **2002**, *51*, 2233–2240. [CrossRef]
22. Kim, H.; Kim, J.J.; Yoon, Y.-S. Emerging therapy for diabetic neuropathy: Cell therapy targeting vessels and nerves. *Endocr. Metab. Immune Disord. Drug Targets* **2012**, *12*, 168–178. [CrossRef]
23. Yagihashi, S.; Mizukami, H.; Sugimoto, K. Mechanism of diabetic neuropathy: Where are we now and where to go? *J. Diabetes Investig.* **2010**, *2*, 18–32. [CrossRef] [PubMed]
24. Woolf, C.J. Central sensitization: Implications for the diagnosis and treatment of pain. *Pain* **2011**, *152*, S2–S15. [CrossRef]

25. Mabie, W.C. Peripheral Neuropathies During Pregnancy. *Clin. Obstet. Gynecol.* **2005**, *48*, 57–66. [CrossRef]
26. Lawrence, J.M.; Contreras, R.; Chen, W.; Sacks, D.A. Trends in the Prevalence of Preexisting Diabetes and Gestational Diabetes Mellitus Among a Racially/Ethnically Diverse Population of Pregnant Women, 1999–2005. *Diabetes Care* **2008**, *31*, 899–904. [CrossRef]
27. Montag, T.W.; Mead, P.B. Postpartum femoral neuropathy. *J. Reprod/Med/* **1981**, *26*, 563–566. [PubMed]
28. Peirce, C.; O'Brien, C.; O'Herlihy, C. Postpartum femoral neuropathy following spontaneous vaginal delivery. *J. Obstet. Gynaecol.* **2010**, *30*, 203–204. [CrossRef]
29. Kc, K.; Shakya, S.; Zhang, H. Gestational Diabetes Mellitus and Macrosomia: A Literature Review. *Ann. Nutr. Metab.* **2015**, *66* (Suppl. 2), 14–20. [CrossRef]
30. Hemachandra, A.; Ellis, D.; Lloyd, C.E.; Orchard, T.J. The Influence of Pregnancy on IDDM Complications. *Diabetes Care* **1995**, *18*, 950–954. [CrossRef] [PubMed]
31. O'Neal, M.A.; Chang, L.Y.; Salajegheh, M.K. Postpartum Spinal Cord, Root, Plexus and Peripheral Nerve Injuries Involving the Lower Extremities: A practical approach. Anesth Analg. *Obstet. Anesthesia Dig.* **2015**, *120*, 141–148. [CrossRef]
32. Wong, C.A.; Scavone, B.M.; Dugan, S.; Smith, J.C.; Prather, H.; Ganchiff, J.N.; McCarthy, R.J. Incidence of Postpartum Lumbosacral Spine and Lower Extremity Nerve Injuries. *Obstet. Gynecol.* **2003**, *101*, 279–288. [CrossRef]
33. Zakowski, M.I. Obstetric-related Neurological Complications. *Int. Anesthesiol. Clin.* **2014**, *52*, 40–60. [CrossRef] [PubMed]
34. Van Diver, T.; Camann, W. Meralgia paresthetica in the parturient. *Int. J. Obstet. Anesthesia* **1995**, *4*, 109–112. [CrossRef] [PubMed]
35. Grothaus, M.C.; Holt, M.; Mekhail, A.O.; Ebraheim, N.A.; Yeasting, R.A. Lateral femoral cutaneous nerve: An anatomic study. *Clin. Orthop. Relat. Res.* **2005**, *437*, 164–168. [CrossRef] [PubMed]
36. Saw, J.-L.; Hale, J.; Madhavan, A.; Ringler, M.D.; Toledano, M.; Naddaf, E. Ischiofemoral impingement syndrome provoked by labor: An unusual case of complete sciatic mononeuropathy. *Neuroradiol. J.* **2022**, *36*, 116–118. [CrossRef] [PubMed]
37. Williams, S.E.; Swetenburg, J.; Blackwell, T.A.; Reynolds, Z.; Black, A.C., Jr. Posterior cutaneous neuropathy in piriformis syndrome: A vascular hypothesis. *Med. Hypotheses* **2020**, *144*, 109924. [CrossRef]
38. Bunch, K.; Hope, E. An Uncommon Case of Bilateral Peroneal Nerve Palsy following Delivery: A Case Report and Review of the Literature. *Case Rep. Obstet. Gynecol.* **2014**, *2014*, 746480. [CrossRef]
39. Brannigan, T.H. Neuropathic pain. In *Merritt's Neurology*, 12th ed; Rowland, L.P., Pedley, T.A., Eds.; Lippincott, Williams, and Wilkins: Philadelphia, Pennsylvania, 2010; p. 840.
40. Gordon, T. Peripheral Nerve Regeneration and Muscle Reinnervation. *Int. J. Mol. Sci.* **2020**, *21*, 8652. [CrossRef]
41. Kim, B.R.; Ha, D.-H.; Kim, J.K.; Kim, Y.H. Comparison of MR findings of acute traumatic peripheral nerve injury and acute compressive neuropathy in a rat model. *PLoS ONE* **2020**, *15*, e0240911. [CrossRef]
42. Jessen, K.R.; Mirsky, R.; Lloyd, A.C. Schwann cells: Development and role in nerve repair. *Cold Spring Harb. Perspect. Biol.* **2015**, *7*, a020487. [CrossRef] [PubMed]
43. Balakrishnan, A.; Belfiore, L.; Chu, T.-H.; Fleming, T.; Midha, R.; Biernaskie, J.; Schuurmans, C. Insights Into the Role and Potential of Schwann Cells for Peripheral Nerve Repair From Studies of Development and Injury. *Front. Mol. Neurosci.* **2021**, *13*. [CrossRef]
44. Wagstaff, L.J.; Gomez-Sanchez, J.A.; Fazal, S.V.; Otto, G.W.; Kilpatrick, A.M.; Michael, K.; Wong, L.Y.; Ma, K.H.; Turmaine, M.; Svaren, J.; et al. Failures of nerve regeneration caused by aging or chronic denervation are rescued by restoring Schwann cell c-Jun. *Elife* **2021**, *10*, e62232. [CrossRef] [PubMed]
45. Molinari, W.J.; Elfar, J.C. The double crush syndrome. *J. Hand Surg.* **2013**, *38*, 799–801. [CrossRef] [PubMed]
46. Kennedy, J.M.; Zochodne, D.W. The regenerative deficit of peripheral nerves in experimental diabetes: Its extent, timing and possible mechanisms. *Brain* **2000**, *123*, 2118–2129. [CrossRef] [PubMed]
47. Zochodne, D.W. Diabetes and failure of axon regeneration in peripheral neurons. *Expert Rev. Endocrinol. Metab.* **2010**, *5*, 7–14. [CrossRef]

International Journal of
Molecular Sciences

MDPI

Article

NAADP-Evoked Ca^{2+} Signaling Leads to Mutant Huntingtin Aggregation and Autophagy Impairment in Murine Astrocytes

Cássia Arruda de Souza Pereira [1,†], Natalia de Castro Medaglia [1,†], Rodrigo Portes Ureshino [2], Claudia Bincoletto [1], Manuela Antonioli [3,4], Gian Maria Fimia [3,5], Mauro Piacentini [3,4], Gustavo José da Silva Pereira [1], Adolfo Garcia Erustes [1,*] and Soraya Soubhi Smaili [1]

[1] Departament of Pharmacology, Escola Paulista de Medicina, Universidade Federal de São Paulo, São Paulo 04044-020, Brazil
[2] Instituto de Ciências Ambientais, Químicas e Farmacêuticas, Universidade Federal de São Paulo, Diadema 09913-030, Brazil
[3] Department of Epidemiology, Preclinical Research and Advanced Diagnostics, National Institute for Infectious Diseases IRCCS "L. Spallanzani", 00149 Rome, Italy
[4] Department of Biology, University of Rome "Tor Vergata", 00133 Rome, Italy
[5] Department of Molecular Medicine, University of Rome "Sapienza", 00185 Rome, Italy
* Correspondence: adolfo.erustes@unifesp.br; Tel.: +55-11-5576-4449
† These authors contributed equally to this work.

Abstract: Huntington's disease (HD) is a progressive neurodegenerative disease characterized by mutations in the huntingtin gene (mHtt), causing an unstable repeat of the CAG trinucleotide, leading to abnormal long repeats of polyglutamine (poly-Q) in the N-terminal region of the huntingtin, which form abnormal conformations and aggregates. Alterations in Ca^{2+} signaling are involved in HD models and the accumulation of mutated huntingtin interferes with Ca^{2+} homeostasis. Lysosomes are intracellular Ca^{2+} storages that participate in endocytic and lysosomal degradation processes, including autophagy. Nicotinic acid adenine dinucleotide phosphate (NAADP) is an intracellular second messenger that promotes Ca^{2+} release from the endo-lysosomal system via Two-Pore Channels (TPCs) activation. Herein, we show the impact of lysosomal Ca^{2+} signals on mHtt aggregation and autophagy blockade in murine astrocytes overexpressing mHtt-Q74. We observed that mHtt-Q74 overexpression causes an increase in NAADP-evoked Ca^{2+} signals and mHtt aggregation, which was inhibited in the presence of Ned-19, a TPC antagonist, or BAPTA-AM, a Ca^{2+} chelator. Additionally, TPC2 silencing revert the mHtt aggregation. Furthermore, mHtt has been shown co-localized with TPC2 which may contribute to its effects on lysosomal homeostasis. Moreover, NAADP-mediated autophagy was also blocked since its function is dependent on lysosomal functionality. Taken together, our data show that increased levels of cytosolic Ca^{2+} mediated by NAADP causes mHtt aggregation. Additionally, mHtt co-localizes with the lysosomes, where it possibly affects organelle functions and impairs autophagy.

Keywords: Huntington's disease; lysosome; NAADP; two-pore channels

Citation: Pereira, C.A.d.S.; Medaglia, N.d.C.; Ureshino, R.P.; Bincoletto, C.; Antonioli, M.; Fimia, G.M.; Piacentini, M.; Pereira, G.J.d.S.; Erustes, A.G.; Smaili, S.S. NAADP-Evoked Ca^{2+} Signaling Leads to Mutant Huntingtin Aggregation and Autophagy Impairment in Murine Astrocytes. *Int. J. Mol. Sci.* **2023**, *24*, 5593. https://doi.org/10.3390/ijms24065593

Academic Editor: Claudia Ricci

Received: 31 December 2022
Revised: 10 February 2023
Accepted: 14 February 2023
Published: 15 March 2023

1. Introduction

Huntington's disease (HD) is a rare autosomal dominant neurodegenerative disease that affects 2.71 individuals per 100,000 [1,2]. HD is clinically characterized by a triad of symptoms that includes motor changes, progressive cognitive loss and psychiatric disorders. Choreic movements is the most characteristic symptom of the disease and consists of involuntary, random and rapid movements in the distal extremities of the limbs [3]. In most cases, HD affects patients aged between 30 to 50 years, and the neurodegeneration progresses irreversibly over a period of 15 to 20 years [4,5].

HD is caused by mutation in the gene encoding huntingtin (Htt), resulting in an expansion of the CAG trinucleotide on the short arm of chromosome 4p16.3 [6]. This

mutation in the Htt gene leads to the abnormal expression of a long chain of polyglutamine (poly-Q) in the N-terminal portion [7], which encodes the mutant form of huntingtin (mHtt) [6]. CAG repeats are variable, while in the non-affected population it ranges from 9 to 35 repeats; in HD patients, these repetitions range from 36 to 55 (even more up to 100) [8].

The mechanisms that lead to neuronal death and the development and progression of HD are related to a toxic gain in mHtt function [9]. It is known that mHtt is prone to form protein aggregates, generate toxic fragments of the N-terminal region, interfere with gene transcription and compromise protein degradation systems [10]. Additionally, HD is also associated with deregulation of calcium (Ca^{2+}) signaling and homeostasis [11–14]. Studies have shown that mHtt can interact with different Ca^{2+} channels, such as voltage-gated Ca^{2+} channels (VGCC) located in plasma membrane [15], and the type 1,4,5-triphosphate receptor 1 (IP_3R1) in the endoplasmic reticulum membrane [12]. Additionally, mHtt can also interact with the outer mitochondrial membrane, affecting the mitochondrial Ca^{2+} buffering and leading to mitochondrial dysfunctions, which includes the opening of the mitochondrial permeability transition pore, causing mitochondrial depolarization and, eventually, the activation of apoptotic pathways of cell death [16]. In a previous study performed by our group, glutamate-induced Ca^{2+} release is higher in cortical slices, corpus callosum and striatum from transgenic R6/1 mice, an in vivo model of HD, when compared to slices from control animals [17].

Lysosomes are acidic organelles whose main function is the degradation of macromolecules, participating in endocytosis, secretory pathways and autophagy [18–20]. Additionally, lysosome and acidic organelles such as endosome play an important role in Ca^2-storage and intracellular signaling [21–23]. The efflux of Ca^{2+} from lysosomes is mediated by ion channels present in the membrane, such as Two-Pore channels (TPCs), which are channels belonging to a superfamily of voltage-gated ion channels [22]. Evidence has revealed that TPCs are activated after their interaction with nicotinic acid adenine dinucleotide phosphate (NAADP) [24–27]. NAADP is a pyridine nucleotide and a potent Ca^{2+} mobilizer that was identified through studies using sea urchin egg homogenates [28,29]. Evidence suggests that the Ca^{2+} mobilized by NAADP comes from acid Ca^{2+} stores. This evidence is supported by the description of TPCs, as well as their location in acid stocks and their permeability to Ca^{2+}, suggesting them as candidates for NAADP-interacting receptors, and, indeed, many studies have shown data consistent with this hypothesis [24,25,30]. Likewise, studies conducted by our group also contributed to describing NAADP as the main agonist of TPCs, where gastric smooth muscle cells and astrocytes were stimulated with NAADP, and the Ca^{2+} released was derived from lysosome and through the TPCs' receptors [31–33]. In addition to its action on Ca^{2+} release, NAADP had a role in inducing autophagy. Pereira and colleagues (2011) demonstrated that NAADP can modulate autophagy in astrocytes through the activating TPC2 receptors since treatment with NAADP promoted the accumulation of autophagic markers LC3-II and Beclin-1; moreover, overexpression of a non-functional TPC2 construct impaired the effects of NAADP [31]. In another study, similar results were found in astrocytes after stimulation with glutamate, suggesting that the induction of autophagy mediated by glutamate involves the participation of NAADP/TPCs signaling [33].

In addition, several studies have correlated the involvement of NAADP with dysfunctional autophagy in neurodegenerative diseases. For example, it has been reported that the overexpression of the protein leucine-rich repeat kinase 2 (LRRK2) promotes the increase of autophagy through Ca^{2+}-dependent protein kinase. Kinase-β (CaMKK-β)/adenosine monophosphate (AMP) activated the pathway of protein kinase (AMPK), which is Ca^{2+} dependent. These effects were similar to the addition of NAADP and were reversed with Ned-19, an NAADP antagonist [34], or through overexpression of a non-functional construct of TPC2 [35]. However, there is no published study that correlates NAADP and HD-mediated Ca^{2+} signaling. Importantly, autophagy is the only mechanism that cells have to remove protein aggregates, including mHtt; however, the impairment of autophagic

function facilitates mHtt accumulation and aggregation, as well as its cytotoxic effects [36]. In this scenario, the NAADP-mediated autophagy could represent an alternative to rescuing defective autophagy, enhancing degradation of mHtt and reducing its cytosolic levels.

Here, we investigated the effects of NAADP/TPC signaling on autophagy and huntingtin protein aggregation in astrocytes. For this purpose, the effect of NAADP in cells overexpressing mHtt-Q74 and the link between TPCs receptors were studied. The effect on mHtt aggregation and autophagy blockade, which may decrease and affect neuroprotection, was also explored.

2. Results

2.1. Overexpression of mHtt-Q74 Enhances NAADP-Mediated Ca^{2+} Release

NAADP is a second messenger capable of interacting with TPCs receptors in acid organelles and promoting Ca^{2+} release [32]. Several studies have associated alterations in Ca^{2+} and NAADP signaling with neurodegenerative diseases; however, this correlation in HD is still unknown. Here, to investigate the connection of NAADP/TPCs and mHtt-Q74 signaling, a murine astrocytes cell line overexpressing pEGFP-mHtt-Q74 or pEGFP (empty vector as control) was loaded with Fura-2 AM. Cells were stimulated with the nicotinic acid adenine dinucleotide phosphate, acetoxymethyl ester (NAADP-AM, 100 nM) in the presence and absence of Ned-19 (1 μM), the antagonist of TPCs. Representative records show that NAADP stimulation promoted an increase in cytosolic Ca^{2+} in astrocytes overexpressing mHtt-Q74, when compared to the control group (Figure 1a). Quantification of maximum Fura-2 fluorescence demonstrates increases of cytosolic Ca^{2+} in cells overexpressing mHtt-Q74, whereas Ned-19 pre-treatment significantly reverses NAADP evoked-Ca^{2+} signals (Figure 1b).

2.2. NAADP Induces mHtt-Q74 Aggregation

Overexpression of mHtt-Q74 in astrocytes promoted changes in NAADP-mediated Ca^{2+} signaling. Thus, we investigated the possible effect of NAADP on mHtt-Q74 aggregation, as well as the participation of Ca^{2+} in this process. Astrocytes overexpressing pEGFP-mHtt-Q74 were treated with NAADP-AM (100 nM, agonist of TPCs), Ned-19 (1 μM, antagonist of TPCs) and BAPTA-AM (10 μM, cytosolic Ca^{2+} chelator) and analyzed under a confocal microscopy. The treatment of NAADP-AM induced the aggregation of mHtt-Q74, when compared to the untreated group (Figure 1c). A large amount of aggregates were distributed in the cytoplasm and in the perinuclear region. To assess the role of NAADP in mHtt-Q74 aggregation, astrocytes were pre-treated with Ned-19, followed by the addition of NAADP-AM. Representative images demonstrate that Ned-19 reversed the NAADP-mediated effect by inhibiting mHtt-Q74 aggregation compared to the NAADP-treated group (Figure 1c). Finally, the role of Ca^{2+} in the aggregation of mHtt-Q74 was also evaluated, using the Ca^{2+} chelator BAPTA-AM, pre-incubated for 30 min, followed by NAADP-AM stimulation. Interestingly, mHtt-Q74 aggregation was suppressed in the presence of BAPTA-AM, as no aggregate was observed in the analyzed cells (Figure 1c). The quantification of mHtt-Q74 aggregates is shown in Figure 1d, where astrocytes stimulated with NAADP-AM showed a significant increase in aggregates, when compared to the control group. Likewise, a statistical difference was detected when the NAADP-stimulated group was compared to groups pre-treated with Ned-19 and BAPTA-AM, which suppressed mHtt-Q74 aggregation.

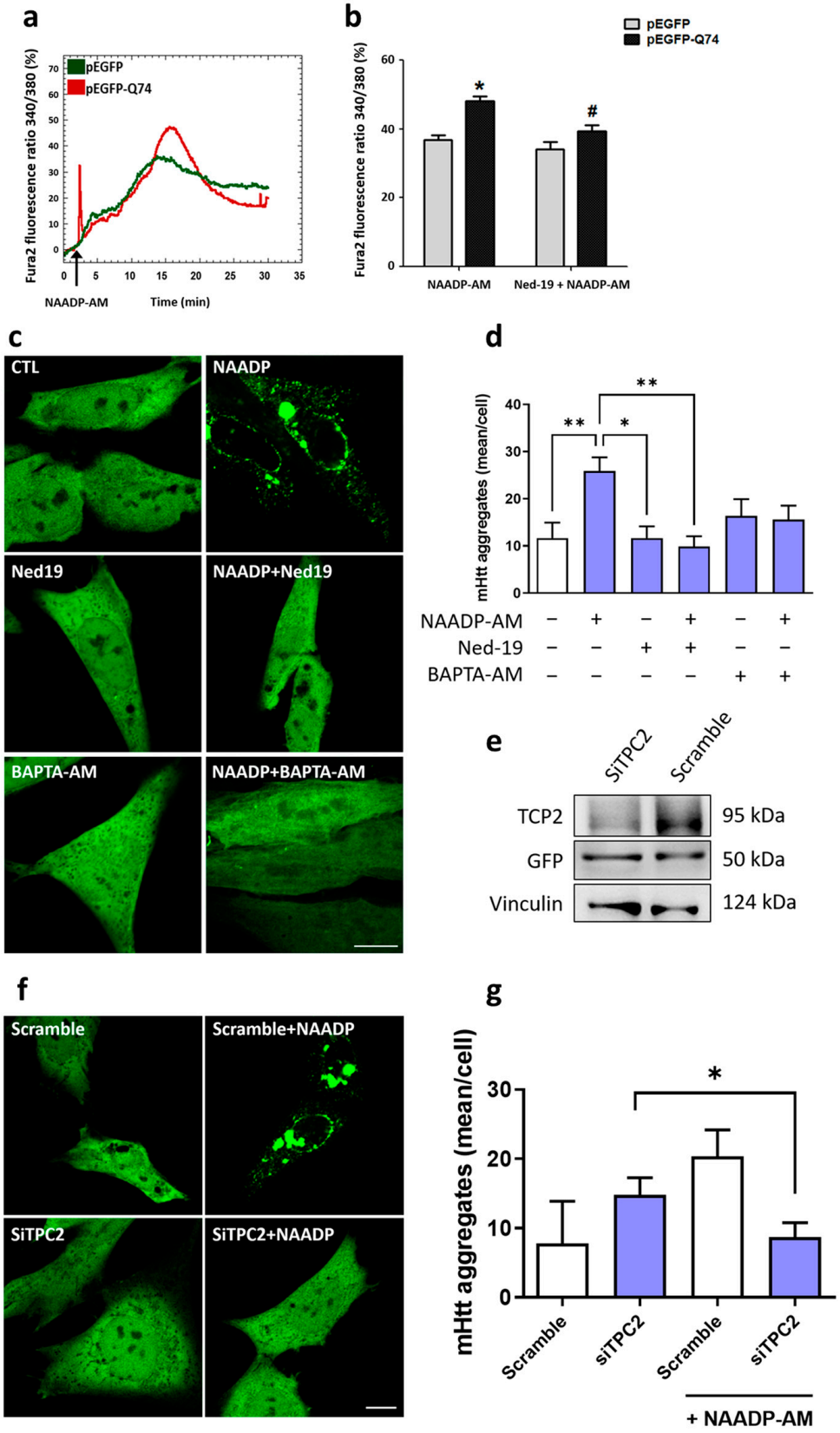

Figure 1. NAADP mediates Ca^{2+} mobilization and mHtt-Q74 aggregation in astrocytes. Astrocytes were transiently transfected with the pEGFP-mHtt-Q74 vector or pEGFP-empty vector, followed by evaluation of Ca^{2+} mobilization and mHtt-Q74 aggregation. Additionally, mHtt-Q74 aggregation was analyzed in

astrocytes overexpressing or silenced for the TPC2 channel. Astrocytes overexpressing pEGFP (empty vector) or pEGFP-mHtt-Q74 were loaded with Fura-2 AM (5 μM), followed by stimulation with nicotinic acid adenine dinucleotide phosphate, acetoxymethyl ester (NAADP-AM, 100 nM) in the presence or absence of Ned-19 (1 μM), a TPCs antagonist. Fura-2 fluorescence was recorded for 30 min, considering the first minute of each experiment as basal fluorescence. (**a**) Representative records of the Fura-2 fluorescence ratio (340/380) of pEGFP (green line) and pEGFP-mHtt-Q74- (red line) overexpressing astrocytes. (**b**) Quantification of the maximum Fura-2 fluorescence ratio after the stimulation with NAADP-AM (100 nM), in the presence or absence of the Ned-19 (1 μM), normalized according to the basal fluorescence. $n = 3$. Data presented as mean ± SEM. One-way ANOVA, followed by Bonferroni post hoc. * $p < 0.05$; # $p < 0.05$. (**c**) Confocal microscopy of astrocytes overexpressing the pEGFP-mHtt-Q74 treated with NAADP-AM (100 nM) and Ned-19 (1 μM), both in the presence or absence of BAPTA-AM (10 μM), used as cytosolic Ca^{2+} chelator. Images were obtained using a Carl Zeiss LSM 780 confocal microscope (Carl Zeiss, Oberkochen, Germany), with 63× magnification. Scale bar: 10 μm. (**d**) Quantification of mHtt-Q74 aggregates (mean/cell) in the studied groups. $n = 3$. Data presented as mean ± SEM. One-way ANOVA, followed by Tukey's post hoc. * $p < 0.05$; ** $p < 0.01$. To evaluate the participation of the TPC2 receptor in mHtt-Q74 aggregation, TPC2 was overexpressed or silenced in the astrocytes overexpressing pEGFP-mHtt-Q74. (**e**) Representative autoradiograms from western blotting analysis of astrocytes overexpressing pEGFP-mHtt-Q74 and silenced for TPC2 receptor, after incubation with anti-TPC2, anti-GFP or anti-vinculin antibodies. (**f**) Confocal images of astrocytes overexpressing pEGFP-mHtt-Q74 treated with NAADP-AM (100 nM), in control and silenced cells for the TPC2 receptor and (**g**) quantification of mHtt-Q74 aggregates in the evaluated groups. $n = 2$. Data presented as mean ± SEM. One-way ANOVA, followed by Tukey's post hoc. * $p < 0.05$. Images were acquired using a Carl Zeiss LSM 780 confocal microscope, with 63× magnification. Scale bar: 10 μm.

Previous results from our group demonstrated that TPC2 is located mainly in lysosomes; in addition, NAADP-mediated Ca^{2+} release is greater in cells that overexpress the TPC2 receptor than in cells overexpressing the TPC1 receptor [30–32]. Thus, to evaluate the participation and role of the TPC2 channel in mHtt-Q74 aggregation, this channel was silenced in astrocytes overexpressing mHtt-Q74, using the siRNA-TPC2 (5′-3′ sequence: GGAAACCUCUUGUCUAUUUTT). Silenced TPC2 cells (Figure 1e) were treated with NAADP-AM (100 nM), and pEGFP-mHtt-Q74 aggregation was evaluated by confocal microscopy. As demonstrated in representative images (Figure 1f) and statistical analysis (Figure 1g), in the astrocytes where TPC2 was silenced (siTPC2), the NAADP-AM did not induce mHtt-Q74 aggregation. However, mHtt aggregation was observed in scramble cells.

2.3. mHtt-Q74 Colocalizes with TPC2 Receptor

It has been reported that mHtt overexpression and presence interact with Ca^{2+} channels, such as IP3R and RYR, modifying their function and cellular Ca^{2+} homeostasis [12,13]. Additionally, the data presented in Figure 1a,b demonstrate that mHtt-Q74 affects NAADP-mediated Ca^{2+} release via TPCs channels. In this way, to verify mHtt-Q74's co-localization and interaction with TPC2 receptors, astrocytes overexpressing mHtt-Q74 were transfected with the RFP-TPC2 construct and observed in confocal microscopy (Figure 2a). Confocal images indicated that mHtt-Q74 partially colocalizes with TPC2 receptors, as demonstrated in the merged and zoomed images. To quantify the colocalized eGFP and RFP fluorescence pixels, the colocalization coefficient was applied, and the weighted colocalization coefficients were calculated. Data showed that mHtt-Q74 partially colocalizes with TPC2, when compared to the control group (RFP-empty).

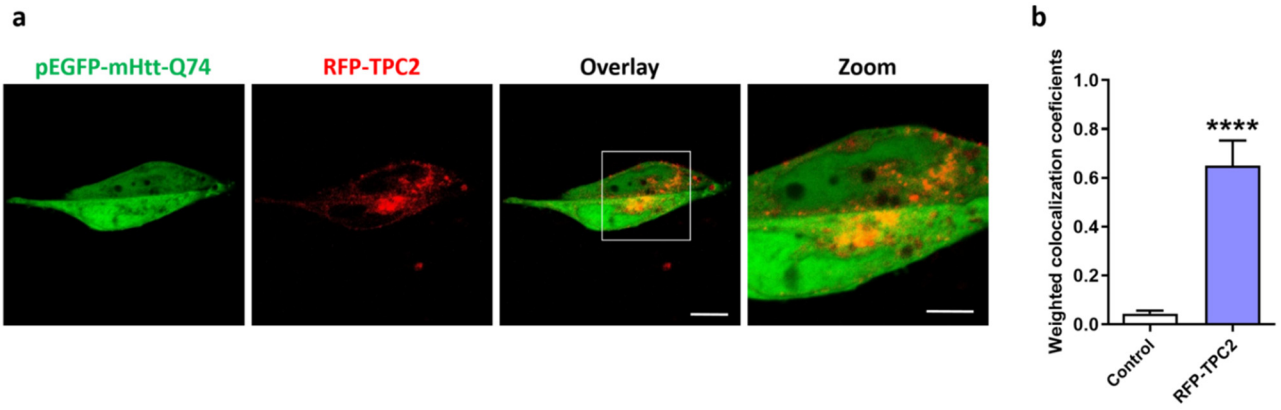

Figure 2. Evaluation of colocalization between the TPC2 receptor and mHtt-Q74. Astrocytes were transfected with pEGFP-mHtt-Q74 and RFP-TPC2 vectors, followed by evaluation of the cells in a confocal microscope. (**a**) Representative images of astrocytes overexpressing mHtt-Q74 protein (pEGFP-mHtt-Q74, green fluorescence) and TPC2 (RFP-TPC2, red fluorescence). The merged images show both fluorescence signals, and digital zoom (2×) on specific areas of interest was applied to demonstrate colocalization between the fluorescence signals. Images were obtained using a Carl Zeiss LSM 780 confocal microscope, with 63× magnification. Scale bar: 10 µm and 5 µm. (**b**) Quantification of colocalization between pEGFP-mHtt-Q74 (green fluorescence) and RFP-TPC2 (red fluorescence), calculated according to the weighted colocalization coefficient. $n = 3$. Data presented as mean ± SEM. Unpaired Student's t test, **** $p < 0.0001$.

2.4. mHtt-Q74 Inhibits Autophagy in Astrocytes

TPC2 has been described as the NAADP receptor in acidic compartments, such as the lysosomes [31,32]. Thus, the autophagic flux mediated by NAADP was evaluated in non-transfected astrocytes, in order to analyze the activation of autophagy in the absence of mHtt-Q74. To overexpress TPC2, astrocytes were transduced with the Myc-TPC2 construct or mCherry (empty vector) if used as the control group. Western blot analysis demonstrated increased Myc expression in the group transduced with the Myc-TPC2 construct, when compared to the control (mCherry) (Figure 3a). Astrocytes were treated with NAADP-AM (100 nM) for 1 and 2 h, in the presence or absence of E64d + Pep A (10 µg/mL) in the last hour of treatment. The results demonstrated that the overexpression of TPC2 promoted the accumulation of LC3-II, which was potentiated after 1 h treatment with NAADP-AM (Figure 3b,c). The groups treated in the presence of E64d + Pep A had a robust accumulation of LC3-II when compared to the control. The p62 analysis showed no statistical differences (Figure 3d). Once the role of TPC2 in the activation of the autophagic flux was demonstrated, the same experiment was performed in astrocytes overexpressing mHtt-Q74. Cells were treated for 1, 2 and 4 h with NAADP-AM (100 nM), in the presence or absence of E64d + Pep A, followed by evaluation of autophagic flux. As demonstrated in Figure 3e,f, NAADP-AM did not induce increases in the autophagic flux in astrocytes overexpressing mHtt-Q74, even in cells treated with E64d + Pep A, indicating an autophagy blockade in the degradative step of autophagy in this model. The p62 evaluation did not demonstrate statistical differences (Figure 3g).

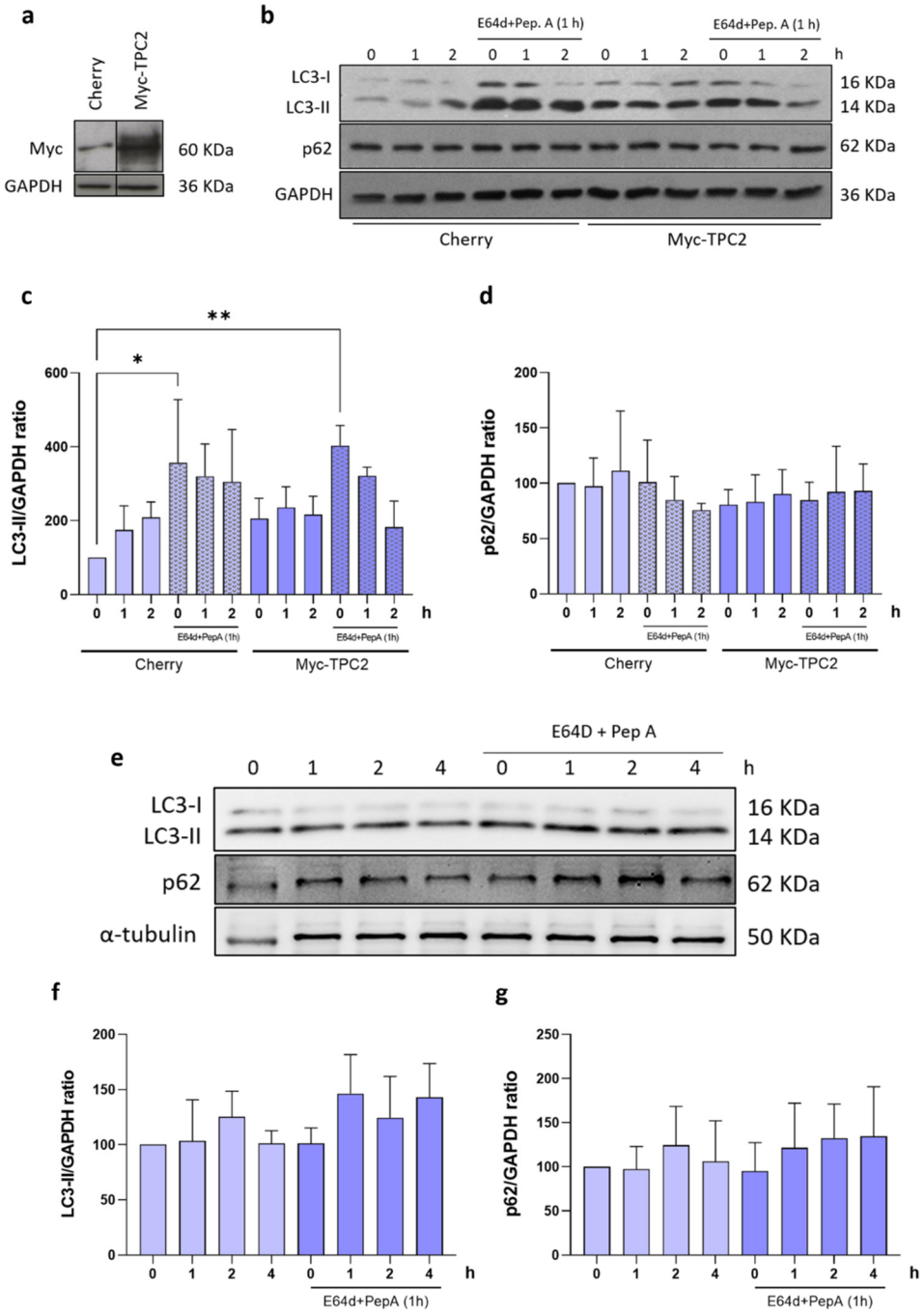

Figure 3. Evaluation of NAADP-induced autophagy in astrocytes overexpressing TPC2 or mHtt-Q74. Western blot analysis of the autophagic flux of astrocytes overexpressing Myc-TPC2 or pEGFP-mHtt-Q74 after treatment with NAADP-AM (100 nM), in the presence or absence of E64d/Pep A. Detection of autophagy was performed by analyzing the levels of LC3 and p62 levels after 1, 2 and 4 h of treatment with NAADP. (**a**) Representative autoradiograms of western blotting analysis of anti-myc and anti-GAPDH antibodies, demonstrating Myc tag protein overexpression in astrocytes transfected with the Myc-TPC2 construct. (**b**) Representative autoradiograms of western blotting analysis of anti-LC3, anti-p62 and anti-GAPDH antibodies in the astrocytes overexpressing Myc-TPC2. (**c**) Quantification of LC3-II and (**d**) p62 after treatments with NAAPD-AM in astrocytes overexpressing Myc-TPC2, both in the presence or absence of E64d/pepstatin A. The experiments were normalized in relation to the GAPDH internal control. $n = 3$. Data presented as mean ± SEM, One-way ANOVA followed by Tukey's

post hoc. * $p < 0.05$; ** $p < 0.01$. The autophagic flux was also evaluated in astrocytes overexpressing mHtt-Q74 after treatments with NAADP for 1, 2 and 4 h, in the presence or absence of E64d/pepstatin A. (**e**) Representative autoradiograms of the western blotting analysis of anti-LC3, anti-p62 and anti-α-tubulin antibodies. (**f**) Quantification of LC3-II and p62 (**g**) after treatments with NAAPD-AM in astrocytes overexpressing mHtt-Q74. The experiments were normalized in relation to the α-tubulin internal control. $n = 3$. Data presented as mean ± SEM, One-way ANOVA followed by Tukey's post hoc.

3. Discussion

The Ca^{2+} ion is an important intracellular second messenger, which is involved in several physiological processes, and its homeostasis is essential to the maintenance of cell functions and viability [37,38]. The intracellular concentrations of Ca^{2+} are finely regulated through the action of pumps and exchangers located in membranes of the major Ca^{2+}-store's organelle and through the action of intracellular second messengers, such as NAADP [39]. Many studies have shown the involvement of acidic organelles and NAADP in neurodegenerative diseases, such as Parkinson's and Alzheimer's disease [40,41], but the involvement is still unknown for the Ca^{2+}/NAADP signaling pathway in HD. Therefore, this study investigates the role of NAADP-mediated Ca^{2+} signaling in an in vitro model of HD and its effects on the aggregation of the mutated huntingtin protein Q74 (mHtt-Q74).

Our data demonstrated that astrocytes overexpressing mHtt-Q74 are more sensitive and presented an increase in cytosolic Ca^{2+} levels after stimulation with NAADP-AM (100 nM) (Figure 1a,b). A similar effect was observed by Pereira and collaborators, who demonstrated that NAADP (100 nM and 1 μM) induced the release and, consequently, the increase of intracellular Ca^{2+} in astrocytes in primary culture [31]. In addition, NAADP-AM promoted a significant increase in mHtt-Q74 aggregates when compared to the control group. However, the combination of NAADP-AM with Ned-19 or BAPTA-AM leads to a reduction of mHtt-Q74 aggregates in astrocytes when compared to the group treated with NAADP-AM. A similar effect was observed when TPC2 was silenced in astrocytes; the formation of mHtt aggregates was reduced (Figure 1f–h). Together, these data suggest the participation of Ca^{2+} in mHtt-Q74 aggregation, which was reverted in the presence of calcium chelator (BAPTA-AM), as well as the possible participation of TPC receptors.

Deregulation in Ca^{2+} signaling is a common characteristic in neurodegenerative disorders, such as Parkinson's disease and Alzheimer's disease [42,43]. In Huntington's disease, mHtt seems to interact with different types of Ca^{2+} receptors and channels, altering their functioning and modifying the intracellular Ca^{2+} signaling [12,13,44,45]. Our results demonstrated colocalization between mHtt-Q74 (pEGFP-mHtt Q74) and TPC2 channels in astrocytes overexpressing RFP-TPC2 constructs. These data suggest a possible physical interaction of mHtt with this receptor, affecting its functioning (Figure 2a,b). Similar results were obtained using the fibroblasts of a LRRK2 G2019S Parkinson's patient, in which lysosomal morphology defects were corrected with molecular TPC2-silencing or pharmacological inhibition of TPCs [40].

It is well known that the interaction of NAADP with the TPCs can induce autophagy in astrocytes [31,33]. In this way, the autophagic flux mediated by NAADP was investigated in an in vitro model of HD. Initially, autophagic flux was evaluated in astrocytes overexpressing the TPC2 channel (Myc-TPC2) to characterize the NAADP-AM response. As expected, cells overexpressing TPC2 channels had an increase in the LC3-II autophagic marker (Figure 3b,c). However, in astrocytes overexpressing mHtt-Q74 and Myc-TPC2, no significant changes were detected in the levels of LC3-II and p62 proteins after the treatment with NAADP-AM at different time-points, indicating the reduction of autophagy in our model (Figure 3e,f). These data may indicate that mHtt affects autophagic signaling and machinery, blocking autophagy in these cells, suggesting that autophagy-mediated NAADP signaling is affected by mHtt. In fact, the reduction of autophagic activity is a common feature in neurodegenerative diseases, where there is an accumulation of protein aggregates [46,47].

The correlation between autophagy and HD has been widely studied, as autophagy induction is often proposed as a therapeutic target of HD in many studies [4,48–50]. The evaluation of autophagy markers performed in patients with HD, the expression levels of genes related to autophagy are increased, such as LAMP2A, LC3I and ULK2 [49]. Studies have shown that wild type Htt plays an important role in autophagy, and the occurrence of mHtt interferes with normal huntingtin functions. This aspect was reported by Wong and Holzbaur, where wild type Htt could act as a regulator of autophagosome transport in neurons, and the depletion of wild type Htt or mHtt expression would lead to dysregulation of this transport and, consequently, would affect and interfere with autophagy degradation [51].

Taken together, our data demonstrated that mHtt-Q74 colocalizes with the TPC2 receptor in lysosomes, consequently affecting the physiological function of this channel, and induces the release of Ca^{2+} from this organelle. Increased levels of Ca^{2+} originating from the lysosome favor mHtt-Q74 aggregation. Additionally, data have demonstrated that there is inhibition of autophagy in astrocytes overexpressing mHtt-Q74. These results are compatible with the hypothesis that lysosomal homeostasis is important to inhibit the mHtt aggregation and to consider autophagy as a potential neuroprotective system.

4. Materials and Methods

4.1. Cell Culture, Transfections and Retroviral Infection

Immortalized astrocytes were cultured in DMEM (Dulbecco's modified Eagle's medium) with high glucose content, supplemented with 10% fetal bovine serum and 1% penicillin/streptomycin and kept at 37 °C in 5% CO_2 humidified atmosphere. Briefly, primary astrocytes were obtained from 4-day-old Wistar rats and immortalized through overexpression of the T antigen [52].

To overexpress mHtt-Q74, astrocytes were transfected with the plasmid pEGFP-mHtt Q74 (3 μg, Cat #40262, Addgene, Watertown, MA, USA) using Lipofectamine 3000 (6 μL), according to the manufacturer's protocol (Thermo Fisher Scientific, Waltham, MA, USA). The control group was prepared with astrocytes transfected with the plasmid pEGFP-empty (Cat #165830; Addgene, Watertown, MA, USA). As previously demonstrated in other studies, the overexpression of nonpathogenic huntingtin (Htt-Q23) does not promote protein aggregation or affect cellular viability, when compared to the mHtt-Q74 [53,54]. Therefore, in the present study, astrocytes transfected with the pEGFP-empty vector were used as the control group. Similarly, astrocytes were also transfected simultaneously with the pEGFP-mHtt Q74 (1.5 μg) and with the plasmid RFP-TPC2 (1.5 μg) using Lipofectamine 2000 (5 μL) according to the manufacturer's protocol (Thermo Fisher Scientific). pEGFP-Q74 was a gift from David Rubinsztein (Addgene plasmid #40262; http://n2t.net/addgene:40262 accessed on 31 December 2022; RRID:Addgene_40262) and pEGFP was a gift from Koen Venken (Addgene plasmid #165830; http://n2t.net/addgene:165830 accessed on 31 December 2022; RRID:Addgene_165830).

The myc-tagged, full-length, wild-type TPC1 and TPC2 constructs were kindly provided by Sandip Patel (UCL, London, UK) [24] and cloned into a modified version of the pLPCX vector (Clontech, Mountain View, CA, USA) [55]. For virus production containing pLPCX-Myc-TPC2, 15 μg retroviral vector was co-transfected with 5 μg expression plasmid for the vesicular stomatitis virus G protein into the 293 gp/bsr cell line using the calcium phosphate method. After 48 h, the supernatant containing the retroviral particles was recovered and supplemented with 4 μg/mL polybrene and stored at −80 °C.

In addition to overexpression assay, TPC2 channel was also silenced in astrocytes overexpressing the mHtt. For this purpose, 1.0×10^5 cells/well were co-transfected using Lipofectamine RNAiMAX (Life Technologies, Carlsbad, CA, USA) (7.5 μL) with pEGFP-mHtt Q74 (1.5 μg) and RNAi siTPC2 (20 nmol; Ambion, Life Technologies), corresponding to TPC2 target sequence (sequence 5′-3′: GGAAACCUCUUGUCUAUUUTT). A scramble sequence was used as a control.

4.2. Ca^{2+} Measurements

To analyze the cytosolic Ca^{2+} mobilization, astrocytes were cultured in 25-mm glass coverslips and loaded with the fluorescent ratiometric indicator Fura-2 AM (5 μM, Thermo Fisher Scientific Cat# F1201) and Pluronic F-127 (20%, Sigma-Aldrich, San Luis, MO, USA) for 30 min at 37 °C in fluorescence buffer (130 mM NaCl; 5.36 mM KCl; 1 mM $MgSO_4$; 1 mM Na_2HPO_4; 1.5 mM $CaCl_2$; 2.5 mM $NaHCO_3$; 1.5 mM albumin; 25 mM glucose and 20 mM HEPES pH 7.4). Fura-2 fluorescence records were performed using a real-time fluorescence microscope (Nikon TE300, Nikon, Tokyo, Japan) coupled to a Coolsnap high-resolution digital camera (RoperSci, Princeton Instruments, Trenton, NJ, USA) at 40× magnification. Fura-2 fluorescence was recorded for 30 min (300 images), with a 6 s interval between images acquisition. The basal Fura-2 fluorescence was recorded in the first 2 min (20 images) of each experiment. Following the establishment of the baseline, cells were stimulated with NAADP-AM (100 nM), in the presence and absence of NED-19 (1 μM), that act as its antagonist. The acquisition of images, data extraction and analysis of regions of interest (ROIs) were performed using the Imaging software BioIP. Only the cells transfected with the pEGFP-mHtt Q74 were analyzed. The data are presented as the maximum fluorescence ratio of Fura-2, normalized according to basal fluorescence. Cells loaded with Fura-2 were excited at 340 nm and 380 nm, and the fluorescence emission was detected at 510 nm.

4.3. Western Blotting

For protein extraction, cells were lysed in RIPA buffer (150 mM NaCl; 1% NP-40; 0.5% deoxycholic acid; 0.1% SDS; 50 mM Tris pH 8.0; 2 mM $MgCl_2$), supplemented with protease and phosphatase inhibitor cocktails, followed by centrifugation to remove cellular debris. Total proteins were quantified using the Bradford assay, and samples were prepared in NuPage LDS sample buffer (Thermo Fisher Scientific). A total of 15–40 μg of each protein sample was subjected to SDS-polyacrylamide gel electrophoresis and transferred onto a nitrocellulose membrane. Immunoblots were blocked in 5% nonfat dry milk for 30 min at room temperature, followed by overnight incubation with primary antibodies: anti-GFP (1:200; Santa Cruz Biotechnology, Dallas, TX, USA; Cat# sc-8334, RRID:AB_641123), anti-vinculin (1:1000; Cell Signaling Technology, Danvers, MA, USA; Cat# 13901, RRID:AB_2728768), anti-LC3B (1:2000; Cell Signaling Technology Cat# 2775, RRID:AB_915950), anti-SQSTM1/p62 (1:2000; MBL International, Woburn, MA, USA; Cat# PM045, RRID:AB_1279301). For internal control, anti-α-tubulin (1:10,000; Sigma-Aldrich Cat# T9026, RRID:AB_477593) and anti-GAPDH (1:10,000; Sigma-Aldrich Cat# G8795, RRID:AB_1078991) were used. Secondary antibodies were incubated 1 h at room temperature: anti-rabbit (1:5000; Thermo Fisher Scientific Cat# 31460, RRID:AB_228341) and anti-mouse (1:5000; Thermo Fisher Scientific Cat# G-21040, RRID:AB_2536527), conjugated with horseradish peroxidase (HRP). The membranes were developed with chemiluminescent substrate (ECL, PerkinElmer, Waltham, MA, USA), and the luminescence bands were captured in a high-resolution photodocumentation system (UVITEC Alliance 4.7, Cambridge, UK). The protein bands were analyzed by densitometry through evaluation of optical intensity using the Alliance software and normalized according each internal control band. Data are presented as the relative expression, comparing to control group.

4.4. mHtt Q74 Aggregation Assay

To quantify the number of aggregates per cell, the astrocytes were plated on 25-mm glass coverslips, and after transfection and/or treatment, the slides were observed. Images were acquired using an LSM 780—Axiovert 200 M confocal microscope (Carl Zeiss, Inc., Oberkochen, Germany) with a 63× oil immersion objective. For pEGFP-mHtt-Q74 visualization, excitation and emission, filters of 488/505–550 nm were used. ZenBlue Lite software (version 2.6) was used for data extraction. Approximately 10 images were acquired in each slide, and the fields were randomly chosen. These images were analyzed in relation to the number of aggregates that each cell presented.

4.5. Colocalization of mHtt-Q74 and TPC2 Receptor

To evaluate the colocalization of pEGFP-mHtt Q74 with RFP-TPC2 receptors, astrocytes were cultured in 25-mm glass coverslips and transfected with the mentioned plasmids. Live cells were observed with a confocal microscope (Zeiss LSM780 Axiovert 200 M, Carl Zeiss) in a 63× magnification. Images were acquired randomly from different locations, and the colocalization evaluation was performed in each cell separately. The analysis was performed using the software ZenBlue Lite software (ZEN Digital Imaging for Light Microscopy, RRID:SCR_013672, version 2.6, Carl Zeiss, Inc., Oberkochen, Germany), and the colocalization was calculated according to weighted colocalization coefficients. Excitation/emission: pEGFP-mHtt-Q74 (488/505 nm) and RFP-TPC2 (543/615 nm).

4.6. Statistical Analysis

Data are presented as mean ± standard error of the mean (SEM). All experiments were performed with a minimum of three independent replicates. Graphical representation, data and analysis were performed using GraphPad Prism (GraphPad Prism, Boston, MA, USA; RRID:SCR_002798), version 5.1, using one-way ANOVA followed by Tukey's post hoc or Bonferroni post hoc or Student's *t* test analysis. Differences between analyzed groups were considered significant when $p < 0.05$.

Author Contributions: Conceptualization, S.S.S., G.J.d.S.P., M.P. and G.M.F.; methodology, A.G.E., C.A.d.S.P., N.d.C.M., G.J.d.S.P. and M.A.; formal analysis, C.A.d.S.P. and N.d.C.M.; investigation, C.A.d.S.P. and N.d.C.M.; writing—original draft preparation, C.A.d.S.P. and A.G.E.; writing—review and editing, C.A.d.S.P., A.G.E., R.P.U., M.A., M.P. and G.M.F.; supervision, S.S.S., G.J.d.S.P., M.P., G.M.F., M.A. and C.B.; project administration, S.S.S. and G.J.d.S.P.; funding acquisition, S.S.S. and G.J.d.S.P. All authors have read and agreed to the published version of the manuscript.

Funding: This research was funded by Fundação de Amparo à Pesquisa do Estado de São Paulo (FAPESP): 2019/02821-8 (SSS); 2017/10863-7; 2019/14722-4 (GJSP); 2020/08840-1 (AGE); 2016/20796-2 (RPU). CASP gratefully acknowledges Coordenação de Aperfeiçoamento de Pessoal de Nível Superior (CAPES) for providing a scholar fellowship (code 001). Facilities from Instituto de Farmacologia e Biologia Molecular (INFAR/UNIFESP) were supported by FAPESP and Financiadora de Estudos e Projetos (FINEP). This study was partially supported by the Ministry of University Program HEALITALIA.

Institutional Review Board Statement: Not applicable.

Informed Consent Statement: Not applicable.

Data Availability Statement: The data that support the findings of this study are available from the corresponding author upon reasonable request.

Acknowledgments: We thank Elizabeth Naomi Kanashiro, Caroline Zito Romera, Ingrid Kazue Mizuno Watanabe, Marina Yukari Kubota, Cícero Ramos dos Santos, Maria de Lurdes dos Santos and Vanessa Christine Gusmão dos Santos for their technical assistance.

Conflicts of Interest: The authors declare no conflict of interest.

References

1. Pringsheim, T.; Wiltshire, K.; Day, L.; Dykeman, J.; Steeves, T.; Jette, N. The incidence and prevalence of Huntington's disease: A systematic review and meta-analysis. *Mov. Disord.* **2012**, *27*, 1083–1091. [CrossRef] [PubMed]
2. Cepeda, C.; Tong, X.P. Huntington's disease: From basic science to therapeutics. *CNS Neurosci. Ther.* **2018**, *24*, 247–249. [CrossRef]
3. Wyant, K.J.; Ridder, A.J.; Dayalu, P. Huntington's Disease-Update on Treatments. *Curr. Neurol. Neurosci. Rep.* **2017**, *17*, 33. [CrossRef]
4. Cortes, C.J.; La Spada, A.R. The many faces of autophagy dysfunction in Huntington's disease: From mechanism to therapy. *Drug Discov. Today* **2014**, *19*, 963–971. [CrossRef] [PubMed]
5. Snowden, J.S. The Neuropsychology of Huntington's Disease. *Arch. Clin. Neuropsychol.* **2017**, *32*, 876–887. [CrossRef] [PubMed]
6. MacDonald, M.E.; Ambrose, C.M.; Duyao, M.P.; Myers, R.H.; Lin, C.; Srinidhi, L.; Barnes, G.; Taylor, S.A.; James, M.; Groot, N.; et al. A novel gene containing a trinucleotide repeat that is expanded and unstable on Huntington's disease chromosomes. *Cell* **1993**, *72*, 971–983. [CrossRef] [PubMed]

7. Gusella, J.F.; Wexler, N.S.; Conneally, P.M.; Naylor, S.L.; Anderson, M.A.; Tanzi, R.E.; Watkins, P.C.; Ottina, K.; Wallace, M.R.; Sakaguchi, A.Y.; et al. A polymorphic DNA marker genetically linked to Huntington's disease. *Nature* **1983**, *306*, 234–238. [CrossRef]
8. Saudou, F.; Humbert, S. The Biology of Huntingtin. *Neuron* **2016**, *89*, 910–926. [CrossRef]
9. Jimenez-Sanchez, M.; Licitra, F.; Underwood, B.R.; Rubinsztein, D.C. Huntington's Disease: Mechanisms of Pathogenesis and Therapeutic Strategies. *Cold Spring Harb. Perspect. Med.* **2017**, *7*, a024240. [CrossRef]
10. Ross, C.A.; Tabrizi, S.J. Huntington's disease: From molecular pathogenesis to clinical treatment. *Lancet Neurol.* **2011**, *10*, 83–98. [CrossRef]
11. Jiang, R.; Diaz-Castro, B.; Looger, L.L.; Khakh, B.S. Dysfunctional Calcium and Glutamate Signaling in Striatal Astrocytes from Huntington's Disease Model Mice. *J. Neurosci.* **2016**, *36*, 3453–3470. [CrossRef] [PubMed]
12. Tang, T.-S.; Tu, H.; Chan, E.Y.; Maximov, A.; Wang, Z.; Wellington, C.L.; Hayden, M.R.; Bezprozvanny, I. Huntingtin and Huntingtin-Associated Protein 1 Influence Neuronal Calcium Signaling Mediated by Inositol-(1,4,5) Triphosphate Receptor Type 1. *Neuron* **2003**, *39*, 227–239. [CrossRef] [PubMed]
13. Suzuki, M.; Nagai, Y.; Wada, K.; Koike, T. Calcium leak through ryanodine receptor is involved in neuronal death induced by mutant huntingtin. *Biochem. Biophys. Res. Commun.* **2012**, *429*, 18–23. [CrossRef] [PubMed]
14. Vigont, V.; Kolobkova, Y.; Skopin, A.; Zimina, O.; Zenin, V.; Glushankova, L.; Kaznacheyeva, E. Both Orai1 and TRPC1 are Involved in Excessive Store-Operated Calcium Entry in Striatal Neurons Expressing Mutant Huntingtin Exon 1. *Front. Physiol.* **2015**, *6*, 337. [CrossRef] [PubMed]
15. Kaltenbach, L.S.; Romero, E.; Becklin, R.R.; Chettier, R.; Bell, R.; Phansalkar, A.; Strand, A.; Torcassi, C.; Savage, J.; Hurlburt, A.; et al. Huntingtin Interacting Proteins Are Genetic Modifiers of Neurodegeneration. *PLoS Genet.* **2007**, *3*, e82. [CrossRef]
16. Carmo, C.; Naia, L.; Lopes, C.; Rego, A.C. Mitochondrial Dysfunction in Huntington's Disease. In *Polyglutamine Disorders*; Advances in Experimental Medicine and Biology; Springer: Cham, Switzerland, 2018; Volume 1049, pp. 59–83. [CrossRef]
17. Rosenstock, T.R.; Bertoncini, C.R.; Teles, A.V.; Hirata, H.; Fernandes, M.J.; Smaili, S.S. Glutamate-induced alterations in Ca2+ signaling are modulated by mitochondrial Ca2+ handling capacity in brain slices of R6/1 transgenic mice. *Eur. J. Neurosci.* **2010**, *32*, 60–70. [CrossRef]
18. Luzio, J.P.; Pryor, P.R.; Bright, N.A. Lysosomes: Fusion and function. *Nat. Rev. Mol. Cell Biol.* **2007**, *8*, 622–632. [CrossRef]
19. Sardiello, M.; Palmieri, M.; Di Ronza, A.; Medina, D.L.; Valenza, M.; Gennarino, V.A.; Di Malta, C.; Donaudy, F.; Embrione, V.; Polishchuk, R.S.; et al. A Gene Network Regulating Lysosomal Biogenesis and Function. *Science* **2009**, *325*, 473–477. [CrossRef]
20. Korolchuk, V.I.; Saiki, S.; Lichtenberg, M.; Siddiqi, F.H.; Roberts, E.A.; Imarisio, S.; Jahreiss, L.; Sarkar, S.; Futter, M.; Menzies, F.M.; et al. Lysosomal positioning coordinates cellular nutrient responses. *Nat. Cell Biol.* **2011**, *13*, 453–460. [CrossRef]
21. Patel, S.; Docampo, R. Acidic calcium stores open for business: Expanding the potential for intracellular Ca2+ signaling. *Trends Cell Biol.* **2010**, *20*, 277–286. [CrossRef]
22. Patel, S. Deviant lysosomal Ca2+ signalling in neurodegeneration. An introduction. *Messenger* **2016**, *5*, 24–29. [CrossRef]
23. Medina, D.L. Lysosomal calcium and autophagy. *Int. Rev. Cell Mol. Biol.* **2021**, *362*, 141–170. [CrossRef] [PubMed]
24. Brailoiu, E.; Churamani, D.; Cai, X.; Schrlau, M.G.; Brailoiu, G.C.; Gao, X.; Hooper, R.; Boulware, M.J.; Dun, N.J.; Marchant, J.S.; et al. Essential requirement for two-pore channel 1 in NAADP-mediated calcium signaling. *J. Cell Biol.* **2009**, *186*, 201–209. [CrossRef] [PubMed]
25. Calcraft, P.J.; Ruas, M.; Pan, Z.; Cheng, X.; Arredouani, A.; Hao, X.; Tang, J.; Rietdorf, K.; Teboul, L.; Chuang, K.-T.; et al. NAADP mobilizes calcium from acidic organelles through two-pore channels. *Nature* **2009**, *459*, 596–600. [CrossRef] [PubMed]
26. Galione, A.; Evans, A.M.; Ma, J.; Parrington, J.; Arredouani, A.; Cheng, X.; Zhu, M.X. The acid test: The discovery of two-pore channels (TPCs) as NAADP-gated endolysosomal Ca2+ release channels. *Pflugers Arch.* **2009**, *458*, 869–876. [CrossRef] [PubMed]
27. Patel, S. Function and dysfunction of two-pore channels. *Sci. Signal.* **2015**, *8*, re7. [CrossRef]
28. Clapper, D.L.; Walseth, T.F.; Dargie, P.J.; Lee, H.C. Pyridine nucleotide metabolites stimulate calcium release from sea urchin egg microsomes desensitized to inositol trisphosphate. *J. Biol. Chem.* **1987**, *262*, 9561–9568. [CrossRef]
29. Lee, H.C.; Walseth, T.F.; Bratt, G.T.; Hayes, R.N.; Clapper, D.L. Structural determination of a cyclic metabolite of NAD^+ with intracellular Ca^{2+}-mobilizing activity. *J. Biol. Chem.* **1989**, *264*, 1608–1615. [CrossRef]
30. Zong, X.; Schieder, M.; Cuny, H.; Fenske, S.; Gruner, C.; Rötzer, K.; Griesbeck, O.; Harz, H.; Biel, M.; Wahl-Schott, C. The two-pore channel TPCN2 mediates NAADP-dependent Ca2+-release from lysosomal stores. *Pflugers Arch.* **2009**, *458*, 891–899. [CrossRef]
31. Pereira, G.J.S.; Hirata, H.; Fimia, G.M.; Do Carmo, L.G.; Bincoletto, C.; Han, S.W.; Stilhano, R.S.; Ureshino, R.P.; Bloor-Young, D.; Churchill, G.; et al. Nicotinic Acid Adenine Dinucleotide Phosphate (NAADP) Regulates Autophagy in Cultured Astrocytes. *J. Biol. Chem.* **2011**, *286*, 27875–27881. [CrossRef]
32. Pereira, G.J.S.; Hirata, H.; Do Carmo, L.G.; Stilhano, R.S.; Ureshino, R.P.; Medaglia, N.C.; Han, S.W.; Churchill, G.; Bincoletto, C.; Patel, S.; et al. NAADP-sensitive two-pore channels are present and functional in gastric smooth muscle cells. *Cell Calcium* **2014**, *56*, 51–58. [CrossRef] [PubMed]
33. Pereira, G.J.S.; Antonioli, M.; Hirata, H.; Ureshino, R.P.; Nascimento, A.R.; Bincoletto, C.; Vescovo, T.; Piacentini, M.; Fimia, G.M.; Smaili, S.S. Glutamate induces autophagy via the two-pore channels in neural cells. *Oncotarget* **2017**, *8*, 12730–12740. [CrossRef] [PubMed]

34. Naylor, E.; Arredouani, A.; Vasudevan, S.R.; Lewis, A.M.; Parkesh, R.; Mizote, A.; Rosen, D.; Thomas, J.M.; Izumi, M.; Ganesan, A.; et al. Identification of a chemical probe for NAADP by virtual screening. *Nat. Chem. Biol.* **2009**, *5*, 220–226. [CrossRef] [PubMed]
35. Gómez-Suaga, P.; Luzón-Toro, B.; Churamani, D.; Zhang, L.; Bloor-Young, D.; Patel, S.; Woodman, P.G.; Churchill, G.C.; Hilfiker, S. Leucine-rich repeat kinase 2 regulates autophagy through a calcium-dependent pathway involving NAADP. *Hum. Mol. Genet.* **2012**, *21*, 511–525. [CrossRef]
36. Djajadikerta, A.; Keshri, S.; Pavel, M.; Prestil, R.; Ryan, L.; Rubinsztein, D.C. Autophagy Induction as a Therapeutic Strategy for Neurodegenerative Diseases. *J. Mol. Biol.* **2020**, *432*, 2799–2821. [CrossRef]
37. Smaili, S.S.; Hsu, Y.-T.; Youle, R.J.; Russell, J.T. Mitochondria in Ca2+ signaling and apoptosis. *J. Bioenerg. Biomembr.* **2000**, *32*, 35–46. [CrossRef]
38. Orrenius, S.; Zhivotovsky, B.; Nicotera, P. Regulation of cell death: The calcium–apoptosis link. *Nat. Rev. Mol. Cell Biol.* **2003**, *4*, 552–565. [CrossRef]
39. Walseth, T.F.; Guse, A.H. NAADP: From Discovery to Mechanism. *Front. Immunol.* **2021**, *12*, 703326. [CrossRef]
40. Hockey, L.N.; Kilpatrick, B.S.; Eden, E.R.; Lin-Moshier, Y.; Brailoiu, G.C.; Brailoiu, E.; Futter, C.E.; Schapira, A.H.; Marchant, J.S.; Patel, S. Dysregulation of lysosomal morphology by pathogenic LRRK2 is corrected by TPC2 inhibition. *J. Cell Sci.* **2015**, *128*, 232–238.
41. Lee, J.H.; McBrayer, M.K.; Wolfe, D.M.; Haslett, L.J.; Kumar, A.; Sato, Y.; Lie, P.P.Y.; Mohan, P.; Coffey, E.E.; Kompella, U.; et al. Presenilin 1 Maintains Lysosomal Ca(2+) Homeostasis via TRPML1 by Regulating vATPase-Mediated Lysosome Acidification. *Cell Rep.* **2015**, *12*, 1430–1444. [CrossRef]
42. Pchitskaya, E.; Popugaeva, E.; Bezprozvanny, I. Calcium signaling and molecular mechanisms underlying neurodegenerative diseases. *Cell Calcium* **2018**, *70*, 87–94. [CrossRef] [PubMed]
43. Ureshino, R.P.; Erustes, A.G.; Bassani, T.B.; Wachilewski, P.; Guarache, G.C.; Nascimento, A.C.; Costa, A.J.; Smaili, S.S.; Pereira, G.J.D.S. The Interplay between Ca2+ Signaling Pathways and Neurodegeneration. *Int. J. Mol. Sci.* **2019**, *20*, 6004. [CrossRef] [PubMed]
44. Tang, T.S.; Slow, E.; Lupu, V.; Stavrovskaya, I.G.; Sugimori, M.; Llinás, R.; Kristal, B.S.; Hayden, M.R.; Bezprozvanny, I. Disturbed Ca2+ signaling and apoptosis of medium spiny neurons in Huntington's disease. *Proc. Natl. Acad. Sci. USA* **2005**, *102*, 2602–2607. [CrossRef] [PubMed]
45. Mackay, J.P.; Nassrallah, W.B.; Raymond, L.A. Cause or compensation?-Altered neuronal Ca^{2+} handling in Huntington's disease. *CNS Neurosci. Ther.* **2018**, *24*, 301–310. [CrossRef]
46. Chu, C.T. Mechanisms of selective autophagy and mitophagy: Implications for neurodegenerative diseases. *Neurobiol. Dis.* **2019**, *122*, 23–34. [CrossRef] [PubMed]
47. Cai, Q.; Ganesan, D. Regulation of neuronal autophagy and the implications in neurodegenerative diseases. *Neurobiol. Dis.* **2022**, *162*, 105582. [CrossRef]
48. Sarkar, S.; Rubinsztein, D.C. Huntington's disease: Degradation of mutant huntingtin by autophagy. *FEBS J.* **2008**, *275*, 4263–4270. [CrossRef]
49. Martin, D.D.; Ladha, S.; Ehrnhoefer, D.E.; Hayden, M.R. Autophagy in Huntington disease and huntingtin in autophagy. *Trends Neurosci.* **2015**, *38*, 26–35. [CrossRef]
50. Croce, K.R.; Yamamoto, A. A role for autophagy in Huntington's disease. *Neurobiol. Dis.* **2019**, *122*, 16–22. [CrossRef]
51. Wong, Y.C.; Holzbaur, E.L.F. The Regulation of Autophagosome Dynamics by Huntingtin and HAP1 Is Disrupted by Expression of Mutant Huntingtin, Leading to Defective Cargo Degradation. *J. Neurosci.* **2014**, *34*, 1293–1305. [CrossRef]
52. Erustes, A.G.; Stefani, F.Y.; Terashima, J.Y.; Stilhano, R.S.; Monteforte, P.T.; da Silva Pereira, G.J.; Han, S.W.; Calgarotto, A.K.; Hsu, Y.-T.; Ureshino, R.P.; et al. Overexpression of α-synuclein in an astrocyte cell line promotes autophagy inhibition and apoptosis. *J. Neurosci. Res.* **2018**, *96*, 160–171. [CrossRef] [PubMed]
53. Lajoie, P.; Snapp, E.L. Formation and Toxicity of Soluble Polyglutamine Oligomers in Living Cells. *PLoS ONE* **2010**, *5*, e15245. [CrossRef] [PubMed]
54. Karachitos, A.; Grobys, D.; Kulczyńska, K.; Sobusiak, A.; Kmita, H. The Association of VDAC with Cell Viability of PC12 Model of Huntington's Disease. *Front. Oncol.* **2016**, *6*, 238. [CrossRef] [PubMed]
55. Antonioli, M.; Albiero, F.; Nazio, F.; Vescovo, T.; Perdomo, A.B.; Corazzari, M.; Marsella, C.; Piselli, P.; Gretzmeier, C.; Dengjel, J.; et al. AMBRA1 Interplay with Cullin E3 Ubiquitin Ligases Regulates Autophagy Dynamics. *Dev. Cell* **2014**, *31*, 734–746. [CrossRef]

International Journal of
Molecular Sciences

MDPI

Article

Origin of Elevated S-Glutathionylated GAPDH in Chronic Neurodegenerative Diseases

Paul A. Hyslop [1,*], Leonard N. Boggs [1] and Michael O. Chaney [2,†]

[1] Arkley Research Laboratories, Arkley BioTek, LLC, 4444 Decatur Blvd., Indianapolis, IN 46241, USA; lboggs@arkleybiotek.com
[2] Eli Lilly Research Laboratories, Eli Lilly & Co., Lilly Corporate Center, Indianapolis, IN 46285, USA; chaney1643@comcast.net
* Correspondence: physlop@arkleybiotek.com
† Retired.

Abstract: H_2O_2-oxidized glyceraldehyde-3-phosphate dehydrogenase (GAPDH) catalytic cysteine residues (C_c(SH) undergo rapid S-glutathionylation. Restoration of the enzyme activity is accomplished by thiol/disulfide S_N2 displacement (directly or enzymatically) forming glutathione disulfide (G(SS)G) and active enzyme, a process that should be facile as C_c(SH) reside on the subunit surface. As S-glutathionylated GAPDH accumulates following ischemic and/or oxidative stress, in vitro/silico approaches have been employed to address this paradox. C_c(SH) residues were selectively oxidized and S-glutathionylated. Kinetics of GAPDH dehydrogenase recovery demonstrated that glutathione is an ineffective reactivator of S-glutathionylated GAPDH compared to dithiothreitol. Molecular dynamic simulations (MDS) demonstrated strong binding interactions between local residues and S-glutathione. A second glutathione was accommodated for thiol/disulfide exchange forming a tightly bound glutathione disulfide G(SS)G. The proximal sulfur centers of G(SS)G and C_c(SH) remained within covalent bonding distance for thiol/disulfide exchange resonance. Both these factors predict inhibition of dissociation of G(SS)G, which was verified by biochemical analysis. MDS also revealed that both S-glutathionylation and bound G(SS)G significantly perturbed subunit secondary structure particularly within the S-loop, region which interacts with other cellular proteins and mediates $NAD(P)^+$ binding specificity. Our data provides a molecular rationale for how oxidative stress elevates S-glutathionylated GAPDH in neurodegenerative diseases and implicates novel targets for therapeutic intervention.

Keywords: glutathione; oxidative stress; redox signaling; glyceraldehyde-3-phosphate dehydrogenase; hydrogen peroxide; neurodegenerative disease; molecular dynamic simulation

Citation: Hyslop, P.A.; Boggs, L.N.; Chaney, M.O. Origin of Elevated S-Glutathionylated GAPDH in Chronic Neurodegenerative Diseases. *Int. J. Mol. Sci.* **2023**, *24*, 5529. https://doi.org/10.3390/ijms24065529

Academic Editor: Claudia Ricci

Received: 2 January 2023
Revised: 30 January 2023
Accepted: 9 March 2023
Published: 14 March 2023

1. Introduction

Exposure of vulnerable cells to reactive oxygen species (ROS) such as H_2O_2 is being increasingly recognized as a common factor associated with the pathophysiology of vascular and neurodegenerative diseases. The redox signaling enzyme glyceraldehyde-3-phosphate dehydrogenase (GAPDH) is involved at multiple levels of redox signaling [1–8]. In a companion publication [9], we identified the mechanism through which H_2O_2 oxidizes GAPDH to a metastable signaling conformer via a two-cysteine switch. Initially, H_2O_2 selectively oxidizes the subunit catalytic cysteine residue C_c(SH) followed by oxidation of the vicinal cysteine C_v(SH) (four residues downstream) to their respective sulfenic acids $C_{c,v}$(SOH). The two sulfenic acids rapidly and irreversibly condense to form an interchain sulfinic ester, inducing an intrachain conformational strain resulting in a new metastable subunit conformer, which we propose forms pro-apoptotic signaling complexes with chaperone proteins [9] that translocate to the nucleus and mitochondria (reviewed in [10,11]).

The major cellular antioxidant thiol, glutathione (G(SH)), reversibly reacts with C_c(SOH) to form S-glutathionylated subunits, thereby blocking H_2O_2 oxidation of C_v(SH)

and the formation of the putative signaling conformer [9]. Reactivation of C_cS-glutathionylated subunits is accomplished by either S_N2 thiol-disulfide exchange by a second molecule of G(SH) or deglutathionylation by a family of G(SH) transferases such as glutaredoxin and thioredoxin. In a recent study [12], following H_2O_2 oxidation of *h*-GAPDH in vitro by the addition of 5 mM G(SH) in the absence and presence of glutaredoxin for 24 h, a modest increase in enzyme reactivation was observed compared to G(SH) on its own. In cellular models of redox stress, the formation of S-glutathionylated GAPDH and its subsequent reactivation has been reported [11,13–16]. S-glutathionylated GAPDH has been shown to translocate to the nucleus and initiate apoptotic signaling via the GAPDH/SitT1/p53 pathway [17]. S-glutathionylated GAPDH is also found in tissues following ischemia reperfusion or chronic neurodegenerative disease [1,18–20], and S-glutathionylated GAPDH in blood samples from patients with Alzheimer's disease (but not healthy controls) was elevated and this correlates with severity and disease progression [21].

In our companion study [9], we noted that the bimolecular rate constant for H_2O_2 oxidation of C_c(SH) located at the hydrophilic surface of the GAPDH subunits was no different from that of cysteine (~10 $M^{-1}s^{-1}$). The elevated C_cS-glutathionylated GAPDH observed after H_2O_2 oxidative stress thus cannot be directly attributable to the enhanced reactivity of GAPDH C_c(SH) to H_2O_2 and furthermore, subunit C_cS-glutathionylation would be expected to be readily reactivated by S_N2 thiol-disulfide exchange by both cellular G(SH) and by enzyme deglutathionylating G(SH) transferases.

For the above reasons, we designed this study with the primary goal of elucidating which factors might contribute to the persistence of S-glutathionylated GAPDH in various pathophysiological conditions. Using biochemical and in silico molecular dynamic simulations (MDS) with a subunit of the crystal structure of human GAPDH (1u8F), we established that the glutathione moiety of S-glutathionylated GAPDH at physiologically relevant intracellular conditions (pH 7, 37 °C and 1–5 mM G(SH)) undergoes S_N2 displacement by a second glutathione molecule and this process is kinetically unfavorable compared with enzyme activation of S-glutathionylated GAPDH with small alkyl thiols such as β-mercaptoethanol. We demonstrate that this observation can be attributable to tight binding interactions between charged and hydrogen donor/acceptor atoms of both glutathione and glutathione disulfide (G(SS)G) and local residues of the GAPDH subunits within the active site pocket. Both S-glutathionylation and accommodation of G(SS)G within the active site results in significant reversable conformational subunit rearrangement with pronounced changes in the cofactor and protein binding S-loop region [22] of the subunit downstream from the active site. Given the central role of GAPDH in energy metabolism and redox signaling, developing a more complete understanding of the biochemical mechanisms giving rise to modified GAPDH with S-glutathione and bound G(SS)G and the consequences thereof may assist in the discovery of novel therapeutic interventions for both acute and chronic vascular and neurodegenerative diseases.

2. Results

2.1. GAPDH Assay

GAPDH was assayed in this study using gluconeogenic substrates as the glycolytic substrate because (D or (DL) glyceraldehyde-3-phoshate (G3P) was unavailable from any vendor when we initiated the study. We encountered difficulty establishing reproducible linear "initial rates" of NADH oxidation in a microtiter plate format (kinetic and equilibrium barriers to substrate flux present in the gluconeogenic compared to glycolytic functions of GAPDH [23] contribute to assay complexity). Therefore, analytical modelling of dose response data for constructing standard curves were used and it yielded a monoexponential decay-to-plateau model, as shown in Figure 1A. The calculated NADH oxidation rate constants were directly proportional to the GAPDH concentration (Figure 1B) over the range required for the sample analysis and the slopes of the linear fit were not significantly different when measured over three separate days. Truncation of the data collection in 10 min segments from 60 min to 10 min did not significantly change the recalculated rate

constants (Figure 1C), and their associated SEM was numerically the smallest at 60 min (Figure 1D), so 60 min was adopted as the standard assay time. The exponential data modelling is useful in a microtiter plate format as the NADH oxidation decay constant for all samples is independent of the relative initiation time of the assay. Using the assay parameters described above, measurements of the interference of the thiols referenced in this study (Figure 1E) revealed that G(SH), cysteine, and dithiothreitol (DTT), had no significant interference when observed over the concentration ranges, while a small ~10% interference was observed with ~1.13 mM β-mercaptoethanol (BME).

2.2. Iodosobenzoic Acid (IOB) Oxidation of GAPDH

The selective oxidation of the active site cysteine residues, C_c(SH) in each subunit of the homotetramer of porcine GAPDH (*p*-GAPDH) results in thiol-reversible formation of stabilized sulfenic acids C_c(SOH), with full recovery of dehydrogenase activity [24]. The use of IOB for selective stoichiometric oxidation of C_c(SH) has been previously described [25]. Treatment of rabbit GAPDH (*r*-GAPDH) with IOB (8:1 mol IOB/mol *r*-GAPDH subunit) at RT for 10 min at pH 7.0 inactivated > 95% of dehydrogenase activity. Restoration of dehydrogenase activity following the removal of excess IOB by spin column buffer exchange (SCBE) was observed to be ~95% after incubation of the oxidized enzyme for at least 1 h following the initiation of oxidation, or after a freeze-thaw cycle prior to incubation with 1 mM DTT for 15 min (requirements for use of this concentration of DTT to achieve maximal enzyme reactivation are shown in Figure 1F).

2.3. Reaction of IOB-Oxidized GAPDH with G(SH)

After incubation of IOB-oxidized *r*-GAPDH with 1.2:1 mol G(SH)/mol GAPDH subunit for 10 min measurement of S-glutathionylated subunits using the Promega Glo assay (Methods and Materials) resulted in approximately four (3.7 ± 0.23, $n = 4$) mol G(SH)/mol. 100% recovery of GAPDH enzyme activity was observed after 15 min incubation with DTT (Figure 1A green bar), and as with the IOB-oxidized enzyme, recovery of the S-glutathionylated enzyme activity after DTT activation was not significantly different compared to the reference native GAPDH activity obtained prior to freeze-thaw.

Recovery of the dehydrogenase activity of S-glutathionylated *r*-GAPDH was demonstrated when incubated in the presence of 0–5 mM G(SH) in the presence or absence of 1 mM DTT for 15 min prior to the GAPDH assay (Figure 2A, red bars). The ability of glutathione to reactivate the dehydrogenase activity of the S-glutathionylated enzyme was augmented compared with DTT (Figure 2A, blue bars). At the highest concentration of G(SH), 42 ± 1.6% dehydrogenase activity was recovered compared with the activation of the IOB oxidized enzyme by 1mM DTT alone (Figure 2A, green bar). Surprisingly, the same post S-glutathionylation concentrations of G(SH) also impaired the ability of 1 mM DTT to dose-dependently reactivate the enzyme, as post-incubation with 5 mM G(SH) and 1 mM DTT only restored 65.2 ± 2.1% to that of DTT alone (Figure 2A, blue bars).

The addition of 1 mM G(SH) $\pm$ 1 mM DTT following S-glutathionylation of oxidized GAPDH was assessed at various time intervals for 1h. The data in Figure 2B shows that incubation with G(SH) $\pm$ 1 mM DTT over 60 min resulted in a time-dependent increase in recovery of dehydrogenase activity. The kinetics of post S-glutathionylated enzyme activity recovery in the presence of 1 mM G(SH) $\pm$ DTT was sluggish, such that at 60 min, only 35.6 ± 2.6% and 69.1.6% was observed $\pm$ DTT, respectively. The approximate intracellular physiological conditions under which reduction of S-glutathionylated of GAPDH by G(SH) would be expected should be in the range of ~ 0.5–5 mM G(SH), pH 7, 37 °C. This demonstrates that, at least with respect to the major intracellular thiol-disulfide S_N2 exchange reaction by G(SH), GAPDH glycolytic activity is compromised after H_2O_2 oxidative stress by slow S-deglutathionylation. Since the low-mw dithiol, DTT was less effective at reactivating S-glutathionylated enzyme in the presence of G(SH) than in its absence, this indicates that steric factors may be responsible for these observations.

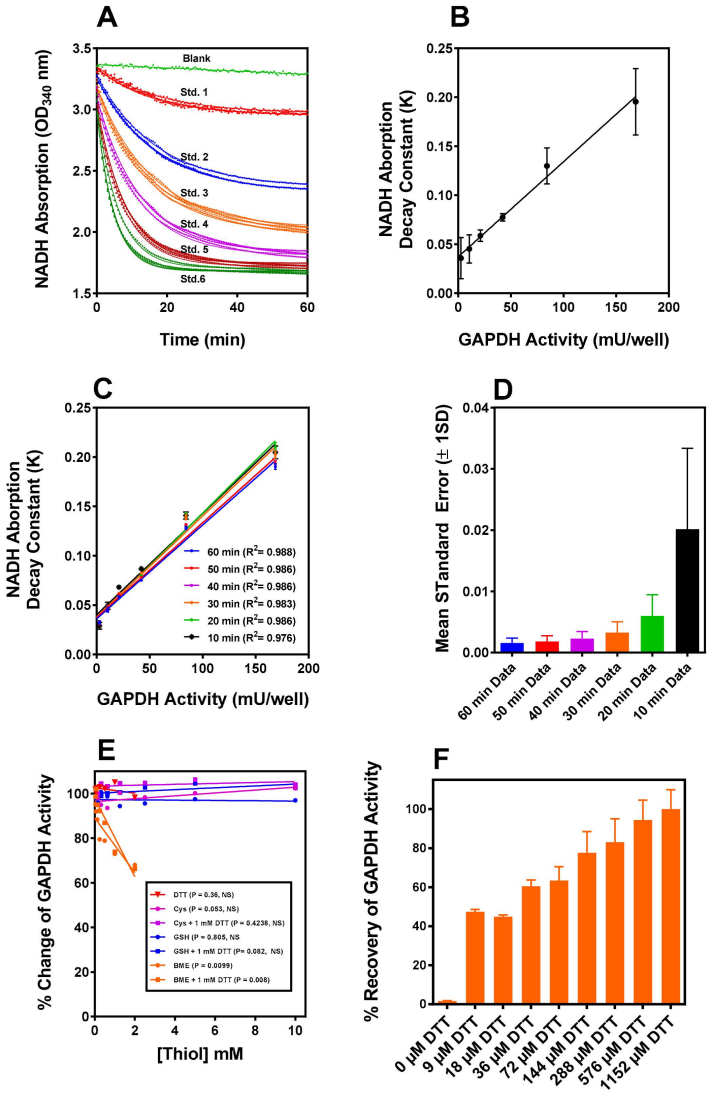

Figure 1. (**A**) The gluconeogenic enzyme GAPDH assay standard curve data generated by following the decrease in NADH absorption over a 60 min time window in the assay coupled to 3-PGA kinase phosphorylation of 3-PGA. The absorption decrease in the absence of GAPDH (blank) was first fitted using linear regression. The interpolated values at each timepoint were added to all concentrations of GAPDH data points from the standard curve and the samples to be measured. (**B**) First, all data sets were corrected for the time-dependent decrease in absorption of the blanks. The data were fitted to a monoexponential decay measured on three separate days. The rate constants calculated from the data in panel (**A**) are directly proportional to the amount of enzyme in the assay in the three experiments, and the slopes are not significantly different. (**C**) As a test of the validity of the data fit model, the 60 min data were truncated in steps of 10 min and the results each successive truncation plotted. (**D**) The SEM's for the rate constants for each truncation obtained from the exponential fit successively declined from a maximum at 10 min to a minimum at 60 min, demonstrating that the data modeling is robust. The value of the exponential rate constant is independent of the assay start time, convenient for manual multiwell microtiter plate kinetic assays. (**E**) The four thiols used in this assay (DTT, BME, G(SH), and Cysteine) are examined for interference in the GAPDH assay. BME interference is observed and noted at concentrations used in the study. (**F**) IOB oxidized GAPDH is reactivated by DTT at various concentrations. Reactivation by 500 µM DTT does not significantly differ from full activation at 1 mM used to assess the % recovery of oxidized GAPDH under various experimental conditions.

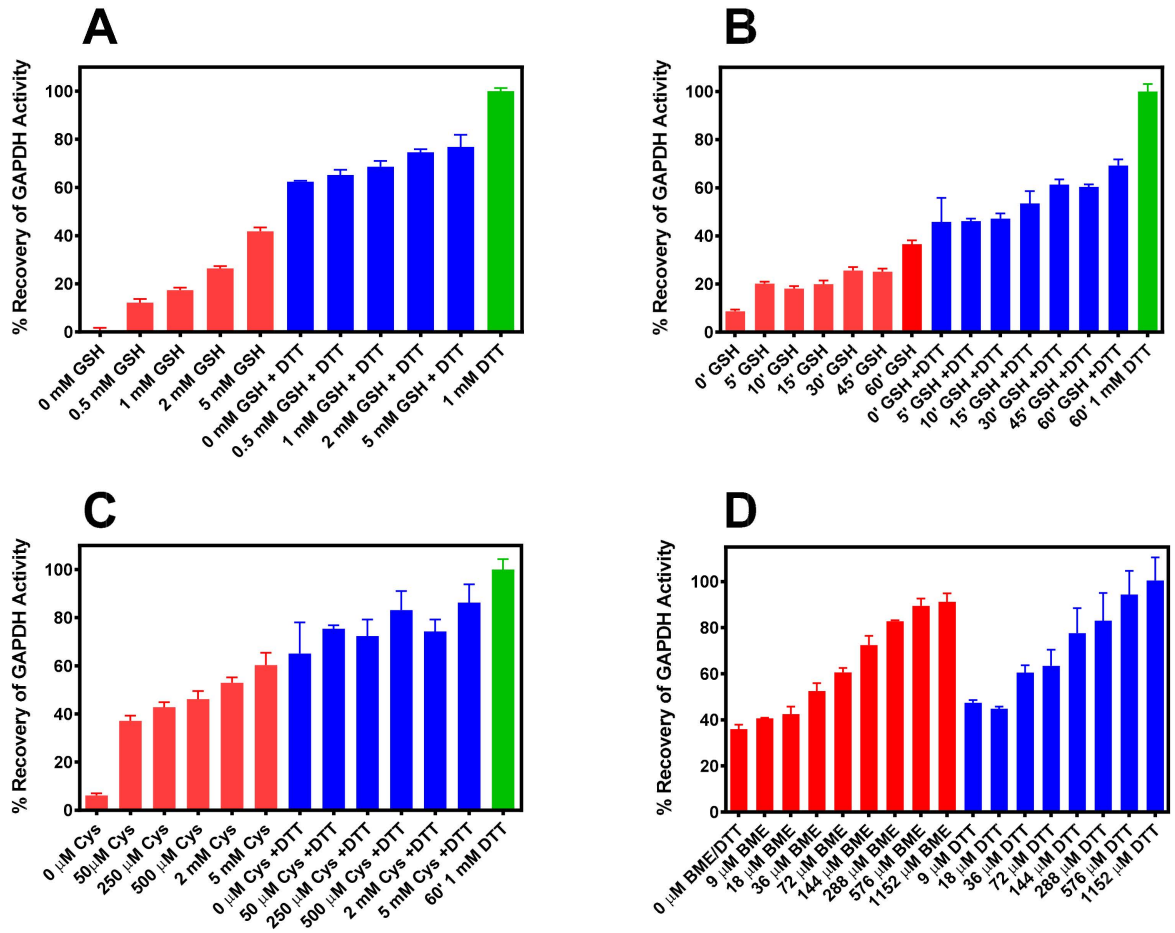

Figure 2. (**A**) Dose response for reactivation of S-glutathionylated GAPDH by G(SH) in the absence (red bars) and presence of 1 mM DTT (blue bars). (**B**) Time course of reactivation of S-glutathionylated GAPDH by 1 mM G(SH) in the absence (red bars) and presence of 1 mM DTT (blue bars). (**C**) Dose response of reactivation of S-cysteinylated GAPDH by cysteine in the absence (red bars) and presence of 1 mM DTT (blue bars). (**D**) Dose response of reactivation of S-mercaptoethanolylated GAPDH by either BME in the absence (red bars) and DTT (blue bars). The data (Mean ± SD, n = 3) are from representative experiments. The green bars in Panels **A**, **B** and **C** represent incubation without G(SH) in the presence of 1 mM DTT.

2.4. Reaction of IOB-Oxidized GAPDH with Cysteine

Qualitatively, similar results were observed following S-cysteinylation of IOB oxidized GAPDH. However, in a post incubation experiment for 15 min with varying concentrations of cysteine ± DTT recovery of S-cysteinylated GAPDH activity was more effective than that observed with G(SH) (Figure 2C). Incubation with 5 mM cysteine restored S-cysteinylated enzyme activity by 60.3 ± 5.15% (Figure 2C red bars. When 1 mM DTT was included in the incubation with cysteine 86.2 ± 2.6% of dehydrogenase activity were recovered (Figure 2C blue bars).

2.5. Reaction of IOB-Oxidized GAPDH with BME and DTT

A dose response study using S-mercaptoethanolated GAPDH was performed with a 15 min. post-incubation with various concentrations of BME or DTT prior to assay (Figure 2D). Recovery of GAPDH activity was significantly increased at lower concentrations of BME or DTT than with either G(SH) or cysteine. 1.152 mM BME (Figure 2D, red bars) restored enzyme activity to levels expected allowing for the small inhibitory effect of BME at the highest concentration observed in Figure 1E, while DTT (Figure 2D blue bars) fully restored GAPDH. A 50% reactivation of enzyme activity was achieved at

~36 μM by both BME and DTT. These latter experiments confirm that both S-glutathionylated and S-cysteinylated GAPDH are resistant to reduction by the two ubiquitous intracellular thiols, G(SH) and cysteine. This observation is particularly relevant to G(SH), because S-glutathionylated GAPDH has been consistently observed in pathological conditions as noted in the introduction section.

2.6. Molecular Dynamic Simulations of G(SH) Docking in the Active Site of Oxidized GAPDH

The crystal structure of an isolated subunit of human GAPDH (*h*-GAPDH) PDB 1u8F was used for in silico analysis, with C152(C_cSH) converted to C152(SOH) using the MOE builder utility. A molecule of glutathione (ligand) was placed in the vicinity of C_c152(SOH), and energy minimized. After 100 ps of molecular dynamics, the structure was annealed, and energy minimized (MDS). The resulting ligand-receptor interactions, the type of interaction, with atomic distances and interaction energies (ΔE) for NAD^+ and G(SH) are listed in Supplementary Tables S1A and S2A, top panel. The 2D representation of the docked ligand is shown in Figure 3A. The relationship between the ligand-receptor value of ΔE and its binding affinity (K_a) is complex (the value of ΔE computed within MOE is a thermodynamic quantity (Methods and Materials) whereas K_a is measured directly from the kinetic equilibrium ($K_a = k_{on}/k_{off}$). It is useful to compare ΔE obtained for G(SH) with that of the NAD^+ cofactor obtained using the same MOE algorithms within the native subunit as a comparator shown in Supplementary Table S1A. The intracellular concentrations of G(SH) and NAD^+ are within the same order of magnitude and both values of ΔE are comparable and the values of K_a for NAD^+ are between 10^{-11} and 10^{-5} M (see Ref. [26]). This indicates that G(SH) is tightly bound within the active site of the enzyme.

The introduction of G(SH) (ligand) into the active site increased the total ΔE for NAD^+ (ligand) and GAPDH between the non-bonded ligand hydrogen atoms and atoms of the local side chains, the polypeptide backbone of the subunit, and solvent increased from −60.5 kcal/mol to −73.2 kcal/mol (Supplementary Tables S1B and Table 1. The G(SH) molecule docked with its sulfur atom at a distance of 4.4 Å (Figure 3A) from the sulfur atom of C152(SOH), within van der Wall's radius for disulfide bond formation ≤ (4.9 Å). The individual ligand bonding energies are shown in Supplementary Table S2A, top panel, with the total ΔE = −77.2 kcal/mol (Table 1). These factors indicate that the docking of glutathione within the proximity of C_c152(SOH) orients the glutathione sulfur atom for nucleophilic attack on C152(SOH) for the formation of mixed disulfide.

2.7. Molecular Dynamic Simulations of Atomic Interactions of S-Glutathione within the Active Site

In the next step, the disulfide bond between the docked glutathione sulfur and C_c(SOH) sulfur was formed within the MOE builder utility and was subject to a second round of MDS and energy minimization. The resulting NAD^+ and S-glutathione moiety interaction binding energies within the active site are shown in Supplementary Tables S1C and S2A, bottom panel, respectively. The total ΔE for NAD^+ docking (Table 1) decreased to −43 kcal/mol, while the total ΔE docking for the docked S-glutathione moiety was 44.3 kcal/mol (Table 1). The 2D representation of the interactions between the S-glutathione moiety and the active site region is shown in Figure 3B.

2.8. Molecular Dynamic Simulations of the Atomic Interactions within the Active Site after Introducing a Second Molecule of G(SH)

A second molecule of glutathione was readily accommodated within the locality of the S-glutathionylated subunit within MOE. After MDS and energy minimization as before, the two glutathione molecules aligned in an anti-parallel formation with respect to each other, with their sulfur centers at 3.56Å, within the van der Waals distance for disulfide bond formation. The G(SH) and the S-glutathionylated moiety and active site residue individual bond ΔE values are listed in Supplementary Table S2B in the top and bottom panels, respectively. The individually calculated total ΔE for the docking of G(SH) and for

local interactions for the S-glutathione were 55.0 kcal/mol and 68.1 kcal/mol, respectively (Table 1).

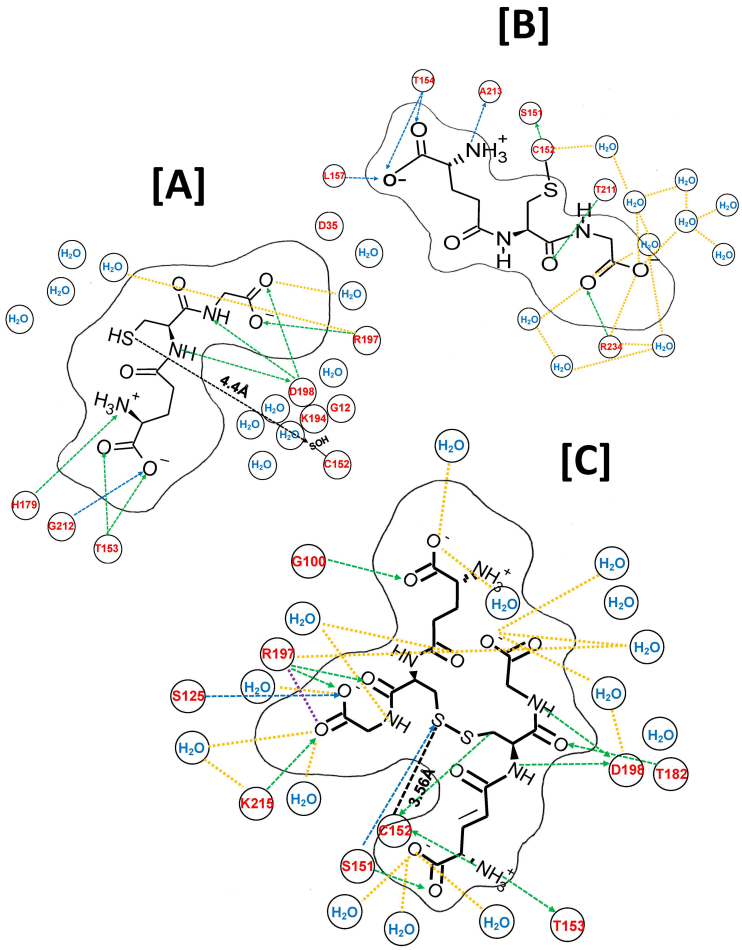

Figure 3. MDS ligand interactions within and around the active site of an isolated subunit of solvated *h*-GAPDH (1u8F) represented in two dimensions. (**A**) A catalytic cysteine residue (C152(SH) GAPDH subunit is converted to C_c(SOH), the initial step of the oxidation of GAPDH by H_2O_2 and a molecule of G(SH) is added to the model. After MDS, the G(SH)-C152(SH) sulfur-sulfur are separated by 4.4 Å, within range of the disulfide bond formation. The H-bond donor and acceptor network are shown in green and blue dotted lines, and the bond lengths are obviously distorted by a 2D rendering. The atomic bond distances and interaction energies are tabulated in Supplementary Tables S1 and S2. The solid black line delineates the van der Walls molecular cross section of G(SH). (**B**) S_N2 nucleophilic attack by G(SH) on sulfenic acid is simulated by the formation of the disulfide bond in MOE, forming C152S-glutathione. (**C**) A second molecule of G(SH) is placed within the active site pocket, and after MDS it is docked in an antiparallel alignment with C152 S-glutathione. S_N2 nucleophilic attack by G(SH) on the S-glutathionylated structure forms a docked G(SS)G ligand and reducesC152(SH) with their nearest sulfur-sulfur distance of 3.56 Å, such that the three sulfurs atoms can undergo thiol-disulfide exchange resonance.

2.9. Molecular Dynamic Simulations of the Atomic Interactions within the Active Site after Breaking the GAPDH S-Glutathione Mixed Disulfide Bond and Formation of Cystine (G(SS)G

The S-glutathione disulfide bond was broken and reformed between the two G(SH) molecules, simulating the S_N2 displacement reaction. This was followed by a third round of MDS and energy minimization. The resulting 2D structure is shown in Figure 3C. The types of interaction, with atomic distances and interaction energies for NAD^+ and G(SS)G) are shown in Supplementary Tables S1D and S2C, respectively. The calculated total ΔE for

NAD^+ was −44.1 kcal/mol, while the ΔE for the docked G(SS)G ligand and local amino acid residues was −85.3 kcal/mol (Table 1).

Table 1. Total interaction energies (ΔE) between all G(SH), G(SS)G, and NAD^+ and the local active site polypeptide backbone and side chain atoms within the GAPDH active site region summarized from Supplementary Tables S1 and S2.

Total Ligand Interaction Energies (ΔE kcal/mol)	NAD^+	G(SH) or G(SS)G
Native GAPDH	−60.5 kcal/mol	-
G(SH) docked in active site with C_c(SH) oxidized to C_cS(OH)	−73.2 kcal/mol	−77.2 kcal/mol
S-glutathionylated C_c(SS)G	−43.0 kcal/mol	−44.3 kcal/mol
G(SH) interactions docked for S_N2 attack on C_c(SS)G	Not calculated	−55.6 kcal/mol
C_c(SS)G interactions with G(SH) docked for S_N2 attack by G(SH)	Not calculated	−68.1 kcal/mol
Glutathione disulfide G(SS)G docked in active site	−44.1 kcal/mol	−85.3 kcal/mol

The sulfur-sulfur distances between the proximal G(SS)G sulfur atom and C_c152 sulfur atom was 3.56 Å, well within the van der Wall's sulfur-sulfur covalent bonding distance (Figure 3C). These observations indicate that the docked G(SS)G and C_c152 can theoretically participate in S_N2 disulfide exchange resonance. The combination of the G(SS)G binding interactions and thiol-disulfide exchange are likely to inhibit dissociation of G(SS)G from the subunit active site and provides an explanation for why G(SH) is a relatively poor reactivator of S-glutathionylated GAPDH.

2.10. Molecular Dynamic Simulations of Cysteine Docking in the Active Site of Oxidized GAPD

If atomic interactions within the active site of GAPDH participate in the slow deglutathionylation process (at least by a thiol-disulfide exchange mechanism), then if the relative atomic interactions within the active site of the enzyme after accommodation of a cysteine molecule follow a similar pattern as G(SH), this would add credence to the hypothesis.

Because of time and resource constraints, fewer parameters were explored with cysteine than with G(SH). After placement of a cysteine molecule within the active site region of *h*-GAPDH with C152 oxidized to C152(SOH), following a round of MDS and energy the total binding interactions between cysteine and atoms within the active site was −22.6 kcal/mol/ (Supplementary Table S3A). After forming the mixed disulfide bond within MOE, the total interaction energies between the S-cysteinylated moiety and the local active site atoms were −23.8 kcal/mol (Supplementary Table S3B). After breaking the S-cysteinylated mixed disulfide bond and forming cystine (C(SS)C), the atomic interaction energies between the dipeptide and local active site atoms increased to −97.1 kcal/mol (Supplementary Table S3C), indicating that as with G(SS)G), C(SS)C was also tightly bound within the active site of GAPDH.

2.11. Measurement of Time-Dependent S-glutathionylated and Non-Covalently Bound G(SH) and G(SS)G to GAPDH

To provide biochemical support for the above conclusions drawn from MDS calculations, IOB oxidized S-glutathionylated *r*-GAPDH was incubated with 1 mM G(SH) for a total 75 min, and samples withdrawn from the incubation very 15 min. Samples were analyzed after SCBE to remove non-GAPDH associated G(SH) and G(SS)G). Denaturation of the sample in the upper chamber of the Microcon® ultrafiltration device allows centrifugal separation of the S-glutathionylated GAPDH remaining in the retentate, while Non-Covalently bound G(SH) and G(SS)G associated with GAPDH can flow through into the eluate. The ratios of oxidized and reduced G(SH) in the samples were then assessed using the Promega Glo assay described in Methods and Materials.

The results are shown in Figure 4 and the measured versus calculated values for the parameters are described in the figure legend. The S-glutathionylation of GAPDH subunits declined over time, whereas bound G(SH) and G(SS)G increased after ~10–15 min incubation with 1 mM G(SH) and then remained relatively constant over the time course of the experiment, which is reflected in the total bound [G(SH)] (Figure 4 top red filled circles), and is calculated as follows: (i) denatured S-glutathionylated GAPDH in the washed retentate and (ii) plus total [G(SH)] + 2 × [G(SS)G] recovered in the eluate. If the assumption is made that the enzyme activity is completely abolished when each GAPDH subunit active site harbors two molecules of G(SH (or 1 molecule of G(SS)G), it is enzymatically inactive; this assumption is consistent with the data obtained in Figure 1A,B. The experimental data indicate that when subunit active sites harbors a tightly bound molecule of G(SS)G or two molecules of tightly bound G(SH) the enzyme activity is inactivated. This may also be true of a single molecule of bound G(SH) in the native enzyme, although this seems unlikely as incubation of native GAPDH with up to 10 mM G(SH) (Figure 1E) had no effect on enzyme activity.

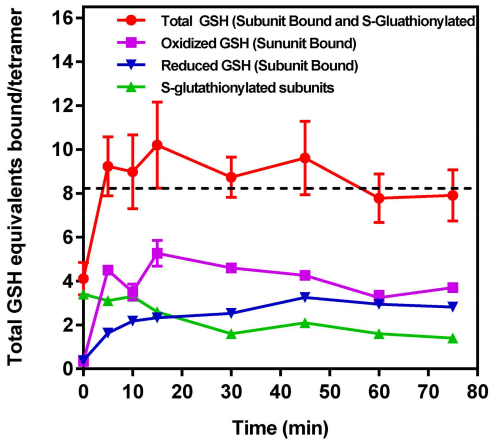

Figure 4. Distribution of S-glutathionylated and bound G(SH) and G(SS)G as a function of time of incubation with 1 mM G(SH). G(SH) and G(SS)G were measured using the Promega oxidized/reduced protocol and reagent kit. (a –▲–) Time course of the decline in total mol of S-glutathionylated subunits GAPDH/mol tetramer measured following the removal of all unbound G(SH) and G(SS)G after subunit denaturation and washing in the retentate following Microcon® spin separation (see text for details). (b –▼–) Time course of unbound reduced G(SH) recovered and measured in the eluate following Microcon® spin separation. (c –■–) Time course of unbound G(SS)G recovered and measured in the eluate following Microcon® spin separation. Note: the data represents 2 mol equivalents of G(SH) derived from 1 mol equivalent of G(SS)G in the Promega protocol). (d –●–) The total number of G(SH) equivalents bound to GAPDH over the time course of the incubation of S-glutathionylated GAPDH with 1 mM G(SH) is shown as the sum of measurements. (a), (b), (c) The associated cumulative SD of the triplicate samples. The black dashed line represents the theoretical maximal G(SH) binding capacity of the four active sites within the GAPDH tetramer. The data show the combined mean values ± SD from two separate experiments with technical triplicates.

This was also true when the native enzyme was pre-incubated with 1 mM G(SS)G for 60 min and was assayed with 1 mM G(SS)G in the assay buffer (Supplementary Figure S1), indicating that G(SS)G cannot bind to the native enzyme, so presumably the conformational rearrangement induced when G(SS)G forms within the active site allows for G(SS)G to dissociate and leave, but not to re-enter when the subunit is restored to its native state.

2.12. Comparison of Secondary Structural Motifs of S-Glutathionylated GAPDH

The entire subunit secondary structure of an S-glutathionylated subunit and one with G(SS)G) bound to the active site of *h*-GAPDH were compared to that of a native subunit. GAPDH subunits are broadly characterized as comprising two domains. The

full 2D sequence alignment of the structural motifs (α-helix, β-sheet, turns, and random coil) are shown linearized in Supplementary Figure S2 (NAD^+ domain) and Supplementary Figure S3 (catalytic domain). A common distinct feature of the comparisons with the native enzyme shows that several α-helical domains within the subunit are interrupted with turns. The results of the sequence alignment superposition matrix of the pairwise RMSD (root mean square distance) of the relative α-carbon atom coordinates showed modest (4–6 Å) perturbations within the NAD^+ binding domain. A major perturbation (7.5–13 Å) was observed within the S-loop (residues 180–203) of the catalytic domain, presumed to interact with cellular proteins [22], and it is also responsible for conferring NAD(P)+ selectivity [27]. Truncated data from Supplementary Figure S3 are shown in Figure 5 for emphasis, and the overall structural ribbon superpositions of the subunit are shown in Figure 6, depicting the S-loop region, showing the short α-helix (W196–G199) in the native subunit converted to turns in the two other superpositions. The calculated averaged RMSD values for all of the amino acids in the subunits perturbed by S-glutathionylation when compared with the native was 2.72 Å, while subunits perturbed by the accommodation of bound G(SS)G was 3.06 Å. The calculated averaged RMSD values for all amino acids comparing the perturbations of subunits S-glutathionylated and G(SS)G decreased to 1.36 Å. While there are secondary structural differences induced by S-glutathionylated subunits and subunits with bound G(SS)G from the inspection of Supplementary Figures S2 and S3, a commonality they share is that they both induce a major perturbation in the S-loop region, evident in Figure 6.

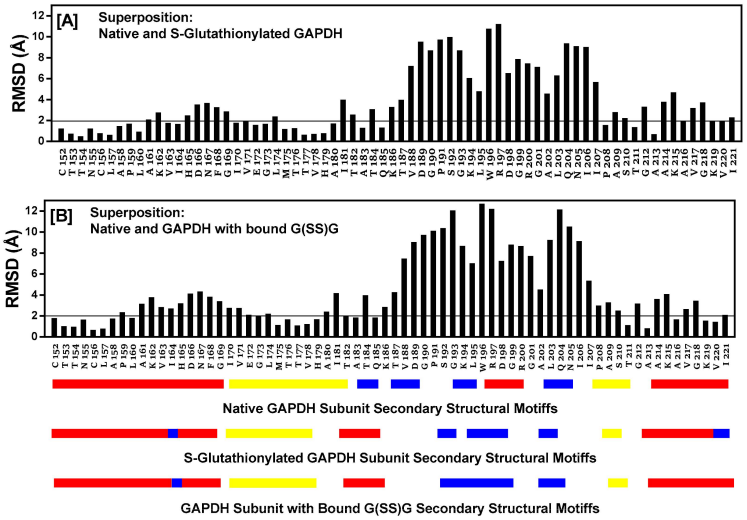

Figure 5. The protein sequence alignment and structure superposition tool in MOE is used to align the native *h*-GAPDH subunit structure with the output from MDS, and the energy minimizes subunit structures for C152S-glutathionylated subunit (Panel [**A**]) and the native *h*-GAPDH subunit structure with the output from MDS and the energy minimizes subunit structure for G(SS)G subunit docked within the active site (Panel [**B**]). The figure shows a truncated version of the full 335-amino acid sequence data shown in Supplementary Figures S2 and S3, to emphasize the region of greatest perturbation and includes all residues in the S-loop region of the subunit (residues 180–203). The root mean square distance (RMSD) for each alignment column (i.e., residue pair) used during the superposition. The RMSD value is represented by a black vertical bar above the pairwise aligned sequences. Closely matching RMSD values are highlighted by a horizontal line cutoff below 2.0 Å, while a larger RMSD excursion (5–13 Å) indicates poor atomic coordinate superposition. The linearized secondary structural features the following: Red α-helix; yellow β-sheet; and blue 2-5 residue turns; while no color is random coil for the three structure superpositions shown below Panel [**B**].

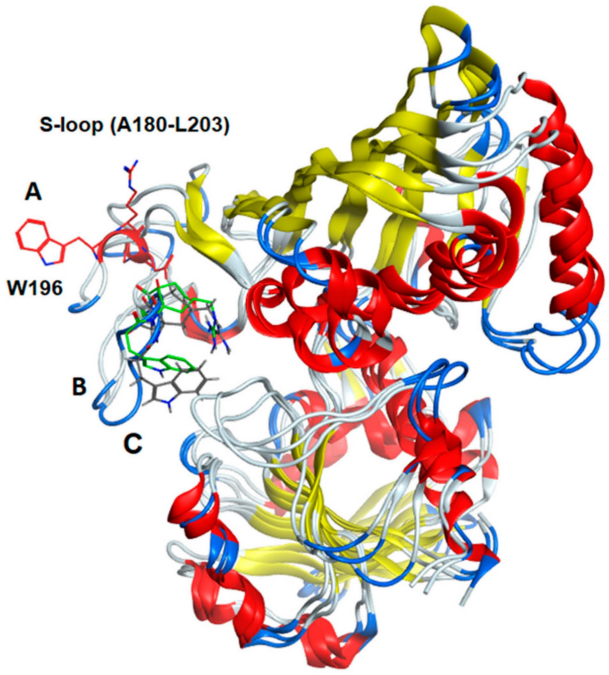

Figure 6. Ribbon diagram of the superimposed subunit structures of GAPDH (**A**) native, (**B**) S-glutathionylated, and (**C**) a subunit with tightly bound G(SS)G in the active site. The figure shows the clear transposition of the S-loop region (residues A180–L203) using of the two modified subunits compared to the native enzyme. The indole side chain of tryptophane W196 is shown as a visual marker for the residue displacement (native subunit is red, S-glutathionylated subunit is green, subunit with G(SS)G bound is black). The short α-helix (W196–R200) in the native subunit is converted to coil and turns in the modified subunits. The S-loop region is of interest because it is a site of protein binding and also mediates $NAD(P)^+$ cofactor binding selectivity.

3. Discussion

Full recovery of the enzyme activity of S-glutathionylated GAPDH was achievable with excess DTT after a 60 min incubation at 37 °C, pH 7, both before and after a freeze-thaw cycle, indicating that any subunit secondary structural perturbations induced by S-glutathionylation or by the accommodation of G(SS)G within the active site pocket were reversible. We used iodosobenzoic acid (IOB) to selectively oxidize C_c(SH) [25], rather than H_2O_2, to avoid the complications introduced by more complex oxidation mechanisms of C_v(SH) and the associated irreversible enzyme activation [9]. The relative ability of thiols to partially reactivate GAPDH activity oxidized with H_2O_2 was first observed to be in the order of G(SH) >>cysteine >BME/DTT [28], and our data are consistent with this result and serve to illustrate that full enzyme activity is recoverable when IOB rather than H_2O_2 is used to oxidize C_c(SH).

The interaction of the S-glutathionylated moiety in GAPDH from *Arabidopsis thalania* with local active site residues was first noted by Zafaginini et al. [29] using infusion of GAPDH crystals with H_2O_2 and G(SH), and again with the caveat that H_2O_2 was used rather than a selective oxidizing agent, provides support for our ab initio MDS analysis and interpretation of S-glutathionylated *h*-GAPDH. An intriguing observation revealed by MDS is that following S_N2 displacement of S-glutathione by a second molecule of G(SH), inhibition of the dissociation of G(SS)G from the active site may be augmented by the additional binding interactions of the glutathione hexapeptide, and also by the proximity of its sulfur atom closest to C_c152, creating a thiol-disulfide exchange resonance between the protein and the hexapeptide atoms. While the limitations of interpreting ΔE in terms of binding affinity are well known, the value obtained for the G(SS)G interaction with the active site of GAPDH (~90 kcal/mol) indicates relatively tight binding. We demonstrate that the results and conclusions drawn from the MDS data are recapitulated

experimentally in vitro, as S-glutathionylation of *r*-GAPDH incubated with 1 mM G(SH) reduced S-glutathionylated subunits over a 75 min incubation with the appearance of non-covalently bound G(SS)G and G(SH), as predicted.

Reversible secondary structural changes induced by S-glutathionylation were first demonstrated by Barinova et al. [12] through measurement of the relative thermal stabilities. Again, H_2O_2 was used as the oxidizing agent and so the complexity of the interpretation of the data with the native enzyme must be considered. However, smaller, but significant, structural perturbations were also observed in the same study when the C156S mutated enzyme was oxidized by H_2O_2 in the presence of G(SH) (where H_2O_2 oxidation of C156 is absent), providing a more direct biochemical validation of our MDS data.

GAPDH modified by S-glutathionylation and bound G(SS)G) are of interest because of the potential for the stabilized modified subunits to interact with cognate partner proteins involved in redox signaling. An analysis of the secondary structure and pairwise amino acid alignment of native *h*-GAPDH and modified with either S-glutathione or bound G(SS)G within the active site region revealed that significantly large perturbations in the secondary structure were especially apparent in the S-loop region (residues A180–L203) containing the short α-helix (W196–R200). The large perturbed relatively unstructured loop protrudes out from the center of the subunits and thus perturbation in this region is a potential site for binding the intracellular cognate partner proteins involved in the redox signaling pathways [22].

On the one hand, S-glutathionylation of partially oxidized GAPDH by H_2O_2 buffers further H_2O_2 oxidation of C_v(SH), preventing irreversible enzyme activation and the adoption of its redox signaling conformer [9]. On the other hand, S-glutathionylation of GAPDH is comprised of glycolytic flux. In a cellular model of H_2O_2 oxidative stress, inhibition of glycolysis was observed to contribute to the depletion of intracellular ATP, which was almost entirely accounted for by GAPDH inactivation [30]. The cellular inactivation was a result of both irreversible and reversible (S-glutathionylation) enzyme inactivation, as well as of a decrease in NAD^+ [31–33]. The physiological significance of S-glutathionylated GAPDH and GAPDH with bound (G(SS)G identified in this study is difficult to evaluate and obviously requires further investigation. In addition, it is likely to be dependent many factors, including the type and of tissue, species and duration of redox stressor (other ROS, nitric oxide etc.), prevailing intracellular G(SH) levels, relative contributions of enzymatic deglutathionylation, and almost certainly many other factors.

The persistence of S-glutathionylated GAPDH has consistently been observed in cellular models of oxidative stress and in tissues from chronic degenerative diseases (introduction). Neurons are particularly dependent on both extracellular glucose and glial-derived glucose and lactate to provide just enough metabolic energy to meet the demand. Inhibiting glycolysis at the triose phosphate step reduces the overall cellular energy charge [30,34] by decreasing mitochondrial substrate availability and by the non-productive consumption of ATP following the phosphorylation of glucose transported into the cell [30]. This is significant because falling neuronal ATP levels disrupt both cytoskeletal organization [35] and integrin-mediated adhesion to the extracellular matrix [36], processes that may contribute to initiating neurodegenerative disease. The pathophysiological reason(s) for the persistence of S-glutathionylated GAPDH is certainly worthy of further investigation, particularly because of its potential impact on vulnerable ischemia intolerant post-mitotic neurons.

At least with respect to non-enzymatic deglutathionylation, our experimental results show (at least in part) the biochemical reasons why S-glutathionylated GAPDH is observed in the tissues and plasma in both acute and chronic degenerative diseases, and we postulate that enzymatic deglutathionylation may also be augmented for the same reasons, but this remains to be investigated and highlights the need to explore the origins and consequences of redox signaling for the identification of novel therapeutic targets to mitigate the devasting impact of chronic neurodegenerative diseases [3,5].

4. Methods and Materials

4.1. GAPDH Sample Preparation and Oxidation

Rabbit GAPDH (Sigma; Cat No. G2267, St. Louis, MO, USA) was prepared fresh as needed for all of the experiments detailed in this work, using the methods below. First, the dry powder was reconstituted at ~1 mg/mL in 1 mM DTT and 1 mM NAD^+ in deionized water and incubated for 30 min at room temperature. Then, the GAPDH samples were centrifuged at 20,000× *g* for 5 min at room temperature to remove any insoluble material. Next, to remove DTT, buffer exchange/desalting was accomplished using a 7000 MW cutoff Pierce Zeba™ Spin Desalt Column resin (Pierce Biotechnology, Rockford, IL, USA), packed in columns, and used according to the manufacturer's instructions. This method will be referred to from here on as Spin Column Buffer Exchange (SCBE). For all GAPDH studies, SCBE was performed using columns equilibrated with 50 mM K^+-HEPES, 1 mM K-EDTA, and 0.1 mM NAD^+ pH 7. Eluate protein concentrations free of DTT were measured using the Pierce (Rockford, IL, USA) BCA protein assay kit, adjusted to 1 mg/mL, and diluted 2.25-fold with K^+-HEPES buffer containing a final eight-fold molar excess of the oxidant, iodosobenzoic acid (IOB). After mixing briefly and incubation for 10 min at room temperature, the resulting oxidized sample was again subjected to SCBE to remove the IOB and the protein concentration was determined.

4.2. Reduction of Oxidized GAPDH

For all the experiments exploring the reduction of oxidized GAPDH, the samples, prepared as described above, were further treated as follows, with either glutathione (G(SH)), L-cysteine (CYS), β-mercaptoethanol (BME), or dithiothreitol (DTT). All of these reducing agents were prepared as stocks in K^+-HEPES buffer, added to oxidized GAPDH to attain the final molar ratio indicated in the figures, and then incubated for 15 min at 37 °C. In the experiments where further treatment or higher concentrations were desired, the reduced samples were further treated by adding 10× stock concentrations of reducing agents to thin-wall PCR tubes and quickly adding the undiluted reduced sample to dilute the agent to 1×. These tubes were mixed briefly then incubated at 37 °C for 10 min in wells of a metal heat block for all concentration response experiments and at the duration indicated for the time course experiments. Afterwards, these incubation samples were analyzed starting as quickly as possible using the kinetic assay described below.

4.3. Kinetic Assay for GAPDH

In order to determine the effect of treatments on GAPDH activity, we prepared a biochemical assay in which the β-NADH absorbance was monitored over time. GAPDH reduced the amount of β-NADH as it was consumed. Therefore, by comparing unknown samples to a standard sample (1 mM DTT and 1 mM EDTA, which was slow-frozen in aliquots at 0.5 mg/mL using 0.2% alkylated BSA [9] and 50 mM trehalose as the cryoprotectant) the specific activity of the GAPDH samples were interpolated. The GAPDH assay buffer (50 mM K^+-HEPES, 130 mM KCl, 3 mM $MgCl_2$, 1 mM K-EDTA, 1 mM potassium phosphate dibasic, 0.1% alkylated BSA, 8 mM 3-phosphoglyceraldehyde, 2 mM β-NADH, and 1.3 mM ATP, pH 7.0, measured at 37 °C) was prepared in a large batch without the 3-phosphoglycerol kinase (3-PGK) and frozen in aliquots. On the day of the assay, an aliquot was thawed at room temperature. To reduce evaporation and start the assay as rapidly as possible, 200 µL water was added to the perimeter wells to clear-bottomed 96-well plates (Greiner Bio One Cat. No. 655090, Monroe, NC, USA) and the plates were warmed in a 37 °C incubator followed by the addition of 5 µL/well of sample or standard, immediately followed by 70 µL of the assay buffer ± 1 mM DTT (also pre-equilibrated to 37 °C). The assay was initiated by the addition of 75 µL/well of 0.5U 3-PGK enzyme (also pre-equilibrated to 37 °C) as quickly as possible. The plate was transferred to a BioTek Synergy HT plate reader (37 °C) and loss of NADH absorption was measured at 430 nm, at 30 s intervals for 60 min.

4.4. Measurement of S-Glutathionylation, Bound G(SH), and Bound G(SS)G to r-GAPDH

IOB-oxidized *r*-GAPDH was prepared exactly as described in Section 4.1. Following the removal of IOB by SCBE, the protein concentrations were determined. Then, the oxidized enzyme was incubated for 15 min with 1:1.2 mol G(SH)/mol *h*-GAPDH subunit followed by incubation with 1 mM G(SH). Both steps were conducted at 37 °C, pH 7. Then, 1 mL of sample was withdrawn from the incubation at time zero and at 15 min intervals for 75 min and was subject to SCBE to remove all non-associated G(SH) from the enzyme. Two aliquots of 0.4 mL sample were added to two YM3 3000 mwco Microcon® centrifugal filters (Millipore Corp, Bedford, MA, USA) followed by 0.1 mL of 0.1 % formic acid/acetonitrile added with rapid pipette mixing to denature the enzyme. After the last time point, the filtration devices were centrifuged at 14,000× *g* at 14 °C for approximately 120 min to for separating the GAPDH subunits (>3000 kDa) in the upper chamber (retentate) from the flow through eluate (lower chamber). The retentates (~15 µL) were reconstituted to 0.5 mL in 0.1% formic acid/acetonitrile. The pairs of eluates' volumes were measured and pooled. The G(SH) content of S-glutathionylated *r*-GAPDH in the retentate was reduced (G(SH)) and the total bound (G(SS)G + G(SH)) was released following denaturation of the enzyme, and were recovered in the eluates, which were measured using the Promega (Madison, WI, USA) assay kit V6611.

4.5. h-GAPDH Active Site Computational Model Methods

The crystal structure of *h*-GAPDH (PDB1u8f) was used as an active site model. The Molecular Operating Environment (MOE) 2020.09 was used to construct, solvate, display, and energetically minimize the model. Merck's Molecular Force Field (MMFF94s with all MOE parameterization was used with a maximum non-bonded cutoff distance of 12.0Å. The GB/VI generalized solvation model with implicit solvent electrostatics was used [37]. All bound water molecules as determined within the crystal structure were included and immersed in a 6 Å spherical shell of TIP3 waters, and 0.175 M KCl was included for the solvation. The complex was gently relaxed by tethering the backbone, then minimizing to an RMS gradient of 0.05 Å. The addition or modification of bonds within the crystal structure were re-parameterized using the Amber12:EHT force field because of its overall increased accuracy, particularly for small molecules. Non-bonded interaction energies (ΔE) between introduced ligands (G(SH), G(SSH), and C152S-glutathione) and the polypeptide chain were computed in MOE using the Extended Hückel Theory (EHT) hydrogen bond model. The EHT output was sigma (q_σ) and pi (q_π) partial charge per atom, along with fractional π bond orders (b_π). These were used to derive donor (ε_{don}) and acceptor (ε_{acc}) strengths for interacting atoms and to predict the acidity of the hydrogen bond donors, as well as the basicity of the hydrogen bond acceptors to compute the interaction energy (ΔE). These were combined with scores for the distance and angle between the groups to generate the individual interaction energy ΔE. The sum of all ligand-solvated protein non-bonding interactions yielded an estimate for free energy of the ligand docking process to the protein and served as a useful predictor of ligand binding affinity.

The protein sequence alignment and structure superposition tool in MOE was used to align the native *h*-GAPDH subunit structure with the output from the MDS and energy minimized subunit structures for the C152S-glutathionylated as well as the subunit with G(SS)G docked within the active site. As the aligned proteins had identical primary sequences, the superposition calculations were for a fully populated alignment positions, i.e., alignment positions with no gaps, and the peptide alpha carbon atom was used for the supposition calculations. "The accent secondary structure matches" feature was enabled to increase the weighting of residues with a matching α-helix and β-sheet. The root mean square distance (RMSD) for each alignment column (i.e., residue pair) used during the superposition is represented by a black vertical bar above the pairwise aligned sequences. Closely matching RMSD values are highlighted by a horizontal line cutoff below 2.0 Å, while larger RMSD excursion (5–11 Å) indicates a poor atomic coordinate superposition.

Supplementary Materials: The following supporting information can be downloaded at: https://www.mdpi.com/article/10.3390/ijms24065529/s1.

Author Contributions: The study was conceptualized by P.A.H. The biochemical experimental data were performed by L.N.B. and P.A.H. M.O.C. and P.A.H. conducted and interpreted the Molecular Dynamic Simulations. P.A.H. wrote the manuscript. All authors have read and agreed to the published version of the manuscript.

Funding: This work was funded entirely by P.A.H. and M.O.C.

Institutional Review Board Statement: Ethical review and approval were waived for this study due to no use of animals, or dangerous or biologically hazardous materials.

Informed Consent Statement: Not applicable.

Data Availability Statement: All data presented in this study are available by written request to P.A.H. (Biochemistry) and M.O.C. Molecular Dynamic Simulations.

Acknowledgments: We thank the Chemical Computing Group for use of their complimentary copy of Molecular Operating Environment (MOE), 2020.09 software (Chemical Computing Group ULC, 1010 Sherbrooke St. West, Suite #910, Montreal, QC, Canada, H3A 2R7, 2020). and assistance to MOC with the molecular dynamic simulations in this study.

Conflicts of Interest: The authors declare no conflict of interest.

References

1. Butterfield, D.A.; Hardas, S.S.; Lange, M.L. Oxidatively modified glyceraldehyde-3-phosphate dehydrogenase (GAPDH) and Alzheimer's disease: Many pathways to neurodegeneration. *J. Alzheimers Dis.* **2010**, *20*, 369–393. [CrossRef] [PubMed]
2. Sirover, M.A. Moonlighting glyceraldehyde-3-phosphate dehydrogenase: Posttranslational modification, protein and nucleic acid interactions in normal cells and in human pathology. *Crit. Rev. Biochem. Mol. Biol.* **2020**, *55*, 354–371. [CrossRef] [PubMed]
3. Gerszon, J.; Rodacka, A. Oxidatively modified glyceraldehyde-3-phosphate dehydrogenase in neurodegenerative processes and the role of low molecular weight compounds in counteracting its aggregation and nuclear translocation. *Ageing Res. Rev.* **2018**, *48*, 21–31. [CrossRef]
4. Semenyuk, P.; Barinova, K.; Muronetz, V. Glycation of alpha-synuclein amplifies the binding with glyceraldehyde-3-phosphate dehydrogenase. *Int. J. Biol. Macromol.* **2019**, *127*, 278–285. [CrossRef]
5. Delport, A.; Kins, S.; Hewer, R. The amyloid precursor protein affects glyceraldehyde 3-phosphate dehydrogenase levels, organelle localisation and thermal stability. *Mol. Biol. Rep.* **2020**, *47*, 3019–3024. [CrossRef]
6. Sekar, S.; Taghibiglou, C. Nuclear accumulation of GAPDH, GluA2 and p53 in post-mortem substantia nigral region of patients with Parkinson's disease. *Neurosci. Lett.* **2020**, *716*, 134641. [CrossRef] [PubMed]
7. Ping, Z.; Fan, H.; Wen, C.; Ji, Z.; Liang, S. GAPDH siRNA Regulates SH-SY5Y Cell Apoptosis Induced by Exogenous alpha-Synuclein Protein. *Neuroscience* **2021**, *469*, 91–102. [CrossRef]
8. Butera, G.; Mullappilly, N.; Masetto, F.; Palmieri, M.; Scupoli, M.T.; Pacchiana, R.; Donadelli, M. Regulation of Autophagy by Nuclear GAPDH and Its Aggregates in Cancer and Neurodegenerative Disorders. *Int. J. Mol. Sci.* **2019**, *20*, 2062. [CrossRef]
9. Hyslop, P.A.; Chaney, M.O. Mechanism of GAPDH Redox Signaling by H2O2 Activation of a Two-Cysteine Switch. *Int. J. Mol. Sci.* **2022**, *23*, 4604. [CrossRef]
10. Sies, H. Role of Metabolic H_2O_2 Generation. *J. Biol. Chem.* **2014**, *289*, 8735–8741. [CrossRef]
11. Tossounian, M.A.; Zhang, B.; Gout, I. The Writers, Readers, and Erasers in Redox Regulation of GAPDH. *Antioxidants* **2020**, *9*, 1288. [CrossRef] [PubMed]
12. Barinova, K.V.; Serebryakova, M.V.; Eldarov, M.A.; Kulikova, A.A.; Mitkevich, V.A.; Muronetz, V.I.; Schmalhausen, E.V. S-glutathionylation of human glyceraldehyde-3-phosphate dehydrogenase and possible role of Cys152-Cys156 disulfide bridge in the active site of the protein. *Biochim. Et Biophys. Acta Gen. Subj.* **2020**, *1864*, 129560. [CrossRef] [PubMed]
13. Schuppe-Koistinen, I.; Gerdes, R.; Moldeus, P.; Cotgreave, I.A. Studies on the reversibility of protein S-thiolation in human endothelial cells. *Arch. Biochem. Biophys.* **1994**, *315*, 226–234. [CrossRef]
14. Brodie, A.E.; Reed, D.J. Reversible oxidation of glyceraldehyde 3-phosphate dehydrogenase thiols in human lung carcinoma cells by hydrogen peroxide. *Biochem. Biophys. Res. Commun.* **1987**, *148*, 120–125. [CrossRef]
15. Brodie, A.E.; Reed, D.J. Cellular recovery of glyceraldehyde-3-phosphate dehydrogenase activity and thiol status after exposure to hydroperoxides. *Arch. Biochem. Biophys.* **1990**, *276*, 212–218. [CrossRef]
16. Townsend, D.M.; Manevich, Y.; He, L.; Hutchens, S.; Pazoles, C.J.; Tew, K.D. Novel Role for Glutathione S-Transferase π. *J. Biol. Chem.* **2009**, *284*, 436–445. [CrossRef]
17. Mustafa Rizvi, S.H.; Shao, D.; Tsukahara, Y.; Pimentel, D.R.; Weisbrod, R.M.; Hamburg, N.M.; McComb, M.E.; Matsui, R.; Bachschmid, M.M. Oxidized GAPDH transfers S-glutathionylation to a nuclear protein Sirtuin-1 leading to apoptosis. *Free Radic. Biol. Med.* **2021**, *174*, 73–83. [CrossRef]

18. Eaton, P.; Byers, H.L.; Leeds, N.; Ward, M.A.; Shattock, M.J. Detection, quantitation, purification, and identification of cardiac proteins S-thiolated during ischemia and reperfusion. *J. Biol. Chem.* **2002**, *277*, 9806–9811. [CrossRef]
19. Newman, S.F.; Sultana, R.; Perluigi, M.; Coccia, R.; Cai, J.; Pierce, W.M.; Klein, J.B.; Turner, D.M.; Butterfield, D.A. An increase in S-glutathionylated proteins in the Alzheimer's disease inferior parietal lobule, a proteomics approach. *J. Neurosci. Res.* **2007**, *85*, 1506–1514. [CrossRef]
20. Nonaka, K.; Kume, N.; Urata, Y.; Seto, S.; Kohno, T.; Honda, S.; Ikeda, S.; Muroya, T.; Ikeda, Y.; Ihara, Y.; et al. Serum levels of S-glutathionylated proteins as a risk-marker for arteriosclerosis obliterans. *Circ. J.* **2007**, *71*, 100–105. [CrossRef]
21. Tsai, C.W.; Tsai, C.F.; Lin, K.H.; Chen, W.J.; Lin, M.S.; Hsieh, C.C.; Lin, C.C. An investigation of the correlation between the S-glutathionylated GAPDH levels in blood and Alzheimer's disease progression. *PLoS ONE* **2020**, *15*, e0233289. [CrossRef] [PubMed]
22. Kim, Y.J. A cryoprotectant induces conformational change in glyceraldehyde-3-phosphate dehydrogenase. *Acta Crystallogr. Sect. F Struct. Biol. Commun.* **2018**, *74*, 277–282. [CrossRef]
23. Smith, C.M.; Velick, S.F. The glyceraldehyde 3-phosphate dehydrogenases of liver and muscle. Cooperative interactions and conditions for functional reversibility. *J. Biol. Chem.* **1972**, *247*, 273–284. [CrossRef]
24. You, K.S.; Benitez, L.V.; McConachie, W.A.; Allison, W.S. The conversion of glyceraldehyde-3-phosphate dehydrogenase to an acylphosphatase by trinitroglycerin and inactivation of this activity by azide and ascorbate. *Biochim. Biophys. Acta* **1975**, *384*, 317–330. [CrossRef]
25. Parker, D.J.; Allison, W.S. The mechanism of inactivation of glyceraldehyde 3-phosphate dehydrogenase by tetrathionate, o-iodosobenzoate, and iodine monochloride. *J. Biol. Chem.* **1969**, *244*, 180–189. [CrossRef] [PubMed]
26. Harris, J.I.; Waters, M. Glyceraldehyde-3-phosphate dehydrogenase. In *The Enzymes*; Boyer, P.D., Ed.; Academic Press: Boca Raton, FL, USA, 1976; Chapter 1; pp. 1–49.
27. Kitatani, T.; Nakamura, Y.; Wada, K.; Kinoshita, T.; Tamoi, M.; Shigeoka, S.; Tada, T. Structure of NADP-dependent glyceraldehyde-3-phosphate dehydrogenase from Synechococcus PCC7942 complexed with NADP. *Acta Crystallogr. Sect. F Struct. Biol. Cryst. Commun.* **2006**, *62*, 315–319. [CrossRef]
28. Vaidyanathan, V.V.; Sastry, P.S.; Ramasarma, T. Regulation of the activity of glyceraldehyde 3-phosphate dehydrogenase by glutathione and H_2O_2. *Mol. Cell Biochem.* **1993**, *129*, 57–65. [CrossRef] [PubMed]
29. Zaffagnini, M.; Marchand, C.H.; Malferrari, M.; Murail, S.; Bonacchi, S.; Genovese, D.; Montalti, M.; Venturoli, G.; Falini, G.; Baaden, M.; et al. Glutathionylation primes soluble glyceraldehyde-3-phosphate dehydrogenase for late collapse into insoluble aggregates. *Proc. Natl. Acad. Sci. USA* **2019**, *116*, 26057–26065. [CrossRef]
30. Hyslop, P.A.; Hinshaw, D.B.; Halsey, W.A., Jr.; Schraufstatter, I.U.; Sauerheber, R.D.; Spragg, R.G.; Jackson, J.H.; Cochrane, C.G. Mechanisms of oxidant-mediated cell injury. The glycolytic and mitochondrial pathways of ADP phosphorylation are major intracellular targets inactivated by hydrogen peroxide. *J. Biol. Chem.* **1988**, *263*, 1665–1675. [CrossRef]
31. Schraufstatter, I.U.; Hinshaw, D.B.; Hyslop, P.A.; Spragg, R.G.; Cochrane, C.G. Glutathione cycle activity and pyridine nucleotide levels in oxidant-induced injury of cells. *J. Clin. Investig.* **1985**, *76*, 1131–1139. [CrossRef]
32. Schraufstatter, I.U.; Hinshaw, D.B.; Hyslop, P.A.; Spragg, R.G.; Cochrane, C.G. Oxidant injury of cells. DNA strand-breaks activate polyadenosine diphosphate-ribose polymerase and lead to depletion of nicotinamide adenine dinucleotide. *J. Clin. Investig.* **1986**, *77*, 1312–1320. [CrossRef] [PubMed]
33. Schraufstatter, I.U.; Hyslop, P.A.; Hinshaw, D.B.; Spragg, R.G.; Sklar, L.A.; Cochrane, C.G. Hydrogen peroxide-induced injury of cells and its prevention by inhibitors of poly(ADP-ribose) polymerase. *Proc. Natl. Acad. Sci. USA* **1986**, *83*, 4908–4912. [CrossRef] [PubMed]
34. Spragg, R.G.; Hinshaw, D.B.; Hyslop, P.A.; Schraufstatter, I.U.; Cochrane, C.G. Alterations in adenosine triphosphate and energy charge in cultured endothelial and P388D1 cells after oxidant injury. *J. Clin. Investig.* **1985**, *76*, 1471–1476. [CrossRef] [PubMed]
35. Hinshaw, D.B.; Miller, M.T.; Omann, G.M.; Beals, T.F.; Hyslop, P.A. A cellular model of oxidant-mediated neuronal injury. *Brain Res.* **1993**, *615*, 13–26. [CrossRef]
36. Zhang, Z.; Turner, D.C.; Drzewiecki, G.J.; Hinshaw, D.B.; Hyslop, P.A. Impairment of integrin-mediated cell-matrix adhesion in oxidant-stressed PC12 cells. *Brain Res.* **1994**, *662*, 189–197. [CrossRef]
37. Labute, P. The generalized Born/volume integral implicit solvent model: Estimation of the free energy of hydration using London dispersion instead of atomic surface area. *J. Comput. Chem.* **2008**, *29*, 1693–1698. [CrossRef]

International Journal of
Molecular Sciences

MDPI

Article

Adaptive Stimulations in a Biophysical Network Model of Parkinson's Disease

Thomas Stojsavljevic [1,*,†], Yixin Guo [2,†] and Dominick Macaluso [3]

[1] Department of Math and Computer Science, Beloit College, 700 College St., Beloit, WI 53511, USA
[2] Department of Mathematics, Drexel University, Philadelphia, PA 19104, USA
[3] Department of Neurosurgery, University of Pennsylvania Health System, Philadelphia, PA 19104, USA
* Correspondence: stojsavljevictg@beloit.edu; Tel.: +1-608-363-2404
† These authors contributed equally to this work.

Abstract: Deep brain stimulation (DBS)—through a surgically implanted electrode to the subthalamic nucleus (STN)—has become a widely used therapeutic option for the treatment of Parkinson's disease and other neurological disorders. The standard conventional high-frequency stimulation (HF) that is currently used has several drawbacks. To overcome the limitations of HF, researchers have been developing closed-loop and demand-controlled, adaptive stimulation protocols wherein the amount of current that is delivered is turned on and off in real-time in accordance with a biophysical signal. Computational modeling of DBS in neural network models is an increasingly important tool in the development of new protocols that aid researchers in animal and clinical studies. In this computational study, we seek to implement a novel technique of DBS where we stimulate the STN in an adaptive fashion using the interspike time of the neurons to control stimulation. Our results show that our protocol eliminates bursts in the synchronized bursting neuronal activity of the STN, which is hypothesized to cause the failure of thalamocortical neurons (TC) to respond properly to excitatory cortical inputs. Further, we are able to significantly decrease the TC relay errors, representing potential therapeutics for Parkinson's disease.

Keywords: Parkinson's disease; deep brain stimulation; adaptive stimulation; multi-site stimulation; thalamocortical relay; basal ganglia model; local field potential

Citation: Stojsavljevic, T.; Guo, Y.; Macaluso, D. Adaptive Stimulations in a Biophysical Network Model of Parkinson's Disease. *Int. J. Mol. Sci.* **2023**, *24*, 5555. https://doi.org/10.3390/ijms24065555

Academic Editor: Claudia Ricci

Received: 31 January 2023
Revised: 3 March 2023
Accepted: 7 March 2023
Published: 14 March 2023

1. Introduction

Deep brain stimulation (DBS) is a therapeutic option for Parkinson's disease (PD) wherein a stimulating electrode is surgically implanted into the subthalamic nucleus (STN), globus pallidus (GP), or thalamus (TC), depending on the more prominent symptoms. The stimulating electrode sends electrical impulses to the targeted regions of the brain [1–3]. At present, the most conventional DBS is done with open-loop methods involving constant high-frequency stimulation (HF). On a neuronal level, the pathophysiology of PD is associated with changes such as increases in synchrony, firing rates, and bursting activity in the basal ganglia [3–6]. DBS may achieve its therapeutic benefits when stimulation is able to disrupt the pathological synchronized bursting in the basal ganglia [7–10]. While this treatment has been effective, there are several drawbacks to HF DBS. In open-loop methods, the stimulation parameters such as duration, amplitude, and frequency of the pulse train are controlled by external forces that are not guided by the changes in the brain's electrical activity resulting from PD [11]. Conventional HF DBS, with high frequency and nonadjustable parameters, may have adverse effects in the proximate region to the stimulation site. Additionally, battery and device shelf-life concerns are present with higher frequency and open-loop DBS [11,12].

A possible remedy is to develop a closed-loop, adaptive system that only administers DBS as necessary. A closed-loop method is a system in which DBS is automatically controlled in accordance with a recorded feedback signal from a targeted region. In this

approach, stimulation is administered only when necessary and is, to an extent, dependent on the measured neuronal activity [13]. Due to the desire for a closed-loop, adaptive system, in vitro and in silico studies have been conducted. In 2013, Little et al. used brain–computer interfaces to monitor the local field potential (LFP) of the STN and to control the administration of DBS to patients with PD. Their results showed statistically significant improvement in motor scores [14]. Later, de Castro et al. employed delayed feedback control algorithms to disrupt unwanted pathological neuronal oscillations within in vitro networks [15]. Current experimental studies aim to identify appropriate biological feedback signals, such as neural oscillating or using the magnitude of the LFP [16–20].

Since other biological signals may be used to monitor and control the administration of adaptive deep brain stimulation (aDBS), we turn to computational models to explore potential avenues. Previous closed-loop computational modeling efforts at DBS have focused on using the amplitude of LFP. In particular, Guo and Rubin studied a multi-site delay feedback DBS in 2011 based on the LFP of the STN population [5,21–23]. Their multi-site delayed feedback stimulation was found to be more beneficial compared to open-loop HF. However, this method lacks an adaptive mechanism because the stimulation remains on the entire time once it is turned on. The primary recent computational studies in aDBS have focused on desynchronizing the STN neurons in parkinsonian networks [13,24–36]. Based on work conducted by Popovych and Tass in 2019, they concluded that using the LFP as a signal to control aDBS can be more efficient in suppressing abnormal synchronization than continuous stimulation [13]. Our work aims to look beyond the desynchronization of PD networks using aDBS. Here, PD networks are computational models of neurons that mimic neuronal patterns of PD in the basal ganglia.

We introduce two novel closed-loop aDBS techniques utilizing the interspike time of model STN neurons to gauge PD neuronal activity and to determine when stimulation is on and off. This will be applied to a small network of conductance-based STN, GP, and TC neurons that, by design, generate parkinsonian activity patterns in the absence of stimulation. While other authors have explored how adaptive stimulation techniques desynchronize neuronal networks in studying PD, we find that our closed-loop aDBS is able to both desynchronize and deburst parkinsonian networks. In our PD networks, we incorporate TC neurons to evaluate the effectiveness of aDBS. Within the setup of our PD networks, the TC fidelity is compromised, with many instances of the TC neurons failing to respond in a one-to-one fashion to excitatory inputs [21,37]. We study how closed-loop aDBS is able to improve TC relay fidelity when properly applied in PD networks. This represents the first work in which the effectiveness of closed-loop aDBS is evaluated based on TC relay fidelity. These results support the idea that adaptive stimulation of STN utilizing an interspike time merits further consideration as a possible alternative to standard forms of DBS for PD.

2. Results

We will be analyzing the proposed adaptive protocols under two different computational parkinsonian network configurations. The first configuration will consist of a network receiving adaptive constant pulse DBS (acDBS) in which the STN neurons have a four-spike burst with an initial TC error index (defined in Section 4.1.3) of 0.39 and 0.37 for the first and second TC cells, respectively. The second network configuration will consist of a network receiving adaptive local field potential DBS (aLFPDBS) in which the STN neurons have a three-spike burst with an initial TC error index of 0.56 for both TC cells. Throughout both computational studies, we will be applying stimulation in a time period we call the treatment window, which will start at 2000 ms and last until 7000 ms. During this time period, the stimulation will be turned on and off according to our adaptive protocols. By using these two network configurations, we can determine how well the proposed adaptive protocols would work in mild to moderate as well as advanced computational parkinsonism. In evaluating the efficacy of acDBS and aLFPDBS, we will examine whether each protocol is able to de-burst the network and under which settings we will see the

largest improvement in the error index in the TC relay. Additionally, we will study how the stimulation changes the total synaptic input of the internal segment of the globus pallidus (GPi) to the TC cells. All model simulations were conducted using XPPAUT, and all model simulation figures were made in MATLAB.

2.1. Adaptive Constant Pulse DBS

In Figure 1, we can see examples of the adaptive constant pulse stimulation profiles when using a stimulation strength of $a_0 = -15$ and an interspike time threshold parameter $intt = 200$ ms.

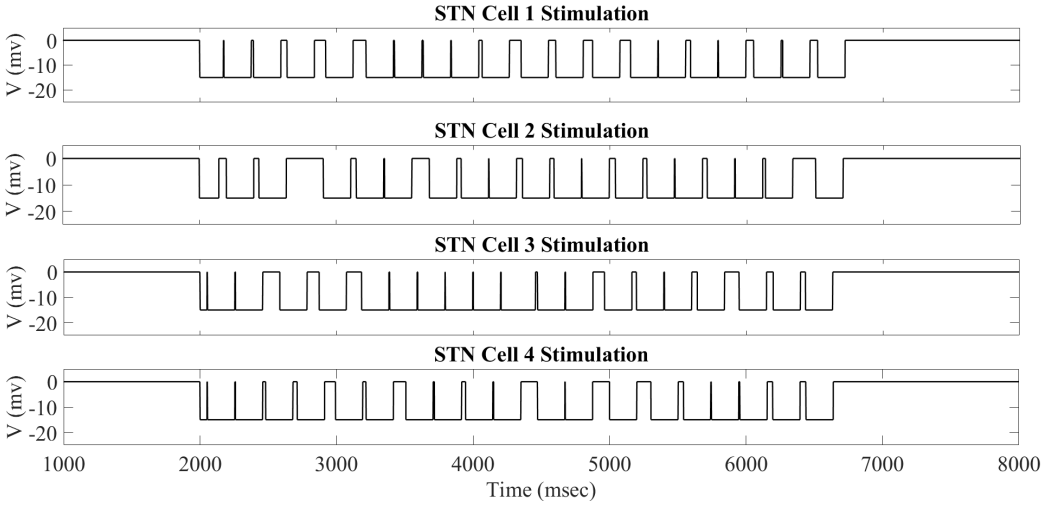

Figure 1. acDBS delivered to STN Cells 1–4 during the time window of 2000 to 7000 ms. Note that the top part of the curve represents the time when the stimulation is turned off, while the bottom part of the curve is when the stimulation is turned on.

During the treatment window of 2000 to 7000 ms, the stimulation currents delivered to neurons 1–4 are different. While not shown, it is the case that all 16 STN neurons will have different times when the stimulation is turned on and off. As outlined in Section 4.2, we use the interspike time—the time between successive STN firings—to determine when the stimulation is turned on and off. This is determined by the threshold parameter *intt*. If the interspike time is larger than the threshold parameter *intt*, then the stimulation is turned off. Otherwise, the stimulation is turned on because we predict that a bursting dynamic is occurring, which we wish to disrupt. Once the stimulation is turned on, the bursting dynamic is broken, and the interspike interval becomes larger than the *intt* threshold and will shut off again. This mechanism allows for neurons coming from the same synchronous groups to receive an individual stimulation based on its own firing pattern. For instance, neurons 1 and 2 belong to the STN_{11} subgroup, while neurons 3 and 4 STN_{12}. However, when studying the stimulation profiles shown in Figure 1, we can see that the times when the stimulation is on and off vary by individual neuron.

When the acDBS protocol is applied to the STN neurons during the treatment window of 2000 to 7000 ms, we observe that the stimulation is able to successfully break the synchronized bursting dynamics observed in our computational parkinsonian state (shown in figure in Section 4.1.3). We are only left with single spike activity at intermittent intervals. An fexample of the membrane potential of STN_1, with its corresponding stimulation profile, is shown in Figure 2. In this instance, the adaptive protocol is working as intended. Examining Figure 2, during the treatment window from 2000 to 7000 ms, bursting activity is suppressed. Once the interspike time exceeds the threshold *intt* and stimulation is turned off, it will remain off until we see the next STN spike and then the stimulation will turn back on to disrupt any potential STN bursting. We apply this throughout the treatment window until we shut the stimulation off at 7000 ms and we see the parkinsonian state of the network resume.

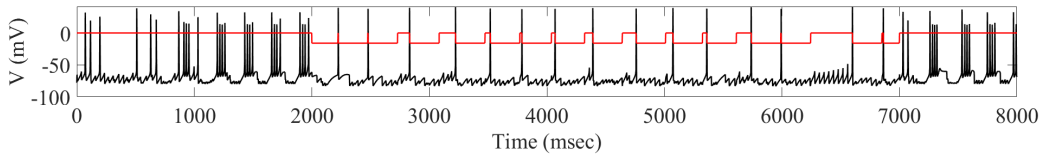

Figure 2. STN_1 membrane potential (black) with corresponding adaptive stimulation received (red) with parameters $a_0 = -16$ and interspike time threshold parameter $intt = 250$ ms. Note that the top part of the red curve represents the time when the stimulation is turned off, while the bottom part of the curve is when the stimulation is turned on.

The overall impact of applying the acDBS throughout the entire 16 STN neurons, along with the changes to the two TC neurons, is shown in Figure 3. Some intermittent single-spike synchronization only occurs in a subgroup of STN neurons. Under the current stimulation settings ($a_0 = -16$, $intt = 250$ ms), the error index for each TC cell is 0.14 and 0.23 for cells 1 and 2, respectively. By changing the synchronized bursting pattern of the STN neurons, we have substantially altered the total synaptic GPi (top traces in blue in Figure 3) input to the TC cells. In Figure 3 (Panels B and C), examining the membrane potentials of TC_1 and TC_2 (black traces) with the excitatory inputs (red traces), the number of failures to respond in a one-to-one fashion in the parkinsonian state (see figure in Section 4.1.3) is greatly improved in the treatment window.

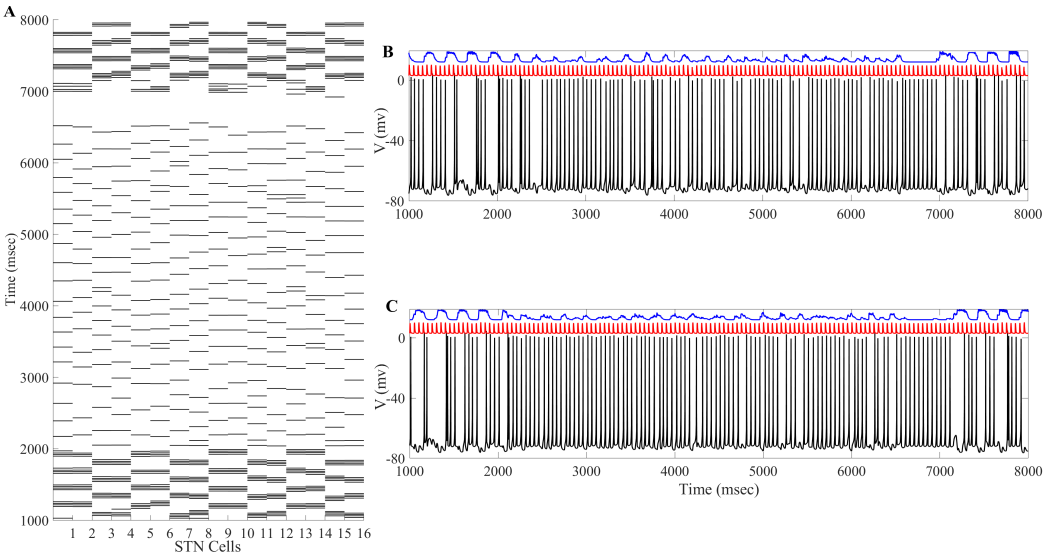

Figure 3. Example of acDBS. (**A**) Spike times of 16 STN neurons. acDBS is on from 2000 to 7000 ms with $a_0 = -16$ and $intt = 250$ ms. Before stimulation, there are two synchronized clusters, as shown in figure panel (a) in Section 4.1.3. During the stimulation period, the bursting dynamic is largely eliminated, and the synchronized clusters no longer exist. Once stimulation is stopped, the synchronized clusters reemerge. (**B**) Relay performance of TC_1. (**C**) Relay performance of TC_2. In both (**B**,**C**), the top trace in blue is the total GPi synaptic input, the middle trace in red is the excitatory signal, and the bottom trace in black is the TC voltage. TC relay performance noticeably improves during the stimulation window.

The changes in STN firing behavior are further reflected in the histograms of sg_1 and sg_2 corresponding to overall GPi synaptic input to the TC neurons (defined in Section 4.1.2). The histograms in Figure 4 with the stimulation show that the distribution has more elements in bin 1 and almost none in bins 5 and 6. Without stimulation, as shown in figure in Section 4.1.2, the histograms have substantially more elements sorted into bins 5 and 6. In the parkinsonian configuration, the overall GPi synaptic input to the TC cell is very phasic and bursty. This can be seen before the treatment window (1000–2000 ms) and after the treatment window (7000–8000 ms) in Figure 4. During the stimulation period,

the phasic and bursty firing pattern seen in the parkinsonian state is interrupted and replaced with a more random pattern. This population-level phenomenon is the result of downstream propagation of the debursted STN neurons. These results indicate that we have significantly altered the firing of the GPi, replacing it with a more randomized firing. The corresponding changes in total GPi synaptic input to the TC cells improve the TC relay responses.

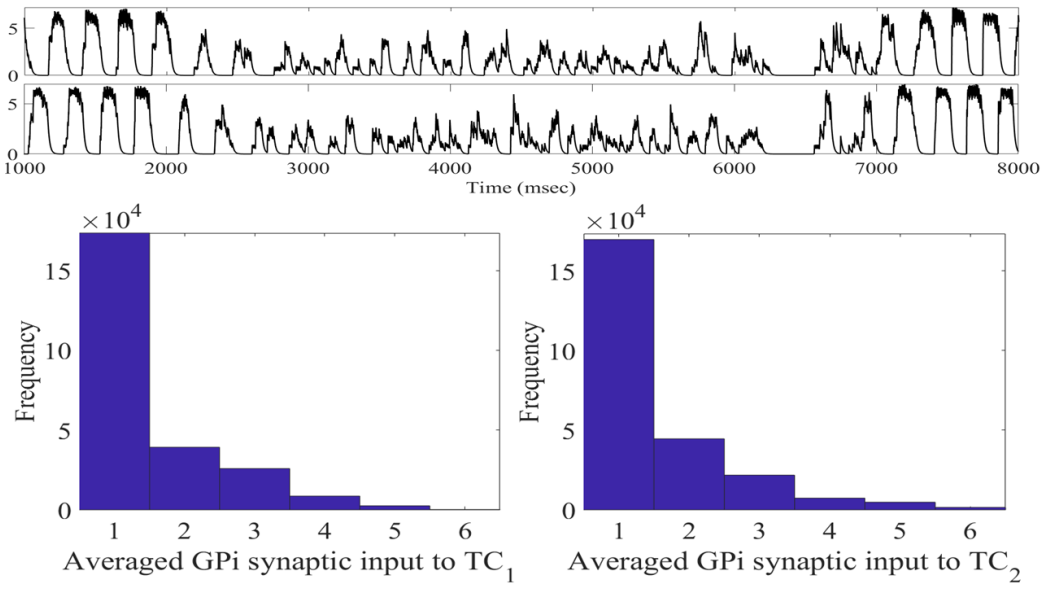

Figure 4. Total GPi synaptic inputs sg_1 and sg_2 (**top traces**) with corresponding histograms of sg_1 (**left**) and sg_2 (**right**) during the treatment window when acDBS was applied with $a_0 = -16$ and $intt = 250$.

Having successfully broken the network parkinsonian state, we next seek to determine how robust this procedure is. Specifically, we seek to identify an effective range of values for the parameters a_0 and $intt$ (the stimulation strength and the interspike time, respectively), under which the network will respond to the stimulation and reduce the TC error index. We are interested in finding a regime of optimal TC performance with relatively weak stimulation amplitude.

As shown in Figure 5, we can see well-separated regions where the error-index is high (0.5 and above), low (0.2 and below), and similar to the parkinsonian state (between 0.3 and 0.4). In contrast with previous work conducted by Guo and Rubin [21], there is a large range of values of interspike threshold times and stimulation strengths that desynchronize and deburst the STN neurons and therefore improve the TC performance. In general, the favorable region of stimulation parameters can be observed in the lower right-hand corner of Figure 5, with stimulation strengths ranging from -11 to -16 and interspike threshold parameters of 250 to 400 ms. The $(intt, a_0)$ parameter pairs in this window behave similarly to our results discussed above.

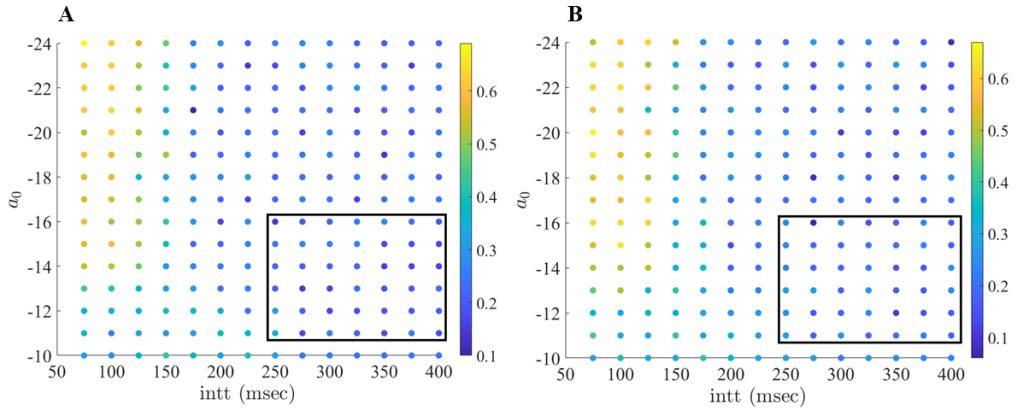

Figure 5. (**A**) Error index values (color coded) for the first TC cell, TC_1 over a range of interspike threshold parameter values *intt* (75–400 ms, with increment 25 ms) and a_0—stimulation strength (-24 to -10, with increments of 1). (**B**) Error index values for the second TC cell, TC_2 over a range of values *intt* (75 to 400 ms, increment 25 ms) and a_0 (-24 to -10, with increment 1). The favorable region of $(intt, a_0)$ pairs is shown in the black box.

When studying Figure 5, we observe that pairing strong stimulation strength with lower interspike interval parameters produces non-optimal results. In these instances, our computational modeling shows that the stimulation to the neurons is occurring in a fashion that induces a different STN bursting pattern, which results in poor TC performance. For example, the $(intt, a_0)$ pair (75, -24) has an error index of 0.69 for TC_1. In Figure 6, we compare the firing of STN_1 with its corresponding stimulation profile. Here we see that the firing in the STN neuron now comes in regular succession. In fact, the new firing pattern is directly induced from the stimulation provided to the STN cell, largely due to the strong stimulation strength and the short interspike intervals.

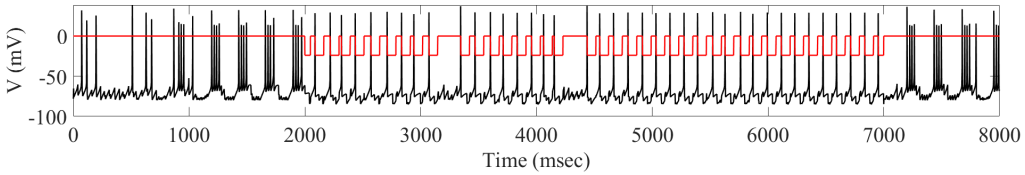

Figure 6. STN_1 membrane potential (black) with corresponding adaptive stimulation received (red) with parameters $a_0 = -24$ and interspike time threshold parameter $intt = 75$ ms. Note that the top part of the red curve represents the time when the stimulation is turned off, while the bottom part of the curve is when the stimulation is turned on.

To better understand the impact that the stimulation-induced firing has on TC performance, we need to study how the induced firing impacts the total GPi synaptic input into the TC neurons. Using the $(intt, a_0)$ pair (75, -24), we compute sg_1 and sg_2 and construct the corresponding histograms. As seen in Figure 7, the total GPi synaptic input to TC_1 and TC_2 is indeed altered from the baseline parkinsonian network with no stimulation. However, unlike the $(intt, a_0)$ pair (250, -16), during the treatment window, we observe that the total synaptic GPi input is still clustered and synchronized. The histograms do not have a pronounced shift in bin 6 to bin 1. While the distribution is shifted in comparison to figure in Section 4.1.2, there are more entries in the middle bins 2–5.

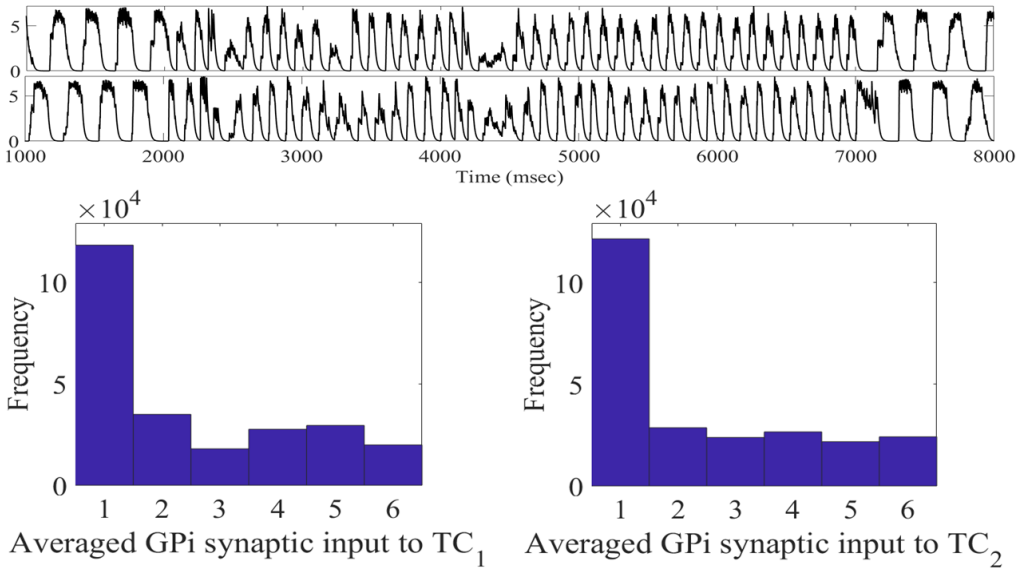

Figure 7. Total GPi synaptic inputs sg_1 and sg_2 (**top traces**) with corresponding histograms of sg_1 (**left**) and sg_2 (**right**) during the treatment window when acDBS was applied with $a_0 = -24$ and $intt = 75$.

This demonstrates that the TC performance is directly attributed to our choice of acDBS parameters. Further, when studying Figure 5, it also suggests that there is a non-linear relationship to how changes in the $(intt, a_0)$ space impact TC performance. In general, we can conclude that there are many combinations of stimulation strengths and interspike threshold parameters that are able to produce improved TC response in acDBS. We see that when the interspike threshold parameter is larger, we can use lower stimulation strengths, which is preferred. Conversely, pairing strong stimulation strengths with a short interspike threshold parameter produces a new firing dynamic bad for TC performance. Thus, there are numerous pairings of parameters, which may induce a theoretical therapeutic benefit.

2.2. Adaptive Multi-Site LFP Stimulation

Unlike the acDBS method discussed above, the adaptive LFP stimulation described by Equation (19) represents a more sophisticated closed-loop DBS. While acDBS is able to stimulate only when necessary, it is unable to adapt the stimulation strength to the amount of abnormal neuronal synchronization. We overcome this limitation by incorporating the recorded LFP signal of the STN neurons. Previous research has assessed the performance of STN stimulation based on recorded LFP signals in terms of its desynchronizing effects on model neurons [13,21,22,31]. This previous work shows that, while there is no clear evidence on how the LFP is related to synaptic and ionic currents of a single neuron, such stimulation is able to greatly reduce phase synchronization [13,22,30,31].

In Figure 8, we can see examples of the aLFPDBS profiles when using a stimulation strength of $a_0 = 6$ and an interspike time threshold parameter $intt = 300$ ms. As with the acDBS results described previously, the stimulation current delivered to neurons 1, 4, 6, and 11 is different during the treatment window of 2000 to 7000 ms. While not shown, it is still the case that all 16 STN neurons will have different times when the stimulation is turned on and off. These differences persist when the neurons are coming from the same stimulation site (Neurons 1 and 6 of the STN_{11} block) or from a different stimulation site but are part of the same synchronous group (Neuron 4 from the STN_{12} block and Neuron 11 from the STN_{21} block). In contrast with acDBS, the amount of current delivered during the stimulation on period is now modulated by the filtered LFP on a delay as the signal is shuffled through the four stimulation sites (see figure in Section 4.3 and Equation (19)).

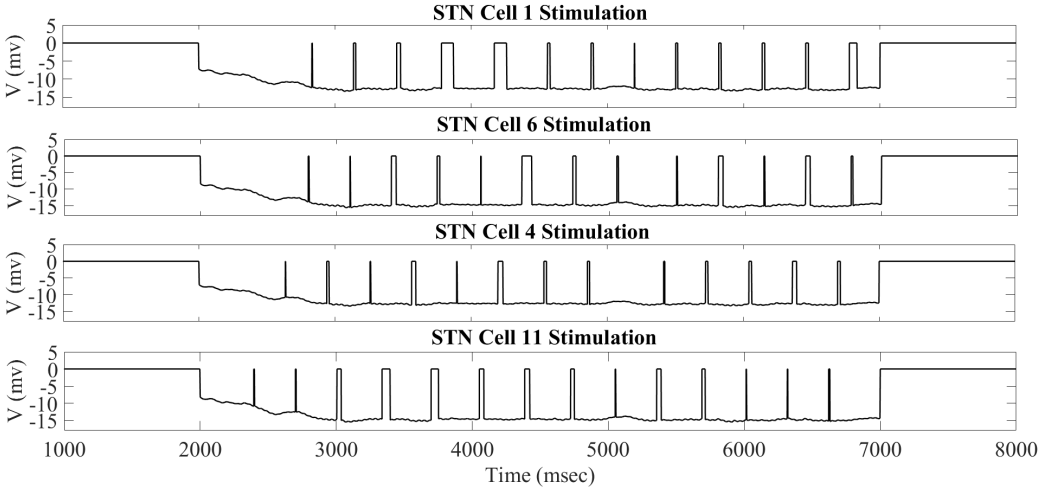

Figure 8. Adaptive local field potential stimulation delivered to STN Cells 1, 4, 6, and 11 arranged by the synchronous group during the time window of 2000 to 7000 ms. Note that the top part of the curve represents the time when the stimulation is turned off, while the bottom part of the curve is when the stimulation is turned on.

When the aLFPDBS protocol is applied to the STN neurons during the treatment window of 2000 to 7000 ms, we again observe that the stimulation is able to successfully break the synchronized bursting dynamics described in Section 4.1.3, and we are left with intermittent single spike activity. An example of the membrane potential of STN_1 with its corresponding stimulation profile (a_0 = 10, $intt$ = 325 ms) is shown in Figure 9. During the treatment window, the amount of stimulation delivered is modulated by the stimulation strength parameter a_0 and by the value of the LFP shown in Figure 10. Throughout the 2000–7000 ms period, the stimulation is turned off when the length between two successive spikes is larger than the interspike time threshold parameter $intt$. This allows for single spikes to occur before switching the stimulation on. When the length between two successive spikes is less than the interspike time threshold $intt$, the stimulation is on to prevent any potential bursting activity.

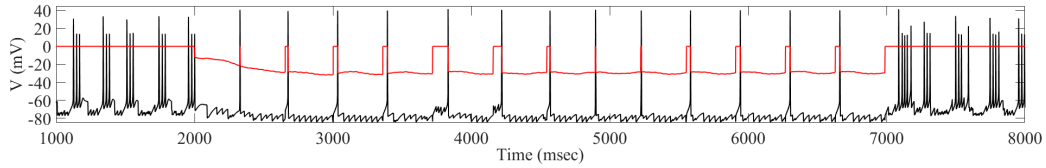

Figure 9. STN_1 membrane potential (black) with corresponding stimulation received (red) with parameters $a_0 = 10$ and interspike time threshold parameter $intt = 325$ ms. Note that the top part of the red curve represents the time when the stimulation is turned off, while the bottom part of the curve is when the stimulation is turned on.

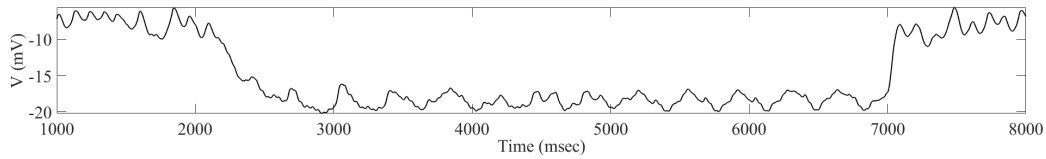

Figure 10. The total filtered local field potential of the 16 STN neurons from 1000 to 8000 ms with aLFPDBS parameters $a_0 = 10$ and $intt = 325$.

The overall impact of applying the aLFPDBS throughout the entire 16 STN neurons, along with the changes to the two TC neurons, is shown in Figure 11. We are able to successfully deburst the network, and there is intermittent single-spike synchronization present in

some subgroups of STN neurons. Under the stimulation settings $a_0 = 6$, $intt = 300$ ms, the error index for each TC cell is 0.13 and 0.2 for cells 1 and 2, respectively. This is a significant reduction from the network parkinsonian state, which had an error index of 0.56 for both model TC neurons.

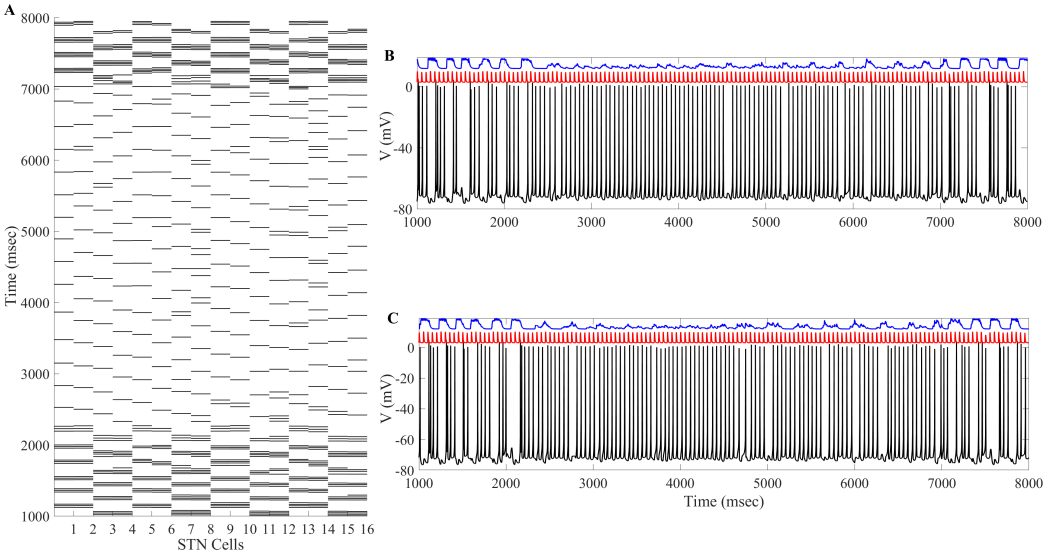

Figure 11. Example of aLFPDBS. (**A**) Spike times of 16 STN neurons. acDBS is on from 2000 to 7000 ms with $a_0 = 6$ and $intt = 300$ ms. Before stimulation, there are two synchronized clusters, as shown in figure panel (a) in Section 4.1.3. During the stimulation period, the bursting dynamic is largely eliminated, and the synchronized clusters no longer exist. Once stimulation is stopped, the synchronized clusters reemerge. (**B**) Relay performance of TC_1. (**C**) Relay performance of TC_2. In both (**B**,**C**), the top trace in blue is the total GPi synaptic input, the middle trace in red is the excitatory signal, and the bottom trace in black is the TC voltage. TC relay performance noticeably improves during the stimulation window.

The changes induced in the STN firing from the aLFPDBS are further reflected in the histograms of sg_1 and sg_2 corresponding to the overall GPi input to the TC neurons. Before the stimulation is turned on and the network is in the parkinsonian state, the GPi input to the TC cells is phasic and bursty. When aLFPDBS is applied, this phasic and bursty input is disrupted and replaced with a more random pattern consistent with what we observed when applying acDBS. Comparing the histograms in Figure 12 and figure in Section 4.1.2, we see that the distribution shifts from having more elements in bins 5 and 6 to more elements in bin 1, resulting in very few elements sorted into bins 5 and 6. This is attributed to the aLFPDBS significantly altering the STN firing pattern producing population-level neuronal changes. The debursting and desynchronization of the STN neurons propagate through the STN-GPe loop to the GPi, which, in turn, feeds into the two TC cells. By debursting and desynchronizing the STN neurons with aLFPDBS, we have greatly improved TC relay during the treatment window.

Having successfully broken the parkinsonian bursting dynamic, we will proceed to determine the robustness of aLFPDBS. We seek to identify an effective range of values for the parameters a_0 and $intt$ under which the network will respond to the aLFPDBS and reduce the TC error index. We are interested in finding a regime of optimal TC performance with relatively weak stimulation amplitude.

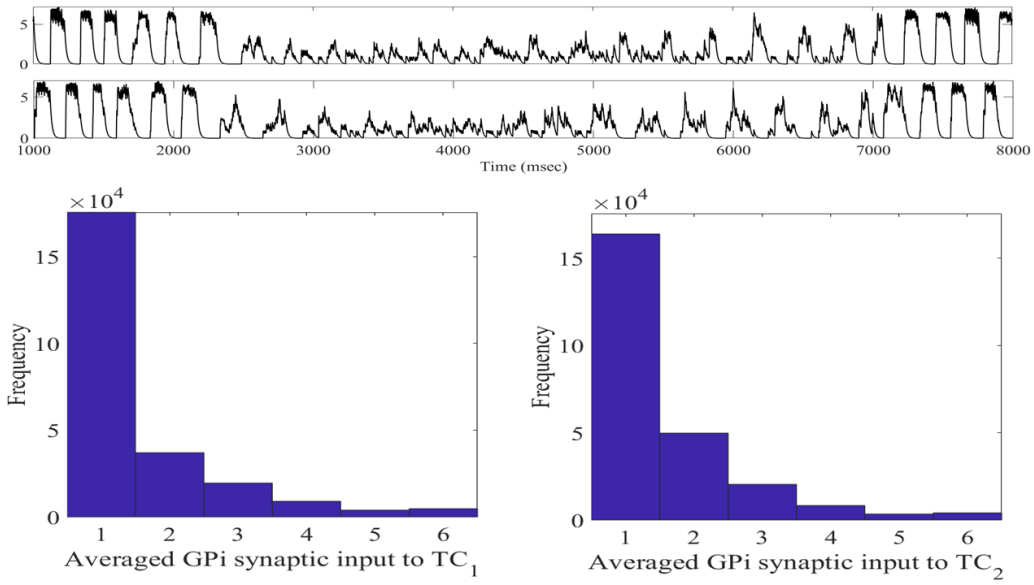

Figure 12. Total GPi synaptic inputs sg_1 and sg_2 (**top traces**) with corresponding histograms of sg_1 (**left**) and sg_2 (**right**) during the treatment window when aLFPDBS was applied with $a_0 = 6$ and $intt = 300$.

When studying Figure 13, we see well-separated regions where the error-index is high (0.6 and above), low (0.2 and below), and similar to the network parkinsonian state (0.4 to 0.5). Consistent with our observations about acDBS, there is a large range of interspike threshold times and stimulation strengths that desynchronize and deburst the STN neurons and improves TC performance. The favorable region spans *intt* values from 250 to 400 ms and stimulation strengths a_0 ranging from 6 to 10. The $(intt, a_0)$ parameter pairs in this window behave similarly to the example of aLFPDBS shown in Figures 8–12.

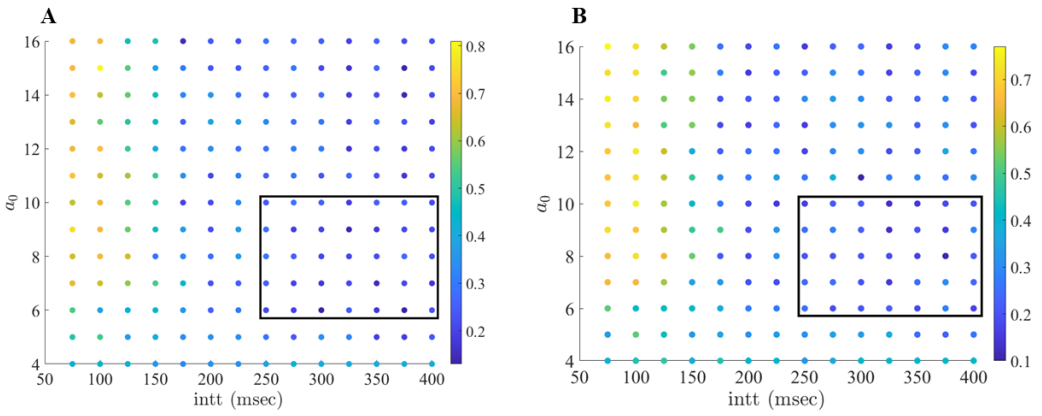

Figure 13. (**A**) Error index values (color coded) for the first TC cell, TC_1 over a range of interspike threshold parameter values *intt* (75 ms to 400 ms, with increment 25 ms) and a_0—stimulation strength (4 to 16, with increment 1). (**B**) Error index values for the second TC cell, TC_2 over a range of values *intt* (75 to 400 ms, increment 25 ms) and a_0 (4 to 16, with increment 1). The favorable region of $(intt, a_0)$ pairs is shown in the black box.

Under the aLFPDBS, pairing strong stimulation strengths with short interspike threshold parameters produces a train of periodic STN spiking throughout the treatment window, which results in pathological GPi outputs. For example, using the $(intt, a_0)$ pair of (100, 15) results in an error index of 0.81 and 0.72 for TC_1 and TC_2, respectively. As shown in Figures 14 and 15, using a strong stimulation strength largely alters the amplitude of the LFP and disrupts the synchronized bursting of the STN neurons. However, the onset of more frequent and regular spiking that the stimulation induces in the STN neurons

results in phasic and bursty GPi inputs to the TC cells. This pattern of firing in the STN and GPi corresponds to large error index values being observed. Another undesirable scenario occurs when a_0 is too small, for instance $a_0 \leq 4$. In this scenario, we observe that aLFPDBS is not strong enough to break the bursting pattern. Furthermore, we lose the adaptive nature of the stimulation because the stimulation is on for the entirety of the treatment window.

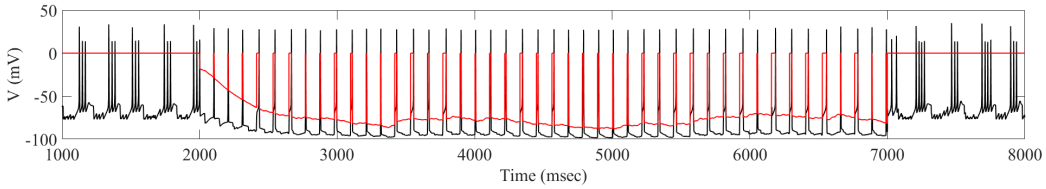

Figure 14. STN_1 membrane potential (black) with corresponding adaptive local field potential stimulation received (red) with parameters $a_0 = 15$ and $intt = 100$. Note that the top part of the red curve represents the time when the stimulation is turned off, while the bottom part of the curve is when the stimulation is turned on.

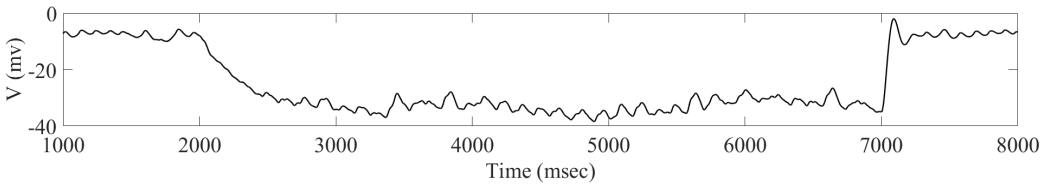

Figure 15. The total filtered local field potential of the 16 STN neurons from 1000 to 8000 ms with aLFPDBS parameters $a_0 = 15$ and $intt = 100$.

2.3. DBS for Heterogeneous TC Cells

To conclude our analysis of this computational study, we investigated the robustness of the proposed adaptive protocols for restoring TC neuron relay responses. We aim to test whether the adaptive stimulations produce the same restoration results with variations of TC neurons. We completed this by generating 40 different model TC neurons with heterogeneity in the parameters g_L, g_{Na}, and g_T. Starting with the baseline values listed in Appendix A, we independently selected new parameters from normal distributions with standard deviations of 0.01, 0.05, and 0.08, as performed in [21,37]. All 40 different TC neurons receive identical GPi inhibition from the upstream basal ganglia loop. For each randomly generated set of parameters for TC neurons, we made a comparison between the parkinsonian network without stimulation and with stimulation. Since we have two parkinsonian networks under study, we paired the weaker parkinsonian configuration with acDBS. The stronger parkinsonian configuration was then compared with the aLFPDBS. It is critical to note that the parameter changes to the downstream TC neurons do not have any impact on the network parkinsonian condition. Based on the network configuration described in figure in Section 4.1, our model TC neurons do not connect back to the upstream STN-GPe loop or the GPi. The TC neurons only receive input from model GPi neurons. We would not expect underlying changes to our model TC neurons to impact the synchronized bursting of the STN neurons.

The results of the heterogeneous TC cell studies are shown in Figure 16. The first row displays the results of the acDBS study, while the second row displays the results of the aLFPDBS study. As seen in Panels A and B, Panel A shows 40 trials for TC_1 and Panel B shows 40 trials for TC_2. A majority of the trials for TC_1 and TC_2 show a moderate reduction in the TC error index from the parkinsonian network without stimulation to the network with acDBS. In Panels C (for TC_1) and D (for TC_2), the majority of the trials for the aLFPDBS show a significant reduction in the TC error index. We observe that the TC error index reduction in aLFPDBS is more significant than in acDBS. One possible explanation for the differences in TC error reduction is due to the nature of the stimulation delivered to

the STN neurons as defined in Equations (16) and (19). While both of these methods are adaptive in that the stimulation is only turned on when necessary, the simplicity of acDBS limits its effectiveness. Comparing Figures 3A and 11A, we observe that while acDBS is able to deburst the STN, there is a degree of isolated single spike STN synchronization. In comparison, when stimulating with aLFPDBS, the amount of isolated single-spike STN synchronization is further reduced.

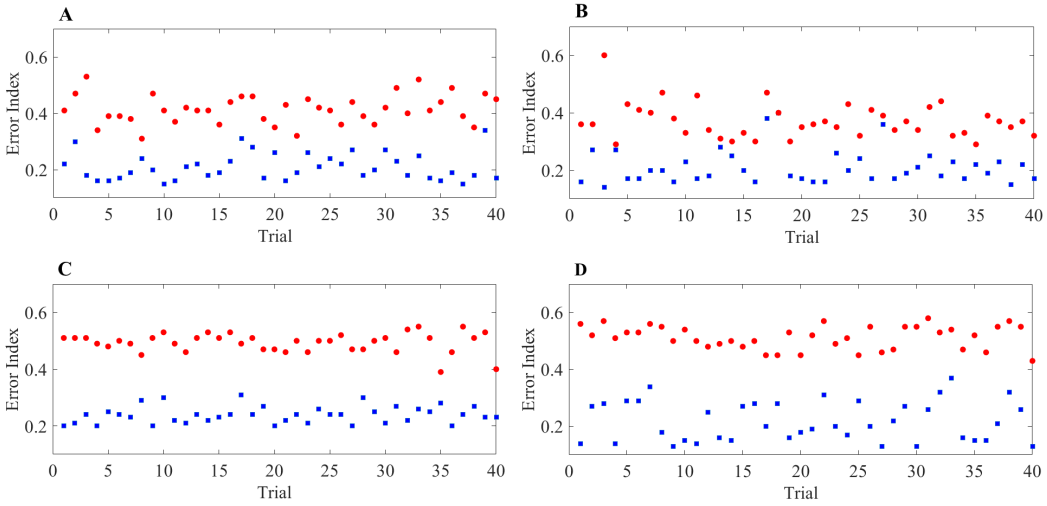

Figure 16. Error index values for 40 model TC neurons with heterogeneous TC parameter values. All baseline values of the TC parameter are given in Appendix A. (**A**) TC_1 heterogeneous error index values without stimulation (red) and with acDBS, Equation (16) (blue). (**B**) TC_2 heterogeneous error index values without stimulation (red) and with acDBS (blue). (**C**) TC_1 heterogeneous error index values without stimulation (red) and with acLFPDBS, Equation (19) (blue). **D** TC_2 heterogeneous error index values without stimulation (red) and with aLFPDBS (blue).

3. Discussion

In this computational study, we investigated the effects of two different adaptive deep brain stimulation techniques—adaptive constant stimulation (acDBS) and adaptive local field potential stimulation (aLFPDBS)—and their effects on the thalamocortical relay. Here, we consider a network of synaptically-connected, conductance-based model neurons from the STN, GPe and GPi in the basal ganglia based on previous modeling work [21,37–39]. The model is parametrized to generate activity patterns featuring synchronized, rhythmic bursts fired by clusters of STN neurons, with different clusters bursting in alternation, which we take to represent a parkinsonian state. Outputs from the GPi are rhythmic (see figures in Sections 4.1.2 and 4.1.3) and inhibit target model TC neurons that also receive excitatory input trains. We observe that the TC neurons are unable to respond reliably to these inputs, in agreement with earlier theory and simulations [21,37,39–49]. Using this framework, we considered two parametrizations of the parkinsonian state. The first network configuration consisted of a four-spike STN bursting pattern with a TC error index of 0.39 and 0.37 for the first and second TC cells, respectively. This configuration, which represents a mild to moderate state of computational parkinsonism, is used to investigate the acDBS mechanism. The second network configuration consisted of a three-spike STN bursting pattern with a TC error index of 0.56 for both model TC neurons. This configuration, representing an advanced state of computational parkinsonism, is used to investigate the aLFPDBS technique.

More recent computational studies on adaptive techniques have focused on stimulation within the STN that desynchronizes the rhythmic bursting dynamics found in the STN-GPe loop [13,24–29,31–36]. In this work, we demonstrate that the two proposed aDBS mechanisms are able to deburst the parkinsonian state and improve the TC error index while stimulation is applied. When these methods are properly tuned, the resulting model STN neurons exhibit single spike firing during the stimulation window. It is apparent that

desynchronization is important to developing effective closed-loop DBS mechanisms; however, our study suggests that desynchronization of the STN neurons alone is not enough to improve thalamocortical relay in our PD networks. In our study, we found that debursting was critical to improving TC relay. Because of the elimination of the bursting dynamic, the combination of debursting and partial desynchronization of the single spikes of the STN neurons is sufficient to restore the TC relay. For both methods under study, our simulations demonstrate that the greatest improvements to the TC error index were achieved when we debursted and desynchronized the STN neurons.

In the present study, all model STN neurons in our PD networks received the same stimulation strength when testing both adaptive mechanisms. Further in silico studies of interest would involve stimulating synchronized subgroups of the STN neurons while leaving other parts of the network unstimulated. Similarly, conducting trials in which all synchronized STN neurons receive different levels of stimulation strength would also be of interest.

Another avenue of interest in aDBS methods is further investigating the detection mechanism for controlling when the stimulation is on and off. Currently, we are determining when stimulation is turned on and off based on an interspike time method. When the interspike time is above a preset threshold, the stimulation is turned off; otherwise, the stimulation is on. This method is an initial investigation for predicting when the STN neurons might exhibit a bursting dynamic we wish to interrupt. Finding novel ways to detect parkinsonian firing is an open problem with many possible avenues of research. Recently, work by Jung et al. in 2023 used whole-brain dynamic modeling and machine learning for the classification of PD [50]. Their study uses a Jensen-Rit model type of interacting excitatory and inhibitory neuronal populations. Their work demonstrates that personalized whole-brain models can serve as an additional source of information relevant to the diagnosis and possibly treatment of PD [50]. As aDBS becomes more widely utilized in personalized medicine and targeted therapies, there will be an increased need to identify beneficial biological feedback signals used in controlling the delivery of stimulation.

At the present moment, there is one commercially available brain stimulation system that provides closed-loop DBS [11]. While research on aDBS is still in its early stages, the preliminary findings suggest that aDBS is superior to the current standard open-loop HF stimulation being used [51–53]. Meta-analysis of the existing studies has proven to be challenging due to the heterogeneity of research methodologies and the small number of studies that have been conducted [52]. The issues surrounding the amount and quality of data available are not new and reflect a continuing challenge in studying STN DBS in Parkinson's disease [54]. While these challenges will persist, experimenters and clinicians will increasingly need to rely on computational models to gain insights and correlations between neuronal activity and physical symptoms.

4. Methods and Materials

4.1. The Network Model

To develop a biologically faithful PD network model, we will adopt the same Hodgkin–Huxley model of basal ganglia thalamic network as in [21,37–39] with modifications to incorporate a variety of adaptive stimulation protocols of the STN neurons. Neurons in the basal ganglia and the thalamus communicate through various excitatory and inhibitory synaptic connections and receive certain external inputs. The basal ganglia circuit consists of GPe, GPi, STN neurons, and striatal input.

As depicted in Figure 17, both the GPi and GPe receive excitatory inputs from the STN. The GPe and GPi are subject to an inhibitory striatal input. There is synaptic coupling among inhibitory GPe neurons, and there is no coupling within the STN population and the GPi population. The TC cell is a relay station whose role is to respond under the GPi inhibition to incoming sensorimotor excitation via corticothalamic projections.

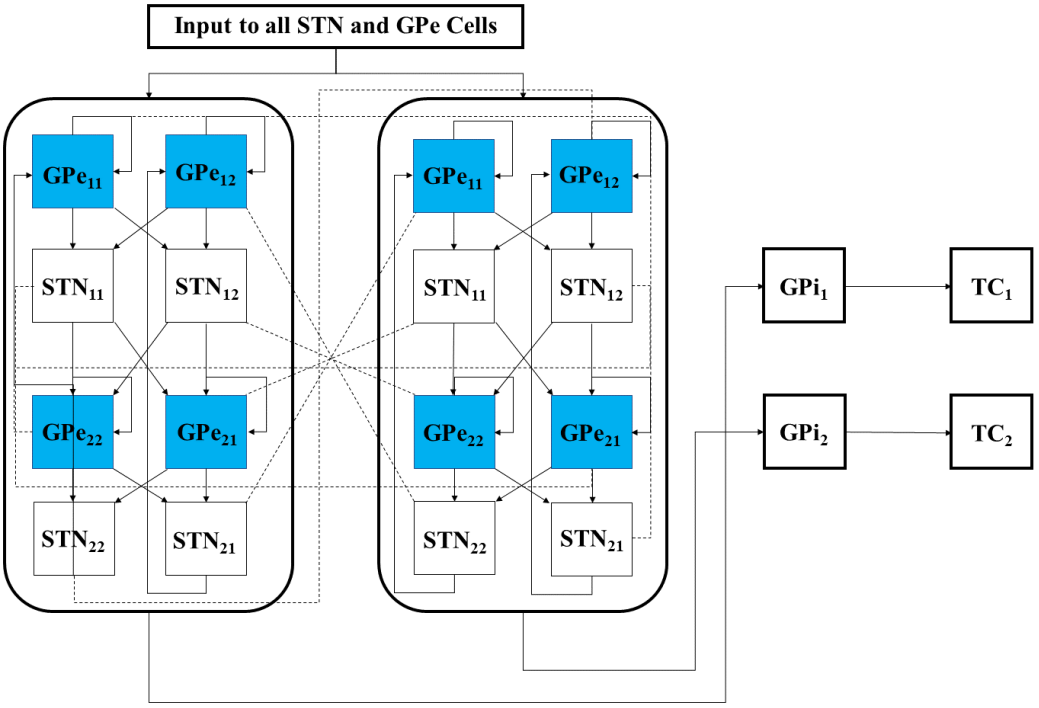

Figure 17. Full network model, including the interconnections between the STN and GPe subnetwork neuronal populations. Each STN and GPe block represents 4 neurons, while the GPi 1 and GPi 2 blocks represent 8 neurons that connect to a single TC cell. The solid lines represent strong synaptic connections, while the dashed lines start from the STN block to the corresponding GPe block, representing weak synaptic connections.

The network model consists of TC, STN, GPe, and GPi neurons. We will first describe the equations of STN, GPe and GPi neurons in the model network [37–39]. We then will present the TC neuron equations [37,39], which will be used to evaluate the DBS effectiveness. All specifics of the functions and parameter values used for each type of neuron in the model are given in Appendix A.

The STN voltage equation that we use takes the form

$$C_m v'_{Sn} = -I_L - I_{Na} - I_K - I_T - I_{Ca} - I_{AHP} - I_{GPe\to STN} + I^{stim}, \quad (1)$$

and was introduced in [38]. All the currents and corresponding kinetics are the same except that we make some parameter adjustments so that STN firing patterns are more similar to those reported in vivo [55–57]. $I_{GPe\to STN}$ is the inhibitory input current from GPe to STN. I^{stim} is the external stimulation applied to STN.

The voltage of each model GPe neuron obeys the equation

$$C_m v'_{Ge} = -I_L - I_{Na} - I_K - I_T - I_{Ca} - I_{AHP} - I_{GPe\to GPe} - I_{STN\to GPe} + I_{app}(t), \quad (2)$$

where $I_{GPe\to GPe}$ is the inhibitory input from other GPe cells, $I_{STN\to GPe}$ is the excitatory input from STN cells, and $I_{app}(t)$ is a time-dependent external current that represents hyperpolarizing striatal input to all GPe cells.

The voltage equation for each model GPi neuron is similar to that for the GPe neurons, namely

$$C_m v'_{Gi} = -I_L - I_{Na} - I_K - I_T - I_{Ca} - I_{AHP} - I_{STN\to GPi} + I_{GPe\to GPi} + I_{appi}(t), \quad (3)$$

where $I_{STN\to GPi}$ represents the excitatory input from STN to GPi, $I_{GPe\to GPi}$ is the inhibitory input from GPe to GPi, and $I_{appi}(t)$ are time-dependent external inputs that represent hyperpolarizing currents from the striatum to all GPi cells. The time-dependent external

currents $I_{app}(t)$ and $I_{appi}(t)$ are different from the constant inputs used in [21,37–39] and will take the form of a square-wave pulse given by

$$I_{appi}(t) = q_1 H(\sin(2\pi(t - t_{off,1})/t_{p,1})))(1 - H(\sin(2\pi(t - t_{off,1})/t_{p,1})), \quad (4)$$

and

$$I_{app}(t) = q_2 H(\sin(2\pi(t - t_{off,2})/t_{p,2})))(1 - H(\sin(2\pi(t - t_{off,2})/t_{p,2})). \quad (5)$$

Here, H is used to denote the Heaviside step function, such that $H(x) = 0$ if $x < 0$ and $H(x) = 1$ if $x > 0$. The parameters q_1 and q_2 in Equations (4) and (5) represent the amplitude of the square wave pulses and are consistent with the constant input values used in [21,37]. The parameters $t_{off,i}$ and $t_{p,i}$, $i = 1, 2$ are used to represent the period and duration of the square-wave pulses and will take on the values $t_{off,1} = 12$ ms, $t_{p,1} = 50$ ms, $t_{off,2} = 6$ ms, and $t_{p,2} = 40$ ms.

The model for each TC neuron takes the form

$$\begin{aligned} C_m v' &= -I_L - I_{Na} - I_K - I_T - I_{GPi\to TC} + I_E + c(t) \\ h' &= (h_\infty(v) - h)/\tau_h(v) \\ r' &= (r_\infty(v) - r)/\tau(v) \end{aligned} \quad (6)$$

In system (6), $I_L = g_L(v - v_L)$, $I_{Na} = g_{Na} m_\infty^3(v) h(v - v_{Na})$, and $I_K = g_K(0.75(1 - h))^4(v - v_K)$ are leak, sodium, and potassium currents, respectively. We apply a standard reduction in our expression for the potassium current to decrease the dimensionality of the model by one variable [58]. The current $I_T = g_T p_\infty^2(v) r(v - v_T)$ is a low-threshold calcium current, where r is the inactivation and $p_\infty^2(v)$ is the activation. The membrane capacitance C_m is normalized to 1 μF/cm^2 in all the neural models included in the current work.

Additional terms in system (6) are inputs that the model TC neuron receives. One is the inhibitory input current from the GPi, $I_{GPi\to TC}$, such that

$$I_{GPi\to TC} = g_{GPi} s_{GPi}(v - V_{GPi}), \quad (7)$$

where g_{GPi} is the constant maximum conductance and V_{GPi} is the synaptic reversal potential. s_{GPi} satisfies the equation

$$s'_{GPi} = \alpha_{GPi}(1 - s_{GPi}) S_\infty(v) - \beta_{GPi} s_{GPi}, \quad (8)$$

where $S_\infty(x) = (1 + e^{-(x+57)/2})^{-1}$.

The other input to the model TC neuron, I_E, represents simulated excitatory sensorimotor signals to the TC neuron. We assume that these are sufficiently strong to induce a spike in the absence of inhibition and therefore may represent synchronized inputs from multiple presynaptic cells. We tune the parameters so that the TC cell yields spontaneous spikes at a rate of roughly 12 Hz in the absence of both inhibitory GPi and excitatory synaptic inputs. The parameter values chosen place the model TC neuron near the transition from silence to spontaneous oscillations. In the model, $I_E = g_E s(v - v_E)$, where $g_E = 0.018$ mS/cm^2 , and s satisfies equation

$$s' = \alpha(1 - s) exc(t) - \beta s \quad (9)$$

where $\alpha = 0.8$ ms^{-1} and $\beta = 0.25$ ms^{-1}. The function $exc(t)$ controls the onset and offset of the excitation: $exc(t) = 1$ during each excitatory input, whereas $exc(t) = 0$ between excitatory inputs. The periodic $exc(t)$ takes the following form:

$$exc(t) = H(\sin(2\pi t/p))(1 - H(\sin(2\pi(t + d)/p))), \quad (10)$$

where the period $p = 50$ ms and duration $d = 5$ ms, and $H(x)$ is the Heaviside step function, such that $H(x) = 0$ if $x < 0$ and $H(x) = 1$ if $x > 0$. Hence, $exc(t) = 1$ from

time 0 up to time d, from time p up to time $p + d$, from time $2p$ up to time $2p + d$, and so on. A similar periodic function was used in previous work [37,39]. A baseline input frequency of 20 Hz is consistent with the high–pass filtering of corticothalamic inputs observed in vivo [59]; at this input rate, the model TC cells rarely fire spontaneous spikes between inputs.

In the following subsections, we focus on three aspects of the PD network model: the coupling structure in the STN–GPe loop, the averaged GPi synaptic input going into a TC relay neuron, and the TC relay error index.

4.1.1. Architecture of Coupling between Individual Neurons

As shown previously in [38], the STN and GPe sub-network can generate both irregular asynchronous and synchronous activity [38,60,61]. Our model builds off of [37], where each STN, GPe, and GPi group includes 16 neurons. We incorporated two relay TC neurons into the parkinsonian network to evaluate the performance of DBS [37,39]. The network model mimics the pathological neuronal activity observed in the basal ganglia in parkinsonian conditions, such as increased firing rate, bursting patterns, and synchronization in STN and GPi neurons [40–49]. We consider this rhythmic clustered regime in STN and GPi as the parkinsonian state and refer to the network in this state as the parkinsonian network. In our simulation results that are presented throughout, we will discard the first 1000 ms to ensure that the network is in the parkinsonian state.

We designed the structure of the STN-GPe loop in the model following the work on clustered rhythms in [38] so that the STN cells will segregate into two rhythmically bursting clusters, with synchronized activity within each cluster. The detailed structure of connections between STN and GPe neurons, along with their connections to the remaining GPi and TC cells, is depicted in Figure 17. In the STN and GPe sub-network, there are both strong and weak synaptic connections built into the architecture of the network. This is reflected in Figure 17 by duplicating the 16 STN and GPe neurons to show the symmetry present in building the strong and weak connections necessary to create two synchronized groups of neurons. We use K_{ij}, where K=GPe or STN, $i = 1, 2$, and $j = 1, 2$, to denote sub-population j within the i-th cluster of type K neurons. For example, the first sub-population of STN cluster one, STN_{11}, sends excitation to the first sub-population of GPe cluster two, GPe_{21}. The same sub-population of STN neurons are also weakly coupled with the other half of the same GPe cluster, GPe_{22}. Each sub-population of STN neurons is connected with two GPe sub-populations in an analogous way. Each sub-population of GPe neurons inhibits one group of STN neurons, as is also illustrated in Figure 17. Within each GPe sub-population GPe_{ij}, there are also local inhibitory connections.

The model also includes 16 GPi neurons, each receiving input from a single corresponding STN neuron. Thus, the rhythmic, bursty, synchronized outputs of each STN cluster induce rhythmic, bursty, synchronized activity in a corresponding group of GPi neurons. These GPi activity patterns mimic those seen experimentally in parkinsonian conditions. The network architecture is set up so that members of each such synchronized GPi group (GPi_1 or GPi_2) send synaptic inhibition to the same TC neuron, and hence each TC neuron receives a rhythmic inhibitory signal in the parkinsonian network (see Figure 17), which disrupts the fidelity of TC relay responses to excitatory inputs.

4.1.2. Averaged GPi Synaptic Input to TC

In our network model, the synaptic input from the GPi to a TC neuron, $I_{GPi\to TC}$, comes from a subgroup of GPi neurons. As illustrated in Figure 17, the first GPi subgroup maps to the first TC cell and the second GPi subgroup maps to the second TC cell. Following [21,37], we will let v_{TC_j} denote the membrane potential of the j-th TC cell. It follows that this input will take the form

$$I_{GPi_j\to TC} = g_{GPi}(v_{TC_j} - v_{GPi}) \sum_{k\in\Omega_j} s^k_{GPi_j},\ j = 1, 2, \tag{11}$$

where each Ω_j is an index set for the neurons in the GPi group, g_{GPi} is the maximal conductance, and v_{GPi} is the synaptic reversal potential for inhibition from the GPi group. Each $s^k_{GPi_j}$ in Equation (11) satisfies the equation

$$s'_{GPi} = \alpha_{GPi}(1 - s_{GPi})S_\infty(\tilde{v}) - \beta_{GPi}s_{GPi}, \tag{12}$$

where $S_\infty(x) = (1 + e^{-(x+57)/2})^{-1}$ and $\tilde{v}$ represents the membrane potential of the k-th GPi neuron from subgroup GPi_j.

Based on the structure of Equation (12), we can see that each $s^k_{GPi_j}$ is between 0 and 1. We define the quantities sg_1 and sg_2 by

$$sg_1 = \sum_{k\in\Omega_1} s^k_{GPi_1}, \tag{13}$$

and

$$sg_2 = \sum_{k\in\Omega_2} s^k_{GPi_2}. \tag{14}$$

Since each $s^k_{GPi_j}$ is between 0 and 1, it follows that sg_1 and sg_2 are each between 0 and 8. In our computational study, we use the variability of the time-average of each sg_i as an indicator of GPi rhythmic bursting activity. We do this by constructing histograms based on the frequency with which each sg_i time series, averaged over 25 ms time windows, takes different values in bins that cover the range of [0, 8]. In analyzing both the parkinsonian state and the adaptive stimulation protocols, we will construct the histograms over the time window during which stimulation is applied from 2000 to 7000 ms. Specifically, we display six bins centered at 1 through 6, respectively, and each represents a subinterval of 1 ms/cm^2, except that all values less than 1.5 are placed in the 1 bin and all values greater than 5.5 are placed into the 6 bin. In the parkinsonian network without external stimulation, the average sg_i values fall into the 1 and 6 bins, as seen in Figure 18.

This result occurs because the GPi firing is both rythmic and bursty (see the top traces in Figure 19). Studying the top traces in blue in Figure 19 in panels B and C, we see that the GPi synaptic output is high during each bursting episode and low in between bursting events. A few values will be sorted into the middle bins 2 through 5 in Figure 18 due to the transition between bursting and quiescent phases. We will show that very different results emerge when our adaptive stimulation protocols are applied to the STN neurons (Figures 4, 7 and 12).

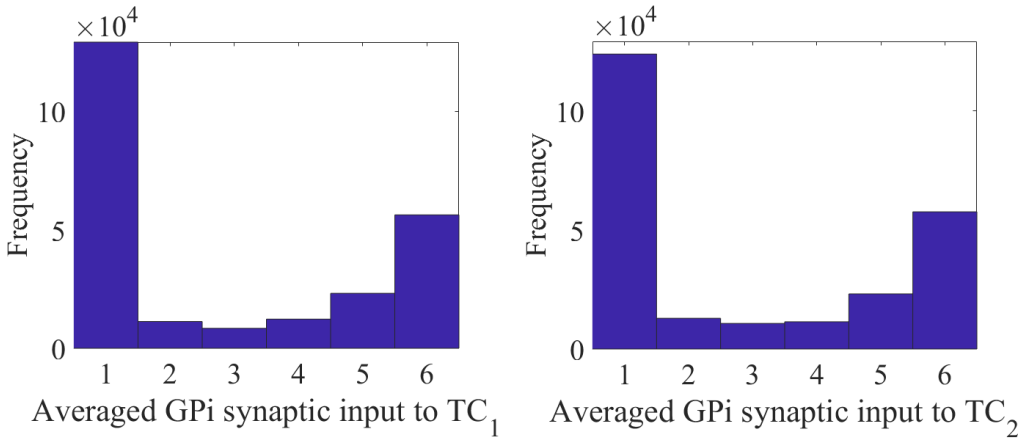

Figure 18. Histograms of sg_1 (**left**) and sg_2 (**right**) in the parkinsonian network, in ms/cm^2. Both histograms include two dominant bins, centered at 1 and 6, due to the quiescent and bursting phases, respectively, of GPi activity.

4.1.3. TC Relay Responses and Error Index

Based on the network architecture described above, the synaptic input from the GPi to the target TC cells is both rhythmic and bursty (see Figure 19 Panels B and C, top curve). While there are instances where the TC neuron fires a single spike in accordance with the excitatory input that it receives (see Figure 19 Panels B and C, middle curve), other excitatory inputs to the TC neuron either result in no spiking activity or firing multiple spikes in response to a single excitatory input. This failure in one-to-one response between excitatory input and TC response is how we will characterize and define TC relay fidelity.

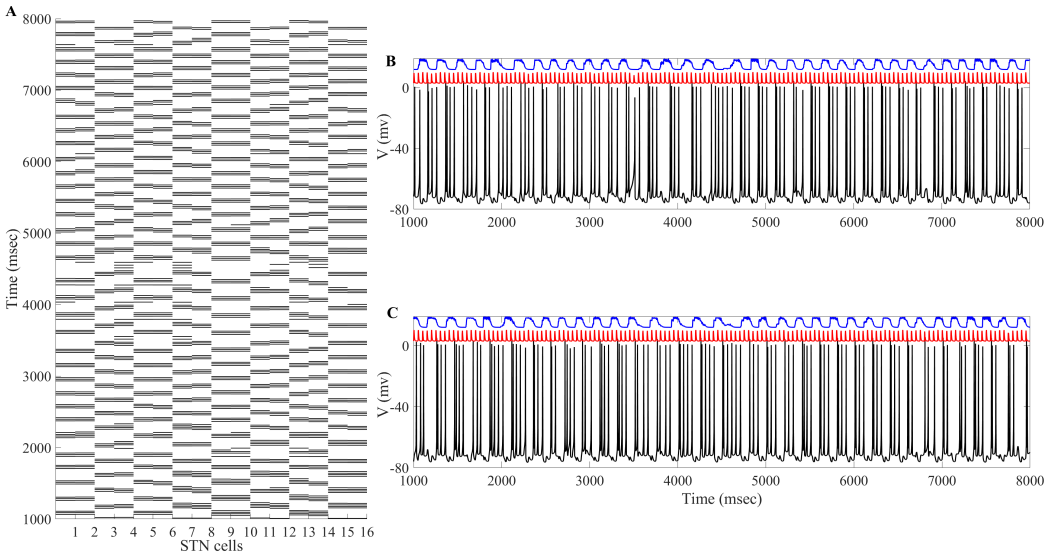

Figure 19. STN clusters in the parkinsonian network. Panel (**A**) shows that the 16 model STN neurons form two synchronized clusters. Panels (**B**,**C**) show the membrane potentials of the two TC neurons (bottom curve, black) responding to excitatory sensorimotor signals (middle curve, red), along with the total synaptic input the corresponding TC cell receives from eight GPi neurons (top curve, blue).

In our computational study, we quantify the relay performance of each TC neuron using a simple error index, which is computed by dividing the total number of errors—instances in which the TC cell either does not fire or fires multiple spikes in response to a single excitatory input—by the total number of excitatory inputs. That is, we define

$$\text{error index} = \frac{b+m}{n}, \tag{15}$$

where n is the total number of excitatory inputs. In Equation (15), b will represent the number of excitatory inputs in which the TC neuron gives a bad response consisting of more than one spike. Typically this will be in the form of a bursting episode but will also include a single-spike response followed after a delay, but before the next input, by additional spikes [37]. The number m in Equation (14) will represent the number of excitatory inputs that are "missed" by the TC neuron. That is, it is the number of excitatory inputs to the TC neuron that results in no corresponding spiking activity during a detection window [37]. Consistent with [37,39], the detection window used in our study extends from the beginning of each excitatory input to 18 ms after each input. This error index was first introduced in [39] and was used previously with the same error detection algorithm to quantify how different patterns of inhibitory GPi signals obtained from experimental recordings of normal and parkinsonian monkeys, with and without DBS [62], affect the TC relay response [37].

Adaptive deep brain stimulation (aDBS) is a closed-loop and demand-controlled method where DBS is turned on and off according to a feedback signal. In this approach, stimulation is administered only when necessary and to an extent dependent on the measured neuronal activity or symptoms [13]. Examples of stimulation trigger events or

biophysical markers include action potentials from the targeted region of the brain and the amplitude of the beta-band local field potential (LFP) of the subthalamic nucleus (STN) measured via implanted electrodes [13]. In this study, we used the interspike time—the time between successive spikes—of the STN neurons to monitor the amount of ongoing abnormal neuronal activity to determine when stimulation will be applied to the network. We chose to use the interspike time between successive STN spikes as our biological signal due to several considerations. First, in our biophysical model, it is not difficult to detect when the action potential occurs. Second, this measurement is coming from the targeted region for stimulation and thus will form a closed feedback loop in the network. This feedback loop will help modulate the stimulation in real-time. Additionally, the use of the interspike time of successive STN neurons as a biological signal to control the adaptive delivery of stimulation has not been studied yet. Using this as our detection method, we aim to not only desynchronize the bursting dynamics of the parkinsonian network but to provide stimulation in such a way that the bursting dynamic of the STN neurons is eliminated completely, and we seek to improve the TC relay performance. The stimulation patterns that we will be testing under this adaptive scheme are constant pulse DBS (acDBS) and local field potential DBS (aLFPDBS) with coordinated reset shuffling.

4.2. Adaptive Constant Pulse DBS

The acDBS is given by the formula

$$I_k^{\text{stim}} = \sum_{i=1}^{N_k} a_0 H(t - t_{i,1})(1 - H(t - t_{i,2})), \tag{16}$$

where a_0 denotes the amplitude of the constant pulses, and H is the Heaviside function, where the times $t_{i,1}$ and $t_{i,2}$ are determined from the spiking mechanism of the STN neurons. These times are identified to track the interspike interval. For the adaptive protocol, if the interspike interval is larger than a preset threshold parameter, then the stimulation is turned off. After the stimulation has been turned off, stimulation will resume if the interspike interval is even smaller than the preset threshold. The corresponding turn-on time is $t_{i,1}$, and the off time is $t_{i,2}$. That is, when $t = t_{i,1}$, $H(t - t_{i,1}) = 1$ and $1 - H(t, t_{i,2}) = 1$, and thus, the stimulation is on, and when $t = t_{i,2}$, $H(t - t_{i,1}) = 0$, and thus, the stimulation will be off.

4.3. Adaptive Multi-Site LFP Stimulation

Local field potentials (LFP) are transient electrical signals generated in nervous and other tissues by the aggregate electrical activity of the individual cells in that tissue (e.g., neurons). Since the LFP reflects the activity of many neurons in the vicinity of the recording electrode, it is therefore useful in studying local network dynamics.

Extracellular potentials are generated by transmembrane currents, and in the presently used volume conductor theory, the system is envisioned as a three-dimensional smooth extracellular continuum where the transmembrane currents are represented as volume currents [63]. In volume conductor theory, the fundamental formula for the contribution of extracellular potential $\phi(\mathbf{r}, t)$ from the activity in an N-neuron model is given by

$$\phi(\mathbf{r}, t) = \frac{1}{4\pi\sigma} \sum_{n=1}^{N} \frac{I_n(t)}{|\mathbf{r} - \mathbf{r}_n|}. \tag{17}$$

Here, $I_n(t)$ denotes the transmembrane current in compartment n positioned at $\mathbf{r}_n$, and σ is the extracellular conductivity.

The measured raw LFP(t) is filtered online by applying a linear damped oscillator

$$\ddot{x} + a\dot{x} + bx = \mu \text{LFP}(t). \tag{18}$$

In the equation above, b approximates the frequency of the LFP oscillations and is expressed by $b = 2\pi/T$ where T is the mean period of the LFP. The parameters a and b are chosen in such a way that $a^2 < 4b$ to guarantee that Equation (18) represents a harmonic oscillator. The parameter μ controls the strength of the stimulation. We first choose the values of $a = 0.0025$ and $b = 0.00136$ so that the period of the harmonic oscillator is the same as the natural frequency of the bursts present in the STN clusters.

The aLFPDBS is given by the formula

$$I_k^{stim} = \frac{\mu}{n} \sum_{i=1}^{N_k} \sum_{k=1}^{4} H(t - t_{i,1})(1 - H(t - t_{i,2}))e^{-2dist(j,k)} x^k(t - (k-1)\tau), \tag{19}$$

where n is the number of STN cells, $dist(j,k)$ is the distance between the jth neuron and the kth stimulation site, and $x^k(t - (k-1)\tau)$ is the time-delayed signal from Equation (18) that is delivered at the kth stimulation site, where τ is the delay and $k = 1, 2, \ldots 4$. Here, we calculate the distance in a two-dimensional Euclidian space. For instance, the distance between STN cell 2 and stimulation site 4 is given by $dist(2,4) = \sqrt{0.25^2 + 0.5^2}$. As before, the times $t_{i,1}$ and $t_{i,2}$ will be identified from the spiking mechanism of the STN neurons to track the interspike interval needed to control the delivery of the adaptive stimulation.

This formula is applied to the STN neurons through four stimulation sites, as illustrated in Figure 20. The 16 model STN neurons are represented by solid circles arranged in a four-by-four grid centered at the plus in the center. The first row on the square grid is STN_1, STN_2, STN_3, and STN_4 from left to right. STN_5–STN_8, STN_9–STN_{12}, and STN_{13}–STN_{16} are in rows 2, 3, and 4, respectively. These neurons are spaced in such a way that the horizontal and vertical distance between any two neurons is 0.1. The four small boxes in Figure 20 are the stimulation sites, numbered 1, 2, 3, and 4, proceeding clockwise from the left. These sites are arranged to be at the center of a smaller two-by-two block formed by the four nearest STN cells.

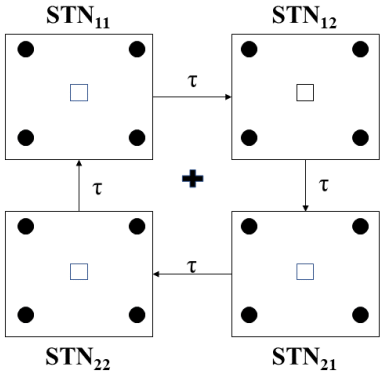

Figure 20. Sixteen STN cells (solid circles) on a square grid with the center (plus sign) where an electrode can measure the local field potential. The four square boxes are the stimulation sites where the signal will be shuffled through in a clockwise fashion. The signal will be on a time delay of τ through each site. In the acDBS protocol (Equation (16)), there is no delay and no shuffling of the stimulation.

Author Contributions: Conceptualization, Y.G.; Methodology, T.S. and Y.G.; Formal analysis, T.S. and Y.G.; Investigation, T.S. and Y.G.; Resources, Y.G.; Writing—original draft, T.S. and D.M.; Writing—review and editing, T.S., Y.G. and D.M.; Visualization, T.S.; Supervision, Y.G.; Project administration, Y.G.; Funding acquisition, T.S. All authors have read and agreed to the published version of the manuscript.

Funding: This research received no external funding.

Institutional Review Board Statement: Not applicable.

Informed Consent Statement: Not applicable.

Data Availability Statement: All the model simulations conducted in this study were completed using XPPAUT. The XPPAUT code is available for use by request to the corresponding author.

Acknowledgments: We thank the journal referees for their constructive feedback that improved the quality of this manuscript. This research was supported in part by the William Keefer Fund at Beloit College.

Conflicts of Interest: The authors declare no conflict of interest.

Abbreviations

The following abbreviations are used in this manuscript:

aDBS	adaptive deep brain stimulation
acDBS	adaptive constant pulse deep brain stimulation
aLFPDBS	adaptive local field potential deep brain stimulation
DBS	deep brain stimulation
GP	globus pallidus
GPe	external segment of the globus pallidus
GPi	internal segment of the globus pallidus
HF	conventional high-frequency stimulation
PD	Parkinson's disease
LFP	local field potential
STN	subthalamic nucleus
TC	thalamacortical neurons

Appendix A

In the following text, we use g_i to denote conductance in mS/cm^2 and v_i to denote reversal potentials in mV, where the subscript i is from the set $\{L, Na, K, Ca, AHP, T, E, GPi, GPe \to GPe, GPe \to STN, GPe \to GPi, STN \to GPe, STN \to GPi\}$. τ with a subscript or both a superscript and a subscript is a time constant in units of ms. All α and β with subscripts are rate constants in units of ms^{-1}. Other parameters are either constants without units or with units given in the following text.

Functions for **TC** neurons in system (6):

$m_\infty(v) = 1/(1+e^{-(v+37)/7})$, $p_\infty(v) = 1/(1+e^{-(v+60)/6.2})$,
$h_\infty(v) = 1/(1+e^{(v+41)/4})$, $r_\infty(v) = 1/(1+e^{(v+84)/4})$,
$\tau_h(v) = 1/(a_h(v)+b_h(v))$, $\tau_r(v) = 0.4(28+e^{-(v+25)/10.5})$,
$a_h(v) = 0.128e^{-(46+v)/18}$, $b_h(v) = 4/(1+e^{-(23+v)/5})$.

Parameters for **TC** neurons:

$g_L = 0.14$, $g_{Na} = 3$, $g_K = 5$, $g_T = 5$, $g_E = 0.018$, $g_{GPi} = 0.009$,
$v_L = -72$, $v_{Na} = 50$, $v_K = -90$, $v_T = 90$, $v_E = 0$, $v_{GPi} = -85$,
$p = 50$ ms, $d = 5$ ms, $win_{off} = 18$ ms.

GPi currents:

$I_L(v) = g_L(v-v_L)$, $I_{Na} = g_{Na}(m_\infty^3(v))h(v-v_{Na})$, $I_K = g_K n^4(v-v_K)$,
$I_T = g_T a_\infty^3(v) r(v-v_{Ca})$, $I_{Ca} = g_{Ca} s_\infty^2(v)(v-v_{Ca})$,
$I_{AHP} = g_{AHP}(v-v_K)([Ca]/([Ca]+k))$,
$I_{STN\to GPi} = g_{STN\to GPi} s_{STN\to GPi}(v-v_{STN\to GPi})$, where $s_{STN\to GPi}$ is listed under STN equations, and
$I_{GPe\to GPi} = g_{GPe\to GPi} s_{GPe\to GPi}(v-v_{GPe\to GPi})$, where $s_{GPe\to GPi}$ is listed under GPe equations.
$I_{appi} = -1$ μA is a constant applied current.

GPi equations and functions:

$n' = \phi_n(n_\infty(v)-n)/\tau_n(v)$, $h' = \phi_h(h_\infty(v)-h)/\tau_h(v)$, $r' = \phi(r_\infty(v)-r)/\tau_r$,
$[Ca]' = \epsilon(-I_{Ca}-I_T-k_{Ca}[Ca])$, $s'_{Gi} = \alpha(1-s_{Gi})S_\infty(v) - \beta_{Gi}s_{Gi}$, where $S_\infty(v)$ is given in Section 2.2.

$X_\infty(v) = 1/(1+e^{-(v-\theta_X)/\sigma_X})$, where $X = m, n, h, r, a, s$, and
$\tau_X(v) = \tau_X^0 + \tau_X^1/(1+e^{-(v-\theta_X^\tau)/\sigma_X^\tau})$, where $X = n, h$.

GPi parameters:

$g_L = 0.1$, $g_{Na} = 120$, $g_K = 30$, $g_T = 0.5$, $g_{Ca} = 0.1$, $g_{AHP} = 30$, $g_{Sn\to Gi} = 0.5$, $g_{Ge\to Gi} = 1$,
$v_L = -55$, $v_{Na} = 55$, $v_K = -80$, $v_{Ca} = 120$, $v_{GPe\to GPi} = -100$, $v_{STN\to GPi} = 0$,
$\tau_n^0 = 0.05$, $\tau_n^1 = 0.27$, $\tau_h^0 = 0.05$, $\tau_h^1 = 0.27$, $\tau_r = 30$,
$\phi_r = 1$, $\phi_n = 0.1$, $\phi_h = 0.05$,
$k_1 = 30$, $k_{Ca} = 15$, $\epsilon = 0.0001$ msec^{-1},
$\theta_r = -70$, $\theta_m = -37$, $\theta_n = -50$, $\theta_h = -58$, $\theta_a = -57$, $\theta_s = -35$, $\alpha = 2$, $\theta_n^\tau = -40$, $\theta_h^\tau = -40$,
$\sigma_m = 10$, $\sigma_n = 14$, $\sigma_h = -12$, $\sigma_r = -2$, $\sigma_a = 2$, $\sigma_s = 2$, $\sigma_n^\tau = -12$, $\sigma_h^\tau = -12$,
$\beta_{GPi} = 0.08$, $k_{Ca} = 15$.

STN currents:

I_L, I_{Na}, I_K, I_{Ca}, I_{AHP} are as given above for the GPi neuron, and $I_T = g_T a_\infty^3(v) b_\infty(r)(v - v_{Ca})$. The synaptic currents from GPe to STN are the following:

$I_{GPe\to STN} = g_{GPe\to STN} \sum_{j\in\Lambda} s^j_{GPe\to STN}(v - v_{STN\to GPe})$, where Λ is a subgroup of GPe cells and $s_{GPe\to STN}$ is given in GPe equations.

For the stimulation current I^{stim}, see details in Sections 4.2 and 4.3.

STN equations and functions:

$n, h, r, [Ca]$ equations and functions $X_\infty(v), \tau_X(v)$ are the same as given above for the GPi neuron, except there is no $r_\infty(v)$ used and we introduce $b_\infty(r) = 1/(1+e^{(r-\theta_b)/\sigma_b}) - 1/(1+e^{-\theta_b/\sigma_b})$.

The synaptic input from STN to GPe and GPi is described as:
$s'_{STN\to GPe} = \alpha_{STN\to GPe}(1 - s_{STN\to GPe}) s_\infty(v - 30) - \beta_{STN\to GPe} s_{STN\to GPe}$,
$s'_{STN\to GPi} = \alpha_{STN\to GPi}(1 - s_{STN\to GPi}) s_\infty(v - 30) - \beta_{STN\to GPi} s_{STN\to GPi}$.

STN Parameters:

$g_L = 2.25$, $g_{Na} = 37.5$, $g_K = 45$, $g_T = 0.5$, $g_{Ca} = 0.5$, $g_{AHP} = 9$, $g_{GPe\to STN} = 0.9$,
$v_L = -60$, $v_{Na} = 55$, $v_K = -80$, $v_{Ca} = 140$, $v_{GPe\to STN} = -100$,
$\tau_n^0 = 1$, $\tau_n^1 = 100$, $\tau_h^0 = 1$, $\tau_h^1 = 500$, $\tau_r^0 = 7.1$, $\tau_r^1 = 17.5$,
$\phi_r = 0.5$, $\phi_n = 0.75$, $\phi_h = 0.75$,
$k_1 = 15$, $k_{Ca} = 22.5$, $\epsilon = 5 \times 10^{-5}$,
$\theta_r = -67$, $\theta_m = -30$, $\theta_n = -32$, $\theta_h = -39$, $\theta_a = -63$, $\theta_s = -39$, $\theta_b = 0.25$,
$\theta_n^\tau = -80$, $\theta_h^\tau = -57$, $\theta_r^\tau = 68$,
$\sigma_m = 15$, $\sigma_n = 8$, $\sigma_h = -3.1$, $\sigma_r = -2$, $\sigma_a = 7.8$, $\sigma_s = 8$, $\sigma_b = 0.07$
$\sigma_n^\tau = -26$, $\sigma_h^\tau = -3$, $\sigma_r^\tau = -2.2$,
$\alpha_{STN\to GPe} = 5$, $\alpha_{STN\to GPi} = 1$, $\beta_{Sn\to Ge} = 1$, $\beta_{STN\to GPi} = 0.05$, $wk = 0.45$.
PHFS parameters: $\rho_1 = 0.7$, $a_1 = 0.9$, $a_0 \in [36, 100]$, $\tau_0 \in [16.5, 60.5]$.
LFP parameters are all given in the text.

GPe currents:

I_L, I_{Na}, I_K, I_{Ca}, I_{AHP} are modeled as given above for the GPi neuron. The synaptic currents to GPe are:

$I_{STN\to GPe} = g_{STN\to GPe} \sum_{j\in\Lambda} s_{STN\to GPe}(v - v_{STN\to GPe})$, where Λ is a subgroup of STN neurons and $s_{STN\to GPe}$ is given under STN equations.

$I_{GPe\to GPe} = g_{GPe\to GPe} \sum_{j\in\Lambda} s_{GPe\to GPe}(v - v_{GPe\to GPe})$ where Λ is a subgroup of STN neurons and $s_{GPe\to GPe}$ is the same as $s_{GPe\to STN}$ given under GPe equations.

$I_{app} = -1.2$ is a constant applied current.

GPe equations and functions:

$n, h, r, [Ca]$ equations and function $X_\infty(v), \tau_X(v)$ are as given above for the GPi neuron.

The synaptic input from STN to GPe and GPi is described as:
$s'_{GPe\to STN} = \alpha_{GPe\to STN}(1 - s_{GPe\to STN}) s_\infty(v - 20) - \beta_{GPe\to STN} s_{GPe\to STN}$,
$s'_{GPe\to GPi} = \alpha_{GPe\to GPi}(1 - s_{GPe\to GPi}) s_\infty(v - 20) - \beta_{GPe\to GPi} s_{GPe\to GPi}$.

GPe parameters:

Most parameters for GPe are the same as those for GPi. We only list those that have different values and the additional ones not present in the GPi model.

$g_{STN\to GPe} = 0.18$, $g_{GPe\to GPe} = 0.01$, $v_{STN\to GPe} = 0$, $v_{GPe\to GPe} = -80$,
$\alpha_{GPe\to STN} = 2$, $\alpha_{GPe\to GPi} = 1$,
$\beta_{GPe\to STN} = 0.04$, $\beta_{GPe\to GPi} = 0.1$.

References

1. McIntyre, C.C.; Hahn, P. Network perspectives on the mechanisms of deep brain stimulation. *Neurobiol. Dis.* **2010**, *38*, 329–337. [CrossRef]
2. Wichmann, T.; DeLong, M.R. Deep brain stimulation for neurologic disorders. *Neuron* **2006**, *52*, 197–204. [CrossRef]
3. Benabid, A.L.; Chabardes, S.; Mitrofanis, J.; Pollak, P. Deep brain stimulation of the subthalamic nucleus for the treatment of Parkinson's disease. *Lancet Neurol.* **2009**, *8*, 67–81. [CrossRef]
4. Volkmann, J. Deep brain stimulation for the treatment of Parkinson's disease. *J. Clin. Neurophys.* **2004**, *21*, 6–17. [CrossRef] [PubMed]
5. Hauptmann, C.; Omel'chenko, O.; Popovych, O.V.; Maistrenko, Y.; Tass, P.A. Control of spatially patterned synchrony with multisite delayed feedback. *Phys. Rev. E* **2007**, *76*, 066209. [CrossRef]
6. Jankovic, J. Parkinson's disease: Clinical features and diagnosis. *J. Neurol. Neurosurg. Psychiatry* **2008**, *79*, 368–376. [CrossRef] [PubMed]
7. Rodriguez-Oroz, M.C.; Obeso, J.A.; Lang, A. E.; Houeto, J.-L.; Pollak, P.; Rehncrona, S.; Kulisevsky, J.; Albanese, A.; Volkmann, J.; Hariz, M.I.; et al. Bilateral deep brain stimulation in Parkinson's disease: A multicentre study with 4 years follow-up. *Brain* **2005**, *128*, 2240–2249. [CrossRef]
8. Deuschl, G.; Schade-Brittinger, C.; Krack, P.; Volkmann, J.; Schäfer, H.; Bötzel, K.; Daniels, C.; Deutschländer, A.; Dillmann, U.; Eisner, W.; et al. A randomized trial of deep-brain stimulation for Parkinson's disease. *N. Engl. J. Med.* **2006**, *355*, 896–908. [CrossRef] [PubMed]
9. Feng, X.; Shea-Brown, E.; Rabitz, H.; Greenwald, B.; Kosut, R. Optimal deep brain stimulation of the subthalamic nucleus—A computational study. *J. Comput. Neurosci.* **2007**, *23*, 265–282. [CrossRef]
10. Feng, X.; Shea-Brown, E.; Rabitz, H.; Greenwald, B.; Kosut, R. Toward closed-loop optimization of deep brain stimulation for Parkinson's disease: Concepts and lessons from a computational model. *J. Neuroeng.* **2007**, *4*, L14–L21. [CrossRef]
11. Parastarfeizabadi, M.; Kouzani, A.Z. Advances in closed-loop deep brain stimulation devices. *J. Neuroeng. Rehabil.* **2017**, *14*, 79. [CrossRef]
12. Bouthour, W.; Megevand, P.; Donoghue, J.; Luscher, C.; Birbaumer, N.; Krack, P. Biomarkers for closed-loop deep brain stimulation in Parkinson disease and beyond. *Nat. Rev. Neurol.* **2019**, *15*, 343–352. [CrossRef] [PubMed]
13. Popovych, O.V.; Tass, P.A. Adaptive delivery of continuous and delayed feedback deep brain stimulation—A computational study. *Sci. Rep.* **2019**, *9*, 10585. [CrossRef]
14. Little, S.; Pogosyan, A.; Neal, S.; Zavala, B.; Ludvic, Z.; Hariz, M.; Foltynie, T.; Limousin, P.; Ashkan, K.; FitzGerald, J.; et al. Adaptive Deep Brain Stimulation in Advanced Parkinson Disease. *Ann. Neurol.* **2013**, *74*, 449–457. [CrossRef] [PubMed]
15. de Castro, D.L.; Aroso, M.; Aguiar, A.P.; Grayden, D.B.; Aguiar, P. A novel closed-loop control algorithm to disrupt pathological neuronal oscillations—Implementation and validation in vitro. *bioRxiv* **2022**. [CrossRef]
16. Piña-Fuentes, D.; van Dijk, J.M.C.; van Zijl, J.C.; Moes, H.R.; van Laar, T.; Oterdoom, D.M.; Little, S.; Brown, P.; Beudel, M. Acute effects of adaptive deep brain stimulation in Parkinson's disease. *Brain Stimul.* **2020**, *13*, 1507–1516. [CrossRef]
17. Guidetti, M.; Marceglia, S.; Loh, A.; Harmsen, I.; Meoni, S.; Foffani, G.; Lozano, A.; Moro, E.; Volkmann, J.; Priori, A. Clinical perspectives of deep brain stimulation. *Brain Stimul.* **2021**, *14*, 1238–1247. [CrossRef] [PubMed]
18. Vissani, M.; Isaias, I.U.; Mazzoni, A. Deep brain stimulation: A review of the open neural engineering challenges. *J. Neural Eng.* **2020**, *17*, 051002. [CrossRef] [PubMed]
19. Shah, A.; Nguyen, T.; Peterman, K.; Khawaldeh, S.; Debove, I.; Shah, S.; Torrecillos, F.; Tan, H.; Pogosyan, A.; Lachenmayer, M.; et al. Combining Multimodal Biomarkers to Guide Deep Brain Stimulation Programming in Parkinson Disease. *Neuromodulation* **2022**, *26* 1–13 . [CrossRef]
20. Lozano, A.M.; Lipsman, N.; Bergman, H.; Brown, P.; Chabardes, S.; Chang, J.W.; Matthews, K.; McIntyre, C.C.; Schlaepfer, T.E.; Schulder, M.; et al. Deep brain stimulation: Current challenges and future directions. *Nat. Rev. Neurol.* **2019**, *15*, 148–160. [CrossRef]
21. Guo, Y.; Rubin, J.E. Multi-site Stimulation of Subthalamic Nucleus Diminishes Thalamocortical Relay Errors in a Biophysical Network. *Neural Netw.* **2011**, *24*, 602–616. [CrossRef] [PubMed]
22. Hauptmann, C.; Popovych, O.; Tass, P.A. Effectively desynchronizing brain stimulation based on a coordinated delayed feedback stimulation via several sites: A computational study. *Biol. Cybern.* **2005**, *93*, 463–470. [CrossRef] [PubMed]
23. Tass, P. A model of desynchronizing deep brain stimulation with a demand-controlled reset of neural subpopulations. *Biol. Cybern.* **2003**, *89*, 81–88. [CrossRef] [PubMed]

24. Asl, M.M.; Valizadeh, A.; Tass, P.A. Decoupling of interacting neuronal populations by time-shifted stimulation through spike-timing-dependent plasticity. *bioRxiv* **2022**. [CrossRef]
25. Fleming, J.E.; Dunn, E.; Lowery, M. Simulation of closed-loop deep brain stimulation schemes for suppression of pathological beta oscillations in Parkinson's disease. *Front. Neurosci.* **2020**, *14*, 166. [CrossRef]
26. Fleming, J.E.; Orłowski, J.; Lowery, M.; Chaillet, A. Self-tuning deep brain stimulation controller for suppression of beta oscillations: Analytical derivation and numerical validation. *Front. Neurosci.* **2020**, *14*, 639. [CrossRef]
27. Khaledi-Nasab, A.; Kromer, J.A.; Tass, P.A. Long-lasting desynchronization of plastic neural networks by random reset stimulation. *Front. Physiol.* **2021**, *11*, 622620. [CrossRef]
28. Kromer, J.; Khaledi-Nasab, A.; Tass, P.A. Impact of number of stimulation sites on long-lasting desynchronization effects of coordinated reset stimulation. *Chaos* **2020**, *30*, 083134. [CrossRef]
29. Liu, C.; Zhao, G.; Zhou, C.; Zhu, X.; Zhang, W.; Wang, J.; Li, H.; Wu, H.; Fietkiewicz, C.; Loparo, K.A. Closing the loop of DBS using the beta oscillations in cortex. *Cogn. Neurodyn.* **2021**, *15*, 1157–1167. [CrossRef]
30. Popovych, O.V.; Lysyansky, B.; Rosenblum, M.; Pikovsky, A.; Tass, P.A. Pulsatile Desynchronizing Delayed Feedback for Closed-Loop Deep Brain Stimulation. *PLoS ONE* **2017**, *12*, e0173363. [CrossRef]
31. Popovych, O.V.; Tass, P.A. Multisite Delayed Feedback for Electrical Brain Stimulation. *Front. Physiol.* **2018**, *9*, 00046. [CrossRef]
32. Rouhani, E.; Fathi, Y. Robust multi-input multi-output adaptive fuzzy terminal sliding mode control of deep brain stimulation in Parkinson's disease: A simulation study. *Sci. Rep.* **2021**, *11*, 21169. [CrossRef]
33. Spiliotis, K.; Starke, J.; Franz, D.; Richter, A.; Köhling, R. Deep brain stimulation for movement disorder treatment: Exploring frequency-dependent efficacy in a computational network model. *Biol. Cybern.* **2022**, *116*, 93–116. [CrossRef]
34. Spiliotis, K.; Butenko, K.; van Rienen, U.; Starke, J.; Köhling, R. Complex network measures reveal optimal targets for deep brain stimulation and identify clusters of collective brain dynamics. *Front. Phys.* **2022**, *10*, 951724. [CrossRef]
35. Toth, K.; Wilson, D. Control of coupled neural oscillations using near-periodic inputs. *Chaos* **2022**, *32*, 033130. [CrossRef]
36. Xia, S.; Zhang, Z. Multiple-site deep brain stimulation with delayed rectangular waveforms for Parkinson's disease. *Electron. Res. Arch.* **2021**, *29*, 3471–3487.
37. Guo, Y.; Rubin, J.E.; McIntyre, C.C.; Vitek, J.L.; Terman, D. Thalamocortical relay fidelity varies across subthalamic nucleus deep brain stimulation protocols in a data-driven computational model. *J. Neurophysiol.* **2008**, *99*, 1477–1492. [CrossRef]
38. Terman, D.; Rubin, J.E.; Yew, A.C.; Wilson, C.J. Activity patterns in a model for the subthalamopallidal network of the basal ganglia. *J. Nerurosci.* **2002**, *22*, 2963–2976. [CrossRef]
39. Rubin, J.E.; Terman, D. High frequency stimulation of the subthalamic nucleus eliminates pathological thalamic rythmicity in a computational model. *J. Comput. Neurosci.* **2004**, *16*, 211–235. [CrossRef]
40. Bergman, H.; Wichmann, T.; Karmon, B.; DeLong, M. The primate subthalamic nucleus. II. Neuronal activity in the mptp model of parkinsonism. *J. Neurophysiol.* **1994**, *72*, 507–520. [CrossRef]
41. Nini, A.; Feingold, A.; Slovin, H.; Bergman, H. Neurons in the globus pallidus do not show correlated activity in the normal monkey, but phase-locked oscillations appear in the MPTP model of parkinsonism. *J. Neurophysiol.* **1995**, *74*, 1800–1805. [CrossRef]
42. Boraud, T.; Bezard, E.; Guehl, D.; Bioulac, B.; Gross, C. Effects of L-dopa on neuronal activity of the globus pallidus externalis (GPe) and globus pallidus internalis (GPi) in the MPTP-treated monkey. *Brain Res.* **1998**, *787*, 157–160. [CrossRef]
43. Wichmann, T.; Bergman, H.; Starr, P.; Subramanian, T.; Watts, R.; DeLong, M. Comparison of MPTP-induced changes in spontaneous neuronal discharge in the internal pallidal segment and in the substantia nigra pars reticulata in primates. *Exp. Brain Res.* **1999**, *125*, 397–409. [CrossRef] [PubMed]
44. Magnin, M.; Morel, A.; Jeanmonod, D. Single-unit analysis of the pallidum, thalamus, and subthalamic nucleus in parkinsonian patients. *Neuroscience* **2000**, *96*, 549–564. [CrossRef] [PubMed]
45. Raz, A.; Vaadia, E.; Bergman, H. Firing patterns and correlations of spontaneous discharge of pallidal neurons in the normal and tremulous 1-methyl-4- phenyl-1,2,3,6 tetrahydropyridine vervet model of parkinsonism. *J. Neurosci.* **2000**, *20*, 8559–8571. [CrossRef] [PubMed]
46. Brown, P.; Oliviero, A.; Mazzone, P.; Insola, A.; Tonali, P.; Lazzaro, V.D. Dopamine dependency of oscillations between subthalamic nucleus and pallidum in Parkinson's disease. *J. Neurosci.* **2001**, *21*, 1033–1038. [CrossRef]
47. Levy, R.; Hutchison, W.; Lozano, A.; Dostrovsky, J. High-frequency synchronization of neuronal activity in the subthalamic nucleus of parkinsonian patients with limb tremor. *J. Neurosci.* **2003**, *20*, 7766–7775. [CrossRef] [PubMed]
48. Hurtado, J.; Rubchinsky, L.; Sigvardt, K.; Wheelock, V.; Pappas, C. Temporal evolution of oscillations and synchrony in GPi/muscle pairs in Parkinson's disease. *J. Neurophysiol.* **2005**, *93*, 1569–1584. [CrossRef]
49. Wichmann, T.; Soares, J. Neuronal firing before and after burst discharges in the monkey basal ganglia is predictably patterned in the normal state and altered in parkinsonism. *J. Neurophysiol.* **2006**, *95*, 2120–2133. [CrossRef]
50. Jung, K.; Florin, E.; Patil, K.R.; Caspers, J.; Rubbert, C.; Eickhoff, C.; Popovych, O. Whole-brain dynamic modelling for classification of Parkinson's disease. *Brain Commun.* **2023**, *5*, fcac331. [CrossRef]
51. van Wijk, B.; de Bie, R.; Beudel, M. A systematic review of local field potential physiomarkers in Parkinson's disease: from clinical correlations to adaptive deep brain stimulation algorithms. *J. Neurol.* **2023**, *270*, 1162–1170. [CrossRef]
52. An, Q.; Yin, Z.; Ma, R.; Fan, H.; Xu, Y.; Gan, Y.; Gao, Y.; Meng, F.; Yang, A.; Jiang, Y.; et al. Adaptive deep brain stimulation for Parkinson's disease: looking back at the past decade on motor outcomes. *J. Neurol.* **2022**, *270*, 1371–1387. [CrossRef]

53. Rosin, B.; Slovik, M.; Mitelman, R.; Rivlin-Etzion, M.; Haber, S.; Israel, Z.; Vaadia, E.; Bergman, H. Closed-loop deep brain stimulation is superior in ameliorating parkinsonism. *Neuron* **2011**, *72*, 370–384. [CrossRef]
54. Hamani, C.; Richter, E.; Schwalb, J.; Lozano, A. Bilateral subthalamic nucleus stimulation for Parkinson's disease:a systematic review of the clinical literature. *Neurosurgery* **2005**, *56*, 1313–1324. [CrossRef] [PubMed]
55. Bevan, M.D.; Jeremy, A.F.; Jérôme, B. Cellular principles underlying normal and pathological activity in the subthalamic nucleus. *Curr. Opin. Neurobiol.* **2006**, *16*, 621–628. [CrossRef] [PubMed]
56. Urbain, N.; Gervasoni, D.; Souliere, F.; Lobo, L.; Rentero, N.; Windels, F.; Astier, B.; Savasta, M.; Fort, P.; Renaud, B. Unrelated course of subthalamic nucleus and globus pallidus neuronal activities across vigilance states in the rat. *Eur. J. Neurosci.* **2000**, *12*, 3361–3374. [CrossRef]
57. Urbain, N.; Rentero, N.; Gervasoni, D.; Renaud, B.; Chouvet, G. The switch of subthalamic neurons from an irregular to a bursting pattern does not solely depend on their GABAergic inputs in the anesthetic-free rat. *J. Neurosci.* **2002**, *22*, 8665–8675. [CrossRef]
58. Rinzel, J. Bursting oscillations in an excitable membrane model. In *Ordinary and Partial Differential Equations*; Sleeman, B., Jarvis, R., Eds.; Springer: New York, NY, USA, 1985; pp. 304–316.
59. Castro-Alamancos, M.; Calcagnotto, M. High-pass filtering of corticothalamic activity by neuromodulators released in the thalamus during arousal: In vitro and in vivo. *J. Neurophysiol.* **2001**, *85*, 1489–1497. [CrossRef]
60. Plenz, D.; Kitai, S. A basal ganglia pacemaker formed by the subthalamic nucleus and external globus pallidus. *Nature* **1999**, *400*, 677–682. [CrossRef] [PubMed]
61. Best, J.; Park, C.; Terman, D.; Wilson, C. Transitions between irregular and rhythmic firing patterns in excitatory-inhibitory neuronal networks. *J. Comput. Neurosci.* **2007**, *23*, 217–235. [CrossRef] [PubMed]
62. Hashimoto, T.; Elder, C.; Okun, M.; Patrick, S.; Vitek, J. Stimulation of the subthalamic nucleus changes the firing pattern of pallidal neurons. *J. Neurosci.* **2003**, *23*, 1916–1923. [CrossRef] [PubMed]
63. Lindén, H.; Pettersen, K.H.; Einevoll, G.T. Intrinsic dendritic filtering gives low-pass power spectra of local field potentials. *J. Comput. Neurosci.* **2010**, *29*, 423–444. [CrossRef] [PubMed]

International Journal of
Molecular Sciences

MDPI

Review

New Pathways Identify Novel Drug Targets for the Prevention and Treatment of Alzheimer's Disease

Botond Penke [1,*], Mária Szűcs [1] and Ferenc Bogár [2]

[1] Department of Medical Chemistry, University of Szeged, Dóm Square 8, H-6720 Szeged, Hungary
[2] ELKH-SZTE Biomimetic Systems Research Group, Eötvös Loránd Research Network (ELKH), Dóm Square 8, H-6720 Szeged, Hungary
* Correspondence: penke.botond@med.u-szeged.hu

Abstract: Alzheimer's disease (AD) is an incurable, progressive neurodegenerative disorder. AD is a complex and multifactorial disease that is responsible for 60–80% of dementia cases. Aging, genetic factors, and epigenetic changes are the main risk factors for AD. Two aggregation-prone proteins play a decisive role in AD pathogenesis: β-amyloid (Aβ) and hyperphosphorylated tau (pTau). Both of them form deposits and diffusible toxic aggregates in the brain. These proteins are the biomarkers of AD. Different hypotheses have tried to explain AD pathogenesis and served as platforms for AD drug research. Experiments demonstrated that both Aβ and pTau might start neurodegenerative processes and are necessary for cognitive decline. The two pathologies act in synergy. Inhibition of the formation of toxic Aβ and pTau aggregates has been an old drug target. Recently, successful Aβ clearance by monoclonal antibodies has raised new hopes for AD treatments if the disease is detected at early stages. More recently, novel targets, e.g., improvements in amyloid clearance from the brain, application of small heat shock proteins (Hsps), modulation of chronic neuroinflammation by different receptor ligands, modulation of microglial phagocytosis, and increase in myelination have been revealed in AD research.

Keywords: Alzheimer's disease; toxic amyloids; Aβ; tau; genetics; amyloid clearance; vascular dysfunction; neuroinflammation; heat shock proteins; drug targets

Citation: Penke, B.; Szűcs, M.; Bogár, F. New Pathways Identify Novel Drug Targets for the Prevention and Treatment of Alzheimer's Disease. *Int. J. Mol. Sci.* **2023**, *24*, 5383. https://doi.org/10.3390/ijms24065383

Academic Editor: Claudia Ricci

Received: 31 January 2023
Revised: 6 March 2023
Accepted: 9 March 2023
Published: 11 March 2023

1. Introduction

Neurodegenerative diseases (NDDs) represent a big part of neurological disorders. NDDs are characterized by the loss of synapses and neurons in the central nervous system (CNS). Neuronal loss often generates the decline of cognitive functions and dementia. Many NDDs have a common central neuropathological event: misfolded, toxic protein aggregates (amyloids) are accumulated in the CNS. NDDs can be regarded as protein homeostasis disorders: the level of several aggregation-prone proteins is increased, and subsequent small conformational changes result in the accumulation of pathogenic, β-structured amyloid proteins. Many amyloid protein structures are self-replicating, display prionoid character, and their aggregated form is propagated from cell to cell (transmissible pathology) [1]. The prionoid propagation of several amyloids (e.g., tau protein and α-synuclein) has been proven. The precise molecular mechanism of the conversion of a nontransmissible protein to the pathogenic prionoid form is not completely understood. Although the native, functionally-folded proteins possess important physiological functions, their misfolded amyloid aggregates are toxic to brain cells. The amyloid structure fundamentally differs from the globular state of these proteins and has remarkable similarities in the molecular and supramolecular organization [2]. Medical research has revealed common disease pathways among NDDs [3]; the most important of them is the accumulation of toxic, misfolded proteins.

Distinct NDDs are coupled to the accumulation of different misfolded amyloid proteins: AD to β-amyloid (Aβ), hyperphosphorylated tau (pTau) and other proteins, Parkinson's disease (PD) to α-synuclein (α-syn), Huntington's disease (HD) to huntingtin, amyotrophic lateral sclerosis (ALS) to SOD-1 or TDP-43, and prion diseases to prion proteins. Amyloid accumulation may also occur in the parenchymal organs of the periphery (e.g., heart and kidneys) and cause the progress of serious diseases. Existing treatments for NDDs are limited and mainly address symptoms rather than causes of the disease. Very recent studies have shown that these diseases are complex and multifactorial, presenting hurdles for discovering novel therapies. In the recent genomic era, novel experimental results have opened up the opportunity for using genetic, epigenetic, transcriptomic, proteomic, metabolomics, and lipidomic data for designing novel drugs for the treatment of NDDs. Developing preventive and, ultimately, disease-modifying therapies for slowing the progression of neurodegeneration in AD and other NDDs seems to be one of the greatest medical needs of our time.

The present review first summarizes our most important knowledge of AD (pathology, genetic background, different hypotheses of the progression of AD, and novel methods for early diagnosis). In the second part, we show novel targets for preventing and/or slowing the progress of AD (e.g., increase in amyloid clearance, inhibition of amyloid formation and accumulation, and modulation of neuroinflammation).

2. Alzheimer's Disease

2.1. Pathology and Classification of AD. Aging and Dementia. The Main Risk Factors of AD

Presently, AD is an incurable and progressive neurodegenerative disorder characterized by mixed proteinopathy, progressive dysfunction and loss of synapses, behavioral dysfunction, memory loss, and rapid cognitive decline [4]. Clinicopathologically, AD is a heterogeneous, multifactorial disease with different pathobiological subtypes. AD is rather a spectrum, a continuum from the preclinical, asymptotic phase via mild cognitive impairment to severe AD dementia [4]. Extremely complex, interrelated, and destructive processes lead to cell death and dementia. Novel strategies emphasize the importance of multitarget therapies for AD treatment due to the heterogeneity of the disease [5].

Excellent reviews based on the results of systematic postmortem analyses summarize the pathology of AD [5–9]. The two most important pathological hallmarks of AD brains were described by A. Alzheimer in 1907. These are the formation of extracellular Aβ deposits (plaques) and intracellular neurofibrillary tangles (NFTs). Different Aβ deposits have been found in the brain and cognitively normal individuals. The distribution of amyloid plaques represents the major difference between cognitively normal individuals and AD patients. All types of cerebral, nonvascular Aβ deposits are referred to as "senile plaques." Cerebral Aβ deposition shows different phases [10]. Diffuse plaques occur in brain regions in β-amyloidosis at early stages, and cored neuritic plaques only occur in later stages of Aβ deposition. Diffuse plaques appear in all phases of deposition. The presence of diffuse plaques is not coupled to AD, while neuritic plaques have been shown to be associated with dementia. Aβ deposits mainly have a complex structure that contains several coaggregating proteins (Apolipoprotein E: APOE, Cathepsin D, and Clusterin), as well as dystrophic neurites and microglia. Other morphological hallmarks are vascular amyloid deposits, neuroinflammation, neuronal loss, and astrogliosis.

AD is classified into early onset (EOAD) and late-onset (LOAD) forms. Both forms possess common pathological features. The symptoms appear before the age of 65 in EOAD and after 65 in LOAD. The different clinical forms of AD have been classified into four subtypes based on the distribution of tau pathology and neuronal loss: typical, minimal atrophy, limbic predominant, and hippocampal spearing subtypes. Deposition of Aβ to extracellular plaques follows different pathways and shows distinct patterns. The specific pattern of tau pathology correlates better than that of Aβ deposition with the clinical symptoms of AD patients (cognitive impairment and memory loss). AD starts when both amyloid and tau pathologies overlap [11]. Several other heterogeneous AD variants have

recently been identified based on the atrophy of different neuronal networks. Age-related copathologies are also frequent (e.g., Lewy bodies and hippocampal sclerosis), which makes it difficult to understand the pathomechanism of AD in individual cases [9].

The neuropathological staging of AD was already performed in 1991 [12] based on the development of tau (NFT) pathology in the brain (stages I to VI). Braak stages show some correlation to the clinically observed severity of dementia. Thal and coworkers demonstrated that the spreading of amyloid deposits in the brain could be predicted and occurs in five stages [13]. Aβ plaques appear in the neocortex in phase 1 (cognitive functions, working memory, speech perception, and language skill). Later, Aβ deposition also occurs in allocortical brain regions (phase 2). Subcortical areas (striatum and basal cholinergic forebrain nuclei) are involved in further depositions (phase 3). In phase 4, several brainstem nuclei (vital functions and relaying neuronal impulses) are affected by the deposition of a high density of plaques, and their level is in good correlation with the symptoms of dementia. Finally, phase 5 is characterized by amyloid depositions in the cerebellum (movement coordination). Biomarkers can monitor the deposition of Aβ plaques and tau in living patients. These studies demonstrate that Aβ and tau pathologies already start decades before symptoms of cognitive decline in AD patients (biomarker-based diagnosis of the preclinical stage, see Section 2.5).

AD is the most common cause of dementia. Although the basic pathophysiological mechanism of AD is not yet clear, many indications address the importance of aging, as well as genetic and environmental factors. Aging seems to be the most important risk factor of AD ("the neurobiology of aging and AD is walking down the same road") [6]. Some of the hallmarks of aging (e.g., mitochondrial dysfunction, low-grade chronic inflammation, and loss of proteostasis) overlap with the hallmarks of AD. Aging, genetic background, and epigenetic changes are the main risk factors for AD.

Normal aging of the brain induces many changes. There are gross and microscopic alterations in the brain structure and metabolism (e.g., volume loss, demyelination, enlargement of ventriculi, dysfunction of the cholinergic system, decreased ligand binding affinity of several receptors, alteration in gene expression, a decrease in synaptic function, lipofuscin accumulation, disturbances of the blood-brain-barrier (BBB) function, an increase in cellular waste, etc.) [14]. Tissue atrophy, alteration in certain neurotransmitters, and dyshomeostasis of the cellular environment accompany normal aging and ultimately result in cognitive decline [14].

Dementia, a common sign of NDDs, is not a part of normal aging. It is very different from the cognitive decline that manifests during normal aging. Dementia is a syndrome of acquired, progressive cognitive impairment, frequently accompanied by depression, loss of memory, orientation, etc., which symptoms result in disruption of basic self-care. There are several modifiable risk factors for dementia, e.g., smoking, diabetes, obesity, depression, and physical inactivity [15].

Aging is accompanied by more and more frequent misfolding and aggregation of proteins [16,17]. Active balancing of protein synthesis and degradation are critical processes in the cells [18]. An adaptive network of functions called protein quality control (PQC) has evolved over millions of years to maintain cellular protein homeostasis (proteostasis). Different chaperones (e.g., heat shock proteins, Hsps) control the correct folding and aggregation of proteins. The vulnerability of the aging brain tissue may be demonstrated by the presence of suboptimal levels of proteostasis components (low levels of aggregation protectors and high levels of aggregation promoters) [19]. If PQC fails, a misfolding process results in the formation of pathogenic aggregates that are divided into two groups: unordered amorphous and rather ordered fibrillar amyloids [16]. Several disease-related amyloids (e.g., β-amyloid peptides) possess a high propensity for irreversible aggregation. It has been uncovered that age-dependent protein aggregation is a common feature of aging [17]. Structural alteration of the peptidic backbone might be one of the reasons for protein aggregation [20]. Spontaneous isomerization and epimerization of the aspartyl residue to D-Asp and L- and D-isoAsp results in modified protein structures with high

protease resistance [21,22]. Hundreds of proteins become highly insoluble during the aging process [23]. Results of systematic postmortem analysis of AD brains demonstrated that two amyloid proteins play a decisive role in the development of AD: Aβ (mainly the 1–40 and 1–42 amino acid peptides) and pTau (see Section 2.3).

2.2. Genetic Background of AD, the Multiplex Model

Both forms of AD show high heritability [24]. The estimated heritability is over 90% for EOAD, and it is in the range of 60–80% for LOAD. Mutations in the amino acid sequence of the amyloid precursor protein (APP) and presenilin (PS) genes (presenilin 1 and 2 proteins are important for APP processing to Aβ) are causative factors for EOAD [8]. About 60 highly penetrant APP mutations have been discovered that are involved in the progress of EOAD. (Interestingly, a protective mutation of APP that decreases Aβ aggregation was found in the Iceland population [25]). PSEN mutations are responsible for 80% of EOAD cases. Over 350 mutations have been identified so far. The amyloid hypothesis is based on the strong genetic evidence of EOAD and Down syndrome. Altered APP processing and Aβ overproduction are in the background of AD.

The genetics of LOAD is much more complex than that of EOAD, and it is the result of combined influences of multiple genetic loci or polygenic effects. Genetic studies have demonstrated that AD is a multicomponent disease [26]. Until 2020, over 50 genetic risk factors have been identified that are responsible for LOAD (multiplex model of AD) [26]. APOE4 was proven to be the strongest single risk factor for LOAD (cholesterol synthesis and transport). It has recently been demonstrated that ApoE4 significantly increases tau pathogenesis and tau-associated neurodegeneration. Global ApoE deficiency is strongly protective [27]. Very recently, it was found that deletion of neuronal ApoE4 drastically reduces tau pathology in pTau overproducing PS19-ED mice [28]. These studies provide evidence that ApoE4 influences a multitude of events in AD progression (Aβ and tau accumulation, neuronal hyperexcitability, and myelin deficits). It was also reported that ApoE4 does not directly drive neurodegeneration, but microglia may mediate the effect of ApoE4 [29]. Interestingly, the majority of the genes/loci are associated with immune functions. For example, the TREM2 (triggering receptor expressed on myeloid cells 2) gene was identified to play a key role in microglia and macrophage function [30]. Genome-wide association studies (GWAS) enable the study of tens of thousands of patients and millions of genetic variations [31]. A two-stage GWAS was performed with 111,326 clinically diagnosed AD patients and 677,663 control individuals [32]. In these studies, 75 AD risk loci were found, of which 42 were new. Over 130 AD-associated loci were identified by GWAS, among them APOE4, TREM2, CR1, CD33, CLU, BIN1, CD2AP, PICALM, SORL1, SP11, RIN3, and more genes in another study [33]. Pathway analysis methods were used for studying genomic associations for identifying disease-relevant processes [33]. It was found that the majority of the genes are associated with immune functions. According to the multiplex model, besides immunity and inflammation, other pathways (for example, endocytosis, cholesterol metabolism and transport, Aβ clearance, tau processing, autophagy, and vascular factors) also participate in AD initiation. Genetic approaches have provided the first convincing evidence that the immune system plays a decisive role in the progression of AD.

Beyond inherited genetics, somatic mutations and diverse epigenetic mechanisms (DNA methylation, histone modification, chromatin remodeling, and long, noncoding RNAs) may participate in aging and neurodegeneration of the brain [34].

2.3. Amyloid Structures. Physiological and Pathophysiological Role of the Aβ and Tau Proteins

Amyloidogenic processing of APP provides a heterogeneous mixture of Aβ peptides of 37 to 43 amino acids. The physiological (neuroprotective) role of the monomeric Aβ 1–42 peptide has been widely reviewed [35–37]. Very recently, a Special Issue of Frontiers in Molecular Neuroscience has been published dealing with the physiological and pathological role of Aβ in detail [38].

Monomeric Aβ 1–42 is a neuropeptide, a physiological neuroprotector. Aβ 1–42 regulates synaptic function, neural circuitry, organelle trafficking, neurogenesis, neuroinflammation, and cognitive processes in picomolar concentrations [38]. Aβ 1–42 in low concentration suppresses microbial infections and can seal leaks in the blood-brain barrier, BBB ("vascular plug") [37,39]. In physiological concentrations, Aβ maintains angiogenesis and vascularization, protects the BBB, promotes recovery after brain injury, and acts as a tumor suppressor [39]. Aβ can be produced intracellularly by APP cleavage. External Aβ can enter the cells by receptor-mediated internalization [40]. Aβ monomers start to aggregate into different Aβ oligomers over a critical concentration [41]. Intracellular Aβ also participates in neurodegenerative processes [42]. The aggregation process provides different Aβ assemblies; in the first step, oligomers (oAβ):

native Aβ monomer → partially folded monomer → transient oAβ → protofibrils (β-sheet → structured oAβ → fibrils (cross-β) → big aggregates, plaques.

Amyloid aggregation has been experimentally studied under in vivo conditions [43]. Amyloid proteins interact with other proteins (cross-seeding) [44]. It was found that cross-seeding plays a key role in amyloid formation. Lipids (e.g., gangliosides and cholesterol) and divalent metal ions (e.g., zinc, copper, and iron) are good nucleators for Aβ (Section 2.4) [45]. Experiments (TEM studies of Aβ aggregates) demonstrated that several D-amino acids (D-Ala, D-Phe, D-Glu, and D-Asp) and DL-selenoMet initiate Aβ aggregation (enantiomeric-induced aggregation [46]). Most of the L-amino acids did not affect amyloid aggregation. Selenium nanoparticles inhibited enantiomeric-induced amyloid aggregation and could be beneficial compounds for AD treatment.

It was demonstrated that protein insolubility and aggregation might be critical for mediating the pathogenesis of NDDs in older ages. Thus, inhibition of the aggregation process seems to be a good target of drug design against NDDs. The very recent development of techniques, such as cryo-EM (cryo-electron microscopy), solid-state NMR (solid-state nuclear magnetic resonance), and AFM (atomic force microscopy), has opened up new ways of understanding amyloid structure [2,47]. Cryo-EM data can be integrated into comparative morphometric AFM image analysis of amyloid fibrils [48]. Cryo-EM studies demonstrated the complex structure and peptide conformation of Aβ fibrils isolated from the brain of AD patients [49–51].

Animal studies demonstrate that oAβ is sufficient and necessary for AD-associated neurodegeneration [52,53]. Aβ oligomers have toxic effects on the brain [41]). They were shown to inhibit axonal transport, cause synaptic damage and dysfunction of neuronal plasticity, Ca^{2+}-dyshomeostasis, oxidative stress, ER stress (endoplasmic reticulum stress), and selective neuronal death. One of the most important effects of oAβ is the promotion of tau-hyperphosphorylation. Oligomeric Aβ interacts with the lipid membrane components (e.g., ganglioside GM1) and directly binds to different receptors [54]. Not all the binding proteins are genuine receptors since Aβ has an intrinsically disordered structure and can associate with many proteins.

The most important pathogenic events induced by toxic oAβ are (1) stimulation of tau-hyperphosphorylation, (2) impairment of mitochondrial function, (3) disruption of Ca^{2+} and protein homeostasis, and (4) induction of autophagy dysfunction. [40].

Another key player in AD progression is the tau protein. Alternative splicing of the human microtubule-associated protein tau (MAPT) gene provides six tau isoforms, which may aggregate into oligomers and filaments [41]. Tau shows a large number of post-translational modifications [55].

The physiological role of tau proteins is widely reviewed [56,57]. As a multifunctional protein, tau plays an important role in physiological processes [41,58]. Tau participates in maintaining DNA integrity, protects and regulates microtubules and axonal transport, interacts with cytoskeletal proteins (e.g., actin and spectrin), and regulates the shape of the cells [39]. Native tau is necessary for normal myelination and also regulates transcription at the cell nucleus. Tau is also a synaptic protein. Very recently, it has been demonstrated that tau plays a basic role in accelerating spine formation, dendritic elongation, and synaptic

plasticity [59]. Native tau modulates NMDA (N-methyl-D-Aspartate) receptor signaling and influences intracellular Ca^{2+} levels. Native tau is a highly soluble protein and not prone to aggregation in its monomeric form. Phosphorylation of tau proteins in specific sites (Thr 231 and Ser 235, 262, 293, 324, and 356) results in the formation of pathological hyperphosphorylated proteins. In a cellular model, Aβ addition was shown to catalyze tau-hyperphosphorylation via activation of protein kinases DYRK1 and Fyn. Hyperphosphorylated tau dissociates from the microtubules and forms toxic assemblies:

abnormally phosphorylated monomer (pTau) → dimer, trimer → small soluble oligomers (oTau) → granular oligomers → straight filaments → paired helical filaments → neurofibrillary tangles.

The monomeric form, filaments, and tangles are probably not toxic; however, the diffusible oligomers are toxic [60]. Recently, several cryo-EM studies have revealed the structure and peptide chain conformation of the helical filaments isolated from an AD brain at the atomic level [61].

Hyperphosphorylated tau aggregates possess several pathophysiological actions:

- Disaggregation and collapse of microtubules. Big tau assemblies may cause a direct physical blockade of axonal transport.
- Loss of DNA protection at the nucleus.
- Increased excitability of neurons.
- Tau may bind to synaptic vesicles and disrupt the synaptic cytoskeleton causing synaptic loss and disturbances of neural circuits.
- Tau causes neuroinflammation.
- Prion-like propagation: tau is able to spread cell to cell, most likely via macropinocytosis and not by receptor support [62]. Several authors propose that AD may be an infectious disease of the brain [63].

It is widely accepted that Aβ and tau proteins have a synergistic effect in the progression of AD: "Aβ is the trigger and tau is the bullet driving AD" [64,65]. It has recently been demonstrated that the presence of both Aβ and tau is necessary for memory decline at the beginning of AD [66]. Aβ and tau crosstalk shows that the two proteins are coupled in the progression of AD.

2.4. The Ever-Changing and Developing Amyloid (and Tau) Hypotheses. Alternative Hypotheses of AD

The importance and complexity of AD triggered the elaboration of a very large number of hypotheses dealing with the pathogenesis of the disease. Strong neuropathological and genetic evidence support the mainstream concept of the amyloid hypothesis of AD. According to the hypothesis, an imbalance in the production and clearance of Aβ results in its overproduction and formation of toxic amyloid assemblies. Aβ accumulation and deposition are the critical initial steps, the central events, and driving factors of the progress of AD [67]. Synaptic loss, chronic neuroinflammation, microgliosis, astrocytosis, neuritic dystrophy, tau-hyperphosphorylation, and formation of NFTs are the consequences of amyloid deposits. The hypothesis has been changed several times over the decades. Originally, the amyloid plaques were proposed to be the culprits of the disease [67], followed by hypothesizing such a role for Aβ oligomers [68]. Although inconsistencies and controversies have been observed, the hypothesis has received continuous support for three decades in the field of AD drug development.

Several experimental studies demonstrated that a pool of intracellular Aβ exists in the brain at the very early stage of AD that may interact with subcellular organelles, thereby affecting their normal function [69]. Novel evidence has suggested that extracellular Aβ has a small impact on AD pathology, and the plaques alone cannot be responsible for the whole pathological process [70]. The "intracellular Aβ (iAβ) hypothesis" assumes that accumulation of iAβ in the brain cells is the earliest sign of AD. The toxic iAβ assemblies trigger tau pathology and the formation of NFTs. The formation of extracellular plaques

only occurs at later stages of the disease [71,72]. Indeed, a series of experiments have proven the formation and accumulation of iAβ, e.g., observation of iAβ by light and fluorescent microscopy, as well as by EM [73]. iAβ is selectively resistant to enzymic degradation and accumulates in a nonfibrillar form in lysosomes [74]. The release of lysosomal proteases is one of the earliest events of iAβ neurotoxicity [75].

The tau hypothesis. Several studies have demonstrated that tau hyperphosphorylation and NFT formation are early events in the development of AD. It was found that pTau cannot bind to the microtubules aggregates to NFTs after truncation of the polypeptide chains [76]. NFTs are toxic and shift APP processing to elevated Aβ production. Experiments demonstrated that pTau is a self-propagating protein with a prionoid character, spreading from cell to cell [77]. The tau (or tau-propagation) hypothesis proposes that pTau dissociates from the microtubules and aggregates to NFTs; this process precedes Aβ plaque formation and drives AD development. It was observed that tau pathology in the brain showed a good correlation with cognitive decline. Moreover, the formation of pTau proved to be the common pathway of different, altered molecular signals [70,78]. According to the tau hypothesis, pTau plays a central role in AD and is the diagnostic and therapeutic target of AD research. Indeed, a shift from the physiological to the pathological level of tau was observed in AD synapses [79].

Most attempts to develop Aβ-targeted drugs for treating AD ended in failure for many years. As a consequence, an inevitable discussion, or rather a debate, started, whether misfolded Aβ or tau amyloids are the culprits, upstream pathogenic causes for driving AD progress. The problems of the amyloid hypothesis in understanding the pathomechanism of LOAD led to a change in the target of drug research from Aβ to tau. However, the experiments with the GSK-3 enzyme inhibitors, such as tideglusib and anti-aggregating agents (methylene blue derivatives: Trx0014 and LMTM), resulted in controversial results, and, thus, did not support the tau hypothesis. As Aβ and tau have neuroprotective effects, it is possible that their overproduction is only a protective response to cellular stress and damage.

Several research groups tried to unify the two hypotheses [79–81]. The "dual pathway hypothesis" of Small and Duff tried to reconcile the two hypotheses. Other research groups "revitalized" the tau hypothesis and provided an integrative model of AD pathogenesis [82]. However, the debate has not ended yet.

The *metal ion hypothesis* connects the two main Alzheimer's hypotheses. Several transition metal ions participate in physiological processes. They play important roles in the maintenance of brain functions and may regulate the development of AD [83]. Postmortem analysis of amyloid plaques demonstrated the accumulation of copper, iron, and zinc by 5.7, 2.8, and 3.1 times compared to the levels of normal brains, respectively [81]. Heavy metal ions can be bound to the His residues of Aβ (His6, His13, and His14) and to pTau [84]. Metal ion imbalance induces Aβ and tau pathologies [85]. Zinc, copper, and iron ions enhance the production of Aβ and subsequently bind to Aβ and tau, promoting their aggregation. The misbalance of these metal ions is connected to the main factors of the pathogenesis of AD (oxidative stress, protein aggregation, mitochondrial dysfunction, energy deficiency, and neuroinflammation) [86]. Accumulation of iron and copper ions can promote cell death by ferroptosis or cuprostosis [87]. Therefore, metal ion chelators as therapeutic agents have been used for treating AD (Section 3). Metal ion chelators are also potential drug candidates for modulating neuroinflammation in AD.

In addition to the above processes, many other factors can affect the occurrence of AD. The results of novel experiments with rhesus monkeys connect the tau and glutamatergic dysregulation hypothesis [88]. Accordingly, vulnerable glutamatergic neurons are responsible for Ca^{2+}-dysregulation, and this event induces the formation of pTau and NFTs. As a consequence, tau pathology might be the key initiating factor for LOAD and suggests that future AD drugs should reduce tau pathology.

The most detailed hypothesis of the initiation and progress of AD was introduced by De Strooper and Karran [89]. The AD continuum includes three stages. First, clearance

problems and proteostasis failure lead to abnormal Aβ and tau formation (biochemical phase). Several genes participate in this process (e.g., APOE4, LRP1, ABCA7, SORL 1, PICALM, and AQP4). In the second phase, each type of brain cell (neurons, microglia, astrocytes, oligodendrocytes, the glioneuronal unit, and the neurovascular unit) participates in the progress of degeneration (cellular phase). These changes result in chronic neuroinflammation, chronic imbalances in neuronal circuitry, cell failure, and cell death. The clinical phase is characterized by hippocampal shrinkage, MRI changes in the brain, alterations of CSF, and dementia. The whole process may take two to three decades.

The history and development of the various AD hypotheses and clinical trials have been excellently reviewed in [90]. The short list of the hypotheses is as follows:

1. Aβ, very probably iAβ, is the initiating factor of AD [66].
2. Loss of cholinergic neurons and neurotransmission are causing factors of AD [91].
3. Deficit of the glutamatergic system [88] triggers tau overproduction.
4. Abnormal phosphorylation of tau proteins is in the background of AD initiation and progress [76].
5. According to the dual cascade hypothesis, cellular processes in the brain cortex simultaneously drive tau and Aβ pathology [80].
6. Metal ion hypothesis: several transition metal ions accelerate amyloid aggregation [84,85].
7. Mitochondrial dysfunction starts a cascade of pathological events in brain cells [92].
8. Chronic neuroinflammation is responsible for the initiation of damage to neurons [93].
9. According to the vascular dysfunction hypothesis, impaired brain circulation and endothelial-mediated processes play central roles in AD pathogenesis [94,95].
10. Impaired amyloid clearance (BBB and glymphatic clearance) is the main cause of amyloid accumulation in AD [96].
11. Aβ peptides are generated in the periphery and enter the brain via the BBB [97].
12. Aging is the main driver of sporadic AD pathogenesis. Each type of brain cell (microglia, astrocytes, and brain vasculature cells) participates in pathophysiological events [89].

We propose that distinct hypotheses might be valid and applicable to understanding the pathology of different forms of AD. In EOAD, the priority of Aβ has already been demonstrated. Well-known mutations of APP, PS1, and PS2 are responsible for the formation of toxic Aβ species, and the familial disease shows autosomal dominant inheritance [98]. The other form of AD, LOAD, is a very heterogeneous disease. It is very probable that not only toxic Aβ can initiate the formation of the "bullet" via tau hyperphosphorylation and NFT formation [64]. Experimental and clinical data have resulted in the consensus that AD is an amyloid-provoked tauopathy. It is agreed that both Aβ and pTau are necessary for cognitive decline [66]. Tau-originated toxic NFT is the common pathway in all subtypes of AD [78]. It can be accepted that either pTau or NFTs alone are able to start AD pathology, e.g., after dysfunction of the glutamatergic system or other stress conditions [88]. However, experimental evidence demonstrates that Aβ (very probably iAβ, which seems to be the earliest sign of pathological events in AD) is the primary factor in starting AD progress in most cases. Figure 1 shows a short summary of the diversity of the possible initiating factors and the pathophysiological processes resulting in cellular dyshomeostasis and cell death.

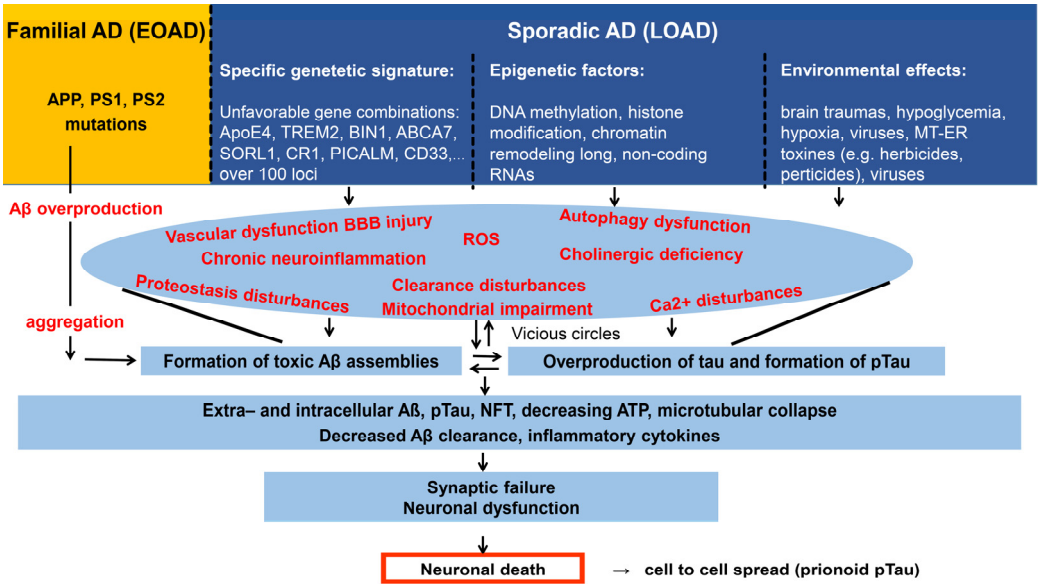

Figure 1. The funnel model of AD. It shows the interrelated destructive processes acting in vicious circles, leading to widespread cell death. In familial AD cases (left side), mutations in APP, presenilin 1 and 2 (PS1 PS2) genes induce Aβ overproduction and formation of toxic aggregates. In the sporadic form (LOAD), aging, unfavorable gene combinations, epigenetic changes, and various environmental factors induce slow changes in the brain. Vascular and autophagy dysfunctions, BBB injury, proteostasis, and clearance disturbances lead to Aβ accumulation and subsequent formation of toxic Aβ and tau assemblies in vicious circles. Microtubular collapse results in synaptic failure, dysfunction, and death of neurons. Aβ and tau act in synergy in the pathological cascades.

2.5. Early Diagnosis of AD, Molecular Biomarkers

Early diagnosis at the preclinical stages of AD is an important issue since amyloid accumulation in the brain begins more than two decades before cognitive decline. AD continuum means that the progress of cognitive decline has several steps [99]:

chronic stress → subjective cognitive decline (SCD) → mild cognitive impairment (MCI) → AD dementia.

Reversal of AD dementia is not possible yet. Contrary, MCI can be reverted to the normal condition [99]. A very early diagnosis may facilitate preventive pharmacological and nonpharmacological treatments before dementia manifests.

Finding and validating standard clinical diagnostic biomarkers is not an easy task, partly owing to the complexity of AD. The diagnostic process has several subsequent steps from detection of cognitive impairment until treatment (laboratory tests, genotyping, neurological examination, cognitive and functional tests, then brain structural imaging, CSF and blood biomarker analysis, and finally diagnosis) [100]. Prediction of AD progression would be essential for planning treatment and medication. However, it has remained a challenging task so far. It is supposed that AD can be diagnosed based only on biomarker abnormalities [101]. In other words, AD diagnosis can be based purely on biology, without cognitive tests.

Diagnostic tools [102]. Brain imaging and fluid biomarker analysis are the most frequently used assays for the detection and staging of the disease. During the last decade, there was a great development in the field of neuroimaging [103]. Precise detection of both Aβ and tau in the blood and brain are essential tools for AD diagnosis. The leading neuroimaging methods have been PET and MRI; less frequently used are CT and SPECT, the latter being a nuclear imaging technique [104]. Functional MRI (fMRI) indirectly measures brain activity and the integrity of brain networks in the MCI stage. Multimodal MRI can be effectively used for the prediction of AD progress [103]. The application and evaluation of different tau biomarkers (tau-PET, CSF- and blood-based markers) have been recently

reviewed [105]. The use of second-generation tau-PET tracers improved our understanding of the heterogeneity of AD and helped for staging the disease. The application of brain imaging techniques is reviewed in the World Alzheimer Report 2021 [106].

It is not rare that cognitively normal patients have degeneration in the cholinergic white matter [107,108]. It is assumed that the integrity of cholinergic pathways might be a good indicator of early changes in AD progress. Individuals without cognitive decline but possessing abnormal Aβ and tau PET images (plaques and NFTs) are also at a high risk of AD [109]. When both Aβ and tau are present in the brain, it can no longer be considered a risk factor but rather a diagnosis [105]. Other approaches, such as electroencephalography (EEG), have also been used for early diagnosis of MCI and AD [110].

The levels of fluid biomarkers of AD (mostly Aβ and tau) can be measured in the cerebrospinal fluid (CSF) and blood. CSF analysis has a disadvantage: it needs invasive treatment (lumbar punction). The routine analytical methods are quantitative measurements of Aβ 1–42, pTau 181, and the ratio of pTau 181/Aβ 1–42 by immunoassay [111,112]. CSF concentration of Aβ peptides can also be measured by the automated tandem mass spectrometry method (HPLC-MS/MS) [113]. The U.S. FDA has recently granted marketing approval for a novel CSF-test (Lumipulse G-amyloid ratio(1–42/1–40) as a cheap alternative to PET for early detection of amyloid accumulation in AD brains [114]). (The Aβ 1–42/1–40 ratio in CSF strongly correlates with the PET status of the brain).

The application of a new blood test, a not complicated binding assay, has recently been published for very early detection of soluble toxic Aβ peptides (SOBA) [115]. Further studies should demonstrate the suitability of the SOBA method for identifying patients at risk of cognitive decline. Parallel work was performed for the detection of Aβ oligomers in mouse brains using a new PET-tracer (a ^{64}Cu-labeled aza-peptide) [116]. This approach gave unbelievably early detection of oAβ increase compared to the standard ^{11}C-PET method.

A radical improvement in blood tests for AD diagnosis has been developed [117]. It was demonstrated that measuring the levels of multiple blood biomarkers (pTau 231; pTau 231 and Aβ 42/40 together) was sufficient for identifying AD pathology. Blood tests were performed with a group of 242 patients and repeated for up to 6 years, along with MRI and cognitive testing. Evaluation of the experimental data gave interesting results: only pTau 217 was related to typical AD pathology over the 6-year testing period. Thus, pTau 217 may be an ideal biomarker in the clinical phases of AD for monitoring disease progression and the protective effects of drug candidates. "The novel blood test will revolutionize the diagnosis of AD" [117].

3. Conventional and Novel Targets for Slowing and/or Preventing the Progress of AD

There are no disease-modifying drugs for AD treatment yet. Existing drugs, e.g., cholinesterase inhibitors (donepezil) and NMDA receptor modulators (memantine), only show a palliative effect. There are serious problems in target identification for the development of AD drugs. Both amyloid proteins (Aβ and tau) possess essential physiological functions in their native state. Therefore, the full blockade of their biosynthesis may cause very severe side effects [118]. The molecular heterogeneity of Aβ and tau assemblies makes target identification very problematic: which species should be targeted to stop neurodegeneration? If aging is the most dangerous risk factor for AD, how can we slow down the natural aging processes? Finally, the lack of a good animal model for AD causes difficulties in translating the results of animal experiments.

Various biochemical pathways that suppress or remove aggregated proteins are now targeted and examined after a series of failed clinical studies with old AD-drug candidates. Several of these pathways of AD are summarized in Figure 1. The application of multitarget Alzheimer's drugs has very recently been widely reviewed [119]. Intracellular Aβ is also a therapeutic target [120].

3.1. Inhibition of the Formation of Toxic Amyloid Aggregates

3.1.1. Decreasing Aβ Production

The first approaches to AD drug development were focused on the partial inhibition of the formation Aβ peptides. Inhibitors of γ- and β-secretases, the key enzymes of amyloidogenic APP processing, have reached phase 2 and phase 3 steps in clinical trials. Although β-Secretase 1 (BACE 1) inhibitors reduced Aβ production, the drug candidates were not able to slow down cognitive decline [118]. γ-Secretase inhibitors (e.g., avagacestat and semagacestat) caused cognitive loss and other severe side effects.

Activation of the nonamyloidogenic pathway of APP procession by activation of α-secretase might be another approach for decreasing Aβ biosynthesis. Unfortunately, the α-secretase enzyme activators also gave discouraging results in the clinical application [121].

3.1.2. Blocking Aβ Aggregation

The mechanism of amyloid protein aggregation has been recently reviewed [122–124]. Targeting Aβ aggregation is a very frequently used strategy in AD drug development [125]. Many natural or synthetic small molecules, peptides, and peptidomimetics were studied for their modulatory effect on Aβ aggregation [118]. Polyphenols, tetracyclines, anthracyclines, and sterols have been used as anti-amyloid compounds [125].

The neuroprotective effect of several natural polyphenols (resveratrol, epigallocatechin, epigallocatechin-3-gallate (EGCG), myricetin, curcumin, and quercetin) has been studied [126]. Myricetin inhibits Aβ nucleation, while resveratrol, curcumin, quercetin, and EGCG inhibit fibril elongation. Resveratrol and curcumin also decrease the hyperphosphorylation and aggregation of tau protein. Most of the polyphenols (besides inhibiting amyloid aggregation) have an antioxidant effect scavenging free oxygen radicals and protecting DNA from oxidative damage. Resveratrol also modulates neuroinflammation and induces adaptive immunity. Unfortunately, the bioavailability of resveratrol and curcumin is very low. Recently resveratrol was combined with selenium nanoparticles (formation of ResSeNPs). The novel combination has good absorption and might improve resveratrol application in AD treatment [127]. Chitosan-containing selenium nanoparticles (Ch-SeNPs) also inhibited D-amino acid enantiomeric-induced amyloid aggregation [46].

Multifunctional metal chelators of the different chemical structures have been designed as potential anti-AD drugs as metal dyshomeostasis contributes to the onset and progression of neurodegeneration [128,129]. Clioquinol, a metal-protein attenuating compound, chelates copper and zinc ions and decreases amyloid aggregation in the brain [130]. PBT2, a clioquinol-related second-generation drug, has been used in clinical studies for the treatment of AD. The Phase 2 study in 42 prodromal AD or mild AD patients gave negative results. However, novel metal chelators might have a better chance. Recent studies with a BBB-permeable silica-cyclen nanochelator gave positive results in a cellular assay [131].

Native state stabilization in a highly crowded cellular environment [124] seems to be a novel method of choice for inhibiting the formation of toxic Aβ aggregates. Peptides designed for mimicking the Aβ amyloid core (ACM-peptides) coaggregate with Aβ 1–42 and form nontoxic nanofibers. Proteases easily degrade these fibers, and thus, ACMs might be ideal anti-amyloid drug candidates ([132]. On the contrary, medin, a known protein, promotes the formation of amyloid aggregates and deposits by coaggregation with Aβ. Researchers hope that medin inhibitors could block the formation of amyloid deposits and may behave as anti-amyloid agents [133]. It has been published very recently that 14-3-3 proteins also bind amyloids, and thus, they can also be targeted as an anti-aggregation approach [134].

3.1.3. Blocking Tau Biosynthesis

Enzyme inhibitors: Tideglusib, a selective inhibitor of the tau-phosphorylating enzyme GSK-3β, was planned to reduce tau-hyperphosphorylation, leading to pTau aggregation and propagation. Tideglusib and similar compounds were able to reduce the amyloid

formation and neuroinflammation. However, the clinical trials have not shown any benefits [118].

3.1.4. Inhibiting Tau Aggregation and Fibrillation

Small molecules, such as a leukomethylene blue derivative (LMTM), have been used as a tau aggregation inhibitor. The treatment was unsuccessful in a group of 800 patients with mild AD in phase 3 clinical trials [135]. Several compounds have been recently studied for inhibiting tau-fibrillation, till now without success [123].

3.1.5. Other Tau-Directed Potential Approaches

Inhibition of the retromer complex, a cargo-sorting protein assembly, increased the toxicity of human tau via increased tau-truncation in an animal model [136]. Retromer deficiency was also connected with tau pathology in Down syndrome patients [137]. There is hope that these results can be translated into AD drug design. Bassoon (BSN), a synaptic scaffold protein, also has an interesting effect: it interacts with tau seeds and contributes to tau propagation and neurotoxicity [138]. In mice, BSN downregulation reduced pathology and propagation by decreasing the stability of tau seeds. The inhibition of BSN-tau interactions might be a novel therapeutic approach for treating AD and other tauopathies.

3.2. Improvement of Amyloid Clearance. Vascular Dysfunction, BBB, and the Glymphatic System

Increased concentration of soluble Aβ (sAβ) in the brain is highly correlative with the severity of neurodegeneration [139], as sAβ seems to be responsible for the deterioration of synaptic function [140]. Two processes contribute to Aβ accumulation in the brain: Aβ production by APP cleavage and transport via the BBB.

3.2.1. Passive Immunotherapy with Monoclonal Antibodies (mAbs)

Passive immunotherapy uses exogenous humanized monoclonal or for the promotion of Aβ clearance from the brain ([141,142]. Several mAbs (Bapineuzumab, Gantenerumab, Aducanumab, Donanemab, Solanezumab, and Crenezumab) have been developed for targeting amyloid plaques against different epitope regions of Aβ [143]. Recently, six mAbs have entered phase 3 trials, and Aducanumab (Biogen) was approved by the U.S. FDA for marketing [142]. However, the European Medicine Agency (EMA) refused the approval of Aducanumab, and it is not authorized in Europe. Aducanumab got approval for 4 years for performing a postapproval confirmatory trial (phase 4 trial). As for the neuroprotective action of humanized mAbs, they target amyloid plaques and not monomers. The main therapeutic hypothesis for the application of hmAbs is that reduction in Aβ and clearance of amyloid plaques would be required for restoring homeostasis in the brain. Aducanumab showed a robust decrease in amyloid burden and full removal of amyloid plaques. Unfortunately, the drug shows a dose-related adverse effect: one-third of the patients showed "amyloid-related imaging abnormalities" (ARIAs) that can be fatal.

Lecanemab (Eisai) treatment, designed to neutralize toxic Aβ protofibrils, has given the best results in clinical studies till now. The phase 3 Clarity trial was performed with 1800 individuals (10 mg/kg mAb infusion every two weeks, 18 months study with early AD patients). This treatment resulted in promising changes in the brain (reduced Aβ and tau scan). However, cellular death was unaffected, and slowing the progress of dementia was modest (only a 0.45 score on the cognition rating scale) [144]. Bleeding in the brain as a potential risk of the lecanemab treatment was present in 22% of patients. The pharmaceutical enterprise Eisai applied for accelerated approval of the drug to the U.S. FDA, and the decision on January 6th this year was "full approval". The success of lecanemab was a big step in AD drug research but initiated a hot debate owing to the modest effect and the risks of application.

3.2.2. Clearance by the BBB and Activation of the Glymphatic System

Dysfunction of the neurovascular unit (NVU) may play a decisive role in AD progress [95]. NVU is a complex system of pial arteries, penetrating arterioles, intraparenchymal arteries, and small capillaries. BBB is a specific brain composition of endothelial cells in NVU, together with pericytes, basement membrane, and astroglial end feet. NVU dysfunction is an essential element of AD pathogenesis and a molecular target for AD therapies by prevention and repair of NVU damage.

Age-related declining efficacy of BBB/proteolytic pathways causes a decrease in CSF-based Aβ clearance in humans [96].

In the late stage of AD patients, the production of Aβ peptides is relatively constant. However, Aβ clearance is impaired. Brain capillary endothelial cells mediate Aβ clearance, leading to Aβ accumulation in the brain. Aβ binding transport proteins, e.g., ApoE and clusterin, as well as receptors (e.g., low-density lipoprotein receptor (LRP1), the receptor for advanced glycosylation end product (RAGE), P-glycoprotein transporter (Pgp or ABCB1)) are expressed in BBB and control Aβ efflux and influx across the BBB.

Aβ deteriorates the components of NVU, and it induces endothelial cell injury by promoting free radical (reactive oxygen species—ROS and reactive nitrogen species—RNS) formation. Deposition of Aβ in BBB contributes to the damage of BBB [145]. Aβ induces the release of inflammatory cytokines and chemokines (that leads to chronic neuroinflammation), impairs BBB, and decreases blood flow by up to 40%. Endothelial cell receptors and transporters may serve as potential therapeutic targets for increasing Aβ clearance [146]. Reduction in RAGE activity and upregulation of LRP1 and Pgp expression will increase Aβ clearance from the brain [146]. Endothelins (ETs, distinctive peptides of 21 amino acids) are well-known vasoconstrictive agents [147]. Endothelin is a novel target of AD drug research: ET-receptor agonists and antagonists proved to be effective for the prevention of AD in preclinical studies [147].

The glymphatic system (GS) is a unique fluid-transport pathway in the brain as it provides access to all brain regions. It uses the network of tunnels created by astrocytes, the interstitial space between cells such as the lymphatic system. GS pathway plays an important role in cleaning waste from the brain [148]. If the GS does not work properly, toxic waste (e.g., Aβ and pTau peptides) is not removed from the brain. ApoE plays a decisive role in removing Aβ assemblies by the glymphatic system. Epigenetic changes (reduced methylation of the APOE gene) are linked to AD progress. Aquaporin 4 (AQP4) water channel is also an important factor for the GS: the loss of polarity of AQP4 reduces GS functions. BBB and the GS interact in solute waste clearance in the late stages of AD [149].

GS fluid transport is suppressed in acute and chronic neuroinflammation [150]. Modulation of brain fluid transport may be a novel target for developing new drugs to fight acute and chronic inflammation in the brain. There is evidence that the presence of increased wasteosomes (or corpora amylacea i.e., amyloid bodies) is an indicator of chronic failure of the GS activity [151]. Chronic lymphatic insufficiency is a risk factor for NDDs, and thus, improvement of the GS is a novel target of AD drug strategies.

3.3. Modulation of Chronic Neuroinflammation

3.3.1. Chronic Neuroinflammation

Chronic neuroinflammation (NI) begins in the second phase of AD progress, in the cellular phase [89]. NI is a protective response against different factors causing CNS damage. NI plays an essential role in AD pathogenesis. The innate immune system represents the first line of defense. It was published in 2015 that chronic comorbidities (e.g., arthritis, atherosclerosis, obesity, and metabolic diseases), as well as low-grade systemic inflammation, are risk factors for subsequent dementia [152]. IL-1β, TNF-α, and other proinflammatory mediators may drive hypothalamic dysfunction, impair neurogenesis, and cause cognitive functional decline [93,152]. Cytokine and chemokine signaling play a decisive role in inflammatory diseases, and therefore, they can drive the processes of AD development [153]. Neuroinflammatory markers [154,155] are very important indicators

of pathological processes of NDDs [154]. External pathogens activate the brain's innate immune system (e.g., microglia and astrocytes) for the protection of brain cells. However, overactivation of the immune cells results in the release of proinflammatory factors (TNF-α, IL-1β, IL-18, NO, and others). Neuroinflammation begins in the cellular phase of AD and is a potential risk for dementia [156,157]. Soluble oAβ can also activate microglia, producing inflammatory cytokines, besides external pathogens [158]. Aβ activates several microglial receptors, such as CD36, and thereby, it triggers the secretion of proinflammatory cytokines, chemokines, and ROS.

Aβ assemblies can trigger the formation of the inflammasome NLRP3, lysosomal disruption, and release of cathepsin-B [158]. Inflammasomes are sensors and regulators of cellular injury and inflammation. Chronic triggering of inflammasomes in the brain tissue leads to an increased level of IL-18 family cytokines [159]. Autophagy dysfunction may be associated with AD pathology, and autophagy activation may suppress neuroinflammation by degrading inflammasomes [160]. The development of small molecular autophagy inducers represents a pharmacological opportunity for the protection of neurons in AD [161].

Microglia (MG) are central players in AD progress [162]. MG has an essential task in the brain which is the perpetual active surveillance of synapses. Since MG are phagocytic cells, they clean the brain tissue from terminally injured neurons, cellular corpses, and debris [163]. MG also has a decisive role in the maturation of the brain by phagocytosis. Deteriorated senescent neurons may cause NI in the AD brain if microglial cleanup does not work properly [164]. Impairment of normal microglial function causes serious effects on normal brain development. MG also regulates myelin growth and integrity in the CNS [165]. MG interacts with neurons and modulates neuronal activity [166]. Absence of MG results in significantly increased brain injury [167]. GWAS studies demonstrated that many of the LOAD risk genes are mainly expressed in MG and not in neurons [168]. "Different AD risk factors converge on the activation response of microglia" [27–29,169].

MG has a mesodermal origin and myeloid nature [170]. Physiological and pathological forms of MG have remarkable morphological diversity. Interleukins activate MG resulting in morphological changes and upregulation of many pro- and anti-inflammatory cytokines. There are several forms of MG: (1) resting and quiescent, homeostatic MG with ramified morphology, (2) disease-associated, pro-phagocytic MG, and (3) dystrophic or primed, aberrant MG, deramified with shortening and loss of branches [171]. Drug researchers should find a suitable form of MG that could serve as a target for neuroprotection.

Astrocytes are the other important immune cells that participate in the neuroinflammatory process and maintain plasticity in the adult brain. Astrocytes serve as targets of future AD drugs [172].

3.3.2. Neuroinflammation and Glial Cells as Targets for AD Drug Development

Modulating neuroinflammation and the activity of glial cells are novel targets in AD research (reviewed in [172,173]). Therapeutic strategies include the use of different anti-inflammatory drugs (e.g., indomethacin, VX-745, OTI-125, candesartan, celecoxib, etanercept, and atomoxetin) in different clinical phases. The newest clinical trials are summarized in [172]. Five experiments are in phase 1, nine in phase 2, and one in phase 3 trial. The following potential drug targets have been identified:

1. TNFα modulation [174].
2. Activation of spleen tyrosine kinase (SYK) for increasing the clearance function of MG [175].
3. Activation of the CX3CR1 (C-X3-C Motif Chemokine Receptor 1) gene for improved MG phagocytotic activity [176].
4. Activation of TREM2 microglial protein for slowing down pTau accumulation and cognitive loss [177].
5. Activation of the PLCG (Phospholipase C γ1) enzyme for promoting the protective function of microglia [178].

6. Mitigation of neuroinflammation by increasing the scavenger functions of MG by targeting INPP5 (Inositol Polyphosphate-5-Phosphatase) enzyme [179].
7. Modulation of astrocyte activity for Aβ degradation and clearance, as well as BBB protection [180].
8. Creating antioxidant molecules for protecting the brain from the degrading effect of ROS by activation of mucosal-associated invariant T-cells (MAIT-cells) [181].
9. Lowering or removing ApoE4 from neurons for decreasing aberrant microglia activation [27–29]

The results of future preclinical and clinical studies will decide which targets prove to be successful in AD drug development.

4. Conclusions and Outlook

An old dream has been to find a master gene or gene combination whose modulation would slow down the aging process, thereby helping to avoid age-related dementia. This type of master gene has not been found yet. AD drug research has reached a turning point now. The novel targets for biomarker and drug research are not amyloid plaques but intracellular proteins (iAβ and oTau) or biochemical pathways. The newest approaches of precise fluid biomarker determinations by cheap clinical mass spectrometry provide a means for the diagnosis of MCI and AD in a large population. It has been widely accepted in recent years that both amyloids (Aβ and pTau assemblies) participate in the progress of AD. In addition, a drug combination ought to be used for reversing MCI or slowing down the development of AD. Novel protein targets (e.g., medin, BSN, PAR-5) should be used for the prevention of amyloid overproduction and the formation of toxic assemblies. Small molecular inducers of small, neuroprotective Hsps (e.g., crystallines: Hsp B4/5) will be used for inhibiting the formation of toxic amyloid aggregates. Increased Aβ clearance with the help of monoclonal Abs might be reached by increasing the penetration of big proteins across the BBB and the cell membrane by specific transporters. Special drugs may be developed to augment the effectivity of oAβ and oTau clearance by the BBB and the glymphatic system from the aging brain. The dangerous effect of chronic inflammation on neuronal death might be inhibited via novel anti-inflammatory agents (e.g., Sig-1R ligands). Microglia, a double-edged sword in the maintenance of brain homeostasis in a suitable form, might be ideal for phagocytotic clearance of brain waste. Identification of the biochemical markers of activated microglia and the main mediators of neuroinflammation provide novel methods for the selective manipulation of microglia in the future. Novel approaches using rejuvenated immune cells and glial phagocytosis by astrocyte-like Bergman glial cells might also increase Aβ clearance. Regulation of ApoE4 effect on cholesterol transport and myelination may help AD patients who have a special ApoE4 gene signature. It is expected that physical methods, e.g., transcranial magnetic stimulation, may also prove to be successful in treating AD.

Currently, there are over 120 different potential new medications for AD in clinical trials. We conclude that over 30 years of intensive experimental work has not provided a genuine breakthrough in AD treatment. A good and suitable animal model of AD for preclinical experiments would be needed. Development of such kind of rodent model mimicking the changes during aging (BBB dysfunction, decreasing Aβ clearance, Aβ and tau overproduction, and NI) could be reached by transgenic techniques [182]. The efficacy of Aβ binding mAbs will be improved during the next years, but their disadvantage is that they only target the extracellular amyloid plaques. The spectrum of drug targets should be widened.

The development of small molecular oral agents for intracellular targets and biological processes (amyloid aggregation, clearance, Hsp, autophagy induction, inflammasomes, etc.) will be the focus of future AD drug research. The development of β- and γ-secretase inhibitors will be abandoned. In the near future, the selection of endangered individuals using genome sequencing and the identification of bad genetic signatures may become feasible. The earliest possible diagnosis (latest in MCI stage) will be necessary for successful

AD treatment as aging is the most important risk factor of AD. We suggest that a single drug cannot be expected to treat all stages of AD. A drug combination strategy with multiple molecular targets should be considered. It may take a couple of years to developing successful AD treatments.

Author Contributions: Conceptualization, B.P.; writing—review and editing, B.P., M.S., F.B., and M.S.; supervision, B.P. All authors have read and agreed to the published version of the manuscript.

Funding: This research was funded by National Research Development and Innovation Office (NKFIH), grant numbers GINOP-2.3.2-15-2016-00060 and GINOP-2.3.2-15-2016-00034.

Institutional Review Board Statement: Not applicable.

Informed Consent Statement: Not applicable.

Data Availability Statement: Data sharing is not applicable to this article.

Conflicts of Interest: The authors declare no conflict of interest.

Abbreviations

APP: amyloid precursor protein, AQP4: aquaporin-4, BSN: bassoon protein, CSF: cerebrospinal fluid, GS: glymphatic system, mAB: monoclonal antibody, MG: microglia, MT: microtubules, NDD: neurodegenerative disease, NI: neuroinflammation, NVU: neurovascular system, and sAβ: soluble Aβ.

References

1. Vaquer-Alicea, J.; Diamond, M.I. Propagation of Protein Aggregation in Neurodegenerative Diseases. *Annu. Rev. Biochem.* **2019**, *88*, 785–810. [CrossRef] [PubMed]
2. Taylor, A.I.P.; Staniforth, R.A. General Principles Underpinning Amyloid Structure. *Front. Neurosci.* **2022**, *16*, 878869. [CrossRef]
3. Bogár, F.; Fülöp, L.; Penke, B. Novel Therapeutic Target for Prevention of Neurodegenerative Diseases: Modulation of Neuroinflammation with Sig-1R Ligands. *Biomolecules* **2022**, *12*, 363. [CrossRef]
4. Small, G.W. Updates in the Management of Mild Cognitive Impairment and Alzheimer Disease. *J. Fam. Pract.* **2022**, *71*, S82–S87. [CrossRef] [PubMed]
5. Ju, Y.; Tam, K. Pathological Mechanisms and Therapeutic Strategies for Alzheimer's Disease. *Neural Regen. Res.* **2022**, *17*, 543. [CrossRef] [PubMed]
6. Kovacs, G. Molecular Pathological Classification of Neurodegenerative Diseases: Turning towards Precision Medicine. *Int. J. Mol. Sci.* **2016**, *17*, 189. [CrossRef] [PubMed]
7. Rahimi, J.; Kovacs, G.G. Prevalence of Mixed Pathologies in the Aging Brain. *Alzheimers Res. Ther.* **2014**, *6*, 82. [CrossRef] [PubMed]
8. Trejo-Lopez, J.A.; Yachnis, A.T.; Prokop, S. Neuropathology of Alzheimer's Disease. *Neurotherapeutics* **2022**, *19*, 173–185. [CrossRef] [PubMed]
9. Jellinger, K.A. Recent Update on the Heterogeneity of the Alzheimer's Disease Spectrum. *J. Neural Transm.* **2022**, *129*, 1–24. [CrossRef] [PubMed]
10. Thal, D.R.; Capetillo-Zarate, E.; Del Tredici, K.; Braak, H. The Development of Amyloid Beta Protein Deposits in the Aged Brain. *Sci. Aging Knowl. Environ.* **2006**, *2006*, re1. [CrossRef] [PubMed]
11. Hojjati, S.H.; Feiz, F.; Ozoria, S.; Razlighi, Q.R. Alzheimer's Disease Neuroimaging Initiative Topographical Overlapping of the Amyloid-β and Tau Pathologies in the Default Mode Network Predicts Alzheimer's Disease with Higher Specificity. *J. Alzheimers Dis. JAD* **2021**, *83*, 407–421. [CrossRef] [PubMed]
12. Braak, H.; Braak, E. Neuropathological Stageing of Alzheimer-Related Changes. *Acta Neuropathol.* **1991**, *82*, 239–259. [CrossRef] [PubMed]
13. Thal, D.R.; Rüb, U.; Orantes, M.; Braak, H. Phases of Aβ-Deposition in the Human Brain and Its Relevance for the Development of AD. *Neurology* **2002**, *58*, 1791–1800. [CrossRef]
14. Lee, J.; Kim, H.-J. Normal Aging Induces Changes in the Brain and Neurodegeneration Progress: Review of the Structural, Biochemical, Metabolic, Cellular, and Molecular Changes. *Front. Aging Neurosci.* **2022**, *14*, 931536. [CrossRef] [PubMed]
15. Livingston, G.; Huntley, J.; Sommerlad, A.; Ames, D.; Ballard, C.; Banerjee, S.; Brayne, C.; Burns, A.; Cohen-Mansfield, J.; Cooper, C.; et al. Dementia Prevention, Intervention, and Care: 2020 Report of the Lancet Commission. *Lancet* **2020**, *396*, 413–446. [CrossRef] [PubMed]
16. Lindner, A.B.; Demarez, A. Protein Aggregation as a Paradigm of Aging. *Biochim. Biophys. Acta BBA Gen. Subj.* **2009**, *1790*, 980–996. [CrossRef] [PubMed]

17. Groh, N.; Bühler, A.; Huang, C.; Li, K.W.; van Nierop, P.; Smit, A.B.; Fändrich, M.; Baumann, F.; David, D.C. Age-Dependent Protein Aggregation Initiates Amyloid-β Aggregation. *Front. Aging Neurosci.* **2017**, *9*, 138. [CrossRef] [PubMed]
18. Kaushik, S.; Cuervo, A.M. Proteostasis and Aging. *Nat. Med.* **2015**, *21*, 1406–1415. [CrossRef]
19. Freer, R.; Sormanni, P.; Vecchi, G.; Ciryam, P.; Dobson, C.M.; Vendruscolo, M. A Protein Homeostasis Signature in Healthy Brains Recapitulates Tissue Vulnerability to Alzheimer's Disease. *Sci. Adv.* **2016**, *2*, e1600947. [CrossRef] [PubMed]
20. Roher, A.E.; Lowenson, J.D.; Clarke, S.; Wolkow, C.; Wang, R.; Cotter, R.J.; Reardon, I.M.; Zürcher-Neely, H.A.; Heinrikson, R.L.; Ball, M.J. Structural Alterations in the Peptide Backbone of Beta-Amyloid Core Protein May Account for Its Deposition and Stability in Alzheimer's Disease. *J. Biol. Chem.* **1993**, *268*, 3072–3083. [CrossRef] [PubMed]
21. Lambeth, T.R.; Riggs, D.L.; Talbert, L.E.; Tang, J.; Coburn, E.; Kang, A.S.; Noll, J.; Augello, C.; Ford, B.D.; Julian, R.R. Spontaneous Isomerization of Long-Lived Proteins Provides a Molecular Mechanism for the Lysosomal Failure Observed in Alzheimer's Disease. *ACS Cent. Sci.* **2019**, *5*, 1387–1395. [CrossRef]
22. Geiger, T.; Clarke, S. Deamidation, Isomerization, and Racemization at Asparaginyl and Aspartyl Residues in Peptides. Succinimide-Linked Reactions That Contribute to Protein Degradation. *J. Biol. Chem.* **1987**, *262*, 785–794. [CrossRef] [PubMed]
23. Truscott, R.J.W.; Schey, K.L.; Friedrich, M.G. Old Proteins in Man: A Field in Its Infancy. *Trends Biochem. Sci.* **2016**, *41*, 654–664. [CrossRef] [PubMed]
24. Neuner, S.M.; Tcw, J.; Goate, A.M. Genetic Architecture of Alzheimer's Disease. *Neurobiol. Dis.* **2020**, *143*, 104976. [CrossRef]
25. Jonsson, T.; Atwal, J.K.; Steinberg, S.; Snaedal, J.; Jonsson, P.V.; Bjornsson, S.; Stefansson, H.; Sulem, P.; Gudbjartsson, D.; Maloney, J.; et al. A Mutation in APP Protects against Alzheimer's Disease and Age-Related Cognitive Decline. *Nature* **2012**, *488*, 96–99. [CrossRef] [PubMed]
26. Sims, R.; Hill, M.; Williams, J. The Multiplex Model of the Genetics of Alzheimer's Disease. *Nat. Neurosci.* **2020**, *23*, 311–322. [CrossRef] [PubMed]
27. Shi, Y.; Yamada, K.; Liddelow, S.A.; Smith, S.T.; Zhao, L.; Luo, W.; Tsai, R.M.; Spina, S.; Grinberg, L.T.; Rojas, J.C.; et al. ApoE4 Markedly Exacerbates Tau-Mediated Neurodegeneration in a Mouse Model of Tauopathy. *Nature* **2017**, *549*, 523–527. [CrossRef]
28. Koutsodendris, N.; Blumenfeld, J.; Agrawal, A.; Traglia, M.; Grone, B.; Zilberter, M.; Yip, O.; Rao, A.; Nelson, M.R.; Hao, Y.; et al. Neuronal APOE4 Removal Protects against Tau-Mediated Gliosis, Neurodegeneration and Myelin Deficits. *Nat. Aging*. *in press*. [CrossRef]
29. Shi, Y.; Manis, M.; Long, J.; Wang, K.; Sullivan, P.M.; Remolina Serrano, J.; Hoyle, R.; Holtzman, D.M. Microglia Drive APOE-Dependent Neurodegeneration in a Tauopathy Mouse Model. *J. Exp. Med.* **2019**, *216*, 2546–2561. [CrossRef]
30. Yeh, F.L.; Hansen, D.V.; Sheng, M. TREM2, Microglia, and Neurodegenerative Diseases. *Trends Mol. Med.* **2017**, *23*, 512–533. [CrossRef]
31. Bellenguez, C.; Grenier-Boley, B.; Lambert, J.-C. Genetics of Alzheimer's Disease: Where We Are, and Where We Are Going. *Curr. Opin. Neurobiol.* **2020**, *61*, 40–48. [CrossRef]
32. Bellenguez, C.; Küçükali, F.; Jansen, I.E.; Kleineidam, L.; Moreno-Grau, S.; Amin, N.; Naj, A.C.; Campos-Martin, R.; Grenier-Boley, B.; Andrade, V.; et al. New Insights into the Genetic Etiology of Alzheimer's Disease and Related Dementias. *Nat. Genet.* **2022**, *54*, 412–436. [CrossRef]
33. Li, Y.; Laws, S.M.; Miles, L.A.; Wiley, J.S.; Huang, X.; Masters, C.L.; Gu, B.J. Genomics of Alzheimer's Disease Implicates the Innate and Adaptive Immune Systems. *Cell Mol. Life Sci.* **2021**, *78*, 7397–7426. [CrossRef]
34. Maity, S.; Farrell, K.; Navabpour, S.; Narayanan, S.N.; Jarome, T.J. Epigenetic Mechanisms in Memory and Cognitive Decline Associated with Aging and Alzheimer's Disease. *Int. J. Mol. Sci.* **2021**, *22*, 12280. [CrossRef]
35. Penke, B.; Bogár, F.; Fülöp, L. β-Amyloid and the Pathomechanisms of Alzheimer's Disease: A Comprehensive View. *Molecules* **2017**, *22*, 1692. [CrossRef] [PubMed]
36. Penke, B.; Bogár, F.; Paragi, G.; Gera, J.; Fülöp, L. Key Peptides and Proteins in Alzheimer's Disease. *Curr. Protein Pept. Sci.* **2019**, *20*, 577–599. [CrossRef] [PubMed]
37. Jeong, H.; Shin, H.; Hong, S.; Kim, Y. Physiological Roles of Monomeric Amyloid-β and Implications for Alzheimer's Disease Therapeutics. *Exp. Neurobiol.* **2022**, *31*, 65–88. [CrossRef]
38. Nichols, R.A.; Gulisano, W.; Puzzo, D. Editorial: Beta Amyloid: From Physiology to Pathogenesis. *Front. Mol. Neurosci.* **2022**, *15*, 876224. [CrossRef]
39. Kent, S.A.; Spires-Jones, T.L.; Durrant, C.S. The Physiological Roles of Tau and Aβ: Implications for Alzheimer's Disease Pathology and Therapeutics. *Acta Neuropathol.* **2020**, *140*, 417–447. [CrossRef]
40. Mohamed Asik, R.; Suganthy, N.; Aarifa, M.A.; Kumar, A.; Szigeti, K.; Mathe, D.; Gulyás, B.; Archunan, G.; Padmanabhan, P. Alzheimer's Disease: A Molecular View of β-Amyloid Induced Morbific Events. *Biomedicines* **2021**, *9*, 1126. [CrossRef] [PubMed]
41. Penke, B.; Szűcs, M.; Bogár, F. Oligomerization and Conformational Change Turn Monomeric β-Amyloid and Tau Proteins Toxic: Their Role in Alzheimer's Pathogenesis. *Molecules* **2020**, *25*, 1659. [CrossRef]
42. Diociaiuti, M.; Bonanni, R.; Cariati, I.; Frank, C.; D'Arcangelo, G. Amyloid Prefibrillar Oligomers: The Surprising Commonalities in Their Structure and Activity. *Int. J. Mol. Sci.* **2021**, *22*, 6435. [CrossRef]
43. Owen, M.C.; Gnutt, D.; Gao, M.; Wärmländer, S.K.T.S.; Jarvet, J.; Gräslund, A.; Winter, R.; Ebbinghaus, S.; Strodel, B. Effects of in Vivo Conditions on Amyloid Aggregation. *Chem. Soc. Rev.* **2019**, *48*, 3946–3996. [CrossRef]
44. Ivanova, M.I.; Lin, Y.; Lee, Y.-H.; Zheng, J.; Ramamoorthy, A. Biophysical Processes Underlying Cross-Seeding in Amyloid Aggregation and Implications in Amyloid Pathology. *Biophys. Chem.* **2021**, *269*, 106507. [CrossRef]

45. Srivastava, A.K.; Pittman, J.M.; Zerweck, J.; Venkata, B.S.; Moore, P.C.; Sachleben, J.R.; Meredith, S.C. B-Amyloid Aggregation and Heterogeneous Nucleation. *Protein Sci.* **2019**, *28*, 1567–1581. [CrossRef]
46. Vicente-Zurdo, D.; Rodríguez-Blázquez, S.; Gómez-Mejía, E.; Rosales-Conrado, N.; León-González, M.E.; Madrid, Y. Neuroprotective Activity of Selenium Nanoparticles against the Effect of Amino Acid Enantiomers in Alzheimer's Disease. *Anal. Bioanal. Chem.* **2022**, *414*, 7573–7584. [CrossRef] [PubMed]
47. Ono, K.; Watanabe-Nakayama, T. Aggregation and Structure of Amyloid β-Protein. *Neurochem. Int.* **2021**, *151*, 105208. [CrossRef] [PubMed]
48. Lutter, L.; Al-Hilaly, Y.K.; Serpell, C.J.; Tuite, M.F.; Wischik, C.M.; Serpell, L.C.; Xue, W.-F. Structural Identification of Individual Helical Amyloid Filaments by Integration of Cryo-Electron Microscopy-Derived Maps in Comparative Morphometric Atomic Force Microscopy Image Analysis. *J. Mol. Biol.* **2022**, *434*, 167466. [CrossRef]
49. Willbold, D.; Strodel, B.; Schröder, G.F.; Hoyer, W.; Heise, H. Amyloid-Type Protein Aggregation and Prion-like Properties of Amyloids. *Chem. Rev.* **2021**, *121*, 8285–8307. [CrossRef]
50. Lövestam, S.; Scheres, S.H.W. High-Throughput Cryo-EM Structure Determination of Amyloids. *Faraday Discuss.* **2022**, *240*, 243–260. [CrossRef] [PubMed]
51. Yang, Y.; Arseni, D.; Zhang, W.; Huang, M.; Lövestam, S.; Schweighauser, M.; Kotecha, A.; Murzin, A.G.; Peak-Chew, S.Y.; Macdonald, J.; et al. Cryo-EM Structures of Amyloid-β 42 Filaments from Human Brains. *Science* **2022**, *375*, 167–172. [CrossRef]
52. Nishitsuji, K.; Tomiyama, T.; Ishibashi, K.; Ito, K.; Teraoka, R.; Lambert, M.P.; Klein, W.L.; Mori, H. The E693Δ Mutation in Amyloid Precursor Protein Increases Intracellular Accumulation of Amyloid β Oligomers and Causes Endoplasmic Reticulum Stress-Induced Apoptosis in Cultured Cells. *Am. J. Pathol.* **2009**, *174*, 957–969. [CrossRef] [PubMed]
53. Tomiyama, T.; Matsuyama, S.; Iso, H.; Umeda, T.; Takuma, H.; Ohnishi, K.; Ishibashi, K.; Teraoka, R.; Sakama, N.; Yamashita, T.; et al. A Mouse Model of Amyloid Oligomers: Their Contribution to Synaptic Alteration, Abnormal Tau Phosphorylation, Glial Activation, and Neuronal Loss In Vivo. *J. Neurosci.* **2010**, *30*, 4845–4856. [CrossRef]
54. Cline, E.N.; Bicca, M.A.; Viola, K.L.; Klein, W.L. The Amyloid-β Oligomer Hypothesis: Beginning of the Third Decade. *J. Alzheimers Dis.* **2018**, *64*, S567–S610. [CrossRef] [PubMed]
55. Arakhamia, T.; Lee, C.E.; Carlomagno, Y.; Duong, D.M.; Kundinger, S.R.; Wang, K.; Williams, D.; DeTure, M.; Dickson, D.W.; Cook, C.N.; et al. Posttranslational Modifications Mediate the Structural Diversity of Tauopathy Strains. *Cell* **2020**, *180*, 633–644.e12. [CrossRef]
56. Tapia-Rojas, C.; Cabezas-Opazo, F.; Deaton, C.A.; Vergara, E.H.; Johnson, G.V.W.; Quintanilla, R.A. It's All about Tau. *Prog. Neurobiol.* **2019**, *175*, 54–76. [CrossRef]
57. Sexton, C.; Snyder, H.; Beher, D.; Boxer, A.L.; Brannelly, P.; Brion, J.; Buée, L.; Cacace, A.M.; Chételat, G.; Citron, M.; et al. Current Directions in Tau Research: Highlights from Tau 2020. *Alzheimers Dement.* **2022**, *18*, 988–1007. [CrossRef]
58. Naseri, N.N.; Wang, H.; Guo, J.; Sharma, M.; Luo, W. The Complexity of Tau in Alzheimer's Disease. *Neurosci. Lett.* **2019**, *705*, 183–194. [CrossRef]
59. Robbins, M.; Clayton, E.; Kaminski Schierle, G.S. Synaptic Tau: A Pathological or Physiological Phenomenon? *Acta Neuropathol. Commun.* **2021**, *9*, 149. [CrossRef]
60. Shafiei, S.S.; Guerrero-Muñoz, M.J.; Castillo-Carranza, D.L. Tau Oligomers: Cytotoxicity, Propagation, and Mitochondrial Damage. *Front. Aging Neurosci.* **2017**, *9*, 83. [CrossRef] [PubMed]
61. Fitzpatrick, A.W.P.; Falcon, B.; He, S.; Murzin, A.G.; Murshudov, G.; Garringer, H.J.; Crowther, R.A.; Ghetti, B.; Goedert, M.; Scheres, S.H.W. Cryo-EM Structures of Tau Filaments from Alzheimer's Disease. *Nature* **2017**, *547*, 185–190. [CrossRef]
62. Zhang, H.; Cao, Y.; Ma, L.; Wei, Y.; Li, H. Possible Mechanisms of Tau Spread and Toxicity in Alzheimer's Disease. *Front. Cell Dev. Biol.* **2021**, *9*, 707268. [CrossRef] [PubMed]
63. Vasili, E.; Dominguez-Meijide, A.; Outeiro, T.F. Spreading of α-Synuclein and Tau: A Systematic Comparison of the Mechanisms Involved. *Front. Mol. Neurosci.* **2019**, *12*, 107. [CrossRef]
64. Roda, A.; Serra-Mir, G.; Montoliu-Gaya, L.; Tiessler, L.; Villegas, S. Amyloid-Beta Peptide and Tau Protein Crosstalk in Alzheimer's Disease. *Neural Regen. Res.* **2022**, *17*, 1666–1674. [CrossRef] [PubMed]
65. Bloom, G.S. Amyloid-β and Tau: The Trigger and Bullet in Alzheimer Disease Pathogenesis. *JAMA Neurol.* **2014**, *71*, 505–508. [CrossRef] [PubMed]
66. Sperling, R.A.; Mormino, E.C.; Schultz, A.P.; Betensky, R.A.; Papp, K.V.; Amariglio, R.E.; Hanseeuw, B.J.; Buckley, R.; Chhatwal, J.; Hedden, T.; et al. The Impact of Amyloid-Beta and Tau on Prospective Cognitive Decline in Older Individuals. *Ann. Neurol.* **2019**, *85*, 181–193. [CrossRef]
67. Hardy, J.; Allsop, D. Amyloid Deposition as the Central Event in the Aetiology of Alzheimer's Disease. *Trends Pharmacol. Sci.* **1991**, *12*, 383–388. [CrossRef]
68. Selkoe, D.J.; Hardy, J. The Amyloid Hypothesis of Alzheimer's Disease at 25 Years. *EMBO Mol. Med.* **2016**, *8*, 595–608. [CrossRef] [PubMed]
69. Penke, B.; Tóth, A.M.; Földi, I.; Szűcs, M.; Janáky, T. Intraneuronal β-Amyloid and Its Interactions with Proteins and Subcellular Organelles: Proteomics and 2DE. *ELECTROPHORESIS* **2012**, *33*, 3608–3616. [CrossRef]
70. Morris, G.P.; Clark, I.A.; Vissel, B. Inconsistencies and Controversies Surrounding the Amyloid Hypothesis of Alzheimer's Disease. *Acta Neuropathol. Commun.* **2014**, *2*, 135. [CrossRef]

71. Hartmann, T. Intracellular Biology of Alzheimer's Disease Amyloid Beta Peptide. *Eur. Arch. Psychiatry Clin. Neurosci.* **1999**, *249*, 291–298. [CrossRef] [PubMed]
72. Friedrich, R.P.; Tepper, K.; Rönicke, R.; Soom, M.; Westermann, M.; Reymann, K.; Kaether, C.; Fändrich, M. Mechanism of Amyloid Plaque Formation Suggests an Intracellular Basis of Aβ Pathogenicity. *Proc. Natl. Acad. Sci. USA* **2010**, *107*, 1942–1947. [CrossRef]
73. Takahashi, R.H.; Nagao, T.; Gouras, G.K. Plaque Formation and the Intraneuronal Accumulation of β-Amyloid in Alzheimer's Disease: Intraneuronal Accumulation of β-Amyloid. *Pathol. Int.* **2017**, *67*, 185–193. [CrossRef] [PubMed]
74. Glabe, C. Intracellular Mechanisms of Amyloid Accumulation and Pathogenesis in Alzheimer's Disease. *J. Mol. Neurosci.* **2001**, *17*, 137–145. [CrossRef] [PubMed]
75. Ditaranto, K.; Tekirian, T.L.; Yang, A.J. Lysosomal Membrane Damage in Soluble Aβ-Mediated Cell Death in Alzheimer's Disease. *Neurobiol. Dis.* **2001**, *8*, 19–31. [CrossRef] [PubMed]
76. Grundke-Iqbal, I.; Iqbal, K.; Tung, Y.C.; Quinlan, M.; Wisniewski, H.M.; Binder, L.I. Abnormal Phosphorylation of the Microtubule-Associated Protein Tau (Tau) in Alzheimer Cytoskeletal Pathology. *Proc. Natl. Acad. Sci. USA* **1986**, *83*, 4913–4917. [CrossRef]
77. Frost, B.; Jacks, R.L.; Diamond, M.I. Propagation of Tau Misfolding from the Outside to the Inside of a Cell. *J. Biol. Chem.* **2009**, *284*, 12845–12852. [CrossRef] [PubMed]
78. Nelson, P.T.; Alafuzoff, I.; Bigio, E.H.; Bouras, C.; Braak, H.; Cairns, N.J.; Castellani, R.J.; Crain, B.J.; Davies, P.; Tredici, K.D.; et al. Correlation of Alzheimer Disease Neuropathologic Changes With Cognitive Status: A Review of the Literature. *J. Neuropathol. Exp. Neurol.* **2012**, *71*, 362–381. [CrossRef]
79. Ittner, L.M.; Ke, Y.D.; Delerue, F.; Bi, M.; Gladbach, A.; van Eersel, J.; Wölfing, H.; Chieng, B.C.; Christie, M.J.; Napier, I.A.; et al. Dendritic Function of Tau Mediates Amyloid-β Toxicity in Alzheimer's Disease Mouse Models. *Cell* **2010**, *142*, 387–397. [CrossRef] [PubMed]
80. Small, S.A.; Duff, K. Linking Aβ and Tau in Late-Onset Alzheimer's Disease: A Dual Pathway Hypothesis. *Neuron* **2008**, *60*, 534–542. [CrossRef]
81. Kametani, F.; Hasegawa, M. Reconsideration of Amyloid Hypothesis and Tau Hypothesis in Alzheimer's Disease. *Front. Neurosci.* **2018**, *12*, 25. [CrossRef]
82. Maccioni, R.B.; Farías, G.; Morales, I.; Navarrete, L. The Revitalized Tau Hypothesis on Alzheimer's Disease. *Arch. Med. Res.* **2010**, *41*, 226–231. [CrossRef] [PubMed]
83. Liu, Y.; Nguyen, M.; Robert, A.; Meunier, B. Metal Ions in Alzheimer's Disease: A Key Role or Not? *Acc. Chem. Res.* **2019**, *52*, 2026–2035. [CrossRef] [PubMed]
84. Singh, S.K.; Balendra, V.; Obaid, A.A.; Esposto, J.; Tikhonova, M.A.; Gautam, N.K.; Poeggeler, B. Copper-Mediated β-Amyloid Toxicity and Its Chelation Therapy in Alzheimer's Disease. *Met. Integr. Biomet. Sci.* **2022**, *14*, mfac018. [CrossRef]
85. Wang, L.; Yin, Y.-L.; Liu, X.-Z.; Shen, P.; Zheng, Y.-G.; Lan, X.-R.; Lu, C.-B.; Wang, J.-Z. Current Understanding of Metal Ions in the Pathogenesis of Alzheimer's Disease. *Transl. Neurodegener.* **2020**, *9*, 10. [CrossRef]
86. Stelmashook, E.V.; Isaev, N.K.; Genrikhs, E.E.; Amelkina, G.A.; Khaspekov, L.G.; Skrebitsky, V.G.; Illarioshkin, S.N. Role of Zinc and Copper Ions in the Pathogenetic Mechanisms of Alzheimer's and Parkinson's Diseases. *Biochem. Mosc.* **2014**, *79*, 391–396. [CrossRef] [PubMed]
87. Chen, L.-L.; Fan, Y.-G.; Zhao, L.-X.; Zhang, Q.; Wang, Z.-Y. The Metal Ion Hypothesis of Alzheimer's Disease and the Anti-Neuroinflammatory Effect of Metal Chelators. *Bioorganic Chem.* **2023**, *131*, 106301. [CrossRef]
88. Arnsten, A.F.T.; Datta, D.; Del Tredici, K.; Braak, H. Hypothesis: Tau Pathology Is an Initiating Factor in Sporadic Alzheimer's Disease. *Alzheimers Dement.* **2021**, *17*, 115–124. [CrossRef]
89. De Strooper, B.; Karran, E. The Cellular Phase of Alzheimer's Disease. *Cell* **2016**, *164*, 603–615. [CrossRef]
90. Liu, P.-P.; Xie, Y.; Meng, X.-Y.; Kang, J.-S. History and Progress of Hypotheses and Clinical Trials for Alzheimer's Disease. *Signal Transduct. Target. Ther.* **2019**, *4*, 29. [CrossRef] [PubMed]
91. Francis, P.T.; Palmer, A.M.; Snape, M.; Wilcock, G.K. The Cholinergic Hypothesis of Alzheimer's Disease: A Review of Progress. *J. Neurol. Neurosurg. Psychiatry* **1999**, *66*, 137–147. [CrossRef] [PubMed]
92. Swerdlow, R.H.; Burns, J.M.; Khan, S.M. The Alzheimer's Disease Mitochondrial Cascade Hypothesis: Progress and Perspectives. *Biochim. Biophys. Acta BBA Mol. Basis Dis.* **2014**, *1842*, 1219–1231. [CrossRef]
93. Heppner, F.L.; Ransohoff, R.M.; Becher, B. Immune Attack: The Role of Inflammation in Alzheimer Disease. *Nat. Rev. Neurosci.* **2015**, *16*, 358–372. [CrossRef]
94. Di Marco, L.Y.; Venneri, A.; Farkas, E.; Evans, P.C.; Marzo, A.; Frangi, A.F. Vascular Dysfunction in the Pathogenesis of Alzheimer's Disease—A Review of Endothelium-Mediated Mechanisms and Ensuing Vicious Circles. *Neurobiol. Dis.* **2015**, *82*, 593–606. [CrossRef] [PubMed]
95. Soto-Rojas, L.O.; Pacheco-Herrero, M.; Martínez-Gómez, P.A.; Campa-Córdoba, B.B.; Apátiga-Pérez, R.; Villegas-Rojas, M.M.; Harrington, C.R.; de la Cruz, F.; Garcés-Ramírez, L.; Luna-Muñoz, J. The Neurovascular Unit Dysfunction in Alzheimer's Disease. *Int. J. Mol. Sci.* **2021**, *22*, 2022. [CrossRef]
96. Elbert, D.L.; Patterson, B.W.; Lucey, B.P.; Benzinger, T.L.S.; Bateman, R.J. Importance of CSF-Based Aβ Clearance with Age in Humans Increases with Declining Efficacy of Blood-Brain Barrier/Proteolytic Pathways. *Commun. Biol.* **2022**, *5*, 98. [CrossRef] [PubMed]

97. Bu, X.-L.; Xiang, Y.; Jin, W.-S.; Wang, J.; Shen, L.-L.; Huang, Z.-L.; Zhang, K.; Liu, Y.-H.; Zeng, F.; Liu, J.-H.; et al. Blood-Derived Amyloid-β Protein Induces Alzheimer's Disease Pathologies. *Mol. Psychiatry* **2018**, *23*, 1948–1956. [CrossRef] [PubMed]
98. Fuller, J.T.; Cronin-Golomb, A.; Gatchel, J.R.; Norton, D.J.; Guzmán-Vélez, E.; Jacobs, H.I.L.; Hanseeuw, B.; Pardilla-Delgado, E.; Artola, A.; Baena, A.; et al. Biological and Cognitive Markers of Presenilin1 E280a Autosomal Dominant Alzheimer's Disease: A Comprehensive Review of the Colombian Kindred. *J. Prev. Alzheimers Dis.* **2019**, *6*, 112–120. [CrossRef] [PubMed]
99. Ávila-Villanueva, M.; Marcos Dolado, A.; Gómez-Ramírez, J.; Fernández-Blázquez, M. Brain Structural and Functional Changes in Cognitive Impairment Due to Alzheimer's Disease. *Front. Psychol.* **2022**, *13*, 886619. [CrossRef]
100. Porsteinsson, A.P.; Isaacson, R.S.; Knox, S.; Sabbagh, M.N.; Rubino, I. Diagnosis of Early Alzheimer's Disease: Clinical Practice in 2021. *J. Prev. Alzheimers Dis.* **2021**, *8*, 371–386. [CrossRef]
101. van der Schaar, J.; Visser, L.N.C.; Bouwman, F.H.; Ket, J.C.F.; Scheltens, P.; Bredenoord, A.L.; van der Flier, W.M. Considerations Regarding a Diagnosis of Alzheimer's Disease before Dementia: A Systematic Review. *Alzheimers Res. Ther.* **2022**, *14*, 31. [CrossRef] [PubMed]
102. Davenport, F.; Gallacher, J.; Kourtzi, Z.; Koychev, I.; Matthews, P.M.; Oxtoby, N.P.; Parkes, L.M.; Priesemann, V.; Rowe, J.B.; Smye, S.W.; et al. Neurodegenerative Disease of the Brain: A Survey of Interdisciplinary Approaches. *J. R. Soc. Interface* **2023**, *20*, 20220406. [CrossRef] [PubMed]
103. Zhou, Y.; Song, Z.; Han, X.; Li, H.; Tang, X. Prediction of Alzheimer's Disease Progression Based on Magnetic Resonance Imaging. *ACS Chem. Neurosci.* **2021**, *12*, 4209–4223. [CrossRef]
104. Turner, R.S.; Stubbs, T.; Davies, D.A.; Albensi, B.C. Potential New Approaches for Diagnosis of Alzheimer's Disease and Related Dementias. *Front. Neurol.* **2020**, *11*, 496. [CrossRef] [PubMed]
105. Ossenkoppele, R.; van der Kant, R.; Hansson, O. Tau Biomarkers in Alzheimer's Disease: Towards Implementation in Clinical Practice and Trials. *Lancet Neurol.* **2022**, *21*, 726–734. [CrossRef]
106. Gauthier, S.; Rosa-Neto, P.; Morais, J.A.; Webster, C. World Alzheimer Report 2021: Journey through the Diagnosis of Dementia 2021. Available online: https://www.alzint.org/u/World-Alzheimer-Report-2021.pdf (accessed on 3 March 2023).
107. Nemy, M.; Cedres, N.; Grothe, M.J.; Muehlboeck, J.-S.; Lindberg, O.; Nedelska, Z.; Stepankova, O.; Vyslouzilova, L.; Eriksdotter, M.; Barroso, J.; et al. Cholinergic White Matter Pathways Make a Stronger Contribution to Attention and Memory in Normal Aging than Cerebrovascular Health and Nucleus Basalis of Meynert. *NeuroImage* **2020**, *211*, 116607. [CrossRef]
108. Cedres, N.; Ferreira, D.; Nemy, M.; Machado, A.; Pereira, J.B.; Shams, S.; Wahlund, L.-O.; Zettergren, A.; Stepankova, O.; Vyslouzilova, L.; et al. Association of Cerebrovascular and Alzheimer Disease Biomarkers With Cholinergic White Matter Degeneration in Cognitively Unimpaired Individuals. *Neurology* **2022**, *99*, e1619–e1629. [CrossRef]
109. Ossenkoppele, R.; Pichet Binette, A.; Groot, C.; Smith, R.; Strandberg, O.; Palmqvist, S.; Stomrud, E.; Tideman, P.; Ohlsson, T.; Jögi, J.; et al. Amyloid and Tau PET-Positive Cognitively Unimpaired Individuals Are at High Risk for Future Cognitive Decline. *Nat. Med.* **2022**, *28*, 2381–2387. [CrossRef]
110. Wang, C.; Xu, T.; Yu, W.; Li, T.; Han, H.; Zhang, M.; Tao, M. Early Diagnosis of Alzheimer's Disease and Mild Cognitive Impairment Based on Electroencephalography: From the Perspective of Event Related Potentials and Deep Learning. *Int. J. Psychophysiol.* **2022**, *182*, 182–189. [CrossRef]
111. Blennow, K.; Shaw, L.M.; Stomrud, E.; Mattsson, N.; Toledo, J.B.; Buck, K.; Wahl, S.; Eichenlaub, U.; Lifke, V.; Simon, M.; et al. Predicting Clinical Decline and Conversion to Alzheimer's Disease or Dementia Using Novel Elecsys Aβ(1–42), PTau and TTau CSF Immunoassays. *Sci. Rep.* **2019**, *9*, 19024. [CrossRef]
112. Veitch, D.P.; Weiner, M.W.; Aisen, P.S.; Beckett, L.A.; DeCarli, C.; Green, R.C.; Harvey, D.; Jack, C.R.; Jagust, W.; Landau, S.M.; et al. Using the Alzheimer's Disease Neuroimaging Initiative to Improve Early Detection, Diagnosis, and Treatment of Alzheimer's Disease. *Alzheimers Dement.* **2022**, *18*, 824–857. [CrossRef]
113. DeMarco, M.L.; Nguyen, Q.; Fok, A.; Hsiung, G.R.; Gugten, J.G. An Automated Clinical Mass Spectrometric Method for Identification and Quantification of Variant and Wild-type Amyloid-β 1-40 and 1-42 Peptides in CSF. *Alzheimers Dement. Diagn. Assess. Dis. Monit.* **2020**, *12*, e12036. [CrossRef]
114. Esquivel, R.N.; Benina, N.; Hawkins, D.M.; De Simone, F.; Le Bastard, N.; Vandijck, M.; Gannon, S.; Latham, J.; Radwan, R.R.; Dickson, D. Clinical Validation of the Lumipulse *G* B-amyloid Ratio (1-42/1-40) in a Subset of ADNI CSF Samples. *Alzheimers Dement.* **2021**, *17*, e055657. [CrossRef]
115. Shea, D.; Colasurdo, E.; Smith, A.; Paschall, C.; Jayadev, S.; Keene, C.D.; Galasko, D.; Ko, A.; Li, G.; Peskind, E.; et al. SOBA: Development and Testing of a Soluble Oligomer Binding Assay for Detection of Amyloidogenic Toxic Oligomers. *Proc. Natl. Acad. Sci. USA* **2022**, *119*, e2213157119. [CrossRef]
116. Habashi, M.; Vutla, S.; Tripathi, K.; Senapati, S.; Chauhan, P.S.; Haviv-Chesner, A.; Richman, M.; Mohand, S.-A.; Dumulon-Perreault, V.; Mulamreddy, R.; et al. Early Diagnosis and Treatment of Alzheimer's Disease by Targeting Toxic Soluble Aβ Oligomers. *Proc. Natl. Acad. Sci. USA* **2022**, *119*, e2210766119. [CrossRef]
117. Ashton, N.J.; Janelidze, S.; Mattsson-Carlgren, N.; Binette, A.P.; Strandberg, O.; Brum, W.S.; Karikari, T.K.; González-Ortiz, F.; Di Molfetta, G.; Meda, F.J.; et al. Differential Roles of Aβ42/40, p-Tau231 and p-Tau217 for Alzheimer's Trial Selection and Disease Monitoring. *Nat. Med.* **2022**, *28*, 2555–2562. [CrossRef]
118. Tatulian, S.A. Challenges and Hopes for Alzheimer's Disease. *Drug Discov. Today* **2022**, *27*, 1027–1043. [CrossRef] [PubMed]
119. Sang, Z.; Wang, K.; Dong, J.; Tang, L. Alzheimer's Disease: Updated Multi-Targets Therapeutics Are in Clinical and in Progress. *Eur. J. Med. Chem.* **2022**, *238*, 114464. [CrossRef] [PubMed]

120. Gallego Villarejo, L.; Bachmann, L.; Marks, D.; Brachthäuser, M.; Geidies, A.; Müller, T. Role of Intracellular Amyloid β as Pathway Modulator, Biomarker, and Therapy Target. *Int. J. Mol. Sci.* **2022**, *23*, 4656. [CrossRef] [PubMed]
121. Jeremic, D.; Jiménez-Díaz, L.; Navarro-López, J.D. Past, Present and Future of Therapeutic Strategies against Amyloid-β Peptides in Alzheimer's Disease: A Systematic Review. *Ageing Res. Rev.* **2021**, *72*, 101496. [CrossRef] [PubMed]
122. Uddin, S.M.; Kabir, T.M.; Rahman, S.M.; Behl, T.; Jeandet, P.; Ashraf, G.M.; Najda, A.; Bin-Jumah, M.N.; El-Seedi, H.R.; Abdel-Daim, M.M. Revisiting the Amyloid Cascade Hypothesis: From Anti-Aβ Therapeutics to Auspicious New Ways for Alzheimer's Disease. *Int. J. Mol. Sci.* **2020**, *21*, 5858. [CrossRef] [PubMed]
123. Ashrafian, H.; Zadeh, E.H.; Khan, R.H. Review on Alzheimer's Disease: Inhibition of Amyloid Beta and Tau Tangle Formation. *Int. J. Biol. Macromol.* **2021**, *167*, 382–394. [CrossRef]
124. Salahuddin, P.; Khan, R.H.; Furkan, M.; Uversky, V.N.; Islam, Z.; Fatima, M.T. Mechanisms of Amyloid Proteins Aggregation and Their Inhibition by Antibodies, Small Molecule Inhibitors, Nano-Particles and Nano-Bodies. *Int. J. Biol. Macromol.* **2021**, *186*, 580–590. [CrossRef] [PubMed]
125. Giorgetti, S.; Greco, C.; Tortora, P.; Aprile, F. Targeting Amyloid Aggregation: An Overview of Strategies and Mechanisms. *Int. J. Mol. Sci.* **2018**, *19*, 2677. [CrossRef] [PubMed]
126. Penke, B.; Bogár, F.; Crul, T.; Sántha, M.; Tóth, E.M.; Vigh, L. Heat Shock Proteins and Autophagy Pathways in Neuroprotection: From Molecular Bases to Pharmacological Interventions. *Int. J. Mol. Sci.* **2018**, *19*, 325. [CrossRef] [PubMed]
127. Yang, L.; Wang, W.; Chen, J.; Wang, N.; Zheng, G. A Comparative Study of Resveratrol and Resveratrol-Functional Selenium Nanoparticles: Inhibiting Amyloid β Aggregation and Reactive Oxygen Species Formation Properties. *J. Biomed. Mater. Res. A* **2018**, *106*, 3034–3041. [CrossRef]
128. Santos, M.A.; Chand, K.; Chaves, S. Recent Progress in Multifunctional Metal Chelators as Potential Drugs for Alzheimer's Disease. *Coord. Chem. Rev.* **2016**, *327*, 287–303. [CrossRef]
129. Wang, Y.; Yang, Y.; Hong, K.H.; Ning, Y.; Yu, P.; Ren, J.; Ji, M.; Cai, J. Design, Synthesis and Evaluation of a Novel Metal Chelator as Multifunctional Agents for the Treatment of Alzheimer's Disease. *Bioorganic Chem.* **2019**, *87*, 720–727. [CrossRef]
130. Lin, G.; Zhu, F.; Kanaan, N.M.; Asano, R.; Shirafuji, N.; Sasaki, H.; Yamaguchi, T.; Enomoto, S.; Endo, Y.; Ueno, A.; et al. Clioquinol Decreases Levels of Phosphorylated, Truncated, and Oligomerized Tau Protein. *Int. J. Mol. Sci.* **2021**, *22*, 12063. [CrossRef] [PubMed]
131. Wang, J.; Wang, K.; Zhu, Z.; He, Y.; Zhang, C.; Guo, Z.; Wang, X. Inhibition of Metal-Induced Amyloid β-Peptide Aggregation by a Blood–Brain Barrier Permeable Silica–Cyclen Nanochelator. *RSC Adv.* **2019**, *9*, 14126–14131. [CrossRef]
132. Taş, K.; Volta, B.D.; Lindner, C.; El Bounkari, O.; Hille, K.; Tian, Y.; Puig-Bosch, X.; Ballmann, M.; Hornung, S.; Ortner, M.; et al. Designed Peptides as Nanomolar Cross-Amyloid Inhibitors Acting via Supramolecular Nanofiber Co-Assembly. *Nat. Commun.* **2022**, *13*, 5004. [CrossRef]
133. Wagner, J.; Degenhardt, K.; Veit, M.; Louros, N.; Konstantoulea, K.; Skodras, A.; Wild, K.; Liu, P.; Obermüller, U.; Bansal, V.; et al. Medin Co-Aggregates with Vascular Amyloid-β in Alzheimer's Disease. *Nature* **2022**, *612*, 123–131. [CrossRef]
134. Ganne, A.; Balasubramaniam, M.; Mainali, N.; Atluri, P.; Shmookler Reis, R.J.; Ayyadevara, S. Physiological Consequences of Targeting 14-3-3 and Its Interacting Partners in Neurodegenerative Diseases. *Int. J. Mol. Sci.* **2022**, *23*, 15457. [CrossRef]
135. Wilcock, G.K.; Gauthier, S.; Frisoni, G.B.; Jia, J.; Hardlund, J.H.; Moebius, H.J.; Bentham, P.; Kook, K.A.; Schelter, B.O.; Wischik, D.J.; et al. Potential of Low Dose Leuco-Methylthioninium Bis(Hydromethanesulphonate) (LMTM) Monotherapy for Treatment of Mild Alzheimer's Disease: Cohort Analysis as Modified Primary Outcome in a Phase III Clinical Trial. *J. Alzheimers Dis.* **2018**, *61*, 435–457. [CrossRef] [PubMed]
136. Asadzadeh, J.; Ruchti, E.; Jiao, W.; Limoni, G.; MacLachlan, C.; Small, S.A.; Knott, G.; Santa-Maria, I.; McCabe, B.D. Retromer Deficiency in Tauopathy Models Enhances the Truncation and Toxicity of Tau. *Nat. Commun.* **2022**, *13*, 5049. [CrossRef] [PubMed]
137. Curtis, M.E.; Smith, T.; Yu, D.; Praticò, D. Association of Retromer Deficiency and Tau Pathology in Down Syndrome. *Ann. Neurol.* **2022**, *91*, 561–567. [CrossRef] [PubMed]
138. Martinez, P.; Patel, H.; You, Y.; Jury, N.; Perkins, A.; Lee-Gosselin, A.; Taylor, X.; You, Y.; Viana Di Prisco, G.; Huang, X.; et al. Bassoon Contributes to Tau-Seed Propagation and Neurotoxicity. *Nat. Neurosci.* **2022**, *25*, 1597–1607. [CrossRef] [PubMed]
139. McLean, C.A.; Cherny, R.A.; Fraser, F.W.; Fuller, S.J.; Smith, M.J.; Beyreuther, K.; Bush, A.I.; Masters, C.L. Soluble Pool of Abeta Amyloid as a Determinant of Severity of Neurodegeneration in Alzheimer's Disease. *Ann. Neurol.* **1999**, *46*, 860–866. [CrossRef]
140. Holscher, C.; Gengler, S.; Gault, V.A.; Harriott, P.; Mallot, H.A. Soluble Beta-Amyloid[25–35] Reversibly Impairs Hippocampal Synaptic Plasticity and Spatial Learning. *Eur. J. Pharmacol.* **2007**, *561*, 85–90. [CrossRef] [PubMed]
141. Bard, F.; Cannon, C.; Barbour, R.; Burke, R.-L.; Games, D.; Grajeda, H.; Guido, T.; Hu, K.; Huang, J.; Johnson-Wood, K.; et al. Peripherally Administered Antibodies against Amyloid β-Peptide Enter the Central Nervous System and Reduce Pathology in a Mouse Model of Alzheimer Disease. *Nat. Med.* **2000**, *6*, 916–919. [CrossRef]
142. Song, C.; Shi, J.; Zhang, P.; Zhang, Y.; Xu, J.; Zhao, L.; Zhang, R.; Wang, H.; Chen, H. Immunotherapy for Alzheimer's Disease: Targeting β-Amyloid and Beyond. *Transl. Neurodegener.* **2022**, *11*, 18. [CrossRef] [PubMed]
143. Karran, E.; De Strooper, B. The Amyloid Hypothesis in Alzheimer Disease: New Insights from New Therapeutics. *Nat. Rev. Drug Discov.* **2022**, *21*, 306–318. [CrossRef]
144. van Dyck, C.H.; Swanson, C.J.; Aisen, P.; Bateman, R.J.; Chen, C.; Gee, M.; Kanekiyo, M.; Li, D.; Reyderman, L.; Cohen, S.; et al. Lecanemab in Early Alzheimer's Disease. *N. Engl. J. Med.* **2023**, *388*, 9–21. [CrossRef] [PubMed]

145. Wang, D.; Chen, F.; Han, Z.; Yin, Z.; Ge, X.; Lei, P. Relationship Between Amyloid-β Deposition and Blood–Brain Barrier Dysfunction in Alzheimer's Disease. *Front. Cell Neurosci.* **2021**, *15*, 695479. [CrossRef] [PubMed]
146. Zhang, Y.-L.; Wang, J.; Zhang, Z.-N.; Su, Q.; Guo, J.-H. The Relationship between Amyloid-Beta and Brain Capillary Endothelial Cells in Alzheimer's Disease. *Neural Regen. Res.* **2022**, *17*, 2355. [CrossRef] [PubMed]
147. Sharma, S.; Behl, T.; Kumar, A.; Sehgal, A.; Singh, S.; Sharma, N.; Bhatia, S.; Al-Harrasi, A.; Bungau, S. Targeting Endothelin in Alzheimer's Disease: A Promising Therapeutic Approach. *BioMed Res. Int.* **2021**, *2021*, 7396580. [CrossRef]
148. Iliff, J.J.; Wang, M.; Liao, Y.; Plogg, B.A.; Peng, W.; Gundersen, G.A.; Benveniste, H.; Vates, G.E.; Deane, R.; Goldman, S.A.; et al. A Paravascular Pathway Facilitates CSF Flow Through the Brain Parenchyma and the Clearance of Interstitial Solutes, Including Amyloid β. *Sci. Transl. Med.* **2012**, *4*, 147ra111. [CrossRef]
149. Verheggen, I.C.M.; Van Boxtel, M.P.J.; Verhey, F.R.J.; Jansen, J.F.A.; Backes, W.H. Interaction between Blood-Brain Barrier and Glymphatic System in Solute Clearance. *Neurosci. Biobehav. Rev.* **2018**, *90*, 26–33. [CrossRef]
150. Mogensen, F.L.-H.; Delle, C.; Nedergaard, M. The Glymphatic System (En)during Inflammation. *Int. J. Mol. Sci.* **2021**, *22*, 7491. [CrossRef] [PubMed]
151. Riba, M.; del Valle, J.; Molina-Porcel, L.; Pelegrí, C.; Vilaplana, J. Wasteosomes (Corpora Amylacea) as a Hallmark of Chronic Glymphatic Insufficiency. *Proc. Natl. Acad. Sci. USA* **2022**, *119*, e2211326119. [CrossRef]
152. Cunningham, C.; Hennessy, E. Co-Morbidity and Systemic Inflammation as Drivers of Cognitive Decline: New Experimental Models Adopting a Broader Paradigm in Dementia Research. *Alzheimers Res. Ther.* **2015**, *7*, 33. [CrossRef]
153. Turner, M.D.; Nedjai, B.; Hurst, T.; Pennington, D.J. Cytokines and Chemokines: At the Crossroads of Cell Signalling and Inflammatory Disease. *Biochim. Biophys. Acta BBA Mol. Cell Res.* **2014**, *1843*, 2563–2582. [CrossRef]
154. Rauf, A.; Badoni, H.; Abu-Izneid, T.; Olatunde, A.; Rahman, M.M.; Painuli, S.; Semwal, P.; Wilairatana, P.; Mubarak, M.S. Neuroinflammatory Markers: Key Indicators in the Pathology of Neurodegenerative Diseases. *Molecules* **2022**, *27*, 3194. [CrossRef]
155. Chen, L.; Deng, H.; Cui, H.; Fang, J.; Zuo, Z.; Deng, J.; Li, Y.; Wang, X.; Zhao, L. Inflammatory Responses and Inflammation-Associated Diseases in Organs. *Oncotarget* **2018**, *9*, 7204–7218. [CrossRef] [PubMed]
156. Penke, B.; Fulop, L.; Szucs, M.; Frecska, E. The Role of Sigma-1 Receptor, an Intracellular Chaperone in Neurodegenerative Diseases. *Curr. Neuropharmacol.* **2017**, *16*, 97–116. [CrossRef] [PubMed]
157. Ahmad, M.A.; Kareem, O.; Khushtar, M.; Akbar, M.; Haque, M.R.; Iqubal, A.; Haider, M.F.; Pottoo, F.H.; Abdulla, F.S.; Al-Haidar, M.B.; et al. Neuroinflammation: A Potential Risk for Dementia. *Int. J. Mol. Sci.* **2022**, *23*, 616. [CrossRef]
158. de Oliveira, J.; Kucharska, E.; Garcez, M.L.; Rodrigues, M.S.; Quevedo, J.; Moreno-Gonzalez, I.; Budni, J. Inflammatory Cascade in Alzheimer's Disease Pathogenesis: A Review of Experimental Findings. *Cells* **2021**, *10*, 2581. [CrossRef]
159. Szabo, A.; O'Connell, K.S.; Ueland, T.; Sheikh, M.A.; Agartz, I.; Andreou, D.; Aukrust, P.; Boye, B.; Bøen, E.; Drange, O.K.; et al. Increased Circulating IL-18 Levels in Severe Mental Disorders Indicate Systemic Inflammasome Activation. *Brain. Behav. Immun.* **2022**, *99*, 299–306. [CrossRef]
160. Cheng, X.; Wei, Y.; Qian, Z.; Han, L. Autophagy Balances Neuroinflammation in Alzheimer's Disease. *Cell Mol. Neurobiol.. in press*. [CrossRef] [PubMed]
161. Panda, C.; Mahapatra, R.K. Bi-Directional Relationship Between Autophagy and Inflammasomes in Neurodegenerative Disorders. *Cell Mol. Neurobiol.* **2023**, *43*, 115–137. [CrossRef] [PubMed]
162. Derecki, N.C.; Katzmarski, N.; Kipnis, J.; Meyer-Luehmann, M. Microglia as a Critical Player in Both Developmental and Late-Life CNS Pathologies. *Acta Neuropathol.* **2014**, *128*, 333–345. [CrossRef] [PubMed]
163. Fekete, R.; Cserép, C.; Lénárt, N.; Tóth, K.; Orsolits, B.; Martinecz, B.; Méhes, E.; Szabó, B.; Németh, V.; Gönci, B.; et al. Microglia Control the Spread of Neurotropic Virus Infection via P2Y12 Signalling and Recruit Monocytes through P2Y12-Independent Mechanisms. *Acta Neuropathol.* **2018**, *136*, 461–482. [CrossRef]
164. Herdy, J.R.; Traxler, L.; Agarwal, R.K.; Karbacher, L.; Schlachetzki, J.C.M.; Boehnke, L.; Zangwill, D.; Galasko, D.; Glass, C.K.; Mertens, J.; et al. Increased Post-Mitotic Senescence in Aged Human Neurons Is a Pathological Feature of Alzheimer's Disease. *Cell Stem Cell* **2022**, *29*, 1637–1652.e6. [CrossRef] [PubMed]
165. McNamara, N.B.; Munro, D.A.D.; Bestard-Cuche, N.; Uyeda, A.; Bogie, J.F.J.; Hoffmann, A.; Holloway, R.K.; Molina-Gonzalez, I.; Askew, K.E.; Mitchell, S.; et al. Microglia Regulate Central Nervous System Myelin Growth and Integrity. *Nature* **2023**, *613*, 120–129. [CrossRef] [PubMed]
166. Cserép, C.; Pósfai, B.; Lénárt, N.; Fekete, R.; László, Z.I.; Lele, Z.; Orsolits, B.; Molnár, G.; Heindl, S.; Schwarcz, A.D.; et al. Microglia Monitor and Protect Neuronal Function through Specialized Somatic Purinergic Junctions. *Science* **2020**, *367*, 528–537. [CrossRef]
167. Spangenberg, E.; Severson, P.L.; Hohsfield, L.A.; Crapser, J.; Zhang, J.; Burton, E.A.; Zhang, Y.; Spevak, W.; Lin, J.; Phan, N.Y.; et al. Sustained Microglial Depletion with CSF1R Inhibitor Impairs Parenchymal Plaque Development in an Alzheimer's Disease Model. *Nat. Commun.* **2019**, *10*, 3758. [CrossRef]
168. Sierksma, A.; Lu, A.; Mancuso, R.; Fattorelli, N.; Thrupp, N.; Salta, E.; Zoco, J.; Blum, D.; Buée, L.; De Strooper, B.; et al. Novel Alzheimer Risk Genes Determine the Microglia Response to Amyloid-β but Not to TAU Pathology. *EMBO Mol. Med.* **2020**, *12*, e10606. [CrossRef] [PubMed]
169. Sala Frigerio, C.; Wolfs, L.; Fattorelli, N.; Thrupp, N.; Voytyuk, I.; Schmidt, I.; Mancuso, R.; Chen, W.-T.; Woodbury, M.E.; Srivastava, G.; et al. The Major Risk Factors for Alzheimer's Disease: Age, Sex, and Genes Modulate the Microglia Response to Aβ Plaques. *Cell Rep.* **2019**, *27*, 1293–1306.e6. [CrossRef] [PubMed]

170. Andreasson, K.I.; Bachstetter, A.D.; Colonna, M.; Ginhoux, F.; Holmes, C.; Lamb, B.; Landreth, G.; Lee, D.C.; Low, D.; Lynch, M.A.; et al. Targeting Innate Immunity for Neurodegenerative Disorders of the Central Nervous System. *J. Neurochem.* **2016**, *138*, 653–693. [CrossRef]
171. Chen, Y.; Colonna, M. Microglia in Alzheimer's Disease at Single-Cell Level. Are There Common Patterns in Humans and Mice? *J. Exp. Med.* **2021**, *218*, e20202717. [CrossRef]
172. Al-Ghraiybah, N.F.; Wang, J.; Alkhalifa, A.E.; Roberts, A.B.; Raj, R.; Yang, E.; Kaddoumi, A. Glial Cell-Mediated Neuroinflammation in Alzheimer's Disease. *Int. J. Mol. Sci.* **2022**, *23*, 10572. [CrossRef]
173. Dhapola, R.; Hota, S.S.; Sarma, P.; Bhattacharyya, A.; Medhi, B.; Reddy, D.H. Recent Advances in Molecular Pathways and Therapeutic Implications Targeting Neuroinflammation for Alzheimer's Disease. *Inflammopharmacology* **2021**, *29*, 1669–1681. [CrossRef] [PubMed]
174. Zelová, H.; Hošek, J. TNF-α Signalling and Inflammation: Interactions between Old Acquaintances. *Inflamm. Res.* **2013**, *62*, 641–651. [CrossRef] [PubMed]
175. Ennerfelt, H.; Frost, E.L.; Shapiro, D.A.; Holliday, C.; Zengeler, K.E.; Voithofer, G.; Bolte, A.C.; Lammert, C.R.; Kulas, J.A.; Ulland, T.K.; et al. SYK Coordinates Neuroprotective Microglial Responses in Neurodegenerative Disease. *Cell* **2022**, *185*, 4135–4152.e22. [CrossRef]
176. Puntambekar, S.S.; Moutinho, M.; Lin, P.B.-C.; Jadhav, V.; Tumbleson-Brink, D.; Balaji, A.; Benito, M.A.; Xu, G.; Oblak, A.; Lasagna-Reeves, C.A.; et al. CX3CR1 Deficiency Aggravates Amyloid Driven Neuronal Pathology and Cognitive Decline in Alzheimer's Disease. *Mol. Neurodegener.* **2022**, *17*, 47. [CrossRef]
177. Pereira, J.B.; Janelidze, S.; Strandberg, O.; Whelan, C.D.; Zetterberg, H.; Blennow, K.; Palmqvist, S.; Stomrud, E.; Mattsson-Carlgren, N.; Hansson, O. Microglial Activation Protects against Accumulation of Tau Aggregates in Nondemented Individuals with Underlying Alzheimer's Disease Pathology. *Nat. Aging* **2022**, *2*, 1138–1144. [CrossRef]
178. Claes, C.; England, W.E.; Danhash, E.P.; Kiani Shabestari, S.; Jairaman, A.; Chadarevian, J.P.; Hasselmann, J.; Tsai, A.P.; Coburn, M.A.; Sanchez, J.; et al. The P522R Protective Variant of PLCG2 Promotes the Expression of Antigen Presentation Genes by Human Microglia in an Alzheimer's Disease Mouse Model. *Alzheimers Dement.* **2022**, *18*, 1765–1778. [CrossRef]
179. Castranio, E.L.; Hasel, P.; Haure-Mirande, J.; Ramirez Jimenez, A.V.; Hamilton, B.W.; Kim, R.D.; Glabe, C.G.; Wang, M.; Zhang, B.; Gandy, S.; et al. Microglial *INPP5D* Limits Plaque Formation and Glial Reactivity in the PSAPP Mouse Model of Alzheimer's Disease. *Alzheimers Dement.. in press*. [CrossRef]
180. Birch, A.M. The Contribution of Astrocytes to Alzheimer's Disease. *Biochem. Soc. Trans.* **2014**, *42*, 1316–1320. [CrossRef] [PubMed]
181. Zhang, Y.; Bailey, J.T.; Xu, E.; Singh, K.; Lavaert, M.; Link, V.M.; D'Souza, S.; Hafiz, A.; Cao, J.; Cao, G.; et al. Mucosal-Associated Invariant T Cells Restrict Reactive Oxidative Damage and Preserve Meningeal Barrier Integrity and Cognitive Function. *Nat. Immunol.* **2022**, *23*, 1714–1725. [CrossRef]
182. Sasaguri, H.; Hashimoto, S.; Watamura, N.; Sato, K.; Takamura, R.; Nagata, K.; Tsubuki, S.; Ohshima, T.; Yoshiki, A.; Sato, K.; et al. Recent Advances in the Modeling of Alzheimer's Disease. *Front. Neurosci.* **2022**, *16*, 807473. [CrossRef] [PubMed]

MDPI
St. Alban-Anlage 66
4052 Basel
Switzerland
www.mdpi.com

International Journal of Molecular Sciences Editorial Office
E-mail: ijms@mdpi.com
www.mdpi.com/journal/ijms

Academic Open
Access Publishing

mdpi.com

ISBN pdfISBN